TECHNICAL DIGEST
1996

INTEGRATED PHOTONICS RESEARCH

APRIL 29–MAY 2, 1996
BOSTON, MASSACHUSETTS

1996 TECHNICAL DIGEST SERIES
VOLUME 6

[illegible]





CO-SPONSORED BY
OPTICAL SOCIETY OF AMERICA
IEEE/LASERS AND ELECTRO-OPTICS SOCIETY

REPORT DOCUMENTATION PAGE

Form Approved
OMB No. 0704-0188

Public reporting burden for this collection of information is estimated to average 1 hour per response, including the time for reviewing instructions, searching existing data sources, gathering and maintaining the data needed, and completing and reviewing the collection of information. Send comments regarding this burden estimate or any other aspect of this collection of information, including suggestions for reducing this burden, to Washington Headquarters Services, Directorate for Information Operations and Reports, 1215 Jefferson Davis Highway, Suite 1204, Arlington, VA 22202-4302, and to the Office of Management and Budget, Paperwork Reduction Project (0704-0188), Washington, DC 20503.

1. AGENCY USE ONLY *(Leave blank)*	2. REPORT DATE	3. REPORT TYPE AND DATES COVERED
	March 17, 1997	Final 03/01/96 - 12/30/96

4. TITLE AND SUBTITLE

Organization of the 1996 Integrated Photonics Research Topical Meeting

5. FUNDING NUMBERS

N00014-96-1-0511

6. AUTHOR(S)

David W. Hennage

7. PERFORMING ORGANIZATION NAME(S) AND ADDRESS(ES)

Optical Society of America
2010 Massachusetts Ave. NW
Washington, DC 20036

8. PERFORMING ORGANIZATION REPORT NUMBER

9. SPONSORING/MONITORING AGENCY NAME(S) AND ADDRESS(ES)

Office of Naval Research
ONR 251: Kirsten I. Johnson
Ballston Centre Tower One
800 North Quincy Street
Arlington, VA 22217-5660

10. SPONSORING/MONITORING AGENCY REPORT NUMBER

11. SUPPLEMENTARY NOTES

12a. DISTRIBUTION/AVAILABILITY STATEMENT

Approved for public release
Distribution unlimited

12b. DISTRIBUTION CODE

13. ABSTRACT *(Maximum 200 words)*

The integrated photonics research topical meeting presented a complete overview of all experimental and theoretical aspects of integrated and guided-wave optics. Some of the topics covered at this meeting were silicon photonics, optical system modeling, simulation of quantum well phenomena, integrated optics and micromachining, parallel optical interconnects and array technology, semiconductor components for fiber in the loop, hybrid packaging of III-V components to single-mode fiber, and components and technologies for wavelength-multiplexed systems.

14. SUBJECT TERMS	15. NUMBER OF PAGES
	16. PRICE CODE

17. SECURITY CLASSIFICATION OF REPORT	18. SECURITY CLASSIFICATION OF THIS PAGE	19. SECURITY CLASSIFICATION OF ABSTRACT	20. LIMITATION OF ABSTRACT
Unclassified	Unclassified	Unclassified	UL

CONFERENCE EDITION

Summaries of the papers

presented at the topical meeting

INTEGRATED PHOTONICS RESEARCH

APRIL 29–MAY 2, 1996
BOSTON, MASSACHUSETTS

1996 TECHNICAL DIGEST SERIES
VOLUME 6

19970318 069





CO-SPONSORED BY
OPTICAL SOCIETY OF AMERICA
IEEE/LASERS AND ELECTRO-OPTICS SOCIETY

Optical Society of America
2010 Massachusetts Avenue NWS
Washington DC 20011-1023

Articles in this publication may be cited in other publications. To facilitate access to the original publication source, the following form for the citation is suggested:

Name of Author(s), "Title of Paper," in *Integrated Photonic Research*, Vol. 6, 1996 OSA Technical Digest Series (Optical Society of America, Washington DC, 1996), pp. xx-xx.

Optical Society of America

ISBN

Conference Edition	1-55752-438-6
Postconference Edition	1-55752-439-4
(Note: Postconference Edition includes postdeadline papers.)	
1996 Technical Digest Series	1-55752-417-3

Library of Congress Catalog Card Number

Conference Edition	95-72759
Postconference Edition	95-72760

Copyright © 1996, Optical Society of America

Individual readers of this digest and libraries acting for them are permitted to make fair use of the material in it, such as to copy an article for use in teaching or research, without payment of fee, provided that such copies are not sold. Copying for sale is subject to payment of copying fees. The code 1-55752-417-3/96/$6.00 gives the per-article copying fee for each copy of the article made beyond the free copying permitted under Sections 107 and 108 of the U.S. Copyright Law. The fee should be paid through the Copyright Clearance Center, Inc., 21 Congress Street, Salem, MA 01970.

Permission is granted to quote excerpts from articles in this digest in scientific works with the customary acknowledgment of the source, including the author's name and the name of the digest, page, year, and name of the Society. Reproduction of figures and tables is likewise permitted in other articles and books provided that the same information is printed with them and notification is given to the Optical Society of America. In addition, the Optical Society may require that permission also be obtained from one of the authors. Address inquiries and notices to Director of Publications, Optical Society of America, 2010 Massachusetts Avenue, NW, Washington, DC 20036-1023. In the case of articles whose authors are employees of the United States Government or its contractors or grantees, the Optical Society of America recognizes the right of the United States Government to retain a nonexclusive, royalty free license to use the author's copyrighted article for United States Government purposes.

Printed in the U.S.A.

Contents

Agenda of Sessions v
IMA Plenary Session 1
IMB Numerical Methods for Guided Wave Optics 7
IMC Symposium on Array-based WDM Devices 31
IMD Passive and Active Component Modeling 57
IME Symposium on WDM Filters 81
IMF Wide-Angle and Vector Propagation Algorithms 107
IMG Symposium on WDM Lasers 127
IMH Poster Session 151
ITuA Symposium on Simulation of Quantum Well Phenomena: Device Applications–Optical Gain in Quantum Wells 239
ITuB Silicon Heterostructure Devices 263
ITuC Symposium on Simulation of Quantum Well Phenomena: Device Applications–Low Dimensional Nanostructures, Spontaneous Emission and Quantum Well Effects 283
ITuD Silicon Waveguides and Interconnect Technologies 303
ITuE Symposium on Simulation of Quantum Well Phenomena: Device Applications–Transverse Modes in Vertical Cavities 323
ITuF Low-Cost Photonic Packaging I 349
ITuG High Speed Devices 363
ITuH Low-Cost Photonic Packaging II 387
IWA Optical Filters and Waveguides 405
IWB Active and Passive Waveguide Devices 427
IWC Polarization Selective Devices 451
IWD Active Semiconductor Devices 473
IWE Diffractive and Reflective Elements 497
IWF Advanced Laser Structures 515
IWG Integrated Optics and Micromachining 537
IWH Symposium on Parallel Optical Interconnects and Avian Technologies 557
IThA Optical System Modeling 571
IThB Symposium on Hybrid Packaging of III-V Components to Single-Mode Fibers 603
IThC Switches and Modulators 625
IThD Semiconductor Components for Fiber in the Loop 641
Key to Authors and Presiders 655

INTEGRATED PHOTONICS RESEARCH
TECHNICAL PROGRAM COMMITTEE

David Yevick, *Queen's University at Kingston, Canada, General Chair*
Robert J. Deri, *Lawrence Livermore National Laboratories, Program Chair*
Anand Gopinath, *University of Minnesota, Program Chair*
Laura Weller-Brophy, *3M Telecom Systems Division, Technical Applications Representative*

SUBCOMMITTEE I: ACTIVE SEMICONDUCTOR DEVICES

Jane Zucker, *AT&T Bell Laboratories, Chair*
Dan Botez, *University of Wisconsin*
S. Chandrasekhar, *Lucent Technology*
Greg Magel, *Texas Instruments*
Monique Renaud, *Alcatel Alstrom, France*
Claude Rolland, *Bell Northern Research, Canada*
Hirohisa Sano, *Hitachi, Japan*
Joseph Shmulovich, *AT&T Bell Laboratories*
Meint Smit, *Delft University of Technology, The Netherlands*
Mike Wale, *GEC-Marconi, UK*
Chung-En Zah, *Bellcore*

SUBCOMMITTEE II: DIELECTRIC WAVEGUIDES AND WAVEGUIDE DEVICES

Fred Heismann, *AT&T Bell Laboratories, Chair*
Catherine H. Bulmer, *Naval Research Laboratory*
Dennis Hall, *University of Rochester*
Winfried H.G. Horsthuis, *Akzo Research Laboratories, The Netherlands*
Janet Lehr Jackel, *Bellcore*
Bahram Jalali, *University of California, Los Angeles*
Yuan P. Li, *AT&T Bell Laboratories*
Leon McCaughan, *University of Wisconsin–Madison*
Patrick Mottier, *LETI, France*
Yasuji Ohmori, *NTT Opto-Electronics Laboratories, Japan*
Ramu V. Ramaswamy, *University of Florida*
Wolfgang Sohler, *University of Paderborn, Germany*
Julian B. Soole, *Bellcore*
Richard Sorel, *USAF Rome Laboratory*
David L. Weidman, *Corning, Inc.*
Laura Weller-Brophy, *3M Corporate Research Laboratories*

SUBCOMMITTEE III: MODELING, NUMERICAL, SIMULATION AND THEORY

Shunji Seki, *NTT Opto-Electronics Laboratories, Japan, Chair*
Sujeet K. Chaudhuri, *University of Waterloo, Canada*
James J. Coleman, *University of Illinois*
Joseph Donnely, *Lincoln Laboratory*
Aly F. Elrefaie, *Bellcore*
Michaeil D. Feit, *Lawrence Livermore National Laboratory*
G. Ronald Hadley, *Sandia National Laboratory*
Jonathan A. Nagel, *AT&T Bell Laboratories*
Yoshiaki Nakano, *University of Tokyo, Japan*
John J. O'Reilly, *University College of London*
Eoin O'Reilly, *University of Surrey*
Klauss Petermann, *Technical University of Berlin, Germany*
K. Alan Shore, *University of Wales, Bangor, UK*
Bjarne Tromborg, *Telecommunication Research Laboratory, Denmark*
Carl M. Weinert, *Heinrich Hertz Institute, Germany*
Alan E. Willner, *University of Southern California*
John Zavada, *U.S. Army Research Office*

SUBCOMMITTEE IV: IMPLEMENTATION OF PHOTONIC COMPONENT TECHNOLOGY: MANUFACTURING, PACKAGING, AND SUBSYSTEM PROTOTYPING

Mark Lowry, *Lawrence Livermore National Laboratories, Chair*
Robert Ade, *United Technologies Photonics*
Philip J. Anthony, *AT&T Bell Laboratories*
Lewis B. Aronson, *Hewlett Packard*
Richard Becker, *Integrated Optics Circuit Consultants*
Ghazi Chaoui, *AT&T Bell Laboratories*
Ian Croston, *Integrated Optical Components, UK*
Paul Haugsjaa, *GTE Laboratories*
Anis Husain, *Advanced Research Projects Agency*
W. J. Tomlinson, *Bellcore*
Marc Verdiell, *Spectra-Diode Laboratories*

IPR ADVISORY COMMITTEE

Steven Korotky, *AT&T Bell Laboratories, Chair*
Stephen R. Forrest, *Princeton University*
Curtis Menyuk, *University of Maryland*
David A. Smith, *Case Western Reserve University*
David Yevick, *Queen's University at Kingston, Canada*
Meint Smit, *Technical University of Delft, The Netherlands*

SUNDAY
APRIL 28, 1996

3rd FLOOR REGISTRATION AREA
6:30–8:30pm
Registration

MONDAY
APRIL 29, 1996

3rd FLOOR REGISTRATION AREA
7:00am–5:30pm
Registration

FAIRFAX A&B
8:15–8:30am
Opening Remarks

8:30–10:00am
IMA • Plenary Session
David O. Yevick, *Queens University, Canada, Presider*

8:30am (Plenary)
IMA1 • The challenging road towards a high-performance WDM technology, T. L. Koch, *SDL, Inc.* Technical issues to be addressed include long-term source channel capacity, wavelength stability and reliability, increased demultiplexer capacity, channel selectivity and decreased loss, and choosing among the rich set of technical possibilities for implementing the new functions of wavelength add-drops, wavelength conversion, and even wavelength cross-connect switches. This talk surveys available technological solutions and new emerging approaches, compared on the basis of fundamental design limitations and practical fabrication and implementation issues that affect both performance and cost. **(p. 2)**

9:15am (Plenary)
IMA2 • How can integrated optics for Telecom become a big business?, Laura Weller-Brophy, *3M Company,* John P. Ryan, *Ryan, Hankin, Kent, Inc.* The deployment of optical fiber in the long-haul, distribution, and drop portions of telecommunications networks is driving the development and manufacture of integrated optic components. In particular, the NTT fiber-in-the-loop program may for the first time bring truly high-volume demand for integrated optic devices and change the nature of this market.This paper looks at the international market forces supporting the scale-up of volume production of integrated optic components, and at the implications for device manufacturers, vendors, and technology developers. We report requirements for further innovation in integrated optics in order to achieve deployment cost targets while improving optical device and network performance. **(p. 3)**

INDEPENDENCE BALLROOM
10:00–10:30am
Coffee Break

FAIRFAX A

10:30am–12:00m
IMB • Numerical Methods for Guided Wave Optics,
Shunji Seki, *NTT Opto-electronics Laboratories, Japan, Presider*

10:30am
IMB1 • Efficient three-dimensional vector-wave analysis of wavelength multiplexers using arrayed-waveguide gratings, W.-K. Wang, F. Tong, *IBM T. J. Watson Research Center.* An efficient three-dimensional analysis of N 3 N arrayed-waveguide grating multi/demultiplexers is presented by use of the vector-wave mode-matching method and the theory of aperture antennas. **(p. 8)**

10:45am
IMB2 • Vectorial analysis of optical waveguide bends using finite-difference method, Sangin Kim, Anand Gopinath, *Univ. Minnesota.* Optical waveguide circular bends are analyzed by solution of the vector Helmhortz equations in terms of transverse components of electric field in the cylindrical coordinates. **(p. 12)**

11:00am
IMB3 • Full vector beam-propagation method for bent channel waveguides, Michael Rivera, *Univ. Arizona.* A finite difference formulation of the full vector wave equation in cylindrical coordinates is presented, which is useful for bent channel waveguide analysis. A Crank-Nicolson scheme with an iterative method is used to solve the problem. Field profiles will be shown for a semiconductor ridge waveguide. **(p. 16)**

11:15am
IMB4 • Numerical implementation of the Bremmer coupling series, Mattheus J. N. van Stralen, Hans Blok, *Delft Univ. Technology,* The Netherlands; Maarten V. de Hoop, Colorado School of Mines. The Bremmer coupling series is proposed as an alternative to beam propagation methods. Its numerical implementation is discussed and applied to model multimode interference combiners. **(p. 20)**

11:30am
IMB5 • The perfectly matched layer boundary condition for the simulation of guided-wave optical devices, W. P. Huang, C. L. Xu, W. Lui, K. Yokoyama, *NTT Opto-electronics Laboratories, Japan.* The perfectly matched layer boundary condition is applied to simulation of guided-wave optical devices by solutions of Helmoltz equation. Its effectiveness is verified by examples. **(p. 24)**

11:45am
IMB6 • Noniterative finite-difference scheme for modal calculations, Wayne W. Lui, Wei-Ping Huang, Kiyoyuki Yokoyama, *NTT Opto-electronics Laboratories, Japan.* A novel finite-difference scheme is derived for the discretization of the Helmholtz equation along the boundary, thereby eliminating the need for any artificially imposed boundary conditions for modal calculations. (p. 27)

12:00m–1:30pm
Lunch on Own

FAIRFAX B

10:30am–12:15pm
IMC • Symposium on Array-based WDM Devices
David L. Weidman, *Corning, Inc., Presider*

10:30am (Invited)
IMC1 • Silica-based planar lightwave circuits for WDM systems, Yasuyuki Inoue, NTT Opto-electronics Laboratories, Japan. Basic wavelength-division multiplexers fabricated with silica-based planar lightwave circuit technologies are described, and their applications are briefly reviewed with emphasis on NTT's achievements. (p. 32)

11:00am
IMC2 • First polymeric phased array wavelength demultiplexer operating at 1550 nm, L. H. Spiekman, M. K. Smit, *Delft Univ. Technology, The Netherlands;* M. B. J. Diemeer, T. H. Hoekstra, *Akzo Nobel Central Research, The Netherlands.* A compact, fiber-compatible polymeric 8 3 8 phased array wavelength demultiplexer for operation in the EDFA window is realized with 9 dB fiber-to-fiber loss and 2 20 dB crosstalk. (p. 36)

11:15am
IMC3 • Filtering Characteristics of virtually imaged phased array, M. Shirasaki, *Fujitsu Laboratories, Ltd., Japan.* A virtually imaged phased array, created through multi-reflection in a thin plate of glass, shows practical characteristics for a high-density WDM filter. Both broad transmission bandwidth and suppressed crosstalk are obtained by use of a split-core output waveguide. (p.40)

11:30am
IMC4 • Use of multimode interference couplers to broaden the pass-band of dispersive integrated, WDM filters J. B. D. Soole, M. R. Amersfoort, H. P. LeBlanc, N. C. Andreadakis, A. Rajhel, C. Caneau, R. Bhat, M. A. Koza, *Bellcore;* C. Youtsey, I. Adesida, *Univ. Illinois.* We discuss the use of multimode interference couplers (MMI) to broaden and flatten the pass-band of integrated wavelength-dispersive WDM filters such as the arrayed waveguide grating. (p. 44)

11:45am
IMC5 • The elimination of sidelobes in the arrayed waveguide WDM, S. Day, J. P. Stagg, D. Moule, S. J. Clements, C. Rogers, S. Ojha, T. Clapp, J. Brook, J. Morley, *BNR Europe Ltd., UK.* Arrayed waveguide WDMs with 4 nm channel spacing are fabricated with better than 2 32 dB of crosstalk. Coupling effects and mask quantization errors are shown to be important parameters that can limit the crosstalk. (p. 48)

12:00m
IMC6 • Loss reduction for phased-array demultiplexers using a double etch technique, C. van Dam, M. K. Smit, *Delft Univ. Technology, The Netherlands:* A. A. M. Staring, E. J. Jansen, J. J. M. Binsma, T. Van Dongen, B. H. Verbeek, *Philips Optoelectronics Centre, The Netherlands.* A method is presented for reducing the loss of phased-array wavelength demultiplexers. Loss reduction of 1.7 dB for TE polarization and 1.3 dB for TM polarization is demonstrated experimentally. (p. 52)

12:15–1:30pm
Lunch on Own

FAIRFAX A

1:30–2:45pm
IMD • Passive and Active Component Modeling
J. M. Zavada, *U.S. Army Research Office, Presider*

1:30pm
IMD1 • Design of planar optical waveguide corners with turning mirrors, Wei Yang, Anand Gopinath, *Univ. Minnesota.* We demonstrate that a wide turning mirror with flared guides provides the lowest excess loss. (p. 58)

1:45pm
IMD2 • Electromagnetic modeling of optical guided-wave controlled micro-strip circuits, Essam S. Tony, Sujeet K. Chaudhuri, *Univ. Waterloo, Canada.* Modeling of the guided wave control of micro-strip circuits is investigated. Techniques for modeling the microwave and optical components of the device are presented. (p. 64)

2:00pm
IMD3 • Dynamic beam propagation method for modeling pulse propagation in flared semiconductor laser amplifiers, S. Balsamo, F. Sartori, G. Perrone, C. Naddeo, I. Montrosset, *Politecnico di Torino, Italy;* C. Giuliano, R. K. Sink, P. Blixt, J. E. Bowers, *Univ. California–Santa Barbara.* We present a dynamic beam propagation method to simulate short-pulse propagation in flared semiconductor laser amplifiers. Examples of results for different structures are shown. (p. 68)

2:15pm
IMD4 • Optoelectronic feedback control of chaotic dynamics in external cavity laser diodes, S. I. Turovets, K. A. Shore, *Univ. Wales,* J. Dellunde, *Univ. Barcelona, Spain.* We show that tailored optoelectronic feedback can be used to effect selection of periodic output in semiconductor lasers in an external cavity configuration. (p. 72)

2:30pm
IMD5 • Wave propagation in a waveguide with a balance of gain and loss, H.-P. Nolting, G. Sztefka, M. Grawert, *Heinrich-Hertz-Institut Germany;* Jiri Ctyroky, *Academy of Sciences of the Czech Republic.* Peculiar wave properties of a waveguide with a balance of gain and loss are described and used to formulate a new BPM benchmark test. (p. 76)

INDEPENDENCE BALLROOM

2:45–3:30pm
Coffee Break

MONDAY
APRIL 29, 1996

FAIRFAX B

1:30–3:00pm
IME • Symposium on WDM Filters
J. L.Jackel, *Bellcore, Presider*

1:30pm
IME1 • An acousto-optic switch with a near-rectangular passband for WDM systems, H. Rashid, D. A. Smith, R. S. Chakravarthy, A. M. Agboatwalla, A. A. Patil, Z. Bao, N. Imam, S. W. Smith, *Case Western Reserve Univ.;* J. E. Baran, J. L. Jackel, *Bellcore;* J. Kallman, *Lawrence Livermore National Laboratory.* We have achieved the most rectangular passband yet reported in an acousto-optic filter. This achievement improves significantly cascadability and wavelength misalignment tolerance in WDM systems. **(p. 82)**

1:45pm
IME2 • Low-sidelobe thermo-optically tunable filter, T. Nakazawa, S. Taniguchi, M. Seino, *Fujitsu Laboratories Ltd., Japan.* We fabricate a polarization-independent tunable filter in x-cut $LiNbO_3$. The sidelobe is 2 24 dB, FWHM is 1 nm, and 10 nm tuning is realized with 6.2 V. **(p. 86)**

2:00pm
IME3 • A temperature-insensitive InGaAsP/InP wavelength filter, H. Tanobe, Y. Kondo, Y. Kadota, H. Yasaka, Y. Yoshikuni, *NTT* Opto-electronics Laboratories, Japan. We report, we believe, the first ever temperature-insensitive InGaAsP/InP wavelength filter. The temperature dependence of the filtering wavelength is less than 0.1 Å/°C. **(p. 90)**

2:15pm
IME4 • Integrated tunable polarization-independent channel dropping filter on InP for WDM systems, Jean-Pierre Weber, Bjorn Stoltz, Olof Oberg, *Ericsson Components AB, Sweden.* A new device that allows the dropping of one out of four wavelength multiplexed channels and the pass through of the others is fabricated with polarization-independent channel positions at 1550 nm in InGaAsP/InP. Bit-error rates measurements are presented. **(p. 94)**

2:30pm
IME5 • Wavelength tunable semiconductor amplifier/filter for add/drop demultiplexing in WDM networks, G. Raybon, U. Koren, R. M. Jopson, B. I. Miller, M. Chien, M. G. Young, R. J. Capik, K. Dreyer, *AT&T Bell Laboratories.* Reconfigurable channel drop in a wavelength-division multiplexed system is demonstrated using a packaged semiconductor pre-amplifier filter. The filter is electrically tunable over 9.5 nm with a 0.9 nm width. No BER penalty was observed when demultiplexing one of five WDM channels spaced by 1.6 nm. **(p. 98)**

2:45pm
IME6 • Silica-based Mach-Zehnder add-drop filter fabricated with UV-induced gratings, Glenn E. Kohnke, Charles H. Henry, Edward J. Laskowski, Russell J. Fischer, Thomas A. Strasser, Alice E. White, *AT&T Bell Laboratories.* Performance of an add-drop filter fabricated in P-doped silica-on-silicon waveguides with UV-induced Bragg gratings is reported. Sidelobe levels of 2 40 dB are achieved with use of double filtering. **(p. 102)**

INDEPENDENCE BALLROOM

3:00–3:30pm
Coffee Break

FAIRFAX A

3:30–5:00pm
IMF • Wide-Angle and Vector Propagation Algorithms
Anand Gopinath, *University of Minnesota, Presider*

3:30pm (Invited)
IMF1 • Limitations of wide-angle BPM in non-uniform systems, Charles Vassallo, *France Telecom/CNET,* France. Wide-angle BPM is reformulated, in good agreement with power conservation and with improved accuracy. Basic limitation is due to evanescent local modes in field expansion. **(p. 108)**

4:00pm
IMF2 • Three-dimensional vectorial wide angle BPM utilizing a multigrid equation solver, P. Lusse, H.-G. Unger, *Technical Univ. Braunschweig, Germany.* An unconditionally stable three-dimensional vectorial wide angle BPM is presented. To solve the large equation systems a multigrid equation solver is used. **(p. 111)**

4:15pm
IMF3 • Technique of improving the multistep method for wide-angle beam propagation, Junji Yamauchi, Minoru Sekiguchi, Jun Shibayama, Hisamatsu Nakano, *Hosei Univ., Japan.* To improve a wide-angle beam propagation method with use of a finite difference technique, the generalized Douglas scheme for variable coefficients is applied to multistep method. **(p. 115)**

4:30pm
IMF4 • Oblique wide-angled beam propagation, T. Anada, T. M. Benson, P. Sewell, *Univ. Nottingham, UK;* P. C. Kendall, Univ. Sheffield, UK. A non-orthogonal coordinate system is introduced that extends the present range of general angled configurations for which beam propagation methods are accurate. **(p. 119)**

4:45pm
IMF5 • Use of higher order Pade approximants for efficient simulation of wide-angle waveguides with step-index profile Igor Ilic, Robert Scarmozzino, Richard M. Osgood Jr., *Columbia Univ.* We present a thorough analysis of the fundamental limits of Pade-based wide angle techniques applied to step index waveguides, and we give guidelines for choice of approximants. **(p. 123)**

FAIRFAX B

3:30–5:15pm
IMG • Symposium on WDM Lasers
Julian B. Soole, *Bellcore, Presider*

3:30pm
IMG1 • An 18-channel multi-frequency laser, M. Zirngibl, C. H. Joyner, C. R. Doerr, L. W. Stulz, H. M. Presby, *AT&T Bell Laboratories.* A multi-frequency laser (MFL) is demonstrated that runs simultaneously cw on 18 channels spaced by 103 GHz. The MFL exhibits a stable and reproducible optical channel spacing as a result of the reproducibility of the waveguide grating router that serves as the intracavity filter element. **(p. 128)**

3:45pm
IMG2 • Chirping of the waveguide grating router for free-spectral-range mode selection in the multifrequency laser, C. R. Doerr, M. Zirngibl, C. H. Joyner, *AT&T Bell Laboratories.* We discuss chirping of the waveguide grating router in the multi-frequency laser for the purpose of controlling the lasing wavelength, and we present experiment results. **(p. 132)**

4:00pm
IMG3 • A compact phased-array-based multiwavelength laser, L. H. Spiekman, M. K. Smit, *Delft Univ. Technology, The Netherlands;* A. A. M. Staring, J. J. M. Binsma, E. J. Jansen, T. van Dongen, *P. J. A.* Thijs, B. H. Verbeek, Philips Optoelectronics Centre, The Netherlands. A phased-array-based multiwavelength laser with nine channels spaced by 400 GHz around 1.55 μm is realized on an area of 3.5 3 2.5 mm^2. Simultaneous dual channel operation is demonstrated. **(p. 136)**

4:15pm
IMG4 • Silica external cavity array transmitters with high-wavelength accuracy, Karen Liu, Stuart D. Brorson, Chaoyu Yue, *IBM T. J. Watson Research Center.* High wavelength accurate waveguide components form the external cavity of directly-modulatable array transmitters to satisfy stringent accuracy requirements of wavelength multiplexed links. **(p. 139)**

4:30pm (Invited)
IMG5 • Wavelength conversion for all-optical networks, Jay M. Wiesenfeld, *AT&T Bell Laboratories.* Experimental results for high-speed (up to 20 Gbit/s) wavelength translation techniques for WDM systems, based on semiconductor optical amplifiers, will be analyzed for performance and signal degradation. Particular methods include cross-gain modulation, cross-phase modulation, and four-wave mixing. **(p. 143)**

5:00pm
IMG6 • High-speed and polarization-insensitive interferometric wavelength converters by MQW optimization, K. Wunstel, G. Laube, W. Idler, K. Daub, E. Lach, K. Dutting, M. Klenk, M. Schilling, *Alcatel Corporate Research Centre, Germany.* Multi-quantum-well layer optimization of wavelength converters with Mach–Zehnder interferometer structure yields polarization-insensitive devices (TE-TM < 1 dB) and first devices operating at 10 Gbit/s. **(p. 147)**

INDEPENDENCE BALLROOM/BOYLSTON PARK CAFE

6:00–7:30pm
Conference Reception

6:00–7:30pm
IMH Poster Session

IMH1 • Compact InP-based waveguide crossings with low crosstalk and low loss, C. van Dam, F. P. G. M. van Ham, F. H. Groen, *Delft Univ. Technology, The Netherlands;* J. J. G. M. van der Tol, *PTT Research, The Netherlands;* I. Moerman, M. K. Smit, *Univ. Gent, Belgium.* Waveguide crossings are fabricated with low crosstalk (<2 30 dB) and low excess loss (< 0.3 dB) for angles down to 30 degrees. Good agreement with predictions based on 2D-BPM simulations is observed. **(p. 152)**

IMH2 • Light propagation in a system of bended single-mode waveguide and straight multimode waveguide with higher refractive index, S. M. Loktev, N. M. Lyndin, V. A. Sychugov, B. A. Usievich, *Russian Academy of Sciences.* Effect of smooth change of buffer thickness along the structure of coupled waveguides with different parameters on transmission characteristics is studied theoretically and demonstrated experimentally. **(p. 156)**

IMH3 • Ultrahigh confinement waveguides for very large scale integrated optics with three-dimensional packaging, Lawrence C. West, Charles W. Roberts, Emil C. Piscani, *Integrated Photonic Systems Inc.* By use of high index ratios, ultrahigh confinement waveguides are created. These UHC waveguides make compact devices, sharp bends, and 100,000 electro-optical components per square centimeter, all with three-dimensional packaging. **(p. 160)**

IMH4 • Structural phase diagrams of proton exchanged waveguides on Z-, X- and Y-cuts of $LiNbO_3$, Yuri, N. Korkishko, V. A. Fedorov, *Moscow Institute of Electronic Technology, Russia;* M. P. De Micheli, *Universite de Nice Sophia Antipolis, France.* It has been shown that $H_xLi_{1-x}NbO_3$ waveguides on Z-, X- and Y-cuts $LiNbO_3$ substrate can present 7, 6, and 4 different crystallographic phases, respectively. **(p. 163)**

IMH5 ◦ Planar waveguide AR lattice filters: advantages and challenges, C. K. Madsen, *AT&T Submarine Systems Inc.;* J. H. Zhao, *Rutgers Univ.* A planar waveguide lattice filter architecture based on ring resonators is investigated. A potential application is for very narrowband filters in WDM systems. **(p. 167)**

IMH6 • Tapered-rib adiabatic-following fiber coupler, R. E. Smith, C. T. Sullivan, G. A. Vawter, G. R. Hadley, J. R. Wendt, B. Snipes, J. F. Klem, *Sandia National Laboratories.* The performance of a fiber to semiconductor waveguide mode converter with losses between 2–3 dB is demonstrated and designs with 0.9 dB loss are discussed. **(p. 171)**

IMH7 ◦ Band-gap tuning in strained piezoelectric quantum well lasers, A. S. Pabla, *Univ. Sheffield, UK.* The spectral characteristics of strained piezoelectric $In_{0.23}Ga_{0.77}As/GaAs$ lasers grown on (111) GaAs are studied. The piezoelectric field allows tuning of the spectral gain and thus offers a new approach to monolithic laser-modulator integration and the fabrication of monolithic multi-wavelength lasers. **(p. 174)**

IMH8 ◦ Optical waveguide interconnects in optoelectronic matrix switches, M. Ersoni, X. Wu, P. E. Jessop, *McMaster Univ., Canada;* J. P. Noad, *Communications Research Centre, Canada.* Multiple in-line GaAs photodetectors are integrated with AlGaAs rib waveguides to distribute optical power evenly among the crosspoints of an optoelectronic matrix switch. **(p. 178)**

IMH9 • Electronanomechanically actuated integrated-optical Mach–Zehnder interferometer, R. Dangel, W. Lukosz, *Swiss Federal Institute of Technology.* We demonstrate electronanomechanically actuated interferometric intensity modulators that are fabricated—without any electro-optic materials—by micromachining of silicon, SiO_2, and (waveguiding) Si_3N_4 films. **(p. 182)**

IMH10 • A standard SPICE model for MQW lasers modeling capture/escape and carrier transport, Kuno Zhu-ber-Okrog, *Siemens AG, Austria.* We describe a circuit simulation model for multiquantum well semiconductor lasers accounting for carrier transport and capture/escape effects. **(p. 186)**

IMH11 • Spectral Green's function approach in the investigation of radiation pattern of a novel circular grating surface-emitting laser, Ali M. Shams-Zadeh-Amiri, W. P. Huang, *Univ. Waterloo, Canada.* A closed-form spectral Green's function in the Hankel transform domain of a multilayered stack is developed to obtain the far field pattern of a novel circular grating surface-emitting laser. **(p. 190)**

IMH12 • Modeling of a passive polarization converter free of longitudinally periodic structure, Marie Fontaine, Velko P. Tzolov, *Univ. Quebec, Canada.* A vectorial finite-element propagation method is applied to optimize the polarization rotation process in a passive polarization converter free of longitudinally periodic structure. **(p. 193)**

IMH13 • Polarization splitting in lossy/gainy multi-quantum well directional coupler, Kwang C. Ho, G. Griffel, T. Tamir, *Polytechnic Univ.* By use of a transmission-line modal description to analyze rigorously lossy/gainy polarization beamsplitters, a novel criterion is developed for the optimal polarization length. **(p. 197)**

IMH14 • Optimization of slab waveguides with given mode width toward low modal birefringence, G. Sarlet, J. Haes, R. Baets, *Univ. Gent, Belgium.* The modal birefringence in slab waveguides is studied for a variety of index profiles. For given mode width the three-layer slab can be optimized to give near-ideal results. **(p. 201)**

IMH15 • Effects of external optical feedback in broad-area lasers, J. Martain-Regalado, G. H. M. van Tartwijk, S. Balle, M. San Miguel, *Univ. Illes Balears, Spain.* External optical feedback is applied to broad-area lasers to permit lateral mode selection and pattern stabilization of the output beam, which usually suffers from undesirable filamentation. **(p. 205)**

IMH16 • Analysis of a lensed coreless fiber by a hybrid technique that involves FD-BPM and FD-TDM, Junji Yamauchi, Koji Nishio, Hisamatsu Nakano, *Hosei Univ., Japan.* A technique of connecting the scalar FD-BPM to the scalar FD-TDM is proposed. The field distribution in a lensed fiber with an AR coating is presented. **(p. 209)**

IMH17 • Characterization of optical filters with two-dimensional confinement, T. Wongcharoen, B. M. A. Rahman, K. T. V. Grattan, *City Univ., UK.* Numerically simulated results are presented for optical filters incorporating nonidentical coupled waveguides with two-dimensional confinement with use of rigorous numerical methods. **(p. 213)**

IMH18 • Octave bandwidth analog link with a monolithic laser/electroabsorption modulator, Roger Helkey, Harold Roussell, Charles Cox III, *MIT Lincoln Laboratory;* Masahiro Aoki, Hirohisa Sano, *Hitachi, Ltd., Japan.* A high performance analog optical link is demonstrated using a monolithic laser/electroabsorption modulator. The spurious-free dynamic range is 116dB x $Hz^{4/5}$. **(p. 217)**

IMH19 • Measurement of linewidth enhancement factor and nonlinear gain of vertical-cavity surface-emitting lasers, Hua Li, *Univ. New Mexico;* David Bossert, *Phillips Laboratory.* The linewidth enhancement factor alpha and nonlinear gain coefficient E of a VCSEL are obtained from the measured normalized phase modulation index versus modulation frequency. **(p. 220)**

IMH20 • Relative intensity noise of an InGaAsP laser over a 22 GHz bandwidth at cryogenic and room temperatures, Gregory E. Obarski, Donald R. Larson, Robert J. Phelan, *NIST.* We show that cryogenic operation of a commercial InGaAsP laser significantly reduces its relative intensity noise within a measurement bandwidth of 22 GHz, indicating its potential for ultrahigh speed optical communications. **(p. 224)**

IMH21 • Investigation of the resolution limit of the hydrogen plasma-induced defect layer intermixing process, A. Saher Helmy, B. S. Ooi, J. H. Marsh, *Univ. Glasgow, UK.* The hydrogen plasma-induced damage layer intermixing is shown to be a viable integration technology. Bandgap shifts can be induced with high spatial resolution (<7 μm). **(p. 228)**

IMH22 • Feasibility of monolithic device integration in GaInP/AlGaInP using photoabsorption induced disordering, Karen McIlvaney, Andrew McKee, A. Catrina Bryce, John H. Marsh, *Univ. Glasgow, UK;* Wynn Jones, *Epitaxial Products International, UK.* A shift of 30 meV in the photoluminescence peak of a 670 nm GaInP/AlGaInP laser structure was obtained by focusing a 5 W Ar laser onto a sample. **(p. 232)**

IMH23 • Guided-wave magneto-optic Bragg diffraction efficiency enhancement using nonuniform bias magnetic field, C. S. Tsai, S. Calciu, Y. S. Lin, *Univ. California-Irvine.* A two to six-fold enhancement in the diffraction efficiency of a guided-wave magneto-optic Bragg cell modulator is achieved with use of a nonuniform bias magnetic field. A diffraction efficiency as high as 60% at an RF drive power of only 0.37 W is measured also. **(p. 235)**

TUESDAY
APRIL 30, 1996

3rd FLOOR REGISTRATION AREA

7:30am–5:30pm
Registration

FAIRFAX A

8:15–10:00am
ITuA • Symposium on Simulation of Quantum Well Phenomena: Device Applications—Optical Gain in Quantum Wells
James J. Coleman, *University of Illinois Urbana-Champaign, Presider*

8:15am (Invited)
ITuA1 • Modeling and experimental characterization of optical gain in InGaAsP-based lasers, M. S. Hybertsen, D. A. Ackerman, G. E. Shtengel, P. A. Morton, R. F. Kazarinov, G. A. Baraff, T. Tanbun-Ek, R. A. Logan, *AT&T Bell Laboratories.* Detailed calculations and measurements of optical gain in bulk and MQW 1.3 μm InGaAsP based lasers are compared, including the temperature sensitivity. **(p. 240)**

8:45am
ITuA2 • The temperature and strain dependence of differential gain in 1.5 mm quantum well lasers, Eoin P. O'Reilly, G. Jones, P. Togher, M. Silver, A. R. Adams, *Univ. Surrey, UK.* Measured gain depends logarithmically on current in long wavelength lasers. The strain and temperature dependence are well described by simple theoretical models. **(p. 243)**

9:00am
ITuA3 • Band structure and modal gain of partially interdiffused InGaAs/GaAs/AlGaAs SWQ lasers, Rafael Gomez-Alcala, Francisco Javier Fraile-Pelaez, *E.T.S.I. Telecomunicacion, Spain;* Ignacio Esquivias-Moscardo, *Univ. Politecnica de Madrid, Spain.* We investigate theoretically the effects of interdiffusion on strained InGaAs-GaAs SQW lasers. The modal gain is evaluated, taking into account valence band mixing. **(p. 246)**

9:15am
ITuA4 • Spin-orbit coupling effects on the optical gain of a cubic GaN quantum-well laser, Doyeol Ahn, *LG Electronics Research Center, Korea.* The optical gain of a cubic GaN quantum-well laser is studied including the spin-orbit (SO) split-off band coupling effects. It is expected that a very narrow separation of the SO band causes undesirable effects, which are discussed. **(p. 250)**

9:30am
ITuA5 • Non-Markovian gain of a quantum-well laser with many-body effects, Doyeol Ahn, *LG Electronics Research Center, Korea.* The optical gain of a quantum-well laser is studied taking into account the valence-band mixing, non-Markovian relaxation, and many-body effects. It is shown that the non-Markovian gain model removes the two anomalies associated with the Lorentzian line shape function with the proper choice of the correlation time. **(p. 254)**

9:45am
ITuA6 • Comparison of well designs for near-infrared (850 nm) semiconductor lasers, T. E. Sale, Y. Ohiso, C. Amano, T. Kurokawa, *NTT Opto-electronics Laboratories, Japan.* We theoretically compare various 850 nm emitting quantum well designs in the $(Al_xGa_{1-x})_yIn_{1-y}As_zP_{1-z}$ system. Materials technology arguments are used to refine the choice further. **(p. 258)**

INDEPENDENCE BALLROOM

10:00–10:30am
Coffee Break/Exhibits

FAIRFAX B

8:30–10:00am
ITuB • Silicon Heterostructure Devices,
Richard A. Soref, *USAF Rome Laboratory, Presider*

8:30am (Invited)
ITuB1 • SiGe/Si heterostructures for photonics, D. C. Houghton, *National Research Council of Canada.* An overview of SiGe/Si materials research and photonic device opportunities are presented, highlighting some recent successes and the challenges ahead. **(p. 264)**

9:00am
ITuB2 • Characterization of GeSi/Si strained layer superlattice avalanche photodiode, F. Y. Huang, Kevin Alt, K. L. Wang, *University of California, Los Angeles.* Device characterization of photoresponse and avalanche multiplication in photodiodes consisting of SiGe/Si strained layer superlattice as both the active absorption and multiplication region. **(p. 265)**

9:15am
ITuB3 • An amorphous silicon/silicon carbide thin-film thermo-optical interferometer at λ = 1.5 mm with 3 MHz bandwidth capability, F. G. Della Corte, I. Rendina, G. Cocorullo, *IRECE-CNR, Italy;* A. Rubino, E. Terzini, *ENEA-CRP, Italy.* A thermo-optical interferometer is realized from a thin-film amorphous silicon/silicon carbide waveguiding structure. Modulation rates of 3MHz are possible with a properly designed device. **(p. 269)**

9:30am
ITuB4 • Guided-wave optical circuits in silicon-on-insulator technology, P. D. Trinh, S. Yegnanarayanan, B. Jalali, *Univ. California–Los Angeles.* We present integrated 3 dB optical directional couplers, a 5 x 9 star coupler, and a Mach–Zehnder wavelength demultiplexer using silicon-on-insulator rib waveguides. These devices show excellent performance characteristics and represent key components for realization of monolithic optoelectronic circuits in a silicon IC-compatible technology. **(p. 273)**

9:45am
ITuB5 • Absorption enhancement in silicon waveguides using metal island films, Howard R. Stuart, Dennis G. Hall, *Univ. Rochester.* A metal island film was used to enhance the absorption characteristics of a silicon waveguide. Measured enhancements reached a factor of 5 in the near-infrared. **(p. 278)**

INDEPENDENCE BALLROOM

10:00am–10:30am
Coffee Break/Exhibits

FAIRFAX A

10:30am–12:00m
ITuC • Symposium on Simulation of Quantum Well Phenomena: Device Applications—Low Dimensional Nanostructures, Spontaneous Emission and Quantum Well Effects
Eoin P. O'Reilly, *University of Surrey, UK, Presider*

10:30am (Invited)
ITuC1 • Low-dimensional nanostructures for integrated optoelectronics applications, Eli Kapon, *Swiss Federal Institute of Technology, Switzerland.* The structure, the optical luminescence and absorption properties, and the application in optoelectronic devices of self-ordered, low-dimensional nanostructures grown on nonplanar substrates are discussed. **(p. 284)**

11:00am
ITuC2 • Features of spontaneous emission in large diameter VCSELs, A. Onischenko, J. Sarma, *Univ. Bath, UK.* Modal field calculations reveal a high level of spontaneous emission along the plane of the multilayer structure, which points to reduced efficiency and larger threshold current density. **(p. 288)**

11:15am
ITuC3 • Spontaneous emission in optical microcavities, H. Rigneault, S. Robert, S. Monneret, *Domaine Univ. Saint Jerome, France.* Spontaneous emission of rare earth atoms confined into resonant planar microcavities is investigated theoretically and experimentally. Strong correlation between microcavity structure and radiation pattern is demonstrated. **(p. 292)**

11:30am
ITuC4 • Impact of quantum confinement and strain effects on the negative chirp parameter of InGaAsP/InP quantum well electroabsorption modulators, Takayuki Yamanaka, Koichi Wakita, Kiyoyuki Yokoyama, *NTT Opto-electronics Laboratories, Japan.* We theoretically demonstrate that, for a wide tensile-strained quantum well structure, a desirable condition exists where the chirp parameter is almost continuously negative independently of electric field strength. **(p. 295)**

11:45am
ITuC5 • Enhanced Stark effect in tensile-strained $Al_xIn_{1-x}As/Ga_yIn_{1-y}As/InP$ quantum well structures, T. Schwander, Bosch Telecom GmbH, Germany; P. Lusse, J. Schuobel, TU Braunschweig, Germany. The enhanced Stark effect in tensile-strained quantum wells is found to be caused by strong carrier-interaction. Optimum performance is achieved with degenerated valence bands at modulator-off-state. **(p. 298)**

12:00m–1:30pm
Lunch on Own

FAIRFAX B

10:30am–12:00m
ITuD • Silicon Waveguides and Interconnect Technologies
Bahram Jalali, *University of California-Los Angeles, Presider*

10:30am (Invited)
ITuD1 • Trends in silica-based optoelectronics hybrid integration, Claude Artigue, *Alcatel Alsthom Recherche, France.* Optoelectronic chips assembly on planar silicon boards opens the way for multi-chips photonic integrated circuits (MPICs); status and trends are reviewed in this presentation. **(p. 304)**

11:00am
ITuD2 • New types of single-mode (movable) and multimode (60-mm-thick) SOI waveguides fabricated using silicon micromachining technology, S. C. Kan, T. T. H. Eng, S. Y. S. Sin, J. Y. L. Ho, I. H. M. Liem, P. W. L. Chan, G. K. L. Wong, *Hong Kong Univ. Science and Technology.* Two low-loss (<0.8 dB/cm) SOI waveguides are fabricated—single-mode movable waveguides used as switches and scanning probes, and multimode SOI waveguides and couplers with 60-μm core. **(p. 307)**

11:15am
ITuD3 • Optical waveguides and components based on porous silicon, H. Arrand, T. M. Benson, T. Anada, *Univ. Nottingham, UK;* M. G. Berger, R. Aren-Fischer, H. G. Munder, H. Luth, *Forschungszentrum Jurlich GmbH, Germany;* A. Loni, R. J. Bozeat, *Defence Research Agency, UK.* Planar optical waveguiding is demonstrated in as-prepared and oxidized porous silicon materials. Additional processing realizes rib waveguides and systems components such as Y-junctions. **(p. 311)**

11:30am
ITuD4 • Diffraction patterns of Si-based polygonal gratings for 1-to-many optical interconnects, Oleg Ershov, Feiming Li, Michael Dubinovsky, Ray T. Chen, *Univ. Texas-Austin.* One micron Si-based polygonal grating couplers are investigated for 1-to-many fanout optical interconnects. Excellent agreement with the scalar diffraction theory is confirmed experimentally. **(p. 315)**

11:45am
ITuD5 • Electro-optic switch constructed with a poled silica-based waveguide on a Si substrate, Makoto Abe, Takeshi Kitagawa, Kuninori Hattori, Akira Himeno, Yasuji Ohmori, *NTT Opto-electronics Laboratories, Japan.* 2 x 2 electro-optic switching is demonstrated in an integrated Mach-Zehnder interferometer constructed with thermally poled GeO_2-doped silica-based channel waveguides on a Si substrate. **(p. 319)**

12:00m–1:30pm
Lunch on Own

FAIRFAX A

1:30–3:00pm
ITuE • Symposium on Simulation of Quantum Well Phenomena: Device Applications—Transverse Modes in Vertical Cavities
Joseph P. Donnelly, *MIT Lincoln Laboratory, Presider*

1:30pm
ITuE1 • Modeling of photon localization in one- to two-dimensional arrays of coupled vertical-cavity lasers, Harald Pier, Eli Kapon, *Swiss Federal Institute of Technology.* Photon localization, arising from disorder in photonic lattices, reduces with increasing dimensionality. One-, two-, and fractal-dimensional arrays of coupled vertical-cavity lasers are discussed. **(p. 324)**

1:45pm
ITuE2 • Transverse multimode dynamics of gain-switched VCSELs, J. Dellunde, J. M. Sancho, *Univ. Barcelona, Spain;* M. C. Torrent, *Univ. Politecnica de Catalunya, Spain;* K. A. Shore, *Univ. Wales, UK.* Numerical simulations demonstrate the significant role played by spatial hole burning and carrier diffusion in the turn-on process of gain-switched multi-transverse VCSELs. **(p. 328)**

2:00pm
ITuE3 • Transverse mode selection in external cavity vertical-cavity surface-emitting lasers, J. Dellunde, *Univ. Barcelona, Spain;* A. Valle, *Univ. Cantabria, Spain;* K. A. Shore, *Univ. Wales, UK.* Analysis of the dynamics of external cavity VCSELs shows that preferential excitation of low-order transverse modes can be effected by appropriate choice of optical feedback delay. **(p. 332)**

2:15pm
ITuE4 • Accurate three-dimensional modeling of transverse mode threshold gain in vertical-cavity surface-emitting lasers, Bart Demeulenaere, Bart Dhoedt, Stefan Goeman, *Univ. Gent, Belgium.* Diffraction effects in vertical-cavity lasers are modeled rigorously. This model is compared with an approximate one and is applied to the transverse mode stability problem. **(p. 336)**

2:30pm
ITuE5 • Modeling of VCSELs by the method of lines, E. Ahlers, S. F. Helfert, R. Pregla, *Fern Univ., Germany.* Vertical-cavity surface-emitting lasers are modeled by the method of lines. Coupling of optical, electrical, and thermal effects is incorporated. **(p. 340)**

2:45pm
ITuE6 • Understanding waveguiding in vertical-cavity surface-emitting lasers, G. Ronald Hadley, K. D. Choquette, K. L. Lear, *Sandia National Laboratories.* We present a fundamentally new understanding of waveguiding in vertical-cavity surface-emitting diode lasers that relates effective index changes inside the cavity to variations in Fabry–Perot resonance frequency. **(p. 344)**

INDEPENDENCE BALLROOM

3:00pm–3:30pm
Coffee Break/Exhibits

FAIRFAX B

2:00–3:00pm
ITuF • Low-Cost Photonic Packaging I
Ian R. Croston, *Integrated Optical Components, UK,Presider*

2:00pm (Invited)
ITuF1 • Novel alignment techniques for packaging and integration of optoelectronic components, Paul O. Haugsjaa, *GTE Laboratories Inc.* This talk reviews alignment techniques recently developed for optoelectronic components that offer the potential for reducing packaging costs and increasing the degree of practical hybrid integration. **(p. 350)**

2:30pm
ITuF2 • Successful development of non-planar lithography for micro-machining applications, J. Shmulovich, J. V. Gates, C. F. Kane, M. A. Cappuzzo, J. M. Szalkowski, *Lucent Technologies, Bell Labs.* We developed a non-planar photolithography approach utilizing a conformal electrophoretic resist. Wafer scale bonding of photodiodes passively aligned to V-grooves using solder bumps was demonstrated. **(p. 354)**

2:45pm
ITuF3 • Thermal study of silicon optical microbenches with on board heaters for soldering, Michael D. Pocha, Oliver T. Strand, John A. Kerns, *Lawrence Livermore National Laboratory.* The combination of selected experimental measurements with finite element simulation provide a thorough understanding of thermal behavior of silicon microbenches with on-board heaters. **(p. 358)**

INDEPENDENCE BALLROOM

3:00–3:30pm
Coffee Break/Exhibits

FAIRFAX A

3:30–5:00pm
ITuG • High Speed Devices
Jane E. Zucker, *AT&T Bell Laboratories, Presider*

3:30pm
ITuG1 • Mach-Zehnder modulator integrated with a gain-coupled DFB laser for 10 Gbit/s, 100 km NDSF transmission at 1.55 μm, D. M. Adams, C. Rolland, N. Puetz, R. S. Moore, J. Yu, F. R. Shepherd, H. B. Kim, S. Bradshaw, *Nortel Technology, Canada.* The first monolithic integration of an interferometric modulator with a gain-coupled distributed-feedback laser to our knowledge is reported. The integrated MZ/DFB is fabricated by butt-coupling in order to minimize design constraints on the MZ and DFB active regions. **(p. 364)**

3:45pm
ITuG2 • Small chirp, low drive-voltage integrated 10 Gbit/s DFB laser and bulk electro-absorption modulator on semi-insulating InP substrate, Olof Sahlen, Lennart Lundqvist, Stefan Funke, *Ericsson Components AB, Sweden.* Laser-integrated bulk absorption InGaAsP modulators on semi-insulating substrate, with 10 dB extinction, 1 V drive voltage for zero bias and 9 GHz bandwidth are reported. **(p. 368)**

4:00pm
ITuG3 • Monolithically integrated nonlinear sagnac interferometer and its application as a 20 Gbit/s all-optical demultiplexer, E. Jahn, N. Agrawal, W. Pieper, H.-J. Ehrke, D. Franke, H. G. Weber, W. Furst, *Heinrich-Hertz-Institut, Germany.* A Sagnac interferometer consisting of a semiconductor laser amplifier and a 3 dB coupler monolithically integrated within a waveguide loop mirror is fabricated and its application as a 20 Gbit/s all-optical demultiplexer is demonstrated. **(p. 372)**

4:15pm
ITuG4 • Novel method for improving the performance of InP/InGaAsP MQW Mach–Zehnder modulators by phase shift engineering, Jun Yu, Claude Rolland, Azmina Somani, Scott Bradshaw, *Bell-Northern Research, Canada;* David Yevick, *Queen's Univ., Canada.* We have simultaneously achieved both an optimized negative frequency chirp and a high extinction ratio in InP/InGaAsP MWQ Mach–Zehnder modulators. **(p. 376)**

4:30pm
ITuG5 • High-speed coplanar Schottky traveling-wave photodetectors, M. Alles, Th. Braasch, D. Jager, *Gerhard-Mercator-Univ. Duisburg, Germany.* Coplanar traveling-wave photodetectors for millimeter wave applications are discussed. Experimentally, a 3-dB-bandwidth of >40 GHz is found at 1.3 μm for an InGaAlAs/InP device with an InGaAs quantum well. **(p. 380)**

4:45pm
ITuG6 • High-speed traveling wave electro-optic intensity modulator with a doped PIN semiconductor junction, G. A. Vawter, V. M. Hietala, J. R. Wendt, B. A. Fuchs, M. Hafich, M. Housel, M. Armendariz, C. T. Sullivan, *Sandia National Laboratories.* A high-electro-optic-efficiency Mach-Zehnder intensity modulator is demonstrated with a bandwidth exceeding 40 GHz. The 1-mm-long modulator has a switching voltage comparable to undoped semiconductor designs of much greater length. **(p. 384)**

FAIRFAX B

3:30–5:00pm
ITuH • Low-Cost Photonic Packaging II
Lewis B. Aronson, *Hewlett Packard, Presider*

3:30pm (Invited)
ITuH1 • Towards low cost single-mode fiber optic components, David G. Parker, *Hewlett Packard Fibre Optic Components, UK.* This paper reviews the key cost components in producing single mode fiber optic transmitters and receivers. Topics such as the use of limited monolithic integration, silicon micromachining, passive optical alignment and low cost circuit technology will be explored. **(p. 388)**

4:00pm
ITuH2 • Low-cost automated fiber pigtailing machine, O. T. Strand, *Lawrence LivermoreNational Laboratory.* This ARPA-funded project has built three machines to perform automated sub-micron alignments and attachments of single-mode fibers to different optoelectronic devices. **(p. 393)**

4:15pm
ITuH3 • Fiber to laser coupling on silicon optical bench platform, G. E. Henein, J. V. Gates, L. J. Mulligan, H. M. Presby, J. F. de Jong, *Lucent Technologies-Bell Labs.* A highly efficient and stable approach is presented to actively couple and solder in position a single mode fiber to a laser chip. **(p. 396)**

4:30pm
ITuH4 • New assembly technology for small surface mount LEDs, P. Rajkomar, *Hewlett Packard.* The Optoelectronics Division of Hewlett-Packard has developed a new technology for making surface mount L.E.D. lamps and indicators whereby the internal wire bond is eliminated. The new technology clears the way for products with enhanced reliability while offering a path to fast and inexpensive proliferations. **(p. 400)**

3rd FLOOR REGISTRATION AREA

7:30 am–5:30pm
Registration

FAIRFAX A

8:45–10:00am
IWA • Optical Filters and Waveguides
K. A. Shore, *University of Wales, UK, Presider*

8:45am
IWA1 • Narrowband transmission filters from highly resonant gratings, J. C. Chen, P. R. Villenueve, H. A. Haus, J. D. Joannopoulos, *Massachusetts Institute of Technology.* The transmission and reflection properties of optical filters with extremely narrow passbands are examined by a FDTD code with quartic perfectly matched layers. **(p. 406)**

9:00am
IWA2 • Improved analysis and design of waveguide Bragg grating filters for wavelength division multiplexing applications, A. Gnazzo, A. Barla, C. De Bernardi, *CSELT S.p.A., Italy.* A refined analysis of amplitude-modulated Bragg grating is presented that includes effective index variations along the filter to predict stopband perturbations. On this basis, integrated filters are designed with nearly ideal response. **(p. 410)**

9:15am
IWA3 • Design of fiber-matched uncladded rib waveguides on InP with polarization-independent fiber coupling loss of 1 dB, C. M. Weinert, *Heinrich-Hertz-Institute, Germany.* A waveguide taper design is presented for uncladded rib waveguides with relaxed fabrication tolerances and polarization-independent fiber mode matching with 1 dB loss. **(p. 414)**

9:30am
IWA4 • Analytical study of birefringence in slab waveguides, J. Buus, *Gayton Photonics Ltd., UK;* J. Haes, R. Baets, *Univ. Gent, UK.* A simple analytical result for the birefringence of a symmetrical slab waveguide is derived and compared with numerical results. **(p. 418)**

9:45am
IWA5 • Reflectivity analysis of optical waveguides with coated and tilted facets using the FD–TD method with the PML absorbing boundary condition, Junji Yamauchi, Shin'ichi Aoki, Hisamatsu Nakano, *Hosei Univ., Japan.* The FD–TD method with a perfectly matched layer absorbing boundary condition allows us to evaluate low power reflectivities from coated and tilted facets. **(p. 422)**

INDEPENDENCE BALLROOM

10:00–10:30am
Coffee Break/Exhibits

FAIRFAX B

8:30–10:00am
IWB • Active and Passive Waveguide Devices
Fred Heismann, *AT&T Bell Laboratories, Presider*

8:30am
IWB1 • Er:LiNbO$_3$ guided wave optical amplifiers pumped at 980 nm, Chi-hung Huang, Leon McCaughan, *Univ. Wisconsin–Madison.* Er-indiffused Ti:$LiNbO_3$ and ZnO:Mg:$LiNbO_3$ channel waveguide amplifiers pumped at 980 nm are reported for the first time to our knowledge. We observed the largest differential gain and pump efficiency to date in this substrate. **(p. 428)**

8:45am
IWB2 • Blue light generation in a lithium tantalate waveguide domain-inverted by heat treatment with a mask, Sang-Yun Yi, Sang-Yung Shin, *Korea Advanced Institute of Science and Technology;* Yong-Sung Jin, Yung-Song Son, *LG Electronics Research Center, Korea.* Blue light is generated with an efficiency 1500%/Wcm^2 in a lithium tantalate waveguide that is periodically domain-inverted by heat treatment with a mask. **(p. 431)**

9:00am
IWB3 • Direct observation of buried refractive-index profiles in annealed proton-exchanged $LiTaO_3$ wave-guides, David B. Maring, Robert F. Tavlykaev, Ramu V. Ramaswamy, *Univ. Florida.* Depth profiles of planar-annealed proton-exchanged waveguides in X-cut $LiTaO_3$ are measured directly by use of a reflectivity technique. For the first time, buried extraordinary profiles are confirmed to exist and ordinary profiles are measured. **(p. 435)**

9:15am
IWB4 • Measurement of complex coupling coefficients of directional coupling by thermo-optic modulation, H. Gnewuch, Univ. *Cambridge, UK;* J. E. Roman, R. D. Harris, J. S. Wilkinson, *Univ. of Southampton, UK;* R. Ulrich, *Technische Univ. Hamburg, Germany.* We demonstrate the measurement of real and complex coupling coefficients in symmetrical directional couplers and strongly absorbing directional couplers by thermo-optic modulation. **(p. 439)**

9:30am
IWB5 • Mechanisms of UV-induced refractive index changes in PECVD silica, M. V. Bazylenko, M. Gross, P. L. Chu, *Univ. New South Wales, Australia;* D. Moss, *Univ. Sydney, Australia.* Ge-doped PECVD silica films can exhibit an increase or decrease in refractive index after UV exposure. Densification/expansion mechanisms are proposed to account for the changes. **(p. 443)**

9:45am
IWB6 • Loss reduction of deeply etched InP/InGaAsP waveguides by CBE regrowth, C. G. M. Vreeburg, Y. S. Oei, T. L. M. Scholtes, *Delft Univ. Technology, The Netherlands;* J. W. Pedersen, *Eindhoven Univ. Technology, The Netherlands;* H. Vonk, C. A. Verschuren, R. T. H. Rongen, M. R. Leys, J. H. Wolter, *Royal PTT Nederland N.V., The Netherlands.* Transmission loss of deeply reactive ion-etched InP/InGaAsP ridge waveguides is reduced significantly by regrowth of InP on the sidewalls with use of chemical beam epitaxy. **(p. 447)**

INDEPENDENCE BALLROOM

10:00–10:30am
Coffee Break/Exhibits

FAIRFAX A

10:30am–12:00m
IWC • Polarization Selective Devices
Ramu V. Ramaswamy, *University of Florida, Presider*

10:30am
IWC1 • Poling-induced waveguide polarizers in electro-optic polymers, Min-Cheol Oh, Sang-Yung Shain, *Korea Advanced Institute of Science and Technology;* Wol-Yon Hwang, Jang-Joo Kim, *Electronics and Telecommunications Research Institute, Korea.* TE-pass and Tm-pass polymeric waveguide polarizers are demonstrated by integration of photobleached polymer waveguides supporting both TE and TM modes and poling-induced polymer waveguides that support either TE or TM modes. **(p. 452)**

10:45am
IWC2 • New metal-free polarization splitter on InGaAsP/InP, Jos J. G. M. van der Tol, Jørgen W. Pedersen, Ed G. Metaal, J. Jan-Willem van Gaalen, *Royal PTT Nederland N.V., The Netherlands;* Y. Siang Oei, Fokke H. Groen, Delft Univ. Technology, The Netherlands. A new directional coupler polarization splitter is presented. It uses the large waveguide birefringence of the first-order modes in a ridge waveguide. Components are 1.5 mm long, showing splitting ratios up to 20 dB (@ 1.5 μm). **(p. 456)**

11:00am (Invited)
IWC3 • Integrated optics versus micro-optics—a comparison, E. C. M. Pennings, A. A. M. Staring, *Philips Optoelectronics Centre, The Netherlands;* M. K. Smit, *Delft Univ. Technology, The Netherlands;* G.-D. Khoe, *Technical Univ. Eindhoven, The Netherlands.* Integrated-optic and micro-optic devices are compared from a market and a technical perspective. A specific performance comparison is made for wavelength demultiplexers. **(p. 460)**

11:30am
IWC4 • High-speed polarization scrambler with adjustable frequency chirp, Fred Heismann, Robert W. Smith, *AT&T Bell Laboratories.* We present a novel electro-optic polarization scrambler that induces a variable amount of common phase modulation in the depolarized output light. Pure phase and polarization modulation are demonstrated at 7.5 GHz. **(p. 464)**

11:45am
IWC5 • Novel compact InP-based polarization converters using ultrashort bends, C. van Dam, L. H. Spiekman, F. P. G. M. van Ham, F. H. Groen, M. K. Smit, *Delft Univ. Technology, The Netherlands;* J. J. G. M. van der Tol, *PTT Research, The Netherlands;* I. Moerman, *Univ. Gent, Belgium;* W. W. Pascher, Fern Univ., Germany; M. Hamacher, H. Heidrich, C. M. Weinert, *Heinrich Herz Institut, Germany.* A novel compact type of polarization converter is realized that uses curved waveguides with small bending radii. Strong polarization conversion (> 85%) is measured with excess loss of only 2.7 dB. **(p. 468)**

12:00m–1:45pm
Lunch on Own

FAIRFAX B

10:30am–12:00m
IWD • Active Semiconductor Devices
S. Chandrasekhar, *Lucent Technologies,/Bell Laboratories,Presider*

10:30am
IWD1 • A gain-clamped, crosstalk free, vertical-cavity lasing semiconductor optical amplifier for WDM applications, J. D. Walker, F. G. Patterson, S. P. Dijaili, R. J. Deri, *Lawrence Livermore National Laboratory.* We have fabricated and tested a semiconductor optical amplifier that is gain clamped by vertical-cavity lasing and amplifies horizontally with 25 dB crosstalk suppression. **(p. 474)**

10:45am
IWD2 • Wavelength accuracy and output power of multiwavelength DFB laser arrays with integrated star couplers and optical amplifiers, M. R. Amersfoort, C. E. Zah, B. Pathak, F. Favire, P. S. D. Lin, A. Rajhel, N. C. Andreadakis, R. Bhat, C. Caneau, M. A. Koza, *Bellcore.* We report the static performance of multiwavelength DFB laser arrays with integrated star couplers and optical amplifiers. Wavelength deviations of ±2 nm or less from the eight-wavelength comb designated by ONTC have been achieved with high yield. High power into a single mode fiber of about –13 dBm and 0 dBm per wavelength has been measured without and with on-chip optical amplification, respectively. **(p. 478)**

11:00am
IWD3 • Flip-chip bonded 0.85-um vertical-cavity surface-emitting laser array using an AlGaAs substrate, Yoshitaka Ohiso, Kouta Tateno,Yoshitaka Kohama, Takashi Kurokawa, *NTT Opto-electronics Laboratories, Japan;* Hideki Tsunetsugu, NTT Interdisciplinary Research Laboratories, Japan. A flip-chip bonded 0.85-um VCSEL array on an AlGaAs substrate demonstrates a power conversion efficiency of 11.7% and a maximum operating temperature of 130 degrees C. **(p. 482)**

11:15am
IWD4 • Integrable polarization-insensitive InGaAsP/InP Mach–Zehnder switch, T. Uitterdik, H. van Brug, F. H. Groen, H. J. Frankena, C. G. M. Vreeburg, *Delft Univ. Technology, The Netherlands;* J. J. G. M. van der Tol, *Royal PTT Nederland N.V., The Netherlands.* A low loss polarization-insensitive InGaAsP/InP Mach-Zehnder switch with a phase shifting efficiency of 14.5 degrees/V mm and crosstalk values around –14 db is presented. **(p. 486)**

11:30am
IWD5 • Terahertz tunable polarization-switching VCSELs, S. Y. Chou, M. Y. Liu, R. C. Shi, L. Zhuang, S. J. Schablitsky, *Univ. Minnesota.* A polarization-switching vertical-cavity surface-emitting laser with a tunable oscillation frequency as high as several terahertz is proposed. The frequency tuning is provided by fabricating the waveplate and a mirror monolithically on a movable microcantilever. **(p. 490)**

11:45am
IWD6 • Cryogenic vertical-cavity laser for low power free-space optical interconnects, Y. A. Akulova, B. J. Thibeault, J. C. Ko, E. Goobar, L. A. Coldren, *Univ. California–Santa Barbara.* By use of limited oxidation in a dielectric apertured structure, single-mode vertical-cavity lasers with submilliamp thresholds over the 77–300 K temperature range are demonstrated. **(p. 494)**

12:00m–1:45pm
Lunch on Own

FAIRFAX A

2:00–3:00pm
IWE • Diffractive and Reflective Elements
Leon McCaughan, *University of Wisconsin–Madison, Presider*

2:00pm
IWE1 • High efficiency focusing waveguide grating coupler with parallelogramic groove profiles, Tingdi Liao, Stephen Sheard, Ming Li, *Univ. Oxford, UK;* Jianguo Zhu, Phil Prewett, *Rutherford Appleton Laboratory, UK.* A high-efficiency focusing waveguide grating coupler with parallelogramic groove profiles and double-layered grating structure is proposed and designed and is fabricated by electron beam lithography. **(p. 498)**

2:15pm
IWE2 • Gratings with parallelogramic-shape grooves for unidirectional coupling in large guidance waveguides, V. A. Sychugov, A. V. Tishchenko, *Russian Academy of Sciences; O. Parriaux, Formerly CSEM, Switzerland.* High-efficiency TE and TM unidirectional coupling is shown to be obtainable in large index difference waveguides loaded by a grating of parallelogramic shape grooves. **(p. 502)**

2:30pm
IWE3 • Periodically segmented tapered waveguide for mode-size transformation and fundamental mode excitation, Ming-Hsien Chou, Mark A. Arbore, Martin M. Fejer, *Stanford Univ.* We report the use of segmented waveguides with axially varying duty cycle to implement adiabatic tapers for mode size transformation. **(p. 506)**

2:45pm
IWE4 • Low-loss GaAs/AlGaAs waveguide corners for compact optical delay lines, J. M. Heaton, M. M. Bourke, S. B. Jones, K. P. Hilton, D. R. Wight, *Defence Research Agency, UK.* We present results of loss measurements for different corner types and sizes and demonstrate the advantages of using near-hyperbolic corners designed to minimize transition losses. **(p. 510)**

INDEPENDENCE BALLROOM

3:00–3:30pm
Coffee Break/Exhibits

FAIRFAX B

1:45–3:00pm
IWF • Advanced Laser Structures
Uziel Koren, *AT&T Bell Laboratories, Presider*

1:45pm
IWF1 • Impact of current blocking structure on the coupling characteristics in 1.3-μm spot-size converted laser diodes, Y. Suzaki, O. Mitomi, Y. Tohmori, H. Okamoto, Y. Kondo, Y. Sakai, M. Okamoto, Y. Kadota, *NTT Opto-electronics Laboratories, Japan.* Impact of buried-heterostructure design on the coupling characteristics are clarified in newly spot-size converted laser diodes. By introduction of proposed design, low-loss-coupling characteristics (<2 dB), with a low threshold current (<6 mA), and a high temperature operation (~100°C) are obtained. **(p. 516)**

2:00pm
IWF3 • Large diameter semiconductor ring lasers in tensile-strained InP/InGaAsP material, Thomas F. Krauss, Hanson Pottinger, A. Catrina Bryce, John H. Marsh, Richard M. De La Rue, *Glasgow Univ., UK;* Chris C. Button, John S. Roberts, *Sheffield Univ., UK.* Semiconductor ring lasers with 3 mm circumference show a threshold current of 110 mA at 1.52 μm. The strained DQW material exhibits a threshold current density of 193 A/cm^2. **(p. 520)**

2:15pm
IWF4 • Output characteristics of high power GaAs/GaAlAs double heterostructure rib-waveguide bow-tie lasers, I. Middlemast, J. Sarma, *Univ. Bath, UK;* P. S. Spencer, *Univ. Wales, UK.* The output characteristics of high-power bow-tie lasers are measured and shown to compare well with theoretical results. **(p. 524)**

2:30pm
IWF5 • A simple, but accurate expression for the static and dynamic chirp in DFB lasers, Geert Morthier, Piet Verhoeve, Roel Baets, *Univ. Gent, Belgium.* An accurate formula for the chirp, resulting from gain suppression, spatial hole burning, and relaxation oscillations, is presented. It shows where and where not to use the effective α-factor and how to include the spatial hole burning contribution. **(p. 529)**

2:45pm
IWF6 • The microstrip laser, D. A. Tauber, A. L. Holmes Jr., J. E. *Bowers, Univ. California-Santa Barbara;* M. Horita, *KDD R&D Laboratories, Japan;* B. I. Miller, *AT&T Bell Laboratories.* We present, we believe, the first results from a novel laser structure, the microstrip laser. This laser incorporates a thick gold layer beneath the lower cladding for excellent high frequency and high-power performance. The lasers are fabricated in the InGaAsP material system and operate at 1.55 μm. **(p. 533)**

INDEPENDENCE BALLROOM

3:00–3:30pm
Coffee Break/Exhibits

FAIRFAX A

3:30–5:15pm
IWG • Integrated Optics and Micromachining
Robert J. Deri, *Lawrence Livermore National Laboratory, Presider*

3:30pm (Invited)
IWG1 • Integrated-optical nanomechanical systems, W. Lukosz, *Swiss Federal Institute of Technology, Switzerland.* Nanometer-variations of the width of an air gap between waveguide and dielectric bridge or cantilever induce effective-refractive-index changes required to IO device operation. **(p. 538)**

4:00pm
IWG2 • Actuated micromachined microreflector with two degrees of freedom for integrated optical systems, Michael J. Daneman, Norman C. Tien, Olav Solgaard, Kam Y. Lau, Richard S. Muller, *Univ. California–Berkeley.* An electrostatically actuated micromachined microreflector is presented. This device positions an optical beam in two dimensions and is intended for self-aligning optical systems on silicon. **(p. 541)**

4:15pm
IWG3 • Design and fabrication of high-performance silicon micromachined resonant microscanners for optical scanning applications, Meng-Hsiung Kjang, Richard S. Muller, Kam Y. Lau, *Univ. California–Berkeley;* Olav Solgaard, *Univ. California–Davis.* We fabricate microma-chined resonant microscanners that have resonant frequencies of 3 kHz and 28° (optical) maximal scan angles. Barcode reading with use of this microscanner is demonstrated. **(p. 545)**

4:30pm
IWG4 • Photonic integrated circuits for optical displacement sensing, Hans P. Zappe, Daniel Hofstetter, *Paul Scherrer Institute, Switzerland.* A photonic circuit for interferometric optical displacement measurement is presented. The chip has a monolithically integrated DBR laser and detector: sub-100-nm measurement resolution is achieved. **(p. 549)**

4:45pm (Invited)
IWG5 • Widely tunable micromachined optical filters, M. S. Wu, E. C. Vail, C. J. Chang-Hasnain, *Stanford Univ.* We demonstrate a surface-normal GaAs Fabry–Perot filter with 70 nm continuous tuning range requiring 5V tuning voltage. Micromechanical tuning is achieved by electrostatically deflecting the top mirror of the resonator which is freely suspended as a cantilever. **(p. 553)**

FAIRFAX B

3:30–5:00pm
IWH • Symposium on Parallel Optical Interconnects and Avian Technologies
Mark Lowry, *Lawrence Livermore National Laboratory, Presider*

3:30pm
IWH1 • POLO—gigabyte/s parallel optical links for multimedia, computer cluster, and switching systems, Kenneth H. Hahn, Robert E. Wilson, Kirk S. Giboney, Tuochuan Huang, Michael R. Tan, Joseph Straznicky, David W. Dolfi, Waguih Ishak, *Hewlett-Packard Laboratories.* Performance results of the 10-channel POLO transceiver module are presented. The design and assembly of the second generation POLO module are discussed. **(p. 558)**

4:00pm
IWH2 • An easily assembled optical device for coupling single-mode planar waveguides to a fiber array, M. Takaya, M. Kihara, S. Nagasawa, *NTT Access Network Systems Laboratories, Japan.* We develop an easily assembled optical coupling device that consists of two mechanically transferable (MT) type connector plugs and a waveguide chip whose ends are passively positioned in a novel plug component compatible with the MT-type connector. **(p. 561)**

4:15pm
IWH3 • Passive alignment technique for all-silicon integrated optics, R. Moosburger, B. Schuppert, U. Fischer, K. Peterman, *Technische Univ. Berlin, Germany.* A self-aligned fiber pigtailing for silicon-based integrated optics with use of a silicon micro-optical bench is demonstrated. An excess loss of <1.5 dB is achieved for standard single-mode fiber/SOI-chip coupling with passive alignment. **(p. 565)**

4:30pm
IWH4 • Passively aligned pin photodetector array's on silicon waferboard platforms, A. J. Negri, J. F. Mehr, G. A. Duchene, M. J. Tabasky, C. A. Armiento, P. O. Haugsjaa, *GTE Laboratories;* D. Yap, H. P. Hsu, W. W. Ng, D. M. Bohmeyer, H. W. Yen, *Hughes Research Laboratories.* This paper describes the assembly process used in the fabrication of microwave frequency, array optical receiver modules using pigtailed fiber ribbon, and pin photodetector arrays mounted on silicon waferboard platforms. Included in this description are the passive fiber alignment and novel characterization techniques used during assembly. **(p. 569)**

3rd FLOOR REGISTRATION AREA

7:30am–5:30pm
Registration

8:00–10:15am
IThA • Optical System Modeling
Curtis Menyuk, *University of Maryland, Presider*

8:00am (Invited)
IThA1 • Modeling the performance of WDM lightwave systems, Fabrizio Forghieri, *AT&T Bell Labs.* Theoretical modeling and split-step simulations are complementary techniques to understand the performance of WDM lightwave systems. Their strengths and weaknesses are discussed and a synergistic approach to their use is described. **(p. 572)**

8:30am
IThA2 • Feasibility of 40 Gbit/s single-channel transmission over embedded standard fiber, Dirk Breuer, Klaus Petermann, *Technische Univ. Berlin, Germany.* We compare two different dispersion compensating techniques—dispersion compensating fibers and optical phase conjugation—for their suitability for future high-speed TDM systems operating at 40 Gbit/s over embedded standard single-mode fiber. **(p. 576)**

8:45am
IThA3 • Novel tapped delay line transmitter pulse shaping for reducing dispersion penalty of a 10 Gbit/s transmission system, Y. R. Zhou, L. R. Watkins, *Univ. Wales, UK.* A tapped delay line for transmitter pulse shaping is proposed to reduce the chromatic dispersion penalty for a 10 Gbit/s system with standard single mode fiber, allowing a transmission distance of 170 km. **(p. 580)**

9:00am
IThA4 • Optical correlation receiver employing phase modulated optical orthogonal codes, Gordon R. Strachan, S. K. Chaudhuri, *Univ. Waterloo, Canada.* The advent of optical amplifiers allows one to construct optical receivers using optical signal processing elements to simplify, and thus increase the bandwidth of, the remaining electrical components while still maintaining the required sensitivity. In this paper we present a novel line coding scheme which is used to implement an all-optical clock recovery circuit and a correlation receiver bank to further increase the channel data rate. **(p. 584)**

9:15am (Invited)
IThA5 • Multiple length scales and averaging in modelling of long-distance optical fiber transmission, Curtis Menyuk, *Univ. Maryland-BC.* Averaging techniques play a key role in modelling long-distance optical fiber transmission. The history and practical applications of this technique are discussed. **(p. 590)**

9:45am
IThA6 • Dynamics of stimulated Brillouin scattering and its effects on fiber supported millimeter-wave communication systems, S. L. Zhang, J. J. O'Reilly, *Univ. College London, UK.* Dynamics of SBS and its effects on fiber-supported millimeter-wave communication systems are studied. More information is provided compared with steady-state analysis. **(p. 594)**

10:00am
IThA7 • Dispersion and self-phase modulation compensation based on a negative nonlinearity, C. Pare, A. Villeneuve, P.-A. Belanger, *Univ. Laval, Canada;* N. J. Doran, *Aston Univ., UK.* We show how a dispersive medium with a negative nonlinear refractive index might be used to compensate for the dispersion and the nonlinear effects resulting from pulse propagation in an optical fiber. **(p. 598)**

INDEPENDENCE BALLROOM

10:15–10:30am
Coffee Break/Exhibits

FAIRFAX B

8:30–10:00am
IThB • Symposium on Hybrid Packaging of III-V Components to Single-Mode Fibers
Joseph Shmulovich, *AT&T Bell Laboratories, Presider*

8:30am (Invited)
IThB1 • Hybrid integration using silica-on-silicon optical motherboards, Carole Jones, Ken Cooper, Maurice Nield, Robert Waller, Jim Rush, John Collins, Phil Fiddyment, Ian Lealman, *BT Laboratories, UK.* The building blocks for micromachined silicon hybrid optical motherboards are described. Examples of motherboard modules developed at BT Laboratories are also discussed. **(p. 604)**

9:00am
IThB2 • Silica-based optical waveguide devices with novel fiber guide structure for alignment-free fiber coupling, N. Kitamura, S. Mizuta, T. Shimoda, M. Kitamura, S. Nakamura, *NEC Corp., Japan.* Silica-based optical waveguide devices with newly designed fiber guide with multiple Si mesas are demonstrated for alignment-free fiber coupling. Average coupling loss as low as 0.36 dB is achieved from 80 devices. **(p. 608)**

9:15am
IThB3 • An integrated opto-electronic transceiver module, R. E. Scotti, P. J. Anthony, J. V. Gates, *Lucent Technologies/Bell Labs;* J. Goodwin, D. Siebert, *AlliedSignal Aerospace Guidance & Control Systems.* We report on a bi-directional single-mode integrated opto-electronic transceiver module being developed under an ARPA Technology Reinvestment Project (TRP). **(p. 612)**

9:30am
IThB4 • Estimation of waveguide loss of 1.3 μm narrow beam lasers fabricated by selective MOCVD, A. Kasukawa, N. Yamanaka, N. Iwai, *Yokohama R&D Laboratories, Japan.* We present the experimental estimation of waveguide loss and high performance (P_{out} > 50 mW, T_{max} = 120°C, FWHM of FFP angles of 11° X 11°) of 1.3 μm integrated vertically tapered waveguide lasers fabricated by selective MOCVD. **(p. 616)**

9:45am

IThB5 • Low-loss and low-cost fiber coupling of 980 nm laser diodes, J-M. Verdiell, M. Ziari, D. F. Welch, *SDL.* We demonstrate packaging techniques for high-efficiency and passive alignment fiber coupling of 980-nm laser diodes. A passive alignment technique for bonding arrays demonstrates 36% coupling and 70 mW power into a silica on silicon waveguide, and a new circular mode laser design demonstrates less than 1 dB coupling loss to a cleaved fiber. **(p. 620)**

INDEPENDENCE BALLROOM

10:00–10:30am
Coffee Break/Exhibits

FAIRFAX A

10:30–11:45am
IThC • Switches and Modulators
Catherine H. Bulmer, *U.S. Naval Research Laboratory, Presider*

10:30am
IThC1 • Reflective linearized modulator, *G. E. Betts,* F. J. O'Donnell, K. G. Ray, *MIT Lincoln Laboratory;* D. K. Lewis, D. E. Bossi, K. Kissa, G. W. Drake, *Uniphase Telecommunication Products.* A simple linearized modulator is made from a lithium niobate Mach–Zehnder interferometric modulator by attachment of a mirror to one end. An 11 dB improvement in linear dynamic range is demonstrated. **(p. 626)**

10:45am (Invited)
IThC2 • Space switching and wavelength routing with polymer components, Marc Donckers, *Akzo Nobel, The Netherlands.* Polymer space switches are available and wavelength multiplexers are under development. The need for these components grows with the importance of dynamic network reconfiguration and the advent of WDM. **(p. 630)**

11:15am
IThC3 • Low crosstalk polymer waveguide optical switch and switching matrix, N. Keil, H. H. Yao, C. Zawadzki, *Heinrich-Hertz-Institut, Germany.* A polymer waveguide thermo-optic 2 3 2 switch exhibiting very low crosstalk (<2 40 dB) at $\lambda = 1.55$ μm is reported and a 4 3 4 switching matrix with a crosstalk of <2 30 dB is demonstrated. **(p. 633)**

11:30am
IThC4 • Crosstalk-reduced digital optical switch with single electrode designed on InP, H.-P. Nolting, M. Gravert, *Heinrich-Hertz-Institut, Germany;* M. Bachmann, M. Renaud, *Alcatel Alsthom Recherche, France.* The integration of a single electrode mode converter into a digital optical switch to reduce the crosstalk to 2 40 dB is proposed and investigated theoretically. **(p. 637)**

FAIRFAX B

10:30am–12:00m
IThD • Semiconductor Components for Fiber in the Loop
Jun Yu, *Bell-Northern Research, Ltd., Canada, Presider*

10:30am (Invited)
IThD1 • Optical hybrid integration technology using a PLC platform and spot-size converted devices, Yasufumi Yamada, *NTT Opto-electronics Laboratories, Japan.* Optical hybrid integration is promising for achieving a low-cost optical module for fiber-to-the-home (FTTH) applications. A planar lightwave circuit (PLC) platform and a spot-size converted semiconductor device are key elements of this technology. This paper reviews recent progress in hybrid integration toward a low-cost optical module. **(p. 642)**

11:00am
IThD2 • A polarization-insensitive semiconductor optical amplifier with integrated electroabsorption modulators, U. Koren, B. I. Miller, M. G. Young, M. Chien, G. Raybon, T. Brenner, R. Ben-Michael, K. Dreyer, R. J. Capik, *AT&T Bell Laboratories.* We demonstrate a 1.55 μm wavelength multiple quantum well semiconductor optical amplifier integrated with bulk layer electroabsorption modulators and passive waveguide beam expanders at the input and output ports. **(p. 645)**

11:15am
IThD3 • Large-spot laser diodes with stable carrier frequency by an external fiber grating, R. Zengerle, H. Burkhard, R. Ries, Ch. Greus, E. Kuphal, *Deutsche Telekom AG, Germany;* B. Hubner, *Univ. Wurzburg, Germany.* A directly modulated semiconductor laser in InP with integrated spot-size adaptation and butt-coupled fiber grating as wavelength reference is presented for operation at bit rates up to 2.5 Gbit/s. **(p. 649)**

11:30am
IThD4 • Re-engineering the receiver: creating a low cost fiber-in-the-loop component, S. Chandrasekhar, Leda Lunardi, *Lucent Technologies/Bell Laboratories.* Semiconductor devices for use in fiber-to-the-home (FTTH) applications need to be made with low cost, high reliability, large volume, and good performance. The receiver is one crucial component. This talk examines issues related to the photodetector and the preamplifier electronics for viable FTTH applications. Both hybrid and monolithic approaches are discussed and potential areas for engineering are enumerated. **(p. 653)**

11:45 am
Closing Remarks

Monday, April 29, 1996

Plenary Session

IMA 8:30 am-10:00 am
Fairfax A&B

David O. Yevick, *Presider*
Queen's University, Canada

The Challenging Road Towards a High-Performance WDM Technology

T.L. Koch
SDL, Inc.

Technical issues to be addressed include long-term source channel capacity, wavelength stability and reliability, increased demultiplexer capacity, channel selectivity and decreased loss, and choosing among the rich set of technical possibilities for implementing the new functions of wavelength add-drops, wavelength conversion, and even wavelength cross-connect switches. This talk surveys available technological solutions and new emerging approaches, compared on the basis of fundamental design limitations and practical fabrication and implementation issues that affect both performance and cost.

How Can Integrated Optics for Telecom Become a Big Business?

Laura A. Weller-Brophy, 3M Telecom Systems Division
John P. Ryan, Ryan Hankin Kent, Inc.

It has been nearly 30 years since the inception of integrated optics, with Shubert and Harris (1) demonstrating planar waveguides in thin dielectric films. Stewart Miller (2) envisioned a "miniature form of laser beam circuitry... [where] photolithographic techniques may permit simultaneous construction of complex circuit patterns." With integrated optics close on the heels of silicon-based electronics, there was reasonable optimism that the lithographic processing that afforded cost-effective mass production for electronics would do the same for integrated optical circuitry. This vision, while not yet realized, is coming closer to maturation (3-5).

The deployment of optical fiber in the long-haul, distribution, and drop portions of telecommunications networks is driving the development and manufacture of integrated optic components. In long-distance networks, where transmission rates are the highest, fiber optics is the dominant transmission medium. This is based on the superior economics afforded in long-distance telecommunications by the high distance-bandwidth product resulting from the combination of singlemode fiber with long-wavelength laser diodes. Even with lightwave systems historically quadrupling transmission speeds every four years, there are routes where rapidly rising demand is soon to outstrip readily available bandwidth.

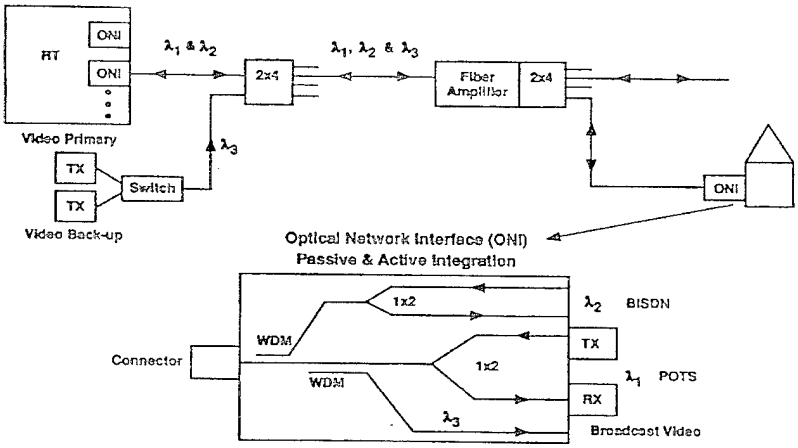
Carriers have several choices to expand upon the 2.5 Gbit/sec capacity of current long-haul networks. These include installing new fiber expanding capacity with TDM devices, and increasing the number of channels with dense WDM (DWDM) systems. Providers such as MCI and Alcatel are exploring the latter, with DWDM systems in trial. MCI currently is deploying four-channel 2.5 Gbit/sec systems to increase capacity by 300 percent. They are working to increase long-haul capacity further through the use of eight channels by the end of the millennium. Alcatel is working on a two-channel, 10Gbit/sec transmission system; the rough equivalent to the eight-channel, 2.5 Gbit/sec system of MCI. Ciena Corp. has introduced a 16-channel DWDM system. In this era of migration to DWDM networks, significant challenges are posed to the technical community that include the need for:

- low-loss dispersion compensation
- low-loss polarization mode dispersion compensation
- optical line amplifiers with flat gain characteristics
- filters and lasers fitting into a standardized wavelength plan for DWDM optical switching
- external modulators for wavelength-stabilized sources
- photonic switches (cross-connects)

To some degree, integrated optics can be used to address these needs with DWDM filters, external modulators, and photonic switches in various degrees of development and production. As one example, DWDM filtering can be achieved using micro-optics, planar waveguide circuits, and fiber-based systems. While arrayed waveguide devices and concatenated Mach-Zehnder circuits have been demonstrated in the laboratory, packaged waveguide devices for multiplexing four or more wavelengths are not yet manufactured in quantity; manufacturing processes remain labor-intensive, and devices are considered "custom". It is unclear whether the DWDM market will expand to support mass production; mass production, with significant factory automation, typically requires individual manufacturing centers to produce 1,000,000 or more devices per year. For deployment in the long-haul networks, there is no one clear integrated waveguide product projected to support mass production of 1,000,000 units/year/manufacturer.

Markets supporting such levels of mass production will most likely be found as fiber is pushed closer to the home. Passive optical access networks such as that illustrated below incorporate waveguide components such as 1XN and 2XN splitters, and WDMs.

Branching Components in Fiber Networks



Ref: Dan Nolan, Corning Inc.

From this figure, it is clear that the most significant emerging market opportunity is the optical network interface (ONI) at the home or pedestal, incorporating both WDM and 1X2 products. In this example, closely following the fiber architecture proposed by NTT, a WDM is used to separate the video and POTS services by wavelength, with the 1X2 allowing bi-directional traffic over a single fiber. Some estimates indicate that the proposed NTT deployment alone will consume in excess of three million waveguide splitters and WDMs annually within the next two to five years. The success of this NTT deployment is expected to spur a wider deployment of the FTTH architecture on a global scale.

The success of this NTT deployment will rest, in part, upon the ability of manufacturers to mass produce integrated optic products with increased efficiency, thereby achieving substantial factory cost reductions. With the major fraction of planar waveguide device manufacturing costs tied to the semi-automated pigtailing, packaging, and testing operations, there is impetus to streamline and automate these processes so to reduce costs. It has been suggested that component price reductions on the order of 80 percent are required to achieve acceptable deployment costs; the 80 percent reduction spans the active and passive waveguide devices, fiber terminations, fiber handling, opto-electronics, etc.

Integrated optic component manufacturers stand to gain significantly from this accelerated deployment of fiber deeper into the access network. From the perspective of the integrated optics community, FTTC and FTTH are the drivers to support scale-up of integrated optic components such as splitters, WDMs, integrated transceivers, integrated transmitters/modulators, and wavelength filtering products.

This paper will look at the international market forces supporting the scale-up of volume production of integrated optic components, and at the implications for device manufacturers, vendors, and technology developers. We also examine the rationale for integrated optics devices, considering the trade-offs in device performance and cost (5).

References:

1. R. Shubert and J. H. Harris, "Optical surface waves on thin films and their application to integrated data processors," IEEE Trans. Microwave Theory and Techniques MTT-16 (12), 1048-1054 (1968).

2. S. E. Miller, "Integrated Optics: An Introduction," Bell Sys. Tech. Journal 48 (7), 2059-2069 (1969).

3. Statistics of Communications Common Carriers. Federal Communications Commission. (1994/1995)

4. C. De Bernardi, "Future developments for integrated optics," CSELT Technical Reports 23 (3), 315-329. (1995)

5. M. Erman, "Prospects for Integrated Optics in Telecom Applications," Proceedings of the 7th European Conference on Integrated Optics, Delft, the Netherlands. April 3-6, 1995. pp 27-32.

6. C. Joffrain, "The challenge of transition to fibre in the loop," Proceedings of the 5th Conference on Optical Hybrid Access Networks. Montreal Quebec, Canada. September 7-9, 1993. pp. 4.13.01 - .05.

Monday, April 29, 1996

Numerical Methods for Guided Wave Optics

IMB 10:30 am-12:00 m
Fairfax A

Shunji Seki, *Presider*
NTT Opto-electronics Laboratories, Japan

Efficient 3-Dimensional Vector-Wave Analysis of Wavelength Multiplexers Using Arrayed-Waveguide Gratings

W.-K. Wang and F. Tong
IBM Thomas J. Watson Research Center, P.O. Box 704, Yorktown Heights, NY 10598
Phone: (914) 784-7718, FAX: (914) 784-6225, E-mail: wangwk@watson.ibm.com

The NxN arrayed-waveguide grating (AWG) multi/demultiplexer [1] has become one of the key integrated-optic components in wavelength-division multiplexing (WDM) communication networks. The reported methods [2]-[4] for the design and performance simulation of AWGs have so far been limited to 2-D scalar-wave analysis using the effective-index method in the vertical direction. In this paper we present a computationally efficient 3-D vector-wave technique for analyzing and designing AWGs including the effects of waveguide-slab junction coupling losses and TE and TM polarizations. Neglecting the effect of waveguide bending, and the loss and mode coupling in the funnel sections, the AWG shown in Fig. 1(a) will be modeled by the equivalent circuit of Fig. 1(b), where the input and output star couplers S and $\bar{S}$ are interconnected by M_{awg} arrayed waveguides with ΔL the incremental length difference. The transmission coefficient T_{ij} of the AWG between waveguide input-i and output-j is thus given within a constant phase term by

$$T_{ij} = \sum_{k=1}^{M_{awg}} S_{ik}\, \bar{S}_{kj}\, e^{-j\beta_c k \Delta L} \tag{1}$$

where β_c is the channel-waveguide propagation constant. The star coupling coefficients S_{ik} and $\bar{S}_{kj}$ are calculated in the geometry of Fig. 1(c). To estimate the waveguide-slab junction coupling loss, suppose the incident waveguide mode is either quasi-TE or quasi-TM (referred to simply as TE and TM in the following) and the slab region in Fig. 1(c) also supports a single TE or TM surface mode vertically. The channel and slab waveguide mode characteristics are first analyzed by the rigorous vector-wave mode-matching method (MMM) [5]. The waveguide mode, when launched into the slab, will predominantly excite the slab surface wave of the same polarization along with a continuum of radiation fields which escape vertically away from the slab near the junction. Since only the slab surface waves can propagate and be coupled into various output waveguides, we can take a projection of the total incident fields on the dominant surface-wave term (assuming negligible reflection), and obtain the aperture field distribution at $z=0^+$ as

TM
$$E_y^a(x,y) = E_y^a(x)\phi_{11}(y)/n_1^2(y),\quad E_y^a(x) = \begin{cases} V_{11}(x) & |x| \le w/2 \\ \sum_{m=1}^{N_{exp}} C_m^{TM} V_{2m}(x), & |x| > w/2 \end{cases} \tag{2.1}$$

TE
$$H_y^a(x,y) = H_y^a(x)\varphi_{11}(y),\qquad H_y^a(x) = \begin{cases} I_{11}(x), & |x| \le w/2 \\ \sum_{m=1}^{N_{exp}} C_m^{TE} I_{2m}(x), & |x| > w/2 \end{cases} \tag{2.2}$$

where $n_i(y)$ is the piece-wise constant material index profile of region-i, $\phi_{im}(y)$ and $\varphi_{im}(y)$ are respectively the E-type and H-type slab mode functions of order m for that region, and $V_{im}(x)$ and

$I_{im}(x)$ are the corresponding x-directional wave function [5]. The projection ratios C_m^{TM} and C_m^{TE} are given by

$$C_m^{TM} = \int \frac{1}{n_2^2(y)} \phi_{2m}(y)\phi_{11}(y)dy$$
$$C_m^{TE} = \int \varphi_{2m}(y)\varphi_{11}(y)dy \qquad (3)$$

The aperture field distributions (2.1) and (2.2) take into account the junction coupling loss from the 3-D channel-waveguide mode to the 2-D slab surface waves. According to the theory of aperture-antennas [6], the far fields resulting from the aperture field in (2.1) or (2.2) can be expanded in a plane-wave spectrum propagating in different directions. When expressed in the cylindrical coordinates associated with the input waveguide, it can be shown by using the stationary phase technique of integration that the y-component of far fields for TM incidence is

$$E_y(r,\theta,y) = \sqrt{\frac{n_s}{r\lambda}}\, e^{-j(\beta_s r-\pi/4)} \cos\theta\, F(\beta_s \sin\theta)\, \phi_{11}(y)/n_1^2(y) \qquad (4)$$

with F the Fourier transform of the aperture fields given by

$$F(\beta_s \sin\theta) = \int_{-\infty}^{\infty} E_y^a(x)\, e^{jx\beta_s \sin\theta} dx \qquad (5)$$

where β_s is the slab surface-wave propagation constant and $n_s=\lambda\beta_s/2\pi$ Similar expressions for TE incidence follow by changing E_y to H_y and $\phi_{11}(y)/n_1^2(y)$ to $\varphi_{11}(y)$ in (4) and (5). The coupling between the input and output waveguides arranged in the far-field zone of each other, as shown in Fig.1(c), can be derived from the Lorentz reciprocity theorem

$$S = \frac{p}{4\pi}\sqrt{\frac{\lambda}{n_s R}}\; e^{-j(\beta_s R-\pi/4)}\, F_i(\beta_s \sin\theta_i) F_o(-\beta_s \sin\alpha_o) \cos\theta_i \cos\alpha_o \qquad (6)$$

where $p=-\omega\mu_o$ for TE and $\omega\varepsilon_o$ for TM. The procedure described above can be applied to both the input and the output star couplers. However, for most reported designs of AWGs, the input star and output star couplers are identical and symmetrically arranged. Therefore we have $S_{ik}= \bar{S}_{ki}$.

The present method of analysis is first applied to a 16x16 AWG with a 7x7 μm core of a core-cladding index difference $\Delta n=0.75\%$. The AWG is designed for $\Delta\lambda=0.8$ nm with a diffraction order M=118 (other structural parameters are given in Fig.2). For this waveguide structure, the convergence studies associated with the MMM confirm that, by using 20 $TE^{(y)}$ and 20 $TM^{(y)}$ slab basis mode functions (i.e. $N_{exp}=20$ in (2.1) and (2.2)), the channel-waveguide mode effective indices of both polarizations converge to within 5×10^{-7} corresponding to the convergence of star coupling coefficient better than 0.01 dB. The required number of arrayed waveguides, $M_{awg}=101$, is determined by the coupling efficiency of the input star. Under these conditions, the AWG transmission coefficients between the center input and various outputs are shown in Fig.2 versus wavelength. The data is essentially identical for both TE and TM polarizations due to low Δn and square core. The calculated center wavelength (at the peak of T_{00}) is $\lambda_{00}=1555.87$ nm in contrast to the measured data $\lambda_{00}=1554.7$ nm [7], the difference can be attributed to a lower Δn in the fabricated waveguide. (Note in [7] the effect due to stress birefringence was eliminated using the polyimide waveplate) The channel spacing shown in Fig.2 is 0.8 nm as designed. The

calculated minimum loss of T_{00} is 0.7 dB as compared to the measured data ~1.7 dB [7] (excluding the fiber coupling loss and loss due to the waveplate), which corresponds to an excess loss of 1 dB. When the measured data and the simulated results are overlaid at the point of minimum loss, very good agreement is seen down to -25 dB. The measured higher crosstalk can be caused by fabrication phase errors [8]. The effect of loss imbalance [9], as also shown in Fig. 2, is plotted in Fig.3 for the transmission T_{ij} between any input-i and any output-j evaluated at their pass wavelengths λ_{ij}. For any fixed input or fixed output, the loss imbalance between the center and the marginal waveguides is about 2.8 dB, which also agrees with the measured data 2-3 dB.

To illustrate the effect of polarization dependence of AWGs, the present analysis is also applied to the design of a 28x28 AWG with high-delta waveguides (Δn=5%). For the structural parameters given in Fig.4, the transmission coefficients T_{0j} for j= -1,0, and 1 are plotted for both TE and TM polarizations. There is about 0.43 nm shift between TE and TM pass wavelengths, which confirms that, in additional to the process-dependent stress birefringence [7], the effect of waveguide shape birefringence is not negligible for AWG devices using high-delta waveguides.

In summary, we have presented an efficient 3-D analysis and design tool for AWG devices using the vector-wave mode-matching method and the theory of aperture antennas. The simulated transmission characteristics, including the loss imbalance, for a low-delta 16x16 AWG, agree well with the measured data. In addition, the effect of waveguide shape birefringence on the polarization wavelength shift in an AWG with high-delta waveguide is illustrated.

The authors wish to thank H. Takahashi for many useful discussions. This work is funded by ARPA contract MD A972-95-C-0001.

References

[1] For an overview of recent progress in AWG-based WDM devices, see B. H. Verbeek and M. K. Smit, "Phased array based WDM devices," in *Dig. 21st Eur. Conf. on Opt. Comm., Brussels, Belgium, Proc. ECOC'95*, pp. 195-202.

[2] C. Dragone, "Efficient NxN star couplers using Fourier optics," *J. Lightwave Technol.*, vol. 7, no. 3, pp. 479-489, Mar. 1989.

[3] C. Dragone, "An NxN optical multiplexer using a planar arrangement of two star couplers," *IEEE Photon. Technol. Lett.*, vol. 3, no. 9, pp. 812-815, Sept. 1991.

[4] H. Takahashi, K. Oda, H. Toba, and Y. Inoue, "Transmission characteristics of arrayed waveguide NxN wavelength multiplexer," *J. Lightwave Technol.*, vol. 13, no. 3, pp. 447-455, Mar. 1995.

[5] W.-K. Wang, H. J. Lee, and P. J. Anthony, "Planar silica-glass optical waveguides with thermally induced lateral mode confinement," to be published in *J. Lightwave Technol.*

[6] R. H. Clarke and J. Brown, *Diffraction Theory and Antennas,* New York: John Wiley & Sons, 1980.

[7] Y. Inoue, Y. Ohmori, M. Kawachi, S. Ando, T. Sawada, and H. Takahashi, "Polarization-insensitive arrayed-waveguide grating multiplexer with polyimide waveplate as TE/TM mode converter," in *Dig. Conf. Integ. Photon. Res., OSA,* Feb. 1994, paper ThE3.

[8] K. Takada, Y. Inoue, H. Yamada, and M. Horiguchi, "Measurement of phase error distributions in silica-based arrayed-waveguide grating multiplexers by using Fourier transform spectroscopy," *Electron. Lett.* vol. 30, no. 20, pp. 1671-1672, Sept. 1994.

[9] O. Ishida and H. Takahashi, "Loss-imbalance equalization in arrayed-waveguide-grating (AWG) multiplexer cascade," *J. Lightwave Technol.*, vol. 13, no. 6, pp. 1155-1163, 1995.

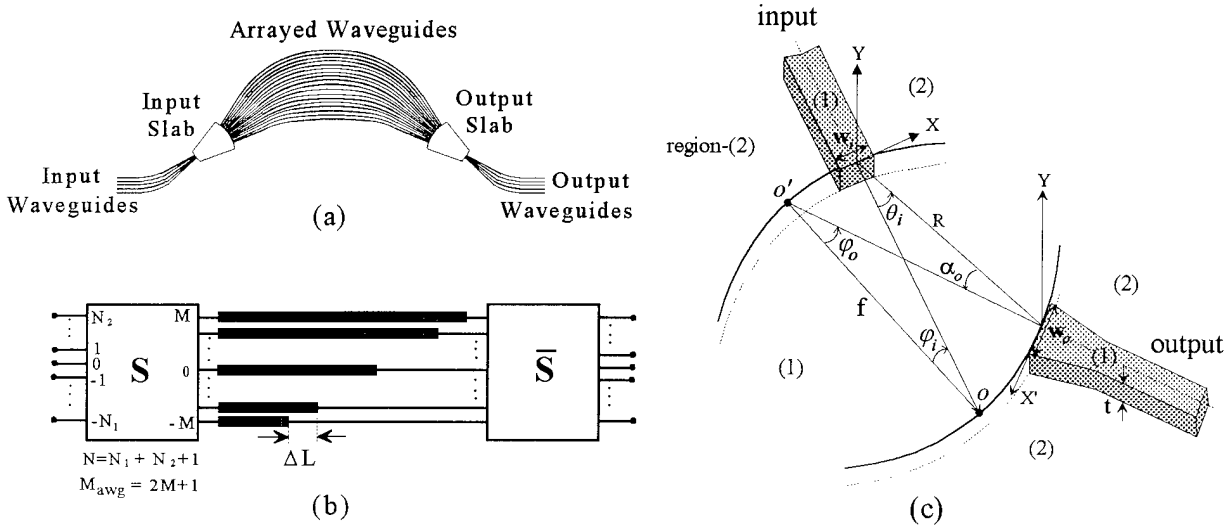


Fig.1 Schematics illustrating (a) the waveguide structures of a typical NxN AWG, (b) the equivalent circuit, and (c) the geometry of coupling through the slab region.

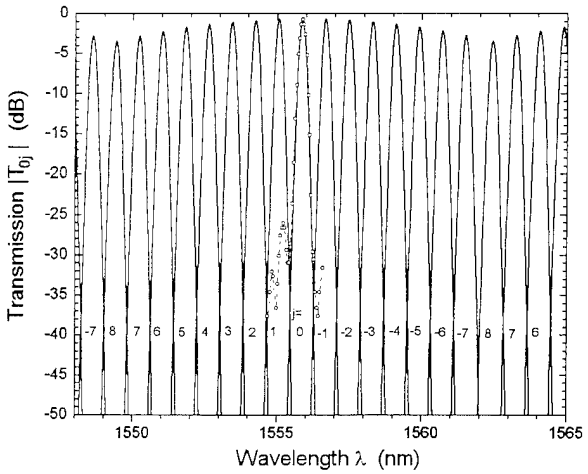


Fig.2 Transmission characteristics T_{0j} of a 16x16 AWG. Solid lines - this analysis, dashed line - measured data from [7]. Input/output waveguides: Δn=0.75%, core 7x7 μm; slab: focal length=9381 μm, waveguide spacing=25 μm; arrayed waveguides: ΔL=126.46 μm, M_{awg}=101, grating order=118.

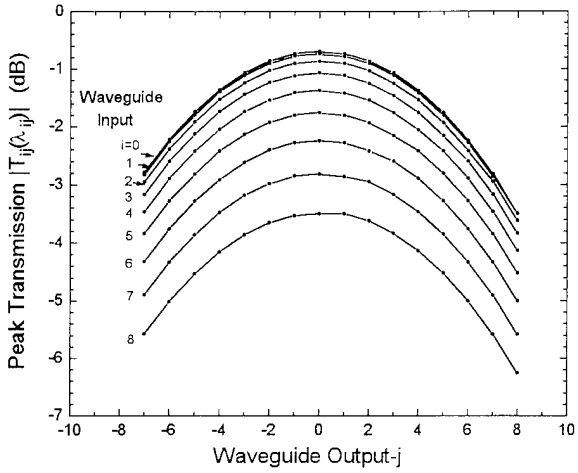


Fig.3 The peak transmission T_{ij} at their pass wavelengths λ_{ij} for the 16x16 AWG of Fig.2.

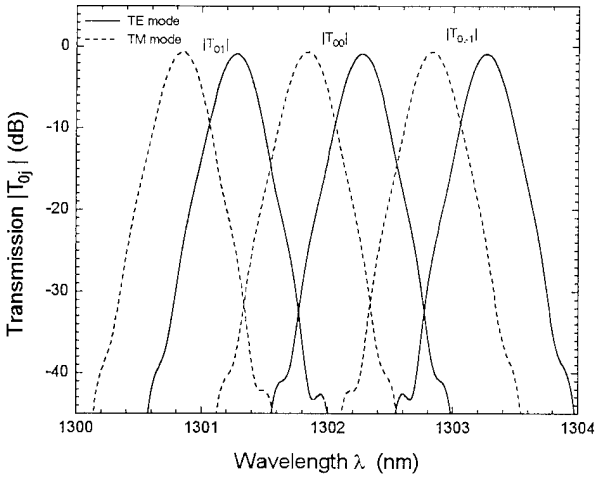


Fig.4 TE and TM transmission characteristics T_{0j} (j=-1,0, and 1) of an AWG with high-delta waveguide. Input/output waveguides: Δn=5%, core 1.2x1.5 μm; slab: focal length=2179 μm, waveguide spacing=8 μm; arrayed waveguides: ΔL=37.14 μm, M_{awg}=201, grating order=42.

Vectorial Analysis of Optical Dielctric Waveguide Bends using Finite-Difference Method

Sangin Kim and Anand Gopinath

University of Minnesota
Department of Electrical Engineering
4-174 EE/CSCI Bldg. 200 Union ST SE
MPLS., MN 55455

I. Introduction

The design of optical dielectric waveguide bends is important in integrated optical circuits. The bends may be used to turn light beem for the desired angle and route it to the desired location. The bends have several advantages over deep-etched turning mirrors: they are easy to fabricate and can be used in buried waveguide structures where mirrors cannot be built. For these reasons, accurate calculation of the loss of optical dielectric waveguide bends is important

Since Marcatili published the first theoretical paper on bends in optical dielectric guides in 1969 [1], a large number of methods have been developed to analyze waveguide bends. Heiblum and Harris [2] used the conformal transformation method in which the curved waveguide is translated into an equivalent straight waveguide with a transformed index profile. Gu *et al.* [3], analyzed a curved ridge waveguide using the method of lines(MoL). The scalar finite-element method (SFEM) has been also applied to curved waveguides [4]. Vectorial analysis of waveguide bends has been performed using method of lines by Pregla *et al.* [5], [6] and vectorial analysis of circularly curved channel waveguides with rectangular cross-section has been done using source-type integral equation method by Blok *et al.* [7].

In this paper, the finite-difference method, which has been widely used for the analysis of straight waveguides, was applied to the full vector analysis of waveguide bends. To construct the boundary conditions at the interfaces where the index profile is discontinuous, the method used by Stern [8] was extended.

II. Formulation

The configuration of the bend is depicted in fig. 1. From Maxwell's equations in the cylindrical coordinates, two Helmholtz equations are derived assuming the lightwave propagates in the θ direction:

$$r2\frac{\partial 2\psi}{\partial r2} + r\frac{\partial \psi}{\partial r} + r2\frac{\partial 2\psi}{\partial z2} + r2k2n2\psi + 2r2\frac{\partial \phi}{\partial z} = \nu 2\psi \qquad (1)$$

$$r2\frac{\partial 2\phi}{\partial r2} + r\frac{\partial \phi}{\partial r} + r2\frac{\partial 2\phi}{\partial z2} + r2k2n2\phi = \nu 2\phi \qquad (2)$$

where $\Psi = rE_r$, $\phi = E_Z$ and ν is the complex angular propagation constant. In deriving above equations, E_θ was eliminated using the divergence equation. By using the finite-difference scheme, above two equations are discretized and a matrix eigenvalue equation is obtained:

$$AX = \nu 2X \qquad (3)$$

where X is an eigenvector which consists of field values at each node in the calculation domain.

III. Boundary conditions

The finite-difference scheme was modified to satisfy the boundary conditions at the internal dielectric interfaces. At all internal interfaces, the continuity of E_θ, H_θ, and the other tangential component of the electric field, and the discontinuity of the normal component of the electric field, were satisfied. The external boundary of the calculation domain was located far from the guiding region and it is assumed the that tangential component of the electric field at the external boundary is zero. A variable spacing mesh was used for this purpose.

IV. Numerical method

To solve the matrix eigenvalue problem (3), the shifted inverse power method [9] was used, in which any desired eigenvalue and corresponding eigenvector can be obtained.

V. Results

The method developed in the above sections was employed to analyze the waveguide bend whose cross section is shown in fig. 1. A guiding layer, GaAs, is on a thick $Al_{0.15}Ga_{0.85}As$ layer. At the wavelength of 1.15 μm, the refractive indexes of GaAs and $Al_{0.15}Ga_{0.85}As$ are 3.44 and 3.35 respectively. Fig. 2 shows the contour plots of the r component of the electric field of waveguide bend whose radii of curvature are 200 μm and 500 μm. We can see that the center of the mode of waveguide shifted to the outer edge of bend in r direction, and the smaller the radius of curvature, the further the center shifts.

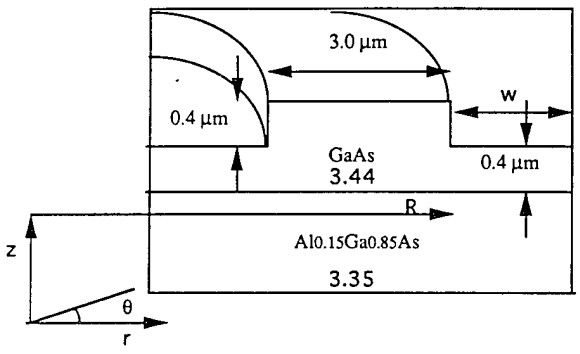


Figure 1 Configuration of waveguide bend

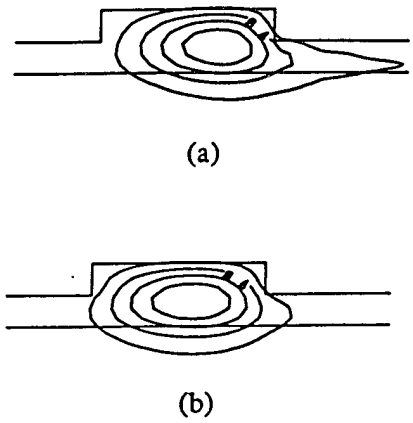


Figure 2 Contour plots of field
(a) contour plot of E_r for R = 200μm
(b) contour plot of E_r for R = 500μm

Effective index of waveguide bend can be defined as

$$n_{eff} = Re(\nu)/(k_0 R) \qquad (4)$$

where k_0 is wave number in free space, $2\pi/\lambda$, and R is the radius of curvature of bend. As shown in fig.1, R is defined as the radius of the outer edge of the waveguide bend. Calculated effective index is plotted as a function of radius of curvature in fig. 3, and it is found that as R increases, effective index tends to that of straight waveguide asymptotically.

The loss of 90° bend due to radiation is obtained by the equation:

$$L_{rad} = 20 \log_{10} \{\exp[(\pi/2)\mathrm{Im}(\nu)]\}. \qquad (5)$$

The radiation loss vs. radius of curvature is plotted in fig. 4. The loss of same structure was calculated by Gu *et al.* [3] and Yamamoto *et al.* [4]. The loss calculated by Gu *et al.* [3] is plotted with our result in fig. 4. Similar results were also reported by Yamamoto *et al.* [4]. For large radius of curvature (R > 200 μm), our result agrees very well with Gu's. For the radius smaller than 200 μm, our calculated loss shows some difference from Gu's, and we surmise that the difference may be due to the external boundary condition, but we are uncertain about this, as changing the distance between the external boundary and the bend edge does not show any difference in radiation losses. As shown in fig. 4, the loss for quasi-TE mode is higher than that for quasi-TM mode. This polarization dependence of the loss arises from the tighter confinement of the field in z direction than in r direction for the waveguide structure considered here.

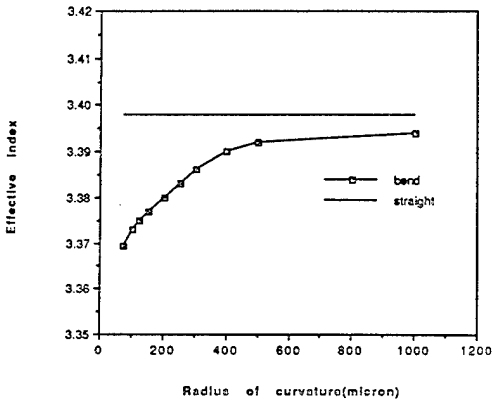


Figure 3 Effective index vs. curvature

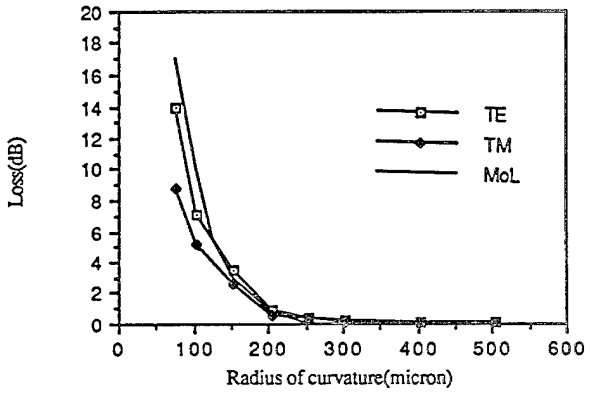


Figure 4 radiation loss vs. curvature

The transition losses of bends due to mode mismatch at various radii of curvature were calculated from overlap integral. The overlap integrals for two differently polarized inputs, quasi-TE mode and quasi-TM mode, were done separately. Since we assumed both ends of the 90° bend are connected with straight guides, the overlap integral was performed twice. The structure considered here is a multi-mode waveguide. For the convenience of calculation, the overlap integral was done using only the fundamental mode of the straight waveguide. The minimized transition loss with optimal offsets at the ends of bend was calculated from the shifted overlap integral. The transition loss and the minimized transition loss with optimal offset was plotted in fig. 5

VI. Conclusion

In this paper, a full vectorial analysis of optical dielectric waveguide bends using the finite-difference method has been developed. The formulation was based on electric field components, E_r and E_z. To set up the boundary conditions at each dielectric interface, the continuity of E_θ, H_θ, and the tangential component of electric field, and the discontinuity of the normal component of electric field were satisfied. The field distributions of the bend shown in fig. 1 were calculated with various radii of curvature and losses were also calculated. By applying optimal offsets at the conjunctions between the straight waveguide and the waveguide bend, we minimized the transition loss.

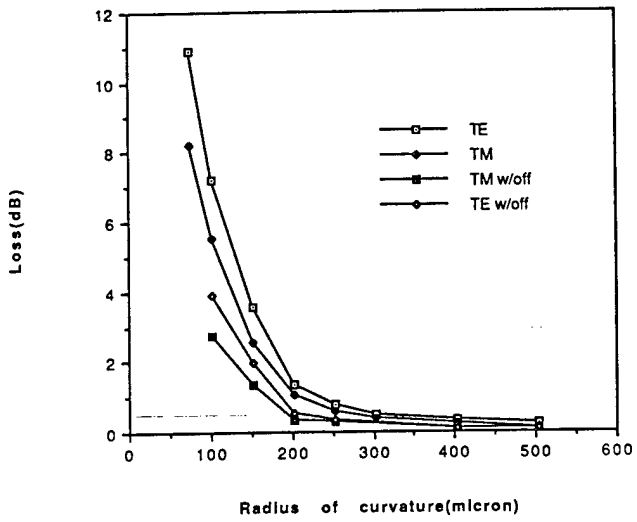


Figure 5 Transition loss vs. curvature

VII. References

[1] E. A. J. Marcatili, "Bends in optical dielectric guides," Bell System Tech. J., vol. 48, pp. 2103-2132, 1969.

[2] M. Heiblum and J. H. Harris, "Analysis of curved waveguides by conformal transformation," IEEE J. Quantum Electron., vol. QE-11, pp. 75-83, 1975.

[3] J. Gu, P. Besse, and H. Melchior, "Method of lines for the ananlysis of the propagation characteristics of curved optical waveguides," IEEE J. Quantum Electron., vol. QE-27, pp. 531-537, Mar, 1991.

[4] T. Yamamoto and M. Koshiba, "Numerical analysis of curvature loss in optical waveguides by finite-element method," J. Lightwave. Technol., vol. 11, pp. 1579-1583, Oct. 1993

[5] W. Pasoher, R. Pregla, "Analysis of curved optical waveguides by the vectorial method of lines," Proc. Int. Cnf. Integrated Optics Optical Fiber Commun., Paris, pp. 237-240, 1991

[6] W. Pasoher, R. Pregla, "Vectorial analysis of bends in optical strip waveguides by the method of lines", Radio Sci, vol. 28, no. 6, pp. 1229-1233, 1993.

[7] Harrie J. M. Bastiaansen, J. Michiel van der Keur, and Hans Blok, "Rigourous, full-vectorial source-type integral equation analysis of circularly curved channel waveguides," IEEE Microwave Theory and Tech., vol. 43, no. 2, pp. 401-409, Feb. 1995.

[8] M. S. Stern, "Semivectorial polarised finite difference method for optical waveguides with arbitrary index profiles," IEE Proc., vol. 135, no. 1, pp. 56-63, Feb. 1988.

[9] J. Wilkinson, "The algebraic eigenvalue problem": Clarendon Press, 1965.

A Full Vector Beam Propagation Method for Bent Channel Waveguides

Michael Rivera
Optical Sciences Center, University of Arizona, Tucson, AZ 85721, USA
Tel: (520)621-8261 Fax: (520)621-4358

I. INTRODUCTION

In the past bent channel waveguides have been modeled with the effective index approximation and the scalar wave equation in the large radius limit [1] as well as using a semivector formulation [2]. Unfortunately, these approaches have obtained limited success. In most cases only qualitative results can be extracted from these models when studying curved channel waveguides. Therefore, more sophisticated numerical techniques are required to predict the quantitative behavior of bent channel waveguides in several, more complicated applications where the vectorial nature of the field may play a role. Examples of some of these applications are semiconductor and polymer ring and microdisk lasers [3,4].

The use of the scalar wave equation in cylindrical coordinates has been demonstrated to be accurate in the numerical determination of both the field profiles and the loss rates [5]. Since current research has led to regions of interest which are well beyond the large radius limit accuracy will certainly become an issue in the near future. With this in mind, implementing a version of the full vector wave equation will certainly become vital for several applications. In this paper a full vector beam propagation method for bent channel waveguides based on Bi-Conjugate Gradient method is presented.

II. THE WAVE EQUATION

In this paper we will use the full vector wave equation in cylindrical coordinates. As it stands this wave equation is not easily reduced into a form that is dependent solely on the transverse components as we would have it in a straight z-invariant structure; coupling from the longitudinal component is explicit in the equations. Fortunately this explicit dependence can be factored out by using other relations [6]. In addition, it is not in a form that is easy to implement numerically. A format that is more appropriate is what is known as the local coordinate system [6] (Figure 1, top view of waveguide). Using the following coordinate transformations: $r=R+x$, $s=R\theta$ and $z=y$, results in the following set of equations in the slowly varying envelope approximation.

X-Component

$$\left\{\nabla_t^2+\left(\frac{3\kappa}{t_s}\right)\frac{\partial}{\partial x}+k_o^2 n^2-\frac{k^2}{t_s^2}+\frac{\kappa^2}{t_s^2}\right\}E_x$$

$$=-\left(\frac{2\kappa}{t_s}+\frac{\partial}{\partial x}\right)[\vec{E}_t\cdot\nabla\ln(n^2)]-\frac{2\kappa}{t_s}\frac{\partial E_y}{\partial y}-\frac{2ik}{t_s^2}\frac{\partial E_x}{\partial s}$$

Y-Component

$$\left\{\nabla_t^2 + \left(\frac{\kappa}{t_s}\right)\frac{\partial}{\partial x} + k_o^2 n^2 - \frac{k^2}{t_s^2}\right\} E_y = -\frac{2ik}{t_s^2}\frac{\partial E_y}{\partial s} - \frac{\partial}{\partial y}\left[\vec{E}_t \cdot \nabla \ln (n^2)\right]$$

where x is measured from the center of the waveguide and R is the radius of curvature, $\kappa = 1/R$ and $t_s = 1 + \kappa x$.

Advantages to this format are: (1) the numerical window can be reduced to within a few microns around the center of the waveguide and (2) the path of propagation is along the center of the waveguide which will give a true representation of the field cross section at every stage.

III. THE ITERATIVE METHOD AND NUMERICAL IMPLEMENTATION

The method used to solve the two coupled equations for bent channel waveguides is the Bi-Conjugate Gradient Method (BiCG). This method follows from a long line of iterative methods used to solve the general problem $\mathbf{Ax}=\mathbf{b}$. It first assumes a solution $\mathbf{x} = \mathbf{x}_0$. Then by constructing a subset of basis vectors at each iteration, based on the residual vector $\mathbf{r} = |\mathbf{Ax}-\mathbf{b}|$, an improved solution to $\mathbf{x} = \mathbf{x}_n$ results. More basis vectors can used to extrapolate what is the actual solution to within a specified tolerance.

For the case at hand, the matrix **A** is a complex non-Hermitian matrix for which there are few iterative methods that will converge. I specifically use BiCGstab, an algorithm created by Van Der Vorst [7] and modified by Gutknecht [8] for complex matrices. The reason is that it has been found to stable for many different types of problems involving matrices of this kind but one underlying disadvantage is the fact that it converges more slowly than other routines.

The numerical implementation of this set of coupled equations is straightforward. A set of linear difference equations results using a modified Crank-Nicolson scheme, with a variable stablity parameter ($0.5 \le \Gamma \le 1.0$), to finite difference the equations. The matrix that is obtained is a sparse banded matrix with 21 non-zero diagonals in its most general form. The location of the main component elements and the coupling terms are shown on the matrix **A** (Fig. 2). The column matrix next to **A** shows the ordering of the elements that make up the field points for both components at level $n+1$. The elements of column vector **b** are defined by the values of the field at the previous level, n.

IV. RESULTS AND DISCUSSION

In Fig. 3 a set of intensity profiles for both polarizations, E_x and E_y, showing the effects of strong bending are present. The calculations are done for a ridge waveguide width $W = 2.0\mu m$, height $H = 1.1\mu m$ and depth $d = 0.2\mu m$, with $n_s = 3.34$, $n_f = 3.44$ and $n_c = 1.0$. The computational window is $4.0\mu m$ by $4.0\mu m$ symmetric around (0,0) and number of points used are $N_x = N_y = 81$. Other parameters are: $\lambda = 1.50\mu m$, $\Delta z = 0.1\mu m$. A stability parameter of $\Gamma = 0.7$ is used.

For each of the polarizations straight and curved waveguide profiles are shown; $R = \infty$ ($\kappa = 0\mu m^{-1}$) and $R = 100\mu m$ ($\kappa = 0.01\mu m^{-1}$). Similar plots for larger radii have been found in the case of strong curvature, $\kappa \ge 0.002\mu m^{-1}$. A simple observation that can be made from looking at the curved

waveguide plots is that the outgoing radiation escapes through the regions of lower index contrast. Knowledge of this may suggest how bent channel waveguides should be designed to reduce losses.

In minor component plots for the curved waveguide there is strong coupling of power into the other polarization showing that the minor component increases drastically in power due to the bending. For the E_x and E_y polarizations the ratios of the field amplitudes (minor/main) are 0.218 and 0.23, respectively. We also notice an obvious breakdown in symmetry of the minor components, going from an asymmetric field to one that is somewhat symmetric with respect to the index profile. For curved waveguides with several modes this would lead to mode conversion (coupling to higher order modes) into the other polarization which could be critical in some applications. These effects would never be predicted using a scalar or semivector formulation.

REFERENCES

[1] K.T. Koai and P.-L. Liu, *J. of Lightwave Tech.*, 7, 1016-1022, (1989) and references therein.

[2] P.-L. Liu and B.-J. Li, *IEEE Photon. Tech. Lett.*, 3, 913-915, (1991).

[3] R.S. Burton, *Fabrication Technologies and Modeling of Integrated Ring-Lasers and Modulators*, PhD Dissertation, Carnegie Mellon University, (1994).

[4] M. Kuwata-Gonokami *et al.*, *Optics Lett.*, **20**, 2093-2095, (1995).

[5] M. Rivera, *J. of Lightwave Tech.*, **13**, 233-238, (1995).

[6] Y. Cheng, W. Lin and Y. Fujii, *J. of Lightwave Tech.*, **8**, 1461-1469, (1990).

[7] H.A. Van der Vorst, *SIAM J. Sci. Statist. Comput.*, **13**, 631-644, (1992).

[8] M.H. Gutknecht, *SIAM J. Sci. Comput.*, **14**, 1020-1033, (1993).

ACKNOWLEDGMENTS

This work is supported by the Optical Data Storage Center, the University of Arizona and the Advanced Technology Program (ATP) of the U.S. Department of Commerce through a grant to the National Storage Industry Consortium (NSIC).

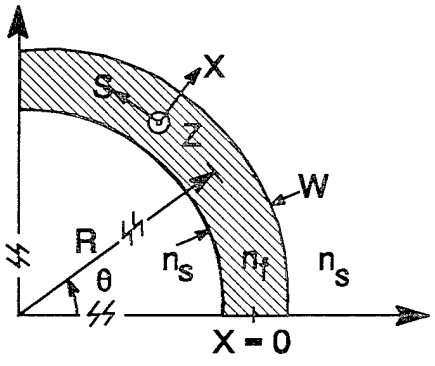


Figure 1

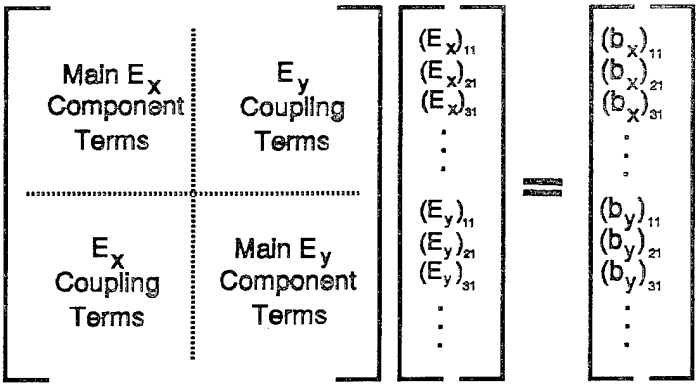


Figure 2

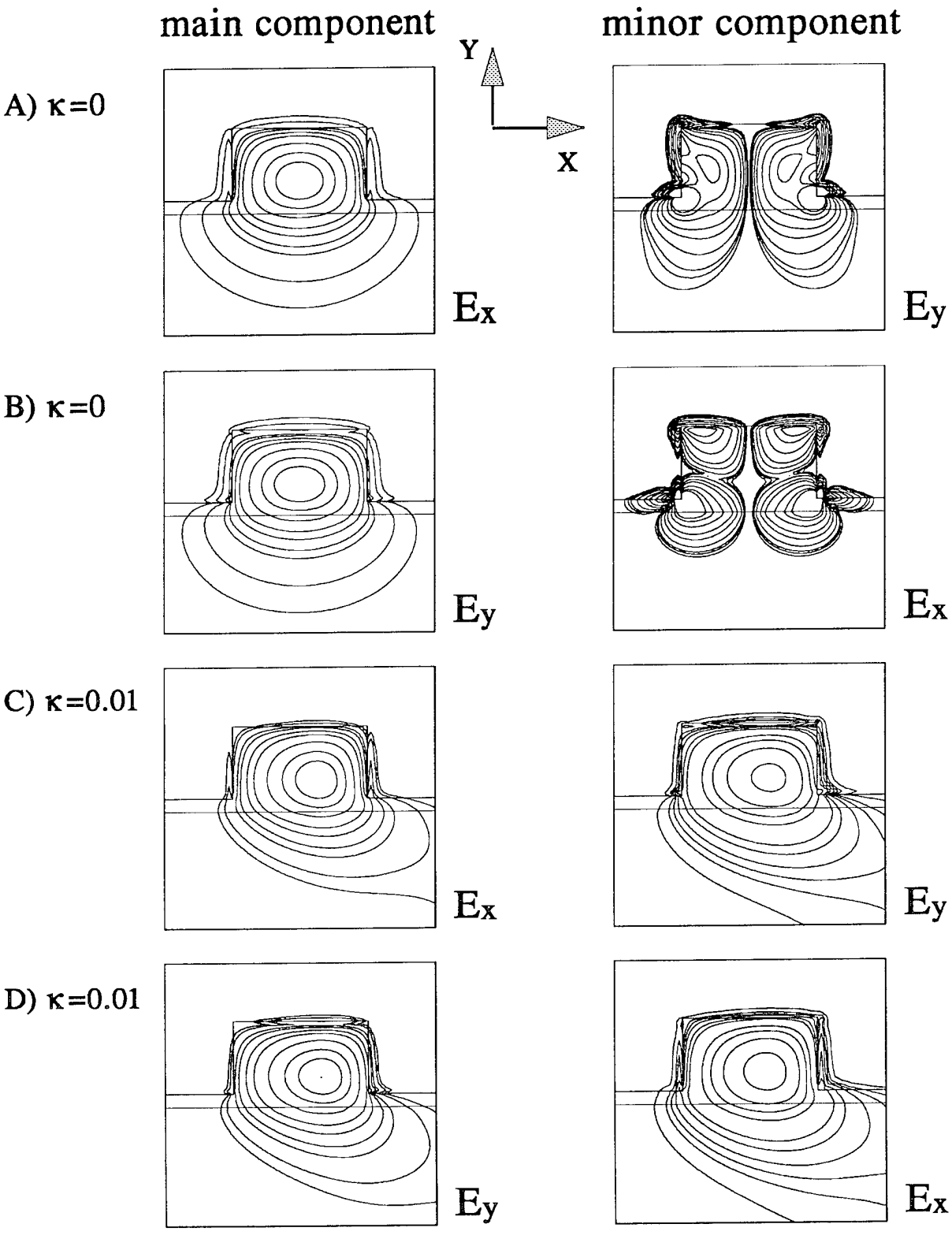


Figure 3. Intensity plots for straight, A and B, and curved, C and D, waveguides. κ in μm^{-1}.

Numerical Implementation of the Bremmer Coupling Series

Mattheus J.N. van Stralen
Laboratory of Electromagnetic Research, Delft University of Technology, Mekelweg 4, P.O.Box 5031, 2600 GA Delft, The Netherlands, Phone: ++31-15 728 4429, Fax: ++31-15 728 6194, E-mail: M.J.N.vanStralen@ET.TUDelft.NL,

Maarten V. de Hoop
Center for Wave Phenomena, Colorado School of Mines, Golden, CO 80401-1887, USA, Phone: (1) 303 273 3933, Fax: (1) 303 273 3478,

Hans Blok
Laboratory of Electromagnetic Research, Delft University of Technology, Mekelweg 4, P.O.Box 5031, 2600 GA Delft, The Netherlands, Phone: ++31-15 728 6291, Fax: ++31-15 728 6194,

Introduction In designing optical communication network devices flexible computational methods are needed to model optical waveguiding structures. Existing methods, like the beam propagation method (BPM), lack the possibility to take the interaction between counter-propagating waves in those structures into account. Recently, the Bremmer coupling series [1] has been proposed as part of a new field decomposition method [2, 3], the first term of which corresponds to the classical beam propagation method. In this paper we discuss the numerical implementation of this series. As an example to show the potential possibilities of the new approach we model the reflection phenomena inside a Multimode Interference (MMI) combiner.

Basic Equations Starting form the Maxwell equations in time domain, we first apply a time-Fourier transform and subsequently decompose the electromagnetic field constituents (for the time being denoted as $\{F_1, F_2\}$) into a wave W^+ propagating in the positive x_3-direction and a wave W^- propagating in the negative x_3-direction

$$\begin{bmatrix} W^+ \\ W^- \end{bmatrix} = \begin{bmatrix} A & A \\ \Gamma & -\Gamma \end{bmatrix}^{-1} \begin{bmatrix} F_1 \\ F_2 \end{bmatrix}. \tag{1}$$

These waves satisfy the first-order matrix equation

$$\partial_3 \begin{bmatrix} W^+ \\ W^- \end{bmatrix} + \mathrm{j}k_\mathrm{o} \begin{bmatrix} \Gamma & 0 \\ 0 & -\Gamma \end{bmatrix} \begin{bmatrix} W^+ \\ W^- \end{bmatrix} = \begin{bmatrix} T & R \\ R & T \end{bmatrix} \begin{bmatrix} W^+ \\ W^- \end{bmatrix}. \tag{2}$$

In case of TE-polarized waves in a 2-dimensional configuration, we have $F_1 = E_2$, $F_2 = -H_1$, $A = \sqrt{\mu_\mathrm{o}/\varepsilon_\mathrm{o}}$, $\Gamma = (\varepsilon_\mathrm{r} + k_\mathrm{o}^{-2}\partial_1^2)^{\frac{1}{2}}$, $T = -R = -\frac{1}{2}\Gamma^{-1}(\partial_3\Gamma)$. The left-hand side of (2) is well known as the forward and backward ("wide-angle") Beam Propagation equations, while the right-hand side describes the interaction between the forward-and backward-propagating waves. In this paper we focuss on taking this interaction term into account. Time-domain results are obtained by an inverse time-Fourier transform.

Bremmer Coupling Series Equation (2) can be rewritten into an integral equation [2]. In compact operator form, this integral equation reads

$$\begin{bmatrix} 1-K_{+,+} & -K_{+,-} \\ -K_{-,+} & 1-K_{-,-} \end{bmatrix} \begin{bmatrix} W^{+} \\ W^{-} \end{bmatrix} (x_1, x_2, x_3) = \begin{bmatrix} W_{+}^{(0)} \\ 0 \end{bmatrix} (x_1, x_2, x_3), \tag{3}$$

where $W_{+}^{(0)}(x_1, x_2, x_3)$ is the transmitted forward wave, which is the only term computed in the Beam Propagation Method. The interaction between the counter-propagating waves is described by the integral operator K. If the norm of this operator K is less than 1, the Neumann expansion can be applied to the inverse of $(1-K)$ at the left-hand side of equation (3). This leads to the Bremmer coupling series

$$W = \sum_{j=0}^{\infty} K^j W^{(0)} = W^{(0)} + KW^{(0)} + K^2 W^{(0)} + \cdots. \tag{4}$$

The jth term can be interpreted as the j-times reflected wave and its relation with the $(j-1)$-times reflected wave is given by

$$W^{(j)} = KW^{(j-1)}, \qquad (j \geq 1), \tag{5}$$

By rewriting the operator K in terms of product integrals [4], a recursive numerical scheme is obtained [5].

Numerical Implementation In order to show the numerical implementation of each term of the Bremmer coupling series, we first investigate one of the 4 elements at the right-hand side of (5), e.g. $K_{+,+}W_{+}^{(j-1)}$. In short-hand notation, we can write

$$(K_{+,+}W_{+}^{(j-1)})(m\Delta x_3) = (PK_{+,+}W_{+}^{(j-1)})((m-1)\Delta x_3) + q(m\Delta x_3), \tag{6}$$

where $P(m\Delta x_3)$ is the propagation operator as used in the Beam Propagation Method and $q(m\Delta x_3)$ is the calculated transmitted field in one unit step along the propagation direction. The computation of q involves the evaluation of the transmission operator T. In a similar way the other terms on the right-hand side of (5) can be determined. The resulting scheme is summarized in a flow chart (see Figure 1).

Numerical Example In our numerical example we have approximated the operator Γ with aid of a third-order Thiele approximation within a local comoving reference frame [6, 7]. For the reflection and transmission operators we have used approximations on principal symbol level [7].

Figure 2 gives a numerical example of the reflections phenomena in a Multimode Inference combiners, as used for instance in semi-conductor ring lasers [8]. Details are given in the corresponding caption.

Conclusion and Discussion We have demonstrated that the field decomposition method together with the Bremmer coupling series allows us to include the interaction between the counter-propagating waves. From results for practical configurations with high reflection phenomena, like the MMI-combiner, we may conclude that only a few terms (2 or 3) of the series already yield good results. The overall computation time is then in the order of 5 or 9 times the BPM computation time, respectively.

- Incident field is given
- Fourier Transform: $t \longrightarrow \omega$
- For every ω
  - decomposition: $F \longrightarrow W$
  - For every term j of Bremmer coupling series, $(j = 0, 1, 2, \cdots)$
    - Initialize the 4 terms in $KW^{(j-1)}$
    - For every forward propagation step m, $(m = 1, 2, \cdots, M)$
      - Compute $(K_{+,+}W_+^{(j-1)})(m\Delta x_3)$ and $(K_{+,-}W_-^{(j-1)})(m\Delta x_3)$
      - $W_+^{(j)}(m\Delta x_3) = (K_{+,+}W_+^{(j-1)} + K_{+,-}W_-^{(j-1)})(m\Delta x_3)$
      - composition $\longrightarrow$ forward propagating part of $F_1^{(j)}$ and $F_2^{(j)}$
      - adding to previous fields + storage
    - For every backward propagation step m, $(m = M-1, \cdots, 0)$
      - Compute $(K_{-,+}W_+^{(j-1)})(m\Delta x_3)$ and $(K_{-,-}W_-^{(j-1)})(m\Delta x_3)$
      - $W_2^{(j)}(m\Delta x_3) = (K_{-,+}W_+^{(j-1)} + K_{-,-}W_-^{(j-1)})(m\Delta x_3)$
      - composition $\longrightarrow$ backward propagating part of $F_1^{(j)}$ and $F_2^{(j)}$
      - adding to previous fields + storage
- Inverse Fourier Transform $\omega \rightarrow t$ yields field at the positions of interest

Figure 1: Flow chart of the numerical implementation of the Bremmer coupling series

References

[1] H. Bremmer, *Comm. Pure Applied Mathematics*, 105–115 (1951).

[2] M.V. de Hoop, submitted to *SIAM J.Appl.Math.* (1995).

[3] M.J.N. van Stralen *et al.*, *International Symposium on Integrated Optics* (Lindau, Germany), 47–56 (1994).

[4] C. DeWitt-Morette *et al.*, *Physics Reports* 255–372 (1979).

[5] M.J.N. van Stralen *et al.*, *Internal Report : Et/EM 1995-18* (available on request).

[6] M.J.N. van Stralen *et al.*, Abstract *ICIAM'95* (Hamburg, Germany), 453 (1995).

[7] M.J.N. van Stralen *et al.*, to be submitted for publication, (1996).

[8] E.C.M. Pennings *et al.*, *IEEE Photonics Technology Letters* 715–718 (1994).

[9] R. van Roijen *et al.*, *Applied Physics Letters*, 1753–1755 (1994).

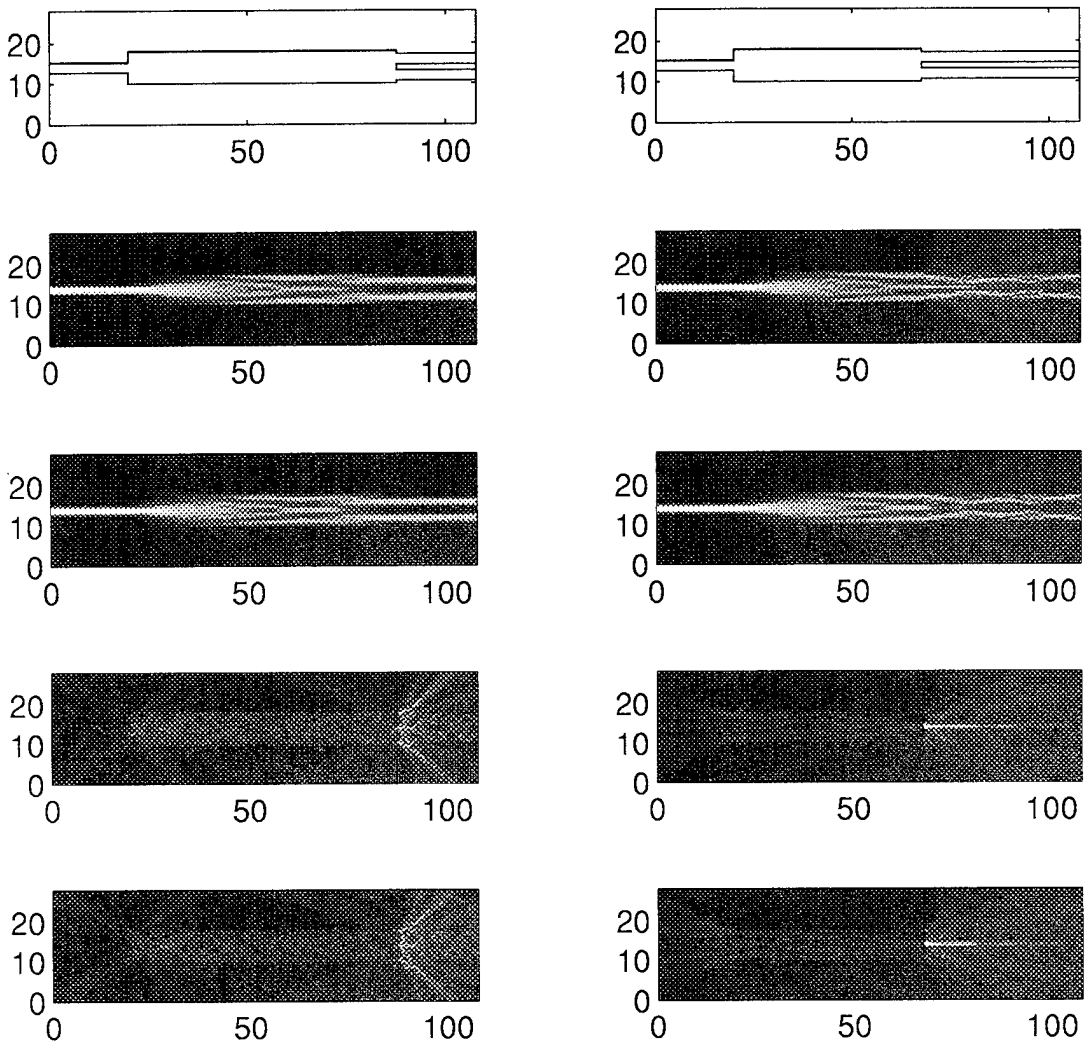


Figure 2: Two MMI-combiners under investigation. The fundamental waveguide mode is launched into the waveguide at the left side of the MMI. The structure is depicted in the first row: $\lambda = 1.55\mu$m, $n_{\mathrm{MMI}} \approx 3.245$, $n_{\mathrm{background}} = 2.0$, $w_{\mathrm{waveguide}} = 2\mu$m, $w_{\mathrm{MMI}} = 8\mu$m, $L_{\mathrm{MMI}} = 67.7\mu$m (left), $L_{\mathrm{MMI}} = 47.7\mu$m (right). The left MMI-combiner was designed for combining two output paths of a ring laser [9]. The right MMI-combiner was shorthened by 20μm in order to elucidate the reflections in an MMI-waveguide. The computed fields ($|E_2|$) corresponds to several terms of the Bremmer coupling series:

- second row: five terms,
- third row: first term only (=BPM),
- fourth row: second term only,
- fifth row: second to fifth term only.

The color scale is magnified by 5 in the two lower right figures. The color scale is magnified by 50 in the two lower left figures. From the last two rows we may conclude that most of the reflection phenomena is included in the second term of the Bremmer coupling series.

The Perfectly Matched Layer (PML) Boundary Condition for the Simulation of Guided-Wave Optical Devices

W. P. Huang[1], C. L. Xu[2], W. W. Lui, and K. Yokoyama

NTT Opto-Electronics Laboratories

3-1, Morinosato Wakamiya, Atsugi, Kanagawa, 243-01, Japan

One of the key issues in implementing a numerical scheme such as the finite-difference method to solve a partial differential equation such as the Helmholtz equation in infinite spatial domain is the numerical boundary condition. Several techniques have been used in the finite-difference beam propagation method. Popular approaches are the absorbing boundary condition (ABC) and the transparent boundary condition (TBC)[1]. Recently, a novel boundary condition, the perfectly matched layer (PML) boundary condition, was proposed by Berenger[2] for the finite-difference time-domain (FDTD) method for Maxwell's equations. The effectiveness of the PML boundary condition was subsequently verified[3]. In this paper, we will show that, the PML provides an attractive addition to the arsenal of tools as a highly effective numerical boundary condition for methods such as the finite-difference beam propagation methods and mode solvers.

The Helmholtz equation for the amplitudes of the transverse fields of the TE waves in two dimension reads

$$\frac{\partial^2}{\partial x^2}\Psi + \frac{\partial^2}{\partial z^2}\Psi + \frac{n^2}{c^2}\omega^2\Psi = 0 \tag{1}$$

where $n = n(x, y, z)$ is the refractive index of the medium and c is the velocity of light in free space. In the perfectly matched layer, the corresponding wave equation is written as

$$\frac{1}{1 - j\sigma_x/\omega\epsilon_o n_p^2}\frac{\partial}{\partial x}\left(\frac{1}{1 - j\sigma_x/\omega\epsilon_o n_p^2}\frac{\partial\Psi}{\partial x}\right) + \frac{1}{1 - j\sigma_z/\omega\epsilon_o n_p^2}\frac{\partial}{\partial z}\left(\frac{1}{1 - j\sigma_z/\omega\epsilon_o n_p^2}\frac{\partial\Psi}{\partial z}\right) + \frac{n_p^2}{c^2}\omega^2\Psi = 0 \tag{2}$$

where n_p is a constant refractive index of the PML medium and can be chosen to be equal to that of the medium adjacent to the perfectly matched layer. σ_x and σ_z are the anisotropic conductivities of the PML. It can be proved that, if we choose the conductivity such that σ_z

[1]On leave from Department of Electrical and Computer Engineering, University of Waterloo, Waterloo, Ontario, Canada

[2]Formerly with Department of Electrical and Computer Engineering, University of Waterloo, Waterloo, Ontario and currently with JDS FETEL, Ottawa, Ontario, Canada

is continuous across an index interface perpendicular to x, then a plane wave incident on the interface experiences no reflection, regardless of the incident angle and the frequency and independent of the conductivities of the media along x. This conclusion is certainly true for an interface between a lossless medium with zero conductivity and a PML medium with a finite conductivity along x. Under the perfectly matching condition, the transmitted field in the PML medium matches perfectly with the wave in the free-space adjacent to it along z and decays exponentially at the rate of $\alpha_{eff} = \sigma_{x2} n_p \sqrt{\mu_o/\epsilon_o}$ along x.

For the application of the PML boundary condition, we implement it for the finite-difference beam propagation method in two-dimension. Eqs. (1) and (2) can be solved by using a Pade recursion procedure. In the PML medium, we have assumed a distribution of the conductivity as $\sigma_x = \sigma_{max}(\rho/\delta)^2$ where δ is the thickness of the PML and ρ is the distance measured from the interface between the computation region and the PML medium. The maximum conductivity σ_{max} may be determined by requiring the reflection coefficient $R(0) = e^{-\frac{2}{3}\sqrt{\frac{\mu_o}{\epsilon_o}} n_p^2 \sigma_{max} \delta}$ to be smaller than a given value.

As a test example, we simulated a Gaussian beam propagating at certain angles with respect to z axis. The input field is assumed to be $\Phi(x,0) = \exp(-x^2/w_o^2)$ with $w_o = 3.0\mu m$. Figures 1a and 1b show the field intensity profiles of the Gaussian beam at 10° and 45°, respectively, simulated by the wide-angle BPM. Solid lines represent the results obtained by using the PML and the dash lines are those by the TBC. The PML layer thickness is $1\mu m$ and the maximum conductivity is $\sigma_{max} = 0.5\Omega^{-1}(\mu m)^{-1}$. The PML layer is terminated by a perfectly reflecting boundary. The discretization is $\Delta x = 0.05\mu m$ and $\Delta z = 0.5\mu m$. The effectiveness of the PML is clearly demonstrated in the simulation results. In comparison, the TBC works well at the small angle and becomes less effective at the large angle.

We have also implemented the PML for calculation of guided and leaky modes in a finite-difference mode solver. It is demonstrated that the PML is particularly effective and useful in the calculation for the leaky modes. The details of the simulation results will be shown in the presentation.

References

[1] G. R. Hadley, "Transparent boundary condition for the beam propagation method," *IEEE J. Quantum Electron.*, vol. 28, no. 1, pp. 363-370, 1992.

[2] J. -P. Berenger, "A perfectly matched layer for the absorption of electromagnetic waves," *J. Computational Phys.*, vol. 114, pp. 185-200, 1994.

[3] D. S. Katz, E. T. Thiele, A. Taflove, "Validation and extension to three dimensions of the Berenger PML absorbing boundary condition for FD-TD meshes," *IEEE Microwave & Guided-Wave Lett.*, vol. 4, no. 8, pp. 268-270, 1994.

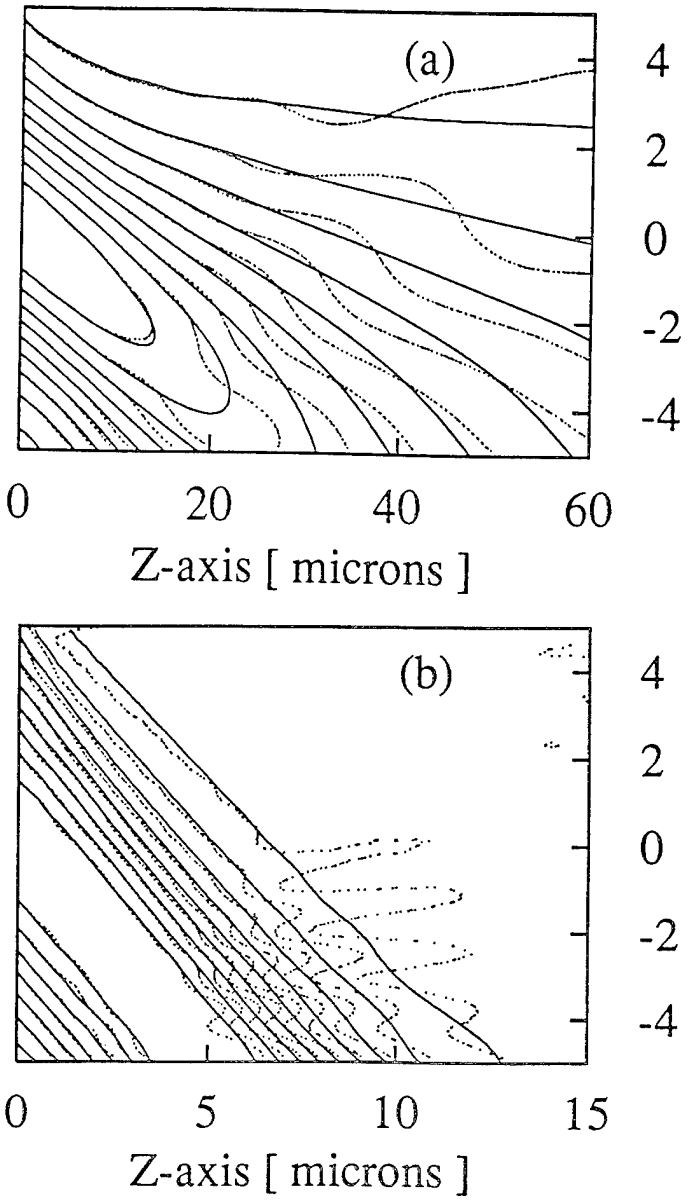


Figure 1: BPM simulation of a Gaussian beam propagating at 10° angle with respect to z-axis. Solid: PML; dash: TBC. (a) 10° angle with respect to z-axis; (b) 45° angle with respect to z-axis. Solid: PML; dash: TBC.

Non-iterative Finite-Difference Scheme for Modal Calculations

Wayne W. Lui, Wei-Ping Huang[1] *and Kiyoyuki Yokoyama*

NTT Opto-electronics Laboratories

3-1 Morinosato, Wakamiya, Atsugi, Kanagawa, Japan.

E-mail address: waynelui @ aecl . ntt . jp

The usual procedure of numerical modal calculations using finite-difference is to first discretize the Helmholtz equation

$$\nabla^2 \phi(\vec{r}) + k^2 n^2(\vec{r})\, \phi(\vec{r}) = \beta^2\, \phi(\vec{r}) \tag{1}$$

by a central-difference scheme, i.e. to approximate the second spatial derivative (assuming a uniform grid) as follows:

$$\frac{\partial^2 \phi}{\partial z^2} = \frac{1}{(\Delta z)^2} [\, \phi(z+\Delta z) - 2\phi(z) + \phi(z-\Delta z)\,] + O[(\Delta z)^2] \tag{2}$$

Here, $n(\vec{r})$ is the refractive index of the medium and $k = 2\pi/\lambda$. Using (2), assuming that the error term is negligible, (1) is reduced to a matrix equation of which the eigenvalues give the propagation constant β. The problem, however, is that at the boundary of the calculation domain where the field beyond which is unknown, (2) is not applicable. Artificially imposed boundary conditions are therefore necessary if (2) is to be used at the boundary.

There have been numerous proposals. Most of them invoke certain physical assumptions, such as (a) zero field at the boundary; (b) exponential decay of the field beyond the calculation domain [1]; and (c) transparent boundary where energy always flows away from the calculation domain [2]. Many of these approaches require an iterative -- often time-consuming -- procedure to enforce the underlying assumptions. Although each approach comes with its set of limitations, each has achieved different degree of accuracy and success.

In this work, we argue that if (1) can be discretized properly at the boundary, it is possible to do away with the physical assumptions -- and the corresponding limitations -- that are implicit in all artificially imposed boundary conditions. This calls for a finite-difference discretization scheme which does not require field information beyond the boundary. Naturally, we turn to the Taylor's series for solution.

This is our methodology. Consider the 1D case and recall the familiar Taylor expansion formula:

$$\phi(z+\delta) = \sum_{m=0}^{m=3} \frac{\delta^m}{m!} \frac{\partial^m \phi}{\partial z^m} - O[(\Delta z)^4] \tag{3}$$

where $\phi(z+\delta)$ is expanded up to four terms. (The sign of the error term is chosen for purpose of convenience.) In view of (3), we consider the following sum:

$$\sum_{m=0}^{m=3} a_m \phi(z+m\,\Delta z) + O[(\Delta z)^4] = \sum_{m=0}^{m=3} b_m (\Delta z)^m \frac{\partial^m \phi}{\partial z^m} \tag{4}$$

where a_m and b_m are parameters to be determined. Neglecting the error term and by comparing coefficients on both sides of (4), a_m and b_m are found to be linearly related:

$$\begin{bmatrix} 1 & 1 & 1 & 1 \\ 0 & 1 & 2 & 3 \\ 0 & 1 & 2^2 & 3^2 \\ 0 & 1 & 2^3 & 3^3 \end{bmatrix} \begin{bmatrix} a_0 \\ a_1 \\ a_2 \\ a_3 \end{bmatrix} = \begin{bmatrix} 0! & 0 & 0 & 0 \\ 0 & 1! & 0 & 0 \\ 0 & 0 & 2! & 0 \\ 0 & 0 & 0 & 3! \end{bmatrix} \begin{bmatrix} b_0 \\ b_1 \\ b_2 \\ b_3 \end{bmatrix} \tag{5}$$

Next, we set the RHS of (4) to be identically equal to $(\Delta z)^2 \frac{\partial^2 \phi}{\partial z^2}$. This is equivalent to simply setting $b_0 = b_1 = b_3 = 0$, $b_2 = 1$. Upon solving (5), (4) can be rewritten as

$$\frac{\partial^2 \phi}{\partial z^2} = \frac{1}{(\Delta z)^2} [\,2\phi(z) - 5\phi(z+\Delta z) + 4\phi(z+2\Delta z) - \phi(z+3\Delta z)\,] + O[(\Delta z)^2] \tag{6a}$$

of which the error term on the RHS is of the same order as that of (2). It can be similarly shown that

$$\frac{\partial^2 \phi}{\partial z^2} = \frac{1}{(\Delta z)^2} [\,2\phi(z) - 5\phi(z-\Delta z) + 4\phi(z-2\Delta z) - \phi(z-3\Delta z)\,] + O[(\Delta z)^2] \tag{6b}$$

Notice that on the RHS of (6a), only field information at locations $z' \geq z$ is required. Likewise, only field information at locations $z' \leq z$ is required on the RHS of (6b). This property allows (6a) and (6b) to properly discretize the wave equation (1) at the boundary.

In general, if more terms are considered in (4), the error term will be of higher order (i.e. smaller) but the number of terms in the discretization scheme will be increased. For instance, if five terms are utilized in (4), we obtain

$$\frac{\partial^2\phi}{\partial z^2} = \frac{1}{12(\Delta z)^2}\left[\,35\phi(z) - 104\phi(z\pm\Delta z) + 114\phi(z\pm 2\Delta z) - 56\phi(z\pm 3\Delta z)\right. \qquad (7)$$
$$\left. + 11\phi(z\pm 4\Delta z)\,\right] + O\left[(\Delta z)^3\right]$$

whereas if six terms are used, the following scheme results:

$$\frac{\partial^2\phi}{\partial z^2} = \frac{1}{12(\Delta z)^2}\left[\,45\phi(z) - 154\phi(z\pm\Delta z) + 214\phi(z\pm 2\Delta z) - 156\phi(z\pm 3\Delta z)\right. \qquad (8)$$
$$\left. + 61\phi(z\pm 4\Delta z) - 10\phi(z\pm 5\Delta z)\,\right] + O\left[(\Delta z)^4\right]$$

If (2) is to be the discretization scheme for the interior points of the calculation domain, (6a) and (6b) are considered sufficiently accurate.

As an illustration, the discretization scheme suggested above is applied towards analysis of an ARROW waveguide. The structure of the ARROW is such that $n = 3.5$ for $z \le 4\,\mu m$ (substrate), $n = 2.01$ for $4\,\mu m \le z \le 4.5\,\mu m$ (AR region), $n = 1.458$ for $4.5\,\mu m \le z \le 8.5\,\mu m$ (guiding layer), and $n = 1$ for $z \ge 8.5\,\mu m$ (vacuum). The calculated field profile using the present method is shown in Fig.1 (dotted curve), where both the leaky nature in the substrate and the evanescent nature in vacuum of the field are predicted. It is also compared against the analytically obtained profile (solid curve). Excellent agreement is observed.

The major difference between the conventional modal calculation method and the one suggested here is the larger matrix bandwidth due to the larger number of terms on the RHS of (6a) and (6b). Savings resulting from the non-iterative nature of this method, on the other hand, is found to more than compensate the extra effort in solving the slightly more difficult eigenvalue problem. More significantly, there is no physical assumption involved. *A priori* knowledge of the field is not necessary as a result.

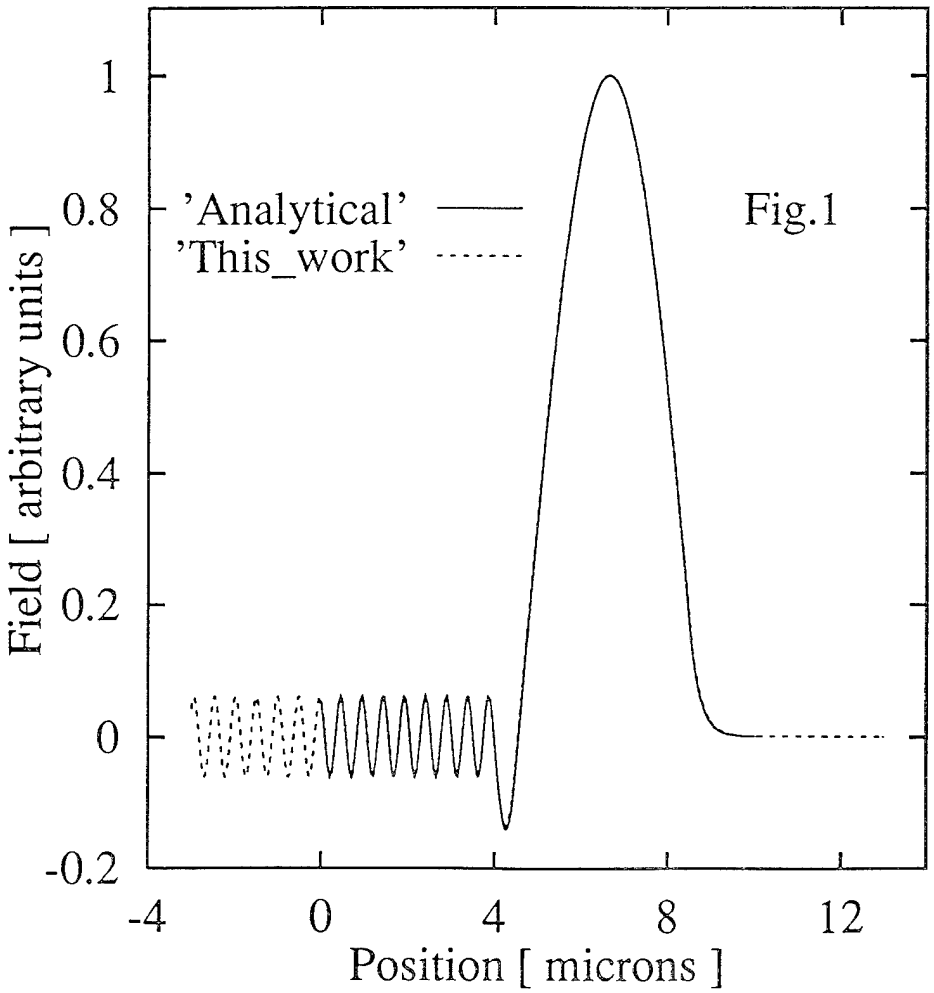
Further details will be discussed at the presentation.

.[1]On leave from Department of Electrical and Computer Engineering, University of Waterloo, Waterloo, Ontario, Canada.

References

[1] M. Stern, "Semi-vectorial polarized finite difference method for optical waveguides with arbitrary index profiles," *IEE Proceedings*, vol.135, pt.J, pp.56-63, (1988).

[2] G.R. Hadley, "Full-vector waveguide modeling using an iterative finite-difference method with transparent boundary conditions," *IEEE J. Lightwave Tech.*, vol.14, pp.465-469, (1995).



Monday, April 29, 1996

Symposium on Array-based WDM Devices

IMC 10:30 am-12:15 pm
Fairfax B

David L. Weidman, *Presider*
Corning, Inc.

Silica-based planar lightwave circuits for WDM systems

Yasuyuki Inoue

NTT Opto-electronics Laboratories,
162 Tokai, Naka-gun, Ibaraki, 319-11 Japan
Telephone: +81-29-287-7687, Fax: +81-29-287-7881
E-Mail: inoue@nttiba.ntt.jp

Introduction

Wavelength-division multiplexing (WDM) systems are attractive for increasing transmission capacity and network flexibility, and they require various kinds of filters. The use of silica-based planar lightwave circuit (PLC) technology [1] is one of the most promising ways to fabricate filters for WDM networks, because PLC devices have low insertion losses, design flexibility, high reliability, and good reproducibility.

Table 1 is a list of the multiplexers constructed with silica-based PLCs, and outlines their features and applications. There are four basic types of wavelength multiplexer. This paper describes these multiplexers and their applications, focusing particularly on NTT's achievements.

Thin Film Filter Embedded Multiplexer

A simple multiplexer can be constructed by using crossed waveguides with a thin film filter embedded at the crossing point. The pass band light of the filter is output from a transmission port and the stop band light is output from a reflection port. This multiplexer has the advantage of an ideal flat and sharp wavelength response originating from multi-interference in the filter.

A subscriber network utilizing 1.3 μm and 1.55 μm wavelength channels is now being intensively investigated. In this case, a prime concern is to reduce the cost of the optical WDM transmitter/receiver module [2]. We are now developing a filter embedded 1.3 /1.55 μm multiplexer in order to reduce the module size and the number of fiber-attachments as shown in Fig.1. Here we use a multilayered dielectric filter evaporated on a polyimide film [3]. The fabricated multiplexer has a low insertion loss of less than 1.1 dB in the 1.23-1.38 μm range for the transmission port and 1.1 dB in the 1.46-1.7 μm range for the reflection port. An extremely low crosstalk of less than -50 dB was also obtained in the 1.50-1.64 μm range for the transmission port. This simple, compact, and high performance multiplexer will enable us to realize a practical 1.3/1.55 μm WDM transmitter/receiver module.

Directional Coupler Type Multiplexer

Another type of 1.3/1.55 μm multiplexer is constructed using a simple directional coupler. This multiplexer dose not require any additional processes such as filter insertion, but its wavelength response is rather sensitive for waveguide fabrication. A fiber-to-fiber insertion loss of 0.5 dB and a crosstalk of -30 dB were obtained experimentally.

Mach-Zehnder Interferometer (MZI) Type Multiplexer

The wavelength response of the asymmetric MZI in Fig.2 is generally sinusoidal as a result of the interference of two beams, therefore it operates as a 2x2 multiplexer [4]. This multiplexer is more flexible in terms of setting the channel wavelength than the directional coupler type. Various channel spacing multiplexers from 1 GHz to 250 nm have already been demonstrated [5]. A thermo-optic (TO) phase shifter equipped on one of the waveguide-arms provides this multiplexer with wavelength response tunability by controlling the relative phase difference between the waveguide-arms. This multiplexer, therefore, operates as a wavelength switch.

In general, silica-based waveguides have stress-induced birefringence, which causes a wavelength response shift between TE/TM modes. This polarization dependence is a crucial problem

for PLC applications in optical networks. We developed two techniques for eliminating the polarization dependence of the multiplexer. One is to control birefringence with an amorphous silicon (a-Si) stress applying film deposited on a waveguide-arm [6]. The polarization dependence can be carefully eliminated by laser-trimming the a-Si film after the multiplexer has been packaged. This removes the need for the a-Si film to be precisely fabricated. The other technique is TE/TM polarization mode conversion at the center of the multiplexer [7]. The converter consists of an 18 μ m waveguide gap and a 15 μ m thick polyimide half waveplate with the principal axis tilted 45 degrees to the substrate plane. The excess loss caused by inserting the converter was 0.3 dB. This method is easily applied to other circuits such as AWG multiplexers.

A 2^N-channel selection filter can be constructed with N MZI multiplexers with N different path differences of ΔL, $\Delta L/2$, $\Delta L/4$,, and $\Delta L/2^{N-1}$ by analogy with micro-wave "periodic-filters". Seven MZIs with different ΔL values were connected in series to form a 10 GHz-spaced 128-channel selective filter. The fiber-to-fiber insertion loss of the reported module was 6.9 dB [8].

A tunable gain equalizer is an attractive application for the asymmetric MZI [9]. This is because a small gain imbalance between multiple wavelength channels is unavoidable in multistage Er-doped fiber amplifiers, and the sinusoidal wavelength transmittance of the MZI can reduce this imbalance. The reported equalizer consists of two tunable couplers, two waveguide arms with a path difference of 64 μ m, and a TO phase shifter on one of the arms, where the extinction ratio can be controlled by the tunable couplers and the wavelength response can be shifted by the TO phase shifter. Recently, another gain equalizer was also demonstrated with a lattice of multiple asymmetric MZIs [10].

Arrayed Waveguide Grating (AWG) Multiplexer

The NxN AWG multiplexer in Fig.3 is very useful in WDM networks since it is capable of simultaneously multiplexing N channels by employing multi-beam interference [11-13]. It consists of N input/output waveguides, two focusing slab waveguides and a phase-array of multiple channel waveguides with a constant path difference ΔL between neighboring waveguides. The input light is radiated in the first slab and then excites the arrayed channel waveguides. After traveling through the arrayed waveguides, the light beams interfere constructively and meet at one focal point in the second slab. The location of this focal point depends on the signal wavelength. The dispersion of the focal position x with respect to the wavelength λ is given by

$$\frac{dx}{d\lambda} = \frac{f \cdot m}{n_s \cdot d} \qquad m = \frac{n_c \cdot \Delta L}{\lambda_0} \qquad (1)$$

where f is the focal length of the slab, m the diffraction order, $n_{s(c)}$ the effective refractive index of the slab (channel waveguide), and d the pitch of the arrayed waveguide grating at the exists. We have fabricated various kinds of multiplexers ranging from 15-nm spacing 8-channel devices to 50-GHz spacing 64-channel devices [14]. The crosstalk to all other channels is less than about -27 dB and the on-chip fiber-to-fiber insertion losses range from 2.1 dB to 3.1 dB, respectively.

The waves caused by four-wave mixing (FWM) result in crosstalk degradation in a WDM transmission system. Unequal channel spacing is an effective way to suppress these FWM waves. Since the dispersion of the focal position x with respect to the wavelength λ is constant in equation (1), a multiplexer with unequal spacing can be achieved by using unequally spaced output waveguides. A multiplexer module has been reported with unequal spacings of 0.8 nm and 0.48 nm and fiber-to-fiber insertion losses of 2.8-3.1 dB [15].

An add-drop multiplexer (ADM) with an AWG multiplexer and loop-back optical paths is a useful application for constructing wavelength-addressed ring or bus networks [16]. Figure 4 shows the basic configuration of the ADM with loop-back paths. N signals introduced into the common input port are first demultiplexed by the AWG multiplexer and then N-1 output signals are looped back to the opposite input ports. The looped-back signals are automatically multiplexed again and fed out to the common output ports. This is because of the symmetric nature of the AWG multiplexer. A desired wavelength channel can be dropped and added by opening the corresponding loop-back path.

An advanced ADM with fold-back optical paths has also been proposed [17]. It offers significant crosstalk reduction and loss-imbalance equalization compared with the ADM with loop-back paths.

A splitter/router is an interesting application of the AWG [18]. The splitter/router in Fig.5, consisting of input/output waveguides, a slab waveguide, an AWG, and a multilayered dielectric filter evaporated on the end face of the AWG, operates as an optical power splitter for a broadcast signal in the pass band of the filter and as a wavelength router for a point-to-point communication signal in the stop band of the filter. This component will be also applied to an optical splitter for a passive double star, where individual lines can be tested by using an optical time domain reflectometer with corresponding wavelength lights.

Summary

Basic wavelength-division multiplexers fabricated with silica-based PLC technologies and their applications have been reviewed. These passive PLC devices, supported by fabrication, design, and packaging technologies will assume an important role in future WDM systems. Finally, it is worth noting that further functional WDM components such as active ADM will be achieved by the hybrid integration of active devices with these PLC devices.

References

[1] M. Kawachi, "Silica waveguides on silicon and their application to integrated-optic components," Opt. and Quantum Electron., vol.22, pp.391-416, 1990.

[2] Y. Yamada et al., "Application of planar lightwave circuit platform to hybrid integrated optical WDM transmitter/receiver module," Electron. Lett., vol.31, pp.1366-1367, 1995.

[3] T. Oguchi et al., "Dielectric multilayered interference filters deposited on polyimide films," Electron. Lett., vol.27, pp.706-707, 1991.

[4] K. Inoue et al., "A four-channel optical waveguide multi/demultiplexer for 5-GHz spaced optical FDM transmission," J. Lightwave Technol., vol.6, pp.339-345, 1988.

[5] N. Takato et al., "Silica-based integrated optic Mach-Zehnder multi/demultiplexer family with channel spacing of 0.01-250 nm," IEEE J. Selected Area in Commun., vol.8, pp.1120-1127, 1990.

[6] M. Kawachi et al., "Laser trimming adjustment of waveguide birefringence in silica integrated-optic ring resonators," CLEO'89, pp.84-85, 1989.

[7] Y. Inoue et al., "Polarization mode converter with polyimide half waveplate in silica-based planar lightwave circuits," IEEE Photon. Technol. Lett., vol.6, pp.626-628, 1994.

[8] H. Toba et al., "A 100-channel optical FDM transmission/distribution at 622 Mb/s over 50 km," J. Lightwave Technol., vol.8, pp.1396-1401, 1990.

[9] K. Inoue et al., "Tunable gain equalization using a Mach-Zehnder optical filter in multistage fiber amplifiers," IEEE Photon. Technol. Lett., vol.3, pp.718-720, 1991.

[10] Y. P. Li et al., "Waveguide EDFA gain equalization filter," Electron. Lett., vol.31, pp.2005-2006, 1995

[11] M. K.Smit, "New focusing and dispersive planar component based on an optical phased array," Electron. Lett., vol.24, pp.385-386, 1988.

[12] H. Takahashi et al., "Arrayed-waveguide grating for wavelength division multi/demultiplexer with nanometre resolution," Electron. Lett., vol.26, pp.87-88, 1990.

[13] C. Dragone, "An NxN optical multiplexer using a planar arrangement of two star couplers," IEEE Photon. Technol. Lett., vol.3, pp.812-815, 1991.

[14] K. Okamoto, "Application of planar lightwave circuits to optical communication systems," ECOC'95, MoB4-1, pp.75-82, 1995.

[15] K. Okamoto et al., "Fabrication of unequal channel spacing arrayed-waveguide grating multiplexer modules," Electron. Lett., vol.31, pp.1464-1465, 1995.

[16] Y. Tachikawa et al., "Arrayed-waveguide grating add-drop multiplexer with loop-back optical paths," Electron. Lett., vol.29, pp.2133-2134, 1993.

[17] O. Ishida et al., "Multichannel frequency-selective switch employing an arrayed-waveguide grating multiplexer with fold-back optical paths," IEEE Photon. Technol. Lett., vol.6, pp.1219-1221, 1994.

[18] Y. Inoue et al., "Silica-based arrayed-waveguide grating circuit as optical splitter/router," Electron. Lett., vol.31, pp.726-727, 1995.

Table 1 Basic wavelength multiplexers with their features and applications

Wavelength Multiplexers	Features	Applications
Thin Film Filter Embedded Type	Flat/Sharp Wavelength Response	1.3/1.55 μ m WDM Transmitter/Receiver
Directional Coupler Type	Simple Structure	—
MZI Type	Switchable, Design Flexibility (from 1.3/1.55WDM to FDM)	Channel Selection Switch, Gain Equalizer, Frequency Discriminator for Stabilizing LD
AWG Type	Single Stage AWG Separate Multi-channels	Multi-channel Multiplexer, ADM, Splitter/Router, Unequal Channel Spacing Multiplexer

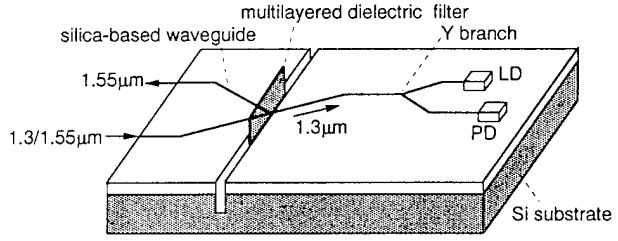


Fig. 1 Configuration of 1.3/1.55 WDM transmitter/receiver for subscriber network

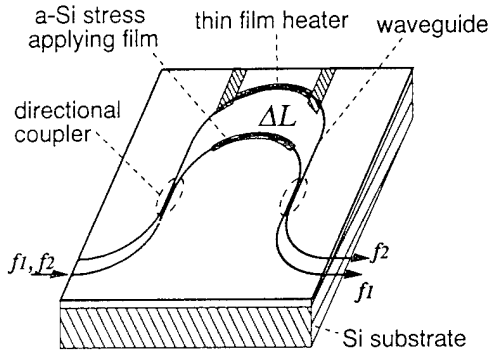


Fig. 2 Configuration of asymmetric Mach-Zehnder interferometer type multiplexer

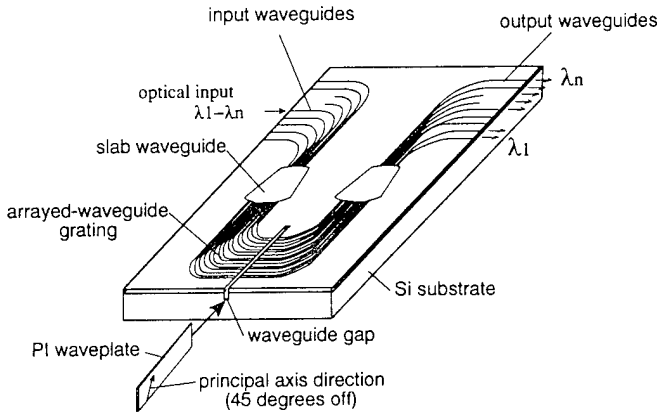


Fig. 3 Configuration of polarization-insensitive arrayed-waveguide grating multiplexer with polyimide half waveplate

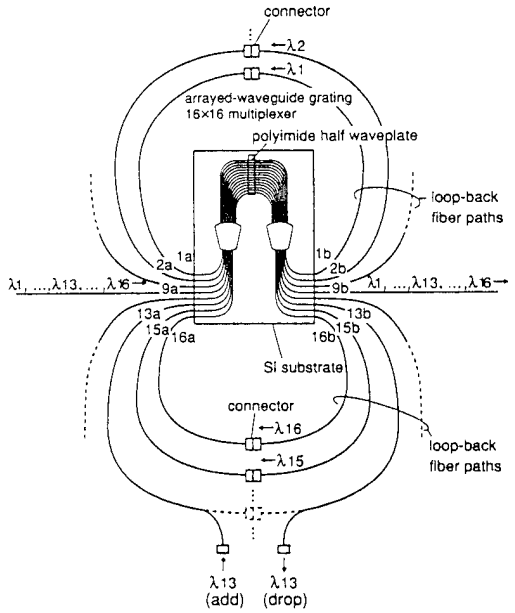


Fig. 4 Add/drop multiplexer (ADM) based on AWG multiplexer with loop-back paths

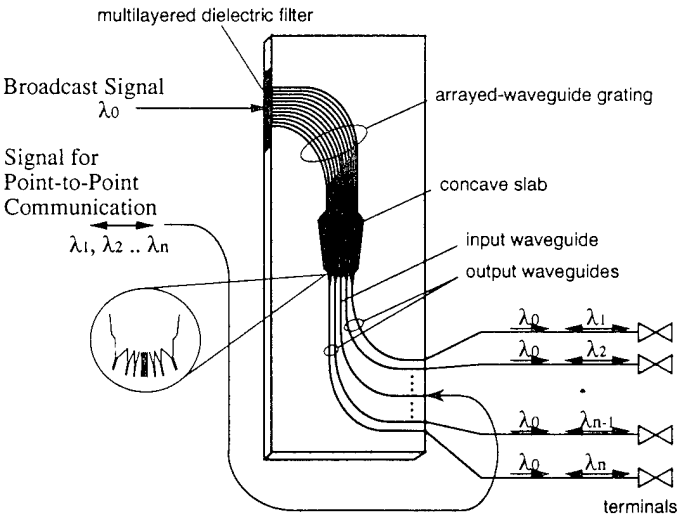


Fig. 5 Layout of splitter/router

FIRST POLYMERIC PHASED ARRAY WAVELENGTH DEMULTIPLEXER OPERATING AT 1550 nm

L.H. Spiekman*, M.B.J. Diemeer, T.H. Hoekstra, and M.K. Smit*
Akzo Nobel Central Research
PO Box 9300, NL-6800 SB Arnhem, The Netherlands
+31 26 366 2685. Fax: +31 26 366 2193
* Dept. of Electrical Engineering
Delft University of Technology, The Netherlands

Introduction:

Wavelength Division Multiplexing (WDM) is widely seen as the next step in broadband optical communications. Essential for WDM systems is the availability of low loss wavelength routers. The Phased Array wavelength demultiplexer [1] has been established as the preferred component for this function.

Fibre-to-fibre loss is an important issue for components in a network, and polymeric components perform well in this respect because waveguide core size and refractive index contrast can be made close to that of standard single mode fibre, allowing for butt coupling losses of a few tenths of a dB. A polymeric Phased Array wavelength demultiplexer with low loss and excellent spectral characteristics has already been presented for the 1.3 μm wavelength window [2]. Recent advances in polymer technology have reduced the hitherto higher absorption losses of the material around 1.55 μm [3], enabling the realisation of high quality components for the important EDFA window as well. The present paper discusses design, fabrication and experimental results for the first polymeric Phased Array wavelength demultiplexer operating around 1.55 μm.

Design:

Phased Array wavelength demultiplexers were designed for realisation in 6 μm×6 μm square waveguide structures with refractive index contrasts of 0.004, 0.006 and 0.008, respectively. The waveguide is strictly monomode for all three structures, the main difference being the minimum allowable bending radius of 4, 2, and 1 cm, respectively, which makes very compact devices possible.

The devices were designed as 8×8 Phased Array wavelength routers, consisting of a dispersive array of waveguides connected to 8 inputs and 8 outputs by two star couplers. The design central wavelength is 1550 nm and the channel spacing is 3.2 nm (400 GHz). The design allows

Refractive index contrast	0.008	0.006	0.004
Minimum bending radius	1 cm	2 cm	4 cm
In/output waveguide pitch	15 μm	18 μm	20 μm
Array waveguide pitch	9 μm	10 μm	11 μm
Focal length	1274 μm	1698 μm	2075 μm
# of array waveguides	50	54	51
Order	50	50	50
Device size (excl. access waveguides)	$2\times0.6\,cm^2$	$3\times0.8\,cm^2$	$5\times0.9\,cm^2$

Table 1: Parameters of the three designed wavelength demultiplexers.

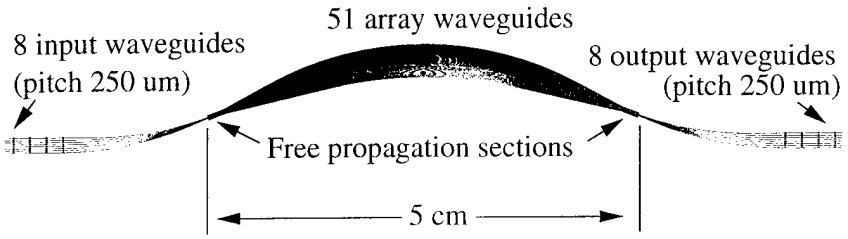


Figure 1: Layout of lowest contrast (largest) 8×8 Phased Array router. If no distortion has taken place in the reprographic process, this is the actual size of the device.

for a maximum on-chip loss of 2 dB for the central channels (due to the coupling loss at the transitions from the star couplers to the array waveguides, pitched 9–11 μm), in addition to a maximum diffraction loss of 2 dB for the outer channels. The parameters of the designs are given in table 1. The pitches of the array and input/output waveguides at the connection to the star couplers are larger for the lower contrast designs in order to avoid crosstalk problems. The free spectral range of the designs is 31 nm, and the devices operate in 50th order. Because square waveguides are used, the demultiplexers are expected to be polarisation independent. Input/output waveguides of the devices are fanned out to a pitch of 250 μm for direct coupling to fibre ribbons.

Figure 1 shows the layout of the lowest contrast (largest) device in actual size.

Fabrication:

The devices are fabricated on a spincoated 4" silicon wafer with Polymer Optoboard Technology developed at Akzo Nobel Electronic Products [3]. After projection lithography and pattern formation, glass plates are glued on both sides of the wafer, which is then diced, yielding waveguides that couple to cleaved fibre with only a few tenths of a dB of loss per coupling, and that show propagation losses lower than 0.6 dB/cm.

Experimental results:

At the moment of writing, only the largest (lowest contrast) device was available for measurement. In figure 2, the transmission curves of all 8 outputs of the device are plotted with light of TM polarisation injected in input 4.

The fibre-to-fibre loss of the device is 9 dB. Reference waveguides running alongside the Phased array show a loss of 6 dB, so the additional loss of the device is 3 dB. Crosstalk is better than 20 dB. The central wavelength of the device is 1553 nm. The design value of 1550 nm can easily be reached due to the thermal tunability properties of the polymeric material.

The small shoulders on the right flanks of the passbands plotted in figure 2 are due to residual TE polarised light coupled in. The device was not polarisation independent, as can be seen in figure 3. Figure 3a shows the TE-TM splitting occuring when linearly polarised light is coupled into the device at an angle of approximately 45°.

At room temperature, 2.5 nm of TE-TM shift was observed. When the device was operated at an elevated temperature, the splitting decreased, and eventually the two peaks could no longer be discerned separately. We believe that the splitting is caused by stress-induced birefringence originating from thermal processing steps in combination with the different thermal expansion coefficients of the polymer and the silicon substrate. Work is in progress to eliminate this effect.

Conclusion:

We have presented the first Phased Array wavelength demultiplexer in polymeric material for the EDFA window (around 1.55 μm), which is very important for telecommunications. The device is an 8×8 router with a channel spacing of 3.2 nm and a central passband of 1553 nm. The fibre-to-fibre insertion loss is 9 dB and its crosstalk is lower than -20 dB. A TE-TM shift of 2.5 nm

was observed at room temperature due to stress effects.

The size of the device is $5 \times 0.9\,cm^2$, excluding access waveguides. Smaller devices are being processed employing higher refractive index contrast for smaller bending radii.

References:

[1] M. Smit, "New focusing and dispersive planar component based on an optical phased array," *Electron. Lett.*, vol. 24, no. 7, pp. 385–386, 1988.

[2] Y. Hida, Y. Inoue, and S. Imamura, "Polymeric arrayed-waveguide grating multiplexer operating around 1.3 μm," *Electron. Lett.*, vol. 30, pp. 959–960, June 1994.

[3] M. B. J. Diemeer, T. Boonstra, M. C. J. M. Donckers, A. M. van Haperen, B. H. M. Hams, T. H. Hoekstra, J. W. Hofstraat, J. C. Lamers, W. Y. Mertens, R. Ramsamoedj, M. vaan Rheede, F. M. M. Suijten, U. E. Wiersum, R. H. Woudenberg, B. Hendriksen, W. H. G. Horsthuis, and H. M. M. Klein Koerkamp, "Low-loss (non)linear optical polymeric waveguide materials and devices," in *Proc. SPIE*, San Diego, USA, 1995.

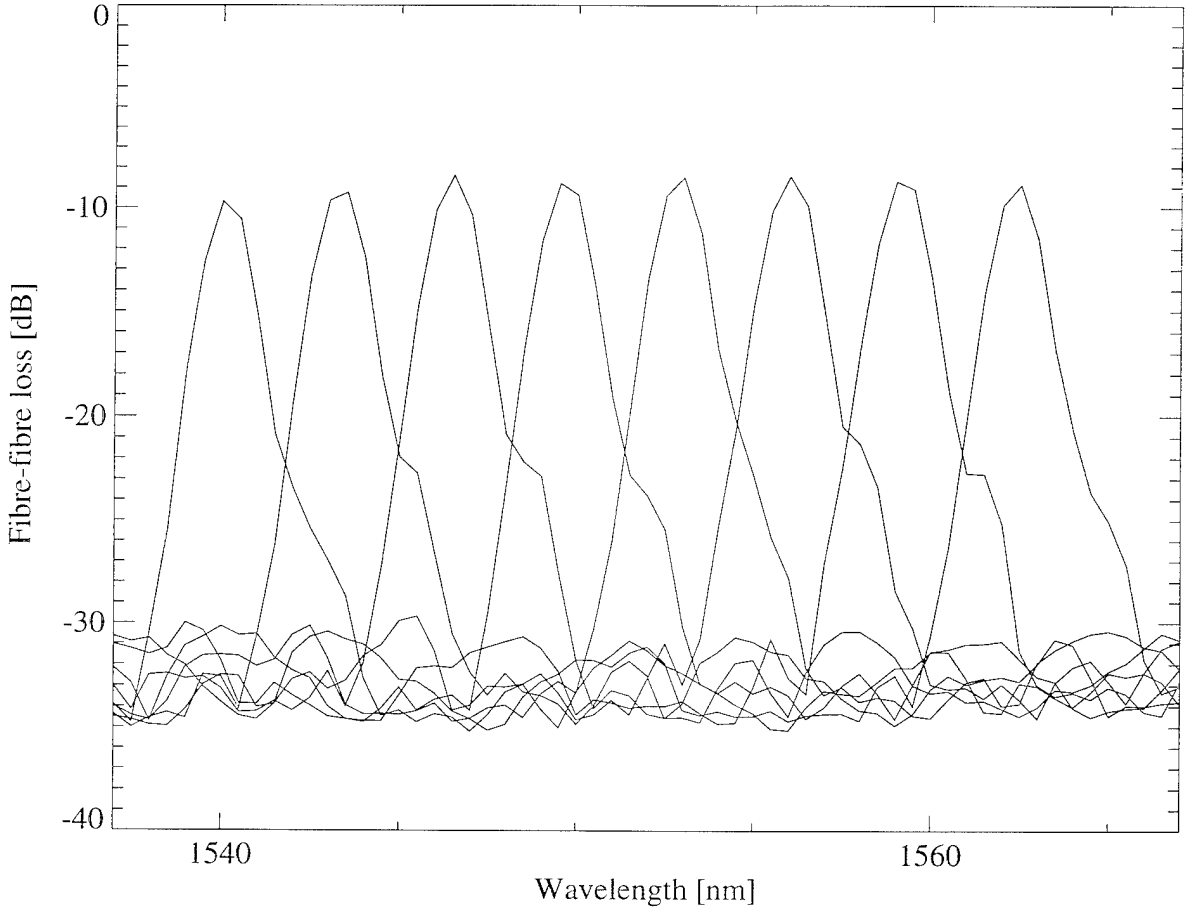


Figure 2: Transmission characteristics (fibre-to-fibre loss) of lowest contrast polymeric Phased Array for TM polarisation.

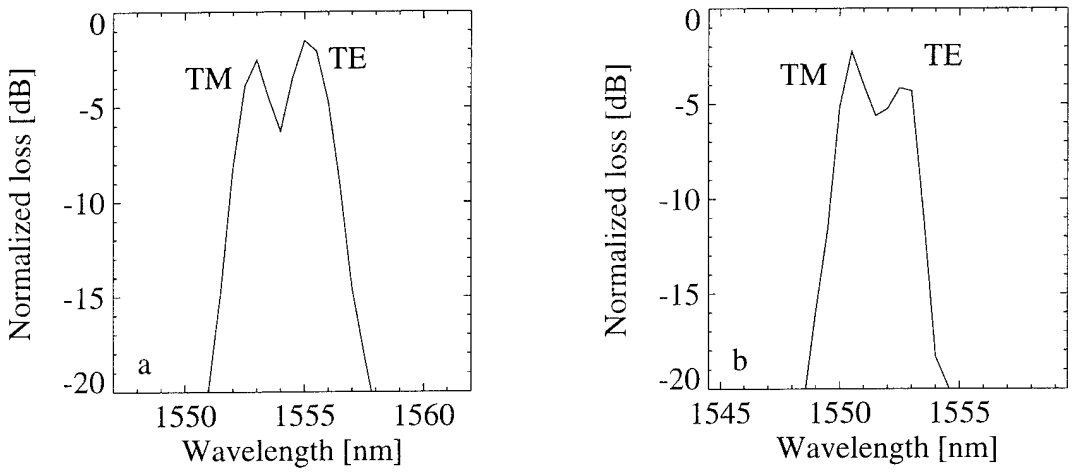


Figure 3: a: TE-TM splitting with linearly polarised light coupled in at an angle of 45°. Left maximum is for TM and right maximum is for TE. b: At elevated temperatures the splitting is reduced.

Filtering Characteristics of Virtually-Imaged Phased-Array

M. Shirasaki

Fujitsu Laboratories Ltd.

4-1-1 Kamikodanaka, Nakahara-ku, Kawasaki, 211-88, Japan
Phone: +81-44-777-1111 ext. 26115
Fax: +81-44-754-2640

One of the most important components in a WDM light transmission system is a wavelength multiplexer/demultiplexer. For a system in which the wavelength bandwidth is limited by the amplifier gain bandwidth or the fiber chromatic dispersion, a narrow channel spacing is required in multi-channel WDM. Other requirements for a WDM filter are low insertion loss, low polarization dependent loss, broad transmission band in each channel, low crosstalk from the neighbor channels, and stability. One possible means for multi-channel, dense WDM filters is a diffraction grating. However, a reflection-type diffraction grating which has a blaze angle of ~30 degrees shows small angular-dispersion, which requires a long light path in a filter[1]. The dispersion can be enhanced with a large blaze angle, and this enhancement was demonstrated by using transmission-type diffraction in a planar waveguide[2,3].

A new scheme based on a virtually-imaged phased-array (VIPA) provides large-angular dispersion, low polarization dependent loss, and stable operation[4]. The VIPA consists of a semi-cylindrical lens and a thin plate of glass as shown in Fig. 1. When the input light is line-focused into the plate with the semi-cylindrical lens, collimated light emerges from the reverse side of the plate. The angle ϕ of the output light varies as the wavelength varies, and this angular dispersion is 10-20 times larger than those of reflection-type diffraction gratings described above. The operating principle of the VIPA is shown in Fig. 2. The thickness t of the glass plate is 50-100 μm. The right surface of the plate is coated with a high reflection film (95% reflectivity or higher). The left surface of the plate is coated with a 100% reflection film except in the light input area which is anti-reflection coated. The input light beam is line-focused on the right surface where the incident angle of the beam center axis inside the plate is θ. To simplify the figure, the refraction at the air-glass boundaries was ignored in Fig. 2. Then

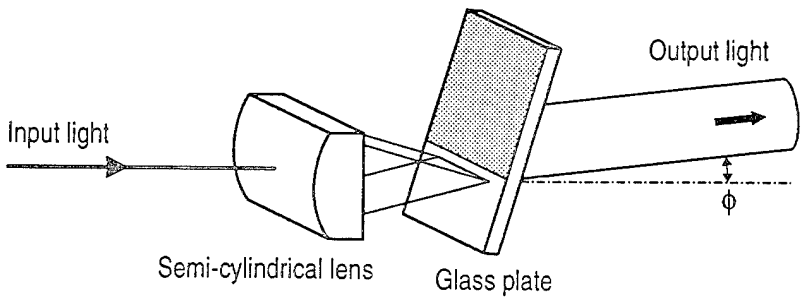


Fig. 1 Schematic of VIPA

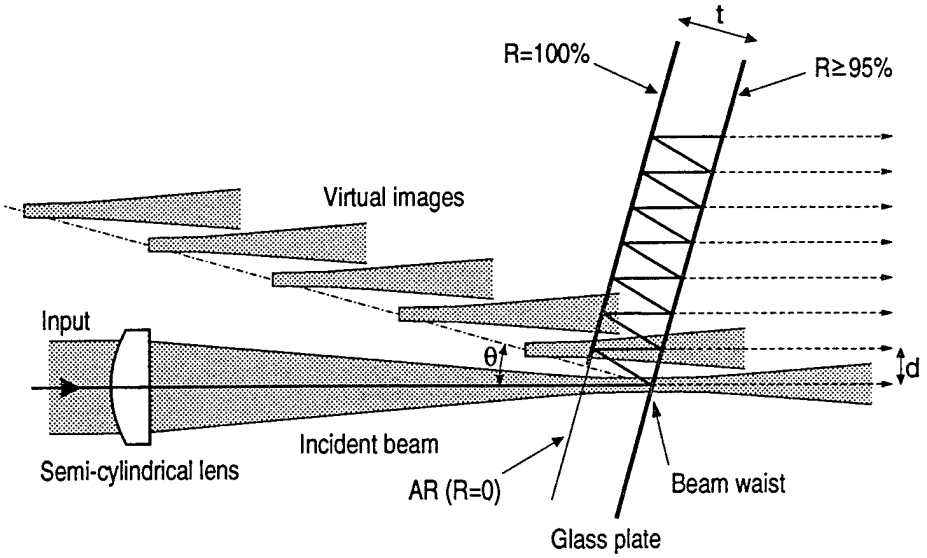


Fig. 2 Details of the VIPA structure

5% of the light passes through the right surface and diverges after the beam waist. 95% of the light is reflected on the surface and, after the second reflection, returns to the same surface with a displacement of d, where $d=2t\sin\theta$. Then 5% of the light passes through again. In a similar way, the incident beam is split into many beams on the different paths. The beam in each path has a beam waist in the virtual image and the virtual images of the beam waist are located along the line which is normal to the plate. The spacing of the virtually-imaged beam waists is 2t. Similar to a phased array, the beams interfere to form collimated light, which propagates at an angle determined by the wavelength.

In the experiment for the 1.55 μm wavelength range, t and θ were 100 μm and 6.4 degrees, respectively. The angular dispersion is a function of θ and the theoretical value is 0.5 degree/nm. The relation between the wavelength and the output angle ϕ was measured and is shown in Fig. 3. The angular dispersion $|d\phi/d\lambda|$ (λ is the wavelength) is 0.5 degree/nm at $\phi=0$ and has good agreement with the theoretical value. Since the change in ϕ is equivalent to the change in nθ (n is the refractive index of the glass), the angular dispersion varies from 0.4 degree/nm to 0.8 degree/nm as a function of ϕ, not of the wavelength.

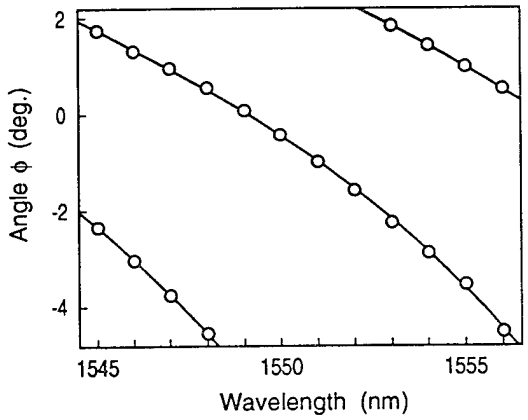


Fig. 3 Output angle vs. wavelength

The VIPA can be used for wavelength demultiplexing. Figure 4 shows an experimental result for 10 channels with a 0.8 nm spacing. In this experiment, the output light from the VIPA was coupled to step index fibers with a lens. The polarization dependent loss was measured to be ~0.1 dB. This result seems to show practical characteristics. It is of importance to theoretically evaluate the insertion loss, the transmission bandwidth, and the

crosstalk. To do this, first, the output field pattern must be calculated. This is done by using a two dimensional model in the plane of Fig. 2. Assuming that the beams diverging from all the virtually-imaged beam waists have the same profile and that its magnitude does not change around the peak direction, the output field traveling in the direction at a deviation angle $\Delta\phi$ is proportional to $1/(1-e^{-\alpha+ikd\Delta\phi})\approx 1/(\alpha-ikd\Delta\phi)$. Here, $k=2\pi/\lambda$, and $e^{-\alpha}$ is the square root of the film reflectivity, which is 0.975 for 95% reflectivity. The approximation is valid for small α and small $kd\Delta\phi$, and thus the output is Lorentzian. A drawback of the Lorentzian output as compared with the Gaussian output is its slow decay in the wings.

The output light is coupled to a fiber or a waveguide with a lens (the focal length is f). The coupling ratio is the square of the overlap integral between the field patterns in the output and in the waveguide mode. When the lateral position of the lens is y, the output field is $e^{iky\Delta\phi/(\alpha-ikd\Delta\phi)}$. Assuming $e^{-\alpha}=0.975$, d=20 μm, f=5 mm, a waveguide width of 5 μm, a waveguide index of 1.5, and an effective index difference of 0.004, the coupling ratio was calculated as a function of the lateral displacement x of the output waveguide (Fig. 5). Here, y is determined to minimize the loss, and this gives y=-410 μm for the above parameters. x can be converted into a wavelength change $\Delta\lambda$ by $\Delta\lambda|d\phi/d\lambda|f=x$. When the angular dispersion is 0.5 degree/nm, 1 μm in x corresponds to a wavelength change of 0.023 nm. The insertion loss is 1.0 dB, and the 1 dB-transmission bandwidth is 4 μm in x. The crosstalk decreases slowly as |x| increases. This crosstalk is due to the wings of the Lorentzian output, and the suppression of the crosstalk is an important issue in the VIPA.

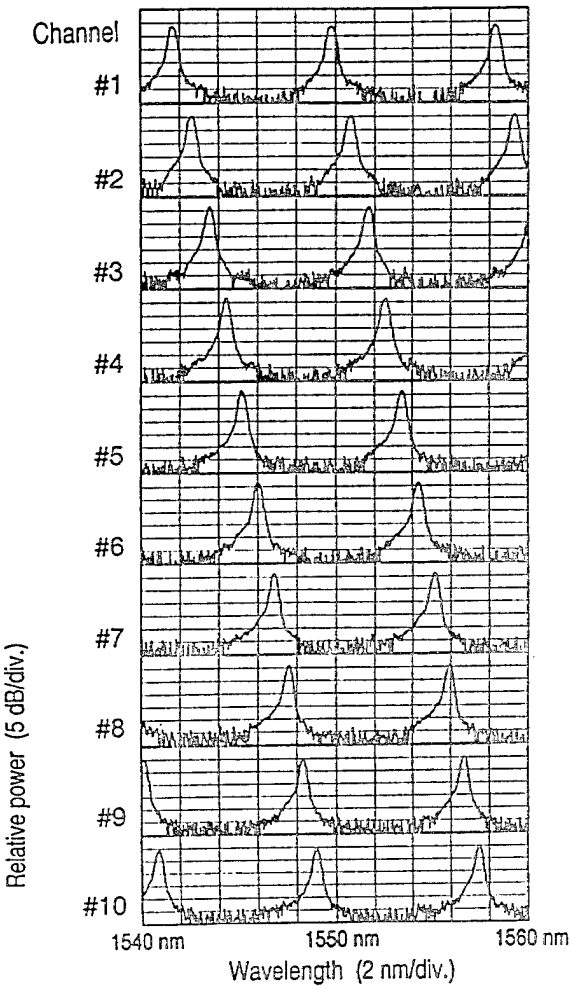


Fig. 4 10 channel demultiplexing

Next, it is shown that both the crosstalk and the transmission bandwidth are improved by using a split-core at the input facet of the output waveguide. Note that the split-core is not necessarily the same as a dual-core waveguide that can possess symmetric and anti-symmetric modes. When the split-core consists of two 5 μm wide sections separated by a 4 μm gap at the input facet, as shown in Fig. 6, the mode pattern will have a dual-peak. Here, the waveguide index n_{WG} is 1.5 and the effective index difference Δn_{eff} is 0.004. The coupling ratio is shown in Fig. 7. Comparing

with Fig. 5, the insertion loss (3.0 dB) is higher and the 1 dB-transmission bandwidth (10.0 μm in x) is broader as expected. An interesting feature is the suppressed crosstalk. (e.g. the crosstalk at x=30 μm is -29 dB in Fig. 5 and below -40 dB in Fig. 7.) This can be understood by considering the phase of the wings in the output field, which changes by a factor of $e^{iky\Delta\phi}$ as described above. Thus, the two peaks of the waveguide mode give opposite contributions to the overlap integral, if the two peaks see a phase difference of π in the wing. With λ=1.55 μm, y=-410 μm, and f=5 mm, the period of the phase change is 18.9 μm along the lens focal plane, and the distance between the mode field peaks in Fig.6 is approximately half of this period.

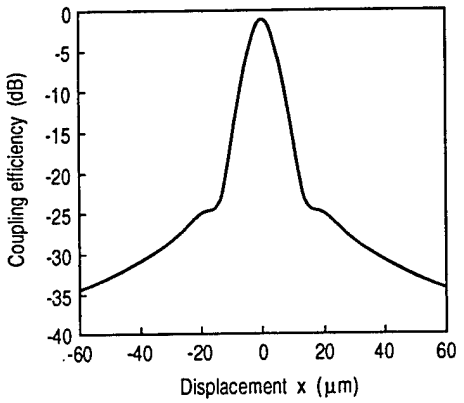


Fig. 5 Coupling to a step index waveguide

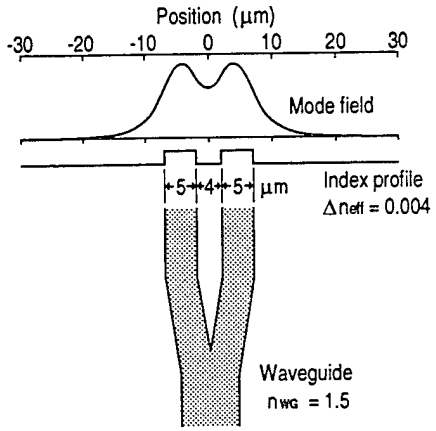


Fig. 6 Output waveguide profile and the mode field

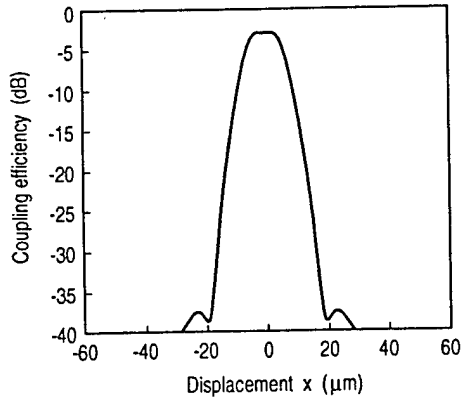


Fig. 7 Coupling to a split-core waveguide

In conclusion, a new scheme based on a virtually-imaged phased-array was analyzed with regard to characteristics for a dense WDM filter. It was found that a split-core output waveguide improved the filtering spectrum remarkably, that is, the transmission bandwidth was broadened and the crosstalk was suppressed.

The author thanks Prof. W-P. Huang for useful discussions, M. Seino and T. Nakazawa for help with the fabrication, and N. Fukushima for help with the measurements.

1. D. R. Wisely, Electron. Lett., Vol. 27, 520 (1991)
2. M. K. Smit, Electron. Lett., Vol. 24, 385 (1988)
3. H. Takahashi et al., Electron. Lett., Vol. 26, 87 (1990)
4. M. Shirasaki, Technical Digest, Microoptics Conference (MOC'95), paper PD3, Hiroshima, Japan

Use of Multimode Interference Couplers to Broaden the Passband of Dispersive Integrated WDM Filters

J.B.D.Soole, M.R.Amersfoort, H.P.LeBlanc, N.C.Andreadakis,
A.Rajhel, C.Caneau, R.Bhat, and M.A.Koza

C.Youtsey and I.Adesida *

Bellcore,
331 Newman Springs Road,
Red Bank, NJ 07701

*CCSM, Beckmann Institute and
Dept. of Electrical and Computer Engineering,
University of Illinois, Urbana IL 61801

Introduction: One of the problems encountered with conventional waveguide-based WDM filters now being developed for use in WDM telecommunications and computer fiber networks is that their spectral passbands are "peaked". Deviation of a signal wavelength from the center of a filter passband thus introduces excess loss. All signal wavelengths and filters have therefore to be very precisely aligned if a high-performance system is to be obtained, which places very tight constraints on both device and system design and operation.

The integrated multi-wavelength filters now being developed operate by dispersing according to wavelength a guided mode carrying wavelength-multiplexed signals, and passing the wavelength-demultiplexed signals out through different single-mode output waveguides. We recently reported that such filters could be "flattened" through the use of an integrated Multimode Interference Coupler (MMI) [1]. In this paper, we describe our approach in more detail, and show how precisely formulated passband flattening may be simply obtained.

Discussion: The arrayed waveguide grating filter, illustrated in Figure 1, is taken as an example of a wavelength-dispersive WDM filter [2]. (The method is also applicable to other dispersive filters, such as the etched grating filter.) The input signal guided mode launched into the planar region P_1 becomes refocussed in region P_2, and dispersed across the conjugate focal line y-y', according to wavelength. See Figure 2. The power coupled into any given output waveguide is determined by the overlap of the focussed spot with the output guide-mode. The filter transmission function, T, is given by the convolution of the focussed field profile $\varphi_o(y)$ and the output guide-mode $\varphi_g(y)$. In the wavelength domain,

$$T(\lambda-\lambda_0) = [\int \varphi_o(y)\, \varphi_g^*(y-Y)\, dy\,]^2 \;/\; (\partial Y/\partial\lambda)\ , \qquad \text{(Eqn 1)}$$

where $(\partial Y/\partial\lambda)$ is the dispersion in the image plane and λ_0 is the peak transmission wavelength.

The case where $\varphi_o(y)$ is a single focussed spot is illustrated in Figure 2.

The task of achieving a flattened or broadened transmission function T thus becomes that of providing the appropriate function $\varphi_O(y)$. As $\varphi_O(y)$ is the image of the input guide mode $\varphi_i(x)$ launched into P_1, this reduces to the task of providing the appropriate mode field $\varphi_i(x)$.

The simplest design approach is provided by assuming the output guide-mode to be Gaussian-like, $\varphi_g(y) \propto \exp(-y^2/y_g^2)$, and $\varphi_O(y)$ to be composed of two separated Gaussians, $\varphi_O(y) \propto \exp(-\{y-Y/2\}^2/y_0^2) + \exp(-\{y+Y/2\}^2/y_0^2)$. Equation 1 then shows that T is also composed the sum of two Gaussians, each with width, $y = (y_0^2 + y_g^2)^{1/2}$ (Eqn. 2). The overall filter shape is determined by the ratio, f, between the Gaussian's separation, Y, and their width, y: $f = Y / y$. As f>0, the filter broadens to yield a flat central region when $f=\sqrt{2}$, and above this the peaks separate to give a shallow central depression. The influence of f on the filter shape is shown in Figure 4.

By introducing a mode field that approximates the two displaced Gaussia $\varphi_O(y)$ illustrated on the l.h.s. of Figure 3 at the input into the planar region P_1, the filter may thus be broadened and flattened. Such a field may be provided by a MMI coupler with a length such as to provide 2-fold imaging, as illustrated in Figure 5 [3]. The spacing between the two-fold MMI images X_{MMI} is preserved by the 1:1 imaging of the filter, so that combining Eqns 2 and 3 we find $X_{MMI} = \sqrt{2}\ (x_i^2 + y_g^2)^{1/2}$ (Eqn. 4) for an ideally flattened filter with $f=\sqrt{2}$. In the case where we have identical input and output guides, this gives $X_{MMI} = 2\ x_i$.

Assuming Gaussian-like guide mode profiles, Eqn. 4 thus determines the MMI required to form a flat filter. In the case of MMI's that provide a high mode-confinement, the MMI width W_{MMI} is simply twice X_{MMI}. For MMI's where the confinement is weaker, $W_{MMI} > 2\ X_{MMI}$, and BPM analysis of the MMI may be used to obtain the W_{MMI} to satisfy Eqn. 4. Evaluation of Eqn 1 using BPM of the MMI to obtain $\varphi_i(x)$ provides a full description of the filter performance.

Demonstration: We have illustrated this method for passband broadening in InP arrayed waveguide filters by forming filters both with and without MMI's. All filters had waveguides composed of 0.2μm-thick 1.25Q cores surrounded by InP cladding. The performance of the filter without the MMI is shown in Figure 6.

The first filter with an MMI had 2μm-wide guides and a 4.5μm-wide MMI. Filter performance is shown in Figure 7. In this case, the filter is still rounded, with the two-fold images provided by the MMI separated by less than that required for a perfectly flat filter. Using the above analysis, $f \sim 0.7\sqrt{2}$, taking the e^{-2} field half-width to approximate x_i, and the associated predicted transmission

function is shown by the light solid line. Calculation of Eqn 1 using a BPM evaluation of φ_0 is also shown, dashed. Both analyses give accurate description of filter performance.

The second MMI filter had 3μm input / output guides and a 6μm MMI, and is shown in Figure 8. It has a substantially flattened central region, with the -1dB passband making up nearly half the -20dB passband. The MMI image peak separation and x_i (in the e^{-2} field half-width approximation) yield $f \sim 0.9\sqrt{2}$, which is close to that for a perfectly flat filter, and the Gaussian approximation again provides a good overall fit. A full PBM evaluation gives a similar filter shape, and also predicts the small dip observable at the filter center, which arises because the field strength between the MMI images is slightly less than given by the Gaussian approximation — a consequence of the moderate field-confinement provided by the MMI.

(Note that the wavelength dispersion is different for the three filters shown; only the filter *shapes* should be compared.)

Summary: We have described how a broadened filter transmission may be obtained by introducing a two-fold imaging MMI. We have also shown that the extent of the broadening may be simply adjusted by setting the relative widths of the MMI and input/ouput guided modes.

Acknowledgement: This work was funded in part by ARPA, contract MDA972-94-3-0036.

---

1) J.B.D.Soole, M.R.Amersfoort, H.P.LeBlanc, N.C.Andreadakis, A.Rajhel, and C.Caneau, *LEOS '95*, post-deadline paper, San Fransisco, Nov '95.

2) M.K.Smit, *Electron. Lett.*, vol. 24, pp. 385-386, 1988.

3) L.B.Soldano and E.C.M.Pennings, *J. Lightwave Tech.*, vol. 13, pp.615-627, 1995.

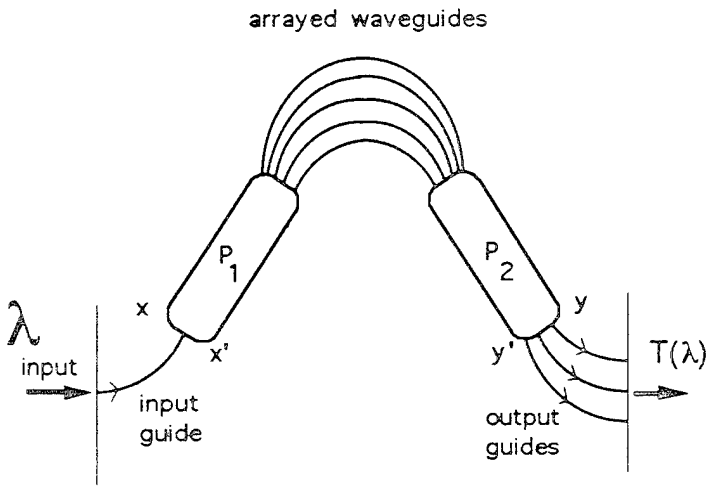


Figure 1. Schematic of arrayed waveguide grating

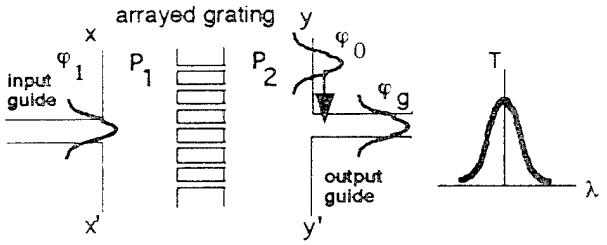


Figure 2. Filter operation

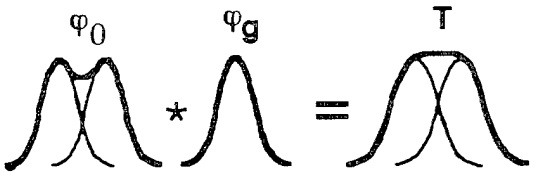


Figure 3. Formation of broadened filter

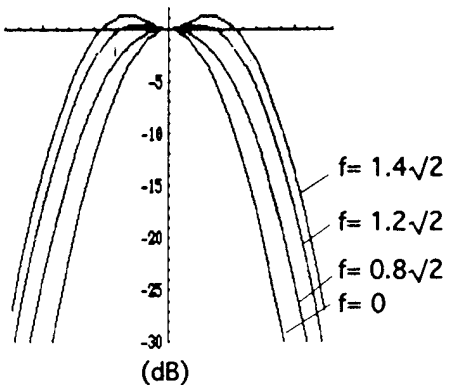


Figure 4. Transmission as function of peak separation

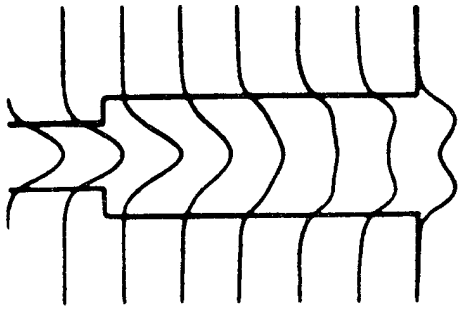


Figure 5. Two-fold imaging of the MMI coupler

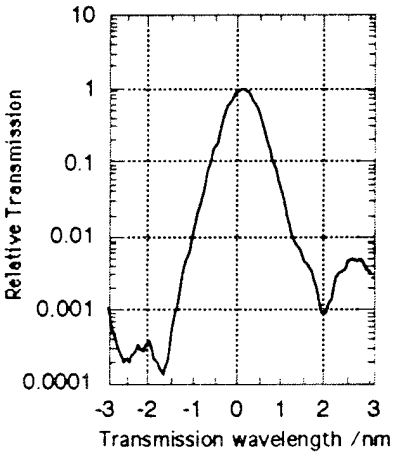


Figure 6. Non-broadened filter.

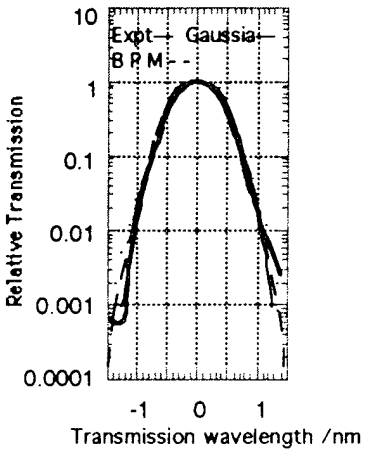


Figure 7. Broadened filter 1.

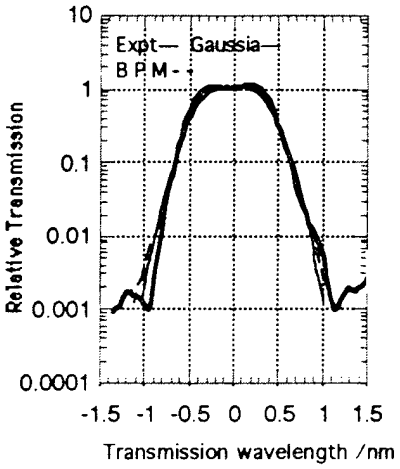


Figure 8. Broadened filter 2.

The elimination of sidelobes in the arrayed waveguide WDM

S. Day, J. P. Stagg, D. Moule, S. J. Clements, C. Rogers, S. Ojha, T. Clapp, J. Brook, J. Morley

BNR Europe Ltd., London Rd., Harlow, Essex, CM17 9NA
Tel 01279 402785 Fax 01279 402765

Introduction

Narrow channel wavelength division multiplexing (WDM) is an attractive technique for increasing the capacity of optical fibre transmission systems. An essential component for WDM systems is a wavelength demultiplexer capable of providing high levels of isolation between adjacent channels. Additionally if the components are to be deployed in large volumes then they will be required to be low cost. Silica-on-silicon technology is an attractive technology for producing such components[1].

The arrayed waveguide grating component which was first proposed by Dragone [2], has been demonstrated to be a promising device for such applications[3]. The component consists of two radiative stars interconnected by an array of waveguides, with a constant path length difference between adjacent waveguides. The radiative stars are the key elements which determine the crosstalk and insertion loss of the WDM component. The field distribution in the input waveguide is approximately gaussian. When the field reaches the planar section of the first radiative star it is no longer confined laterally and diverges. The far field, which is also approximately gaussian, is launched into the grating array of waveguides. The number of grating waveguides needs to be sufficient to capture all of the far field. If there are not enough waveguides in the grating section, then the insertion loss of the component increases and also when the light is focused in the second star sidebands are produced.

An 8 channel WDM with 4 nm channel spacing was designed using 5 μm high waveguides with a Δn of 7×10^{-3}. The radiative star had a radius of 3.3 mm, with 17 μm wide waveguides arranged on a 21 μm pitch. The WDM had 24 waveguides in the grating section. The overlap integral between the modefields of adjacent waveguides is close to -30 dB, thus the WDM would be expected to have a similar level of adjacent channel isolation. Modelling of the radiative star indicated that there were sufficient arms in the grating section to suppress the sidelobes below -30 dB. However experimentally it was observed that the isolation was close to -22 dB.

Offset of phase centre due to coupling

As the waveguides come together in the input radiative star, then light can couple into adjacent waveguides. Without coupling, the input field starts to diverge when it reaches the planar region. Coupling offsets the focal position of the input field, so that it appears to originate within the array of input waveguides. In the output radiative star, as the output waveguides fanout from each other, light is able to couple into adjacent waveguides, reducing the isolation. The coupling was modelled using a beam propagation model (BPMCAD), which predicted a reduction in isolation to about -25 dB.

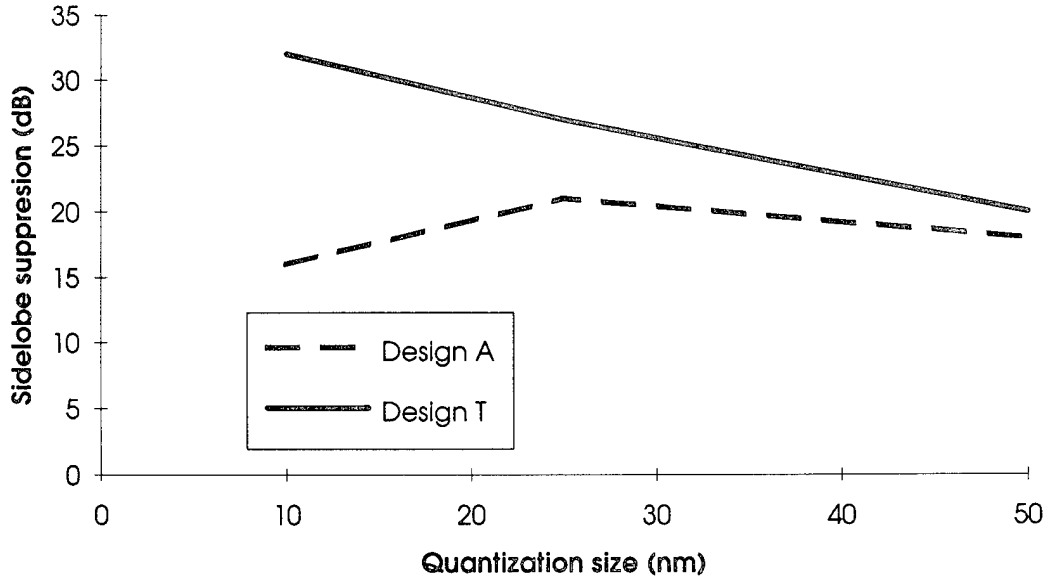
Two methods can be used to correct for coupling effects. Firstly they can be eliminated by increasing the spacing between waveguides. Secondly they can be compensated for by moving the two surfaces of the radiative star together, so that instead of each member of the two waveguide arrays pointing at the end of the central waveguide in the opposite array, they are pointing towards the offset focal point. Both of these methods have been investigated experimentally and further design iterations have been produced.

Phase errors

Modelling of random phase errors showed that to achieve good sidelobe suppression, it is necessary to control the optical path length to better than ± 20 nm, over a length of several centimetres. The optical path length is controlled by several factors. Firstly there is the actual physical path, which is determined by the mask and secondly there are fluctuations caused by variations in the refractive index.

The generation of the mask is intensely dependent upon software. Initially a software package is used which calculates the start and end co-ordinates of each waveguide. The second stage is to transform the waveguide path into an array of grid co-ordinates which are used to define the actual mask writing process. Errors can occur in the calculation of the initial path, all the routines used were carefully verified and where possible different methods were used to calculate the values of co-ordinates. The second part of the mask generation involves the quantization of the data, the quantization size being a key parameter. The first mask written using the BNR electron beam machine had used a quantization of 50 nm. The BNR facility is capable of using quantizations as small as 10 nm, although the mask writing time increases from 1 hr/WDM to 9 hrs/WDM. A test mask was fabricated containing 2 different WDM devices each one being written three times with quantizations of 10, 25 and 50 nm. Figure 1 below shows measured sidelobe level against quantization size

Figure 1 : Measured sidelobe level against quantization size



For 5 of the 6 components made, there is excellent correlation between the sidelobe suppression and the quantization size, the sidelobe suppression increasing linearly as the

quantization size decreases. As the quantization size reduces, the measured performances will approach the theoretical limit for a particular design. Hence for design A, which is limited by coupling effects, the improvement is not as great as for T.

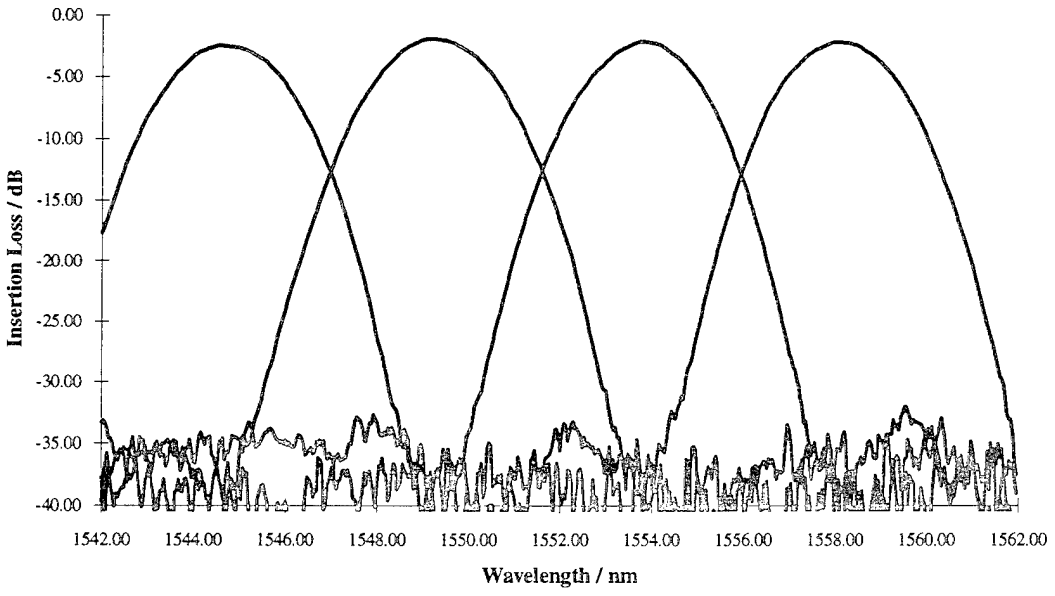
However when design A was made, with a 10 nm quantization size, worse sidelobe suppression was achieved. The data was checked, but no obvious reason was found for this anomalous result. One possibility could be that because the write time is about 9 hours, there is a greater probability of the electron beam machine being affected by a random voltage spike. Due to the failure to identify the mechanism in this case, the final mask was fabricated using a 25 nm quantization. Quantization is a key factor in sidelobe suppression and there is potential for improvement with further work.

Although it has not been possible to quantify the effect of small scale random process variations. The results from this test mask would suggest that such effects are of much less importance than mask errors.

Elimination of coupling effects

In this design, the waveguide pitch was increased, which significantly reduces coupling effects. From the modelling of coupling effects, the changes relative to the initial design should give an improvement in isolation of about 10 dB. This was very close to the actual improvement to give an isolation of -32 dB, as shown below in figure 2. This is one of the best isolation results reported for this kind of device and demonstrates the levels of performance required by practical systems.

Figure 2 : 4 channel WDM with 4 nm channel spacing, isolation of -32 dB



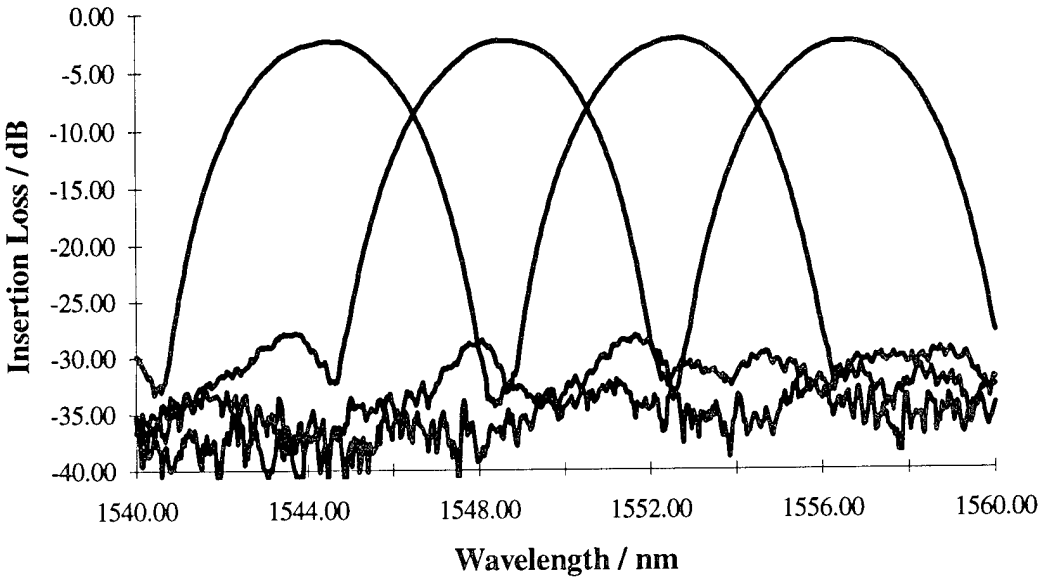
I104\Al2

Phase centre compensation

The response of the WDM was modelled by summing all of the amplitude components in each arm of the grating section and introducing a correction for phase centre offset. This modelling

predicted that sidelobes would be produced at -22 dB for a phase centre offset of 100 μm. A series of 3 designs were produced where the two surfaces of the radiative star were offset in 50 μm steps from 0 to 100 μm, to compensate for phase centre displacements. This series shows a steady improvement in sidelobe suppression, indicating that as predicted, phase offsets are a limiting factor. By fitting a parabola to the experimental points it was possible to infer that a 100 μm offset is very close to the optimum phase centre compensation. This device had an isolation greater than -27 dB, as illustrated below in figure 3. The use of phase centre compensation has reduced the sidelobes, in addition this device has a 50 % wider passband than the first design.

Figure 3: Insertion loss for 4 channel WDM, with phase centre compensation



Conclusions

Two approaches have been used to reduce sidelobes caused by coupling effects in the arrayed waveguide WDM. One method is to eliminate them by spacing the waveguides sufficiently far apart, this approach has led to an adjacent channel isolation of greater than -32 dB. The second approach has been to compensate for phase centre offsets, via the use of corrections to the radiative stars. Using the second approach an isolation of -27 dB has been achieved, with the additional benefit of a 50% increase in passband. Additionally phase errors due to quantization errors in masks have been shown to be an important parameter in achieving good levels of isolation

Acknowledgements

The authors would like to thank the directors of BNR Europe Limited for permission to publish this paper. This work was partially funded under RACE 2001.

---

[1] Grant, M. 'Low loss coupling of ribbon fibres to silica on silicon integrated optics using preferentially etched v-grooves'. Integrated Photonics Research 92 Proc, April 92

[2] Dragone C. 'An N x N optical multiplexer using a planar arrangement of two star couplers' IEEE Photonics Technology Letters, V3 N9, Sept 1991

[3] K. Okamato 'Fabrication of a 64 x 64 arrayed waveguide grating multiplexer on silicon' elect let.

Loss reduction for phased-array demultiplexers using a double etch technique

C. van Dam, A. A. M. Staring*, E. J. Jansen*, J. J. M. Binsma*, T. van Dongen*, M. K. Smit and B. H. Verbeek*

Delft University of Technology, Dept. of Electrical Engineering
P.O. Box 5031, NL-2600 GA Delft, The Netherlands
Phone: +31 - 15 - 2787089, Fax: +31 - 15 - 2784046
*Philips Optoelectronics Centre, Eindhoven, The Netherlands

Introduction

Wavelength Division Multiplexing (WDM) is an effective technique to exploit the huge bandwidth of optical fibres. Key components in such WDM-systems are demultiplexers which spatially separate the different wavelength channels. Phased-array demultiplexers combine ease of fabrication and low insertion losses. Silica-based phased-array demultiplexers are realised with low losses from 2-3 dB [1,2]. InP-based demultiplexers show slightly higher on-chip losses of 4-6 dB [3,4]. In addition they have considerably higher fibre coupling losses (several dB's), but the advantage of InP-based demultiplexers is that they can be integrated with active components. Earlier we reported a low-loss demultiplexer with reduced fibre coupling loss by applying deeply etched InGaAsP waveguides with a relatively large core and a low index contrast, which had an almost circular mode profile [5]. The component had 4-5 dB on-chip loss and fibre coupling loss of about 1 dB to a tapered fibre. In this article we report a method to further reduce the on-chip losses.

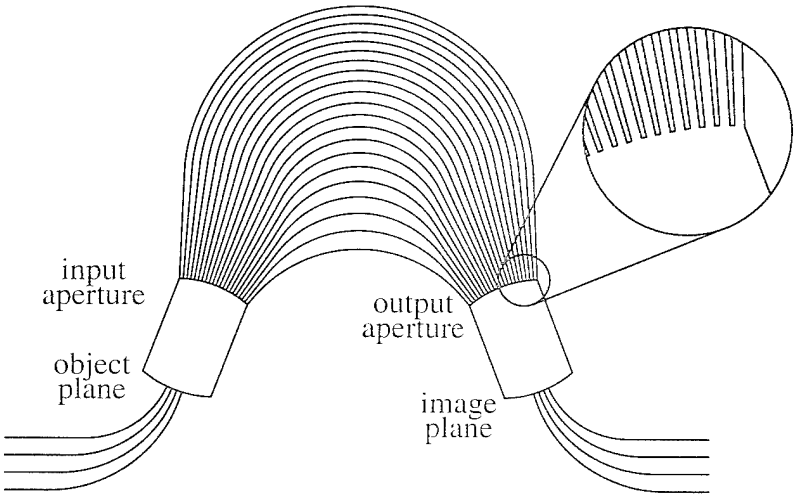


Figure 1. Schematic layout of the phased-array demultiplexer.

Design

Most of the on-chip loss occurs at the junctions between the array and the slab guide, the so-called free propagation region (FPR), as shown in the inset of figure 1. At this junction the field in the waveguide section shows a very deep modulation (figure 2a, solid line) due to the deep trenches between the array waveguides.

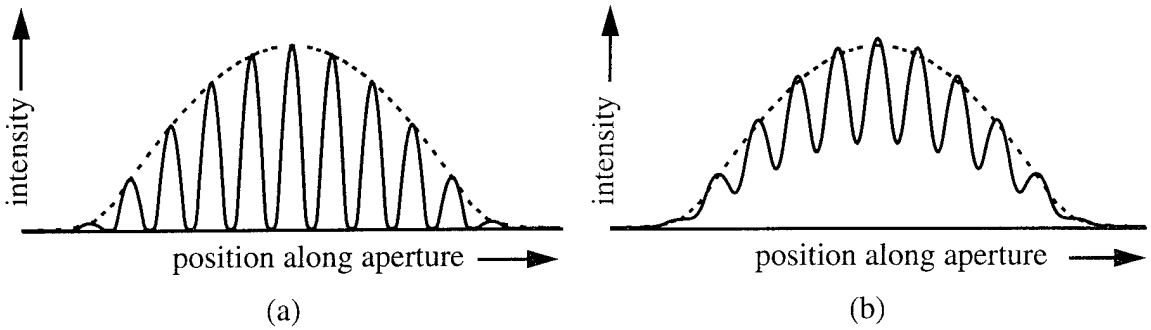


Figure 2. Fields at the aperture: sum field of the array waveguides (solid line), and the field required for efficient coupling to the receiver waveguide order (dashed line). In (a) the the fields are shown for the deeply etched waveguide structure. The coupling efficiency can be improved by a using a shallowly etched waveguide structure, as shown in (b).

The ripple in the field pattern causes a considerable fraction of the power to be radiated into adjacent orders. The dashed line depicts the field corresponding to the dominant order, which couples efficiently into a receiver waveguide. The coupling efficiency is found from the overlap of the two fields. The overlap is increased by filling the zeroes between the individual waveguide modes (figure 2b, solid line). This can be done by inserting a shallowly etched transition region (TR) between the deeply etched array waveguides and the FPR, as shown in figure 3. This method has been applied before to waveguide bends, in order to reduce the bending and scattering losses [6].

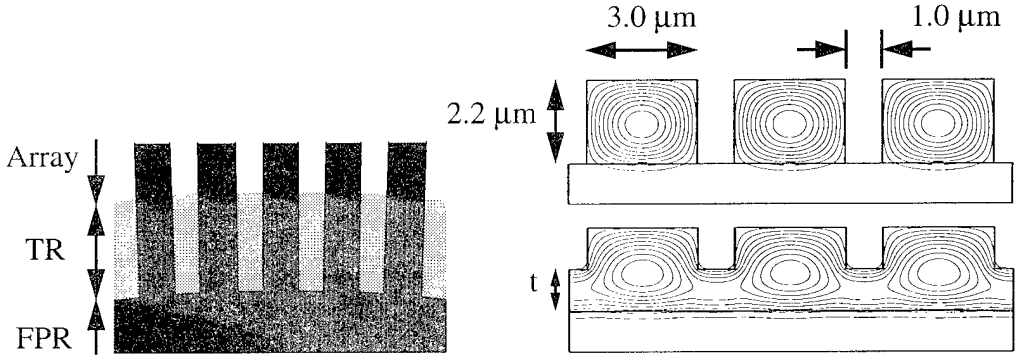


Figure 3. Detail of the transition region (TR) at the junction between the array waveguides and the free propagation region (FPR) (left, topview). Also shown are the field distributions in the waveguide structure as used for the array waveguides (upper right) and for the waveguides in the transition region (lower right).

Now the coupling between the FPR and the array waveguides takes place in two steps. First the fields in the array waveguides couple to the fields of the TR waveguides, and then these fields couple to the dominant order in the FPR. By increasing the thickness t of the TR, the efficiency of the latter coupling increases due to the fact that the exponential tails of the fields in the TR waveguides extend further into the film next to the waveguides, resulting in filling the zeroes between the individual waveguide modes. This TR thickness dependency of the coupling efficiency is shown in figure 4a (dashed line), where coupling losses for two slab-array junctions - at input and output aperture - are shown (only for TE polarisation). However, the

coupling efficiency of the elliptical waveguide fields in the TR to the circular waveguide fields in the deeply etched array waveguides decreases with increasing TR thickness t (figure 4a, dotted line), and an optimum in the combined coupling efficiency can be found (figure 4a, solid line). The total coupling efficiency for t = 0 μm, i.e. without TR, is 3.5 dB. A similar graph can be obtained for TM polarisation. In figure 4b the total loss reduction is shown for both TE and TM polarisation. The optimum TR thickness is 1.1 μm, resulting in a predicted loss reduction of 2.2 dB for TE polarisation, and 1.9 dB for TM polarisation..

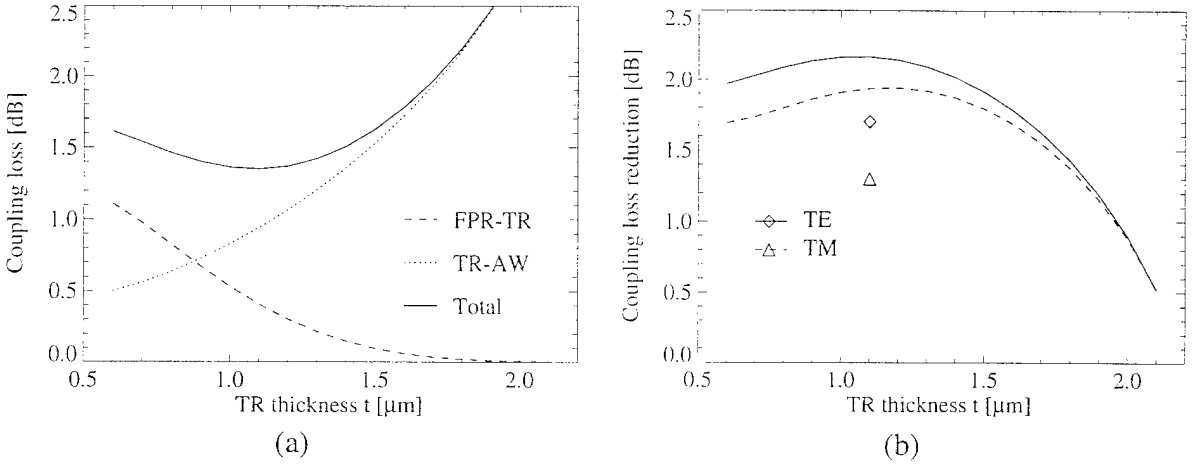


Figure 4. Coupling losses versus TR film thickness. In (a) the losses are shown for two slab-array junctions for TE polarisation: the dashed line depicts the coupling between the FPR and the TR, and the dotted line the coupling between the TR and array waveguides (AR). The solid line shows the combined loss. In (b) the total predicted loss reduction is shown for TE polarisation (solid line) and TM polarisation (dashed line). Also shown is the measured reduction for TE (diamond) and TM polarisation (triangle).

Fabrication

Two phased-array demultiplexers have been fabricated using raised strip waveguides in LP-OMVPE grown undoped InGaAsP(λ_g = 1.02 μm) on InP substrate, one of which was used for the double etch experiment. The devices have 8 wavelength channels with a 2 nm channel spacing. The width and thickness of the raised strip waveguides are chosen as 3.0 μm and 2.2 μm respectively, to obtain zero birefringence. The etch depth for the TR was chosen 1.1 μm, yielding an optimum TR thickness of 1.1 μm. The length of the TR was chosen 10 μm, which is - according to BPM analysis - sufficiently short to get rid of the radiation modes excited at the first junction. The waveguides are reactive ion etched (RIE) using Cl_2 for smooth sidewalls and low scattering losses, resulting in an optical loss of 2 dB/cm both for TE and TM polarisation. Due to the high lateral index contrast, small bending radii can be used (200 to 500 μm), giving an array size of 1.0x1.3 mm^2, measured from object plane to image plane, and an overall device size of 1.2x3.3 mm^2 because the input and output waveguides are positioned with a 250 μm pitch for tapered fibre ribbon coupling.

Experiments

Figure 4b shows the experimental improvement obtained. It can be seen that the reduction of the insertion loss is 1.7 dB for TE polarisation and 1.3 dB for TM polarisation, which is only

0.6 dB less than predicted. The gap between the waveguides was larger than in a previous design [5], which resulted in a slightly higher on-chip loss of 6 and 7 dB for TE and TM polarisation respectively, for the device with the transition region. Crosstalk values are -25 dB or better.

Conclusion

We have demonstrated a method to reduce the insertion loss of phased-array demultiplexers. In this method an intermediate section with a shallow etch depth is inserted at the junction between the free propagation region and the array waveguides, resulting in lower coupling losses. Feasibility of the concept is demonstrated experimentally for an 8 channel demultiplexer with 2 nm channel spacing employing non-birefringent InGaAsP(λ_g = 1.02 μm)-on-InP raised strip waveguides. The measured on-chip loss is 7.7 and 8.3 dB for TE and TM polarisation respectively, for the device without the transition region. The device with transition regions showed an on-chip loss of 6 and 7 dB, resulting in a reduction of 1.7 dB and 1.3 dB for TE and TM polarisation respectively. This is only 0.6 dB less than predicted by theory.

Acknowledgement

Part of this work has been carried out in the RACE 2070 MUNDI (Multiplexed Network for Distributive and Interactive Services) project.

References

[1] K. Okamoto, M. Ishii, Y. Hibino, Y. Ohmori, and H. Toba, "Fabrication of unequal channel spacing arrayed-waveguide grating multiplexer modules", *Electron. Lett.*, vol. 31, pp. 1464-1465, August 1995.

[2] K. Okamoto, M. Ishii, Y. Hibino, and Y. Ohmori, "Fabrication of variable bandwidth filters using arrayed-waveguide gratings", *Electron. Lett.*, vol. 31, pp. 1592-1594, August 1995.

[3] M. R. Amersfoort, C. R. de Boer, B. H. Verbeek, P. Demeester, A. Looyen, and J. J. G. M. van der Tol, "Low-loss phased-array based 4-channel wavelength demultiplexer integrated with photodetectors", *IEEE Photon. Technol. Lett.*, vol. 6, pp. 62-64, January 1994.

[4] H. Bissessur, F. Gaborit, B. Martin, and G. Ripoche, "Polarisation-independent phased-array demultiplexer on InP with high fabrication tolerance", *Electron. Lett.*, vol. 31, pp. 1372-1373, August 1995.

[5] B. H. Verbeek, A. A. M. Staring, E. J. Jansen, R. van Roijen, J. J. M. Binsma, T. van Dongen, M. R. Amersfoort, C. van Dam, and M. K. Smit, "Large bandwidth polarisation independent and compact 8 channel PHASAR demultiplexer/filter", In *OFC/IOOC '94 Technical Digest, Postdeadline papers*, pp. 63–66, San Jose, U.S.A., February 20-25 1994.

[6] E. C. M. Pennings, J. van Schoonhoven, J. W. M. van Uffelen, and M. K. Smit, "Reduced bending and scattering losses in new optical 'double-ridge' waveguide", *El. Lett.*, vol. 25, pp. 746-747, May 1989.

Monday, April 29, 1996

Passive and Active Component Modeling

IMD 1:30 pm-2:45 pm
Fairfax A

J.M. Zavada, *Presider*
U.S. Army Research Office

Design of Planar Optical Waveguide Corners with Turning Mirrors

Wei Yang*, Anand Gopinath
University of Minnesota
Department of Electrical Engineering
Minneapolis, MN 55455

currently* Honeywell Technology Center
12001 State Highway 55
Plymouth, MN 55441

1 Introduction

Integrated optical circuits use planar optical waveguides to perform routing, and other functional operations on the optical signals. In the routing function, these guides have to convey signals from one location on the circuit to another, and these involve the use of bends and corners. It is known that sharp discontinuities in optical waveguides result in losses in the form of radiation, and the design of these bends and corners to minimize is of considerable importance.

In this paper, we discuss the design of the corner bend which uses a turning mirror, and the form that the turning mirror is shown in Figure 1. The analysis of these structures is performed using the boundary integral method outlined in an earlier publication [1]. The method has been extended to allow the analysis of both the quasi-TE and quasi-TM modes of operation, and we therefore describe the method and present the results obtained on the corner bend. We provide a brief outline of the method used for the TM mode case only. A more detailed description of the method with results on a variety of structures including the quasi-TE mode structures will be discussed elsewhere [2].

2 Analysis Method

Consider a region comprising of piecewise homogeneous domains, $m = 1, 2, 3...$, with propagation constants β_m, which are separated by a series of boundaries. In the case of nonmagnetic dielectric structures β_m is given by $\omega n_m/c_0$, where n_m is the index of the mth domain, ω is the radial frequency of the propagating wave, and c_0 is the velocity of light in free space. Given any point r_0 in domain m, by Green's theorem, the scalar field can be expressed in terms of the boundary values:

$$\phi(r_0) = \int (\phi(r)\frac{\partial G_m(r - r_0)}{\partial n} - G_m(r - r_0)\frac{\partial \phi(r)}{\partial n})dS \tag{1}$$

where the integral is performed on the boundary and G_n is the Green function in the domain, which is $exp(j\beta_m r))/r$ for 3-D and $H_0(\beta_m r)$ for 2-D, and the complete solution requires that all the boundary values are known. We set N points on the boundaries, and for simplicity these points are uniformly spaced, and each point occupies a unit area (or unit length for 2-D domain). The scalar field, and its normal gradient at point i are denoted by ϕ_i and $\psi = \partial\phi/\partial n$. Note that since these values are shared by both sides of the boundary, continuous boundary conditions are applied. We also define operator $\delta_{ij} = 1$ for boundary point i and j on the same domain, and $\delta_{ij} = 0$ otherwise. Applying Green's theorem, and replacing the integral in equation 1 with a summation for boundary point i, the scalar field ϕ_i can be evaluated from either left or right side of the boundary. It can be proved that for j on the left:

$$\frac{1}{2}\phi_i = \sum_{j \neq i} \phi_j \frac{\partial G_l(r_j - r_i)}{\partial n}\delta_{ij} - \sum_{j \neq i} G_l(r_j - r_i)\psi_j\delta_{ij} + S_{li} \tag{2}$$

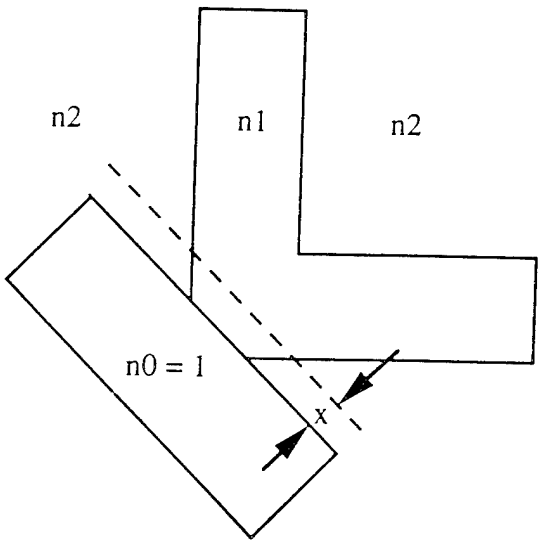


Figure 1: Effective index of right angle bend with turning mirror, guide is 3 μm wide, and the effective indices of the guide and outer regions are 3.3, and 3.295 respectively, with the mirror region of index 1.0

and for j on the right:

$$\frac{1}{2}\phi_i = -\sum_{j\neq i}\phi_j \frac{\partial G_r(r_j - r_i)}{\partial n}\delta_{ij} + \sum_{j\neq i} G_l(r_j - r_i)\psi_j\delta_{ij} + S_{ri} \tag{3}$$

where G_l and G_r are Green functions in the left and right side domains, S_l and S_r are left and right side integral contributions from the sources, which are boundary nodes with known field values. The sign change in equation 3 is due to the definition of normal direction. Linear system of 2N equations with 2N unknowns (ϕ_i, ψ_i) in equations 2, 3 can be explicitly solved. Note that evaluation of the matrix elements is merely a task of calculating Green functions for pairs of points, and since many points may not "see" each other $\delta_{ij} = 0$, the matrix is sparse in most structures. With the TE mode, which has the electric field in the plane of the paper, additional boundary conditions need to be imposed, and these will be outlined in detailed elsewhere [2] .

3 Results

Using this method, we have been able to examine a waveguide with a right angle corner, as shown in Figure 1, together with the turning mirror. Since the method is two dimensional, we have used the concept of effective indices, also shown in the figure. The guide is single mode, 3 μm wide, effective index of 3.3, and the outer regions have an effective index of 3.295, and the wavelength of the propagating mode is 850 nm. For this case with a reduced mirror size of the form shown in Figure 2, the calculated results of the fields are shown in Figure 3. The loss is calculated by taking the overlap integral of the field at the output end with the fundamental mode field. The flared guide structure shown in Figure 4 has the lowest loss, and the results of the fields in the guide are shown in Figure 5. In practice the roughness loss at the turning mirror also needs to be added to this loss. The location of the turning

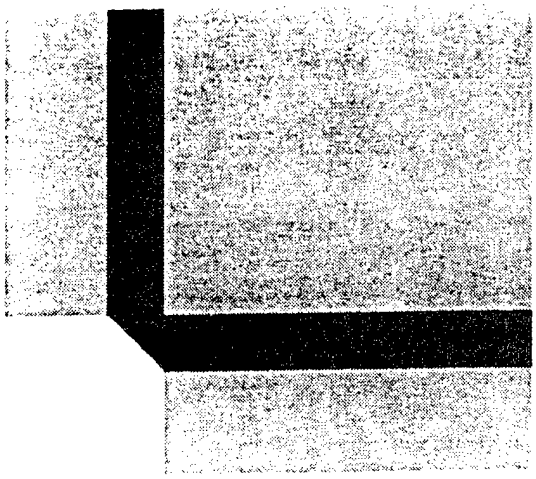


Figure 2: Small turning mirror, with cut away section for the corner bend structure of Figure 1

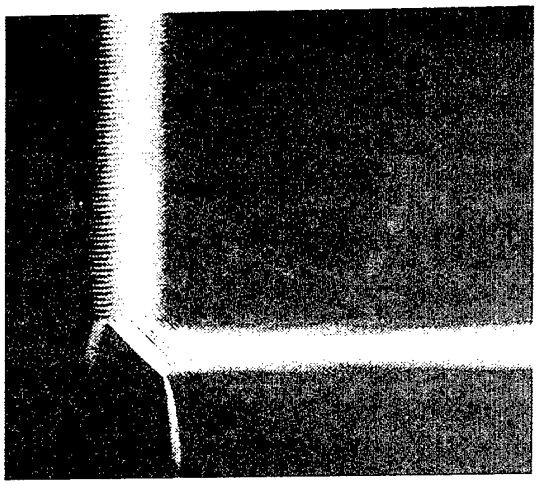


Figure 3: Fields in the small turning mirror, with cut away section for the corner bend structure of Figure 2

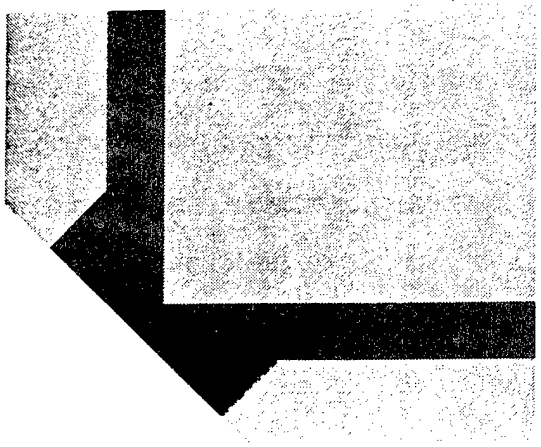


Figure 4: Flared waveguide structure with a wide turning mirror for the corner bend structure of Figure 1

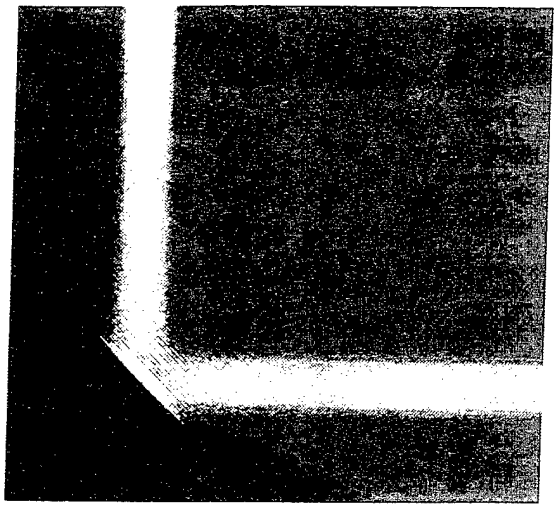


Figure 5: Fields in the flared waveguide structure with a wide turning mirror for the corner bend structure of Figure 4

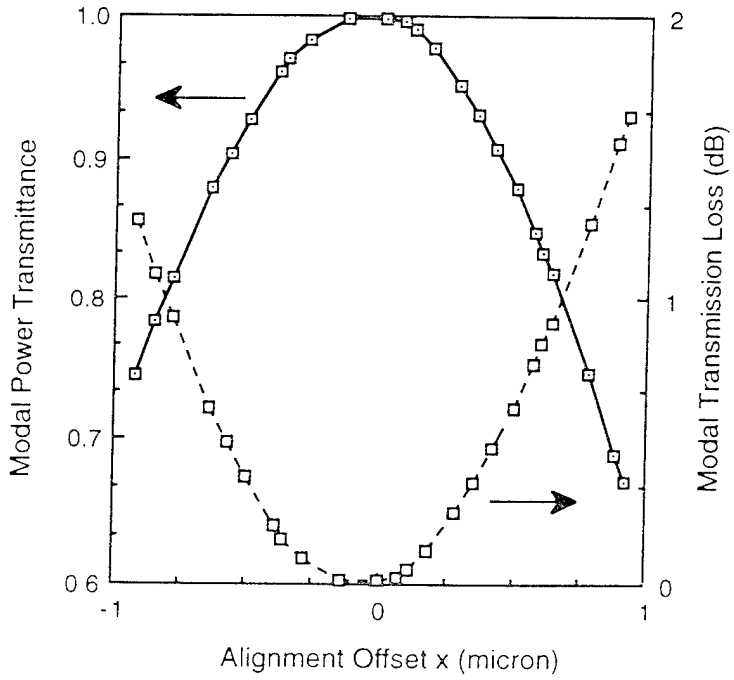


Figure 6: Effect of misalignment of the wide turning mirror in the flared waveguide structure corner bend structure of Figure 4.

mirror in the corner has an optimum position as shown in Figure 6. The calculations were performed for the TM mode cases, and the losses are similar for the TE case.

4 Summary

We have shown that the losses for the reduced mirror size turning mirror results in additional loss, and that the flared guide results in the least loss, and also has an optimum position for the wide turning mirror.

5 Acknowledgements

This work was supported in part by ARPA (through a subcontract with SDL, San Jose, CA), and the University of Minnesota Institute of Technology.

References

[1] W. Yang, A. Gopinath, "A boundary integral method for propagation problems in integrated optical structures", IEEE Photon. Tech. Lett., Vol. 7, pp. 777-779, 1995.

[2] W. Yang, A. **Gopinath,** " A boundary integral method for dielectric waveguide problems", under review.
also W. Yang, "Investigation of components in integrated optoelectronic circuits", Ph. D. Thesis, University of Minnesota, Department of Electrical Engineering, Minneapolis, MN, August 1995.

Electromagnetic Modeling of Optical Guided-wave controlled Microstrip Circuits

Essam S. Tony & Sujeet K. Chaudhuri
Electrical and Computer Engineering Department, University of Waterloo
Waterloo, Ontario, Canada, N2L 3G1.
Phone: (519) 888 4567 FAX: (519) 746 3077

1 Introduction

Optical control of microwave circuits is a fast-growing research area. The aim is to develop microwave devices capable of performing high-speed/high-frequency tasks needed in emerging communication and signal processing systems.

Several authors have proposed the use external bulk illumination for control of microwave devices. External illumination, however, is an inefficient approach to achieve that task. Intergrated guided-wave optical control has been proposed to achieve better and efficient control. Also, composite devices and more complicated control mechanisms could be implemented using guided wave optics.

In this paper, modeling of the optical guided wave control of microstrip circuits is investigated. Techniques for modeling the microwave and optical components of the device, as well as modeling of the interaction between the optical and microwave signals are presented.

2 Basic Device Configuration

Consider the configuration in Fig. 1. The figure shows a microstrip line with a gap in its top metalization. Light is guided in a low-loss dielectric region of the substrate, where it couples into a parallel waveguide just below the gap. The waveguide into which it couples is made of a photosensitive semiconductor material. Consequently, optical energy will be absorbed, and a plasma of electrical carriers will be generated. The capability of shaping the optical guided mode profile allows for a certain degree of freedom in profiling this plasma distribution, in order to best utilize the optical energy available. Due to the proximity of the optical mode to the metal surface, the optical signal will suffer some attenuation. Some techniques may be used to minimize this effect. For example, away from the coupling region, the optical energy

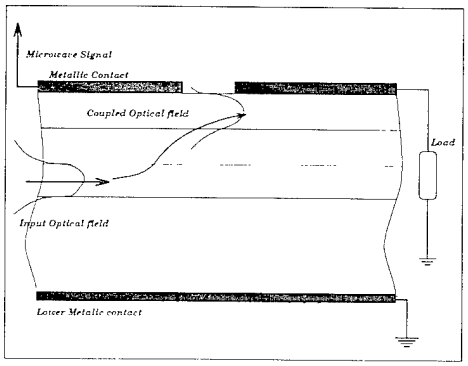


Figure 1: A cross-section in an optically controlled microstrip switch

should be guided in a strongly-guided mode. Also, TE modes are prefered over TM modes since they are less sensitive to the existence of a metallic surface. Further, the optical-energy could be made to approach the surface with in the gap region only, using bends in the waveguide structure for example, as shown in Fig. 2. For these considerations, a directional coupler appears to be a suitable choice of the optical guiding system.

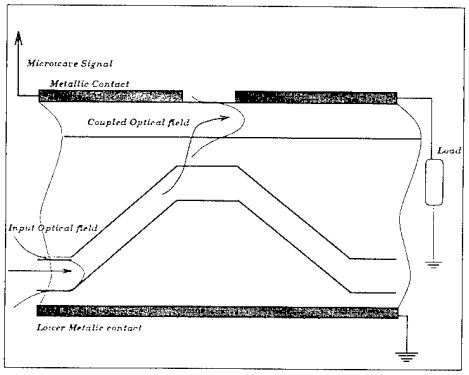


Figure 2: A cross-section in an optically controlled microstrip switch with input bended guide.

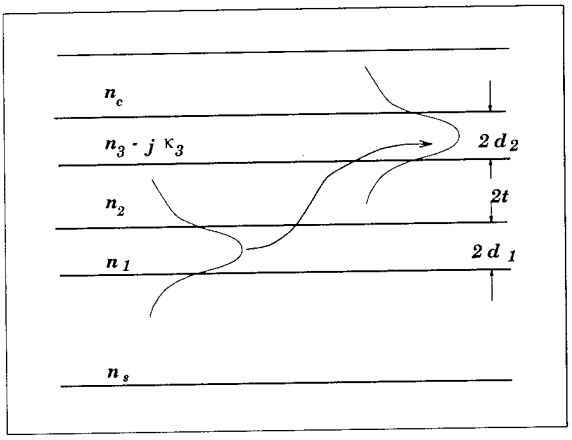


Figure 3: A cross-section in a directional coupler with an absorbing layer

3 Modeling of the Optical Component

Consider the directional coupler shown in Fig. 3. The input waveguide, into which a TE wave at $\lambda = 830$ nm is launched, has a core of thickness $2d_1 = 1$ μm and an index $\tilde{n_1}$= 3.65. The second guide, into which the optical energy couples, has a thickness of $2d_2 = 1$ μm and an index $n_3 - j\kappa_3 = 3.65 - j\ 0.0684$ (GaAs at λ= 830 nm). The separating cladding has an index n_2 =3.63. The width of the separation layer between the two guides, $2t$, is variable. These are typical values of double heterostructure with GaAs/AlGaAs MQW materials. Refractive index values between 3.66 and 3.15 can be obtained by varying the *Al* composition in $Al_xGa_{1-x}As$ from x =0.0 to x=0.7 at a wavelength of $\approx$ 826 nm. The two dimensional optical models are suitable for the analysis of the system, since the width of the microstrip wire is wide enough to make the underneath optical guide essentially a 2-D structure. Using the above data, the input field distribution could be calculated, and supplied to a Vector Beam Propagation Method (VBPM) numerical simulator. Fig. 4 depicts the case where the guides separation,$2t$, is 0.6 μm. Fig. 5 and Fig. 6 depict the cases where $2t$ =0.3 and 1.5 μm respectively. For $2t$=1.5 μm, the coupling length,L_c, is 4.7 mm. For $2t$ =0.3 μm,L_c= 686.7 μm and for $2t$ =0.6 μm it is 3.363 mm.

From these simulations, the rate at which optical energy is being coupled and absorbed in the GaAs layer is calculated. This in turn would give an estimate of the photogenerated conductivity, $\sigma(z)$, and the conductance, G_b in that layer. The amount of power absorbed in the *GaAs* layer along the gap length is depicted in Fig. 7. The rate of absorption of this power, $\frac{\Delta P_a}{\Delta z}$, is proportional to the conductivity $\sigma(z)$ at each point along the gap. The linear portion of the curves depicted in Fig. 7 are the regions where the plasma is evenly distributed, and hence the conductance is relatively constant. The portion at which the curve's slope is almost zero indicates dark regions with high resistivity. The quantity $\frac{\Delta P_a}{\Delta z} \propto \Delta G_b$, was calculated and plotted in Fig. 8. If within a certain small length segment, Δz along the gap width, a certain amount of optical power, ΔP_a has been absorbed, the conductivity of this segment would be $\Delta G_b(z) = \frac{\sigma(z)A}{\Delta z}$, where A is the area normal to the propagation direction. The conductivity of the gap region is determined by a series of these segments. By adding up these series conductances, we get the total gap conductance, G_b.

$$\frac{1}{G_b} = \sum_{i=1}^{n} \frac{1}{\Delta G_b} = \int_0^b \frac{dz}{\sigma(z)A} \qquad (1)$$

where b is the length of the gap. From Figs. 7 and 8, it is evident that coupling strength affects the carriers distribution along the gap, and hence it could be used to design an evenly distributed plasma across the gap. Depending on the gap length, the coupling strength could be adjusted accordingly. This topic is one of the areas that would require thorough investigation in the future research work, in order to come up with an optimized set of parameters such as the gap length, and guided wave parameters that satisfies a set of conditions on power handling capability, speed, impedance level,..etc.

4 Modeling of the Microwave Component

The effect of the light-generated conductivity on the microwave power transmission can be studied using full wave analysis of the transmission line discontinuity in the presence of the plasma of carriers within the discontinuity. This was done numerically for free space illumination [1] and could be extended to the guided wave case. Full wave analysis of the gap discontinuity was conducted [2] and could be extende to the case where the gap is partially conducting due to the presence of the photo-generated carriers. It is also suggested by Platte and others [3] to use a simple π equivalent circuit as that shown in figure 9 to model the microwave gap. This equivalent circuit consists of several gap and shunt conductances that describe the performance of the real gap structure as a first order approximation. The power trans-

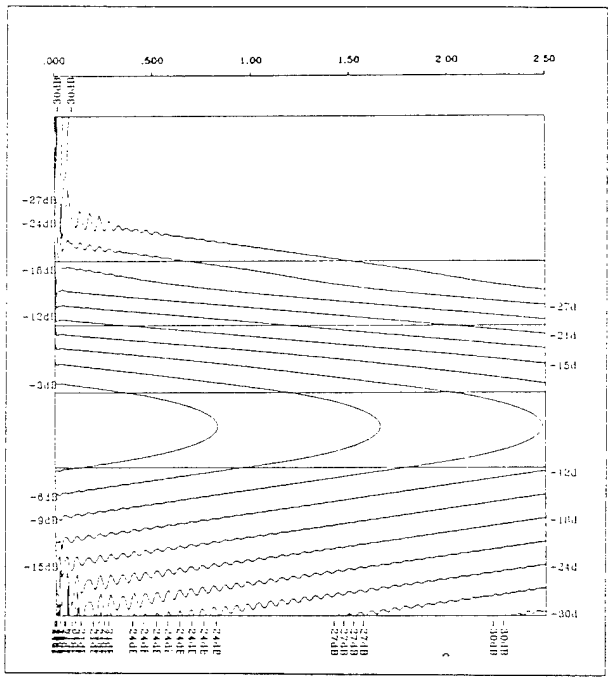


Figure 4: A contour plot for the E_y field in a directional coupler with the top guide being an absorbing layer. Optical power is launched into the lower guide, and is being absorbed while being coupled into the upper guide. guide separation is 0.6μm

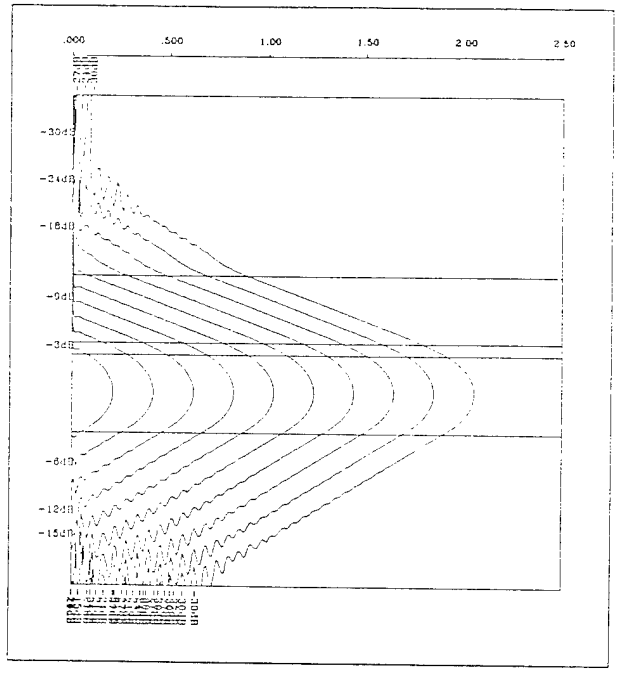


Figure 5: A contour plot for the E_y field. All parameters are as before except for separation $= 0.3\mu$m.

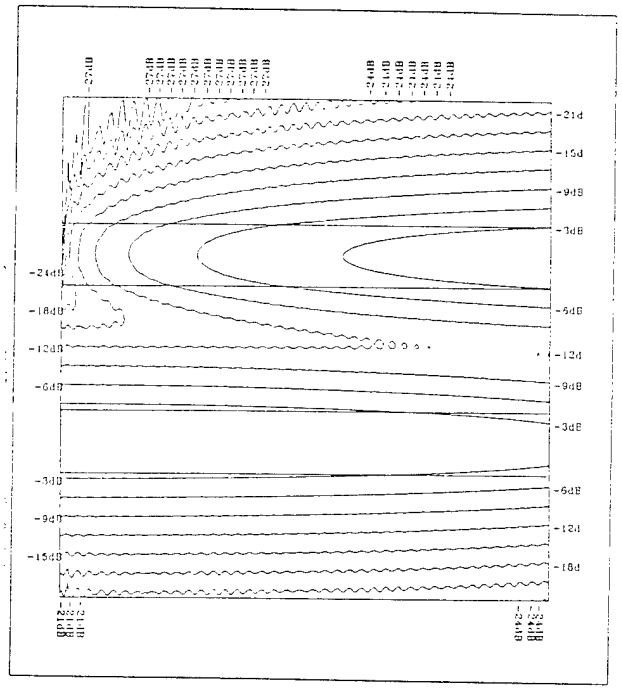


Figure 6: A contour plot for the E_y field. All parameters are as before except for separation $= 1.5\mu$m.

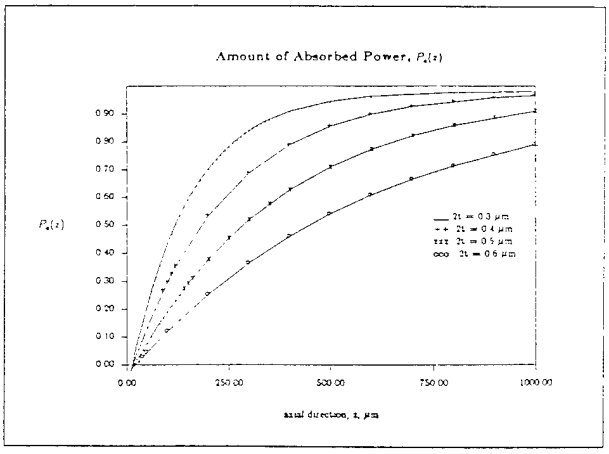


Figure 7: The amount of power absorbed along the gap length.

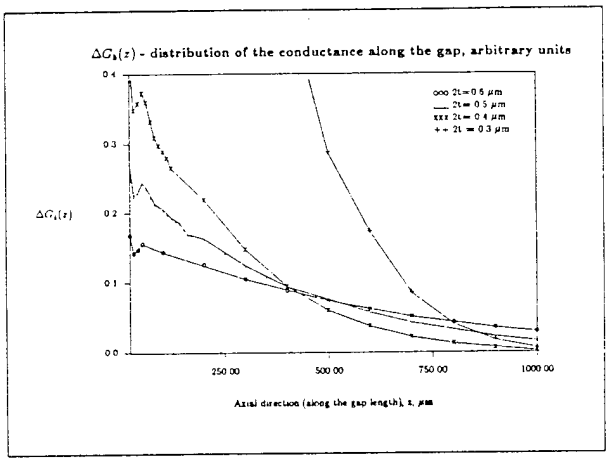


Figure 8: The variation of photo-induced conductance $G_b(z)$ along the axial direction, z.

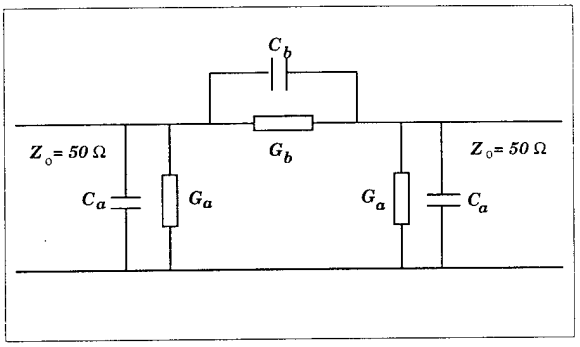


Figure 9: The π equivalent circuit of the configuration shown in the previous figure

mission through the laser excited plasma layer is described by the lumped conductance G_b, and shunting effects caused by greater absorption depths is taken into account through the shunt conductance G_a. To include the feature of the dark microstrip gap, the gap capacitance C_b and the shunt capacitance C_a are introduced [4]. In most cases, however, and using gap widths of 0.1 mm, C_a and C_b are in the order of 0.01 pF [4]. For signal frequencies of up to 10 GHz, or even more, these capacitances may be neglected [5]. This is always the case as long as the induced photoconductivity satisfies the conditions $G_b >> \omega C_b$ and $\omega C_a Z_o << 1$, where Z_o is the line characteristic impedance. The first condition ensures that the impedance level between the ON and OFF states are highly distinctive, which is a basic condition for achieving an effective switching. If this condition is not satisfied, the photo-excited microwave power transmission would barely exceed the residual "dark" power transmission through the gap capacitance. The second condition ensures that the shunt capacitive reactance is much higher than the transmission line impedance.

For the matched operating conditions, i.e., with signal source impedance and load impedance equal to the transmission line characteristic impedance, Z_o, it could be shown that the power transmission coefficient, based on the S parameter concepts, is given by

$$|S_{12}| = \frac{P_1}{P_2} = \frac{(2Z_oG_b)^2}{[(1+Z_oG_a)(1+Z_oG_a+2Z_oG_b)]^2} \quad (2)$$

where G_a and G_b are dependent on the optical pulse energy and the optical wavelength. The above equation does not take into account the insertion losses due to the microstrip line.

References

[1] Y. Shin, K. Nickerson, C. Wu, J. Litva, and D. Conn, "Full-wave analysis of optically controlled semiconductor coplanar waveguides," *1993 IEEE Antennas and Propagation International Symposium*, vol. 2, pp. 838–841, 1993.

[2] R. W. Jackson and D. M. Pozar, "Full-wave analysis of microstrip open-end and gap discontinuities," *IEEE Transactions on Microwave Theory and Techniques*, vol. 33, pp. 1036–1042, 1985.

[3] W. Platte, "On the excitation-dependent decay of photo-conductivity in laser-controlled solid-state switches," *Frequenz*, vol. 32, pp. 57–62, 1978.

[4] M. Maeda, "An analysis of gap in microstrip transmission lines," *IEEE Transactions on Microwave Theory and Techniques*, vol. MTT-20, pp. 390–396, 1972.

[5] W. Platte, "Spectral dependence of microwave power transmission in laser controlled solid-state microstrip switches," *Solid-State and Electron Devices*, vol. 2, pp. 97–103, 1978.

Dynamic Beam Propagation Method for Modelling Pulse Propagation in Flared Semiconductor Laser Amplifiers

S. Balsamo, F. Sartori, G. Perrone, C. Naddeo, I. Montrosset
Politecnico di Torino, Dipartimento di Elettronica,
C.so Duca degli Abruzzi 24, 10129 Torino, I
tel. +39-11-5644132, fax +39-11-5644134, email: sartori@ealpha.polito.it

C. Giuliano, R.K. Sink, P. Blixt, J.E. Bowers
Dept. of Electrical and Comp. Engineering,
University of California at S. Barbara,
Santa Barbara, CA, 93106, USA

I. Introduction

Mode-locked semiconductor laser diodes are excellent for generating, e.g., solitons and blue light by second-harmonic generation in bulk crystals. However, until recently, the output pulse energy has been limited by the low saturation energy (about 1 pJ) of single lateral-mode semiconductor amplifiers. By using flared semiconductor laser-diode amplifiers, the saturation energy, and thereby the output power can be increased by two orders of magnitude [1],[2].

So far, no detailed modelling has been performed for these devices, due to the lack of a dynamic Beam Propagation Method (BPM), necessary for this highly multimode and nonlinear device.

It is important that a semiconductor laser amplifier (SLA) has a large gain and does not distort the pulse shape. Good modelling will allow us to achieve these two goals. In this paper, we present simulations of short pulse propagation in travelling-wave SLAs using a Dynamic BPM. Based on these simulations, SLAs have been designed and fabricated and are currently under measurement. The paper is organized as follows: in section II we present the derivation of the model and the numerical method; in section III we show some examples of the results and in section IV we draw some conclusions.

II. Theoretical model and numerical technique

Our dynamic BPM is based on two coupled equations [3]: 1) a scalar time-domain wave equation that describes the propagation of the electromagnetic field and 2) a rate equation that describes the carrier induced nonlinear dynamic phenomena that are relevant in the propagation of picosecond pulses. The wave equation approach allows us to consider the complex field amplitude dynamics - such as chirping - that is usually neglected in the photon density rate equation. We applied the paraxial approximation and the effective index method, including refractive index dispersion up to the second order and a parabolic gain profile in frequency, to obtain an equivalent problem in two spatial and one temporal coordinates [4]. Furthermore, we introduced a time frame T moving with the pulse group velocity.

The rate equation approximation for the carrier dynamics holds for pulse durations longer than the intraband relaxation time τ_{in} (i.e. about 100 fs). To obtain an analytical expression for the time–dependent gain of the active medium, we also neglected the diffusion and recombination terms. This is correct for low repetition rates and pulses much shorter than the carrier lifetime in the conduction band, which is usually longer than 500 ps. This means that our model can give correct results for pulse durations between 1 and 50 ps.

The final equation is:

$$\frac{\partial F}{\partial z} = H\,F$$

where the H operator has the following expression

$$H = a\frac{\partial^2}{\partial x^2} + b(x,z) + c\frac{\partial^2}{\partial T^2} + d(x,z,T)\left(1 + e\frac{\partial^2}{\partial T^2}\right) - f$$

Here z is the longitudinal coordinate, x the transversal lateral position, $F(x,T,z)$ the complex field envelope, a accounts for the diffraction, b for the lateral index guiding, c for the chromatic material dispersion, d for the gain with saturation, e for gain dispersion and f for the internal material losses. The gain coefficient d is a complex number to include the linewidth enhancement factor α, which is responsible for the self–focusing of the field. The analytical expression of $d(x,z,T)$ is the following:

$$d(x,z,T) = g_0(1+\mathrm{i}\alpha)\exp\left\{-\frac{1}{U_{\mathrm{sat}}}\int_{-\infty}^{T}|F(x,\tau,z)|^2\ \mathrm{d}\tau\right\}$$

where g_0 is the unsaturated gain and U_{sat} is the saturation energy expressed in pJ/μm.

The numerical solution is based on a Locally One Dimensional (LOD) [5] symmetrized split-step method, that reduces the solution of the 3D problem to that of a sequence of three 2D equations: a spatial, a temporal, and a nonlinear one. This approach allows us to choose the optimal technique for solving each equation and to use 2D transparent boundary conditions (TBC) [6] instead of the more cumbersome 3D ones. The possibility of applying the TBC to the spatial and temporal equations is quite important because we need to simulate correctly the outgoing radiated modes due to the high multimodality of the structure.

In our case, the first two equations have been solved by a finite difference scheme with TBC modified to consider a medium with gain dispersion. The nonlinear equation has been solved by Newton's method.

III. Results

We have analyzed both gain and index guided structures with different material parameters in order to investigate the effects of saturation and self–focusing.

We first simulated a 1 mm–long GaAs power amplifier with a 4 μm–wide input and 68 μm–wide output linearly flared TiPtAu contact.

The working wavelength is 0.85 μm and the input field is Gaussian with a temporal and spatial FWHM of 3.4 ps and 10 μm, respectively.

An example of the comparison between index and gain guided structures for the same value of the Linewidth Enhancement Factor (LEF= 2) is shown in Figs. 1, 2, 3, 4.

Index–guided amplifiers have very sharp pulse shapes (Fig. 1) and highly distorted phase profiles (Fig. 3), due to the intense self–focusing of the strongly confined optical field.

On the other hand, gain–guided devices give smoother pulse shapes (Fig. 2) (apart from the ripple superimposed on the peak that is due to a filamentation phenomenon) with quasi–parabolic phase profiles (Fig. 4), thanks to the reduced confinement of the field. Their drawback is the lower amplification compared to the index–guided ones.

Since for obtaining the maximum power coupled into an optical fiber using a lens, the ideal field shape should be Gaussian with a nearly–parabolic phase profile like the one of gain–guided devices, in the rest of the paper we focus our attention on these ones.

We next considered two cases of gain–guided devices with different input pulse energy (1 pJ and 4 pJ) keeping the saturation energy (4 pJ) and the Linewidth Enhancement Factor (LEF=2) constant. In this case, we simulated a 2 mm–long, 4 μm–wide input, 132 μm–wide output linearly flared amplifier.

The comparison between the spatial profiles is shown in Fig. 5 and proves that, thanks to the low LEF value, both cases provide high amplification with little pulse distorsion. The temporal profiles (Fig. 6) clearly show the tails due to self-focusing and gain saturation.

IV. Conclusions

We have derived a dynamic BPM to simulate picosecond pulse propagation in travelling wave semiconductor laser amplifiers and we have shown its application to the analysis of flared gain guided devices.

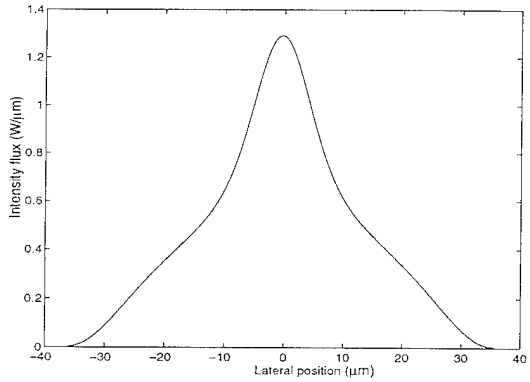


Figure 1: Index guided device output field profile.

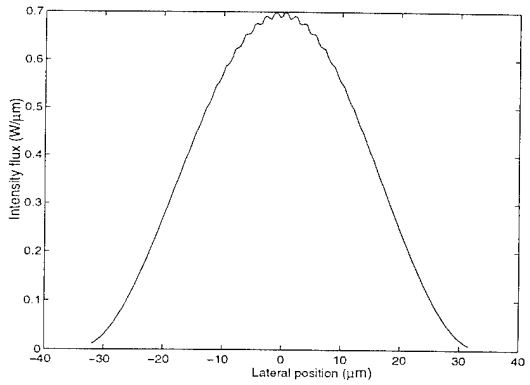


Figure 2: Gain guided device output field profile.

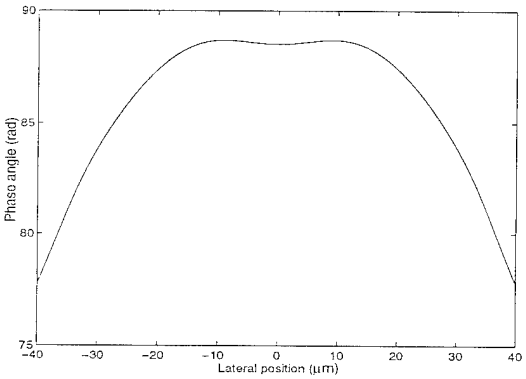


Figure 3: Index guided device output phase profile.

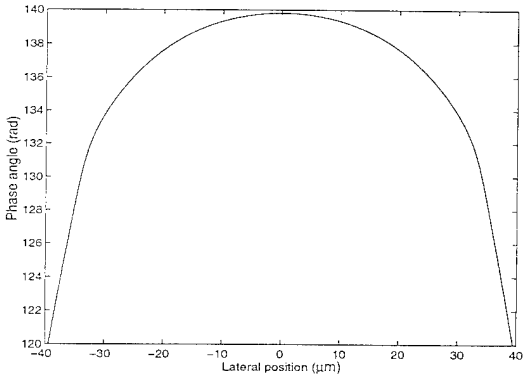


Figure 4: Gain guided device output phase profile.

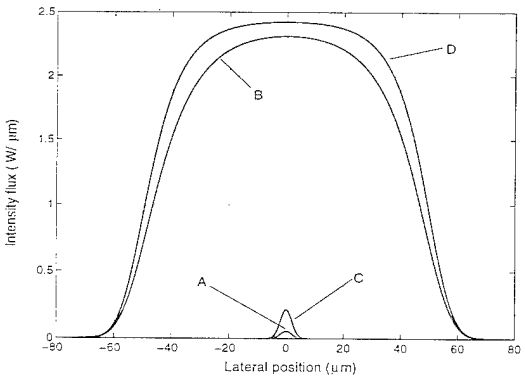


Figure 5: Comparison between the spatial profiles for 1 pJ (A input field- B output field) and for 4 pJ (C input field - D output field) input energy.

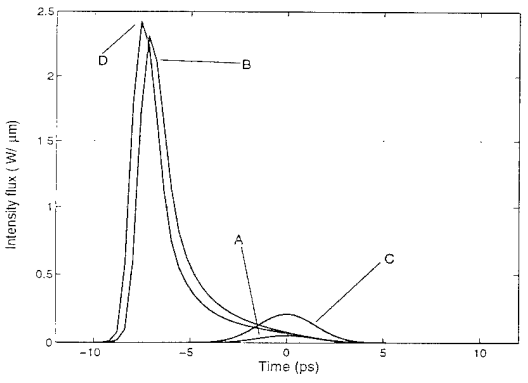


Figure 6: Comparison between the temporal profiles for 1 pJ (A input field - B output field) and for 4 pJ (C input field- D output field) input energy.

References

[1] A. Mar, R. Helkey, J. Bowers, D. Mehuys, and D. Welch, "Mode-locked operation of a master oscillator power amplifier," *IEEE Photon. Technol. Lett.*, vol. 6, pp. 1067-1069, 1994.

[2] L. Goldberg, D. Mehuys, and D. Welch, "High power mode-locked compound laser using a tapered semiconductor amplifier," *IEEE Photon. Technol. Lett.*, vol. 6, pp. 1070-1072, 1994.

[3] G.P.Agrawal, "Effect of gain dispersion on ultrashort pulse amplification in semiconductor laser amplifiers", *IEEE J.Quantum Electron.*, vol. 27, pp. 1843–1849, 1991.

[4] W.P. Huang, C.L. Xu, J. Chrostowsky, "A time-domain propagating scheme for simulation of dynamics of optical guided-wave devices," *IEEE Photon. Techn. Lett.*, vol. 5, pp. 1071-1073, 1993.

[5] A.R. Mitchell, "Computational methods in partial differential equations," *Wiley*, New York, 1969.

[6] G.R. Hadley, "Transparent boundary condition for the beam propagation method," *IEEE J. Quantum Electron.*, vol. 28, pp. 363–370, 1992.

OPTOELECTRONIC-FEEDBACK CONTROL OF CHAOTIC DYNAMICS IN EXTERNAL CAVITY LASER DIODES

S.I.Turovets (+) , J.Dellunde (*) and K.A.Shore

University of Wales, Bangor, School of Electronic Engineering and Computer Systems
BANGOR,LL57 1UT, Wales, UK

(*) Departament d'Estructura i Const. de la Materia, Facultat de Fisica,
Universitat de Barcelona, Diagonal 647,E-08028 Barcelona, Spain

(+) Permanent address : Institute of Physics, Academy of Sciences,
70 Skarina Ave., Minsk 220072, Belarus.

Introduction : Secure communication systems based upon chaotic encryption of data have recently attracted interest . An efficient algorithm for improving the locking rate between receiver and transmitter of such a system has been reported previously [1] and consideration has been given to techniques for the control of the nonlinear dynamics of lasers in general [2,3] and , in particular , laser diodes [4,5] which can function as practical transmitters in chaotic optical data encryption systems .In the present work an investigation has been undertaken of the use of continuous optoelectronic feedback in selecting periodic dynamics in external cavity laser diodes subject to conventional optical feedback .Other work has explored the control of chaos in external cavity laser diodes using occasional proportional feedback [6] and direct modulation [7,8].

Model : It is assumed that the laser operates in a single longitudinal mode and is subject to optical feedback from an external mirror. A rate equation treatment of this configuration has recently been developed to take into account feedback effects in

modulated external cavity laser diodes [5,9] . The laser is taken to be supplied with a DC injection current $I_{DC} = 2\ I_{th}$, where I_{th} is the threshold current. Delayed optoelectronic feedback is used to slightly modifiy the driving current at time t, according to the output power that was emitted at a previous time $t-\tau_{el}$. Using the proportionality between the output power and the cavity photon density , s(t) , the laser driving current is then given as :

$$I(t) = I_{DC}\left[1 - x\frac{[s(t) - s(t-\tau_{el})]}{s_0}\right] \qquad (1)$$

Where x is the control parameter. The photon density s_0 of the solitary laser under the DC driving current is taken as a reference.

Results : It is well known that with increase of the level of optical feedback the laser dynamics undergoes a sequence of period-doubling bifurcations culminating in chaotic behaviour [4-6]. The effect of applying additional optoelectronic feedback in the form (1) to a laser in the chaotic regime is shown in Figure 1 . As the control parameter is increased by relatively small values in a step-wise manner the chaotic dynamics is successively replaced by period 4 , period 2 and period 1 dynamics.

The second parameter which may be used to control the dynamics is the delay time of the optoelectronic feedback. Figure 2 shows the bifurcation diagram for a laser with the fixed optoelectronic feedback strength but with the feedback delay τ_{el} being adiabatically varied. It is seen that reverse bifurcation sequences appear over a number of ranges of the feedback delay. This demonstrates that the laser diode dynamics can be 'tuned' or rapidly switched to a chosen dynamical regimes including effecting transitions from chaos to periodic regimes and vice versa. Examination of

corresponding results for the time dependence of the laser light output power and control signal amplitudes confirm that periodic dynamics can be extracted from chaos using corrections to a pumping current which are typically less than 1% of DC injection current even when the control parameter was changed suddenly (eg when modulated by rectangular pulses).

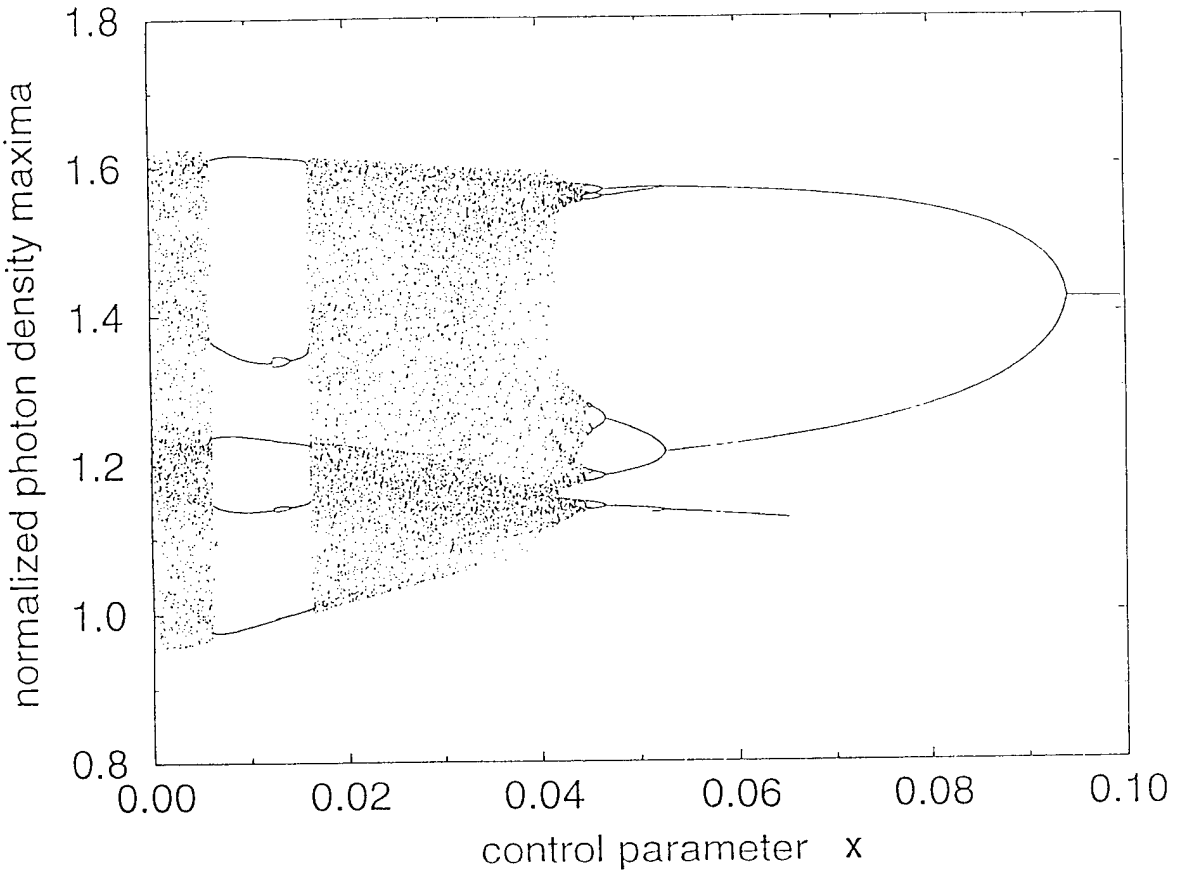
In conclusion, control of coherence collapse and selection of stable periodic outputs of semiconductor lasers subject to weak optical feedback has been demonstrated. In comparison with synchronization by external modulation the present approach is seen to possess significant engineering advantages in that it does not require additional high frequency sources, imposes a modest requirement on the bandwidth of the electronic components in the feedback loop and is amenable to optoelectronic integration.The approach also offers a novel means for performing electronic to optical information conversion .

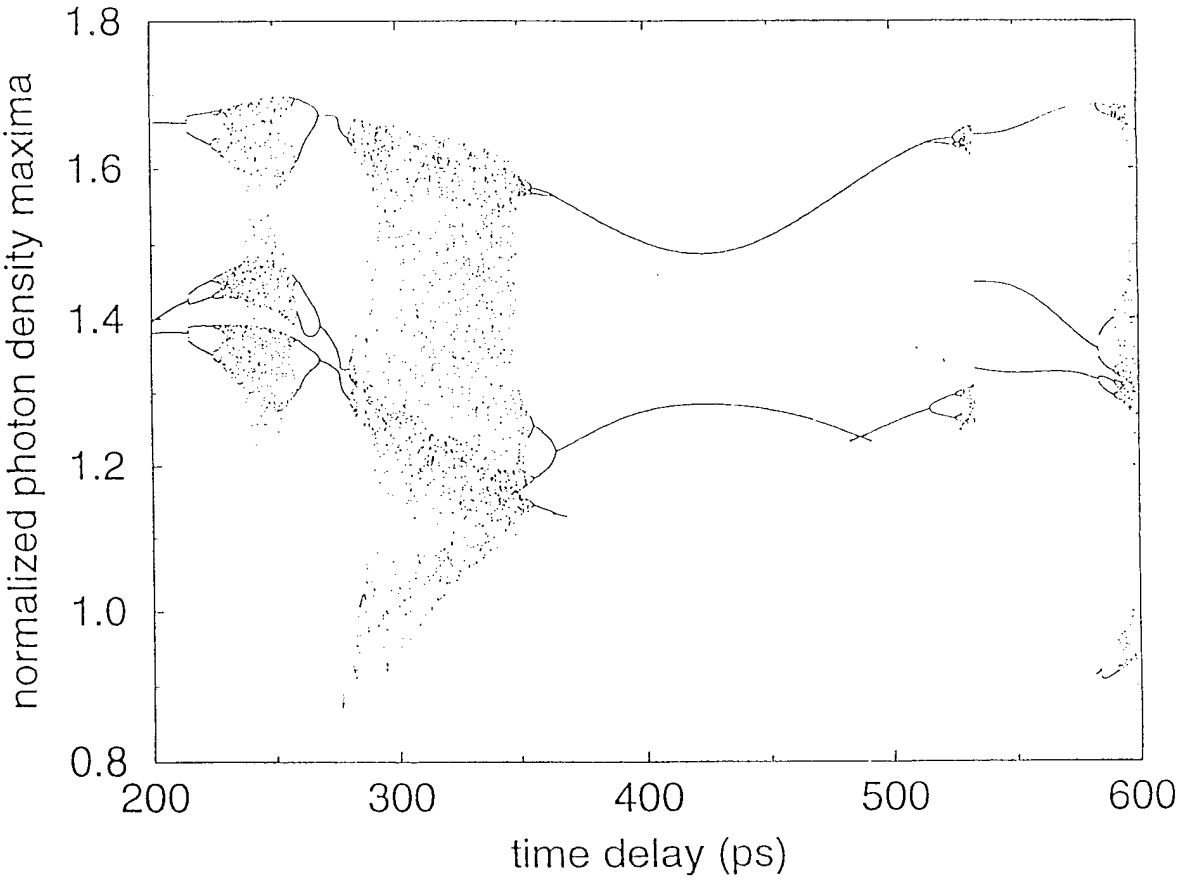
Acknowledgements

S.I.Turovets acknowledges financial support from the Royal Society , London,UK, which permitted a visit to the University of Wales, Bangor where this work was carried out. J.Dellunde undertook this with support from CICYT, Spain , Project PB93-0769-C02-01.

References

1) K.A.Shore and D.T.Wright, Electron.Lett ,**30**,1203-1204, 1994
2) V.N.Chizhevsky and S.I. Turovets, Phys. Rev. A , 50, 1840-1843,1994
3) V.N. Chizhevsky and S.I. Turovets, Opt. Commun., **102**,175-182, 1993
4) L.N.Langley ,S.Turovets and K.A.Shore,Optics Letts., **20**,725-727,1995
5) L.N.Langley ,S.Turovets and K.A.Shore,IEE Proc., Optoelect.,**142**,157-161, 1995
6) G.R. Gray, A.T.Ryan, G.P. Agrawal, and E.C. Gagein: Chaos in Optics , SPIE Proc. Vol.2039, (ed. R.Roy), 45-57,1993
7) N.Watanabe and K.Karaki,Optics Letts., **20**,725-727,1995.
8) Y.Liu, N.Kikuchi and J.Ohtsubo,Phys. Rev. E,**51**,R2697-R2700,1995
9) L.N.Langley and K.A.Shore ,IEEE Journal of Lightwave Technology,**11**,434-441 ,1993


normalized photon density maxima
1.8
1.6
1.4
1.2
1.0
0.8
0.00
0.02
0.04
0.06
0.08
0.10
control parameter x


normalized photon density maxima
1.8
1.6
1.4
1.2
1.0
0.8
200
300
400
500
600
time delay (ps)

Wave Propagation in a Waveguide with a Balance of Gain and Loss

H. - P. Nolting, G. Sztefka, M. Grawert, Heinrich-Hertz Institut für Nachrichtentechnik Berlin GmbH
Einsteinufer 37, 10587 Berlin, Germany, +(4930) 31002 427
Jiri Ctyroky, Institute of Radio Engineering and Electronics, Academy of Sciences of the Czech Republic, Chaberska 57, 182 51 Praha 8, Czech Republic, Tel.: +(422) 688 1804

Introduction

A waveguide problem with a balance between loss and gain has been defined by one of the authors (H.-P. N.) in the COST 240, Working Group 2, to study the mode behaviour in the case of complex refractive index and to compare different approaches. This problem is many-layered in both senses of the word. We will not discuss the numerical aspects of finding *all* roots[1] of the dispersion equation, we will give a quasi-analytic solution for the branching point of the dispersion diagram, define a new BPM benchmark test, and discuss the peculiar wave behaviour of this waveguide.

Definition of the task

The waveguide structure is shown in Figure 1: two layers with mutually complex conjugate refractive indices are surrounded with a slightly lower real refractive index. The exact values of all parameters are given in Figure 1. The imaginary parts of refractive indices of guiding layers vary in a very broad range: in terms of the absorption (gain) coefficient α, between zero and $\pm 10^4$ cm^{-1}. The task is to find effective refractive indices and mode fields of TE modes for any α in this interval.

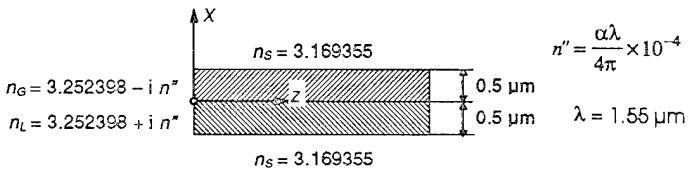


Figure 1: Two-layer waveguide with gain and loss

Quasi-analytic solution

A large number of well-known methods can be used to solve the task[2]. In the most straightforward method, the electric field distribution of a guided mode in the waveguide is expressed in the form

$$\begin{aligned} x \le -d: E &= A\exp\left[k\gamma_S(x+d)\right], & -d < x \le 0: \quad E &= B_1\cos k\gamma_L x + B_2 \sin k\gamma_L \\ x > d: \quad E &= D\exp\left[-k\gamma_S(x+d)\right], & 0 < x \le d: \quad E &= C_1\cos k\gamma_G x + C_2 \sin k\gamma_G x \end{aligned} \tag{1}$$

where

$\gamma_S = \sqrt{\varepsilon_{eff} - \varepsilon_S}$, $\gamma_L = \sqrt{\varepsilon_L - \varepsilon_{eff}}$, $\gamma_G = \sqrt{\varepsilon_G - \varepsilon_{eff}}$, $\varepsilon_L = \left(n + in''\right)^2$, $\varepsilon_G = \varepsilon_L^*$, $\varepsilon_{eff} = N_{eff}^2$, $k = (2\pi)/\lambda$, and the sign of N_{eff} is chosen so that $\mathrm{Re}\{N_{eff}\} > 0$.

The conditions of continuity of the field E and its derivative at $x = 0$ and $x = \pm d$ give a set of homogeneous linear equations for unknown amplitudes A, B_1, B_2, C_1, C_2, D. To get a non-trivial solution, the determinant of this set of equations must be equal to zero. It leads to the dispersion equation of the form

$$\begin{aligned} \Phi\left(\varepsilon_{ef}, \alpha\right) = {} & \gamma_G\left(\gamma_S\cos k\gamma_G d - \gamma_G \sin k\gamma_G d\right)\left(\gamma_S \sin k\gamma_L d + \gamma_L \cos k\gamma_L d\right) \\ & + \gamma_L\left(\gamma_S\cos k\gamma_L d - \gamma_L \sin k\gamma_L d\right)\left(\gamma_S \sin k\gamma_G d + \gamma_G \cos k\gamma_G d\right) = 0 \end{aligned} \tag{2}$$

Having this equation numerically solved, the field amplitudes A, B_1, B_2, C_1, C_2, D can be calculated, and the field distribution is then explicitly given by (1).

The calculated dependencies of real and imaginary parts of effective refractive indices are plotted versus the absorption coefficient α in Figure 2.

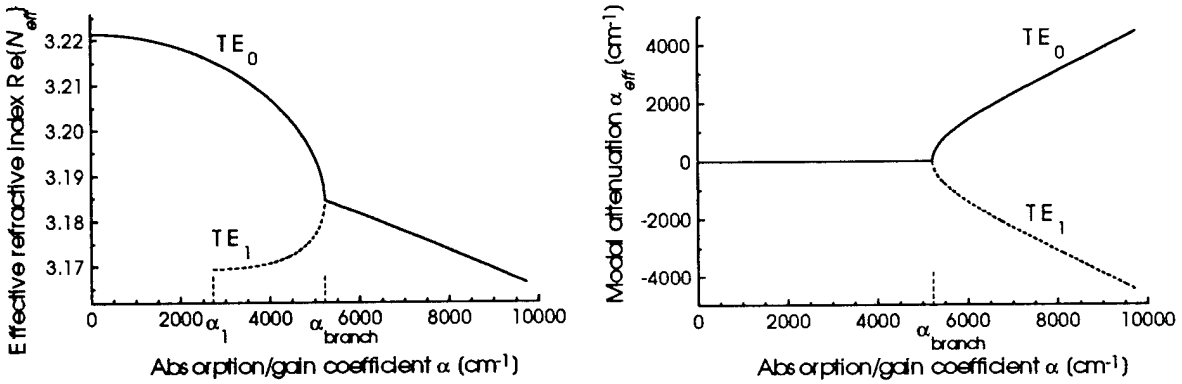


Figure 2: Effective refractive indices $\mathrm{Re}\{N_{eff}\}$ and $\alpha_{eff}=(4\pi/\lambda)\mathrm{Im}\{N_{eff}\}$ versus α

It is seen that for values of $\alpha < \alpha_1 = 2725$ cm^{-1}, the waveguide is *single-mode* and the mode propagates without loss or gain. In the interval $\alpha_1 < \alpha \le \alpha_{branch} = 5226.3$ cm^{-1}, the waveguide supports *two modes with real effective indices*, and finally, for very large values of $\alpha > \alpha_{branch}$, the two modes have mutually complex-conjugate effective indices. With increasing attenuation/gain in the waveguiding layers above α_1, the effective refractive indices and the mode fields approach to each other, and at $\alpha = \alpha_{branch}$ *both effective indices degenerate into a single real value.* For even larger α, one mode is attenuated while the other one grows, but both propagate with the same velocity. The mode field distributions are correspondingly concentrated in the layer with loss and gain, respectively. The mode field distributions for $\alpha = 5000$ cm^{-1} (which is close to α_{branch}) and $\alpha = 7000$ cm^{-1} are plotted in Figure 3.

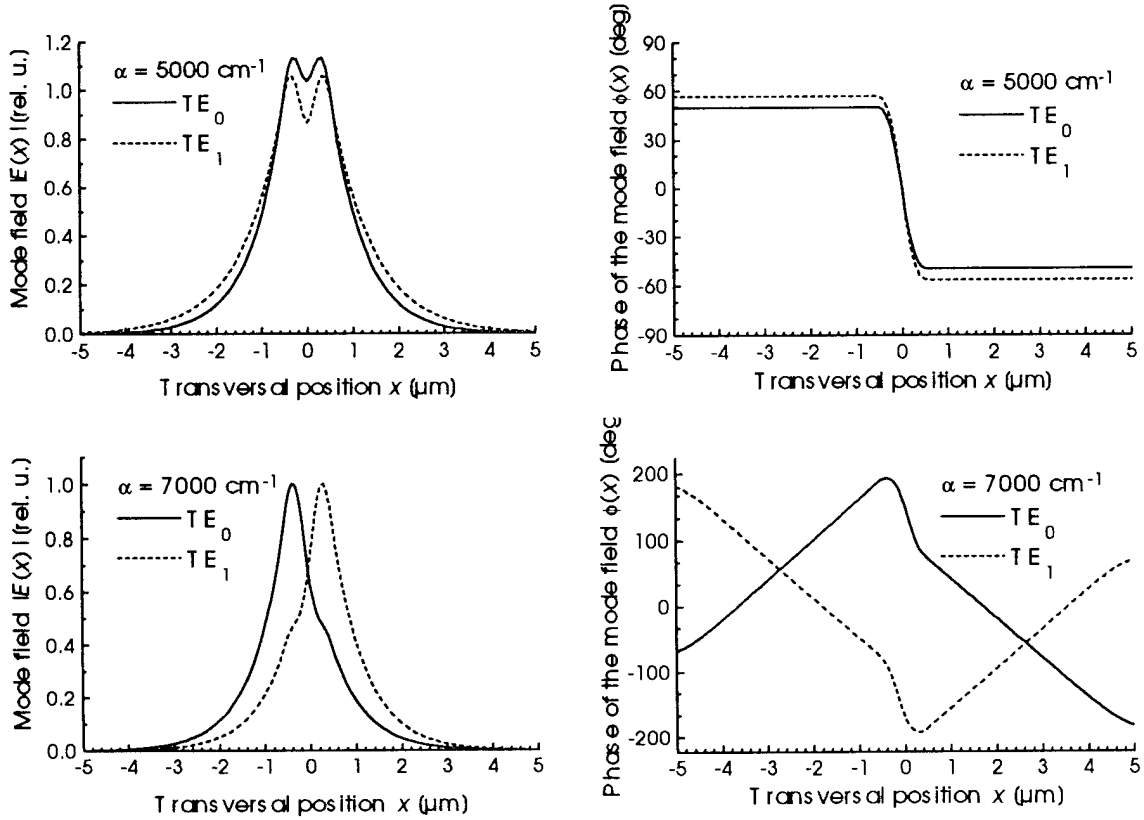


Figure 3: Module and phase of the modal field distributions for $\alpha = 5000$ cm^{-1} (close to α_{branch}) and $\alpha = 7000$ cm^{-1} (greater than α_{branch})

From the asymptotic behaviour of mode fields for $\alpha \to \alpha_{branch}$ we can deduce that at α_{branch}, the mode fields are degenerate, and the orthogonality condition reduces to the "self-orthogonality"

$$\int_{-\infty}^{\infty} E^2(x)dx = 0$$

From Fig. 2 it is seen that at the branch point α_{branch}, $d\varepsilon_{eff}/d\alpha \to \pm\infty$. Since $d\varepsilon_{eff}/d\alpha = -(\partial\Phi/\partial\alpha)/(\partial\Phi/\partial\varepsilon_{eff})$ as follows from the dispersion equation (2), it means that $\partial\Phi/\partial\varepsilon_{eff} = 0$. We get the critical value of α_{branch} by solving a set of two complex transcendental equations

$$\Phi(\varepsilon_{eff},\alpha) = 0, \quad \partial\Phi/\partial\varepsilon_{eff} = 0 \tag{3}$$

for ε_{eff} and α. Their (numerical) solution gives $\alpha_{branch} = 5226.302\ cm^{-1}$, $\varepsilon_{eff} = 10.1412428\ cm^{-1}$. The behaviour of the dispersion curves in Fig. 2 can be easily explained by the following arguments: Since $\Phi(\varepsilon_{eff},\alpha)$ is a regular function of the complex variable ε_{eff} and a smooth function of α, it can be expanded into the Taylor (Laurent) series. It follows from (3), however, that in the expansion in the vicinity of the branching point the corresponding two terms vanish. The dispersion equation can thus be approximated by

$$\Phi(\varepsilon_{eff},\alpha) \approx \Phi_{\alpha}'(\alpha - \alpha_{branch}) + \frac{1}{2}\Phi_{\varepsilon_{eff}}''(\varepsilon_{eff} - \varepsilon_{eff,branch})^2 = 0, \tag{4}$$

where $\Phi_{\alpha}' = \partial\Phi(\varepsilon_{eff,branch},\alpha_{branch})/\partial\alpha$, $\Phi_{\varepsilon_{eff}}'' = \partial^2\Phi(\varepsilon_{eff,branch},\alpha_{branch})/\partial\varepsilon_{eff}$. From (4) it follows that the approximate solution of the dispersion equation near α_{branch} is

$$\varepsilon_{eff} \cong \varepsilon_{eff,branch} \pm i\sqrt{(2\Phi_{\alpha}'/\Phi_{\varepsilon_{eff}}'')(\alpha - \alpha_{branch})}, \tag{5}$$

where $2\Phi_{\alpha}'/\Phi_{\varepsilon_{eff}}'' \approx 5.6753\times10^{-5}$ cm.

BPM benchmark test for complex refractive index

This problem can be used for defining of a new benchmark test[3] for the beam propagation method (BPM), because we know the quasi-analytic solution (3). This test is complementary to the two tests published earlier. It is focused on the imaginary part of the refractive index, which was always zero in the previous tests. The definition of the tasks is:

Calculate the wave behaviour for various values of the coefficient α of a gain-loss waveguide, which is placed between two lossless (single-mode) input and output waveguides with identical real parts of the refractive index. From the dispersion diagram we know that there is a branch point α_{branch} which divides the results into two parts. For $\alpha<\alpha_{branch}$ we have two *lossless* modes with similar field distributions, and we thus observe a beat

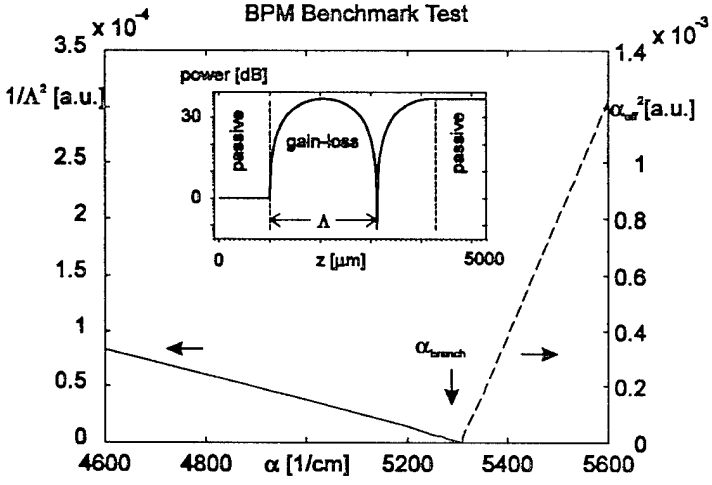


Figure 4: BPM benchmark test with beat length Λ and α_{eff} as a function of α. The insert demonstrates the strong attenuation / amplification behaviour of the gain-loss waveguide at α=5306 cm^{-1} from -10 dB < 0 dB (start) < 30dB.

length Λ, which is increasing for increasing values of α. We can easily determine α_{branch} from (5) by plotting $1/\Lambda^2$ over α, as is shown in Fig. 4, left part. For $\alpha > \alpha_{branch}$ we have a superposition of an amplified and an attenuated modes, where the amplified will survive, and we can thus determine the effective gain constant α_{eff} as a function α from a plot of α_{eff}^2 as is shown in Fig. 4, right part. We used a FD-BPM algorithm to perform this benchmark test, and we found the value of $5306<\alpha_{branch}<5307$ [cm^{-1}], which is slightly different from the quasi-analytic solution.

Wave growth in the gain-loss waveguide with "lossless" eigenmodes

The calculation of the passive waveguide/gain-loss waveguide/passive waveguide structure used for the BPM test for $\alpha<\alpha_{branch}$ shows a variation of the transmitted power P propagating along the z-direction between $P_{min}<P_{start}<P_{max}$. Notice that the two eigenmodes of the gain-loss waveguide have zero imaginary parts and that we start with 0 dB power in a real passive waveguide. How can we explain this growth behaviour, shown in the insert of Fig. 4, where we have $P_{min} \leq -10$ dB and $P_{max} > 30$ dB? Investigation with an eigenmode expansion method like the BEP[4] shows:

Following the notation of[5] (with l = number of the section, i,k = number of modes), we can write the amplitude expansion coefficient a_{ik} at the interface of the passive/gain-loss waveguide as:

$$ {}^{l+1,l}a_{ik} = \int_{-\infty}^{\infty} {}^{l+1}E_i(x)\cdot{}^{l}E_k(x)dx \Big/ \left(\sqrt{\int_{-\infty}^{\infty} {}^{l+1}E_i(x)\cdot{}^{l+1}E_i(x)dx} \cdot \sqrt{\int_{-\infty}^{\infty} {}^{l}E_k(x)\cdot{}^{l}E_k(x)dx} \right). $$

We have calculated the squared absolute value of the amplitude expansion coefficients a_{ik} at the interface passive/gain-loss waveguide in Figure 5 and observe a strong increase for α approaching α_{branch}. As a driving force we identify that

$$ V = 1\Big/\sqrt{\int_{-\infty}^{\infty} {}^{l+1}E_i(x)\,{}^{l+1}E_i(x)dx} \rightarrow \infty $$

due to the "self-orthogonality". We can think of the two modes as of two large numbers $E_1 \equiv E_2 = E_1 + \tau$ with $\tau << E_1$. By interference we get $P_{min} \equiv \tau^2 << 1$ and $P_{max} \equiv |E_1|^2 >> 1$. The asymptotic behaviour of the modes for α aproaching α_{branch} is as follows: the beat length Λ approaches to infinity, and for $z \rightarrow \infty$ the field amplitude growths to infinity, too.

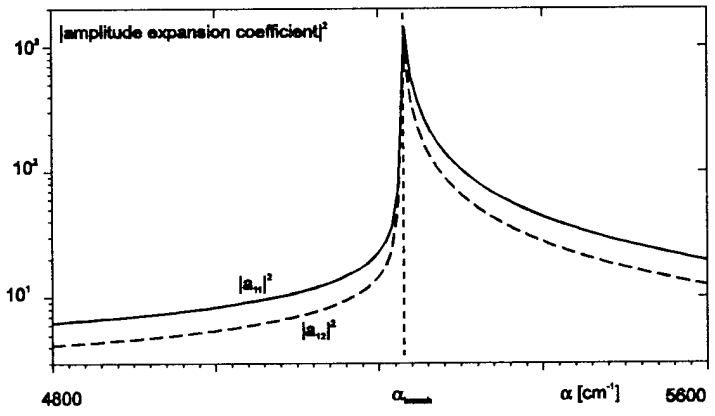


Figure 5: Asymptotic behaviour of the squared absolute value of the amplitude expansion coefficients a_{ik} as a function of α.

---

[1] R.E.Smith, S.N.Houde-Walter, and G.W.Forbes, *Opt. Lett.* Vol. 16, pp.1316–1318, 1993

[2] R. Collin: *Field theory of guided waves*. Academic Press, New York 1960

[3] H.-P. Nolting, R. März, "Results of Benchmark Tests for Different Numerical BPM Algorithms", *IEEE J. Lightwave Technology*, vol.13, No.2, pp.216–224, 1995

[4] G. Sztefka, H.-P. Nolting, "Bidirectional Eigenmode Propagation for Large Refractive Index Steps", *IEEE Photon. Technol. Lett.*, Vol 5, No. 5, pp. 554–557, 1993

[5] H.-P. Nolting, M. Grawert, "A Comparison between Different Methods to Calculate Grating Assisted Asymmetrical Couplers", Linear and Nonlinear Integrated Optics, 11–13 April 1994 Lindau 94, Germany, Proceedings Europto Series Vol 2212, pp 328–336

Monday, April 29, 1996

Symposium on WDM Filters

IME 1:30 pm-3:00 pm
Fairfax B

J.L. Jackel, *Presider*
Bellcore

An Acousto-Optic Switch With a Near Rectangular Passband for WDM Systems

H. Rashid, D. A. Smith, R. S. Chakravarthy, A. M. Agboatwalla, A. A. Patil, Z. Bao, N. Imam and S. W. Smith, J. E. Baran* , J. L. Jackel* and J. Kallman**
Dept. of Electrical Engineering, Case Western Reserve University, Cleveland, OH 44106
*Bellcore, 331 Newman Springs Rd., Red Bank, NJ 07701
**Lawrence Livermore National Laboratories, Livermore, CA

Summary. Large-scale WDM systems contain wavelength-selective filters, switches and multiplexers which must be tolerant of moderate wavelength channel misalignment and can be cascaded without severe accumulated shrinkage of the effective passband width. These requirements demand that wavelength-selective components possess nearly rectangular spectral profiles. In this paper, we describe the flattest acousto-optic wavelength-routing switch yet reported. A multi-cycle SAW directional-coupler-weighted AOTF was fabricated on XY lithium niobate which posessed a 3-dB width of 2.52 nm and a -20-dB width of 0.89 nm. For comparison, an ideal apodized AOTF with the same 3-dB width would have a -20 dB width of only 0.33 nm. In this paper we describe WDM switch requirements for transmission band flatness, present our filter design and device evaluation and compare our results with the work of previous authors.

Crosstalk and Passband Shape. Figure 1 shows the operation of a WDM switch on two wavelengths, λ_{bar} which is a channel passing unfiltered through the switch and remains in the bar state, and λ_{cross} which is coupled to the opposite or cross-state port of the switch. In the acousto-optic switch (AOS), switching occurs for wavelengths for which TE-TM photoelastic interconversion is phase-matched with an acoustic grating of period $\Lambda=\lambda/\Delta n$, in which Δn is the substrate birefringence [1]. From the point of view of real WDM systems, crosstalk between channels leads directly to system degradation, and it is important to relate WDM switch passband shape to interchannel crosstalk. Consider the schematic passband of Fig. 2a, in which the filter is optimized for switching at λ_0 which is near the system channel λ_{cross} and far from the unswitched neighbor λ_{bar}. In the AOS, peak switching at λ_0 occurs for an acoustic frequency obeying $F = V_s\lambda_0 / \Delta n$. The bar-state transmission curve identifies the fraction of intensity ε_{bar} at λ_{cross} which remains in the bar state, while the fraction of λ_{bar} which has been induced to switch by the switching at λ_0 is ε_{cross}, determined by reading the cross-state transmission profile at λ_{bar}. Switch performance can be identified by specifying a target crosstalk level ε_c and then examining the passband shape in order to obtain the key parameters of wavelength misalignment tolerance $\Delta\lambda_{tol}\big|_c = \Delta\lambda_{bar}\big|_c$ (the range of wavelength window over which switching extinction exceeds ε_c) and minimum interchannel separation for which the unswitched channels remain in the bar state with extinction exceeding ε_c : $\Delta\lambda_{sep}\big|_c = (\Delta\lambda_{bar}\big|_c + \Delta\lambda_{cross}\big|_c)/2$. This definition of interchannel separation allows for interchannel crosstalk to be low enough even at the maximum tolerable wavelength misalignment, as depicted in Fig. 2b. A further term, the rectangularity r can be defined as $r(c) = \Delta\lambda_{tol} / \Delta\lambda_{sep}\big|_c$; for a perfect rectangular filter $r \to 1$ for all values of c . How long r remains large, as c becomes more stringent, is a practical measure of rectangularity.

Passband Engineering. Sidelobe suppression or peak flattening can be realized by controlling the amplitude and phase of the envelope of the photoelastic grating which constitutes the interaction region of an AOTF [1]. For example, sidelobe suppression can be achieved by imbedding the active optical waveguide of the WDM filter in the cross arm of a SAW directional coupler so that the observed interaction strength is apodized with a tapered onset and cutoff. Adjusting the weighting function affects the depth of sidelobe suppression [2]. Theoretical calculations by G. H. Song predicted that a rectangular filter would require a tapered-onset of the AO interaction strength followed by three cycles of an oscillating acoustic interaction strength with an overall exponential decay envelope [3]. In a recent experiment, Song's proposed coupling potential was successfully tested by using only two cycles of a 20 micron gap surface acoustic wave directional coupler, in which a single partial acoustic absorber was placed between SAW intensity cycles to simulate a decay envelope, and the tapered onset of Song's design was ignored [4]. Jackel had a filter with a 1.78-nm 3-dB width and a bar-state width (wavelength misalignment tolerance) of 0.67 nm at -15 dB and 0.30 nm at -20 dB.

In our experiments, we have designed an improved filter (Figure 3a) which maintains the qualitative features of Song's proposal and which coupled-mode theory led us to believe would have superb rectangularity but would be just 39 mm in length [5]. Improvements over Jackel's work incorporated in this device are (1) incorporation of a linear tapered onset, (2) three full cycles of SAW amplitude and (3) a much shorter interaction by using a zero gap SAW coupler instead of the more gradually oscillating 20 micron gap coupler.

Device fabrication and evaluation. The multi-cycle SAW-coupler-based AOTF generates the SAW in an IDT located in an isolated acoustic waveguide which evanescently couples into a zero-gap two-SAW-mode coupler which causes the SAW intensity to oscillate over an imbedded optical waveguide. The device shown in Figure 4 was fabricated on X-cut, Y-propagating lithium niobate. Acoustic cladding layers were formed by diffusing a 1800Å titanium stripe for a total of 30 hours at 1050°C. Optical waveguides were formed using 950Å of Ti and a 10-hour diffusion at the same temperature. The SAW intensity profile over the optical waveguide under study was modeled using an optical beam propagation program which treated all dimensions as correct, but which imagined the SAW beam to be an optical mode with "free-space" wavelength 33.2 μm, so that the artificial cladding index (1.6) yielded the correct 20-μm SAW period in the device. The "core" index of 1.605 was chosen to obtain agreement with the observed SAW oscillation. By varying the modeled point acoustic attenuation at each null, the passband flatness could be optimized. Maximum-flatness passbands are shown in Fig. 3b for one, two and three cycles of SAW excitation. It is clear from the figure that the flatness improves as the number of cycles increases.

Experiment. The SAW intensity profile was monitored by a short-pulse RF probe technique which provided a direct real-time plot of SAW intensity vs. position along the active waveguide [6][7]. Discrete rubylith strip absorbers of 0.5 mm width were placed at the SAW intensity nulls while monitoring the transmitted SAW power using a second IDT at the far end of the device. Adjusting the width of the absorber strips allowed us to vary the attenuation. The position dependence of birefringence was monitored by finding the local resonant frequency at each SAW peak. Often, devices suffer from high sidelobe levels due to birefringence nonuniformity across the interaction region. Anticipating birefringence variations, we placed nichrome heater coils above each peak and arranged to adjust the current through each coil independently to perform local temperature tuning of Δn. The filter passband was evaluated at various levels of partial absorber attenuation and while varying the birefringence to obtain best flatness. Birefringence was monitored whenever an important result was obtained. Figure 4 depicts the tuning/probing apparatus. The filter shape was obtained (see Fig. 5) by employing the spontaneous emission spectrum of an erbium amplifier as the optical source and observing the passband or band-reject spectra using an optical spectrum analyzer.

Results. In experiments to date, we have seen dramatic improvement of passband flatness in moving from one to two cycles, but it appears that uncompensated birefringence variations have made three-cycle devices actually worse than two-cycle ones. The effective device length for two cycles is only 27.5 mm, and the passband for the uncompensated device and the far deeper notch for the compensated device is shown in Fig. 6a. Figure 6b compares the one and best two cycle passband shapes. Table 1 compares the passband widths at various crosstalk levels for the one- and two-cycle devices. We compared the results obtained with the temperature-compensated two-cycle, tapered-onset, zero-gap SAW-coupler-apodized filter with the best reported previous results [Jackel] in the last row of Table 1. Jackel et al.'s results have been normalized so that the 3-dB widths agree (Their actual 3-dB filter width was 1.78 nm). Their normalized passband shapes are superimposed on ours in Fig. 7, and the rectangularity parameter is plotted for the experimental observations of Table 1 in Fig. 8.

Discussion. A number of observations can be made for completeness. (1) The wavelength-misalignment tolerance benefit of passband flattening exacts a penalty in sidelobe skirt level, but, as all these extinctions are much smaller than the better-than-30-dB extinction required to reduce the effects of interchannel coherent crosstalk, it will still be necessary to use spatial switch dilation. (2) We have further studied the effect of passband shape on intermodulation and find that the closer the rectangularity is to one, the worse the intermod. We are investigating whether this is a fundamental limitation. (3) The placement of the optical waveguide in the center of the lower half of the SAW waveguide is not optimum, according to our modeling of the SAW amplitude, and in future designs, we will move the optical waveguide toward the SAW guide center. (4) The best flatness was achieved, surprisingly,

for a birefrinence nonuniformity worse than that measured for the "uncompensated" profile. This is not yet understood.

[1] D. A. Smith et al., "Evolution of the acousto-optic wavelength-routing switch", to be published in *J. Lightwave Technol.* , March, 1996. [2] H. Herrmann et al., *J. Lightwave Technol.*, vol. 13, no. 3, pp. 364-374, 1995. [3] G. H. Song, *J. Lightwave Technol.*, vol. 13, pp. 470-480, 1995. [4] J. L. Jackel et al., *Photon.Technol. Lett.* , vol. 7, pp.318-320, 1995. [5] R. S. Chakravarthy et al., *Proc. 7th European Conf. on Integrated Optics* , (Delft, The Netherlands, Apr. 3-6, 1995). [6] L. B. Aronson et al., Proc. *Integrated Photonics Res. Conf.*, postdeadline paper PD6 (Dana Point, CA, Feb. 23-25, 1995). [7] H. Rashid et al., Proc. LEOS'95 (San Francisco, CA, Nov., 1995).

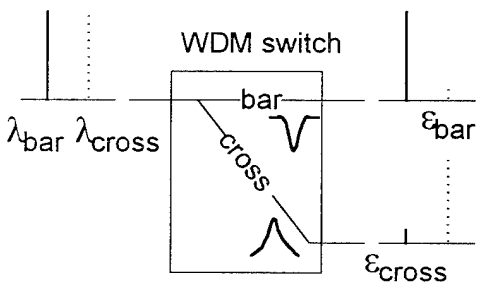


Fig. 1. *Wavelength channels remain in the bar state or are switched to the cross state with residual fractions as shown.*

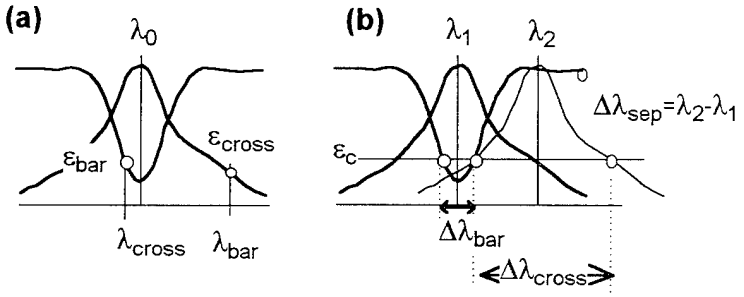


Fig. 2. *(a) Bar and cross state extinctions defined; (b) Depiction of wavelength misalignment tolerance and channel separation required for a given crosstalk criterion.*

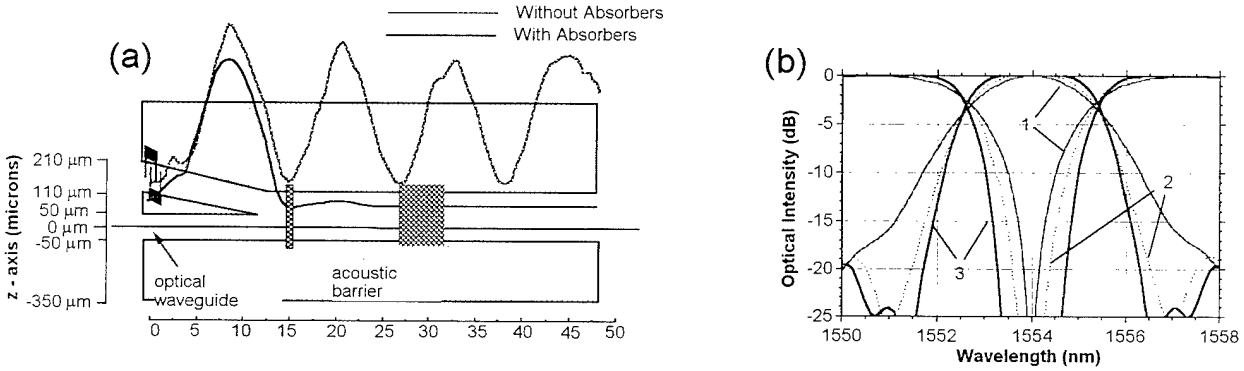


Fig. 3. *(a) Schematic of the multi-cycle SAW-coupler--based AOTF showing measured SAW intensity profile before and after step attenuators were put in place. (b) predicted bar and cross state passband shapes for 1,2 and 3 cycles with optimum attenuation chosen.*

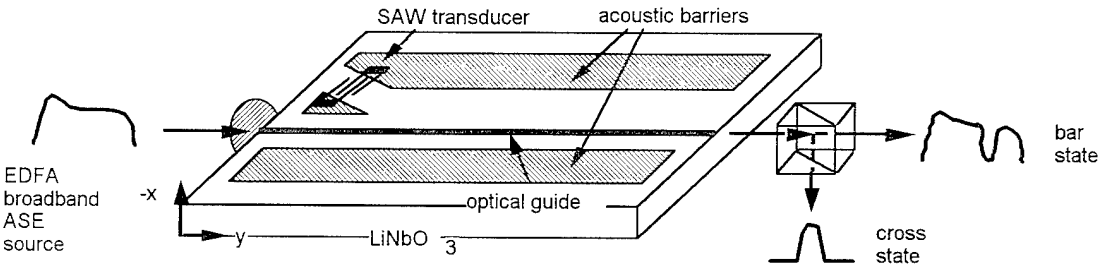


Fig. 4. *Passband evaluation using EDFA ASE probe.*

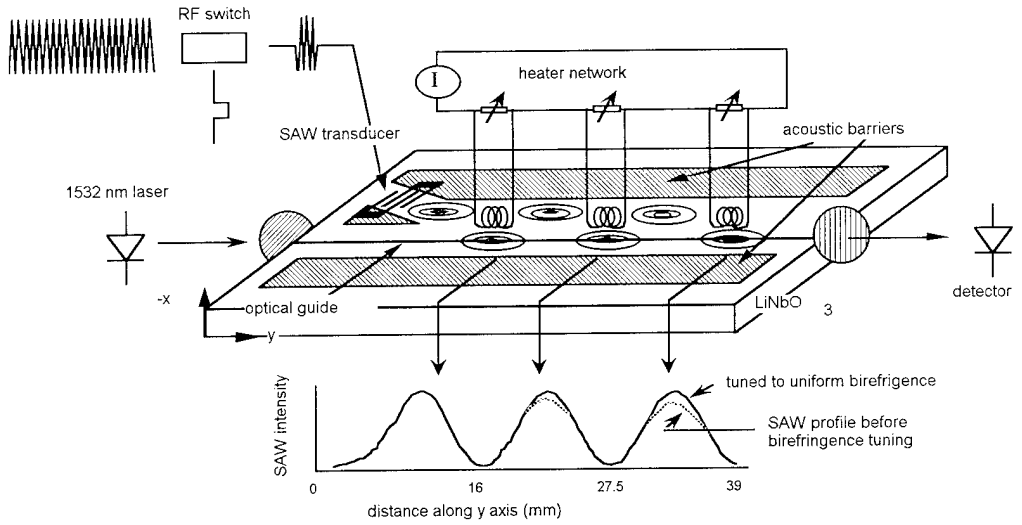


Fig. 5. *Birefringence tuning by separately heating SAW peaks. The pulse probe scheme is also shown.*

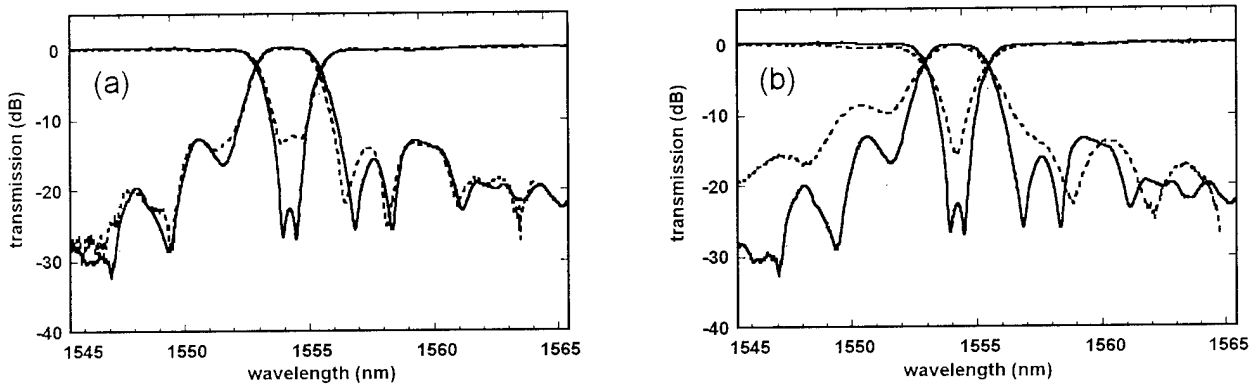


Fig. 6. *(a) Passband shapes before (dashed) and after (solid) birefringence tuning, (b) comparison of one (dashed) and two (solid) cycle passband shapes.*

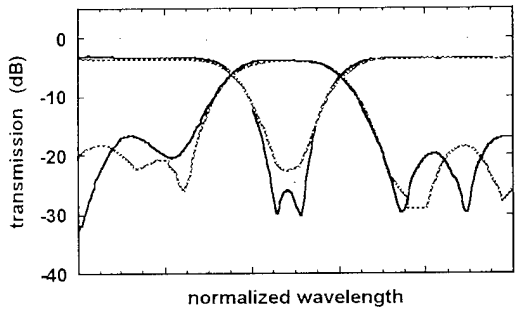


Fig. 7. *Comparison of our passbands (solid) with those of Ref. 4 (dashed). Curves are normalized to the same 3-dB level.*

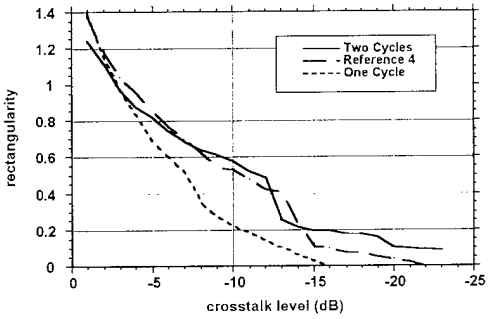


Fig. 8. *Comparison of the rectangularity for one cycle operation, two cycle operation and Ref. 4.*

# cycles	-3 dB width	-10 dB width	-15 dB width	-20 dB width
one	2.52 nm	0.89	0.22	N/A
two	2.52	1.56	1.11	0.89
two [ref 4]	2.52	1.26	0.95	0.42

Table 1. *Comparison of bar-state widths of one-cycle and two-cycle devices.*

Low-Sidelobe Thermo-Optically Tunable Filter

T. Nakazawa, S. Taniguchi, and M. Seino

Fujitsu Laboratories Ltd.
64 Nishiwaki, Ohkubo-cho, Akashi 674, Japan
Phone: +81-78-934-8252
Fax: +81-78-934-3314
E-mail: tdnaka@flab.fujitsu.co.jp

1. Introduction

Tunable narrowband filters will be used in a variety of applications such as wavelength-division multiplexed (WDM) optical communication systems. Ti:$LiNbO_3$ electro-optically tunable filters (EOTF) are potential candidates for such devices [1]. However, they require some improvements in sidelobe suppression, drive-voltage reduction, narrow passband, and polarization independence for practical use.

In this paper, we demonstrate a low-sidelobe, low-drive-voltage, polarization-independent tunable filter that features a new type of electrode structure.

2. Structure

The configuration of our filter is shown in Figure 1. This filter is fabricated in X-cut $LiNbO_3$ and consists of polarization beam splitters (PBS), TE/TM mode converters and a heater. In this polarization-diversity configuration, the filtered output is guided to the cross-waveguide (port 2).

The PBS was a zero gap coupler, as shown in Figure 2. We use an interdigital structure electrode between the two PBSs as a mode converter. In order to suppressed the sidelobe we employed a withdrawal electrode, in which the fingers are removed so that the density of fingers may be distributed to reflect the shape of the appropriate weighting function [2]. We found that a Gaussian function as a weighting function gives good sidelobe suppression characteristics, base on calculations. Figure 3 shows the schematic diagram of this withdrawal electrode.

In a conventional EOTF, the electro-optical tuner has the disadvantage that it requires a large tuning voltage. We considered a thermo-optically tuning with a heater, because the temperature dependence of $LiNbO_3$ birefringence is large. To realize this effect in devices, we set a heater near the waveguides. This heater also doubles as a pad for the withdrawal electrodes.

3. Fabrication and measurement

The waveguides and PBSs were fabricated by titanium indiffusion. We deposited a buffer layer, then formed an Au withdrawal electrode and a heater by evaporation. The length of the electrode was 40 mm and the electric resistance of the heater was 87 Ω.

Figure 4 shows the measured characteristics of the filtered light (port 2) for both the TE and TM inputs. The sidelobe is less than -24 dB for both polarization inputs and the polarization-dependent loss is less than 1 dB. A FWHM of 1 nm was obtained. The sidelobe was reduced drastically compared with a conventional filter (about a -10dB sidelobe). In this measurement, a conversion efficiency greater than 98% was achieved with a mode conversion voltage (V_{MC}) of 4.1 V.

Figure 5 shows the tuning characteristics by applying a voltage to the heater. By increasing the heater voltage (V_H), the center wavelength of the peak shifted towards the shorter wavelengths. To obtain the 10 nm wavelength shift, we only required a tuning voltage of 6.2 V and a mode conversion voltage of only 1.3 V. In this tuning, no degradation of bandwidth was observed. In order to keep the high conversion efficiency, V_{MC} must be changed in correspondence with V_H.

Figure 6 shows the relationship between the heater power and the shift of the center wavelength, where the vertical axis on the right shows the predicted temperature of the waveguides. This graph shows that the shift is linear with the heater power and that a 10 nm shift is obtained with the power of 430 mW. Hence, it follows that tuning with a heater can reduce the voltage by a factor of about one hundred, compared with a conventional EOTF.

Finally we evaluated the response of tuning. Figure 7 shows the step response of the filter to the heater voltage square wave. The time constant is in the order of 10 - 50 ms.

4. Conclusion

We demonstrated a low-sidelobe, polarization-independent thermo-optically tunable filter. We employed a withdrawal electrode of 40 mm as a mode converter in which the density of fingers was distributed. We obtained a sidelobe of less than -24 dB for a Gaussian weighting function and a FWHM of 1 nm for both polarizations. We achieved a reduction of the tuning voltage by employing thermo-optical tuning using a heater near the waveguides. For a 10 nm shift, we only required a tuning voltage of 6.2 V (430mW) and the mode conversion voltage of 1.3 V. This means that the tuning voltage was reduced by a factor of about one hundred, compared with a conventional EOTF.

References

1) W.Warzanskyj et al., Appl.Phys.Lett., 53 , pp.13-15 (1988).
2) T.Nakazawa et al., to be accepted in Photonics Switching'96.

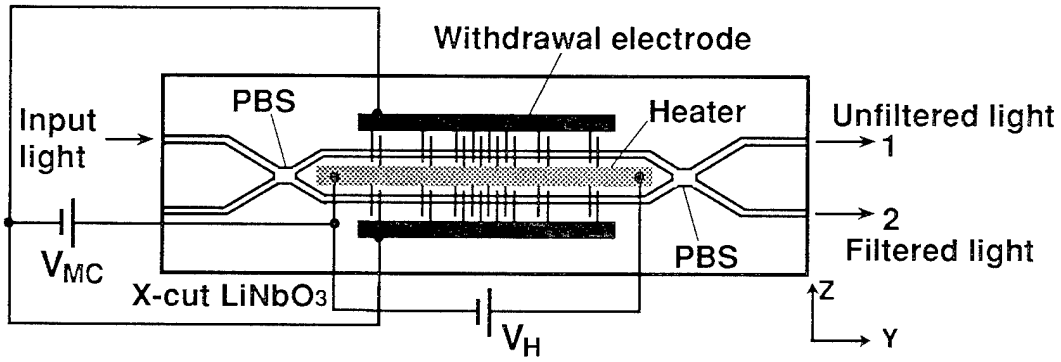


Fig.1. Tunable filter configuration.

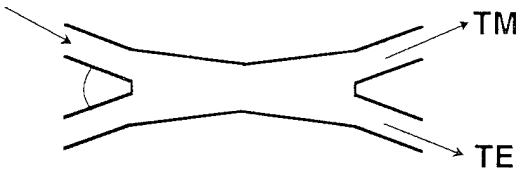


Fig.2. PBS structure.

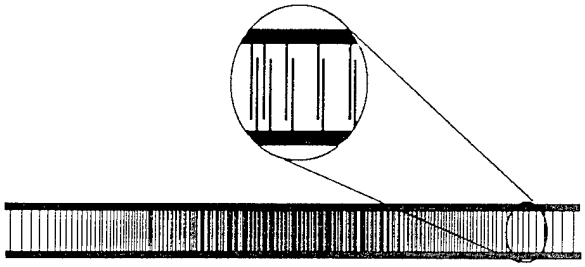
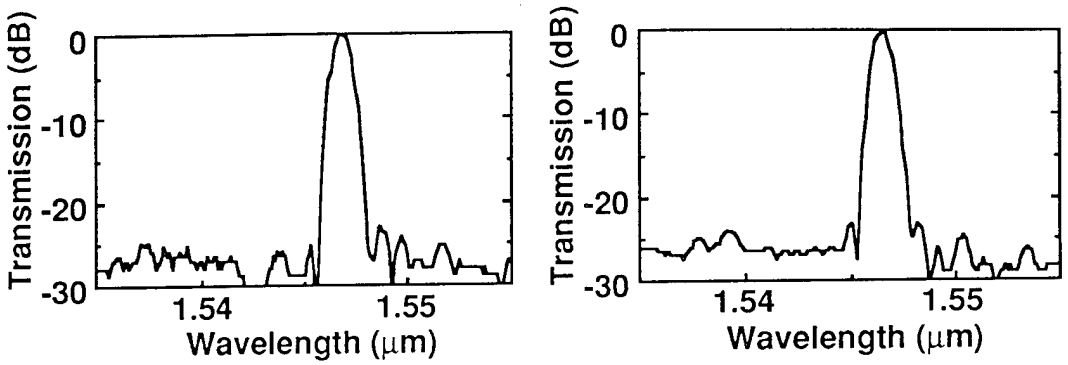


Fig.3. Diagram of the withdrawal electrode.



(a) TE mode light input (b) TM mode light input

Fig.4. Filter characteristics.

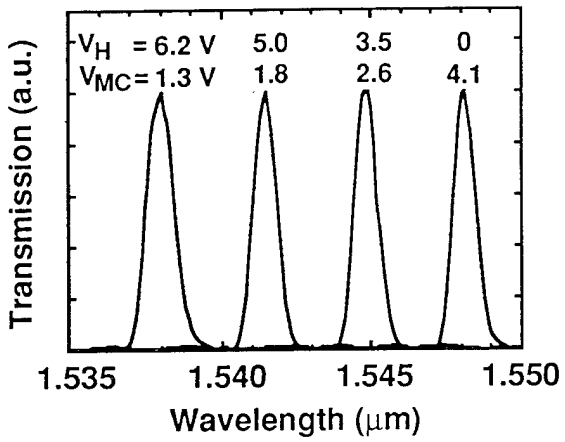


Fig.5. Characteristics of tuning.

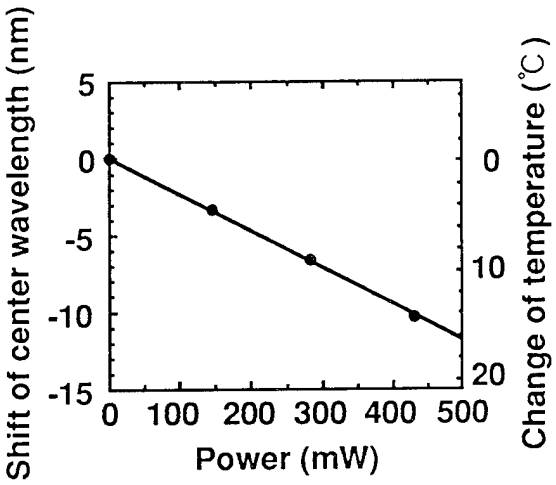


Fig.6. Shift of center wavelength versus heater power.

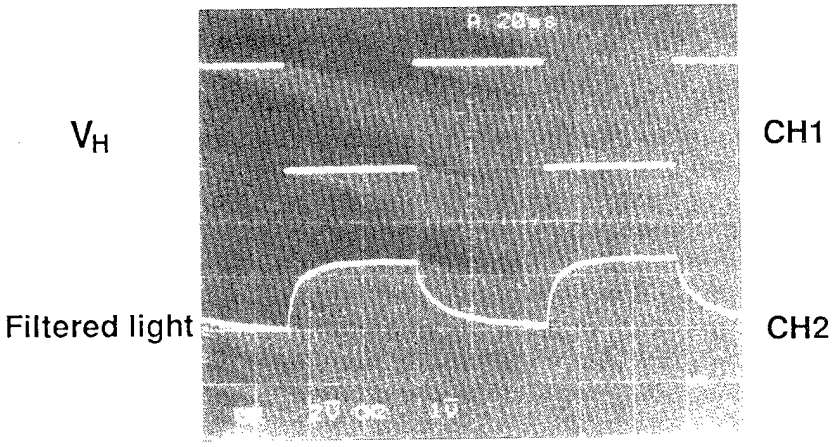


Fig.7. Response of tuning.

A Temperature Insensitive InGaAsP/InP Wavelength Filter

H. Tanobe, Y. Kondo, Y. Kadota,
H. Yasaka and Y. Yoshikuni

NTT Opto-electronics Laboratories
3-1, Morinosato Wakamiya, Atsugi-shi
Kanagawa Pref., 243-01 Japan
Tel. +81 462 40 3152
Fax. +81 462 40 4302
E-mail: htanobe@aecl.ntt.jp

1. Introduction

Wavelength change due to temperature fluctuations in semiconductor lightwave devices is a problem for building high-density wavelength division multiplexed (WDM) fiber optic network systems. The wavelength of the laser diodes and the central wavelength of the semiconductor wavelength filter has a typical temperature dependence of 1 Å/°C or higher. Thus, a temperature insensitive lightwave device is required. However, the study of temperature insensitive lightwave devices has been very limited; the only existing one we know of was in the silica-based material field. In that study, a polymer of which the refractive index varies negatively with respect to temprature (i.e. $dn/dT < 0$) was used to construct a silica-based temperature insensitive waveguide[1]. On the other hand, in the semiconductor field, such negative dn/dT characteristics are rare. Moreover, it has been said that it is impossible to build temperature insensitive lightwave devices using the InGaAsP/InP system. However, semiconductor temperature insensitive lightwave devices are attractive and suitable for the monolithic integration of active and passive devices. To overcome the above mentioned problems, we propose a novel temperature insensitive optical filter (TIOF) with InGaAsP/InP system.

2. Design Principle

The fundamental schematic structure of the TIOF is shown in Fig. 1. The TIOF consists of a Mach-Zehnder (MZ) interferometer with two waveguides. Instead of introducing a material that has a negative dn/dT value, we use two waveguides with different dn/dT values: low and high. The waveguide with low dn/dT value is used for the longer waveguide and the one with the high dn/dT value is used for shorter waveguide, for a 1.55-μm-band TIOF, a InGaAsP(λ_g=1.3 μm) core and InGaAsP(λ_g=1.1 μm) core were chosen for the waveguide with the high and low dn/dT values, respectively.

The filtering wavelength of a typical MZ filter is determined from the difference between the optical path length distances of two waveguides. Generally, as the temperature increases, the refractive index of the semiconductor increases. Thus, a red-shift in the filtering wavelength can be seen. In the case of the TIOF, however, due to the dn/dT difference, this effect can be canceled out under the condition that is simply expressed by

$$\frac{\frac{\partial n_{eq_1.1Q}}{\partial T}}{\frac{\partial n_{eq_1.3Q}}{\partial T}} = \frac{L'}{L'+\Delta L} \quad \cdots\cdots \quad (1)$$

where, $n_{eq_1.xQ}$ is the equivalent refractive index of the each corresponding waveguide.

3. TIOF Structure

The actual structure of the proposed TIOF and cross sections of the waveguides are schematically shown in Figs. 2 and 3, respectively. Each waveguide has a buried-rib structure. To build the Mach-Zehnder interferometer, a pair of arc waveguides with the same radius 3.75 mm is linearly shifted and connected to each other at the waveguide ends by two linear waveguides. The InGaAsP(λ_g=1.3 μm) core waveguide with the larger dn/dT value is introduced into the shorter waveguide of the TIOF filter. To make a junction between the InGaAsP(λ_g=1.3 μm) core and InGaAsP(λ_g=1.1 μm) core, the 0.3-μm-thick core regions are butt jointed. Then, a 0.1-μm-thick intermediate InP layer is grown on the core layer. The common InGaAsP(λ_g=1.1 μm) rib which is 0.23-μm-thick and 1.5-μm-width is laid on the InP layer. A Cl_2 RIE system was used to form the rib. Finally, the rib was buried with a 1.5-μm-thick InP layer. All of the layers are un-doped epitaxial layers and were grown by low pressure MOCVD. The TIOFs were then thinned and AuGe/Au backwafer metallization for bonding was carried out. After cleaving to set single TIOFs, samples were bonded to Si heatsinks with AuSn for the temperature dependence measurement.

4. Characterization

We measured transmission spectra of the TIOF at temperatures from 25 to 45 °C. In the measurement, we used a 1.55-μm TE-polarized tunable laser. Typical measured spectra with 100 GHz FSR are shown in Fig. 4 (no AR coating).

The filtering wavelength temperature dependence of a MZ filter and the TIOF are shown in Fig. 5. The measured MZ filter as a reference device is a modified TIOF without

InGaAsP(λ_g=1.3 μm) core region (i.e. L'=0). As can be clearly seen, the conventional MZ filter has a well known temperature dependence of 1 Å/°C or higher with a red-shift. On the other hand, in the case of the TIOF, it is improved to less than 0.1 Å/°C. To our knowledge, this is the first time a lightwave device with less than 0.1 Å/°C temperature dependence has been built using InGaAsP/InP alloy semiconductor.

We also measured the temperature dependence of TIOFs varying the length of the waveguide with InGaAsP(λ_g=1.3 μm) core to verify the TIOF design principle. The results of this measurement are shown in Fig. 6. The optimum length of the waveguide with a InGaAsP(λ_g=1.3 μm) core for the TIOF is represented by " L' ", and all of the InGaAsP(λ_g=1.3 μm) core waveguide length in the modified TIOFs are normalized by " L' ". By extending the waveguide length with InGaAsP(λ_g=1.3 μm) core, the temperature dependence of the filtered wavelength were changed greatly. Moreover, another TIOF with a longer InGaAsP(λ_g=1.3 μm) core waveguide exhibited an increasing rate of filtering wavelength shift for shorter wavelengths. This blue-shift phenomena is in good agreement with the principle of the TIOF.

5. Results

We have demonstrated, for the first time, a temperature insensitive wavelength filter with InGaAsP/InP alloy semiconductor. The device exhibits temperature insensitive characteristics of < 0.1Å/°C. A blue-shift temperature dependence of the filtered wavelength was also obtained in the modified TIOF. These two phenomena are in good agreement with the design principle.

References

[1] Y. Kokubun et al., Electron. Lett., Vol. 30, pp. 1223-1224, Jul., 1994.

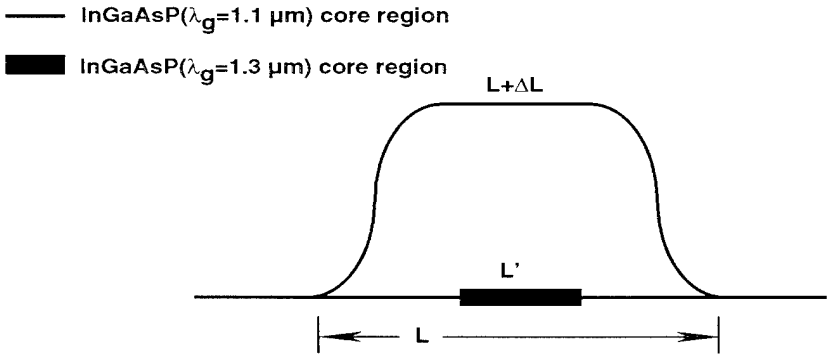


Figure 1: Schematic of the fundamental TIOF structure model

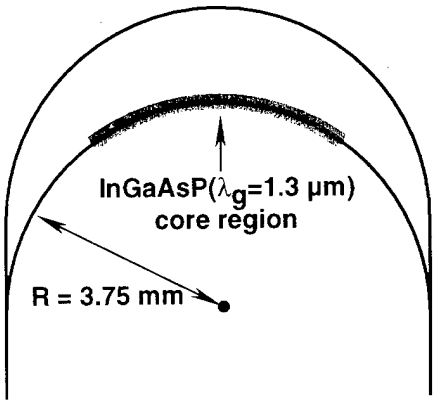


Figure 2: Schematic structure of the proposed TIOF

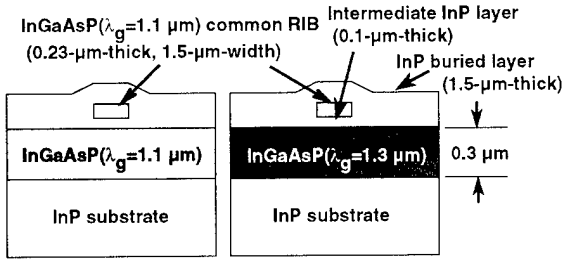


Figure 3: Cross section of rib waveguides in the TIOF

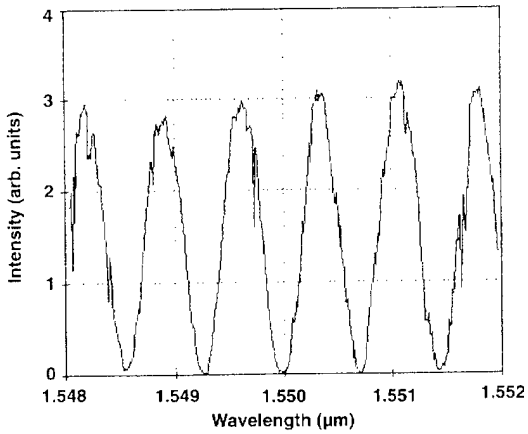


Figure 4: Transmission spectra of the TIOF

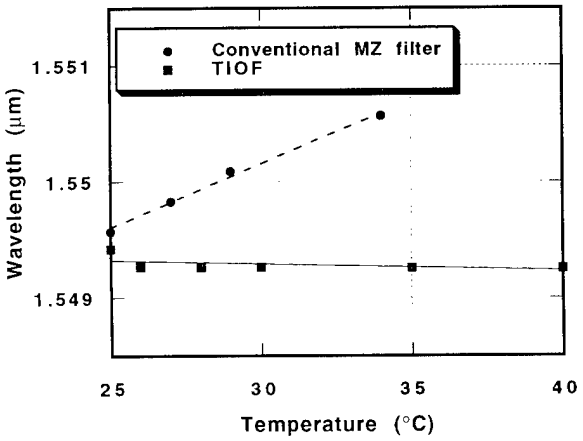


Figure 5: Filtering wavelength dependence against temperature for a conventional MZ filter and the TIOF

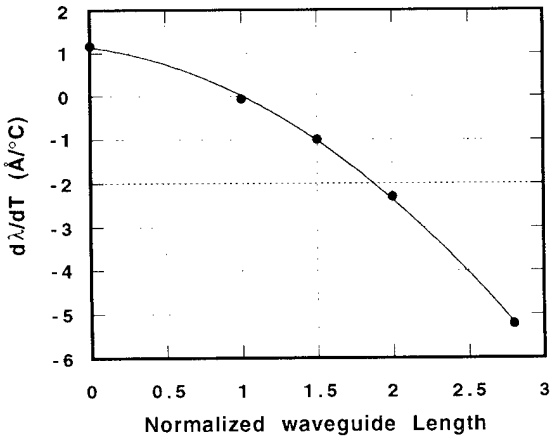


Figure 6: Filtering wavelength varying characteristics respect to temperature against normalized InGaAsP(λ_g=1.3 μm) core waveguide Length (L').

Integrated tunable polarization-independent channel dropping filter on InP for WDM systems

Jean-Pierre Weber
Ericsson Components AB, Fiber Optics Research Center,
S-164 81 Kista, Sweden (+46-8-757-4513, Fax: +46-8-757-4764)
Björn Stoltz, Olof Öberg
Ericsson Components AB, Opto and RF Power Products,
S-164 81 Kista, Sweden (+46-8-757-4061)

An important element in optical transmission networks based on Wavelength Division Multiplexing (WDM) is the Optical Add-Drop Multiplexer (OADM). It allows the selective dropping of one or several wavelength channels (fixed or selectable) and the addition of new signals at the same wavelengths. To reduce cost, an integrated optics solution would be preferable to discrete components. Several technologies can be used, including acousto-optic devices in $LiNbO_3$ [1], planar diffraction gratings in InGaAsP/InP [2] or SiO_2/Si [3], and arrayed-waveguides, also in InGaAsP/InP [4] or SiO_2/Si. One of the most advanced examples to date is a 16 channels device in SiO_2/Si [5] using three arrayed-waveguide grating demultiplexers on the same chip (80 by 65 mm).

In this paper, we present a new device that can realize the most difficult part of an OADM: the drop function. It is fabricated in InGaAsP/InP, allowing a smaller chip size (in our case only 3.4 by 1.5 mm) than SiO_2/Si or $LiNbO_3$. It also allows the integration of amplifiers and detectors on-chip. The device schematic is shown in Fig. 1: the input light is split using a 3 dB splitter and each branch passes through a Multi-Grating Filter (MGF) [6, 7, 8]. The 3-dB splitters are either Y-junctions or Multi-Mode Interference (MMI) splitters [9]. One branch is the drop branch (transmitting the wavelength to be dropped) and the other the through branch (transmitting the other wavelengths). Amplifiers are integrated at the input and at each output. Tapers have been added to improve coupling between the chip and the fibers.

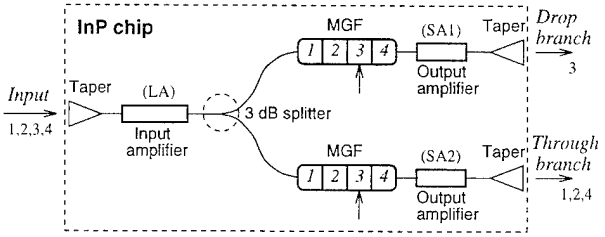


Figure 1: *Schematic of the channel dropping device.*

Each MGF consists of four Bragg gratings in series in a waveguide. In the drop branch, each grating center wavelength corresponds to one channel wavelength, so that all channels are blocked. The dropped channel is selected by injecting current in the corresponding grating, which changes the effective index and thus the center wavelength and allows the transmission of that channel, as shown in Fig. 2 (see [6, 7, 8] for more details). In the through branch, the center wavelengths of the gratings are placed on the long wavelength side of the channels, so that all channels pass through. To block the dropped channel, current is injected in the corresponding grating to make its center wavelength coincide with the channel wavelength, and thus reflect most of it (see Fig. 2). The channel positions are made polarization-independent by designing the waveguide to have the same effective index for TE and TM [6, 7].

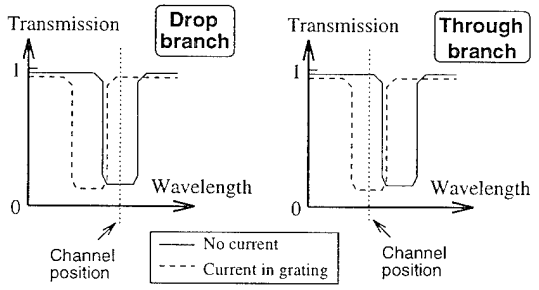


Figure 2: *Current injection opens a channel in the drop branch but closes it in the through branch.*

The fabrication procedure is similar to the one described in [7], but with some additions to form the tapers. The devices are made on a n-type InP substrate using low pressure MOVPE (Metal Organic Vapour Phase Epitaxy) for all the epitaxial growths. First the layers for the amplifier sections are grown: lower n-InP cladding, 0.6 μm n-InGaAsP (1.1 μm) waveguide

Dropped channel	Drop branch						Through branch					
	Chip losses [dB]	On/off ratio [dB]	Crosstalk [dB] from channel				Worst crosstalk [dB]	On/off ratio [dB]	Chip losses [dB] in channel			
			1	2	3	4			1	2	3	4
1	8.8	22.4	–	-21.9	-22.0	-21.9	-17.6	23.1	–	10.8	9.3	6.9
2	8.1	20.5	-23.3	–	-22.9	-22.5	-19.3	20.4	7.5	–	8.8	7.3
3	8.7	19.5	-22.4	-21.6	–	-21.6	-18.2	22.5	7.1	8.5	–	5.6
4	8.4	19.0	-22.3	-20.9	-22.6	–	-14.6	20.1	8.3	9.1	5.5	–

Table 2: *Chip coupled input power= -9.3 dBm (tunable laser), T= 20 °C with currents LA= 60 mA, SA1= SA2= 30 mA and 30 mA for grating tuning. The losses are the estimated on-chip losses, the through branch crosstalk is the worst case channel crosstalk.*

layer, 50 nm n-InP, 50 nm n-InGaAsP (1.4 μm) grating layer, 0.1 μm n-InP, 0.2 μm undoped InGaAsP (1.58 μm) active layer and top p-InP cladding. All n dopings are 10^{18} cm^{-3} and the p doping is 6×10^{17} cm^{-3}. The regions outside the amplifiers are etched down to the grating layer and the gratings are formed in the filters by electron-beam lithography and etching in the grating layer. Then 50 nm n-InP is regrown over the gratings, followed by a 0.5 μm undoped InGaAsP (1.2 μm) top waveguide layer and a top p-InP cladding layer. The top waveguide layer is then etched to form the taper shown in Fig. 3 and Fe-doped InP is regrown to planarize the surface. The 0.7 μm wide waveguides, the Y-junction (or the 45.8 μm by 6 μm MMI) and the tapers are then defined by electron-beam lithography and etched using reactive ion etching. The bend radiuses are all 300 μm and the waveguides terminate about 40 μm from the facets to reduce reflection (window structure). After etching of the top p cladding between sections (for electrical isolation), semi-insulating (Fe doped) InP is selectively grown for current confinement. Then the top p contact layers are grown and metalization is done (the resulting waveguide cross-section is shown in Fig. 3). Finally the contact layers are removed between the sections and a thick Fe-doped InP layer (about 10 μm) is grown over the window regions to avoid internal reflection from the top surface of the chip. Each grating section is 400 μm long, the input amplifier (LA) is 400 μm long and the output amplifiers (SA1 and SA2) are 200 μm long. The devices were not anti-reflection coated and were mounted and bonded on a Si sub-carrier.

Channel number	Wavelength [nm]	Transparency [mA] LA	SA1	SA2
1	1539.7	10.66	4.97	5.03
2	1543.7	10.02	4.65	4.75
3	1547.7	9.38	4.37	4.47
4	1551.7	8.83	4.10	4.22

Table 1: *Channel wavelengths and amplifier transparency currents at T= 20 °C.*

Using polarization maintaining fiber tapers to couple light in and out of the device and the spontaneous emission from an EDFA as the light source, we measured bewtween 0.1 and 0.25 nm difference in center wavelength between TE and TM on most of the devices. This, and the gratings'center wavelength shift to a shorter value than designed, is probably due to an over-etching of the waveguide down to a 0.6 μm width [6, 7]. The channel wavelengths are spaced by 4.0 nm (see Table 1). Temperature sensitivity of the channel positions is about 0.1 nm/K. One of the best devices (Y-junction, with 0.25 nm TE/TM shift but low losses) was selected for detailed measurements.

Chip to tapered fibers coupling losses were estimated by measuring the ratio of the spontaneous emission power from the amplifiers coupled in the fiber to the total power collected by a lens (NA= 0.4, f= 16 mm). This gave us a lower bound on the losses of 9.3 dB for the input (LA), 3.3 dB for the drop branch (SA1) and 4.2 dB for the through branch (SA2). Previous devices without taper structures on the chip had about 15 dB coupling loss per facet with the same fiber tapers.

A tunable laser was used to measure the transparency currents of the long (LA) and the short (SA1 and SA2) amplifiers at each channel wavelength (Table 1) by the modulation method. Then the gain and gain saturation of each amplifier was studied by measuring the transmission as a function of current and input optical power (with the other amplifier biased at transparency). The gain curves for channel

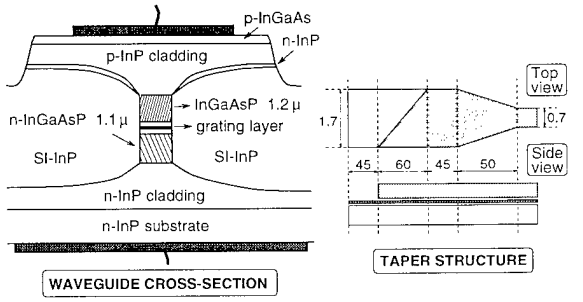


Figure 3: *Waveguide and taper structure.*

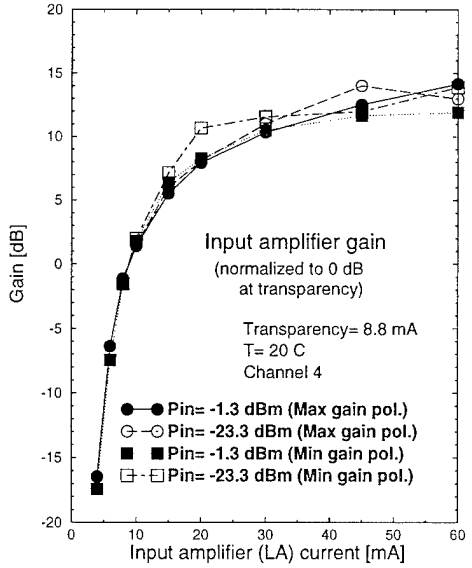


Figure 4: *Input amplifier gain curves.*

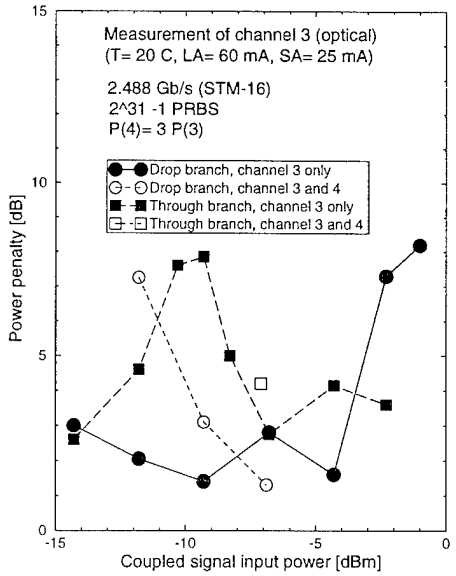


Figure 5: *Power penalties compared to back-to-back.*

4 (normalized to unity gain at transparency) of the long (input) amplifier (LA) are shown in Fig. 4 for the polarization of maximum transmission and the one of minimum transmission, at two coupled input powers (-1.3 and -23.3 dBm). The maximum gain (above transparency) was about 14 dB (LA) and 7.5 dB (SA1 and SA2) in the maximum gain polarization and about 12 dB (LA) and 6.5 dB (SA1, SA2) in the minimum gain polarization. Gain saturation was negligible for the output amplifiers (within measurement errors) and at most about 2 dB in the input amplifier (LA) for the powers we were able to couple in the chip (up to -1 dBm CW optical power).

Table 2 shows the worst case crosstalk (for any polarization combination) and the estimated chip losses for the drop and the through branches. Measurements were made at T= 20 °C, with LA= 60 mA, SA1= 30 mA, SA2= 30 mA and grating currents of 30 mA. The chip-coupled laser input power was about -9.3 dBm. The polarization dependence of the losses was typically between 1 and 3 dB (due in part to the polarization dependence of the amplifiers'gain)

The next step in the device evaluation was to measure the power penalty in transmission experiments at 2.488 Gb/s (STM-16) caused by the crosstalk and the spontaneous emission in the chip. The signal was always in channel 3 and generated by a tunable DBR laser and an external $LiNbO_3$ modulator (both fabricated at Ericsson Components). The perturbation in channel 4 was generated by an integrated DFB/electro-absorption modulator device [10], modulated with the same signal but inverted and delayed. The two channels were combined in 3 dB coupler and boosted with an EDFA. In all the measurements the two channels had parallel polarizations and were injected in the maximum gain polarization state. (Analysis of previous measurements on single MGF [8] has shown that the polarization effects were entirely due to the gain differences only.) The receiver was a commercial Ericsson STM-16 receiver with an APD detector and a phase-lock loop for clock recovery. Back-to-back sensitivity at a bit-error rate (BER) of 10^{-9} was measured to be -32.9 dBm (taken as reference for the power penalties). The STM-16 measurements were all made with $2^{31} - 1$ Pseudo-Random Bit Sequences (PRBS).

The measured penalties, at a BER of 10^{-9}, are shown in Fig. 5, as a function of the channel 3 chip coupled average input power (estimated errors on the penalties: $\pm$ 1 dB). Both single channel and two channel operation are shown for the drop and the through branch. When present, the perturbation (channel 4) had 3 times the power of the signal (+4.8 dB) to simulate a worst case four channels'operation. In the drop branch case, current was injected in grating 3 to transmit channel 3 (channel 4 was measured to be 19 dB below channel 3 at the output of the drop branch). For the through branch, current was injected in grating 4 to block channel 4 (channel 4 was 17.5 dB below channel 3 at the output of the through branch). The measured range of coupled input powers was limited at the high end to about 0 dBm (due to the maximum power out of the EDFA, about 9 dBm, and the input coupling loss, about 9.3 dB). The low end was limited by the high total fiber-to-fiber loss of about 22.5 dB, giving a bad signal-to-noise ratio in the receiver. This could be improved by better fiber-to-chip coupling. The limited range of input powers makes any conclusion difficult. In addition, some resonances (probably due to reflections, see [11]) seem to be also

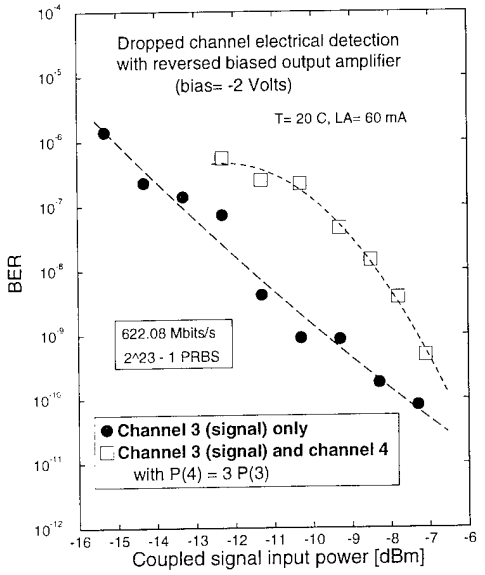


Figure 6: *Electrical BER curves.*

present. All we can say is that the best results (about 2 dB penalty) are close to the best results of the single MGF [8].

Finally, we demonstrated the possibility of using the reverse-biased output amplifier of the drop branch (SA1) as a photo-detector to get an integrated solution and avoid additional coupling losses and the cost of an external photo-detector. This is only a demonstration of principle since the chip was not mounted for high speed operation. Using a probe, we managed to measure single and double channel BER curves at 622 Mbits/s (STM-4), with a $2^{23}-1$ PRBS sequence (longer sequences had problems due to the electrical bandwidth of the system). Except for the bit rate and the PRBS length, the transmitter was the same as for the 2.488 Gb/s measurements, i.e., with channel 4 (when present) having 4.8 dB more power than channel 3. The electrical detection chain consisted of the SA1 amplifier (contacted by a probe), reverse-biased with 2 Volts through a bias tee (160 kHz–40 GHz). The signal was then amplified by a chain of three amplifiers (20 dB gain each, 20 kHz–2 GHz) with a variable attenuator (11 dB max) and filtered by a 622 Mbits/s SDH filter before being fed into the BER measurement system (and a sampling oscilloscope).

The measured BER curves as a function of the estimated coupled average input power to the chip are shown in Fig. 6 for channel 3 alone and for channel 3 plus channel 4. Bias currents were: LA= 60 mA, grating 3 in both branches= 30 mA, T= 20 °C, 2 Volts reverse bias on SA1 (typical DC current 50 to 120 μA with light injected). We see that the penalty due to the perturbation was 2.4 dB at a BER of 10^{-9}. This penalty is not due to the channel 4 light reaching the detector (since it is more than 17 dB below the signal, see above), but to cross-gain saturation in the input amplifier. This was causing power dependent waveform distortion in the electrical signal applied to the BER measurement system (observed with the sampling oscilloscope). The same problem was observed previously in single MGF devices [8]. In addition, some resonances due to reflections seem also to be present. Exact interpretation of the measured BER curves is difficult due to the interaction between the effects of electrical noise, spontaneous emission noise (from LA), (cross–)gain saturation and reflections.

Summary: We have fabricated an integrated InGaAsP/InP device performing the drop function of an OADM node, around 1550 nm. The device has four polarization-independent channels 4 nm apart with electrical selection of the dropped channel. Optical measurements at 2.488 Gbits/s (STM-16) of the drop and through branches showed power penalties (at BER= 10^{-9}) down to 2 dB for single channel operation and a few dB more for multi-channel (due to cross-gain saturation in the input amplifier). We also demonstrated on-chip electrical detection of the dropped channel (by reverse-biasing the output amplifier) at 622 Mbits/s (STM-4). Multi-channel operation showed a 2.4 dB power penalty (at BER= 10^{-9}) compared to single channel, again due to cross-gain saturation in the input amplifier.

This work was supported in part by the RACE MWTN (R2028) project.

References

[1] A. d'Alessandro *et al*, IEEE Photon. Technol. Lett., 6 (3), March 1994, pp 390–393.

[2] C. Cremer *et al*, Electron. Lett., 30 (19), 15 Sept 1994, pp 1625–1626.

[3] P.C. Clemens *et al*, IEEE Photon. Technol. Lett., 6 (9), Sept 1994, pp 1109–1111.

[4] H. Bissessur *et al*, Electron. Lett., 30 (4), 17 Feb 1994, pp 336–337.

[5] K. Okamoto *et al*, OFC'95, San Diego (CA), Feb. 1995, post-dealine PD10.

[6] J.-P. Weber *et al*, Electron. Lett., 31 (3), 2 Feb 1995, pp 220–221.

[7] J.-P. Weber *et al*, IPR'95, Dana Point (CA), Feb. 1995, Vol. 7, 1995 OSA Techn. Digests, paper PD–4.

[8] J.-P. Weber *et al*, *"Power penalties measurements of a four-channel Multi-Grating filter with WDM signals at 2.488 Gb/s"*, to appear in IEEE Photon. Technol. Lett., 7 (12), Dec 1995.

[9] L.C. Soldano and E. Pennings, J. Lightwave Technol., 12 (4), April 1995, pp 615–627.

[10] P. Ojala *et al*, Electron. Lett., 29 (10), 13 May 1993, pp 859–860.

[11] Lars Gillner, ECOC'95, Brussels, Sep 1995, paper Mo.L.3.6, pp 119–122.

A wavelength tunable semiconductor amplifier/filter for add/drop demultiplexing in WDM networks

G. Raybon, U. Koren, R. M. Jopson, B. I. Miller, M. Chien
M. G. Young, R. J. Capik, K. Dreyer

AT&T Bell Laboratories, Crawford Hill Laboratory
791 Holmdel-Keyport Rd, Holmdel, NJ 07733
(908) 888-7221

The ability to add and drop wavelength channels in a wavelength division multiplexed (WDM) network is of great importance to achieve successful routing of wavelengths [1]. Several types of add/drop multiplexers have been demonstrated such as those using fiber grating filters and circulators [2], and those using arrayed waveguide technology [3]. The function of these add/drop multiplexers is to provide optical selection (drop) and addition (add) of a particular wavelength channel without interference from adjacent channels. The filter is a key building block for use in the drop demultiplexer as well as in wavelength selective receivers [4]. A fast tuning semiconductor filter may be the best practical solution since it can combine the filter functionality with compactness, low cost and low polarization dependent loss. Additionally, through integration more functionality such as amplification and detection can be provided on a single chip. Here we present a semiconductor amplifier/filter which can be used an element in an add/drop multiplexer to provide gain and electrical tunability over 9.5 nm. Channel dropping and high receiver sensitivity is demonstrated using a circulator and the amplifier/filter in a five channel WDM system operating at 50 Mbits/s.

The amplifier/filter shown in Fig. 1 is designed to reduce polarization dependence. The filter is fabricated with lattice matched 1.42 quaternary InGaAsP core layer which has a square 0.7 x 0.7 μm lateral cross section and a first order Bragg section etched beneath the 1.42 core layer. The peak Bragg wavelengths for TE and TM polarization differ by only 1 Angstrom [5] and the spectral width of the filter response is measured to be approximately 0.9 nm FWHM. The amplifier is fabricated to reduce polarization dependence by growing strained-layer multiple quantum wells (MQW) with alternating tensile and compressive strain [6]. The amplifier and filter sections are 400 μm and 350 μm respectively and anti-reflection coatings are applied to each facet. The device is packaged in a standard butterfly package with a lensed-end single mode fiber coupled only to the output of the amplifier. To cascade this

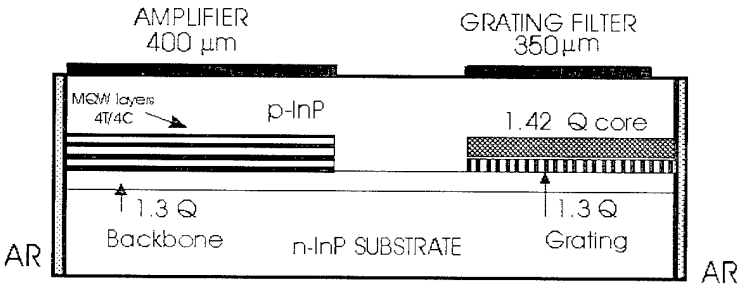


Fig. 1: Schematic diagram of amplifier/filter device.

device for user in an add/drop function, fiber would also be coupled to the filter section to recover the out of band signals. The selected wavelength is reflected by the filter and amplified twice in the amplifier. Peak gain is achieved with approximately 70 mA bias to the amplifier. Fiber to-fiber gain is measured to be 4.2 dB for small tuning currents.

The performance of the amplifier/filter was evaluated as the key component in the drop function of an add/drop multiplexer. A schematic of the experimental set-up is shown in Fig. 2. where the amplifier/filter is used in conjunction with a circulator to perform the drop function. Typically the add function would follow the filter with the add being performed using another circulator [2]. Here to demonstrate channel selection, five wavelengths with a channel spacing of 1.6 nm have been multiplexed onto a single fiber using two sources. One source is modulated using a pulse pattern generator (PPG) at 50 Mbits/s and is the channel which is demultiplexed and tested for error rate. The four other wavelengths are provide by four channels of a semiconductor multi-frequency laser (MFL) [7] and are also modulated with pseudorandom data at 50 Mbits/s to simulate interfering channels. By separating the two signal sources, any crosstalk associated with the source of optical interference can be ignored and only the effects due to incomplete channel drop

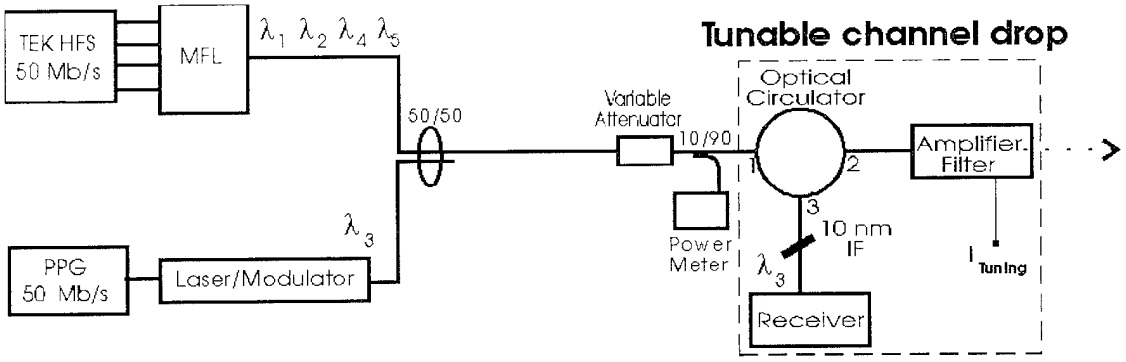


Fig. 2: Schematic of experimental WDM system with tunable channel drop.

can be examined. The two signals are passively multiplexed using a 3 dB fiber coupler. A variable optical attenuator and optical power meter are placed before the drop for error rate measurements and a broad 10 nm interference filter (IF) is placed in front a commercial 50 Mbit/s receiver to filter unwanted amplified spontaneous emission (ASE) emitted by the amplifier. This filter is wide enough to accommodate selection of any of the five wavelengths without manual tuning. The amplifier/filter is a reflective filter and the desired channel is reflected back to the circulator and exits port 3 where the signal is received. Figure 3 illustrates the selection of the channels by simple adjustment of the current to the tuning section of the filter. At the input to the amplifier/filter, the amplitude of each channel is adjusted to within +/- 1 dB as shown in Fig. 3a. Figs. 3b-d show the selection of wavelength channels λ_1, λ_2, and λ_3 respectively by simple electrical tuning of the filter from 13 mA to 5 mA. Unfortunately, the two highest channels available fell out of the tuning range of the filter because the filter tunes to shorter wavelengths with

increased tuning current. The filter is capable of tuning approximately 8.0 nm with 50 mA and a maximum tuning range of 9.5 nm as previously reported [5]. Each channel can be selected with at least 10 dB rejection of the adjacent channels. At this bit rate this crosstalk should lead to a negligible penalty in receiver sensitivity.

Bit-error-rate (BER) was measured on the center wavelength (λ_3) to determine if a sensitivity penalty due to optical crosstalk caused by incomplete demultiplexing would be observed. Fig. 4 shows the BER plotted as a function of received optical power as measured at the input to the circulator. For comparison a baseline receiver sensitivity curve is plotted (▲)for the case when no interfering wavelengths are transmitted and the transmission line is connected directly to the receiver. At 50 Mbit/s, this receiver has a sensitivity of -44.4 dBm at a BER=$1x10^{-9}$. The data for the drop demultiplexer is shown for two cases. One is for all channels transmitted (■) and the other is when only the signal channel is transmitted (●). There is no penalty observed for the demultiplexing and the receiver sensitivity is -35.7 dBm at a BER=$1x10^{-9}$. The difference in sensitivity between the receiver baseline and the dropped channel is mostly due to signal-to-noise degradation caused by unfiltered ASE from the optical amplifier coupled with a very high sensitivity commercial receiver. Despite being far from the quantum limit, this represents a significant improvement over previously reported sensitivities for integrated WDM receivers [4] where sensitivity was low due excessive optical losses.

In summary, we have demonstrated penalty free wavelength demultiplexing at 50 Mbit/s using an integrated amplifier/filter. The structure can be implemented as an add/drop filter in reconfigurable WDM networks requiring fast wavelength tuning and low polarization dependence.

References

1. W. I. Way, et. al., *Photon. Technol. Lett.*, 1992, **4**, (4), pp. 402-405.
2. M. J. Chawki, et. al., ECOC'95-Brussels, Belgium, pp. 47-50.
3. K. Oda, et. al., ECOC'95, Brussels, Belgium, pp. 59-62.
4. F. Tong, et. al., ECOC'95 Brussuls Belgium, pp. 203-206.
5. U. Koren, et. al., LEOS '95, San Francisco, PD 1.4.
6. M. A. Newkirk, et. al., *Photon. Technol. Lett.*, 1993, **4**, pp. 406-408.
7. M. Zirngibl, et. al., *Electron. Lett.*, 1992, 28 (11), pp. 1007-1008.

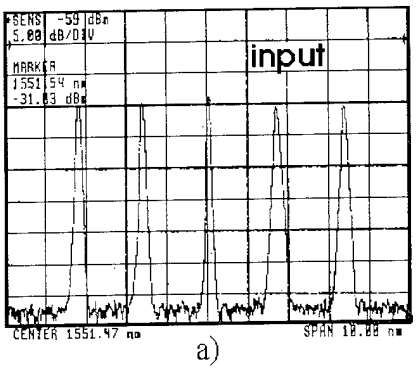


Fig. 3: Optical spectrum measured at a) the input to the amplifier/filter, b) -d) at the output of the circulator port 3 showing demultiplexing of the first three wavelength channels by electrical tuning. Inset shows tuning current for each wavelength selection. Vertical scale: 5 dB/div, Horizontal scale: 1 nm/div.

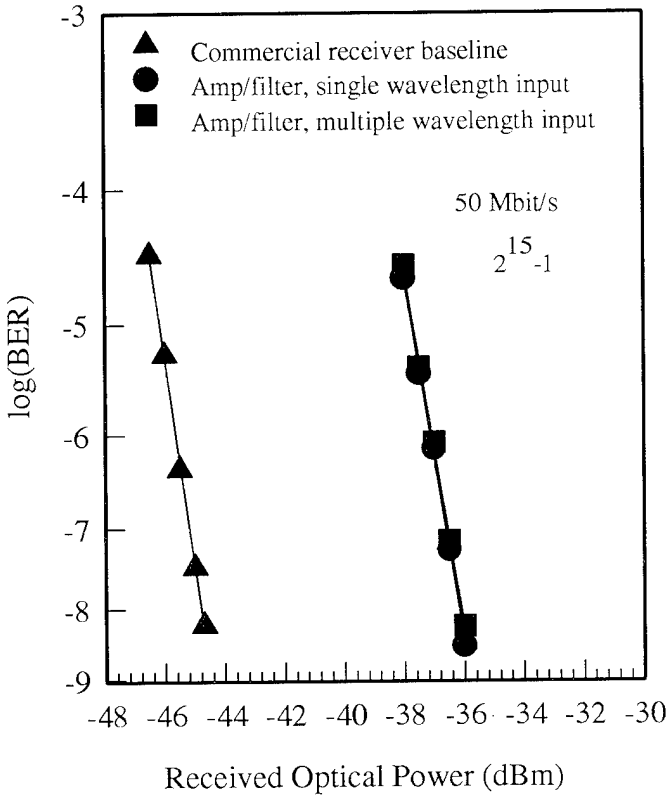


Fig. 4: BER measurement of channel drop with and without adjacent channels compared to the baseline sensitivity of the commercial receiver.

Silica based Mach-Zehnder add-drop filter fabricated with UV-induced gratings

Glenn E. Kohnke, Charles H. Henry, Edward J. Laskowski,
Russell J. Fischer, Thomas A. Strasser, and Alice E. White
AT&T Bell Laboratories, 600 Mountain Avenue, Murray Hill, NJ 07974
Tel: (908) 582-6095 Fax: (908) 582-2783 E-mail: gek@allwise.att.com

Introduction

Add-drop filters are critical components for wavelength-division-multiplexed optical communications systems. It is of interest to develop narrow bandwidth devices with good isolation and crosstalk performance and minimal insertion loss. A Mach-Zehnder interferometer with UV-induced gratings is an attractive add-drop technology.[1] Adjacent channel isolation greater than 20 dB at 100 GHz and transmitted isolation less than -20 dB has been demonstrated in a fiber-based device.[2] However, fiber interferometers suffer from sensitivity to environmental changes due to polarization effects and also require UV trimming to account for arm length differences.

Planar waveguide based devices with a similar design have been demonstrated.[3] These are more robust than fiber-based devices and can be fabricated with equal arm lengths. The grating length in the previous work was the primary limitation, resulting in grating spectra which were not simultaneously narrow and highly reflecting. The planar geometry is especially attractive for these devices since it easily allows double filtering as was previously demonstrated with elliptical Bragg reflectors.[4] In this work, we report a double filtered Mach-Zehnder based add-drop filter incorporating UV-induced gratings that has exceptionally low sidelobe levels and good dropped channel transmitted isolation.

Device Design and Fabrication

The device design is shown schematically in Fig. 1. Although this device is actually a four-port device, our experimental design contains two additional ports to use in monitoring grating growth and to allow for measurement of the individual Mach-Zehnder interferometers, MZ-A and MZ-B. In operation as an add-drop filter, the multichannel input enters through port 1 and leaves through the cross port 5. The dropped channel exits port 6 and the added channel is inserted through port 4. The arms of the interferometer are spaced by 30 μm to allow simultaneous grating exposure in both arms.

The device is fabricated in P_2O_5-doped silica-on-silicon with waveguide dimensions of 6x6 μm and a core-cladding index difference, Δ=0.6%. The P-doped material system is unusual with respect to its photosensitivity in that the UV-induced index change is initially quite slow and therefore results in improved index modulation.[5] To enhance the photosensitivity of the P-doped waveguides at longer wavelengths, they were loaded with 2.5 mole-% deuterium.[5,6] UV exposure was performed at 210 nm using a frequency-doubled dye laser pumped by an excimer laser. To the best of our knowledge, this is the first demonstration of photosensitivity of P-doped silica at 210 nm. Waveguide gratings were formed by exposing the waveguides through a fused silica phase mask having surface relief gratings positioned over the two interferometer arm regions. The exposure beam was roughly Gaussian with a full-width at half maximum of approximately 6 mm. The gratings were exposed until they reached a 3 dB width of 1.3 nm corresponding to an induced index change of approximately $1.6x10^{-3}$. Following exposure, the sample was annealed at 120 °C for 24 hours to remove any residual deuterium and stabilize the induced index change.

Measurements

The device was characterized by butt-coupling fiber ribbon connectors to the waveguides and examining the outputs of various ports using an Erbium-doped-fiber amplified spontaneous emission source and an optical spectrum analyzer with 0.1 nm resolution. The individual grating reflectivity spectra were measured independently by coupling into port 2 and out of port 3 for MZ-A and into port 4 and out of port 5 for MZ-B. This type of coupling corresponds to adding a channel. These spectra are plotted normalized in Fig. 2. The oscillatory structure on the short wavelength side of the spectra is due to Fabry-Perot effects.[7]

The device transmission and dropped channel spectra were measured by coupling into port 1. The spectra were normalized relative to transmission through a straight waveguide to eliminate coupling losses. As described above, the transmitted spectrum appears in port 5 and the dropped channel spectrum exits port 6. The measured spectra are plotted in Fig. 3. The transmitted spectrum has a 3 dB width of 1.4 nm and a minimum transmission of -25 dB. This transmitted isolation is an improvement of 10 dB over previous planar devices.[3] The feature appearing in the vicinity of 1525 nm is caused by radiation mode coupling.[7] The insertion loss of ~1.5 dB is a combined result of non-ideal 3 dB couplers on the interferometer, path length differences introduced by different gratings in the interferometer arms, and UV-induced loss. The dropped channel spectrum has a 3 dB width of 1 nm which is significantly narrower than the individual Mach-Zehnder grating widths of 1.4 nm in Fig. 2. This narrowing is caused by small differences in shape and position of the two spectra. The insertion loss of ~4 dB is caused by the same

factors as for the transmitted signal and is not due to low reflectivity gratings. The double filtering is clearly demonstrated by the extremely low sidelobe levels of -40 dB within 200 GHz of the peak. As expected, this level is two times lower than the single device sidelobe levels in Fig. 2.

Because of its reduced sidelobe levels and improved dropped channel transmitted isolation, this device represents significant progress in Mach-Zehnder based add-drop filters. Further optimization in coupler design and grating fabrication will result in additional performance enhancements. The planar waveguide geometry provides an inherently stable interferometer that is relatively simple to fabricate using established processing techniques. This work demonstrates that a small wafer area can yield a high quality device and suggests that silica-based planar waveguide devices are a low-cost and viable add-drop technology.

References

1. D. C. Johnson, K. O. Hill, F. Bilodeau, and S. Faucher, *Electron. Lett.* **23**, 668 (1987).
2. F. Bilodeau, D. C. Johnson, S. Theriault, B. Malo, J. Albert, and K. O. Hill, *IEEE Photon. Technol. Lett.* **7**, 388 (1995).
3. R. Kashyap, G. D. Maxwell, and B. J. Ainslie, *IEEE Photon. Technol. Lett.* **5**, 192 (1993).
4. C. H. Henry, R. F. Kazarinov, Y. Shani, R. C. Kistler, V. Pol, and K. J. Orlowsky, *J. Lightwave Technol.* **8**, 748 (1990).
5. T. A. Strasser, A. E. White, M. F. Yan, P. J. Lemaire, and T. Erdogan, in *Conference on Optical Fiber Communication*, 1995 Technical Digest Series, Vol. 8 (Optical Society of America, Washington, D.C., 1995), paper WN2.
6. B. Malo, J. Albert, F. Bilodeau, T. Kitagawa, D. C. Johnson, K. O. Hill, K. Hattori, Y. Hibino, and S. Gujrathi, *Appl. Phys. Lett.* **65**, 394 (1994).
7. V. Mizrahi and J. E. Sipe, *J. Lightwave Technol.* **11**, 1513 (1993).

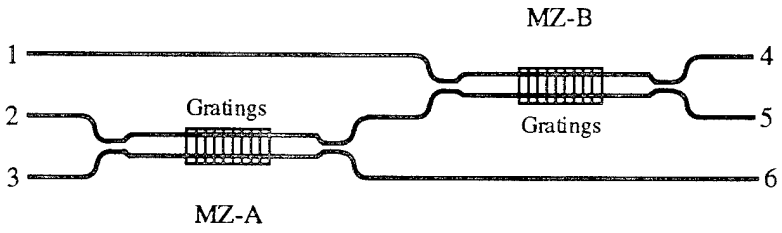


Figure 1. Schematic illustration of a double filtered add-drop device using Mach-Zehnder interferometers with UV-induced Bragg gratings.

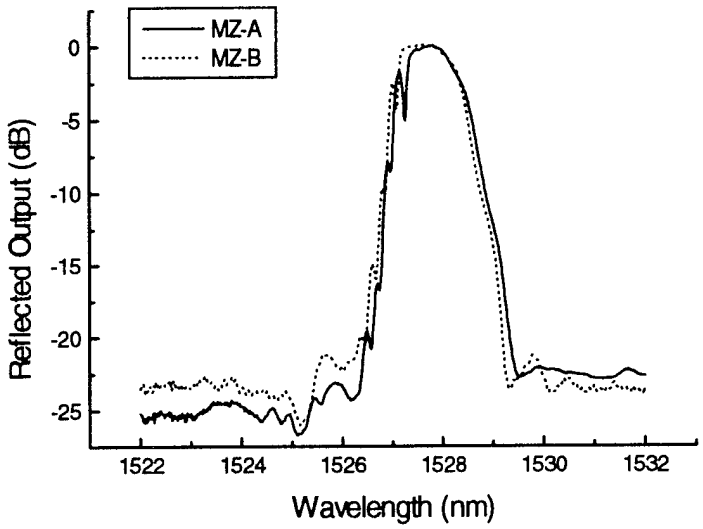


Figure 2. Added channel spectrum for MZ-A and MZ-B showing single Mach-Zehnder performance of less than -20 dB sidelobe levels.

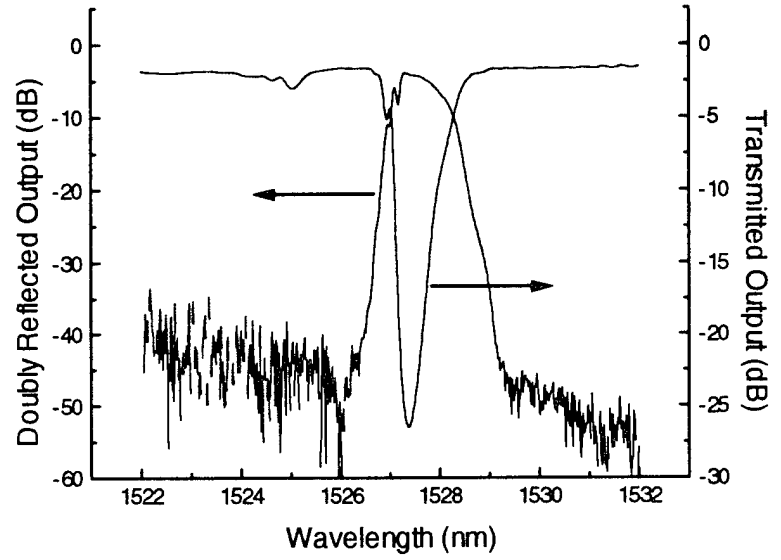


Figure 3. Spectral output of dropped channel (port 6) and transmitted channels (port 5) for input at port 1. A transmitted isolation of -25 dB and sidelobe level of -40 dB are achieved for a 1 nm dropped channel 3 dB width.

Monday, April 29, 1996

Wide-Angle and Vector Propagation Algorithms

IMF 3:30 pm-5:00 pm
Fairfax A

Anand Gopinath, *Presider*
University of Minnesota

The limitations of wide-angle BPM in non-uniform systems

Charles Vassallo
France Telecom/CNET, 2 av. Pierre Marzin, 22307 Lannion, France

This paper proposes a reformulation for the BPM which allows to partly remedy the deficiencies of the classical theory and to understand its basic limitations for wide angle propagation. Only scalar fields in lossless systems are considered.

Deficiencies of classical BPM

Instead of solving the full Helmholtz equation $(\partial_z^2 + \mathbf{H}^2)\Phi(x,z) = 0$, with $\mathbf{H}^2 = \partial_x^2 + k^2 n^2(x,z)$, the classical wide-angle BPM attempts at solving $\partial_z \Phi = -i\mathbf{H}\Phi$. In the case of non-uniform systems, $\mathbf{H}$ depends on z and it is obvious that BPM fields are not exact solutions of the full Helmholtz equation. A related effect is far more annoying: since $\mathbf{H}$ is generally replaced with an Hermitian approximation, the squared L^2 norm $<|\Phi|^2>$ is automatically constant, which is not compatible with the conservation of the carried power, namely $\Re e <i\Phi^* \partial_z \Phi>$. For instance, in the case of adiabatic propagation of a mode in a bent waveguide, $<|\Phi|^2>$ should vary as $1/\cos\theta$ where θ is the tilting angle of the local guide axis.

Converging properties of classical BPM are puzzling. Decreasing the sampling step δx or the integration step δz does not systematically improve the computation, and different behaviours are observed which mainly depend on the guidance. In strong guidance, the accuracy is not improved when the non-paraxiality order is increased in the computation.

Reformulation

The first stage consists in splitting the field into two parts Φ_a and Φ_b, such that

$$\Phi = \Phi_a + \Phi_b \tag{1}$$

$$\partial_z \Phi = -i\mathbf{H}\cdot(\Phi_a - \Phi_b)\,. \tag{2}$$

Φ_a and Φ_b can be identified with exact forward and backward propagating waves only in the case of z-uniform systems. Then the Helmholtz equation can be replaced with two coupled equations for Φ_a and Φ_b:

$$\partial_z \Phi_a = -i\mathbf{H}\cdot\Phi_a - \frac{1}{2}\mathbf{H}^{-1}\cdot\partial_z\mathbf{H}\cdot(\Phi_a - \Phi_b) \tag{3}$$

$$\partial_z \Phi_b = +i\mathbf{H}\cdot\Phi_a + \frac{1}{2}\mathbf{H}^{-1}\cdot\partial_z\mathbf{H}\cdot(\Phi_a - \Phi_b)\,. \tag{4}$$

If Φ_b is neglected at this stage, we exactly recover the classical BPM formalism, including the L^2 norm paradox. This can be circumvented by introducing new unknown fields

$$\Psi_a = \mathbf{H}^{1/2} \cdot \Phi_a \tag{5}$$

and similarly $\Psi_b = \mathbf{H}^{1/2} \cdot \Phi_b$. The interest of these new fields is that, whenever $\mathbf{H}$ can be considered Hermitian, the carried power takes the form

$$P = <|\Psi_a|^2> - <|\Psi_b|^2> \ . \tag{6}$$

The propagation equation then becomes

$$\partial_z \Psi_a = -i\mathbf{H} \cdot \Psi_a + \mathbf{p} \cdot \Psi_a + \mathbf{q} \cdot \Psi_b \tag{7}$$

$$\partial_z \Psi_b = +i\mathbf{H} \cdot \Psi_a + \mathbf{p} \cdot \Psi_b + \mathbf{q} \cdot \Psi_a \ , \tag{8}$$

where $\mathbf{p}$ and $\mathbf{q}$ are corrective operators. If we neglect the "backward" part Ψ_b together with the corrective operator $\mathbf{p}$, again we recover the BPM equation for the new field Ψ_a, but the conservation of L^2 norm is now in complete agreement with the power conservation.

This means that classical BPM can be run provided that the physical input field Φ is replaced by the corresponding Ψ through the action of $\mathbf{H}^{1/2}$, and, conversely, that the output field Ψ is converted into a physical Φ. Evaluating $\mathbf{H}^{1/2}$ for wide angle operation is not easy, but this can be skipped whenever input and output fields are normal modes of waveguides parallel to z-axis (Φ and Ψ then are proportional).

BPM validity

As a by-product of this approach, we can check the basic assumption of BPM, namely that "backward propagating" fields must be negligible. Indeed Eqs.(1–2) can be exactly solved in problems where the field Φ is known analytically; for instance one gets $2\Phi_b = \Phi - i\mathbf{H}^{-1} \cdot \partial_z \Phi$. We applied this process to the case of a tilted slab waveguide and we obtained the following results for the ratio $(<|\Phi_b|^2> / <|\Phi_a|^2>)^{1/2}$:

Tilt angle	10°	20°	30°	40°
Δ=0.01	0.000	0.001	0.001	0.003
Δ=0.10	0.005	0.007	0.038	0.055

This table gives the order of the best error that we can expect with BPM. Of course, we get these numbers with an exact form for $\mathbf{H}$, i.e. derived from an expansion in terms of exact local normal modes:

$$\mathbf{H} \cdot \Phi = \sum_j \beta_j <\Phi \phi_j> \phi_j(x) \ , \tag{9}$$

where the ϕ_j are the eigenvectors of $\partial_x^2 + k^2 n^2$ at z. The derivation of local normal modes also allows us to evaluate the importance of local evanescent modes in the field, through the computation of the projection $\Phi_{a,ev}$ of Φ_a over the set of local evanescent modes, and the tabulation of $\rho = (<|\Phi_{a,ev}|^2> / <|\Phi_a|^2>)^{1/2}$. We got the following values:

Tilt angle	10°	20°	30°	40°
Δ=0.01	0.000	0.001	0.001	0.003
Δ=0.10	0.003	0.004	0.037	0.051

A significant occurrence of local evanescent modes means a lot of troubles in BPM. The propagation matrix $\mathbf{H}$ can no longer be considered Hermitian, so that $<|\Psi_a|^2>$ is no longer the carried power; also such an occurrence implies a noticeable excitation of local modes near cutoff, that most practical wide-angle approximations of $\mathbf{H}$ are unable to deal with. Lastly, a part of the carried power by the complete Φ must correspond to these local evanescent modes, which requires the occurrence of backward propagating evanescent modes —hence a significant Φ_b, opposite to the basic assumption for BPM. So, the two tables are strongly correlated and they lead to the same conclusions: highly accurate calculations should be possible in weakly guiding systems, even for large tilt angles ($\sim 40°$), but not in strongly guiding systems.

Empirical confirmation

The last part of the work is an empirical investigation through various computations on tilted slab waveguides and comparisons with exact analytical fields. Several forms were used for $\mathbf{H}$ and $\mathbf{H}^{1/2}$, either exact modal forms or various Padé approximations, with orders up to 10 in non-paraxiality and up to 4 in δz [1,2]. The main conclusions can be summarized as follows:

- In weak guidance ($\Delta \lesssim 0.01$), the convergence irregularities are smoothed out by the new theory and very accurate results (error $< 1\%$ for fields) can be obtained by using small enough δx and δz, even for a tilt angle of 45°, provided that one uses a sufficiently non-paraxial approximation of $\mathbf{H}$; also, δz^4-accurate propagators are very efficient and allow to use larger δz.
- In strong guidance ($\Delta \sim 0.1$), the accuracy is basically limited. The new theory brings a slight improvement only for low tilt angles ($\theta < 20$–$30°$). Also it restores the logic that approximate $\mathbf{H}$ with higher order in non-paraxiality lead to better results, though with little effect beyond the 2nd-order. On the other hand, since one cannot expect a high accuracy, one can use relatively large δx and δz.

Another important point was to check whether the corrective term $\mathbf{p}$ in Eqs.(7–8) is really negligible. We found that either it has no effect (weak guidance) or it has little importance in front of other basic limitations (strong guidance).

References

[1] G.R. Hadley, *"Multistep method for wide-angle beam propagation"*, Opt. Lett. 17 (1992) 1743–1745

[2] D. Yevick and B. Hermansson, *"Convergence properties of wide-angle techniques"*, IEEE Photonics Technol. Lett. 6 (1994) 1457–1459

3D Vectorial Wide Angle BPM Utilizing a Multi-Grid Equation Solver

P. Lüsse and H.-G. Unger

TU Braunschweig, Institut für Hochfrequenztechnik
Postfach 3329, 38023 Braunschweig, Germany
Phone: +49 531 391 2493, FAX: +49 531 391 5841

Abstract

In this article, a 3D vectorial wide angle BPM is presented. By using an unconditionally stable Crank-Nicholson discretisation scheme in z-direction, a large, sparse linear equation system has to be solved for each propagation step . This can efficently be done by using a multi-grid equation solver. The application of the method is also shown.

Introduction

Integrated optical waveguide devices are key components for applications ranging from high bandwidth communication systems to optical sensing. The design of waveguide components such as directional couplers, wavelength selective couplers, or different types of phase and absorption modulators requires reliable numerical methods. Besides the modal analysis of waveguides [1], the computation of the propagating field is a powerful and popular approach (e. g. [2, 3]).

Theory

In our simulations, the transverse magnetic field is used because of its continuity even at dielectric boundaries. In a homogeneous region, the Helmholtz equations

$$\nabla^2 H_x + n^2 k^2 H_x = 0 \tag{1}$$
$$\nabla^2 H_y + n^2 k^2 H_y = 0 \quad . \tag{2}$$

are valid. In the slowly varying envelope approximation, a plane wave in z-direction $\exp(-jkn_b z)$ is split off from the equations (1) and (2):

$$\frac{\partial^2 \Psi_x}{\partial z^2} - 2jkn_b \frac{\partial \Psi_x}{\partial z} + \left(\frac{\partial^2}{\partial x^2} + \frac{\partial^2}{\partial y^2} + (n^2 - n_b^2)k^2 \right) \Psi_x = 0 \tag{3}$$

$$\frac{\partial^2 \Psi_y}{\partial z^2} - 2jkn_b \frac{\partial \Psi_y}{\partial z} + \left(\frac{\partial^2}{\partial x^2} + \frac{\partial^2}{\partial y^2} + (n^2 - n_b^2)k^2 \right) \Psi_y = 0 \quad . \tag{4}$$

Equations (3) and (4) can be combined to the operator equation

$$\frac{\partial}{\partial z} \left(1 + \frac{j}{2kn_b} \frac{\partial}{\partial z} \right) \Psi = -\frac{j}{kn_b} \mathbf{A} \Psi \quad . \tag{5}$$

Ψ_x and Ψ_y are coupled by the operator $\mathbf{A}$ at dielectric boundaries. Details for the transverse discretisation can be found in [1]. Transparent boundary condition are used in all simulations [4].

By applying a standard Crank-Nicholson discretisation scheme in z-direction and using a Padé-(1,1)-recursion [5] to account for the second derivative, the following equation system is obtained for the n-th propagation step:

$$\left(1+\left(\frac{1}{(2kn_b)^2}+\frac{j\alpha\Delta z}{2kn_b}\right)\mathbf{A}\right)\Psi_{\mathbf{n+1}}=\left(1+\left(\frac{1}{(2kn_b)^2}-\frac{j(1-\alpha)\Delta z}{2kn_b}\right)\mathbf{A}\right)\Psi_{\mathbf{n}} \qquad (6)$$

By summing up the left and right sides in (6), the linear equation system

$$\mathbf{L}u=f \qquad (7)$$

is obtained. For each popagation step, eq. (7) has to be solved. Since the sparse coefficient matrix $\mathbf{L}$ is unsymmetrical, standard equation solvers like Jacobi, Gauss-Seidel, SOR, or a CG-method are not applicable, because they demand a positiv definite coefficient matrix. Equation solvers like BiCG-Stab or GMRES converge too slowly for matrices of a rank larger than, about 5000. Therefore a powerful multi-grid method has to be utilized to solve equation (7). With this algorithm, costs depend only linearly ($O(n)$) on the number of unknows [6].
In Fig. 1 a multi-grid iteration is sketched. A semi-iterative approach [6, page 243] is used as smoothing iteration. Special attention has to be paid to the prolongation and restriction. For convergence, the order of the interpolating scheme has to be larger than two times the order of the differential operator [6, page 149]. On the nonuniform grid, we use bicubic Newton interpolation polynoms [7] for the prolongation. The restriction is formulated as the adjoint operation of the prolongation. The equation system on the coarsest grid is solved by BiCG method. For solving equation (7), typically 20 to 40 vector matrix multiplications are needed on the finest grid, mainly depending on the largest refractive index step.

Results

As a first example, transparent boundary conditions are tested. Homogeneous material is excited with a Gaussian intensity distribution with a phase tilt of 12.5 degrees to the propagation direction (see Fig. 2). After 35 μm, the field leaves the computational window, which is shown in Fig. 3. No reflections can be seen in the resolution of the picture. In this example, only 20 vector matrix multiplications are needed on the finest grid for solving the equation system (7) with a defect lower 10^{-12}.
In the second example, a 3dB coupler is considered. The structure is sketched in Fig. 4. For the input waveguide, the fundamental HE-mode is calculated [1]. The absolute value is given in Fig. 5, which represents the excitation of the three coupled waveguides. After 620 μm, the power is nearly split equally between both output ports. The structure is sampled with 93 points in x-direction and 83 points in y-direction on a nonuniform grid. Here, 40 vector matrix multiplications are needed on the finest grid to perform one propagation step.

Conclusion

In this article, an efficient 3D vectorial wide angle BPM is presented. By applying a Crank-Nicholson discretization scheme in z-direction, an unconditionally stable formulation is used. For each propagation step, a large sparse equation system has to be solved. This is done by a multi-grid equation solver. For this algorithm, the cost depends only linearly on the number of unknowns. Application of the method is shown.

REFERENCES

[1] P. Lüsse, P. Stuwe, J. Schüle, and H.-G. Unger: "Analysis of vectorial mode fields in optical waveguides by a new finite difference method", *J. Lightwave Technol.*, vol. 12, pp. 487-494, 1994

[2] W. P. Huang, C. L. Xu, S. T. Chu, and S. K. Chaudhuri: "The finite-dif"|ference vector beam propagation method: analysis and assessment", *IEEE J. Lightwave Technol.*, vol. 10, pp. 295-305, 1992.

[3] D. Yevick: "Forward wide-angle light propagation in semiconductor rib waveguides", *Opt. Lett.*, vol. 15, pp. 174-176, 1990.

[4] G. R. Hadley: "Transparent boundary condition for the beam propagation method", *IEEE J. Quantum Electron.*, vol. 28, pp. 363-370, 1992.

[5] G. R. Hadley: "Wide-angle beam propagation using Padé approximant operators", *Opt. Lett.*, vol. 17, pp. 1426-1428, 1992.

[6] W. Hackbusch: *Multi-grid methods and applications*, Springer, Berlin, 1985

[7] H. R. Schwarz: *Numerical analysis: a comprehensive introduction*, Wiley, Chichester, 1989

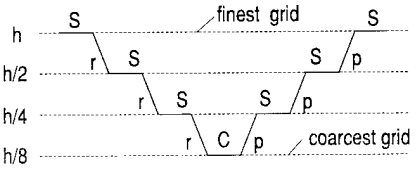


Fig. 1: Multi-grid iteration step with S: smoothing iteration, r: restriction, p: prolongation, C: conventional equation solver

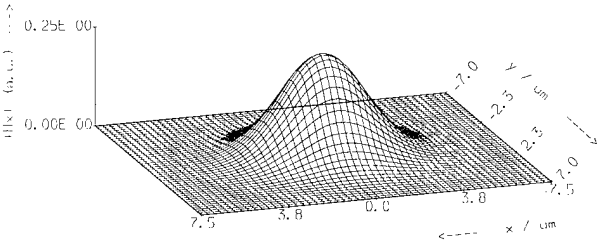


Fig. 2: Absolute value of H_x at $z = 0$ μm

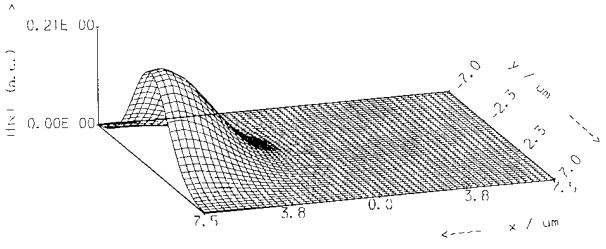


Fig. 3: Absolute value of H_x at $z = 35$ μm

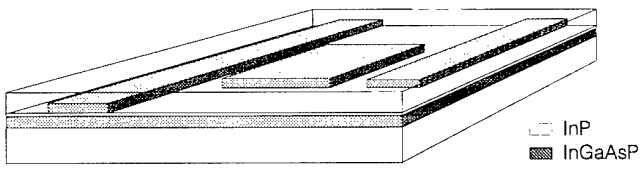


Fig. 4: 3dB coupler

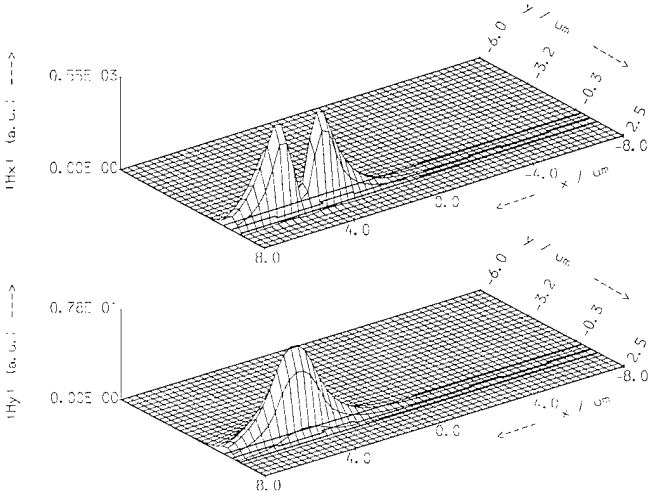


Fig. 5: Transverse magnetic field at $z = 0$ μm. Only part of the computational window is shown

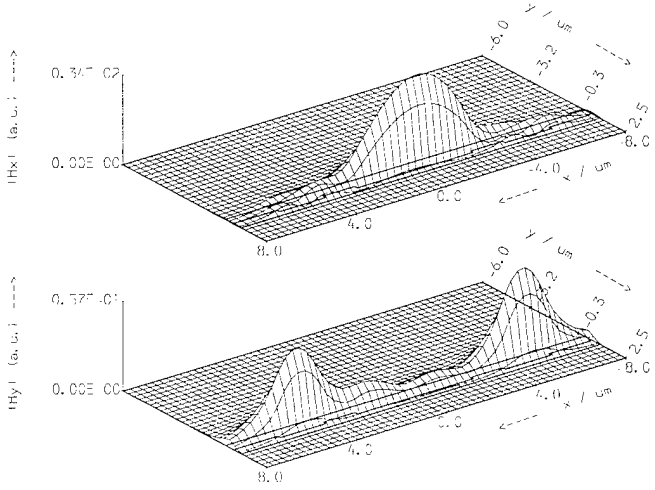


Fig. 6: Transverse magnetic field at $z = 620$ μm

Technique of improving the multistep method for wide-angle beam propagation

Junji Yamauchi, Minoru Sekiguchi, Jun Shibayama
and Hisamatsu Nakano

College of Engineering, Hosei University, 3-7-2, Kajino-cho, Koganei, Tokyo 184, Japan
Tel: 423-87-6190, Fax: 423-87-6048

1 Introduction

The beam-propagation method (BPM) has successfully been used to analyze various optical waveguides. Since the conventional paraxial approximation restricts the application, several techniques have been proposed to treat wide-angle beam propagation [1]-[7]. Of them a so-called multistep method [4] in which the Padé approximant operator is factored into a series of simpler Padé (1,1) operators has an advantage that it allows paraxiallike solution techniques, such as the Thomas algorithm. The previous formulation is, however, based on the Crank-Nicholson (CN) scheme with a truncation error of $O(\Delta x)^2$ in the transverse direction.

Recently we developed an improved BPM based on the generalized Douglas (GD) scheme for variable coefficients [8], and studied the possibility of applying GD scheme to a wide-angle beam propagation analysis [9]. The GD scheme ensures a truncation error of $O(\Delta x)^4$ with substantial improvement in accuracy.

The purpose of this paper is to apply the GD scheme to the multistep method for wide-angle beam propagation, and to demonstrate the effectiveness of the present method. The propagation of TE_1 mode in a tilted step-index waveguide [10] is analyzed to assess the numerical accuracy.

2 Formulation

The method begins with the scalar propagation equation obtained using a Padé (n,n) approximation of the Helmholtz operator. Then, an Nth-order Padé propagator may be decomposed into an N-step algorithm for which the kth partial step takes the form [4]

$$E^{m+k/N} = \frac{1 + a_k P}{1 + a_k^* P} E^{m+(k-1)/N} \tag{1}$$

in which $P = \partial^2/\partial x^2 + \nu$, where $\nu = k_0^2[n^2(x,z) - n_0^2]$. k_0 is the free space wavenumber, $n(x,z)$ is the index profile, and n_0 is the reference refractive index. The superscript m indicates position along the z axis. The a's can be determined by the one-time solution of an Nth-order complex algebraic equation.

Eq.(1) can be restored to the following differential equation

$$\frac{\partial E}{\partial z} = \frac{2jIm\{a_k\}P}{(1 + Re\{a_k\}P)\Delta z/N} E \quad . \tag{2}$$

We apply the GD scheme to Eq.(2). Following the procedure described in Ref.[9], we finally obtain

$$\begin{aligned} & C_{i+1}^{m+k/N} E_{i+1}^{m+k/N} + C_i^{m+k/N} E_i^{m+k/N} + C_{i-1}^{m+k/N} E_{i-1}^{m+k/N} \\ =& C_{i+1}^{m+(k-1)/N} E_{i+1}^{m+(k-1)/N} + C_i^{m+(k-1)/N} E_i^{m+(k-1)/N} + C_{i-1}^{m+(k-1)/N} E_{i-1}^{m+(k-1)/N} \end{aligned} \tag{3}$$

where

$$C_{i\pm1}^{m+(k-1)/N} = \frac{1}{12} + \Gamma_k \left(\frac{1}{\Delta x^2} + \frac{1}{12} \nu_{i\pm1} \right), \qquad C_i^{m+(k-1)/N} = \frac{5}{6} - \Gamma_k \left(\frac{2}{\Delta x^2} - \frac{5}{6} \nu_i \right),$$

in which

$$\Gamma_k = \begin{array}{ll} a_k & for \quad m + (k-1)/N \\ a_k^* & for \quad m + k/N \end{array} .$$

Eq.(3) can be solved by efficient techniques such as the Thomas algorithm, so that the computational time is almost identical to that in the conventional method based on the CN scheme. A transparent boundary condition [11] can easily be incorporated.

3 Numerical results

We consider a tilted step-index waveguide shown in Fig.1. The core width is designated as $2D$, and the refractive indices of the core and cladding are chosen to be $N_{CO} = 1.002$ and $N_{CL} = 1.000$, respectively. A wavelength of $\lambda = 1\ \mu m$ is used. The reference refractive index is chosen to be that in the cladding. To assess the accuracy, we calculate the coupling efficiency at a propagation distance of 100 μm. In the case of no calculation error, the guided-mode field continues to propagate without any distortion, so that the efficiency becomes unity. The numerical parameters to be used are as follows. The propagation step length is $\Delta z = 0.1\ \mu m$, the transverse sampling width is $\Delta x = D/(84 \cos\theta) = D'/84$, and the number of transverse sampling points is 1800.

Fig.2 shows the coupling efficiency for TE_1 mode as a function of tilt angle θ. The core width is taken to be $2D = 15.092\ \mu m$, so that the normalized frequency is $V = 3.0$. Figs.2(a) and (b) are the cases for the GD and CN schemes, respectively. It is clearly seen that the increase in the number of steps leads to the improvement in accuracy. It is worth mentioning that the GD scheme achieves higher accuracy than the CN scheme in spite of the same discretization mesh.

To clarify the reason why the GD scheme improves the coupling efficiency, we illustrate the propagating field obtained using the three-step method in Fig.3. The tilt angle is taken to be $\theta = 40°$. The field obtained by the GD scheme propagates with the mode profile being maintained, while that by the CN scheme not only deforms but also shifts toward the $-x$ direction.

As a further test on the accuracy, we calculate the phase error accumulated as the field propagates. The phase is evaluated using the maximum field at a propagation distance of 100 μm. The results as a function of the number of steps are shown in Fig.4. The tilt angle is 40 degrees. In this Figure, 0-step corresponds to the paraxial approximation. We can again find that the accuracy improves as the number of steps is increased, and

the GD scheme achieves higher accuracy than the CN scheme. For example, the error is evaluated to be -0.7% for the three-step method with the GD scheme, while that with the CN scheme is at best -6.9%.

It is known that a wide-angle scheme has an advantage that the numerical results are not sensitive to the choice of the reference refractive index n_0. To confirm this fact, we also evaluate the reference-index dependence of the coupling efficiency and the phase error using the GD scheme. Calculations are made for $\theta = 40°$ at a propagation distance of 100 μm. Figs.5 and 6 clearly show that the present results are almost independent of n_0, while the scheme on the basis of the paraxial approximation yields relatively good results only when n_0 is chosen to be $\beta \cos\theta / k_0$, where β is the propagation constant of the eigenmode of the waveguide. In other words, a wide-angle scheme has an advantage that the problem involving radiation modes can be treated more accurately than that based on the paraxial approximation.

4 Conclusion

The generalized Douglas scheme for variable coefficients has been applied to a multistep method for wide-angle beam propagation. The coupling efficiency and the phase error in a tilted step-index waveguide are evaluated to assess the numerical accuracy. The present method offers further improvement in the analysis of wide-angle beam propagation compared with the conventional approach, while maintaining almost the same computational efficiency.

References

[1] D. Yevick and M. Glasner, Opt. Lett., 15, pp.174-176, 1990.
[2] G.R. Hadley, Opt. Lett., 17, pp.1426-1428, 1992.
[3] H.J.W.M. Hoekstra et al., Opt. Commun., 97, pp.301-303, 1993.
[4] G.R. Hadley, Opt. Lett., 17, pp.1743-1745, 1992.
[5] W.P. Huang and C.L. Xu, Photon. Tech. Lett., 4, pp.1118-1120, 1992.
[6] Y. Chung and N. Dagli, Photon. Tech. Lett., 6, pp.540-542, 1994.
[7] D. Yevick and B. Hermansson, Photon. Tech. Lett., 6, pp.1457-1459, 1994.
[8] J. Yamauchi et al., Photon. Tech. Lett., 7, pp.661-663, 1995.
[9] J. Yamauchi et al., Opt. Lett., 20, pp.7-9, 1995.
[10] H.P. Nolting and R. März, J. Lightwave Tech., 13, pp.216-224, 1995.
[11] G.R. Hadley, Opt. Lett., 16, pp.624-626, 1991.

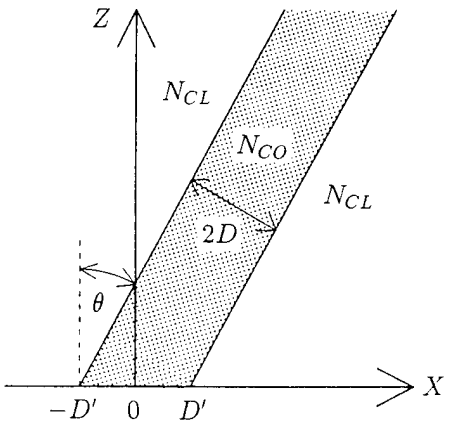


Fig.1 Configuration of a tilted step-index slab waveguide.

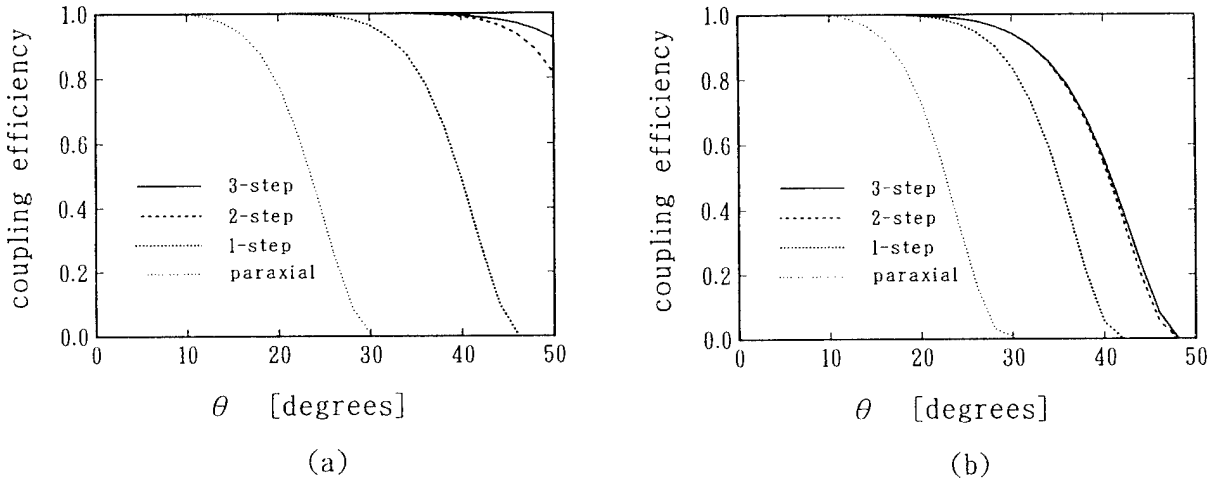


Fig.2 Coupling efficiency for TE_1 mode as a function of tilt angle θ: (a) generalized Douglas scheme and (b) Crank-Nicholson scheme.

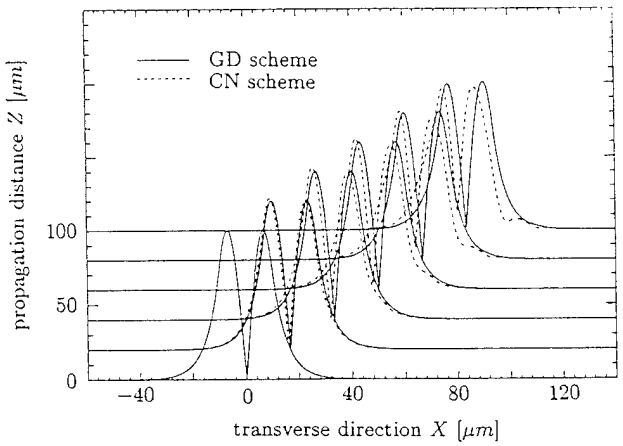


Fig.3 Propagating field distributions for TE_1 mode.

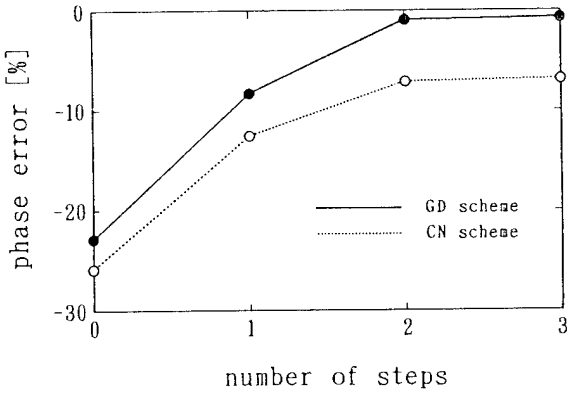


Fig.4 Phase error for TE_1 mode observed at a propagation distance of 100 μm.

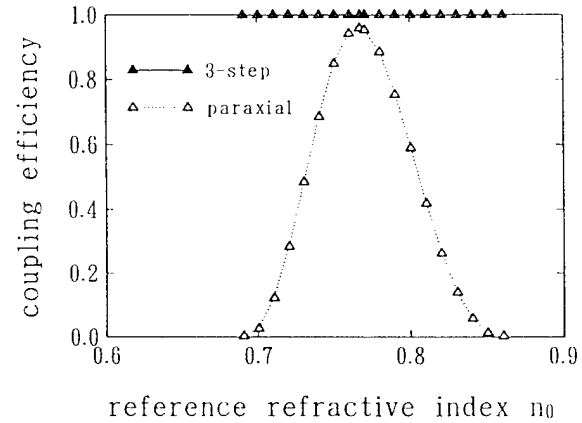


Fig.5 Coupling efficiency as a function of reference refractive index.

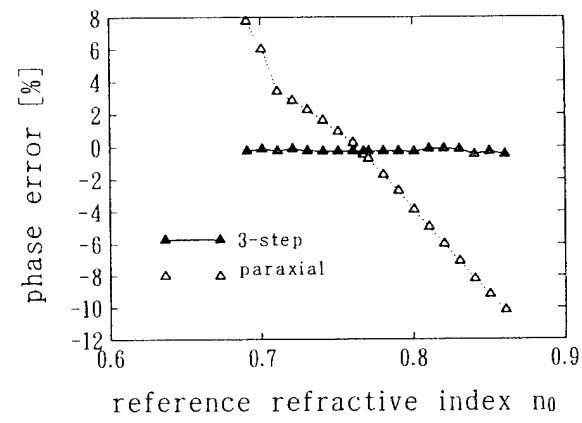


Fig.6 Phase error as a function of reference refractive index.

Oblique Wide Angled Beam Propagation

T Anada, T M Benson, P Sewell: Department of Electrical and Electronic Engineering, University of Nottingham, Nottingham NG7 2RD, UK

P C Kendall: Department of Electronic and Electrical Engineering, University of Sheffield, PO Box 600, Sheffield S1 4DU,UK

Introduction

The applications and systems specifications for photonic integrated circuits (PIC's) continue to grow. This places an increasing demand on the complexity and compactness of such circuits and necessitates the accurate analysis of curved, intersecting, branching and coupled guided wave structures and waveguide directional changes incorporating mirrors. To enable study of such configurations 'wide angle' beam propagation methods (BPM) have been introduced [1-6] but these become less accurate as the angle the waveguide makes to the propagation direction specified in the simulation increases. In this paper we introduce an oblique coordinate transformation which extends the range of structures which can be accurately modelled within BPM and show that the transformation provides the following important advantages when applying BPM in the design of general photonic integrated circuits incorporating angled waveguide sections:

- An extra degree of freedom within configuration and method.
- Treatment of tilted waveguides with any tilt angle without staircase approximation.
- Matching of the propagation direction of each waveguide section to the propagation direction of the model. This is in contrast to all standard BPM algorithms where the resulting phase shift $\beta \sin\theta \Delta x$ can vary rapidly in the transverse direction, leading to significant errors unless a fine discretisation is used. Consequently the present method achieves equivalent accuracy for a much coarser mesh size giving considerable run-time and memory advantages.
- A coordinate system which moves with the waveguide. This aids the implementation of transparent boundary conditions [7] and inherently allows the waveguide to be maintained in the centre of the problem workspace.
- The basic concept readily extends to other non-orthogonal systems and other propagation algorithms, including three dimensions, and is not restricted by contrast in permittivity.

Application of Non-Standard Coordinates to Wide Angle Beam Propagation.

We illustrate the method using a two dimensional, scalar wide-angle FD propagation algorithm [1-5]. Consider propagation in a z′ direction at angle θ to the z axis (inset Fig 1(a)). Use a rotated coordinate system $z' = x\sin\theta + z\cos\theta$, $x' = -z\sin\theta + x\cos\theta$. Then introduce an oblique coordinate system (u,y,w), where $u = x'\sec\theta = x - z\tan\theta$ and $w = z$, and a solution of the form $E = F_o(x',z')\exp(-j\,k_b\,z') = F(u,w)\exp[-j\,k_b(w\sec\theta + u\sin\theta)]$ to the scalar wave equation where $k_b = k_o\,n$ with k_o the free space wave vector and n is a reference refractive index. We obtain after some manipulation:

$$2jk_b\cos\theta\frac{\partial F}{\partial w} - \frac{\partial^2 F}{\partial w^2} = \sec^2\theta\,\frac{\partial^2 F}{\partial u^2} - 2\tan\theta\frac{\partial^2 F}{\partial u\partial w} + (k^2 - k_b^2)F \qquad (1)$$

Approximating for $\partial^2F/\partial w^2$ following the approach and notation of [4] we find:

$$2jk_b\cos\theta\,(L^2 + (2k_b\cos\theta)^{-2}\,M)\frac{\partial F}{\partial w} = L\,M\,F \qquad (2)$$

where L is the linear operator:

$$LF = F - \frac{j\tan\theta}{k_b\cos\theta}\,\frac{\partial F}{\partial u} \qquad (3)$$

and M is the linear operator:

$$MF = \sec^2\theta\frac{\partial^2 F}{\partial u^2} + (k^2 - k_b^2)F \qquad (4)$$

To obtain a tridiagonal implementation of equation (2) using the Crank Nicolson scheme divide (2) by L then take L^{-1} to be 1 in the small term $(2k_b\cos\theta)^{-2}L^{-1}M$, giving

$$2jk_b\cos\theta\,[L + (2k_b\cos\theta)^{-2}]\frac{\partial F}{\partial w} = MF \qquad (5)$$

Equation (5) reduces to those of [1,4] for θ=0 and its implementation requires minimal additional computational effort. The coordinate system can readily be varied locally when

studying piecewise constant problems.

Applcations

We illustrate the utility of our new method using illustrative applications.

In the first of these the diffraction of a focused Gaussian beam of wavelength 0.633μm and initial spot size 1μm travelling at an angle of 45° in a homogeneous region of refractive index 1.5 is studied. Figure 1(a) shows that the beam profile calculated with the present method after a propagation distance of 30 μm agrees perfectly with the analytical solution obtained by Fourier transformation. The present results were obtained using a relatively course mesh size (0.025 μm in the u direction and 0.05μm in the w direction)and only 500 FD points in the u direction. Figure 1(b) shows that results from a standard wide-angled BPM algorithm and classical FDBPM agree substantially less well with the exact solution than those results from the present method. We find our method provides similar improvements in performance for the treatment of propagation in tilted waveguides.

In the second example we study the practical OEIC example of the transmission coefficient of a symmetric Y-junction. Using non-orthogonal coordinates this is handled without staircase approximation. Figure 2 shows the variation in the proportion of power remaining in the fundamental modes of the output guides after traversing the Y-junction whose half cross-section is shown in the inset to the figure. The solid curve shows results from the present method, the dashed one from a conventional paraxial BPM. We attribute the discrepancy between the two curves to a combination of the staircase and paraxial approximations in the paraxial BPM calculations.

References

1. YEVICK, D and GLASNER M :"Analysis of forward wide-angle light propagation in semiconductor rib waveguides and integrated-optic structures" Electronics Letters, 25, 1989, 1611-1613.

2. HADLEY, G R: "Multistep method for wide angle beam propagation" Optics Letts. 17, 1992, 1743-1745.

3. THYLEN L and LEE C M: "Beam-propagation method based on matrix diagonalization" J. Opt. Soc. Am A, 9, 1992, 142-146

4. VASSALLO C: "Reformulation for the beam propagation method" J. Opt. Soc. Am A, 1993, 2208-2216.

5. CHUNG Y and DAGLI N: "A wide angle propagation technique using an explicit finite difference scheme" IEEE Photonics Tech Letter, 6, 1994, 540- 542.

6. HUANG W, XU C, CHU S-T and CHAUDHURI S K: " The finite-difference vector beam propagation method; Analysis and assessment" J. Lightwave Tech 10, 1992, 295-305, 1992.

7. HADLEY G R:" Transparent boundary condition for the beam propagation method" IEEE IEEE J. Quantum, Electron. 28, 1992, 363-370.

Acknowledgement.

The authors thank EPSRC for the financial support of part of this work under research grant G/J74602

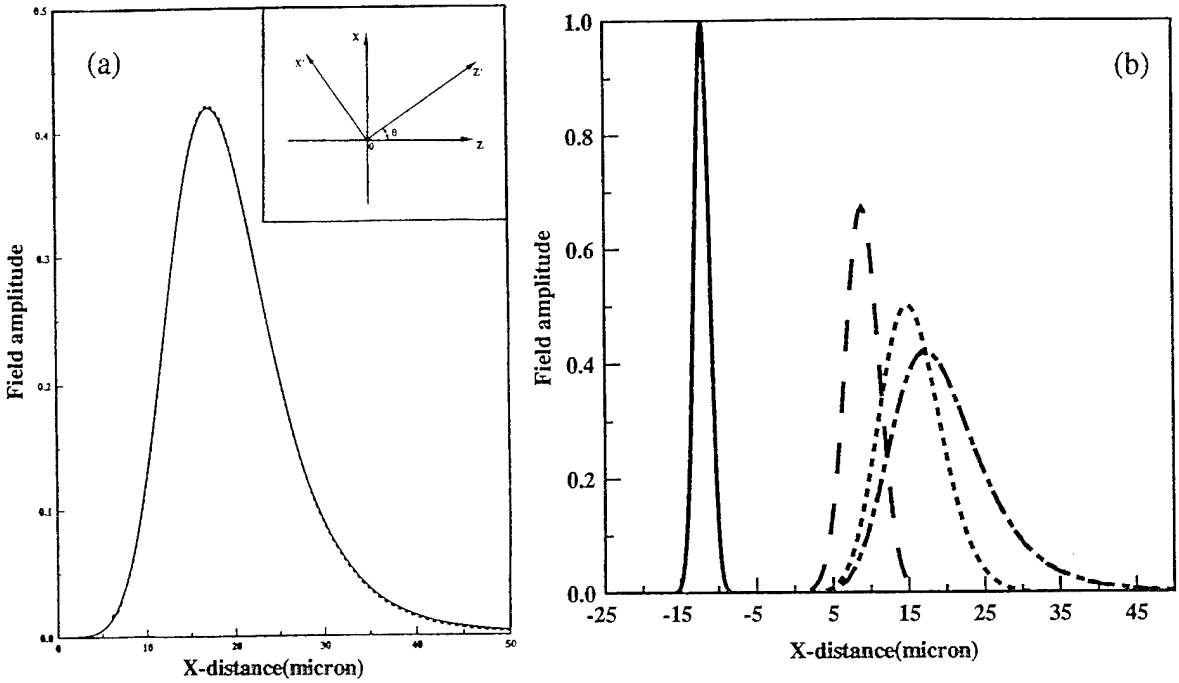


Figure 1(a) Output beam profile of angled Gaussian beam, solid line exact solution dashed line present propagation method. Inset: Definition of coordinate systems. (b) Comparison of input field (solid line) and output field distribution calculated using standard FDBPM (— -), standard wide angled BPM (- - - - -) and present method (— - —)

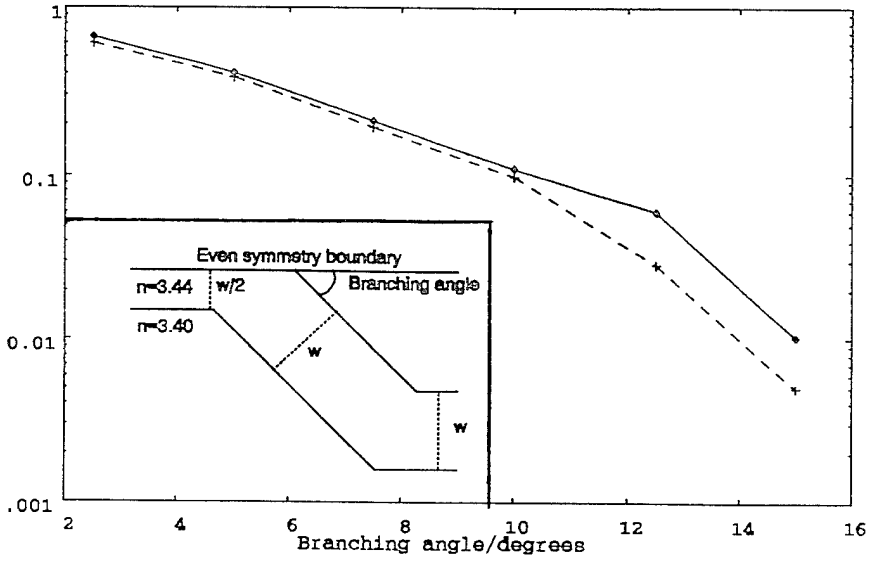


Figure 2. The proportion of the power remaining in the output waveguides after traversing a symmetric Y junction whose half section is shown in the inset. w=1μm λ=1.15 μm

Use of Higher Order Padé Approximants for Efficient Simulation of Wide-Angle Waveguides with Step-Index Profile

Igor Ilić, Robert Scarmozzino, Richard M. Osgood, Jr.
Room 1312 Mudd Building
Columbia University
500 W. 120th St.
New York, New York 10027-6623

1. INTRODUCTION

An important challenge in computer-aided design and simulation of advanced waveguiding circuits is to perform efficient calculations of arbitrarily shaped, wide-angled structures using effective computational numerical schemes. The finite-difference beam propagation method using the paraxial approximation[1] has been applied successfully to treat photonics integrated circuits with shallow angles. Recent extension of this technique based on the Padé approximants[2,3] of the square root operator in the scalar one-way wave equation, specifically the multistep method of implementation by Hadley[4] have made wide-angle propagation possible with a significant improvement in accuracy. To derive the full benefit of this technique requires a thorough understanding of its limitations. We previously[5] derived analytic expressions which measure the accuracy that can be achieved for different Padé orders and showed that the error is composed of a fundamental part and a part dependent on the reference wavenumber. In this paper, we perform an exhaustive study to test these scaling laws. We show that there is an additional error which fundamentally limits the accuracy of the solution and which is not reduced with higher Padé approximants. From these results we have now obtained useful recommendations on the best application of higher order Padé approximants to achieve an acceptable absolute error for wide-angle waveguides with step-index profile.

2. ANALYSIS

The test example for analytical development and numerical experiments was a uniform, slab waveguide tilted at an angle from the propagation direction for the finite difference beam propagation method. This geometry often appears as standard benchmark in the literature [6] since an exact analytical solution is known.

In our previous work we have identified the two main terms for the error in the one-way equation: the first one,

$$T_{ref} = \frac{\bar{k} - \beta\cos\phi}{\bar{k}} \tag{1}$$

which expresses the error that derives from the choice of the reference wavenumber k, and for

the case at hand this error can be eliminated by choosing $\bar{k} = \beta\cos\phi$. The second term,

$$T_{fund} = \frac{\gamma \sin\phi}{\bar{k}} \tag{2}$$

represents a fundamental angular error limit which cannot be eliminated by any particular choice of reference wavenumber or numerical parameters. However, both terms can be significantly reduced by applying higher order Padé approximants. We further present a new error term which appears as a result of the derivatives of the index profile present in the analysis of the higher Padé orders. This term scales approximately with

$$T_d = 2\sqrt{\frac{\Delta n}{n}}\sin\phi \tag{3}$$

and is not reduced by higher Padé orders thus representing the ultimate error limit.

3. SIMULATION RESULTS AND COMPARISON

Figure 1 shows simulation results for case of the reference wavenumber choice as $\beta\cos\phi$ so that only the fundamental error, T_{fund}, and the higher-order derivatives error, T_d, remain. The Padé(1,0) results ideally follow the equation for the normalized angular error:

$$e = 2q\left(\frac{q}{2}\right)^{m+n} \tag{4}$$

However, Padé order (1,1) and higher do not show the same benefit produced by Eq. 4. Instead, they are limited by the new error term, Eq. 3, thus higher order approximants do not improve accuracy.

For the case when $\bar{k} \neq \beta\cos\phi$, the term involving T_{ref} becomes dominant and limits the error until the ultimate limit of Eq. 3 is reached. This is illustrated in Fig. 2 where we plot the error achieved by approximants of different Padé order for the waveguide tilted at 40°. Further examples illustrating the dependence on waveguide parameters, such as $\Delta n/n$, will be presented in the talk.

4. CONCLUSIONS

This paper discusses the fundamental limits of the Padé-based approximation of the wave equation as applied to wide angle propagation in step-index waveguides. For a given angle a portion of the error can be eliminated by a proper choice of the reference wavenumber, however a fundamental error that increases with the angle remains. This fundamental error is composed of an angular part reducible by higher order Padé approximants, and a portion which is not. The

later is due to the additional field derivatives that are introduced by the higher order Padé operators and field discontinuities at the walls of the waveguide and Padé orders higher then (1,1) do not improve the accuracy of the calculation. However, in the more general case where the wavenumber error term cannot be eliminated, higher order Padé approximants, for example P(2,2), P(3,3), and P(4,4), further reduce the absolute error thus justifying the higher cost in CPU time required.

5. ACKNOWLEDGEMENT

The funding for the work performed was provided by the Advanced Research Project Agency (ARPA).

6. REFERENCES:

[1] Robert Scarmozzino and Richard M. Osgood, Jr., "Comparison of finite-difference and Fourier-transform solutions of the parabolic wave equation with emphasis on integrated-optics problems", *J.Opt. Soc. Am.*, vol. A-8, pp. 724-729 (1991)

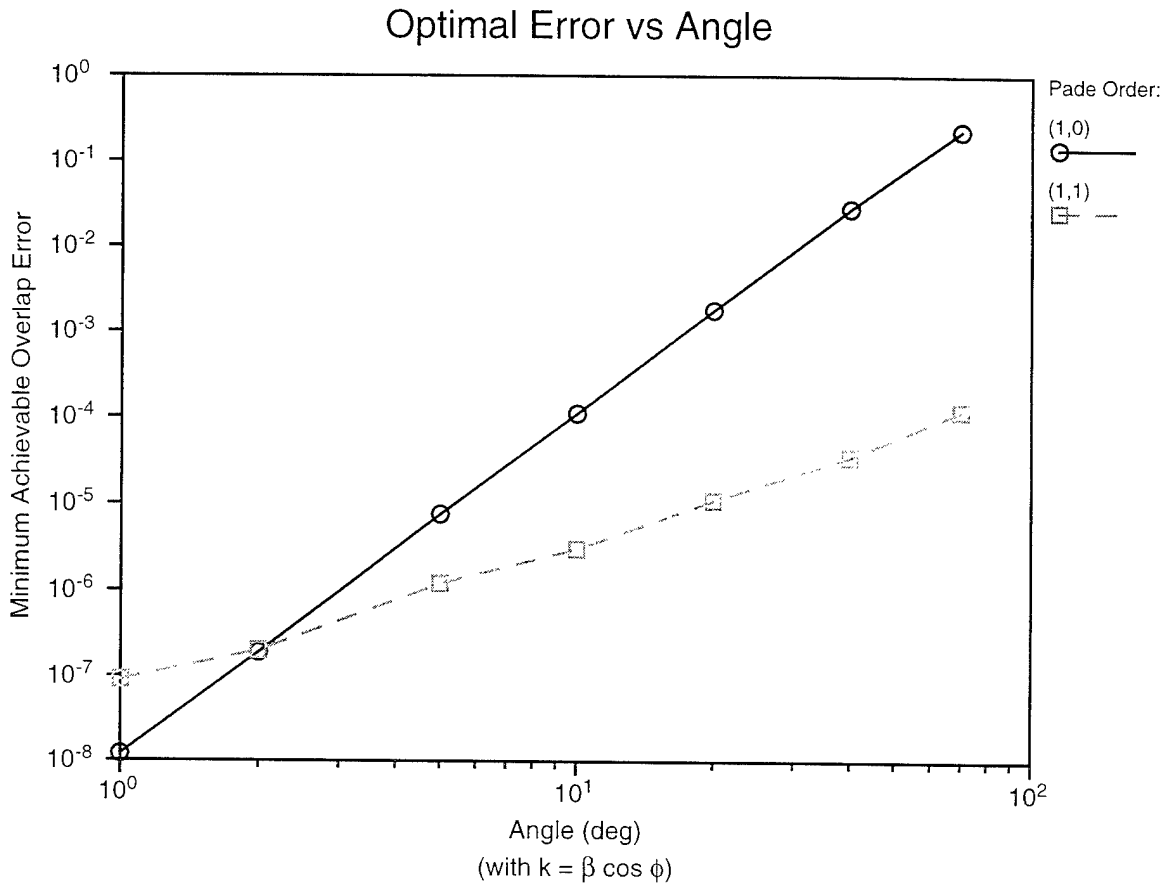
[2] G. Ronald Hadley, "Wide-angle beam propagation using Padé approximant operators", *J. Opt. Soc. Am.*, vol. 17, no. 20, pp. 1426-1428 (1992)

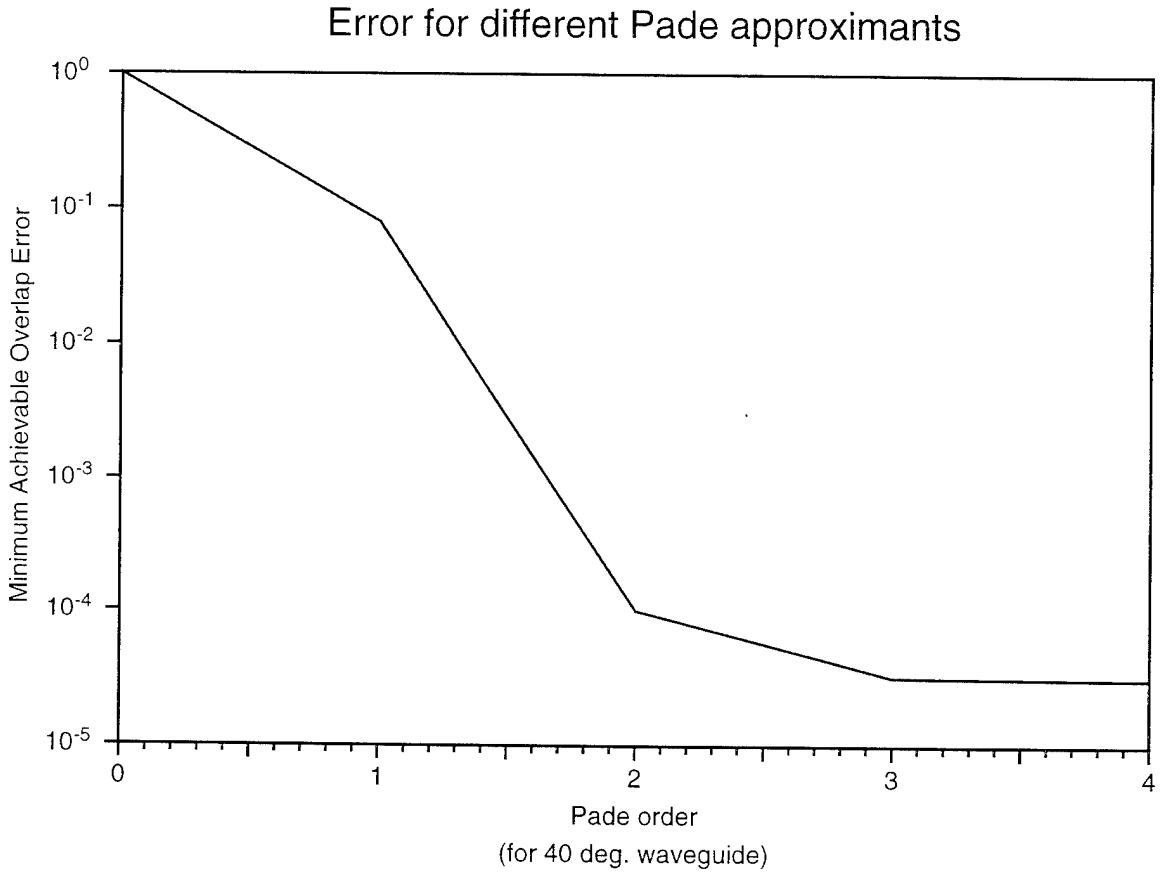
[3] David Yevick, M.Glasner, and B. Hermansson, "Finite difference generalized Padé approximant propagation methods", *Integrated Photonics Research*, vol. 10, pp. 42-45 (1992)

[4] G. Ronald Hadley, "Multistep method for wide-angle beam propagation", *Opt. Lett.*, vol. 17, no. 24, pp. 1743-1745 (1992)

[5] Igor Ilić, Robert Scarmozzino, Richard M. Osgood,Jr., "Wide angle beam propagation modeling of variable-angle photonics circuits", *Integrated Photonics Research*, vol. 13, (1995)

[6] H.P. Nolting et al, *Integrated Photonics Research*, vol. 12, (1994)


Optimal Error vs Angle
Minimum Achievable Overlap Error
10^{0}
10^{-1}
10^{-2}
10^{-3}
10^{-4}
10^{-5}
10^{-6}
10^{-7}
10^{-8}
10^{0}
10^{1}
10^{2}
Angle (deg)
(with k = β cos ϕ)
Pade Order:
(1,0)
(1,1)


Error for different Pade approximants
Minimum Achievable Overlap Error
10^{0}
10^{-1}
10^{-2}
10^{-3}
10^{-4}
10^{-5}
0
1
2
3
4
Pade order
(for 40 deg. waveguide)

Monday, April 29, 1996

Symposium on WDM Lasers

IMG 3:30 pm-5:15 pm
Fairfax B

Julian B. Soole, *Presider*
Bellcore

A 18 Channel Multi Frequency Laser

M. Zirngibl, C.H. Joyner, C.R. Doerr, L.W. Stulz, H.M. Presby
AT&T Bell Laboratories, Holmdel NJ, 07733
Tel. 908 888 7153, FAX 908 888 7074, e.mail mz@big.att.com

Multifrequency lasers (MFL) (1) are attractive sources for wavelength division multiplexed (WDM) systems because they can simultaneously deliver many densely spaced optical wavelength channels (2) each of which can be independently modulated. An important characteristic of MFLs is that the relative channel spacing is defined by the geometry of the intracavity waveguide grating router and, therefore, is very stable and reproducible. In this paper, we present and characterize a MFL that can simultaneously oscillate on 18 channels.

The design of MFLs requires several trade-offs. First, one would like to have the filter bandwidth of the intracavity waveguide grating router (WGR) as narrow as possible. As explained in Reference 3, a narrow filter bandwidth guarantees that the laser locks on a single longitudinal mode, regardless of how many longitudinal modes are contained within that filter bandwidth. On the other hand, the free spectral range (FSR) or periodicity of the WGR should be large so that the selectivity of the amplifier gain profile is sufficient to choose lasing in only one passband of the WGR. In our design, the FSR is uniformly filled with channels for a wavelength at 1560 nm (channel "wrap-around"). The resolution of the WGR filter for our design is given approximately by FSR/3N, where N is the number of channels. Based on our experimental data, we find that the FSR should be larger than 1850 GHz (15 nm) and the filter bandwidth narrower than 50 GHz (0.4 nm) (3) to satisfy both, single longitudinal stability and single passband lasing. In view of this trade-off, we decided on a 24- channel laser with 100 GHz (0.8 nm) channel spacing at 1560 nm and a free spectral range of 2400 GHz (19.2 nm).

Note that for low bit-rate applications like local access (4), single mode stability may not be necessary. Also, it might be possible to suppress multipassband (MPB) lasing by employing a chirped router design (5), which would considerably relax the above described trade-off. In general, MPB is worse for high threshold devices since the gain profile of a semiconductor amplifier becomes less selective for a high population inversion.

We have previously reported on the MFL fabrication (6). The chip with 24 channels, described here, measures 9x18 mm^2 (Fig. 1). The amplifier sections are 1 mm long. Three ternary quantum wells, 0.8 % compressively strained, provide gain. The transition between amplifiers and passive waveguides is laterally tapered to avoid reflections. During the last, p-type, regrowth step, SiO_2 stripes run on top of the passive waveguides and between the amplifiers to prevent p-type material from growing there. This helps to keep the passive waveguide losses low and increases the electrical isolation between amplifiers to more than 1 MΩ. The active stripe width of the amplifier is 1 μm. The 540 μm thick chips are presently not thinned down to facilitate handling. The devices are fully packaged and can be temperature controlled via a TE-cooler.

The cw threshold of the MFL was 82 mA total (41 mA per amplifier) for single channel operation. Channel 1 did not oscillate after packaging. Out of the 24 channels, 5 channels had to be eliminated because of MPB. Even for a large FSR, there will always be some channels, where the gain difference in different passbands is too small to clearly favor one passband over the other. In Fig. 2, we display the wavelength comb for simultaneous cw oscillation on 18 channels. The output amplifier runs at 162 mA bias current. The bias currents of the individual, wavelength selective amplifiers are adjusted to equalize the output powers. Most of these amplifiers are biased between 30 and 40 mA. The channels that are geometrically located at the edges (channels 2, 3, 23, 24) had to be driven by up to 60 mA current, because the router insertion

loss is higher for these channels. The measured power in the fiber was - 2 dBm (or -14.6 dBm per channel). By thinning down the sample, we believe that the output power can be significantly increased because the cooling of the chip will be more effective.

The experimental channel spacing is 103 GHz. The increase of channel spacing from the design value of 100 GHz is caused by the fact that the absolute lasing wavelength is lower (around 1515 nm) than what we assumed for the design, which in turn increases the channel spacing. Indeed, the angle of the first Brillouin zone (7) is proportional to λ, where λ is the absolute channel wavelength. The channel spacing, on the other hand, is determined by the geometrical separation of the output waveguides on the router. If the MFL is designed for "wrap around" at a given wavelength, say 1560 nm, the optical channel spacing in frequency is given by FSR/N. However, for a lasing wavelength λ_{las} different from the design wavelength, the experimental channel spacing will be changed by a factor $\lambda_{design}/\lambda_{las}$ from the design value. In our case, the channel spacing should therefore be 103 GHz (1560/1515x100GHz=103 GHz) , which is in perfect agreement with the experimental value. The channel spacing reproducibility from wafer-to-wafer is better than 1 GHz. For an application where the laser has to be matched to a passive router in a remote node (4), the router, too, would exhibit an increase of channel spacing for lower wavelength (for exactly the same reasons as above) so that there should not be any difficulty to align the MFL wavelength comb to the router channels.

All channels are stable single mode. The longitudinal mode spacing is 1.7 GHz. The full width half maximum of the intracavity filter due to the WGR is 35 GHz. In Fig. 3, we plot the spectrum over a larger scale to show side modes created by the next passbands. They are suppressed by at least 20 dB. Signal-to-noise ratio of the laser is 30 dB. The laser can be directly modulated at 1.24 Gbps as evidenced by the eye-diagram in Fig. 4, making this MFL a potential 20 Gbps WDM source. The cross-talk in the common output amplifier can be eliminated by using a feed-forward drive scheme (8).

To make the MFL high performance, the photonic integration has to produce a low loss passive waveguide, a high gain amplifier, that is single mode in the transverse direction, and a smooth, reflection-free transition between the amplifier and the passive waveguide. These three elements have to be separately measured in order to better understand and further optimize the device performance. The waveguides have losses around 4 dB/cm, up from 1 dB/cm for waveguides that have not undergone any of the processing steps necessary for the integration. The doping levels (Zn and Fe) are mainly responsible for the increased losses. These losses bring the multiplexer insertion loss to about 10 dB. The amplifiers showed a threshold current density of 1200 kA/cm^2 when cleaved as 1 mm Fabry Perot laser bars without coatings. Their differential quantum efficiency was 26 %, and they deliver 20 mW power per facet at 200 mA drive current. The photoluminescence of the wafer is peaked at 1560 nm. However, the MFL lasing wavelength is around 1515 nm. The intracavity loss of the MFL is believed to be responsible for the shift to lower wavelength (compared to the photolumiscence wavelength), because the amplifier has to operate under high inversion which in turn, increases the mean energy of the electron distribution in the conduction band. The active-passive transition is the most difficult to characterize. Right now, this transition causes a 1.7 dB ripple in the amplified spontaneous emission spectrum of the output amplifier (when all the other amplifiers are turned off and the output amplifier runs at 162 mA). It is crucial to keep this ripple as small as possible, because it competes with the intracavity filtering from the router and may destroy single-mode lasing stability. The threshold current density does not significantly increase for Fabry-Perot lasers with a short piece of passive waveguide attached, showing thereby that the transition loss is small. We believe that further optimizing of the layer structure, processing and mask design can still produce significant improvement of the MFL performance: increasing output power, lowering threshold and increasing the number of channels.

In conclusion, we have reported on a MFL that operates simultaneously on 18 channels. Each channel can be directly modulated at 1.24 Gbps. The inherently stable and reproducible channel spacing of this device is a major advantage when it come to manufacturability and reliability of sources for dense WDM systems.

Figure captions:
Fig. 1: Schematic drawing of the MFL with 24 channels.
Fig. 2: Output spectrum for 18 channels simultaneously lasing
Fig. 3: Output spectrum over larger wavelength range.
Fig. 4: Eye-diagram of one of the channels modulated at 1.2 Gbps.

References:

(1) B. Glance, I.P. Kaminow, R.W. Wilson, "Applications of the integrated waveguide grating router", J. of Lightwave Technology, Vol. 12, No. 6, pp. 957-962, 1994.

(2) M. Zirngibl, C.H. Joyner, L.W. Stulz, " Demonstration of a 9x200 Mbit/s wavelength division multiplexed transmitter", Electron. Lett., vol 30, pp. 1484, 1994.

(3) C.R. Doerr, M. Zirngibl, C.H. Joyner, "Single Longitudinal-Mode Stability Via Wave Mixing in Long-Cavity Semiconductor Lasers", IEEE Photon. Technol. Lett., Vol. 7, pp. 962-964, 1995.

(4) M. Zirngibl, C.H. Joyner, L.W. Stulz, C. Dragone, "LARNet, a Local Access Router Network", IEEE Photon. Technol. Lett., vol. 7, pp. 215-217, 1995.

(5) C.R. Doerr, M. Zirngibl, C.H. Joyner, "Chirping of the waveguide grating router for free spectral range mode selection in the multi-frequency laser ", to appear in IEEE Photon. Technol. Lett.

(6) M. Zirngibl, C.H. Joyner, L.W. Stulz, U. Koren, M.-D. Chien, M.G. Young and B.I. Miller, " Digitally Tunable Laser based on the Integration of a Waveguide Grating Multiplexer", IEEE Photon. Technol. Lett., vol.6, pp. 516-518, 1994.

(7) C. Dragone, "Efficiency of a Periodic Array with Nearly Ideal Element Pattern", IEEE Photon. Technol. Lett., vol.1, pp. 238-240, 1989.

(8) C.R. Doerr, C.H. Joyner, M. Zirngibl, L.W. Stulz, H.M. Presby, "Elimination of Signal Crosstalk form Carrier Density Changes in the Shared Semiconductor Amplifier of Multifrequency Signal Sources", IEEE Photon. Technol. Lett., vol.7, pp.1131-1133, 1995.

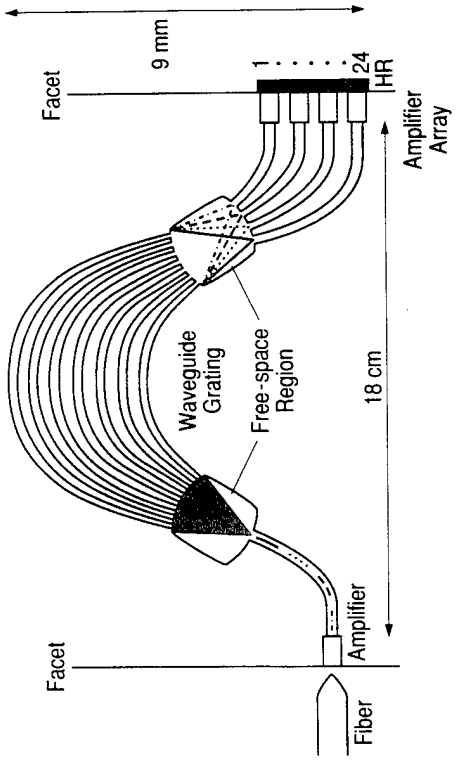


Fig. 1

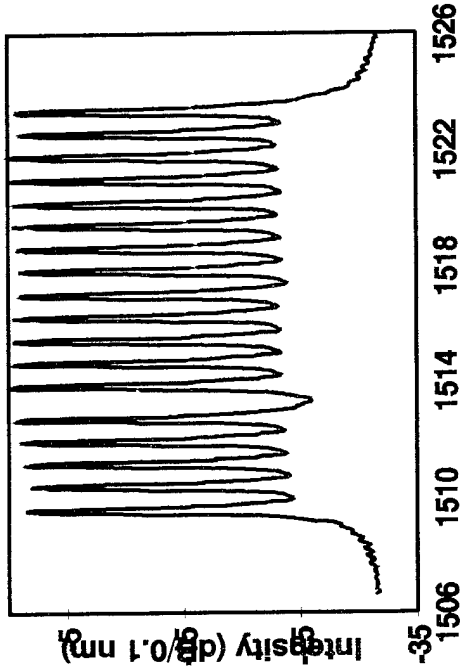


Fig. 2

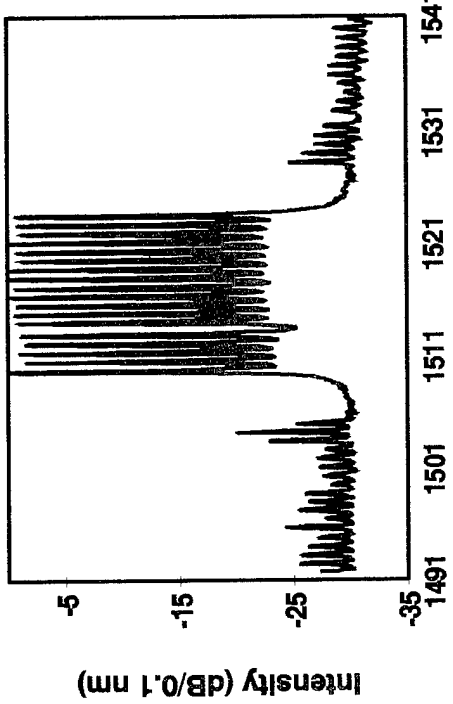


Fig. 3

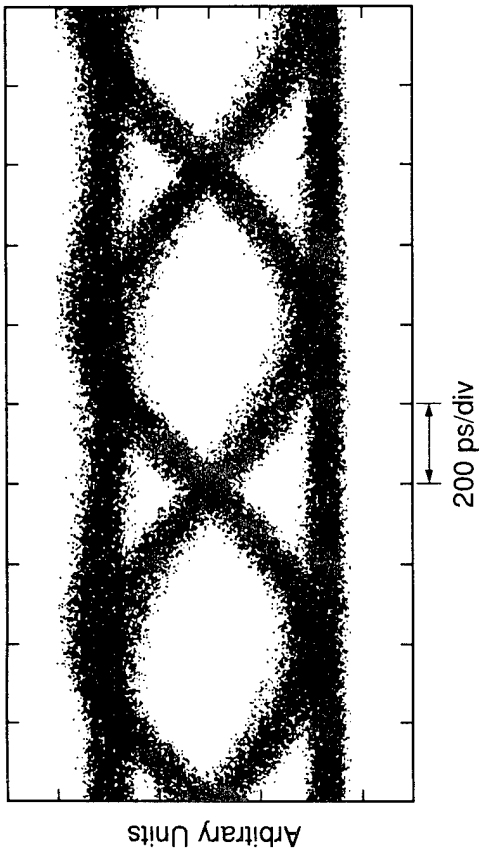


Fig. 4

Chirping of the waveguide grating router for free-spectral-range mode selection in the multi-frequency laser

C. R. Doerr, M. Zirngibl, and C. H. Joyner

AT&T Bell Laboratories, Crawford Hill Laboratory
791 Holmdel-Keyport Road, Holmdel, NJ 07733-0400
(908) 888-7067, FAX: (908) 888-7007, e-mail: crdoerr@big.att.com

The multi-frequency waveguide grating router laser (MFL)[1] consists of a waveguide grating router[2-4] integrated with semiconductor amplifiers. N ports at one end of the router terminate in optical amplifiers with cleaved mirror facets, and one port at the other end terminates in a partially reflecting mirror, or possibly an additional optical amplifier. Each of the N resonant cavities provides a different intracavity filter frequency due to the router. These intracavity filters are precisely spaced with respect to each other, resulting in an MFL output consisting of N precisely spaced laser frequencies.

However, the transmission peaks of the router-based intracavity filters repeat with a periodicity equal to the router free-spectral range. In which and in how many passbands laser oscillation occurs for each channel is determined only by the amplifiers. This makes it difficult to control the absolute lasing wavelength, and multiple passband lasing results in instability in the laser output[5].

We wish to modify the router so that the intracavity filter in each channel has one dominant passband, with all the other passbands exhibiting higher loss, and we wish to control which passband in each channel has the highest transmission. These goals can be achieved by chirping the router.

The waveguide grating router is a device with N_1 inputs and N_2 outputs that consists of M waveguides of varying lengths connecting two star couplers. For the following analysis, we limit ourselves to NxN routers with channels evenly spaced in frequency, free-spectral ranges equal to N times the channel spacing, and even M. Following the work of Dragone[4], one can write the amplitude transmission between port p on one end of the router and port q on the other as

$$t_{p,q} = \sum_{m=1}^{M} P_m \exp\left(j \frac{2\pi n}{c} l_m f\right) \exp\left[j \frac{2\pi}{N}(p-q)m\right] \qquad (1)$$

where f is the optical frequency, P_m is the optical power in the mth arm normalized to the total power, n is the index of refraction, c is the speed of light in vacuum, and l_m is the length of the mth arm. In the simplest router design, $l_m = m\Delta l + C$, where Δl and C are constants. The offset value C does not affect the router response and is left out in all following equations. $T_{p,q} = |t_{p,q}|^2$ in such a router has equal-height transmission peaks (passbands) that occur at $f = [k - (p-q)/N]c/(n\Delta l)$, where k is an integer.

To change the relative passband heights, we require a non-uniform distribution of

l_m. Such a concept of using non-uniformity to modulate a filter response has been applied to many devices, such as distributed feedback lasers[6], weighted couplers[7], and beamsteerers[8]. One of the unique features of the present case is that the router is a NxN device.

The constraints we impose on the design for controlling the passband heights are that we can control only l_m and that $l_m<l_{m+1} - \varepsilon$, where $\varepsilon>0$. To help create and evaluate a design, we make the following substitution for l_m: $l_m = (m + \alpha_m)\Delta l_t$. Thus α_m is the deviation from a non-chirped "test" grating. If we constrain ourselves to evaluate $t_{p,q}$ only at the frequencies where a non-chirped router with $l_m=m\Delta l_t$ would have its passband peaks, then Eq. (1) reduces to

$$t_{p,q\ env} = t_{p,q}(f=[k-(p-q)/N]c/(n\Delta l_t)) = \sum_{m=1}^{M} P_m \exp\left(j\frac{2\pi n}{c}\alpha_m \Delta l_t f\right) \qquad (2)$$

The overall envelope of the passband peaks for a design can be found by taking the largest magnitude of $t_{p,q\ env}$ for all Δl_t at each f.

For example, one chirp design is to separate the router grating arms into two separate gratings with slightly different periods. Light passing through the two gratings will add coherently over only certain frequency ranges. For such a design, $l_m = m\Delta l_a + (M/2 - m)\Delta l_b$ for m=1,...,M/2, and $l_m = m\Delta l_a + (m - M/2)\Delta l_b$ for m=M/2+1,...,M, where Δl_a and Δl_b are constants.

A more general chirp design is

$$l_m = m\Delta l_a + \text{round}\left[g(m)\Delta l_a \frac{nf_c}{c}\right]\frac{c}{nf_c} \qquad (3)$$

where g is an arbitrary function of m with a small average g(m+1)-g(m), round is a function that rounds its argument to the nearest integer, and f_c is the desired peak wavelength of the passband envelope. Δl_a determines the channel spacing and channel alignment in the envelope, and g(m) determines the envelope shape. The advantage of this design is that one can independently control passband envelope width and location. For the two-grating design, $g(m) = \gamma_{2grat}(1 - 2m/M)$ for m=1,...,M/2, and $\gamma_{2grat}(2m/M - 1)$ for m=M/2+1,...,M. Figure 1a shows $T_{p,q}$, $T_{p,q\ env}(\Delta l_t=\Delta l_a)$, and $T_{p,q\ env}(\Delta l_t=\Delta l_a+\Delta l_b)$ vs. wavelength for an N=10, M=36 two-grating-chirped router with $\gamma_{2grat}=M\Delta l_b/(2\Delta l_a) \approx 1$and P_m a Gaussian distribution.

Another design that can use Eq. (3) is the M-grating design, in which g(m+1)-g(m) changes linearly. For this case $g(m) = \gamma_{Mgrat}[m(m+1)/M - m]$, where, like γ_{2grat}, γ_{Mgrat} is a constant that adjusts the envelope width. Figure 1b shows $T_{p,q}$ and $T_{p,q\ env}(\Delta l_t=\Delta l_a)$ vs. wavelength for an M-grating design. The envelope repeats with period f_c.

A two-grating design was fabricated in InP using buried rib waveguides with N=10, M=36, and a channel spacing of 100 GHz. One channel from a non-chirped router is shown in Fig. 2a, and all 10 channels of the two-grating chirped router are

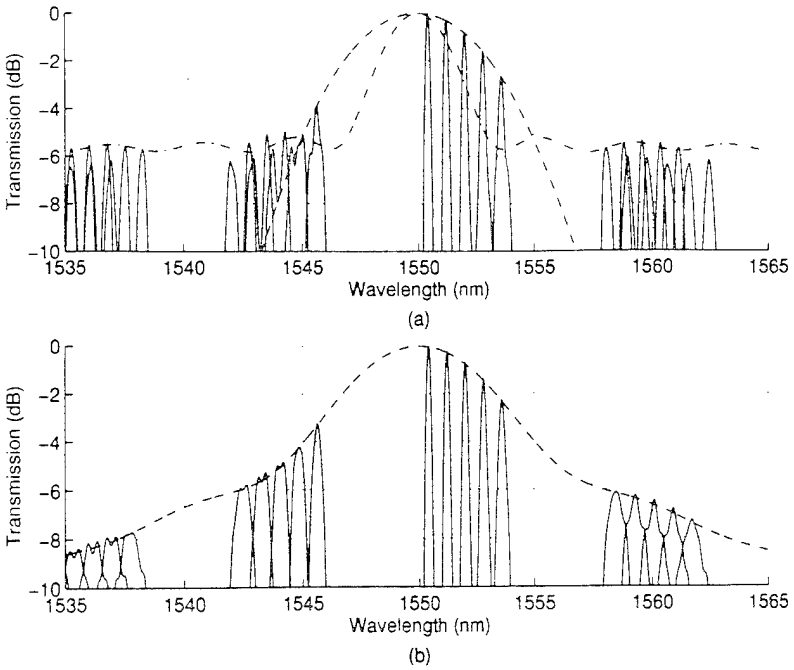


Fig. 1. Theoretical $T_{p,q}$ vs. free-space wavelength for a two-grating chirped router (a), and an M-grating chirped router (b) with M=36 and N=10. Only 5 of the channels (solid lines) are shown; the other 5 channels are symmetric about 1550 nm. The dashed line shows $T_{p,q\ env}(\Delta l_t=\Delta l_a)$, and the dash-dot line in (a) shows $T_{p,q\ env}(\Delta l_t=\Delta l_a+\Delta l_b)$.

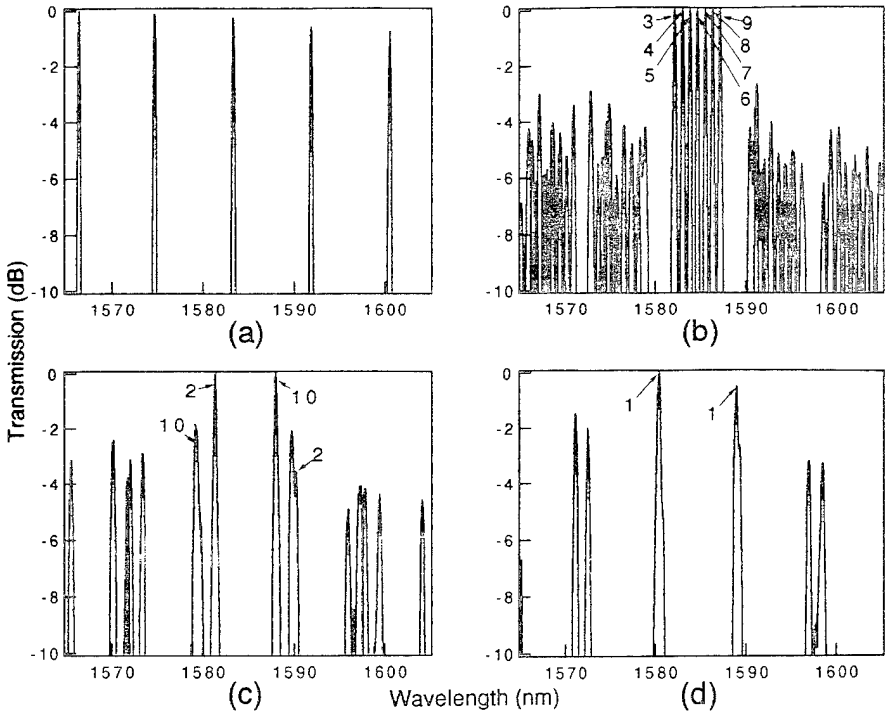


Fig. 2. Experimental results from a two-grating chirped router with M=36, N=10 covering five free-spectral ranges. (b)-(d) show the ten different channels measured by sending broadband light into port p=6 on one side of the router and measuring the spectrum of the TE light from each of the 10 ports on the other side. q is shown on the plots. (a) shows the response from an equivalent non-chirped router. All the plots are adjusted so their peaks are at 0 dB.

shown in Figs. 2b-d. Seven (q=3,...,9) of the channels have extinction ratios less than about -3 dB, two (q=2,10) have extinction ratios of -2 dB, and the tenth (q=1) has nearly equal passbands. These extinction ratios are about 1-2 dB worse than predicted by the theory, which we believe is caused by small phase errors in the fabricated grating. The envelope and passband positions were repeatable to approximately ±0.5 nm from chip to chip (whether on the same wafer or different wafers). The total on-chip loss is about 6±1 dB between center channels, and the loss is about the same for the unchirped and chirped router for the channels at the center of the chirp envelope.

In conclusion, chirping of the router in an MFL is similar to placing a highly controllable, wide band-pass filter into the laser. It reduces the number of channels that oscillate in more than one router passband and gives precise control over the absolute lasing wavelength.

References

[1] M. Zirngibl, B. Glance, L. W. Stulz, C. H. Joyner, G. Raybon, and I. P. Kaminow, *Characterization of a multiwavelength waveguide grating router laser*, IEEE Photon. Tech. Lett. **6**, 1082-1084 (1994).

[2] A. R. Vellekoop and M. K. Smit, *Four-channel integrated-optic wavelength demultiplexer with weak polarization dependence*, J. Lightwave Technol. **9**, 310-314 (1991).

[3] H. Takahashi, S. Suzuki, K. Kato, I. Nishi, *Arrayed-waveguide grating for wavelength division multi/demultiplexer with nanometre resolution*, Electron. Lett. **26**, 87-88 (1990).

[4] C. Dragone, *An N x N optical multiplexer using a planar arrangement of two star couplers*, IEEE Photon. Tech. Lett. **3**, 812-814 (1991).

[5] C. R. Doerr, M. Zirngibl, and C. H. Joyner, *Single longitudinal-mode stability via wave mixing in long-cavity semiconductor lasers*, IEEE Photon. Tech. Lett. **7**, 962-964 (1995).

[6] H. A. Haus and C. V. Shank, *Antisymmetric taper of distributed feedback lasers*, IEEE J. Quant. Electron. **QE-12**, 532-539 (1976).

[7] R. C. Alferness and P. S. Cross, *Filter characteristics of codirectionally coupled waveguides with weighted coupling*, IEEE J. Quant. Electron. **QE-14**, 843-847 (1978).

[8] J. H. Abeles and R. J. Deri, *Suppression of sidelobes in the far-field radiation patterns of optical waveguide arrays*, Appl. Phys. Lett. **53**, 1375-1377 (1988).

A COMPACT PHASED ARRAY BASED MULTI-WAVELENGTH LASER

L.H. Spiekman, A.A.M. Staring,* J.J.M. Binsma,* E.J. Jansen,* T. van Dongen,*
P.J.A. Thijs,* M.K. Smit, and B.H. Verbeek*
Dept. of Electrical Engineering, Delft University of Technology
Mekelweg 4, NL-2628 CD Delft, The Netherlands
spiekman@et.tudelft.nl, +31 15 278 6106, fax +31 15 278 4046
* Philips Optoelectronics Centre
Prof. Holstlaan 4, NL-5656 AA Eindhoven, The Netherlands

Introduction:

Wavelength Division Multiplexing (WDM) is widely regarded as a promising option to increase the bandwidth and flexibility of broadband optical communication systems. In such systems, multi wavelength laser sources [1], both for selectable single wavelength and simultaneous multiple wavelength operation, will be important components.

Several monolithically integrated solutions of launching multiple wavelengths into a single fibre have been demonstrated. Among these are integration of DBR lasers with a star coupler [2], and an etched grating [3] or a Phased Array wavelength multiplexer [4, 5] in the laser cavity. Previous devices have been fabricated using QW-loaded [4] or Selective Area Epitaxy-grown [5] embedded waveguides. Due to the relatively small index contrast of such waveguides, a rather large device size of $10 \times 4\,\mathrm{mm}^2$ results.

In this paper, devices are presented which employ a simple ridge waveguide structure, enabling a compact Phased Array design due to a high index contrast.

Design and fabrication:

As shown schematically in Fig. 1, the passive part of the device consists of an 11×1 Phased Array wavelength multiplexer having a channel spacing of 400 GHz (3.2 nm), and a free spectral range (FSR) of 38.75 nm. It comprises 50 array waveguides with a minimum bending radius of $500\,\mu\mathrm{m}$. The two outer input waveguides are used for testing purposes, while the 9 inner input arms are fit with $500\,\mu\mathrm{m}$ long gain sections. Total device size is only $3.5 \times 2.5\,\mathrm{mm}^2$.

In addition to a small device size, the ridge waveguide structure in both the active and passive parts of the device leads to a simple fabrication scheme. The complete structure (active + passive) is grown in 3 epitaxy steps. A 120 nm thick InGaAsP laser active layer with $\lambda_{\mathrm{gap}} = 1.55\,\mu\mathrm{m}$ is grown onto an n-type InP substrate by means of Low-Pressure OMVPE. After defining the active regions using wet chemical etching, 230 nm InGaAsP with $\lambda_{\mathrm{gap}} = 1.30\,\mu\mathrm{m}$ is grown, butt-jointed to the active layer, and the entire structure is overgrown with a $1.4\,\mu\mathrm{m}$ thick p-InP cladding layer. Stable TE mode operation [6] is obtained using ridges of $2.5\,\mu\mathrm{m}$ in width and $1.35\,\mu\mathrm{m}$ in height, which are etched by means of reactive ion etching. Finally, the laser contact metallisation is fabicated. For characterisation, chips with as-cleaved facets are soldered onto copper carriers providing 8 leads for electrical contacts.

Experimental results:

Figure 2 shows the response of a discrete, passive Phased Array. The 11 channels have a spacing of 400 GHz around the central wavelength of 1547 nm, with a crosstalk less than -20 dB. Fibre-to-fibre insertion loss (using two lensed fibres) is 24.7 dB for the best channel, and increases with channel number due to the increasing path length (see Fig. 1). This yields an estimated waveguide loss of 20 dB/cm, which is supported by the results of Fabry-Pérot contrast measurements

on straight waveguides. This relatively high loss is attributed to the p-doped InP cladding layer, which was grown over the entire structure for simplicity of processing.

As shown in Fig. 3, single-mode operation with a side mode suppression of approximately 20 dB is obtained for 6 out of 8 adressable channels. The width of the individual peaks results from the 0.1 nm resolution of the optical spectrum analyser used for the measurements. Threshold current for the devices, operated at 25°C, is 120 mA for channel 2 and increases to 150 mA for channel 7, due to the increasing waveguide loss with increasing length of the passive part of the cavity. Discrete laser arrays (i.e. without passive waveguides; length 500 μm) uniformly exhibit threshold currents of 38 mA. Finally, for channel 2, at 200 mA approximately 0.15 mW of output power is coupled into a lensed standard single mode fibre.

Stable dual channel operation could be obtained for any combination of lasing channels at a device temperature of 16°C, as shown in Fig. 4 for channel 2 and 3. Device heating resulting from the high operating currents prevented lasing at more than two wavelengths.

Conclusion:

A compact multi-wavelength laser has been fabricated in a simple ridge waveguide structure, exhibiting stable single mode operation at 6 out of 9 discrete wavelengths spaced by 400 GHz. Simultaneous operation at two independently lasing wavelengths has been demonstrated.

Acknowledgements:

Technical assistance of A. van Leerdam is gratefully acknowledged. Part of this work has been supported by the RACE project R2070 MUNDI.

References:

[1] J. B. D. Soole and C.-E. Zah, "Multiwavelength semiconductor lasers advance rapidly," *Laser Focus World*, vol. 30, pp. S9–S15, June 1994.

[2] M. G. Young, U. Koren, B. I. Miller, M. A. Newkirk, M. Chien, M. Zirngibl, C. Dragone, B. Tell, H. M. Presby, and G. Raybon, "A 16 × 1 wavelength division multiplexer with integrated distributed bragg reflector lasers and electroabsorption modulators," *IEEE Photon. Technol. Lett.*, vol. 5, pp. 908–910, Aug. 1993.

[3] K. R. Poguntke, J. B. D. Soole, A. Scherer, H. P. LeBlanc, C. Caneau, R. Bhat, and M. A. Koza, "Simultaneous multiple wavelength operation of a multistripe array grating integrated cavity laser," *Appl. Phys. Lett.*, vol. 62, pp. 2024–2026, Apr. 1993.

[4] M. Zirngibl and C. N. Joyner, "12 frequency WDM laser based on a transmissive waveguide grating router," *Electron. Lett.*, vol. 30, pp. 701–702, Apr. 1994.

[5] C. H. Joyner, M. Zirngibl, and J. C. Centanni, "An 8-channel digitally tunable transmitter with electroabsorption modulated output by selective-area epitaxy," *IEEE Photon. Technol. Lett.*, vol. 7, pp. 1013–1015, Sept. 1995.

[6] M.-C. Amann, "Polarization control in ridge waveguide laser diodes," *Appl. Phys. Lett.*, vol. 50, pp. 1038–1040, Apr. 1987.

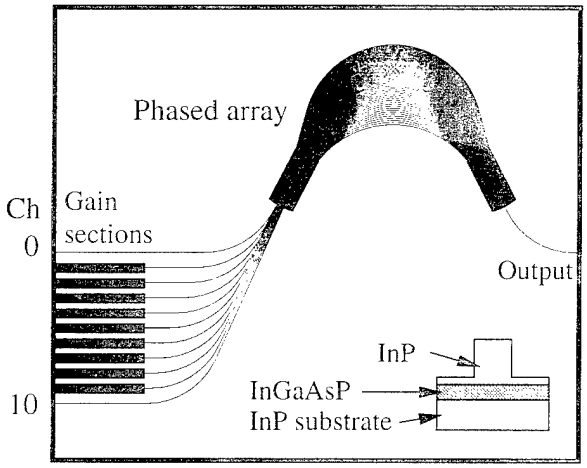


Figure 1: Schematic diagram of ridge waveguide multi-wavelength laser.

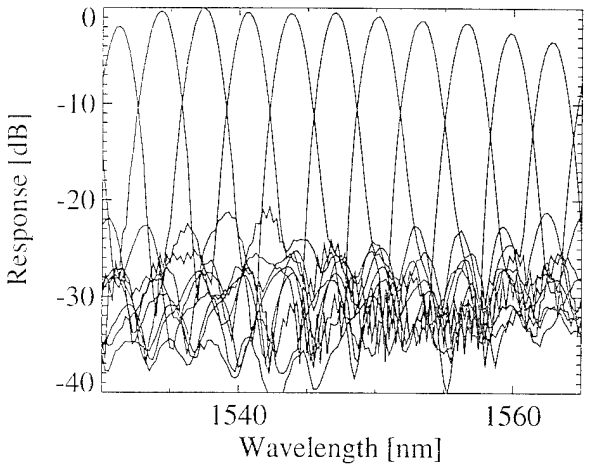


Figure 2: Response of a discrete phased array.

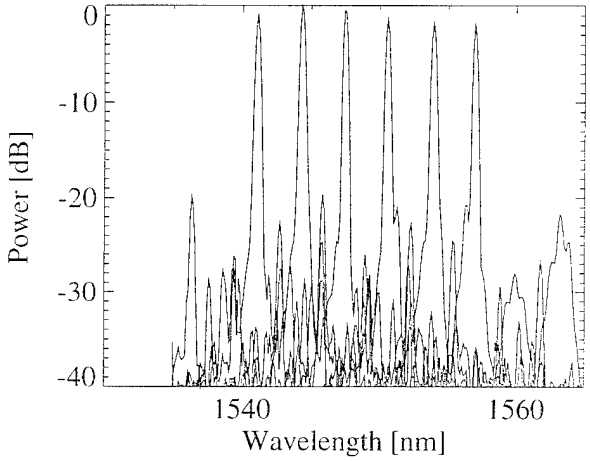


Figure 3: Spectra of the individual channels at 175 mA gain current.

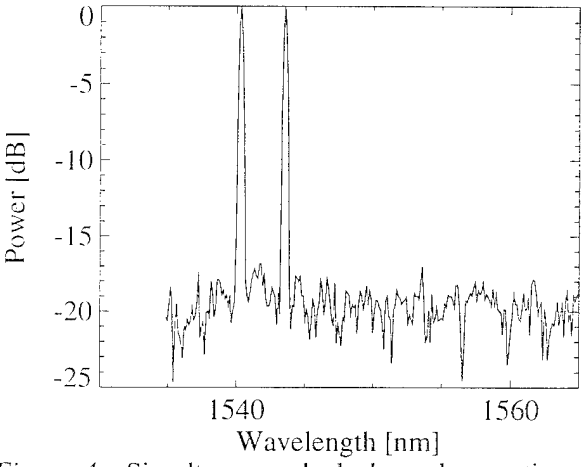


Figure 4: Simultaneous dual channel operation; $I_{ch\,2} = 165\,mA$, $I_{ch\,3} = 154\,mA$.

Silica External Cavity Array Transmitters with High Wavelength Accuracy

Karen Liu, Stuart D. Brorson, Chaoyu Yue
IBM T. J. Watson Research Center
P. O. Box 704
Yorktown Heights, NY 10598
Tel (914) 784-7378
Fax (914) 784-6225

SYSTEM REQUIREMENTS: Directly-modulated semiconductor diode lasers are ideal sources for digital data communications, but sources for wavelength-division multiplexing (WDM) have additional stringent requirements on wavelength. The most obvious of these requirements is wavelength accuracy upon manufacture. Maintaining the wavelength stability over life may be even harder to ensure. Also, the dynamic properties of the laser frequency, both in terms of high-speed chirp and low-speed thermal drift, need to be guaranteed.

Arrays of wavelength-distinct arrays of DFB's are being developed for WDM.[1,2] One major issue with this approach is that temperature-tuning cannot be used to correct relative errors within the array. The best reported data on the wavelength accuracy is a standard deviation of 0.18 nm for six-element arrays.[1] This is still large compared to the accuracies demonstrated in waveguide gratings used for multiplexing and demultiplexing.[3] Therefore, these systems will require individually temperature tunable lasers unless the array accuracies can be improved.

As an example of the target requirements for a dense WDM system, we consider a 32-channel simple link which uses silica waveguide arrayed-waveguide gratings at either end as multiplexer and demultiplexer. Experimentally, measurements were done on such a link constructed of two arrayed waveguide gratings (AWG) loaned to us by NTT Opto-electronics Labs. The gratings have channels spaced 0.8 nm (100 GHz) apart with approximately 0.29 nm FWHM. If we (arbitrarily) allow a 1 dB "mismatch loss" penalty through the mux and demux, the lasers need to be within ± 0.06 nm of the grating passband peak.

If direct modulation is used, the target accuracy may need to be reduced further.The details of a DFB laser's dynamic spectra have been found to cause additional penalties in a link. Unlike conventional transmission, these penalties result from the wavelength selective nature of the link (not fiber dispersion) and may occur even at low speeds and short distances. We have observed this with a bit error rate measurement taken at 200 Mb/s with a commercial DFB laser driven with an extinction ratio of 10 and an average power in the fiber pigtail of -3 dBm. In the experiment, the laser was maintained at constant temperature and drive conditions, but the AWG's were temperature tuned to achieve mismatch between the WDM link and the laser. ***With the power at the receiver held constant***, a BER rate degradation was seen for detuning in either direction. This "de-tuning penalty" in addition to the "mismatch penalty" already mentioned above was of comparable magnitude. A de-tuning penalty of 1 dB corresponded to 0.055 nm between laser and WDM link under the test conditions above, but will depend on the particular DFB used.

AWG LASER: We propose to use the same AWG which is used as the multiplexer to define the laser array wavelengths by forming an external cavity as shown in Fig. 1. It consists of a semiconductor laser array (with highly reflective back mirror and anti-reflection front facet coatings) coupled to the silica waveguide grating. On the end of the fiber pigtail butted to the waveguide is a reflective coating which acts as the output coupler of all the laser cavities. Recently, a slightly different silica external cavity AWG laser which minimized the number of laser diodes was demonstrated.[4] The silica AWG laser is the hybrid version of the previously demonstrated integrated semiconductor waveguide grating lasers[5,6]

One advantage of using the same make of grating to define the laser wavelengths as to perform the multiplexing/ demultiplexing functions is that some small systematic errors in wavelength would be in common and would not lead to either mismatch or detuning penalties. Wavelength errors in the grating can be divided in several categories:

TYPE 1: overall wavelength shift of the entire device due to fabrication errors such as material composition, waveguide layer thickness and waveguide width
TYPE 2: reproducible wavelength errors of individual channels due to mask inaccuracies
TYPE 3: truly random individual channel variations.

Type 1 errors are typically much larger than the other types but the overall shift of the whole array can be corrected coarsely by choosing a different input, and finely by temperature tuning of the grating. In considering the laser requirements, we assume that these errors have already been corrected to achieve matching between multiplexer and demultiplexer. Our point here is that this external cavity design is self-correctly for Type 2 errors because the laser transmitter wavelength will automatically track the multiplexer. As an example, the NTT multiplexer and demultiplexer used in the link experiment described above had Type 1 errors correctable by 10 C (~ .1 nm) of temperature tuning between mux and demux, and showed type 2 errors of $< \pm$ 0.05 nm (limited by measurement accuracy) from nominal channel wavelength but Type 3 errors (errors uncorrelated between mux and demux) caused random differences between the two components with a σ of 0.02 nm (again limited by measurement accuracy.)

PHOTOREFRACTIVE BRAGG GRATING LASER: The device of Fig. 1 has some disadvantages. First, the wavelength characteristics of high-order gratings such as the arrayed-waveguide type are periodic. As reported[5,6] the external cavity lasing wavelengths are not uniquely defined. Also, the long cavity length (5 cm typical) in standard low-loss silica material limits the modulation speed possible. Another version of the external cavity laser uses UV-written photorefractive Bragg gratings in the waveguide to define the laser wavelength[7]. This technique uses a low-order grating and thus does not have the wavelength ambiguity problem of the arrayed-waveguide grating. With the shorter cavity, 2.4 Gb/s modulation was possible. We propose that these gratings should be written in the multiplexer AWG at the end nearest the laser diode array as shown in Fig. 2. The purpose is to put the dominant type 1 effective index error in common between the Bragg grating and the multiplexer.

EXPERIMENTAL RESULTS: So far, we have assumed that the accuracy of the external cavity wavelengths are directly translated to the wavelength of the laser. But there are additional factors that must be considered. The gain curve of the diodes including residual ripple from the laser facet will pull the lasing wavelength. Nonlinearities due to wave-mixing have been shown to bias the wavelength towards longer wavelengths.[6]

An initial experiment to study the wavelength accuracy relative to the external cavity wavelength was done using a single HR/AR coated laser diode and a fiber with a photorefractive grating. The fiber was lensed to increase coupling efficiency to over 50% but was not AR coated. Without the fiber grating, the diode gain peak is centered at 1560 nm and shows no lasing up to 300 mA. The low current case in Fig. 3 shows the transmission spectrum of the grating which has 0.1 nm BW as well as the residual ripple due to the diode. Based on rf spectra at the onset of multimode behavior, the effective cavity length is 2 cm. Above threshold, the laser wavelength is matched within .02 nm of the grating center. The peak wavelength as measured by an Advantest wavement shows a dependence on drive currents as shown in Fig. 4, but remains within 0.02 nm.

The above behavior occurs when the fiber position has been optimized for minimum threshold. It was also noted that another (multi-mode) behavior occurs at high currents when the fiber position is optimized for high power output at high (>140 mA) currents. The multimode state is characterized by typically 6 dB higher output power, wider linewidth (multi-longitudinal mode), peak wavelength longer by 0.08 nm, and high intensity noise. The spectral difference between the two states both taken at 140 mA is shown in Fig. 5.

This work was supported by ARPA contract MDA972-95-C-001.

REFERENCES

1. M. G. Young et al, "Wavelength uniformity in $\lambda/4$ shifted DFB laser array WDM transmitters", Electronics Letters, V. 31, No. 20 pp.1750 - 1752, Sept. 1995

2. C. E. Zah et al., "Monolithic integrated multiwavelength laser arrays for WDM lightwave systems", Optoelectron. Devices Tech., V. 9, No. 2, June 1994

3. J. B. D. Soole et al, "Wavelength precision of monlithic InP grating multiplxer/demultiplexers", Electronics Letters, V. 30, N. 8, pp. 664-6, April 1994

4. Y. Tachikawa and K. Okamoto, "32 wavelength tunable arrayed-waveguide grating based on special input/output arrangement", Electronics Letters, V. 31, No. 19, pp. 1665 - 1666

5. J. B. D. Soole et al, "Multiple-stripe array grating in cavity (MAGIC) laser: a new semiconductor laser for WDM applications", Electronics Letters, V. 28, N. 19, pp. 1805-1807, Sept. 1992

6. C. R. Doerr et al, "Single Longitudinal-Mode Stability Via Wave Mixing in Long-Cavity Semiconductor Lasers", IEEE Photon. Tech. Letters, V. 7, No. 9, pp. 962-4, Sept. 1995

7. G.D. Maxwell et al, "Demonstration of a semconductor external caivty laser using a UV written grating in a planar silica waveguide", Electronics Letters, V. 30 N. 18, pp. 1486-7, Sept. 1994

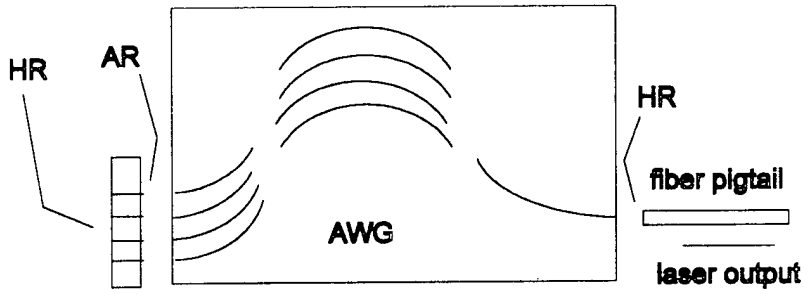


Fig. 1 AWG laser concept

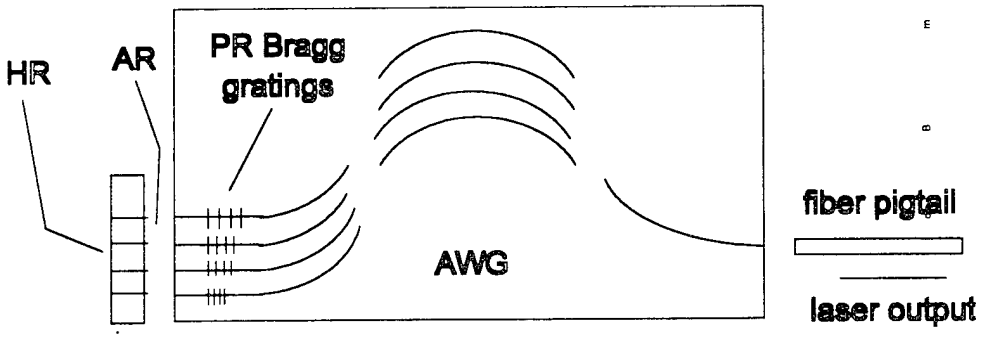


Fig. 2 Photorefractive Bragg gratings in AWG multiplexer

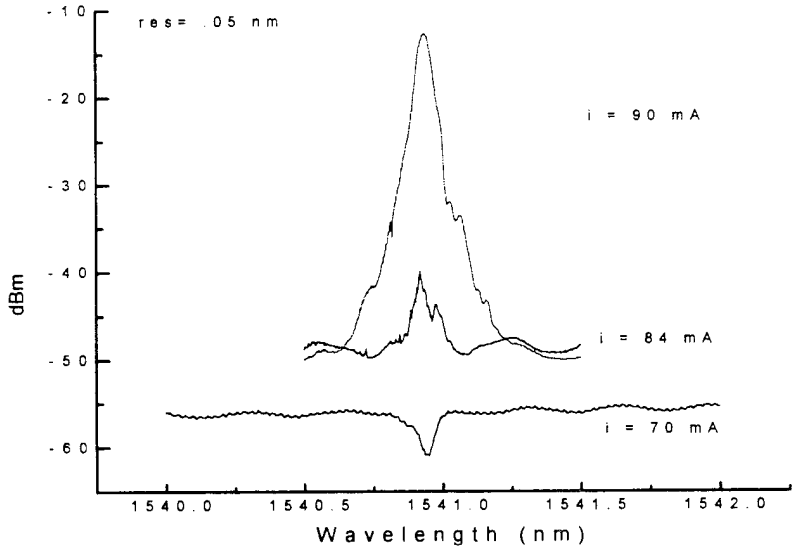


Fig. 3 Fiber Bragg laser spectra below, at and above threshold

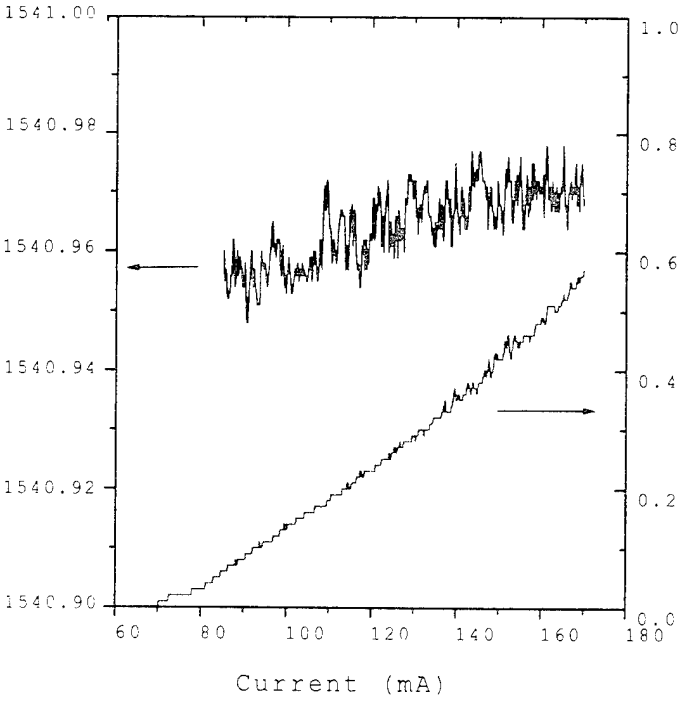


Fig. 4 Peak wavelength and output power for fiber Bragg laser

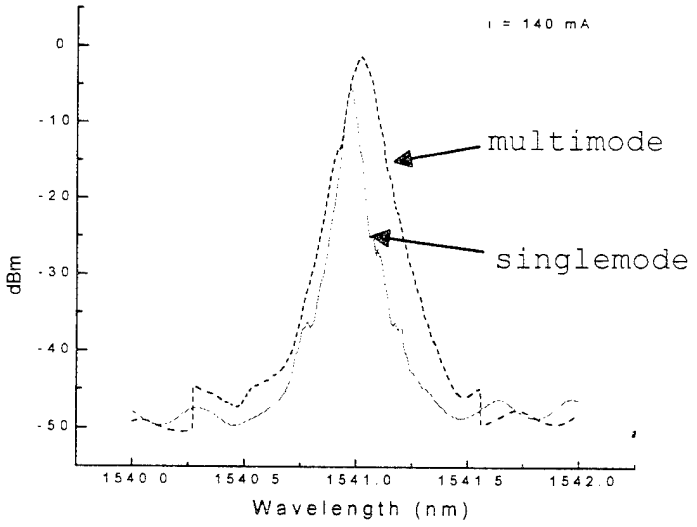


Fig. 5 Difference in spectra for different operating states at 140 mA.

Wavelength Conversion for All-Optical Networks

Jay M. Wiesenfeld
AT&T Bell Laboratories
Crawford Hill Laboratory
Holmdel, NJ 07733

The dynamic exchange of signals between different wavelength channels will become a crucial feature in the development of WDM optical networks. Such a wavelength conversion function will be particularly important for applications involving frequency re-use and wavelength/spatial routing. Additionally, wavelength conversion will simplify the operation of future photonic cross-connects and permit their operation in a non-blocking mode. To minimize their deleterious effects on the optical network, wavelength converters should support the level of optical "transparency" required by the network and produce little degradation on the signal channel.

Techniques based on semiconductor optical amplifiers (SOA's) are most promising candidates for the function of wavelength conversion [1]. In particular, nonlinearities in SOA's applied to wavelength conversion are cross-gain modulation (XGM), cross-phase modulation (XPM) and four-wave mixing (FWM). Cross-gain modulation and cross-phase modulation rely on carrier density dynamics within the SOA, while FWM relies on carrier intraband dynamics for the wavelength conversion range of interest for optical networks.

The simplest technique is XGM, in which a signal reduces the carrier density within the SOA by stimulated emission, thereby imposing a gain modulation on a second, independently tunable, cw input to the amplifier (the probe), which becomes the wavelength-converted output [2-4]. Using XGM, wavelength conversion, to both longer and shorter wavelength, has been demonstrated for signals at bit rates up to 20 Gb/s.[5] Two problems associated with XGM are extinction ratio degradation [6] and chirp, produced by the phase modulation that necessarily

accompanies gain modulation in a SOA [7]. This technique requires only a single SOA, is bit-rate transparent up to a maximum of perhaps 20 Gb/s, and is effective only for intensity modulated formats.

In a second technique, the phase modulation caused by the signal-induced carrier depletion is used to advantage. To use this cross-phase modulation (XPM) to produce intensity modulation on the probe requires an interferometric configuration, in which one or two SOA's is placed inside a Michaelson or Mach-Zehnder interferometer. [8,9] While the first demonstration of XPM for wavelength conversion used discrete SOA's and optical fiber couplers to construct interferometers [8,9], recent significant progress has been achieved by the fabrication of monolithically integrated SOA interferometers, of both the Michaelson [10] and Mach-Zehnder configurations [11-13]. With these devices the extinction ratio can be enhanced by the interferometric transfer function [12] and the chirp is controlled, so that transmission over dispersive fiber at high bit rate is possible [10-12]. Wavelength conversion by XPM in interferometric configurations is bit-rate transparent up to at least 10 Gb/s [10, 14], but, as with XGM, functions only for intensity modulated formats.

Wavelength conversion using FWM in a single SOA [15, 16] functions for both intensity modulated and frequency modulated data formats. For digital intensity modulated signals the extinction ratio of the input signal is preserved. However, the conversion efficiency can vary by more than 20 dB over a range of wavelength translation of 10 nm [16]. Moreover, because of the possibly small conversion efficiency and the presence of ASE noise from the SOA, the signal-to-noise ratio can be a limiting factor [1, 17]. Nevertheless, signal wavelengths have been translated by FWM in SOA's at bit rates of 622 Mb/s [18] and at rates to 10 Gb/s [19].

In this presentation, recent applications of SOA's to wavelength translation will be presented. Particular attention will be directed to issues of flexibility, transparency, and signal degradation.

References

1. J. M. Wiesenfeld, Int. J. High Speed Electronics and Systems, **7**, xxx (1996).

2. M. Koga, N. Tokura, and K. Nawata, Appl. Opt., **27**, 3964 (1988).

3. B. Glance, J. M. Wiesenfeld, U. Koren, A. H. Gnauck, H. M. Presby, and A. Jourdan, Electron. Lett., **28**, 1714 (1992).

4. C. Joergensen, T. Durhuus, C. Braagaard, B. Mikkelsen, and K. E. Stubkjaer, IEEE Photonics Tech. Lett., **5**, 657 (1993).

5. J. M. Wiesenfeld, J. S. Perino, A. H. Gnauck, and B. Glance, Electron. Lett., **30**, 720 (1994).

6. J. M. Wiesenfeld, B. Glance, J. S. Perino, and A. H. Gnauck, IEEE Photonics Tech. Lett., **5**, 1300 (1993).

7. J. S. Perino, J. M. Wiesenfeld, and B. Glance, Electron. Lett., **30**, 256 (1994).

8. B. Mikkelsen, T. Durhuus, C. Joergensen, R. J. S. Pedersen, C. Braagaard, and K. E. Stubkjaer, Electron. Lett., **30**, 260 (1994).

9. T. Durhuus, C. Joergensen, B. Mikkelsen, R. J. S. Pedersen, and K. E. Stubkjaer, IEEE Photonics Tech. Lett., **6**, 53 (1994).

10. B. Mikkelsen, T. Durhuus, C. Joergensen, R. J. S. Pedersen, S. L. Danielsen, K. E. Stubkjaer, M. Gustavsson, W. van Berlo, and M. Janson, Proc. 20th Eur. Conf. Opt. Comm., Vol. 4, p. 67, post-deadline, 1994.

11. F. Ratovelomanana, N. Vodjdani, A. Enard, G. Glastre, D. Rondi, R. Blondeau, C. Joergensen, T. Durhuus, B. Mikkelsen, K. E. Stubkjaer, A. Jourdan, and G. Soulage, IEEE Photonics Tech. Lett., **7**, 992 (1995).

12. W. Idler, M. Schilling, K. Daub, D. Baums, U. Korner, E. Lach, G. Laube, and K. Wunstel, Electron. Lett., **31**, 454 (1995).

13. X. Pan, J. M. Wiesenfeld, J. S. Perino, T. L. Koch, G. Raybon, U. Koren, M. Chien, M. Young, B. I. Miller, and C. A. Burrus, IEEE Photonics Tech. Lett., **7**, 995 (1995).

14. C. Joergensen, S. L. Danielsen, T. Durhuus, B. Mikkelsen, K. E. Stubkjaer, N. Vodjdani, F. Ratovelomanana, A. Enard, G. Glastre, D. Rondi, and R. Blondeau, Proc. IOOC '95, paper ThB3-3, p. 58 (1995).

15. L. Tiejmeijer, Appl. Phys. Lett., **59**, 499 (1991).

16. J. Zhou, N. Park, K. J. Vahala, M. A. Newkirk, and B. I. Miller, Electron. Lett., **30**, 859 (1994).

17. J. Zhou, N. Park, K. J. Vahala, M. A. Newkirk, and B. I. Miller, IEEE Photonics Tech. Lett., **6**, 984 (1994).

18. M. C. Tatham, G. Sherlock, and L. D. Westbrook, IEEE Photonics Tech. Lett., **5**, 1303 (1993).

19. R. Ludwig and G. Raybon, Electron. Lett., **30**, 338 (1994).

High speed and polarisation insensitive interferometric wavelength converters by MQW optimisation

K.Wünstel, G.Laube, W.Idler, K.Daub, E.Lach, K.Dütting, M.Klenk, M.Schilling

Alcatel Corporate Research Centre

Adress: Alcatel SEL, Lorenzstrasse 10, D-70435 Stuttgart, Germany
Phone: (+49)711-821-46142, Fax: (+49)711-821-46355

Introduction: Amongst various types of wavelength converters presently investigated, interferometric wavelength converters have shown most enormous progress in the recent period /1/. Availability of these devices is strongly demanded for optical routing and switching demonstrators as well as for WDM experiments. System requirements such as polarisation insensitivity and high speed wavelength conversion up to 10 Gb/s are crucial for success of these components.

The interferometric devices are formed by monolithic integration of semiconductor optical amplifiers (SOAs) in a waveguide structure yielding a Michelson or Mach Zehnder (MZI) interferometer /2,3,4/. The choise of a MQW structure for the interferometer waveguides layers and SOA segments provides enhanced design and processing flexibility compared to standard bulk devices. MQW based MZI wavelength converters have recently shown signal regeneration capabilites up to 5 Gb/s /5/. MQW devices have still to be optimised concerning polarisation insensitivity and high speed operation up to 10 Gb/s.

Principle of wavelength conversion with 3-port MZI: Wavelength conversion achieved by cross phase modulation with SOAs in a discrete Mach Zehnder Interferometer configuration has been reported in /6/. First monolithic integration of SOAs coupled with active waveguides (2-port version with segments 1 to 4, cf. fig.1) has been realised by /7/. In the present version, a 5th segment (s. fig.1) has been additionally integrated to perform injection of the input signal in only one of the MZI branches.

Due to the all active configuration of our MZI, the input and output segments 1,3,5 can be operated as optical amplifiers with potential for compensation of losses arising from splitter/ combiner and input/output coupling. Furthermore, signal level adaptation at the inputs and output of the interferometer is possible.

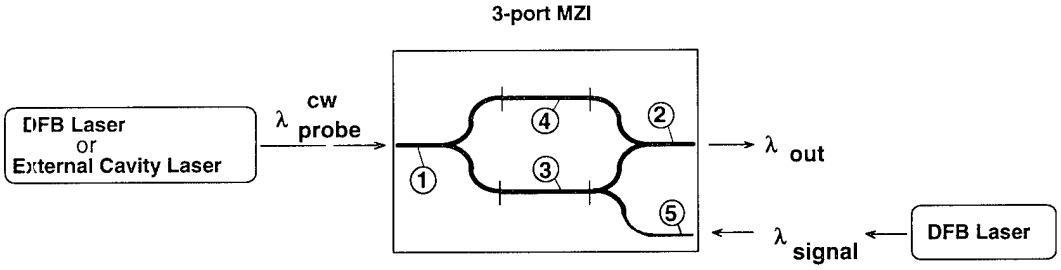


Fig. 1: 3-port Mach-Zehnder interferometer chip operated in contra-directional injection

We operate the 3-port MZI in contra-directional injection scheme (fig.1). In this mode, no optical filter is required at the output to suppress signal wavelength from control wavelength

/8/. Signal power injection only into one MZI branch (branch 3, see fig.1) modulates the refractive index (via carrier density). Thus the counter running control wavelength is phase modulated in branch 3 with respect to branch 4, resulting in amplitude modulation of the control wavelength at the output of the MZI (segment 2). By the more efficient cross phase modulation in the 3-port MZI compared to a 2-port MZI high modulation depth can be realized by optimum choice of bias conditions of the MZI /5/.

Device Fabrication: For the input/output and interferometer waveguides, an identical waveguide layer stack containing the (InGaAs/InGaAsP) MQW active layers is grown in one single step by LP MOVPE on full 2 inch n-InP substrates. Compact ($L \leq 3mm$) monolithic wavelength converters were fabricated. The lateral device geometry (buried ridge stripe) is formed by applying a CH_4/H_2 RIE process before final MOVPE regrowth. The wafer processing is completed using our conventional technology as reported in /2/. Finally, anti-reflection coating of both facets is performed.

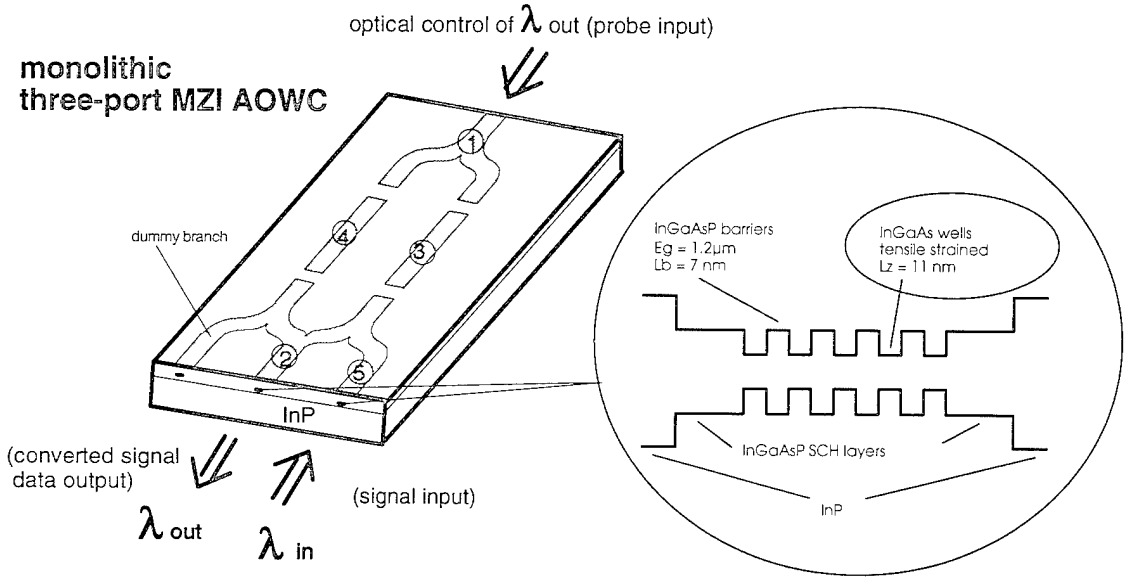


Fig. 2: Schematic view of all-optical wavelength converter (AOWC)

Device optimisation for polarisation insensitivity:
Typical values for conventional MQW-structures are > 10 dB polarisation dependence, whereas < 1 dB is required for specific system applications. Therefore, the MQW structure has to be properly designed to equally support TE and TM. This design has to take into account influences on the polarisation sensitivity arising from the MQW layer stack and the actual waveguide geometry.

As shown in /9/ for discrete MQW-based optical amplifiers, polarisation insensitive operation can be achieved by introduction of small amounts of tensile strain in the wells, resulting in a bandstructure modification (for light and heavy hole bands). A similar technique was applied in the present work for fabrication of completely integrated MZI AOWCs. A schematic band diagram of a typical 5 well structure is shown in fig.2. The MQW core is sandwiched by separate confinement layers of the same composition as the unstrained barrier layers (Eg = 1.2 µm). By fine adjustment of tensile strain (varied between -0.3 and -0.45%) the optimum

conditions to achieve equalized gain for TE and TM modes have been identified for our structures (including MQW and waveguide effects).

Assessment of static and dynamic all-optical wavelength conversion performance has been done for MZI devices with different strain. The basic functionality was comparable to previous polarization dependent devices /2,5/. The best results with the smallest TE-TM difference are obtained for wavelength converters with -0.34% tensile strain. For such a device the interferometric characteristic under electrical control is shown in fig.3 for TE and TM optical probe inputs. In wavelength conversion experiments, the probe input polarisation was held at a constant level (e.g. TE) whereas the polarisation states of the (modulated) input signal were varied between TE and TM. As a result, TE-TM values $\leq$ 1 dB for the output intensity variation were achieved (fig.4) independently of the signal intensity. With these new polarisation-insensitive components, penalty-free 2.5 Gbit/s all-optical wavelength conversion including extinction ratio improvement was verified in system experiments.

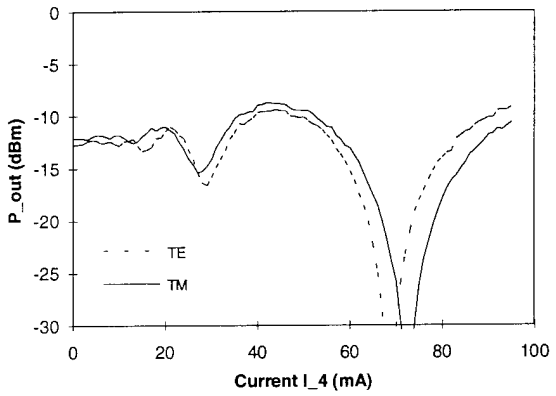


Fig.3: Interferometric response of a MZI under electrical control for TE and TM probe inputs

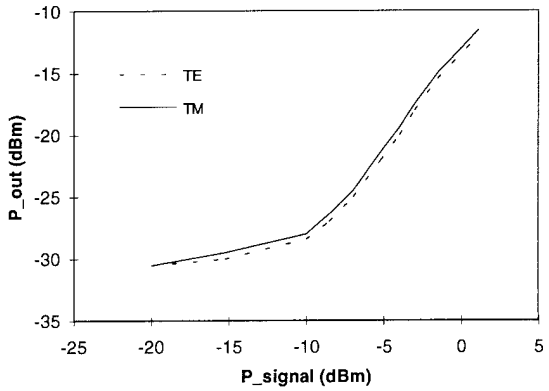


Fig.4: Wavelength converter output signal (P_out) for TE and TM polarised signal input (P_signal)

Device optimisation for high speed operation:
Wavelength conversion speed is directly related to the SOA properties in the interferometer branches 3 and 4. High photon density resulting in short response time as described in /1/ can be achieved by increasing the active volume (increased confinement factor) and by increasing the differential gain. Both effects are achievable by increasing the well number of the MQW stack from formerly 5 well (fig.2) to e.g. 10 wells as chosen in our approach.

The realised devices were characterised in the following way: The 10 Gb/s input data were generated by fast external modulation of a DFB laser using an InP based MQW electro-absorption modulator. The 3-port MZI converter was operated in contradirectional configuration as depicted in fig.1. In the present study good ER improvement capabilities up to 5.5 dB (from 7 dB to 12.5 dB) are verified for the first time at 10 Gb/s. The rise and fall times derived from the MZI output pulse pattern are about 50 ps. Fine adjustment of the strain for the 10 well structure is expected to yield polarisation insensitivity in analogy to the above described 5 well structure. The optical pulse pattern and eye diagram of a wavelength converted 10 Gb/s signal are shown in fig.5 and 6, respectively.

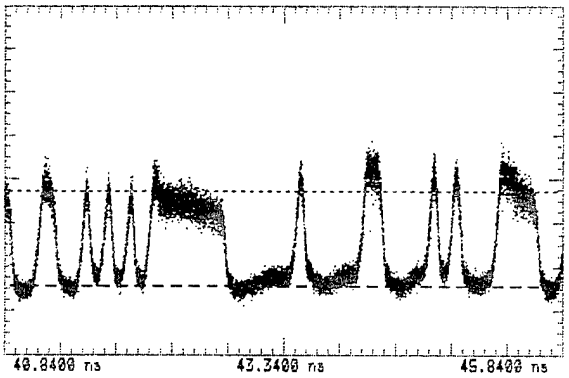


Fig.5: Pulse pattern of 10 Gb/s wavelength converted signal

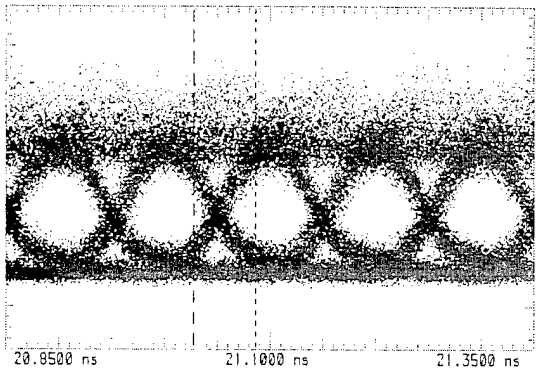


Fig.6: Optical eye diagram of 10 Gb/s wavelength converted signal

Summary:
Monolithic integrated Mach Zehnder interferometer devices have been developed for efficient wavelength conversion. The all active waveguide structure has been realised using a MQW layer stack. Optimisation for polarisation insensitivity was achieved by applying appropriate tensile strain in the quantum wells. MQW layer optimisation has been also performed for high speed (10 Gb/s) operation. To reach this goal, differential gain and confinement factor have been increased by introducing a 10 well layer stack.The decribed approach has thus proven as capable to fulfil major requirements for highly ambitious system applications.
This work was partially supported by BMBF (project 01 BP 442) and European ACTS project 043 (KEOPS).

References:

/1/ K.E.Stubkjaer et al., "Optical wavelength converters and their applications", IOOC'95,inv. paper ThB3-1,Proc.pp.54-55,Hong Kong, 1995
/2/ M. Schilling et al.: "Wavelength converter based on integrated all active 3-port Mach-Zehnder interferometer", Electron. Lett., Vol.30, No.25, 1994, pp. 2128-2129
/3/ N.Vodjdani et al. "Integrated optics all optical wavelength converters", Proc.7th.Eur.Conf.on Int.Opt. (ECIO'95), p.261
/4/ X.Pan et al "Dynamic operation of a three-port, integrated Mach-Zehnder Wavelength converter" IEEE PTL, Vol 7, pp995-997, Sept.95
/5/ W.Idler et al. "Compact monolithic wavelength converter with strong signal improve ment including chirp compression", ECOC'95, Brussels, paper We.L.1.1. (Sept.1995)
/6/ T.Durhuus et al., "Optical wavelength Conversion in SOAs in a Mach Zehnder Configuration" IEEE Photonics Technol. Lett., 1994, 6, pp.53-55
/7/ M. Schilling et al.: "Monolithic MZI based optical wavelength converter operated at 2,5 Gbit/s with extinction ratio improvement and low penalty", Proc. ECOC `94 , Firenze 1994, Vol. 2, pp. 647-650
/8/ W. Idler et al.: "Signal Quality and BER Performance Improvement by Wavelength Conversion with an Integrated 3-Port Mach-Zehnder Interferometer", Electron. Lett. Vol.31, No.6, 1995, pp. 454-455
/9/ M.Joma et al., "Polarization insensitive semiconductor laser amplifiers with tensile strained InGaAsP/InGaAsP multiple quantum well structure", Appl.Phys.Lett. vol.62 (2),pp.121-122, 1993

Monday, April 29, 1996

Poster Session

IMH 6:00 pm-7:30 pm
Independence Ballroom

Compact InP-based waveguide crossings with low crosstalk and low loss

C. van Dam, F.P.G.M. van Ham, F.H. Groen*, J.J.G.M. van der Tol†, I. Moerman‡, M.K. Smit

Delft University of Technology, Dept. of Electrical Engineering
P.O. Box 5031, NL-2600 GA Delft, The Netherlands
Phone: +31 - 15 - 2787089, Fax: +31 - 15 - 2784046

*Delft University of Technology, Department of Applied Physics

†PTT Research, Leidschendam.

‡Department for Information Technology, IMEC-University of Gent, Belgium

Introduction

Optical waveguide crossings are becoming increasingly important due to the increasing complexity of optical chips. In switching matrices [1], multiwavelength add drop filters [2] and optical crossconnects [3] worst-case paths may contain more than five or even ten crossings. In fibre-matched waveguides structures as used in lithium niobate or silica-based technology, crossings with very low crosstalk and loss can be realised [4,5]. We have found that in highly integrated semiconductor devices crossings may contribute significantly to the loss and crosstalk performance. In this paper we present the results of a series of experiments for design of high-performance semiconductor waveguide crossings.

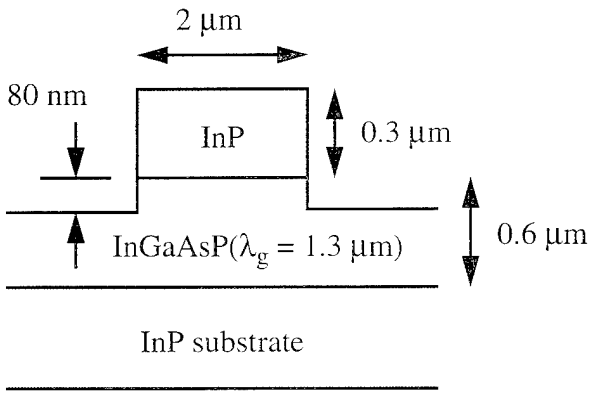


Figure 1. Schematic diagram of the used waveguide structure.

Design

We performed our experiments using a ridge-type waveguide structure as depicted in figure 1. The performance of waveguide crossings realised in this structure has been analysed using two methods. Firstly, the theory of Multiple Scattering Interaction (MSI) [6] was used in combination with a 2D Effective Index Method (EIM). From the analysis it can be found that for specific values of the intersection angle - also referred to as magic angle - the crosstalk vanishes. For the analysed waveguide structure the MSI predicts a magic angle at 10-11 degrees and one at 30-35 degrees, as depicted by dashed lines in graphs (a) and (b) of

figure 2. Secondly, a 2D Beam Propagation Method (BPM) was used for comparison. The results of this analysis are shown as solid lines in the same graphs. It can be seen from these graphs that the BPM does not predict a magic angle at 10-11 degrees. The fabrication tolerance of the magic angle was investigated by analysing the effect of a change in the width of the waveguide. A 0.2 μm change in the waveguide width results in a shift of the magic angle of 1 degree. We investigated the crossings experimentally in an interval of a few degrees around both predicted magic angles. For more accurate measurement of the excess loss five crossings were placed in series.

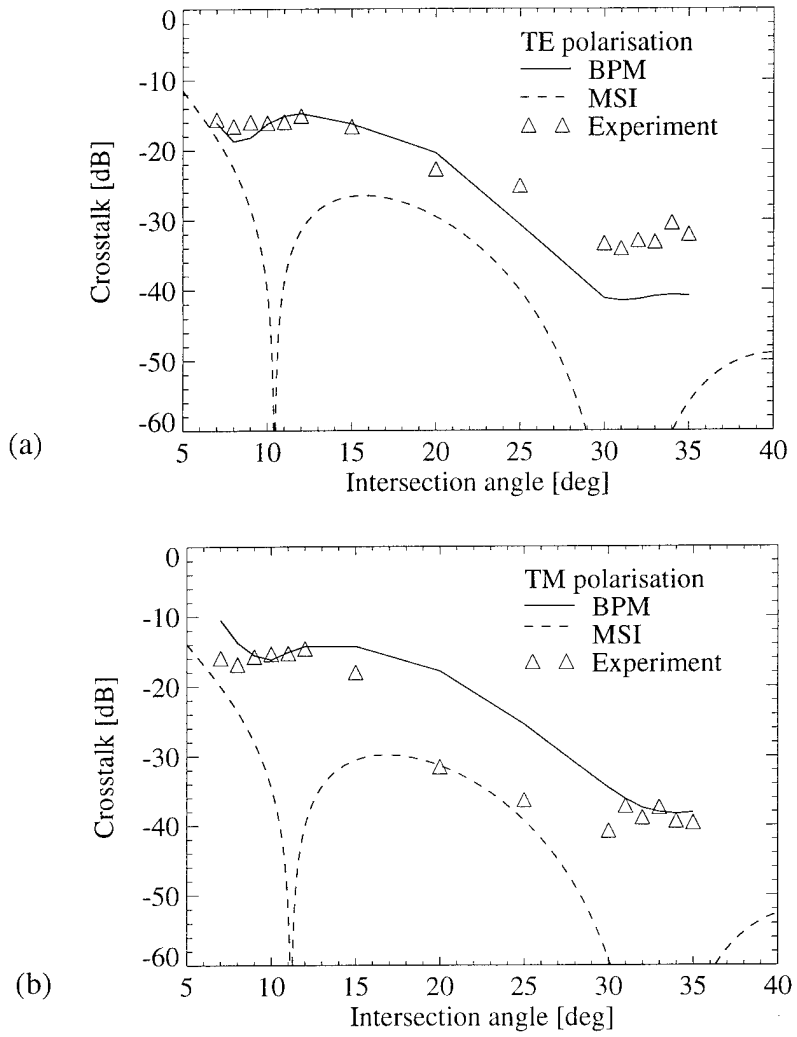


Figure 2. Crosstalk values versus intersection angles, for TE polarisation (a) and for TM polarisation (b). Lines denote predictions: 2D-BPM simulations (solid line) and theory according to [4] (dashed line).

Fabrication

Waveguide crossings have been fabricated in a MOCVD-grown InP/InGaAsP(λ_g = 1.3 μm)/ InP ridge waveguide structure. A 100 nm thick PE-CVD deposited SiNx film was used as masking layer, and waveguides were RIE etched using CH_4/H_2 to a depth of 80 nm into the guiding layer employing an etch/descum process to reduce the scattering losses [7]. Waveguide losses were measured 1.8 dB/cm for both TE and TM polarisation.

Experimental results

A Fabry-Perot laser operating at 1508 nm was used to measure the crosstalk and excess loss of the crossings. Measurement results of the crosstalk are shown in graphs (a) and (b) of figure 2 for TE and TM polarisation, respectively. Crosstalk values lower than -30 dB are measured for angles greater than 30 degrees. It can be seen that the MSI gives a good prediction of the position of the magic angles, whereas the BPM also gives a good quantitative prediction. Figure 3 shows the excess loss, which reduces to values of less than 0.3 dB for intersection angles greater than 30 degrees for both TE and TM polarisation.

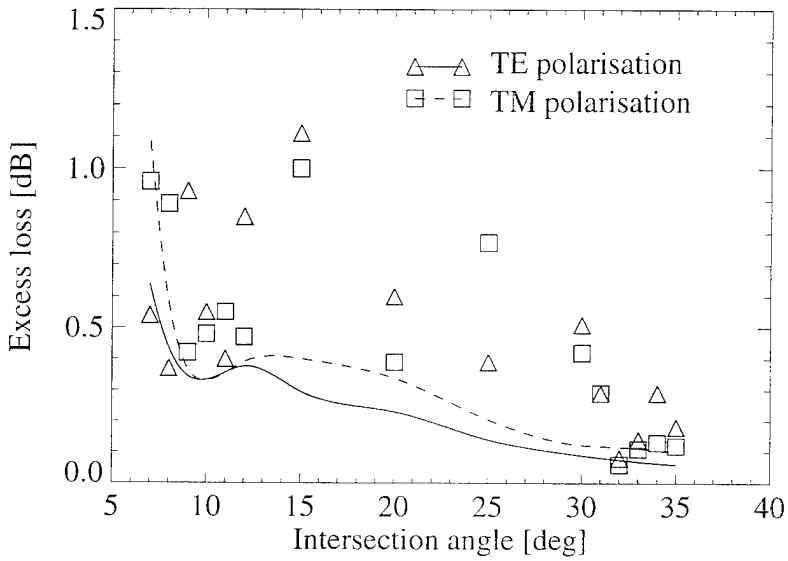


Figure 3. Excess loss of the crossings: lines denote 2D-BPM predictions.

Conclusion

Waveguide crossings with small intersection angles have been fabricated in a InP-based waveguide structure. Measurements yielded crosstalk values of less than -30 dB and excess loss values of less than 0.3 dB for intersection angles down to 30 degrees, for both TE and TM polarisation. It is shown that the MSI correctly predicts the magic angles. A 2D-BPM gives a good quantitative fit to the experimental results. Further improvement of semiconductor waveguide crossing performance will gain importance with increasing complexity of circuit designs.

References

[1] L. H. Spiekman, A. A. M. Staring, C. van Dam, E. J. Jansen, J. J. M. Binsma, M. K. Smit, and B. H. Verbeek, "Space-switching using wavelength conversion at 2.5 Gb/s and integrated phased array routing", In *Proc. 21st Eur. Conf. on Opt. Comm. (ECOC '95)*, pp. 1055-1058, Brussels, Belgium, September 17-21 1995.

[2] K. Okamoto, K. Takiguchi, and Y. Ohmori, "16-channel optical add/drop multiplexer using silica-based arrayed-waveguide grating", *Electron. Lett.*, vol. 31, pp. 723-724, April 1995.

[3] G. Depovere, M. Tomesen, R. v. Gils, N. Wauters, D. Vercauteren, and P. Demeester, "Laboratory demonstration of a 2.5-GBit/s SDH-compatible optical cross-connect network", In *Proc. 20th Eur. Conf. on Opt. Comm. (ECOC '94)*, pp. 571-574, Firenze,

Italy, September 25-29 1994.

[4] S. S. Gevorgyan, and A. B. Hovsepyan, "The optical power distribution and scattering losses in symmetrical channel waveguide X-junctions", *Opt. and Quant. El.*, vol. 23, pp. 649-656, January 1991.

[5] G.A. Bogert, "Ti:$LiNbO_3$ intersecting waveguides", *El. Lett.*, vol. 23, pp. 72-73, January 1987.

[6] N. Agrawal, L. McCaughan, and S. R. Seshadri, "A multiple scattering interaction analysis of intersecting waveguides", *J. Appl. Phys.*, vol. 62, pp. 2187-2193, September 1987.

[7] Y. S. Oei, C. van Dam, F. P. van Ham, L. H. Spiekman, B. H. Verbeek, F. H. Groen, E. G. Metaal, and J. W. Pedersen, "Improved RIE technique for controlled roughness and anisotropy in InP-based devices", Procs. 18th State-of-the-art Program on Compound Semiconductors (SOTAPOCS XVIII), May 16-21, Honolulu, U.S.A., Volume 93-27, pp. 134-141, 1993.

Light propagation in a system of bended singlemode waveguide and straight multimode waveguide with higher refractive index

S.M.Loktev, N.M.Lyndin, V.A.Sychugov, B.A.Usievich.

General Physics Institute of Russian Academy of Sciences, Vavilov street 38, 117942, Moscow, Russia, Phone:(095) 132-81-13, Fax: (095) 135-02-70

Introduction.

Waveguide structure, consisting of two coupled waveguides was extensively studied [1-2]. Nowadays many practically useful integrated optics devices are based on it. Recently this structure attracted the attention of researchers again because several new possibilities of its usage were found. The subject of investigation is a pair of waveguides: singlemode waveguide with low refraction index and multimode waveguide formed by layer with high refraction index. The practical realization of this structure is a singlemode fiber with the side polished core and a waveguide layer coupled with this fiber. In recent times some very interesting optical devices (filtering, lasing) were realized on the basis of this system [3-6]. Nevertheless the details of light transmission through this structure remain non completely understood up to now. The aim of this work is theoretical and experimental study of the light propagation in the structure taking in to account variation of the coupling coefficient with distance. We consider propagation for TE-modes.

Theoretical part and calculation results.

Usually real structures of two coupled waveguides have the transition regions at the input and output where the coupling coefficient varies from zero to maximum value (fig. 1a). Transmission of the structure is ratio between the output radiation power and the input radiation power in singlemode waveguide: $T=P_{out}/P_{in}$. Let us begin with simpler structure: single mode planar waveguide with low refractive index and multimode planar waveguide with high refractive index (fig.1b).

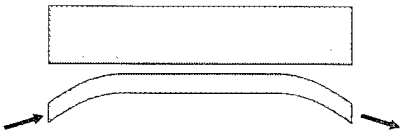


Figure 1a.

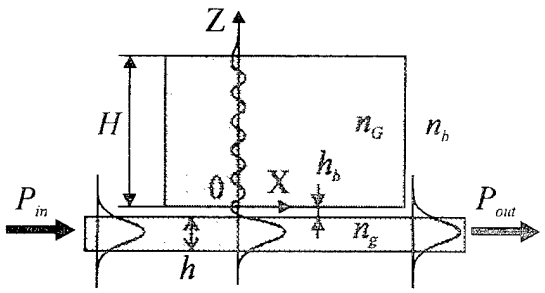


Figure 1b.

Structure parameters are n_G =2,2; n_g =1,47; n_b =1,46; H=4 μm; h=2 μm, buffer layer thickness h_b=2 μm, $l=L_c/2$=972 μm at λ=0,8 μm (L_c - coupling length). There are two main cases:

1. Modes in these waveguides are in resonance. In this situation two modes of whole structure ("symmetrical" and "antisymmetrical") will be excited with approximately equal amplitudes (see fig 2 curves 1,2). During their propagation along the structure phase difference between these modes arises due to different effective refractive indices that leads to energy exchange between the waveguides. When the distance l equals $L_c/2$ most of light power is transferred to the thick waveguide and scattered at its end which corresponds to a dips in the transmission characteristics (see fig. 2b).
2. Modes in the waveguides are far from resonance. In this case only one mode of the structure is important (see fig.1b) and great part of the energy propagates

in the singlemode waveguide. Overlap integral of this mode and the mode of the singlemode waveguide at the input-output of the structure is near unity which provides 96-97% light transmission. Let us define it as "transmission" mode (fig.5 curve 1)

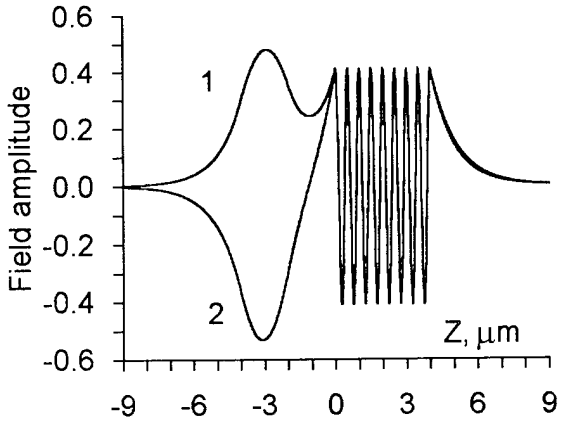


Figure 2

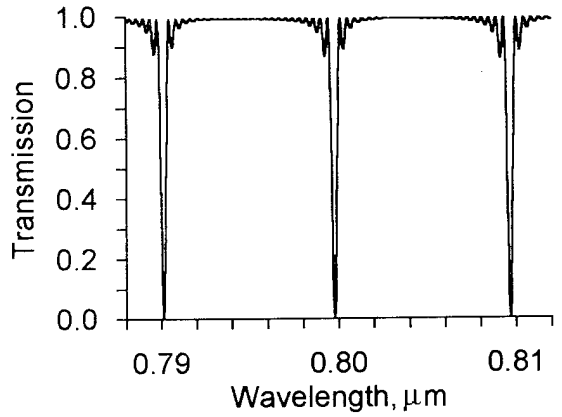


Figure 3

The analysis of calculation results (fig.3) gives, that the distance between the dips is determined by the following formula [4]:

$$\Delta\lambda = \frac{\lambda^2}{2H\sqrt{n_g^2 - n^2}}, \qquad (1)$$

where $n = (n_a^* - n_s^*)/2$, and n_s^*, n_a^* - effective refractive indices of "symmetrical" and "antisymmetrical" modes respectively.

The width of these dips is determined by the coupling coefficient that depends on buffer layer thickness. The interference of structure modes with lower orders (total energy about 3-4%) leads to small variations inside the transition region.

Now we will consider the structure with the smooth transition from separate to coupled waveguides (see fig.1b). For calculations of the transmission $T(\lambda)$ we used the cross section method where the buffer thickness difference at the adjacent sections was 0.01 μm and structure parameters were believed constant at each section. The thickness of the buffer layer at the structure input-output was equal 5 μm so that the coupling coefficient was practically negligible. The length of the sections was chosen so that the parabolic dependence of buffer layer thickness along the structure was provided. The whole structure length was equal 10 mm and the equivalent bend radius of the singlemode waveguide R was approximately 1 m.

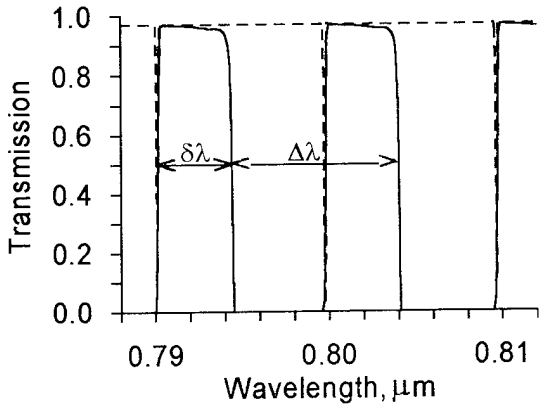


Figure 4a

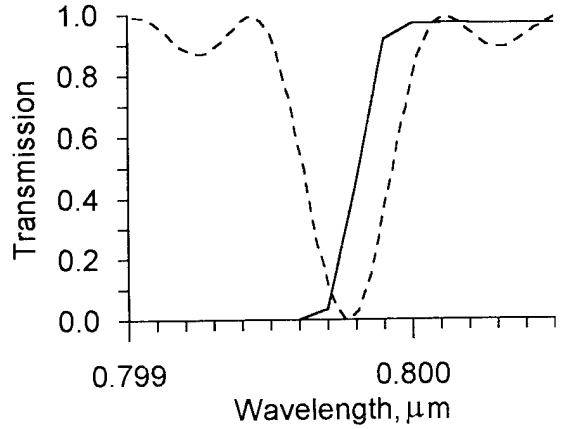


Figure 4b

The wavelength dependence of transmission for this structure is shown in fig.4a,b for two cases:

1) Minimum value of buffer layer thickness h_b is 1 μm. The dependence T(λ) (dashed curve) is analogous to the dependence for the structure with the constant buffer layer thickness, however width of the dips is less and determined by the large (h_b=5 μm) buffer layer thickness at the structure input-output.
2) Minimum value of buffer layer thickness is h_b=0 μm and the minimum thickness of the singlemode waveguide h_{min} equals 1 μm (that is, waveguide layer is partially removed). In this situation T(λ) appearance (solid curve) changes completely. The transmission curve consists of equidistant peaks.

We should note that the peak width $\delta\lambda$ increases with the thickness of multimode waveguide and at H=70-80 μm becomes close to $\Delta\lambda$ ($\Delta\lambda$ is spectral distance between adjacent peaks).

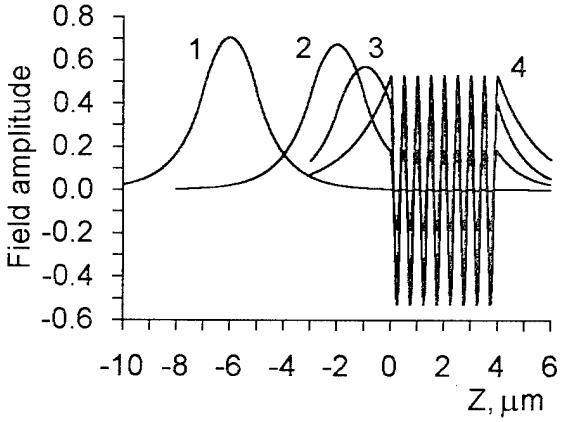


Figure 5

The transformation of "transmission" mode field distribution along the structure (without singlemode waveguide in its middle i.e., h_{min}=0 μm) is shown on fig.5. Wavelength was chosen to be 0.8 μm to ensure maximum transmission (Fig. 4a, 4b).

Experimental results.

Test structure for experimental investigation consists of side polished singlemode fiber at wavelength 633 nm and liquid multimode waveguide with refractive index n_G=1.50 (see Fig.6).

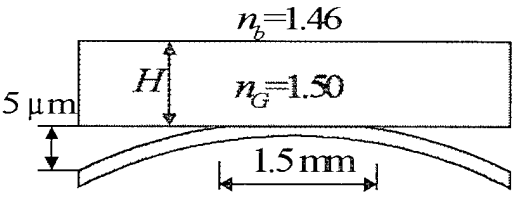


Figure 6

Fiber core was partially removed so with air on the its top the transmission was less then 60% and 10% for TE and TM polarization respectively. A polarization controller was placed at the input fiber. Micropositioner was used to change multimode waveguide thickness H. This approach [7] is simpler for interpretation of the results then the spectral one.

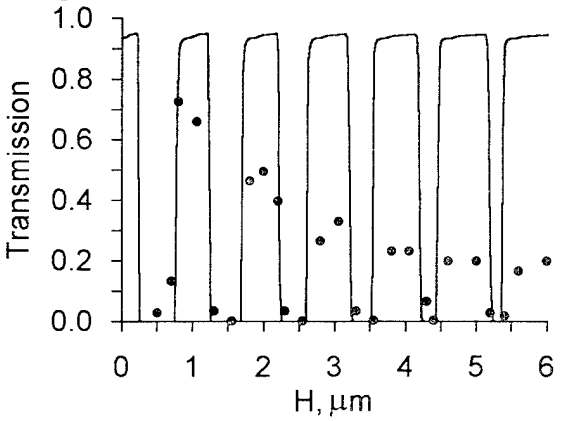


Figure 7a

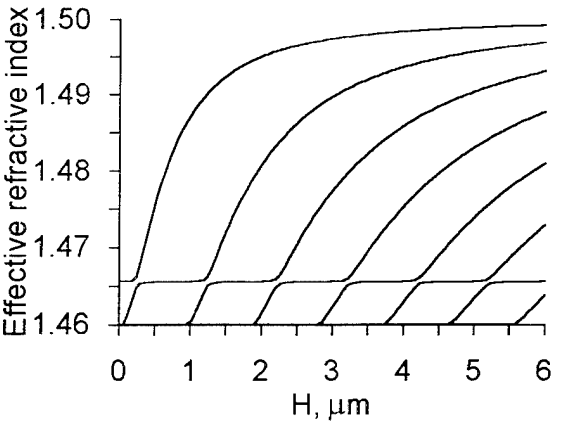


Figure 7b

We present results of measurements (dots) and PC simulation (solid curve) for TE polarization in fig.7a. In the middle of the structure the thickness of singlemode waveguide reduces so in this part of the structure total number of modes decreases by one. Outside the transition intervals of *H* "transmission" mode has maximum mode order and cuts off in the middle of the structure. In the regions of transparency "transmission" mode is not the mode of highest order and it propagates from the beginning to the end of the structure. Dispersion curves (see fig. 7b) calculated for the structure with buffer layer thickness h_b=1.5μm illustrate this fact. We suppose that the diminishing of the peaks amplitudes with thickness of multimode waveguide is a result of small radius of curvature of side-polished fiber (~30mm) and small size of its core (less than 3μm). Hence conditions for adiabatic transformation of "transmission" mode and its channeling are violated. Despite the fact that our calculations were made for planar waveguides, there is a good agreement of peaks widths and their positions with experimental results.

Conclusion

We investigated the system of two coupled waveguides, one of them was singlemode with small index change and the other was multimode with large index change. Distance between the waveguides was varied according to bend of thin waveguide. We found that in the large wavelength range light propagates in the structure in the form of "transmission" mode that hold most of the energy in the singlemode waveguide at the ends of the structure and almost completely transferred it into the multimode waveguide in the middle of the device.

The proposed structure seems to be very promising for employing in waveguide laser. Active layer of the laser can be multimode slab waveguide which is coupled with optical fiber, channel or singlemode slab waveguide.

Acknowledgments

Authors acknowledge the financial support of RFBR, Grants N 95-02-06173 and N 94-02-03648.

References

1. Parriaux O., Gidon S., Kuznetsov A.A. Appl. Optics, 20, 2420, (1981)
2. Peschel U., Peschel T., Lederer F. Proceedings 7th European Conference on Integrated Optics, April 3-6, 1995, Delft, The Netherlands, p.161.
3. Mc. Callion K., Johnstone W., Thursby G. Electron. Lett., 28, 410, (1992)
4. Mc. Callion K., Johnstone W., Fawcelt G. Optics Letters 19, 542, (1994)
5. Gloag A., Langford N., Mc. Callion K., Johnstone W. Optics Letters 19, 801, (1994)
6. Das A.K., Ganguly A.K. Optics Letters 18,2110,(1994)
7. Svakhin A.S., Sychugov V.A. Zhurnal Tekhnicheskoy Fiziki, 57, 1191, (1987), in Russian

ULTRA HIGH CONFINEMENT WAVEGUIDES FOR VERY LARGE SCALE INTEGRATED OPTICS (VLSIO) WITH THREE DIMENSIONAL PACKAGING

Lawrence C. West, Integrated Photonic Systems Inc., PO Box 717 Clarksburg, NJ 08510 (609) 259-1654; Charles W. Roberts, Emil C. Piscani, Integrated Photonic Systems Inc., 1325 Campus Parkway, Suite 214, Wall Township, NJ 07719 (908) 919-1479

INTRODUCTION:

By use of very high index ratios between the cladding and guide, Ultra High Confinement (UHC) waveguides[1] can be created, leading to compact devices and sharp bends. Furthermore, with the use of diffractive optics, these Very Large Scale Integrated Optical (VLSIO) circuits[2] can be interconnected in three dimensional stacks with high density connectivity. A non-uniform grating coupler between a compact waveguide mode and a large Gaussian profile single mode beam is designed and tested. This coupler is a critical component for interconnects, allowing efficient coupling between various beam shapes and compact devices. The size of UHC integrated optical devices is 10 to 100 times smaller per cubic wavelength than present waveguides and resonators, resulting in much higher speed and lower power. These UHC waveguides and components are analyzed using 3D Vector Field Finite Element Methods and microwave scaled experiments.[3]

ULTRA HIGH CONFINEMENT (UHC) WAVEGUIDES:

In spite of the offered promise of high density integration of optical components, two-dimensional lateral connectivity to date has nowhere approached that of VLSI electronics. We show that by use of high refractive index ratios between guide and cladding, Ultra High Confinement (UHC) waveguides can be created.[1] Ultra High Confinement is defined here as confinement of light in a waveguide with an effective cross-section less than a tenth of a squared free-space wavelength or a resonator volume less than a cubic free-space wavelength (see Fig. 1). Because of the high confinement, a full vector field analysis of the mode is essential for accuracy. A practical implementation of an UHC waveguide in the mid-infrared region uses Ge with refractive index 4.0 on GaAs with refractive index 3.27. The Ge waveguide can be deposited on top of GaAs substrate via UHV E-Beam evaporation. The Ge/GaAs UHC waveguide geometry can scale to the near-infrared as lithography resolution improves to 0.1 μm with the use of GaAs with refractive index 3.6 as the waveguide on AlAs with refractive index 2.9.

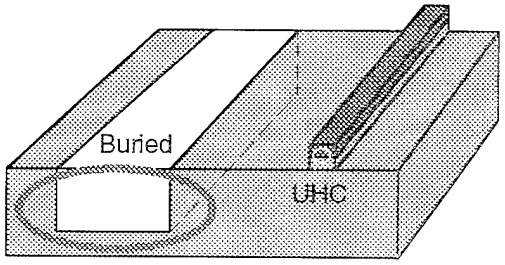


Figure 1. Note UHC waveguides have a mode area (indicated by ellipse) 20 times smaller than the typical buried waveguide.

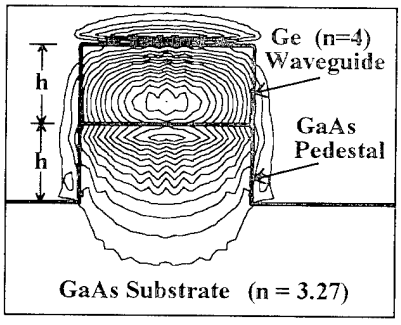


Figure 2. An UHC pedestal waveguide with vertical mode component.

Using the numerical analysis[3] and microwave experiments we show that a large index ratio confines the light into a waveguide with dimensions as small as fraction of the wavelength of light. Figure 2 shows the electric field profile for the vector component in the vertical direction derived numerically using a custom (EMFlex) finite element method (FEM) time domain program. An approximate mode was generated and propagated down the guide until steady state was achieved. The effective index of

the mode was calculated from the linear phase shift with distance. This procedure was repeated for several ratios of waveguide height to free space wavelength. The new UHC waveguide properties are verified with microwave scaled experiments. Waveguides are created with dielectric materials in the 4 GHz microwave region with the same dielectric constant as Ge (4.0) and GaAs (3.27). Identical propagation experiments are performed using FEM and real microwave waveguides. The effective index, n_{eff}, measured in both cases. Note the waveguide size scaling from the microwave to infrared optics is a perfect scaling. The results are shown in Figure 3. These results show good confinement (n_{eff} > 3.27) when h/l is greater than 0.170. In practice, we use h/l between 2.0 and 2.1.

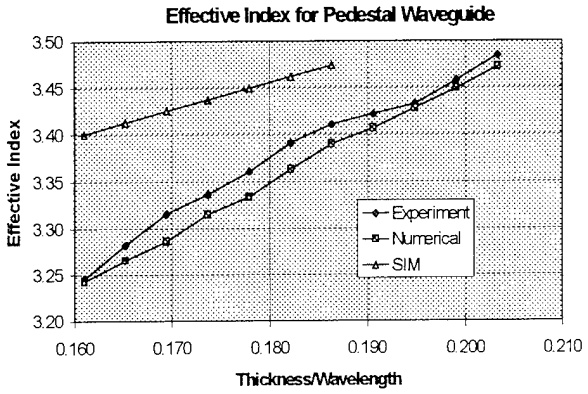


Figure 3. The comparison of FEM, Theory, and Exp.

3D COUPLING INTO UHC WAVEGUIDES:

Coupling into the UHC waveguides is a major practical obstacle to their fabrication and testing. The usual buried waveguide mode has relative large size of one to three free space wavelengths that allows direct output from a cleaved edge. In contrast, the UHC waveguide has a dimension that is about 0.2 by 0.3 free space wavelengths, which does not allow efficient edge coupling. Instead, the UHC waveguide for 10 μm light is first adiabatically tapered from 3.7 μm wide rectangular mode to 13.5 μm wide slab mode over a length of 40 μm with 98 % efficiency. This wide mode is then scattered at a 21 degree angle into the substrate with a non-uniform, but periodic grating coupler. The scattering strength of the coupler teeth is continuously increased as the light propagates so as to radiate a Gaussian intensity profile with a diameter of 120 μm. The angle in the substrate is greater than the total internal reflection angle to ensure no radiation to the air side of the coupler. The highly elliptical spot size is then coupled to a round Gaussian profile beam with a diameter of 120 μm by use of an aspheric off-axis elliptical four level Fresnel lens on the back side of the substrate. The 120 μm diameter mid-infrared beam can propagate 2 mm in free space without diffracting, allowing wide tolerance in spacing of the chip stack and allowing over 3000 couplers/cm^2 to be created.

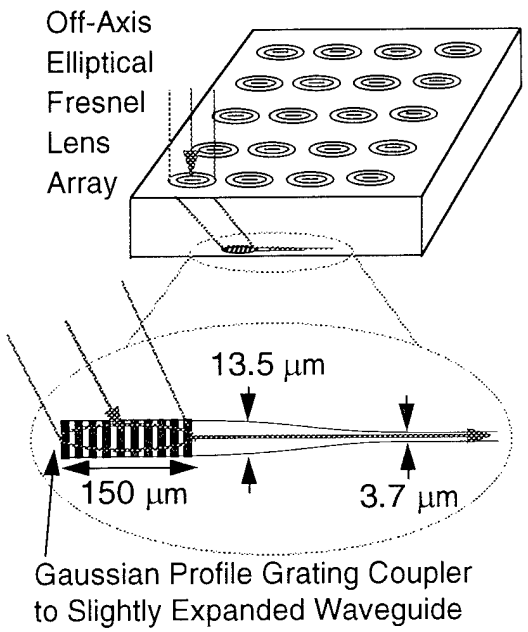


Figure 4. Coupling to UHC waveguide with a normal incidence 120 mm diameter beam.

The large 10 μm wavelength allows periodic but non-uniform grating couplers to radiate a profile better matched to a Gaussian for improved efficiency. The design uses 33 teeth with a 4.5 μm period and two masks with two etch depths of 0.2 μm and 0.45 μm for sufficient range of tooth coupling. The design starts with measure of single tooth scattering coefficients for transmission, reflection, and scatter, including phase shifts. The fully assembled Gaussian coupler is then modeled with EMFlex in two dimensions for a slab waveguide. The output of this coupler was

measured for Gaussian diameter and overlap. The final design had a Gaussian overlap into the desired beam of 85 %. The losses were from scatter to air, backwards scatter down the waveguide, backwards scatter into the substrate, uncoupled transmission in the waveguide, and non-Gaussian components of the scattered beam. Each of these scatter losses are less than a few percent. The coupler uses teeth with a width near that of a half wave in the waveguide because the 1.5 μm width simplifies fabrication and has minimum back scatter down the waveguide (see Figs. 5, 6 and 7).

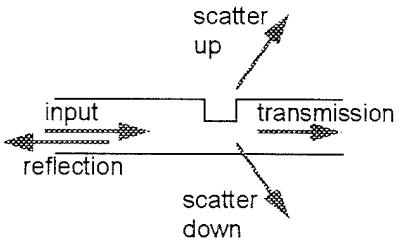


Figure 5. Single tooth model for calculating coupling coefficients.

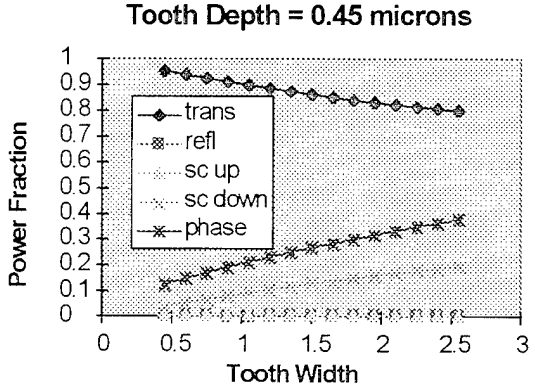


Figure 6. Single tooth transmission, phase shift, and scatter to the substrate for a 0.45 μm depth.

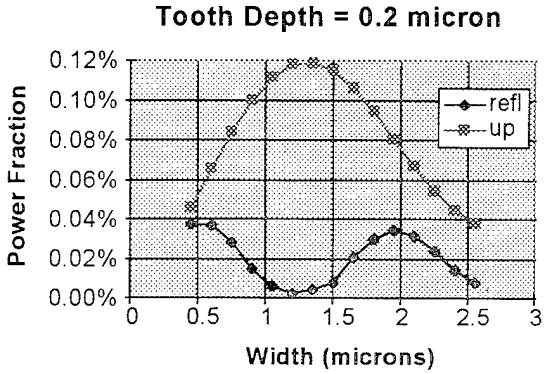


Figure 7. Single tooth reflection and scatter to air expanded for the 0.2 μm deep tooth.

VERY LARGE SCALE INTEGRATED OPTICS (VLSIO):

One of the most significant advantages of the high index of refraction is the ability to create waveguide bends with a radius of less than one free space wavelength. FEM modeling and microwave experiments show that a right angle bend with a radius of 7.5 μm for 10 μm light has a 90% efficiency single mode transmission. This tight bend allows dense components for VLSIO.

The UHC waveguide has several advantages in opto-electronic device improvement due to its small size. We will show the UHC waveguides are capable of creating resonators with volumes less then one tenth of a cubic free space wavelength, 1000 times smaller than VCSELs. The 20 times smaller beam diameter improves gain and other optical properties by a similar factor. The capacitance of the devices is also much reduced, improving the bandwidth of opto-electronic devices to near 1 THz in frequency response. Because of lithography resolution, near-infrared use of UHC concepts may not be viable until the availability of 0.1 μm linewidth lithography.

REFERENCES:

[1] A. D. Chaudhari, L. C. West, C. W. Roberts, and Y. Li, "Highly compact optical waveguides with a novel pedestal geometry," *IEEE Phot. Tech. Lett.*, vol. 7, pp. 526-528, 1995.

[2] L.C. West, C. W. Roberts, J. P. Dunkel, "Manufacture of Very Large Scale Integrated Optics (VLSIO) with Three Dimensional Packaging," *Proceedings of the Conference on Manufacturing Process Development in Photonics*, Huntsville, AL, November 1-2, 1994

[3] Wojcik, G., Mould, J. Jr., West, L. C., "Time-Domain Finite Element Modeling of 3D Integrated Optical Devices," *Integrated Photonics Research Tech. Digest*, W.D.1. Optical Society of America, eds., pp. 112-115, 1993.

Structural phase diagrams of proton exchanged waveguides on Z- , X- and Y-cuts of $LiNbO_3$

Yu. N. Korkishko and V. A. Fedorov

Moscow Institute of Electronic Technology (Engineering University), Chemistry Department,
103498 Moscow, Zelenograd, RUSSIA
Tel.(007-095) 532 99 62, Fax. (007-095) 530 22 33
e-mail: korkishk@chem.miet.zgrad.ru, fedorov@chem.miet.zgrad.ru

M.P. De Micheli

C.N.R.S.- Université de Nice Sophia Antipolis, Laboratoire de Physique de la Matière Condensée
06108 Nice Cedex 2, FRANCE
Tel.(33) 93 52 98 82 , Fax.(33) 93 52 98 08, e-mail:demicheli@naxos.unice.fr

Introduction. The proton-exchange (PE) technique[1] has been of considerable interest recently for the fabrication of integrated optics devices in lithium niobate and lithium tantalate. During the past ten years, a lot of attempts have been made to characterize the PE process in $LiNbO_3$. However, in the known reports, several fundamental issues. have not been addressed, the published structural investigations of PE $LiNbO_3$ waveguides being uncompleted and restricted to particular fabrication process.

Unfortunately, the results obtained by Rice and Jackel [2,3] for powders cannot be applied directly to the single crystalline waveguides. Indeed, the strains induced by the substrate-guide interface substantially modify the proton concentration and the crystalline structure of the exchanged layer.

This work allowed identifying different crystallographic phases of the proton exchanged layers in $LiNbO_3$, considering that there is a phase jump when gradually varying the proton concentration in the exchange layer, causes a sudden variation of the cell parameters, even if the crystallographic system is conserved [4,5]. Such approach allowed us to identify and describe different phases in $H_xLi_{1-x}TaO_3$ waveguides [6,7]. The most interesting for waveguide fabrication is that most of these discontinuities and phase jumps can already be seen on a rather simple diagram, which we shall call the structural phase diagram, where the index increase Δn_e is plotted as a function of the strain normal to the substrate surface ε''_{33}. We shall present these diagrams for the different useful orientations of $LiNbO_3$.

To realize the PE waveguides, one can use either a simple exchange, varying the temperature and the acidity of the bath and the duration of the exchange to modify the parameters of the waveguide, or one can use a two step process, where the exchange is followed by annealing whose duration and temperature further modify the waveguide parameters.

Direct exchange. In order to control the acidity of the melt, it is important to work in conditions where the used product are stable. This restricts the number of possible acids, and to vary the bath acidity on the large scale, we used two kind of melts: (i) benzoic acid (B.A.) melted at 300°C in sealed ampoule whose acidity can be reduced by adding up to 5% of lithium benzoate (L.B.); (ii) glycerine bath around 200°C, whose acidity can be increased by adding $KHSO_4$ (up to 25 g/l) and decreased by adding LiCl (up to 10 g/l). Glycerine solution containing 4.5 g/l $KHSO_4$ have an acidity similar to that of the pure benzoic acid melt.

The obtained planar waveguides were than characterized using a standard prism coupling set-up to measure the modes effective indices at 633 nm and the extraordinary refractive index profiles were reconstructed using the IWKB technique [8]. To improve the precision, the surface increments Δn_e were determined for each sample as the average between the IWKB value and the value calculated using the K.S Chiang method [9] .

To investigate the crystal structure we recorded rocking curves for different planes using a double crystal X-ray diffractometer DRON-3 (Cu $K\alpha_1$ radiation).

The six components of the strain tensor in the surface-layer structures can then be extracted from the system of 2N-1 equations determined by analyzing the rocking curves obtained from N different planes [10] (with the condition N>3). This leads to rather complicated calculations, but a lot of important information can already be obtained from the observation of ε''_{33} , the strain perpendicular to the substrate surface, which is directly deduced from the rocking curves , measuring the angular distance $\Delta\theta_{hkl}$ between the substrate peak and exchange layer peak: $\varepsilon''_{33} = -\Delta\theta_{hkl} \cdot ctg\theta_{hkl}$ (Fig.1). In most cases we observed that in PE $LiNbO_3$ waveguides on X-, Y- and Z-cuts the in- plane deformations ε''_{11} , ε''_{22} and ε''_{12} are negligible (here the axis x_3'' is normal to the plane of

the interface and the planar orthogonal axes x_1'' and x_2'' define this plane and are chosen arbitrarily to form together with x_3'' a right-handed orthogonal set of axes).

In Fig.2 we plotted the surface extraordinary index increase as a function of this strain for Z-cut and X-cut substrates. Note, that $H_XLi_{1-X}NbO_3$ with equal composition on X- and Y-cuts gives similar deformations ε''_{33} [4-6] and phase diagram for Y-cut $LiNbO_3$ is similar to one for X-cut except the regions where the waveguides can not be obtained due to surface damage . We see that five different crystalline phases (α and β_1 to β_4) can be obtained on Z-cut $LiNbO_3$ and four phases (α and β_1 to β_3) on X-cut by direct exchange. Only two phases β_1 and α can be realized by direct exchange on Y-cut. Future increasing of proton concentration leads to surface damage.

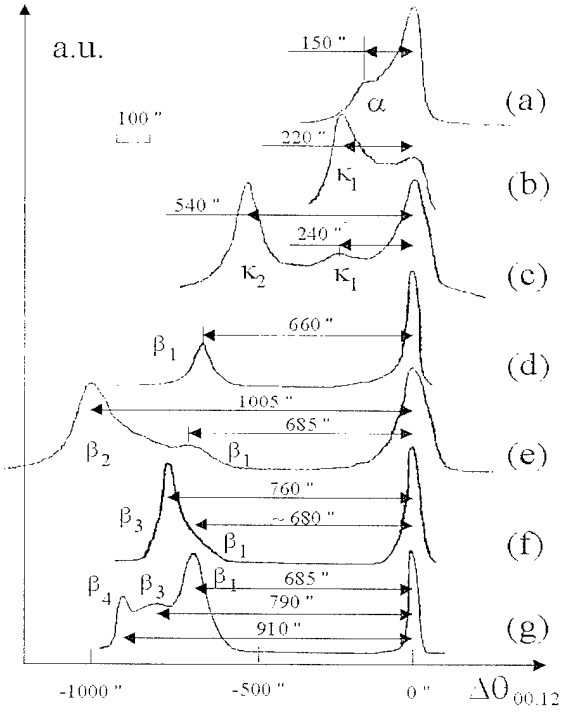


Fig.1. Typical rocking curves for PE Z-cut $LiNbO_3$ structures prepared under conditions, corresponding to formation of different $H_XLi_{1-X}NbO_3$ phases: (a) PE: B.A.+ 2.6% L.B., T_{PE}=300° C, t_{PE}=25 h; (b) PE: Glycerin + $KHSO_4$ (3 g/l) , T_{PE} =220° C, t_{PE}=25 h. Annealing - T_A=330° C, t_A =80 h; (c) PE: Glycerin + $KHSO_4$ (3 g/l) , T_{PE} =220° C, t_{PE}=25 h. Annealing - T_A=330° C, t_A=30 h; (d) PE: B.A.+ 1.0% L.B., T_{PE}=300°C, t_{PE}=10 h; (e) PE: B.A., T_{PE} =300° C, t_{PE}=1 h; (f) PE: Glycerin + $KHSO_4$ (10 g/l) , T_{PE} =220° C, t_{PE}=25 h; (g) PE: $NH_4H_2PO_4$ melt, T_{PE} =230° C ,t_{PE}=3 h.

PE $LiNbO_3$ waveguides can be assigned to two families: the low concentration family and the high proton concentration family. The phases κ_1 and κ_2 and can be achieved by annealing only.

Low proton concentration layers. The low proton concentration as exchanged layers give graded index profile waveguides with maximum index increase lower then 0.03. Crystallographic parameters also varies gradually but remain very similar to those of substrate: ε''_{33} is hardly measurable on the rocking curves. The crystallographic phase which correspond to the α-phase identified by C.Rice and J.Jackel[2,3] , can be obtained using the low acidic bath such as benzoic acid melts at 300°C and containing at least 2.5% of lithium benzoate or by annealing. The corresponding waveguides are very low loss, and according to very small modification of the crystalline cell one can expect that the electro-optic and the non-linear coefficients are not or very little affected by the exchange[11].

High proton concentration layers. In this case, the situation is more complicated, and we see in Figure 1 that 4 different phases β_1 to β_4 have been identified on Z-cut $LiNbO_3$. Only the β_1 -phase can be present alone on top of the structure, the exchanged layer is then homogeneous and the index profile is step like. The β_2 and β_3 phases can be found only in combination with β_1 phase, organized as a sublayers, for the rocking curves presenting two peaks with more or less signal coming a graded or disordered intermediate area (Fig.1). The β_4 phase can be found only in combination with two lower proton concentrated phases β_3 and β_1 . The exchanged layer is then stratified in two or three homogeneous layers presenting two or three different indices, which has been verified by slowly removing the surface layer by successive polishing.

Note, that stress-free lattice constants **a** and **c** in the β_2- and β_1 -phases are so, that in the β_2-phase $\Delta c/\Delta a > 1$, and sufficiently larger than it in β_1-phase, where $\Delta c/\Delta a < 1$ [12], and the strained states realized in waveguides on Z- and X-cuts are quite different (Fig.2): in PE layers on X-cut ε''_{33} (β_2 -phase) < ε''_{33} (β_1 -phase) and on Z-cut : ε''_{33} (β_2-phase) > ε''_{33} (β_1- phase). This leads to rather unexpected situation when layer with larger proton concentration exhibits the lower deformation ε''_{33} on X-cut (Fig.2). However, the larger deformation ε''_{33} on Z-cut corresponds to larger proton concentration (Fig.2).

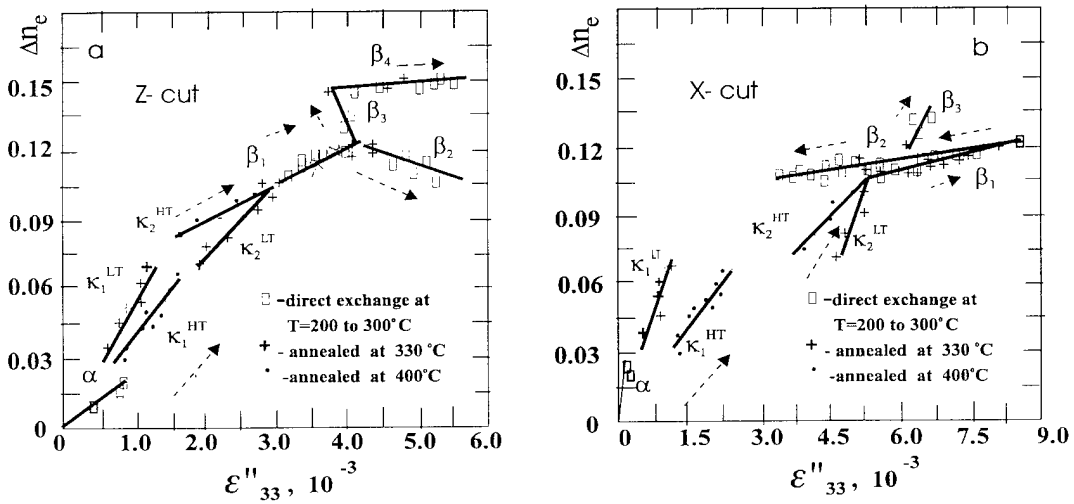


Fig. 2. Phase diagrams of $H_xLi_{1-x}NbO_3$ on Z⊥ (a) and X⊥ (b) substrates. They give the dependence of the index variation Δn_e measured at $\lambda = 632.8$ nm versus the deformations ε''_{33} normal to surface plane. The arrows show the directions in which proton concentration increases.

In each of these phases the relationship between ε''_{33} and Δn_e is linear but with very different parameters.

When the exchange layer is a pure β_1 -phase, the -O-H absorption spectra present only one sharp polarized peak around 3505 cm^{-1} , but in other three phases we could observed a broad absorption band centered at 3240 cm^{-1} which is the signature of randomly distributed protons in the crystal which might induce instabilities or interfere with the properties of the waveguide.

As shown in Table 1, using Z-cut substrates, one goes from β_1 to β_4 -phase by increasing the acidity of the melt.

Table 1. PE conditions to realize different $H_xLi_{1-x}NbO_3$ phases.

Phase	Lithium Benzoate in Benzoic acid melt (300° C)	$KHSO_4$ in glycerine	Others
α	>2.5 %		
β_1	1 to 2.5 %		stearic acid, oleic acid
β_2	0%	0 to 4 g/l	
β_3		8 to 15 g/l	cinnamic acid
β_4		↑ 20 g/l	phosphoric, pyroposphoric acids, ammonium dihydrophosphate

We were able to observe that the propagation losses which are higher than 1 dB/cm than the β_2 -phase is present, are in the order of 0.5 dB/cm only in the β_1 -phase. One has also to expect very different electro-optic and nonlinear properties of these waveguides. This possibility of having waveguides presenting the same index profile but with very different crystalline structure is responsible for great variety of appreciation's concerning PE waveguides one can find in literature of the past ten years.

Influence of annealing. Another important fabrication parameter of PE waveguides is the annealing. Actually, most of the published results were obtained using heavily annealed PE waveguides, whose index profile indicates that they are in the α -phase. During the annealing, the sample is heated up to temperature generally higher than the exchange temperature. If the annealing is long, the main effect of the temperature increase is to increase the mobility of the protons which diffuse deeper in the crystal, lowering the proton concentration. It is than possible by annealing either to involve in a given phase or to go from a high concentration phase to a low concentration phase.

For example, starting in the β_2 -phase one can reach the β_1 -phase. Under certain annealing conditions the anomalous refractive index increasing have been observed [13].

By further annealing at the temperatures up to 330°C we were able to observe two layers in the crystallographic phases [4,5] we call here as κ_1^{LT} and κ_2^{LT}- phases (low temperature modifications) which cannot be observed by direct proton exchange. By annealing at the temperatures above 380°C the high temperature modification of these phases we call κ_1^{HT} and κ_2^{HT} (high temperature modifications) were observed [4,5]. Note, that the phase transition $\kappa_1^{LT} \rightarrow \kappa_1^{HT}$ is not sharp and after annealing at 350°C an intermediate state was realized.

Fig.2 shows, that in contrast to κ_1 -phase, where $\varepsilon''_{33}(\kappa_1^{LT}) < \varepsilon''_{33}(\kappa_1^{HT})$, the low temperature κ_2 -phase characterized by larger deformations on both X- (Y-) and Z-cuts: $\varepsilon''_{33}(\kappa_2^{LT}) > \varepsilon''_{33}(\kappa_2^{HT})$. The κ_2 phases can be found only in combination with κ_1 . Further annealing leads to disappearing of κ_2 -phase. The associated waveguides also present graded index profiles with surface index increasing ranging between 0.03 and 0.07 and quite important mode coupling and propagation losses (in the order of several dB/cm). During the future annealing, a layer in the α -phase forms at the interface with the substrate, and the κ_1 -phase progressively disappears to let place to a high quality pure α -phase layer, similar to layers produced by direct exchange.

The plot Δn_e on Δn_o obtained for annealed PE waveguides clear exhibits the discontinuity around $\Delta n_e = 0.03$ (Fig.3), corresponds to $\kappa_1 - \alpha$ phase boundary. [14]

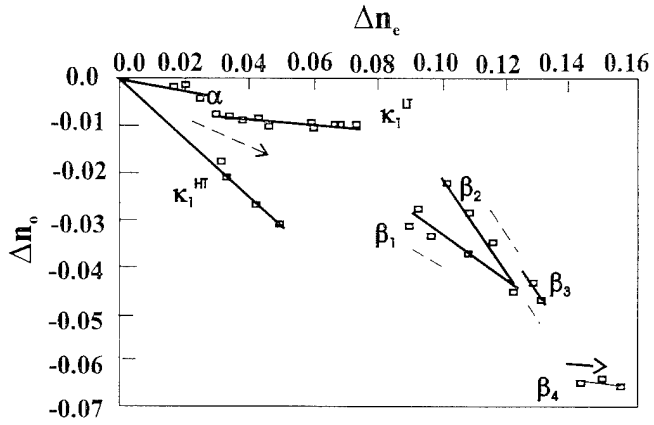


Fig.3. The plot Δn_e versus Δn_o for different $H_xLi_{1-x}NbO_3$ phases. The arrows show the directions in which proton concentration increases.

By using dark m-line interferometric analysis for waveguides with step-like index profiles[15] and reverse exchange for graded waveguides[14] the ordinary indices in all $H_xLi_{1-x}NbO_3$ phases have been obtained.

Conclusion. We think that appearing due to lattice parameters mismatch stresses lead to dividing of equilibrium β-phase and all observed β_i phases are subdivision of β - phase identified by C.Rice and J.Jackel[2,3] for powders. Evidently, the phase mixture (α+β) can not exist in single crystalline layers and in this proton concentration interval the single crystalline phases κ_1 and κ_2 are realized.

References

1. J.L.Jackel, C.E.Rice and J.J.Veselka, *Appl.Phys.Lett.*, **41**, pp.607-608, (1982).
2. C.E.Rice and J.L.Jackel, *Mat.Res.Bull.*, **19**, pp.591-597, (1984).
3. C.E.Rice, *J.Solid State Chemistry*, **64**, pp.188-199, (1986).
4. V.A.Fedorov and Yu.N.Korkishko, *Proceedings of SPIE*, **2291**, pp.243-255 (1994).
5. V.A.Fedorov and Yu.N.Korkishko, *Proceedings of SPIE*, **2401**, pp.216-226 (1995).
6. V.A.Fedorov and Yu.N.Korkishko, *Ferroelectrics*, **160**, pp.185-208 (1994).
7. K.El Hadi, P.Baldi, S.Nouh, M.P.De Micheli, A.Leycuras, V.A.Fedorov and Yu.N.Korkishko, *Optics Letters*, **20**, pp.1698-1700 (1995).
8. J.M.White and P.F.Heidrich, *Appl.Optics*, **15**, pp.151-155, (1976).
9. K.S.Chiang, *J. Lightwave Techn.*, **3**, pp.385-391, (1985).
10. V.A.Fedorov, V.A.Ganshin and Yu.N.Korkishko, *Physica status solidi(a)*, **135**, pp.493-505, (1993).
11. P.G.Suchoski, T.K.Findakly and F.J.Leonberger, *Optics Letters*, **13**, pp. 1050-1052, (1988).
12. V.A.Fedorov and Yu.N.Korkishko, to be published.
13. Yu.N.Korkishko, V.A.Fedorov and M.P.De Micheli, *Electronics Letters*, **31**, pp.1603-1604, (1995).
14. Yu.N.Korkishko, V.A.Fedorov, S.V.Katin and A.V.Kondrat'ev, *Proceedings of ECIO'95*, Delft, The Netherlands, April 3-6, pp.395-398 (1995).
15. J.Olivares, M.A.Díaz-García and J.M.Cabrera, *Opt.Commun.*, **92**, pp.40-44 (1992).

Planar Waveguide AR Lattice Filters: Advantages and Challenges

Christi K. Madsen[a,b] and Jian H. Zhao[b]

a) AT&T Submarine Systems, Inc., Holmdel, NJ 07733
b) Department of Electrical and Computer Engineering, Rutgers University, Piscataway, NJ 08854

A planar waveguide lattice filter architecture based on ring resonators has been investigated. A potential application is for very narrowband filters in WDM systems and networks. The merits of the architecture are described, and practical considerations for realizing such filters are discussed including the design for non-zero waveguide loss and compensation of fabrication variations. The proposed architecture is shown in Fig. 1 for a third order filter. The architecture is similar to fiber architectures [1,2]; however, the waveguide layout minimizes the ring length so that the maximum Free Spectral Range (FSR) can be achieved given the bend radius limit for a particular fabrication process. When described in the Z-domain, the transfer functions for E_{o1}/E_{i1} and E_{o2}/E_{i2} are Autoregressive (AR) responses having only poles, while E_{o1}/E_{i2} and E_{o2}/E_{i1} are Autoregressive Moving Average (ARMA) responses having both poles and zeroes. The architecture is general in the sense that it can be extended to any number of stages and the location of the poles can be set by determining appropriate coupling ratios and phases for each stage using a filter synthesis algorithm previously described [3].

The following desired characteristics are used to compare the proposed architecture against other planar waveguide filters which have been demonstrated:

1) require as few stages as possible for a particular set of passband/stopband requirements
2) general architecture: extendable to higher orders and control over pole and/or zero locations
3) meet various FSR requirements
4) low passband loss
5) a direct synthesis algorithm
6) ability to test individual stages after fabrication for compensating errors

Planar waveguide filters based on Mach Zehnder Interferometers [4], waveguide array multiplexers [5], and transversal filters [6] are MA filters. It is well known that for the same number of stages, an ARMA filter can provide a flatter passband, sharper rolloff, and better stopband rejection compared to MA filters. For comparison, a third order MA filter can provide a minimum rejection of 13 dB and a FWHM of 0.24*FSR while a third order AR filter can provide a minimum rejection of 25 dB and a FWHM of 0.19*FSR. Because the bend radius is limited for current silica-based waveguides to around 4mm, a concern is increasing the achievable FSR for AR filters. Several architectures using the Vernier effect have been demonstrated [7]; however, these are not general architectures and the passband width is very narrow since the largest ring dominates the passband characteristics. With respect to passband loss, lattice architectures offer significantly better performance compared to cascaded single stages or transversal filters. A comparison of three cascaded single stage AR filters to a three stage lattice filter shows that the lattice architecture can achieve 100% passband transmission for a lossless filter while a tradeoff exists for the cascade architecture between peak transmission and fit to a desired filter function

[3]. A direct synthesis algorithm has been derived for the AR lattice filter architecture which includes ring loss and terms for relative phase differences between stages [3].

When fabricated, variations in the effective index contribute to random phase variations between stages. The magnitude of $\sigma_{\Delta\phi}$ depends on the fabrication process and is proportional to the square root of the ring length [8]. Fabrication errors cause the relative phase between stages to be different in a lattice filter which can render it unusable if the errors cannot be compensated. Waveguide heaters allow the phase to be modified after fabrication; however, a method to determine the needed phase compensation after fabrication is required. An analysis algorithm for the AR lattice filter which determines both the coupling ratios and phase errors based on the measured AR magnitude response has been reported [3]. This algorithm is applied to measurements on an as-fabricated third order filter below.

The third order filter was designed and passed on to Photonic Integration Research, Inc. for fabrication using Ge-doped SiO_2 on a Si substrate with a core-to-cladding refractive index difference of Δ=0.75%. Test couplers with the same design as those used in the filter were placed on the chip so that they could be measured independently of the filter function. Straight waveguides were also included to estimate the fiber-to-waveguide coupling loss. The magnitude responses were measured using a tunable laser to step in approximately 0.001 nm increments and a wavemeter. The group delay was measured by amplitude modulating the input at 100 MHz and detecting the change in phase of the detected signal as a function of wavelength.

The as-fabricated N=3 AR response for one FSR is shown in Fig. 2 for both the vertical and horizontal polarizations. The phase errors relative to ϕ_1 were calculated from the analysis algorithm to be $\phi_{2,3}$={0.8,-1.1} radians for the horizontal and {-0.1,-2.0} radians for the vertical polarization. The change in phase with applied power to the waveguide heater was calibrated. Then, the necessary power was calculated and applied to minimize the phase difference between the stages. Since there is a large waveguide birefringence, both polarizations cannot be compensated with the same heater settings in general. The compensation was set for the vertical polarization. The results are shown in Fig. 3 for the AR and ARMA#1 (E_{o2}/E_{i1}) magnitude responses. The difference in the calculated phase errors between stages on the optimized response was reduced to 0.1 radians. The peak filter transmission increased from -4.9 dB to -2.7 dB and the maximum rejection relative to the peak transmission increased from 15.9 dB to 21.3 dB. By optimizing the coupling ratios for a given ring loss, the peak transmission can be optimized and the rejection increased. For example, coupling ratios of κ={0.548,0.166,0.166,0.548} and a loss of 0.5 dB/ring would yield a peak transmission of -1.9 dB and a maximum rejection of 33.3 dB. The optimum passband transmission for the AR response occurs when the zeroes of the ARMA response are on the unit circle. The stopband rejection is degraded as the zeroes move away from the unit circle.

One difficulty in applying the analysis algorithm is that there are 2^N possible solutions for the coupling ratios and phase terms based on the AR magnitude response. The test couplers, adjacent to the filter, were used to identify the particular solution. However, if the solutions have very similar coupling ratios, an alternate method is needed. The particular solution is easily distinguished by measuring either ARMA group delay response. The group delay for the ARMA#1 response is shown in Fig. 4. The location of the ARMA zeroes with respect to the unit circle can be determined by the sign of the group delay assuming that the zeroes are closer to the

unit circle than the poles. For example, the vertical polarization has a dominantly negative group delay implying that the zeroes have magnitudes less than one. This points to the minimum phase solution as the particular solution from 8 possible solutions.

The first general AR planar waveguide filter was demonstrated. Its distinct advantages compared to other planar waveguide architectures is the smaller number of stages for a given stopband rejection and control over the passband width. In addition, fabrication errors can be compensated using an analysis algorithm combined with waveguide heaters or alternate methods to vary the refractive index in a particular stage. This is significantly different than other technologies, such as thin film filters, where there is no control over the filter shape after fabrication. The major disadvantage is the maximum FSR, currently <0.1 nm, which is limited by the maximum refractive index difference for silica waveguide fabrication processes. Other waveguide material systems which allow tighter bend radii and alternate structures to create the ring, such as mirrors and gratings, need to be explored to increase the maximum FSR.

References

[1] K.P. Jackson, S.A. Newton, B. Moslehi, M. Tur, C.C. Cutler, J.W. Goodman and H.J. Shaw, "Optical Fiber Delay-Line Signal Processing," *IEEE Trans. Microwave Theory and Techniques*, vol. 33, pp. 193-209, 1985.

[2] B. Moslehi, J.W. Goodman, M. Tur and H.J. Shaw, "Fiber-Optic Lattice Signal Processing," *Proc. IEEE*, vol. 72, pp. 909-930, 1984.

[3] C.K. Madsen and J.H. Zhao, "A General Planar Waveguide Autoregressive Optical Filter," to be published in the *J. Lightwave Technol.*.

[4] M. Kuznetsov, "Cascaded Coupler Mach-Zehnder Channel Dropping Filters for Wavelength-Division-Multiplexed Optical Systems," *J. Lightwave Technol.*, Vol.12, No. 2, Feb. 1994, pp. 226-230.

[5] C. Dragone, C.A. Edwards and R.C. Kistler, *IEEE Photonics Technology Letters*, vol. 3, pp. 896-899 (1992).

[6] K. Sasayama, M. Okuno, and K. Habara, "Coherent Optical Transversal Filter Using Silica-Based Waveguides for High-Speed Signal Processing," *J. Lightwave Technol.*, Vol. 9, No. 10, Oct. 1991, pp. 1225-1230.

[7] K. Oda, N. Takato, H. Toba, K. Nosu, "A Wide-Band Guided-Wave Periodic Multi/Demultiplexer with a Ring Resonator for Optical FDM Transmission Systems," *J. Lightwave Technol.*, vol. 6, pp. 1016-1022, 1988.

[8] R. Adar, C.H. Henry, M.A. Milbrodt, and R.C. Kistler, "Phase Coherence of Optical Waveguides," *J. Lightwave Technol.*, Vol. 12, No. 4, April 1994, pp. 603-606.

Figure 1. N=3 AR Lattice Filter Architecture

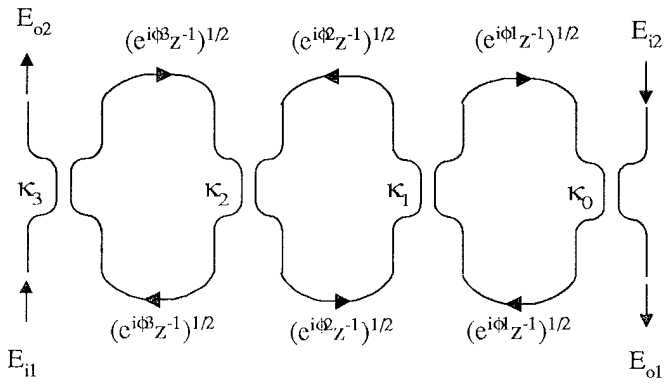


Figure 2. As-fabricated AR Magnitude Response

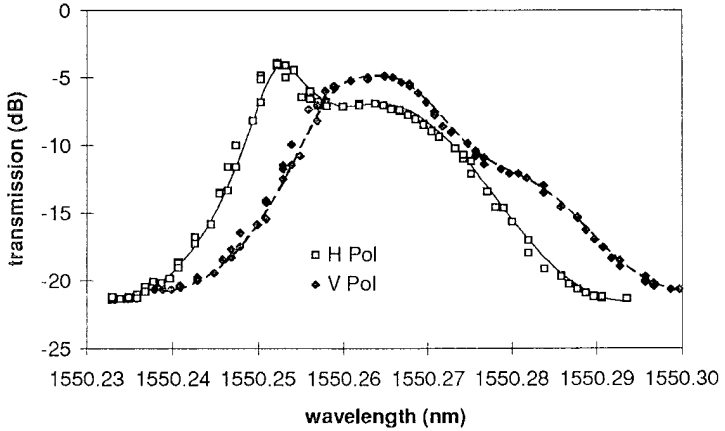


Figure 3. Compensated Magnitude Responses

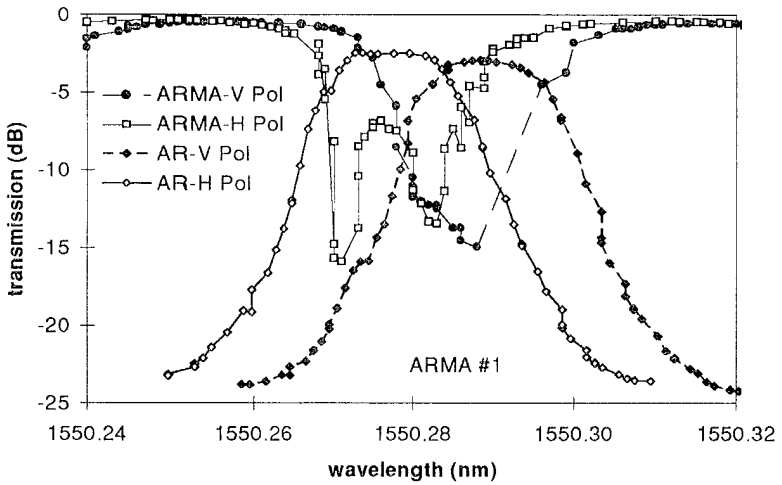
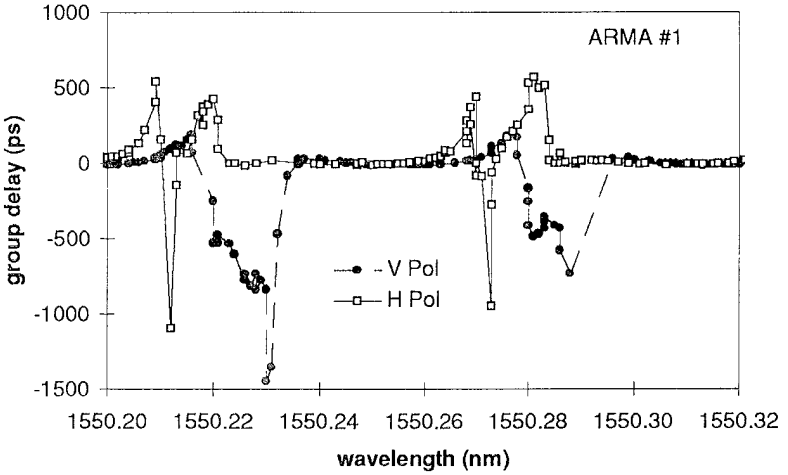


Figure 4. ARMA Group Delay for Compensated Filter



Tapered-Rib Adiabatic-Following Fiber Coupler

R. E. Smith, C. T. Sullivan, G. A. Vawter, G. R. Hadley,
J. R. Wendt, B. Snipes, and J.F. Klem

Sandia National Laboratories
Albuquerque, NM 87185-0603

Abstract - We present the design and experimental verification of a Tapered-Rib Adiabatic-Following Fiber Coupler (TRAFFiC). This device is a monolithically integratable structure fabricated in AlGaAs designed to increase the coupling efficiency of conventional optical fibers to tightly confined semiconductor waveguide devices. This approach offers the possibility of significantly reducing fiber butt coupling losses from the typical values of 7 to 10 dB to values of 0.5 to 3 dB. This long-standing packaging problem is one of the major impediments to the widespread acceptance of semiconductor-based optoelectronics. Moreover, the design can be implemented with minimal increase in fabrication complexity since it uses only epitaxial growth, lithography and etching.

The absence of an efficient and low cost means of connecting optical fibers to semiconductor waveguide devices, e.g. diode lasers and Photonic Integrated Circuits (PICs), currently poses one of the largest barriers to wide scale commercialization of semiconductor optoelectronic devices. This problem arises because of the small size of semiconductor waveguides compared to optical fibers. The 1-2 μm elliptical modal spot of typical semiconductor waveguides is neither well-sized nor shaped to match to the standard 8 μm circular modal spot of conventional single mode optical fibers. Directly coupling light from a fiber to the small waveguide typically results in 7 to 10 dB insertion loss. Non-integrated solutions that improve this coupling, often increase coupling at the cost of tight alignment requirements (< 1 μm) and are thus prohibitively expensive.

Recently several groups have presented devices that address this problem with a variety of monolithic approaches. An excellent survey of these is provided by Ref. 1. Our designs, shown in Fig. 1, are essentially Shani-Henry couplers,[2] similar to that discussed in Ref. 3, but with several modifications to increase performance and process tolerance.

Many tapered mode converters of this type require very sharp taper points, and the rounding of these points increases the losses substantially. We have avoided this potential process intolerant problem in our device designs. Figs. 2 shows the effect of a finite taper width on the overlap of the conventional fiber mode with the mesa mode. Notice that coupling losses are low and constant for taper end widths less than 1.8 μm.

The major theoretical source of loss in our designs are caused by stair-stepping brought about by pixelization in the lithographic processes. This effect is shown in Fig. 3. It is worth pointing out that the excess loss due to pixelization can be minimized in the design process and that it scales linearly with pixel size.

We have fabricated and tested devices exhibiting losses of approximately 2-3 dB (0.5 dB to mesa overlap loss + 0.8 dB excess taper loss + ~1.2 dB estimated material/ waveguide loss). The devices currently being fabricated incorporate lower-loss waveguide designs, have improved coupling to fiber and excess pixelization taper loss. These devices have predicted fiber-to-waveguide coupling losses to 0.9 dB (0.2 dB fiber to mesa overlap loss + 0.5 excess taper loss + 0.2 dB estimated material/waveguide loss). Furthermore, for these new designs a ±10% variation in our most critical processing dimension brings about a variation of only ±0.15 dB respectively.

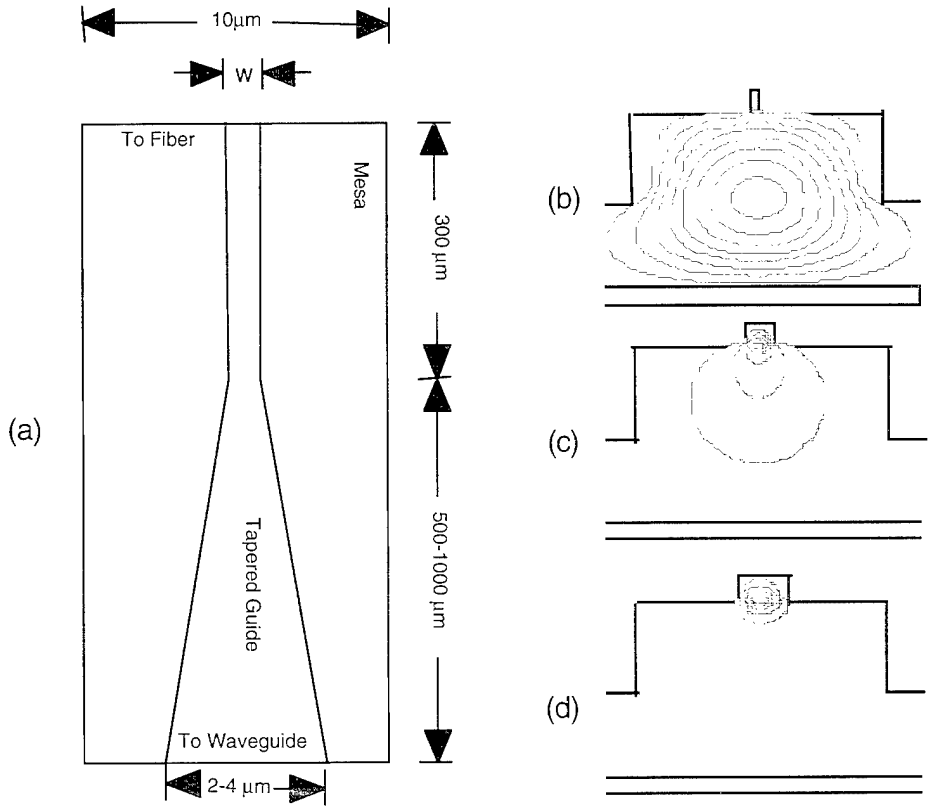


Fig. 1 A schematic representation of the (TRAFFiC) device. (a) Top View. (b) A cross section showing the mesa mode, which is the fundamental mode of the device for rib widths < 1.8 μm for the device discussed in Fig. 2-3. (c) A cross section showing the fundamental mode in transition from the mesa to the rib. This transition occurs at rib widths of 1.8-2.1 μm. (d) A cross section showing the fundamental mode confined to the rib, widths of greater than 2.1 μm.

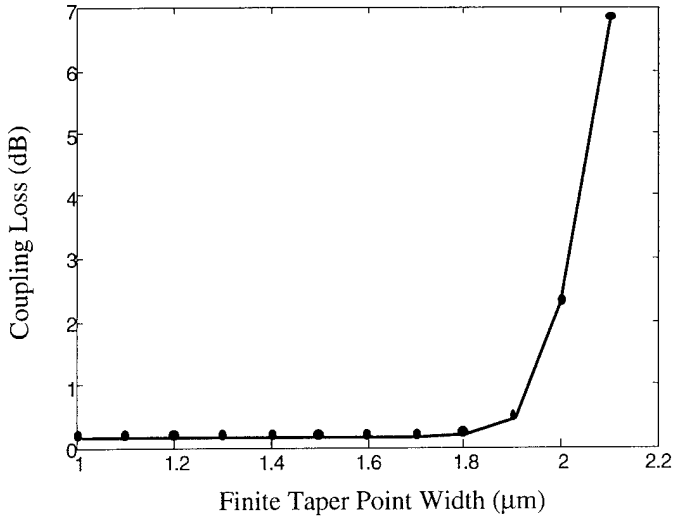


Fig. 2 The effect of finite taper point width on fiber-to-mesa waveguide coupling. For all rib waveguide widths less than 1.8 μm the fundamental mode is confined to the mesa where it has good overlap with conventional fiber.

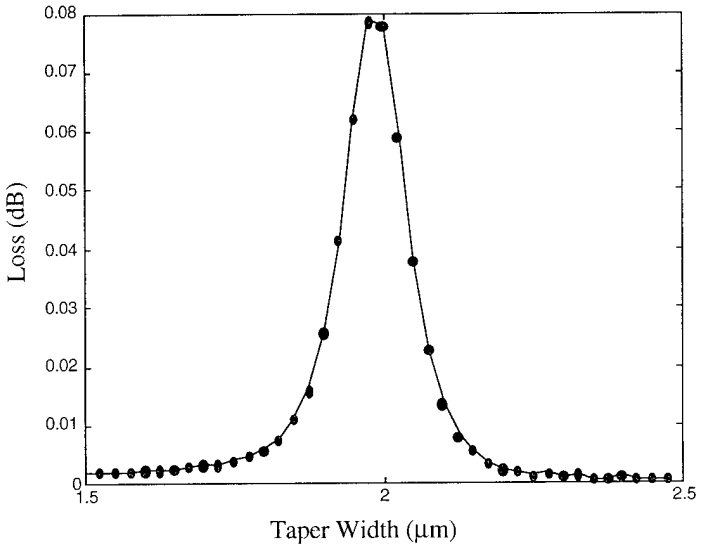


Fig. 3 Excess taper loss at each pixel step. The lateral tapering of the upper rib waveguide is comprised of a series of discrete steps. The size of the steps is defined by the pixel size of the lithographic mask. This figure shows the loss associated with each of the (0.025 μm) steps. The sum of these individual losses sets an lower bound on the excess taper loss.

[1] LEOS, IEEE Laser and Electro-Optics Society 1995 meteing, Vol 1,EMGW1-2.
[2] Y. Shani, C. H. Henery, R. C. Kristler, K. J Orlowsky, and Ackerman, *Phys. Lett.* **55**. pp 2389-2391,1989.
[3] R.N. Thurston, Eli Kapon and Arie Shahar, *Opt. Lett.*, vol. 16, pp.306-308, 1991.

This work was supported by the United States Department of Energy under Contract DE-AC04-94AL85000.

Band-gap Tuning in Strained Piezoelectric Quantum Well Lasers

A.S. Pabla

Department of Electronic & Electrical Engineering
University of Sheffield
Mappin Street
Sheffield. S1 3JD. U.K.
Tel: (44) 114 282 5241; Fax: (44) 114 272 6391
e-mail: a.pabla@sheffield.ac.uk

The accumulation of electron-hole charge within a strained piezoelectric quantum well establishes a dipole which opposes the strain-generated electric field [1]. Such structures therefore exhibit a carrier-density dependent blue-shift of the inter-band transitions [1,2]. In this paper this field-screening process is studied using forward-biased current injection in strained piezoelectric quantum well lasers. The implications of the findings for various optoelectronic applications are outlined.

This study is based on the separate confinement heterostructure quantum well diode depicted in Fig.1. The choice of indium composition and the (111)B substrate establishes a field across the quantum well of expected to be ≈ 220kV/cm after accounting for an expected 30% reduction in the piezoelectric constant for $In_{0.23}Ga_{0.77}As$ [3].

Broad-area cleaved-facet lasers of 66μm width and various lengths were prepared by standard techniques. Room temperature pulsed electroluminescence (EL) spectra were recorded from the end-facets of the lasers under test. In this configuration the emission spectrum is modified by amplification and re-absorption as it passes through the waveguide. While the peak in the electroluminescence response of such a structure does not directly correspond to the peak in the gain spectrum (or the absorption edge), its blue-shift with injection current is, nevertheless, a useful guide to the extent of the in-well field screening that is occuring.

Fig.2. shows a schematic plan representation of a bar of cleaved facet lasers with cavity lengths of 1000μm. Because of the {110} family of cleavage planes some of these lasers have *non-parallel* facets. In our case, however, these devices prove to be a fortunate 'by-product'. EL spectra measured at different current densities are shown in Fig.3 for a laser with *parallel* facets. The EL peak undergoes a blue-shift with increasing current density, indicating that the field screening effect associated with in-well charge accumulation prevails over any red-shift that may be expected from forward-biasing of the diode. The spectral width narrows until a

lasing mode appears at 1023nm. Further increases in current yield a linear increase in the output power per facet, but *no* further spectral shift.

To establish whether there is an unscreened "residual" field across the quantum well at threshold we have recorded the spectral shift from an adjacent *non-parallel* facet laser. Fig.4. compares the observed EL-shift for both of these devices. The peak positions are comparable below the threshold of the parallel facet. The non-parallel facet laser, however, which offers a comparatively poorer facet reflectivity, does not achieve threshold over this range of current densities. Instead, the EL-peak proceeds to shift beyond that of the parallel-facet laser. In contrast, the spectral shift in the parallel-facet device is arrested once lasing is achieved because the in-well carrier concentration is "pinned" preventing any further field-screening. Thus, by effectively raising the lasing threshold in the non-parallel facet device and consequently allowing higher in-well carrier densities, we are able to conclude that there is indeed a residual unscreened electric field across the quantum well at the lasing threshold of the parallel facet laser.

Further evidence for partial field-screening at threshold is provided by simply examining the spectral characteristics of lasers of differing cavity length. The spectral gain per unit length is determined, in part, by the carrier concentration, which is also the parameter which controls the degree of field-screening. Thus, the threshold round-trip gain is satisfied for *different* in-well carrier concentrations, resulting in a *cavity-length dependence of the lasing wavelength.* We see this to be the case in Fig.5 which plots the lasing wavelength as a function of cavity length and the threshold current density. Since the Fabry-Perot mode-spacing (typically less than 1nm) is considerably smaller than the 22nm spectral range observed, this lasing wavelength dependence on cavity length can only be explained by gain-spectrum tuning associated with field-screening in the piezoelectric quantum well. In essence, this is a simple approach to fabricating monolithic multi-wavelength lasers. Furthermore, by controlling the overall gain-length product at threshold in a 3-terminal device, it should prove possible to adjust the intra-cavity gain/loss and allow quasi-continous tunability between the Fabry-Perot modes.

This demonstrated ability to control the band-gap in piezoelectric quantum well lasers has has potential applications in optoelectronic integration. For example, monolithic laser-modulator integration can be achieved, if there is a residual electric field in the quantum well once lasing occurs. Since the piezoelectric field offers a means of blue-shifting the absorption edge [3], the output of the piezoelectric quantum well laser will be modulated if, by applying sufficient reverse bias to a monolithically integrated modulator, the well field can be reduced to below that of the laser [4].

References

[1] D.L.Smith & C.Mailhiot, "Optical properties of strained-layer superlattices with growth axis along [111]", *Physical Review Letters*, vol.58, no.12, pp.1264--7, 1987

[2] I.Sela, D.E.Watkins, B.K.Laurich, D.L.Smith, S.Subbanna & H.Kroemer, "Excitonic optical nonlinearity induced by internal field screening in (211) oriented strained-layer superlattices", *Applied Physics Letters*, vol.58, no.17, pp.684-6, 1991

[3] A.S.Pabla, J.L.Sanchez-rojas, J.Woodhead, R.Grey, J.P.R.David, G.J.Rees, G.Hill, M.A.Pate & P.N.Robson, "Tailoring of internal fields in InGaAs/GaAs multi-well structures grown on (111)B GaAs", *Applied Physics Letters*, vol.63, no.6, pp.752-4, 1993

[4] A.S.Pabla, R.Grey, J.Woodhead, E.A.Khoo, J.P.R.David & G.J.Rees, *unpublished*

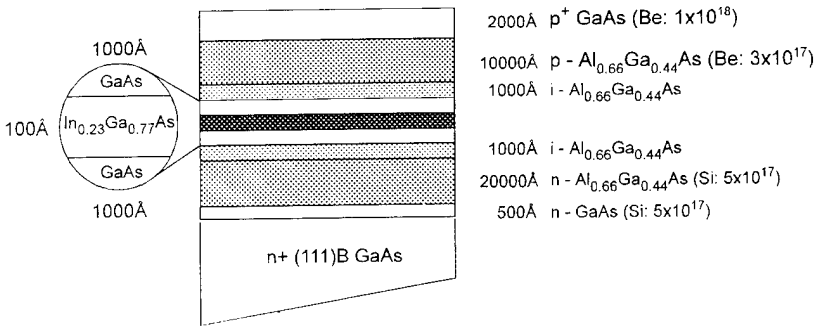


Fig.1: Layer structure of the SCH laser

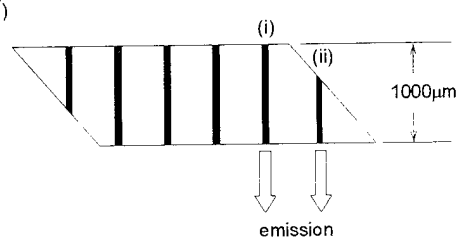


Fig.2: Schematic representation of a bar of cleaved lasers (i) parallel facets, (ii) non-parallel facets

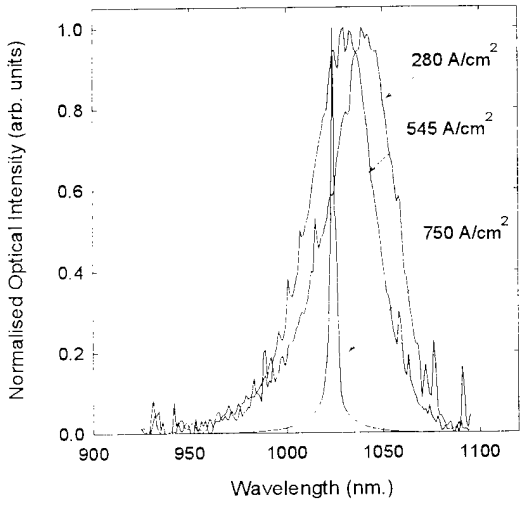


Fig.3: EL spectra from parallel-facet laser

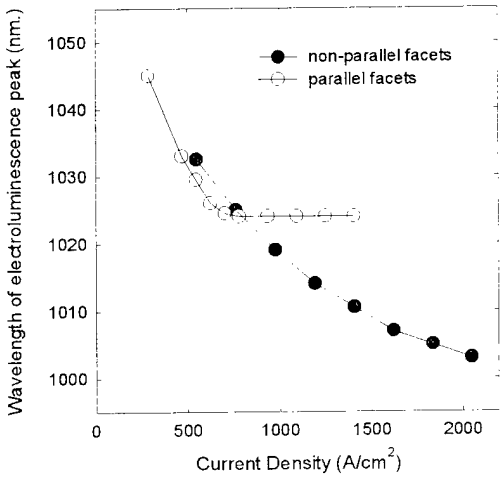


Fig.4: EL peak position vs current density

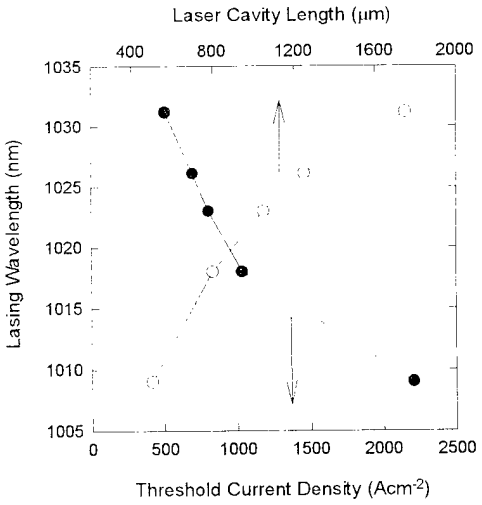


Fig.5 : Cavity length and threshold current density dependence of the lasing wavelength

Optical Waveguide Interconnects in Optoelectronic Matrix Switches

M. Ersoni, X. Wu and P.E. Jessop
Centre for Electrophotonic Materials and Devices
McMaster University, Hamilton, Ontario, CANADA L8S 4L7
(905)525-9140 FAX: (905)527-8409

J.P. Noad
Communications Research Centre
P.O. Box 11490, Station H, Ottawa, Ontario, CANADA K2H 8S2
(613)998-2154 FAX: (613)990-8382

Introduction

An optoelectronic matrix switch consists of an interconnected array of photodiodes or photoconductors. In an $N \times N$ switch each of N input lightwave signals is divided among all of the detectors in a row of the matrix by a passive optical distribution network. All of the detectors in a column are electrically connected so that their output signals are summed. Switching action is based on using the detectors bias voltages to switch their responsivities. Connections are made simply by biasing the detectors at the desired crosspoints. High data rate transmission ($> 1\ GHz$) and excellent interchannel isolation ($> 60\ dB$) have been demonstrated in a 10×10 switching matrix [1].

The optical signals are normally distributed using a network of optical fiber splitters. However, for matrix switches with a large number of elements the complexity of the fiber network and the need to align fibers precisely to the individual detector elements are obstacles to practical implementation. Manufacturing costs could be reduced and reliability improved by integrating optical waveguides into the matrix structure to distribute the lightwave signal on-chip without the use of optical fiber splitters. Waveguide coupling also eliminates the problem of metal contacts shadowing some of the input light. In this paper we report on the integration of AlGaAs rib waveguides into a 4×4 array of GaAs metal-semiconductor-metal (MSM) detectors.

Device Design

Figure 1 illustrates the structure of the combined MSM detector and integrated waveguide. A 0.75 μm thick $Al_{0.15}Ga_{0.85}As$ waveguide layer, $Al_{0.20}Ga_{0.80}As$ cladding layers and a 0.4 μm thick GaAs absorbing layer were grown on undoped GaAs substrates by metal-organic chemical vapour deposition. A series of straight parallel rib waveguides was patterned using wet chemical etching. The absorbing layer was removed everywhere except for small mesas distributed along the waveguides to form the detector elements. Prior to metallization a dielectric layer was deposited with windows opened above the mesas for the interdigital metal-semiconductor contacts. The metal was Ti:Pt:Au with 2 μm finger width and spacing. Where the GaAs layer is removed the waveguides support a single transverse mode while in the detector regions we calculate that there are two modes. Assuming an

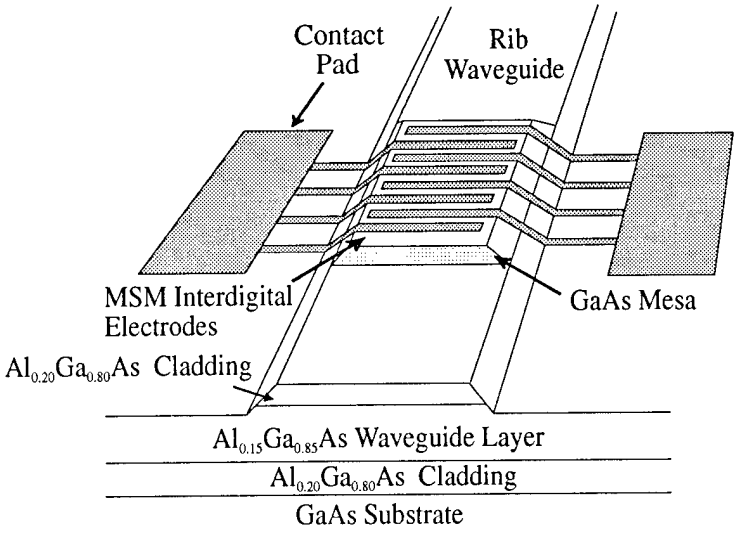


Figure 1: Structure of the waveguide-coupled MSM photodetector

absorption coefficient of $10^4\ cm^{-1}$ for GaAs, the beam propagation method as well as a mode expansion method [2] were used to determine the optical attenuation in the detector regions as a function of the upper cladding layer thickness. A cladding thickness of 0.3 μm was selected based on its calculated 3 dB absorption length of approximately 100 μm.

Figure 2 illustrates a 4×4 matrix switch that was fabricated using ten micron wide parallel waveguides spaced 300 μm apart. Along each waveguide the detector lengths were 45, 63, 106 and 177 μm. These values were selected in an effort to equalize the power absorbed in each detector in spite of the decrease in optical power along the guide.

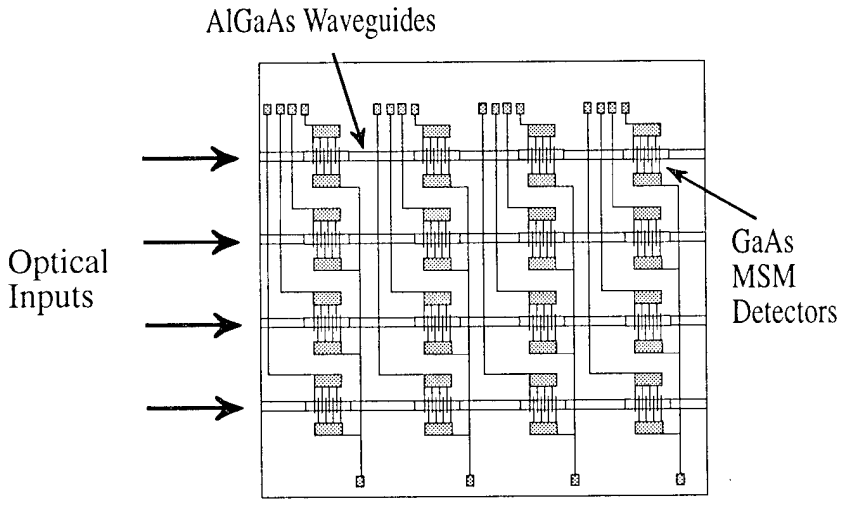


Figure 2: Layout of a waveguide-coupled 4×4 optoelectronic matrix

Experimental Results

Several test structures were located on the chip adjacent to the matrix switch. Among these were straight passive waveguides containing no detector elements. By performing cut-back experiments on these we determined that the propagation loss in the passive sections was less than 2 dB/cm at a wavelength of 820 nm. The attenuation in the detector sections was measured by comparing the photocurrents in a pair of identical detectors that were located in-line on a common waveguide. In a separate test structure a chain of several small electrically isolated MSM detectors was fabricated on a single GaAs mesa. Their relative photocurrents exhibited an exponential decay from which the attenuation coefficient in the detector regions was inferred. The result obtained was $\alpha = 115 \pm 16\ cm^{-1}$, which corresponds to 3 dB absorption length of of 60 μm. A responsivity of 0.1 A/W in a 100 μm long detector element was measured at a modulation frequency of 1 GHz using a lightwave analyzer.

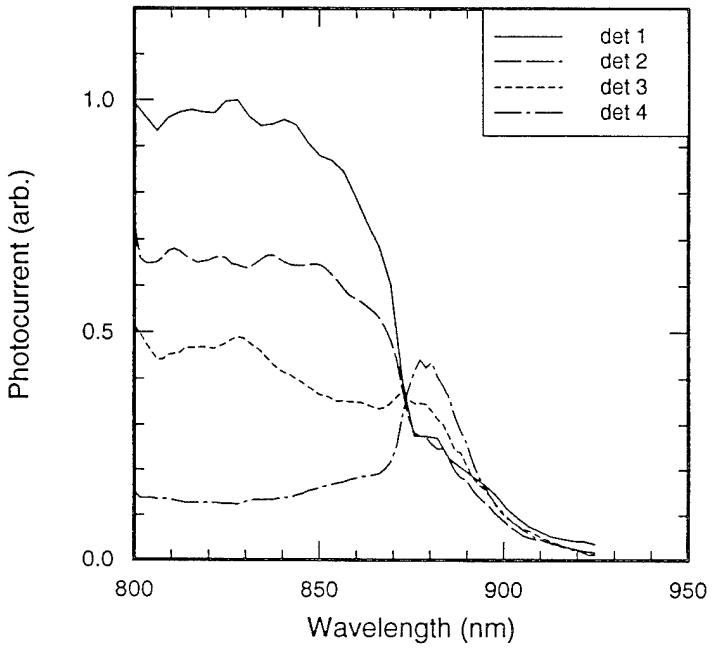


Figure 3: Photocurrent as a function of wavelength in each of four photodetectors located in-line on a single waveguide. Signals are normalized to constant input power

The observed attenuation coefficient was larger than the value that was assumed in designing the detector lengths. Consequently, at a wavelength of 820 nm, the leading detectors in a row of the 4×4 matrix switch extracted more power from the waveguide than did the trailing detectors. This imbalance could be corrected by increasing the upper cladding layer thickness to reduce the coupling to the GaAs layer. In order to simulate a wide range of coupling strengths the 820 nm diode laser was replaced by a titanium:sapphire laser that could be tuned continuously on either side of the GaAs band edge. Figure 3 shows

the photocurrents in the four in-line detectors as a function of wavelength. For each curve the detector under test was biased at five Volts while the other three detectors were not biased. As the wavelength increases the absorption in the lead detector decreases allowing more light to reach the subsequent detectors. At wavelengths near 873 nm the optical power delivered to the four detectors is very nearly balanced as is desired in an optoelectronic matrix switch.

At short wavelengths, well below the band edge of GaAs, the fraction of the input power that is absorbed in each detector is independent of its bias voltage. At these wavelengths, a well-designed matrix switch will share the input power evenly among all of the detectors along a given waveguide. For wavelengths at or above 880 nm, near the GaAs band edge, the optical absorption coefficient is significantly greater in high electric fields than it is in zero field due to the Franz-Keldysh effect. This effect can enhance the absorption in detectors that are biased in their on-state relative to the absorption in the off-state detectors. Thus more efficient use can be made of the available input power. We observed that for a wavelength of 880 nm a 280 μm long detector transmitted 30% more light when biased at zero Volts than it did at five Volts. The photocurrent in subsequent detectors on the same waveguide was correspondingly increased. This difference will be increased by modifying the MSM electrode configuration to improve the overlap between the waveguide mode and the DC electric field. The potential exists for fabricating nearly transparent optoelectronic switches that do not absorb any signal in the off-state.

In summary, we have demonstrated the use of integrated optical waveguides for optical signal distribution in a 4×4 optoelectronic matrix switch. Uniform power division was achieved by optimizing the lengths of the individual detector elements and good responsivity was obtained for modulation frequencies greater than 1 GHz. The feasibility of using the Franz-Keldysh effect to enhance the fraction of the optical power coupled into the on-state detectors was demonstrated.

References

[1] M. Veilleux and R.I. MacDonald, "An Optoelectronic Switching Matrix With High Isolation", *IEEE J. Lightwave Technol., 10*, 988-991 (1992).

[2] W. Ng, A. Narayanan, R.R. Hayes, D. Persechini and D. Yip, "High-Efficiency Waveguide-Coupled $\lambda = 1.3\ \mu m\ In_xGa_{1-x}As/GaAs$ MSM Detector Exhibiting Large Extinction Ratios at L and X Band", *IEEE Photon. Technol. Lett., 5*, 514-517 (1993).

Electro-nanomechanically actuated integrated-optical Mach-Zehnder interferometer

R. Dangel and W. Lukosz
Optics Laboratory, Swiss Federal Institute of Technology, CH-8093 Zürich, Switzerland
phone: ++41-1-633 28 10 fax: ++41-1-633 11 12

Introduction

We report on intensity modulation with Mach-Zehnder interferometers comprising Si_3N_4 rib waveguides on oxidized silicon wafers (SiO_2/Si) as substrates. No electro-optic materials are required. The phase shifts are induced nanomechanically by varying the width d of an air gap between a dielectric plate E and a section of a rib waveguide [1]. The "effective-refractive-index-shifting" element E is realized in the form of a cantilever fabricated by etching of oxidized silicon wafers (SiO_2/Si); the cantilever is elastically deflected under electrostatic forces.

Previously, we had worked with elements E in form of bridges (made of SiO_2/Si) spanned over a planar (slab) or rib waveguide made of dipcoated SiO_2-TiO_2 films on SiO_2/Si substrates; we demonstrated electro-nanomechanically actuated intensity modulation with a difference or polarimetric interferometer [2,3].

All experiments are performed at wavelength λ = 633 nm.

Waveguide fabrication

Planar Si_3N_4 waveguides with thicknesses of d_F = 162...164 nm and refractive index n_F = 2.013 grown by an LPCVD process on oxidized silicon substrates (SiO_2/Si) were procured from CSEM, Neuchâtel. The 2.02 µm thick SiO_2 buffer layers of refractive index n_{BL} = 1.46 had been grown by wet oxidation.

We fabricated rib waveguides (see Fig. 1) and Mach-Zehnder interferometers comprising rib waveguides and Y-junctions (see Fig. 2) by etching the planar Si_3N_4 waveguides in buffered hydrofluoric acid (BHF). The ribs were protected by a positive photoresist (Shipley, Microposit® SP25-15) irradiated in contact exposure through a chromium mask.

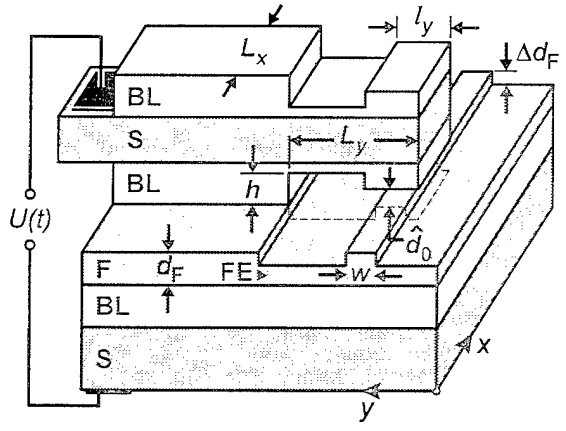


Fig. 1. Rib waveguide with electro-nano-mechanically actuated effective-refractive-index-shifting element E in form of a cantilever.

S, silicon wafer; BL, SiO_2 buffer layer;
F, waveguiding film of thickness d_F;
FE, etched film; Δd_F, rib height; w, rib width.
L_x, L_y, l_y, lateral dimensions of cantilever;
h, depth of etched channel;
$\hat{d}_0$, initial air-gap width.
$U(t)$, time-dependent applied voltage.

We determined the thicknesses d_{FE} and d_F, respectively, of the etched and non-etched (waveguiding) films FE and F by prism incoupling. The difference $\Delta d_F \equiv d_F - d_{FE}$ gave the value of the step or rib height ($\Delta d_F = 3...18$ nm). For step heights of $\Delta d_F = 6...18$ nm, scanning experiments with a mechanical stylus instrument (Alpha-Step 200 from Tencor Instruments) confirmed the results of the optical measurements; the etch rate r_{BHF} was determined to be $r_{BHF} = 0.4$ nm/min at room temperature. With the prism-incoupling method, we also measured the refractive indices n_F and n_{FE} of the etched and non-etched films and found them to be equal, i.e., $n_F = n_{FE}$. Previously, we had worked with SiO_2-TiO_2 rib waveguides produced by BHF-etching of dipcoated SiO_2-TiO_2 planar waveguiding films. With that material, however, we found that etching reduces the thickness but also the refractive index of the etched film FE [3].

We fabricated rib waveguides with widths $w = 1.5...10$ µm and rib heights $\Delta d_F = 3...6$ nm. With the prism-outcoupling method, we investigated the number of transverse modes propagating in the rib waveguides. Light was end-fire coupled into the waveguides and outcoupled by the prism. The resulting "*m*-lines" show how many different transverse modes propagate in the rib waveguide. Previously, we had used a grating coupler instead of a prism for analogous measurements of SiO_2-TiO_2 rib waveguides [3]. With the prism-outcoupling method we found that Si_3N_4 rib waveguides with widths of $w = 1.5...2.0$ µm and rib heights of $\Delta d_F = 3.0$ nm are monomode waveguides.

Mach-Zehnder interferometers comprising monomode rib waveguides and Y-junctions were etched; the interferometers were 35 mm long, and the distance between the two legs was 500 µm (see Fig. 2).

Fabrication of effective-refractive-index-shifting elements

The effective-refractive-index-shifting elements E were made of oxidized, 390 µm thick silicon wafers with 3.5 µm thick SiO_2 layers. The cantilever with a hammer-like head with breadth of l_y = 0.4 mm was realized by a two-stage etching process in BHF. The symmetric form of the cantilever was chosen in order to minimize any undesirable deformation. To facilitate free movement of the cantilever, a channel of depth h = 0.7 µm or 1.4 µm, respectively, was provided between the hammer-like head and the base of the

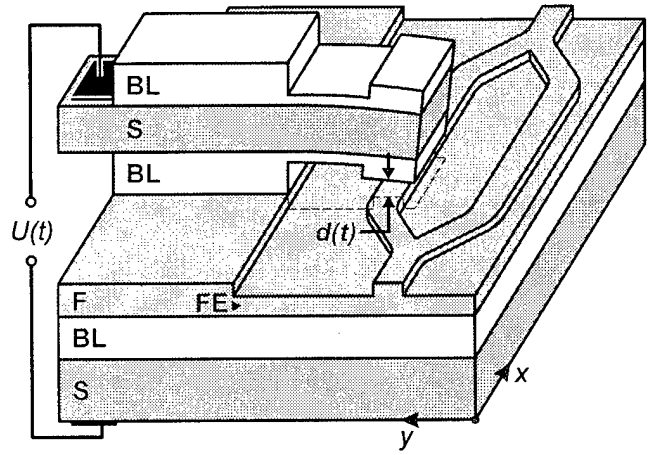


Fig. 2. Mach-Zehnder interferometer with electro-nanomechanically actuated effective-refractive-index-shifting element E in form of a cantilever projecting over one leg of the interferometer.

d(t), time-dependent air-gap width.

cantilever. The air-gap width $\hat{d}_0$ between the hammer-like head of the undeflected cantilever and the rib waveguide was $\hat{d}_0$ = 180 nm. The cantilevers, with widths of L_x = 3...5 mm and lengths of L_y = 1.26 or 2.52 mm, respectively, were attached to the waveguide by optical contact bonding.

Modulation experiments

Electro-nanomechanical actuation

We apply the electric voltage $U(t) = U_0 + \Delta U(t)$ to the condenser formed by the conducting silicon part of the element E (cantilever) and the waveguide substrate (Si), respectively. The resulting electrostatic pressure is $p(t) \propto [U(t)]^2 \approx U_0^2 + 2U_0\Delta U(t)$. The gap width is reduced from its initial value $\hat{d}_0$, defined by the etching process, to $d(t) = d_0 + \Delta d(t)$ where d_0 is the median gap width which is adjusted with the d.c. voltage U_0. The time-dependent voltage $\Delta U(t)$ induces gap-width variations $\Delta d(t) = C_p\Delta p(t) \propto C_pU_0\Delta U(t)$, where C_p is the frequency-dependent compliance of the cantilever, and thus, effective-refractive-index changes $\Delta N_j(t) = (\partial N_j/\partial d) \cdot \Delta d(t)$ where j = TE or TM [1]. A guided mode propagating under the element E experiences a time-dependent phase shift $\Delta\Phi_j(t) = 2\pi(L_x/\lambda)\Delta N_j(t)$.

Mach-Zehnder interferometer

The Mach-Zehnder interferometer transforms the phase modulation $\Delta\Phi(t)$ into an intensity modulation. The output power of the Mach-Zehnder is proportional to $1 + \cos\{\Delta\Phi(t) + \Delta\Phi_0\}$ where $\Delta\Phi_0$ is a constant phase shift, which is adjusted by a small change of the d.c. voltage U_0. In the points of operation I and III (where $\Delta\Phi_0 = -\pi/2$ and $+\pi/2$, respectively), the output-power variations are linearly proportional to small phase shifts $\Delta\Phi(t)$. In point of operation II (where $\Delta\Phi_0 = \pi$), the interferometer's response is quadratic for small phase shifts $\Delta\Phi(t)$.

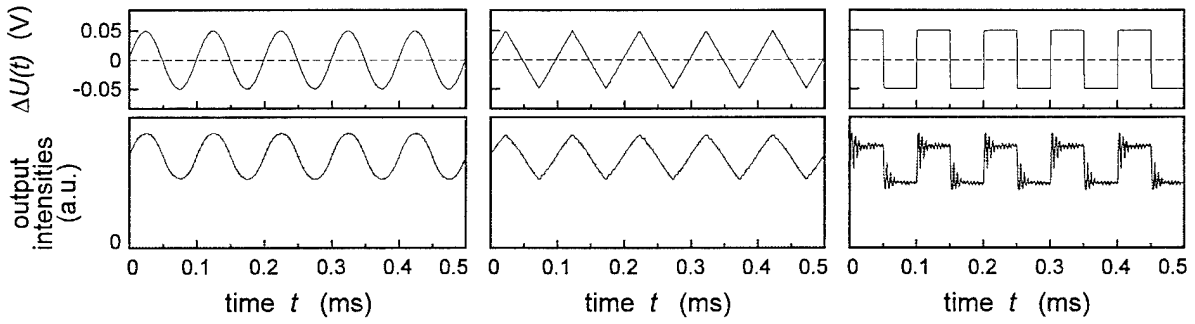


Fig. 3. Intensity-modulation experiments with Mach-Zehnder interferometer. TM_{00} modes; λ = 633 nm. Point of operation I, $\Delta\Phi_0 = -\pi/2$.

$\Delta U(t)$, time-dependent applied voltage; U_0 = 50 V, d.c. voltage; f = 10.0 kHz, fundamental frequency. Shown are the output intensities for sinusoidal, saw-tooth and square-wave voltages $\Delta U(t)$.

Results of intensity-modulation experiments with TM_{00} modes are shown in Figs. 3 and 4. In Fig. 3, the periodic input signals $\Delta U(t)$ of different form have a fundamental frequency $f = 10$ kHz which is smaller than the 1st (mechanical) resonance frequency $f_r \approx 85$ kHz of the cantilever. The response time of the system is about $\Delta t = 100$ µs. The frequency response of the cantilever seems to be linear up to frequencies of about 10 kHz. Therefore, the electro-nanomechanically actuated interferometric modulator can be used for input signals $\Delta U(t)$ of arbitrary form up to this frequency. But for sinusoidal input signals $\Delta U(t)$, modulation at much higher frequencies is attainable. Fig. 4 shows that for sinusoidal input signals $\Delta U(t)$ at a frequency $f = 2.0$ MHz well above the 1st resonance frequency f_r an intensity modulation results.

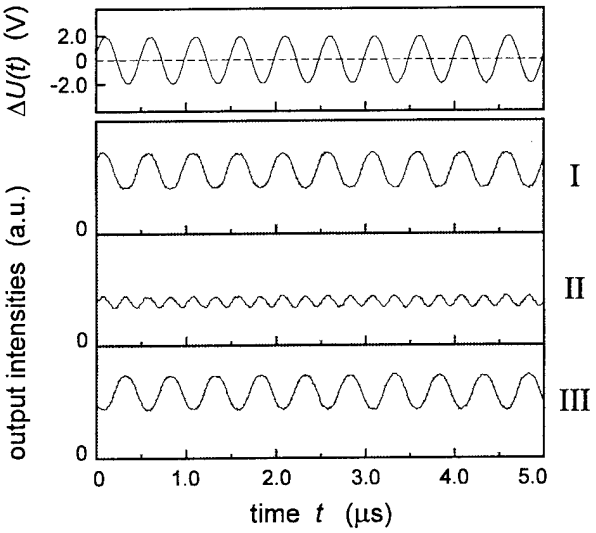


Fig. 4. Intensity-modulation experiments as in Fig. 3 with a higher modulation frequency of $f = 2.0$ MHz.

$\Delta U(t)$, sinusoidally time-dependent applied voltage; $U_0 = 70$ V, d.c. voltage. Shown are the output intensities versus time t at different points of operation I, II, and III, where the constant phase shifts are $\Delta\Phi_0 = -\pi/2$, π, and $\pi/2$, respectively.

Conclusions

We demonstrated electro-nanomechanically actuated intensity modulators with Mach-Zehnder interferometers comprising Si_3N_4 rib waveguides. With the present design of the effective-refractive-index-shifting element E in form of a micromachined cantilever made of silicon and SiO_2, response times of about 100 µs were achieved.

References

[1] W. Lukosz, "Integrated-Optical Nanomechanical Systems," Integrated Photonics Research, Boston, April 29 - May 3, 1996, and "Integrated-Optical Nanomechanical Devices as Modulators, Switches, and Tunable Frequency Filters, and as Acoustical Sensors," Proc. SPIE Vol. 1793 (1992), 214-234 [OE/Fibers '92, Boston].

[2] P. Pliska, R. Dangel, and W. Lukosz, "Electro-Nanomechanically Actuated Integrated-Optical Modulators, Switches, and Deflectors and Tunable Fabry-Perot Interferometers," Proceedings European Conference on Integrated Optics (ECIO '93), Neuchâtel, April 1993; paper: 14-30.

[3] R. Dangel and W. Lukosz, "SiO_2-TiO_2 Rib-Waveguides for Electrostatically Actuated Integrated-Optical Nanomechanical Devices," 7th European Conference on Integrated Optics (ECIO '95), Delft, April 1995, Conf. Proc. p. 371-374.

A Standard SPICE Model for MQW Lasers Modeling Capture/Escape and Carrier Transport

Kuno Zhuber-Okrog

SIEMENS AG Austria, EZE TNT-4, P.O.Box 326, A-1031 Wien, Austria
Tel +43 1 1707 37503
Fax +43 1 1707 55120
on leave from Technische Universität Graz, Institut für Nachrichtentechnik und Wellenausbreitung, Inffeldgasse 12, A-8010 Graz, Austria

1. Introduction

MQW lasers show a different electrical behaviour than bulk lasers [1] which cannot be modeled with previous circuit simulation models. Electron and hole densities are different, even in undoped structures (see e.g. [2] and [3]). Hence it is necessary to extend existing simulation models with emphasis on the electrical behavior. Rigorous simulations however, require large amounts of calculation time for deriving a DC characteristic with suitable resolution.

The model is the application of a new semiconductor device simulator for quasineutral structures including MQW layers with an extension for simple single-mode modeling of the optical behaviour. It is implemented in a standard SPICE circuit simulation program. The model is applied to a Fabry-Perot laser diode and compared to measured data.

Carrier transport is **not** modeled using a rate equation approach which would simulate only diffusion but not electric field-induced drift current. Furthermore, the influence of independent SCH layers on both sides of the active layer is taken into account.

The device is treated as layers which are each modeled by three simulation circuit parts taking over specific simulation tasks. An overview of the circuit parts is shown on Fig. 1.

2. Continuity and optical circuit (Fig. 2)

This circuit part models the continuity equation and the optical behavior. It is equivalent to rate equations for all carrier and photon densities of each layer.

The model uses two unconfined (three-dimensional) and a number of confined (two-dimensional) carrier populations in the active MQW region and electron and hole populations in seperate confinement layers. Quasineutrality is assumed in all layers, which imposes a single equation making the carrier densities linear dependent with an offset representing doping.

Simple single-mode rate equations with nonlinear gain have been applied. The optical gain is a polynomial of the confined electrons and holes taking part in the lasing action. Additional spontaneous emission collected by the broad-area detector is modeled by an extra branch resulting in excellent of sub-threshold differential L/I curve (Fig. 5).

3. Fermi level circuit (Fig. 3)

Fermi levels are referenced to a single freely chosen single level in mid-gap. Based on excess carrier densities relative to the carrier densities if the Fermi level were at the reference level, the Fermi levels are modeled by diodes with intrinsic series resistance, following a method described in [4].

Capture/escape currents are modeled by a new method. The basic current is proportional to the difference between the unconfined population and the theoretical value of the unconfined population if the Fermi level were at the position of the actual Fermi level of confined states. This current is supposed to model phonon scattering accurately, and may be modified e.g. by multiplication by a polynomial function of unconfined carrier densities to model carrier-carrier interaction accurately.

4. Electrical terminal circuit (Fig. 4)

Combined drift/diffusion currents are modeled proportional to mobility and Fermi level gradient [5].

5. Application to undoped 1.55 μm InGaAsP MQW lasers

A quantum-mechanical analysis showed two hole states and a single confined electron state in the structure under investigation. The unstrained InGaAs well was 4.6 nm and the 1.3 μm InGaAsP barrier was 17.5 nm wide.

Due to strongly different concentration of electrons and holes, an effective reduction of differential gain by a factor of 1.6 has been found compared with an investigation based on an optical modulation response measurement method [6].

With this laser, there was no significant roll-off due to carrier transport.

Fig. 6 shows a comparison of various simulation runs and measured lasers. Fig. 7 shows frequency response curves of optical power output and various carrier densities.

6. Numerical convergence

Static caracteristics have been obtained by transient analysis starting at very low current levels. It is important to use many points on the stimulus curve, since the solution should not skip to the unphysical branch with negative photon density.

SPICE assumes infinite resistance of current sources in finding an initial bias point. Making an AC analysis to obtain the frequency response, a real bias bias point has to be found with a carrier transport conductivity many orders of magnitude larger than at reference condition. The circuit needs modification, transfering conductance from the current source to real resistors.

7. Conclusion

The proposed circuit gives a pictorial impression of more detailed MQW laser modeling. Still there remains a mismatch to measured electrical characteristics. It seems to be necessary to

include leakage, which has been done in another work [7] with algebraically assigned elements, which is sold as an option by many SPICE vendors.

The measurements were done at Tele Danmark Research, Denmark. This was partly supported by the European Community COMETT programme.

8. References

[1] S. Weisser, I. Esquivias, P.J. Tasker, J.D. Ralston, B. Romero, J. Rosenzweig, "Impedance Characterstics of Quantum-Well Lasers,"
IEEE Photon. Technol. Lett. **6** (1994), no. 12, p. 1421-1423.

[2] N. Tessler, G. Eisenstein, "On Carrier Injection and Gain Dynamics in Quantum Well Lasers,"
IEEE J. Quantum Electron. **29** (1993), no. 6, p. 1586-1595.

[3] N. Suzuki, M. Ishikawa, "A frequency response model in multiquantum well lasers with unequilibrium carrier transport,"
Optical and Quantum Electronics **26** (1994), no.7, p. 789-803.

[4] R.S. Tucker, "Circuit model of double-heterojunction laser below threshold,"
IEE Proc. **128** Pt. I (1981), no. 3, p. 101-106

[5] S.M. Sze, "Physics of Semiconductor Devices," Wiley 1981.

[6] C.B. Su, J. Eom, C.H. Lange, C.B. Kim, R.B. Lauer, W.C. Rideout, J.S. LaCourse, "Characterization of the Dynamics of Semiconductor Lasers Using Optical Modulation,"
IEEE J. Quantum Electron. **28** (1992), no. 1, p. 118-127.

[7] N. Bewtra, D.A. Suda, G.L. Tan, F. Chatenoud, J.M. Xu, "Modeling of Quantum-Well Lasers with Electro-Opto-Thermal Interaction,"
IEEE J. Sel. Topics Quantum Electron. **1** (1995), no. 2, p. 331-340.

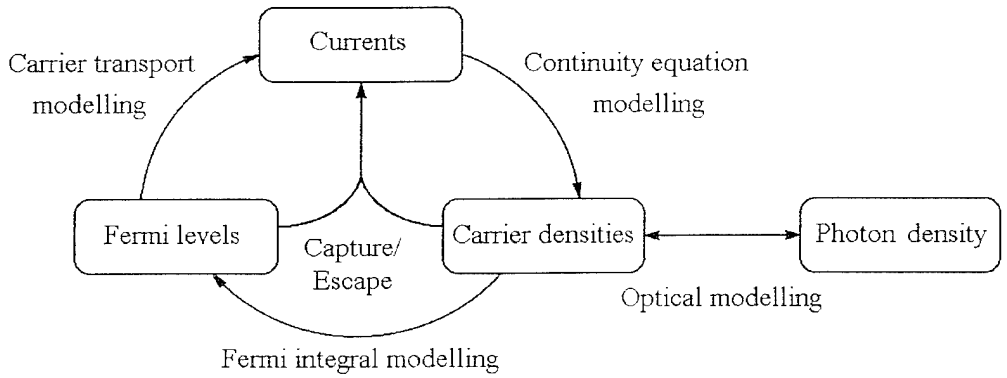


Figure 1. Interaction of modeling circuit parts.

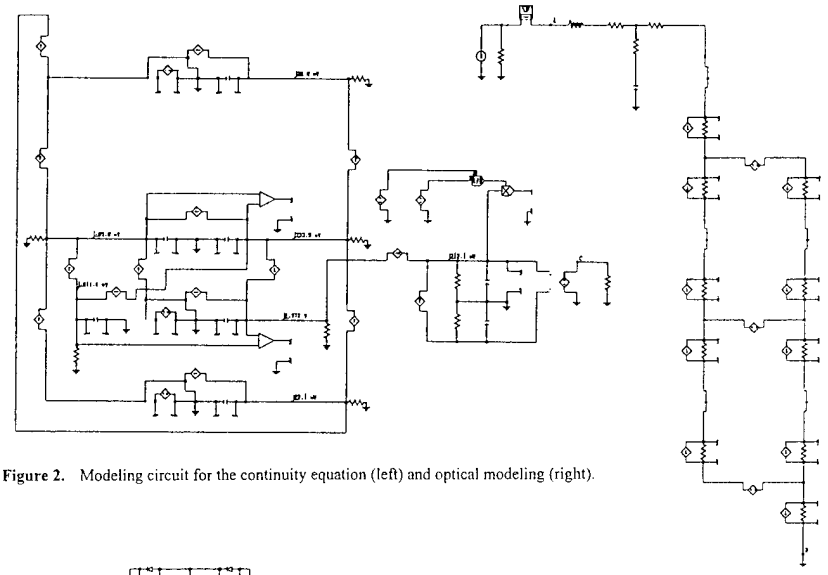


Figure 2. Modeling circuit for the continuity equation (left) and optical modeling (right).

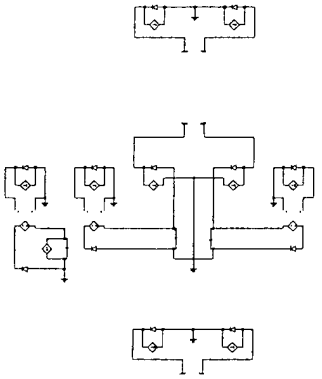


Figure 3. Modeling circuit for Fermi levels and the basic capture/escape currents.

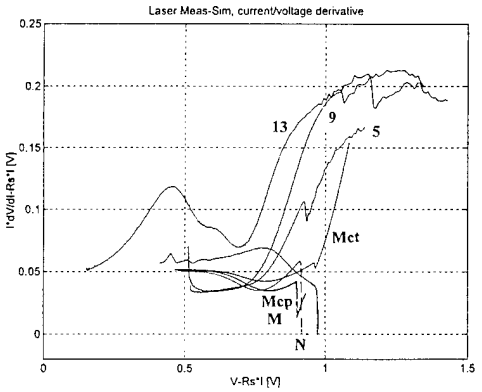


Figure 6. Voltage/Current derivative $I\frac{dV}{dI}$ versus voltage. Series resistance has been subtracted. A **number** denotes the number of quantum wells of measured lasers. Zero is a bulk 1.3 µm laser, thirteen is a laser with a p-doped active region. **N** denotes a model neither taking into account carrier transport nor capture/escape. **M** denotes the reference model. **Mcp** exaggerates capture times by a factor of 10. **Mct** exaggerates the influence of carrier transport by assuming a lower mobility divided by 10.

Figure 4. Electrical circuit part with true voltages and modeling of drift/diffusion currents. Electrical parasitics have been added in the upper left corner.

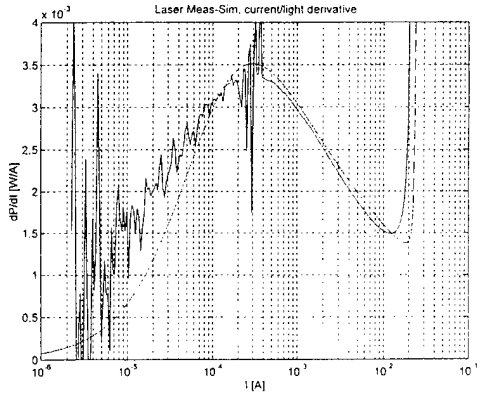


Figure 5. Sub-threshold differential L/I curve $\frac{dP}{dI}$ versus I.

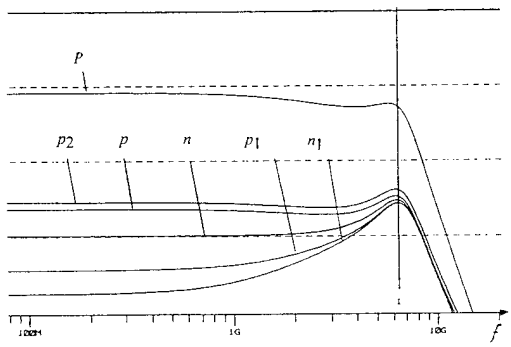


Figure 7. Frequency response (arbitrary units, 10 dB/div.). The curves show the optical power (top), second confined holes, unconfined holes, unconfined electrons, first confined holes, confined electrons (bottom). The marker is at 6.38 GHz.

Spectral Green's Function Approach in the Investigation of Radiation Pattern of a Novel Circular Grating Surface Emitting Laser

Ali M. Shams-Zadeh-Amiri, W. P. Huang

Department of Electrical and Computer Engineering
University of Waterloo, Waterloo, Ontario, N2L 3G1, Canada
Tel: (519)888-4567, Ex: 3819, Fax: (519)746-3077

Introduction

Grating coupled surface emitting lasers (SELs) are desirable for high power applications due to their large emitting areas. The advantages of these kinds of optical sources in comparison with the conventional edge-emitting lasers have caused an interest in geometries to fully develop their potentials. Among these geometries, circular grating SELs (CGSELs) have additional advantage of producing a low divergence circularly symmetric beam. Recently, a novel CGSEL with the emission from the center has been reported [1] . The schematic view of this new geometry is illustrated in Fig.1. Surface emission is produced by the presence of second-order circular grating at the center of the structure. The annular active region surrounding the second-order grating provides optical gain, and the first-order circular grating section which encloses both the annular region and the central region is largely responsible for producing the optical feedback. The most obvious advantage of this new design in comparison with the previous CGSELs is that the emitting region is located at the center of the laser.

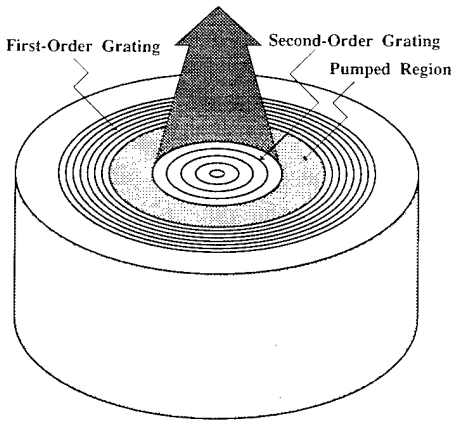


Figure 1: Schematic view of the new CGSEL

To obtain important design criteria and predict the characteristic behavior of this kind of CGSELs, thorough analysis and modeling is needed. As a first step, this paper attempts to

obtain the laser modes and its far field pattern at threshold.

Formulation

The approach employed in this paper consists of two parts. In the first part, appropriate coupled-mode (CM) equations have been solved in each region and the laser characteristic equation has been obtained by applying the boundary conditions at the interfaces between neighboring regions and those at the center and the edge of the laser. To include the effect of radiation field on the resonant modes, we have modified the CM equations reported in the investigation of first-order resonant circular grating [2]-[4]. These modified equations are valid in the limit of large radius approximation. Therefore, the laser gain and its frequency obtained via these equations are more accurate than those obtained simply by ignoring the radiation field. In order to obtain the radiation pattern of the laser, its resonant frequency and resonant modes have been used to model the second order grating as an equivalent volume current source in a planar multilayered structure. To make this model applicable, in the second part of our approach, a closed-form spectral Green's function (Hankel transform domain) has been developed for an arbitrary planar multilayered stack.

Spectral Green's function

We have developed spectral Green's function for an arbitrary multilayered structure in the Hankel transform domain. The idea behind such a development is based on the method first used for predicting the characteristic behavior of a circular patch conductor printed on a grounded dielectric slab [5]. The use of two recurrence formulas for Bessel functions

$$\frac{n}{\rho}B_n(\rho) = \frac{1}{2}[B_{n+1}(\rho) + B_{n-1}(\rho)]$$
$$\frac{dB_n(\rho)}{d\rho} = -\frac{1}{2}[B_{n+1}(\rho) - B_{n-1}(\rho)]$$

are the fundamental principles on which this method is based. It was originally applied to a surface current excitation of a single-layered structure. By using the method of matrix formulation for layered structures, we have extended this method to obtain the closed-form Green's function for arbitrary number of layers, surrounded by substrate from the bottom and by cladding from the top. In addition, we have considered the volume current excitation. The only restriction of this method is that no transverse component of exciting current is allowed. This restriction, however, is not a limiting factor for our purposes because the dominant TE laser mode does not produce such a component. We have also corrected the formulas related to the radiation pattern in the original work [5]. Strictly speaking, obtaining the radiation pattern requires inverse Hankel transform, which was not done in that work.

Radiation Pattern

Based on the method described above, we have obtained the radiation pattern at threshold of a circularly symmetric beam for three different structures. In order to see the dependence of

the radiation pattern on the aperture area, all electrical and geometrical parameters of three CGSELs are kept constant except for radii r_c of the central regions. The radii were chosen $10\lambda_1$, $20\lambda_2$, and $30\lambda_3$, where λ_i $(i = 1, 2, 3)$ are the lasing wavelengths. The parameters are chosen such that the lasing wavelengths are near 1.55 μm. In each case, the excitation of the laser is such that the amplitude of the resonant modes at the center of the laser are the same. As illustrated in Fig.2, the divergence of the beam is less than 1° FWHM in almost all cases.

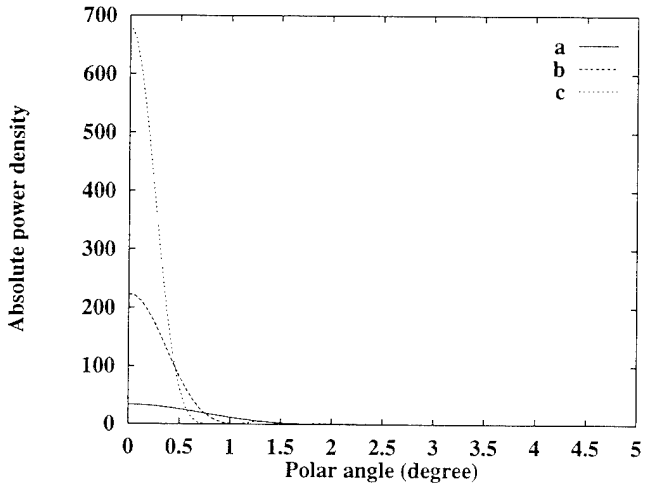


Figure 2: Radiation pattern of a CGSEL with three different central radii, r_c. (a) $r_c = 10\lambda_1$, (b) $r_c = 20\lambda_2$, (c) $r_c = 30\lambda_3$.

Conclusion

The second-order grating profile has been modeled as an equivalent current source exciting a multilayered stack in a novel CGSEL. The far field pattern of the laser has been found from the spectral Green's function (Hankel transform domain) of a multilayered stack. More detailed discussion about the method and results will be presented at the conference.

Acknowledgement

The authors would like to thank Dr. Xun Li for his comments and suggestions.

References

[1] C. Wu, et al., *Jpn. J. Appl. Phys.* vol. 33, Part 2, No. 3B, pp. L 427-L 429, 15 march 1994.

[2] T. Erdogan, et al., *IEEE, J. Quantum Electron.*, vol. 28, pp. 612 -623, March 1993.

[3] C. Wu, et al., *IEEE, J. Quantum Electron.*, vol. 29, pp. 2596-2606, Oct. 1993

[4] X. M. Gong, et al., *IEEE, J. Quantum Electron.*, vol. 30, pp. 1212-1218, May 1994

[5] K. Araki, et al., *IEEE, Trans. Antennas Propagat.*, vol. Ap-29, pp. 84-89, Jan. 1981.

Modeling of a Passive Polarization Converter Free of Longitudinally-Periodic Structure

Marie Fontaine and Velko P. Tzolov, Université du Québec à Hull, C.P. 1250, Succursale B, Hull (Québec) , Canada J8X 3X7, Tel: (819) 773-1626, Fax: (819) 773-1638

Recently, there has been increased interest in the analysis of passive polarization converters made with longitudinally-periodic structures owing their great polarization conversion efficiency. Three kinds of passive polarization converters made with periodic structures are presently reported in the literature: asymmetric loading section converters, tilted waveguiding section converters and asymmetric angled facet section converters. The most promising version so far is the angled facet converter recently proposed by van der Tol et al [1,2]. This polarization converter contains a series of N waveguide sections with right-asymmetric (RAS) and left-asymmetric (LAS) cross-sections with angled facets. Simplified structure of RAS and LAS cross-sections with angled facet are shown in Fig. 1. For any converters made of longitudinally-periodic structures, the main factors limiting the performance of the devices are the losses which occur at the junction between the neighboring sections and the difficulty of fabricating the multi-section devices. In this paper, using a vectorial finite-element propagation method to model angled facet converters, it is shown that polarization rotation effects in such devices can be maximized with an appropriate choice of the facet angle α and the base rib width w. Optimization of structure design achieves a device free of longitudinally-periodic structure with a very short converting length and low losses.

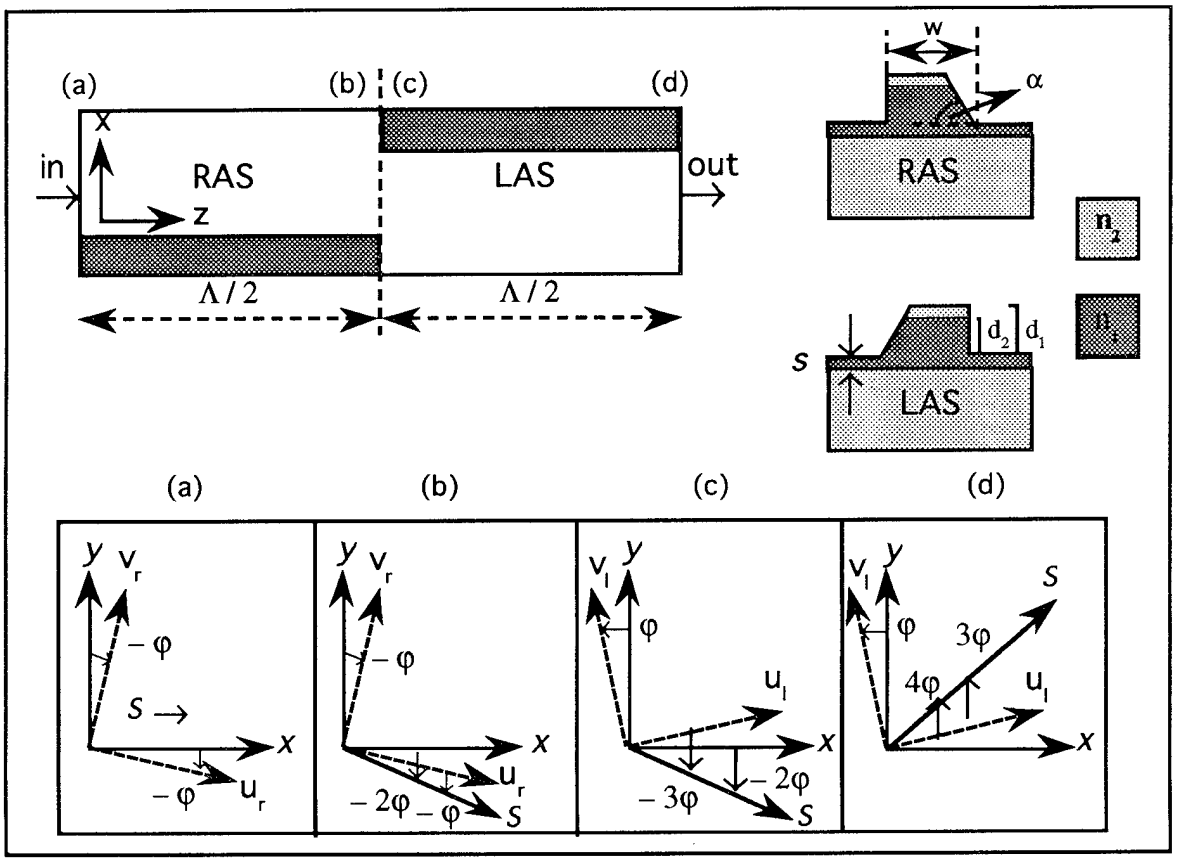


Fig. 1 Above: Top view of one section of a angle facet converter with two subsections (RAS and LAS). Below: The orientation of the optical axis u_r, v_r for RAS (or u_l, v_l for LAS), x and y axis and the polarization state of the propagating signal S for 4 stages (a, b, c, d) along the propagation.

In the following we describe the operating principle of passive polarization converters which is based on a well-known property of birefringent optical devices: if a linearly polarized signal is launched into a longitudinally invariant waveguide and the input polarization state makes an angle ψ (counter-clock-wise) with respect to one of the optical axes of the device, after a propagation length equal to half of beat-length, the output polarization state of the signal makes an angle $-\psi$ (clock-wise) with respect to the same optical axes. To date, all passive polarization converters analyzed in the literature have been based on the use of asymmetric cross-section waveguide structures. The facet angle structure illustrated in Fig. 1 is an example. The asymmetry in the cross-section of the waveguide structure produces a rotation of its optical axis around a fixed coordinate system defined as the Cartesian coordinate system having the x axis parallel and the y axis perpendicular to the epitaxial layers of the waveguide. As shown in Fig. 1, the optical axis u_r and v_r of the facet angle structure are rotated at an angle $-\varphi$ (clockwise) with respect to the x and y axis. Let us consider a longitudinally-periodic structure with a period Λ (the beat-length of the waveguide) having two subsections: a right-asymmetric-structure (RAS) and a left-asymmetric-structure (LAS) respectively (Fig. 1 above). In Fig. 1 (a-d), the optical axes for RAS and LAS are identified as u_r, v_r and u_l, v_l respectively. The optical axis rotation is an angle of $-\varphi$ for RAS (Fig. 1a) and an angle of φ for LAS (Fig. 1c). If an x-polarized signal is launched in the RAS, making an angle of φ in relation to the u_r optical axis (Fig. 1a), the output polarization state at the end of RAS subsection (half-beat-length) is rotated by an angle of $-\varphi$ with respect to the optical axes u_r and by an angle of -2φ with respect to the x axis (input polarization state (Fig. 1b). When the optical signal enters the LAS subsection, the polarization state of the signal makes an angle of -3φ with respect to the optical axes u_l (Fig. 1c). At the end of the LAS subsection, the output polarization state is rotated by an angle of 3φ regarding the optical axes u_l and then by an angle of 4φ in relation to the x axis (input polarization state). In summary, one section of a passive polarization converter, having a length equal to the beat-length Λ, rotates the input polarization state by an angle of 4φ, assuming that φ is the angle between the optical axis of the structure and the linearly-polarized input signal. If N is the number of sections presented, the converted power P_c can be expressed as:

$$P_c = \sin^2(4\varphi N) \qquad (1).$$

The main objective of this paper is to model a waveguide having optical axes (eigenstates) rotated at an angle $\varphi = 45°$ with respect to the fixed coordinate system of the device (x, y in Fig. 1); according to Eq. (1) a 90° polarization rotation after half a period $\Lambda/2$ (or half the beat-length) will then be ensured. As a consequence, no longitudinally-periodic perturbation structures would be further required. In such a case, because of the absence of any junctions, the losses are expected to be reduced. To simulate the polarization rotation, we solve the two following differential equations using a three-dimensional propagation method based on a finite-element numerical scheme:

$$2i\beta\frac{\partial e_x}{\partial z} = \frac{\partial}{\partial x}\left\{-\frac{\partial e_x}{\partial x} - e_x\frac{\partial}{\partial x}\left[\ln\left(n^2\right)\right] - e_y\frac{\partial}{\partial y}\left[\ln\left(n^2\right)\right]\right\} + \frac{\partial}{\partial y}\left\{-\frac{\partial e_x}{\partial y}\right\} - \left(k^2n^2 - \beta^2\right)e_x \qquad (2a)$$

$$2i\beta\frac{\partial e_y}{\partial z} = \frac{\partial}{\partial x}\left\{-\frac{\partial e_y}{\partial x}\right\} + \frac{\partial}{\partial y}\left\{-\frac{\partial e_y}{\partial y} - e_x\frac{\partial}{\partial x}\left[\ln\left(n^2\right)\right] - e_y\frac{\partial}{\partial y}\left[\ln\left(n^2\right)\right]\right\} - \left(k^2n^2 - \beta^2\right)e_y \qquad (2b).$$

The parameters of the cross-section of the angle facet rib waveguide we analyzed are as follows (Fig. 1): The top layer is InP ($n_2 = 3.27$), the layer below is InGaAsP ($n_2 = 3.4$) grown on InP ($n_2 = 3.27$). The geometrical parameters are: d_1 = 1 μm, d_2 = 0.8 μm and s = 0.2 μm. The operation wavelength is $\lambda = 1.5\ \mu m$. We vary two parameters to optimize the polarization rotation

capability of the device. These parameters are the facet angle α and the base rib width w. In Fig. (2a) we present the variation of the two lowest order propagation constants for a device having $\alpha = 75°$ as a function of the rib width w. Here we introduce a parameter R related to the rotation angle of the optical axis of the waveguide with respect the x and y axes:

$$R = \frac{\int_{A_w} n^2(x,y)\, e_x^2(x,y)\, dx\, dy}{\int_{A_w} n^2(x,y)\, e_y^2(x,y)\, dx\, dy} \qquad (3),$$

where $n(x,y)$ is the refractive index distribution and $e_x(x,y)$ and $e_y(x,y)$ are the distributions of the transversal electrical field components. The integrals are taken on the area A_w of the computational window. If $R << 1$, the corresponding eigenstate is principally polarized along the y axis; if $R = 1$, the optical axes of the corresponding eigenstate are rotated at 45° with respect to x or y; and finally if $R >> 1$, the corresponding eigenstate is principally polarized along the x axis. From the plot of the rotation parameter R as a function of the width of the rib-waveguide, as illustrated in Fig. 2b, we can conclude that a width w = 1.81 μm yields a 45° rotation of the optical axes. Consequently, this structure is expected to provide 90° polarization rotation in half the period without the use of any longitudinally-periodic structures.

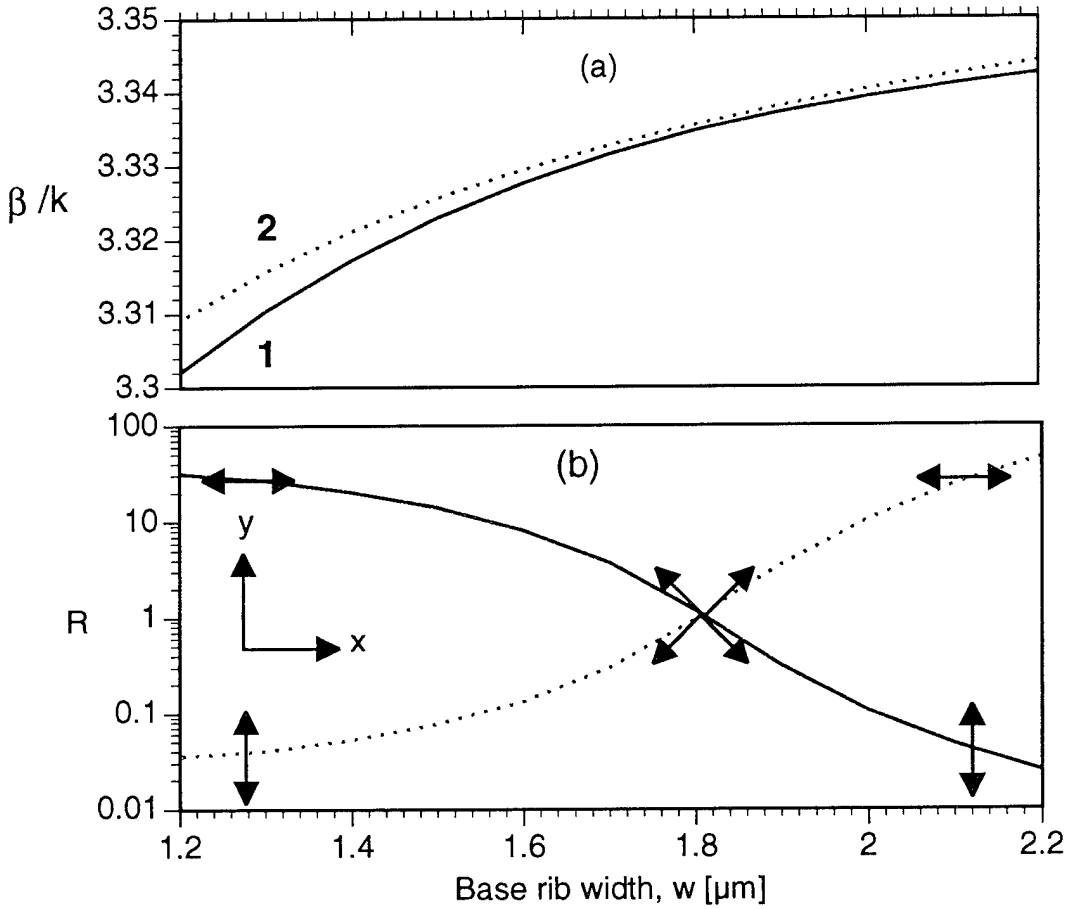


Fig. 2 The variation of: a) the normalized propagation constants for the two lowest order polarization modes and b) the optical axes rotation parameter R for the same eigenstates as a function of the rib width. The eigenstates are identified as 1 - solid line and 2 - dotted line. The arrows in b) give an indication of the current orientation of the corresponding eigenstate with respect to x and y axis.

Different facet angle converters optimized to have 45° rotation of the optical axis have been simulated. In Fig. 3 we present the propagation simulation for a structure having having a facet angle $\alpha = 45°$, a rib base width w = 2.0 μm. The relative powers along the x and y axes are presented as a function of the propagation distance. A 90° polarization rotation (100% power transfer) can be observed after a distance of less than 0.25 mm, corresponding to half the waveguide beat-length. For all the devices, variations of $\pm 0.1 \mu m$ in the optimized rib base width yields a power transfer of 92-93% instead of 100%. Therefore, tight tolerances are not expected when designing pratically the devices.

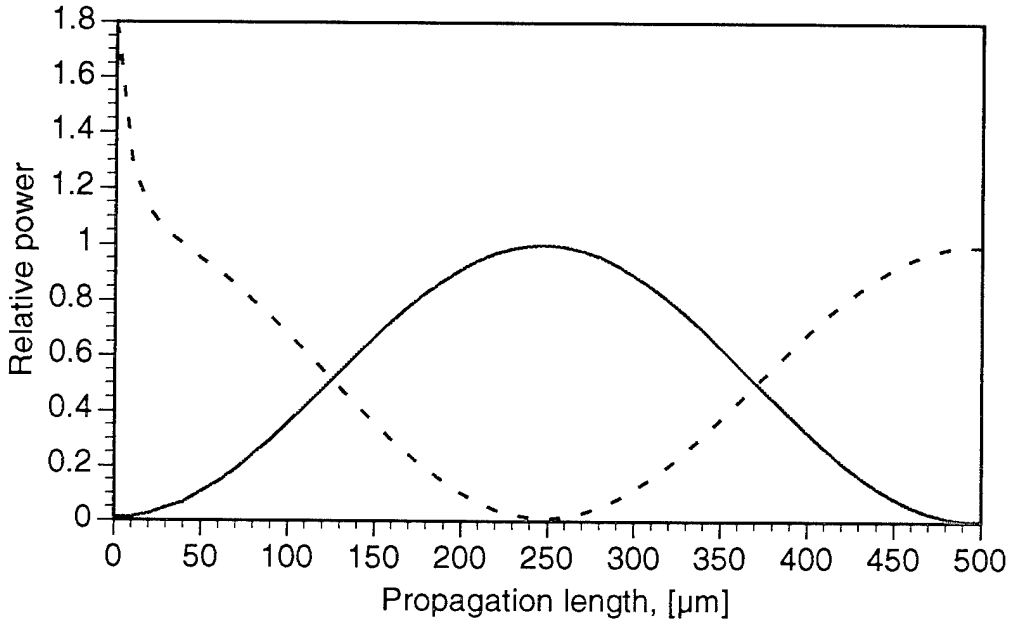


Fig. 3 The relative power along x - dashed line and along y - solid line as a function of the propagation length

To summarize, based on a vectorial analysis, the operating principle of passive polarization converters have been presented in terms of optical axis orientation. This analysis reveals that an appropriate geometrical configuration can be deduced to optimize the polarization conversion process. As a result, a passive polarization converter free of longitudinally-periodic structures has been proposed. The device is expected to have superior features as a passive polarization converter:

(i) a very short length (0.25 mm total length)
(ii) no junctions
(iii) no period-to-period coupling losses since no multi-section structure is required.

References:

1. J. J. G. M. van der Tol, J. W. Pedersen, E.G. Metaal, F. Hakimzadeh, Y.S. OEI and I. Moerman, IEEE Photon. Technol. Lett. 7(1), 32-34 (1995).

2. J. J. G. M. van der Tol, F. Hakimzadeh, J. W. Pedersen, D. Li, and H. van Brug, IEEE Photon. Technol. Lett. 7(8), 893-895 (1995).

Polarization Splitting in Lossy/Gainy MQW Directional Couplers

Kwang C. Ho, G. Griffel and T. Tamir
Polytechnic University, Brooklyn, NY 11201

1. Introduction

Optical polarizers consisting of directional couplers are of great interest as guided-wave devices in optical signal processing systems. By splitting the input signal into two orthogonal TE and TM modes, the output signals can be used in a high-speed optical communication for single-mode transmission. The pertinent behavior, which relies on the difference between propagation constants, was analyzed by using coupled-mode theory to evaluate the coupling lengths for the two polarizations [1] [2]. However, this approach is often insufficiently accurate, and it may not provide full information on all the physical effects encountered in devices containing lossy and/or gainy media, such as semiconductor based materials.

In this paper, we present a transmission-line modal description (TLMD) to rigorously analyze the mode polarization effects in $GaAs/Al_xGa_{1-x}As$ heterostructure waveguides using MQW layers as a secondary guiding channel, as shown schematically in Fig. 1. By defining a useful and accurate mode suppression ratio for the supermodes that determine the polarization effects, our results show that a very effective splitting of the two polarization states can be implemented.

2. Modal Derivation of the Optimal Polarization Length

Stratified semiconductor guiding structures are subject to material loss due to *inter-band* (α_{qi}) and *free-carrier* (α_{qf}) absorption [3] in the guiding layers. For structures containing layers identified by an index q, the complex dielectric constants can be expressed in terms of the total loss $\alpha_q = \alpha_{qi} + \alpha_{qf}$, as given [4] by

$$\epsilon_q = \epsilon_q' + i\epsilon_q'' = \left[n_q^2 - \left(\frac{\alpha_q}{2k_o}\right)^2\right] + i\left[\frac{n_q\alpha_q}{k_o} + \frac{\sigma_q}{\omega\epsilon_o}\right] \quad , \tag{1}$$

where a time variation $e^{-i\omega t}$ is implied, k_o is the wavenumber in vacuum. For dielectric materials, $\epsilon_q' > 0$ and ϵ_q'' is positive or negative depending on whether the material is lossy or gainy, respectively.

A typical MQW directional coupler, as shown in Fig. 1, consists of several dielectric layers identified by $q = p$ (for the primary guide), uc (for the upper cladding), lw (for the low-bandgap layer), hw (for the high-bandgap layer) and lc (for the lower cladding). For a heterostructure optical coupler ($\sigma_q \approx 0$), the complex propagation constant $k_z = \beta + i\alpha$ of the composite structure can be calculated by applying Eq. (1) and the transverse resonance condition [5]

$$Y_{up} + Y_{dn} = 0 \quad , \tag{2}$$

where Y_{up} indicates the admittance looking up at an arbitrary layer boundary, and Y_{dn} represents admittance looking down at that point.

As the current injected into the structure increases, the negative imaginary components ϵ_{lw}'' of ϵ_{lw}, which affects the gain component in the MQW structure, become more negative. The resulting gain in the medium causes the net positive attenuation α to also decrease. At a critical

value $\epsilon''_{lw,c}$ of ϵ''_{lw}, the gain overcomes the absorption losses and the guided wave travels without attenuation along the longitudinal z direction, i.e., $\alpha = 0$. Larger current intensities generate values of $\epsilon''_{lw} < \epsilon''_{lw,c}$ that cause α to become negative, in which case the wave amplitude increases as it progresses along z.

For optical parameters as given in Table 1, we plot in Fig. 2 the attenuation $\alpha\lambda$ at the phase-match points ($\lambda_p = 0.8733\ \mu m$ for TE and $\lambda_p = 0.7398\ \mu m$ for TM modes) as a function of the gain component $-\epsilon''_{lw}$ associated with the quantum wells. We note that $\alpha\lambda$ is positive or negative according to whether $-\epsilon''_{lw}$ is smaller or larger than the critical values $-\epsilon''_{lw,c} =$ (0.033, 0.034) for even (symmetric) TE/TM modes and (0.043, 0.045) for odd (anti-symmetric) modes, respectively. Absorption losses presented at $-\epsilon''_{lw,c} = 0$ produce net positive attenuations $\alpha\lambda = (6.44 \times 10^{-4}, 6.48 \times 10^{-4})$ for even TE/TM modes and $(5.69 \times 10^{-4}, 5.84 \times 10^{-4})$ for odd modes. These losses are balanced out by transparency gain of the wells at the critical values of $-\epsilon''_{lw,c}$. Since the results in Fig. 3 were generated by solving Eq. (2) for the given structure, they are based on a rigorous solution of the pertinent boundary-value problem.

To determine optimal beamsplitting conditions, we assume that the geometry is two-dimensional ($\frac{\partial}{\partial y} = 0$), and a wave is incident into the primary guide. The transverse modal fields can be expressed by the transmission-line modal functions [6]

$$\left.\begin{aligned} \mathbf{E}_c(x,z) &= \varepsilon_c(x)\left[V_s(z)\mathbf{e}_s(x) + V_a(z)\mathbf{e}_a(x)\right] \\ \mathbf{H}_c(x,z) &= \rho\left[I_s(z)\mathbf{h}_s(x) + I_a(z)\mathbf{h}_a(x)\right] \end{aligned}\right\} \quad \text{for } 0 \le z \le z_o\ ,$$

$$\mathbf{E}_r(x,z) = \varepsilon_r(x)V_r(z)\mathbf{e}_r(x)\ ,\quad \mathbf{H}_r(x,z) = \rho I_r(z)\mathbf{h}_r(x) \qquad \text{for } z < 0 \text{ and } z > z_o \tag{3}$$

where the subscript $r = [in,\ out]$ for the input or output section, s and a represent the even and the odd modes while $\rho = [-1, 1]$ and $\varepsilon(x) = [1, \epsilon_j^{-1}(x)]$ for TE/TM modes, respectively.

A modal field incident at the junction boundary $z = 0$ from the primary waveguide generates supermodes that propagate independently along z. The power of these supermodes decays or grows exponentially due to the loss or gain in the guiding structure, and is transmitted through the primary and/or secondary channel at $z = z_o$. Then, using the boundary conditions at $z = 0$ and $z = z_o$ and neglecting reflections, we obtain

$$\begin{aligned} &\varepsilon_{in}V_{in}(0)\mathbf{e}_{in}(x) \cong \varepsilon_c(x)\left[V_s(0)\mathbf{e}_s(x) + V_a(0)\mathbf{e}_a(x)\right]\ , \\ &I_{in}(0)\mathbf{h}_{in}(x) \cong I_s(0)\mathbf{h}_s(x) + I_a(0)\mathbf{h}_a(x)\ , \\ &\varepsilon_{out}V_{out}(z_o)\mathbf{e}_{out}(x) \cong \varepsilon_c(x)\left[V_s(z_o)\mathbf{e}_s(x) + V_a(z_o)\mathbf{e}_a(x)\right]\ , \\ &I_{out}(z_o)\mathbf{h}_{out}(x) \cong I_s(z_o)\mathbf{h}_s(x) + I_a(z_o)\mathbf{h}_a(x)\ . \end{aligned} \tag{4}$$

Applying to Eq. (4) the power normalization and field orthogonality conditions

$$\int_{cs} \varepsilon_{out}(x)|\mathbf{g}_{out}(x)|^2\ dS = 1\ , \qquad \int_{cs} \varepsilon_c(x)\mathbf{g}_n \cdot \mathbf{g}_m\ dS = C_n\delta_{nm}\ , \tag{5}$$

we obtain the modal voltages and currents given by

$$\frac{V_{out}(z_o)}{V_{in}(0)} = \frac{e^{ik_{z,s}z_o}}{C_s}T^{(s)}_{in,c} + \frac{e^{ik_{z,a}z_o}}{C_a}T^{(a)}_{in,c}\ , \qquad \frac{I_{out}(z_o)}{I_{in}(0)} = \frac{e^{ik_{z,s}z_o}}{C_s}T^{(s)}_{c,out} + \frac{e^{ik_{z,a}z_o}}{C_a}T^{(a)}_{c,out} \tag{6}$$

where C_n is an appropriate normalization constant, $\mathbf{g}(x)$ represents $\mathbf{e}(x)$ or $\mathbf{h}(x)$, and the transformation constant $T^{(m)}_{a,b}$ between modal functions is given by

$$T^{(m)}_{a,b} = \left[\int_{cs} \varepsilon_a\mathbf{g}_{in} \cdot \mathbf{g}_m\ dS\right]\left[\int_{cs} \varepsilon_b\mathbf{g}^*_{out} \cdot \mathbf{g}_m\ dS\right]\ . \tag{7}$$

As a result, we can define a novel *mode suppression ratio* M_{sr} to determine the optimized polarization length L_{op} by

$$M_{sr} = \begin{cases} \eta_{te}/\eta_{tm} , & \text{for TM mode suppression} , \\ \eta_{tm}/\eta_{te} , & \text{for TE mode suppression} , \end{cases} \tag{8}$$

where the coupling efficiency η is defined as

$$\eta = \frac{V_{out} I^*_{out}}{V_{in} I^*_{in}} . \tag{9}$$

To obtain optimum transfer conditions, we assume that TE and TM modes having the same amount of power are fed through the primary channel simultaneously at the input terminal. After propagating over the length z_o of the coupler, the field separates into the two guiding channels at the output terminal. The value of z_o in which this field splits into a TM mode in one of the output channels and a TE mode in the other defines the optimal polarization length L_{op} that maximizes the mode suppression ratio M_{sr}.

3. Numerical Results and Conclusion

To explore the TE/TM polarization beamsplitting in a MQW lossy/gainy optical coupler, we have applied the rigorous TLMD method using parameters as given in Table 1. We limit ourselves to the case of TE mode emitted from the secondary waveguide (*TM mode suppression*). The schematic configuration is shown in Fig. 1(b). The alternative situation for *TE mode suppression* has a larger optimal polarization length.

A gain polarization beamsplitter with 4 quantum wells, operating wavelength $\lambda_p = 0.8733\ \mu m$, and $-\epsilon''_{lw} = 0.05$ was evaluated, as shown in Fig. 3. We note that the suppression ratio peak is located at $L_{op} = 194.2\ \mu m$ (vertical solid line), rather than at $L_p = 202\ \mu m$ as obtained by the conventional coupled-mode method (vertical dotted line). We also found that the difference becomes more appreciable for lossy cases. We conclude that the rigorous analytical method provides a powerful tool, which yields accurate results that may not be achieved otherwise.

References

[1] F.Ghirardi *et al.*, "Polarization Splitter Based on Modal Birefringence in InP/InGaAsP Optical Waveguide," *IEEE Photon. Technol. Lett.*, Vol.5, pp. 1047-1049, 1993.

[2] A.N.Miliou *et al.*, "A 1.3-μm Directional Coupler Polarization Splitter by Ion Exchange," *J. Lightwave Technol.*, LT-11, pp. 220-225, 1993.

[3] W.P.Dumke, "Interband Transitions and Maser Action," *Physics Review*, Vol.127, pp. 1559-1563, 1962.

[4] M.J.Adams and M.Cross, "Electromagnetic Theory of Heterostructure Injection Lasers," *Solid-State Electronics*, Vol.14, pp. 865-883, 1971.

[5] T.Tamir, "Beam and Waveguide Couplers," in *Integrated Optics*, pp. 107-110, Springer-Verlag, 1979.

[6] L.B.Felsen and N.Marcuvitz, *Radiation and Scattering of Waves*, pp. 187-190, IEEE Press, 1994.

Layer	Material	x	$\mathbf{n, p}(cm^{-3})$	$\mathbf{t}(\mu m)$
Primary Guide	$p^+ - Al_xGa_{1-x}As$	0.1	$p^+ = 2.3 \times 10^{19}$	$t_p = 0.4$
Upper Cladding	$p - Al_xGa_{1-x}As$	0.2	$p = 1.83 \times 10^{19}$	$t_{uc} = 0.8$
Secondary Guide	$pure - GaAs$	0	0	$t_{lw} = 8 \times 10^{-3}$
	$pure - Al_xGa_{1-x}As$	0.2	0	$t_{hw} = 1 \times 10^{-2}$
Lower Cladding	$n - Al_xGa_{1-x}As$	0.2	$n = 1 \times 10^{18}$	$t_{lc} = 0.2$
Substrate	$n - Al_xGa_{1-x}As$	0.4	$n = 1 \times 10^{18}$	n/a

Table 1: Optical parameters for numerical analysis at $E_p = 1.29\ eV$ and $T = 298\ ^oK$.

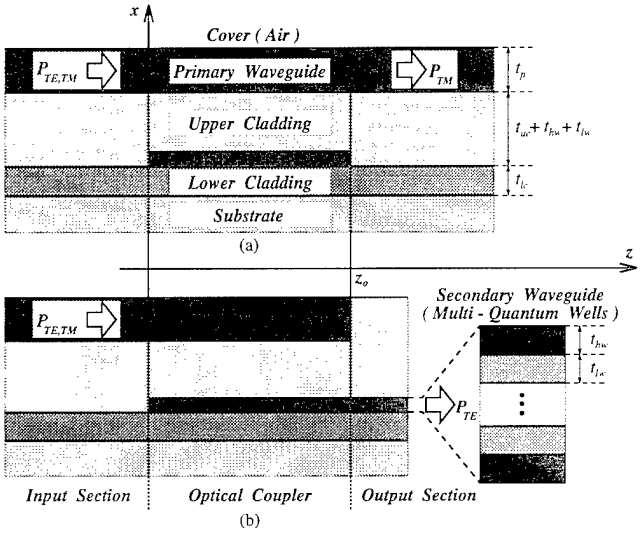
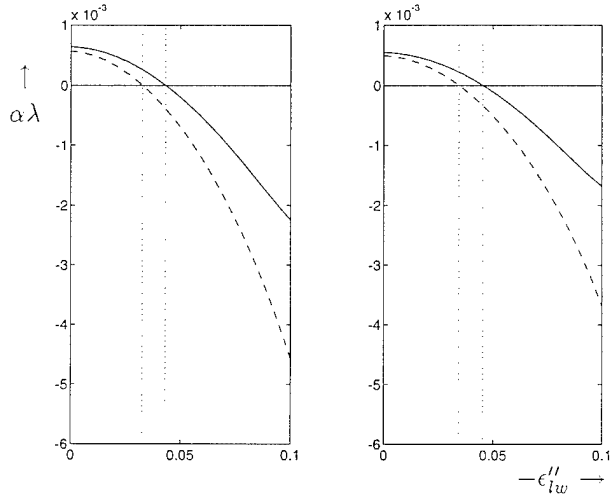


Figure 1: MWQ optical directional polarizers with identical input guides but different output guides : (a) Primary waveguide only, (b) Primary waveguide for input and secondary waveguide for output.



(a) TE mode (b) TM mode

Figure 2: Variation of $\alpha\lambda$ as a function of $-\epsilon''_{lw}$. The solid or dashed lines represent even or odd modes. Vertical dotted lines show the critical gain values.

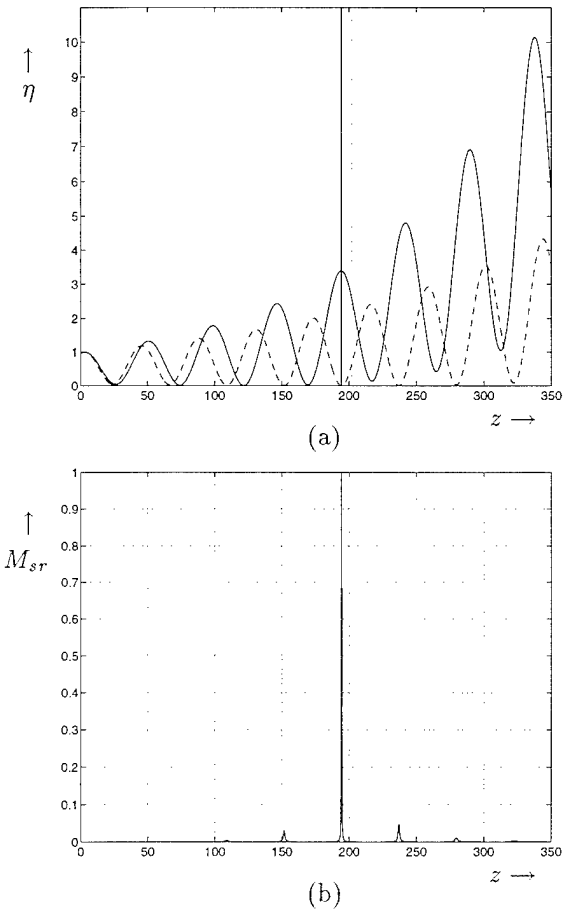


Figure 3: (a) Coupling efficiency η for TE mode (solid line) and TM mode (dashed line); (b) TM mode suppression ratio M_{sr} as a function of z at $-\epsilon''_{lw} = 0.05$. Vertical solid and dotted lines in (a) represent our results and coupled-mode results for polarization lengths, respectively.

Optimisation of Slab Waveguides with Given Mode Width towards Low Modal Birefringence

G. Sarlet, J. Haes and R. Baets
University of Gent-IMEC, Department of Information Technology
Sint-Pietersnieuwstraat 41, B-9000 Gent, Belgium
Tel: +32-9-264 33 16 Fax: +32-9-264 35 93
E-mail: Jan.Haes@intec.rug.ac.be

Introduction - A well known characteristic of optical fibres is that they do not maintain the polarisation of the transmitted light. Therefore an important requirement of integrated optical circuits in optical fibre systems is that they have to be polarisation independent, i.e. their operation is the same for all polarisations of the incoming light. Unfortunately, integrated optical waveguides always show modal birefringence. In an optical bandpass-filter based on interference this causes for example a shift in the wavelength for maximal transfer between TE and TM modes.

In channel waveguides one can reduce this modal birefringence by using circular or square waveguides. As a second possibility one can optimise the height h and width w of a ridge waveguide. For particular values of w and h the difference in effective index vanishes. However, the polarisation dispersion increases rapidly when w or h show small deviations from the optimal values. A third method consists in using anisotropic materials to compensate the birefringence caused by the waveguide.

In this paper we focus our attention on slab waveguides, because one could consider these as a 'worst-case' when compared to channel waveguides. Further, one could expect, when using a slab waveguide with low polarisation dispersion as a basis for the optimisation of a channel waveguide with respect to modal birefringence, the channel guide birefringence will be lower and the optimum less sensitive to variations in design parameters.

Recently, a simple analytic result for slab waveguide modal birefringence was derived [1]. In this paper we adopt a more numerical approach. We will compare the modal birefringence of a class of step index slab waveguides, which all have a given value for the mode width, and compare them with a parabolic index waveguide, which is found to be optimal in terms of birefringence. A general rule for optimal polarisation dispersion will be formulated for step index slab waveguides.

Approach - We study waves propagating along the z-axis in slab waveguides, with transversal index variation along the x-axis. A simple symmetric 3-layer slab waveguide has, for a given wavelength, three degrees of freedom in the refractive index profile: the core index n_1, the cladding index n_2 and the core width $2a$. In order to be able to compare different refractive index profiles in terms of modal birefringence, we have to choose a fair basis of comparison. This is done by requiring all structures to have equal mode width w_{90} and equal effective index n_{eff} of the TE_0 mode. The condition of constant mode width originates from the observation that TE and TM effective indices can be made arbitrarily close to each other by forcing the waveguide structure to cut-off ($n_{eff} \rightarrow n_2$) or to extreme guidance ($n_{eff} \rightarrow n_1$). The effective index level is also kept constant to allow for a fair comparison between different

waveguide structures. For structures which are symmetric relative to the yz-plane, we define the mode width w_{90} with the relation:

$$\int_{-w_{90}/2}^{w_{90}/2} |E_y(x)|^2 dx = 0.9 \int_{-\infty}^{+\infty} |E_y(x)|^2 dx \qquad (1)$$

For asymmetric 3-layer slabs, with air superstrate, the surface between core (high refractive index) and superstrate (at $x = 0$) is taken as upper boundary for the integration and $-w_{90}$ as lower boundary. In this case the electric field will extend very little into the superstrate, because of the large difference in refractive index.

The wavelength equals 1.55 μm. The effective index of the TE_0 was fixed at a value of 3.20, which is a typical value for InP/InGaAsP-based waveguides. The conclusions of this paper are independent however of the precise choice of this value.

Results - *1. Parabolic Index Profile.* The first profile we consider is the parabolic index profile, where the variation of the refractive index is described by:

$$n(x) = \sqrt{n_1^2 - (x/\alpha)^2} \qquad (2)$$

This profile has two advantages: we have only two degrees of freedom (n_1 and α) and there exist analytical expressions for the effective indices of TE (exact) and TM modes (approximate) [2]. For given values of the TE_0 effective index and mode width we calculate n_1 and α, from which the modal birefringence $\Delta n_{eff} = n_{eff}(TE_0) - n_{eff}(TM_0)$ is derived, as plotted in figure 1. These values will be used as reference values for the modal birefringence in the following.

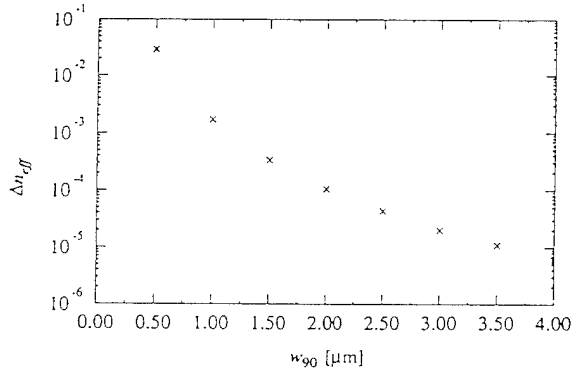
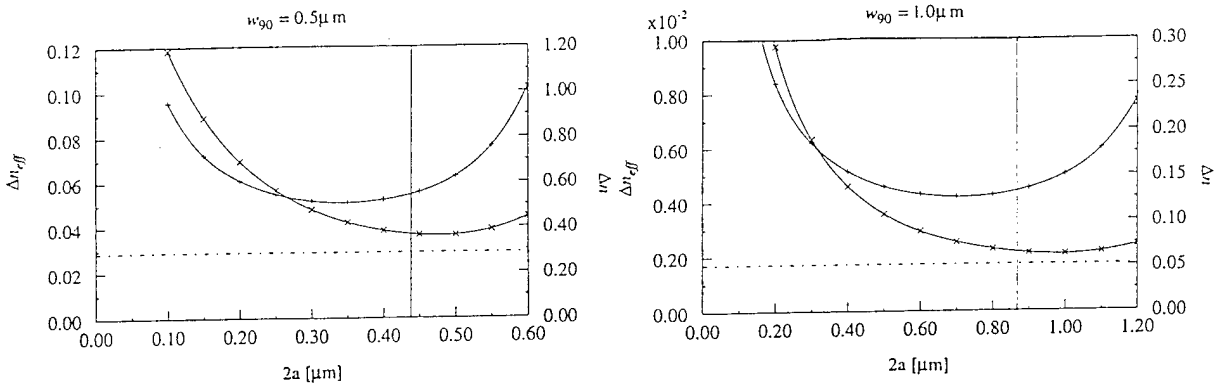


Figure 1: Modal birefringence Δn_{eff} of the parabolic index profile as a function of the mode width of the TE_0 mode.

2. Symmetric 3-layer Slab. We studied the waveguide for three different values of w_{90} = 0.5, 1.0 and 2.0 μm. For given values of the TE_0 mode effective index, mode width and for variable core width we calculated the refractive indices n_1 and n_2. For each pair of indices we then evaluated the modal birefringence, see figure 2. In each graph we also indicated the range of the core width for which the waveguide is single moded (left of the vertical line).

We see that in each case the polarisation dispersion decreases with increasing core width, and diminishing refractive index contrast, and approaches the value for the parabolic profile when the core width is near to the mode width. It is also observed that the modal birefringence of a symmetric 3-layer slab will be lowest near to the cut-off of the TE_1 mode.



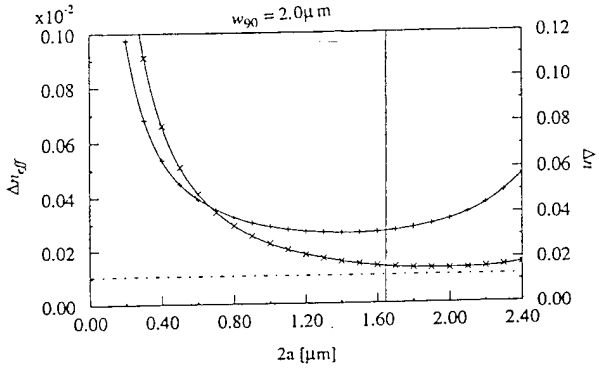
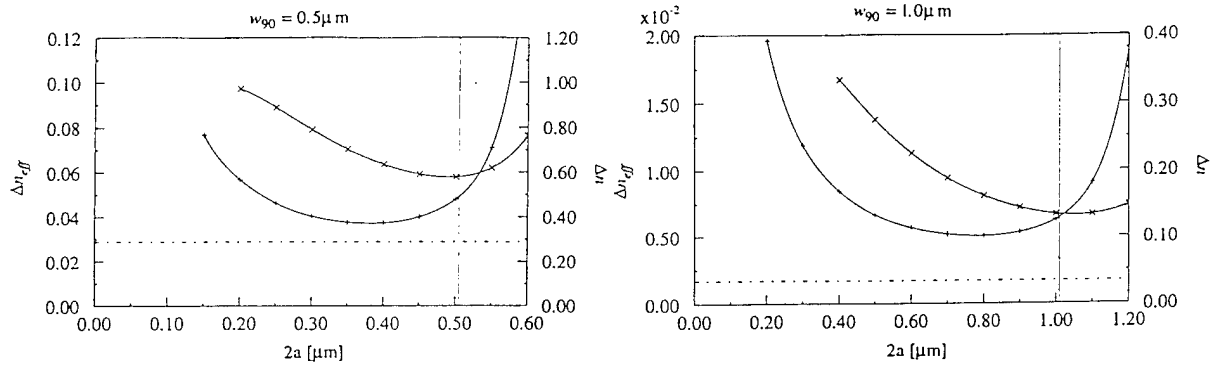


Figure 2: Symmetric 3-layer slab. Modal birefringence Δn_{eff} (×, left axis) and refractive index contrast $\Delta n = n_1 - n_2$ (+, right axis) as a function of the core width $2a$ for three values of the TE_0 mode width w_{90}. The dashed-dotted horizontal line shows the corresponding value of the parabolic index profile birefringence. All waveguides are single moded left of the vertical line.



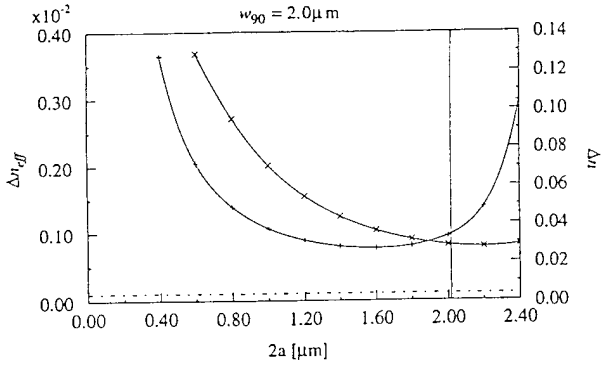


Figure 3: Asymmetric 3-layer slab. Modal birefringence Δn_{eff} (×, left axis) and refractive index contrast $\Delta n = n_1 - n_2$ (+, right axis) as a function of the core width $2a$ for three values of the TE_0 mode width w_{90}. The dashed-dotted horizontal line shows the corresponding value of the parabolic index profile birefringence. All waveguides are single moded left of the vertical line.

3. Asymmetric 3-layer Slab. If we repeat the calculations for an asymmetric 3-layer slab, where the refractive index on one side of the core is 1, and on the other side n_2, we obtain the results shown in figure 3. Again we see that the modal birefringence is lowest near to the cut-off of the TE_1 mode. Compared to the symmetric structure, the asymmetric structure has a stronger birefringence for the higher mode widths, with comparable index contrast.

4. 5-Layer Index Profiles. Here we consider symmetric 5-layer slabs (see figure 4). The idea is that, for a symmetric 3-layer slab the TM effective index is always lower than the TE index, implying that the TM has a slightly larger mode width. The TM mode therefore extends more in the cladding regions than the TE mode of the same order. By increasing the refractive index in the cladding regions or by applying a dip in the centre of the core index profile, one hopes that the TE and TM effective indices will approach each other. Some results for a mode width of 1.0 μm are given in table 1. We see that the modal birefringence gets worse as the refractive index profile moves further away from the more monotonous behaviour of the parabolic index. The modal birefringence always exceeds that of the 3-layer slab.

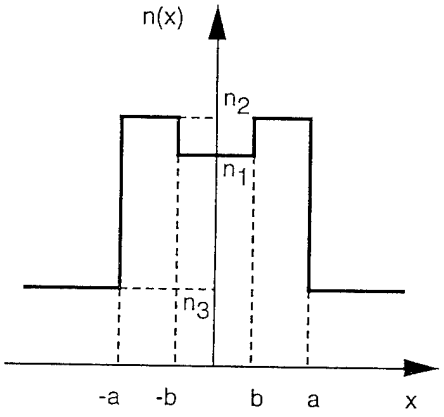


Figure 4: 5-layer refractive index profile.

2a [μm]	2b [μm]	n_1	n_2	n_3	Δn_{eff}
0.50	0.00	-	3.277327	3.139905	0.003566
	0.05	3.25	3.281115	3.139620	0.003621
		3.20	3.287848	3.139112	0.003919
		3.15	3.294334	3.138621	0.004468
		3.10	3.300584	3.138145	0.005258
	0.10	3.25	3.286006	3.139271	0.003692
		3.20	3.301155	3.138157	0.004373
		3.15	3.315422	3.137097	0.005585
		3.10	3.328873	3.136089	0.007272

Table 1: Modal birefringence for the symmetric 5-layers slab ($w_{90} = 1.0\mu m$). The first row gives the birefringence of the corresponding 3-layer slab.

Conclusion - In this paper the optimisation of the modal birefringence of slab waveguides was discussed. The birefringence of the parabolic index profile was considered as a reference. To make a fair comparison two conditions were imposed on the fundamental slab mode. The TE effective index level as well as the mode width were fixed. It was shown that the modal birefringence of a single mode symmetric 3-layer slab is minimal at the onset of the first order mode. This leads to the conclusion that waveguides with large core width and low index contrast show lower modal birefringence than thinner waveguides with higher index contrast. We also found that the birefringence of the parabolic index profile can be considered as a lower boundary and that the birefringence of strongly asymmetric slab waveguides is significantly larger than the birefringence of the corresponding symmetric slab, especially for higher mode widths.

Acknowledgement - J. Haes is a doctoral fellow of the Flemish IWT.

References

[1] J. Buus, J. Haes and R. Baets, "Analytic study of birefringence in slab waveguides", *submitted for publication.*

[2] M.J. Adams, *An Introduction to Optical Waveguides*, John Wiley & Sons, Chichester, 1981.

Effects of External Optical Feedback in Broad Area Lasers

J. Martín-Regalado[†], G.H.M. van Tartwijk[†,*], S. Balle[†,‡] and M. san Miguel[†,‡]

[†]Departament de Física, Universitat de les Illes Balears, E-07071 Palma de Mallorca, Spain

[‡]Instituto Mediterraneo de Estudios Avanzados, IMEDEA (CSIC-UIB), E-07071 Palma de Mallorca, Spain

[*]Current address: The Institute of Optics, University of Rochester, Rochester, NY 14627, USA

Considerable effort has been recently focused on the development of coherent laser sources for applications which require high output powers such as free-space communications systems. Broad-area lasers have been proposed as possible candidates because they have wider injection regions than conventional lasers, so a large amount of stimulated photons can be generated. However, both the lack of guiding control of the optical mode and the spatial hole burning effect favor the simultaneous oscillation of several lateral modes when the laser is driven higher above threshold [1,2]. As a consequence, the output beam profile develops filamentation [3] which limits the operativity of these lasers devices. A reduction in the number of excited lateral modes is desirable in order to increase the spectral purity and spatial coherence of such lasers. Operation in the fundamental single-lobe lateral mode can provide spatially-coherent diffraction-limited high-power laser sources, but it requires a control mechanism of the excited lateral modes in these devices.

Optical feedback from an external cavity, where a laser diode is exposed to optical feedback by reflecting a part of the output beam back into the laser cavity, has been shown to yield single longitudinal mode operation, tuning of the lasing frequency, and substantial linewidth narrowing in Fabry-Perot multi-longitudinal mode lasers [4]. This highly coherent state is the result of the nonlinear interaction of the longitudinal modes of the laser cavity and the external cavity modes. In this work we study the possibility of lateral mode control and selection in broad area lasers through external optical feedback, in order to improve the optical characteristics of the laser beam of these lasers.

We model the spatio-temporal dynamics of the broad-area laser by the semiclassical

Maxwell-Bloch equations for a two-level homogeneously broadened single mode laser [5]. The external optical feedback is incorporated to the field equation in the Lang–Kobayashi weak feedback approximation [6]. The equations of the model are solved numerically for a 30 μm wide, broad area laser for several injection currents. The reflectivity of both laser facets is $R = 32.0\%$. A low reflectivity external mirror of $R_{ext} = 0.34\%$ is used in all the simulations. The external cavity length, $L_{ext} = \frac{c\tau}{2}$, is chosen in such a way that the separation between external cavity modes, $\Delta\nu = \tau^{-1} = 70$ GHz, is larger than the width of the free-running laser spectrum. For such external cavity length ($L_{ext} \sim 1$ mm), the feedback coefficient [7] is C = 0.45 < 1, ensuring that only one external cavity mode is active."

Initially, the laser is switched on at t=0 ns from the transparency level (Fig. 1a) by applying an injection current of 1.1 I_{th}. The system presents relaxation oscillations towards

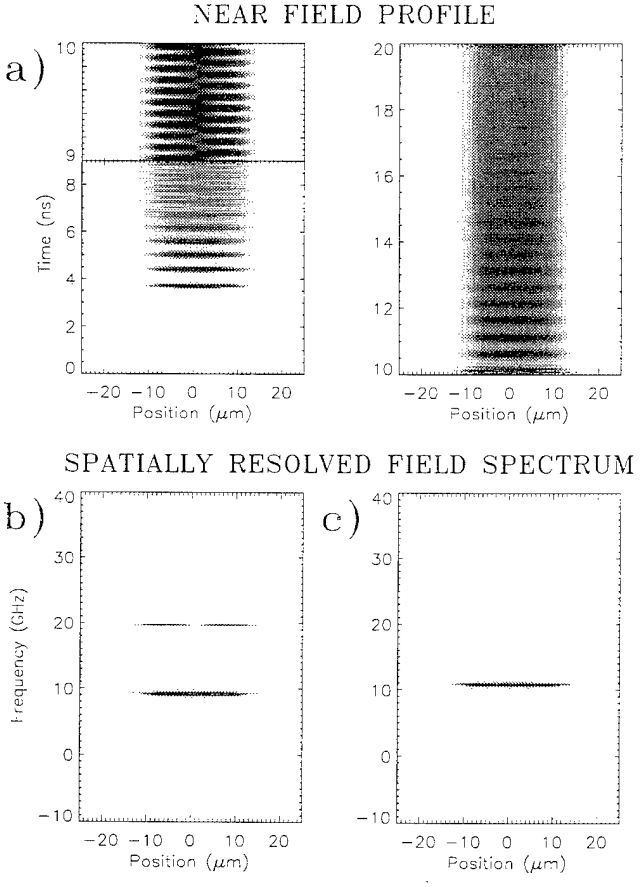


FIG. 1. *Effect of external optical feedback at I=1.1 I_{th}. a) Time-resolved lateral near-field intensity pattern. External optical feedback is applied at t=10 ns. Associated field spectrum for b) no optical feedback; c) weak optical feedback with $\phi_{fb} = 0$.*

the steady state, which, due to spatial hole burning, consists of a single intensity lobe moving periodically across the stripe. The spatially resolved field spectrum associated to this dynamics (Fig. 1b) shows the coexistence of the fundamental and the second order lateral modes of the laser cavity. Weak optical feedback is applied at t=10 ns (Fig. 1a). The two-mode dynamics previously described in absence of feedback is washed out before t=10.5 ns. After some relaxation oscillations, the system reaches fundamental mode operation (see Fig. 1c) at t= 16 ns. Pattern stabilization is achieve due to the strong interaction of the fundamental mode of the free-running laser and an external cavity mode located at ν_i= 0 GHz. This well-behaved state is stable in a wide range of feedback phase values (variations of L_{ext} within half a wavelength that can be experimentally produced by a PZT, produce a change in the feedback phase $\phi_{fb} = \omega_o \tau_{ext}$ from 0 to 2π).

When the injected current is increased to I=1.3 I_{th} in absence of feedback, the third order lateral mode is simultaneously excited with the fundamental and second order mode (Fig. 2a). After applying optical feedback at t=10 ns we leave the system to relax to its steady state. Different situations are observed depending on the value of ϕ_{fb}. For $\phi_{fb} = \pi$ (Fig. 2b), an external cavity mode is located at the frequency ν_{i+1}=61.25 GHz, which excites the fourth order lateral mode at expense of the third order mode. A small change of the cavity length to give $\phi_{fb} = \frac{3\pi}{4}$ shifts the external cavity mode to 43.75 GHz, close to the frequency of the third order lateral mode which becomes strongly excited it (Fig. 2c). Finally, suppression of the third order mode is achieved for any value of the feedback phase between $\frac{3\pi}{2}$ and $\frac{\pi}{4}$. However, the highest linewidth narrowing of the lateral modes is obtained for $\phi_{fb} = \frac{7\pi}{4}$, which is shown in Fig. 2d.

For higher injection levels, the same type of behavior as shown in Fig. 2 has been observed, but with a higher number of lateral modes simultaneously excited.

In summary, we have shown that a certain degree of lateral mode control and pattern stabilization can be achieved in broad area lasers by applying external optical feedback.

Aknowledgments: This work has been partially supported by CICYT Projects No. TIC93/0744, and PB94-1167 (Spain), and European Union HCM Grant CHRX-CT-93-0114

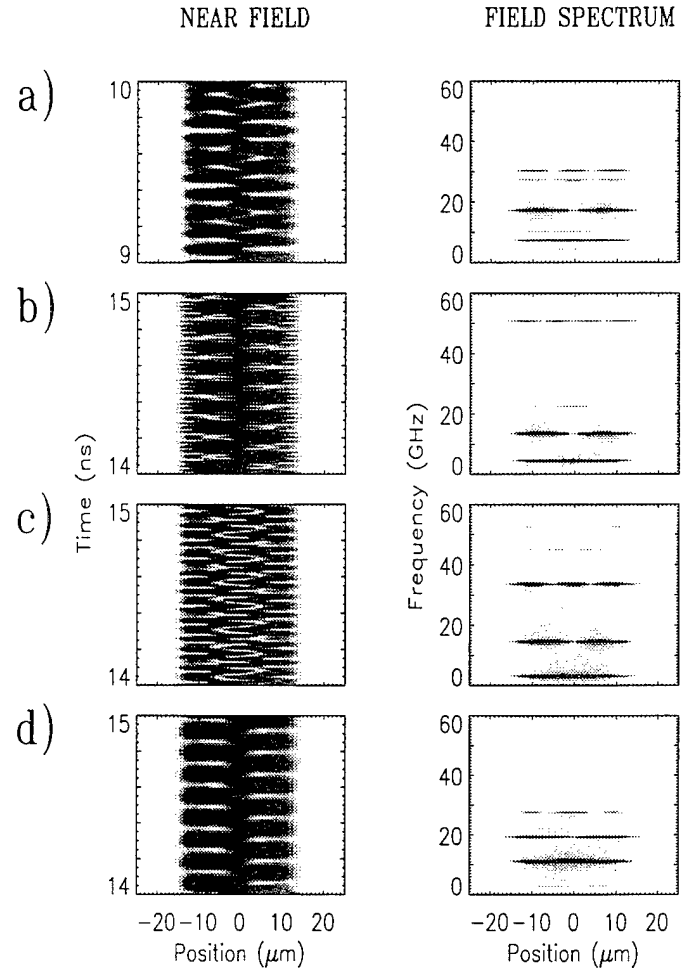


FIG. 2. *Time-resolved lateral near-field intensity pattern and spatially-resolved field spectra for I=1.3 I_{th}. a) Absence of feedback. Weak optical feedback with b) $\phi_{fb} = \frac{\pi}{2}$, c) $\phi_{fb} = \frac{3\pi}{4}$, and d) $\phi_{fb} = \frac{7\pi}{4}$. The other feedback parameters are those of Fig. 1b*

II. BIBLIOGRAPHY

[1] Chang-Hasnain, C.J., *et al, Appl. Phys. Lett.*,**54**, p. 205, 1989

[2] Hess, O., *et al, IEEE J. Quantum Electron.*,**31**, p. 35, 1995

[3] Fisher, I., *et al, Non linear Dynamics in Optical Systems*, Paper TD2, June 1995, Rochester, New York, USA

[4] Goldberg, L., *et al, IEEE J. Quantum Electron.*,**18**, p. 555, 1982; Wyatt, R., *et al, Electron. Lett.*,**19**, p. 110, 1983

[5] Jakobsen, P.K., *et al, Phys. Rev. A.*, **45**, p. 8129, 1992; Martin-Regalado , J., *et al*, "Spatio-temporal dynamics of gain-guided semiconductor laser arrays", to appear in *IEEE J. Quantum Electron.*, 1996 Martin-Regalado , J., *et al*, "Modeling spatio-temporal dynamics of gain-guided multistripe and broad area lasers", to appear in *IEE Proc. Optoelectronics*, 1996

[6] Lang, R., *et al, IEEE J. Quantum Electron.*,**23**, p. 347, 1981

[7] Petterman, K., "Laser diode modulation and noise", *Kluwer Academic Publishers*, Chapt. 9, 1988

Analysis of a lensed coreless fiber by a hybrid technique that involves FD-BPM and FD-TDM

Junji Yamauchi, Koji Nishio and Hisamatsu Nakano

College of Engineering, Hosei University, 3-7-2, Kajino-cho, Koganei, Tokyo 184, Japan
Tel: 432-87-6190, Fax: 423-87-6048

1 Introduction

The finite-difference beam-propagation method (FD-BPM) [1] and the finite-difference time-domain method (FD-TDM) [2] are powerful tools of analyzing the propagating beam in an optical waveguide. The FD-BPM based on the Crank-Nicholson scheme has the advantage of unconditional stability. Since the FD-BPM assumes only travelling waves, reflected waves generated at longitudinal discontinuities have been neglected.

On the other hand, the FD-TDM that directly solves the Maxwell's equations is accurate since no approximation is introduced with respect to polarization and propagating beam direction, but it requires enormous computation time and memories for the simulation of large structures. Recently, a scalar FD-TDM [3] was formulated and it was extended to the cylindrical coordinate system [4]. Compared with the vector FD-TDM, the scalar FD-TDM requires less memory and is computationally more efficient. It should be noted, however, that compared with the FD-BPM, the improvement in computational efficiency is not still enough.

The purpose of this paper is to propose a hybrid technique that involves a scalar FD-BPM with a Padé approximant operator [5] and a scalar FD-TDM in the cylindrical coordinate system [4], and to demonstrate the effectiveness of this technique. In particular, the present technique is more efficient than the conventional FD-TDM when we analyze large structures with a longitudinal discontinuity in which the reflected waves cannot be neglected. As an application, the propagating field in a lensed coreless fiber [6]-[8] is analyzed. Furthermore, we reveal the effects of an antireflection (AR) coating [9] on the fields in the lens.

2 Technique of connecting FD-BPM to FD-TDM

We describe the method of utilizing the field obtained from the FD-BPM as the incident field in the FD-TDM. For the FD-BPM, the electric field $E(r,\phi,z)$ at a connecting position ($z=l$) of the FD-BPM and the FD-TDM is expressed as

$$E(r,\phi,l) = \psi(x,\phi,l)\exp(-jk_0n_0l), \tag{1}$$

where k_0 is a wavenumber in free space and n_0 is the appropriately chosen reference refractive-index. In this paper, such reference refractive-index is chosen to be the cladding refractive-index. Separating the electric field into an amplitude term $\bar{E}(r,\phi,l)$ and a phase term $\varphi(r,\phi,l)$, Eq.(1) is rewritten as

$$E(r,\phi,l) = \bar{E}(r,\phi,l)\exp[-j\varphi(r,\phi,l)]. \tag{2}$$

On the other hand, the electric field for the scalar FD-TDM can be expressed as

$$E(r,\phi,z,t) = E(r,\phi,z)\exp(j\omega t), \tag{3}$$

where ω is the angular frequency. Substituting Eq.(2) into Eq.(3), and changing it into the expression of an instantaneous value, we get the following equation as the incident field for the FD-TDM at the connecting position

$$E(r,\phi,l,t) = \bar{E}(r,\phi,l)\sin[k_0ct + \varphi(r,\phi,l)]. \tag{4}$$

As will be shown later, the direct use of Eq.(4), however, gives rise to considerable parasitic waves due to the existence of the phase term φ, so that it takes a long computational time to get a steady-state field distribution. In order to reduce the amount of parasitic waves, the source excitation is started using the following modified procedure. We introduce a gradual

excitation method [10], i.e., Eq.(4) is multiplied by a sine function of the quarter period, so that we use

$$E(r,\phi,l,t) = \bar{E}(r,\phi,l)\sin[k_0 ct + \varphi(r,\phi,l)]\sin(\pi ct/2\Delta\tau), \qquad for \quad ct \leq \Delta\tau \tag{5}$$

where $\Delta\tau/c$ is a rising time. Eq.(5) together with Eq.(4) is used as the incident field in the FD-TDM region.

To confirm the validity of the hybrid technique, we first consider a coreless fiber connected with a single-mode fiber whose core radius is $\rho = 5\mu$m, as shown in Fig.1. The refractive indices of core and cladding are $n_{co} = 1.504$ and $n_{cl} = 1.50$, respectively. A wavelength of $\lambda = 1.55\mu$m is used, so that the normalized frequency is $V \simeq 2.22$. The input field is the fundamental mode LP_{01}. The connecting position of the FD-BPM and the FD-TDM is chosen to be $l = 150\mu$m. The incident field for the FD-TDM is launched at $z = 150\mu$m toward $+z$ direction using a similar technique described in Ref. [11], so that we can separate the computational region for the FD-TDM into the total field and the reflected field regions. The computation parameters are taken to be $\Delta r = \Delta z = \rho/200 = 0.025\mu$m and $c\Delta t = 0.031\mu$m in the FD-TDM region. The same discretization mesh is also used for the FD-BPM region. The number of transverse grid points is 2000.

We demonstrate the effectiveness of the gradual excitation method in the FD-TDM region. Fig.2 shows the time-dependent variation of the parasitic-wave power observed in the reflected field region. The power is normarized by the input power. In this Figure, the data for $\Delta\tau = 0\mu$m corresponds to the case where only Eq.(4) is used. It is worth mentioning that use of the gradual excitation drastically reduces the parasitic waves. From this numerical test, we choose $\Delta\tau = 9.3\mu$m in the following.

Fig.3 shows a comparison between the field obtained from the hybrid technique and the field obtained when only the FD-BPM is used. The field is evaluated at $z = 157\mu$m. It is found that the two curves are almost indistinguishable. Further calculation shows that the phase variation also agrees well to each other. From the above-mentioned results, it can be said that the field obtained from the FD-BPM is satisfactorily connected to that in the FD-TDM.

3 Analysis of a lensed coreless fiber

As an application of the present technique, we analyze a hemispherically-ended coreless fiber shown in Fig.4. The coreless fiber is identical to that in Fig.1 with the exception of a coreless-fiber length of $l = 200\mu$m. The hemispherical lens tipped on the coreless-fiber endface is formed by the adjustment of a lens radius r_L and a center angle θ_L. The refractive index of the lens is the same as that of the cladding.

Fig.5 shows the field distribution in the coreless fiber calculated by the FD-BPM. It is seen that the field spreads and the constant phase plane is distorted with the propagation.

Using the hybrid technique, the field obtained from the FD-BPM is connected to that in the FD-TDM. Fig.6 shows the field distribution ($ct = 62\mu$m) for $r_L = 40\mu$m and $\theta_L = 60°$ in the FD-TDM region. In Fig.6(a), we can observe the complicated field distribution in the lens. This is due to the reflected waves caused at the lens endface with air. The reflected power of the fundamental mode is calculated to be 4.2%. Fig.6(b) shows that the phase variation is gradually modified because the local velocity of a light in the lens is different from that in air. It is demonstrated that the lens operates as a phase adjustment element.

Fig.7 shows the far-field patterns radiated from the fibers with the lens ($r_L = 40\mu$m and $\theta_L = 60°$) and without the lens. Due to the phase adjustment effect, the beam radiated from the lensed fiber is sharper than that from the fiber without the lens.

Finally, we treat a lensed fiber with an AR coating. Taking account of impedance matching between the waveguide and the air, the refractive index of the AR coating is chosen to be 1.225, and the AR layer thickness is 0.325μm. The field distribution ($ct = 62\mu$m) for the lens coated with the AR layer is shown in Fig.8. In contrast to Fig.6(a), the standing wave is not observed in the lens. It is found that the reflected fields are successfully suppressed due to the AR coating, and the reflected power from the endface is reduced to be 0.01%.

4 Conclusions

We have proposed a technique of connecting the scalar FD-BPM to the scalar FD-TDM in the cylindrical coordinate system. This hybrid technique enables us to analyze large structures

with a longitudinal discontinuity and has the advantage of computational efficiency compared with the conventional technique in which only the FD-TDM is applied to large structures. As an application, a hemispherically-ended coreless fiber has been analyzed and discussed.

References

[1] Y.Chung and N.Dagli, J. Quantum Electron., 26, pp.1335-1339, 1990.

[2] K.S.Yee, Trans. Antennas and Propag., AP-14, pp.302-307, 1966.

[3] W.P.Huang et al., Photon. Tech. Lett., 3, pp.524-526, 1991.

[4] J.Yamauchi et al., Photon. Tech. Lett., 8, to be published.

[5] G.R.Hadley, Opt. Lett., 17, pp.1426-1428, 1992.

[6] G.Wenke and Y.Zhu, Appl. Opt., 22, pp.3837-3844, 1983.

[7] J.Yamada et al., J. Quantum Electron., QE-16, pp.1067-1072, 1980.

[8] K.Shiraishi et al., J. Lightwave Tech., 13, pp.1736-1744, 1995.

[9] J.Yamauchi et al., Photon. Tech. Lett., 8, to be published.

[10] Y.Naka et al., Asia Pacific Microwave Conference, SO7-2, 1995.

[11] S.T.Chu et al., Computer Physics Com., 68, pp.451-484, 1991.

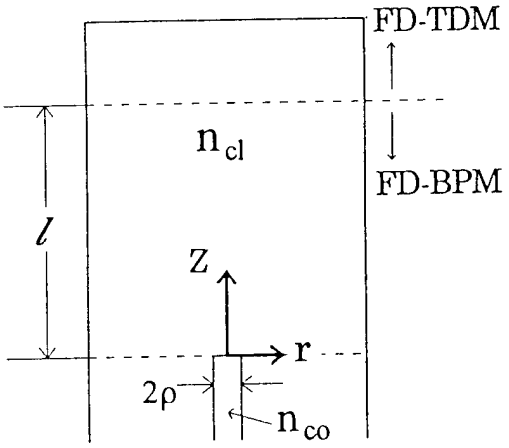


Fig.1 Configuration of a coreless fiber.

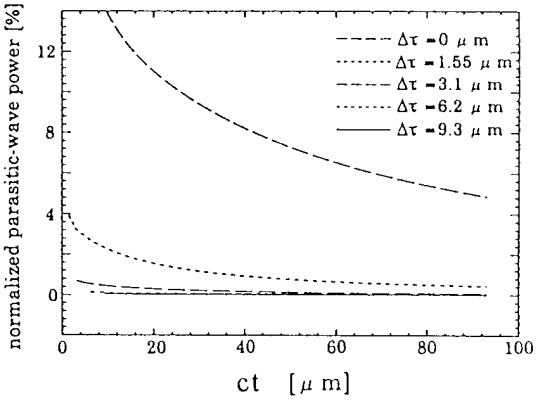


Fig.2 Time-dependent variation of the parasitic-wave power observed in the reflected field region.

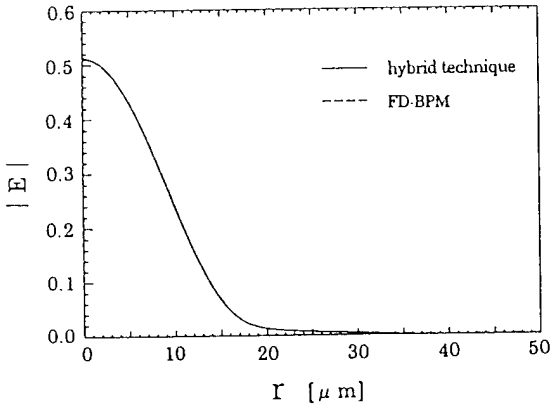


Fig.3 Comparison between the propagating fields obtained from the hybrid technique and the FD-BPM ($z = 157\mu m$).

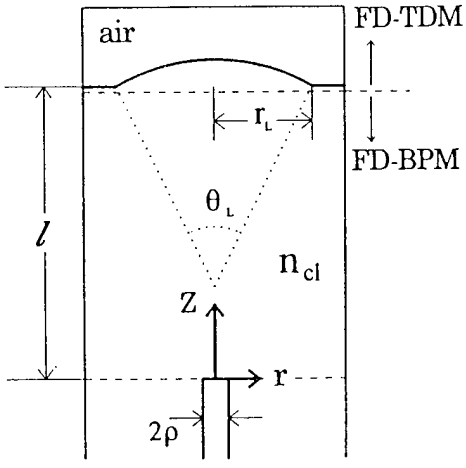
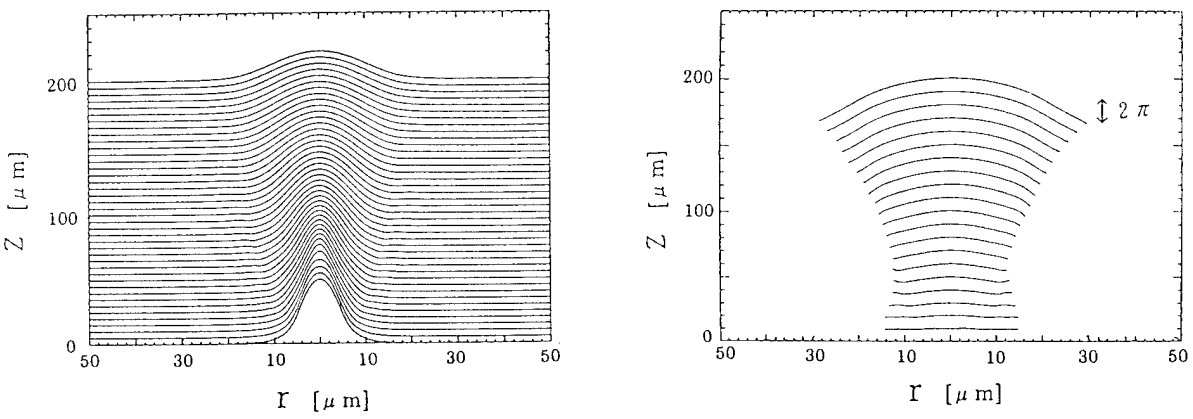
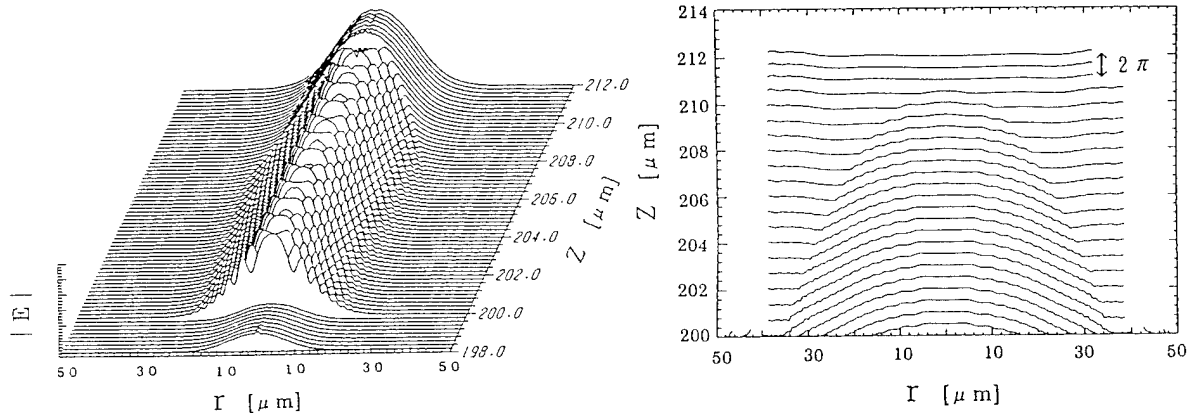


Fig.4 Configuration of a hemispherically-ended coreless fiber.



(a) field (b) phase

Fig.5 Field and phase distributions in the coreless fiber.



(a) field (b) phase

Fig.6 Field and phase distributions in the lens ($r_L = 40\mu m$ and $\theta_L = 60°$).

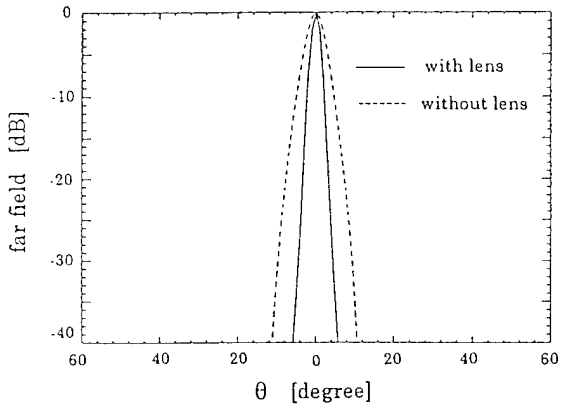


Fig.7 Comparison in the far-field pattern.

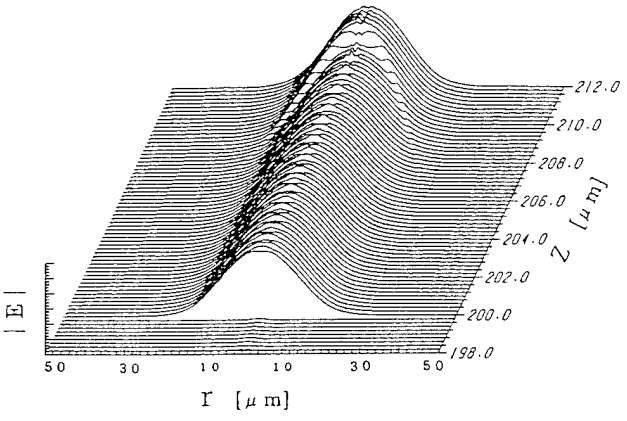


Fig.8 Field distribution in the lens coated with the AR layer.

Characterization of optical filters with two-dimensional confinement

T Wongcharoen, B M A Rahman and K T V Grattan
Department of Electrical, Electronic and Information Engineering
City University
Northampton Square, London EC1V 0HB, UK
Tel: +44-171-477-8123 Fax: +44-171-477-8568

Introduction

Directional couplers are key elements in the design of many important optical devices such as power combiners, power splitters, modulators, switches, polarizers and filters. Inherently, the directional coupler is a frequency dependent device and the wavelength dependency of its coupling ratios finds application in the construction of wavelength-division multi/demultiplexer for exploiting the broad bandwidth available from an optical-fiber network. The material dispersion, waveguide dispersion, and the mode confinement of a waveguide mode change with the system operating frequency. This also changes the coupling coefficients and hence the coupling length for a pair of coupled waveguides. However, the frequency sensitivity of the power transfer efficiency is small, when the guides are identical, since only the effect of coupling length variation is utilized, as the two guides are always phased matched. On the other hand, if the guides are nonidentical, but phase matched only at the design frequency, then their power transfer efficiency will be very sensitive with the operating wavelength and it can be used as a realistic narrow band-width filter. So far most of the published simulation work is on the use of planar structures [1,2], and these are not suitable for practical applications. However, Burke *et al.* [3] have presented results for a nonsynchronous optical filter incorporating rib waveguides and using the spectral index method for the simulations. In the work presented in this paper, an accurate characterization of optical filters is carried out by using nonidentical coupled waveguides with two-dimensional confinement but using the more rigorous finite element method and the least squares boundary residual method.

The Finite Element Method

The finite element method (FEM) is a very powerful tool throughout engineering for its flexibility and versatility and increasingly is being used for characterizing a wide range of practical optical guided-wave devices. In using the finite element method, the region of concern is subdivided into a patchwork of a number of subregions called elements. These elements each can be of various shapes, and sizes and using many such elements, any cross-section with a complex boundary can be accurately represented. Each element can have different refractive index, loss or gain factor, anisotropy or nonlinearity, so a wide range of practical waveguides can be characterized. By using the vector H-field formulation [4], accurate propagation constants and modal field profiles can be obtained for the isolated modes or even for the supermodes. The vector supermodes of the complete super-structure may be obtained and these supermodes maintain their orthogonality even when the guides are strongly coupled and also when the guides are not identical.

The Least Squares Boundary Residual Method

The power transfer between two coupled waveguides can be accurately estimated by using the accurate eigenvalues and eigenvectors by the finite element method along with the application of the coupled mode theory or the least squares boundary residual (LSBR) method [5]. Here it is assumed that a single isolated waveguide is butt-coupled to a directional coupler section. The incident field profile from the isolated waveguide excites two supermodes in the directional coupler section and the least squares boundary residual (LSBR) method is used to obtain coefficients of the two excited supermodes. The LSBR is a powerful numerical method used to find the scattering coefficients from a waveguide discontinuity. In this case the continuity of the tangential components of both, the Electric and Magnetic fields are enforced in a least squares sense. From the amplitude of the two excited supermodes, power carried by the two guides along the axial direction can be calculated.

Results

In this paper, two directional coupler based optical filters using nonidentical waveguides, with one and two-dimensional confinement in InGaAsP/InP system is studied. First a planar structure, earlier investigated by other workers is considered to compare our results, and then, another example of two coupled waveguides with two-dimensional confinement is considered.

In the first example, two slab waveguides *A* and *B* of film widths *a* and *b* are separated by a distance, *s*. The refractive indices of the guides A and B, the separating region and the cladding region are given by n_a, n_b, n_s, and n_c, respectively. The materials that make up the waveguides considered here are InGaAsP, for the guiding layers and InP for the cladding and separation layers. The refractive indices n_a and n_b for the two guiding layers, when lattice matched to InP, are calculated by using the formulae given by Broberg and Lindgren [6]. The refractive index of InP in the cladding and separation layers is determined by the formula given by Glembocki and Piller [7]. In this example, the widths of the two guides are 0.53 μm and 1.6 μm, with arsenic contents (y) of 0.25 and 0.15 respectively considered. The refractive indices of both the guides *A* and *B* and that of the substrate and claddings decrease with the wavelength, but their rate of changes are different. For this dimension and material combination, two isolated guides are phase matched at a wavelength of 1.3 μm. At this wavelength, the guide *A*, guide *B*, the separation region and the cladding refractive indices are 3.30970, 3.26799, 3.20483, and 3.20483 respectively.

Figure 1 shows the variation of the coupling length with the operating frequency for this structure. It can be observed that the coupling length is a maximum at a wavelength of 1.3 μm and decreases for other wavelength. Further, the coupling length is higher for the larger waveguide separation with sharp resonant features. When the wavelength is far from the resonance value, the coupling length is not sensitive to the separation, *s*. It can also be noted that coupling lengths are smaller for all other nonphase matching wavelengths for similar waveguide separations. Only TE modes are considered in this example.

Figure 2 shows the coefficients of the two supermodes, for different operating wavelengths for the waveguide separation, s = 1.4 μm. *B1* and *B2* are the modal coefficients of the excited even-like and odd-like supermodes, respectively. It can be observed that, when λ = 1.3 μm, *B1* and *B2* are nearly equal to 0.7, nearly a half of the power is carried by each of the supermodes. However, as the wavelength moves away from the phase matching frequency, the power carried by each supermodes become unbalanced. The maximum power transfer between the guides may be calculated from the supermode coefficients and is shown in Figure 3. It can be observed that nearly 100% power transfer is possible at the design frequency, which is, λ_0 = 1.3 μm. However, the power transfer at other frequencies is quite small, and the filter bandwidth can be reduced further by increasing the waveguide separation, *s*, or by making the phase difference between two guides more frequency sensitive. Our result agrees very well with that of Huang [2], who used a more computer-intensive beam propagation method.

In the second example, two nonidentical coupled waveguides with two dimensional confinement are considered and the schematic diagram is shown in Figure 4. The frequency-dependent refractive indices of the lattice matched InGaAsP guides and InP cladding are calculated, as discussed earlier for the planar guides. The width of both the guides is considered to 3.0 μm, but their arsenic contents (y) were 0.25 and 0.15 respectively. The height of the top waveguide, *a*, is considered to be 0.53 μm and the height of the second waveguide, h_2, is varied to obtain the required phase matching at the design wavelength 1.3 μm.

The accurate vector finite element method is used to find the modal solutions of the isolated waveguides at a wavelength of 1.3 μm. In this case 3200 first order triangles have been used to represent a quarter of the waveguides. The variation of their propagation constants for the quasi-TE (Hy11) modes is shown in Figure 5. It can be seen that when the second guide height, h_2 = 1.58 μm, the two isolated guides are phase matched, which is close to the value 1.6 μm for the slab waveguides. Next the supermodes of the coupled structure are calculated by using the finite element method. It can be emphasized that the coupling length obtained by using the finite element method is accurate, even when the guides are not identical or they are strongly coupled. The variation of the coupling length with the operational wavelength is shown for two different waveguide separations, *s*, in Figure 6 and features similar to the planar example can also be observed.

The supermodes at the phase matching wavelength, λ= 1.3 μm, are shown in Figure 7, when s=1.5 μm. Figure 7(a) shows the even-mode of the coupled structure, where as figure 7(b) shows the odd-mode of the coupled structure. It can be observed that both the waveguides carry equal power, although the guide cross-sections are

different, however, they are phase matched. Figures 8(a) and (b) show the supermode profiles when the operating wavelength is 1.28 μm. It can be observed that first supermode which is even-like, is more concentrated in the top waveguide, which has a higher index at this wavelength. Similarly the second supermode, which is odd-like is more concentrated in the lower waveguide. Similarly, it can be noted that, when $\lambda = 1.32$ μm, the first supermode, which is even-like is now more concentrated in the lower waveguide.

Finally, the coefficients of the supermodes excited and the overall power transfer efficiency for different operating wavelengths are given in the Table for s = 1.5 μm. It can be noticed that in a similar way to the planar example, at the phase matching condition, super modes' coefficients are nearly equal, whereas for other wavelengths their values differ widely. Their large difference is responsible for only a small amount of power transfer between the guides at non-phase-matching wavelengths.

λ (μm)	B1	B2	P_{out}
1.28	0.25890	0.96589	0.04929
1.29	0.48486	0.87456	0.70425
1.30	0.80929	0.58735	0.90573
1.31	0.93392	0.35744	0.22894
1.32	0.96723	0.25385	0.01226

Conclusion

A rigorous numerical procedure is presented for the accurate characterization of optical filters using nonidentical waveguides. Practical and important photonic devices use waveguides with two-dimensional confinement and their use warrants more accurate design tool to assist in their development and further optimization. Due to the inherent versatility of the approach presented here, it will be applicable to a wide range of important photonic devices.

References

[1] B Broberg *et al.*, *J Lightwave Technol.*, **LT-4**, pp.196-203, 1986.
[2] W P Huang *et al.*, *IEEE J. Quantum Electron.*, **QE-28**, pp.1527-1532, 1992.
[3] S V Burke *et al.*, , *IEE Proceedings* - J, **vol.139**, pp.59-65, 1992.
[4] B M A Rahman and J B Davies, *J. Lightwave Technol.*, **LT-2**, pp.682-688, 1984.
[5] B M A Rahman and J B Davies, *J. Lightwave Technol.*, **LT-6**, pp.52-57, 1988.
[6] B Broberg and S Lindgren, *J Appl. Phys.*, **55**, pp.3376-3381, 1984.
[7] O J Glembocki and H Piller, Indium Phosphide (InP), Editor: E D Palik, Handbook of Optical Constants of Solids, New York, Acadmic Press, 1985.

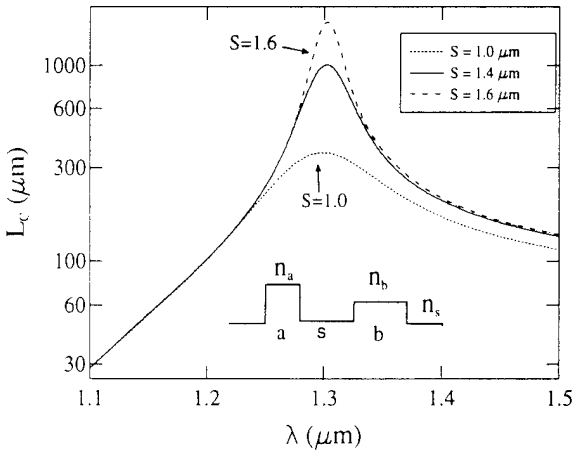


Fig. 1 Variation of the coupling length with λ.

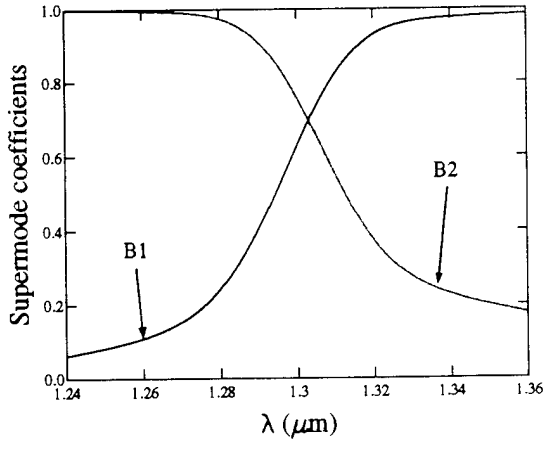


Fig. 2 Variation of the supermode coefficients with λ.

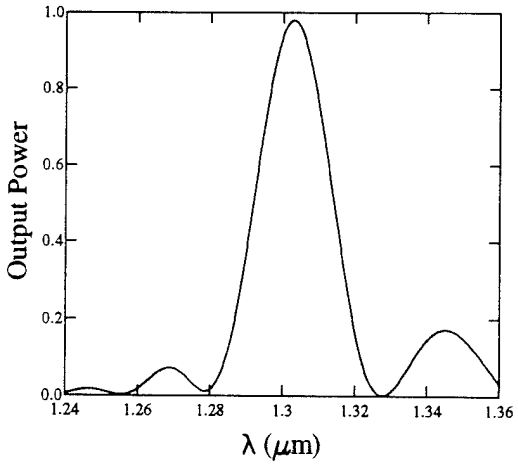


Fig. 3 Variation of the power transfer efficiency with λ.

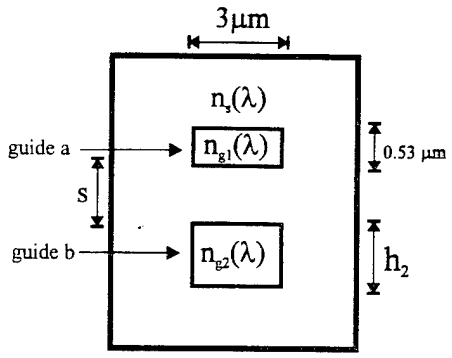


Fig. 4 A schematic diagram of two coupled nonidentical waveguides.

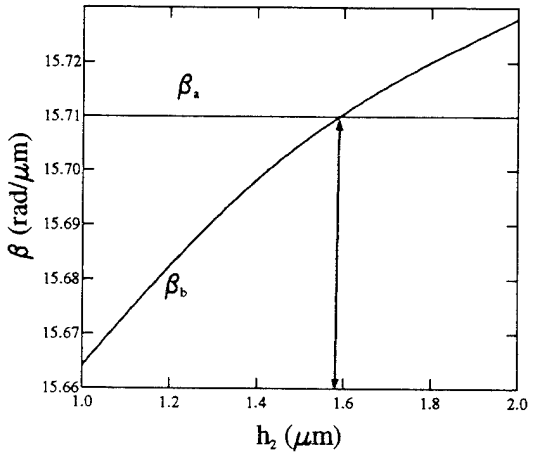


Fig. 5 Variation of the propagation constants with h_2.

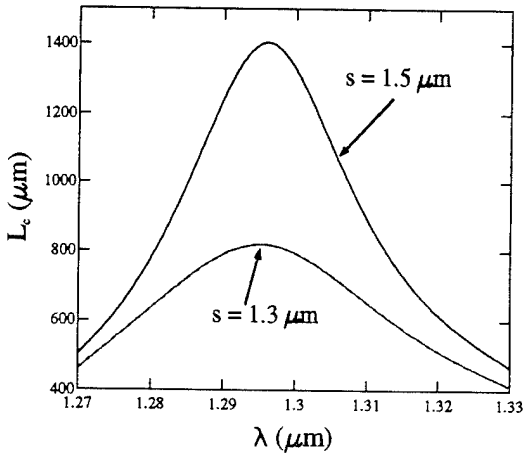


Fig. 6 Variation of the coupling length with λ for the waveguides with 2-D confinement.

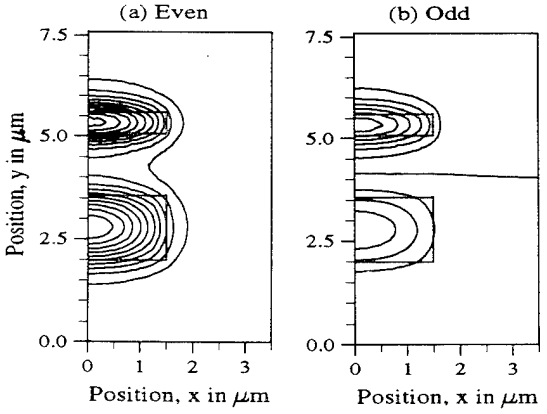


Fig. 7 (a) First supermode and (b) Second supermode at λ = 1.30 μm.

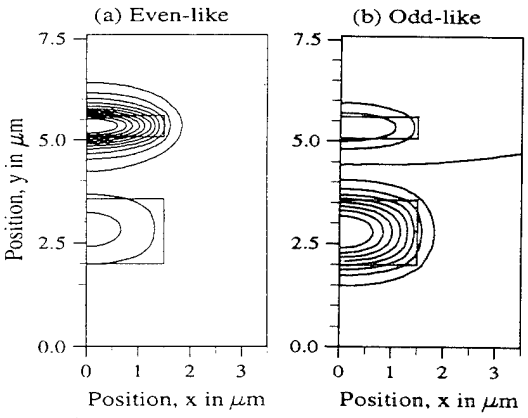


Fig. 8 (a) First supermode and (b) Second supermode at λ = 1.28 μm.

Octave Bandwidth Analog Link with a Monolithic Laser/Electroabsorption Modulator

Roger Helkey, Harold Roussell, Charles Cox III
Lincoln Laboratory, Massachusetts Institute of Technology
Lexington MA 02173

Masahiro Aoki, Hirohisa Sano
Central Research Laboratory, Hitachi, Ltd., Kokubunji, Tokyo 185, Japan

High linearity RF analog links are of great interest for remoting cellular radio and personal communications systems base stations. Electroabsorption modulators have been demonstrated to give high linearity when used in external modulation analog optical links[1]. Monolithically integrated laser/electroabsorption modulators have been demonstrated to be useful for long-haul multi-gigabit digital communications[2,3]. Integrated laser/modulators have been demonstrated for analog applications up to 10MHz[4]. In this paper, we demonstrate a monolithically integrated laser/electroabsorption modulator for high-frequency analog link applications. The monolithic laser/modulator is shown to offer good linearity with considerably reduced size and weight compared to an external electroabsorption modulator with a Nd:YAG pump laser.

The 1.55μm laser and modulator were grown by metal organic vapor phase epitaxy (MOVPE). The active region of the laser and modulator consist of seven InGaAs quantum wells. The electroabsorption (EA) modulator is based on the quantum-confinement Stark effect (QCSE), using selective area growth to control the in-plane bandgap energy[5].

The experimental configuration is shown in Fig. 1. The laser bias was 85mA, and the modulator was reversed-biased at .91V. The estimated optical power into the electroabsorption modulator was 14mW. The output of the laser/modulator was coupled into a 200m optical fiber using a micromachined fiber lens. The fiber output was angle-cleaved and used to illuminate an analog photodetector. The photodetector had a reverse bias of 4V and a photocurrent of 0.4mA.

The dynamic range was characterized for an octave bandwidth 450MHz link. Unlike ordinary Mach-Zender modulators, electroabsorption modulators have a null in third-order nonlinearity for finite transmission[1]. The absorber bias was set to this

high linearity point. The intermodulation products were produced by the fifth-order nonlinearity, resulting in intermodulation products with a slope of five. The resulting spurious-free dynamic range was 116dB•$Hz^{4/5}$. This is lower than the SFDR of 123dB•$Hz^{4/5}$ measured using a bulk electroabsorption external modulator pumped by a 34mW Nd:YAG laser[1].

The performance of the monolithic laser/modulator is lower than if the same device were used as an external modulator due to the higher relative intensity noise (RIN) of a semiconductor laser. The SFDR would be increased to ~118dB•$Hz^{4/5}$ if it were used with an external modulator with a 14mW Nd:YAG laser as the optical source. The SFDR of the link could be further increased by obtaining higher power from the pump laser.

In summary, a monolithic laser/electroabsorption modulator has been demonstrated as a compact, efficient source for high linearity analog links. This work was prepared for the Department of the Air Force under Contract F19628-95-C-002.

References

1. S. A. Pappert et al., IEEE/LEOS RF Optoelectronics Topical Meeting, **WC3**, (1995).

2. M. Aoki et al., *Electron. Lett.* **29**, 1983 (1993).

3. W. T. Tsang et al., IEEE MTT-S Symposium Digest, 247 (1995).

4. G. C. Wilson et al., Conference on Optical Fiber Communication, **TuF1** (1995).

5. M. Aoki et al., *IEEE J. Quantum Electron.* **27**, 2281 (1993).

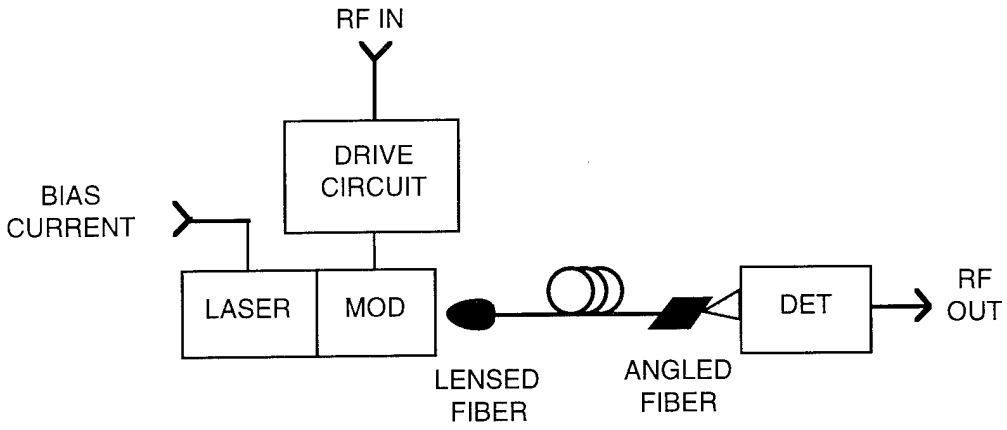


Fig. 1. Experimental configuration for the analog fiber link using a monolithic laser/electroabsorption modulator.

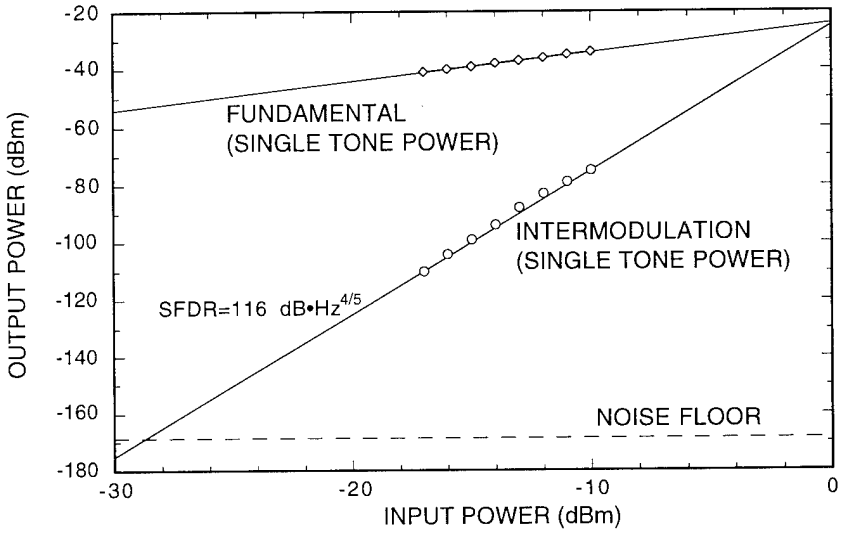


Fig. 2. Spurious-free dynamic range at 450MHz using the monolithic laser/electroabsorption modulator.

Measurement of Linewidth Enhancement Factor and Nonlinear Gain of Vertical Cavity Surface Emitting Lasers

Hua Li[a)] and David Bossert[b)]

a) Center for High Technology Materials,The University of New Mexico,Albuquerque, NM 87131-6081,
Tel: (505)277-3418, e-mail: huali@chtm.eece.unm.edu

b)Phillips Laboratory, LIDA, Kirtland Air Force Base, Albuquerque, NM 87117-5776,
Tel: (505)846-4314, e-mail: bossert@plk.af.mil

A high frequency current modulation technique was used to measure the linewidth enhancement factor of vertical cavity surface emitting lasers. It is found that the ratio of the phase modulation index β to the amplitude modulation index m/2 is a strong function of modulation frequency Ω, due to the presence of nonlinear gain, as reported for many kinds of edge-emitting semiconductor lasers[1,2]. The linewidth enhancement factor and nonlinear gain coefficient were obtained from measurements of $2\beta/m$ versus Ω. The measured nonlinear gain of the VCSEL device was found to decrease for an increased pump level.

Single mode rate equations[3] were used for small signal analysis with the inclusion of a nonlinear gain term to the net gain. Various mechanisms of nonlinear gain have been reported, such as spectral hole burning, carrier heating, carrier transport, and nonuniform distribution of photon density[4,5,6,7]. We use a phenomenological expression to the describe nonlinearity in gain which encompasses all of the above mechanisms to first order; the equations are given by:

$$\frac{dI(t)}{dt} = \left\{G_N\left[N(t)-N_0\right]\left[1-\epsilon I(t)\right] - G_N\left(N_{th}-N_0\right)\right\}I(t) \tag{1}$$

$$\frac{d\Phi(t)}{dt} = \frac{\alpha}{2}G_N\left[N(t)-N_0\right] \tag{2}$$

$$\frac{dN(t)}{dt} = J - \frac{N(t)}{\tau_s} - G_N\left[N(t)-N_0\right]\left[1-\epsilon I(t)\right]I(t) \tag{3}$$

Here $I(t)$ is the photon number, $\Phi(t)$ is the relative phase of the electrical field, $N(t)$ and N_{th} are instantaneous carrier number and carrier number at threshold, and N_0 is value of N for transparency. The total gain includes a linear part as $G=G_N[N(t)-N_0]$, where $G_N=\partial G/\partial N$, with the unit of s^{-1} and a nonlinear gain term $-G\epsilon I(t)$. ϵ is the nonlinear gain coefficient. The frequency dependence of nonlinear gain is ignored here because the time scale associated with nonlinear gain is sub-picosecond, much faster than the current modulation. α is the linewidth enhancement factor, J is the pump rate and τ_s is the carrier lifetime. The spontaneous emission noise terms are ignored in the equations (1)-(3).

For the small signal analysis we define $I(t)=I_s+i(t)$, $\Phi(t)=\omega_s t+\varphi(t)$, $N(t)=N_s+n(t)$, where I_S, ω_S and N_S are the steady state values for intensity, frequency and carrier number. If the intensity and phase are modulated by direct current modulation at frequency Ω, then $I(t)=I_S[1+m\cdot\cos(\Omega t)]$ and $\Phi(t)=\omega_s t+\beta\cdot\cos(\Omega t+\theta)$. Here, m and β are the intensity and phase modulation index. Therefore $i(t)=mI_S\cdot\cos(\Omega t)$, $\varphi(t)=\beta\cdot\cos(\Omega t+\theta)$, the amplitude of $di(t)/dt$ and $d\varphi(t)/dt$ are $\Omega\cdot mI_S$ and $\Omega\cdot\beta$. Inserting these values into (1-3) to first order, we obtain:

$$\left(\frac{2\beta}{m}\right)^2 = \alpha^2\left(1+\epsilon I_s\right)^2\left[1+\frac{\left(G\epsilon I_s\right)^2}{\Omega^2}\right] \tag{4}$$

This result is identical with that reported[1] for edge-emitting lasers, except that cross saturation effects can be ignored in the case of a VCSEL as it is single mode. Because ϵI_s is a small number, normally in the order of 0.01-0.1, $\alpha(1+\epsilon I_s)\approx\alpha$ is a reasonable approximation in the measurement. Let us define

$$S=G\epsilon I_s/2\pi, \tag{5}$$

and we can obtain S by measuring $2\beta/m$ versus f ($2\pi f=\Omega$).

A single mode VCSEL (4-QW, 10μm window size and 15μm implant size)[8] operating at ~840nm at 300K ambient temperature was used in the experiment. The VCSEL was operating in a single mode, where one polarization emission dominated. Modulation of the pump current created an intensity and phase modulation in the VCSEL emission. The intensity modulation index m was measured using a Schottky photodetector (model 1404, NewFocus). The DC photocurrent was read from the 50Ω terminator, while the AC photocurrent was read by a spectrum analyzer (Tektronik 2755P) and calibrated by a network analyzer (HP 8720A). The optical spectrum of the laser emission was measured using a scanning Fabry-Perot interferometer. The value of β was obtained from the ratio of the center carrier peak in the spectrum to the side peaks[9,10].

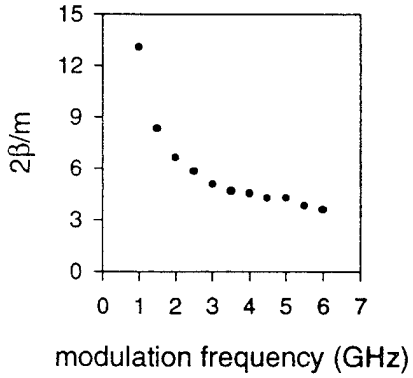


Fig.1. Measured normalized phase modulation index $2\beta/m$ versus modulation frequency f for a single mode VCSEL. The pump level is $I=1.32\cdot I_{th}$, the output power is P=0.46mW.

Fig.1 shows one measured curve of $2\beta/m$ versus f for the VCSEL. It is seen that $2\beta/m$ is a strong function of modulation frequency f. From equation (4) it is clear that as $f\rightarrow\infty$, $2\beta/m\rightarrow\alpha$. We then plotted the data as $(2\beta/m)^2$ versus $1/f^2$ and obtained a straight line with the intercept corresponding to α^2 and the slope to α^2S^2. Fig.2 shows two typical measured curves.

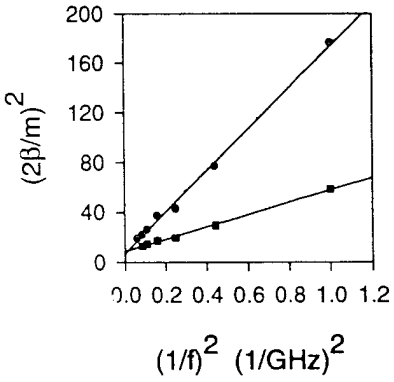


Fig. 2. Measured $(2\beta/m)^2$ versus $1/f^2$. The data • are with $I=1.13\cdot I_{th}$ and P=0.2mW, the data ▪ are: $I=1.47\cdot I_{th}$ and P=0.58mW. The solid lines are fitting lines with the interception of α^2 and the slope of α^2S^2 (see text).

It is clear that the value of α at different power levels is convergent. The average α value of several measurements at different power levels was $\alpha=2.7\pm0.5$.

Fig.3 gives the gain compression S for the VCSEL as the function of output power level. It is seen that S increases initially for increasing power, then decreases dramatically. This might be because higher order nonlinear gain terms should be included, or that the nonlinear gain coefficient ϵ is dependent on the differential gain[11]. It is well known that thermal effects cause an obvious decrease in differential gain with increasing pump for a CW-running VCSEL, causing the observed decrease of the nonlinear gain. It is reasonable to assume that the first order approximation is correct for very low power levels. Then the ϵ value can be obtained from the low power data. Knowing the quantum efficiency and output coupling efficiency, $\epsilon = 7.9\times10^{-6}$ was obtained for an output power P=0.2mW. We estimate the active volume as $V=1.38\times10^{-11}$ cm^3, giving $\epsilon \cdot V=1.1\times10^{-16}$ cm^3.

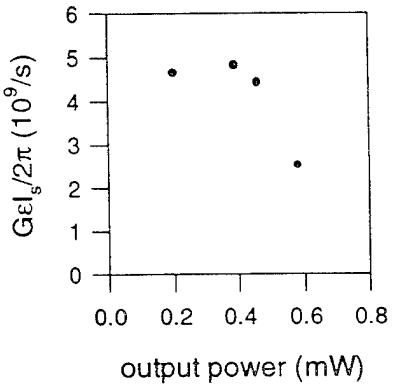


Fig.3. Measured nonlinear gain $S=G\epsilon I_s/2\pi$ $(10^9\ s^{-1})$ versus output power $P(mW)$. The corresponding pump level are: $I=1.13\cdot I_{th}$, $1.25\cdot I_{th}$, $1.32\cdot I_{th}$, and $1.47\cdot I_{th}$,, respectively.

Although high frequency modulation technique has been used for α measurements of single mode lasers for a long time, we found that it is still difficult to reduce the measurement error, mainly because the absolute AC power of laser emission is required. The system for high frequency power measurement should be calibrated carefully. An error of 2dB for the AC power measurement was estimated in our experiment, which causes a error of ~20% in final results.

The nonlinear gain of a VCSEL running CW shows abnormal behavior. As we discussed above, that may be a result of a decrease in differential gain for increasing pump current. However, the severe thermal effects in VCSEL can also cause changes in other laser parameters such as threshold gain, lasing wavelength, refractive index (therefore waveguide structure), etc. This makes quantitative analysis of nonlinear gain quite difficult. Further work will be needed to study nonlinear gain in VCSELs.

References:

[1] C. B. Su, V. Lanzisera, R. Olshansky, Electronics Letters, vol. **21**, pp.893-895, 26th September, 1985.
[2] T. L. Koch and R. A. Linke, Appl. Phys. Lett., **48**(10), pp.613-615, March 1986.
[3] C. H. Henry, IEEE Journal of Quantum Electronics, vol. QE-**19**, pp.1391-1397(1983).
[4] Francois Girardin, Guang-Hua Duan, Philippe Gallion, Anne Talneau and Abdallah Ougazzaden, Appl. Phys. Lett. **67**(6), pp.771-773, 7 August 1995.

[5] Chin B. Su, Appl. Phys. Lett. **53**(11), pp.950-952, 12 September 1988.
[6] A. D'Ottavi, E. Iannone, A. Mecozzi, S. Scotti, P. Spano, J. Landreau, A. Ougazzaden, and J. C. Bouley, Appl. Phys. Lett. **64**(19), pp.2492-2494, 9 May 1994.
[7] Chin-Yi Tsai, Chin-Yao Tsai, Yu-Hwa Lo, Robert M. Spencer, and Lester F. Eastman, IEEE Journal of Selected Topics in quantum Electronics, vol. **1**, pp.316-330, June 1995.
[8] Hua Li, Timothy L. Lucas, John G. McInerney, and Robert A. Morgan, Chaos, Solitons & Fractals, vol. **4**, nos 8/9, pp.1619-1636, 1994.
[9] Christoph Harder, Kerry Vahala, and Amnon Yariv, Appl. Phys. Lett. **42**(4), pp.328-330, 15 February 1983.
[10]B. Moller, E. Zeeb, U. Fiedler, T. Hackbarth, and K. J. Ebeling, IEEE Photonics Technology Letters, vol. **6**, no. 8, pp.921-923, 1994.
[11]Gary wang, Radhakrishnan Nagarajan, Dan Tauber, and John Bowers, IEEE Photonics Technology Letters, vol. **5**, no. 6, pp.642-645, 1993.

Relative Intensity Noise of an InGaAsP Laser over a 22 GHz Bandwidth at Cryogenic and Room Temperature

Gregory E. Obarski, Donald R. Larson, and Robert J. Phelan
Optoelectronics Division, National Institute of Standards & Technology,
M.S. 815.01, 325 Broadway, Boulder, Colorado 80303
(303)497-5747, fax (303)497-3387

Cryogenic operation of semiconductor lasers offers the potential for greater bandwidth due to improved frequency modulation response,[1,2] lower threshold current, and higher power efficiency[3] over that of room temperature operation. The 3 dB electrical modulation bandwidth can be determined from the relaxation oscillation frequency as located from the peak in the relative intensity noise (RIN) spectrum.[4] In this report we show that the cryogenic RIN of a commercial 1.5 μm InGaAsP laser is significantly reduced below room temperature values over a major portion of a 22 GHz measurement bandwidth, yielding increased potential for ultrahigh speed modulation. Low RIN lasers are also useful for determining the optimum performance of advanced photodetectors, for measuring noise figure of optical fiber amplifiers, and as reference standards for the comparison and evaluation of RIN measurements.

We define the RIN[5,6] of a laser of output power p(t) and fluctuation δp(t) as the ratio of the mean square of the fluctuation to the square of the average power, or RIN = $<\delta p(t)^2>/<p(t)>^2$. In the electrical domain, the RIN at some arbitrary frequency is obtained by weighting the intensity noise per unit bandwidth $\delta P(\nu)$ from an rf electrical spectrum analyzer with the appropriate system frequency response $w(\nu)$ and dividing by the electrical dc power P. Thus $RIN(\nu) = w(\nu)\delta P(\nu)/P$.

Figure 1 is a schematic of our RIN measurement system.[7] A p-type-down InGaAsP laser, driven by a battery-operated constant current input, is cooled to 77 K by mounting it on a heat sink in the vacuum chamber of a cryostat filled with liquid nitrogen. The light is collimated inside the chamber with a micro-lens in thermal contact with the laser mount. The emerging beam is optically isolated and focussed onto a 25 GHz bandwidth photodetector. A biastee sends the dc portion of the detector output to a voltmeter while the ac portion is preamplified and recorded with a 26 GHz spectrum analyzer. By careful determination of the system's frequency response $w(\nu)$, we conclude that measurement uncertainty over a 22 GHz bandwidth is $\pm$ 3 dB.

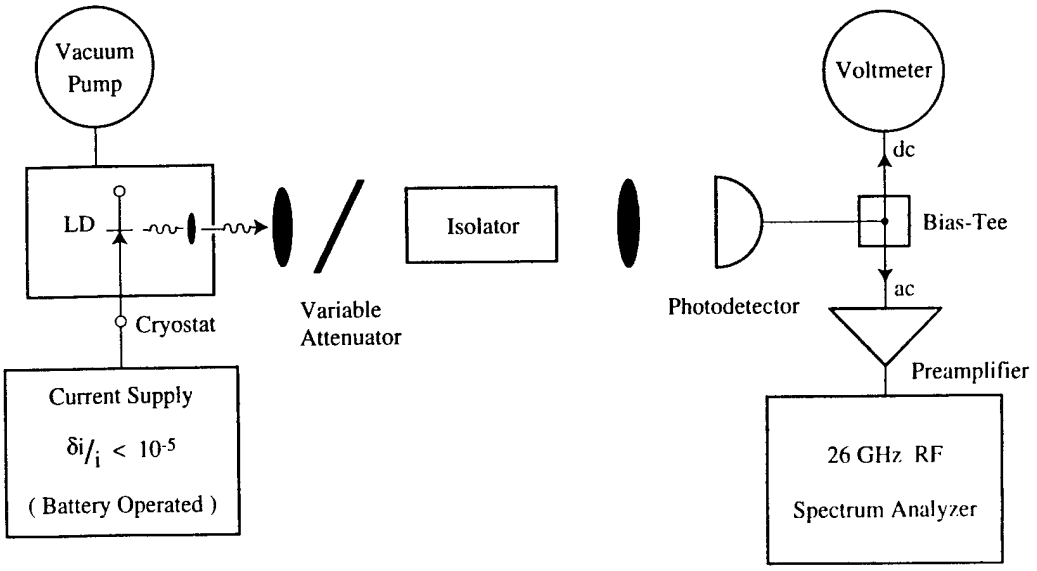


Fig 1: Cryogenic RIN measurement system.

Results: Figure 2 shows the dependence of the laser's optical power output on drive current at cryogenic (77 K) and room (300 K) temperature. At 300 K the threshold current is ≈ 15.5 mA; at 77 K it has fallen to ≈ 0.75 mA, showing a large increase in external quantum efficiency. In Figures 3 and 4, we compare drive current dependence of the 300 K and 77 K RIN at 2 and 22 GHz respectively. For each frequency, the RIN at 77 K is significantly lower than at 300 K for currents many times above threshold. At 77 K, as current is increased beyond the corresponding room temperature threshold value, the RIN reduction begins to decrease. For 2 GHz (Fig. 2) with current at 22.7 mA, the power output increases from ≈ 1.2 mW to ≈ 5 mW while the RIN (Fig. 3) decreases by ≈ 22 dB/Hz.

In Figure 5, we compare the 77 K and 300 K RIN from 1 to 22 GHz. The drive current is set so that optical power outputs are equal (≈ 3.4 mW) at both temperatures: 36.7 mA at 300 K and 17 mA at 77 K. The maximum peak in the 300 K RIN spectrum locates the relaxation oscillation frequency at $\Omega_r \approx 5.5$ GHz, with a 3 dB electrical bandwidth of 8.5 GHz.[4] At 77 K the RIN reduction is significant for frequencies to ≈ 11 GHz, with the maximum reduction of ≈ 14 dB/Hz occurring at $\Omega_r \approx 5.5$ GHz. Near 20 GHz the slight difference observed falls within measurement uncertainty. The absence of a RIN peak anywhere within the 22 GHz measurement bandwidth indicates that Ω_r has risen to >22 GHz, and that the integrated RIN over the entire bandwidth is significantly reduced.

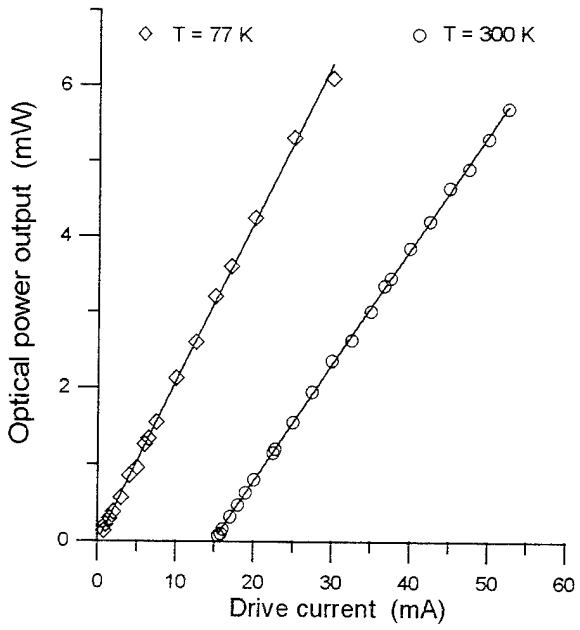


Fig. 2: Optical power output vs. drive current at 300 K and at 77 K.

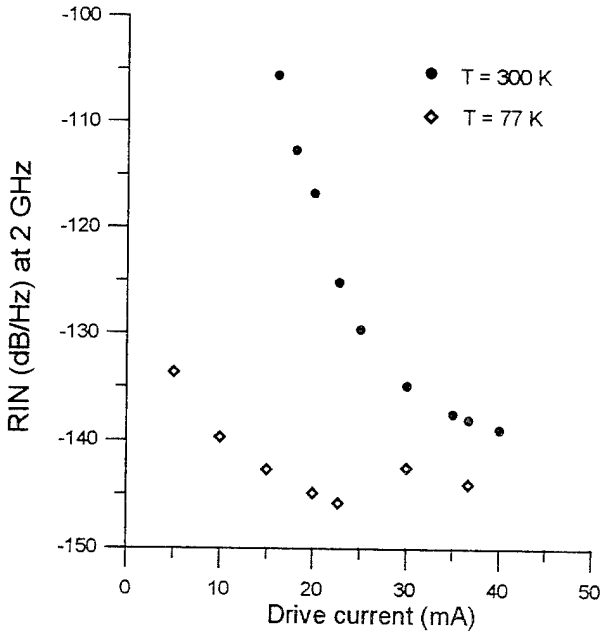


Fig 3: 2 GHz RIN dependence on drive current at 300 and 77 K .

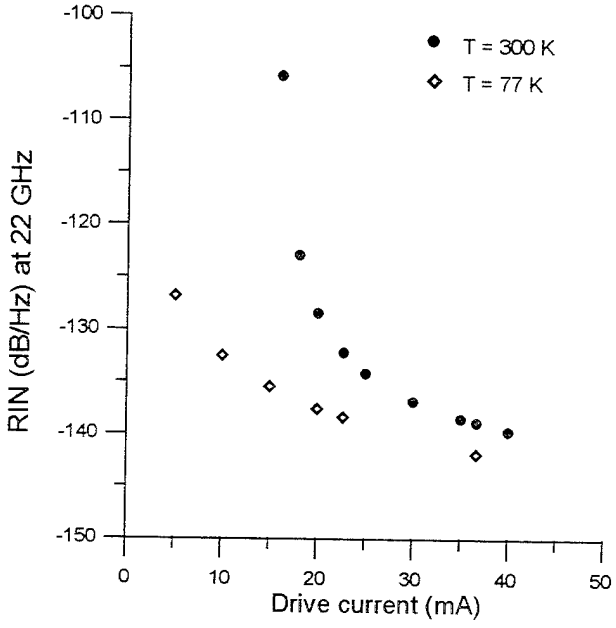


Fig 4: 22 GHz RIN dependence on drive current at 300 and 77 K .

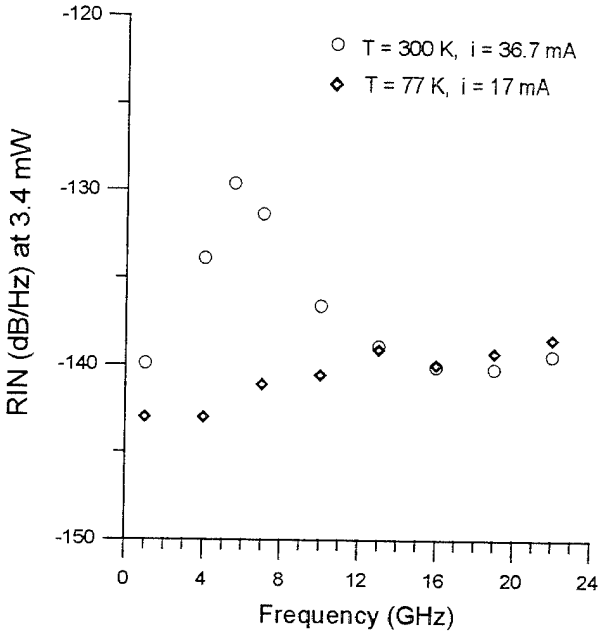


Fig 5: Cryogenic (77 K) and room temperature (300 K) RIN at same optical power output (3.4 mW).

Conclusion

Cryogenic operation of a commercial 1.5 μm InGaAsP laser significantly reduces its RIN at frequencies to $\approx$11 GHz and its integrated RIN over a 22 GHz measurement bandwidth. The large RIN peak occuring at the relaxation oscillation frequency at room temperature vanishes within the 22 GHz bandwidth at 77 K. Such behavior indicates strong potential for applications in ultrahigh speed optical communications.

References

1 M. A. Newkirk and K. J. Vahala, Appl. Phys. Lett. **54**(7), 600 (1989).

2 R. Yu, R. Nagarajan, T. Reynolds, J. E. Bowers, M. Shakouri, J. Park, K. Y. Lau, C. Zah, W. Zou, and J. Merz, IEEE MTT-S Digest (45) 1995.

3 B. Lu, W. Luo, C. Hlian Cheng, R.P. Schneider, S.P. Kilcoyne, K.L. Lear, and J.C. Zolper, CLEO '95, paper CTuB6, Baltimore, Maryland.

4 E. Goobar, C. Mahon, F. H. Peters, M. G. Peters, and L. Coldren, IEEE Phot Tech Lett. **7**(8), 851 (1995).

5 K. Petermann, Laser Diode Modulation and Noise (Kluwar Academic Publishers, Boston, 1991), pp. 152-157.

6 G. P. Agrawal and N. K. Dutta, Semiconductor Lasers (Van Nostrand Reinhold, New York, 1993), pp. 255-258.

7 G. E. Obarski, R. J. Phelan, and D. R. Larson, OSA Annual Meeting 1995, paper WVV74, Portland, Oregon.

Investigation of the resolution limit of the hydrogen Plasma Induced Defect Layer Intermixing Process

A. Saher Helmy, B. S. Ooi, and J. H. Marsh
Department of Electronics and Electrical Engineering, University of Glasgow, Glasgow G12 8QQ, Scotland, UK.

Introduction

Different schemes for realising photonic and optoelectronic integrated Circuits (OEICs & PICs) have been studied to replace the well known etch and overgrowth technique. The latter is usually associated with low efficiencies due to the nonradiative centres generated at the regrown interfaces and poor yield performance. Quantum well intermixing (QWI) has been developed so it is now a major contender for replacing the etch and regrowth method. Various QWI techniques have been developed [1]-[3]—one of these is to use point defects created by exposure to a hydrogen for layer intermixing; such a process has been used to realise PICs and OEICs [4] in materials with profiles that incorporate quantum wells at depths typical to those used for realising laser diodes (about 1 μm deep).

Hydrogen plasma induced defect layer intermixing is based on introducing point defects [5] into sections of the material exposed to the hydrogen plasma glow discharge in a reactive ion etching machine. The point defects then propagate through the material by annealing the sample in a rapid thermal annealer (RTA). During the annealing step, QWI takes place due to the exchange of Ga and Al atoms between the wells and the cladding.

Process Analysis

By exposing the sample to the H_2 plasma, defects are generated with an exponential depth profile [6]. Such defects include group III vacancies and interstitials, which are the major contributors to the QWI process [7]. Hydrogen forms both positive and neutral ions in the sample, leading to the following reactions in materials doped with the p-type dopants zinc and carbon [11]:

$$[C/Zn]_{Ga}^{-} + H^{+} \rightarrow \left\{[C/Zn]_{Ga}H\right\}^{\circ},$$

$$[C/Zn]_{Ga}^{-} + h^{+} + H^{\circ} \rightarrow \left\{[C/Zn]_{Ga}H\right\}^{\circ}.$$

The formation of the new bonds passivates the free carriers in the semiconductor. Hydrogen also causes passivation of deep level traps, consequently increasing the nonradiative life-time. Both the shallow and deep level traps are reactivated after the annealing step, which takes place at 850 °C. Passivated shallow and deep level traps are activated at 400 °C and 600 °C respectively [13]. The hydrogen depth range can be verified experimentally by using deuterons in an identical process together with SIMS measurements. In our process the sections in which it is desired to retain the wafer original features, usually for active gain sections, are capped with SrF_2. Strontium fluoride has been shown to be a suitable capping layer to screen the plasma from the sample surface. The hydrogen plasma range in the SrF_2 was computed using the TRIM ion implantation simulation program and found to be ~25 nm [8].

Subsequently the samples are annealed in the RTA. During the fast controlled heating of the samples (which are placed under GaAs caps to provide an As over-pressure) the group III point defects introduced during the plasma exposure move both towards the surface of the

sample, where they are released, and inwards towards the quantum wells. The profile of the defects after the annealing stage is currently under investigation, but it is not expected to have an *erfc* profile as in the case of impurity free vacancy disordering (IFVD), since the boundary conditions are different [9]. The defects that move down through the material leading to intermixing in quantum well region. Hydrogen was used as the implantation species since it has a low atomic mass. The low mass provides a low cross-over energy between the two energy loss mechanisms that implanted species experience. At high energies, at the beginning of the implantation track, the ion-electron interaction is the dominant energy loss mechanism. At lower energies, towards the end of the implantation track, atomic interactions are the main cause of the ion energy loss: such an interaction results in Frenkel pair type of defect [10]. The Frenkel pair defect is an essential factor for the QWI process. On the other hand, the concentration of defects introduced by hydrogen ion bombardment is low. This necessitates several cycles of plasma exposure and annealing to introduce an adequate number of defects to have the desired magnitudes of intermixing.

Bandgap tuned 75 μm oxide stripe laser diodes have been fabricated [4], by using this process. Shifts of about 25 nm were achieved, with the internal laser loss remaining unchanged at around 9.8 cm^{-1}. Such a shift was achieved after 8 cycles of exposure to the hydrogen plasma. However further knowledge of the process and its resolution limit for quantum wells at the desired depths is necessary for properly utilising it.

Experiments and Results

SrF_2 gratings, with periods ranging from 14 μm to 22 μm, were fabricated on the surface of the sample with a 1:1 ratio. The material used was a typical laser with a double quantum well (DQW) as the active layer at a depth of 0.9 μm. The aluminium concentration in the barrier was 43 %. The samples underwent 6 cycles of plasma exposure and RTA. Shifts of about 25 nm between the capped and uncapped layers were observed. The 77 K PL measurement results can be seen in Fig. 2. The grating samples should result in QWI with a repetitive profile—one region intermixed and the other is not non-intermixed as shown in Fig. 1. We therefore expect a two peaked PL spectrum resulting from recombination in the two regions. As can be seen in Fig. 2, the grating sample PL spectrum is indeed dual peaked. The longer wavelength peak has the higher intensity, since it corresponds to the narrowest bandgap region in the sample into which carriers diffuse prior to recombination. The grating spacing at which the two peaks overlap should represent the resolution limit.

As we expected from the description of the process, the peaks are well separated, even for the 14 μm pitch grating—the resolution limit is therefore considerably less than 7 μm. The limit of fairly close material profile for the IFVD process using a similar intermixing inhibitor cap SrF_2, was reported to be about 5 μm [12]. The process in hand, as expected, shows the potential to possess a higher resolution than that of the IFVD process. It should be noted that the comparison is done using the same intermixing inhibitor cap, SrF_2, in an attempt to eliminate the thermal stress factor introduced by the capping layer during the RTA stage.

Conclusion

We have demonstrated the potential of the plasma induced defect layer intermixing process as a promising candidate for high resolution, large bandgap shift quantum well intermixing process. Simple grating experiment was used to reveal the resolution limit of the process. Thus such features should allow the realisation of OEIC and PIC related processes, which were otherwise realised using etched and regrowth, higher order DFB and DBR gratings as well high precision external cavities are anticipated applications for such a process. TEM measurements will be made to examine the true resolution limit of the process, and a ridge waveguide laser with an extended cavity intermixed using the process is in the process of being tested.

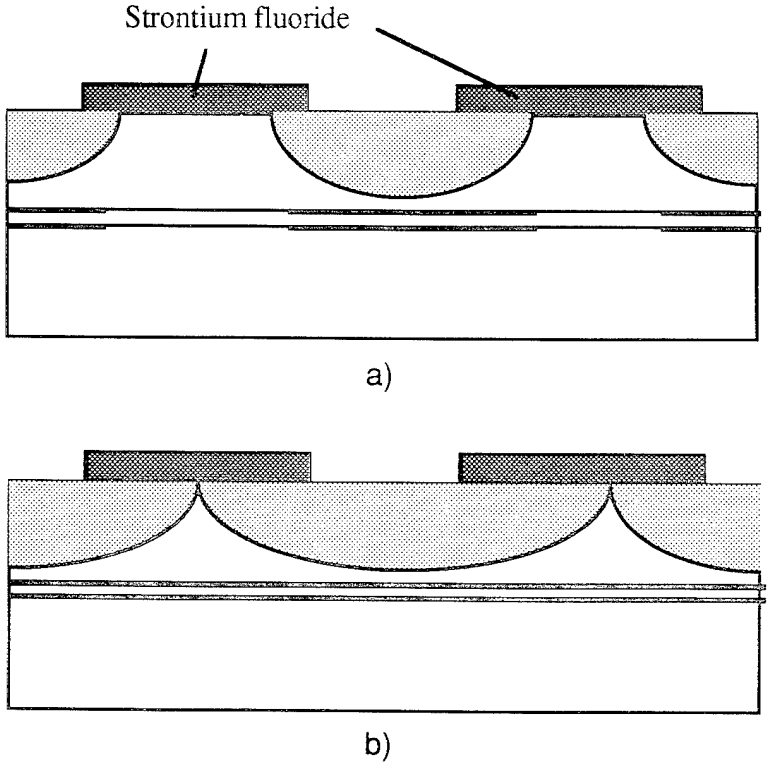


Fig. 1 A schematic for the quantum well profile at, a) partial intermixing b) complete intermixing at the resolution limit. The thick lines represent intermixed wells and the thin ones represent as-grown wells.

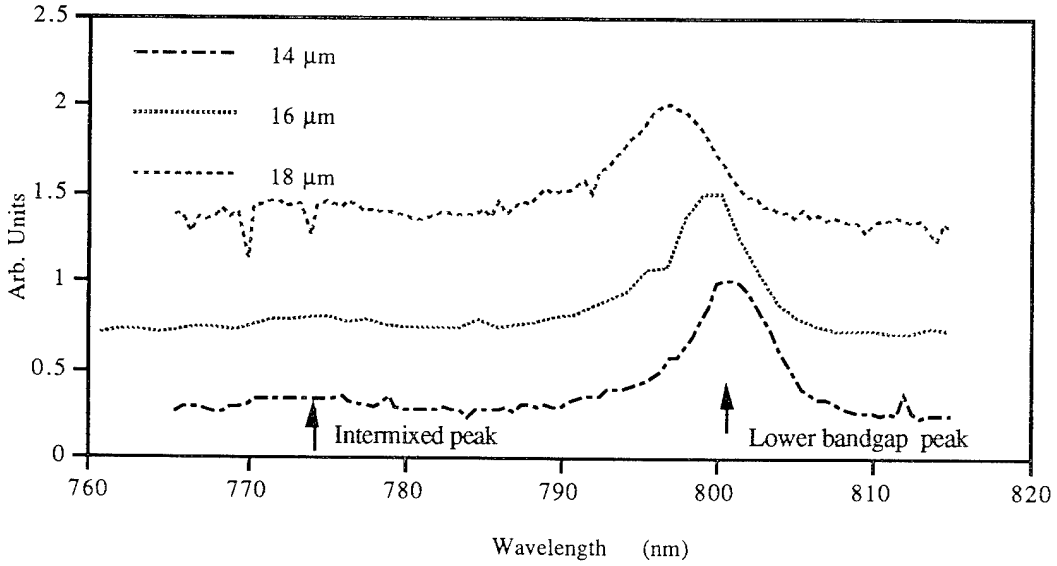


Fig. 2 PL Spectrum of three grating sizes showing two peaked spectrum with both peaks collapsing as the period of the grating decreases.

References

[1] J.H. Marsh et al., Optical and Quantum Electronics, Vol. 23, p S941, 1991.
[2] I. Gontijo et al., Electronics Letters, Vol. 30, p 145, 1994.
[3] C.J. McLean et al., Electronics Letters, Vol. 29, p 1657, 1993.

[4] B.S. Ooi et al., Electronics Letters, Vol. 31, p 449, 1995.
[5] D. Lootens et al., J. Appl. Phys., Vol. 70, p22, 1991.
[6] M. Rahman et al., Mat. Res. Soc. Symp. Proc., Vol. 279, P 775, 1993.
[7] D.G. Deppe &Holonyak Jr., J. Appl. Phys., Vol. 64, p R93, 1988.
[8] B.S. Ooi , Ph.D. Thesis University of GLasgow, Chapter V, 1995.
[9} A. Saher Helmy, M.Sc. Thesis, University of GLasgow, Chapter III, 1995.
[10] Mayer, Eriksson, & Davies, " Ion Implantation," Academic Press, 1970.
[11] R. Rahbi et al., Physica B, Vol. 170, p135, 1991.
[12] B. S. Ooi et al., IEEE Photonics Technology Letters, Vol. 7, p 944, 1995.
[13] W.C. Dautremont et al., Appl. Phys. Lett. Vol. 49, p 1098, 1986.

Feasibility of monolithic device integration in GaInP/AlGaInP using Photoabsorption Induced Disordering

Karen McIlvaney, Andrew McKee, A. Catrina Bryce and John H. Marsh
Department of Electronics and Electrical Engineering, University of Glasgow, Glasgow G12 8QQ

Wynn Jones
Epitaxial Products International , Cardiff, Wales

Introduction

Lasers operating in the visible region 633 nm-670 nm are in demand for such applications as optical disk systems, laser beam printing and optical sources for pumping solid-state lasers[1], including Cr:LISAF and Cr:LISCAF lasers. As in other wavelength regions, it would be of obvious advantage to bandgap shift regions of the as-grown structures to form low-loss modulator and coupler sections, and non-absorbing mirrors for high power operation. In this paper we present for the first time, to our knowledge, quantum well intermixing using photoabsorption induced disordering (PAID) in the GaInP/AlGaInP. This technique has already been successfully developed for use in the InGaAsP/InP. In the process, the sample is irradiated with a high-power laser whose wavelength is larger than the bandgap of the layers in the epitaxial semiconductor structure. The layers are intermixed when heat is generated by carrier cooling and non-radiative recombination. Large blue-shifts of the bandgap can be obtained and both bandgap tuned lasers[2] and modulators[3] have been demonstrated using PAID in the InGaAsP system with a Nd:YAG laser used to induce intermixing . The optical source used for the GaInP/AlGaInP system was an argon ion laser operating CW.

Layer Structure

The layer investigated is shown in below in Figure 1. The structure was grown on a GaAs substrate and contained a single 80 Å $Ga_{0.43}In_{0.57}P$ quantum well with 1 μm thick AlGaInP cladding layers. Lasers fabricated from the material had a threshold current density of 325 A/cm^2.

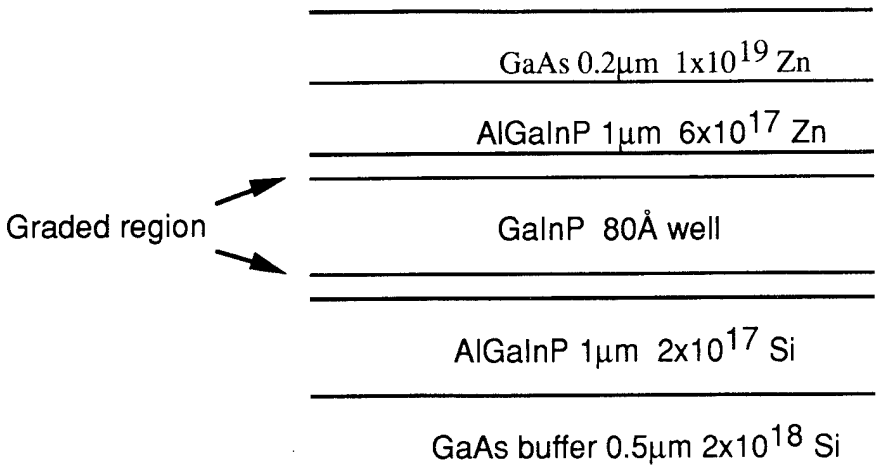


Figure 1 Diagram of layer structure used for intermixing

Experimental Set-up

A layer of silica (200 nm) was deposited on the samples to prevent damage to the surface during the intermixing process and to encapsulate any As from the cap layer which may be released due to heat. The photoluminescence of the sample was measured at 77 K and found to be 650 nm. The sample was then placed on a ceramic plate on a hotplate at a temperature of 250 °C. A thermocouple was placed in contact with the sample to monitor the temperature throughout the experiment. The output from the argon ion laser (5 W, all lines) was initially incident onto the sample with a beam diameter of 3 mm. A control sample was also placed on the hotplate to monitor the effect of low temperature heating on the structure over the duration of the experiment. This raised the temperature of the sample to 670 °C. The sample was exposed to the laser beam for a range of times between 1 and 20 minutes. In all cases the PL remained unchanged and no damage was observed on the sample. Next the laser beam was more tightly focused to a diameter of 0.5 mm, and the temperature of the sample rose to 850°C. No shift in the PL was observed for periods of 5 minutes and less. After 15 minutes exposure to the laser, a shift in the PL peak of 10 nm (30 meV) was observed, as shown in Figure 2. In this case some damage was observed on the surface possibly because the layer of silica was too thin. 500 nm thick layers will be used in future experiments.

Conclusion

Intermixing has been demonstrated using the PAID process for the GaInP/AlGaInP material system. A shift of 30 meV was obtained using a 5 W argon ion laser as the intermixing source. A control sample was used to eliminate the possibility that low temperature annealing of the sample on the hotplate was occurring. It is intended to use this intermixing technique to fabricate non-absorbing mirrors at the facets of a laser device, allowing high power operation to be achieved.

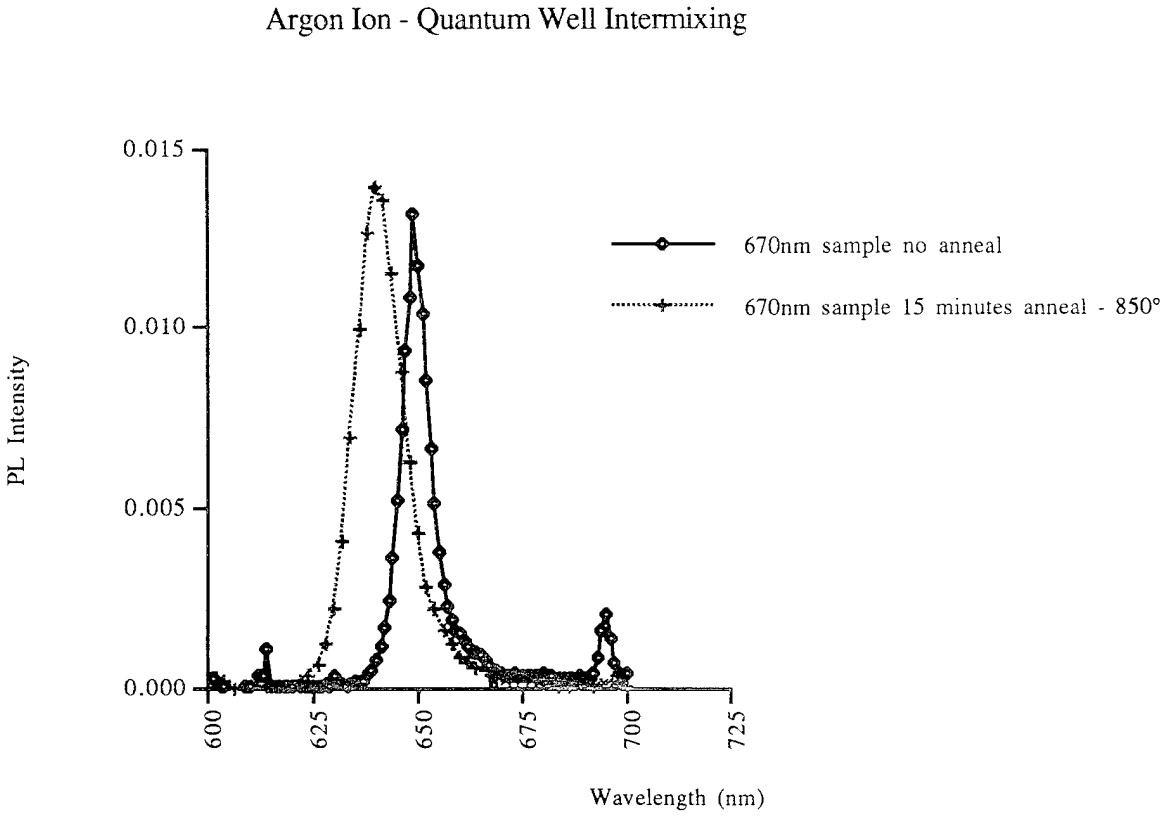


Figure 2 PL spectra of sample before and after annealing with an argon ion laser

References

[1]S.S. Ou, J.J. Yang, M.Jansen, C.Hess, P. Hayashida, C. Tu and F. Alverez, "High power, reliable 645nm compressively strained GaInP/GaAlInP laser diodes", *Electronics Letters*, **30**, 1303-1305, (1994)

[2]A. McKee, C. J. McLean, A. C. Bryce, R. M. De La Rue, C. Button and J. H. Marsh : "High quality *GaInAs/GaInAsP quantum well lasers wavelength tuned using photo-absorption induced disordering"—Appl Phys Lett*, **65**, 2263-2265 (1994).

3G. Lullo, A. McKee, C. J. McLean, A. C Bryce, C. Button and J. H. Marsh: "Fabrication of electroabsorption optical modulators using laser disordered GaInAs/GaInAsP multiple quantum well structures"—*Electron Lett*, **30**, 1623-1625 (1994).

Guided-Wave Magnetooptic Bragg Diffraction Efficiency Enhancement Using Nonuniform Bias Magnetic Field *

C.S. Tsai, S. Calciu, and Y.S. Lin
Department of Electrical and Computer Engineering
and Institute for Surface and Interface Science
University of California
Irvine, CA 92717
Tel #: (714) 824-5144; Fax # (714) 824-3732

Magnetoopic (MO) interactions between guided-optical waves and magnetostatic waves (MSWs) in a suitable magnetic substrate such as the yttrium iron garnet-gadolinium gallium garnet (YIG-GGG) waveguides [1] has continued to be a subject of considerable interest [2]. MSW can be readily and efficiently generated by applying a microwave signal to a microstrip line transducer, deposited directly on or brought over the YIG-GGG waveguide substrate. For the YIG-GGG waveguide substrate, the carrier frequency of the MSW can be tuned, typically from 0.5 to around 20 GHz, by simply varying an external DC bias magnetic field. MO Bragg diffractions result from the moving optical gratings induced by the MSW through the Faraday and Cotton-Mouton effects [3] in a manner similar to guided-wave acoustooptic (AO) Bragg diffractions in which the surface acoustic waves (SAW) induce moving optical gratings through the photoelastic effects [4]. In analogy with the AO Bragg cells, the resulting MO modulators are called the MO Bragg cells [5]. Such YIG-GGG-based MO Bragg cells have demonstrated the following unique advantages in comparison to their AO counterparts: (1) A large range of tunable carrier frequency (0.5 to around 20 GHz) may be obtained by varying the bias magnetic field. When used as a modulator such high and tunable carrier frequencies with the MO devices allow direct processing at the carrier frequency of wideband RF signals and, thus, eliminate the need for indirect processing via frequency down-conversion as is required with the AO devices, (2) A large MO bandwidth may be realized by means of a simpler transducer, and (3) much higher and electronically tunable modulation/switching and scanning speeds are achievable because the velocity of propagation for the MSWs can be higher than that of the SAWs by one to three orders of magnitude. Consequently, such MO Bragg cell modulators possess the potential for unique applications in wideband real-time RF signal processing and high-speed multiport optical switching. [2]

* This work was supported by the ONR

However, the MO Bragg diffraction efficiency (commonly defined as the Bragg diffracted light power per RF drive power in percentage) that has been reported heretofore was relatively low. For example, at an RF drive power of one watt a 10% diffraction efficiency for the MO Bragg cell versus a 80% diffraction efficiency for the AO Bragg cell has been typical. [4,5]. Thus, from the standpoint of practical application, it is desirable to achieve as high a diffraction efficiency at as low an RF drive power as possible. In this paper we report a new technique for enhancement of the MO Bragg diffraction efficiency using a nonuniform bias magnetic field. Enhancement of MO diffraction efficiency by as much as six times and a diffraction efficiency as high as 60% have been achieved.

We have found that the inferior MO Bragg diffraction efficiency, in comparison to the AO Bragg cell counterpart, is a result of the large angular beam spread (or wave vector spread) of the MSWs generated by a conventional transducer. For a MSW transducer with aperture L, the angular beam spread θ of the MSW generated is roughly given by (Λ/L) in radian in which Λ designates the wavelength of the MSW. Since for a given RF drive frequency, the wavelength of the MSW is significantly larger than that of the corresponding SAW, the angular beam spread of the MSW (from identical transducer aperture L) is also correspondingly larger. Now, at a given RF drive frequency the wave vector of the incident light wave finds only a small angular range of the wave vector of the MSW, within the large angular beam spread, to satisfy the Bragg condition and undergo Bragg diffraction. As a result, all of the MSW powers that associate with the remaining range of wave vector spread do not contribute to Bragg diffraction, and are considered wasted. The physical mechanism just described suggests that in order to increase the MO Bragg diffraction efficiency the angular beam spread of the MSW must be reduced.

We have employed a nonuniform bias magnetic field to reduce the angular beam spread of the MSW and, thus, enhance the MO Bragg diffraction. Since the velocity of propagation of the MSW is a sensitive function of the bias magnetic field, a nonuniform magnetic field will modify the wavefront of the MSW and, thus, create a lensing effect upon the MSW which in turn reduces its angular beam spread. In this work the nonuniform bias magnetic field was facilitated by using a nonuniform airgap, in which the YIG-GGG MO Bragg cell sample of 5.0 mm transducer aperture was inserted, in a compact Sm-Co magnetic circuit. A two-to-six-fold increase in the MO Bragg diffraction efficiency over that measured using a uniform bias magnetic field of comparable strength has been accomplished. For example, Fig. 1 shows the experimental data for the cases with uniform

and nonuniform bias magnetic fields at the carrier center frequency of 2.3 GHz, indicating a diffraction efficiency enhancement by six times. Fig. 2 is the plot of diffraction efficiency versus RF drive power. A diffraction efficiency as high as 60% has been achieved at an RF drive power of only 0.37 watt. Thus, a sixteen-fold enhancement in diffraction efficiency per watt RF drive power has been achieved when compared to the typical earlier performance figure of 10% at 1.0 watt RF drive power obtained using a uniform bias magnetic field [5]. Finally, the measured frequency responses indicate that the nonuniform magnetic field has had only a minor effect on the bandwidth (approximately 500 Mhz) of the MO Bragg cell.

In summary, theoretical and experimental results on a new technique for greatly enhancing the diffraction efficiency of guided-wave magnetooptic Bragg cell modulators are presented.

Acknowledgement

We acknowledge the technical assistance provided by Jae Yoo.

References

[1] P. K. Tien, R.J. Martin, R. Wolfe, R.C. LeCraw, and S.L. Bank, "Optical Waveguides of Crystal Garnet Films," Appl. Phys. Lett; 21, 207-209 (1972).

[2] See, for example, the many references cited in C.S. Tsai, "Recent Advances in Guided-Wave Magnetooptic Interactions, Devices and Applications," Photonics and Optoelectronics; 1, 51-66 (1993).

[3] C.S. Tsai, D. Young, W. Chen, L. Adkins, C.C. Lee, and H. Glass, "Noncollinear Magnetooptic Interaction of Guided-Optical Wave and Magnetostatic Surface Waves in YIG/GGG Waveguide," Appl. Phys. Letters; 47, 651-54 (1985).

[4] C.S. Tsai, "Integrated Acoustooptic Circuits and Applications," IEEE Trans. on UFFC; 39, 529-53 (1992).

[5] C.S. Tsai and D. Young, "Magnetostatic-Forward Volume Wave-Based Guided-Wave Magnetooptic Bragg Cells and Applications to Communication and Signal Processing," IEEE Trans. on MIT; 38, 560-70 (1990).

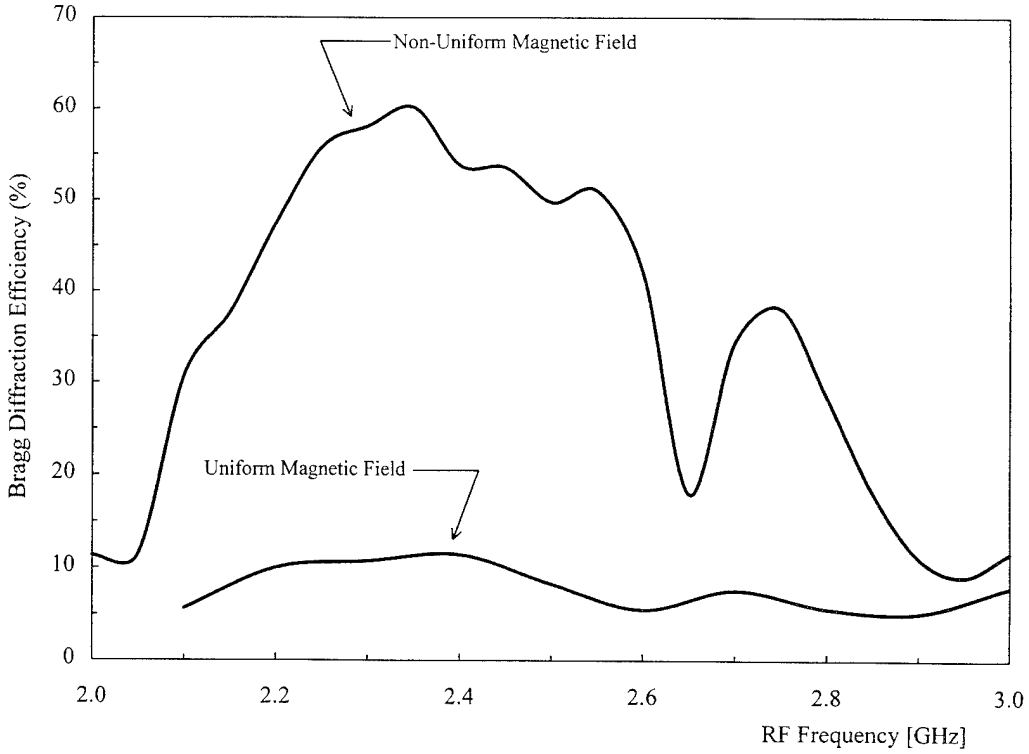


Fig.1 Magnetooptic Bragg Diffraction Efficiency Enhancement Using Non-Uniform Bias Magnetic Field

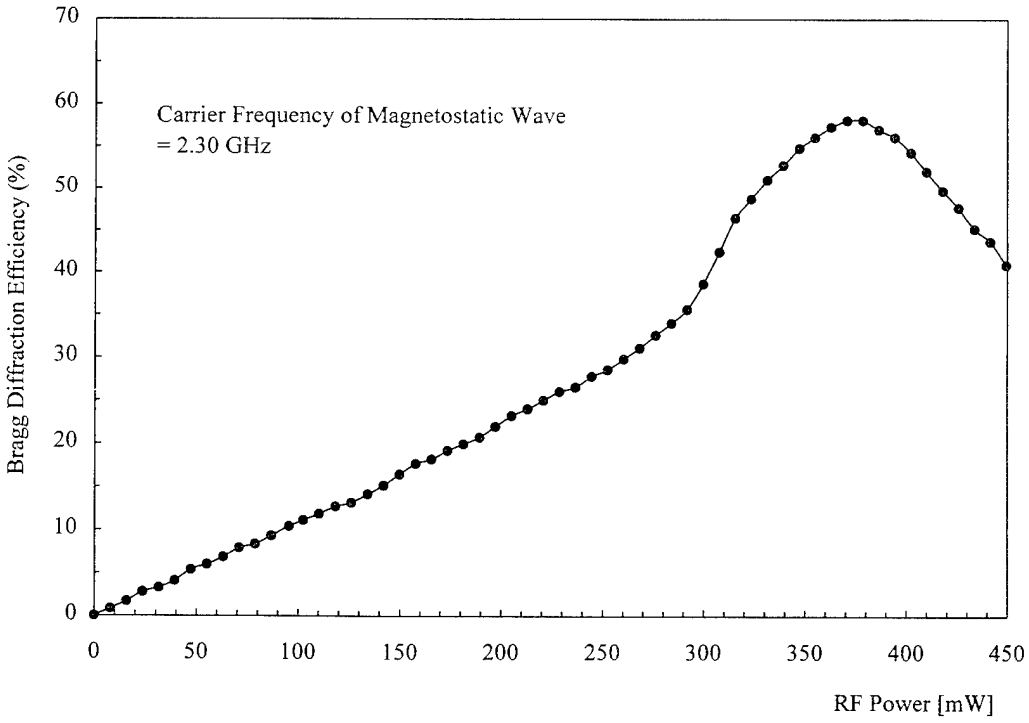


Fig.2 Magnetooptic Bragg Diffraction Efficiency Versus RF Drive Power Under Non-Uniform Magnetic Field

Symposium on Simulation of Quantum Well Phenomena: Device Applications—Optical Gain in Quantum Wells

ITuA 8:15 am-10:00 am
Fairfax A

James J. Coleman, *Presider*
University of Illinois, Urbana–Champaign

Modeling and Experimental Characterization of Optical Gain in InGaAsP-Based Lasers

M. S. Hybertsen, D.A. Ackerman, G.E. Shtengel, P.A. Morton,
R.F. Kazarinov, G.A. Baraff, T. Tanbun-Ek and R.A. Logan

AT&T Bell Laboratories, Murray Hill, New Jersey, 07974

Modeling of laser performance has become increasingly important as the performance requirements for lasers in telecommunications applications have become more demanding. The utility of modeling properties such as optical gain is tied to the use of multiquantum well (MQW) structures to improve laser performance. A multidimensional design space must be mapped out. At the same time, development of low cost, uncooled laser modules highlights the temperature dependence of laser performance. The T_0 parameter empirically describes the temperature sensitivity through $I_{th} = I_0 \exp(T/T_0)$. For InGaAsP based lasers, T_0 of 60-80 K near room temperature indicates substantial degradation of laser performance at elevated temperatures.

Here we review our experimental and theoretical results for 1.3 μm InGaAsP based lasers, both bulk active and MQW devices [1-6]. We systematically compare the models with the data in order to provide an assessment of conventional gain models for these systems. We address the temperature sensitivity of laser performance finding that the temperature dependence of material gain is important in determining the low value of T_0.

Devices used in this study consisted of MQW and bulk active 1.3μm capped mesa buried heterostructure Fabry-Perot lasers with cavities of ~1 μm width and ~300 μm length surrounded by conventional InP current blocking layers. Lasers exhibit low current leakage with internal efficiency remaining high (~80%) over the measured temperature range (25-85 C). For each device, the modal gain and loss, as well as the spontaneous emission, were measured as a function of current below threshold. A direct determination of the transparency energy yields the average quasifermi level separation in the active region. The average carrier density in the active region was determined by integrating the measured differential lifetime over current, taking account of the internal efficiency and correcting for the effect of the finite load impedance.

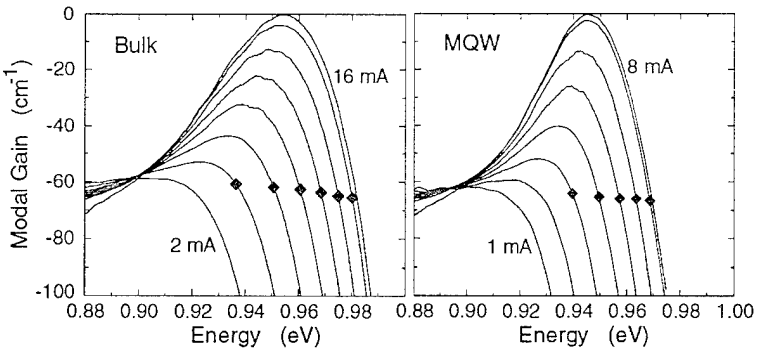


Figure 1. Families of measured gain spectra as a function of photon energy for the indicated ranges of device current for a bulk and a MQW active laser at 25 C.

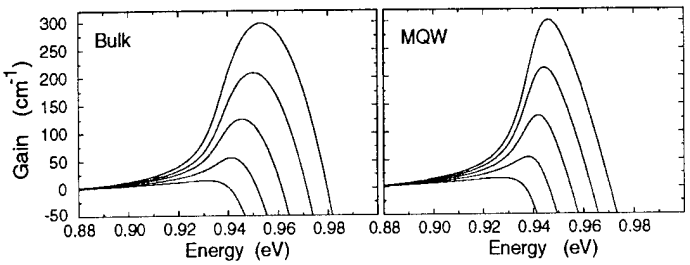


Figure 2. Calculated gain spectra for bulk active and MQW (superlattice approximation) active layer materials. Carrier densities: n = p = 1.2, 1.4, 1.6, 1.8 and 2.0 $\times$ 10^{18} cm^{-3} for the bulk case; n = p = 0.7, 0.8, 0.9, 1.0 and 1.1 $\times$ 10^{18} cm^{-3} for the superlattice case.

The electronic states for each constituent material are represented by an eight band $\mathbf{k}\cdot\mathbf{p}$ model. The needed input parameters are: (1) the Luttinger parameters which describe the light and heavy hole masses, (2) the momentum matrix element connecting the s-like and p-like bulk states at the zone center, (3) the conduction band effective mass, (4) the fundamental band gap, and (5) the spin-orbit splitting of the zone center valence band states. Incorporation of epitaxial strain requires knowledge of several deformation potentials. The electronic states for heterostructures are calculated using the envelope function approximation. This Hamiltonian naturally accounts for the non-parabolicity of the bands and the light hole to heavy hole mixing. The widely used axial approximation has been tested as a special case and found to be sufficiently accurate in the present context. Self consistent calculations have been done for MQW structures to account for spill-over of carriers into the SCL regions of the active layer. The quasifermi levels are determined for each pumping level and the optical absorption and spontaneous emission are then computed following the usual density matrix formulation. Broadening is included phenomenologically with a constant dephasing time of 0.1 ps, incorporated in such a way as to preserve the transparency energy. The many-body contribution to the quasifermi level separation is included as an overall shift.

Figure 1 summarizes some of the basic experimental gain data. Modal gain, including mirror and distributed losses, is shown as a function of photon energy for a set of subthreshold currents. The direct measurement of the transparency energy for each current yields the diamonds. At these energies, the material gain is zero, so the modal gain corresponds to the other modal losses. For each current, the peak gain achieved by pumping the active material is obtained as the difference between the peak and the point indicated by the diamond.

Bulk active lasers are modeled by quaternary composition $(In_{0.53}Ga_{0.47}As)_{0.6}(InP)_{0.4}$. The MQW region of the laser diode can be modeled for some purposes by an extended superlattice. This allows analysis of many of the features in the electronic structure. However, accurate treatment of these laser structures must self consistently include the SCL regions. Examples of calculated gain spectra are shown in Fig. 2. The range of density roughly covers the region from transparency to threshold. Qualitatively, the results agree well with the experimental curves. In particular, the MQW gain spectra are systematically narrower. However, quantitative comparison shows that the calculated spectra are too narrow. This can not be trivially resolved by a faster dephasing time (larger Lorentzian broadening) because the low energy tail has the wrong shape.

For the bulk active case, the measured chemical potential (quasifermi level separation) and the peak modal gain are shown as a function of density in Fig. 3. The calculated results are shown for comparison, where an acceptor band has been included in the determination of the hole quasifermi level with $N_A = 1\times10^{18}$ cm^{-3} and $E_A = 40$ meV, roughly representative of Zn in the present alloys. The calculated quasifermi level separation, including a many-body correction,

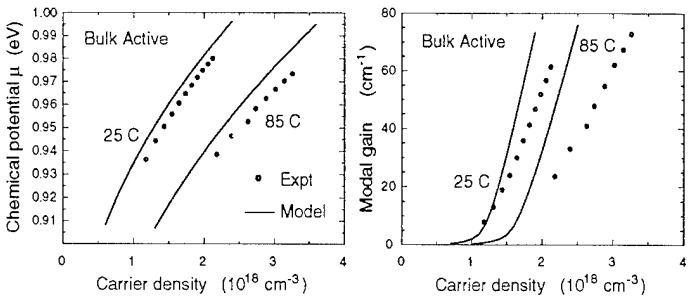


Figure 3. Comparison of the model (lines) to experiment (solid circles) for the chemical potential and peak modal gain as a function of density for the bulk active 1.3 μm device at room temperature and 85 C.

agrees well with the measured transparency energy as a function of density and temperature. This suggests that the calculated density of states is accurate for the bulk material. Similarly, detailed comparisons to various experiments for the MQW case demonstrate the accuracy of the calculated electronic structure. The calculated peak modal gain at room temperature yields a differential gain which is larger than experiment. Since the spontaneous emission spectra are well reproduced overall, this is largely be due to the discrepancy between theory and experiment for the width and shape of the gain spectra. The measured gain as a function of density at 85 C indicates a substantial temperature sensitivity which the model underestimates. The differential gain is measured to drop noticeably with a corresponding increase in the threshold carrier density. The measurements for the MQW based devices show similar trends.

The key open physical issue in the model is the broadening of the gain. A theory beyond the simple dephasing time approximation is clearly required. In addition, inhomogeneous broadening may be important, including the role of p-type dopants (Zn) and or other fluctuations in material composition. The observed temperature dependence of the gain is a key contribution to the overall low value of T_0 for these lasers.

[1] D.A. Ackerman, P.A. Morton, G.E. Shtengel, M.S. Hybertsen, R.F. Kazarinov, T. Tanbun-Ek and R.A. Logan, "Analysis of T_0 in 1.3 μm multi-quantum-well and bulk active lasers," *Appl. Phys. Lett.*, vol. 66, pp. 2613-2615, 1995.

[2] D.A. Ackerman, G.E. Shtengel, M.S. Hybertsen, P.A. Morton, R.F. Kazarinov, T. Tanbun-Ek and R.A. Logan, "Analysis of gain in determining T_0 in 1.3μm semiconductor lasers," *IEEE J. of Selected Topics in Quantum Electronics,* vol. 1, pp. 250-263, 1995.

[3] M.S. Hybertsen, R.F. Kazarinov, G.A. Baraff, D.A. Ackerman, G.E. Shtengel, P.A. Morton, T. Tanbun-Ek and R.A. Logan, "Modeling of gain for InGaAsP based lasers," *SPIE Proceedings Series,* vol. 2399, pp. 132-145, 1995.

[4] G.E. Shtengel and D.A. Ackerman, "Internal optical loss measurements in 1.3 μm InGaAsP lasers," *Electron. Lett.*, vol. 31, pp. 1157-1159, 1995.

[5] G.E. Shtengel, D.A. Ackerman, P.A. Morton, E.J. Flynn, and M.S. Hybertsen, "Impedance-corrected carrier lifetime measurements in semiconductor lasers," to be published, *Appl. Phys. Lett.*, vol. 67, pp. 1506-1508, 1995.

[6] G.E. Shtengel, D.A. Ackerman, and P.A. Morton, "True Carrier Lifetime Measurements of Semiconductor lasers," *Electron. Lett.*, vol. 31, pp. 1747-1748, 1995.

The temperature and strain dependence of differential gain in 1.5μm quantum well lasers.

Eoin P. O'Reilly, G. Jones, P. Togher, M. Silver and A.R. Adams
Department of Physics, University of Surrey, Guildford GU2 5XH, U.K.

Tel. 44-1483-259406 Fax 44-1483-259501 email e.oreilly@surrey.ac.uk

The temperature sensitivity of long wavelength (1.5μm) semiconductor lasers, denoted by the characteristic temperature, T_o, has remained poor, with T_o values typically ranging from 40K up to a maximum of order 100K. There still remains controversy as to the cause of this temperature sensitivity. Several groups have suggested that the problem is due to the differential gain decreasing rapidly with increasing temperature [1-2], or is due to the temperature dependence of a strong stimulated emission component below threshold [3]. However, this work has involved lasers with low T_o values, of order 40K, and so it has not yet been convincingly demonstrated as to what is the limiting mechanism for lasers with higher T_o values. We have provided direct evidence in a previous paper that the radiative component of the threshold current is perfectly well behaved in 1.5μm strained and unstrained quantum well lasers, with a characteristic temperature, T_o, close to 300K at room temperature [4]. The high values and strong temperature dependence of the threshold currents must then be due to non-radiative recombination paths, in particular Auger recombination.

We use two different methods to investigate the variation of gain with current density in long wavelength lasers, investigating separately the influence of strain and of temperature. In each case, we find that the gain characteristics are perfectly well behaved, and consistent with Auger recombination being the dominant current path. Our results show that the strain dependence of the differential gain is well explained by conventional theoretical models and that there is no evidence in the devices studied for a rapid decrease in differential gain with temperature; rather, the differential gain is inversely proportional to temperature, as predicted by simple models.

1 McIlroy Analysis of Strain Dependence

Because the threshold gain varies with cavity length, L, measurement of threshold current density against L allows the determination of the gain, g, as a function of current density, g(J) [5]. It has been shown that the threshold current increases much more rapidly as the cavity length decreases in InP-based lasers [6] than in the case of GaAs-based devices [5]. In practice the measured variations with cavity length in lattice-matched and compressively strained layers are typically a factor of 3-4 larger than those observed in GaAs. The measured variations in tensile-strained devices emitting about 1.5μm are much improved, being about a factor of two better than in the lattice-matched case [7]. Using a modified analysis based on the work of McIlroy *et al* [5], we present calculations which show that the observed differences between compressive and tensile strain are well explained by the calculated variation with strain of the optical confinement factor, Γ, and the differential gain at transparency, dg/dn (n_{tr}). More detailed comaprisons with experiment support Auger recombination as the dominant contribution to the threshold current density in these 1.5μm

devices. We extend our analysis to show that the magnitude of the Auger coefficients and their variation with strain are comparable to those obtained using other techniques.

2 Hakki-Paoli Analysis of Temperature Dependence

Using the Hakki-Paoli technique [8], we have measured g(J) as a function of temperature for several 1.5μm quantum well lasers. Both simple theoretical analysis and experiment suggest a logarithmic relationship between gain, g, and current density, J, in quantum well lasers

$$g = g_o \ln(J/J_{tr}) \qquad (1)$$

where J_{tr} is the transparency current density and g_o is a device parameter which, in an ideal laser, should be independent of temperature. All of the devices studied had T_o values of order 65K. The coefficient g_o was in all cases found to be virtually independent of temperature between 20 and 60°C, confirming that the differential gain did not have an anomalous temperature dependence. By contrast, the transparency curent density, J_{tr}, varied strongly with temperature, with the measured variation being entirely consistent with that predicted from a simple model which assumes phonon-assisted Auger recombination to be the dominant recombination mechanism [9].

Conclusion

The modal gain is found by two different experimental techniques to have a logarithmic dependence on drive current in 1.5μm quantum well lasers. The experimentally measured strain dependence of the differential gain with respect to current is well explained, both qualitatively and quantitatively, by the calculated variation with strain of the differential gain with respect to carrier density. More detailed comparison with experiment supports Auger recombination as the dominant contribution to the threshold current density. The measured variation of gain with temperature is also best explained for devices with characteristic temperature T_o of order 60K by the differential gain having only a weak temperature dependence, with Auger recombination dominant.

Acknowledgements - This work was supported by the Engineering and Physical Sciences Research Council (UK). We are grateful to BNR (Harlow) and NorTel (Paignton) for CASE studentships to support GJ and PT respectively.

REFERENCES

[1] Y. Zou, J.S. Osinski, P. Godzinski, P.D. Dapkus, W. Rideout, W.F. Sharfin and F.D. Crawford, Appl. Phys. Lett. **62**, 175 (1993)

[2] D.A. Ackerman, G.E. Shtengel, M.S. Hybertsen, P.A. Morton, R.F. Kazarinov, T. Tanbun-Ek and R.A. Logan, IEEE J. Selected Topics in Quantum Electron. **1**, 250 (1995)

[3] J. O'Gorman, A.F. Levi, S. Schmitt-Rink, T. Tanbun-Ek, D.L. Coblentz, R.A. Logan,

Appl. Phys. Lett. **60**, 157 (1993)

[4] J. Braithwaite, M. Silver, V.A. Wilkinson, E.P. O'Reilly and A.R. Adams, Appl. Phys. Lett. **67**, December 1995

[5] P.W.A. McIlroy, A. Kurobe and Y. Uematsu, IEEE J. Quantum Electronics **21**, 1958 (1985)

[6] A.T.R. Briggs, P.D. Greene and J.M. Jowett, IEEE Photon. Tech. Lett. 4, 423 (1993)

[7] A.D. Smith, A.T.R. Briggs, A. Vranic and K. Scarrott, 5th. European Workshop on MOVPE, Malmo, June 1993

[8] B.W. Hakki and T.L. Paoli, J. Appl. Phys. **46**, 1299 (1975)

[9] E.P. O'Reilly and M. Silver, Appl. Phys. Lett. **63**, 3318 (1993)

Bandstructure and Modal Gain of Partially Interdiffused InGaAs/GaAs/AlGaAs SQW Lasers

Rafael Gómez-Alcalá (Phone: +34-86-812165, FAX: +34-86-812116)
E.T.S.I. Telecomunicación.
Campus Universitario, s/n
E-36200 VIGO (SPAIN)
Francisco Javier Fraile-Peláez (Phone: +34-86-812139, FAX: +34-86-812116)
E.T.S.I. Telecomunicación.
Campus Universitario, s/n
E-36200 VIGO (SPAIN)
Ignacio Esquivias-Moscardó (Phone: +34-1-3367339, FAX: +34-1-3367319)
Departamento de Tecnología Fotónica, Universidad Politécnica de Madrid
Ciudad Universitaria, s/n
28040 MADRID (SPAIN)

Interdiffusion is a fabrication technique which is gaining interest in many applications [4] [5] [7] [3] [6]. It modifies the composition of the quantum well yielding a non square potential profile [9]. In order to analyze the effect of interdiffusion on quantum well properties the diffusion length (L_d) is used as a parameter. This is the product of the annealing time and the diffusion coefficient.

In this work we calculate the bandstructure of a $In_{0.2}Ga_{0.8}As/GaAs$ interdiffused quantum well for different diffusion lengths, and a well width of 10 nm, with the finite element method [8]. The conduction subbands are supposed parabolic, whereas for the valence band we include band mixing in our calculations [1]. The energy levels for the conduction band and the corresponding for the valence band (at $k = 0$) are plotted as a function of the diffusion length in figure 1. We can see a maximum in the value of the energy subbands at $L_d \simeq 2$ nm for both conduction and valence bands. This has been previously noted in [10] for the interdiffused GaAs/AlGaAs quantum wells. The valence subbands structure is shown in figure 2 for several diffusion lengths.

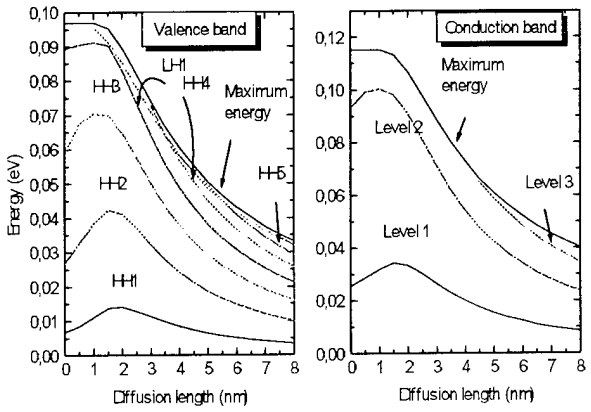


Figure 1. The energy levels for different diffusion lengths.

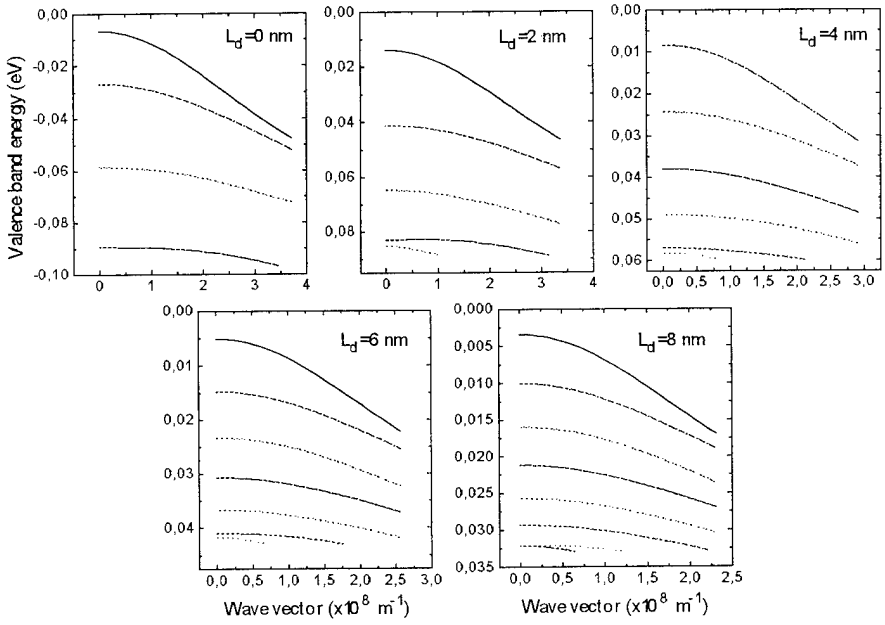


Figure 2. Valence subbands structure for diffusion lengths of 0, 2, 4 and 6 nm.

In order to calculate the modal gain we suppose a SCH SQW structure with a cladding of $Al_{0.2}Ga_{0.8}As$ and a core width of 0.8 μm in order to obtain a monomode solution for the optical field. The modal gain was evaluated using the model of Aversa and Iizuka [2], which we have extended to account for valence band mixing. In figure 3 is plotted the TE modal gain as a function of the sheet carrier density. We can see the theoretical improve of the differential modal gain as we increase the diffusion length up to a value (for $L_d \simeq 5$ nm) where the slope keeps constant but the transparency carrier density increases. An optimum L_d exists which give us a maximum of differential gain.

In conclusion, our calculations predict an improve of the laser performance for partially interdiffused SQW strained-layer lasers.

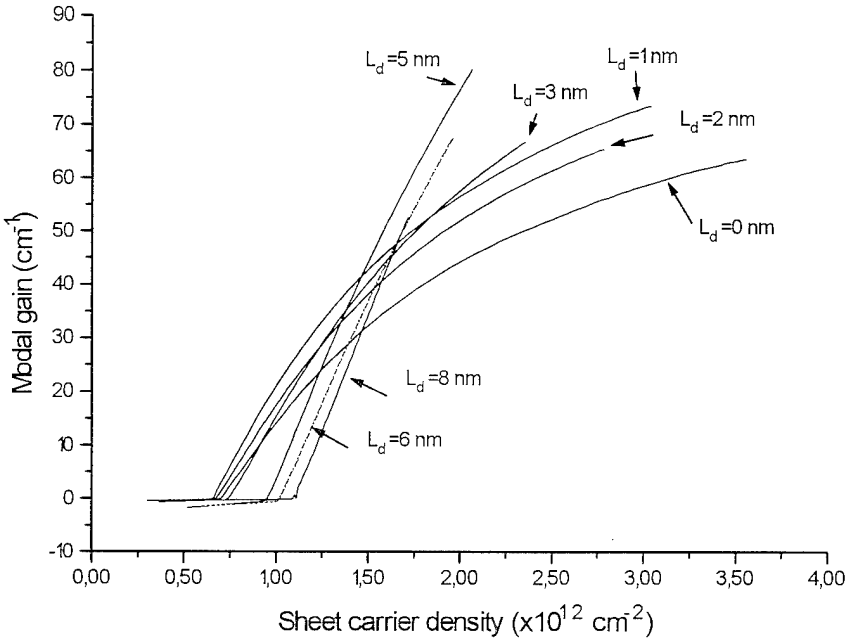


Figure 3. The modal gain as a function of the sheet carrier density for several diffusion lengths.

References

[1] R. Gomez Alcala, C. Mejuto Vila, and F.J. Fraile Pelaez. Valence band-structure of disordered quantum wells. *Superlattices and Microstructures*, 17(3):277–283, 1995.

[2] C. Aversa and K. Iizuka. Gain of TE-TM modes in quantum-well lasers. *IEEE Journal of Quantum Electronics*, 28(9):1864–1873, 1992.

[3] S. Brukner, J.D. Ralston, S. Weisser, J. Rosenzweig, E.C. Larkins, R.E. Sah, and J. Fleissner. Wavelength tuning of high-speed InGaAs-GaAs-AlGaAs pseudomorphic MQW lasers via impurity-free interdiffusion. *IEEE Photonics Technology Letters*, 7(9):941–943, 1995.

[4] A.C. Bryce, J.H. Marsh, R. Gwilliam, and R.W. Glew. Impurity induced disordering in InGaAs/InGaAlAs quantum wells using implanted flurine and boron. *IEE Proceedings-J*, 138:87–90, 1991.

[5] K. Kash, B. Tell, P. Grabble, E.A. Dobisz, H.G. Craighead, and M.C. Tamargo. Aluminium ion-implantation enhanced intermixing of GaAs-AlGaAs quantum-well structures. *Journal of Applied Physics*, 63:190–194, 1988.

[6] J. Micallef, E.H. Li, and B.L. Weiss. Polarisation dependent interband optical absorption in strained nonsquare InGaAs/GaAs quantum well. *Electronics Letters*, 28(6):526–528, 1992.

[7] Y. Nagai, K. Shigihara, S. Karakida, S. Kakimoto, M. Otsubo, and K. Ikeda. Characteristics of laser diodes with partially intermixed GaAs-AlGaAs quantum well. *IEEE Journal of Quantum Electronics*, 31:1364–1370, 1995.

[8] K. Nakamura, A. Shimizu, M. Koshiba, and K. Hayata. Finite-element analysis of quantum wells of arbitrary semiconductors with arbitrary potential profiles. *IEEE Journal of Quantum Electronics*, 25(5):889–895, 1989.

[9] T.E. Schlesinger and T. Kuech. Determination of the interdiffusion of al and ga in undoped (Al,Ga) As/ GaAs quantum well. *Applied Physics Letters*, 49:519–521, 1986.

[10] A.P. Zhao, S.R. Cvetkovic, and Z.Y. Yang. Finite-element calculation of the influence of interdiffusion on eigenstates in a GaAs/AlxGa1-xAs single-quantum-well structure. *Optical and Quantum Electronics*, 25:845–851, 1993.

Spin-orbit coupling effects on the optical gain of a cubic GaN quantum-well laser

Doyeol Ahn

LG Electronics Research Center
16 Woomyeon, Seocho-Gu
Seoul 137-140, Republic of Korea

III-V nitrides such as GaN or InGaN are attractive for their potential optoelectronic device applications in the blue-green or near-ultraviolet spectrum. Because of its very narrow spin-orbit(SO) split off energy (10 meV), the coupling effects in the valence band of GaN is expected to be quite pronounced. Recently, the Luttinger valence-band parameters γ_1, γ_2, and γ_3 of a cubic phase of GaN, a knowledge of which is necessary for the calculation of the valence-band structures, are calculated from a semi-empirical five level $\mathbf{k}\cdot\mathbf{p}$ approach [1].

In this work, the effects of a very strong spin-orbit (SO) split-off band coupling on the valence-band structure and the optical gain of a 100Å cubic GaN quantum-well are studied theoretically within the 6x6 Luttinger-Kohn model [2]. Firstly, the valence band structure of a cubic GaN quantum well is calculated using the recently developed 6x6 Luttinger-Kohn model [2] which takes into account the spin-orbit (SO)split-off coupling. Secondly, the optical gain of a GaN quantum well is calculated from the complex optical susceptibility obtained by the density matrix formalism [3].

The results of our valence-subband calculation for a 100 Å cubic GaN quantum well surrounded by lattice-matched GaAlN barriers versus in-plane wave vector (in unit of $2\pi/a_0$) are shown in Fig. 1. Here a_0 is the lattice constant of the active layer. We consider a quantum well of width L_z grown along the [001] direction and valence band is

assumed to be isotropic in the in-plane wave vector. It has been customary to label the subbands according to their character at the zone center. It is also well known that the SO band is coupled to the light hole band and is decoupled from the heavy hole band at $k_{\|} = 0$. We have found that it is not entirely correct to label the subbands as "light hole" or "spin-orbit" especially for GaN for which the spin-orbit split off energy is very small (10 meV) and as a result there is no pure "light hole" or "spin-orbit" bands even at the zone center when the coupling effects are considered. In this letter, we propose to denote the subbands which are the coupled states of "light hole" and "spin-orbit" bands as "LS" and "SL". Here "LS" or "SL" is the acronym for "light-hole-spin-orbit" and the first letter denotes the dominant component of the wave function.

In Fig. 2, the calculated peak optical gains are shown for unstrained GaN and ZnSe quantum wells and strained GaN quantum well for comparison. The widths of both quantum wells are assumed to be 100 Å. In this figure, we note that the transparent level n_{tr}, the carrier density required to reach zero gain in the material, of an unstrained GaN quantum well (8.37×10^{18} cm^{-3}) is much higher than that (5.54×10^{18} cm^{-3}) of an unstrained ZnSe quantum well.

There seem to be two factors which cause the inferior gain of a GaN quantum well as compared with that of a ZnSe quantum well: (1) the conduction-band electron mass (0.2 m) of a GaN quantum well is heavier than that (0.14 m) of a ZnSe quantum well and (2) because of the very narrow separation (10 meV) between the SO band and the heavy - and light- hole bands of GaN, the injected holes into the valence band will easily occupy the SO band which may not contribute to the lasing mode of a GaN quantum well laser.

In order to improve the optical gain of a GaN quantum-well laser, we propose a combination of strain and the use of alloy to reduce the electron and hole mass and to increase the SO band separation: (1) use of compressive strained quantum well to reduce the heavy hole effective mass, (2) employ alloy to increase the SO band separation and (3) reduce the conduction-band effective mass. Alloys such as GaNAs or GaNP may be considered as a candidate.

With the compressive strain potential of -30 meV, the transparent level n_{tr} is expected to be reduced to 6.81 x 10^{18} cm^{-3} from the unstrained level of 8.54 x 10^{18} cm^{-3}. The compressive strain potential of -30 meV corresponds to the lattice mismatch of around -1 % and would be obtainable employing InGaN alloy.

Fig. 3 shows the peak linear gains for the TE modes as functions of the injected carrier density for the SO band separation of (i) 0.01 eV (dashed line), (ii) 0.1 eV (dotted line), and (iii) 0.2 (eV) (solid line) for a hypothetical 100 Å quantum well employing GaN based alloys. When the SO band separation is increased to 0.1 eV from 0.01 eV , the transparent level n_{tr} is expected to be reduced to 7.05 x 10^{18} cm^{-3} . One can further reduce n_{tr} to 6.73x 10^{18} cm^{-3} with the SO separation of 0.2 eV.

It seems that preventing the valence-band leakage of the injected holes to the SO band could be as effective as the use of strained-layer in reducing the lasing threshold of GaN quantum-well lasers. It should be so because the reduction of the hole (or electron) mass or the prevention of the SO band from filling increases the separation of quasi-Fermi levels F_C - F_V such that Bernard-Duraffourg condition for the lasing is satisfied at lower injected carrier density.

References

[1] D. Ahn, presented at the 22nd International Symposium on Compound Semiconductors, Cheju island, Korea, Aug. 28 - Sept. 2, 1995.

[2] D. Ahn, S. J. Yoon, S. L. Chuang, and C. S. Chang, J. Appl. Phys 78, 2489 (1995).

[3] D. Ahn and S. L. Chuang, IEEE J. Quantum Electron. 24, 2400 (1988).

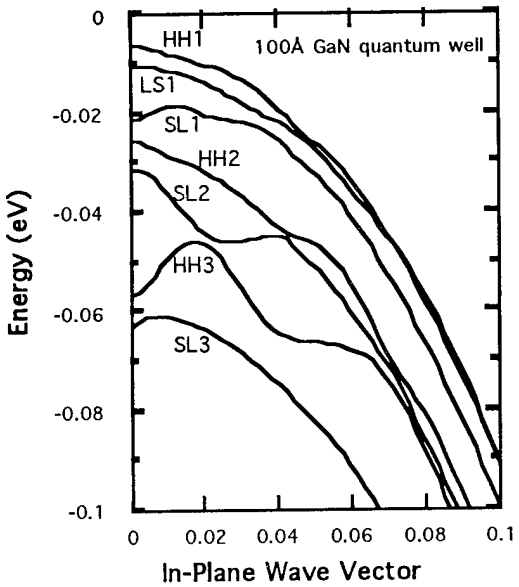


Fig. 1 The valence-band structure of a 100Å cubic GaN quantum well

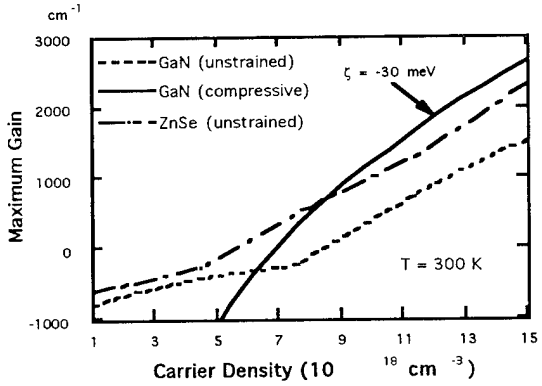


Fig.2 Peak gain profiles of unstrained GaN, compressive strained GaN, and unstrained ZnSe quantum wells

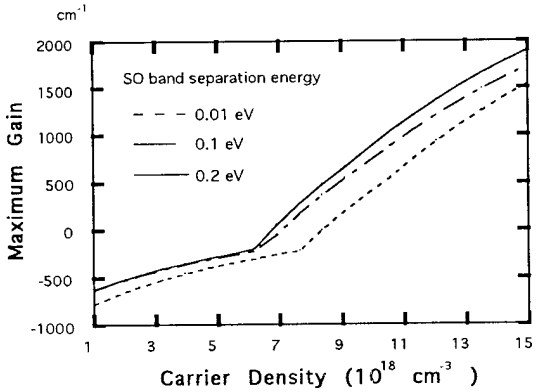


Fig. 3 Peak gain for a hypothetical GaN quantum well with various SO separation

Non-Markovian gain of a quantum-well laser with many-body effects

Doyeol Ahn
LG Electronics Research Center
16 Woomyeon, Seocho-Gu
Seoul 137-140
Republic of Korea
E-mail: dahn@goldstar.co.kr

It was pointed out by Yamanishi and Lee [1] that the optical gain spectra calculated with the Lorentzian line shape function deviate from the experimental results. Especially, an anomalous absorption region appears at photon energies below the band-gap in the gain spectra as long as the Lorentzian line shape is used. Moreover, the detailed balance between absorption and emission of photons requires that the transparency point in the gain spectra coincide with the Fermi (or quasi Fermi) -level energy [2,3]. In general, the gain spectra with the Lorentzian do not satisfy the detailed balance condition, either.

In this work, we present a model for the optical gain of a quantum-well laser taking into account the non-Markovian relaxation, many-body effects, and the valence-band mixing employing the 6x6 Luttinger-Kohn Hamiltonian. The optical gain and the line shape function of the quantum well under an external optical field are derived from recently developed time-convolutionless quantum-kinetic equations [4] for electron-hole pairs near the band edge. Many-body effects such as band-gap renormalization and excitonic enhancement are included by taking into account the Coulomb interaction in the Hartree-Fock approximation. In this work, the plasma screening of the Coulomb interaction is not considered and this makes the calculation of the many-body effects to be overestimated. Unnormalized single-particle energies are obtained using the multiband effective approximation, i.e., a parabolic band structure for electrons and a 6x6 Luttinger-Kohn

model for holes [5]. The latter includes the spin-orbit (SO) split-off band coupling effects on the valence-band structure. Conventionally, the optical gain of a quantum-well laser is calculated using the density matrix formalism. The linear gain is the result of $k_{\parallel}$-space integration of the product of the absolute square of the dipole matrix element, the Fermi function difference between electrons and hole , and the Lorentzian line shape function.

Recently, the optical gain and the line shape function of a driven semiconductor were derived from the time-convolutionless (TCL) quantum-kinetic equations for the interband polarization taking into account the many-body effects [4]. We integrate the equation of motion for the interband pair amplitude directly to obtain the optical gain assuming the quasi-equilibrium or adiabatic approximation and discuss the interference effects on the line shape between the external driving field and the stochastic reservoir of the system.

The optical gain $g(\omega)$ is obtained after some lengthy mathematical manipulations and is given by [4]

$$g(\omega) = \frac{\omega\mu c}{n_r}\frac{2}{V}\sum_k \frac{\mathrm{Re}\ \Xi\ (0,\Delta_k)}{1-\mathrm{Re}\ q_{1k}(0)}\ |\mu(k)|^2\ [1+\mathrm{Re}\ g_2(\infty,\Delta_k)][n^o_{ck} - n^o_{vk}] \quad (1)$$

$$\text{with} \quad \mathrm{Re}\ q_{1k}(0) \approx \sum_{k'} V_s(k-k')\mathrm{Re}\ \Xi\ (0,\Delta_{k'})[n^o_{ck'} - n^o_{vk'}] \quad (2)$$

where μ is the permeability, n_r is the refractive index, c is the speed of light in free space, V is the volume, and ε_0 is the permittivity of free space. In equation (1), $\mathrm{Re}\ \Xi\ (0,\Delta_k)$ is the line shape function that describes the spectral shape of the optical gain in a driven semiconductor and $\Delta_k = E_c(k) - E_v(k) - \omega$. The denominator [1- $\mathrm{Re}\ q_{1k}(0)$] describes the gain enhancement due to the excitonic effects caused by the attractive Coulomb interaction and the factor (1 + $\mathrm{Re}\ g_2(\infty,\Delta_k)$) describes the gain (or line shape) enhancement due to the interaction between the optical field and the stochastic reservoir of the system.

It was shown [4] that the line shape of the gain spectra is Gaussian for the simplest non-Markovian quantum kinetics:

$$\mathrm{Re}\ \Xi\ (0,\Delta_k) = \sqrt{\frac{\tau_c\ \pi}{2\gamma_{cv}(k)}}\ \exp\left(-\frac{\tau_c \Delta_k^2}{2\gamma_{cv}(k)} \right). \qquad (3)$$

where τ_c is the correlation time for the intraband relaxation

and

$$\gamma_{vc}(k) = \frac{1}{2}\ \{\ \frac{1}{\tau_v(k)} + \frac{1}{\tau_c(k)}\ \}.$$

As a numerical example, we have calculated the band-structure, the band-gap renormalization (BGR), and the optical gain spectra of a lattice-matched 60 Å $In_{0.53}Ga_{0.47}As$ quantum well surrounded by InP outer barriers.

In Fig. 1, we plot the calculated optical gain spectra for the three cases of: (i) Markovian model with Lorentzian line shape function (dashed line), (ii) non-Markovian model (dotted line), and (iii) non-Markovian model with excitonic enhancement (solid line) for the correlation time τ_c = 20 fs. The intraband relaxation time of 0.1 ps and the carrier density of 3 x 10^{18} cm^{-3} are assumed throughout the calculation and the renormalization of the band-gap energy is taken care of in all three cases. The correlation time is inversely proportional to the energy transfer in the intraband frequency fluctuations. Since the typical energy transfer for the intraband process is on the order of k_BT, we get the correlation time of approximately 20 fs from the uncertainty relation. We do not specify the explicit form of the intraband relaxation in this paper and the recent calculations of the intraband relaxation can be used.

In the absence of spectral broadening the optical gain spectra are related to the spontaneous emission spectra from the detailed balance between absorption and emission of photons [3]. One of the remarkable feature of this relation is that there is a transparency point in the gain spectra which coincide with the Fermi (or quasi-Fermi) - level separation

that suggests the carriers and the photons are in thermal (or quasi) equilibrium [2,3]. For the carrier density of 3×10^{18} cm^{-3} the Fermi-level separation is 0.8752 eV for the quantum-well structure. Then the optical gain spectra calculated with the Lorentzian line shape function have two anomalies: unnatural absorption region below the band-gap energy and mismatch of the transparency point of the gain with the Fermi-level separation, the latter suggests that the carriers and the photons are not in thermal (or quasi) equilibrium. It is seen that the two anomalies associated with the Lorentzian line shape are removed in the non-Markovian model with many-body effects.

References

[1] M. Yamada and Y. Suematsu, J. Appl. Phys. 52, 2653 (1981).

[2] P. Rees and P. Blood, IEEE J. Quantum Electron. 31, 1047 (1995).

[3] C. H. Henry, R. A. Rogan, and F. R. Merritt, J. Appl. Phys. 51, 3042 (1980).

[4] D. Ahn, IEEE J. Selected Topics in Quantum Electron. 1, 301 (1995).

[5] D. Ahn, S. J. Yoon, S. L. Chuang and C. S. Chang, J. Appl. Phys. 78, 2489 (1995).

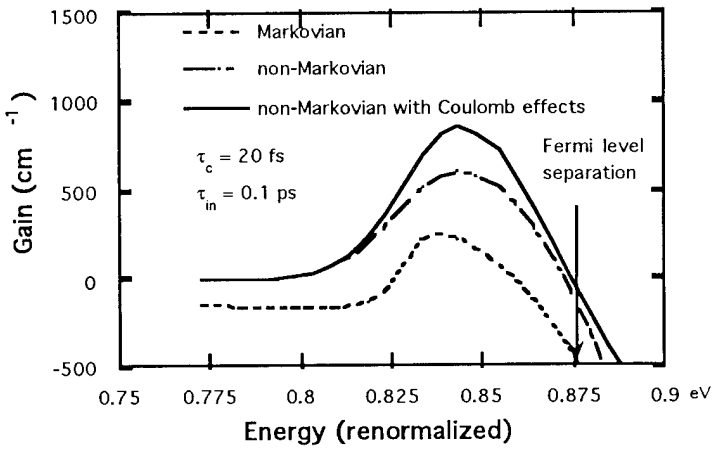


Fig.2 We plot the calculated optical gain spectra for the three cases of: (i) Markovian model with Lorentzian line shape function (dashed line), (ii) non-Markovian model (dotted line), and (iii) non-Markovian model with excitonic enhancement (solid line) for the correlation time τ_c = 20 fs.

Comparison of Quantum Well Designs for Near Infra-red (850nm) Semiconductor Lasers

T. E. Sale, Y.Ohiso, C. Amano & T. Kurokawa.
NTT Optoelectronics Laboratories.
3-1 Morinosato Wakamiya, Atsugi-Shi, Kanagawa-Ken, 243-01, JAPAN.
Tel: +81-462-40-3221. Fax: +81-462-40-3259. e-mail: sale@aecl.ntt.jp.

The near infra-red wavelengths of 800 to 850nm are important because of the diversity of compatible modulators and detectors which can be produced in both Si and GaAs based materials and the ease of integration with driving and amplification circuitry. GaAs and Si based circuits can allow very high speed operation and low noise figures of complex circuitry. Thus 850nm laser sources are important for developing highly parallel interconnections over short distances (several cms to several tens of metres).

In this paper we consider the optimum quantum well composition for operation in this band. Because of the interest in high density interconnections we consider mainly the case for vertical cavity surface emitting lasers (VCSELs). VCSELs are readily produced in high density two dimensional arrays. Their emission can efficiently be coupled into optical-fibres without the need for external optics. In contrast with conventional edge emitting lasers (EELs), VCSEL modes cannot efficiently interact with TM mode gain (E-field polarized perpendicular to quantum well).

We consider materials available in the quitnernary $(Al_xGa_{1-x})_yIn_{1-y}As_zP_{1-z}$ system (see fig. 1) which covers all of the conventional semiconductor compounds which can be used as emitters at this wavelength. We examine the quantum well designs described in table 1. All are grown pseudomorphically on {100} GaAs, the only suitable common substrate material.

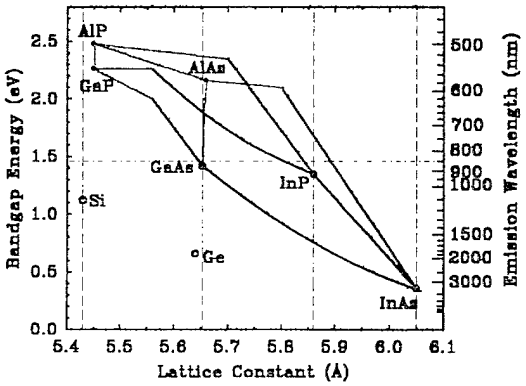


Fig. 1. Bandgap vs. lattice constant for common III-Vs.

The design of these wells is engineered to produce an e_1h_1 transition at 850nm (except for *2* & *7*). The ground states in each of the wells are calculated by solving the effective mass equation[1]:

$$\left[\tan\left(\frac{L\sqrt{2m_wE}}{2\eta}\right)\right]^{\pm 1} \mu\frac{m_w}{m_b}\sqrt{\frac{V-E}{E}} = 0$$

at both material interfaces. The material parameters are a 3D interpolation of the binary parameters listed in Landolt-Börnstein[2], using ternary and quaternary bowing parameters where known. The hole

Well / Barrier	Well (x,y,z)	Barrier (x,y,z)	λ (nm)	Width (Å)	ID
GaAs / AlGaAs	(0,1,1)	(0.3,1,1)	850	100	1
InGaAs / AlGaAs	(0,0.9,1)	(0.3,1,1)	850	49	2*
InAlGaAs / AlGaAs	(0.2,0.75,1)	(0.3,1,1)	850	85	3†
InGaAsP / InGaP	(0,0.47,0.41)	(0,0.515,0)	850	85	4†
GaAsP / InGaP	(0,1,0.85)	(0,0.515,0)	800	85	5‡
GaAs / InGaP	(0,1,1)	(0,0.515,0)	850	100	6
InGaAs / GaAs	(0,0.75,1)	(0,1,1)	1026	85	7†

Table1. Quantum well designs used in calculations. Compressive (ε=1.7%† & ε=0.6%) and tensile (ε= -0.64%‡) strained $(Al_xGa_{1-x})_yIn_{1-y}As_zP_{1-z}$ wells are indicated.*

masses are deduced from Lüttinger parameters. From fig. 1 we see that tensile material with the same bandgap as GaAs is not possible. Thus well *5* (GaAsP) emits at the shorter wavelength of 800nm.

The valence band structure is calculated using an infinite well approximation which effectively decouples the in-plane and out-of-plane effects and greatly simplifies the solution[3,1]. This method can be used to accurately determine the dispersion around the zone centre where this mixing is smallest. The approximation is poorer for high values of momentum and for narrow wells. At low carrier densities, where carriers largely fill states around the zone centre, the effect of this error is small. A four band model (hh_1 hh_2 hh_3 & lh_1) is used. The smallest spin-orbit splitting is 180meV and so is ignored.

Gain spectra are calculated using the density of sates functions deduced from the band structure. The transition matrix element is calculated from the Kane bulk value[4,5] with due consideration taken for the polarization effects in the quantum well[6]. Since the density of states in a real quantum well is not constant within a sub-band, the maximum gain g_{max} does not necessarily correspond to zero momentum.

Results and discussion

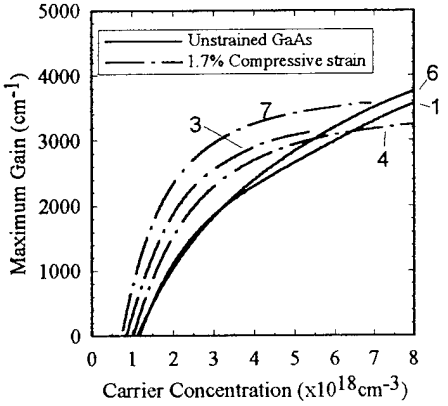


Fig. 2. TE Gain of unstrained and compressively strained QWs.

In fig. 2. we show g_{max} values calculated for the 1.7% compressive and unstrained well designs. As expected, the two GaAs based quantum wells have almost identical gain. In practice, the higher bandgap cladding of well *6* will result in lower carrier losses. By adding indium to the well the compressive strain increases the *lh-hh* splitting by around 100meV. This effect is well known[7]; the parasitic *lh* states are displaced to much higher energy and the reduced *lh* interaction with the *hh* result in a lower density of *hh* states. Thus in well *7* we see a reduced transparency density (n_o) and an

increased differential gain (g_d). To maintain the wavelength at 850nm Al is added to the well (in well *3*). A consequential increase in mass parameters means that some of the improvement is lost. Well *4* is a similar design in the Al-free InGaAsP / InP system. A further increase in the mass parameters means that a little more performance is lost. All three of these wells outperform the unstrained wells at gains typical for those in a VCSEL or EEL (500 to 1000cm^{-1}) in terms of both carrier density and differential gain (the latter affects the dynamic performance).

Recently, several authors have demonstrated GaInAsP QW based devices emitting at 780 [8] and 980nm [9]. The major attraction of this system being the ability to include strain in the active layer and to remove aluminium from the structure. Of particular interest to VCSELs is the possibility to create atomically ordered phosphide based materials by a suitable choice of growth conditions; this provides a strong anisotropy to the band structure along a particular axis of the quantum well[10] and enables the polarization to be fixed reliably over a large array of devices. Gain improvements due to changes in the distribution of valence states are also expected.

Aluminium containing compounds are typically heavily contaminated with oxygen or carbon impurities which limit their ability to be efficient emitters[11]. By use of high-purity reagents and low temperature MOCVD growth, high quality AlGaAs based wells may be grown with more than 30% Al in the well[12,13]. The high field density at the output facet of an EEL can cause rapid degradation of aluminium compounds resulting in poor ageing characteristics. Careful passivation of the laser facet can prevent this problem[14]. In a VCSEL such degradation is not a problem because of the thick DBR stacks and the low photon density at the emitting surface.

Unfortunately for the AlGaInAs well, an In precursor of suitable purity to avoid oxygen contamination has yet to be found[15]. Thus in the InGaAs / AlGaAs well (number *2*), we attempt to spatially separate the conflicting Al and In species. Even so, Al and In growth conditions are only compatible when low oxygen Al reagents are available[10,11,12]. Careful switching of the gas flows is necessary to prevent mixing of these two group III precursors. Thin interfacial GaAs layers may be required to achieve high quality wells. Since a large quantum confinement is required achieve 850nm emission, the carrier wave functions will penetrate deeply into the Al containing barriers. This type of well will be highly susceptible to broadening effects due to monolayer fluctuations and other interface defects which will reduce the available gain. Thus we limit the minimum well width to around 45Å, in which case the maximum strain available is 0.68%. Wavelengths shorter than 850nm are only possible with very narrow wells.

In fig. 3 we show the results for this type of well (number *2*). The *lh* level is electron like over a wide momentum range

producing a high density of states at low energies as well as a heavy *hh* band. Hence n_o is relatively large, but the large g_d will allow fast switching. The gain spectrum of this well is narrower (more triangular) than that of the other wells; broadening effects due to lifetime and well fluctuation effects will reduce g_d more severely.

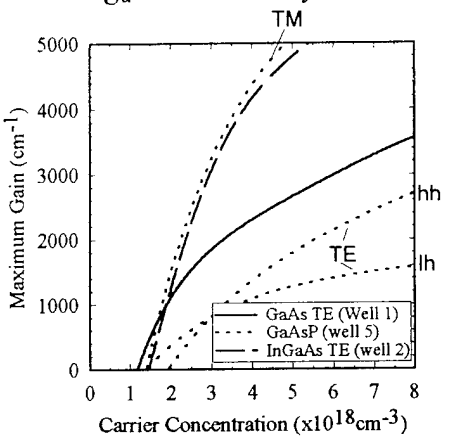


Fig. 3. Gain of GaAsP and InGaAs QWs.

Also in fig. 3 is the relation for the tensile strained well. Because of the low lying *lh* states, only in the TM mode is there significant gain. This type of well is only of use in edge-emitting lasers. Compared to other wells, g_d is improved by a factor $\sim 3/2$ because of the reduced degrees of freedom for the *lh*. Because of the limited degree of strain the *lh* & *hh* ground states are only separated by 7meV, thus n_o is higher than for an unstrained well. Only by operating at much shorter wavelengths can the full advantages of tensile strain be realized.

Conclusion

For operation at 850nm there are a number of options. Compressively strained wells provide the best solution, but current growth technology can provide higher quality Al-free materials which, numerically, provide less advantage over unstrained GaAs wells. Some of the growth problems involved with Al containing wells may be overcome with narrow InGaAs wells but higher thresholds may be expected. Tensile strained wells are only useful for wavelengths much shorter than 800nm and only in EELs.

At this meeting we will present results based on a finite well bandstructure model and include broadening effects on the gain of the narrow wells. We will also attempt to estimate carrier losses, based on parameters typical for current MBE and MOCVD grown material.

[1] *Optical gain in III-V bulk and quantum well semiconductors*, S.W.Corzine, R.H.Yan & L.A.Coldren, in *Quantum Well Lasers*, P.S.Zory Jr. Ed.,
[2] *Landolt-Börnstein*, **17a**, *Physics of group IV elements and III-V compounds*, E.O.Madelung Ed.
[3] E.P.O'Reilly, Semicond. Sci. Technol., **4**, pp121-137, 1989.
[4] E.O.Kane, Phys. Rev., **131**, pp79-78, 1963.
[5] A.R.Adams, Electron. Lett., **22**, pp249-250, 1986.
[6] P.Rees, PhD Thesis, University of Wales, 1993.
[7] E.Yablonovitch & E.O.Kane, J.Lightwave Technol., **6**, pp1292-1299, 1988.
[8] R.P.Schneider Jr. & M.Hagerott-Crawford, Electron. Lett., **31**, pp554-555, 1995.
[9] G.Zhang, J.Näppi, A.Ovtchinnikov & H.Asonen, Electron. Lett., **29**, pp429-430, 1993.
[10] A.T.Meney, E.P.O'Reilly & K.J.Ebeling, Electron. Lett., **31**, pp461-462, 1995.
[11] P.L.Tihanyi, F.C.Jain, M.J.Robinson, J.E.Dixon, J.E.Williams, K.Meehan, M.S.O'Neill, L.S.Heath & D.M.Beyea, Photon. Technol. Lett., **6**, pp775-777, 1994.
[12] J.S.Roberts, J.P.R.David, T.E.Sale & P.Tihanyi, J.Crystal Growth, **143**, pp135-140, 1993.
[13] T.E.Sale, J.P.R.David, J.S.Roberts, CLEO '95, OSA Technical Digests, **15**, 77-78, 1995.
[14] J.S.Major Jr., W.J.Gignac, B.Li, Z.Huan, V.Gulgazov, D.F.Welch, R.Craig & D.Scrifes, IEEE Catalog 95TH8014, p151.
[15] J.S.Roberts, C.C.Button & A.C.Chew, J.Crystal Growth, **135**, pp365-366, 1994.

Tuesday, April 30, 1996

Silicon Heterostructure Devices

ITuB 8:30 am-10:00 am
Fairfax B

Richard A. Soref, *Presider*
U.S.A.F. Rome Laboratory

SiGe/Si Heterostructures for Photonics

D.C. Houghton
Institute for Microstructural Sciences
National Research Council of Canada, Ottawa

An overview of SiGe/Si materials research and photonic device opportunities will be presented, highlighting some recent successes and the challenges ahead. Recent progress in Si-based architectures for potential optoelectronic device applications will be reviewed. Novel photonic devices will be discussed, illustrating the potential for SiGe integration with mainstream Si integrated circuits. Epitaxy at low temperatures (less than 600°C) permits the growth of highly strained $Si_{(1-x)}Ge_{(x)}$/Si multilayers. These exhibit unique optical and electrical properties characteristic of the alloy composition, the tetragonal distortion of the crystal lattice, and the periodicity in the growth direction. However, the built-in strain in SiGe/Si is both a blessing and a curse: band-structure tailoring is available but the penalties are a rigid critical-strain thickness limit and a modest thermal budget for processing. Bandgap shifting utilizing local ion implantation and rapid thermal annealing for wavelength-selective photodetectors in WDM applications and rare-earth doping of waveguides for possible on-chip emitter/amplifier applications at 1.3 and 1.55 microns will be presented. Photoluminescence from SiGe quantum wells has proved to be invaluable in determination of band gaps, band offsets, and integrity of strained SiGe/Si heterostructures. In addition, low-temperature SiGe/Si epitaxial growth by traditional molecular beam epitaxy (MBE) and the now commercially available UHV chemical vapor deposition (Leybold) will be compared.

CHARACTERIZATION OF GeSi/Si STRAIED LAYER SUPERLATTICE AVALANCHE PHOTODIODE

F.Y. HUANG, KEVIN ALT, and K.L. WANG

Device Research Laboratory, Electrical Engineering Department
University of California at Los Angeles
Los Angeles, CA 90095-1594
phone: (310) 206-7987, Fax: (310) 206-8495

We report the material and device characterization of SiGe/Si strained layer superlattice (SLS) avalanche photodiodes (APDs). The active absorption and multiplication region of the device consists of ten periods of $Si_{0.5}Ge_{0.5}$/Si SLS. The device exhibits an optical response at 1.3 μm and has a cutoff at 1.5 μm at normal incidence. The device shows a linear photoresponse as a function of the load resistance upto 0.1 MΩ. Avalanche breakdown as evidenced by the positive temperature dependence of the breakdown voltage has been demonstrated. The temperature coefficient of the breakdown voltage is measured to be 0.01 V/K. Multiplication factors in excess of 50 have been obtained. The measured excess noise factor is even lower than that of Si, due to the enhanced ionization ratio in this SLS-APD as compared to that in bulk Si.

Because of the high gain and low noise features provided by the APDs as optical receivers, APDs based on Si, GaAs, and InP have been extensively studied. In order to obtain sufficient optical absorption for applications in fiber optical communication and optical interconnects, narrow bandgap materials such as GeSi and InGaAs have been widely used as the absorption region. Besides the compatibility of the SiGe with the advanced Si based IC processing, Si APDs also offer additional advantage of low noise factor among the commonly known materials. However, it has been recognized that to achieve appreciable optical response at 1.3 and possibly 1.55 um wavelengths, SiGe/Si strained layer superlattice with high Ge content of more than 50% has to be used in the photodetectors based on Si substrate. The large lattice mismatch between the Ge and Si constitutes a major obstacle in the device design and material growth for detectors which require a large thickness of the absorption region. Previous work has been focused on a waveguide structure wherein the light is incident laterally onto the device to increase the absorption length. And initial results have been reported on the avalanche multiplication [1,2]. Here we will demonstrate the feasibility of 1.3 um wavelength detection using the SiGe/Si SLS at a normal incidence. Detailed studies of avalanche and gain properties, such as the temperature dependence of the breakdown voltage, the multiplication factor, and also the noise factor of the SLS photodiode will be reported.

The device structure is shown schematically in Fig. 1. The epitaxial layers were grown by a Perkin Elmer 425B molecular beam epitaxy (MBE) system. Details about the layer structure and materials growth were reported else where [3]. The feature important to our SLS-APD is the ten-period GeSi/Si SLS. The design of the SLS, which consists of 100-A SiGe with 50% Ge sandwiched between 400 A Si, is to achieve a large optical absorption at long wavelengths (which means a high Ge mole fraction), a large overall absorption thickness, and at the same time, to keep the layers coherently strained without the generation of misfit dislocations. The quality of the SLS has been characterized by low-temperature photoluminescence (PL) spectrum. The PL spectrum reveals no dislocation line at 4.2 K.

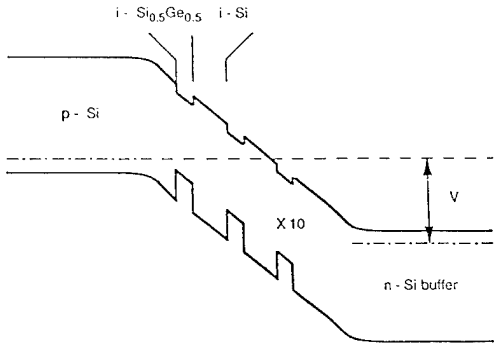


Fig. 1 Schematic structure of the strained layer superlattice SiGe/Si avalanche photodiode

Devices were fabricated using standard photolithographic techniques and plasma dry etching. Devices with SiO_2 for surface passivation were deposited by plasma enhanced chemical vapor deposition (PECVD). Both square and circular mesas with different mesa sizes were fabricated.

The photoresponse spectrum of the device is shown in Fig. 2. The device shows a response peak at about 0.8 um. Without reverse bias the response at 1.3 um diminishes. At a reverse bias of 5 V, the response extends to 1.3 um and has a cutoff at around 1.5 um. The bias induced response increase at a small bias is due to the carrier trapping of holes in the valence band.

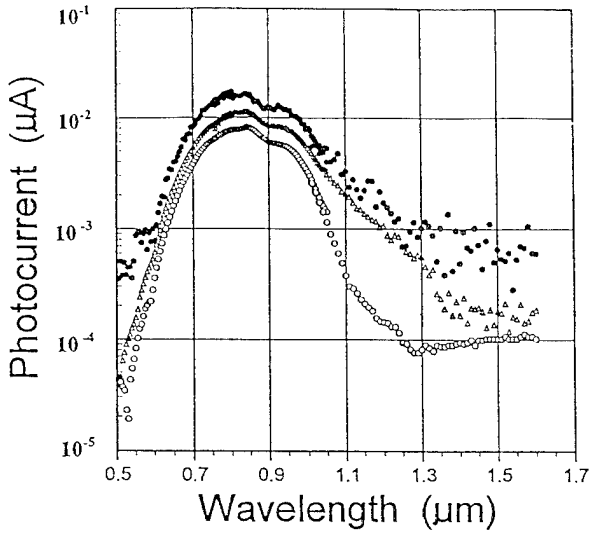


Fig. 2 Photoresponse of the device at 0, 5, and 8 V.

The photoresponse spectrum of the device is measured through the photovoltage across an external load resistor by a lock-in amplifier. Becasue of the finite resistance, especially in the case of a large leakage current in the SLS photodetectors, the linear response region of the load resistance should be determined. The photovoltage across the load resistor under different resistances are shown in Fig.3. It can be seen from Fig.3(a) that under a low load resistance the photocurrent increases as the applied bias increase. As the load resistance increases the photoresponse increases at a small bias and becomes saturated at a certain voltage. As the bias further increases, the photocurrent decrease. This implies that the load resistance is no longer substantially larger than the resistance of the photodetector. The linear regime of the load resistance upto about 0.1 MΩ is shown in Fig.3(b).

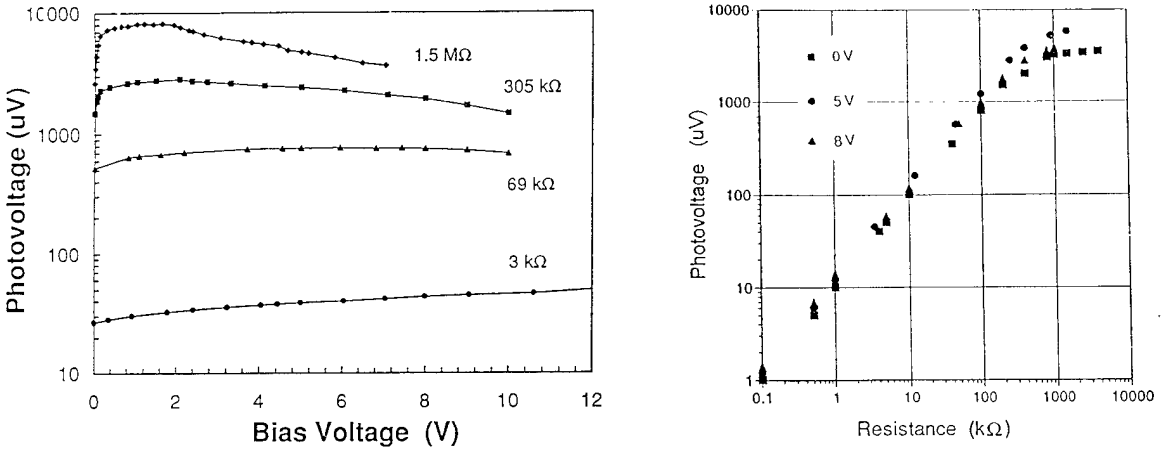


Fig. 3 (a) Photovoltage across a load resistor as a function of the external bias voltage.
(b) Photovoltage as a function of the load resistance under different bias. The photovoltage is a linear function of the resistance upto about 100 kΩ.

Electrical properties of the device were characterized by a HP-4142. The I-V curve shows a sharp breakdown at about 21 V at 295 K. As the temperature decreases the breakdown voltage decreases, which is the signature of avalanche breakdown due to a longer mean free path of carriers at lower temperatures. The temperature dependence of the breakdown voltage is shown in Fig. 4. The breakdown voltage is determined at that point where the current has over an order-of-magnitude increase and is limited only by the external resistance. The temperature coefficient of the breakdown voltage ($\Delta V_B/\Delta T$) is 0.011 V/K. For comparison, the corresponding coefficient in Si is 0.024 - 0.03 V/K [4].

The photocurrent response of the device under illumination of a mode-locked Ti-sapphire laser at 0.8 μm wavelength is shown in the inset of Fig. 5 for different illumination powers. Avalanche gain exceeding 50 was obtained before the onset of microplasmas. Initial result on the excess noise factors of the SLS-APDs was obtained by a HP 8592A spectrum analyzer set at 200

kHz center frequency with a 10 kHz bandwidth. Measurements have shown that at a gain of 30 the excess noise factor is smaller than 2.5, which is even lower than that of bulk Si. A possible explanation is due to the enhanced hole scattering in the valence band due to the heterobarriers.

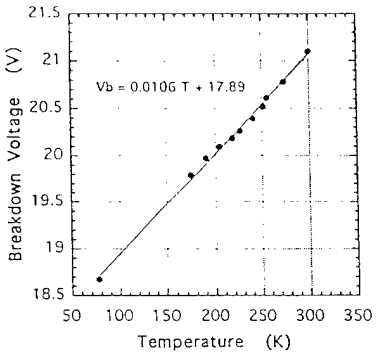


Fig. 4 Temperature dependence of breakdown voltage for the SLS-APDs. The positive temperature coefficient indicates the avalanche breakdown.

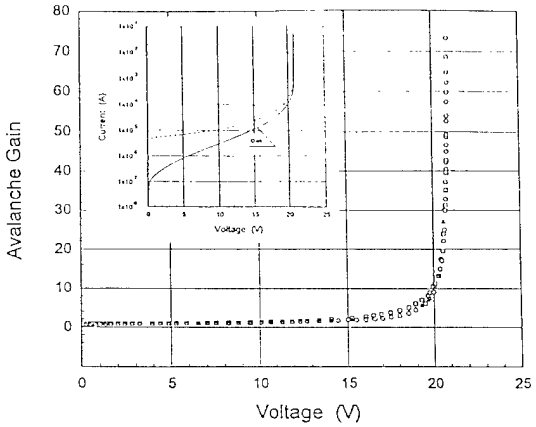


Fig. 5 Avalanche multipkication factor as a function of external voltage.

In conclusion, we have investigated the gain properties of GeSi/Si strain-layer superlattice avalanche photodiodes. A multiplication factor in excess of 50 has been demonstrated. The device also exhibits an extremely low excess noise factor due to the structure-induced enhancement of the electron-hole ionization ratio. With further reduction of dark current the superior features of low noise and high gain, along with response at 1.3 μm, will make these devices very attractive for applications as optical receivers in Si-based optoelectronic integrated circuits (OEICs).

REFERENCES

[1] J.C. Campbell, A.G. Dentai, W.S. Holden, and B.L. Kasper, *Electron Lett.*, vol. 19, pp. 818-820, 1983.
[2] B. Jalali, L. Naval, and A.F.J. Levi,*J. Lightwave Technology*, vol. 12, pp. 930-935, 1994.
[3] F.Y. Huang, X. Zhu, M.O. Tanner, and K.L. Wang, *Appl. Phys. Lett.*, vol. 67, pp. 566-568, 1995.
[4] A. Goetzberger, B. McDonald, R. Haitz, and R.M. Scarlet*J. Appl. Phys.*, vol. 34, pp.1591, 1963.

An amorphous silicon/silicon carbide thin-film thermo-optical interferometer at λ=1.5 μm with 3 MHz bandwidth capability.

G. Cocorullo
IRECE-CNR, Via Diocleziano 328, 80124 Naples, Italy,
and *DEIS-University of Calabria, 87036 Rende (CS), Italy*
ph.: +39 81 5707999, fax: +39 81 5705734

F. G. Della Corte, I. Rendina
IRECE -CNR, Via Diocleziano 328, 80124 Naples, Italy
ph.: +39 81 5707999, fax: +39 81 5705734

A. Rubino, E. Terzini
ENEA-CRP, P. O. Box 32, 80055 Portici, Naples, Italy
ph. +39 81 7723227, fax: +39 81 7766902

The optoelectronic properties of hydrogenated amorphous silicon (α-Si:H) has been always considered almost exclusively for the fabrication of wide-area low-cost photovoltaic panels. For this reason the optical characteristics of this material has been extensively studied mainly in the wavelength range from 300 to 750 nm. In recent times, however, interesting applications have been proposed in the optical communication area, especially for photon detection at the visible wavelength of 670 nm. The strong absorption coefficient of α-Si:H, close to 10^4 cm^{-1} at this wavelength, allows in fact the realization of thin photodetectors, then particularly suitable for the realization of on-chip point-to-point optical interconnections [1].

α-Si:H, however, shows interesting characteristics which make it attractive for lightwave communication purposes also at the near infrared wavelengths of 1.3 and 1.5 μm, i.e. those wavelengths for which fiber silica presents the lowest optical absorption. As a direct-gap material, for instance, α-Si:H, whose optical bandgap corresponds to λ=0.82 μm, shows a low absorption coefficient at those wavelengths, usually lower than 50 cm^{-1}. Moreover, advances made in the deposition technology by low temperature Plasma Enhanced Chemical Vapor Deposition (PECVD) allow today the growth of undoped layers of α-Si:H characterized by an extremely low density of gap states, and then by a low subband-gap optical absorption. The result is that thin films of this material can be easily grown today with an absorption coefficient even lower than 0.5 cm^{-1} at λ=1.5 μm [2].

Another interesting point to consider is the possibility, offered by the same technology, of realizing heterostructures in conjunction with α-SiC:H and α-SiGe:H, whose bandgaps can be tailored to cover the entire energy spectrum between 1.0 and 2.2 eV. Thanks to the low temperature required for the deposition (often below 200 °C), stacks of these materials can be virtually deposited on any substrate, including crystalline silicon (c-Si).

Finally, α-Si:H possesses a very high thermo-optical coefficient, a characteristic which, as will be shown hereafter, allows the realization of an effective amplitude modulation by means of an interferencial thermo-optical modulator.

In this paper we present an α-Si:H/α-SiC:H planar waveguiding structure, deposited on a c-Si substrate, which has served as the base for the realization of a waveguide and a light intensity modulator. The compatibility of such devices with standard microelectronic IC's is made possible by the low temperatures required for the deposition of the stack, paving the way to the integration of optics and electronics on the same silicon chip, a challenge that needs to be won to allow the diffusion at any level of low-cost optical interconnection systems.

A cross section of the realized planar waveguide is shown in Fig. 1. It consists of a 3 μm thick undoped α-Si:H core layer, between two undoped α-SiC:H cladding layers. The low refractive index of α-SiC and the good quality of the undoped α-Si:H confer strong confinement and small losses to the waveguide at λ=1.5 μm.. We demonstrate that this structure can constitute the base for the realization of new α-Si:H based active guided-wave components. Preliminary experimental results on thermo-optical induced modulation in such a structure are shown. 3-D thermal simulations are reported which indicate that, thanks to the high thermal conductivity of silicon and silicon-carbon, the maximum switching frequency of a modulator derived from this waveguide is beyond 3 MHz. Finally, a measure of the previously unavailable thermo-optic coefficient of α-Si:H at this wavelength is given.

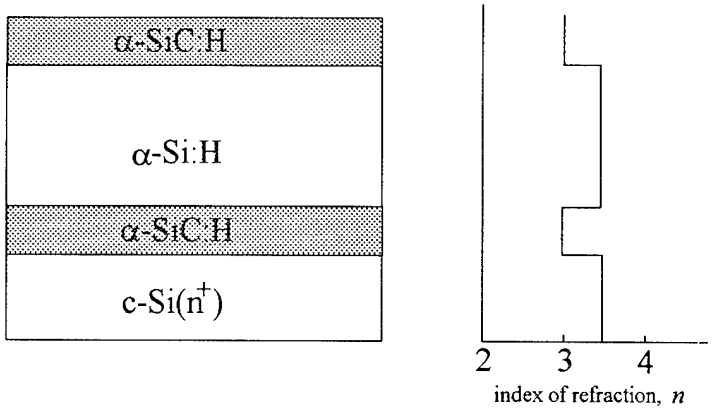


Fig. 1 Cross section of the thin-film structure realized. The profile of the refractive index allows a strong confinement of the radiation propagation into this waveguide.

For the deposition of the stack we used a three-chambers RF (13.56 MHz) PECVD reactor. The substrate was a 150-μm-thick Sb-doped c-Si wafer (ρ=0.025 Ω·cm). After loading, the 300-nm-thick intrinsic α-SiC was deposited in a 70% CH_4 and 30% SiH_4 atmosphere. The α-Si layer was deposited in a different chamber. Subsequently, 300 nm of intrinsic α-SiC were deposited in the same conditions as before. Temperature and pressure were 180°C and 700 mTorr respectively for all steps, while RF power ranged from 2 to 4 W. The deposition time was 5h 20min. At the end of the process the adhesion of the thin amorphous layer to the crystalline substrate was very good.

The values of the refractive index *n*, measured at λ=1.5 μm on separate sample films deposited in the same conditions, were 3.4 for undoped α-Si and 3.0 for undoped α-SiC.

Waveguides of various lengths were obtained by substrate cleaving. The radiation of a 1 mW, λ=1.5 μm, DFB laser diode, pigtailed to a 5-μm-core monomode fiber, was butt-coupled to each waveguide for testing. The transmitted light was collected at the output by a 50-μm-core multimode fiber and detected by an InGaAs photodiode. Preliminary measurements done on these samples allowed to determine that the propagation losses were ~2 dB/cm. This value was substantially confirmed by an estimate of the losses performed by means of a numerical waveguide design software, based on the effective index method. Assuming for the undoped α-Si:H an absorption coefficient $\alpha \approx 0.2\ cm^{-1}$ at λ=1.5 μm, found for

films deposited in equivalent conditions [2], these simulations allowed to predict an attenuation of ~1 dB/cm for the TE_0 mode.

Fabry-Perot-like characteristics were observed for the shortest waveguides ($l < 2$ mm) when they were heated and the transmitted intensity vs. temperature was plotted. One of these plots is reported in Fig. 2 for a 1700-μm-long waveguide. It shows a periodic amplitude modulation of the transmitted light, unambiguously due to the thermo-optic effect in a Fabry-Perot optical cavity. In this case the modulation depth is shown to be limited to less than 9%. Though modulation depths of up to 15% could be measured, this value seems to be still rather small. We believe that this result is to be attributed to the low *finesse* of our test cavities, whose mirrors did not receive any polishing treatment.

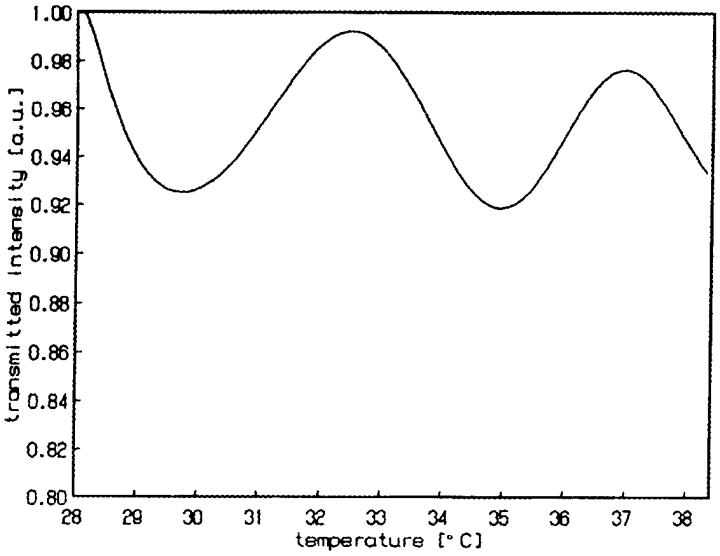


Fig. 2 Relative transmitted light intensity vs. device temperature. The wavelength is λ=1.5 μm and the device length is 1700 μm.

The plot in Fig. 2 has allowed the determination of the thermo-optical coefficient $(\partial n/\partial T)$ of the undoped α-Si:H. To our knowledge experimental data at the infrared communication wavelengths are not available to date.

The technique adopted here is the same described in [3]. With n=3.4, and a thermal expansion coefficient $(\partial l/\partial T)/l$ of $2.6 \cdot 10^{-6}$ K^{-1}, we could determine $\partial n/\partial T \approx 9 \cdot 10^{-5}$ K^{-1} at λ=1.5. It follows that α-Si shows a weaker thermo-optic effect with respect to its crystalline counterpart ($1.9 \cdot 10^{-4}$ K^{-1}) [3]. Nevertheless, this effect is stronger than in other usual thermo-optical materials, like $LiNbO_3$ and soda-lime-glasses.

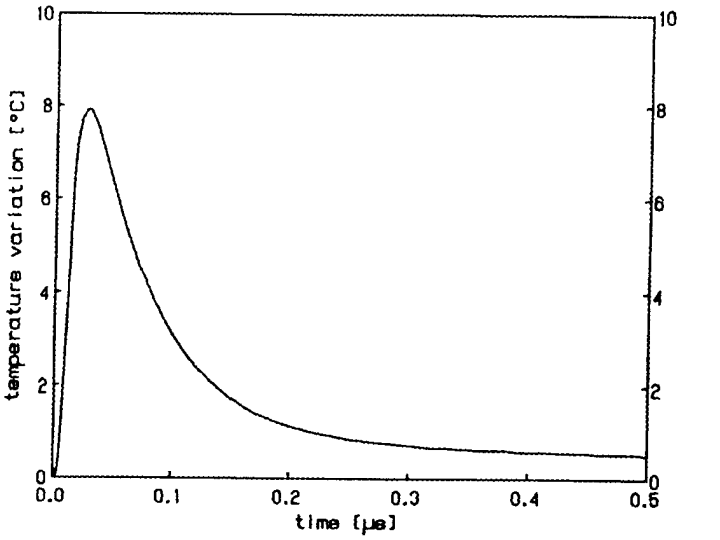


Fig. 3 Temperature transient inside a 500 μm long cavity subject to 15 ns heat pulse with an energy of 50 nJ. For λ=1.5μm, a temperature variation ΔT=8°C produces a complete detuning inside a cavity with this length.

Light intensity modulation via thermo-optic effect in a Fabry-Perot structure has been already successfully proposed in crystalline silicon by several researcher, at frequencies up to few tens of kilohertz [4], [5]. However, this group recently demonstrated, both theoretically and experimentally, that bandwidths in excess of 700 kHz can be obtained through the careful design of the device [6], thanks to the

high thermal conductivity k of silicon (k_{Si}=1.5 W/cm°C), even higher than that of many metals, which allows to maintain very low time constants for the thermal transients.

Starting from these considerations, a modulator based on the waveguiding structure proposed in this work is expected to allow even faster operations, thanks to the higher thermal conductivity of SiC (k_{SiC}=5 W/cm°C). In order to examine the effect of the thin α-SiC bottom layer on the transient thermal behavior of the stack, grown on a c-Si substrate, the numerical thermal analysis of a modulator obtainable by photolithographic definition out of the waveguide proposed here, was performed by means of the 3-D heat transfer simulator already tuned and tested in [7].

In Fig. 3 the calculated thermal response of a 500-μm-long device is shown. In this simulation a 15 ns current pulse is applied to a thin resistive film at the top of the waveguide. The film heating by Joule effect causes a temperature variation of the underlying waveguide core sufficient to produce a complete detuning of the 500-μm-long cavity. It is seen that driving pulses with repetition periods of ~300 ns can be applied, and therefore operation rates in excess of 3 MHz are possible.

In conclusion, PECVD deposited stacks of α-SiC:H/α-Si:H/α-SiC:H thin films have been demonstrated to posses good waveguiding characteristics and low attenuation (~2 dB/cm) at λ=1.5 μm, when they are optimized for low gap states concentration. Starting from these waveguides, interferometric thermo-optical light intensity modulation has been also achieved through Fabry-Perot cavities of various lengths. Numerical thermal simulations have allowed to determine that modulation rates in excess of 3 MHz are possible in these devices, thanks to the high thermal conductivity of both silicon and silicon carbide.

REFERENCES

[1] D. S. Shen, S. T. Kowel, C. A. Eldering, "Amorphous silicon thin-film photodetectors for optical interconnection", *Optical Engineering,* vol. 34, no. 3, pp. 881-886, 1995.

[2] A. Asano, M . Stutzman, "Depth profiling of nonuniform optical absorption in thin films: Application to hydrogenated amorphous silicon", *J. Appl. Phys.*, vol. 70, no. 9, pp. 5025-5034, 1991.

[3] G. Cocorullo, I. Rendina, "Thermo-optical modulation at 1.5 μm in silicon etalon", *El. Lett.*, vol. 28, no. 1, pp. 83-84, 1992.

[4] G. V. Treyz, "Silicon Mach-Zehnder waveguide interferometers operating at 1.3 μm", *El. Lett.*, vol. 27, no. 2, pp.118-120, 1991.

[5] U. Fisher, T. Zinke, B. Schuppert, K. Petermann, "Singlemode optical switches based on SOI waveguides with large cross-section", *El. Lett.*, vol. 30, no. 5, pp. 406-408, 1994.

[6] G. Cocorullo, M. Iodice, I. Rendina, P. M. Sarro, "Silicon thermooptical micromodulator with 700 kHz -3dB bandwidth" , *IEEE Photon. Technol. Lett.*, vol. 7, no. 4, pp. 363-365, 1995.

[7] G. Cocorullo, M. Iodice, I. Rendina, "All-silicon Fabry-Perot modulator based on thermo-optic effect", *Opt. Lett.*, vol. 19 no. 6, pp. 420-422, 1994.

Guided-wave Optical Circuits in Silicon-on-Insulator Technology

P. D. Trinh, S. Yegnanarayanan, and B. Jalali

Department of Electrical Engineering
University of California at Los Angeles
Los Angeles, California 90095-1594
Phone: (310)-206-4554
Fax: (310)-206-8495
Email: siva@ee.ucla.edu

Silicon-on-insulator (SOI) structures offer the unique ability to integrate long wavelength photonic devices into the CMOS integrated circuit (IC) process. The large index step between SiO_2 and Si ($\Delta n \sim 2.0$) permits the use of thin layers (< 1.0 μm cladding) in $SiO_2/Si/SiO_2$ waveguide structures, making them compatible with VLSI technology. This large index step does not prevent single-mode wave propagation and single mode waveguides with low loss have been demonstrated at $\lambda = 1.55$ μm [1]. Further, the use of Si-Ge heterostructures permits the realisation of Si-based optoelectronic detectors in the 1.2 to 1.6 μm wavelength range [2]. Therefore, development of optical and optoelectronic devices in SOI offers a path towards low-cost, monolithic optoelectronic circuits. We report here the fabrication of a number of guided wave optical circuits in SOI technology including 3 dB directional couplers with excess insertion loss of ~1.9dB at $\lambda = 1.55$ μm, an asymmetric Mach-Zehnder wavelength filter, and a 5 x 9 integrated optical star coupler with excess insertion loss of 1.3 dB and good uniformity. These optical circuits are used in cascaded Mach- Zehnder wavelength filters and phased-array waveguide grating filters for wavelength-division-multiplexed (WDM) networks .

The starting material is a bond and etchback silicon-on-insulator (BESOI) wafer with a SiO_2 thickness of 1μm and a Si thickness of 5μm. The rib waveguides were formed using a two step Reactive Ion Etching (RIE) process and single-mode behaviour was clearly observed. The propagation loss through straight SOI ribs was measured using the conventional cut-back technique and found to be 0.2 dB/cm at λ=1.3μm. Directional couplers with waveguide separation of 2.5 μm and coupling section lengths ranging from 150 to 400 μm were fabricated. Fig.1 shows a comparison between experiment and BPM simulation of the power transfer efficiency as a function of coupling length . These 3 dB couplers may be used as building blocks for asymmetric arm

Mach-Zehnder wavelength filters. A preliminary 1:2 wavelength filter at $\lambda = 1.55$ μm with a channel separation of 4.0 nm was realised. Fig. 2 shows a schematic of the Mach-Zehnder filter, in the inset, and the filter characteristics. The measured crosstalk is 18 dB. With improved 3dB couplers the crosstalk performance is expected to be enhanced. A 5 x 9 star coupler was also fabricated. The coupler consists of arrays of channel waveguides separated by a radiative slab region [3]. This geometry permits a large number of channels in a compact device. The 5 x 9 star coupler operates at $\lambda = 1.55$ μm and has an average excess insertion loss $\alpha \sim 1.3$ dB and an output power variance $\sigma \sim 1.4$ dB (The insertion loss reported here does not include the inevitable 1:9 power split loss of ~9.5 dB). Fig. 3 shows the measured near-field image (a) and line scan (b) for each of the 9 output waveguides of the star coupler with light coupled into the center input waveguide.

References

[1] Soref, R. A., Schmidtchen, J., and Petermann K. : "Large Single-mode rib waveguides in GeSi-Si and Si-on-SiO_2", IEEE Journal of Quantum Electronics, 1991, **27**, pp. 1971 - 1974

[2] Jalali, B., Naval, L., and Levi, A. F. J. : "Si - based receivers for optical data links", Journal of Lightwave Technology, 1994, **12**, pp. 930 - 935

[3] Dragone, C., Henry, C. H., Kaminow, I. P., and Kistler, R. C. : "Efficient multichannel integrated optic star coupler on silicon", IEEE Photonics Technology Letters, 1989, **1**, pp. 241 - 243

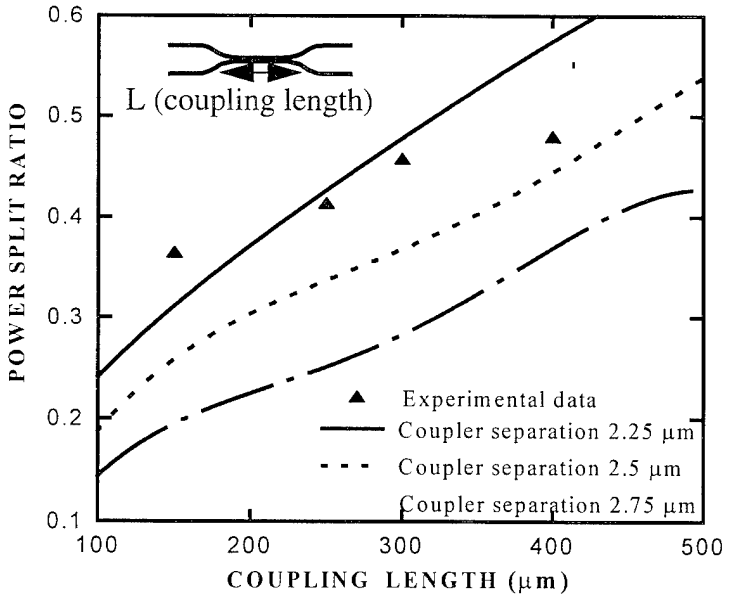


Fig. 1 Power split ratio versus coupling length for SOI directional coupler. Lines show results of BPM simulations.

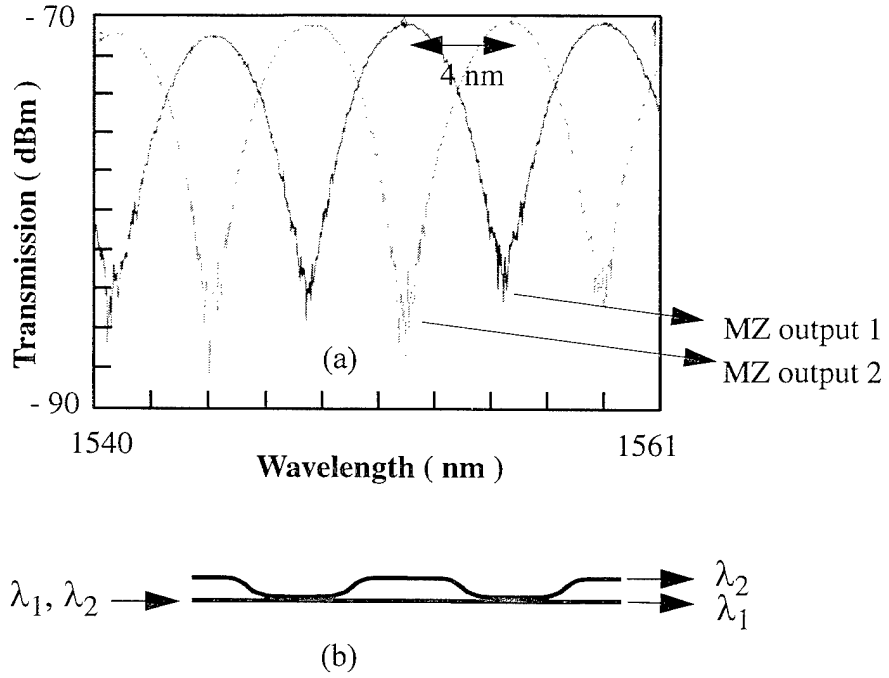


Fig. 2 (a) Mach-Zehnder 1:2 filter (λ=1.55 μm) with channel spacing of 4 nm (FSR = 8 nm).
(b) Schematic of asymmetric arm Mach-Zehnder wavelength filter.

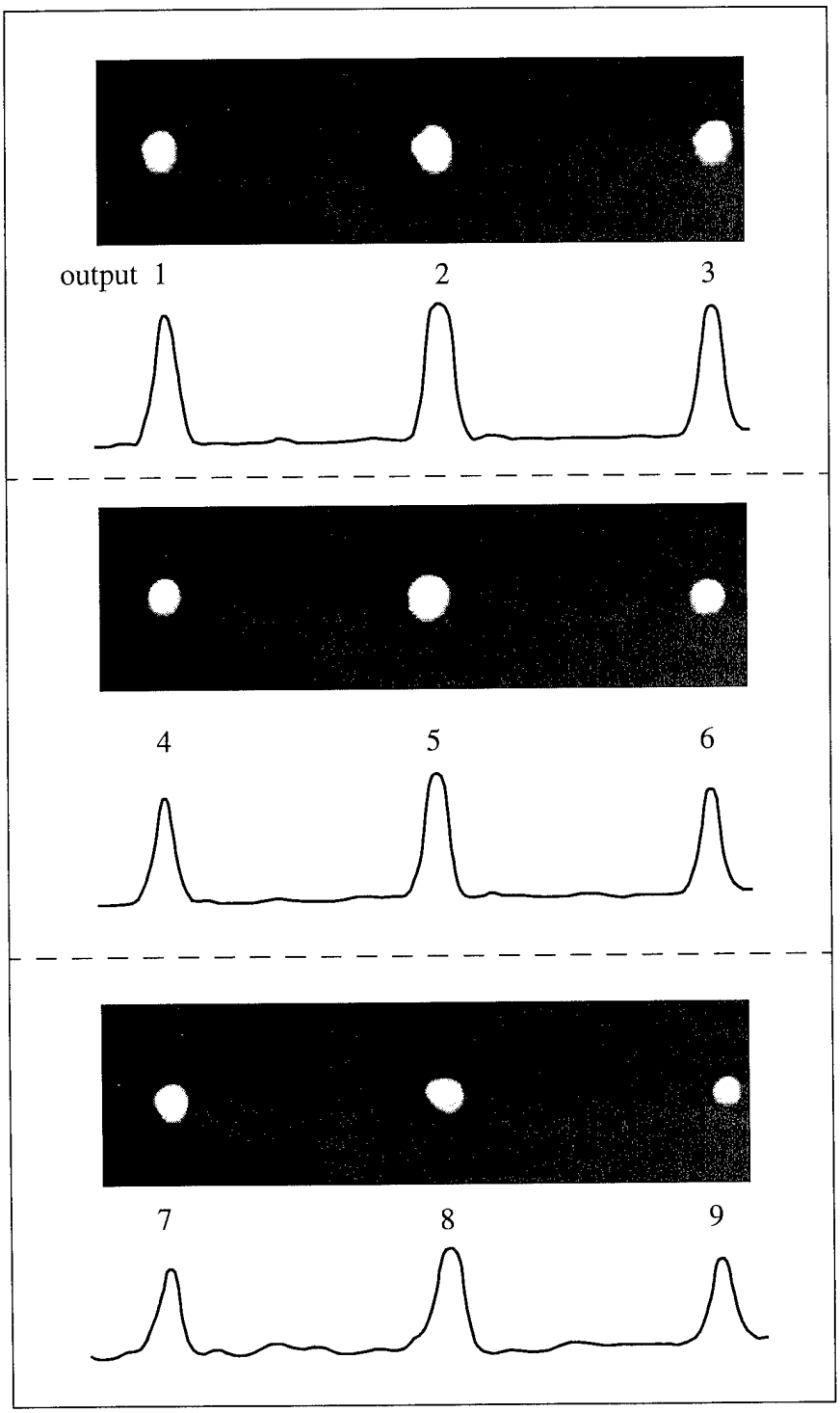


Fig. 3 Measured near-field image and line-trace of output waveguides of the 5 x 9 star coupler.(λ = 1.55 μm)

Absorption Enhancement in Silicon Waveguides Using Metal Island Films

Howard R. Stuart and Dennis G. Hall
The Institute of Optics
University of Rochester
Rochester, NY 14627

HRS: (716) 275-5561
DGH: (716) 275-2134
Fax: (716) 273-1072

Introduction

A fluorescent dye molecule placed within 1000Å of a metal surface is highly damped, due to the efficient energy transfer from the dye to the surface plasmon (SP) mode of the metal.[1] This process is a non-radiative coupling of the SP to the near-field of the oscillating dipole. Dipole-SP coupling has also been observed for the case of a metal island film adjacent to a metal surface (the metal particles in the island film act as dipole oscillators when excited by light).[2] The notion of dipole-SP coupling can be extended to dipole-waveguide coupling. This coupling is familiar to microwave antenna designers: when an antenna is mounted on a dielectric substrate, a significant portion of the radiation from the antenna can be trapped by the guided modes of the substrate.[3] In this paper, we will demonstrate that dipole-waveguide coupling can be used to enhance the absorption properties of silicon waveguide structures.

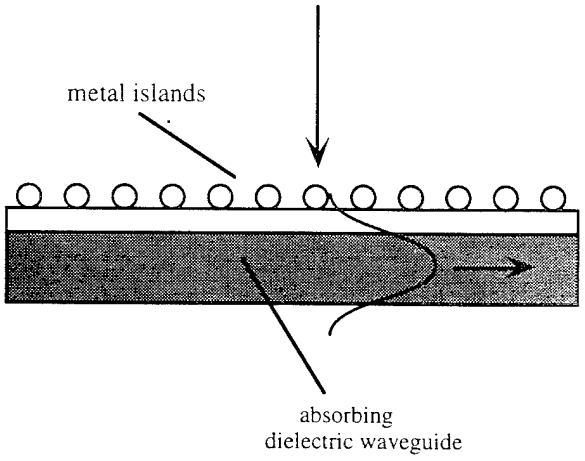


Figure 1. Metal island "antennas" can help to couple incident light into an adjacent waveguide structure.

The proposed idea is shown in Figure 1. A metal island film is mounted on an absorbing dielectric waveguide, with an intermediate spacer layer. Absorption in the waveguide is governed by the absorption coefficient of the material, and the path length of the incident light. In the absence of the island film, this path length is related to the thickness of the waveguide. The metal islands placed adjacent to the waveguide can act like antennas, collecting the incident radiation and then transferring the energy into the waveguide modes of the structure. Once the light is coupled into the waveguide modes it is "trapped", and this trapping can lead to longer path lengths inside the material, and therefore, enhanced absorption. The light-trapping abilities of this structure will be limited by two factors. The first is the ability of the islands to effectively transfer their energy into the waveguide. Dipole coupling into an all-dielectric waveguide structure has never been demonstrated experimentally in the optical regime. However, recent calculations have shown that the coupling probabilities can be as high as 90% for certain geometries similar to that in Figure 1.[4] The second factor is the ability of the waveguide to absorb the light before it is coupled back out of the structure by the island layer. The islands, which couple light efficiently *into* the structure, will, by reciprocity, also couple the waveguide modes *out* into radiated light. These two conflicting demands should lead to the existence of an optimal spacer thickness for maximizing absorption by the structure.

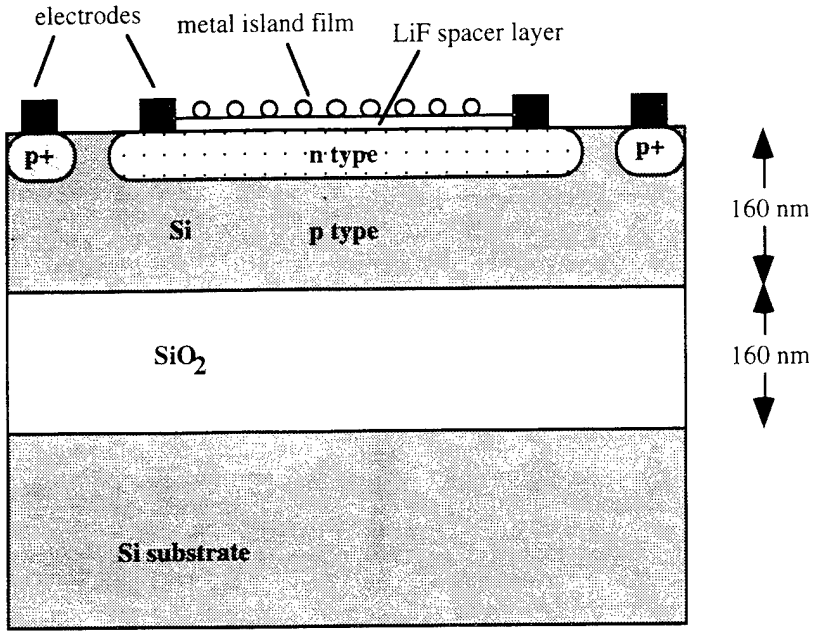


Figure 2. SOI solar cell design. The thin silicon layer acts as a waveguide, supporting 3 TE and 4 TM modes at 560 nm. Because of the SiO_2 layer, all contacts must be made at the top of the cell.

Experimental Results

In order to study the dipole-waveguide coupling process, and the possibility of absorption enhancements, a solar cell was fabricated in a silicon waveguide structure (Figure 2). A bonded silicon-on-insulator (SOI) wafer was used, with a silicon layer thickness of 160 nm. Takato *et al.* have reported fabrication of a solar cell on a 3 μm thick SOI wafer, with a design similar to that in Figure 6, using thermal diffusion.[5] For our cell, ion implantation was used in order to achieve an extremely shallow junction. An initial boron implantation ($5x10^{12}$ cm^{-2} at 25 keV) was used to create a high background doping within the entire waveguide. The shallow emitter was formed by a masked arsenic implantation ($1x10^{15}$ cm^{-2} at 10 keV), and the p+ contact regions were formed by a masked boron implantation ($5x10^{15}$ cm^{-2} at 25 keV). The implanted sample was annealed in a three step process (550°C for 60 minutes, 850°C for 15 minutes, 550°C for 60 minutes).[6] The electrodes were made by electron beam deposition of titanium (400Å) and silver (1 μm).[7] The cells exhibit high open circuit voltages, but very low short circuit currents; this behavior is expected for such a thin cell. The cells also exhibit extremely high series resistances, due to the lateral design of the junction (made necessary by the SOI structure), coupled with the thinness of the waveguide. While such resistances would be unacceptable in a commercial cell, they did not interfere with the goals of this study.

Vacuum deposition was used to create the LiF spacer layer as well as the metal island layer. The metal islands were created by evaporating a very thin coating (30 - 125 Å) of the given metal (either gold or silver) onto a portion of the cell, and annealing the sample under flowing nitrogen for 2 hours at 300°C. The annealing step is necessary to allow the thin metal layer to coalesce into islands. Transmission spectra of two typical island layers are shown in Figure 3 for reference. A tungsten-halogen lamp, put through a monochromator and chopped, was used to illuminate a small (1x1mm) region of the cell, and the voltage produced by the cell across a 50 ohm load was measured using a lock-in amplifier. The spectral response of the cells was measured both in regions with the island coating and in those without the island coating. The addition of the LiF layer alone had only a small effect on the cell response. The measured photocurrent for the two cases (with islands and without islands) was compared and used to

derive the enhancement factor. The results obtained for the enhancements are shown in Figure 4. The two curves are for gold (100Å island layer) and silver (125Å island layer), each with a 300Å LiF spacer layer. Enhancements as high as a factor of 5 are seen in the near infrared with smaller enhancements in the visible. Each curve has a cross-over point in the visible, below which the photocurrent is *reduced* by the presence of the island layer.

Discussion

The areas of greatest enhancement in Figure 4 do not correspond directly to the areas of largest absorption in the metal island spectra in Figure 3. There are a number of possible explanations for this. The presence of the silicon layer is likely perturbing the spectral behavior of the islands.[8] This applies especially to the silver island curve, which shows virtually no absorption at 800 nm in Figure 3, but a large enhancement value at that wavelength. Visual examination of the silver island-coated solar cells offers some evidence of this phenomenon (a dramatic difference in color is seen for these samples as compared to the islands on glass slides). The silicon layer also absorbs light much less efficiently in the infrared, so that the potential for enhancement in this region is much greater than in the visible. The modal structure of the SOI material is different for different wavelengths, and this may affect the efficiency of the coupling process. The refractive index of the island layer shifts dramatically as one moves from above to below the resonance point, and this may relate to the difference in behavior as one moves to shorter wavelengths.

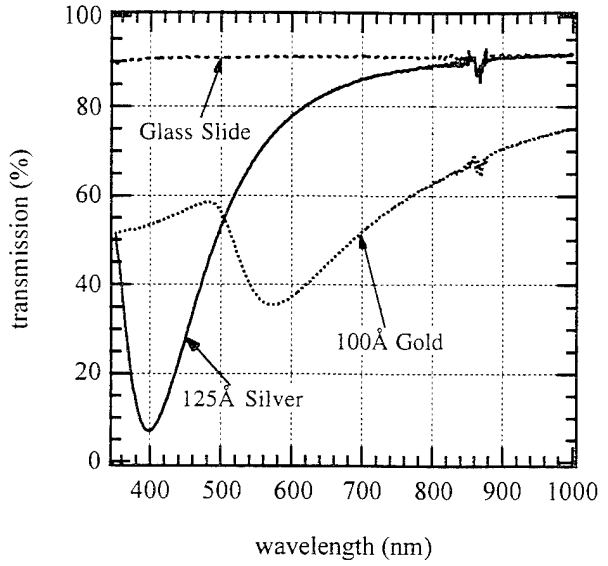


Figure 3 Transmission spectra of metal island films. The substrate in each case is a glass slide with a 300Å LiF layer. The transmission of a bare glass slide is shown for reference.

The key question raised by these results is whether the enhancements that we see are due to the coupling of the metal islands to the waveguide modes of the structure. An alternative explanation would be that the enhancements are due simply to random scattering introduced by the presence of the small island particles. However, this conjecture is not consistent with the results seen at longer wavelengths. Above 900 nm, the enhancement drops off sharply. In this region, the silicon layer is a very poor absorber, and could be well served by scattering enhancements. The sharp falloff *is* consistent with the decrease in island absorption at longer wavelengths, which supports the waveguide coupling hypothesis.

Another explanation is that the island layer is acting as a type of anti-reflection (AR) coating. A comparison with the normal reflectance spectrum of the plain SOI sample reveals that some of the peaks and dips in the enhancement curves correspond to peaks and dips in the SOI reflectance. These features are a result of interference in the multilayer structure, and the presence of the island layer will tend to perturb these features, reducing the reflectance at some points and increasing it at others. This effect can be measured, by taking reflectance measurements of the island-coated cells. Measurements have revealed that the *total* enhancement (shown in Figure 4) exceeds the purely AR enhancement at all wavelengths (supporting the waveguide coupling hypothesis). Some degree of the measured AR enhancement may also be due to coupling effects. Further modeling of this system will be necessary to unravel these effects.

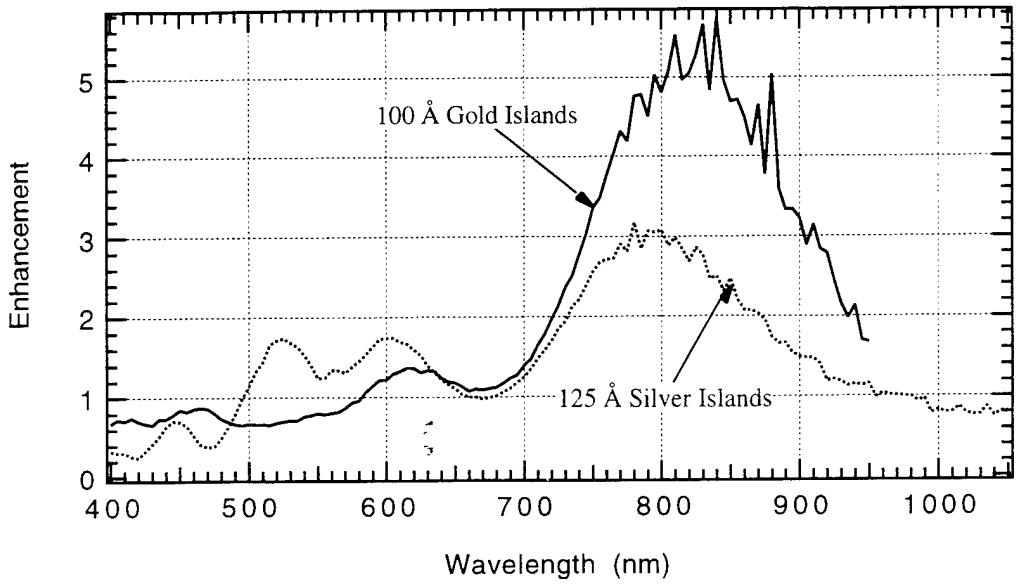


Figure 4 Measured enhancements due to the presence of the metal island layer. Enhancement is defined as the ratio of the photocurrent of the cell-LiF-island structure to that of the cell-LiF structure. The LiF thickness is 300Å for both curves.

Conclusions

This absorption enhancement mechanism has potential applications in any scheme that requires coupling optical energy into a very small dielectric region. Thin film solar cells are only one example. High speed photodetectors require very small device dimensions to achieve their fast response. The trade-off between sensitivity and response speed could be circumvented by using island coupling to enhance absorption. Another idea would be to use this technique in the optical pumping of waveguide lasers. The island layer would be chosen to absorb the pump wavelength, but to have no effect at the lasing wavelength. Thus, the coupling of the pump light into a waveguide structure could be enhanced, but the laser light would not be affected.

This research was supported by the Rochester Gas and Electric Corp. One of us (HRS) acknowledges the support of the Fannie and John Hertz Foundation.

References

1. R.R. Chance, A. Prock, and R. Silbey, in *Advances in Chemical Physics*, ed. I. Prigogine and S.A. Rice (Wiley, New York, 1978) Vol. 37, p. 1. W.H. Weber and C.F. Eagen, Opt. Lett. **4**, 236 (1979).
2. W.R. Holland and D.G. Hall, Phys. Rev. B **27**, 7765 (1983). S.L. McCarthy and J. Lambe, Appl. Phys. Lett. **30**, 427 (1977).
3. E.R. Brown, C.D. Parker, and E. Yablonovitch, J. Opt. Soc. Am. B **10**, 404 (1993).
4. K.G. Sullivan, private communication.
5. H. Takato *et al.*, Jpn. J. Appl. Phys. **33**, 1396 (1994).
6. A.R. Kirkpatrick, J.A. Minnucci, and A.C. Greenwald, *Proc. 14th IEEE Photovoltaic Specialists Conference*, p. 820 (1980).,
7. H.J. Hovel, in *Semiconductors and Semimetals, Volume 11, Solar Cells*, ed. R.K. Willardson and A.C. Beer, (Academic Press, New York, 1975) p. 207.
8. P. Royer, J.P. Goudonnet, R.J. Warmack, and T.L. Ferrell, Phys. Rev. B **35**, 3753 (1987).

Symposium on Simulation of Quantum Well Phenomena: Device Applications—Low Dimensional Nanostructures, Spontaneous Emission and Quantum Well Effects

ITuC 10:30 am-12:00 m
Fairfax A

Eoin P. O'Reilly, *Presider*
University of Surrey, U.K.

Low-Dimensional Nanostructures for Integrated Optoelectronics Applications

Eli Kapon
Institute of Micro and Optoelectronics
Department of Physics
Swiss Federal Institute of Technology
1015 Lausanne, Switzerland

Low-dimensional semiconductor quantum nanostructures, particularly quantum wires (QWRs) and quantum dots (QDs), have been predicted to exhibit many properties useful for applications in novel optoelectronic devices [1]. The potential advantage of these structured materials arises from the extremely small volume of their charge carrier confinement regions as well as the modification in their optical absorption and emission spectra owing to the multi-dimensional quantum confinement. The expected narrowing in the absorption and luminescence spectra, the increase in exciton binding energy, new possibilities for control of polarization anisotropy, the enhanced peak absorption and optical gain, and the reduced transparency current should be useful for improving the performance and reducing the power consumption of optical modulators, switches and lasers. The potential for power consumption reduction is especially attractive for the realization of densely-packed integrated optoelectronic circuits.

The main difficulty in this area, however, has been the extremely demanding requirements set on the dimensions and the uniformity of such low-dimensional structures. For typical III-V compound QWRs and QDs, achieving subband separations of at least several $kT_{room\text{-}temperature}$ and maintaining the sharp DOS profile requires lateral dimensions smaller than about 20 nm and size variations as small as one or two monatomic layers. This talk discusses the realization, the optical properties and the optoelectronic device applications of such GaAs/AlGaAs and InGaAs/GaAs QWR structures made using self-ordering during organometallic chemical vapor deposition (OMCVD) on nonplanar substrates.

Our fabrication approach is based on the *in situ* formation of lateral potential wells due to controlled lateral thickness variations of quantum wells (QWs) grown on nonplanar substrates [2]. The resulting lateral variation in confinement energy serves to confine both electrons and holes to the thicker parts of the wells. In contrast to lithography-based etching and regrowth techniques, the resulting lateral interfaces are defect-free and have a quality comparable to those of conventional QWs. To achieve the extremely narrow channels required for inducing lateral *quantum* confinement, the self-limiting surface profile of AlGaAs layers grown by OMCVD in [01$\bar{1}$]-oriented grooves etched on (100)-GaAs substrates is utilized [3]. The radius of curvature at the bottom of the groove can be controlled by selecting the growth conditions and the Al content, with values as low as 5 nm and uniformity of better than ±5%. GaAs QW layers grown in such sharp

grooves yield a crescent-shaped QWRs with size and shape determined solely by the growth conditions and independent of the details of lithography [4] (see Fig. 1). Low-pressure OMCVD is particularly effective in achieving faceted QWR interfaces, well defined within one to two monolayers [5] (see Fig. 2). Closely related to the self-ordering of these QWR structures is the self-ordering of "vertical" AlGaAs QWs (VQWs) at the intersection of certain crystal facets, due to facet-induced segregation of group III atoms. Similarly, strained-layer QWRs were also formed by growth of InGaAs/AlGaAs and InGaAs/GaAs heterostructures on nonplanar GaAs substrates. Cross-sectional and topographical atomic force microscope (AFM) studies of these structures will be presented.

The optical luminescence and absorption properties of these self-ordered QWs and QWRs were investigated using low-temperature, cw and time-resolved photoluminescence (PL), PL excitation (PLE) and cathodoluminescence techniques. Low-temperature PL linewidths as narrow as 6 meV, comparable to those of QWs of similar thickness grown side-by-side, have been measured. The PLE spectra exhibit distinct absorption peaks at the QWR one-dimensional (1D) subbands, with subband separation in agreement with model calculations of the electron-heavy hole transition energies in these structures [6]. Clear polarization anisotropy of the PLE spectra, for pump beams linearly polarized parallel and perpendicular to the wire axis, is a further evidence for 2D confinement in these wires. This anisotropy arises from the larger matrix element corresponding to electron-heavy hole transitions, compared to that for electron-light hole transitions, for light polarized along the wire axis (and *vice versa* for perpendicular polarization). The VQW structures also exhibit distinct PL lines which can be attributed to carrier recombination in their Ga-rich cores. Observation of the temperature dependence of the PL intensity as well as time-resolved PL spectra of these structures indicate efficient carrier transfer from the VQWs to adjacent QWRs, suggesting a means for increasing the efficiency of QWR carrier capture by using 2D barrier material [7].

Three types of device applications of these self-ordered quantum structures will be presented, namely, QWR lasers [8], VQW lasers [9], and infrared intersubband transition devices based on VQWs [10] and QWRs [11]. Prospects for extending this fabrication approach for achieving QD structures of controllable size and positions will also be discussed.

References:

1. see, e.g., E. Kapon, M. Walther, J. Christen, M. Grundmann, C. Caneau, D.M. Hwang, E. Colas, R. Bhat, G.H. Song and D. Bimberg, Superlattices and Microstructures **12**, 491 (1992), and references therein.
2. E. Kapon, M.C. Tamargo and D.M. Hwang, Appl. Phys. Lett. **50**, 347 (1987).
3. E. Kapon, G. Biasiol, D.M. Hwang, M. Walther and E. Colas, Solid State Electronics (in print).
4. E. Kapon, D.M. Hwang and R. Bhat, Phys. Rev. Lett. **63**, 430 (1989).

5. A. Gustafsson, F. Reinhardt, G. Biasiol and E. Kapon, Appl. Phys. Lett. **67**, 18 December (1995).
6. D. Oberli, F. Vouilloz, M.-A. Dupertuis, C.J. Fall and E. Kapon, Nuovo Cimento D (in print).
7. M. Walther, E. Kapon, J. Christen, D.M. Hwang and R. Bhat, Appl. Phys. Lett. 60, 521 (1992); J. Christen, E. Kapon, E. Colas, D.M. Hwang, L. Schiavone, M. Grundmann and D. Bimberg, Surf. Sci. **267**, 257 (1992).
8. E. Kapon, OPTOELECTRONICS- Devices and Technologies **8**, 429 (1993).
9. E. Kapon, B. Dwir, H. Pier, A. Gustafsson and J.M. Bonnard, Quantum Electronics Laser Sciences Conference (QELS '95), Baltimore, Maryland, May 1995.
10. V. Berger, G. Vermeire, P. Demeester and C. Weisbuch, Appl. Phys. Lett. **66**, 218 (1995).
11. A. Sa'ar, A. Givant, S. Calderon, O. Ben-Shalom, E. Kapon, A. Gustafsson, D. Oberli and C. Caneau, Superlattices and Microstructures (in print).

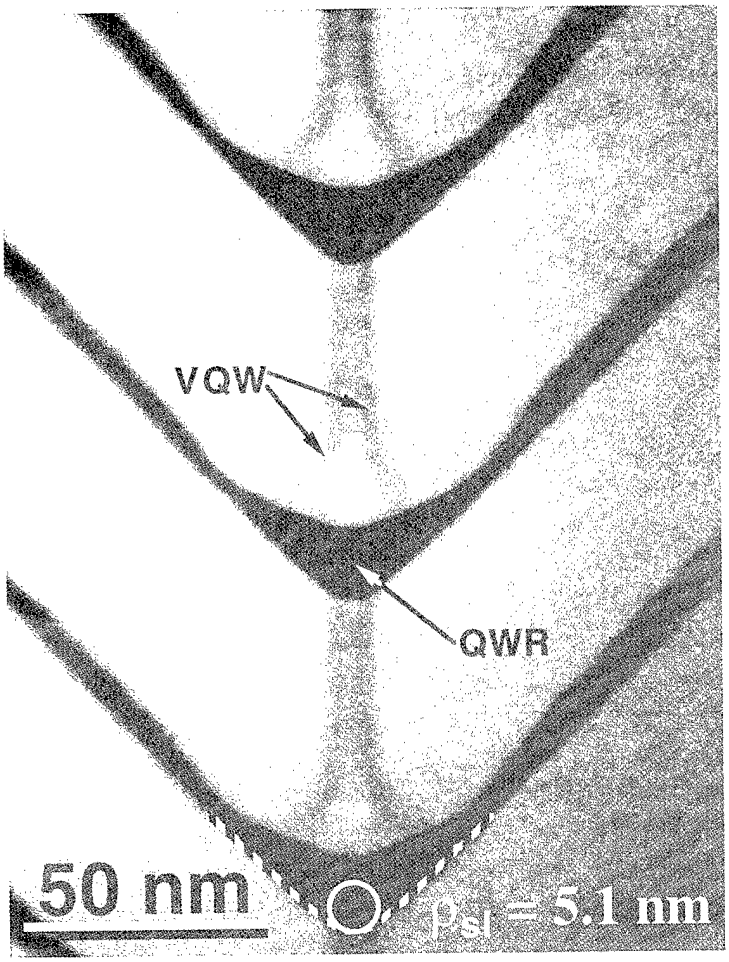
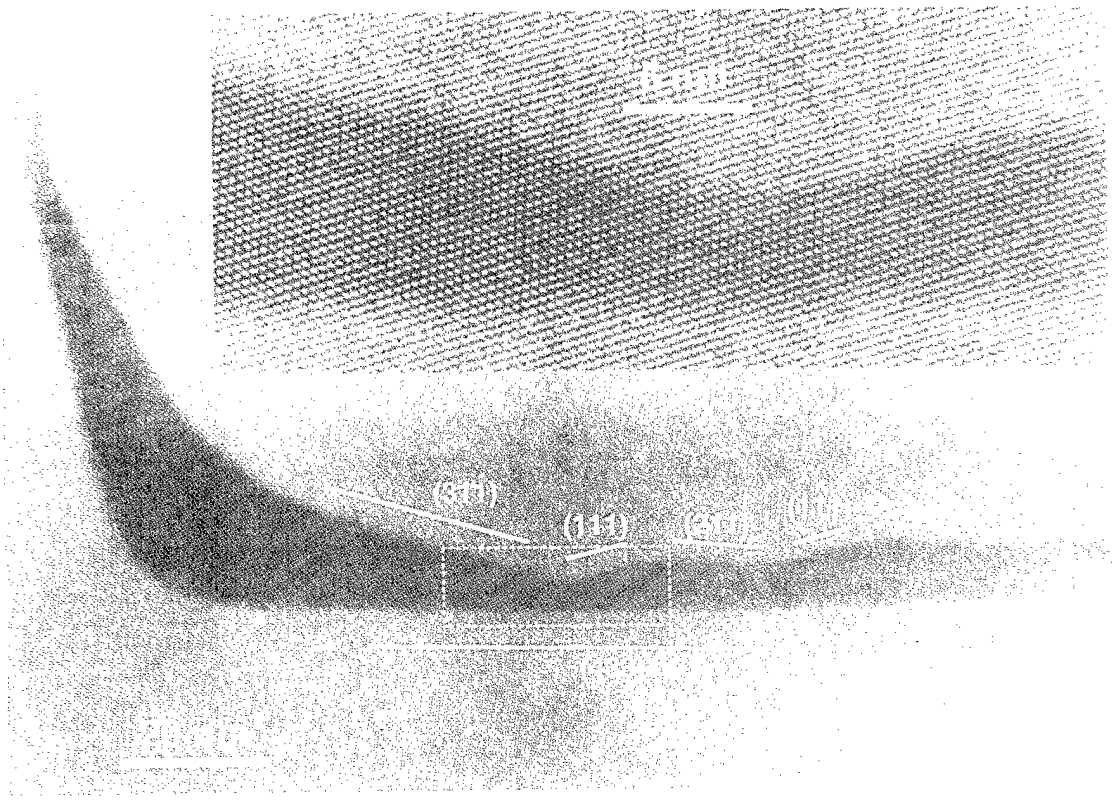


Figure 1 (left). Dark field TEM image of vertically-stacked GaAs/$Al_{0.42}Ga_{0.58}As$ QWRs grown at 20 mbar and 650°C. The hyperbolic fit to the lower interface of the QWR is also shown.

Figure 2 (below). High resolution TEM image of a GaAs/$Al_{0.42}Ga_{0.58}As$ QWR as well as the side QW of a structure grown at 20 mbar and 765°C. The crystal planes of the facets are indicated. The inset shows a high magnification view of the QWR-to-QW necking. The inset also demonstrates the interface quality.



Features of Spontaneous Emission in Large Diameter VCSELs

A.Onischenko & J.Sarma
School of Electronic and Electrical Engineering, University of Bath
Bath - BA2 7AY, England, U.K.
Phone: (44)(1225) 826863; Fax: (44)(1225) 826305

1 Introduction

VCSELs have shown great promise as optical sources for a variety of important optoelectronic applications and therefore continue to be under continuous development. There is also very considerable scientific interest in VCSELs which explains the continuing intensive research investigations. This interest is motivated, in particular, by the intriguing physics associated with the significant modification of emission characteristics that can be achieved with 3-dimensional micro-cavity structures. However, for a variety of reasons some of even the recently fabricated VCSELs tend to have large diameters ($D = 10-100\mu m$) but which are still very short along the longitudinal direction [1, 2]. Recent experimental results [3] and preliminary theoretical analysis [4] suggest that, unlike for traditional, small diameter ($D < 10\mu m$) VCSELs, the larger diameter devices have in-plane propagation of emitted light which may significantly affect device operational characteristics.

A proper understanding of the phenomenon requires an accurate calculation of the enhancement of spontaneous emission (SE) in large diameter VCSELs. Because of the quite complex geometries of cavities of the actual, fabricated devices, different researchers have applied pertinently different approximations for calculating SE. For example, a model that is suitable for air-post (index guide) VCSELs having small diameter ($D < 10\mu m$) is presented in references [5, 6]. For large diameter VCSELs the physical radial boundary may, in the present context, be reasonably assumed to be absent. Hence a planar multi-layer structure (PMLS) is usually used as a suitable model for the large diameter VCSELs [7] - [10]. However, there appears to be no published analysis which takes in to account the proper mode spectrum of the PMLS that includes both discrete and the continuum modes [11, 12] - hence an accurate estimate of the in-plane (IP) and in-face (IF) emission is not available. Further, various researchers have used the two-level atom dipole moment for SE calculations which is not really suited to the band-band optical transitions in a semiconductor [13]. The present paper incorporates both the transition characteristics for the QW active layer and the appropriate mode spectrum. Results of calculations of IP and IF SE for both λ- and $\lambda/2$-cavities are presented.

School of Electronic & Electrical Engineering, University of Bath, Bath, BA2 7AY, England, UK.

2 Theoretical model

The most consistent consideration of SE can be provided by the well known quantum mechanics approach developed (for a two level atom in free space) in [14].

In accordance with quantum mechanics

postulates the system *electron-hole pair - field* can be in two states:

- $|i\rangle = |0, \psi_c(\mathbf{p})\rangle$ - the electron is in the conduction band and field oscillators are in a ground state.
- $\langle f| = \langle 1_{\mathbf{k}}, \psi_v(\mathbf{p})|$ - the electron is in the valence band and a photon having a wavevector $\mathbf{k}$ and a frequency $\omega = c|\mathbf{k}|$ is emitted,

where $\psi_{c,v}(\mathbf{p})$ are wavefunction of an electron and hole respectively and $\mathbf{p}$ is the momentum vector. Transition rate between the initial $|i\rangle$ and final $\langle f|$ states is given by Fermi's Golden Rule:

$$W_{\mathbf{k},\mathbf{p}} = \frac{2\pi}{\hbar} \| \langle f | \widehat{V}_{int} | i \rangle \|^2 \, \delta\left(E_c(\mathbf{p}) - E_v(\mathbf{p}) - h\omega_{\mathbf{k}}\right), \quad (1)$$

where δ is the Dirac delta function, $E_c(\mathbf{p})$ and $E_v(\mathbf{p})$ are the energies of an electron in the conduction and valence bands respectively, $\widehat{V}_{int} = -\frac{q}{m}(\mathbf{A_k} \bullet \hat{\mathbf{P}})$, q and m are the electron charge and mass, respectively. $\mathbf{A_k}$ is the vector potential and $\hat{\mathbf{P}}$ is the momentum operator.

The refractive index profile of the PMLS for a $\lambda/2$-cavity is shown in Fig.1:

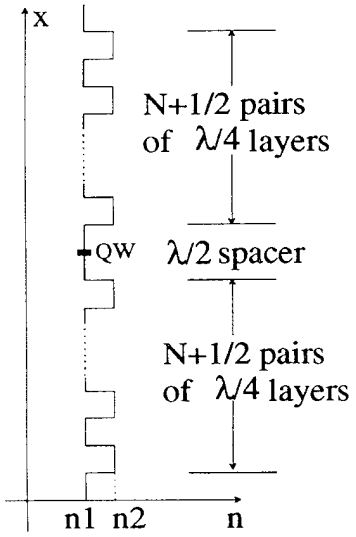


Fig.1

Note that the QW (active region) is positioned at the center of the spacer and this is the configuration that is used for the calculations. In the case of a λ-cavity the spacer has refractive index n_2 and the Bragg reflectors have N pairs of the $\lambda/4$-layers.

The vector potential $\mathbf{A_k}$ for the optical (electromagnetic) field is taken to correspond to $(TE)_x$ polarisation and has the form:

$$\mathbf{A_k} = \mathbf{e}_E a_{\mathbf{k}}^{\dagger} A_0 F_{\mathbf{k}}(x) e^{i\beta \bullet \mathbf{r}} + c.c., \quad (2)$$

where A_0 is the normalisation constant and $\mathbf{e}_E$ is a unity vector in the plane of the layers. The usual application of the Lorentz gauge establishes that the electric field vector is thus also along the direction of the vector potential; $a_{\mathbf{k}}^{\dagger}$ is a creation operator for the optical mode $\mathbf{k}$; the propapagation vector is $\beta = (0, k_y, k_z)$; $\mathbf{r} = (0, y, z)$ and c.c. implies complex conjugate. $F_{\mathbf{k}}(x)$ is a solution to the one dimensional wave equation in x for the multi-layer structure if a plane wave-like field distribution along any one chosen linear direction in the y-z plane is used in eqn. (2). The boundary conditions for $F_{\mathbf{k}}(x)$ are that $|F| \to 0$ as $|x| \to \infty$ (for discrete/bound modes) and F is finite as $|x| \to \infty$ (for continuum/radiation) modes (and correspondingly for the field derivative).

We will assume that electrons and holes in the QW are in an equilibrium determined by the quasi-Fermi levels E_{fc} and E_{fv}, respectively. Probability of SE can be found as

$$W = \frac{1}{N} \sum_{\mathbf{k},\mathbf{p}} W_{\mathbf{k},\mathbf{p}} f_c (1 - f_v) = W_0(\eta_w + \eta_r) \quad (3)$$

where N is the concentration of the electron-hole pairs, $f_{c,v}$ are Fermi-Dirac occupation probability functions for conduction and valence bands, W_0 is the probability of the SE from the QW in an infinite media, η_w and η_r give a relative part of the SE into the bound and radiation modes, respectively.

The radiation modes form a continuum set of $0 \leq \beta \leq n_1 k_0$ and the summation in equation (3) gives:

$$\eta_r = \int_0^{\infty} \int_0^{\pi} \sin\theta \, |a_\theta(\omega)|^2 g(\omega) \, d\theta d\omega, \quad (4)$$

where $|a(\omega)|^2$ represents the enhancement in the SE for a single mode, $g(\omega)$ is oscillator strength and $\sin\theta = \beta/(k_0 n_1)$. Features of the SE angular distribution for a $\lambda/2$-cavity and $N = 14$ are as shown, Fig.2.

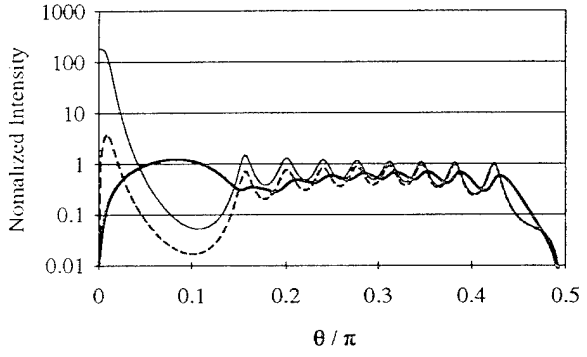


Fig.2

In Fig.2 the thin line represents $|a_\theta(\omega)|^2$ versus θ with $\omega = \omega_{BR}$; ω_{BR} is the Bragg frequency for plane waves propagating purely along x (i.e., $\beta = 0$). Hence θ as defined above may be viewed as a wave propagating in the region $|x| \to \infty$ at an angle θ with respect to the x-axis; the dashed line represents $\sin\theta |a_\theta(\omega)|^2$; and the thick line represents the integrand in eqn. (4) integrated over all ω which then gives the angular distribution for the total SE. Note that the case represented by the thin line has a maximum SE enhancement at $\theta = 0$ while the maximum for the dashed line case is at a small but finite value of θ. However, the most interesting result is presented by the thick line in Fig.2 which indicates that if the total SE is considered then the angular distribution of SE is extremely small for $\theta = 0$, in spite of the fact that the thin line shows a maximum at $\theta = 0$.

The bound mode propagate in the plane of the layers ($\theta = \pi/2$) and form a discrete set of $n_1 k_0 \leq \beta_n \leq n_2 k_0$. In this case the equation (3) gives:

$$\eta_w = 2\pi \int_0^{\infty} \sum_n |a_n(\omega)|^2 g(\omega) \, d\omega, \quad (5)$$

where n is a (discrete) mode number.

η_w and η_r as a function of the number of Bragg reflector pairs, N, for $\lambda/2$- and λ-cavities are plotted in Fig.3:

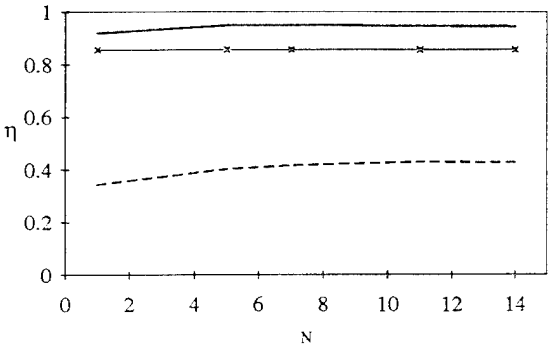


Fig.3a λ - cavity

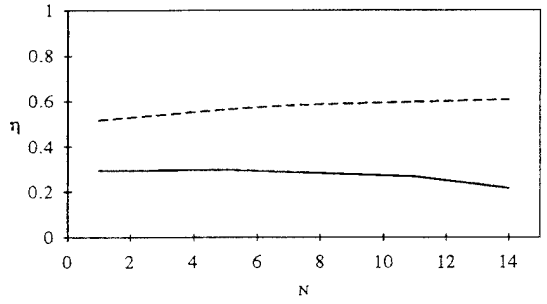


Fig.3b λ/2 - cavity

For both $\lambda/2$- and λ- cavities most of the bound mode solutions have $F_k(x)$ which have the predominant peaks outside the spacer region. However, interestingly, only for the λ-cavity is there a particular bound mode solution which has a single peak and this is in the spacer. With reference to Fig.3a, the above explains the existence of large SE in to this bound mode in particular (crosses) and hence the large value of SE in the totality of bound modes for the λ-cavity (solid line). The broken line gives the SE in to the radiation modes. Note from Fig.3b that even for the the $\lambda/2$-cavity, SE in to the radiation modes (broken line) is comparable to that in the bound modes (solid line) and hence cannot

be neglected, contrary to normal assumption.

3 Conclusion

The SE in a PMLS, as a model of the large diameter VCSELs, has been analysed for both $\lambda/2$- and λ-cavities taking into account proper mode spectrum of the structure and the optical spectrum of a QW. The SE in to bound modes is comparable with the SE in to radiation modes.

Density of radiation modes ($\sim \sin\theta$) and the relatively broad optical spectrum of the QW results in the high level of SE in the radiation modes having a finite propagation in the plane of the layers. Due to specifically large aspect ratio of the active region of the large diameter VCSELs, these radiation and bound modes can have an amplification that is comparable with that of the "$\beta = 0$" radiation modes. This results in additional losses of the pumped energy, thus increasing threshold current and decreasing device efficiency.

4 Acknowledgement

A.Onischenko is supported by a EPSRC (UK) Research Grant No.GR/J50149.

References

[1] R. S. Geels, B. J. Thibeault, S. W. Corzine, J. W. Scott and L. A. Coldren, *IEEE J. Quantum Electron.*, vol. QE-29, pp.2977-2987, Dec. 1993.

[2] T. E. Sale, J. Woodhead, R. Gray and P. N. Robson, *IEEE Photon. Technol. Letters*, vol. 4, pp.1192-1194, Nov. 1992.

[3] T. Zhang, J. G. Wohlbier, Kent D. Choquette and N. Tabatabae, *IEEE J. of Select. Topics in Quant. Electronics*, v.1, No.2, pp.606-614, June 1995.

[4] A. I. Onischenko and J. Sarma, *IEE Proceedings, pt.J, Optoelectronics*, accepted for publication.

[5] T. Baba, T. Hamano, F. Koyama and K. Iga, *IEEE J. Quantum Electron.*, vol. QE-27, pp.1347-1358, June 1991.

[6] T. Baba, T. Hamano, F. Koyama and K. Iga, *IEEE J. Quantum Electron.*, vol. QE-28, pp.1310-1319, May 1992.

[7] S. D. Brorson, H. Yokoyama and E. P. Ippen, *IEEE J. Quantum Electron.*, vol. QE-26, pp.1492-1499, Sept. 1990.

[8] C. C. Lin, D. G. Deppe and C. Lei, *IEEE J. Quantum Electron.*, vol. QE-30, pp.2304-2313, Oct. 1994.

[9] G. Bjork, *IEEE J. Quantum Electron.*, vol. QE-30, pp.2314-2318, Oct. 1994.

[10] Y. Yamamoto, S. Machida, G. Bjork, *Opt. Quantum Electrocs.*, vol. 24, pp.S215-S243, 1992.

[11] D. Marcuse, *Light transmission optics*, Van Nostrand Reinhold Company: New York-Cincinnati-Toronto-London-Melbourne, 1982.

[12] R. E. Collin, *Field Theory of Guided Waves*, 2nd Ed., New York: IEEE Press, 1991, pp.716-718.

[13] F. Bassani and G. Pastori Parravicini, *Electronic states and optical transitions in solids*. Pergamon Press: Oxford - New York - Toronto - Sydney - Braunschweig, 1975.

[14] W. Heitler, *The quantum theory of radiation*. Oxford University Press: Oxford, 1973.

Spontaneous emission in optical microcavities

H. Rigneault, S.Robert, S.Monneret

Ecole Nationale Supérieure de Physique de Marseille
Laboratoire d'Optique des Surfaces et des Couches Minces. Domaine Universitaire de Saint Jérôme - URA CNRS n° 1120 - 13397 - Marseille cedex 20 - France
phone: (33)91 28 83 28 -fax: (33)91 28 80 67 -E.mail: herve.rigneault@enspm.u-3mrs.fr

1 - Introduction

Optical microcavities are resonators that have at least one dimension on the order of a single optical wavelength. These structures enable one to control the optical emission properties of materials placed inside them. They can for example, modify the spatial distribution of radiation power, change the spectral width of the emitted light, and enhance or suppress the spontaneous emission rate [1]. In addition to being attractive for studying the fundamental physics of the interaction between luminescent atoms and vacuum field, optical microcavities hold technological promise for constructing novel kinds of light emitting devices.
This paper is divided into two parts. In part 2, we present a classical description of the spontaneous emission of luminescent atoms located inside a planar microcavity. An other electromagnetic formulation derived from scattering theory will be presented at the conference and can be found elsewhere [2].
In part 3 we give some radiation patterns of rare earth atoms (erbium) implanted in a multi-dielectric microcavity [3], and we investigate the power emitted into the guided modes of the structure.

2 - Modal analysis of spontaneous emission in planar multilayer structures

Consider the stack of dielectric films schematically drawn in **figure 1**. The surrounding media (air and substrate) are labeled as subscripts a and s. The spontaneous emission process of an atom located inside the stack will result in a field which can be expanded on a complete set of modal fields of this planar structure.
The complete set of modal fields of a lossless multilayer dielectric structure includes an infinite number of radiation modes and evanescent modes, as well as a finite number of guided modes [4]. The evanescent modes are neglected in this analysis since they do not carry power far away from the guide.
For the radiation modes, since they are propagation modal fields, the fields in both the air and the substrate must be standing waves in the direction normal to the layers. In this case, these fields vary only by a phase factor when they propagate along the x direction. These fields can be described by a superposition of two plane waves which have the same cross power through the yz plane. These two waves are incoming towards the stack respectively from the air and from the substrate. Since the total field is a standing wave in the outer medium, the power in the outgoing waves is a superposition of incoming power reflected by the stack plus incoming power transmitted across the stack from the opposite side.
The radiation modes can be classified into modes radiated in all space, namely the full radiation modes ES ($0< \beta <2\pi n_a/\lambda_0$), and into modes radiated in the substrate, namely the substrate

radiation modes ER ($2\pi n_a/\lambda_0 < \beta < 2\pi n_S/\lambda_0$), where β is the propagation constant of the considered modal field, which remains constant is every media. Figures 1-a and 1-b show respectively a schematic view of the full radiation modes and of the substrate radiation modes. Figure 1-c shows a guided mode EG for which ($2\pi n_S/\lambda_0 < \beta < 2\pi n_H/\lambda_0$), where n_H is the highest refractive index of the stack.

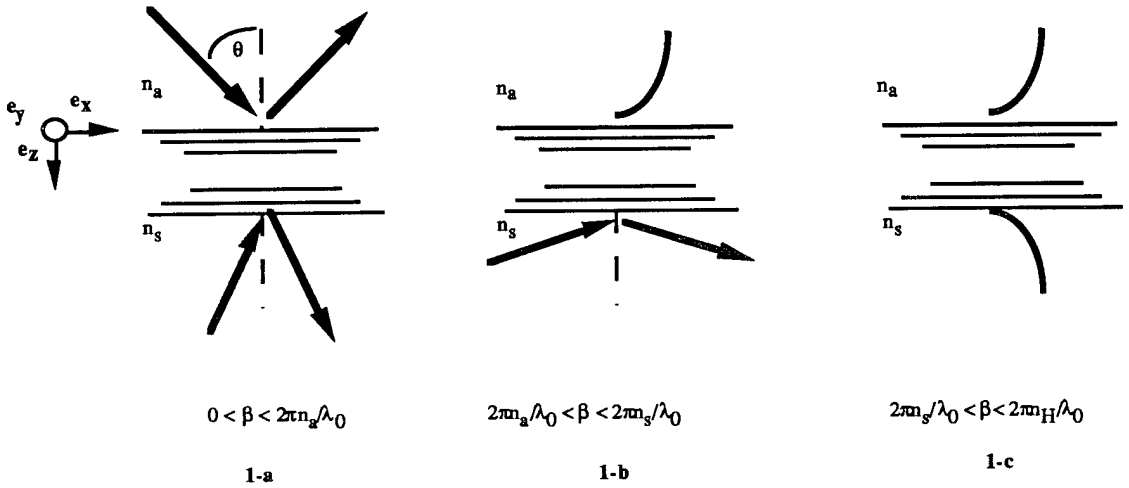


Figure 1: Schematic view of the full radiation modes (a), the substrate radiation modes (b) and the guided modes (c) of a planar dielectric structure.

As previously mentioned, we will now use this complete set to expand the total field emitted by the atom, which will be considered here as a dipole. This will allow us to get the emitted power into each modal field. By integration over all these modal fields, we will be able to compute the total emitted power, which can be expressed as:

$$P = \frac{q^2 a_0^2 \omega_0^2}{32\pi^3 \varepsilon_0 n^2(z_0)} \left[\sum_{\beta} \int_{k_p} \delta(\omega_0 - \omega_k) \left| \mathbf{e}.\mathbf{EG}(\mathbf{r}_0, \mathbf{k}_p) \right|^2 d\mathbf{k}_p + \int_{k_a} \delta(\omega_0 - \omega_k) \left| \mathbf{e}.\mathbf{ES}(\mathbf{r}_0, \mathbf{k}_a) \right|^2 d\mathbf{k}_a + \int_{k_s} \delta(\omega_0 - \omega_k) \left| \mathbf{e}.\mathbf{ER}(\mathbf{r}_0, \mathbf{k}_s) \right|^2 d\mathbf{k}_s \right]$$

where ω_0 is the dipole bare frequency, a_0 is the dipole amplitude, q is the electron charge, $n(z_0)$ is the refractive index where the dipole is located, and **e** is the dipole vector.

2 - Numerical and experimental results

The sources considered here are rare earth atoms (erbium) located into resonant dielectric structures by ion implantation.

Let us first consider a luminescent atom ($\lambda_0 = 1.55\mu m$) located in free space. Because there is no boundaries confinement, the radiation pattern (in a plane perpendicular to the dipole vector **e**) is isotropic (see figure 2 (a)). Let us consider now the same atom located in a $\lambda/2$ microcavity. More precisely, this cavity is HLHLHL 2H LHLHLH where H and L stand respectively for a high ($n_H = 2.2$) and low ($n_L = 1.45$) refractive index layer whose optical thickness is $\lambda_0/4$. Because this structure is resonant in normal direction, the radiation pattern of the dipole is in normal direction is enhanced up to 18 times compared to its free space value (see figure 2 (b)).

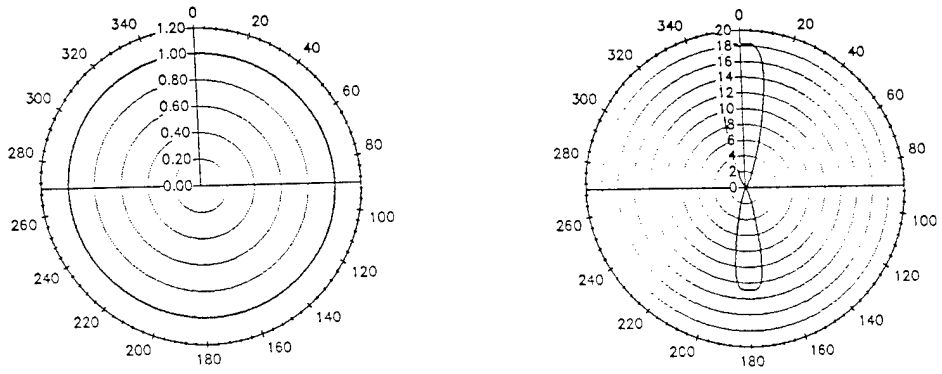


figure 2: (a) radiation pattern of an erbium atom in free space; (b) radiation pattern of an erbium atom in a resonant microcavity.

In other words the spontaneous emission is controled and the atom is forced by the microcavity to emit its photon in a direction normal to the stack. From a quantum point of view, this is due to the extreme vacuum confinement realized by this device.

By the way, we have investigated the radiation that can exit the stack through running waves in the semi infinite outer media. We have seen theoretically that the atom can also relax by emitting its light in some guided modes of the structure. In order to confirm our theory, we have implemented an experiment to measure the power emitted by spontaneous emission into the guided modes. Figure 3 shows the experimental set up where a group of atoms are excited by a cw argon laser. A scatterometer type apparatus allows us to measure the radiation pattern in the air. A high index prism (rutile) is set on the microcavity, few mm far from the excited atoms, and decouples the light along various angles θ according to the guided modes. A detector permits to obtain the guided power emitted in these guided fields.

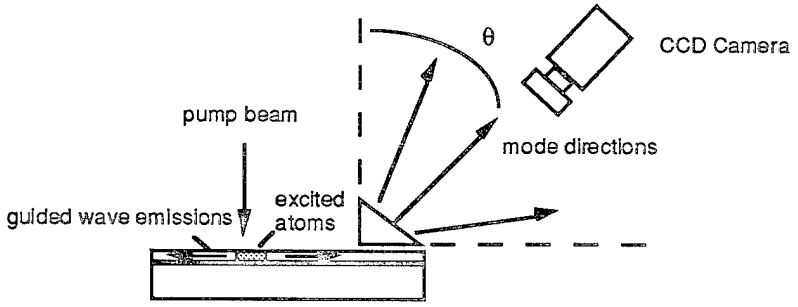


figure 3: experimental apparatus to measure the emission into the guided modes

Results of these experiments will be presented where it will be shown that the amount of power emitted into those guided modes is important, and drastically diminishes the emission in normal direction. We will present also some new structures, which should avoid this emission into the guided modes, in order to make efficient luminescent micro devices in vertical direction.

[1] Yamamoto Y., Slusher R. E., Physics Today (1993) 66-73
[2] Amra C., J. Opt. Soc. Am. A **10** (1993) 365-374
[3] Rigneault H., Amra C., Pelletier E., Flory F., Cathelinaud M., Roux L., in Quantum optics in wavelength scale structures (Plenum Press, C.Weisbush and J.Rarity editors, 1996
[4] D.Marcuse, *Light Transmission Optics* (Van Nostrand Reinhold, New York, 1972)

Impact of Quantum Confinement and Strain Effects on the Negative Chirp Parameter of InGaAsP/InP QW Electroabsorption Modulators

Takayuki Yamanaka, Koichi Wakita, and Kiyoyuki Yokoyama
NTT Opto-electronics Laboratories
3-1, Morinosato Wakamiya, Atsugi-shi, Kanagawa, 243-01 JAPAN
Tel:+81-462-40-4403, Fax:+81-462-40-2859, E-mail:tyama@aecl.ntt.jp

I. Introduction

For dispersion-free transmission with a standard fiber in the 1.55 μm window, a light source capable of negative-chirp modulation is strongly desired. External modulation by electroabsorption (EA) modulators [1]-[5] has attracted much interest because it provides negative-chirp modulation where the averaged values of chirp parameter are negative. The problem is that the conventional negative-chirp modulation using larger bias-voltage and/or detuning to smaller wavelengths is accompanied by excessive propagation loss. To solve these problems, we aim to establish a design guideline for quantum well (QW) EA modulators that makes it possible to attain the ideal situation where the negative chirp parameters are independent of the applied electric fields. In this paper, the impact of quantum confinement and/or strain effects on the chirp parameter for TE-polarized small-signal modulation by using InGaAsP quaternary material is analyzed theoretically. Based on the analysis, we predict that a combination of a wide well and tensile strain will provide almost a continuously negative field-independent chirp parameter.

II. Theoretical Formalism

In EA materials, under a small change of electric field strength δF, chirp parameter β_C at the wavelength of incident light λ_0 is defined as $\beta_C = (4\pi/\lambda_0)(\delta n/\delta\alpha)_{\lambda=\lambda_0}$, where $\delta\alpha$ and δn are the induced changes in the absorption coefficient $\alpha(\lambda, F)$ and in the refractive index $n(\lambda, F)$, respectively, where λ denotes wavelength. Electroabsorption spectra $\alpha(\lambda, F)$ over a wide wavelength range are calculated to properly evaluate δn by the Kramers-Krönig (K-K) transformation [6] and β_C. Two remarkable features of the InGaAsP quaternary material system are low barrier height for conduction electrons and strong valence-subband nonparabolicity due to coupling among hole states. Recently, we showed that weak electron confinement in InP-based QW structures is a main cause of the spectral broadening of α [7]. With these facts in mind, the optical transition strengths including excitonic effect are calculated to give the α-spectra for TE polarization, taking into account the field-induced broadening (FB) in the conduction subband structures and the field-dependent valence subband structures [7]. With the calculated α-spectra, K-K integration is performed with the help of the sum rule.

III. Possibility of Negative Chirp Parameter

From the definition of β_C, $\delta n(\lambda_0) < 0$ is required to get negative β_C under biased conditions ($\delta\alpha > 0$). In order to satisfy this condition, we manipulate the well width L_w (the quantum confinement effect) and the amount of strain ε (the strain effect). The analyzed

QW structures are composed of a single $In_{1-x}Ga_xAs_yP_{1-y}$ well embedded in InGaAsP (lattice matched to InP, $\lambda_g = 1.1$ μm) barriers. Well material compositions x and y are varied independently of L_w so as to keep their exciton band gap energy at about 1.5 μm when $F = 0$. Here, δF is set to 2 kV/cm.

First, the quantum confinement effect on β_C is examined. The integrand in K-K transformation is expressed as $(\lambda_0^2/2\pi^2)[\delta\alpha(\lambda, F)/(\lambda_0^2 - \lambda^2)]$. Large variation in $\delta\alpha$ of the integrand due to a large red Stark shift is necessary for $\delta n(\lambda_0)$ to become negative. In Fig. 1, the calculated F dependence of β_C at λ_0= 1.55 μm is shown for lattice-matched QW's with different L_w's. Note the trend of decreasing β_C with increasing L_w. β_C for the QW with L_w= 12 nm crosses zero at half the value that β_C for the QW with L_w= 6 nm does. The reason for this trend is in enhanced red Stark shift nonlinearly proportional to L_w. The wider the well is, the faster the spectra of $\delta\alpha$ shift toward longer wavelengths across λ_0 become. As a result, the integrand contributes to reducing δn. Figure 1 indicates that the larger red Stark shift due to well widening makes it easier for β_C to turn negative at smaller F. Further reduction in β_C down to a negative value in the lower F range is possible by increasing L_w to more than 12 nm. However, because the Stark shift $\propto F^2$, the impact of widening the well on reducing β_C becomes less effective when F is low. To obtain negative β_C values in the low F range, we turn our attention to the strain effect when L_w= 12 nm. When L_w is enlarged, the quantum confinement degrades. On the other hand, the strain-induced change in $\delta\alpha$ becomes more enhanced in the wider QW. L_w of 12 nm is the compromise that extracts the best of both the quantum confinement and strain effects as is discussed next.

Figure 2 shows the pure effect of tensile strain on β_C, where the dependence of β_C on F up to 75 kV/cm for lattice-matched and tensile-strained QW's with different ε's is plotted. In the figure, β_C is found to be sensitive to ε. Note the case of ε= 0.4 % where β_C is almost continuously negative over the entire range of F. These results suggest that a wide QW with 0.4 % tensile strain is very promising for achieving negative β_C characteristics in the low F region. We have also found out that compressive strain in the wide QW can reduce β_C, but its impact is not large enough to bring negative β_C values over the whole F range. Further details will be discussed in the presentation.

IV. Conclusion

We have theoretically examined the possibility of negative chirp characteristics for InGaAsP QW-EA modulators at an operating wavelength of 1.55 μm. We conclude that a combination of the well width of 12 nm and 0.4% tensile strain brings about almost a continuously negative chirp parameter for all field strengths.

References

[1] F. Dorgeuille et al, IEEE J. Quantum Electron, **QE-30**, 2565 (1994).
[2] J. A. J. Fells et al, Electron. Lett. **30**, 1168 (1994).
[3] K. Morito et al, Electron. Lett. **31**, 975 (1995).
[4] J. J. M. Binsma et al, Conference Proceedings of IPRM'95, paper FB1.1 (1995).
[5] K. Yamada et al, IEEE Photon. Technol. Lett., **7**, 1157 (1995).
[6] D. C. Hutchings et al, Opt. Quantum Electron. **24**, 1 (1992)
[7] T. Yamanaka et al, Appl. Phys. Lett.. **65**, 1540 (1994)

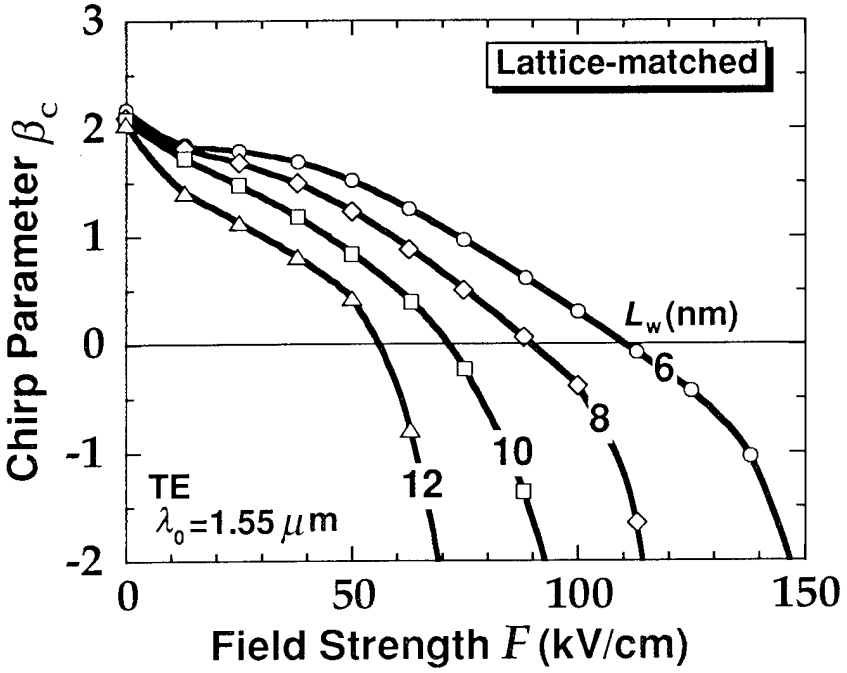


Fig. 1 Variation in chirp parameter at 1.55 μm for lattice-matched InGaAsP QW with changing field strength using well width as a parameter.

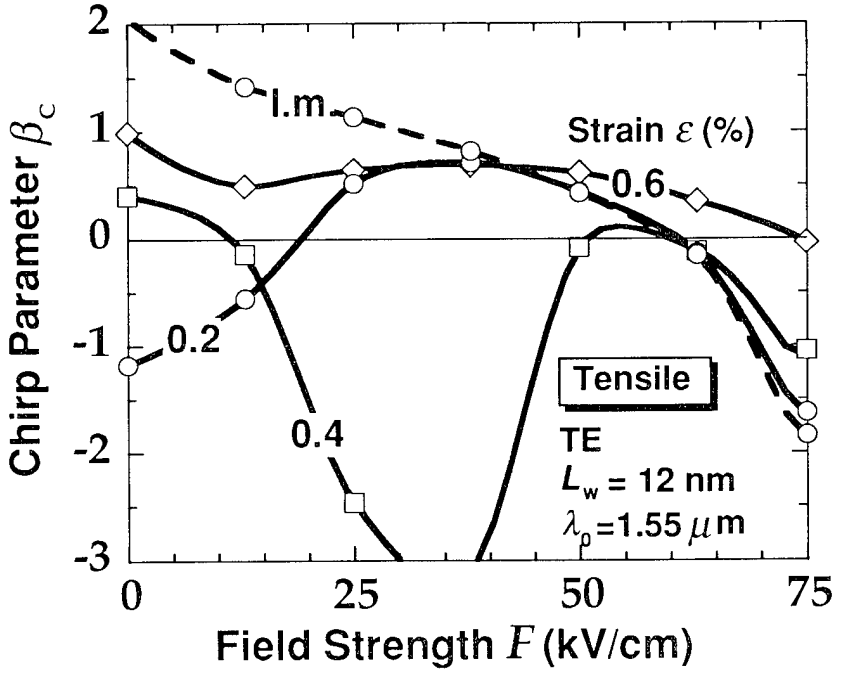


Fig. 2 Variation in chirp parameter at 1.55 μm for lattice-matched and tensile-strained InGaAsP QW's with changing field strength using amount of strain as a parameter. l.m. means lattice match.

Enhanced Stark-Effect in Tensile Strained $Al_xIn_{1-x}As$/ $Ga_yIn_{1-y}As$/ InP - Quantum Well Structures

T. Schwander
Bosch Telecom GmbH, Gerberstr. 33, D-71522 Backnang
Tel.: +49 7191 133878, Fax.: +49 7191 133044
P. Lüsse, J. Schöbel
Institut für Hochfrequenztechnik, TU Braunschweig
Germany

Introduction:

Electroabsorption modulators (EAMs) of the Quantum-Confined Stark-Effect type [1, 2] are most favorable for high-bitrate distribution-networks [3] which require transmitters with high bandwidth, high extinction ratio and controlled chirp [4, 5]. For high-bitrate applications a strong Stark-shift is needed at low drive-voltages for an effective intensity modulation at high extinction ratios. The bandwidth of the EAMs is mainly determined by their intrinsic depletion layer capacity. Devices for high-bitrate applications with large intrinsic layer thicknesses need enhanced Stark-shift efficiencies of at least 0.70 nm/(kV/cm), because only moderate fieldstrengths can be achieved in the quantum well region. The use of Si-bipolar driver-ICs in commercial applications limits the modulation-voltage swing to 2 V, and an adjustment of absorption and chirp, using a bias-voltage, is not practicable.

The application of biaxial strain to thin epitaxial layers can help to improve the quality of quantum-well semiconductor devices [6]. In the field of EAMs, tensile strained layers have been used mainly for polarisation independent devices [7, 8]. Moreover, these devices showed superior modulation efficiencies in linear polarized light. This work gives a theoretical approach to this enhanced Stark-Effect, presenting novel design criteria for tensile strained quantum wells, offering very high Stark-shift efficiencies between 0.70 nm/(kV/cm) and 0.80 nm/(kV/cm). The predicted modulation behaviour is compared with experimental results.

Theoretical Background:

Band structures are calculated with the kp-method in the envelope function approximation [9]. The conduction band is assumed decoupled and is treated with an effective-mass model. Based on the theory of Luttinger-Kohn and Bir-Pikus, the valence band structure is described by a 6x6 Hamiltonian, which includes the k- and strain-induced couplings between heavy-hole, light-hole and split-off bands [10]. In the axial approximation the problem reduces to two sets of three coupled differential equations.

We apply the finite-difference method using equidistant discretization and appropriate boundary conditions at layer interfaces and obtain sparse Hermitian matrices [11]. Eigenstates are computed for a set of k values, so that the subbands can be approximated by polynomials. In the calculation of fundamental absorption a derivative of a polynomial substitutes the valence-band effective mass.

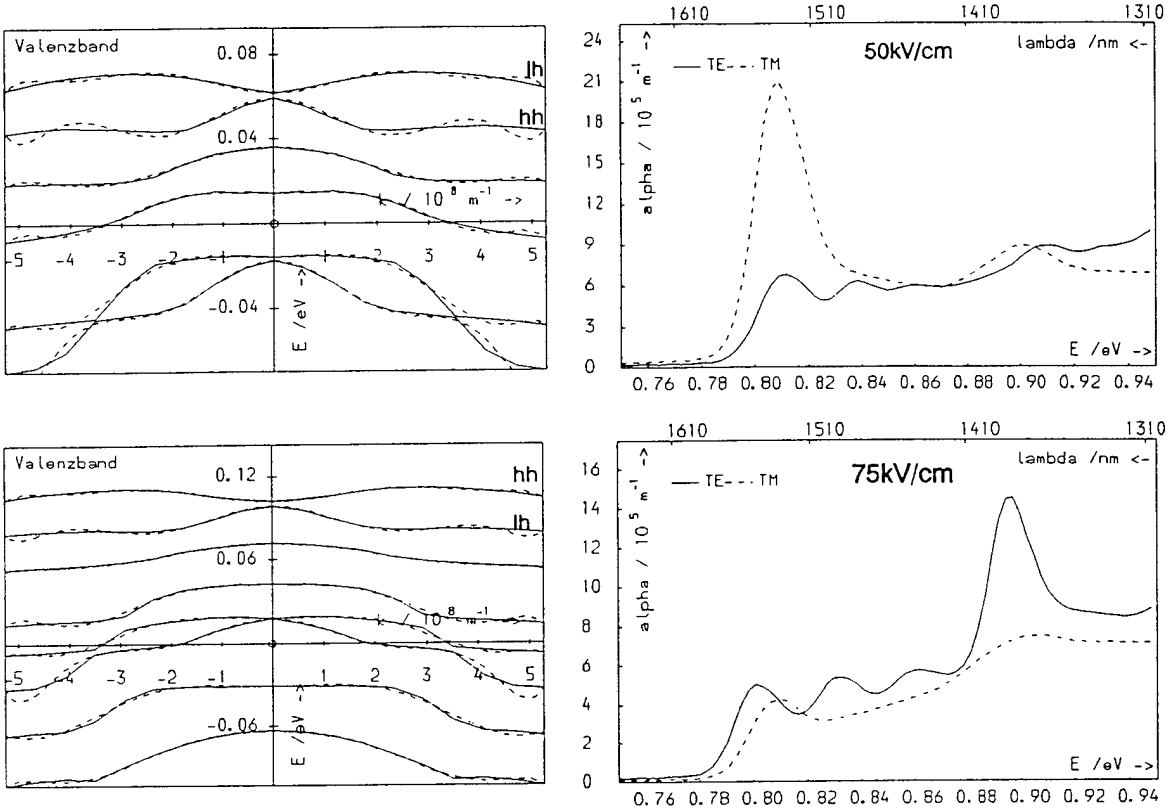


Fig. 1: Calculated valence-bands and absorption spectra of a 13 nm $Ga_{0.53}In_{0.47}As$ quantum well at fieldstrengths of 50 kV/cm and 75 kV/cm

Excitonic states are calculated by a variational method [9]. The exciton Hamiltonian is newly formulated for nonparabolic valence-band dispersion. The linewidth broadening is assumed to be inhomogenous with a Gaussian shape of 8 meV width (HWHM) for light-hole and spilt-off-band transitions and 7 meV for heavy-hole transitions, respectively.

Simulation Results:

Fig. 1 shows calculated valence-band dispersions and the corresponding absorption spectra for TE- (straight line) and TM-polarisation (dotted line) at 50 kV/cm and 75 kV/cm in a 13 nm $Ga_{0.53}In_{0,47}As$ quantum-well situated in strain-compensating AlInAs-barrieres with 35 % Aluminium content. The dotted lines in the valence-band diagrams represent the 8 th-order polynomial approximations used for the calculation of the absorption spectra.

The interaction between the two topmost light-hole and heavy-hole subbands, which reach the degeneration state between 50 kV/cm and 75 kV/cm, leads to a dramatic change of the effective mass at the band edge. The negative heavy-hole mass at 75 kV/cm fieldstrength results in an extremum of the combined density-of-states. This leads to a relatively high excitonic off-state absorption for TE-polarised light, in spite of the decreased transition-matrix element in the field-distorted quantum wells. The increase of heavy-hole mass between the on- and the off-state supports the TE-electroabsorption in a very effective way. In contrast, the TM-absorption dramatically drops down for fieldstrengths exceeding the degeneration at about 62 kV/cm, according to the decreasing light-hole mass. A Stark-Shift of 50 nm is achieved at 75 kV/cm with an absorption change of 4000 cm^{-1} at 1.55 μm (Fig. 2).

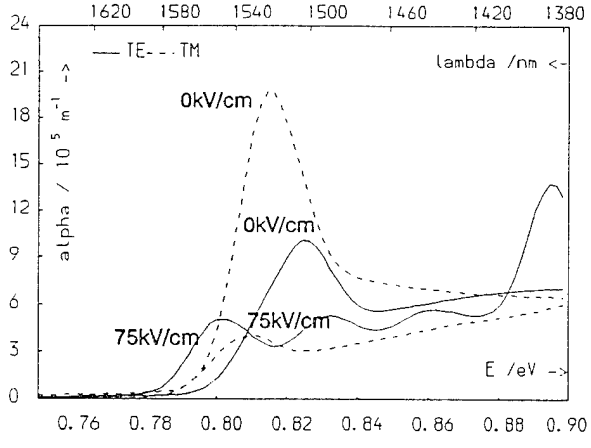


Fig. 2: Calculated Absorptionspectra of a 13 nm $Ga_{0.53}In_{0.47}As$-QW for 0 kV/cm and 75 kV/cm

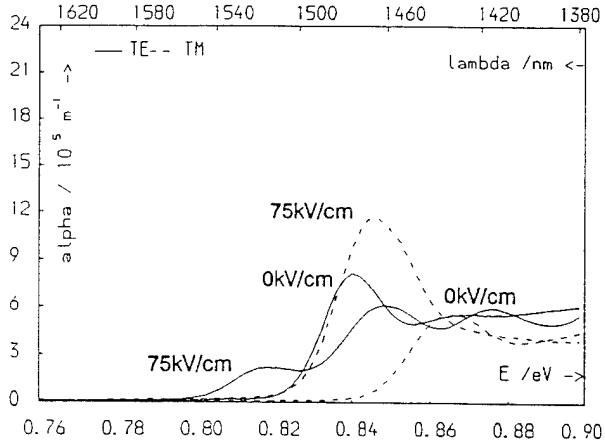


Fig. 3: Calculated Absorptionspectra of a quaternary 13 nm $Ga_{0.42}Al_{0.05}In_{0.52}As$-QW at 0 kV/cm and 75 kV/cm

To stress the difference, Fig. 3 shows calculated absorption spectra of a quaternary, lattice matched $Ga_{0.42}Al_{0.05}In_{0.52}As$ quantum well of 13 nm width without electric field and for 75 kV/cm. The off-state TM-absorption in the excitonic resonance is much higher than in the tensile strained device due to the larger light-hole transition-matrix element and the interaction between the light holes and the second heavy-hole subband. In contrast to the absorption of TM-polarized light, the TE-absorption at 75 kV/cm is approximately three times higher in the tensile strained device, resulting in a three times stronger absorption modulation.

In principle, this result keeps valid even under high temperature conditions, simulated with exciton linewidths of 25 meV.

Device processing:

Samples are grown on 2-inch S-doped InP substrates in a solid-source MBE. The structures consist of a 120 nm-thick Si-doped $(Al_{0.48}In_{0.52}As)_{0.5}$ $(Ga_{0.47}In_{0.53}As)_{0.5}$ short-period superlattice buffer with a superlattice period of 3 nm, followed by the investigated MQW structures. The overall thickness of the intrinsic zone was adjusted to approximately 300 nm by an undoped $Al_{0.48}In_{0.52}As$ cover layer. Subsequently, the 1.2 μm InP cladding layer and a 150 nm $Ga_{0.47}In_{0.52}As$ contact-layer (both Be-doped) are grown. Ridge-waveguides are formed by a combination of a CH_4/H_2-RIE process and $HCl{:}H_3PO_4{:}CH_3COOH$ wet-chemical etching. For the p-contacts a Ti Pt Au-metallisation is applied to the ridge. The EAMs are characterized by photocurrent and transmission experiments. Modulation efficiencies exceeding 10 dB/V have been achieved at 1540 nm wavelength in 300 nm long tensile-strained quantum-well EAMs with 51 % Gallium content. Both, TE- and TM-absorption characteristics are nearly identical, so that the device could be driven as polarisation independent EAM too.

Conclusion:
Tensile strained quantum wells, with degenerated subbands at the modulator off-state are most favorite for high-bitrate EAMs in the 1.55 μm wavelength range. The predicted Stark-Shift in 13 nm $Ga_{0.53}In_{0.47}As$ quantum wells in 5 nm $Al_{0.35}In_{0.65}As$ barriers amounts to 50 nm for 75 kV/cm with an absorption modulation of 4000 cm^{-1}, due to strong light-hole heavy-hole interactions at the modulator off-state. This enhanced Stark-Effect allows wide intrinsic layers with low depletion-layer capacity, which is mandatory for high bitrate devices. Modulation efficiencies exceeding 10 dB/V have been achieved in devices corresponing to the above mentioned design. As expected, these EAMs additionally show polarisation independent modulation characteristics.

References

[1] D.A.B. Miller et al: Electric Field Dependence of Optical Absorption Near the Band Gap of Quantum-Well Structures; Phys. Rev. B, Vol. 32, pp. 1043.

[2] J.S. Weiner, D.A.B. Miller, D.S. Chemla: Quadratic electro-optic effect due to the quantum-confined Stark effect in quantum wells; Appl. Phys. Lett., Vol. 50, No. 13, März 1987, p. 842-844.

[3] W. Bambach, K. Krull, H.G. Zielinski: DIAMANT - a novel concept for digital TV-Distribution; Proc. ECOC 1992, Berlin, pp. 577.

[4] A.H. Gnauck, R.W. Tkach, M. Mazurczyk: Interplay of Chirp and Self Phase Modulation in Dispersion-Limited Optical Transmission Systems; Proc. ECOC'93, Montreux, Switzerland, Vol. 2, p. 105-109

[5] F. Dorgeuille and F. Devaux: On the Transmission Performances of a Multiple-Quantum-Well Electroabsorption Modulator; IEEE J. of Quant. El., Vol. 30, No. 11, 1994, p. 2565-2572.

[6] E.P. O'Reilly: Valence band engineering in strained-layer structures; Semicon. Sci. Tech., Vol. 4, 1989, p. 121-137.

[7] F. Devaux, S. Chelles, A. Ougazzaden, A. Mircea, M. Carr, F. Huet, A. Carenco, Y. Sorel, J.F. Kerdiles and M. Henry: Full Polarization Insensitivity of a 20 Gb/s Strained-MQW Electroabsorption Modulator; IEEE Phot. Tech. Lett., Vol. 6, No. 10, 1994, p. 1203-1205.

[8] H. Haisch et al: Record Bandwidth (42 GHz measured) and Polarisation Insensitive (< 0,4 dB) Tensile Strained InGaAsP MQW Ridge Waveguide Electroabsorption Modulator for Ultra-High Bitrate TDM Systems; Proc. of 21 st ECOC'95, Brussels, Vol. 3, Post Deadline Papers, pp. 1027.

[9] G. Bastard, J.A. Brum: Electronic States in Semiconductor Heterostructures; IEEE J. of Quantum El., Vol. QE-22, No. 9, 1986, pp. 1625.

[10] : C.-S. Chang, S.L. Chuang: Modeling of Strained Quantum-Well Lasers with Spin-Orbit Coupling, IEEE J. of Selected Topics in Quantum Electronics, Vol. 1, No. 2, 1995, p. 218-229.

[11] : P. Lüsse, J. Schöbel, H.-G. Unger: Numerische Berechnung des spektralen Absorptionsverlaufs von allgemeinen Quantenfilmstrukturen aus III/V-Halbleitern, confernce contribution to Kleinheubacher Tagung, Kleinheubach, Germany, 1995

Silicon Waveguides and Interconnect Technologies

ITuD 10:30 am-12:00 m
Fairfax B

Bahram Jalali, *Presider*
University of California–Los Angeles

Trends in silica-based optoelectronics hybrid integration

Claude Artigue

Alcatel Alsthom Recherche, Route de Nozay, 91460, Marcoussis, France

I. INTRODUCTION

Revisiting the future All-Optical Network within its Transport, Switching and Access functionalities or considering the increasing demand for Datacommunications, it appears that a wide range of optoelectronic components with balanced performances and costs will be required. Concerning this balance, it has been recognised that package structures based on silicon boards might contribute to a generic and flexible technological approach. The more popular has been the flip-chip assembly of optoelectronic components on silicon boards with V-grooves in order to perform passive, and therefore cost-effective alignment with single mode fibers [1]. More recently [2, 3, 4, 5, 6], it has been proposed to extend this approach to silicon boards with integrated silica waveguides. This opens the way for the planar integration of several Photonic Integrated Circuits (PICs) [7, 8] that is, several monolithically integrated optoelectronic circuits (figure 1). This approach can be considered as the photonic counterpart of the Multi-chip Module Integrated Circuits (MMICs) approach previously developed for electrical chips. These new photonic circuits might be therefore described as Multi-chips Photonic Integrated Devices (MPICs).

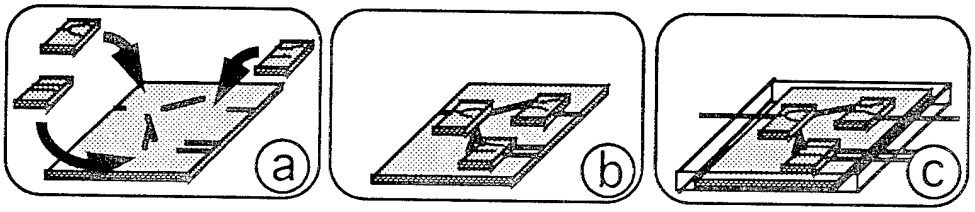


figure 1 : After PICs assembly on the silica on silicon boards (1-a), the MPICs are obtained (1-b) and packaged (1-c)

MPICs are attractive because they specifically address an identified bottle-neck which is the PICs packaging. On the one hand, the silica on silicon boards used in MPICs bring with it the functionality of low-loss integrated optics [9, 10, 11] ; therefore it is necessary to identify the best complementarities or functionalities sharing between MPICs and the PICs they integrate. On the other hand, MPICs have to fit gently with the overall optoelectronic package for which the usual difficulty is to search an optimum in a sea of constraints.

Starting from the more recent progress on silicon boards and silica on silicon passive components, this presentation reviews the present status on MPICs and some possible future prospects.

II. SILICON MOTHERBOARDS and SILICA ON SILICON INTEGRATED OPTICS

Silicon wafers are well-suited as optoelectronic submounts due to their thermal dissipation and thermal expansion coefficients which are close to those of III-V materials, their mechanical properties that involve hardness, mastered wafers polishing, possible structuration by established wet or dry etching processes, compatibility with lines and bumps definition for flip-chip assembly. Additionally, Si wafer cost is relatively low and a wide range of manufacturing equipments issued from the electronic activity are available.

An usual process for these silicon optoelectronic submounts involves some optional structuring steps that include V-grooves' anisotropic wet-etching for fiber passive alignment [12], wet [13] or dry [14] etched indentations for optoelectronic chips passive alignment or recessed areas allowing electrical lines access under the flip-chip mounted optolectronic components. The lines and bumps on the board are interfaced by proper pads with a multilayer structure [15] involving in general an adhesion layer, a barrier preventing for metal diffusion between bumps and lines, and finally a passivation layer.

The silicon board structure is generally chosen together with an on-board assembly strategy that can lie from purely active alignment techniques (i.e. activation of a laser for alignment with a single mode fiber) [16] to passive alignment techniques [13, 14, 17, 18, 21] with many possible trade-offs between alignment accuracy, board process complexity, etc...

It must also be underlined that some of the more recent progress on PIC's will directly benefit to MPICs. Illustration of it are tapered waveguide devices [19, 21] that improve optical coupling with single mode fibers, self-aligned patterns [18] or indentation [21] which constitute a more accurate reference for the alignment between MPICs and single mode fibers or silica waveguides.

Silica on silicon integrated devices have been fabricated mainly using Chemical Vapor Deposition (CVD) [9, 11, 22, 23, 24] or Flame Hydrolysis Deposition (FHD) [10, 25, 27]. CVD processes have the potential of a lower process temperature which makes them attractive for the fabrication of optical waveguides with reduced birefringence ; also on board integration with electrical interconnections can be considered. However, using CVD, voids appear in the case of burried waveguides [23, 24] which might then limit the performance reproductibility of the silica based integrated circuits (i.e. : directional couplers).

III. MULTI-CHIP PHOTONIC INTEGRATED CIRCUITS (MPICs)

MPICs have emerged from increased systems needs (reduced packaging cost, higher systems functionalities) and this has been possible from the simultaneous progress of more conventional components (PICs, Passive optical components). The MPICs concept has been pioneered by laboratories which had already mastered the silica on silicon passive components [25, 26, 2] from which the MPICs board technology is derived.

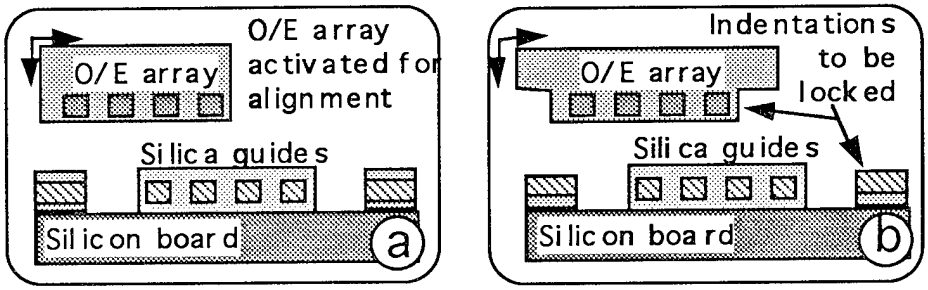


figure 2 : Flip-chip assembly of O/E components onto a Silica on silicon motherboard using active alignment (2-a) or passive alignment (2-b) techniques

A proper design of MPICs boards is a complex problem. Concerning the alignment of optoelectronic components on the silica on silicon boards, a few microns alignment tolerance is accepted for multi-mode coupling as required in some datacom applications ; in this case, passive alignment techniques are attractive [4]. Concerning single mode operation where alignment tolerances are in the micron range or even lower, the debate is still open between active [5, 27] or passive [6, 28] onboard alignment approaches (figure 2). Thermal dissipation also is a concern due to the low thermal conductivity associated to the use of silica layers. Finally, passive alignment techniques have been also proposed for the fiber alignment at the edge of the silica on silicon board [29 , 30].

Acknowledgments :
The author would like to thank S. Valette, P. Mottier and G. Grand from CEA-LETI (France), F. Mallecot, D. Tregoat and all is colleagues from the Alcatel Corporate Research Center for fruitful discussions and collaboration on the development of Multi-chips Photonic Integrated Circuits.

References

[1] K. Lösch, "Potential and implementation of optical Technologies for high bitrate short distance interconnects", Proc. ECOC'95, Tu.A.1.3, pp 165-171
[2] C.H. Henry, "Glass Waveguides on Silicon for Hybrid Optical Packaging", JLT, Vol. 7, N°10, Oct. 1989, pp1530-1539
[3] C. Artigue and G. Grand, "Optoelectronic Packaging Using Silicon Platforms", Proc. EFOC&N'95, Vol. 3, pp 50-51
[4] K.P. Jackson et al., "A High-Density, Four-Channel, OEIC Transceiver Module Utilizing Planar-Processed Optical Waveguides and Flip-Chip, Solder-Bump Technology", J.L.T., Vol. 12, N°7, July 1994,pp11185-1191
[5] I. Ogawa, "Reduction of Waveguide Facet Reflection in Optical Hybrid Circuit Using Saw-Toothed Angled Facet", IEEE Photonics Technology Letters, Vol. 7, N°1, pp 44-46, January 1995
[6] F. Mallecot et al., " Hybrid silica multiwavelength optical source realized by passive alignment techniques", Proc. OFC'95, ThB3, p227
[7] M. Erman, "Prospect for Integrated Optics in Telecom Applications", ECIO'95, Tu P1, pp27-32
[8] D. Trommer, "Photonic Integration on InP", Proc. ECIO'95, Tu A3, pp 93-98
[9] P. Mottier, "Integrated optics at the Laboratoire d'Electronique, de Technologie et d'Instrumentation", International Journal of Optoelectronics, 1994, volume 9, number 2, pp 125-134
[10] M. Kawachi, "Recents Progress in Planar Lightwave Circuits", IOOC-95, ThB1-1, pp 30-33
[11] C.H. Henry, "Recent Advances in Integrated Optics on Silicon", E-FOC 90, pp11-14
[12] J.D. Crow et al., "Gallium arsenide laser-array-on-silicon package", Applied Optics, 1 february 1978, Vol. 17, N°3, pp 479-485
[13] H. Kaufmann et al., "Self-adjusted permanent attachment of fibres to GaAs waveguide components", El. Lett., 5th June 1986 Vol. 22, N°12, pp 642-644
[14] C.A. Armiento et al., "Passive coupling of InGaAsP/InP laser array and single mode fibres using silicon waferboard", El. Lett., 6th June 1991, Vol. 27, N°12, pp 1109-1111
[15] J. P. Hall and all., "Hybrid Micropackaging for Optoelectronic Multi-Chip Modules", IPR'95, IFE1-1, pp 240-242
[16] D.E. Bossi, "Progress Report on the ARPA/NCAICM Automated Optoelectronics Packaging Project", IPR'95, IThE1-1, pp 70-72
[17] A. Ambrosy et al., "Reliability Investigations of Au/Au Thermo Compression Flip Chip Bonded Laser Diode Arrays for Parallel Optical Links", Proc. ECOC'95, We.P.30, pp 725-728
[18] M.S. Cohen et al., "Improvments in Index Alignment Method for Laser-Fiber Array Packaging", IEEE TRans. on Comp., Pack. and Man. Technology-, Part B, Vol 17, N°3, August 1994, pp402-411
[19] I. Moerman, "III-V semiconductor waveguiding devices using adiabatic tapers", Microelectronics Journal, 25 (1994), pp 675-690
[20] P.C. Clemens et al., "8-Channel Optical Demultiplexer Realized as SiO2/Si Flat-Field Spectrograph", IEEE Photonic Technology Letters, Vol. 6, N°9, Sept. 1994, pp1109-1111
[21] M.J. Robertson et al., "Passive Aligment of a Tapered 1.55µm Laser with coupling efficiency greater than 50%", Proc. ECIO'95, Th P1(Post-deadline paper), pp 5-8
[22] H. Moisan et al., "Low Temperature Fabrication of GeO2-doped Silica Optical Waveguide Using Microwave Plasma",Proc. ECIO'95, TuPo, pp 201-204
[23] J. Magerand et al., "Integrated polarization insensitive 1.3µm/1.55µm duplexer on silica-based technology", Proc. Int. Symp. on Integrated Optics, Lindau, Germany, 11-15 April 1994
[24] P.R. Wensley et al., "Improved Waveguide Technolgy for Silica-on-Silicon Integrated Optics", ECIO'93, Neuchatel
[25] H. Terui et al., "Hybrid Integration of a Laser Diode and a High-Silica Multimode Optical Channel Waveguide on Silicon", El. Lett., 18th July 1985, Vol. 21, N°15, pp 646-648
[26] S. Valette et al., "Integrated optics and microelectronics : toward an integration on a single chip", SPIE Vol. 864, Advanced Optoelectronic Technology (1987), pp125-130
[27] J. Yoshida et al., "Packaging and Reliabibilty of Photonic Components for Subscriber Network Systems", IEEE Trans. on Comp., Hyb. and Man. Tech., Vol.16, N°8, Dec. 1993, pp 778-782
[28] C. Jones et al., "An Optical Transceiver on a Silicon Motherboard", Proc. ECIO'95, ThC4, pp591-594
[29] G. Grand et al., "New Method for Low Cost and Efficient Optical Connections Between Single Mode Fibres and Silica Waveguides", El. Lett., 3rd January 1991, Vol.27, N°1, pp16-17
[30] A. Sugita et al., "Circuits with Fiber-Guiding Grooves", Fiber & Int. Optic, Vol.13, 1994, pp347-354

New Types of Singlemode (Movable) and Multmode (60-μm thick) SOI Waveguides Fabricated using Silicon Micromachining Technology

S.C. Kan, T.T.H. Eng, S.Y.S. Sin, J.Y.L. Ho, I.H.M. Liem, P.W.L. Chan, and G.K.L. Wong
Dept. of Physics, The Hong Kong University of Science and Technology, Clear Water Bay, Hong Kong, Phone: (852) 2358-7493, Fax: (852) 2358-1652, Email: phskan@usthk.ust.hk

Advantages of integrated optical devices based on silicon technology have been well recognized and discussed [1]. In particular, excellent properties of waveguides based on Silicon-On-Insulator (SOI) structures have been demonstrated. In this paper, we report on the demonstration of two new types of SOI waveguides for various applications.

I. Single Movable SOI waveguide with a rib-beam structure

Movable SOI waveguides have been proposed by Watts et al. [2] and demonstrated by Eng et al. [3] recently. Applications such as optical switches and scanning probes have also been demonstrated [4-5]. However, the movable SOI waveguides developed so far all have a simple trapezoidal cross-section of tens of μm^2. At λ=1300nm, these waveguides support multi-mode propagation. However, for high performance applications, single mode propagation is often necessary. The first demonstration in this paper is the singlemode propagation in a low-loss movable SOI waveguide with a new rib-beam structure.

The new movable waveguide designed for singlemode propagation is shown in Fig.1. It consists of two sections in tandem: a conventional rib waveguide section followed by a rib-beam cantilever section. The conventional rib waveguide section acts as a mode filter to remove the cladding mode confined by the beam structure.

The singlemode criterion for SOI rib waveguide with large cross-sectional area was derived by R. A. Soref *et al* [6]: $W/H < 0.3 + r / (1-r^2)^{1/2}$, where W is the rib width, H is the rib height, and r is the ratio of the rib height to the core thickness. For our rib waveguides and rib-beam waveguides, W = 4μm, H = 5μm, and r = 0.6. Therefore, the above singlemode criterion is satisfied.

The fabrication process (Fig. 2) starts with a commercial SOI wafer with an undoped (6-8 Ω-cm), 5μm thick, <100> silicon on top, and a 1μm thick SiO_2 underneath. A 3000Å thermal oxide layer is first grown on the wafer and patterned into an array of 4μm-wide strips along (110) direction by photolithography and buffered HF etching. The rib structure with a 2μm-height is obtained by KOH etching. Owing to the crystal orientation, the side slope of the ribs yields 54.7°, thus resulting in a base width of 6.8μm. The beam structure with beam width of 17μm in the rib-beam cantilever section is obtained by a second photolithography and the RIE silicon etching using photoresist as masking material. The sample is then cleaved into 8mm-long bars with its ends polished. Finally, the SiO_2 underneath the silicon beams is etched by buffered HF.

The waveguide loss at λ=1300nm is measured to be less than 2.4dB/cm. The polarization dependence (between TE and TM) of the loss is less than 5%. The intensity of the TM mode that is coupled into the TE mode or vice versa is less than 0.6%.

The measured intensity profile using an IR camera is shown in Fig.3. In both the vertical and lateral directions, the profile is single lobe in shape. The single lobe shape of the intensity profile implies that the rib-beam waveguide supports predominately the propagation of the fundamental mode in both the vertical and horizontal directions. This profile is found to be identical to that of a conventional rib waveguide that we fabricated with the same rib dimension within 5%. It also agrees well with our simulation result from Beam Propagation Method.

We also using the singlemode movable waveguide as a scanning optical probe to scan over the near field of an optical fiber mechanically in the lateral direction. The result is shown in Fig.4. A mechanical optical switch can also be constructed in this way [2,4].

II. Multimode SOI waveguides with a 60-micron thick single crystal Si core

The second demonstration in this paper is the development of low-loss thick multimode SOI waveguides that has a core size comparable to that of the conventional multimode optical fibers. One of the applications is for multimode optical interconnect.

The SOI waveguides developed previously all have a very thin core layer (less than 20 μm) and are not for suitable for the multimode communication systems. In order to optimize the optical coupling, the core size of the waveguides should be comparable to that of the conventional multimode optical fibers, i.e., at least 50 μm.

The low-loss thick multimode waveguides that we fabricated (Fig.5) consist of a waveguide core (an undoped Si beam) with a trapezoidal cross section on top of a 1 μm thick oxide of a Si wafer. The core thickness ranges from 25 to 60 μm. The top surface of the silicon core is a (100) surface. The width of the top surface ranges from 3 to 60 μm. A simple 4-port waveguide coupler device in a cross-junction form (Fig.5) is also fabricated.

The fabrication process of the waveguides consists of two steps. The first step is to fabricate a Bond-and-Etchback Silicon-On-Insulator (BESOI) wafer [7] for the vertical optical confinement. A 0.5-μm thick thermal oxide layer is first grown on two (100) Si wafers. The two oxidized surfaces of two wafers are then bonded together at 25°C. The bonded pair is then annealed at about 1000°C for 30 min in N_2 . The Si layer on one side of the sandwiched oxide is first chemically etched to a desired thickness in KOH solution. The waveguide can be as thick as the starting wafer, i.e., 500 μm or as thin as less than 1 μm. The etched surface is finally polished using Chemo-Mechanical Polisher.

The second step in the fabrication process is to build a beam structure. A 1500Å thick LPCVD Si_3N_4 film is first deposited on a BESOI wafer and then patterned into masking lines by photolithography and SF_6 plasma-etching. The masking lines have width ranging from 3 to 60 μm and are aligned along <110>. Si waveguide beams with trapezoidal cross-section are then obtained in KOH solution. The two end facets of the waveguides are finally polished mechanically.

We first measure the optical loss (λ=1300nm) of the Si waveguides. For Si waveguides with core thickness ranging from 25 to 60 μm and top width ranging from 3 to 60 μm wide, the waveguide loss is smaller than the uncertainty (0.8dB/cm) involved in our measurement. Therefore, we conclude that the loss is less than 0.8 dB/cm. The near field at the output end of the waveguide is shown in Fig.6.

In order to demonstrate the application of these Si multimode waveguides, we fabricate a simple multimode waveguide coupler device in a cross-junction form (Fig.5). The core thickness are 60 μm. The waveguide channel from A to B has a top width of 60 μm and is aligned with the <110> direction. The waveguide channel from C to D has a top width of 80 μm. The angle of intersection between AB and CD is 2.5°. The results are shown in Table 1. The listed values are the optical power inside the Si waveguides. We assume 31% optical power reflection at the Si/air interfaces.

Input Port	Optical Power (inside input port)	Optical Power (inside port B)	Optical Power (inside port D)	Splting Ratio
Port A	32.4	21.1	3.5	6:1
Port B	34.7	6	7.4	0.8:1

For the case of injecting optical power from port A, the waveguide channel CD serves well as a waveguide tap in which about 11% of the input power is tapped off from the main waveguide channel AB. For the case of injecting optical power from port C, we find that the excess loss is significantly higher.

REFERENCES

[1] R.A.Soref, J.P.Lorenzo, "Silicon guided-wave optics", Solid State Tech. vol.31,pp.95-98 (1988).

[2] R.Watts, A.L.Robinson, R.A.Soref, "Electromechanical optical switching and modulation in micromachined silicon-on-insulator waveguides", IEEE Int.SOI Conf. Proceedings., p.62 (1991).

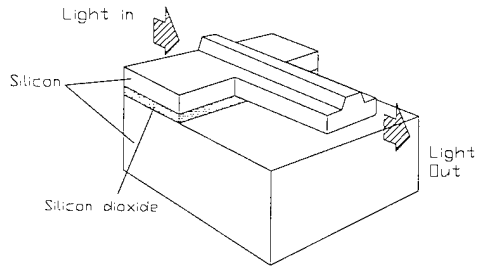
[3] T.T.H.Eng, S.C.Kan, G.K.L.Wong, "Surface-micromachined epitaxial silicon cantilevers as movable optical waveguides on silicon-on-insulator substrates", Sensors & Actuators, A99 (1995).

[4] T.T.H.Eng, S. Y. S. Sin, S. C. Kan, G. K. L. Wong, "Micromechanical optical switching with voltage control using SOI movable integrated optical waveguides", IEEE Photon. Technol. Lett., vol. 7 (1995).

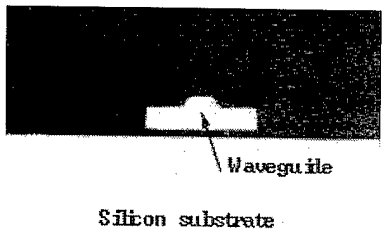
[5] T.T.H.Eng, S.C.Kan, G.K.L.Wong, "Micro-optical Scanning Probe using SOI Movable Waveguides", Paper D-2, Fifth Microoptics Conf., Oct 18-20, Hiroshima, Japan (1995).

[6] R.A.Soref, J.Schmidtchen, and K.Petermann, "Large singlemode waveguides in Ge-Si-Si and Si-on-SiO_2", J. Quantum Electron.,QE-27, pp.1971-4 (1991).

[7] C. Harendt, C. E. Hunt, W. Appel, H. Graf, B. Hofflinger, and E. Penteker, "Silicon on insulator material by wafer bonding", J. Electronic Materials, vol. 20, pp. 267-277 (1991).



(a)



(b)

Fig.1 (a) Singlemode Rib-Beam Cantilever Waveguide (b) Cross-Section

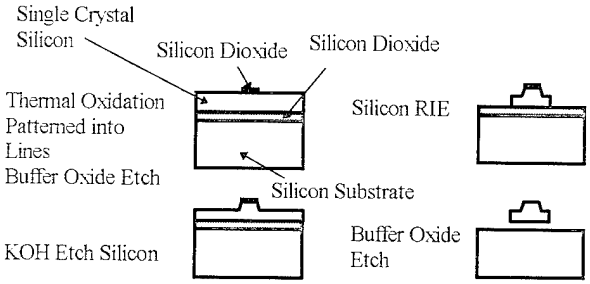


Fig. 2 Fabrication Procedure

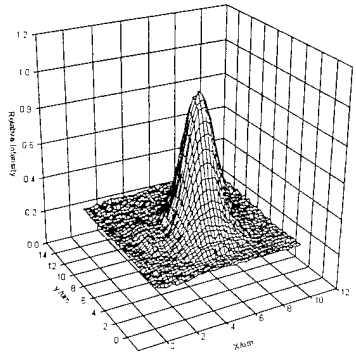


Fig. 3 3-D Intensity profile

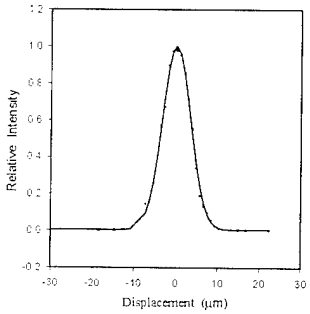


Fig.4 Collected Power vs. Displacement

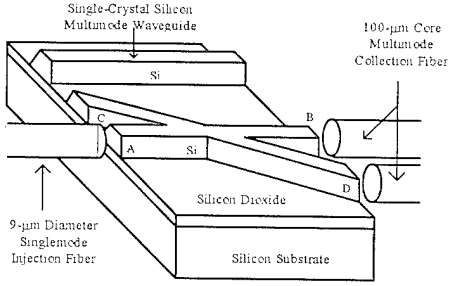
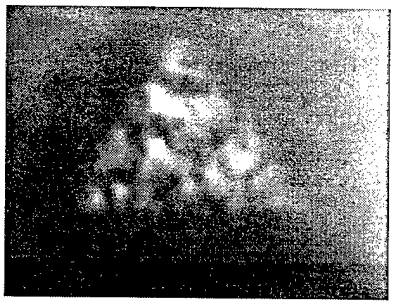


Fig.5 Thick Multimode SOI Waveguide Devices



(a)



(b)

Fig.6 Near Field at the Output End of Multimode SOI Waveguide (a) Singlemode Fiber Input (b) Multimode Fiber Input.

Optical Waveguides and Components Based on Porous Silicon

H Arrand, T M Benson, T Anada: Department of Electrical and Electronic Engineering, University of Nottingham, Nottingham NG7 2RD, UK

M Krueger, M G Berger, R Aren-Fischer, H G Munder H Luth: Forschungszentrum Jurlich GmbH, D-52425, Jurlich, FRG

A Loni, R J Bozeat: Defence Research Agency, St Andrews Road, Malvern, Worcestershire WR14 3PS, UK

Introduction

Porous silicon offers many potential advantages for the realisation of optoelectronic circuits and systems. Foremost is the demonstration of photoluminescence [1] and solid state electroluminescent devices [2,3] which, when married with silicon based photodetectors and the well established electronic fabrication processes, has opened up the possibility for the realisation of monolithic all-silicon optoelectronic integrated circuits (OEIC's). Another important feature is the ability to selectively produce insulating regions in CMOS circuitry by converting the porous silicon to silicon dioxide by oxidation. Oxidation of porous silicon also provides a new route to the realisation of the basic building block for all optoelectronic circuits - the optical waveguide.

The refractive index of porous silicon varies widely with the porosity of the material [4,5] which can, in turn, be varied controllably [6]. Subsequent oxidation offers the designer an extra degree of freedom and may be advantageous since the optical properties of as-prepared porous silicon material have been shown to vary with time [7]. Porous silicon material thus provides great flexibility for the realisation of waveguides and derived devices such as splitters and couplers. In this paper we describe the design, fabrication and testing of planar and single mode rib optical waveguides in porous silicon materials and, by using the illustrative example of a Y-junction splitter, show how, once this base waveguide technology is established, systems components for optoelectronic integrated circuits (OEIC's) can be readily realised. Importantly these devices do not resort to the epitaxy or implantation processes which were a feature of previous porous silicon based waveguide designs [8] and therefore offer significant processing and cost advantages.

Formation and Testing of Planar (Slab) Waveguides

To produce a planar optical waveguide it is necessary to form a region with a refractive index which is higher than that of its surroundings. In the case of porous silicon layers on a silicon wafer a low refractive index buffer layer of sufficient thickness is required to isolate the waveguiding region optically from the high refractive index substrate.

Bondarenko and co-workers [9] reported the formation of optical waveguides in silicon wafers which were masked before anodization and subsequently oxidised. We have extended this work to oxidised porous silicon layers which were prepared from p^+ substrates of resistivity 5-15 mΩcm, by anodising with a uniform current of 30 mAcm^{-2} and a 20% ethanoic HF solution, to produce a 5μm thick layer of nominal uniform porosity 54%. Planar optical waveguiding was observed in the resulting structure at both 0.633 μm and 1.28 μm wavelengths. The TE mode power attenuation coefficient, measured using a cut-back method, at the visible

wavelength was around 0.8 cm^{-1}. Prism coupling measurements confirm the presence of two guided TE modes (with effective indices 1.4554 and 1.4513) and one guided TM mode (with effective index 1.4551) at this wavelength. At 1.28 μm wavelength the waveguide was observed to be leaky and the power attenuation coefficient evaluated was over 5 cm^{-1}. The waveguide formation mechanism in these structures is not clear. Ellipsometry measurements at 0.633 μm suggest the presence of a layer of higher refractive index approximately 0.5 μm thick near the surface of the wafer but these predictions are not consistent with a measured full width half intensity beam width of approximately 4μm nor the measured effective refractive indices.

Multi-layer slab waveguides can be also be produced by using the variation of microscopic structure and in particular porosity with anodization current density [5]. In these structures the porosity can be controlled and refractive index predicted from porosity using a Bruggeman approximation. The relationships obtained for the samples produced under the present study, based on (100) p-type silicon (0.2 Ωcm), are shown in Figure 1. By changing current density abruptly during the anodization process three-layer slab waveguides comprising a waveguiding layer of 62% porosity sandwiched between upper and lower cladding layers of porosity 75% were produced. Two samples were produced, the first with a guiding layer thickness of 0.5 μm and the second with a guiding layer thickness of 2 μm. In the as-prepared state these exhibited (lossy) waveguiding at 1.28 μm but after subsequent oxidation for 2 hours at 870 °C losses were substantially reduced and waveguiding also observed at visible wavelengths.

SEM studies of the layered waveguide structure reveals that the interface between the guiding and cladding porous silicon layers shows a roughness with an amplitude of 50-100 nm. This is known to give rise to unwanted scattering loss and in an attempt to reduce this a slab waveguide having a graded refractive index was designed and fabricated.

The planar waveguide with graded index profile, which will function at 633 nm after oxidation and which can be subsequently etched to form strip loaded waveguides with additional lateral confinement, was designed. For oxidised porous silicon we again estimate refractive index using a Bruggeman approximation. The design refractive index profile chosen for the oxidised structure was $n = 1.17 + (0.0859/(\cosh^2(3.89x))$ for $-0.3 \leq x\ \mu m \leq 0.5$. Here the origin is taken to be the centre of the guiding region [10]. A uniform upper cladding region of measured refractive index 1.449 and thickness 0.5 μm (which can be subsequently etch to form a strip load) and a lower cladding of refractive index 1.373 and thickness 6.3 μm (the optical buffer) were also incorporated in the wafer prepared. The as-prepared wafer showed lossy waveguiding at 1.28μm and, as with the three layer slab waveguide, waveguiding was extended to visible wavelengths and losses were substantially reduced following oxidation.

Processing and Testing of Strip Loaded Waveguides

In order to demonstrate practical devices for OEIC's it is required to provide waveguides with additional lateral confinement. This may be conveniently achieved in the (oxidised) porous silicon multi-layers by partially etching the upper cladding layer to provide strip loaded waveguide structures. When defining a strip load it is usual to define an etch mask photolithographically followed by a wet or dry etch process. It was found, however, that porous silicon reacted with our photoresist developer. In order to overcome this, the as-prepared wafers were coated with a 50nm layer of silicon nitride by PECVD at 300 °C. The nitride layer and strip load waveguides were patterned by reactive ion etching with Freon 14 + 8-12% O_2 to a total depth of 0.5 μm. Waveguides for visible wavelengths were prepared by

subsequent oxidation at 800 °C in air for 80 minutes. Waveguide widths of between 2 and 100 μm were studied. Waveguides with smaller widths (typically below 6μm) were found to be single-moded in agreement with theoretical predictions. Losses measured were similar to those found for the equivalent planar structures.

Study of Y-Junction Splitters

Using the basic strip-loaded waveguides functional devices can be realised. This is illustrated using Y-junctions. A set of Y-junctions having waveguide widths 2, 3, and 4 μm, a range of initial separation angles 5°, 10° or 15° (relatively large in a OEIC context) and which followed sine curves to separate the output waveguides to a distance of 50 μm were fabricated. Figure 2 shows the output near field intensity pattern measured for an oxidised sample with 3 μm wide guides and an initial separation angle of 10°. All configurations show the expected splitting performance and detailed work is underway to understand how curvature and fabrication tolerance contribute to additional losses observed experimentally.

Conclusion

Porous silicon continues to emerge as an important and versatile material for electronic and optoelectronic applications. In this paper we have demonstrated that planar optical waveguides operating over a range of wavelengths can be readily produced in these materials without recourse to epitaxy and therefore at low cost. Subsequent standard processing effects the fabrication of single mode rib waveguides with additional lateral confinement. These form the basic building blocks of functional elements for optoelectronic circuits.

Acknowledgement

The authors acknowledge the contributions to this study made by D F Clark and G Hill.

References

[1] Canham LT, "Silicon quantum wire array fabrication by electrochemical and chemical dissolution of wafers", Appl Phys Lett, 57[10], 1046-1048, 1990.

[2] Kalkhoran NM, "Porous silicon-based optoelectronic devices: processing and characterization", Mat Res Soc Symp Proc, 283, 1993.

[3] Loni A, Simons AJ, Cox TI, Calcott PDJ, Canham, LT , "Electroluminescent porous silicon device with an external quantum efficiency greater than 0.1% under CW operation", Elec. Lett, 31, 1288, 1995.

[4] Badoz PA, Bensahel D, Bomchil G, Ferrieu F, Halimaoui A, Perret P, Regolini JL, Sagnes I and Vincent G, "Characterization of porous silicon: structural, optical and electrical properties", Mat Res Soc Symp Proc, 283, 97-108, 1993.

[5] Loni A, Berger MG, Arens-Fischer R, Munder H, Luth H, Arrand H and
Benson TM, "Optical waveguide properties of porous silicon multilayers", to be published in Thin Solid Films.

[6] Berger MG "Formation and properties of porous silicon superlattices" Mat Res Soc Symp Proc, Fall meeting, 1994.

[7] Canham LT, Houlton MR, Leong WY, Pickering C and Keen JM, "Atmospheric impregnation of porous silicon at room temperature", J Appl Phys, 70[1], 422-431, 1991.

[8] Loni A, Bozeat RJ, Krueger M, Berger MG, Arens-Fischer R, Munder H, Luth H, Arrand H and Benson TM, Application of porous silicon technology to optical waveguiding, IEE Colloquium on Microengineering Applications in Optoelectronics, 27th Feb, 1996 (submitted).

[9] Bondarenko VP, Varichenko VS, Dorofeev AM, Kazyuchits NM, Labunov VA and Stel'makh VF, "Integrated optical waveguide fabricated with porous silicon", Tech Phys Lett, 19(7), 463-464, 1993.

[10] Kogelnik H "Theory of optical waveguides' in T Tamir (ed) "Guided-wave Optoelectronics", Springer-Verlag, 2nd edn 1990, p52.

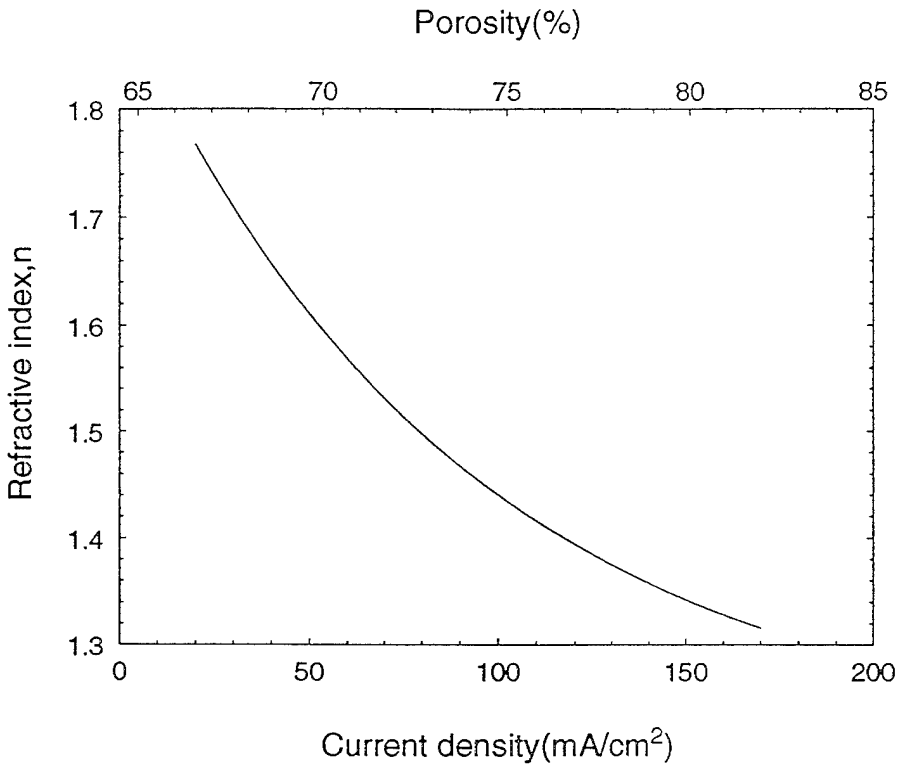


Figure 1: Refractive index of porous silicon prepared form 0.2 Ωcm p-type silicon wafer in 1 HF: 1 H_2O:2 C_2H_5 OH electrolyte, as a function of anodisation current density and porosity.

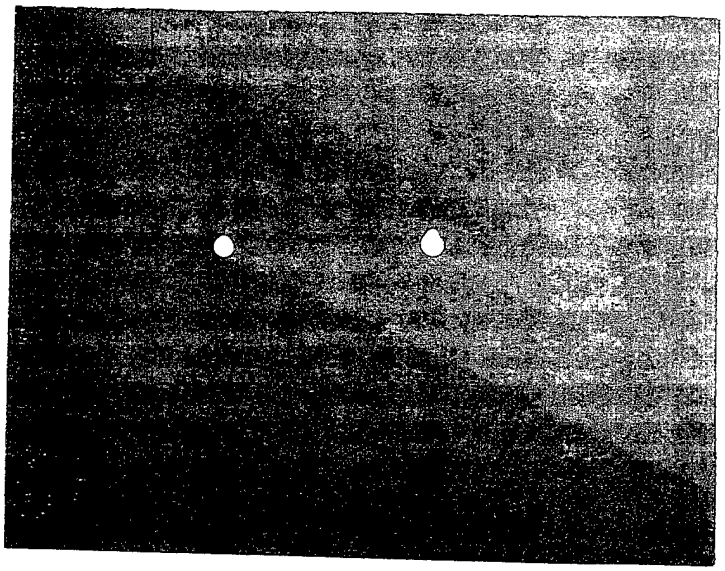


Figure 2: Near-field output at wavelength 0.633 μm from an oxidised porous silicon Y-junction formed using 3μm wide guides. The output guide separation is 50 μm.

Diffraction Patterns of Si-based Polygonal Grating for 1-to-many Optical Interconnects

Oleg Ershov, Feiming Li, Michael Dubinovsky, Ray T. Chen
Microelectronics Research Center
Department of Electrical and Computer Engineering
University of Texas at Austin
Austin, TX 78758
Phone: (512)4717035 Fax: (512)4718575

With the advent of higher clock speeds and distributed multiprocessor computer architectures, a great deal of interest has arisen in synchronously distributing a clock signal over all the processors in a computer with an acceptable clock skew [1]. Unfortunately, at clock speeds above 500 MHz, a synchronous global clock distribution system is very difficult to attain using electrical interconnects due to their inherent limitations. Because of the high bandwidth capability in optical signals, various guided wave optical clock distribution schemes have been investigated to alleviate such a problem. Photopolymer-based multiplexed volume holograms [2], surface relief gratings working at different diffraction orders [3] have been employed to achieve massive fanouts. However, due to the nature of non-multiplexibility, a surface relief grating is primarily employed as 1-to-1 interconnect device with relatively low interconnectivity [4]. For 1-to-many fanout optical interconnects employing surface relief material with a single fanout node, a new device configuration is needed to solve this problem.

Polygonal grating structures for optical clock signal distribution have been investigated recently [5,6]. These authors demonstrated specific advantages of free space optical interconnects using diffractive optical elements. A suitable packaging of these structures provides the desired optical clock signal distribution while a high diffraction efficiency is maintained. On the other hand some papers are dedicated to study Gaussian beam diffraction from planar gratings [7-9]. The objective of this paper is to address the diffraction patterns observed in various 1-to-many fanouts using polygonal planar grating structures with Gaussian beams as the input light sources.

We outline in Figures 1(a) and 1(b), respectively, the experimental setup and the three dimensional (3D) view of the detailed structure of the Si-based 1-micron period input/output grating couplers. The input coupler is a square grating, containing four triangular gratings with grating vectors perpendicular to the adjacent ones, while the output couplers are four linear gratings apart from the input grating. All surface relief gratings were etched into the Si wafer by techniques described early [6]. A SEM photograph of the microstructure of the fabricated square grating is illustrated in Fig.2. In the experimental scheme, 1.3 μm semiconductor laser beam after the spatial filtration and expansion had a diameter of 6 mm and the full divergent angle of 0.34×10^{-3} rad. After focusing by a lens with a focal length of 100 mm, the laser beam was coupled surface-normally into Si-substrate by the square grating coupler containing four triangular gratings. Four surface-normal fanout beams were observed. The square grating converted surface-normal incoming beam into four substrate guided waves which zig-zagged along four phase-matching directions. The four fanout beams were picked up by four output gratings. These four surface-normal output beams were detected by Vidicon camera together with a laser beam analyzer (LBA). The micro-objective lens M served to enlarge the observed image and to enhance the LBA measurement resolution.

The zig-zag beam path in the Si substrate is governed by grating diffraction theory and total internal reflection (TIR), which is displayed in Fig.3. Here, only the two corresponding triangular gratings which diffract the input clock signal beam to the indicated direction are plotted. For the considered case with an 1 micron grating period, the angle of the first diffraction order is calculated

to be $\theta_1 = 21.8^0$, larger than the critical angle θ_c of TIR in Si substrate ($\theta_c = 16.6^0$). The whole zig-zag propagation beam path was estimated to be about 15 mm. As we can see, for each pair of the polygonal gratings shown in the left top of the sketch (Fig.3), two diffraction spots should be observed along the surface normal direction. The double-spot appearance is due to the two 1st order diffractions activated by two oppositely-structured triangular gratings. This conclusion is confirmed by the observations described below and should be valid for any polygonal structures with an even number of triangle grating facets .

In order to further investigate the observed results, we performed theoretical calculation on the diffraction patterns equivalent to the experimental setting. There are two processes that result in the diffraction patterns observed. The first is the grating diffraction which is controlled by the required phase-matching condition and the second is the diffraction pattern generated by finite apertures which are defined by the triangular segments affiliated with the polygonal gratings. From the point of view of optoelectronic interconnects, both effects are pivotal in system design. The direction defined by the grating diffraction determines the precise location of fanout beams while the aperture-related diffraction patterns dictate the effective area of the photodetector to be implemented.

Because the aperture size is much larger than the wavelength, we used only scalar diffraction approach. We also assumed that output beam shape is independent of the polarization states of the incident beam. The aperture of one pair of the triangular gratings with opposite facets locate in the plane defined by (ξ, η). Consider an incident Gaussian beam propagates along z direction with low divergence; the paraxial approximation can be used. The diffraction pattern u(x,y,z) in the image plane (x, y) derived from Fresnel integral [10] is given by:

$$u(x,y,z) = \frac{i}{\lambda z}\iint_{\Omega} u(\xi,\eta,0)\exp\{-i(k/2z)[(x-\xi)^2+(y-\eta)^2]\}d\xi d\eta \qquad (1)$$

where $u(\xi,\eta,0)$ is the wave field within the double triangular apertures (z=0), k is the wave vector, and Ω is the effective aperture area.

The normalized surface-normally incident TEM_{00} Gaussian beam is characterized at the aperture plane by the expression:

$$u(\xi,\eta,0) = \exp[-(\xi^2+\eta^2)\beta] \qquad (2)$$

where

$$\beta = \frac{1}{w^2} - \frac{ik}{2R}, \qquad w^2 = w_0^2[1+(\lambda z_0/\pi w_0^2)^2], \qquad R = \frac{z_0^2 + (\pi w_0^2/\lambda)^2}{z_0}.$$

Here, w is the beam width at any distance z; z_0 is the distance from the aperture plane to the beam waist w_0, and R is the radius of the spherical wave front .

If the beam waist is located at the aperture plane, we have:

$$u(\xi,\eta,0) = \exp[-(\xi^2+\eta^2)/w_0^2] \qquad (3)$$

Substituting Equations (2) and (3) into Equation (1), we obtain the Fourier-transformation that is used for our simulations:

$$u(x,y,z) \approx \frac{\exp[-\pi i(x^2+y^2/\lambda z)]}{z} F_{x/\lambda z, y/\lambda z}\{\exp[-(\xi^2+\eta^2)(\beta + i\pi/\lambda z)]\} \qquad (4)$$

In equation (4), $F_{\alpha,\gamma}\{f(\xi,\eta)\}$ is defined by:

$$F_{\alpha,\gamma}\{f(\xi,\eta)\} = \iint_{\Omega} f(\xi,\eta)\exp[-2\pi i(\xi\alpha+\eta\gamma)]d\xi d\eta$$

For diffracted field calculation, we use a known fast Fourier transform (FFT) method delineated in [11].

The calculated output diffraction pattern for an image planes at z=5mm is shown in Fig.4. Fig.5a shows the 3D experimental pictures of diffracted beam profiles in the near field ($z \approx 5mm$) from 1 micron grating, for 100 mm focused incident beam. The parameters used in the calculation (Fig.4) were the same as those used in measurement in Fig.5a. Apparently they are in excellent agreement. In Fig.5a we see two diffraction spots limited by the aperture of output rectangular grating with a lateral size of 0.3 mm. This demonstrated image structure was observed for all four surface-normal fanout beams. We also used an output couple prism instead of an output grating to directly couple out the guided wave. The prism was placed between the input square grating and output rectangular grating and the distance from it to the input grating can be adjusted from 1 mm to about 5 mm. The resulting output beam profile is shown in Fig.5b, which is similar to Fig.5a and in good agreement with calculation. The peaks are broadened because the image was taken about 5 mm after the prism surface and the actual path was longer.

In conclusion, we demonstrated in this paper the fanout beam profiles in the proposed optical clock signal distribution scheme using Si-based polygonal grating couplers. Double diffraction spots occurred for a polygonal grating with an even number of grating facets. This effect is further confirmed by the scalar diffraction theory.

This research is sponsored by ONR, ARPA and Radiant Reaserch, Inc..

References:

1. S.Koh, H.Carter, J.Boyd, Opt.Eng., v.33, no.5, p1587, 1994.
2. Suning Tang, Ray T.Chen, Appl.Phys.Letters, v. 66, no.22, p.2931, 1994.
3. S.Walker, J.Jahns, L.Li, et al., Appl.Opt., v.32, no.14, p.2494, 1993.
4. J.Morris, M.Feldman, W.Welch et al., Proc.SPIE, v.1849, p.48, 1994.
5. H.Zarschizky, C.Gerndt, A.Steammer, H.Schneider, SPIE Proc., v.1732, p.297, 1992.
6. L.Graham, O.Ershov, S.Tang, R.Chen, Proc. SPIE, v. 2400, p.140, 1995.
7. R.Chu, JOSA, v.66, No.3, p.220, 1976.
8. L.Li, M.Gupta, Appl. Opt., v.29, No.36, p.5320, 1990.
9. E.Kriezis, P.Pandelakis, A.Papagiannakis, JOSA. v.A11, No.2, p.630, 1994.
10. H.Haus, "Waves and Fields in Optoelectronics", Prentice-Hall, 1984.
11. D.Dudgeon, R.Mersereau, "Multidimensional digital signal processing", Prentice Hall, 1984.

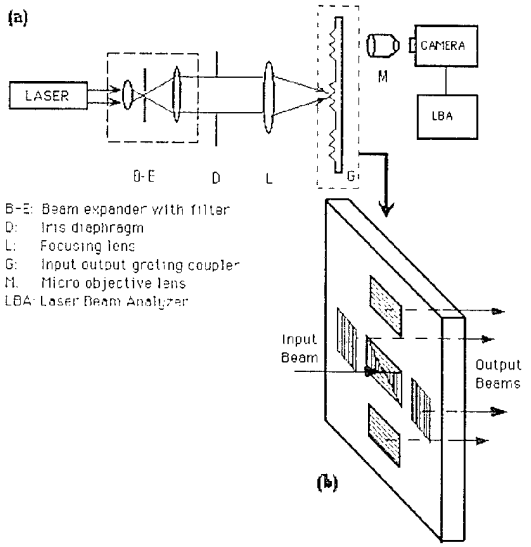


Fig.1. (a) Experimental setup. (b) Structure of input/output grating coupler.

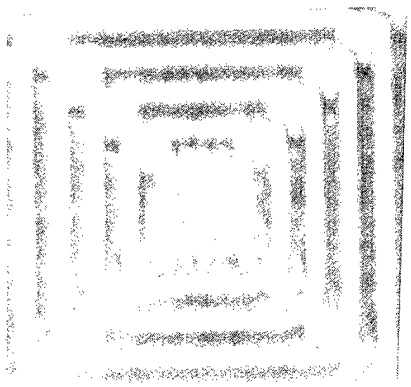


Fig.2. SEM photograph of the square grating structure.

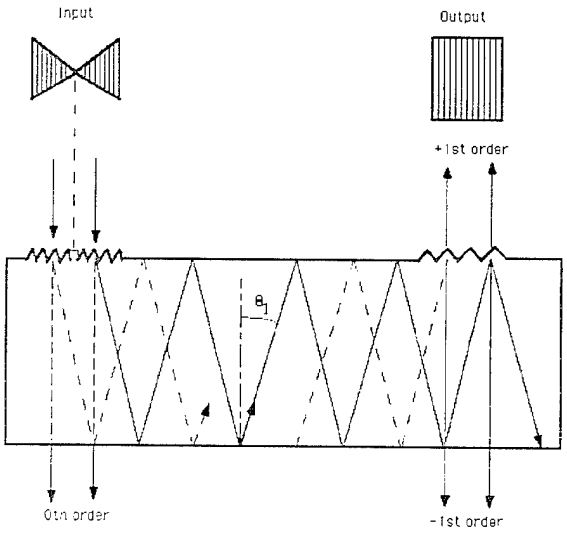


Fig.3. Beam path in Si substrate.

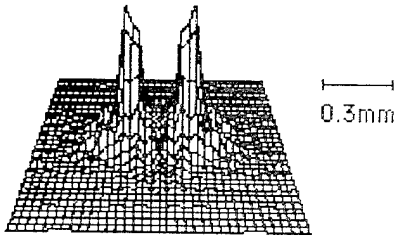


Fig.4. Calculated 3D image of diffracted beam profile when z=5mm. 100mm incident beam

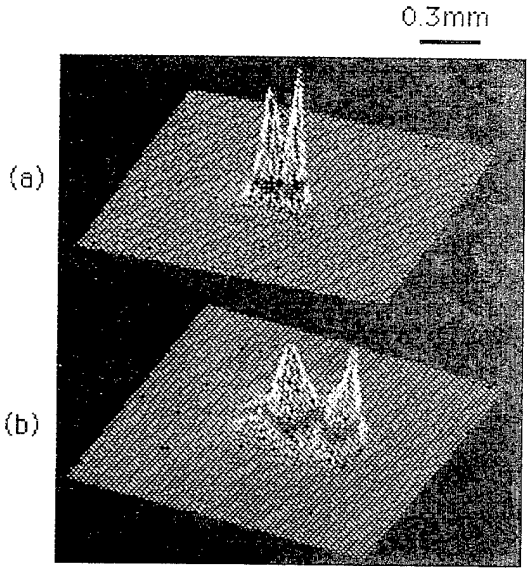


Fig.5. 3D pictures of double-spot diffracted beams by 1-micron grating.
(a) coupled out by grating.
(b) coupled out by prism.

Electro-optic switch constructed with a poled silica-based waveguide on a Si substrate

Makoto ABE, Takeshi KITAGAWA, Kuninori HATTORI, Akira HIMENO and Yasuji OHMORI

NTT Opto-electronics Laboratories
Tokai, Naka-Gun, Ibaraki, 319-11 Japan
TEL +81-29-287-7402
FAX +81-29-287-7871
E-mail abem@nttiba.ntt.jp

I. Introduction

Low-loss silica waveguides on silicon are used to produce a variety of planar lightwave circuits (PLCs), including optical splitters, thermooptic switches, filters and routers, which are useful devices for constructing optical communication networks [1]. The introduction of the high-speed optical effect into silica-based waveguides will extend the possible PLC functions with a fast switching operation.

Recently, considerable interest has been shown in applying the linear electro-optic effect in poled silica-based glass to optical devices. Although electro-optic phase modulation has been observed in poled silica with bulk, fiber and planar waveguide geometries [2]-[7], no integrated intensity modulators or switches have yet been reported. It is important to developed integrated waveguide devices and also to understand the mechanism of the electro-optic effect, which exhibits electro-optic coefficients scattered over a wide range between 0.002 [2] and 6pm/V[6][7].

In this paper, we report successful 2x2 electro-optic switching in thermally poled GeO_2-doped silica-based channel waveguides on Si which we achieved by using an integrated Mach-Zehnder interferometer (MZI) configuration.

II. Experimental

An MZI, which was composed of two 3dB-directional couplers and two waveguide-arms with the same length was constructed with GeO_2-doped silica-based channel waveguides on a Si substrate. One waveguide-arm of the MZI included an electro-optic phase shifter. The layout of the waveguide MZI and the phase shifter cross section are shown schematically in Fig. 1 (a) and (b), respectively. The MZI was fabricated by flame hydrolysis deposition (FHD) and reactive ion etching (RIE) techniques [1]. The 7 μm square core was formed using GeO_2-doped silica glass with a refractive index 0.7% greater than that of the silica cladding. The 36 cm- long

phase shifter was equipped with two electrodes; one was a Au thin film electrode formed on one waveguide-arm of the MZI and the other was a Si substrate with a low resistivity. The glass between the two electrodes was 36 μm thick. The gap between the Au thin film electrode and the core was 9 μm. The size of the integrated MZI on the Si substrate was 75 mm x 60 mm. In order to induce the electro-optic effect, the silica-based waveguide in the phase shifter was thermally poled at 300 °C by applying a voltage of 4 kV between the electrodes for 2 hours.

After the poling process, we measured the MZI transmission characteristics at a wavelength of 1.55 μm by applying a voltage between the electrodes. 1.55 μm light from a laser diode was introduced into the MZI by a polarization maintaining fiber through a polarizer. The output light from the MZI was detected with a photodiode through a single mode fiber.

III. Results and Discussion

Figure 2 shows the TM-polarized output powers against the applied voltage. The open and closed circles represent the output optical power from output port 1 (through port) and output port 2 (cross port), respectively. Output port switching was observed at a switching voltage of 1700 V. The extinction ratio and the loss were 20 dB and 4 dB, respectively. The sinusoidal relationship between the output powers and the applied voltage indicates that the optical phase shift was caused by the linear electro-optic effect. The optical phase shift of the MZI can be described by

$$\Delta\phi = 2\pi \frac{\eta \frac{1}{2} r\, n_e^3 \frac{V}{d} L}{\lambda}$$

where $\Delta\phi$ is the shift of the optical phase in the MZI, r is an electro-optic coefficient, n_e is the effective refractive index of the core, V is the applied electrical voltage of the glass layer, d is the thickness of the glass layer, L is the interaction length, that is the Au thin film electrode length, η is the spacial overlap factor between the poled region and the waveguide mode, and λ is the measurement wavelength. Assuming the value of the overlap factor η to be 1, the electro-optic coefficient estimated from the MZI optical response in the TM mode is 0.02 pm/V. This value is in the range of the reported electro-optic coefficients. The weak electro-optic effect may be due to the high quality of the GeO_2-doped silica formed by FHD which contains very few impurities or defects, since the nonlinearity is thought to originate from charge migration or the dipole orientation in the glass [8].

Figure 3 shows the switching response of the MZI when a pulsed voltage of 100 V was applied. The upper and lower lines represent the applied voltage and the MZI output power, respectively. The rise and fall times of the output light were both shorter than 100 ns. This response is similar to the temporal change of the driving voltage. High speed switching over 1 order of magnitude faster may be possible by reducing the RC constant.

The thermal stability of the electro-optic coefficient was examined in the poled waveguide. The waveguide was heat treated for periods of 30 minutes at successively higher temperatures with an interval of 100 °C. The measured electro-optic coefficients are shown in fig. 4. No reduction was observed in the electro-optic coefficient after 30 minutes annealing at 300 °C. The electro-optic coefficient decreased to 50 % of its initial value at a temperature of 400 °C.

IV. Conclusion

Electro-optic switching in a GeO_2-doped silica integrated waveguide MZI on Si was demonstrated for the first time. The switching voltage was 1700 V in the 1.55μm wavelength region with an extinction ratio of 20 dB. The switching response time was less than 100 ns. Improvement in the electro-optic coefficient to the maximum value reported for GeO_2-doped silica fiber [6]-[7] will reduce the length-voltage product by a factor of more than 100 and will extend the possible PLC applications, which will be useful for constructing optical communication networks.

References

1. M. Kawachi, Opt. Quantum. Electron., **22**, 2106 (1990).

2. L. Li and D. N. Payne, IGWO '89, 130 (1989)

3. A. C. Liu, M. J. F. Digonnet, and G. S. Kino, Opt. Lett. **19**, 466 (1994).

4. X.-C. Long, R. A. Myers, and S. R. J. Brueck, Electron. Lett. **30**, 2162(1994).

5. P. G. Kazansky, P. St. J. Russel, L. Dong, and C. N. Pannell, Electron. Lett. **31**, 62 (1995).

6. T. Fujiwara, D. Wong, Y. Zhao, S. Fleming, S. Poole, and M. Sceats, CLEO /Pacific Rim '95, **FE5**, 177 (1995).

7. T. Fujiwara, D. Wong, Y. Zhao, S. Fleming, S. Poole, and M. Sceats, Electron. Lett. **31**, 573 (1995).

8. P. G. Kazansky and P. St. J. Russel, Opt. Comm., 110, 611(1994).

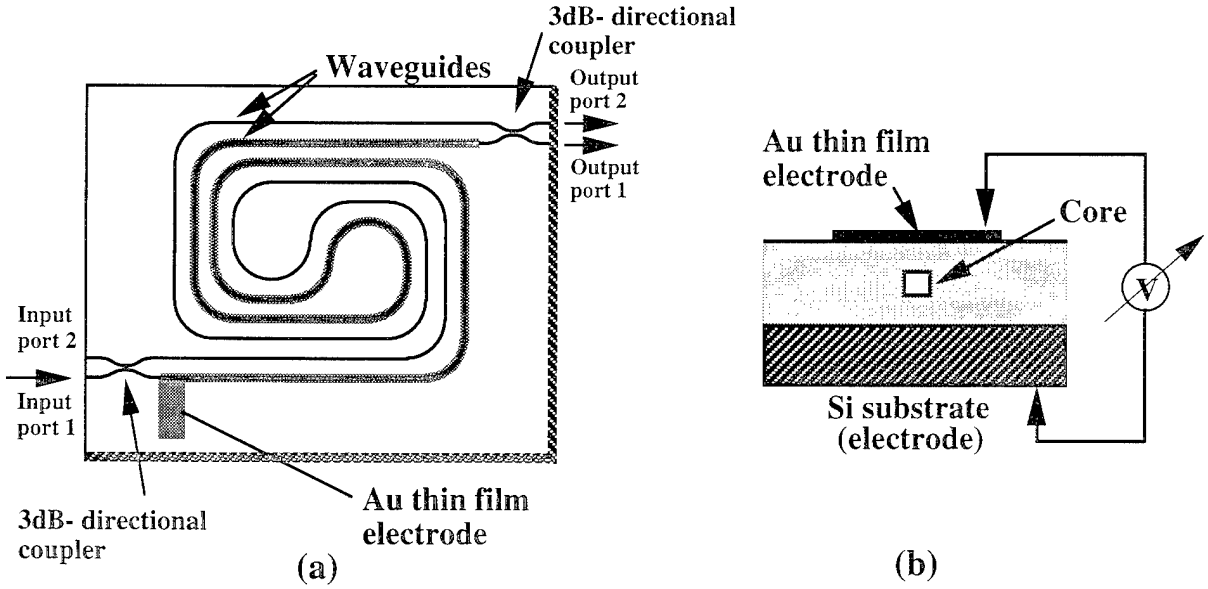


Figure 1 A silica-based waveguide Mach-Zehnder interferometer on Si with a phase shifter (a) schematic layout of the MZI (b) cross sectional view of the phase shifter

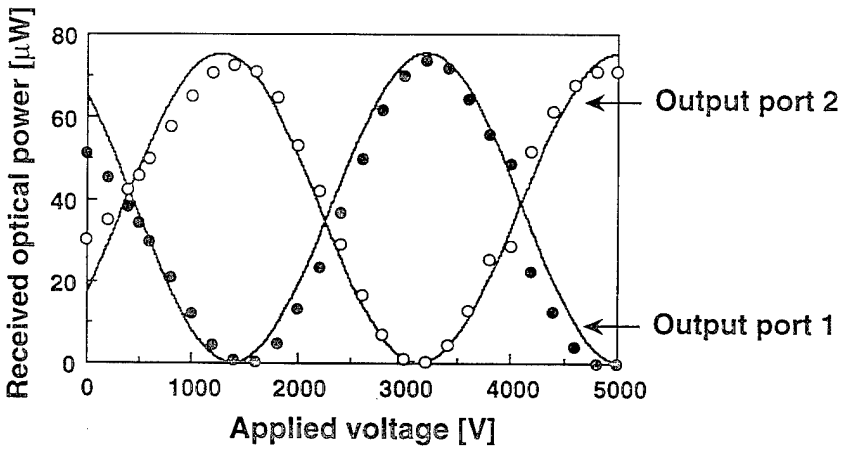


Figure 2 The MZI output powers vs the applied voltage. The open and closed circles represent the output optical power from output port 1 and output port 2, respectively.

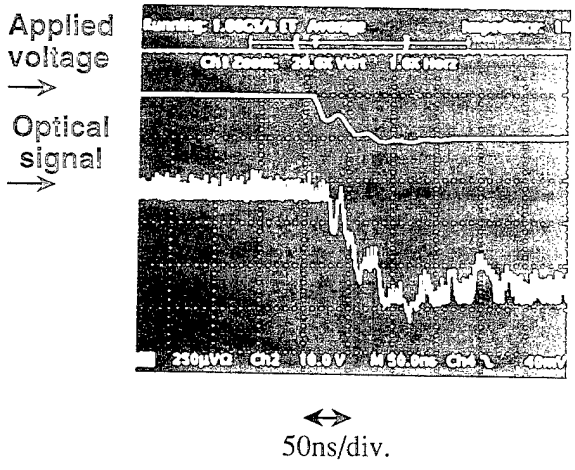


Figure 3 The temporal response of an MZI driven with a pulsed voltage

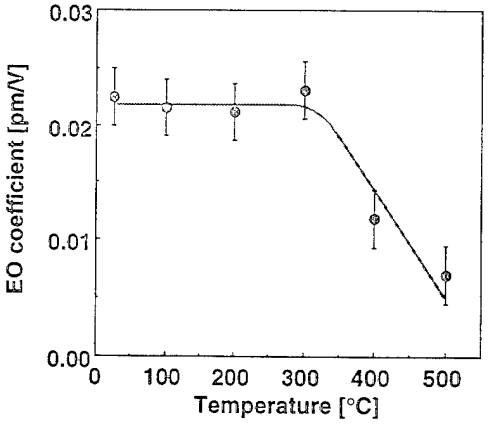


Figure 4 The EO coefficient vs. annealing temperature

Tuesday, April 30, 1996

Symposium on Simulation of Quantum Well Phenomena: Device Applications—Transverse Modes in Vertical Cavities

ITuE 1:30 pm-3:00 pm
Fairfax A

Joseph P. Donnelly, *Presider*
MIT Lincoln Laboratory

Modeling of photon localization in one- to two-dimensional arrays of coupled vertical cavity lasers

Harald Pier

Tel.: +41 21 693 5483
Fax: +41 21 693 5480

Eli Kapon

Tel.: +41 21 693 3388
Fax.: +41 21 693 4525

Institute of Micro- and Optoelectronics
Department of Physics
Swiss Federal Institute of Technology (EPFL)

CH - 1015 Lausanne (SWITZERLAND)

Introduction

Photonic lattices in the optical wavelength regime can be experimentally realized by periodically modulating the reflectivity of the top mirror of a broad area vertical cavity surface emitting laser (VCSEL) structure. Each lattice element is represented by a lasing pixel whose cavity is defined by locally enhancing the mirror reflectivity using, e.g., etching [1] or metal layer deposition [2]. The sizes of such mirror elements are of the order of a few μm. Diffraction at the mirror edges then leads to an overlap of the electromagnetic fields of adjacent lasers. Due to this coupling among the array elements, a band of array "supermodes" is formed.

Electrically pumped, patterned mirror VCSEL arrays have been demonstrated, and showed a superior spatial coherence as compared with broad area VCSELs [3]. They exhibit a high degree of supermode selectivity, due to the difference in cavity losses of the various array modes. Furthermore, the spatial coherence was greatly improved in two dimensional (2D) arrays as compared with 1D arrays [4] of such lasers. This was attributed to a reduced degree of photon localization, caused by inadvertent fluctuations in refractive index across the array, as the array dimensionality is increased from 1 to 2.
This dependence of photon localization on dimensionality is considered in detail in the present paper. We present results of modeling of such photonic lattices, and establish quantitatively the impact of disorder on the localization for one-, two- and fractal-dimensional arrays.

The Model

Our simulations are based on coupled mode theory [5], which successfully simulates the experimental near- and far-fields of patterned mirror VCSEL arrays [2]. Each laser is represented by a 2D waveguide mode (propagation constant β_i) placed at a given site on a square lattice, and the optical coupling is represented by the coupling coefficients κ_{ij}. The dimensionality of the array is varied either by adding rows to a 1D structure or by using fractal lattices (with a finite fractal depth). Disorder effects are modeled by choosing different distributions of β_i across the array. We study the simplest case of a single optical "impurity", where all β_i are identical except for the impurity site, for which $\beta_{imp} = \beta_i + \Delta\beta$, as well as random disorder distributions. The array supermodes are evaluated by finding the eigenvectors and eigenvalues of the coupling matrix $\boldsymbol{M}$ of size QxQ (Q being the total number of lasers), with diagonal elements β_i and off-diagonal elements κ_{ij} [5, 6].

The photon localization effects are studied by investigating the near field patterns as well as the localization length L_{loc} associated with the decay of the supermode envelope due to the disorder. For the case of a single impurity, this length is defined by the distance from the impurity position (measured in lattice constants), for which this envelope drops by a factor of 1/e:

$$\frac{E(L_{loc})}{E_{imp}} = \frac{1}{e}$$

Another useful measure of the degree of localization is the far-field distribution, which is proportional to the Fourier-transform of the supermode near-field distribution. In particular, we use the full width at half maximum (FWHM) of the far-field lobes as a representative parameter of the localized mode.

Results

The near-field intensity distributions of the fundamental supermode in several (Mx25) arrays

containing a single optical impurity are shown in Fig. 1a. The position of the impurity is indicated by the arrow. This system describes, e.g., an inadvertent defect in an otherwise perfectly uniform VCSEL array. Starting from a 1D-system (M=1), we observe a strongly localized mode near the impurity site. On adding rows, the supermode gradually delocalizes and becomes nearly completely delocalized for the 2D (25x25) array case. This decreasing degree of localization results from the larger effective coupling among elements due to the availability of more coupling routes in a 2D system. However, the localization effect is strongly position dependent, as shown by the near-fields for the two different impurity sites in figure 1a,b (8x25). The boundary conditions result in a smaller impact of an impurity located near the array edge.

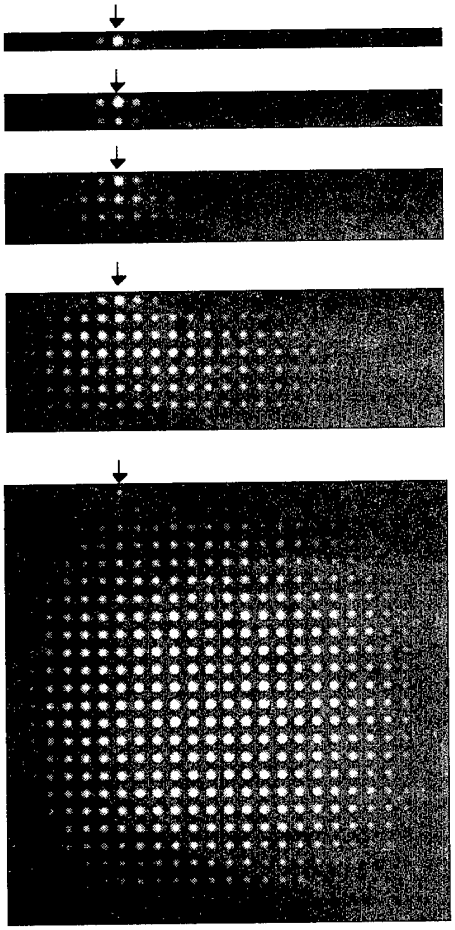


Figure 1a: *Near field intensity plots of 1x, 2x, 4x, 8x, 25x25 arrays with impurity $\Delta\beta = 2\kappa$ at position (1, 7), marked with an arrow.*

Similar simulations of the near-field localization for the different supermodes in the presence of array disorder show that the modes localize at different parts of the array, depending on their propagation constants; the supermodes with the higher propagation constants localize at areas characterized by larger (local) values of the effective index.



Figure 1b: *Same for 8x25, impurity position (4,7).*

The localization lengths for the fundamental supermode for Mx25 arrays with single impurities are plotted in Fig. 2 as a function of the number of array rows M. The impurity site is kept at the center of the array, and three cases with increasing effective perturbation $\Delta\beta = 2\kappa$, 3κ, and 4κ are considered. The localization length, always measured in the long dimension of the array, increases as the number of rows M increases, and eventually reaches asymptotically the 2D value. It decreases on increasing $\Delta\beta$, reaching earlier the 2D value due to the smaller influence of the boundaries.

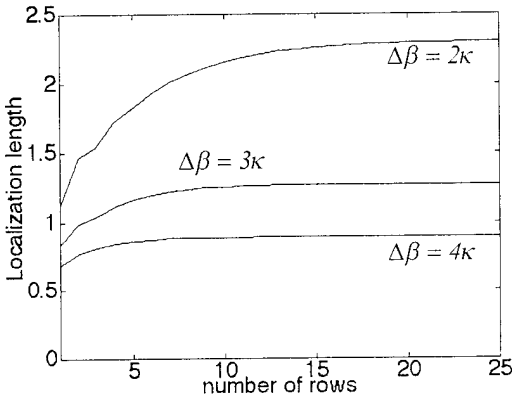


Figure 2: *Localization lengths for impurity positions (M/2, 13) or ((M+1)/2, 13) versus number of rows in Mx25 laser arrays. $\Delta\beta = 2\kappa$, 3κ, 4κ.*

The supermode localization manifests itself in the broadening of the lobes of the far-field patterns, as shown in Fig. 3. In this case, we consider the highest-order supermode of the structures of Fig. 1 (single impurity case). These supermodes are characterized by out-of-phase nearest neighbors and hence exhibit the typical double- or four-lobed far-field patterns. The FWHM of each lobe decreases from 1.1 deg to 0.2 deg as the dimensionality is increased from one to two. A dramatic narrowing of the far-fields of similar array structures has also been observed experimentally [5, see discussion].

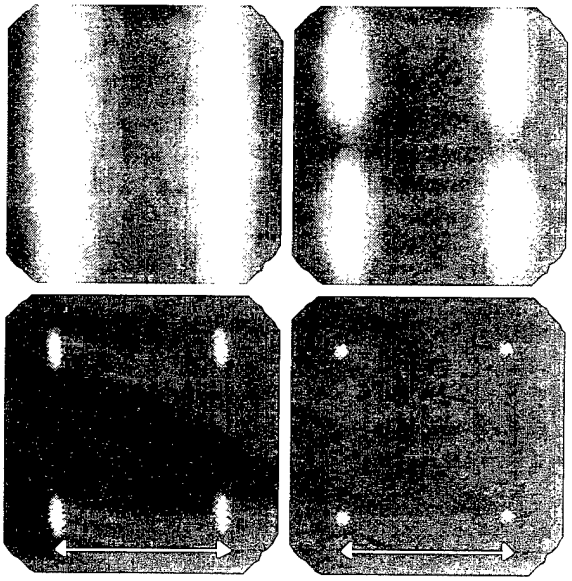


Figure 3: *Calculated far fields of 1, 2, 8, 25x25 of the arrays in figure 1a, highest order mode (wavelength=980nm, pitch=5μm). The arrows indicate 11°.*

Although the case of a single optical impurity serves to illustrate the basic features of the localization, in practical structures the disorder is distributed randomly throughout the array due to inadvertent wafer and lithography defects. We calculated the FWHM for such a randomly disordered array, with $-\Delta\beta_{\max} \le \Delta\beta \le +\Delta\beta_{\max}$.

Figure 4 shows the FWHM of the far-field of the fundamental supermode, averaged over a large number of random disorder distributions with the same $\Delta\beta_{max}$, as a function of the disorder parameter for several Mx25 array structures.

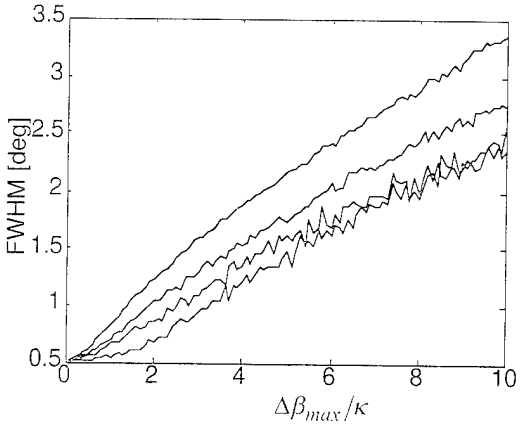


Figure 4: *Width of the far field lobes in 1x25, 2x25, 4x25 and 25x25 (from top to bottom) arrays versus disorder, calculated along the long dimension of the array.*

The FWHM increases with increasing disorder as the near-field becomes more localized. However, the far-field broadening decreases as the number of rows increases. The FWHM for the 4x25 arrays is practically indistinguishable from that of the square array (for the strong disorder regime), in agreement with the saturation in L_{loc} shown in Fig. 2 for ≥4 rows and $\Delta\beta = 4\kappa$. For practical considerations, this means that the coupling among the array elements should be as strong as possible to avoid having any influences of inadvertent fluctuations.

Since the above results clearly demonstrate a reduced degree of localization for 2D structures as compared with 1D ones, it is natural to expect that structures with intermediate dimensionality will exhibit an "intermediate behavior". The transition between the case of 1D and 2D can be illustrated by adding rows to a 1D case, as discussed above. In that case, however, the boundaries play an important role. An intermediate dimensionality structure free of such outer boundary effects is a fractal array, such as the Sierpinski carpet shown in Fig. 5.

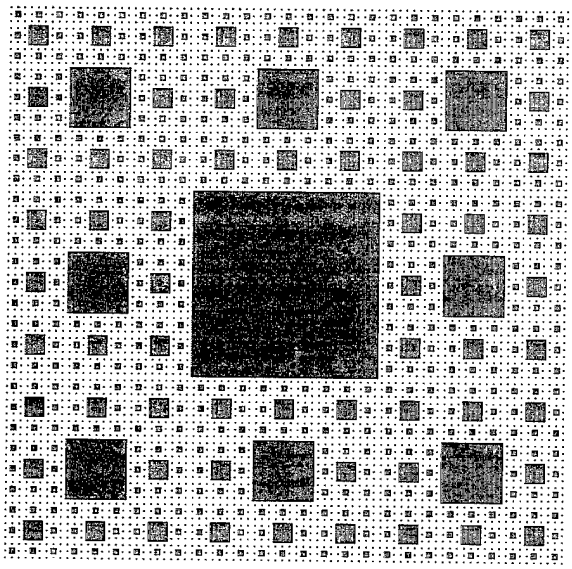


Figure 5: *Regular Sierpinski carpet of depth 6, b=3, n=1. The white areas are the laser positions (Haussdorff-dimension is 1.89).*

In this structure, bxb blocks form the substructure of the fractal, from which n units are removed, which corresponds to a Haussdorff-dimensionality

$$D_H = \frac{\ln\left(b^2 - n\right)}{\ln b}$$

The near-field distribution of the fundamental supermode in the fractal array of Fig. 5, in which a single impurity is introduced in an otherwise uniform index distribution, is shown in Fig. 6. Localization of the mode around the impurity site is observed in this fractal case as well, however, the details of the

localized mode pattern depend on the fractal structure and the position of the impurity within the fractal array, which lacks translational symmetry.

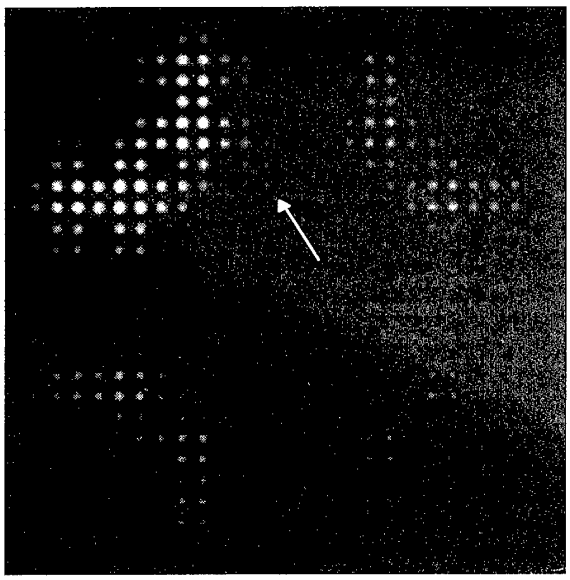


Figure 5: *Near field intensity distribution of a homogeneous fractal with one impurity at position (9,13), marked with an arrow. The Haussdorff-dimension is 1.89*

The direct relation between the degree of localization and the dimensionality is demonstrated in Fig. 7, which shows the FWHM as a function of the single impurity $\Delta\beta$, for 1D and 2D square arrays (27x27 elements) as well as for fractal arrays with intermediate dimensionalities $D_H = 1.77$ and $D_H = 1.89$.

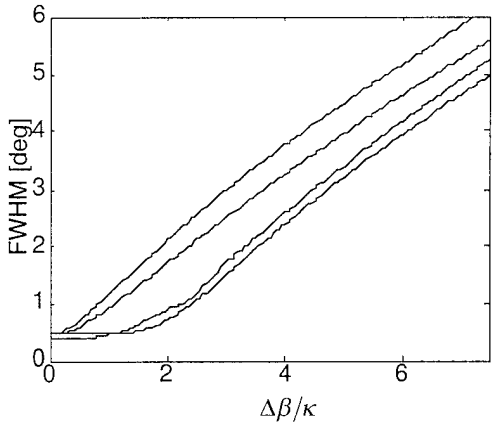


Figure 7: *Comparison of far field widths of arrays with different dimensionalities. From top to bottom: D_H = 1, 1.77, 1.89, 2*

For weakly localized modes the localization in the fractal structures strongly depends on the impurity position, but for a stronger perturbation a clear increase in the FWHM with decreasing dimensionality is observed.

Discussion

The degree of supermode localization discussed above is reflected in the broadening of the corresponding supermode far-field patterns. As already experimentally observed in [4], the far-field of a 1D VCSEL array structure is indeed significantly broader than that of a 2D array. However, our model accounts only for part of this broadening mechanism. The disorder in the array induces localization of the different supermodes in different parts of the disordered array. Gain saturation then results in simultaneous oscillation of several supermodes, which are mutually incoherent. The far-field pattern corresponds to a superposition of those of the individual supermodes, which yields a larger broadening than that predicted by the broadening in each supermode far-field due to the localization effects. In fact, the disorder-induced localization gives rise to both the direct and the gain-saturation induced broadening mechanisms.

Conclusion

In summary, we investigated the effect of dimensionality on photon localization in VCSEL array structures using coupled-mode models. We used near field patterns, localization lengths and far-field distributions to characterize the localization effects in lumped and distributed disordering cases. We showed that the degree of photon localization is dircetly related to the dimensionality of the structure, with lower-dimensionality structures showing stronger localization. The impact of these localization effects on the coherence properties of phase-locked VCSEL arrays was also discussed.

References

[1] P. L. Gourley, M. E. Warren, G. A. Vawter, T. M. Brennan and B. E. Hammons, *Appl. Phys. Lett.* **60**, 2714

[2] M. Orenstein, E. Kapon, N. G. Stoffel, J. P. Harbison, L. T. Florez and J. Wullert, *Appl. Phys. Lett.* **58**, 804 (1991)

[3] M. Orenstein, E. Kapon, J.P. Harbison, L.T. Florez and N.G. Stoffel, *Appl. Phys. Lett.* **60**, 1535 (1992)

[4] M. Orenstein, E. Kapon, L.T. Florez, J.P. Harbison and N.G. Stoffel, *Integrated Photonics Research Topical Meeting, Monterey, Cal.*, April 1991, paper TuF5

[5] A. Hardy, W. Streifer, *J. Lightwave. Techn.* **LT-3**, (5), 1135 (1985)

[6] H.J. Yoo, J.R. Hayes, E.G. Paek, A. Scherer and Y.S. Kwon, *IEEE J. Quantum Electron.* **26**, (6) 1039 (1990)

Transverse Multimode Dynamics of Gain-Switched VCSELs

J. Dellunde, M.C. Torrent*, J.M. Sancho and K.A. Shore**
Departament d'Estructura i Constituents de la Matèria, Facultat de Física, Universitat de Barcelona, Diagonal 647, E-08028 Barcelona, Spain.
Phone: (343) 4021183 Fax: (343) 4021198
* *Departament de Física i Enginyeria Nuclear, EUETIT, Universitat Politècnica de Catalunya, Colom 1, E-08222 Terrassa, Spain.*
Phone: (343) 7398222 Fax: (343) 7398225
** *School of Electronic Engineering and Computer Systems, University of Wales, Bangor LL57 1UT, Wales, U.K.*
Phone: (44) 1248 382618 Fax: (44) 1248 361429

The manufacture of vertical-cavity surface-emitting semiconductor lasers (VCSELs) lasing around 1550 μm, where the silica optical fibers exhibit a minimum in the optical losses, is under active research [1]. VCSELs operating at that wavelength are expected to offer a good performance as optical emitters in optical communication systems working at Gbit/s rates. Several advantages become evident. Because of their cylindrical geometry, good matching with standard monomode optical fibers has been demonstrated, with power losses lower than 10%. The surface emission characteristics of VCSELs allow integrability in two-dimensional laser arrays. Investigations of the performance of VCSELs under current modulation or gain-switching operation are important to characterize possible improvements with respect to the widely used edge-emitting lasers (EELs). One of the drawbacks of EELs is the natural tendency to lase in several longitudinal modes under large signal modulation, even when the side mode suppression ratio (SMSR) during steady-state operation is large [2]. Although transient multimode operation can be efficiently suppressed by using DFB structures, any damage in the AR-coatings on the laser facets can trigger the appearance of side modes.

Due to their short cavity length VCSELs are expected to oscillate in a single longitudinal mode. Typical diameters of the active region, however, permit the appearance of several transverse modes. During steady-state operation, the dominant mode depends on the injection current density and the geometry of the contact. For a disc geometry contact, the gain is in principle higher for the lowest order mode (LP_{01}), with circular symmetry and a single lobe. At large injection currents, however, side modes appear because of spatial holeburning and carrier diffusion [3, 4]. Two modes can coexist with a significant output power only when their spatial overlapping is small. In this work, the multimode dynamics during the laser turn-on following the laser gain-switching is investigated. A detailed description of the model can be found in [4]. The carrier density is considered to depend both on time and space, while the mode amplitudes change only with time. The change in device behavior due to variation in the radius of the injection current disc is considered. Only the two lowest order modes, LP_{01} and LP_{11}, are expected to have a significant modal gain in the described geometry.

The simulation of the complete model in [4] requires long computational time, which can be significantly reduced by expanding the carrier number in a series of Bessel functions,

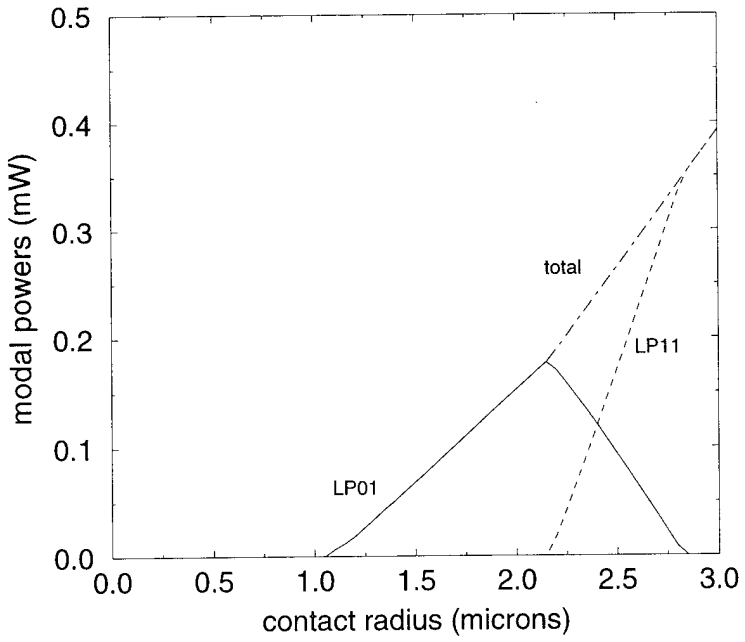


Figure 1: Modal powers in steady-state operation

as described in [5]. The resulting simplified model allows the calculation of threshold gains, output powers during steady-state operation and fully incorporates the effect of spatial holeburning and carrier diffusion as well. Additionally, the numerical simulations require less computational time, an important feature when a huge number of turn-on events is involved. In figure 1 the modal powers during steady-state operation are plotted with a current density of 20 A/m^2, for several contact radii. Emission is single mode up to a radius of 2.1 μm, approximately. If the contact radius is increased beyond this value, the side mode appears due to spatial holeburning at high output powers. We are interested in the gain-switched operation, so that the current density is suddenly changed from 4 A/m^2 (0.7 times threshold) to 20 A/m^2 (3.5 times threshold). The contact radius is set at 2.3 μm, where the SMSR during steady-state operation is very low. The carrier density profiles before and after the gain-switching are shown in figure 2, where holeburning effects become evident. A typical time trace of the modal powers after the laser switch-on is shown in figure 3. Laser emission is monomode up to the third power overshoot, when the side mode appears. The modal gain of the LP_{01} always reach the threshold value before the LP_{11} mode, so that the probability of turn-on, triggered by random spontaneous emission events, is considerably higher. Only during rare late turn-on events, lying in the long time tail of the probability density function (PDF) of turn-on times, can the side mode lase before the main mode. 10^4 turn-on events were simulated and the side mode power was recorded when the total power reached a reference value (0.1 mW). The histogram is plotted in figure 4.

In optical communication systems, the appearance of a side mode with a significant power during the detection process can lead to an error. An error is considered when the side mode power is higher than that of the main mode. According to the obtained results, the VCSEL exhibits single mode operation during pulsed operation, in spite of their multimode operation during steady-state operation. This is a consequence of spatial holeburning and carrier diffusion effects, which only appear when a significant output power is being emitted by the laser. The reported results predict a good performance of VCSELs as emitters in high speed optical communication systems, with a low bit error rate.

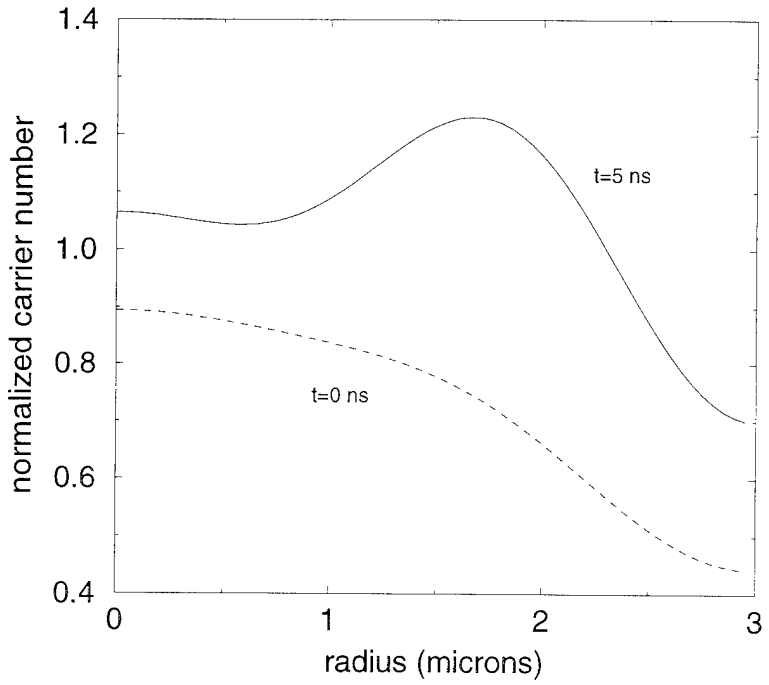


Figure 2: Carrier profiles before and after the laser switch-on

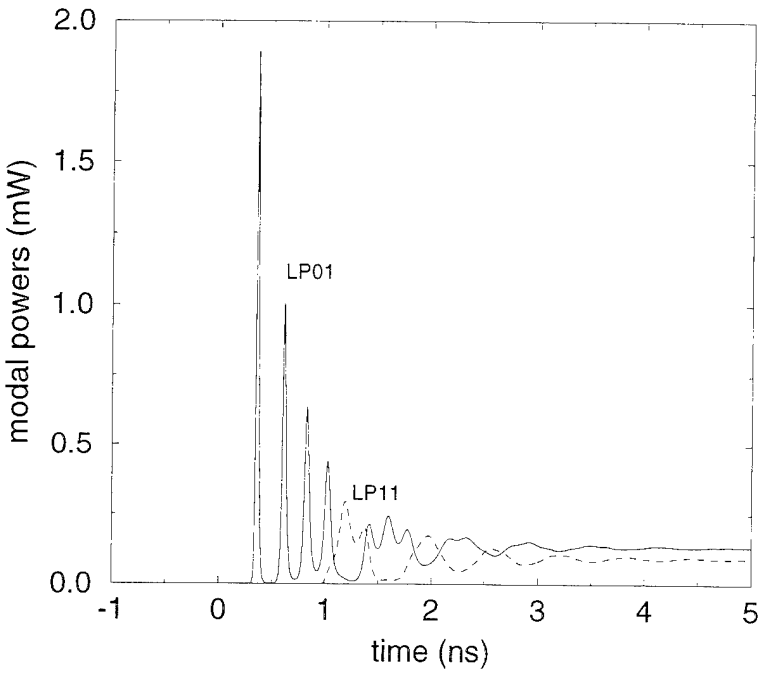


Figure 3: Modal powers after the laser switch-on.

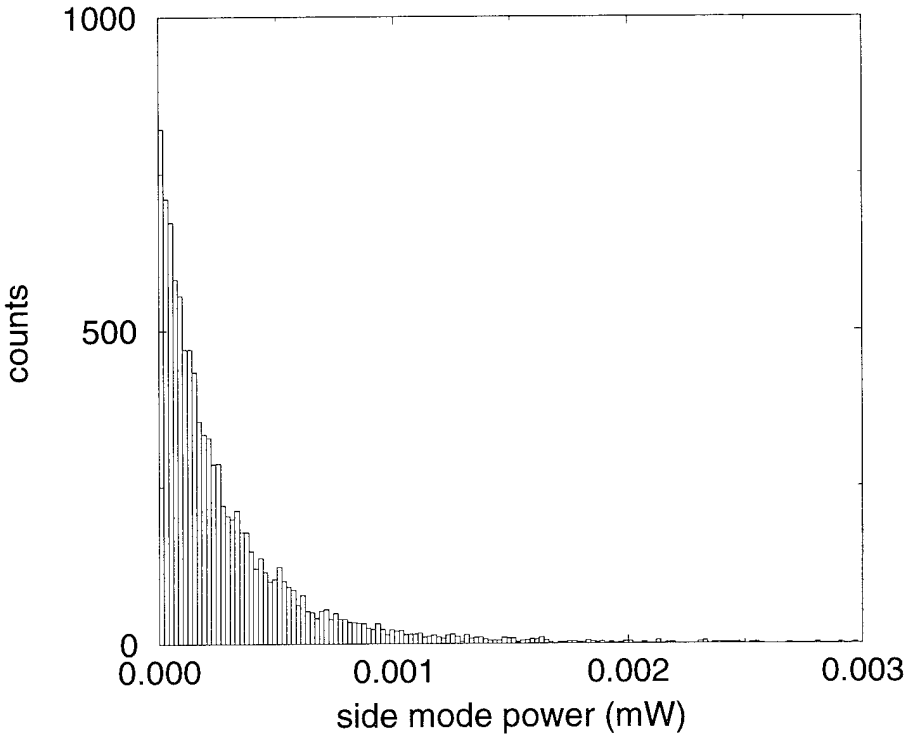


Figure 4: Side mode power probability at the threshold time

References

[1] M.A.Fisher, Y.Z.Huang, A.J.Dann, D.J.Elton, M.J.Harlow, S.D.Perrin, J.Reed, I.Reid, H.J.Wickes and M.J.Adams, *1.5 μm Vertical-Cavity Surface-Emitting Lasers*, Technical digest of the OSA Semiconductor Lasers Topical meeting, August 1995, paper TuD2.

[2] A.Valle, C.R.Mirasso and L.Pesquera, *Mode Partition Noise of Nearly Single-Mode Semiconductor-Lasers Modulated at GHz Rates*, IEEE Journal of Quantum Electronics **QE-31** (1995), 876-885.

[3] A.Valle, J.Sarma and K.A.Shore, *Dynamics of transverse mode competition in vertical cavity surface emitting semiconductor lasers*, Optics Communications **115** (1995), 297-302.

[4] A.Valle, J.Sarma and K.A.Shore, *Spatial Holeburning Effects on the Dynamics of Vertical Cavity Surface-Emitting Laser Diodes*, IEEE Journal of Quantum Electronics **QE-31** (1995), 1423-1431.

[5] K.Moriki, H.Nakahara, T.Hattori and K.Iga, *Single Transverse Mode Condition of Surface-Emitting Injection Lasers*, Electronics and Communications in Japan (Part 2) **71** (1988), 81-90.

TRANSVERSE MODE EXCITATION IN EXTERNAL CAVITY VERTICAL CAVITY SURFACE EMITTING LASERS

J. Dellunde (*) , A. Valle (+) and K.A.Shore (++)

(*) Departmento d'Estructura i Const. de la Materia, Facultat de Fisica , Universidad de Barcelona,Diagonal 647,E-08028 Barcelona,Catalunya,Spain

(+) Instituto de Fisica de Cantabria ,CSIC-UC and Departamento de Fisica Moderna , Universidad de Cantabria ,E-39005 Santander ,Spain

(++)University of Wales,Bangor ,School of Electronic Eng. & Computer Systems BANGOR LL57 1UT ,Wales,UK

Tel: + 44 1248 382618 ; Fax + 44 1248 361429 ; email : alan@sees.bangor.ac.uk

Introduction

The recent rapid advances in performance of vertical cavity surface emitting lasers (VCSELs) have permitted consideration to be given to novel applications of such devices in, for example, optical data links and two-dimensional optical switching. In such applications consideration must be given to the effects of optical feedback on device operating characteristics.The transverse mode structure of stand-alone VCSELs has been studied quite extensively but modifications of that mode structure due to optical feedback have received rather less attention.This contribution reports a theoretical study which has been performed of the multimode dynamics and steady state transverse mode selection in Vertical Cavity Surface Emitting Lasers (VCSELs) subject to weak optical feedback in an external cavity configuration. Attention is focussed on the competition between the two lowest order modes (LP_{01} and LP_{11}) appropriate to the chosen circularly symmetric VCSEL structure. It is shown that preferential excitation of either mode can be effected by appropriate choice of optical

feedback delay. Opportunities for enhancing modal discrimination by adjusting the strength of optical feedback are also presented.

Model

The model utilised in the work reported here incorporates both spatial depedence of carrier and optical field profiles and time delay effects associated with weak optical feedback. In the former respect the model is seen as an extension of earlier work on VCSEL transverse mode dynamics [1-3] whilst the incorporation of optical feedback using the Lang-Kobayashi equations makes contact with complementary work on edge emitting lasers [4-6].

Results

Simulations have been performed of the dynamical evolution of the transverse mode structure in disc-geometry external cavity VCSELs. Depending upon the phase of the returned light with respect to that emitted from the laser the effect of the optical feedback can be either to increase or decrease the laser threshold [see eg , 4]. For this structure the frequency detuning between transverse modes is about 240 Ghz and it is found that the modes can be enhanced or suppressed essentially in unison for small external cavity round trip times,τ ,whilst for larger values it is possible to enhance one mode and suppress the other as is illustrated in Figure 1.It can be seen that selection of either mode can be effected by appropriate choice of external cavity round trip time. For selection of single mode emission in the LP_{01} mode, with a central lobe, it is found that some τ allow a broader range of injection currents than for the solitary VCSEL, before the LP_{11} mode starts lasing.

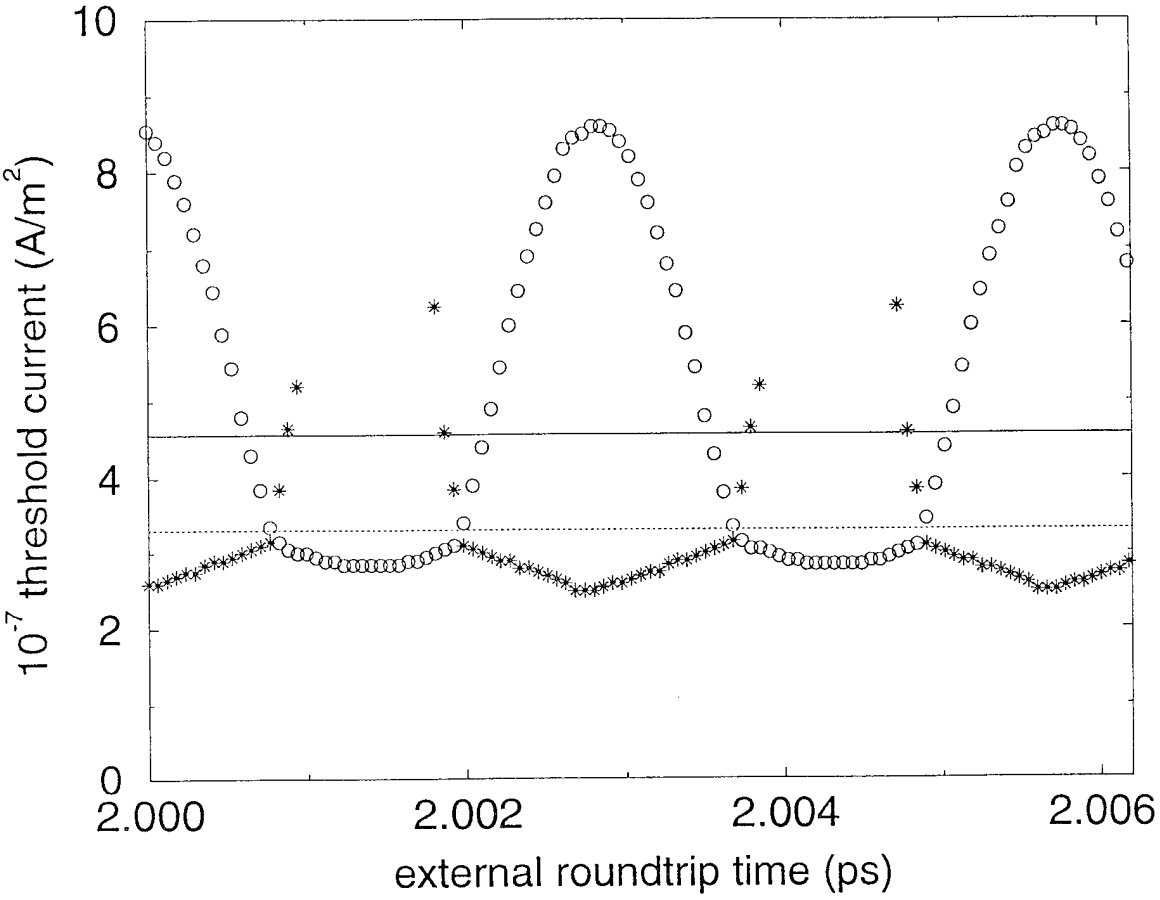
The second principal parameter which characterises the behaviour of external cavity lasers is the strength of the optical feedback.Results here are obtained for a fixed external cavity length corresponding to a roundtrip time of 2 ps. Figure 2 shows the threshold currents for the two modes involved at different feedback strengths, when the LP_{01} mode is enhanced by selecting a suitable external roundtrip time. A reduction in the threshold current of the LP_{01} mode becomes evident at around κ_i=0.03 ps^{-1}, while the threshold current of the LP_{11} mode increases continuously for lower values of the feedback strength.Further results will be presented which indicate the range of maximum and minimum value of the threshold current which can be obtained for the respective modes. In particular it is found that a decrease of the threshold current for the LP_{01} mode is only possible at rather strong feedback levels.

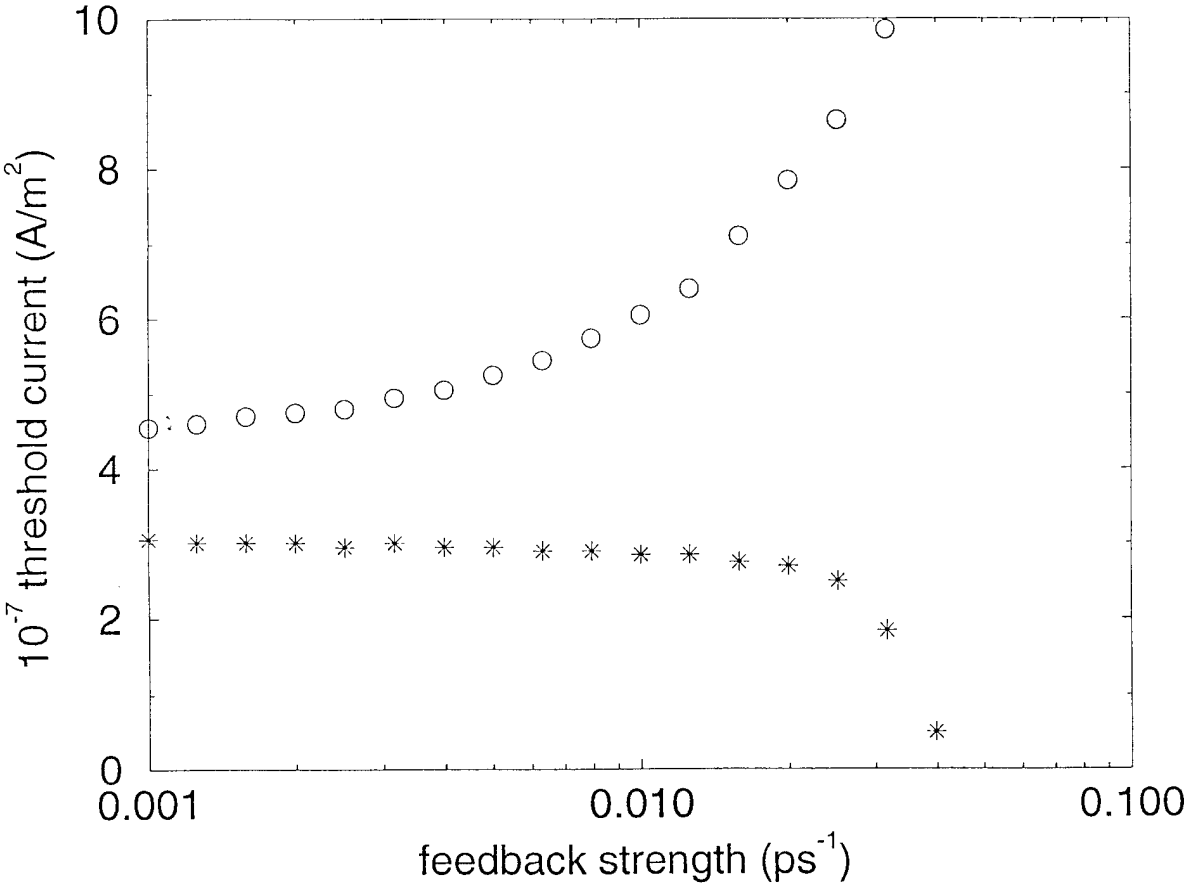
Acknowledgements

J.Dellunde undertook this work with support from CICYT, project PB93-0769-C02-01. A.Valle acknowledges support from the DGICYT, Spain under the Programme 'Becas de Formacion de Personal Investigador en el Extranjero ' and from the CICYT project TIC95-0563-C05-01. This work was also supported by the UK EPSRC under grant GR/J50149.

References

1) A.Valle, J.Sarma and K.A.Shore, Optics Communications **115**, 297-302,1995.
2) A.Valle, J.Sarma and K.A.Shore, ,IEEE J.Quant.Electron. **QE-31**,1423-1431,1995.
3) A.Valle, J.Sarma and K.A.Shore, J.Opt.Soc.America B,**12**,1741-1746,1995
4) E. Hernandez-Garcia , C.Mirasso, K.A.Shore and M.San Miguel,IEEE J. Quantum Electronics **QE-30**, 1994,241-248.
5) L.N.Langley and K.A.Shore,IEEE Journal of Lightwave Technology **LT-11**,434-441,1993
6) L.N.Langley, K.A.Shore and J.Mork , Optics Letters **19**, 2137-2139, 1994


10
8
6
4
2
0
10^{-7} threshold current (A/m^2)
2.000
2.002
2.004
2.006
external roundtrip time (ps)


10
8
6
4
2
0
10^{-7} threshold current (A/m^2)
0.001
0.010
0.100
feedback strength (ps^{-1})

Accurate Three-Dimensional Modeling of Transverse Mode Threshold Gain in Vertical Cavity Surface Emitting Lasers

Bart Demeulenaere, Bart Dhoedt, Stefan Goeman and Roel Baets
University of Gent - IMEC
Dept. of Information Technology (INTEC)
St.-Pietersnieuwstraat 41, 9000 Gent, Belgium
tel. +32 9 264 3316 fax : +32 9 264 3593

1) Introduction

Vertical cavity surface emitting lasers (VCSEL's) are very promising devices for parallel optical data links. Their main qualities are wafer scale testability, inherent single longitudinal mode operation, low threshold current, low beam divergence and their easy integration in two-dimensional arrays. Due to their intrinsic symmetry and quite large emission area problems arise however concerning the transverse mode stability. Unless specific measures are taken to prevent this higher order transverse modes start lasing already slightly above threshold thereby deteriorating the beam properties (e.g. divergence) and increasing the noise. It is obvious that this behaviour is unwanted. One way of solving this problem is by introducing mode selective scattering or loss in the cavity [1,2,3,4]. It is therefore important to be able to model the threshold gain of the different transverse modes in such cavities. In this paper we present an accurate vectorial model capable of predicting threshold gain and illustrate is with a few examples.

2) Theory

Fig.1a shows a very general VCSEL geometry. It is a layered structure that is epitaxially grown on a semiconductor substrate and that has a circular symmetry. The bottom mirror and the active layer have an infinite lateral extent while the top mirror has a finite radius thus allowing for top emission and easy carrier injection by means of a ring contact. In this geometry light diffracts in two different ways. First there is the spreading of a beam of finite radius in the bottom mirror whereby the reflectivity of the bottom mirror is reduced as compared to plane wave incidence. Second there is the scattering effect that occurs at the interface between two layers in case the radial refractive index profile of both layers is different. Our model describes both effects and is based on a vectorial solution of Maxwell's equations for the cavity eigenmodes of the complete three-dimensional structure consisting of the top mirror stack, the bottom mirror stack and the active region (i.e. the quantum well and its cladding layers).

Only a very concise description of the model will be given here. For further details we refer to [5]. We use a modal expansion of the field in each layer of the structure. By imposing the boundary conditions at each interface we obtain the reflection and transmission properties of all interfaces in the structure. From these we then obtain the reflection and transmission properties of a stack of layers via a recursion procedure. Since we use a modal expansion to describe the field the reflection and transmission properties of a stack of layers are expressed as NxN matrices describing the coupling of all modes in the layer below the stack to themselves (reflection) and to the modes of the layer above the stack (transmission). N is the number of modes used in the expansion of the fields. If we repeat this procedure for the top mirror stack, the bottom mirror stack and the active region we obtain the following relations :

$$\begin{pmatrix} A_{down}^{cl1} \\ A_{up}^{cl1} \end{pmatrix} = \begin{pmatrix} T_1 & T_2 \\ T_3 & T_4 \end{pmatrix} \begin{pmatrix} A_{down}^{cl2} \\ A_{up}^{cl2} \end{pmatrix} \quad (1)$$

$$A_{up}^{cl2} = R_{bot} \cdot A_{down}^{cl2} \quad (2)$$

$$A_{down}^{cl1} = R_{top} \cdot A_{up}^{cl1} \quad (3)$$

in which A_{up}^{cl1}, A_{down}^{cl1}, A_{up}^{cl2}, A_{down}^{cl2} stand for the upward and downward propagating waves in both cladding layers and T_1, T_2, T_3, T_4 stand for NxN matrices relating the N upward and N downward travelling waves in both cladding layers. All phase rotations due to propagation through the quantum well as well as through both cladding layers are contained in these four matrices as well as reflections at the interfaces between the quantum well and the cladding layers. (2) and (3) express the mirror reflections. From these relations it is easily deduced that when looking for the cavity eigenmodes we have to solve the eigenvalue problem for the following cavity roundtrip matrix :

$$R_{top}\left(T_3 + T_4 R_{bot}\right)\left(T_1 + T_2 R_{bot}\right)^{-1} \quad (4)$$

When the phase of the eigenvalue γ is a multiple of 2π a cavity eigenmode is found. For the cold cavity the amplitude of γ will be smaller than 1. Only when we provide gain in the quantum well can the amplitude of γ be equal to 1. This expresses the threshold condition in this very general cavity. The amplitude of γ takes into account all losses : absorption in the cavity and mirrors, diffraction loss and mirror transmission loss. Therefore the modal threshold gain can be approximately written as $g_{th}=-\ln|\gamma|/(2L_{qw})$, with L_{qw} the quantum well thickness and the factor of 2 in the denominator assuming that the quantum well is at the antinode of the cavity standing wave pattern.

An approximate way that is very often used to estimate the threshold modal gain is to obtain approximate values for the mirror power reflectivities R_1 and R_2 and to use the formula $g_{th}=-\ln(R_1.R_2)/(4L_{qw})$. The mirror power reflectivities are often estimated by calculating the power reflectivity for a waveguide mode when hitting a laterally infinite Bragg mirror [5,6].

3) Numerical examples

In this section we present two examples to illustrate the strength and versatility of the above outlined method. The first example deals with the structure depicted in fig.1a. We will present results concerning the threshold modal gain using both the approximate and the exact theory. The second example deals with the structure of fig.1b.

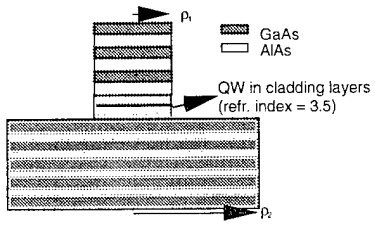
Fig.1a shows a VCSEL structure that has a bottom mirror of radius ρ_2 and a top mirror of radius ρ_1. Such a structure has the advantage that both electrical contacts are on the sane side of the substrate. Both are DBR-mirrors made from alternating layers of AlAs (index of refraction 2.9) and GaAs (index of refraction 3.5). The operating wavelength is taken to be 980nm and the thickness of the quantum well is 5nm. This structure is modeled with both the fully rigorous model and with the approximate model that was mentioned at the end of section 2. In the approximate model we consider a circular waveguide of the same radius as the top mirror (2μm) and assume that its fundamental mode is a good approximation to the actual lowest order lasing mode. The top mirror has 20 periods while the bottom mirror has 30 periods and its radius is varied between that of the 2μm and 8μm. When using the rigorous model we first look for the appropriate cavity thickness for having a resonance at λ=980nm. Having found the

thickness of the cavity we look for the mode with the lowest threshold gain and consider that to be the lowest order lasing mode. Fig.2a shows the threshold modal gain of the lowest order lasing mode according to both models. We notice that for a radius of the bottom mirror that is comparable to that of the top mirror both models agree very well. Once the bottom mirror becomes too large in the lateral direction the results of both models diverge. Apparently the lasing mode is not well modeled anymore by the fundamental waveguide mode but is made up from a superposition of several modes in order to adjust itself as well as possible to the large difference in radius between both mirrors.

Next we present results that can only be obtained with the full model. The idea to provide for transverse mode selection by using an optical window on top of the cavity [1] is extended by distributing the optical window over the top mirror. Fig.1b shows two possible VCSEL-structures that consist of a laterally infinite lower mirror, a laterally infinite active region and a top mirror with a radius of 3μm. The bottom mirror is a 30 period GaAs/AlAs DBR stack and the top mirror is a 20 period GaAs/AlAs stack ($n_2=n_3=2.9$). This structure is the structure without AlAs-oxidation. The structure with partial AlAs-oxidation in the top mirror has $n_2=2.9$ and $n_3=1.55$ and the oxidised region is 1μm deep. In this last structure the bottom mirror is unaffected. The partial oxidation of the AlAs in the top mirror provides for an additional lateral step in refractive index in these layers that should affect higher order modes more severely than the lowest order mode. This provides for mode selective diffraction. For both structures the thickness of the GaAs layers is 70nm while the AlAs layers are 84.483nm thick whether partial oxidation has occurred or not. The thickness of the active region (quantum well and both cladding layers) is 281nm (λ-cavity) with a 5nm thick quantum well. This way the structures are meant to operate at λ=980nm. For both structures a wavelength scan was performed between 970nm and 990nm to determine the cavity resonances and the cavity losses of the resonances using the rigorous model described in section 2. From the cavity losses suffered by each resonance the threshold modal gain for that resonance was calculated as described in section 2. Fig.2b shows a threshold gain versus wavelength plot for the lowest order cavity resonances of both the structure with and without partial oxidation in the top mirror. We see from fig.2b that for both structures the actual operating wavelength will be slightly smaller than 980nm : without oxidation the lowest threshold gain is for λ=979.14nm and with oxidation for λ=977.02nm. The threshold gain for the lowest order mode in the structure with oxidation (1164.72 cm^{-1}) is about 2 times smaller than in the structure without oxidation (2044.39 cm^{-1}). In the laser with partial oxidation the threshold gain difference between the lowest order mode and the next higher order mode is about 4 times larger than in the laser without oxidation. It should be clear that the oxidation process induces significant changes in the behaviour of the cavity modes.

4) Conclusion

In this paper we presented an accurate cavity model for VCSEL's based on a vectorial solution of Maxwell's equations. With this model we can calculate the threshold model gain of the lowest order and higher order cavity modes. Two structures were studied with this model. In a first example the exact results were compared to results from an approximate model showing the region of breakdown of the approximate model. In a second example a structure with partial AlAs oxidation was compared to one without oxidation showing the profound change in the modal gain for the different transverse modes due to the oxidation process.



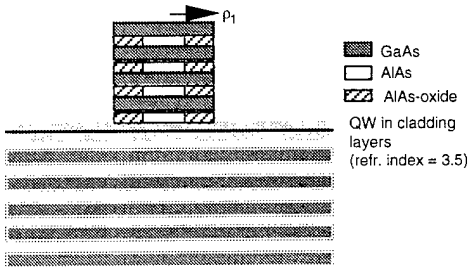
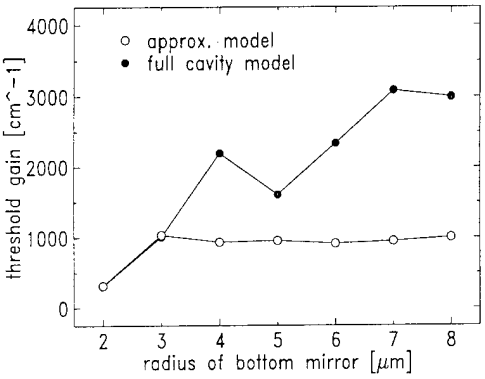


Fig.1a Fig.1b

Fig.1 : Two VCSEL-structures. Fig.1a shows a structure with two mirrors of finite radius, while fig.1b has a bottom mirror of infinite radius and a top mirror that is partially oxidised.



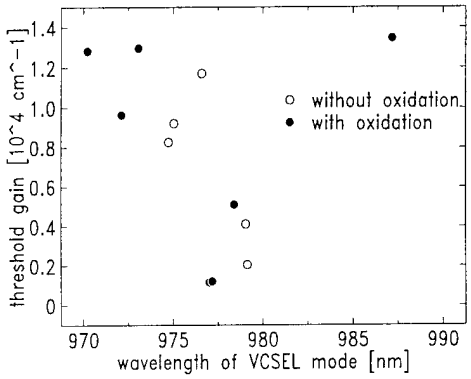


Fig.2a Fig.2b

Fig.2 : Threshold modal gain for the lowest order lasing mode of the structures shown in fig.1. Fig.2a compares an approximate and a rigorous modeling of the structure of fig.1a while fig.2b shows the behaviour of the structure from fig.1b with and without partial oxidation.

References

[1] R.A. Morgan et al., IEEE Phot. Tech. Lett., vol.4, no.4, pp.374-377, 1993

[2] D.L. Huffaker et al., Appl. Phys. Lett., vol.65, no.21, pp.2642-2644, 1994

[3] Y.A. Wu et al., IEEE Journ. of Selected Topics in Quantum Electronics, vol.1, no.2, pp.629-637, 1995

[4] D.L. Huffaker et al., Appl. Phys. Lett., vol. 65, no. 13, pp.1611-1613, 1994

[5] B. Demeulenaere et al., to be published

[6] R.R. Burton et al., IEE Proceedings - Optoelectronics, vol. 142, no. 2, pp.77-81, 1995

Modelling of VCSELs by the Method of Lines

E. Ahlers, S. F. Helfert and R. Pregla
Allgemeine und Theoretische Elektrotechnik
FernUniversität, Hagen
58084 Hagen
Telephone: +49 2371 566 256
Fax: +49 2371 51898

The Vertical Cavity Surface Emitting Lasers (VCSEL) have certain important advantages over the edge emitting lasers [1] and were a subject of extended research activities recently.

This paper describes a numerical analysis model for VCSEL diodes based on the Method of Lines [2] with high degree of accuracy. The characteristics of the model are:

- all calculations are done in cylindrical coordinates
- for the optical modelling
  - a solution of the vectorial wave equation is performed
  - a bidirectional solution is used
  - multireflections are incorporated
  - all guided modes and radiating modes are considered
- the current density in the whole structure is computed with respect to the different materials and different temperatures
- the temperature profile resulting from the optical and electrical losses is modelled
- in the active layer the rate equation with the coupling to the optical model is solved
- a coupling of optical, electrical and thermal effects is incorporated

For accurate modelling of the different effects in the laser structure three coupled submodels are used

- the optical submodel
- the electronic submodel
- the thermal submodel

All submodels analyze the structure by splitting it into a number of homogenous layers in z-direction. In each layer the parameters may be different and dependent on the radius.
The whole analysis model with the coupling of the submodels is sketched in Fig. 1.
At first the electronic submodel calculates the current density in the whole structure. Each layer is thereby represented by an electrical conductivity which is a function of the radius and the temperature.
In the active region the rate equation is solved under consideration with the electrical part of the optical field. The algorithm to solve this equation is described later. From the rate equation we get the carrier density which produces an optical gain that leads to a new complex refractive index. The gain is not only a function of the carrier density, a function of the temperature is implemented and can be extended to other parameters.
For the new refractive index distribution the optical model yields the resonator wavelength and the optical field.

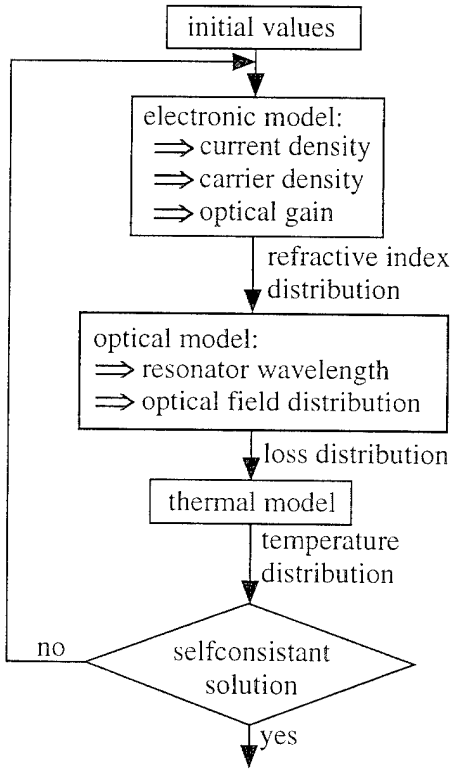


Figure 1: Flow chart of the whole analysis model

The optical and electrical losses are the input of the thermal model which calculates the temperature profile in the structure. As in the electronic model each layer is described by a thermal conductivity which is a function of the radius and temperature.

The new temperature distribution changes the parameters of the other submodels and a new iteration step has to be performed. Iterations must be done until a selfconsistent solution is obtained.

The optical resonator

As written above the structure is splitted in z-direction in a number of layers in which the refractive index is independent of z. In each layer we can compute the analytical solution of the wave equation as shown in [3]. With this solution we can transform the tangential fields from one side of a layer to the other side. This leads to certain numerical problems. A numerically stable algorithm is to transform admittances. We can define a admittance matrix $\mathbf{Y}$ with

$$\mathbf{H}_t = \mathbf{Y}\mathbf{E}_t$$

where $\mathbf{H}_t$ and $\mathbf{E}_t$ are the tangential field components. This matrix can transformed over a layer according to

$$\mathbf{Y}_A = -\boldsymbol{y}_1 - \boldsymbol{y}_2(\mathbf{Y}_B - \boldsymbol{y}_1)^{-1}\boldsymbol{y}_2 \tag{1}$$

$$\mathbf{Y}_B = \boldsymbol{y}_1 - \boldsymbol{y}_2(\mathbf{Y}_A + \boldsymbol{y}_1)^{-1}\boldsymbol{y}_2 \tag{2}$$

with

$\mathbf{Y}_A$ = admittance matrix at $z = z_A$ $\quad$ $\boldsymbol{y}_1 = \widehat{\boldsymbol{T}}\boldsymbol{\Gamma}\tanh^{-1}(\boldsymbol{\Gamma}d)\boldsymbol{R}^{-1}$

$\mathbf{Y}_B$ = admittance matrix at $z = z_A + d$ $\quad$ $\boldsymbol{y}_2 = \widehat{\boldsymbol{T}}\boldsymbol{\Gamma}\sinh^{-1}(\boldsymbol{\Gamma}d)\boldsymbol{R}^{-1}$

$\widehat{\boldsymbol{T}}, \boldsymbol{\Gamma}$ and $\boldsymbol{R}$ are known from the analytical solution and are defined in [3].

At the upper and lower boundary of the structure we set a wave in $+z$ and $-z$-direction, respectively.

upper boundary $(+z)$: $\overline{\Psi}_u = e^{-\Gamma\overline{z}}\mathbf{A} \implies \mathbf{Y}_{u0} = -\widehat{\boldsymbol{T}}\boldsymbol{\Gamma}\widehat{\boldsymbol{T}}^{-1}$

lower boundary $(-z)$: $\overline{\Psi}_l = e^{\Gamma\overline{z}}\mathbf{A} \implies \mathbf{Y}_{l0} = \widehat{\boldsymbol{T}}\boldsymbol{\Gamma}\widehat{\boldsymbol{T}}^{-1}$

Now $\mathbf{Y}_{u0}$ is transformed over n layers with eq. 1 and $\mathbf{Y}_{l0}$ over m layers with eq. 2 into a matching plane. In this matching plane the tangential fields must be continuous leading to the equation

$$(\mathbf{Y}_{un} - \mathbf{Y}_{lm})\mathbf{E}_t = \mathbf{0}$$

which has a nontrivial solution if and only if

$$\det(\mathbf{Y}_{un} - \mathbf{Y}_{lm}) = 0 \tag{3}$$

To find the resonator wavelength we have to vary the wavelength until eq. 3 is fulfilled.

The active region

In the active region the carrier density must fulfil the rate equation

$$D\frac{1}{r}\frac{\partial}{\partial r}\left(r\frac{\partial N}{\partial r}\right) = -\frac{J}{qd} + \frac{N}{\tau_{nr}} + BN^2 + CN^3 + gb|E|^2 \tag{4}$$

with

D	:	diffusion coefficient	N	:	carrier density
τ_{nr}	:	livetime of nonradiative emission	J	:	current density
B	:	spontaneous emission coefficient	C	:	Auger coefficient
g	:	optical gain	b	:	normalization factor
$\lvert E\rvert^2$	:	square of the magnitude of the electric field			

Discretizing all parameters in the rate equation the solution procedure is reduced to finding the zeros of the function

$$\mathbf{F} = h^{-2}\boldsymbol{D}\boldsymbol{P}\mathbf{N} - (qd)^{-1}\mathbf{J} + \tau_{nr}^{-1}\mathbf{N} + \boldsymbol{B}\mathbf{N}^2 + \boldsymbol{C}\mathbf{N}^3 + g\boldsymbol{b}|\mathbf{E}|^2 \stackrel{!}{=} \mathbf{0} \tag{5}$$

where $\boldsymbol{P}$ denotes the second derivative with respect to r in cylindrical coordinates. The zeros of eq. 5 can be found very efficiently with the Newton algorithm. It should be noted that D, τ_{nr}, B and

C depend on the radius and can additionally be a function of other parameters like temperature, wavelength, carrier density, etc. So it is easy to include measured functions in the program which leads to a realistic modelling.

For a given current density $\mathbf{J}$ in the active region the resulting wavelength can be calculated with the algorithm sketched in Fig. 2.

The rate equation is solved with initial values for the square of the magnitute of the electrical field, which is calculated to $b \cdot |\mathbf{E}|^2$ where $\mathbf{E}$ is the result of the optical model. The carrier density leads (with some other parameters) to an optical gain which produces a new refractive index distribution. Now the resonance wavelength with this index distribution is calculated. The following action depends on the imaginary part ($\Im$) of the wavelength λ:

$\Im(\lambda) = 0$ All losses are compensated with the optical gain. The selfconsistent result is optained and the iteration process can be stopped.

$\Im(\lambda) < 0$ The loss is higher than the gain. We can increase the gain by decreasing b (which produces a higher N in the solution of the rate equation). If b is already very small the current density is to small for laser operation and the iteration can be stopped.

$\Im(\lambda) > 0$ The gain is higher than the loss. We must decrease the gain by increasing b and perform a new iteration step.

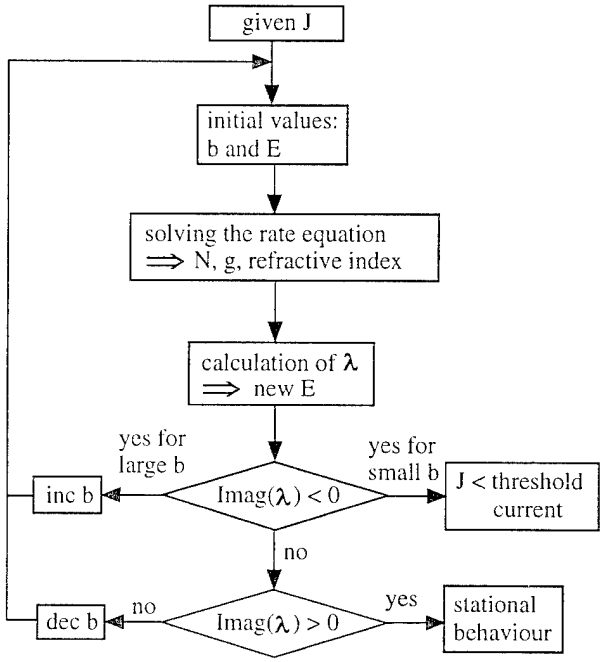


Figure 2: Flow chart for finding the resulting wavelength by given current density

The electronic and thermal submodel

The algorithms in the electronic and thermal submodel are similar to each other so they will be discussed here together.

In both models the corresponding equation in a layer is solved and a transformation from the top and the bottom to a matching plane is carried out. This is rather similar to the optical submodel.

To calculate the temperature increase the heat equation

$$\frac{\partial^2 \vartheta}{\partial z^2} + \frac{1}{\lambda_c} \frac{1}{r} \frac{\partial}{\partial r} \left(r \lambda_c \frac{\partial}{\partial r} \vartheta \right) = \frac{Q}{\lambda_c} \qquad (6)$$

with

λ_c : thermal conductivity
ϑ : temperature increase
Q : loss density

must be solved in each layer.
At the interface of two layers ϑ and $\lambda_c \frac{\partial \vartheta}{\partial z}$ must be constant.

To calculate the electrical potential distribution the Laplace equation

$$\frac{\partial^2 U}{\partial z^2} + \frac{1}{\sigma_c} \frac{1}{r} \frac{\partial}{\partial r} \left(r \sigma_c \frac{\partial}{\partial r} U \right) = 0 \qquad (7)$$

with

σ_c : electrical conductivity
U : electrical potential

must be solved in each layer.
At the interface of two layers U and $\sigma \frac{\partial U}{\partial z}$ must be constant.

In both models the corresponding equation in a layer is solved by disretizing in r-direction and transforming to the principal axis. As in the optical submodel we define a kind of admittance matrix which represents the relation between both constant components and transform this from the top and the bottom into a matching plane.

Unlike the optical submodel we don't need to equate the determinant to zero because there is no unknown parameter in the admittance matrix. Thus the resulting equation can be solved and the temperature and electrical potential in the whole structure can be calculated. The current density is then obtained from the electrical potential with

$$\vec{J} = -\sigma(\nabla U)$$

Results

Some results illustrating the use of electrical and optical submodel are shown in Fig. 3 and Fig. 4

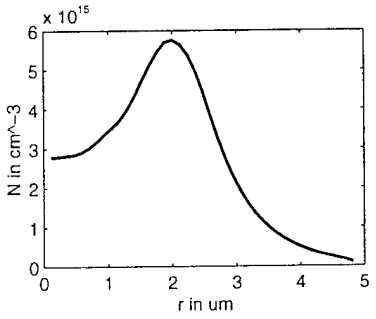


Figure 3: Example for the carrier density in the active region

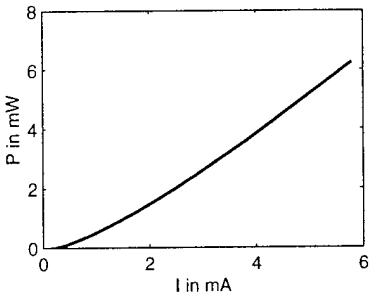
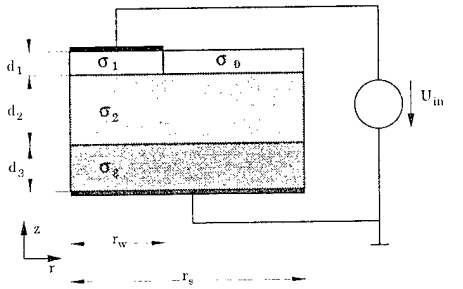


Figure 4: Optical output power as function of current

Fig. 3 shows the carrier density in the active region obtained from the rate equation for a current density higher than the threshold one. The spatial hole burning is clearly seen.

In Fig. 4 the optical output power over the top mirror is plotted vs. current I.



$d_1 =$ 1.0 μm
$d_2 =$ 2.5 μm
$d_3 =$ 2.0 μm
$r_w =$ 5 μm
$r_s =$ 50 μm
$\sigma_0 =$ 0 μm
$\sigma_1 =$ 117 S/cm
$\sigma_2 =$ 3.7 S/cm
$\sigma_3 =$ 7.4 S/cm

Figure 5: Parameters of the structure

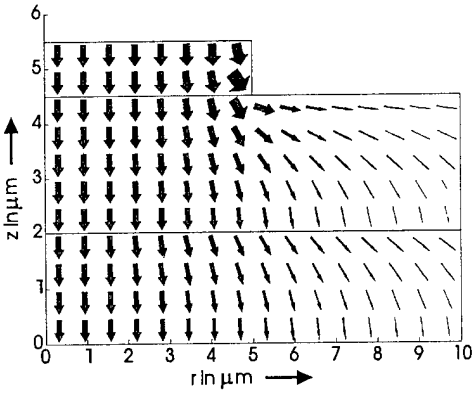


Figure 6: Current density

Fig. 6 shows the current density in the structure sketched in Fig. 5. calculated from the electronic submodel.

References

[1] K. Iga and F. Koyama, "Surface Emitting Semiconductor Lasers", In: *IEEE J. Quantum Electron.*, vol. 24, no. 8, pp. 1845–1855, Sept. 1988.

[2] R. Pregla and W. Pascher, "The Method of Lines", in *Numerical Techniques for Microwave and Millimeter Wave Passive Structures*, T. Itoh, Ed., pp. 381–446. J. Wiley Publ., New York, USA, 1989.

[3] R. Pregla and E. Ahlers, "New Vector-BPM in Cylindrical Coordinates Based on the Method of Lines", in *Integr. Photo. Rescar. Technic. Digest*, Dana Point, USA, Feb. 1995, vol. 7, pp. 23–25.

Understanding Waveguiding in Vertical-Cavity Surface-Emitting Lasers

G. Ronald Hadley
K. D. Choquette
K. L. Lear
Sandia National Laboratories
Albuquerque, New Mexico 87185-5800
(505)844-4015
FAX (505)844-8985

Vertical-cavity surface-emitting lasers (vcsels) are presently the subject of intense research due to their potential as compact, efficient, astigmatic laser sources for a number of important applications. Interest in these devices has increased still further due to recent reports of record-low thresholds[1] and record-high wall-plug efficiencies[2]. Most of the prevalent vcsel designs operate in multiple lateral modes, however, limiting their usefulness. In general, little attention has been paid to lateral mode discrimination in vcsels, partly because of the need for addressing other more pressing issues, and partly due to the lack of a fundamental understanding of waveguiding and the physics of optical confinement in such devices. Here, we present the first theoretical treatment of waveguiding in vcsels that properly includes the effects of the resonant cavity. The resulting treatment immediately suggests new designs for leaky-mode (antiguided) vcsels that should result in devices operating in the fundamental mode to powers much higher than presently attainable.

Our treatment of waveguiding follows from an effective index model[3] based on approximate separation of the relevant Helmholtz Equation in a manner similar but not identical to the well-known derivation for edge-emitting lasers.

The treatment for vcsels differs due to the presence of a short resonant cavity, resulting in an expression for the effective index that depends in an essential way upon variations in optical cavity length. Although similar effects occur for edge-emitters, the much longer cavity length renders the effects unimportant. This treatment results in the simple formula[3]

$$\frac{\Delta n}{n} = \frac{\Delta \lambda_0}{\lambda_0} \tag{1}$$

in which the relative variation in effective index occurring in different parts of the vcsel cavity is equal to the relative change in Fabry-Perot resonance wavelength in these regions. This result implies that *regions of high or low effective index may be designed into a vcsel merely by engineering changes in optical cavity length*. This view is entirely contrary to the conventional wisdom that supposes that waveguiding may only be affected by the introduction of material of different index along the cavity length. The latter approach does of course result in effective index differences through its influence on the resonant wavelength, but requires much more difficult processing.

The concept embodied in Equation (1) may be better understood with the aid of a simple example in which the more complicated vcsel cavity is idealized as a simple cavity with discrete mirrors as shown in Fig. 1. Radiation resonant in the left-most region that diffracts into the lengthened region is non-resonant unless the wavevector tilts at the angle shown in the figure so as to maintain the Fabry-Perot resonance condition in this region. But this picture is equivalent to an effective index picture in which the index in the lengthened region is increased over that in the left-most region by an amount such that θ becomes the critical angle. This index increase is found to be identical to the result described in Equation (1) above.

The Above discussion reveals that index increases in vcsels may be engineered by etching and unilateral regrowth of dielectric material (Fig. 2), with the index step being defined not by the properties of the dielectric, but rather by the depth of the etch. This has profound implications for the fabrication of leaky-mode vcsels. The latter are of interest because of their predicted higher lateral mode discrimination that should result in fundamental mode operation to higher powers. Previous attempts to fabricate such devices by etching completely through the mirror stack and regrowing high-index material[4] have only been partially successful due to the obvious processing difficulties involved. In contrast, since effective cavity lengths for most current vcsel designs are usually under 2 μm, an etch of only 30 nm is sufficient to affect an index change of about 0.05. Following such a shallow etch, the remaining mirror structure may then be deposited. It also follows that index guided devices may be fabricated in the same manner by merely reversing the etch profile.

An additional potentially important use of leaky-mode coupling in vcsels is for inter-element coupling of 2-D arrays, which would provide much higher fundamental mode output powers with a minimum of excess radiation loss. The shallow etch process described above could be used to fabricate arrays as well, either in a rectangular pattern or as a series of concentric rings separated by anti-guided regions for strong leaky-mode coupling.

1. G. M. Yang, M. H. MacDougal and P. D. Dapkus, *Electron. Lett.* 31(11)p886(1995).
2. K. L. Lear, K. D. Choquette, R. P. Schneider, Jr., S. P. Kilcoyne, and K. M. Geib, *Electron. Lett.* 31, p208(1995).
3. G. R. Hadley, *Optics Lett.* **20**(13),p1483(1995).
4. C. J. Chang-Hasnain, Y. A. Wu, and G. S. Li, *Appl. Phys. Lett.* 63(10),p1307(1993).

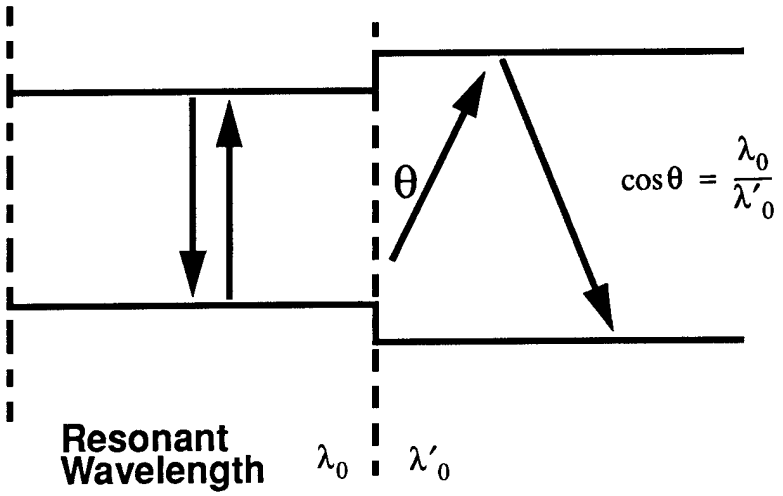


Fig. 1. Schematic diagram of a simplified vcsel cavity whose optically lengthened region (on the right) behaves as if it were the same length as the region on the left, but with an increased index of refraction

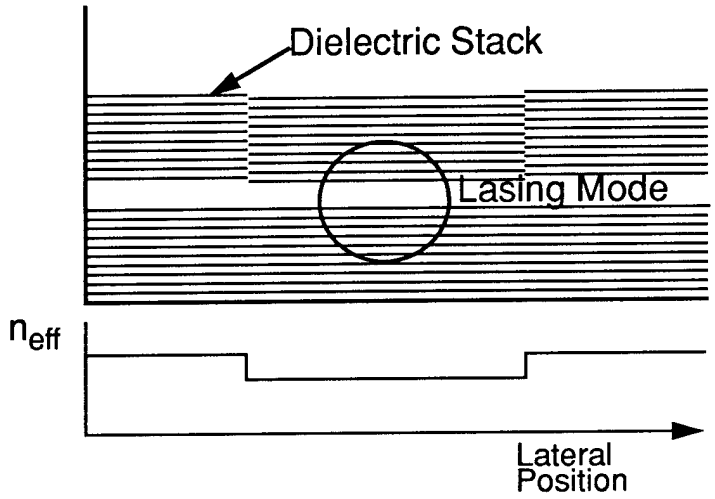


Fig. 2. Schematic diagram of leaky-mode vcsel produced by patterning the cavity region followed by regrowth of a dielectric stack.

Tuesday, April 30, 1996

Low-Cost Photonic Packaging I

ITuF 2:00 pm-3:00 pm
Fairfax B

Ian R. Croston, *Presider*
Integrated Optical Components, U.K.

Novel Alignment Techniques for Packaging and Integration of Optoelectronic Components

Paul O. Haugsjaa

GTE Laboratories Incorporated
40 Sylvan Road, Waltham, MA 02254
Telephone: 617-466-2512
E-mail: phaugsjaa@gte.com

Introduction

The cost of critical alignment techniques required in the packaging of optoelectronic components has been one of the most important contributors to the high cost of these components. Recently, efforts have been undertaken around the world to develop novel techniques to reduce the complexity of alignment procedures and thereby reduce the costs of optical and optoelectronic components. Most of these aligned packaging techniques utilize platforms that while providing enhanced alignment capabilities, also allow the potential for increased hybrid integration. It is the purpose of this paper to review some of these newly evolving techniques that show particular promise or capture the imagination.

Passive Alignment Techniques

Active alignment, accomplished with the powering of optoelectronic components or otherwise passing light through them, generally requires careful, iterative movements of components to optimize the coupling. As such, it is a good way to get the ultimate in coupling performance out of a system but costs for labor, equipment and precision machined assembly parts may be excessive. On the other hand, passive alignment does not introduce the complexities of operating devices during the packaging operations and may significantly reduce the cost of packaging. Several techniques that allow for the passive alignment of optoelectronic components will be reviewed.

Passive allignment techniques have been developed, for example, that utilize micromachined silicon waferboard substrates[1], specially fabricated optoelectronic components[2, 3, 4], complementary structures on platforms and devices[5], solder bump alignment forces[6], controlled height solder pads[7], and visual alignment fiducials[8]. One of the important recent developments affecting the practicality of passive alignment techniques involves the use of expanded mode lasers to give a better match to single-mode optical fiber than conventional lasers.[9,10]

Novel Alignment Techniques

It is also possible to simplify the alignment of complex optical systems by use of platforms and bearings[11], silicon V-groove carriers[12], filled plastic fiber array connectors[13], and glued interface attachment techniques[14] to thereby also reduce component costs. A review of some of this work will be provided.

Platform Selection and Preparation

Selection of the substrate for aligned packaging and hybrid integration must be carefully considered since it must fulfill a variety of functions and it must be capable of being easily fabricated with microscopic features and tolerances. Issues involving chip attachment, wire bonding, flip-chip solder bonding, passive and active optoelectronic alignment, electronic chip bonding, control of reflections, internal package atmosphere, minimization of undesired electronic parasitic impedances etc. must all be considered It is also useful to consider including optical connectors in the finished packaging concept[15, 16] and providing a means of electronic interconnection that is entirely consistent with interconnections to other hybrid subassemblies or MCMs.

Ceramic substrates can represent a good choice for use as a packaging platform. Certainly the technology for metal patterning and fabricating appropriately shaped ceramic platforms has been well developed for use in the hybrid circuit and MCM industries. Additionally, technology for the machining of precision grooves for the alignment of optical fibers and other package elements into ceramic, glass or other substrates makes them acceptable for platforms with micrometer alignment requirements.

Silicon substrates are often utilized as packaging platforms. Besides having suitable thermomechanical properties, silicon is often used as a substrate for optical waveguides using glass[17, 18] or polymeric depositions.[19] Silicon substrates may contain built-in electronic components such as termination resistors, decoupling capacitors, and transistors. An added advantage offered by silicon substrates is the substantial capability for micromachining V-grooves, precision micro stops, and a variety of optical elements[20]. Techniques used include orientation dependent etching of the single crystal substrate to reveal precisely angled crystal planes useful for alignment of optical fibers, spherical lenses, optical waveguides and etc.[21,22] The micromachining capability may also be applied to formation of pyramidal fiducial cavities that when combined with small alignment spheres can provide registration between several substrates [23] Alternatively, optical fiber glass rods can provide alignment between two or more silicon substrates with precision etched V-grooves.[24] Recently, micromachined optical components

have also been fabricated on silicon substrates with built-in passive alignment capabilities.[25]

Plastic substrates have been applied to the fabrication of optical connectors for both single and multimode optical fiber.[26] These quite precise and stable plastic alignment subassemblies with precision pin registration are molded with new, dimensionally stable, silica-filled polymer materials. Plastic materials of this sort should thus also be considered as a possible integration platform for use in optoelectronic packaging.

References

[1]C. Armiento, A. Negri, M. Tabasky, R. Boudreau, M. Rothman, T. Fitzgerald, and P. Haugsjaa, "Gigabit Transmitter Array Modules on Silicon Waferboard," *IEEE Transactions on Components, Hybrids, and Manufacturing Technology*, Vol. 15, No.6 , pp 1072-1080, (1992).

[2]M. Rothman, J. Thompson, and C. Armiento, 'Multichamber RIE Processing for InGaAsP Ridge Waveguide Laser Arrays," *Mat. Res. Soc. Symp. Proc.* Vol. 240, pp 341-348, (1992).

[3] "Temporal and Spectral Characteristics of Back-Illuminated InGaAs Metal-Semiconductor-Metal Photodetectors," M. Hargis, S. Ralph, J. Woodall, D. McInturff, A. Negri, and P. Haugsjaa, *IEEE Photonics Tech. Lett.*, vol. 8, pp. 110 - 112, (1996)

[4]" M. Rothman, C. Shieh, A. Negri, J. Thompson, C. Armiento, R. Holmstrom and J. Kaur, "Monolithically Integrated Laser/Rear Facet Monitor Arrays with V-Groove for Passive Optical Fiber Alignment", *IEEE Photonics Technology Lett.*, Vol. 5, No. 2, pp. 169-172 (Feb. 1993).

[5] C. Armiento, M. Tabasky, C. Jaganath,P. Haugsjaa, T. Fitzgerald, C. Shieh, V. Barry, M. Rothman, A. Negri, and H. Lockwood, "Passive Coupling of InGaAsP/InP Laser array and singlemode fibres using Silicon Waferboard," *Electron. Lett.*, 27, p. 1109-1111, (June 6, 1991).

[6]K. Jackson, E. Flint, M. Cina, D. Lacey, Y. Kwark, J. Trewhella, T. Caulfield, P. Buchmann, C. Harder, and P. Vettiger, "A High-Density, Four-Channel, OEIC Transceiver Module Utilizing Planar-Processed Optical Waveguides and Flip-Chip, Solder-Bump Technology," *J. Lightwave Tech.* Vol. 12, pp. 1185-1191, (1994).

[7]G. Nakagawa, K. Miura, S. Sasaki, and M. Yano, "Lens-coupled Laser-diode Module integrated on Silicon Platform," *Proceed. SPIE Laser Diode Chip and Packaging Conference* 2610, pp 59-64, (1995).

[8]M. Cohen, et al. *Photonics Tech. Letters*, Vo. 3, pp. 985 - 987 (1991).

[9] I. Collins, R. Payne, C. Ford, A. Thurlow, I Lealman, P. Fiddyment, "Technology developments for low-cost laser packaging," *Technical Digest of the 1995 Conference on Optical Fiber Communications*, pp. 222 - 221, (1995).

[10] I. F. Lealman, C. P. Seltzer, L. J. Rivers, M. J. Harlow and S. D. Perring, "Low threshold current 1.6 μm InGaAsP/InP coupling to cleaed single mode fibre," *Electron. Lett.*, vol 30, pp 973-975, (1994).

[11]H. Karstensen, C. Hanke, M. Honsberg, J. Krop, J. Wieland, M. Blaser, P. Weger, and J. Popp, 'Parallel Optical Interconnection for Uncoded Data Transmission with 1 Gb/s-per-Channel Capacity, High Dynamic Range, and Low Power Consumption," *J. Lightwave Tech.* Vol 13, pp. 1017 - 1030, (1995).

[12]S. Hall, R. Lane H. Wang, and A. Gareri, "Assembly of Laser-Fiber Arrays," *J. Lightwave Tech.* Vol. 12, pp. 1820 - 1826, (1994).

[13]T. Satake, and P. Blubaugh, "New Applications for Miniature Multifiber Connector," *Proceedings of 1993 LEOS Annual Meeting*, pp. 179-180, (1993).

[14]N. Mekada, M. Seino, Y. Kubota, and H. Nakajima, "Paractical method of waveguide-to-fiber connection: direct preparation of waveguide endface by cutting machine and reinforcement using ruby beads," *Applied Optics*, Vol 29, pp 5096-5101, (1990).

[15]Y. Wong, et. al., "Technology Development of a High Density 32-Channel 16 Gbps Optical Data Link for Optical Interconnections Applications for the Optoelectronic Technology Consortium (OETC)," *J. Lightwave Technology*, Vol. 13, pp 995 - 1016, (1995).

[16]M. Kihara, S. Nagasawa, and T. Tanifuji, "Compact, demountable optical coupling between single-mode, planar waveguides and miltifiber," *Proceedings of the Conference on Optical Fiber Communications*, pp 214 - 215, (1995).

[17]C. Henry, G. Blonder, and R. Kazarinov, "Glass Waveguides on Silicon for Hybrid Optical Packaging," *Journal of Lightwave Technology*, Vol. 7, No. 10, pp. 1530-1539, (1989).

[18] N. Takato, M. Yasu, and M. Kawatchi, "Low-Loss High-Silica, Single-Mode Channel Waveguides," *Electronics Letters*, Vol 22, pp 321-322 (1986).

[19] W. Feng, S. Lin, R. B. Hooker, and A. R. Mickelson, "Study of Channel Waveguide Performance in Nonlinear Optical Polymer Films", *App. Optics*, Vol 34, (1995)

[20] L.Lin, S. Lee, K. Pister, and M. Wu. "Micromachined Micro-Optical Bench for Optoelectronic Packaging," *Proceedings of the IEEE Laser and Electro-Optics Socitey Annual Meeting*, pp 219-220, (1994).

[21]S. Mino, K. Yoshino, Y. Yamada, M. Yasu, and K. Moriwaki, "Opto-Electronic Hybrid Integrated Laser Diode Module using Silica-on-Terraced-Silicon Platform, *Proceedings of the IEEE Laser and Electro-Optics Socitey Annual Meeting*, pp 271-272, (1994).

[22] C. Jones, K. Cooper, M. Nield, J. Ruch, J. Collins, I. Hall, A. McDonna, and S. Brown, "Hybrid Integration of Optical and Electronic Compoenents on Silicon Motherboard," *Proceedings of the IEEE Laser and Electro-Optics Socitey Annual Meeting*, pp 273-274, (1994).

[23] M.F. Dautaras, G. Blonder, Y-H Wong, Y. Chen, "A Self-Aligned Optical Subassembly for Multi-Mode Devices," *IEEE Trans. on CPMT, Part B*, Vol 18, pp. 552 - 557, (1995).

[24]R. Carson, P. Seigal, D. Craft and M. Lovejoy, "Future Manufacturing Techniques for Stacked MCM Interconnections," *Journal of Metals*, pp. 51-55, (June, 1994)

[25]S. Lee, L. Lin, M. Wu, "Micromachined Three-Dimensional Micrograting for Free-Space Integrated Mirco-Optics," *Technical Digest of the 1995 Optical Fiber Communication Conference*, pp. 229 - 230, (1995).

[26] S. Nagasawa, Y. Yokoyama, F. Ashiya, and T. Satake, " A Single-Mode multifinger Push-on Connector with Low Insertion- and high Return-Losses," *Proceedings of the 17th European Conference on Optical Communications*, pp 49-52, (1991).

SUCCESSFUL DEVELOPMENT OF NON-PLANAR LITHOGRAPHY FOR MICRO-MACHINING APPLICATIONS.

J. Shmulovich, J. V. Gates, C. F. Kane, M. A. Cappuzzo, and J. M. Szalkowski
Lucent Technologies, Bell Labs
600 Mountain Avenue, Murray Hill, NJ 07974.
Tel: (908)582-4635; Fax: (908)582-7994

Silicon micro-machined Optical Sub-Assemblies (OSA) are becoming increasingly popular in packaging of photonic devices. Good thermal conductivity of silicon, for heat sinking, ability to etch precisely controlled grooves, for fiber alignment, availability of good quality wafers, developed processing technology, and batch processing are some of the advantages that are inherent to this approach, which we call Silicon Optical Bench (SiOB) technology. It is often desirable to be able to define photolithographically patterns in close proximity to deep grooves or at the bottom of such grooves. Typical features required are: wire bonding pads, device soldering pads, alignment marks, turning mirrors, thin film heaters, coplanar microstrips, etc.

However, the conventional spin-on photoresists do not work on highly non-planar surfaces. Steps in the wafer surface lead to substantial variation of the local resist thickness during spin coating. In particular, V-grooves etched in the surface of silicon wafers, typically more than 150μm deep, present a topography that these photoresists cannot uniformly coat. The resist tends to thin out along the edges of the groove, while becoming much thicker in the low lying areas. This nonuniform distribution of photoresist does not allow for creating a well controlled resist pattern simultaneously in the high and low areas of the wafer in a single step.

To solve this problem we successfully utilized electrophoretic photoresist. Developed primarily for fine line applications in the printed wiring board industry, electrophoretic resists (ED resists) are electrically deposited photoresists with the ability to uniformly coat electrically conductive surfaces with nonplanar topographies.[1,2] Electrophoretic resist deposition occurs when an electric potential is applied across two electrodes submerged in a solution of the resist. When the voltage is applied, the resist is attracted to the negative electrode where it adheres and coats the electrode surface. The reaction is self limiting in nature such that when the deposited resist reaches a certain thickness, the negative electrode becomes insulated from the resist solution causing the deposition reaction to cease.[3] The final thickness of the deposited resist is determined primarily by a combination of the bath temperature and applied voltage. In general, increasing the temperature of the resist solution, or decreasing the applied voltage will decrease the deposited resist thickness.

The conformal coating capability of electrophoretic resists allow the micro-machined wafers to be patterned following steps similar to conventional photoresist processing once the resist has been deposited. In this communication we will describe the application of the ED resist technology to the fabrication of PIN-PAC OSA. PIN-PAC utilizes an etched V-groove for fiber alignment and attachment, and a metallized end of a V-groove as a turning mirror, directing the light from the fiber toward the photodetector mounted on top of the groove and bridging it. The photodetectors were passively aligned to the turning mirrors by solder bumps formed on solder pads that were accurately registered lithographically in relation to the mirror. The PIN-PAC OSA requires metal to be patterned in the V-groove, as well as on the surface of the wafer in close proximity to the groove. Commercially available Shipley Eagle 2100 ED resist was used in all lithography steps. The details of resist deposition, exposure and developing are readily available from Shipley.

PIN-PAC OSAs were fabricated from 500μm thick, 125mm, <100> silicon wafers. Prior to metal deposition V-grooves, 190μm deep and 272 μm wide, were etched in the surface of the wafers for fiber attachment. After the V-grooves have been etched in the starting wafers, a 10 μm

thick SiO_2 film was grown on the wafer surface by High Pressure Oxidation (HIPOX). The base metal Ti/Pt 1000/2000Å was sputtered on the wafers, and after deposition the wafers were coated with a layer of ED resist. The patterned resist is shown in Figure 1 after exposure and development(developer Shipley Eagle 2005 at 40°C) but prior to the metal's etch. The turning mirror and bonding pads are clearly visible in the figure. The Pt layer was etched by ion milling in a Technics Ion Miller, with the resist acting as the etch mask. The wafer was positioned perpendicular to the ion beam to ensure that the metal at the bottom of the groove is milled. Without stripping the resist, Ti was etched in a solution of 100:1 HF (H_2O:49wt% HF) for approximately 1 minute. After the metals have been etched, the resist was stripped in Eagle 2009 Remover at 85°C for 10 minutes. At the next step a 10,000Å layer of gold was sputtered on the wafers, and etched in diluted aqua regia, using resist as a mask. The gold is used to lower the resistivity of the interconnects and to allow wire bonding. The next step is solder dam layer deposition and patterning. Non-wettable oxidized films of Cr or Ti have been used to form the solder dams. The Au/Sn solder was evaporated on the bonding pads and on part of the solder dam area, using lift-off technique. After solder deposition the solder was reflowed to form solder bumps by heating the devices above the solder melting temperature and causing the solder to dewet from the solder dams. Utilization of solder dams and solder reflow step allows to reduce the deposited layer thickness well bellow the required bump height by concentrating solder from a larger dam area into the area of the smaller bonding pad.

The final patterned OSA with solder bumps is shown in Figure 2. Two V-grooves are visible as black horizontal rectangular strips. On both sides of the grooves rectangular elongated bonding sites for the photodiode are positioned. In them the small dark squares are the reflown solder bumps which are surrounded by lighter dark areas that are the uncovered solder dams. The triangles are alignment marks for positioning the photodiode. A close-up of the solder bonding site before and after reflow is shown in Figures 3a and 3b, respectively In Figure 3a we can see on the left a part of the gold pad and the large, grainy, dark square on the right is as deposited solder. A small uncovered portion of the solder dam is seen as a white stripe between them. The entire solder dam area is visible around the solder in Figure 3b.

A general view of a part of a PIN-PAC silicon OSA wafer populated with photodiodes is shown in Figure 4. The devices were first tack-bonded onto the bonding pads, then the assembly was put in an oven and the solder was reflown, allowing the solder bumps to passively align all the devices at once. The devices were wire bonded and electrically tested on the silicon wafer. After test the wafer was mounted on tape, diced into individual OSAs, cleaned on tape, and finally picked from the tape to be used in packages. No wire bonds loss or electric damage to the photodetectors were incurred in the separation process.

Our ability to pattern thin films over highly non-planar topographies extends the applications of the SiOB technology. It enables high level integration of a number of features critical to the batch packaging of photonic devices, such as V-grooves, solder sites, wire bonding pads, etc., leading to their low cost manufacturing.

References

1. J. M. Collins,"Printed Circuit Fabrication", **62**, March 1991.
2. J. Murray,"Printed Circuit Fabrication", **44**, June 1991.
3. Eagle 2100 ED Photoresist Technical Information Sheet, available from Shipley Co.

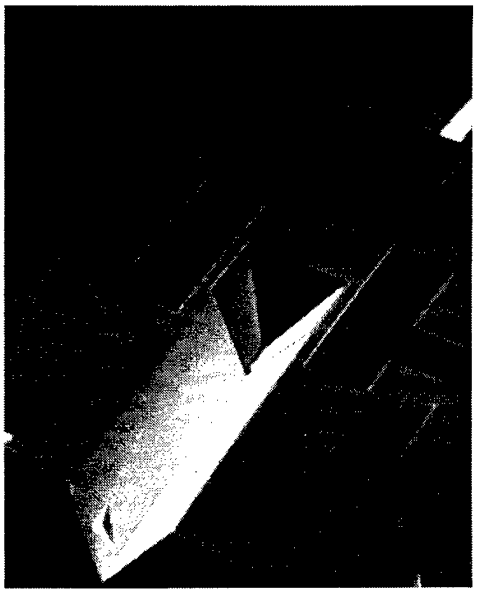


Figure 1. SEM micrograph of patterned electrophoretic resist

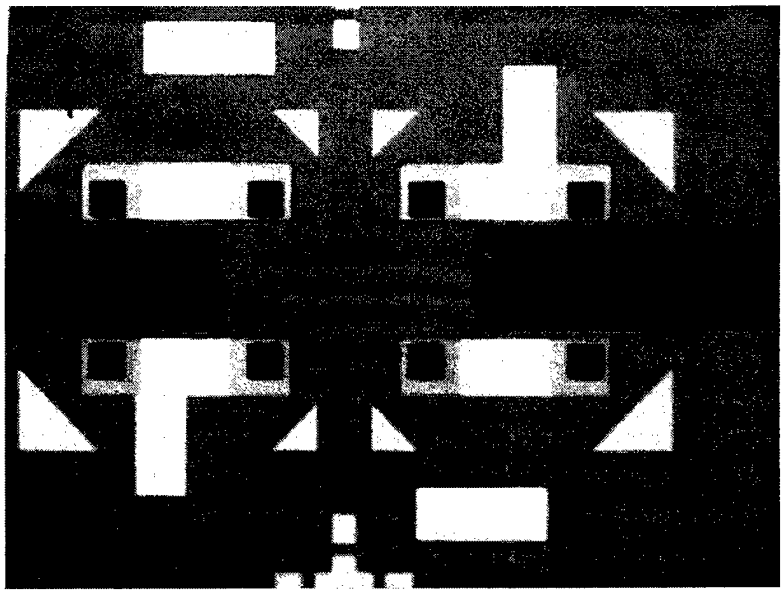
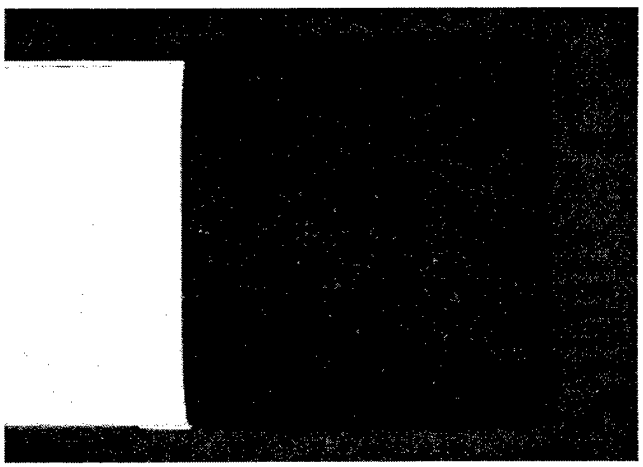


Figure 2. Top view of patterned Optical Sub-Assembly after solder bumps reflow



a) Solder pad showing deposited solder



b) Solder pad showing reflowed solder

Figure 3. Micrographs of Optical Sub-Assembly solder bonding pad before and after solder reflow

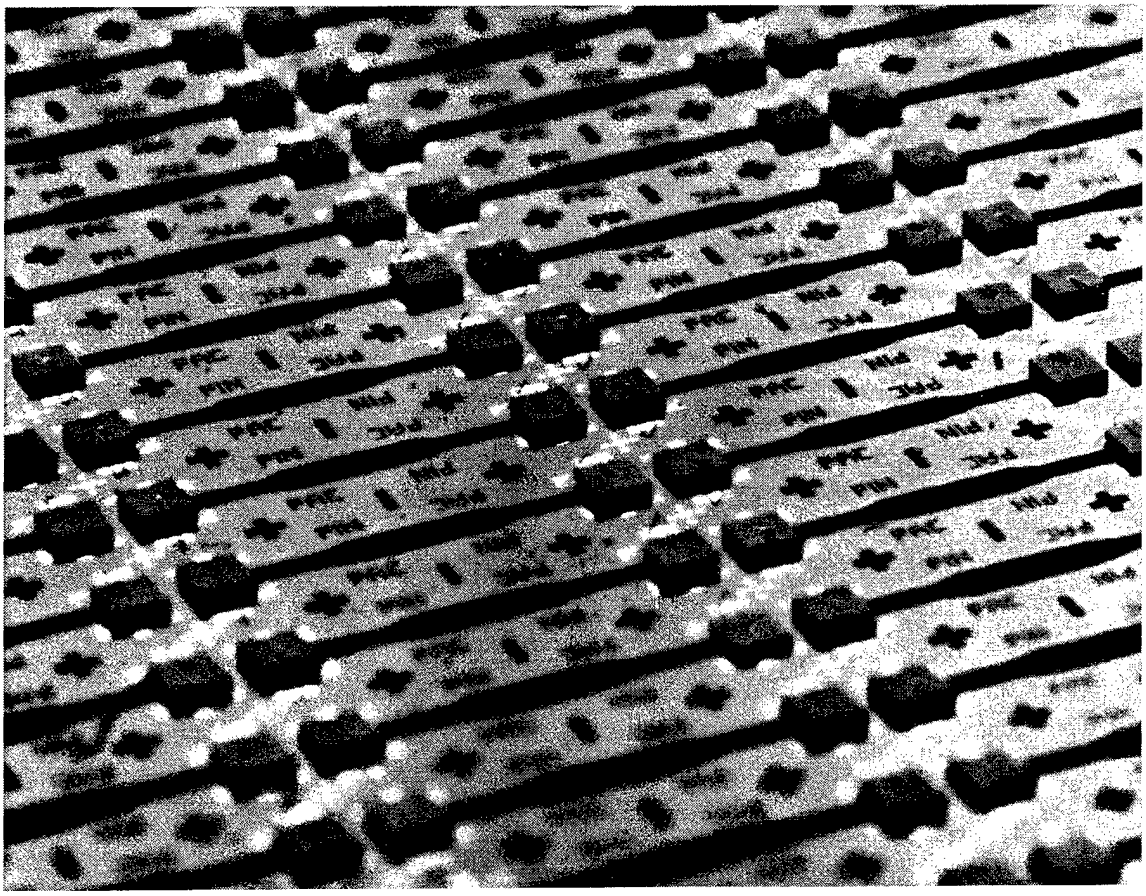


Figure 4. Processed silicon wafer populated with photodetectors

Thermal Study of Silicon Optical Microbenches with on Board Heaters for Soldering

Michael D. Pocha, Oliver T. Strand and John A. Kerns
Lawrence Livermore National Laboratory
P.O. Box 808, L-222, Livermore, CA 94550
(510) 422-8664, FAX (510) 422-2783

Introduction

High-precision packaging of optoelectronic (OE) components is a labor-intensive and expensive process. We believe that the pigtailing process must be automated to realize a significant reduction in the cost of OE packages. We are addressing issues of automating the fiber pigtailing process on silicon waferboards or microbenches. While we are initially concentrating on laser diodes, the same techniques are applicable to other OE devices. This paper focuses on reflowing solders for the attachment of OE components on silicon microbenches. Nearly ten years ago, miniature metallic heaters to reflow solder for the attachment of OE components on ceramic waferboards were developed [1]. We have recently developed miniature polysilicon heaters which are compatible with silicon microbenches [2]. These miniature heaters avoid the problem of raising the entire microbench to the solder melting point to attach components. Most importantly, these miniature heaters are completely compatible with automating the attachment process.

Designing silicon microbenches with on-board heaters requires some care. The thermal properties of the microbench itself along with all coatings on the surface and any heatsinking materials must be understood. The heaters must operate in a current and voltage regime compatible with the overall characteristics of the OE package. Inadvertently reflowing solder in unanticipated locations may occur unless the thermal behavior of the microbench is thoroughly known. This paper, then, describes an experimental and theoretical study we have performed on these silicon microbenches which gives us a complete picture of their thermal behavior. We have two goals. First, we want to understand the temperature distribution on our existing microbench designs. Secondly we want to develop a computational tool to model the thermal behavior and help us to design future microbenches. The next section describes the geometry of our existing silicon microbenches and the following section describes the theoretical thermal model we are using and simulations to extend our experimental results. The final sections present the results of the experiments and their comparison with the model.

Structure and construction of microbenches

Construction of our silicon microbenches begins with single-crystal silicon wafers as a substrate. We use a standard silicon wafer thickness of 400-500μm. Wells and pedestals are etched into the silicon as needed to approximately align, in the vertical direction, the optical axis of the various components to be mounted. Next a thick layer of silicon dioxide (SiO_2) is deposited and etched to provide some degree of thermal isolation of other areas from the heaters. The thermal resistance of SiO_2 is approximately two orders of magnitude greater than that of silicon so a 5μm thick layer of SiO_2 is thermally equivalent to a 500μm thick layer of silicon. With plasma-assisted Chemical Vapor Deposition, it is possible to deposit layers of SiO_2 up to 20-30μm thick. We generally use a thickness of 5-10μm depending on the needs of each application.

The heaters are made by depositing, doping, and patterning an approximately 1μm thick layer of polycrystalline silicon (polysilicon). The doping is adjusted to result in a resistance of the heaters of approximately 10-50Ω. Resistors in this range give the greatest control at the temperatures of interest with standard laboratory power supplies. A final metal layer of a standard Cr/Au or Ti/Au metallization completes the interconnect

structure to provide electrical connections to the heaters and a layer of metal that is strongly adherent to both silicon and SiO_2 and to which most standard solders will adhere.

Figure 1 shows the top view of a typical microbench. The overall dimensions are about 6mm x 13mm. The spacing between the mounting location of the laser diode and the nearest heater is approximately 1mm and the second heater is about 5mm away from the first. By judicious choice of solders and power to the heaters we can solder the laser diode, a thermistor, and metal coated fiber to the top as well as a thermoelectric cooler to the bottom of the microbench with just these two heaters. Using this technique we have been able to achieve sub-micron tolerance of conically tapered fiber actively aligned and attached with coupling efficiencies as high as 65%.

Thermal Modeling and Simulation

A mechanical finite-element modeling code called COSMOS/M[3] was used to develop a predictive model of the temperature response of the silicon microbench to various heating pulses. Full three dimensional simulation is needed to account for all the heat flow in the structure, however we found that we could simplify the model by approximating the three dimensional physical structure as a two dimensional axisymmetric problem. This was justified because the microbench is thin compared to its overall width and length dimensions. Heat penetrates quickly through the thin wafer and then spreads radially outward. Our strategy here was to compare the model to measured results at two extremes of heatsinking. First, heat sinking only around the edge of the microbench simulates minimum cooling where just natural convection of air provides the cooling. Second, heat sinking under the entire microbench provides much larger thermal losses and simulates the attachment of the microbench to a real package. For comparison with our experiments, we modeled different types of heatsink materials including glass, brass, and a thermal-electric cooler. We did not permanently solder the microbenches to the heatsinks, so that the benches and the heatsinks could be reused. The microbenches were attached to the heat sinks by either a thin layer of silicone grease or thermal epoxy.

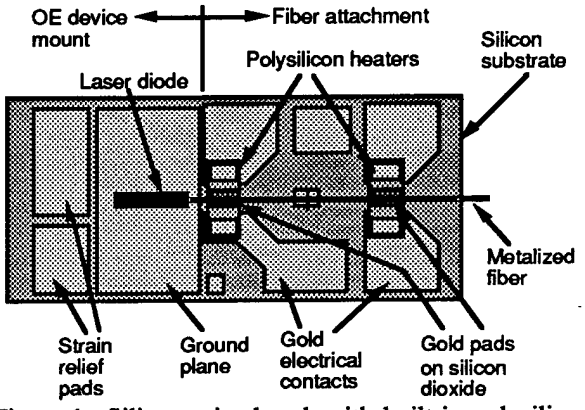


Figure 1. Silicon microbench with built-in polysilicon heaters for manufacturable solder reflow.

Because the edge boundaries of the microbench are relatively far from the heat source we can use a circular heat source in the model to approximate the actual rectangular heat source. This gives accurate central temperatures, relative edge temperatures at the source boundary, and accurate temperatures far from the source. Local temperature prediction at the heater determines the melt or remelt of the solder, while temperatures far from the heater determine the fate of the other solder junctions on the microbench.

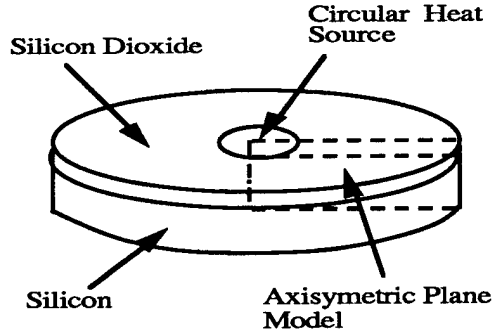


Figure 2. Thermal model of the silicon microbench showing the cylindrical approximation to the physical model and the planar section used in the simulation. Heat is removed by natural convection from the top surface and by a heat sink located under the microbench.

The thermal model developed for the microbench assumes axial symmetry and is a plane section cut radially from a cylindrical piece of silicon. A sketch of the axisymmetric

model is shown in Figure 2. The height of the rectangular plane is equal to the thickness of the silicon (450 μm) plus a 25 μm height that approximates the 5 μm insulation layer of silicon dioxide. The insulation layer was purposely made thicker so that fewer nodes would be required in the simulation. The material properties of the insulation were adjusted to match the thermal properties of the 5 μm silicon dioxide layer. Natural convection heat transfer removes some heat from the surface of the microbench but the majority of the heat is removed through contact resistance with heat sinks located near the bottom edges of the microbench or under the microbench. The contact resistance between the microbench and a heat sink is a large thermal barrier to heat flow. This resistance is difficult to predict accurately because of uncertainties in the gap height between contacting parts. For this study, the contact resistance was the only variable in the model used to match the data.

We are running COSMOS/M on a Macintosh II with a 16 MHz 68030 processor and a math co-processor. On this somewhat primitive platform we can perform steady state simulations in less than 10 minutes and transient simulations in less than 30 minutes.

Experimental Setup

The experimental data was gathered using a flexible IEEE-488 bus controlled measurement system. Measurements were taken of temperature vs. time with a variety of applied electrical power pulses and at several locations on the microbench. For transient measurements shorter than one second we found that it was necessary to attach miniature chip thermistors to the microbench. The thermal response time of even the smallest thermocouple we had available was too long (several seconds). Thermistors, however, are restricted to a temperature range below 150°C. So, for short pulses our experimental data is restricted to that range. We can extrapolate the experimental data to higher temperatures with the computer simulations. Three chip thermistors were mounted on each microbench tested: one on top of the central heater, the next approximately 2mm away on the diode mounting pad, and the third on one of the strain relief pads about 5mm from the heater.

Experimental Results

Due to limitation of space, only a few sample results are described here; additional results will be presented at the conference. Figure 3

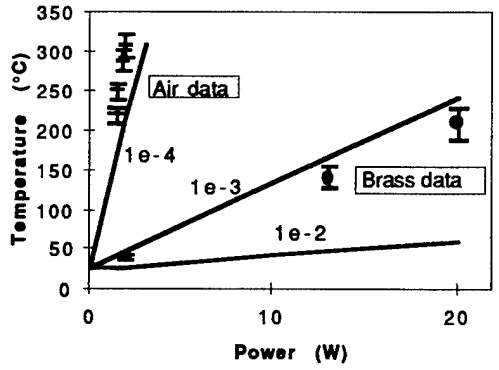


Figure 3. Simulated and experimental plot of steady state temperature with various values of cooling coefficients to represent heatsinking.

shows a plot of steady state temperature vs. electrical power applied to the heater for several different cooling coefficients in units of W/mm^2-°C. The experimental data allows determination of the effective cooling coefficients. From such plots we can calibrate the model for a particular cooling mechanism. Using this model, we can make this kind of plot for any location on the microbench.

Figure 4 shows the decrease in temperature with distance away from a heater for different electrical pulse lengths. This

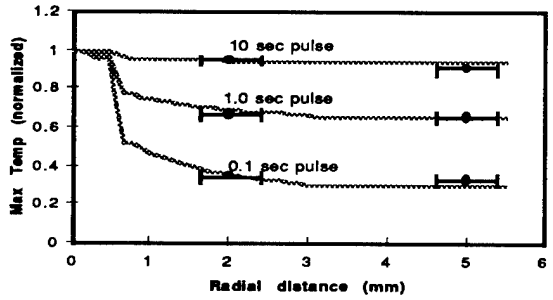


Figure 4. Typical plot of normalized temperature vs. radial position for various lengths of electrical pulses applied to the heater

information allows one to determine how far apart to design the attachment points of

components which must be soldered sequentially in time. One wants to maintain the first component at a temperature lower than the melting point of the solder while attaching subsequent components. As one would expect, a short pulse results in a larger decrease in temperature with distance because the heat is initially concentrated only at the heater.

Conclusion

An experimental and theoretical study has been conducted of the thermal behavior of silicon microbenches with on-board heaters for solder reflow. The combination of selected experimental measurements with finite element simulation of the thermal behavior of the structure allows us to gain a good understanding of temperature distributions on the microbench under various conditions of power applied to heaters and for different heatsinks. The result is an accurate predictive model of the silicon microbench.

Acknowledgments

The authors would like to thank their colleagues Leslie Jones, Kirk Kleint, and Ronald Tilley for help in fabricating microbenches and taking experimental data. This work was performed under the auspices of the U.S. Department of Energy by Lawrence Livermore National Laboratory under contract No. W-7405-Eng-48.

References

1. S. Enochs, "A packaging technique to achieve stable single-mode fiber to laser alignment," *SPIE Integration and Packaging of Optoelectronic Devices, Vol. 703*, p 42 (1986).

2. M. Lowry, et. al., "Low-Cost Packaging of High-Performance Optoelectronic Components," IPR-95 *Technical Digest, Vol. 7*, pp.77-79, Feb. 23-25, 1995

3. Available from Structural Research Analysis Corp., 1661 Lincoln Blvd., Suite 200, Santa Monica, CA 90404, Phone: (310) 452-2158

High Speed Devices

ITuG 3:30 pm-5:00 pm
Fairfax A

Jane E. Zucker, *Presider*
AT&T Bell Laboratories

Mach-Zehnder modulator integrated with a gain-coupled DFB laser for 10 Gbit/s, 100 km NDSF transmission at 1.55 μm

D. M. Adams, C. Rolland, N. Puetz, R. S. Moore, J. Yu, F. R. Shepherd, H. B. Kim, and S. Bradshaw

Advanced Technology Laboratory, Nortel Technology,
P.O. Box 3511, Station C, Ottawa, K1Y 4H7, Canada
phone: (613) 763-8651 fax: (613) 763-4147 email: adams@nortel.ca

Introduction

The monolithic integration of lasers and modulators in InGaAsP/InP is an attractive approach for the manufacture of compact, low-chirp sources with low packaging cost for high bit rate fiber transmission systems. For the control of chirp, the use of an interferometric Mach-Zehnder (MZ) modulator provides more flexibility than modulation by electro-absorption [1]. Zucker *et al.* have demonstrated a MZ modulator integrated with a superposed DBR laser [2], and more recently Tambun-Ek *et al.* have reported a MZ integrated with an optical amplifier and a conventional DFB laser, fabricated by selective area growth [3]. Although both of these implementations offer the advantage of a small number of growth steps, the designs of the MZ and laser active regions are mutually constrained. In contrast, integration by butt-coupling virtually eliminates design constraints, allowing the DFB laser and modulator active regions to be independently optimized with respect to the choice of the number of quantum wells, the quantum well and barrier compositions, the doping profiles, and the optical confinement factors.

In this paper, we present the first monolithically integrated MZ/DFB device fabricated by butt-coupling. We also report the first high-speed and long-distance operation for an integrated MZ/DFB device. The chosen MZ modulator design provides high bandwidth and low excess losses [4]. For the light source, gain-coupled (GC) DFB lasers were selected because they provide high single mode yield [5], high side mode suppression [6], relatively low sensitivity to external reflections [7], and an external quantum efficiency which can be enhanced by the application of a high-reflectivity coating to the back facet. With the integrated MZ/DFB we demonstrate 10 Gbit/s transmission over 100 km of non-dispersion-shifted fiber (NDSF) at λ=1.55 μm.

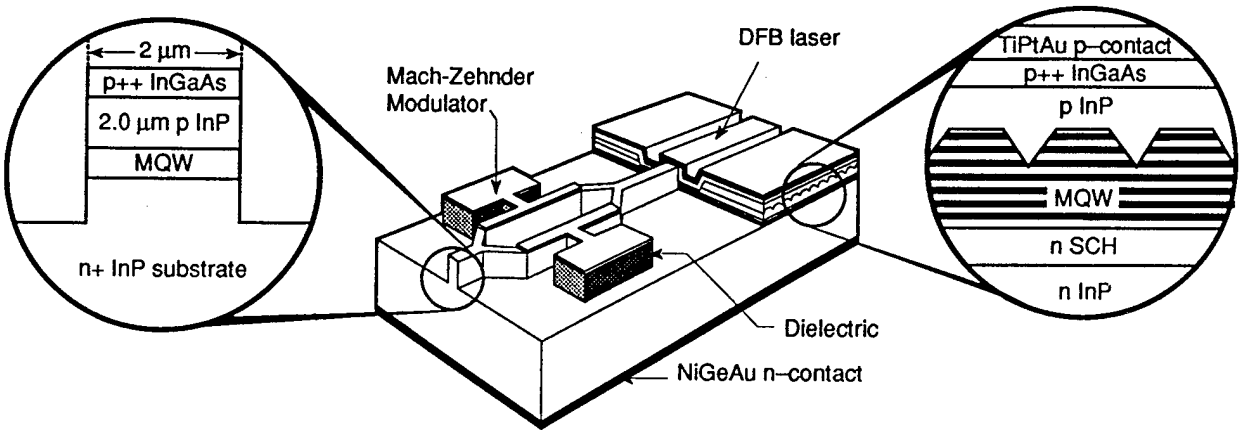


Figure 1: Schematic diagram of the Mach-Zehnder modulator which is monolithically integrated with a gain-coupled distributed feedback laser.

Device structure and fabrication

The integrated MZ/DFB structure is illustrated in Figure 1. The fabrication involves a total of 4 low-pressure MOCVD epitaxial steps. The first two epitaxial steps constitute the laser active region growth and the overgrowth of the first-order DFB grating. Trenches are etched to accommodate the MZ active region, which is deposited in the third growth. The p-type InP ridge and InGaAs p-contact layers, which are common to both the ridge-waveguide DFB and MZ, are added in the fourth growth. The MZ length is 1.5 mm, and the dimensions and the definition process of the waveguides in the MZ region is identical to that reported previously [4]. The MZ material (both quantum wells and ridges) show excellent planarity everywhere, except for a small transition region within 0.5 μm of the butt-joint. The optical coupling loss at the butt-coupling joint between the laser and MZ was measured to be as low as 0.75 dB (1.2 dB typical). The GC-DFB lasers have a ridge height and width of approximately 2 μm.

The MZ active region consists of twenty 95 A InGaAsP quantum wells separated by 80 A InP barriers, with a photoluminescence emission peak at $\lambda = 1.45$ μm. The voltage swing to one arm which was required to achieve maximum extinction of 17.7 dB was 4.57 Volts. The total insertion losses from the integrated laser into a tapered fiber aligned to the MZ output is estimated to be 12.8 ± 2.4 dB.

The DFB has a "truncated-well" gain-coupled active region structure, having 3 of its 7 compressively strained quantum wells etched by the grating. The GC-DFB's

exhibited a single mode yield of 90% (SMSR>35 dB) at I=100 mA for a sample size of 304 integrated devices, consistent with the yield reported for standalone GC-DFB's of similar design [5]. With the MZ/DFB having the front facet anti-reflection coated and the back facet uncoated, optical powers slightly in excess of 0.5 mW into tapered fiber have been achieved for a laser bias current of 125 mA. Additional power would be available with the use of a high reflectivity coating on the laser back facet. A typical DFB spectrum obtained from the front facet of an integrated MZ/DFB is shown in Fig. 2.

Transmission Experiment

The integrated MZ/DFB chip was attached p-side-up on a carrier patterned with co-planar transmission lines terminated with a 50 Ohm resistor. The DFB was biased at 100 mA and the heatsink temperature was set at 20 C. The MZ arms were driven differentially at 10 Gbit/s from -4.0V to -2.0V and -3.8V to -5.8V by the output of a pseudo-random bit sequence generator (PRBS). Under these conditions, the extinction ratio was 10.8 dB.

The fiber-coupled MZ/DFB output signal was followed by an optical isolator, an erbium doped fiber amplifier (EDFA), and an optical bandpass filter (1.5 nm FWHM) to reduce the amplified spontaneous emission noise from the EDFA. The waveform at 0 km for a PRBS pattern length of 2^7-1 is shown by the eye-diagram in Fig. 3(a). The eye-diagram obtained by a Tektronix SD-46 photodetector after 80 km and 100 km of NDSF is given in Figs. 3(b) and 3(c), respectively. An optical receiver based on a SAGCM APD [8] with an HBT preamplifier (500 Ohm transimpedance) was employed to assess the dispersion penalty after transmission through the NDSF. The BER vs. received power curves at 0, 80 km, and 100 km all obeyed a classic logarithmic waterfall form, with no evidence of BER flooring. The displacement between the BER curves for 0 km and 100 km revealed a penalty of only 0.8 dB, which is in reasonable agreement with the performance of a discrete III-V MZ device [9].

Conclusion

An InGaAsP/InP MZ modulator integrated by butt-coupling with a gain-coupled distributed-feedback laser has been demonstrated for the first time. 10 Gbit/s transmission over 100 km of NDSF at λ=1.55 μm is achieved with a receiver penalty of less than 1 dB. Approximately 90% of the integrated gain-coupled DFB's lase in a single longitudinal mode at 100 mA.

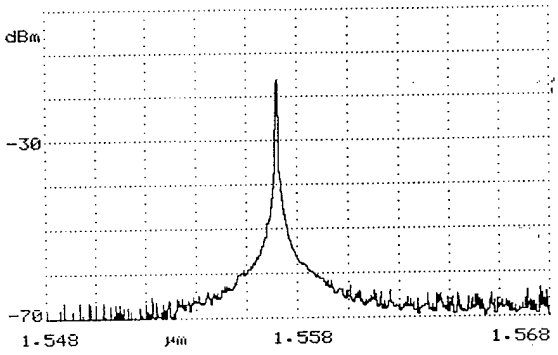
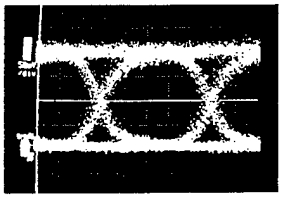
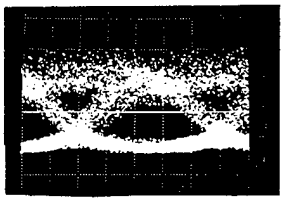


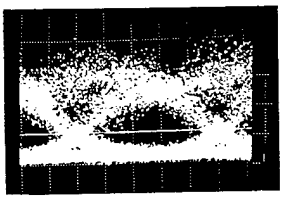
Figure 2. Typical power versus wavelength spectrum measured from the front facet of the integrated MZ/DFB at I=120 mA and T=20 C. The vertical scale is 10 dB per division.



a) 0 km



b) 80 km NDSF



c) 100 km NDSF

Figure 3: Received optical eye diagram at 10 GBit/s after: a) 0 km, b) 80 km, and c) 100 km of NDSF

References:

[1] Cartledge, J. C., Rolland, C. R., Lemerle, S., Solheim, A., IEEE Phot.. Tech. Lett., 1994, 6, pp. 282-284.
[2] Zucker, J. E., Jones, K. L., Newkirk, M. A., Gnall, R. P., Miller, B. I., Yound, M. G., Koren, U., Burrus, C. A., and Tell, B., Electron. Lett., 1992, **28**, pp. 1888-1889.
[3] Tanbun-Ek, P. F., Sciortino, P. F., Sergent, A. M., Wecht, K. W., Wisk, P., Chen, Y. K., Bethea, C. G., and Sputz, S. K., IEEE Phot. Tech. Lett., 1995, **7**, pp. 1019-1021.
[4] Rolland, C., Moore, R. S., Shepherd, F., and Hillier, G., Electron. Lett., 1993, **29**, pp. 471-472.
[5] Adams, D. M., and Makino, T., Electron. Lett., 1995, **31**, pp. 976-977.
[6] Lu, H., Blaauw, C., and Makino, T., IEEE Photon. Tech. Lett., 1995, 7, pp. 613-615.
[7] Li, G.-P., Makino, T., Lu, H., Hong, J., and Huang, W., Proc. of the SPIE, 1994, **2148**, pp. 238-245.
[8] Tarof, L. E., Bruce, R., Knight, D. G., Yu, J., Kim, H. B., and Baird, T., IEEE Phot. Tech. Lett., 1995, **7**, pp. 1330-1332.
[9] Rolland, C. R., O'Sullivan, M. S., Kim, H. B., Moore, R. S., and Hillier, G., OFC '93, San Diego CA, 1993, paper PD 27.

Small chirp, low drive-voltage integrated 10 Gb/s DFB laser and bulk electro-absorption modulator on semi-insulating InP substrate

Olof Sahlén, Lennart Lundqvist and Stefan Funke
Ericsson Components AB, S-164 81 Kista, Sweden
Telephone: + 46 8 757 5000. Telefax: + 46 8 757 4764.

Introduction: Integrated lasers and electro-absorption modulators have attained large interest, [1]-[8], for long distance, high bitrate transmission. In this paper we report on monolithically integrated DFB lasers and bulk modulators on semi-insulating (SI) InP substrate. The main reasons to develop SI-substrate devices are (i) the reduced stray capacitances, (ii) possibilities to make arrays, (iii) easier integration with co-planar microwave waveguides, (iv) future integration with InP Heterojunction Bipolar Transistor (HBT) drive stages. By proper optimisation (i.e. choice of bandgap wavelength of the modulator with respect to the DFB lasing wavelength) we obtain zero-bias operation with low drive voltage and small chirp. Short modulator (150 μm) devices have a 3-dB bandwidth of up to 19 GHz and can be operated with a voltage swing from 0 to -2 V with 10 dB extinction ratio, and have good transmission properties in 10 Gb/s transmission experiments. In particular they operate penalty-free at 40 km standard fibre. With long modulator (300 μm) devices, less than 1 V drive voltage for 10 dB extinction with >9 GHz modulation bandwidth can be obtained. We believe this is the lowest drive voltage reported for integrated bulk modulators useful for 10 Gb/s. The temperature dependence is also investigated and conclusions made regarding the usefulness in WDM applications.

Design and fabrication: Figures 1 and 2 show cross-sections of the DFB section and of the modulator section, respectively. First, a 2.8 μm thick, n-doped (varying from $3\bullet10^{18}$ cm^{-3} at the bottom to $1\bullet10^{18}$ cm^{-3} close to the active layer) InP layer is grown. A 0.15 μm thick, undoped, active quaternary layer with luminescence wavelength of 1.55 μm (Q1.55), a 0.12 μm thick p-doped ($2\bullet10^{17}$ cm^{-3}) InP layer and a 0.028 μm thick Q1.30 grating layer follow. After grating definition with electron-beam lithography and wet etching, InP regrowth over the grating takes place. The grating includes a symmetrically placed quarter-wave shift. Subsequently, 400 μm long lasers are defined by etching down into the bottom n-doped InP layer. The modulator and passive sections are formed by butt-joint growth of a 0.16 μm thick undoped Q1.48 layer, a 0.04 μm thick undoped Q1.05 layer (to avoid hole pile-up) and a thin p-InP ($2\bullet10^{17}$ cm^{-3}) layer. Subsequently, 1.3 μm wide waveguides are formed. Current-blocking, 1.7 μm thick SI-InP and 0.5 μm thick n-InP ($1\bullet10^{18}$ cm^{-3}) are regrown around the waveguide mesa. Finally p-InP ($1\bullet10^{18}$ cm^{-3}) and p-InGaAs contact layers are grown. MOVPE is used throughout for the epitaxy. A sequence of reactive ion etching (RIE) steps is used to obtain the geometry in Figures 1 and 2. The modulator is terminated with a window-structure and anti-reflection coating.

Short integrated modulator (150 μm) performance: The small-signal 3-dB bandwidth of short devices (150 μm long modulator) was up to 19 GHz (measured with 50 Ω parallel load). The threshold current was typically 22 mA at 293 K, and the DFB emission wavelength was around 1530 nm. The side-mode suppression ratio typically exceeded 40 dB. Figure 3 displays the extinction and chirp (measured with the method in [9]) as function of modulator bias. About 10 dB extinction was obtained when operating the modulator between 0 and -2 V. The chirping parameter varied from 0.3 to -0.45.

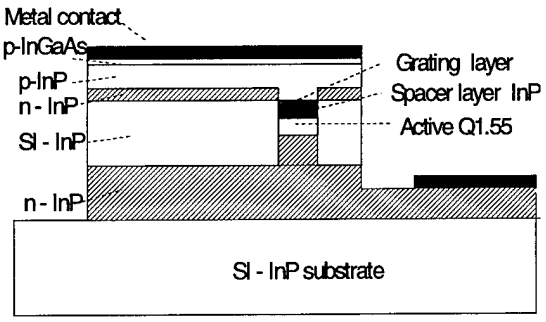


Figure 1. Laser cross-section.

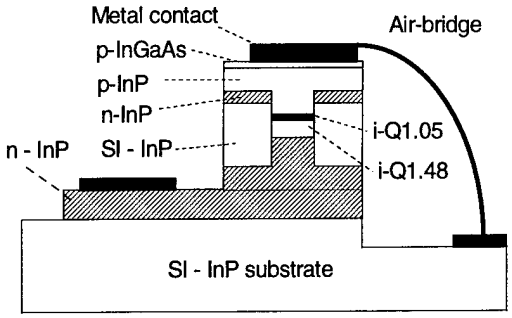


Figure 2. Modulator cross-section.

Transmission experiments: A 150 µm device operated at 293 K , with 125 mA DFB laser current, was driven from 0 V to slightly below -2 V, to give 11 dB extinction ratio, with a 10 Gb/s, PRBS 2^7-1 sequence. The chip mean output power was 0 dBm. The experimental set-up consisted of the transmitter chip, an Erbium-Doped Fibre Amplifier (EDFA) giving +6 dBm mean output power (thus assuring linear transmission), standard (i.e. non-dispersion-shifted) transmission fibre, an EDFA pre-amplifier followed by a wide-band 50 Ω receiver and electrical amplifiers. For 41 km transmission no significant penalty was seen, whereas a penalty of 2.5 dB (+/- 0.5 dB) was obtained at 71 km. Figure 4 shows the measured Bit Error Rate (BER). The measured penalties obtained agree well with calculated penalties (based on the chirp and extinction functions in Figure 3).

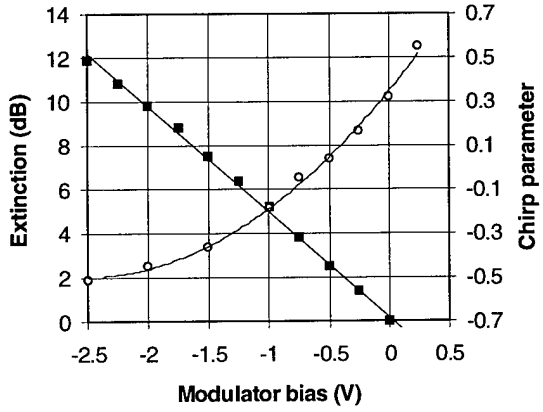


Figure 3. Extinction ratio (solid squares, left axis) and chirp parameter (open circles, right axis) as function of applied modulator bias, for an integrated 150 µm long modulator integrated with a DFB laser.

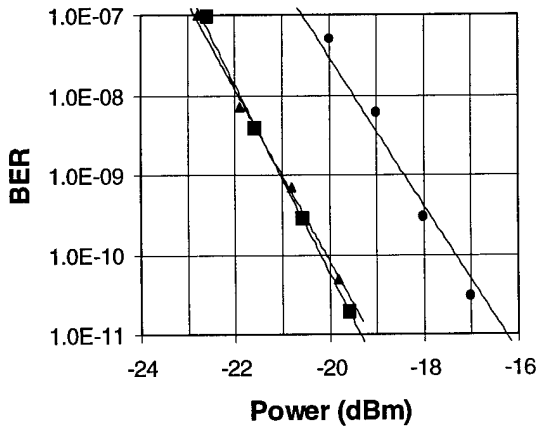


Figure 4. Bit Error Rate (BER) as function of received mean power at 0 km (triangles), 41 km (squares) and 71 km (closed circles) transmission on a standard fibre. 150 µm long integrated modulator, operated with 11 dB extinction ratio and at zero bias.

Temperature dependence: The temperature dependence gives information on how critically the device must be controlled. Also, when the temperature is changed, the wavelength detuning between the DFB laser and the modulator bandgap changes. The DFB laser emission wavelength changes little (≈1 Å / K) whereas the modulator bandgap changes much more (≈6 Å / K), so that one gets information on the performance if it should be used in wavelength-tuneable transmitters (i.e. arrays of wavelength-shifted DFB or DBR lasers).

Figure 5 shows the insertion loss (defined as the absorption loss determined by measuring the photocurrent) at zero bias and the chirp parameter measured at a bias giving 3 dB extinction (relative to zero bias), as functions of chip temperature. One can show that the chirp at a voltage giving 3 dB extinction can be used as a roughly representative, effective chirp parameter under digital modulation. We have done full transmission simulations - using field-dependent chirp parameters - in order to verify this. (Other groups have also suggested using various average chirp parameters [10].) Figure 6 shows the modulator bias voltage required for 3 dB and 10 dB extinction, for the 150 μm long device. The conclusion is that the devices can be used in a temperature range > 20 K, or equivalently in a wavelength range > 10 nm, in 40 km standard fibre 10 Gb/s systems.

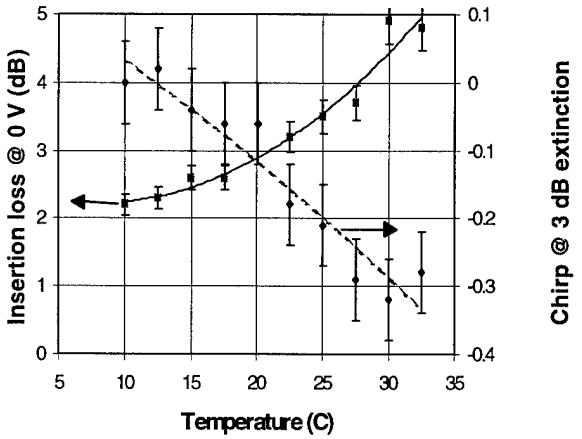


Figure 5. Insertion loss (left) and chirp parameter at 3 dB extinction (right) as function of chip temperature, for a 150 μm long modulator + DFB. AR coating used.

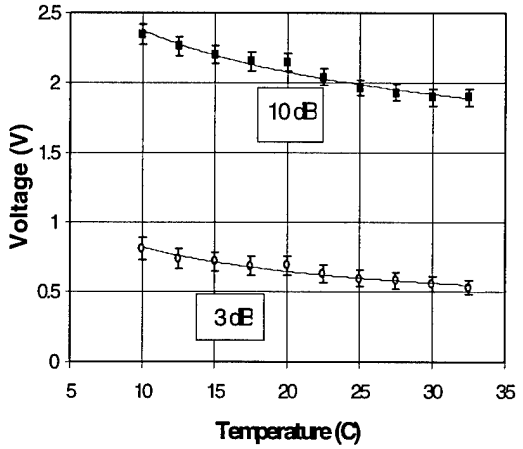


Figure 6. Voltage (relative to zero bias) for 3 dB and 10 dB extinction, as function of temperature, for a 150 μm long modulator + DFB. AR coating used.

Integration with long (300 μm) modulator For 10 Gb/s applications, a modulation bandwidth of 7 - 8 GHz is in principle sufficient (although higher bandwidth is useful, i.e. to facilitate the modulator driving and avoid electrical reflections). We therefore fabricated devices similar to the ones above, with 300 μm long modulator sections. Figures 7 and 8 show the corresponding results for the longer modulator, as shown for the shorter device in Figures 5 and 6. The 3-dB modulation bandwidth was larger than 9 GHz. The waviness on the chirp function in Figure 7 is due to that this device was yet not AR coated. Thus the influence of reflection-induced wavelength deviations in the DFB laser is apparent in Figure 7: When the temperature is changed, the phase of the reflected light is modified and hence the (effective) chirp parameter. These oscillations will disappear after AR coating. From Figure 8 it is seen that less than 1 V drive voltage for 10 dB extinction can be obtained with

properly designed 10 Gb/s bulk modulator integrated with a DFB laser on semi-insulating substrate (similar low drive voltage has been obtained for stand-alone bulk modulators [11], using high-mesa ridge structures with polyimide burying layer).

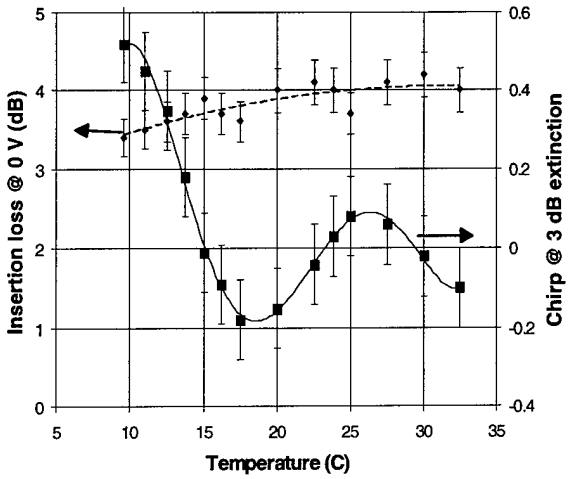


Figure 7. Insertion loss (left) and chirp parameter at 3 dB extinction (right) as function of chip temperature, for a 300 μm long modulator+DFB. No AR coating.

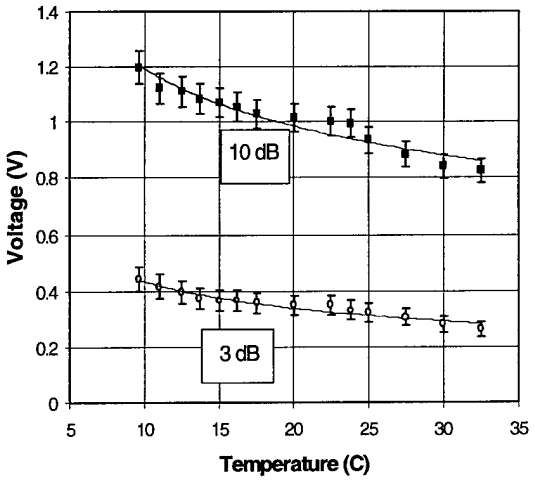


Figure 8. Voltage (relative to zero bias) for 3 dB and 10 dB extinction, as function of temperature, for a 300 μm long modulator+DFB. No AR coating.

Conclusion: DFB lasers integrated with nearly optimised bulk modulators on SI InP substrate show promising performance for 10 Gb/s systems in terms of drive voltage and chirping. Short devices, with up to 19 GHz modulation bandwidth, can be operated with zero bias and 2 V swing in 10 Gb/s systems in a 20 K or, equivalently a 10 nm, window. With a longer device, less than 1 V swing at zero bias is sufficient for 10 dB extinction, while the modulation bandwidth remains sufficient for 10 Gb/s.

[1] Ojala, P., Pettersson, C., Stoltz, B., Mörner, A.-C., Janson, M., and Sahlén, O., Electron. Lett., vol. 29, no. 10, pp. 859-860 (1993).

[2] Aoki, M. and Sano, H., Technical Digest from OFC'95, San Diego, CA, USA, February 26 - March 3, 1995, paper TuF5.

[3] Ramdane, A., Ougazzaden, A., Devaux, F., Delorme, F., Schneider, M., Landreau, J., Electron. Lett., vol. 30, no. 23, pp 1980-1981 (1994).

[4] Kakaoka, T., Miyamoto, Y., Hagimoto, K, Sato, K., Kotaka, I., Wakita, K., Electron. Lett., vol 30., no. 11, pp 872 - 873 (1994).

[5] Reichmann, K. C. , Magill, P. D. , Koren, U., Miller, B. I., Young M., Newkirk, and M., Chien, M. D., IEEE Photon. Techn. Lett., vol. 5, no. 9, pp. 1098-1100 (1993).

[6] Kuindersma, P. I., Mols, P. P. G., v. d. Hofstad, G. L. A., Cuypers, G., Tomesen, M., v. Dongen, and T., Binsma, J. J. M., Electron. Lett., vol. 29, no. 21, pp. 1876-1878 (1993).

[7] Clesca, B., Gauchard., S, Rodrigues, V., Lesterlin, D., Kuhn, E., Bodere, A., Haisch H., Satzke, K., and Vinchant, J.-F., Proc. ECOC'95, Brussels, Belgium, September 17-21, 1995, paper, Th.A.3.8.

[8] Morito, K., Sahara, R., Sato, K., Kotaki, Y and Soda, H., Proc. ECOC'95, Brussels, Belgium, September 17-21, 1995, paper Th.B.2.1.

[9] Devaux, F., Sorel, Y., Kerdiles, J. F., J. Lightwave Techn., vol. 11, no. 12, pp. 1937-1940 (1993).

[10] Dorgeuille, F., and Devaux, F., J. Quant. Electron., vol. 30, no. 11, pp 2565-2572 (1994).

[11] Yamada, K., Murai, H., Nakamura, K., Matsui, Y., and Ogawa, Y., Electron. Lett., vol 31, no. 3, pp 237 - 238 (1995).

Monolithically Integrated Nonlinear Sagnac Interferometer and its Application as a 20 Gbit/s All-Optical Demultiplexer

E. Jahn, N. Agrawal, W. Pieper, H.-J. Ehrke, D. Franke, H. G. Weber, and W. Fürst
Heinrich-Hertz-Institut für Nachrichtentechnik Berlin GmbH
Einsteinufer 37, D-10587 Berlin, Federal Republic of Germany

Introduction: All-optical switching devices are expected to play an important role in future optical time-division multiplexing (OTDM) networks. Interferometer arrangements consisting of one or two semiconductor laser amplifiers (SLA) are very attractive for this purpose. Here, the cross-phase modulation due to the gain-saturation nonlinearity of SLAs provides the differential phase shift required for interferometric switching. The first of such devices was configured as a Sagnac interferometer by using an SLA in a fiber loop mirror (SLALOM) [1]. Subsequently, SLALOM devices were used as demulitiplexers in high bit rate OTDM experiments [2-5]. So far, these devices have been assembled using discrete SLA components. Other interferometer arrangements like Mach-Zehnder interferometer (MZI) or Michelson interferometer with SLAs provide additional flexibility but require their realization as integrated devices for stable operation. Recently, we developed an integrated MZI device and demonstrated its use in 40 Gbit/s to 5 Gbit/s demultiplexing and add/drop multiplexing experiments [6-7]. In this paper, we report the first monolithically integrated nonlinear Sagnac interferometer (NSI) and its application as a 20 Gbit/s all-optical demultiplexer.Such a demultiplexer requires only half the number of SLAs and 3-dB couplers as compared to the MZI devices.

Principle of Operation: Figure 1 shows schematically the InGaAsP/InP Sagnac interferometer consisting of a single SLA and a 3-dB coupler monolithically integrated within a waveguide loop. After passing through the 3-dB coupler, data (D) and control (C) pulses are divided into clockwise (CLW) and counter-clockwise (CCW) travelling pulses which after traversing the loop mirror interfere in the 3-dB coupler. Since the SLA is located asymmetrically within the loop, the CLW and CCW pulses pass through the SLA at different

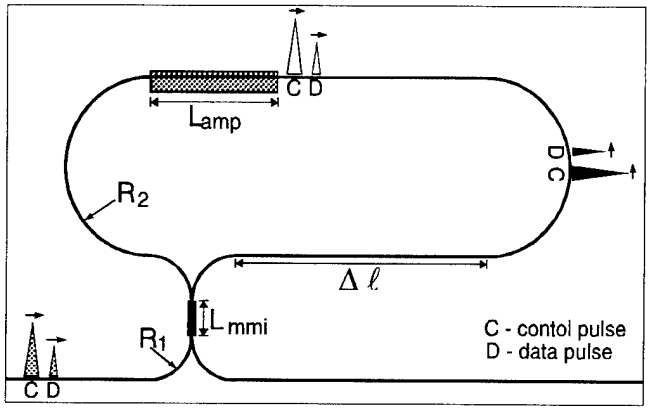


Fig.1: Schematic of Sagnac interferometer device for all-optical demultiplexing

times. It follows that the CLW and CCW data pulses experience the unsaturated and saturated (due to control pulses) gains of the SLA, respectively (cf. Fig. 1). This difference in gain saturation induces a differential phase-shift, which causes the data pulses to be transmitted to the output port. Thus a demultiplexing operation is achieved. The energy of data pulses is taken to be sufficiently small such that they do not saturate the SLA and hence are reflected back to the input port in the absence of control pulses.

Device design and fabrication: Bulk InGaAsP quaternary layers buried within InP cladding layers with approximate bandgap wavelengths of 1.55 μm and 1.3 μm were used as core of the active and passive waveguides, respectively. Single mode waveguides require large loop radii due to the inverse relationship between mode confinement and bend losses. Therefore, we employed double-moded (only in lateral direction) passive waveguides and chose the bend radii (R_1=250 μm, R_2=500 μm) in such a way that the losses for the fundamental and first order modes are small and large, respectively. Thus, by using the concept of mode-filtering by circular bends we realized very compact low-loss bends together with single mode operation within the Sagnac interferometer. Moreover, multi-mode-interference (MMI) devices were employed as 3-dB couplers due to their compact size and low polarization sensitivity. The amplifying and MMI sections were 750 μm and 204 μm long, respectively. The SLA is asymmetrically placed in the loop with Δl=1.5 mm, such that the time delay (switching window) between CLW and CCW travelling pulses is about 30 ps. Note that a 40 % saving of chip area is achieved by inverting the coupler and input/output waveguides so that they are inside the loop. Both standard and inverted interferometers were successfully fabricated. A butt coupling scheme was used for the integration of active/passive sections. After defining the active and passive sections by a combination of wet and reactive ion etching, selective epitaxy was performed using a SiN_x mask to grow the semi-insulating Fe:InP blocking layers. All epitaxial layers (3 steps) were grown by low pressure ($2x10^3$ Pa) metalorganic vapor phase epitaxy (MOVPE) at 670°C. A TiO_2/SiO_2 double layer coating was employed as anti-reflection coating for both facets.

Pump-probe and demultiplexing experiments: In order to study the switching window under dynamic conditions, a pump-probe experiment was performed at 5 GHz. Both pump and probe pulses were injected through the input port of the NSI. These pulses were derived from two tunable hybrid mode-locked semiconductor lasers (TMLL) which are described in reference 8. The measured output power of the NSI as a function of pump-probe delay is shown in Fig. 2. This figure indicates a contrast between the on and off states to be better than 11 dB and a switching window of ≈30 ps as expected. The experimental set up for the demultiplexing experiment using an inverted interferometer is shown in Fig. 3. An optical pulse stream (λ=1532 nm) was generated by the TMLL with 3 ps pulses and a repetition rate of 5 GHz. These pulses were intensity modulated with a pseudo random bit sequence (PRBS) having a word length of 2^{31}-1 using an external modulator. The so obtained 5 Gbit/s data

signal was then multiplexed by a fiber delay line multiplexer to a 10 or 20 Gbit/s data signal. This data signal was coupled into the NSI device at the port 1 with a definite state of polarisation. A circulator was used to couple in control pulses (λ=1555 nm) and couple out the demultiplexed data pulses via port 2 of the NSI. The estimated optical power coupled into the interferometer was 0 dBm for the control pulses after taking into account fiber-chip coupling losses of about 7 dB at each port. Figure 4 shows bit error rate (BER) measurements on the demultiplexed data signal versus the received power. A power penalty of 2.5 dB due to demultiplexing can be seen at 20 Gbit/s as compared to the back-to-back measurements. The inset in Fig. 4 shows an eye-diagram for the 20 Gbit/s experiment. Note that there is a clear eye-opening with no indication of crosstalk. In all experiments the synchronisation of data pulses and control pulses was done manually such that an optimum BER performance is obtained.

Conclusions: We have realized a demultiplexer photonic integrated circuit (PIC) by monolithic integration of a semiconductor laser amplifier within a Sagnac interferometer. The potential application of this PIC in high capacity OTDM systems is demonstrated by successfully performing an error-free demultiplexing experiment from 20 Gbit/s to 5 Gbit/s. By suitable modifications of the present design such nonlinear SLALOM devices can be readily improved to achieve polarization independence, superior contrast ratios, reduced fiber-chip coupling losses, and operation at much higher bit-rates.

Acknowledgements: This work was supported by the Land Berlin and the Bundesministerium für Bildung, Wissenschaft, Forschung und Technologie of the Fed. Rep. of Germany under contract 01 BP436/1.

References:

[1] M. Eiselt, 'Optical loop mirror with semiconductor laser amplifier', Electron. Lett. 1992, 28 (16) pp. 1505-1507.

[2] J. P. Sokoloff, I. Glesk, and P. R. Prucnal, 'Performance of a 50 Gbit/s optical time domain multiplexed system using a Terahertz optical asymmetric demultiplexer', IEEE Photon. Technol. Lett. 1994, 6 (1), pp. 98-100.

[3] M. Eiselt, W. Pieper, and H. G. Weber, 'All-optical demultiplexing with a semiconductor laser amplifier in a loop mirror', Electron. Lett. 1993, 29 (13) pp. 1167-1168.

[4] A. D. Ellis, D.M. Spirit, 'Compact 40 Gbit/s optical demultiplexer using a GaInAsP optical amplifier', Electron. Lett. 1993, 29 (24) pp. 2115-2116.

[5] K. Suzuki, K. Iwatsuki, S. Nishi, and M. Saruwatari, 'Error-free demultiplexing of 160 Gbit/s pulse signal using optical loop mirror including semiconductor laser amplifier', Electron. Lett. 1994, 30 (18) pp. 1501-1503.

[6] E. Jahn, N. Agrawal, M. Arbert, H.-J. Ehrke, D. Franke, R. Ludwig, W. Pieper, H.G. Weber, and C.M. Weinert, '40 Gbit/s all-optical demultiplexing using a monolithically integrated Mach-Zehnder interferometer with semiconductor laser amplifiers', Electron. Lett. 1995, 31 (21), pp. 1857-1858.

[7] E. Jahn, N. Agrawal, H.-J. Ehrke, R. Ludwig, W. Pieper, and H.G. Weber, 'Monolithically integrated Mach-Zehnder interferometer as a 20 Gbit/s all-optical add/drop multiplexer for OTDM systems', IEEE LEOS 1995 Annual Meeting, San Francisco, California, post-deadline paper PD1.6.
[8] R. Ludwig and A. Ehrhardt, 'Turn-key-ready wavelength-, repetition rate- and pulsewidth- tunable femtosecond hybrid modelocked laser', Electron. Lett. 1995, 31 (14), pp. 1165-1167.

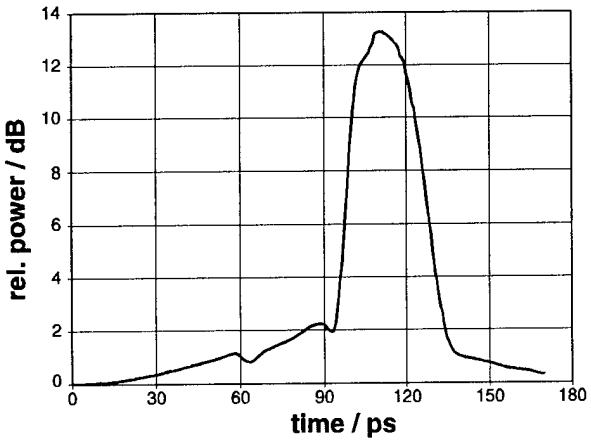


Fig. 2: Results of pump-probe experiment

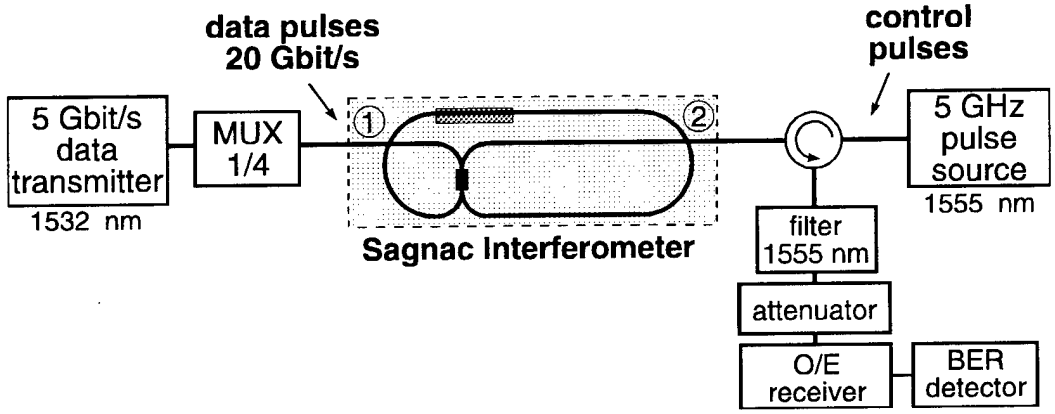


Fig. 3 Experimental set-up for demultiplexing experiment

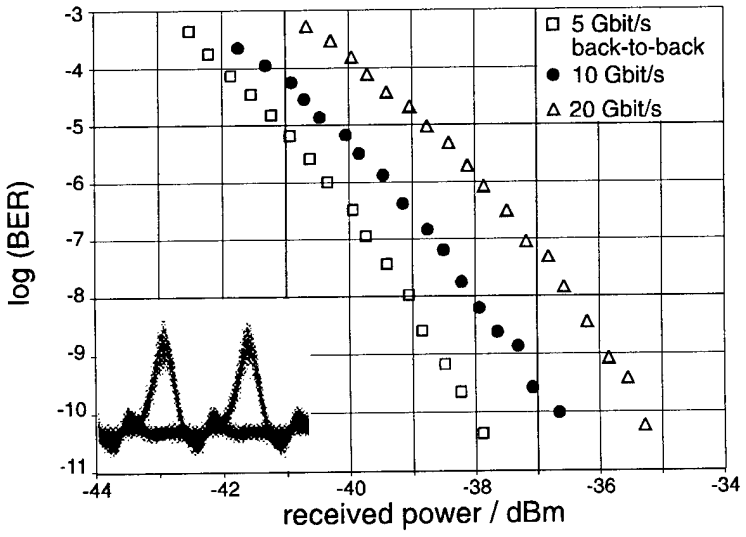


Fig. 4: Bit-error rate measurements and eye-diagram for demultiplexing of 20 Gbit/s, and 10 Gbit/s to 5 Gbit/s

A Novel Method for Improving the Performance of InP/InGaAsP Multiple-Quantum-Well Mach-Zehnder Modulators by Phase Shift Engineering

Jun Yu, Claude Rolland, David Yevick*, Azmina Somani, Scott Bradshaw

Bell Northern Research, Advanced Technology Laboratory, Ottawa, Ont. K1Y 4H7, Canada

*Queen's University, Department of Electrical Engineering, Kingston, Ont. K7L 3N6, Canada

Introduction: Semiconductor external modulators are increasingly employed in high speed and long haul optical fiber communication. A highly desirable feature of an external light modulator is the ability to generate a signal with a negative frequency chirp. Mach-Zehnder (MZ) III-V multiple-quantum-well (MQW) modulators are thus increasingly attractive relative to other modulator designs because of their adjustable frequency chirp, low drive voltage, small size, long term reliability and potential for integration with laser sources[1, 2, 3, 4]. Unfortunately, in III-V MQW MZ modulators where the two arms of the interferometer are of equal length and the power splitting ratio 50%, the nonlinear electrooptic effect imparts a small positive chirp under symmetric push-pull operation. While negative chirp can be induced by designing the Y-junction to inject less optical power into the more deeply biased modulator arm and employing a small amount of overdrive,[5] the back-to-back extinction ratio is degraded. In this paper we demonstrate that by increasing the length of one of the modulator arms such that the transmitted optical signal is shifted by π relative to the other arm, an optimal chirp can be obtained while maintaining a high extinction ratio.

Results:

We consider in this paper an InP/InGaAsP MQW Mach-Zehnder modulator with a structure identical to that discussed in [3] except that one modulator arm is elongated to produce the required relative π phase shift at the $\lambda = 1.56\mu$m operating wavelength. This additional waveguide length is given in terms of the modal refractive index n_{eff} by

$$\frac{\lambda}{2n_{eff}} = \frac{1.56}{2 \times 3.23}\mu\text{m} = 0.241\mu\text{m} \tag{1}$$

Here, we will demonstrate the advantages of this π phase shift by qualitatively analyzing the frequency chirp performance. In a semiconductor phase modulator the larger phase change in a push-pull configuration occurs in the more deeply DC-biased arm because of the nonlinear nature of the quantum confined Stark effect. Further, for a single-mode waveguide, the total optical field at the output of the modulator can be regarded to a first approximation as a weighted summation of the optical field from the two separate arms. The weight factors depend on the power splitting ratio of the two Y-junctions and the photo-absorption in the modulation section.

In Fig. 1(a) , we display the frequency chirp from both arms in a conventional III-V MQW MZ modulator. The device is driven in a push-pull configuration and is switched from an off to an on state. The device reaches the "on" or "push" state when both arms

are biased equally. The phase of the optical field in a given arm, which we label arm 1, is thus decreased when the device is switched from an "off" to "on" state so that the change in frequency $\Delta\nu_1 > 0$ and consequently the optical field is blue-shifted. By the same reasoning $\Delta\nu_2 < 0$ and the optical field is red-shifted in arm 2. For equal voltage push-pull operation, $|\Delta\nu_1| > |\Delta\nu_2|$ as a result of the nonlinearity of the electrooptic effect. Even though the photo-absorption is larger in the more deeply-biased arm 1 compared to the arm 2, if the Y-junction splits the power equally, the overall effect is to blue-shift a fraction of the power present in the rising edge of the optical pulse.

To generate instead a red-shifted rising edge and hence a negative frequency chirp in a III-V MQW Mach-Zehnder modulator, an asymmetric power splitting in the Y-junction can be employed[5]. This method reduces the optical power in arm 1, so that the red-shift in arm 2 dominates the behavior of the rising edge. However, since less power is then inserted into arm 1 while the photo-absorption in this arm is also larger, the extinction ratio of such a modulator is $\approx$ 10dB [4].

Fig. 1(b) illustrates our novel approach and shows the frequency chirp from both arms of a π phase shifted III-V MQW MZ modulator. The device is switched on when both arms reach the pull-state. The phase of the optical field in arm 1 is thus decreased when the device is switched from the "off" to "on" state so that $\Delta\nu_1 < 0$, red-shifting the optical field in arm 1. At the same time, $\Delta\nu_2 > 0$ and the optical field is blue-shifted in arm 2. Since now $|\Delta\nu_1| > |\Delta\nu_2|$, again as a result of the nonlinearity of the electrooptic effect, the rising edge of the optical pulse is red-shifted. Although such a π phase shifted modulator has a theoretically infinite extinction ratio for a symmetric Y-junction, in practice, to obtain sufficient negative frequency chirp, slightly more power must be directed into arm 1. This small asymmetry does not however significantly affect the extinction ratio.

Having established the basic principle of operation of the phase-shifted modulator, we now present the actual device characteristics. TE-polarized light from a 1.56μm DFB laser was coupled through a 10μm-radius tapered fiber into an MZ modulator. Light was coupled out of the modulator using a similar tapered fiber resulting in an overall insertion loss of 11.2dB. As expected, the modulator is in the off-state at zero applied voltage with a switching voltage of $\approx$ 4.0V. The DC extinction ratios is measured to be 15.8dB and 16.1dB for arm 1 and arm 2, respectively.

The chirp characteristic of the modulator was investigated using a scanning Fabry-Perot filter that transforms frequency modulation into amplitude modulation.[6] The 3dB bandwidth of the filter was 0.43nm. The modulator was mounted on a high speed carrier and driven in a push-pull configuration using a long sequence of ones and zeros from a 12 GHz HP-70843 pattern generator. After the bias-tee each arm received a 1.6V peak-to-peak signal having less than a 40ps rise and fall time and an average bias of ≈ -3.0V in arm 1 and ≈ -1.0V in arm 2. Fig. 2 shows the intensity waveform and time-resolved frequency chirp. The magnitude of the red-shifted transient chirp on the rising edge of the waveform is approximately 3GHz. This is the first chirp measurement published for a III-V MZ modulator.

Finally we examined the 10Gbit/s NRZ transmission performance of a modulator co-packaged with a 1557nm strained-layer MQW DFB laser. Measurements were performed using a standard single mode fiber with zero dispersion at 1310nm and 17ps/(nm km) at 1550nm. The modulator was driven with a peak-to-peak amplitude of 1.4V and average

biases on arms 1 and 2 of -3.2V and -0.7V respectively. This choice gives an AC extinction ratio of 15.1dB. The same device produced a DC extinction ratio of 18dB. Fig. 3 shows the 0km and 85km eye diagrams obtained using a 32GHz high-speed PIN detector. The performance of the transmitter with larger dispersion was also investigated. Fig. 4 shows the receiver sensitivity at 10^{-9} BER and 10Gb/s versus distance in conventional fiber. Like other system measurements using prechirped sources, the curve initially shows improvement in receiver sensitivity up to a distance of $\approx$ 105km. At 120km, the dispersion penalty is only 0.7dB.

Conclusions: By introducing a π phase shift in an III-V MZ device, we have simultaneously achieved excellent extinction ratio and the required spectral characteristics for 10Gb/s operation. Extinction ratios of $>$ 16dB are routinely achieved while transmission over 120km of conventional fiber gives only a 0.7dB of dispersion penalty. We have thus demonstrated a high-performance optical source with the spectral and waveform characteristics required for emerging high-bandwidth transport systems.

Acknowledgement: The authors would like to thank Norbert Puetz for device growth, Ronald Moore and Bob Foster for device processing, Kin-Wai Leong for the help of setting up frequency chirp measurement, and Adnan Akhtar, Jeffery Yu, Hyung Kim, Keith Anderson, Gen Ribakovs, Frank Shepherd for stimulating discussions.

References

[1] J.E. Zucker, K.L.Jones, M.Newkirk, R.P. Gnall, B.I.Miller, M.G. Young, U.Koren, C.A.Burrus and B. Tell, "Quantum well interferometric modulator monolithically integrated with 1.55μm tunable distributed reflector laser", Electron. Lett.,**28**, pp1888-1889, (1992).

[2] H.Sano, H.Inoue, S.Tsuji and K.Ishida, "InGaAs/InAlAs MQW Mach-Zehnder optical modulator for 10Gbit/s long haul transmission systems", OFC'92, San Jose, California, 1992, ThG4

[3] C. Rolland, R.S.Moore, F.Shepherd and G.Hiller, "10Gbit/s 1.56μm multiquantum well InP/InGaAsP Mach-Zehnder optical modulator", Electron. Lett.,**29**, pp471-472, (1993).

[4] C. Rolland, M.S. O'Sullivan, H.B. Kim, R.S.Moore and G.Hiller, "10Gbit/s , 120km normal fiber transmission experiment using a 1.56μm multiquantum well InP/InGaAsP Mach-Zehnder modulator", OFC'93, PD-27

[5] J.C Cartledge, C. Rolland, S. Lemerle and A. Solheim: " Theoretical performance of 10Gb/s lightwave systems using a III-V semiconductor Mach-Zehnder modulator", IEEE Photon. Technol. Lett., **6** pp282-284, (1994).

[6] N.S. Bergano, "Wavelength discriminator method for measuring dynamic chirp in DFB lasers," Electron. Lett.,**24**(20), pp1296-1297, (1988).

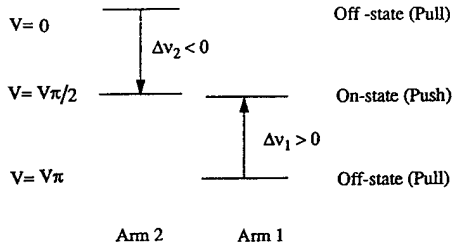


Fig. 1(a) Push-pull drive configuration for conventional MZ

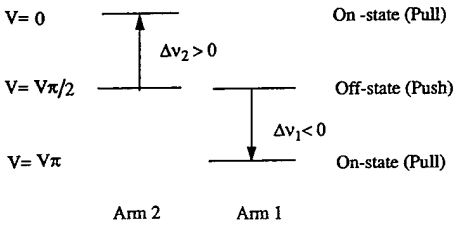


Fig. 1(b) Push-pull drive configuration for π phase shifted MZ

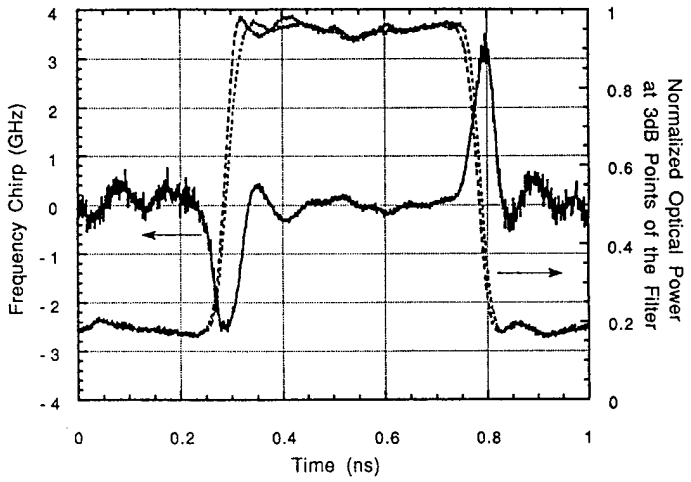


Fig.2 Time resolved frequency chirp measurement

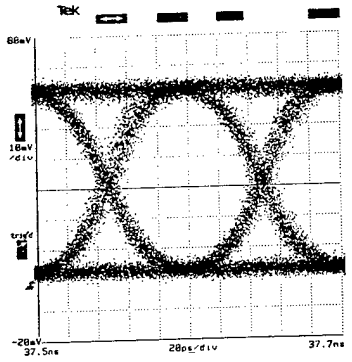


Fig.3 (a) Eye diagram at 0km

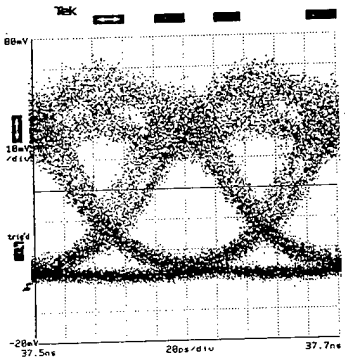


Fig.3(b) Eye diagram at 85km

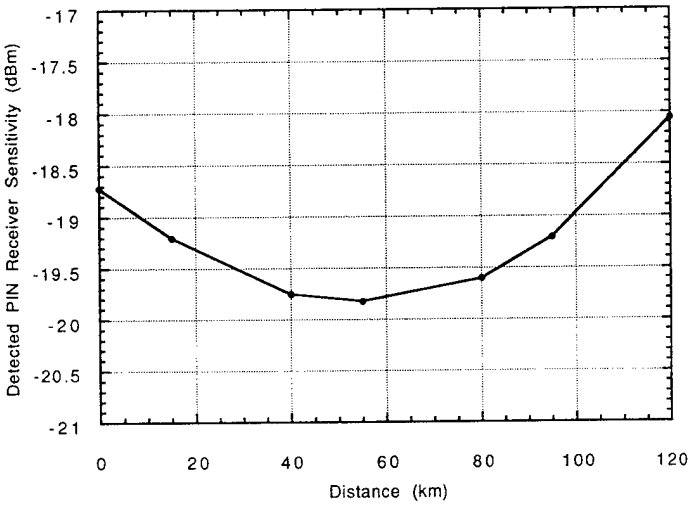


Fig.4 Variation of detected PIN receiver sensitivity with increasing dispersion

High-speed Coplanar Schottky Travelling-Wave Photodetectors

M. Alles, Th. Braasch, and D. Jäger

Fachgebiet Optoelektronik
Gerhard-Mercator-Universität Duisburg
Kommandantenstraße 60, D-47048 Duisburg, Germany
Phone: +49-203-379-2340, Fax: +49-203-379-2409

Introduction

Recently, a growing interest has been given to the development of travelling-wave photodetectors. In [1] Wu et al. report on a AlGaAs/GaAs travelling-wave photodetector array consisting of 27 discrete pin photodiodes periodically arranged along an electrical and an optical waveguide. The measured pulse response is 50 ps resulting in a 3dB-bandwidth of about 20 GHz. Hietala et al. [2] describe a coplanar travelling-wave photodetector on GaAs substrate with a 3dB-bandwidth of 4.8 GHz at 1 µm. Bowers et al. [3] have studied a 7 µm long waveguide photodetector on GaAs with a bandwidth of about 170 GHz at 0.83 µm.
In this paper, we discuss the characteristics of a coplanar InGaAlAs/InP Schottky travelling-wave photodetector with a cut-off frequency > 40 GHz at 1.3 µm.

1. Schottky travelling-wave photodetector

The general outline of the coplanar travelling-wave photodetector is shown in Fig. 1. It consists of an electrical coplanar waveguide coupled to an optical waveguide (hatched region). The ground metalizations form ohmic contacts to the semiconductor and the center conductor a Schottky contact. As a result, the electric bias field of this diode is concentrated in the depletion layer containing the optical waveguide underneath the center conductor. Optical waveguiding is achieved using a strip loaded waveguide including an optical absorbing layer.

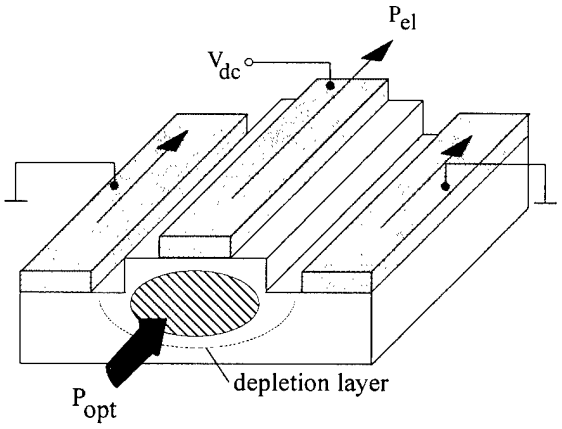


Fig. 1: Sketch of the travelling-wave photodetector. P_{opt} and P_{el} are the input optical and output electrical power, respectively.

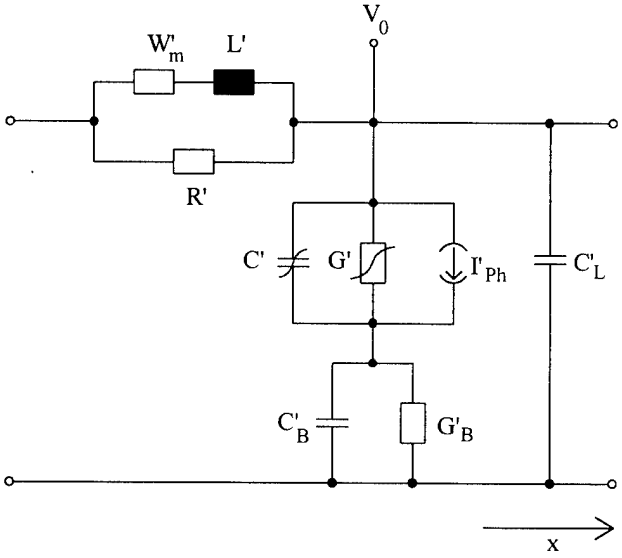


Fig. 2: Equivalent circuit of the travelling-wave photodetector [4]. All elements are per unit length.

2. Simulation

The equivalent circuit for electrical wave propagation on the travelling-wave photodetector is shown in Fig. 2. The impedances W'_m and R' describe the longitudinal ohmic losses in the metalization and the semiconductor, respectively. The inductance of the electrical waveguide is considered by the inductance L'. The capacitance C'_L describes the electric field in air of the coplanar line, and the capacitance C' and the conductance G' the electrical behaviour of the depletion layer. Additionally, a conductance G'_B and a capacitance C'_B are introduced for the bulk material. The impressed current source $I'_{ph}(x,t)$ describes the opto-electric conversion. In case of the travelling-wave photodetector the distributed generation of electron-hole-pairs results in a wave for the generated photocurrent.
The travelling-wave photodetector exhibits highest bandwidth and optimum power conversion under phase matching condition, which occurs when the electrical and optical waves travel with the same phase velocity.
In Fig. 3 the calculated phase velocity of a Schottky contact coplanar waveguide are shown for different gap widths d and center conductor widths w using the equivalent circuit model and the material constants of the travelling-wave photodetector in Fig. 4. Phase matching can be achieved because the Schottky capacitance C' leads to slow-wave effects [5]. Hence, phase matching is obtained by a careful design of the microwave structure, as the properties of the optical waveguide are fixed due to the given structure and material constants. From Fig. 3 one concludes that phase matching is achievable, for a gap width and a center conductor width of 5 µm.

3. Device strucure

The structure of the travelling-wave photodetector is shown in Fig. 4. A 600 nm InGaAlAs n-doped optical waveguiding layer, a 30 nm InGaAs absorbing quantum-well layer, and a 400 nm InAlAs cladding layer are grown on semiinsulating InP-substrate. The metalization

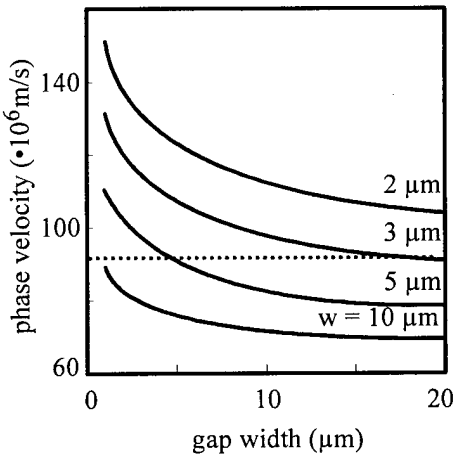


Fig. 3: Calculated microwave phase velocity versus gap width. Parameter is the center conductor width w. The points of intersection with the dotted line (optical phase velocity) show the phase matching condition.

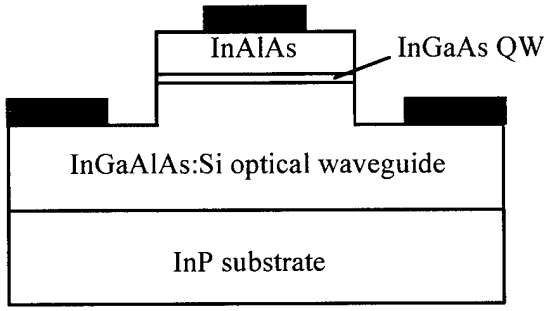


Fig. 4: Sketch of the travelling-wave photo-detector.

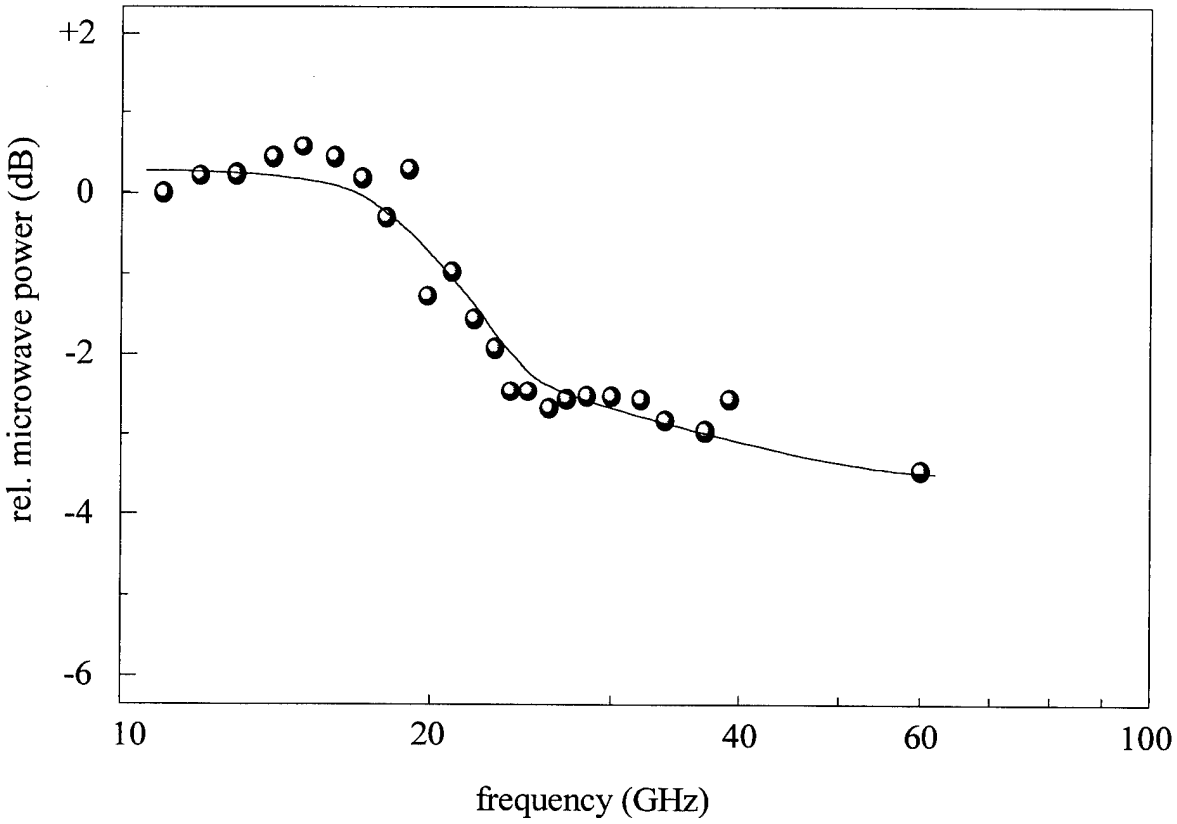


Fig. 5: Measured frequency response of the travelling-wave photodetector.

consists of GeNiAu for the ohmic contacts and PtTiPtAu for the Schottky contact.
For hybrid integration the electrical transmission line is flip-chip- or wire-bonded to other semiconductor circuits. Monolithic integration is also possible, when the travelling-wave photodetector is grown on top of a HEMT- or HFET-structure. The optical absorption in the HFET- or HEMT-layers can be reduced by growing an ARROW-structure as a reflecting cladding layer between microwave and optical layers [6].

4. Measurements

Measurements of the optoelectronic characteristics of the travelling-wave photodetectors are carried out using a heterodyne setup with two diode-pumped 1.3 µm YAG-lasers and a spectrum analyzer. The wavelengths of the two lasers are tunable, generating beating frequencies up to 60 GHz. The generated electrical signals are measured via an on-wafer prober and the spectrum analyzer. The result for a travelling-wave photodetector with a device length of about 1 mm is shown in Fig. 5. Obviously, the 3dB bandwidth is > 40 GHz. In contrast to usual RC-limited photodetectors the travelling-wave photodetector shows only a slight decay in the frequency response. We conclude therefore, that the photodetector can be used up to frequencies of 60 GHz and possibly above.
Finally, it should be mentioned that the low frequency impedance of the travelling-wave photodetector with a device length of 1mm lead to a calculated 3dB-bandwidth of merely 2 GHz. This bandwidth is much lower than the measured bandwidth indicating the functionality of the travelling-wave principle.

5. Summary

In this paper we have shown, that travelling-wave photodetectors can meet the current requirements for ultra-high-speed operation. In particular we have found, that travelling-wave photodetectors are not limited by the usual RC-time constant. Microwave properties determine the bandwidth and the input impedance is given by the characteristic impedance of the transmission line. Due to the Schottky contact waveguide, slow wave properties arise, which allow a phase matched design of the travelling-wave photodetector. As a result, the travelling-wave photodetector shows a 3dB bandwidth > 40 GHz, which to our knowledge is the highest bandwidth reported up to now for a device with a length of 1 mm.

6. References

[1] N. Mysoor, T. Vang, S. Forouhar, L. Lin, M. Wu, "High power photodetectors for space communications applications", 1995 IEEE/LEOS Summer Topical Meeting Dig., Keystone Resort, Colorado, USA, pp. 23-24

[2] V.M. Hietala, G. Allen, T.M. Brennan, B.E. Hammons, "Traveling-wave photodetectors for high-power, large-bandwidth applications", IEEE Trans. Microwave Theory and Techn., Vol. 43, 1995, pp. 2291-2298

[3] K.S. Giboney, R.L. Nagarajan, T.E. Reynolds, S.T. Allen, R.P. Mirin, M.J.W. Rodwell, J.E. Bowers, "Travelling-wave photodetector with 172-GHz bandwidth and 76-GHz bandwidth-efficiency product", IEEE Phot. Techn. Lett., Vol. 7, 1995, pp. 412-414

[4] D. Jäger, R. Hülsewede, and R. Kremer, "Travelling-wave MMIC Schottky, MSM and pn diodes for microwave and optoelectronic applications", Proc. CAS '93, Bukarest, pp. 19-29, 1993

[5] D. Jäger, "Slow-wave propagation along variable Scchottky contact microstrip line", IEEE Trans. Microwave Theory and Techn., Vol. 24, 1976, pp. 566-573

[6] R. Freye, Th. Delonge, H. Fouckhardt, "Two-dimensional ARROWS", J. Opt. Comm., 1994

High Speed Traveling Wave Electrooptic Intensity Modulator with a Doped PIN Semiconductor Junction

G.A. Vawter, V.M. Hietala, J.R. Wendt, B.A. Fuchs, M. Hafich,
M. Housel, M. Armendariz and C.T. Sullivan

Sandia National Laboratories, P.O. Box 5800, MS 0603
Albuquerque, NM 87185-0603, ph. (505) 844-9004; fax 844-8985

Extremely fast modulation response of optical phase delay in a waveguide modulator is required for photonic integrated circuits (PICs) to operate with mm-wave signals. Single phase modulators, paired phase modulators in a Mach-Zehnder interferometer, or more complex arrangements can be used for mm-wave modulation of light in either phase, amplitude, or frequency. Standard lumped-element devices are bandwidth limited by the RC time-constant of the structure. Distributed, or traveling-wave designs have been developed to surpass the RC limit. With distributed structures the bandwidth limit is determined by loss of phase synchronism between the optical and RF wavefronts within the length of the device. The generally different propagation constants of the optical and RF waves leads to a limiting length-bandwidth product in the modulation response. In the limit of zero velocity mismatch the modulation bandwidth is then limited by RF loss in the transmission line. Velocity matching in undoped or low-doped semiconductor optoelectronic modulators typically involves use of a slow-wave transmission line electrode structure. Several successful techniques have been developed[1-2], but undoped structures offer low electrooptic efficiency, resulting in undesirably large devices. We disclose a device using doped semiconductor structures to increase efficiency in a traveling-wave modulator. This new design is demonstrated to have a bandwidth greater than 40 GHz in a Mach-Zehnder intensity modulator operating at 1.32 μm wavelength while maintaining V_π = 10V with a phase modulator section only 1mm-long.

Electrooptic efficiency can be dramatically increased through the appropriate use of doping in a semiconductor optical waveguide. A *p-i-n* junction centered on the optical mode of the waveguide concentrates the applied electric field within the optical mode, yielding higher optical phase shift per unit applied voltage compared to undoped waveguides. The improved efficiency permits the use of shorter modulators for a given applied voltage. Use of doped waveguides does increase the optical loss but the overall loss of the device can be similar to an undoped design due the reduced length.[3]

Figure (1) shows the cross-section of the optical phase modulator used in the high-speed Mach-Zehnder. The waveguide comprises an (Al,Ga)As cutoff-mesa rib optical waveguide.[4] A *p-i-n* junction with a 0.6 μm undoped thickness is centered on the 0.2 μm thick GaAs waveguide core. The upper waveguide rib is 2 μm wide, the waveguide mesa is 10 μm wide. The microwave transmission line comprises a 14 μm-wide Au strip balanced on the waveguide and ground-plane metalization contacting a continuous n^+ GaAs layer placed below the etched mesa. Vertical and horizontal spacing between the ground metalization and the center strip, is used to control the microwave phase velocity. The intrinsic region thickness also has a strong influence on the microwave phase velocity. However, this thickness is kept at a practical minimum in order to maintain the desired high optical modulation efficiency.

A quasi-TEM transmission-line model was used to predict the transmission line characteristics and phase modulation response versus frequency. At 30 GHz, the microwave index, loss and characteristic impedance are calculated to be 3.31, 2 dB/mm and (22 - 0.56j) Ohms respectively. The microwave index is well matched with the optical modal index of 3.3134 at the 1.32 μm wavelength calculated using a two-dimensional finite difference technique. Using theoretical transmission-line losses, ideal impedance matching at the source and load and a fixed electrooptic efficiency, the model indicates that a 1 mm-long device would have a bandwidth

between 50 and 100 GHz (Figure 2). This model is expected to overestimate the bandwidth to some extent as the RF loss is known to increase with frequency.

Mach-Zehnder intensity modulators were fabricated using epitaxial layers grown by molecular-beam-epitaxy. All etching was by chlorine reactive ion beam etching. A PMGI-based air-bridge metal plating technique was used to create the central metal strip balanced on the waveguide rib. The transmission line was terminated at both ends with pads placed directly on the semi-insulating substrate for Cascade microprobes. Final cleaved devices were 3 mm in length including the 1 mm-long phase modulator, input and output waveguides and optical power combiners/splitters occupied the remaining length. The two arms of the Mach-Zehnder were driven asymmetrically with one arm held to ground potential and the other comprising the high-speed phase modulator.

Small signal electrical response was measured to 40 GHz using an amplitude modulated microwave signal[5] and a DC-bias of -10 V. As seen in Figure (3), the response is fairly flat out to 20 GHz with a peak at 30 GHz. The device does not show a -3dB roll-off within the 40 Ghz measured frequency range. The peak at 30 GHz is most likely a resonance caused by the use of 50 Ohm probes, cables and output termination on the 22 Ohm transmission-line structure. This impedance mismatch was not included in the model of Figure (2). Use of proper impedance-matching techniques should flatten the resonance, providing a more uniform frequency response. S-parameter measurements up to 20 GHz were performed using a network analyzer. From this data, the measured RF loss of a 1 mm-long device is seen to increase monotonically from 1.3 to 2.4 dB/mm between 10 and 20 GHz.

In conclusion, a Mach-Zehnder intensity modulator at 1.32 μm wavelength has been demonstrated with a modulation bandwidth greater than 40 Ghz. The device uses a doped *p-i-n* semiconductor junction for high electrooptic modulation efficiency and small overall size. The 1 mm-long modulator section has a V_π = 10V, comparable to undoped semiconductor designs of much greater length.

This work was supported by the United States Department of Energy under Contract DE-AC04-94AL8500.

References:

[1] R.G. Walker, Proceedings of the IEEE Lasers and Electrooptics Society 1995 Annual Meeting, Vol. 1, pp. 120-121, San Fransisco, CA, Oct. 30-Nov. 2, 1995.

[2] R. Spickermann, S. Sakamoto, M. Peters and N. Dagli, Proceedings of the IEEE Lasers and Electrooptics Society 1995 Annual Meeting, Vol. 1, pp. 118-119, San Fransisco, CA, Oct. 30-Nov. 2, 1995.

[3] G.A. Vawter, V.M. Hietala, S.H. Kravitz, M.G. Armendariz, Proceedings of the International 1994 IEEE MTT-S Topical meeting on Optical Microwave Interactions, pp. 3-6, Ile de France, France, Nov. 21-23, 1994.

[4] G.A. Vawter, R.E. Smith, B. Fuchs, J.R. Wendt, M. Hafich, G.R. Hadley, Proceedings of the IEEE Lasers and Electrooptics Society 1995 Annual Meeting, Vol. 1, pp. 137-138, San Fransisco, CA, Oct. 30-Nov. 2, 1995.

[5] S. Uehara, Applied Optics, Vol. 17, No. 1, pp. 68-71, 1978

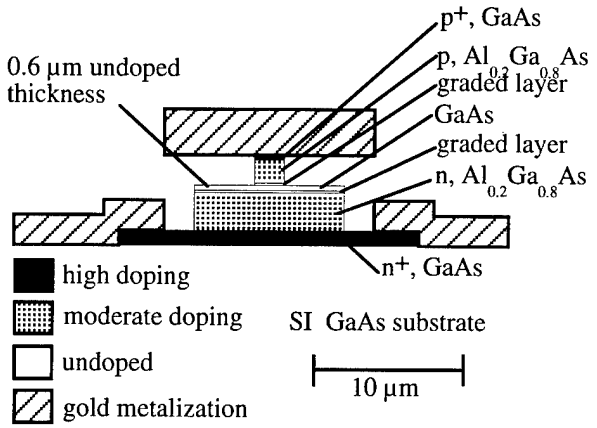


Figure 1: Cross-section view of the traveling-wave phased modulator with doped *p-i-n* waveguide design. Figure is drawn approximatly to scale. The outer Au ground-plane metalizations extend beyond the edges of the drawing.

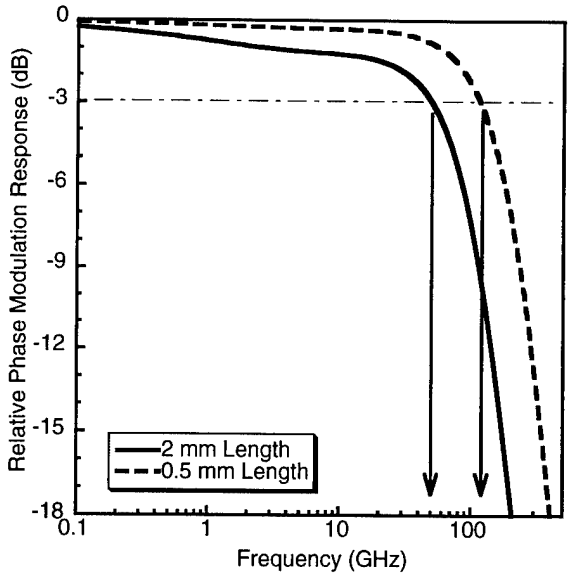


Figure 2. Theoretical traveling-wave phase modulator response as function of frequency. Dashed line is 0.5 mm long device. Solid line is 2 mm long device.

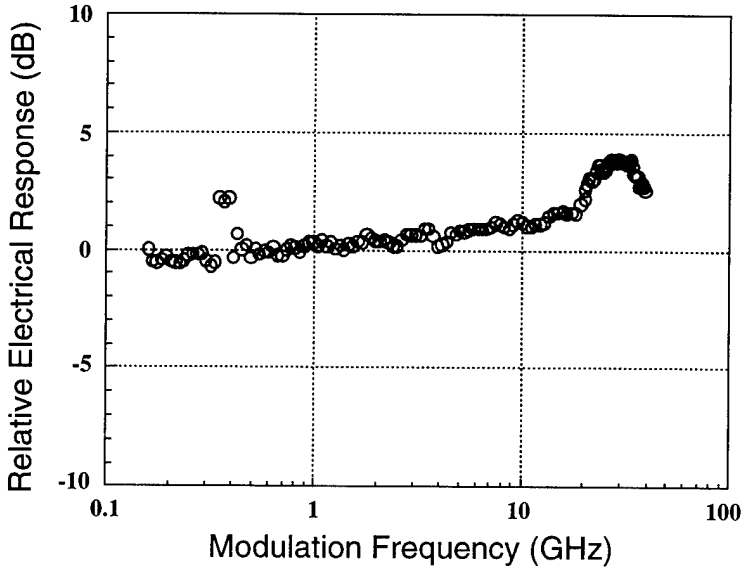


Figure 3: Relative small-signal electrical response of a Mach-Zehnder intensity modulator employing a 1 mm-long phase modulator of the design in Figure (1). Data spans 150 Mhz to 40 GHz.

Low-Cost Photonic Packaging II

ITuH 3:30 pm-5:00 pm
Fairfax B

Lewis B. Aronson, *Presider*
Hewlett Packard

Towards Low Cost Single-Mode Fibre Optic Components

David G. Parker

Hewlett Packard Fibre Optic Components
White House Road
Ipswich
England

1. Introduction

The advantages of using fibre optic technology for communication are widely publicised. Proponents discuss at length the seemingly endless bandwidth potential, long distance capability, inherent security, future proofing through upgrades such as Wave Division Multiplexing (WDM) etc. Competing technologies such as wireless will raise debate over infrastructure, conventional copper is entrenched for broadband broadcast distribution and the bandwidth of twisted pair solutions seems to continue to push upwards.

In long haul or back bone applications there is little doubt that fibre is the technology of choice. The real debate is the optimum solution for what is often termed "the last mile(s)". This again will depend on the success of competing technologies, resolution of regulatory issues which clearly distort the who, when and why ? of deployment strategy and ultimately cost. This paper will concentrate on one cost element : that of single mode fibre optic components. However, I must stress that this is but one factor in the deployment argument. The paper will concentrate on active Transmitter and Receiver Components.

2. The Requirements for Single Mode Components

The choice of components is influenced by several notable factors :-

- Cost
- Complexity : How much complexity or functionality is to be included within the O-E element or added at the system level ?
- Reliability

- Commercial issues : These often include vendor performance criteria such as delivery and partnership arrangements

The relative emphasis depends upon the market segment. For example, for an undersea application reliability become all pervasive. Cost, however, dominates the argument the further into the network one considers as the total cost of the fibre link is shared amongst fewer customers.

The choices available depend upon the specification requirements of the component. However, there are several common themes. Figure 1. represents a generic single mode fibre optic Transmitter and a proposed evolutionary equivalent. These can be summarised as follows :-

Active device : One of the biggest trade-offs is in this area. The cost of the active laser is driven by the cost of material (including Epitaxial layers), fabrication and test cost. In general this amounts to around $\$1/mm^2$ where large area epitaxy is employed, such as MOVPE. The dominant total cost is in the yield of the resultant devices. Providing that this is maintained at reasonable levels then the biggest contribution to cost reduction from the active element is to enable low cost packaging (see below).

Sub Package : The challenge is to maintain high coupling efficiencies over a wide temperature range (typically -40 to +85°C) and life. In our example this has been achieved by modifying the beam shape to better match the NA of the fibre. Lasers that operate at high temperature with low threshold currents and little degradation (high To) also enable the use of inexpensive heatsinking material. It may be possible to utilise this material to form the primary chassis to hold both the laser and the fibre e.g. Si micromachining.

Circuits : The requirements of the laser such as lower threshold currents, and the increasing performance of low cost IC technologies such as CMOS should allow significant reduction in the cost of IC's incorporated into EO modules.

Interconnect : Traditional chips and wire hybrids have already given way to SMT's. In our example this has been extended to a leadframe to further reduce cost.

Outer Package : Current experience dictates the use of an hermetic enclosure. This fundamental remit is currently being challenged.

3. A State of the Art Receiver Solution

At Hewlett Packard the approach outlined in 2. has already been implemented for a receiver solution. Figure 2. shows an exploded view. The receiver is built directly onto a leadframe using precision placement of the Photodetector element. The preamp and passive components are then added prior to encapsulation. During the transfer moulding a lens is formed in the encapsulant which is passively aligned to the

position of the Photodetector. This assembly is then clipped onto a simple external housing with fibre assembly. The manufacturing process is highly mechanised. The product replaces a conventional chip and wire or TO+ PCB approach saving around 50% of the cost. Hence, this approach has met its objectives of utilising available technology to produce a scaleable, low cost component.

4. The Role of Integration

The approach shown in Figure 1. does utilise a low level of integration ; in that a laser is integrated with a monitor diode and a waveguide. This low level of integration would clearly enable the "hybrid" approach discussed. Currently, however, the performance of the module would be compromised. For example such a laser would be processed using dry etched facets which have yet to be demonstrated to exhibit the low threshold currents and high operating temperature of conventional cleaved facets (e.g. Ith of 20-25mA @ 25°C vs. 5-8mA for conventional devices [4]). Herein lies a key challenge for process development activities.

There are examples where a higher level of integration becomes a more compelling argument. In figure 3 the evolution of a bi-directional module is outlined. The first step from a spliced solution to a "hybrid" is difficult and may be an inappropriate compromise. The integrated one chip solution may well be the complete enabler for such an approach. The challenge remains to achieve the performance required by the system needs at a lower total cost.

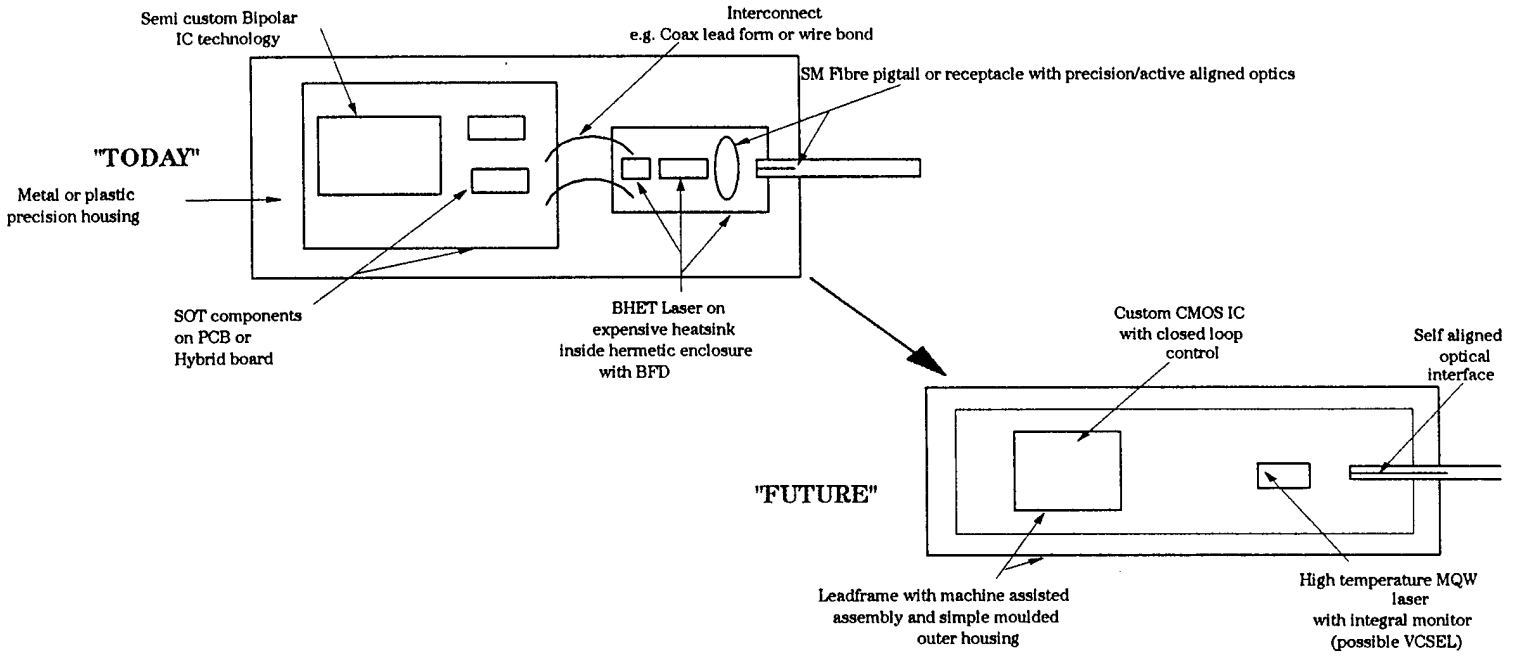
5. Conclusion

The key to cost is Total Cost. Solutions must meet the customer need in terms of cost-performance trade-offs whilst maintaining quality and reliability standards that are well established. Integrated photonics can act as an enabler providing the performance of the module is not adversely affected, and in some instances may have genuine advantages.

Acknowledgment
I am grateful for the contribution of David Chown, Richard Ash and Bob Musk in the formulation of this paper.

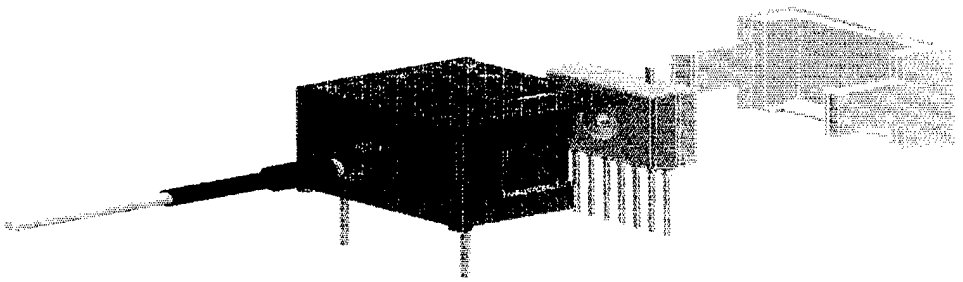
• **Figure 1.**

Transmitter Module Evolution



• **Figure 2.**

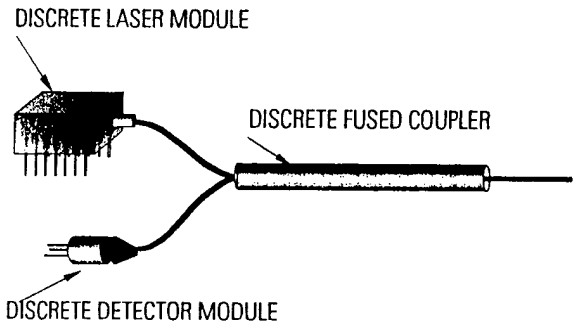
Leadframe Based Optical Receiver

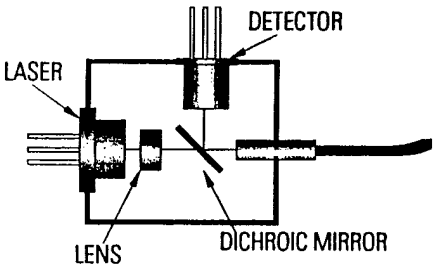


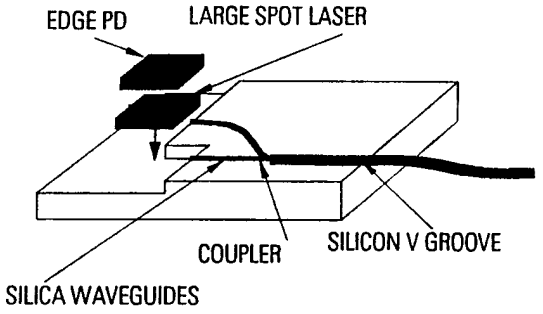
HEWLETT PACKARD

BI-DIRECTIONAL MODULE IMPLEMENTATION

FIGURE 3.







DISCRETE VERSION

OVERALL MODULE SIZE
approx. 150x100x25mm

BULK OPTICS

OVERALL MODULE SIZE
approx. 15x15x10 mm

OIC

OVERALL MODULE SIZE
approx. 10X6X3 mm

LOW-COST AUTOMATED FIBER PIGTAILING MACHINE

Oliver T. Strand
Lawrence Livermore National Laboratory
Livermore, CA

Introduction

At present, the high cost of optoelectronic (OE) devices is caused in part by the labor-intensive processes involved with packaging. Automating the packaging processes should result in a significant cost reduction. One of the most labor-intensive steps is aligning and attaching the fiber to the OE device, the so-called pigtailing process. The goal of this 2-year ARPA-funded project is to design and build 3 low-cost machines to perform sub-micron alignments and attachments of single-mode fibers to different OE devices. These Automated Fiber Pigtailing Machines (AFPMs) are intended to be compatible with a manufacturing environment and have a modular design for standardization of parts and machine vision for maximum flexibility. This work is a collaboration among Uniphase Telecommunications Products (formerly United Technologies Photonics, UTP), Ortel, Newport/Klinger, the Massachusetts Institute of Technology Manufacturing Institute (MIT), and Lawrence Livermore National Laboratory (LLNL). UTP and Ortel are the industrial partners for whom two of the AFPMs are being built. MIT and LLNL make up the design and assembly team of the project, while Newport/Klinger is a potential manufacturer of the AFPM and provides guidance to ensure that the design of the AFPM is marketable and compatible with a manufacturing environment. The AFPM for UTP will pigtail $LiNbO_3$ waveguide devices and the AFPM for Ortel will pigtail photodiodes. Both of these machines will contain proprietary information, so the third AFPM, to reside at LLNL, will pigtail a non-proprietary waveguide device for demonstrations to US industry.

AFPM Design

The AFPM (Figure 1) is designed to be low-cost (<$150K), modular, flexible, and compatible with a manufacturing environment. The performance goals of the AFPM are to perform each pigtailing operation in less than 3 minutes (including the epoxy curing time) and to operate unattended for up to 1 hour. During the alignment operation, the OE device is held fixed while the ends of the fibers are moved by the high-precision stages. These machines incorporate a 2-step procedure to perform sub-micron alignments. The first step uses computer vision to align the fiber sufficiently close (few microns) to the OE device to couple light between the fiber and the device; the second step then achieves the sub-micron alignment by maximizing the light throughput. The overall design of the AFPM was carefully considered to minimize the requirements for high-precision machining tolerances; this greatly reduced the cost of building the AFPM. The modular nature of the AFPM means that each machine may be easily customized for a particular application.

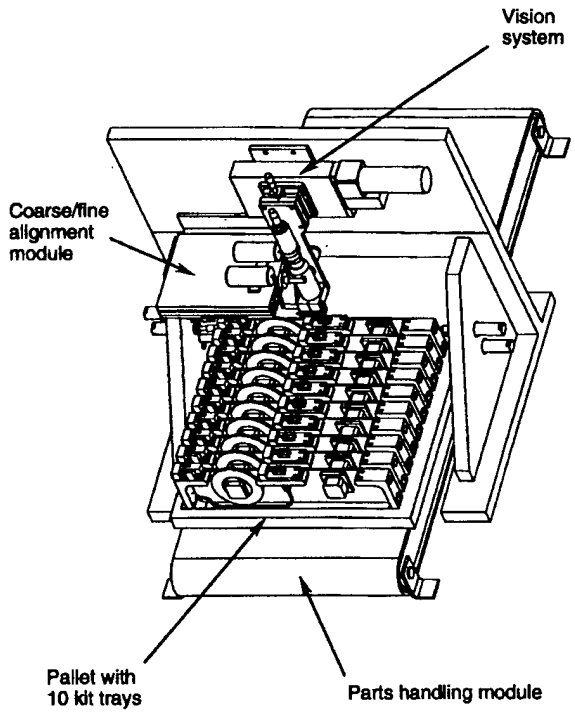


Figure 1. The Ortel AFPM has one high-precision stage mounted on the left side of the frame.

For this project, a basic set of modules was designed to build prototype AFPMs which can pigtail devices with 3 very different geometries including a photodiode and two different types of waveguide devices; a different set of the same modules would allow laser diodes to be pigtailed, for example. Considerable effort was put into the parts handling scheme which allows the AFPM to operate unattended for significant amounts of time. A conveyor system is provided to deliver the OE devices to the alignment stages and vision system. A description of several modules is given in the following sub-sections.

Vision Module

The vision system greatly reduces mechanical fixturing constraints by requiring the critical components to be positioned only within the field of view of the camera. The field of view for all 3 AFPMs is approximately 1 mm by 1.2 mm with approximately 2 micron resolution (Figure 2). Achieving mechanical precisions sufficient to locate the OE device and the ends of the fibers within this field of view is fairly straightforward. Object-recognition algorithms written by LLNL allow the AFPM to determine the initial locations of the OE device and the fiber; this image analysis takes between 1 second to 6 seconds, depending upon the complexity of the image. The 2-micron resolution of the vision system allows the fiber to be moved to within a few microns of the desired initial position. This is sufficiently accurate to ensure that some coupling of light between the OE device and the fiber will occur. At this point, the AFPM switches to active feedback to perform the sub-micron alignment, that is, the AFPM performs a series of peak-finding motions until the coupling efficiency is maximized.

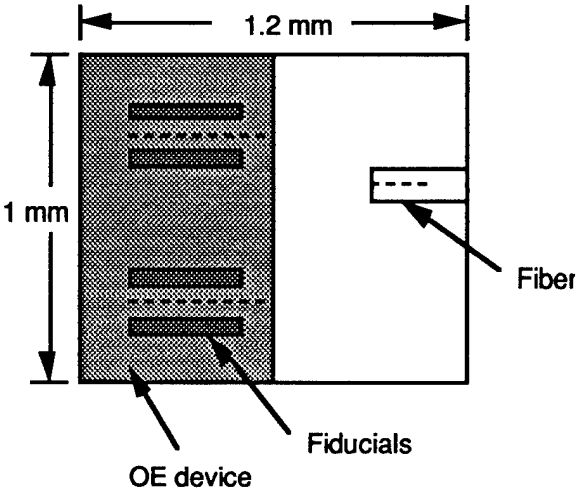


Figure 2. This schematic of a camera image shows the waveguide device on the left side of the image and the end of a fiber on the right side. Fiducials indicate where the invisible waveguides are located. The dotted lines indicate the computer-found locations for the waveguides and the fiber end.

High-precision Stages

The high-precision stages were designed and built by MIT after extensive discussions with UTP and Ortel regarding the required resolution and range. The required resolution was determined by the mode size of the UTP waveguide device operating at 830 nm and the corresponding single-mode fiber to be pigtailed. The resolution of the stages needs to be a small fraction of the waveguide dimensions to ensure high coupling efficiencies. For the AFPMs, the chosen resolutions for the stages were 0.1 micron in the lateral dimensions and 0.5 micron in the longitudinal dimension. The range of the stages was determined by the working volume required by the AFPM to access the interior of the 14-pin DIP package of the Ortel photodiode; for this project, the range of the high-precision stages was chosen to be 25 mm in each of three translation directions. The issue of whether to include fiber roll in the AFPM created considerable discussion. Ultimately, roll was not included for this project once satisfactory mechanical fixturing was designed to accommodate this degree of freedom.

Parts Handling

One of the original design criteria for the AFPM was that it should operate unattended for at least an hour; this implies that at least 20 pigtails will be performed without operator intervention. The issue of parts handling and feeding becomes important for an automated

system compatible with a manufacturing environment. Many aspects of the electronics industry are fully automated in terms of feeding parts to the assembly stage, so the technology is well developed. For this project, however, a parts handling scheme was developed which relies upon the operator to load the OE device and the fibers into a tray, the so-called kit tray (Figure 3). A set of six loaded kit trays is placed onto a pallet by the operator who then places the pallet onto the conveyor system of the AFPM. The conveyor system may be chosen to have any length necessary to allow the desired time of unattended operation.

The kit tray is designed for easy placement of the OE device and the fibers with sufficient accuracy to allow alignment by the AFPM. The overall design of the kit tray is standard for all applications. The tray body is cast from hard plastic which allows 25 micron repeatability of the placement of the OE device with respect to the vision system from tray to tray. The kit tray can hold up to four spools of fiber depending upon the type of OE device to be pigtailed. Unfortunately, every OE device has a different geometry so no standardization of the kit tray was possible for the fixture to hold the device. The kit tray body is designed to accommodate a device cartridge which fits onto the top of the kit tray; the device cartridge is one of the few AFPM components which must be custom designed for each OE device application.

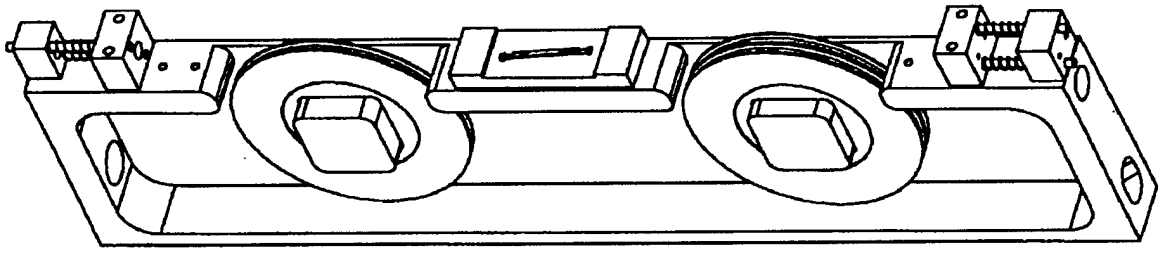


Figure 3. The kit tray measures 15" long by 3.5" high by 1" thick. The tray body is standard for all applications while only the device cartridge in the center is customized for each OE device. The fiber spools can hold at least 2 meters of fiber.

Summary

Three Automated Fiber Pigtailing Machines (AFPMs) have been designed and built under this ARPA-funded project. The AFPM enables many of the critical technologies to perform automated sub-micron fiber pigtailing compatible with a low-cost manufacturing environment. These technologies include low-cost high-precision stages, computer vision to replace the labor-intensive coarse alignment, and many details of parts handling and feeding. Subsequent generations of the AFPM may build upon the design concepts developed here to pigtail fibers to OE devices in more complicated geometries. For example, all applications for this project use epoxy to attach the fibers, so no applications using solder or laser welding have been considered. Also, the stages to manipulate the fibers provide only 3 axes of translation, so no rotational degrees of freedom are available, including the very important roll axis for polarization-dependent applications. The AFPM to reside at LLNL will be used for demonstrations to US industry and for further development of AFPM capabilities.

Acknowledgments

The author wishes to thank Andy Yang and Anis Husein of the Advanced Research Projects Agency for funding this project. Other team members in this collaboration include Andre Sharon at MIT, Don Bossi at UTP, Ron Moeller at Ortel, and Randy Heyler at Newport/Klinger. At Lawrence Livermore National Laboratory, this work was performed in part under the auspices of the U.S. Department of Energy under contract No. W-7405-Eng-48.

FIBER TO LASER COUPLING ON SILICON OPTICAL BENCH PLATFORM

G.E. Henein, J.V. Gates, L.J. Mulligan, H.M. Presby and J.F. de Jong

Lucent Technologies- Bell Labs
600 Mountain Avenue
Murray Hill, NJ 07974
USA
(Tel: 908-582-2236, Fax: 908-582 7774, E-mail: henein@allwise.att.com)

INTRODUCTION

The key requirements for field-deployable fiber optic components are high fiber power, high stability/reliability and low-cost manufacturability. Among the contributing factors, a critical role is played by the fiber-to-laser coupling since it is both a discontinuity in the optical path at the material level and in the manufacturing process sequence. The fiber-coupling approach presented here meets these three requirements: the high fiber power arises from the lensing of the fiber tip, the stability is achieved through the use of a single platform and solder securing both the laser and the fiber, and the manufacturability from batch wafer-level chip assembly and batch fiber soldering technique resulting in a low labor cost.

After a description of the pieceparts involved and of the actual fiber attachment process, coupling and stability results are presented for 1300 nm MQW and 980nm laser chips.

PIECEPARTS

Silicon Bench

A common platform[1] is used for the laser chip, backface monitor photodiode and fiber, consisting of a silicon bench 2.16x1.7 mm in size. The benches are processed on 125 mm diameter/500 μm-thick silicon wafers and are equipped with metallized electrical access pads, bonding sites, evaporated solder, solder dams and an integral microstrip heater for fiber attachment. The metallization consists of sputtered Ti/TiN/Pt/Au thin film. The evaporated solder at the chip sites is eutectic AuSn (80 wt.% Au) 6 μm thick and is confined by a Cr thin film dam. The on-board heater consists of a Cr strip deposited over a 2 μm-thick SiO_2 layer serving as thermal isolation between the fiber and the laser sites. The heater is capable of melting a 0.0035 mm^3 AuSn solder. The thermal isolation between the fiber and the laser sites allows the laser to emit light for active fiber alignment. The overall stability of the assembly arises from 1) the common (hard) solder, 2) the common Si platform and 3) the close proximity of the bonding sites for the laser and the fiber (620 μm center-to-center spacing).

In order to minimize handling and increase uniformity of assembly, chip assembly is performed at the Si wafer level. The Si wafer is populated by tack-bonding several hundred laser and PIN chips epi-side up. The wafer is then heated in a controlled atmosphere to reflow the evaporated solder. The chips are then wire-bonded and the PIN tested and inked at the wafer level. Only then is the wafer diced into individual optical sub-assemblies (OSA) for testing and fiber attacment. A 125 mm wafer contains ~2,000 OSAs. We have limited ourselves so far to 1/4 wafers with excellent yields. A close-up view of such a "populated" wafer is shown in Fig. 1.

Fiber

Two different types of single mode fibers are used for the 1300 nm MQW (FP and DFB) lasers and the 980 nm pump lasers and are lensed by two different techniques. At 1300 nm, the fiber tip is chemically etched in a solution which etches the cladding faster than the core resulting in the lens shown in Fig. 2. This lens routinely couples ~75% of the light and the lensing

uniformity results mostly from the well-controlled doping profile of the glass. It is produced in a batch process (1,000 fibers per batch). At 980 nm, we used a CO_2 laser to micromachine [2] the fiber tip in such a way as to obtain a hyperbolic profile, achieving coupling efficiencies of 90%. A view of this lens is shown in Fig. 3. These lenses are fabricated individually but the actual lensing operation takes only a few seconds.

After lensing, both types of fibers are metallized by plating. The metallization is electroless and consists of ~ 4 μm of Ni capped by ~ 0.2 μm of Au.

FIBER ATTACHMENT OPERATION

After dicing, the OSAs are loaded and temporary-wire bonded onto 10-position batch cartridges. A AuSn solder preform is then tacked at the fiber bond site. The equipment used consists of a piezo-controlled stage holding the fiber, a second stage holding the cartridge, standard electro-optic equipment for laser bias and power detection, video cameras and a power supply to feed the strip heater. The operation is computer-controlled, including fine adjustments in the fiber position (0.1 μm steps). The cartridge arrangement allows the pigtailing of the 10 lasers in succession. Each laser is biased for active alignment and the current through the strip heater is raised until the preform melts: typically, the current is ~1 A and the voltage ~7V. A reducing atmosphere is used to prevent oxidation. The fiber is then brought in close proximity with the laser facet using manual verniers. Fine and final alignment is performed by moving the fiber in the molten solder using piezo positioners. When peak power is detected, power to the strip heater is removed and the solder instantly frozen . It is to be noted that only spontaneous light is used during the alignment (a few μW) due to the laser temperature (~200°C). The procedure is then repeated with the next laser. The cycle time for this operation is 5 minutes allowing therefore 12 operations per hour. A simple calculation shows that the relative movement of the fiber tip during cooling is ~0.08 μm along the vertical resulting in a negligible coupling loss (~2 %).

A fiber-pigtailed 1300 nm OSA is shown in Fig.4. After removal from the cartridge, the OSAs are packaged in low-profile ceramic packages for uncooled operation.

RESULTS

Coupling Efficiency

Distributions of final coupling efficiency for 1300 nm lasers are shown in Fig. 5. The 45 experimental devices were fiber-attached with the goal of maximizing power, independent of the time required, whereas, for the 101 model devices, the goal was to freeze the solder within 60 seconds as is presently done on the production line. As can be seen from these results, the coupling achieved routinely is 61±11%. Higher coupling is achievable by tailoring the lens etching, but at the expense of displacement sensitivity. Similar data taken for the 980 nm lasers show a coupling efficiency of ~ 80% with the CO_2 laser micromachined fiber.

Alignment Sensitivity

The sensitivity to displacement was measured in the three directions for both laser types. The coupling is extremely sensitive to displacement in the x and y directions (while quite insensitive along the optical axis z.) The 3dB drop-off is ~0.7-0.9 μm, forcing the alignment to be stable to within ~0.2 μm in actual field devices.

Mechanical Stability

The stability of the pigtail was measured over temperature from -40 to 85°C for six 1300 nm lasers and is shown in Fig. 6. The tracking error is the change in the ratio of the coupled power out of the fiber to the optical power out of the back facet, the latter being measured by the PIN monitor diode and kept constant during the temperature scan. The measurement therefore reflects both the fiber movement relative to the laser, as well as the changes in the laser front-to-back ratio and its far-field variations with temperature. The total excursion from perfect stability is ~±8 %. We attribute ~2% to pure fiber movement (less

than 0.1 μm) and the remaining 6% to laser variations.

The solid stability of our approach was further tested by subjecting 50 packaged devices to 500 temperature cycles from -40 to 85°C as per the Bellcore specification. The data was acquired in terms of relative change in output power before and after cycling, measured at a fixed backface monitor current. A total of 48 devices exhibited less than 0.5 dB change, thus passing the test. The two failures observed were due to fissures visible in the fiber metallization and were not directly related to the fiber attachment process.

Mechanical Strength

Of the devices referred to above, 25 were subsequently subjected to the Bellcore mechanical shock and vibration tests with 100% success rate (maximum power change observed 0.33 dB).

The strength of the fiber attachment was measured on over 100 devices using the fiber pull test. The data shows a mean of 630 grams with a standard deviation of 135 grams. In nearly every instance, the failure mode is a clean delamination of the metallization from the fiber, not rupture through the solder bond itself. Accounting for the solder-wetted area on the OSA, the pull force represents a shear stress of 150 MPa. The yield stress of AuSn solder is ~215 MPa, in agreement with the above rupture observation.

CONCLUSION

The approach described here is attractive for high volume/low cost packaging of fiber-pigtailed components. We have transferred this technology to the manufacturing facility where, to date, over 3,000 devices have been fabricated. Aside from the performance advantages described earlier, it is the low cost of this technology which makes it truly attractive . It comprises only five pieceparts which are low cost. The Si bench uses well-established Si processing techniques. The wafer-level assembly drastically reduces handling of individual pieceparts. The fiber attachment requires only a modest capital investment and yields, in the present approach, one part every 5 minutes.

REFERENCES

1. J.V. Gates et al., "Uncooled laser packaging based on silicon optical bench technology", Proceedings of SPIE's Photonics East 1995 symposium.

2. H. Presby and C.A. Edwards, "Near 100% efficient fiber microlenses", Electron. Lett. 28,p. 582, 1992.

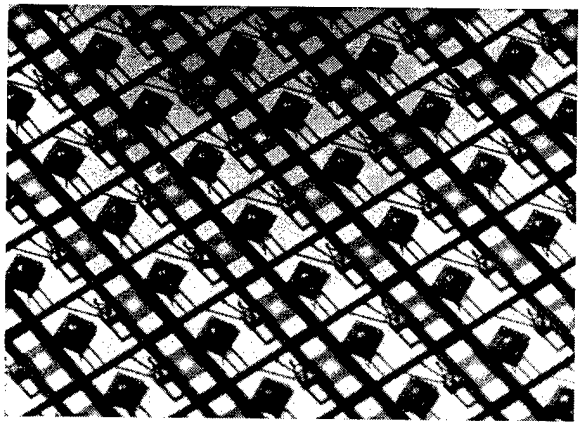


Fig. 1 Wafer-level chip assembly

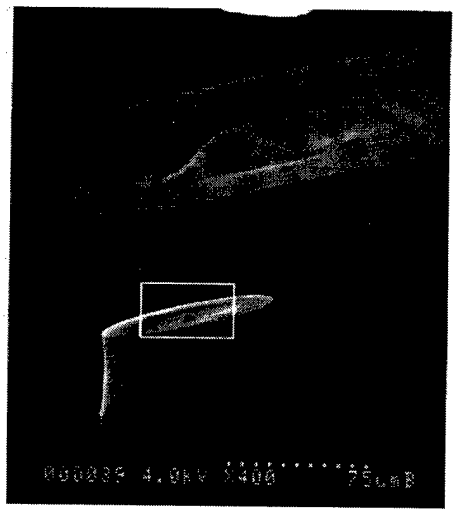


Fig. 2 Etched lens for 1300 nm lasers

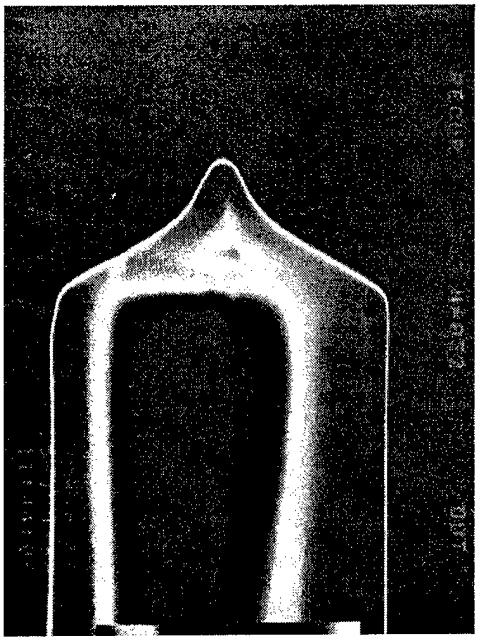


Fig. 3 CO_2 laser lensed fiber for 980 nm

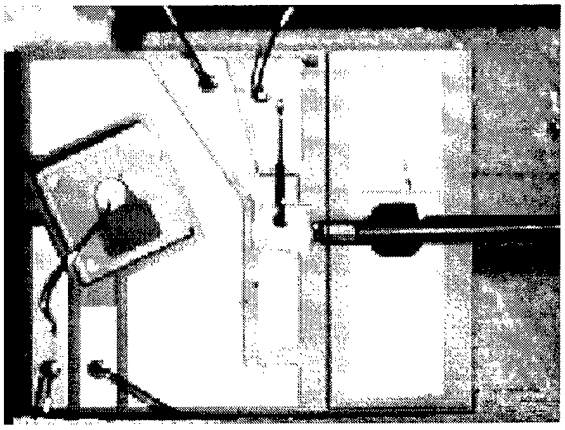


Fig. 4 Fibered 1300 nm OSA

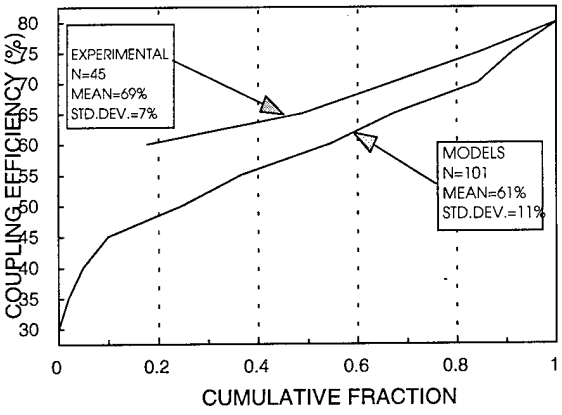


Fig. 5 Coupling efficiency for 1300 nm

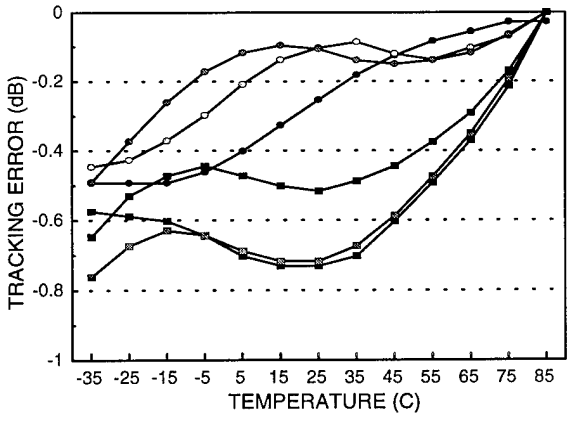


Fig. 6 Coupling stability for 1300 nm lasers

NEW ASSEMBLY TECHNOLOGY FOR SMALL SURFACE MOUNT LEDS.

P.Rajkomar
OptoElectronics Division
Hewlett Packard, San Jose,California

Abstract:
The Optoelectronics Division of Hewlett-Packard has developed a new technology for making surface mount L.E.D lamps and indicators whereby the internal wire bond is eliminated. The new technology clears the way for products with enhanced reliability while offering a path to fast and inexpensive proliferations. That will enable OED to increase its range of products in a fast growing market.

Introduction:

OED is a vertically integrated manufacturer of LED lamps, indicators and displays, mostly for thru' hole applications. In the last few years there has been a dramatic increase in the demand for surface mount LED lamps. While OED offers numerous products in the high performance arena, its range was not as extensive in the low end where most of the growth has been [>150M/ month]. However OED did not want to provide just a me-too approach. We felt that we had to offer a technological breakthrough that would contibute to the high volume-low cost segment of the market and could further extend the market for surface mount leds.

Development:

Our approach included the elimination of the wire bond,the weakest link in the traditional chip and wire assembly of LED lamps for quality and reliability. Connections in the new scheme are through solder joints.[Figure 1]. We believe that elimination of the wire widens our choices for handling and further processing once the chip has been put down.

The obvious problem is that the chip is on its side and requires a totally different means of placement. As we want to solder chips down to a board as opposed to wire bonding, the first crucial element was a solderable chip. The integration of those two aspects of development proved to be more challenging than we had anticipated. During the development phase, most of the emphasis in Wafer Fab R &D centered around developing the processes and fixturings that would produce material that could be used on the Die Attach machine with ease. While the obvious work necessary was accomplished early, there were many more changes that were necessary once the DA machine was fully operational. Die size changes, problems with pattern recognition, strict sawing quality needs as well as increasing volumes and an increasingly exacting die presentation requirement were issues that had to be addressed and resolved without compromise. The need for a sound and well engineered setup in the Front End [See Figure 2] was imperative.

The Die Attach machine has been,without any doubt, the center of attraction for most of the development phase . It exemplifies (1) faith, in that we even attempted to develop it after several experienced vendors expressed doubts about its feasibility (2) innovation, in that we knew that die presentation would require new , original fixturing , new process and materials (3) top design capabilities, for the technical depth , and (4) top notch tool shop, for meeting the fine workmanship standards imposed by the designers. See Figures 3 and 4 . The machine rate is presently 5000 placements per hour which is comparable to that of standard , commercial equipment.

Another major area of development centered around the soldering process. The search for an appropriate solder was initially driven by the inconsistent solder joint after soldering with eutectic tin/ lead solder. In order to develop a robust Surface Mount led that could be mounted by IR as well as wave Solder, it was felt that we also had to use a high temperature solder with a melting point above normal soldering temperatures (260 Deg C). Using life testing and cross sectioning of soldered metal structures as indicators , we finally settled on Lead Indium .

While the solderable chip, die presentation , the DA machine and the high temp solder form the essential base of the new platform, there are several other areas where major efforts were necessary. We chose the encapsulation process rather than transfer molding early in the program because of the frequent changes we had to make to the boards. Design time,tooling costs as well as capital equipment expenditure were thus minimized.

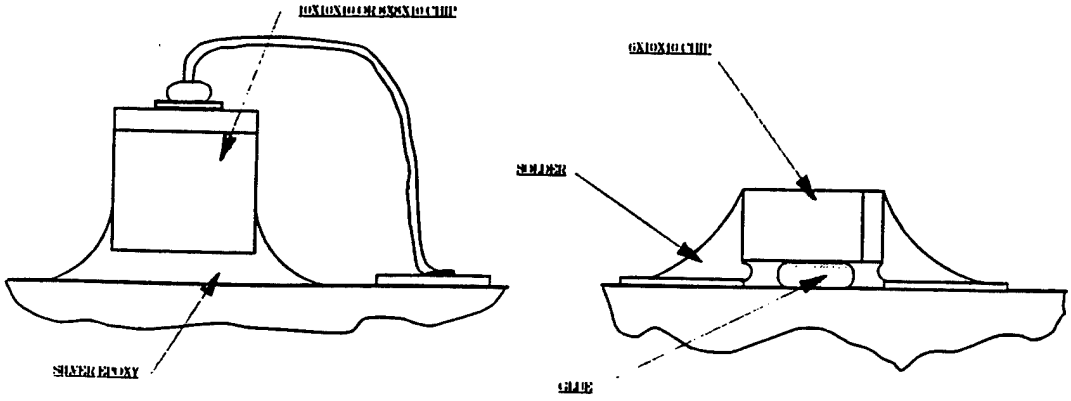
The use of a rubber mold for encapsulation has been around for a long time but we adapted the method and coupled it with some innovative fixturing to give an inexpensive, flexible casting for surface mount lamps. Changes in device size and addition of features such as a lens or profile changes can be accommodated fairly easily. At this point, apart from some mechanization, little effort has been made to automate the process.

During the initial phase, we used a small FR4 solder plated board built by a special process developed together with a local vendor. The choice of Pb/In forced us to use a high temperature [BT] laminate. A larger board was designed and tooled up with an approved vendor overseas. The last significant change was a switch from tin / lead plating to gold plating and as a consequence,the design was simplified and it may be possible to source a cheaper board. The switch to gold plating was made because we could not control the thickness of the board after soldering due to inconsistent build up of solder at the back. We decided to plug the plated through hole after die attach with a water soluble mask which we washed off after wave solder. The existing process is crude but could be improved considerably. One area where the vendor played a crucial role was in the development of the high temperature soldering process. Since we are using Lead Indium at a temperature above 300 degrees C, we have added a nitrogen blanket to minimize dross. Since our features are so small, we cannot tolerate any foreign material.

Conclusion:

This development program allowed us the opportunity to seek innovative approaches to existing and new problems. Most of our effort was spent in areas where there was no existing

equipment or process. To speed up the essential development, we chose to use the same testing and packaging equipment/process as our existing parts for now. We have programs in place to design and develop,amongst other things : faster testing , cheaper, dedicated tape and reel mechanisms, gang sawing , and a robotic cell for part handling. The response from the customers has been very favorable . From a customer's point of view,this part is a drop-in replacement for existing aparts. As such, the challenge now is to meet cost and delivery targets. We have an aggressive cost reduction in place as well as a sharp ramp rate to meet expectations of a very dynamic market.



(a) Existing (b) New

Figure 1 Construction Details

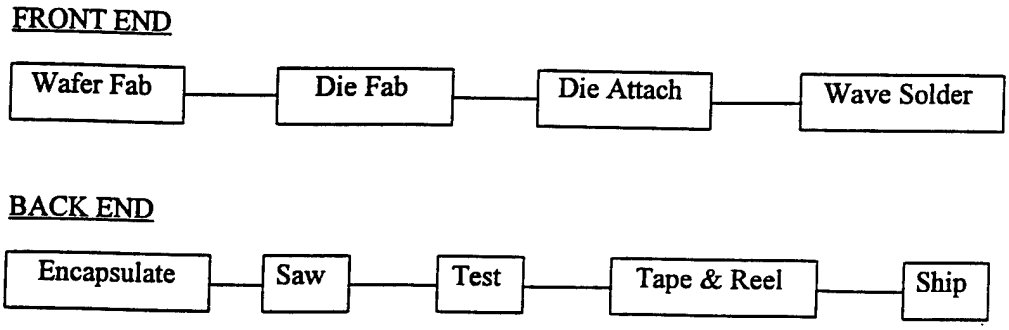


Figure 2 Flow Charts

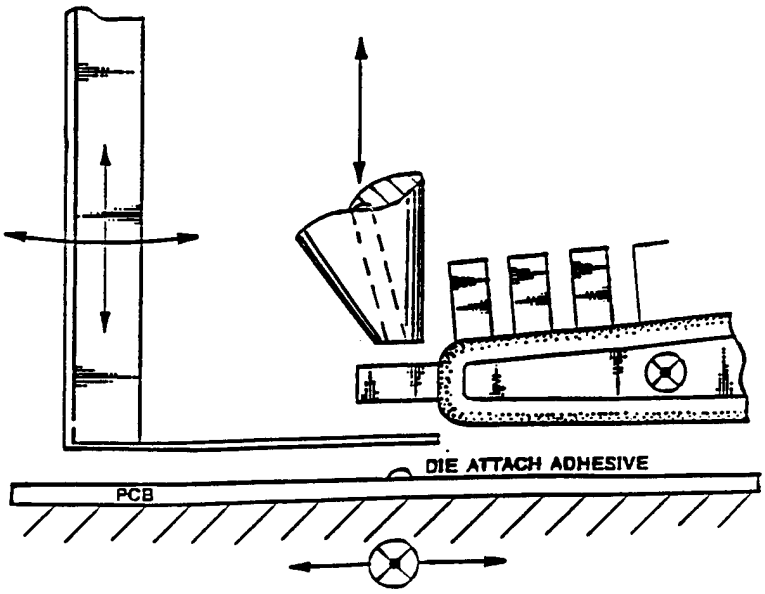
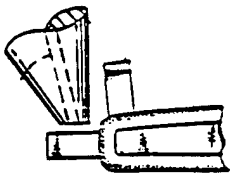
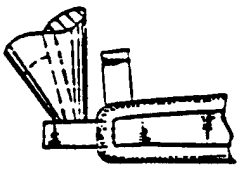


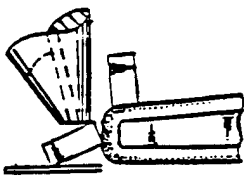
Figure 3 Die Attach Machine Features



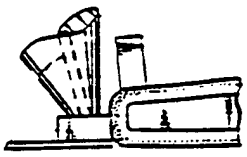
(a) Die in position



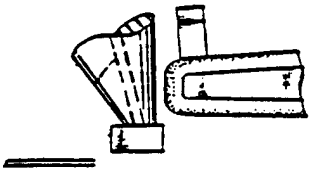
(b) Collet moves down



(c) Shelf slides under die



(d) Die clamped between collet and shelf



(e) Shelf moves out collet travels down with die

Figure 4 Die Attach Sequences

Wednesday, May 1, 1996

Optical Filters and Waveguides

IWA 8:45 am-10:00 am
Fairfax A

K.A. Shore, *Presider*
University of Wales, U.K.

Narrow-band transmission filters from highly resonant gratings

J. C. Chen, P. R. Villenueve, H. A. Haus and J. D. Joannopoulos
Office 36-351
Research Laboratory of Electronics
Center for Material Science and Engineering
Massachusetts Institute of Technology
Cambridge, MA 02139
phone: (617) 253-2585, fax: (617) 253-9611, email: haus@mit.edu

Gratings implemented on silicon-on-insulator (SOI) structures have been used for waveguide coupling.[1] Gratings can also form the end mirrors of DFB and DBR lasers. Recently, channel dropping filters have been fabricated in silicon from gratings with a quarter wave shift.[2] Such resonant gratings transmit one frequency but reflect the others that fall within the "stop band" or band gap. In order for the stop bands to cover the 40 nm spectrum of erbium amplifers, deep gratings or large index modulations are needed. As the grating strength increases, light tends to radiate into the substrate.

Here we design and model a transmission filter whose stop band exceeds 100 nm yet whose radiation losses are kept low. The quality factor — number of optical cycles for energy to decay to $1/e$ — is over 13,000. We present the transmission spectrum of such a filter using a finite difference time domain (FDTD) program with a new quartic perfectly matched layer (PML)[3] boundary condition.

1 Quartic Perfectly Matched Layers

Optical gratings have been studied with a variety of analytic techniques: coupled mode theory, transfer matrices, etc. But the radiation properties of gratings are difficult to treat without resorting to numerical techniques. The finite difference time domain method allows for the computation of a wide frequency spectrum in a single simulation.

The standard way to simulate an open or unbounded region uses the Mur second-order absorbing boundary condition (ABC).[4] Waves may be reflected from the computational border back into the computational domain. These spurious reflections become particularly noticeable when the index of refraction changes along the border or when a waveguide crosses the border. These reflections can give rise to Fabry Perot fringes and long simulations can suffer from instabilities.[3] Recently, Berenger formulated the perfectly matched layer (PML)[5] to model open boundary conditions. The PML method uses an artificial conductor that absorbs incident fields. These fields are split into two components, of which only one "sees" the conductor. To minimize back reflections, Berenger[5] and Pekel and Mittra[6] suggest that increasing the spatial profile of this conductivity quadratically (with a power of $n = 2$) is preferable to both uniform and linear profiles. As a result, quadratic gradations are the norm.[7–9] We[3] show that at least, in our situation, quartic ($n = 4$) conductivity profiles are far superior to quadratic ones.

Using Berenger's notation,[5] the conductivity σ can be expressed as

$$\sigma(\rho) = \sigma_{\max} \left(\frac{\rho}{\delta}\right)^n,$$

where δ is the PML thickness, $\sigma_{\max}$ is the maximum conductivity or the conductivity at the edge, and n is the order of the polynomial which describes the conductivity profile. ρ varies from 0 at the edge of the solution domain to δ next to the perfectly conducting outer boundary. The field is completely reflected at the perfectly conducting outer boundary, where

the tangential electric field is zero. As a result, the theoretical reflected field amplitude is

$$R(\theta) = \exp\left(-\frac{2}{n+1}\frac{\sigma_m \delta}{\epsilon c}\cos(\theta)\right),$$

where θ is the angle of incidence, ϵ is the electric permittivity, and c is the speed of light.

To measure the actual reflections, we send light down a GaAs waveguide ($n = 3.4$) that was surrounded by air (figure 1). Various numerical boundary conditions were tried in succession on the four borders. The Mur second-order ABC[10] was implemented in a 2D, scalar FDTD.[11] Both quadratic and quartic PML's were chosen to have a theoretical reflectivity of $R(0) = 10^{-6}$ and a layer thickness of $\delta = 12$ grid points. Following the example of Taflove *et al.*,[12] we set the conductivity in the GaAs region ϵ higher than that in air. All of these simulations were performed for 2D FDTD. The reflected and initial TE electric fields, E_z (where z is normal to simulation domain), are plotted with solid lines while the TM magnetic fields, H_z, are denoted with dashed lines (figure 2). For $R(0) = 10^{-6}$ and $\delta = 12$, the quartic (n=4) PML produces the least reflections — two orders of magnitude less than the quadratic (n=2) PML and over four orders of magnitude less than a Mur second-order ABC. The reflections from the quartic PML are less than 2×10^{-6} for both TE and TM waves, from 50 to 250 THz.

2 Optical filter characteristics

We use this FDTD with the improved PML boundaries to model the 2D cross section depicted in figure 3. The top layer is silicon (0.315 μm thick with $n_{eff} = 3$). This waveguiding layer is sandwiched by air on the top and by silicon dioxide (0.85 μm thick and $n_{eff} = 1.45$) on the bottom. Beneath the SiO_2 is the silicon substrate. Such a multi-layer structure can be commercially fabricated by flip chip bonding. The indices used in this simulation are similar also to GaAs systems with buried Al_2O_3. A quarter wave phase shift divides an otherwise sixty period grating in two. These gratings are deep with a 10% index modulation ($n_{eff} = 3$ to $n_{eff} = 2.7$). Such a grating can be implemented by the conventional horizontal grooves or by some side notches.[13] The grating period is 0.315 μm, which can be defined by electron beam lithography. The overall device is less than 20 μm long, so within a small region many of these filters can be cascaded.

This structure is simulated by FDTD with the before-mentioned quartic PML boundary condition. In particular, the time step is $\Delta t = 0.07071$ fs while in space, the increments are $\Delta x = 0.03150\,\mu$m and $\Delta y = \Delta x$. The source or input excitation is a sine function whose envelope is a gaussian pulse.[3,13] Figure 4 plots the reflected and transmitted powers for this grating. Notice that with over two million steps, the reflection coefficient is very flat between 1490 and 1600 nm; the borders do not reflect nor set up Fabry-Perot cavities. Also, there is little noise; the spectra are clearly discernible. The transmission resonance at 1547 nm is adequately resolved, with 0.054 nm (or 6.7 GHz) resolution. At the peak, the transmitted power is 0.642 while the reflected power is 0.054. The radiated power is 0.304 and includes losses to higher order guided modes and radiation to the substrate.

Figure 5 is a gray scale contour plot of the electric field (normal to the page) in such a filter. This plot shows the resonator mode at transmission resonance where the radiation losses are the highest. The field coupling to (or reaching) the substrate is negligible. The thin silicon oxide layer confines the light to the top silicon layer rather well. The quality factor as measured from the decay of the resonator's power is $Q = 13,900$. Because the power in a Bragg grating decays exponentially from its quarter wave shift, the radiation can be reduced and the transmission can be increased, simply by shortening the grating. However, this will lead to more radiation from the grating–waveguide border, lowering the quality factor.

3 Conclusion

We have showed that quartic gradations in Perfectly Matched Layers can reduce spurious reflections by two orders of magnitude. This permits the solution of highly resonant, notch filters. These transmission filters have 110 nm stop bands and quality factors over 13,000.

Acknowledgments

J.C. Chen appreciates conversations with Ms. Jee-hoon Krska, Mr. Jim Foresi and Mr. Paul Martin on fabrication issues. These simulations ran on the NSF San Diego Supercomputer Center's Cray

C90. This work is supported in part by the MRSEC Program of the NSF under award number DMR 94-00334 and the Army Research Office grant number DAAH04-93-G-0262.

References

[1] R. M. Emmons and D. G. Hall. *IEEE J. Quant. Electron.*, 28(1):164–75, 1992.

[2] J. N. Damask, J. Ferrera, V. V. Wong, H. I. Smith, and H. A. Haus. *Proceedings of the SPIE — The International Society for Optical Engineering*, 2213:137–51, 1994.

[3] J. C. Chen and K. Li. Quartic perfectly matched layers for dielectric waveguides and gratings. to be published in *Microwave Opt. Technol. Lett.*.

[4] G. Mur. *IEEE Trans. Electromag. Compat.*, EMC-23(4):377–82, 1981.

[5] J.-P. Berenger. *J. Computat. Phys.*, 114(2):185–200, 1994.

[6] Ü. Pekel and R. Mittra. *Microwave Opt. Technol. Lett.*, 9(3):117–22, 1995.

[7] W. C. Chew and W. H. Weedon. *Microwave Opt. Technol. Lett.*, 7(13):599–604, 1994.

[8] E. A. Navarro, C. Wu, P. Y. Chung, and J. Litva. *Electron. Lett.*, 30(20):1654–6, 1994.

[9] W. V. Andrew, C. A. Balanis, and P. A. Tirkas. *IEEE Microwave Guided Wave Lett.*, 5(6):192–4, 1995.

[10] B. Engquist and A. Majda. *Math. Computat.*, 31(139):629–51, 1977.

[11] J. C. Chen, H. A. Haus, J. N. Winn, S. Fan, and J. D. Joannopoulos. T. Tamir, G. Griffel, and H. Bertoni, editors, *Guided-Wave Optoelectronics: Device Characterization, Analysis and Design*, 477–83. Plenum Press, 1995.

[12] C. E. Reuter, R. M. Joseph, E. T. Thiele, D. S. Katz, and A. Taflove. *IEEE Microwave Guided Wave Lett.*, 4(10):344–6, 1994.

[13] J. C. Chen, H. A. Haus, S. Fan, P. R. Villeneuve, and J. D. Joannopoulos. Optical filters from photonic band gap air bridges. submitted to *J. Lightwave Technol.*, 1995.

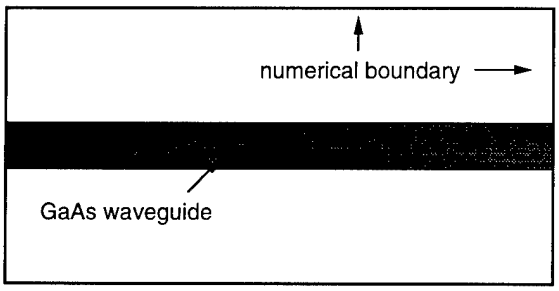


Figure 1: GaAs waveguide surrounded by air.

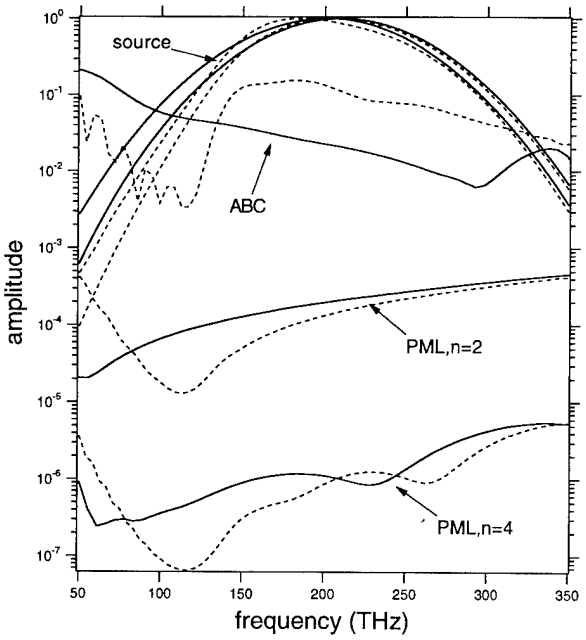


Figure 2: In a straight, GaAs waveguide, amplitudes reflected for various frequencies due to a Mur second-order ABC, a quadratic ($n = 2$) PML, and a quartic ($n = 4$) PML. Solid lines denote TE E_Z and dashed lines are for TM H_Z.

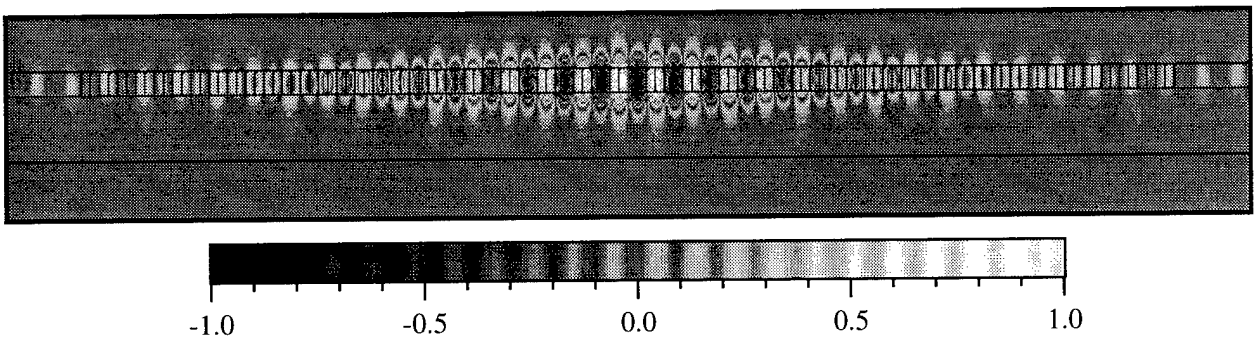


Figure 5: Grayscale contour of electric field normal to page, at resonant frequency.

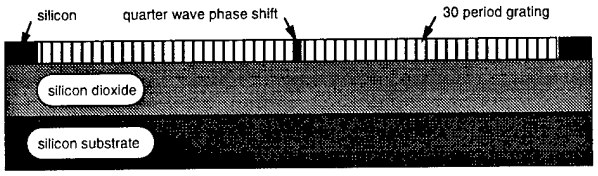


Figure 3: Quarter wave shifted (resonant) grating on silicon-on-insulator (SOI).

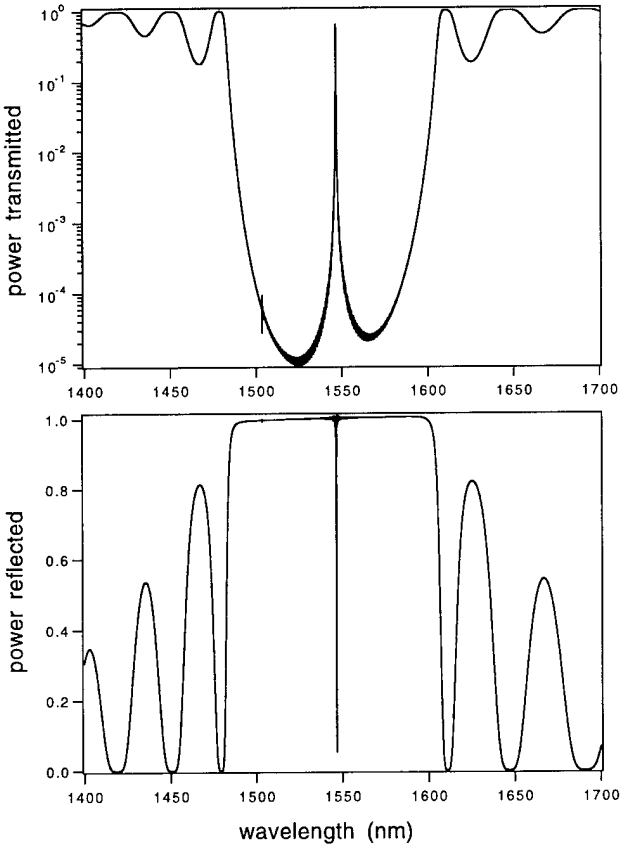


Figure 4: Transmitted and reflected powers of resonant, silicon-on-insulator grating.

Improved Analysis and Design of Waveguide Bragg Grating Filters for Wavelength Division Multiplexing Applications

A.Gnazzo, A.Barla, C.De Bernardi
CSELT S.p.A., Via G.Reiss Romoli 274, 10148 TORINO - ITALY
Phone + 39 11 228 7320 - Fax + 39 11 228 5085

1. Introduction

Waveguide Bragg gratings are attracting increased attention as narrow-band filters to separate different channels in closely-spaced wavelength-division-multiplexing (WDM) systems. In fact grating filters directly written into Ge-doped optical fibers are already available and exhibit quite attractive features. However, the added structural flexibility inherent in integrated optical waveguides can offer an even increased variety of device and subsystem architecture and performance.

Usually current models [1] describe Bragg gratings by means of a single effective modal index for the forward- and backward propagating mode (in the single-mode waveguide case) along the entire filter; while this is correct for uniform gratings, it is not adequate to describe accurately the characteristics of apodized filters, which are based on modulated-amplitude gratings, i.e. structures with varying groove depth or index change.

In this paper a refined analysis of Bragg planar waveguide gratings is described, which takes into account the consequences of effective index variations along apodized filters, and shows the difference in their predicted spectral response. On this basis, nearly ideal integrated filters are designed.

2. Theoretical approach

The spectral response of a uniform grating varies approximately as a sinc squared function; this exhibits sidelobes of such an amplitude that limits excessively the minimum spacing between adjacent WDM channels to avoid intolerable cross-talk levels. To overcome this limitation, apodized filters can be designed [2], in which the amplitude of the grating (or the refractive index variation, if it is an index-modulated or phase grating) changes along its length in appropriate ways, achieving a strong suppression of sidelobes and approaching an ideal, rectangular-shaped response.

As well known [3], the propagation in periodic corrugated waveguides can be described analytically, and the spectral reflectivity of these structures can be expressed as:

$$r(\lambda) = \frac{\left|\kappa \cdot Sinh(S \cdot L)\right|^2}{\left|S \cdot Cosh(S \cdot L) - i \cdot \Delta\beta \cdot Sinh(S \cdot L)\right|^2} \qquad (1)$$

where κ is the coupling coefficient between the forward and backward propagating modes, L is the length of the grating, $S = \sqrt{|\kappa|^2 - \Delta\beta^2}$, $\Delta\beta = \beta - \frac{\pi}{\Lambda}$, β is the fundamental mode propagation constant, and Λ the spatial period of the grating.

For non-periodic gratings there are no known analytical solutions, and the spectral response must be found numerically. A straightforward approach [4] approximates the non-uniform grating by a number of sections, each assumed with a (slightly different) constant value of κ and $\Delta\beta$; each section can therefore be described analytically, and for every section a

2x2 transfer matrix is generated. The action of the entire grating is then described by a transfer matrix obtained by multiplying all the matrices of the individual sections.

By choosing appropriately the number of sections, the quality of the approximation can be adapted to the requirements, and different shape functions can be analyzed to find the required apodized response. For example, it can be found that, by means of a gaussian-shaped coupling coefficient, a symmetric response with low sidelobes can be achieved [1].

However, in this case the effective index is not constant along the filter, but depends on the local groove depth, or on the local refractive index modulation amplitude, unless appropriate guide parameters are varied along the grating coherently with its amplitude. This effect, which is often neglected, has to be taken into account for a correct modeling.

To design appropriately such apodized filters, we have included this effect, in the calculation of the response of Bragg gratings. The analysis has been performed on three-layer planar waveguide structures, with the following parameters: n_s=1.5000, n_g=1.5330, n_c=1, d=3 μm, where n_s, n_g and n_c are the substrate, guiding layer and cover refractive indices, respectively, and d is the guiding layer thickness; the resulting effective index for TE mode is n_{eff}=1.5210 at 1550 nm. The grating parameters are the following: period Λ=509.5 nm, maximum depth g_0=200 nm, total length L=10 mm, rectangular profile with mark/space ratio = 1, and modified gaussian envelope $g(z)$ calculated to get:

$$\kappa(z) = 17.3 \cdot e^{-16\left(\frac{z-L/2}{L}\right)^2} \qquad (2)$$

The local effective index is calculated in each uniform grating section and a maximum effective index variation $\Delta n_{eff}=5.85\cdot10^{-4}$ is found; Fig 1a) shows the results of the conventional calculations, while Fig 1b) shows the spectral characteristics corrected for the effective index variations.

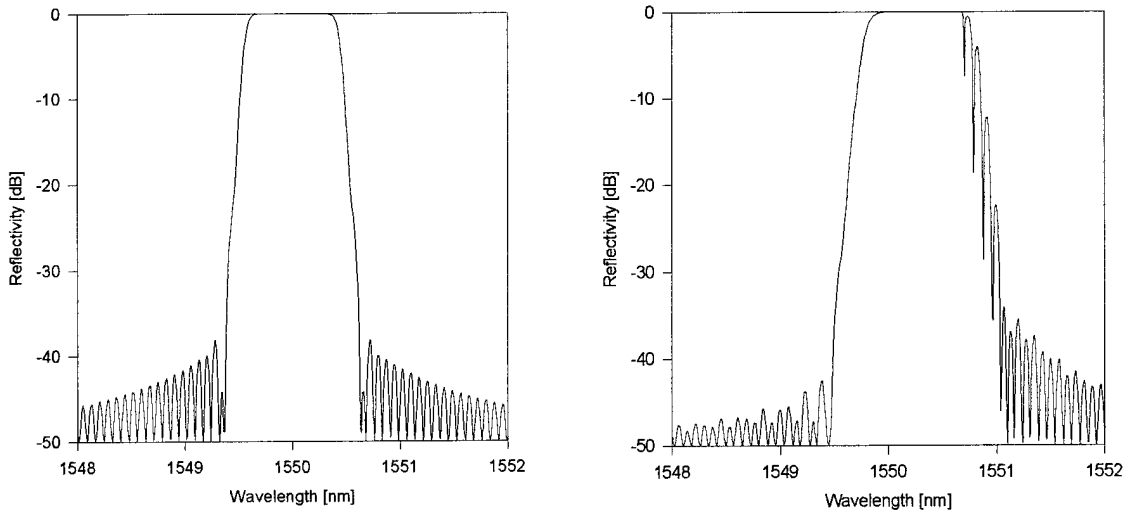


Fig. 1. Calculated spectral reflectivity of a Bragg planar waveguide grating (see text for parameter values). a) response neglecting variations of n_{eff} along the grating; b) corrected response using appropriate $n_{eff}(z)$ values.

The improved calculation shows a fine structure on one side of the reflection peak, which is direct consequence of the non-uniformity of n_{eff}. This fine structure corresponds exactly to what has been observed in fibers with photoinduced gratings [5]. The fact that in the present case the fine structure appears on the longer wavelength side of the peak, while for fibers it is on the shorter side, comes from the fact that for photoimprinted fibers the effective index increases with the grating amplitude, while the opposite happens for etched waveguide gratings.

The fine structure could be eliminated by changing the guide parameters to keep a constant n_{eff}, as done in [5] for apodized fiber filters, but this is difficult to implement in a technological process for planar waveguides.

A much more practical solution is to introduce a small linear chirp in the grating: a nearly ideal stopband shape can be achieved, free from sidelobes and ripples, as in the example shown in Fig. 2.

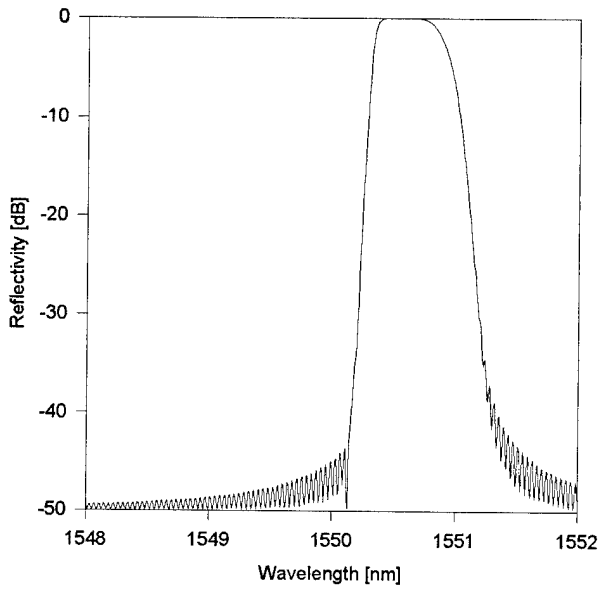


Fig 2. Spectral characteristics of an amplitude-modulated, linearly chirped Bragg planar waveguide grating for TE polarization. Waveguides parameters as described in the text; grating parameters are as follows: L=20 mm, $g(z)=100\cdot\exp[-16(z/L-1/2)^2]$ nm, $\Lambda(z)=(509.9-0.2\ z/L)$ nm, maximum $\Delta n_{eff}=2.86\cdot10^{-4}$.

The model has been extended to two-dimensional waveguide gratings, including polarization effects, using the effective index and Marcatili's method; real doped-silica strip waveguide Bragg filters are currently being designed, and their details will be described later.

3. Conclusions

We have implemented an improved model for the modeling and design of apodized, amplitude modulated planar waveguide Bragg grating filters; this model takes into account the variation of the effective index along the grating, and explains the perturbations observed experimentally in photoinduced fiber grating filters. Using this method, nearly ideal filters based on linearly chirped waveguide gratings have been designed.

References

[1] F. Ouellette, J.F. Cliche, S. Gagnon, "All-Fiber Devices for Chromatic Dispersion Compensation Based on Chirped Distribuited Resonant Coupling", *IEEE Journal of Lightwave Technology*, Vol.12, pp. 1728-1738, 1995.

[2] B. Malo, S. Thériault, D.C. Johnson, F. Bilodeau, J. Albert, K.O. Hill, "Apodized in-fibre Bragg grating reflectors photoimprinted using a phase mask", *Electronics Letters*, Vol.31, pp. 223-225, 1995

[3] A. Yariv, M. Nakamura, "Periodic structures for integrated optics", *IEEE Journal of Quantum Electronics*, Vol. QE-13, pp. 233-253, 1977.

[4] L.A. Weller-Brophy, D.G. Hall, "Analysis of waveguide grating: a comparison of the results of Rouard's method and coupled-mode theory",*J. Opt. Soc. Am. A*, Vol.4, pp. 60-65, 1987.

[5] V. Mizrahi, J.E. Sipe, "Optical properties of photosensitive fiber phase gratings", *IEEE Journal of Lightwave Technology*, Vol. 11, pp. 1513-1517, 1993.

Design of fibre matched uncladded rib waveguides on InP with polarization independent fibre coupling loss of 1 dB

C. M. Weinert

**Heinrich-Hertz-Institut für Nachrichtentechnik Berlin GmbH,
Einsteinufer 37, 10587 Berlin, Germany, Tel. xx 30 31002-255**

Low cost fabrication of photonic integrated circuits for future subscriber systems require efficient coupling of the single mode fibre to the chip as well as large alignment tolerances. This can be achieved by increasing the spot size of the waveguiude to the spot size of the fiber using an integrated spot size transformer. For buried waveguide structures such as lasers or amplifiers this can be done by gradually decreasing the waveguide thickness which leads to an adiabatic mode expansion /1-3/. More complex integrated photonic circuits, however, mostly have uncladded rib waveguides. If this type of waveguide is etched down in order to achieve spot size matching, the cutoff properties of the asymmetric layer structure make it impossible to achieve a large spot size and to make the waveguide-fibre coupling polarization independent. A concept for lateral tapering of uncladded waveguides has been proposed by Thurston and coworkers /4/. However, it is restricted to channel waveguides only. In addition, the design outlined in /4/ requires layers with refractive index differences as small as 0.01 which is not feasable for standard MOVPE growth techniques of InGaAsP/InP. In this work we theoretically investigate taper waveguides suitable for vertical tapering and propose a new waveguide design which can be used to fabricate tapers with polarization independent coupling to the fibre for arbitrary uncladded rib or channel waveguides.

The problem of mode expansion for uncladded waveguides can be shown by simple slab calculations. For an uncladded slab waveguide of InGaAsP (λ_Q=1.06 µm) core material grown on InP the mode size of the optical field exhibits a very steep increase close to the cutoff thickness of the waveguide core. For TE and TM polarized light and for 1.55 µm wavelength the cutoff thickness is 0.452 µm and 0.525 µm, respectively. Therefore mode expansion occurs at different values of the waveguide core layer thickness for TE and TM. Consequently, vertical tapering of uncladded waveguides is expected to have strong polarization dependence for the coupling to the fibre.

The problem of vertical cutoff can be overcome by introducing thin guiding layers beneath the waveguide core as shown by the 3D taper structure in fig. 1(a). At the chip port, the waveguide core has a large thickness and the optical wave is not influenced by the thin guiding layers. However, as the waveguide layer thickness in the

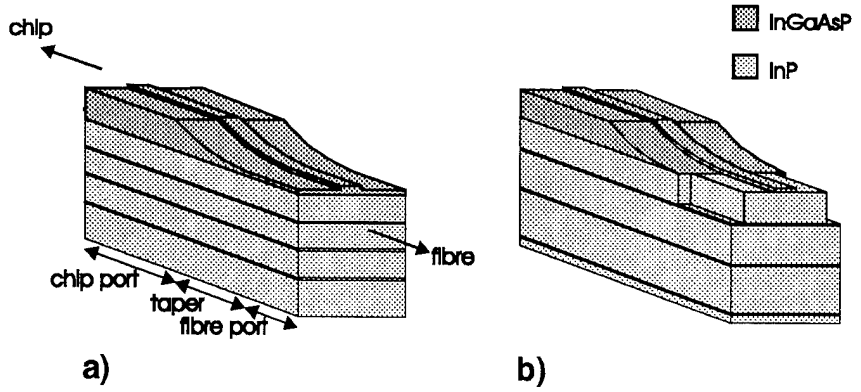


Fig .1: Taper structures for uncladded rib waveguides. a) Polarization dependent structure as given in /5/.
b) Improved taper structure for polarization independent mode matching

taper section decreases, the light spot is extended horizontally and also vertically into the substrate. Now the guiding layers become effective by avoiding vertical cutoff. Such a structure which was optimized for TE

polarization has recently been fabricated /5/. A minimum coupling loss to a butt coupled fibre of about 2 dB was found for TE polarization, however,the coupling loss for TM polarization was several dBs higher. Therefore a modified taper design will be presented here with which a polarization independent fibre coupling loss of 1 dB can be achieved.

In order to analyze the taper structures and to test the polarization independence of the waveguides the scalar two-dimensional Finite Difference Method (2D FDM) has been used to calculate the modal fields of waveguides and fiber. Choice of the integration mesh needs much care since the tails of the fields extend up to 50 µm whereas the waveguide thickness can be in the nm range. Therefore an equidistant mesh with narrowly spaced mesh points is chosen in the vicinity of the waveguide and mesh points with exponentially increasing spacings are used in the tails of the fields. The calculation window has been chosen to be 160 µm x 80 µm and the eigenmode calculation has been performed with an accuracy of 10^{-7} in the propagation constant. All calculations are done for a wavelength of 1.55µm.

First, the standard monomode step index fibre (SMF) is calculated. The core diameter is 8.7 µm, the refractive indices of core and cladding are 1.4681 and 1.4650 respectively. The calculated spot diameter, -defined as the diameter for which the field has decayed to 1/e of the maximum value-, is 11.4µm. The same mesh is used for the calculations of the waveguides and for evaluation of the two-dimensional overlap between normalized fields of waveguide and fibre. The square of the overlap measures the fiber coupling loss due to the mismatch in mode size which in the following will be denoted as fibre matching loss. Losses due to the radiation along the vertical tapering section are not considered in this work. However, from the mode expansion characteristics as given by the subsequent cross section calculations it becomes apparent that for an adiabatic spot size transformer tapering has to be very smooth when approaching the fibre port (c.f. fig 1). Such vertical tapering curves can be achieved by the ion beam shadow etching technique as described in /6/.

The new taper design is shown in fig. 1 (b). Compared to fig. 1 (a) the guiding layers (GL) are now inequidistantly spaced below the core layer (CL) and both core and guiding layers are of λ_Q=1.06µm material. For this optimized taper design, the fields for TE and TM polarization are calculated along the taper. Fig. 2 depicts both the vertical and lateral spot enlargement for the waveguide film thickness t as it decreases from the chip port to the the fibre port. The horizontal (d_x) and vertical (d_y) spot size diameters and the loss due to mode mismatch are shown as function of the waveguide film thickness t. If t approaches zero d_y approaches a constant value given by the locations of the guiding layers. On the other hand, the horizontal spot diameter d_x increases but has no cutoff, since in lateral dimension the waveguide is symmetric. However, it is seen that the minimum for the fibre matching losses for TE and TM polarization are at different values of t. The loss curves for both polarizations intersect at t=35 nm and a common fibre matching loss of about 2 dB can be achieved.

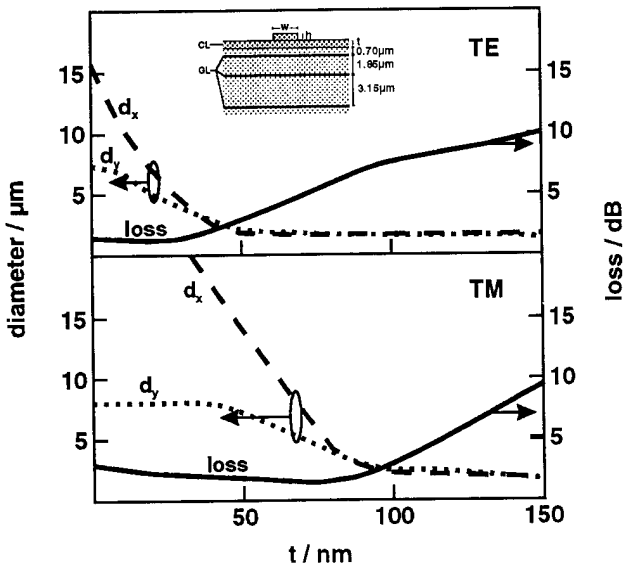


Fig. 2: Calculated light spot diameters d_x and d_y and mode matching loss to SMF versus film thickness t for TE and TM polarization . The core layer (CL)and guiding layers (GL) shown in the cross section are of λ_Q=1.06 µm quaternary material.

As seen from fig. 3, for this kind of uncladded waveguide tapers the center of gravity of the light spot is moved downward into the substrate as shown by the field isoline plots in different taper sections. This is an essential difference compared to buried waveguide tapers for which the center of gravity remains in the central core region.

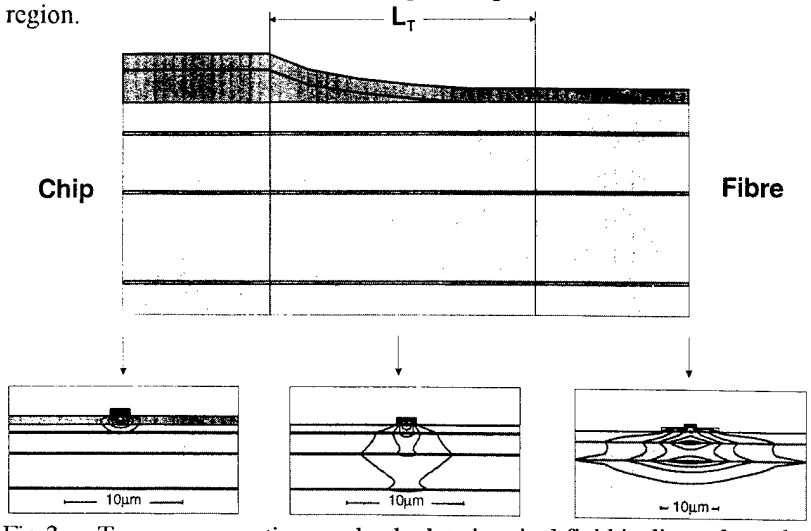


Fig.3: Taper cross sections and calculated optical field isolines along the taper structure. Note the migration of the field maximum from the cladding layer into the guiding layers.

We will now further improve this taper waveguide structure to achieve a polarization independent fibre matching loss of only 1 dB. It is fabricated as shown in fig. 1 (b) by first tapering the waveguide film thickness down to zero. From fig. 2 we see that the loss for the TM ploarized wave is 3.2 dB wheras for TE it is only 1.7 dB since the spot size diameter for TM is much larger than the one of the fibre. We now add an additional rib of 13 µm width by etching down the InP layer completely down to the first guiding layer. (see fig. 1(b)). Because of its large lateral spot size only the TM spot is decreased by this additional rib. Therefore this additional rib acts as a TM-focussing rib and from the 2D FDM calculations we find that the fibre matching losses now decrease to 1.1 dB and are equal for both TE and TM polarization.

Besides the decrease of fibre coupling loss to 1 dB, the advantage of this improved waveguide structure is the fact that vertical etching of the waveguide film layer need not be precisely controlled as to achieve the exact thickness for which the taper is polarization independent. In the new structure the quaternary film layer is always etched down completely and the underlying InP layer can act as an etch detection layer. In addition, we now show by the calculations that the same polarization independent losses can be achieved for rib waveguides with ribs of different width and composition as long as the guiding layers and the TM-focussing rib remain

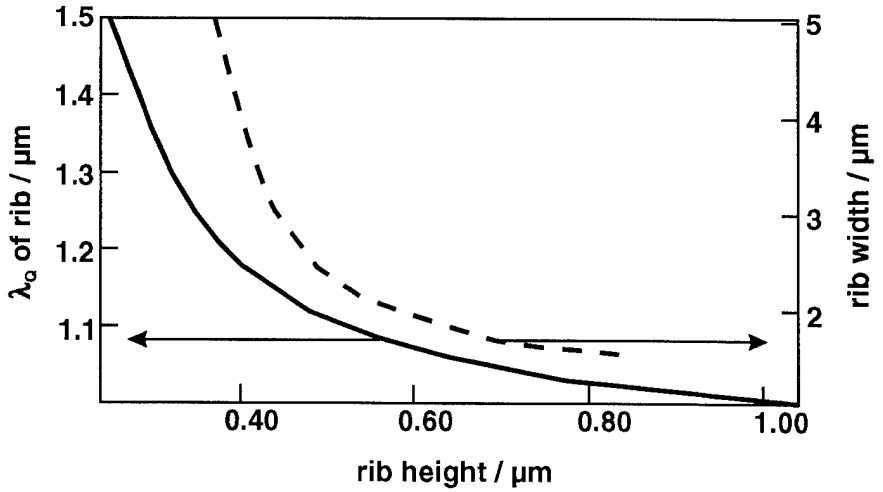


Fig. 4 : Design rules for the rib structure of optimized taper waveguides: quaternary material composition λ_Q versus rib height for a 2 µm wide rib (solid line) and rib width versus rib height for λ_Q=1.06 µm material (dashed line). The guiding layers remain unaltered as given in fig. 2.

unaltered. The results of the 2D FDM calculations for taper waveguides with different rib width and different material composition of the waveguide layer are depicted in fig. 4 (the TM-focussing rib is the same as above and the guiding layers are always λ_Q=1.06 µm material and remain at the position shown in the inset of fig 2). From the solid curve in fig. 4 we can find the rib height for a given material composition to design a polarization independent taper with rib width of 2 µm and 1 dB fibre mode matching loss. From the dashed curve in fig. 4 the rib width for the optimal taper rib waveguide of λ_Q=1.06 µm composition is given as a function of the rib height. Using these curves and the data for the guiding layers given in fig. 2, polarization independent taper structures can be designed for different rib waveguides.

Concluding, we have shown a taper waveguide design for InGaAsP/InP with relaxed fabrication tolerances which can be used for tapering uncladded rib waveguides of different width and material composition. Polarization independent coupling to the fibre with a mode matching loss of 1 dB is achieved.

Acknowledgements
This work was supported by the German Ministry of Research and Technology and the Senat of Berlin.

[1] T. L. Koch, U.Koren, G. Eisenstein, M. G. Young, M. Oron, C. R. Giles, and B. I. Miller, "Tapered waveguide InGaAsP Multiple-Quantum-Well lasers", IEEE Photon. Technology Lett., vol. 2 , pp. 88-90, 1990.

[2] L. Mörl, L. Ahlers, P. Albrecht, H. Engel, H.J. Hensel, H.-P. Nolting and F. Reier, Proc. OFC/IOOC'93 San Jose, USA, Feb., pp.212-213, 1993

[3] P. Doussiere, P. Garabedian, C. Graver, D. Bonnevie, T. Fillion, E. Derouin, M. Monnot, J. G. Provost, D. Leclerc, and M. Klenk, IEEE Photon. Technology Lett., **vol. 6** , pp. 170-172, 1994.

[4] R. N. Thurston, E. Kapon, and A. Shahar, Opt. Lett. **16**, pp. 306-308, 1991

[5] L. Mörl, C. M. Weinert, F. Reier, L. Stoll, and H.-P. Nolting , 21 st European Conference on Optical Communication ECOC'95, Brussels, paper Tu P22, 1995

[6] G. Wenger, L. Stoll, B. Weiss, R. Müller-Nawrath, S. Eichinger, J. Müller, B. Acklin, G. Müller, J. Lightwave Technol. **12**, pp. 1782-1790, 1994

Analytical study of birefringence in slab waveguides

J Buus, Gayton Photonics Ltd
6 Baker Street, Gayton, Northants, NN7 3EZ, UK
Tel +44 (0)1604 859253, Fax +44 (0)1604 859256, email 100340.331@compuserve.com

J Haes and R Baets, University of Gent-IMEC
Department of Information Technology, Sint-Pietersnieuwstraat 41, B-9000 Gent, Belgium
Tel +32 9 264 3316, Fax +32 9 264 3593, email jan.haes@intec.rug.ac.be

Introduction

For a number of optoelectronic components it is important to estimate the amount of waveguide birefringence in order to reduce or eliminate a possible polarization dependence. Several important structures (e.g. buried or ridge) can be analysed with sufficient accuracy by the effective index method which reduces the original 2-D problem to two 1-D problems. We therefore look at waveguide birefringence for the 1-D case.

First a general expression is derived by using a simple perturbation argument. Based on this result a very simple expression is derived for the case of a symmetric slab structure. The accuracy of this expression is examined by comparing with numerical results.

Birefringence cannot be eliminated for the slab case, optimisation with respect to low birefringence is discussed in [1].

General 1-D structure

For the TE case (polarization parallel to the y-axis, propagation in the z-direction, and index variation n(x) in the x-direction) the field component Φ and the propagation constant β are found by solving

$$\frac{d^2\Phi}{dx^2} + \left(k^2 n^2(x) - \beta^2\right)\Phi = 0 \qquad (1)$$

where $k=2\pi/\lambda$ is the wave number. For the TM case an addition term appears, given by

$$\frac{d}{dx}\left(\frac{\Phi}{n^2(x)}\frac{dn^2(x)}{dx}\right) \qquad (2)$$

We consider this term as a perturbation to the index profile, with Φ being the solution for the TE case, and assume that the field is normalised (i.e. $\int_{-\infty}^{\infty}\Phi^2(x)dx = 1$). Standard perturbation theory then gives

$$\Delta = n^2_{eff,TE} - n^2_{eff,TM} = -\int_{-\infty}^{\infty} \frac{1}{k^2\Phi}\frac{d}{dx}\left(\frac{\Phi}{n^2(x)}\frac{dn^2(x)}{dx}\right)\Phi^2 dx \qquad (3)$$

Integrating by parts, using the fact that Φ vanishes at infinity, and replacing $1/n^2(x)$ by $1/n^2_{eff,TE}$ gives the general result

$$\Delta \approx \frac{1}{2k^2 n^2_{eff,TE}} \int_{-\infty}^{\infty} \frac{d\Phi^2}{dx}\frac{dn^2}{dx} dx \qquad (4)$$

Symmetric slab

For a symmetric slab, with an index given by

$$n(x)=n_1 \text{ for } |x| \le |d/2 \text{ and } n(x)=n_2 \text{ for } |x|>d/2 \qquad (5)$$

we have (with δ denoting the Dirac delta function)

$$\frac{dn^2}{dx} = \left(n_1^2 - n_2^2\right)\left(\delta\left(-\frac{d}{2}\right) - \delta\left(\frac{d}{2}\right)\right) \qquad (6)$$

This leads to

$$\Delta \approx \frac{n_1^2 - n_2^2}{k^2 n^2_{eff,TE}} \frac{d\Phi^2}{dx}\bigg|_{x=\frac{d}{2}} \qquad (7)$$

Inserting the slab solution for Φ, and using normalised parameters (see for example [2]) gives

$$\Delta \approx 2\frac{\left(n_1^2 - n_2^2\right)^2}{n^2_{eff,TE}} \frac{b(1-b)}{1+v\sqrt{b}} \qquad (8)$$

Here v is the normalised frequency $v = \frac{kd}{2}\sqrt{n_1^2 - n_2^2}$ and b is the normalised propagation constant. If the index difference is moderate eq (8) can be approximated by

$$\frac{n_{eff,TE} - n_{eff,TM}}{n_{eff,TE}} \approx 4\left(\frac{n_1 - n_2}{n_{eff,TE}}\right)^2 \frac{b(1-b)}{1+v\sqrt{b}} \qquad (9)$$

Examples

The second part of the right hand side of eq (9) contains normalised parameters, and depends on the normalised frequency v only. We refer to this as the normalised birefringence factor. Figure 1 shows a comparison of the approximate result (9) with a direct numerical solution for

a fixed (and large) index difference, corresponding to a typical semiconductor laser or amplifier structure. The v-dependence of the relative birefringence is dominated by the normalised birefringence factor.

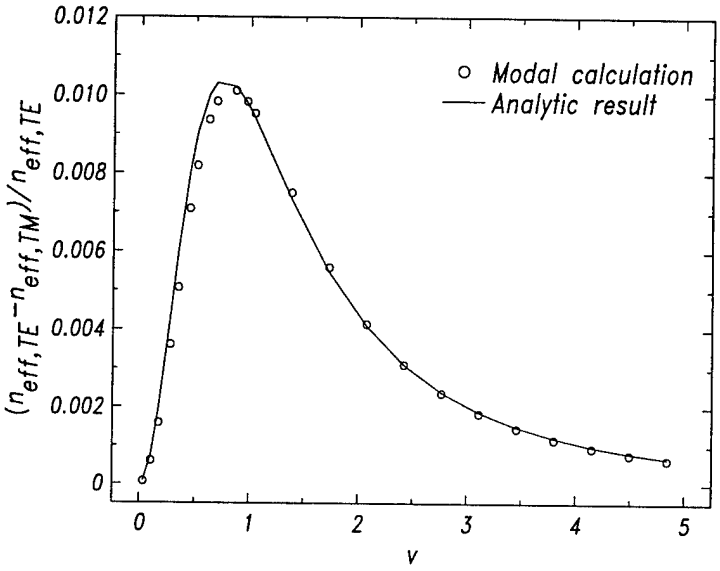


Figure 1 Relative birefringence as a function of the normalised frequency for core index 3.6, cladding index 3.17, wavelength 1.55μm; points: direct calculation, line: prediction from eq. (9).

Next the value of v is kept constant by varying the index difference and the slab thickness simultaneously. The square root of the relative birefringence is then shown as a function of the relative index difference in figure 2, the expression given by eq (9) predicts a straight line.

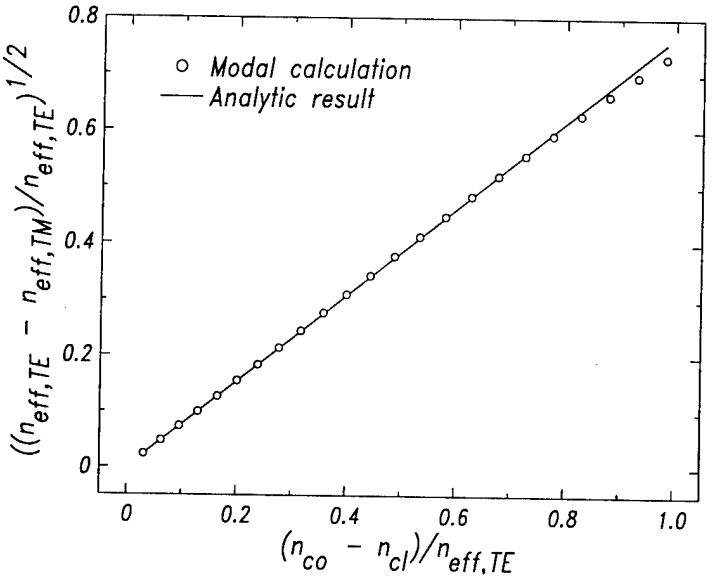


Figure 2 The square root of the relative birefringence shown as a function of the relative index difference for v=1; points: direct calculation, line: prediction from eq. (9).

Discussion and conclusion

We have derived a general expression for birefringence in a planar waveguide, and from this found a very simple expression for the birefringence in the important special case of a symmetrical slab. The result consists of two factors, the first being the square of the relative index difference, and the second being an expression consisting entirely of normalised parameters. We have shown that this result is in excellent agreement with the numerical solution. Consequently it is sufficient to solve for the TE case and then apply a simple correction to get the TM propagation constant and the birefringence, it is not necessary to solve the TM problem directly.

The general result expressed in eq. (4), offers some insight into the general problem of birefringence minimisation. It shows that the derivative of the intensity should be low in places where the refractive index varies. This is shown very clearly in the result for the slab waveguide given by eq. (9) since the normalised birefringence factor is minimised for $b \rightarrow 0$ and for $b \rightarrow 1$. Equation (4) also allows a simple evaluation of waveguide birefringence for other waveguide structures where the field distribution for the TE mode is known.

References

[1] G Sarlet, J Haes, R Baets, "Optimisation of slab waveguides with given mode width towards low modal birefringence", submitted for publication.

[2] M J Adams "An introduction to optical waveguides", Wiley, Chichester, 1981.

Reflectivity analysis of optical waveguides with coated and tilted facets using the FD-TD method with the PML absorbing boundary condition

Junji Yamauchi, Shin'ichi Aoki and Hisamatsu Nakano

College of Engineering, Hosei University, 3-7-2, Kajino-cho, Koganei, Tokyo 184, Japan
Tel: 423-87-6190, Fax: 423-87-6048

1 Introduction

Considerable attention has been paid to reflection problems at the facets of optical waveguides [1]-[3]. Recently, the finite-difference time-domain (FD-TD) method was used to analyze optical waveguides with an antireflection (AR) coating[4][5]. The numerical modeling has an advantage of applicability to arbitrary structures with sufficient accuracy. It should be noted, however, that the performance of the absorbing boundary condition (ABC) used with the FD-TD method determines the dynamic range of the numerical simulation. Widening the dynamic range is crucial to the evaluation of low power reflectivities, particularly for a tilted AR coating.

Berenger[6] recently published the perfectly matched layer ABC (PML-ABC). The improved performance of the PML-ABC relative to any earlier technique has been verified in optical waveguides [7][8].

The purpose of this paper is to analyze the reflection problems of optical waveguides with coated and tilted facets using the FD-TD method, and to demonstrate the simulation having an increased dynamic range over that for the conventional Mur-ABC[9]. The present results are also compared with other analytical results.

2 Discussion

We consider the reflection problems for a single-layer AR coating. The configuration to be investigated is a two-dimensional symmetric waveguide whose facet is coated with an AR coating of thickness L, as shown in Fig.1. A tilt angle of the facet is designated as θ. The +z propagating incident wave is generated on the incidence plane indicated by a dotted line in Fig.1, so that the computation region is divided into the reflected field and total field regions.

The PML is a nonphysical lossy medium adjacent to the outer grid boundary. The PML region is located outside the waveguide geometry shown in Fig.1. Within the PML, the electromagnetic waves rapidly decay without varing the velocity and field impedance, so that the outgoing waves vanish. Throughout this paper, the PML thickness is taken to be 16 cells with a theoretical reflection coefficient $R(0) = 10^{-6}$[6].

We first compare the performance of the PML-ABC with that of Mur-ABC. The refractive indices of the core, cladding, and AR layer are chosen to be $N_{CO} = 3.6$,

$N_{CL} = 3.564$, and $N_{AC} = \sqrt{N_E} = 1.8938$ (N_E is the effective index of the waveguide), respectively. The tilt angle is fixed to be $\theta = 0°$. A wavelength of $\lambda = 1.55\mu m$ is used and the normalized frequency is taken to be $V = 1.5$. Fig.2 shows the comparison in the power reflectivity as a function of coating thickness L, when the TE_0 wave is excited. From each set of data, it is seen that the reflectivities become minimums when the coating thickness L is around $0.206\mu m$, or $\lambda_g/4$. It should be noted, however, that the simulations using the PML-ABC have a dynamic range over that for the Mur-ABC's.

We next compare the results obtained from the present method with those from the other approach [1] to confirm the validity of our numerical results. The geometrical parameters are $N_{CO} = 3.512$, $N_{CL} = 3.17$, $N_{AC} = 1.8739$, $L = 0.224\mu m$ and $2D = 0.25\mu m$. Fig.3 shows the wavelength dependence of reflectivities for TE and TM waves. In this case the AR coating is optimized for TE wave. Good agreement is found to exist between the present results and those in Ref.[1] for both polarizations.

Since the effectiveness of the PML-ABC has been verified, we apply the present method to a tilted facet with an AR coating. The reflectivity as a function of tilt angle θ is shown in Fig.4(a). TE_0 wave excitation whose wavelength is $\lambda = 1.55\mu m$ is considered. The geometrical parameters are the same as those in Fig.2 (The coating thickness is optimized for $\theta = 0°$). For comparison, the data without the AR coating is also shown in Fig.4(b). It is clear that the tilted facet with the AR coating achieves an extremely low power reflectivity of less than 10^{-6}. The AR coating reduces the reflectivity by two orders of magnitude.

Steady-state field distributions with and without an AR coating are shown in Fig.5. The typical results for a tilt angle of 8° are presented. The field is expressed with the sinusoidal steady-state amplitude, which can be obtained by the numerical integration of a time-dependent signal over one period. It is seen that the reflected field observed in Fig.5(b) is greatly reduced in Fig.5(a) due to the AR coating.

The effect of the AR coating thickness on the reflectivity is shown in Fig.6. The tilt angle is taken to be 8°. It is found that the optimum thickness for $\theta = 8°$ is nearly the same as that for $\theta = 0°$.

Final consideration is given to the wavelength dependence for both polarizations. Fig.7 shows the reflectivity for $\theta = 8°$ as a function of wavelength. Calculation shows that the wavelength at which the minimum reflectivity is observed for TE wave is slightly different from that for TM wave. It should be noted, however, that the low power reflectivities are obtained over a wide range of wavelengths for both polarizations.

3 Conclusions

We have demonstrated that the FD-TD method with the perfectly-matched layer absorbing boundary condition (PML-ABC) is a powerful tool for designing optical waveguides with coated and tilted facets. The use of PML-ABC allows us to evaluate low power reflectivities, as compared with the conventional ABC's. We have also shown the suppression of the reflected field from the facet due to an AR coating. Further calculation shows the wavelength dependence of reflectivity for both polarizations.

References

[1] C.Vassallo, Electron. Lett., 24, pp.62-64, 1988
[2] C.E.Zah et al., Electron. Lett., 24, pp.1275-1276, 1988
[3] P.Kaczmarski et al., Electron. Lett., 25, pp.716-717, 1989
[4] J.Yamauchi et al., Integrated Photonics Research, pp.120-123, 1993
[5] J.Yamauchi et al., Photon. Tech. Lett., 2, 1996
[6] J.P.Berenger, J. Comput. Phy., 114, pp.185-200, 1994
[7] C.E.Reuter et al., Microwave and Guided Wave Lett., 4, pp.344-346, 1994
[8] Y.Naka et al., Paper of Tech. Meeting, IEE Japan, EMT95-2, pp.7-12, 1995
[9] G.Mur, IEEE Trans. Electromagn. Compat., EMC-23, pp.377-382, 1981

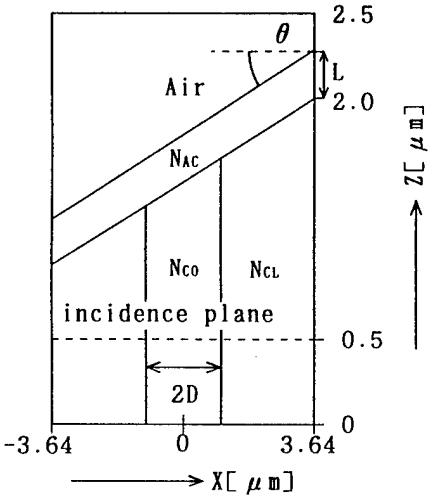


Fig.1 Configuration of coated and tilted facets

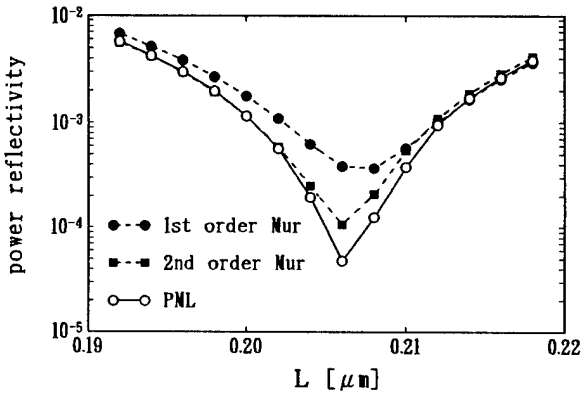


Fig.2 Comparison in reflectivity among ABC's ($\theta = 0°$)

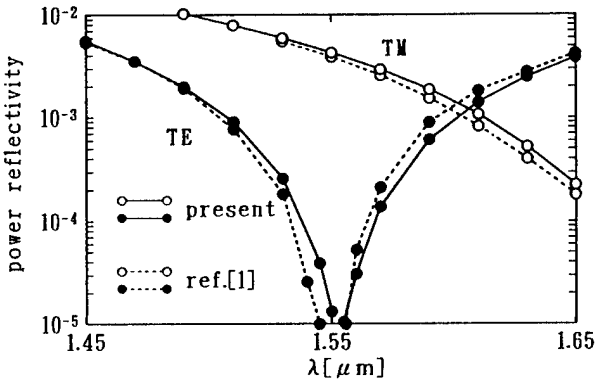
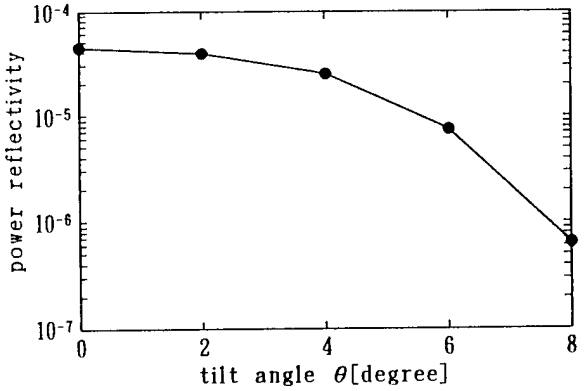


Fig.3 Comparison in reflectivity between the present results and those in ref.[1] ($\theta = 0°$)



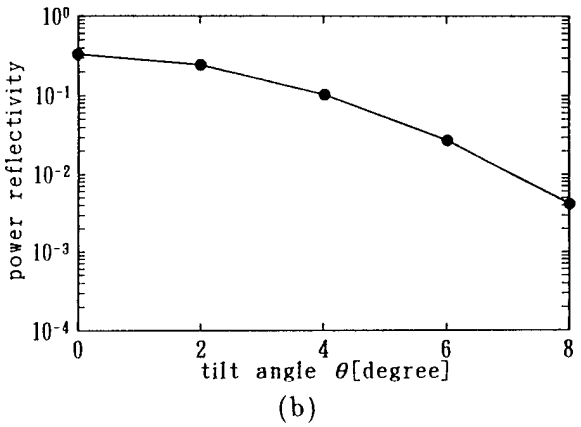
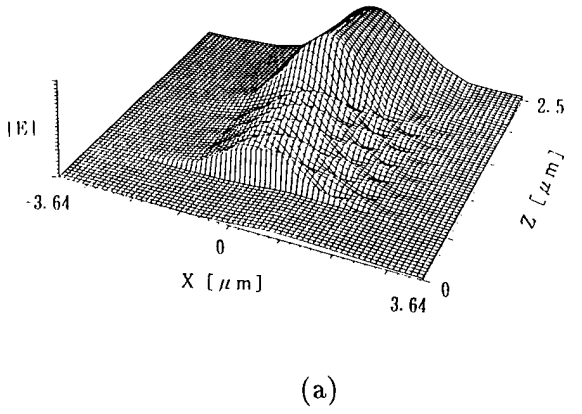


Fig.4 Reflectivities as a function of tilt angle θ (a)with coating and (b) without coating



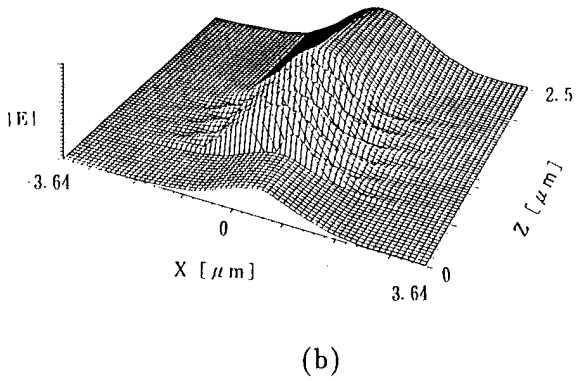


Fig.5 Steady-state field distributions (a)with coating and (b) without coating ($\theta = 8°$)

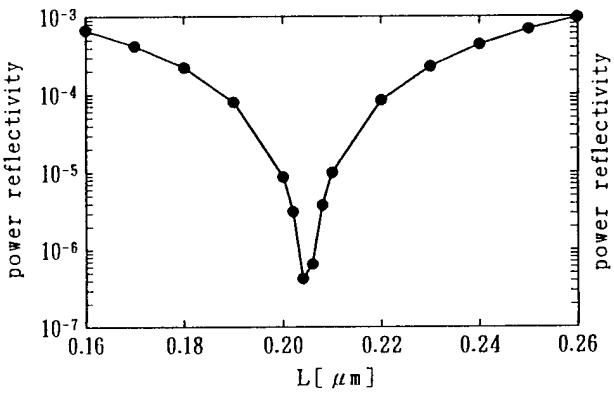


Fig.6 Reflectivity as a function of AR coating thickness($\theta = 8°$)

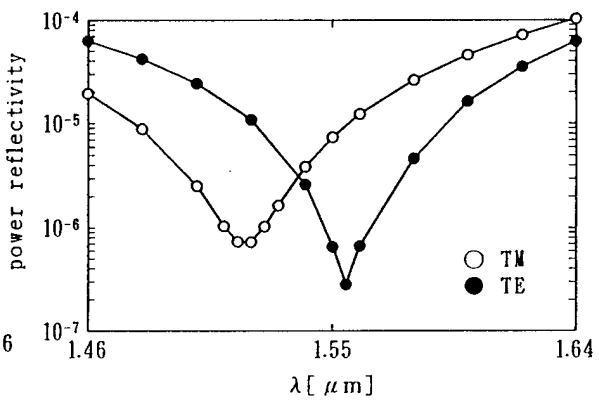


Fig.7 Reflectivity as a function of wavelength ($\theta = 8°$)

Wednesday, May 1, 1996

Active and Passive Waveguide Devices

IWB 8:30 am-10:00 am
Fairfax B

Fred Heismann, *Presider*
AT&T Bell Laboratories

Er:$LiNbO_3$ Guided Wave Optical Amplifiers Pumped at 980nm

Chi-hung Huang and Leon McCaughan
Department of Electrical and Computer Engineering
University of Wisconsin-Madison
Madison, Wisconsin 53706
Tel: (608) 263-3982, FAX: (608) 265-2614

Introduction: The development of Er-doped fiber amplifiers and fiber lasers[1,2] has recently spawned interest in $LiNbO_3$-based integrated optic versions of these devices[3,4]. A variety of guided traveling wave amplifiers and lasers pumped at 1.48μm, have been demonstrated.[5-7] Model calculations and measurements of Er-doped fibers have shown[8,9], however, that the 980nm pump wavelength has a higher efficiency and lower noise figure than 1480nm due to the absence of pump induced stimulated emission. In model calculations similar to Ref. 4, we recently found that a 980nm pump should have a higher slope efficiency than a 1480nm in $LiNbO_3$ waveguides. This Letter reports the experimental results of the optical gain in Er-indiffused Ti:$LiNbO_3$ and ZnO:Mg:$LiNbO_3$ channel waveguides pumped around 980nm.

Sample fabrication: A 15nm thick planar Er film was ion-beam sputtered over half of the -z face of commercial $LiNbO_3$ substrates and then thermally diffused in a tube furnace at 1100°C for 90 hours with 1.0L/min of flowing oxygen bubbled through 20cm of water. Optical waveguides were formed by thermal in-diffusion of 810Å thick Ti stripes at 1025°C for 7.5 hours with the same atmosphere as in the Er diffusion. Waveguides in the Er-free half were used to estimate the coupled pump power. For the ZnO:Mg:$LiNbO_3$ waveguide, the Er was diffused for 300 hours on 5mol% Mg bulk-doped substrate, and 220nm ZnO stripes were diffused at 940°C for 10 minutes.

Sample measurement: The absorption cross sections of Er-doped $LiNbO_3$ were first measured from a bulk doped sample, as shown in Fig. 1. The σ-polarization at 980nm is obviously preferable for pumping the $^4I_{11/2}$ level of the Er^{3+} ions.

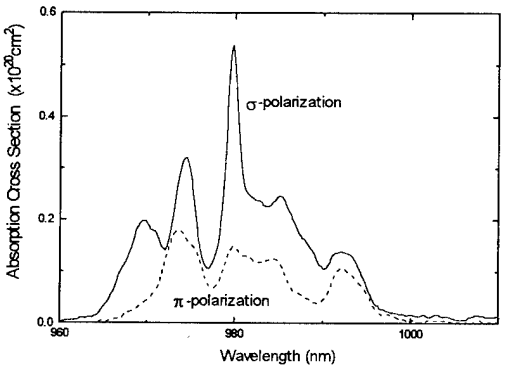


Fig. 1. Absorption cross sections of bulk doped Er:$LiNbO_3$ at two polarizations.

A tunable Ti:sapphire laser operated around 980nm is used as the pump source. The lifetime of the 1532nm fluorescence in the both types of waveguides was measured to be 2.7ms, comparable to that reported in Ref. 5. Green up-converted light was observed due to the excited state absorption at the $^4I_{13/2}$ level of the Er^{3+} ions.

A forward pump-and-probe measurement scheme for estimating the small signal optical gain is shown in Fig. 2. A compensator allows the adjustment of the pumping polarization. The signal light and pump light are combined by a 1530nm/980nm wavelength division multiplexer (WDM), whose output is single-mode for both the signal and the pump light. No coating is used on either end of the sample, so the pump light makes only a single pass. The mode profiles of the signal and pump light used for model calculations were also measured with an IR vidicon.

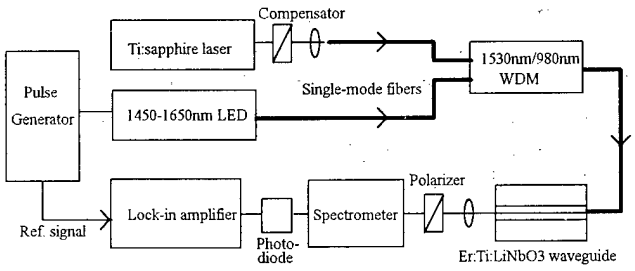


Fig. 2. The pump-and-probe setup for measuring the optical gain of the Er:$LiNbO_3$ waveguides.

A simple method was used to estimate the pump intensity necessary to reach zero-gain (or transparency). We adjusted the pump power so that when we scanned the transmitted signal, a flat spectrum around 1532nm was obtained. The transmitted signal level at this pump power therefore corresponds to the zero-gain level, and the pump intensity is the transparency pump power. Gain is measured relative to this level. This method, however, ignores fiber-waveguide coupling loss and the scattering loss (typically 0.2-0.4 dB/cm)[5], both of which are approximately wavelength-independent around 1532nm.

Results: The measured optical gain of an ~8 μm wide, 1.7cm long Ti- diffused waveguide is shown in Fig. 3. The transparency pump power is less than 25mW. At the maximum available coupled pump power of 80mW (σ-polarization), a gain of 2.7±0.2dB at 1531.6nm along σ-polarization is obtained. This 1.6dB/cm performance is over two times better than the previous result using 1480nm single-pass pumping.[5] The gain fluctuation at high pump power, shown in Fig. 2 by error bars, is mainly due to the photorefractive effect, which continuously changes the coupling and the optical mode structure in the $LiNbO_3$ waveguide. A gain of 4.7dB was obtained for about 1 second before the photorefractive effect takes place. We speculate that this larger gain is due to better coupling efficiency of pump power before the photorefractive damage.

A model calculation similar to Ref. 4 is shown in Fig. 3, in which the pump induced stimulated emission is included for the 1484nm pumping. We can see that 980nm pumping has a much better gain performance than 1484nm, although it shows some instability at high pump power due to the photorefractive effect.

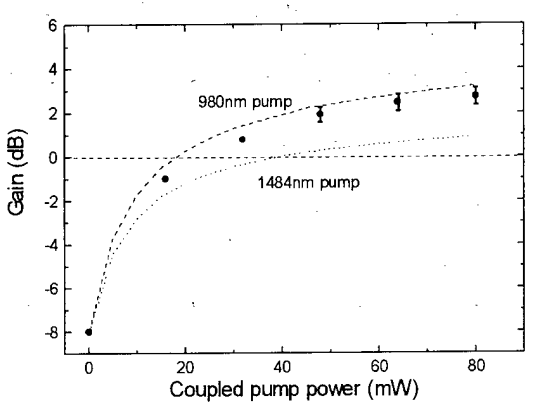


Fig. 3. The measured optical gain of a 1.7cm long Er:Ti:$LiNbO_3$ waveguide. The dashed lines show the calculated results for both 980nm and 1484nm pump.

The excitation gain spectrum, obtained by scanning the pumping wavelength, is shown in Fig. 4. Good amplification performance can be obtained over a range of ~3nm, a broad window for diode laser pumping. It is also interesting to note that the peak in the excitation spectrum occurs several Å lower than the peak observed from bulk Er-doped samples (shown as a dotted line of Fig. 4). This suggests that the Ti dopant may have a small effect on the Er spectrum. In fact, the peak in the optical gain spectrum at 1531.6nm is also ~3-4Å higher than the fluorescence peak obtained from bulk Er-doped samples.

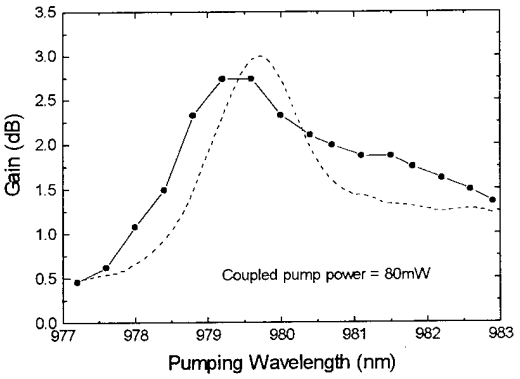


Fig. 4. The excitation gain spectrum of the Er:Ti:$LiNbO_3$ waveguide (–•–). The dotted line is measured from bulk Er-doped $LiNbO_3$ samples.

In order to overcome the problem caused by the photorefractive effect, we also tested the ZnO:Mg:$LiNbO_3$ waveguides[10]. A very stable gain of 1.8dB (at π-polarization) over 2.1cm long, ~9μm wide, waveguide was obtained with 60mW coupled power (at σ-polarization), as shown in Fig. 5, which suggests a promising performance on this type of waveguides. This sample, however, shows a slightly rough surface after the long Er diffusion, which may cause a larger scattering loss. We have not yet attempted to optimize the mode profiles of this waveguide to achieve a higher pump efficiency.

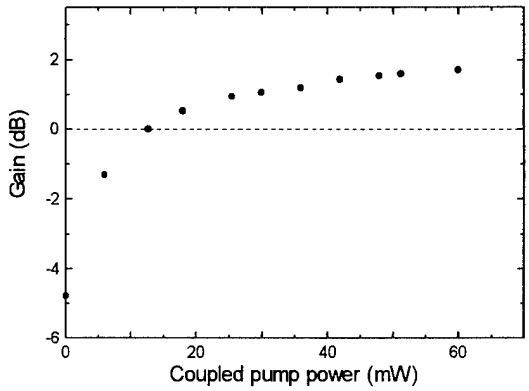


Fig. 5. The measured optical gain of a 2.1cm long Er:ZnO:Mg:$LiNbO_3$ waveguide using 980nm pump.

Conclusion: We have demonstrated, for the first time, the optical gain in Er-indiffused $LiNbO_3$ channel waveguides pumped at 980nm. A small signal gain of 1.6dB/cm is obtained with 80mW pump power on Ti waveguides, whose performance is limited by photorefractive effect. Er-indiffused ZnO:Mg:$LiNbO_3$ channel waveguides, however, show no photorefractive effect. Positive gain is observed with moderate pump power.

References:

[1] B. J. Ainalie, "A review of the fabrication and properties of erbium-doped fibers for optical amplifiers," *J. of Lightwave Technol.*, 1991, **9**, (2), pp. 220-238.

[2] K. Iwatsuki, "Er-doped superfluorescent fiber laser pumped by 1.48 μm laser diode," *Photon. Technol. Lett.*, 1990, **2**, (4), pp. 237-238.

[3] R. Brinkmann, W. Sohler, and H. Suche, "Continuous-wave erbium-diffused $LiNbO_3$ waveguide laser," *Electron. Lett.*, 1991, **27**, (5), pp. 415-417.

[4] C. H. Huang, D. M. Gill, and L. McCaughan, "Evaluation of absorption and emission cross section of Er-doped $LiNbO_3$ for application to integrated optic amplifiers," *J. of Lightwave Technol.*, 1994, **12**, (5), pp. 803-809.

[5] M. Dinand and W. Sohler, "Theoretical modeling of optical amplification in Er-doped Ti:$LiNbO_3$ waveguides," *J. Quantum Electron.*, 1994, **30**, (5), pp. 1267-1276.

[6] H. Suche, L. Baumann, D. Hiller, and W. Sohler, "Modelocked Er:Ti:$LiNbO_3$-waveguide laser," *Electron. Lett.*, 1993, **29**, (12), pp. 1111-1112.

[7] R. Brinkmann, M. Dinand, L. Baumann, Ch. Harizi, W. Sohler, and H. Suche, "Acoustically tunable wavelength filter with gain," *Photon. Technol. Lett.*, 1994, **6**, (4), pp. 519-521.

[8] M. Yamada, M. Shimizu, T. Takeshita, M. Okayasu, M. Horiguchi, S. Uehara, and E. Sugita, "Er^{3+}-Doped Fiber Amplifier Pumped by 0.98μm Laser Diodes," *Photon. Technol. Lett.*, 1989, **1**, (12), pp. 422-424.

[9] M. Yamada, M. Shimizu, M. Okayasu, T. Takeshita, M. Horiguchi, Y. Tachikawa, and E. Sugita, "Noise Characteristics of Er^{3+}-Doped Fiber Amplifier Pumped by 0.98μm and 1.48μm Laser Diodes," *Photon. Technol. Lett.*, 1989, **2**, (3), pp. 205-207.

[10] W. M. Young, M. M. Fejer, M. J. F. Digonnet, A. F. Marshall, and R. S. Feigelson, " Fabrication, Characterization and Index Profile Modeling of High-Damage Resistance Zn-Diffused Waveguide in Congruent and MgO:Lithium Niobate," *J. of Lighwave Technol.*, 1992, **10**, (9), pp. 1238-1246.

Blue Light Generation in a Lithium Tantalate Waveguide Domain-Inverted by Heat Treatment with a Mask

Sang-Yun Yi and Sang-Yung Shin
Department of Electrical Engineering, Korea Advanced Institute of Science and Technology
371-1, Kusong-Dong, Yusung-Gu, Taejon, 305-701, Korea
(Fax) +82-42-869-3410

Yong-Sung Jin and Yung-Sung Son
Devices and Materials Laboratory, LG Electronics Research Center
16 Woomyeon-Dong, Seocho-Gu, Seoul, 137-140, Korea
(Fax) +82-2-578-5513

The quasi-phase-matched second-harmonic generation(QPM-SHG) in a periodically domain-inverted waveguide is a promising technique to get a compact blue light source. It has been already demonstrated in $LiNbO_3$ and $LiTaO_3$ waveguides. $LiTaO_3$ is a favorable nonlinear optic crystal owing to its high optical damage resistance and high nonlinearity.

The domain grating for the first order QPM can be formed on -c face of $LiTaO_3$ by selective proton exchange and quick heat treatment[1]. Then, channel waveguides are formed perpendicular to the domain grating. $LiTaO_3$ waveguides fabricated by proton exchange(PE) and a short-time annealing may have a tight mode confinement[1] that is required to achieve a high conversion efficiency. The conversion efficiency over 1000 %/Wcm^2 is expected by a theoretical calculation[2]. However, the reported efficiency is about 230 %/Wcm^2. A possible explanation for this difference is a reduced nonlinearity due to the PE process for domain inversion(DI) and waveguide formation[3]. It is reported that the nonlinearity of $LiTaO_3$ is severely degraded near the crystal surface by a high PE rate, and the damaged nonlinearity cannot be recovered in the whole waveguide cross-section by the conventional short-time annealing[3]. For example, if a device has zero nonlinearity from surface to 1 μm depth due to the damaged nonlinearity[3], the calculated efficiency is lower than 200 %/Wcm^2. This is similar to the reported values. Therefore, it is desirable to reduce the amount of PE to fully utilize the original nonlinearity in $LiTaO_3$.

In this paper, we report an efficient second-harmonic blue light generation in a $LiTaO_3$ QPM waveguide. To preserve the nonlinearity the QPM waveguide is fabricated with a small amount of PE. To reduce the amount of PE in fabricating the QPM-SHG device, a Ta-SiO_2 mask is used for the domain grating and a SiO_2 mask for the waveguide. In a QPM-SHG waveguide with a length of 8 mm, the second-harmonic blue light of 1 mW at 429 nm is generated with the fundamental wave power of 10.3 mW. Its normalized efficiency is 1500 %/Wcm^2 which is the highest value for $LiTaO_3$ devices reported to date.

Recently, we reported DI formed by using the heat treatment with a Ta-SiO_2 mask[4]. Fig. 1 shows the effect of the mask for the diffusion flux during the heat treatment for the DI. In case of the heat treatment with the mask(Fig. 1(a)), the mask promotes proton diffusion into the substrate by suppressing proton diffusion out of the substrate. On the other hand, in case of the heat treatment without the mask(Fig. 1(b)), the indiffusion flux will be lowered by the proton outdiffusion. According to the DI mechanism[5] in $LiTaO_3$, the enhanced indiffusion causes a strong poling field inside the substrate, and it results in a deep DI. For the same DI depth the heat treatment with the mask requires less amount of initial PE than that without the mask. Typically, the amount of PE is reduced to about 50 % of that used in a conventional DI process without the mask.

Previously, we also proposed proton diffusion(PD) with a SiO_2 mask to fabricate good quality waveguides[6]. This process uses a small amount of initial PE owing to the proton-conserving property of the SiO_2 mask. PD is carried out at a high temperature using the SiO_2 mask above the waveguide channel. During PD the SiO_2 mask promotes proton indiffusion by inhibiting proton outdiffusion, which facilitates the appropriate index increase for guided modes in the depth direction. By using this process, good waveguides in Y-cut $LiNbO_3$ were demonstrated without surface damage and the degradation of electrooptic effect[6]. On the other hand, the annealed proton exchange(APE) method has some difficulty in fabricating Y-cut $LiNbO_3$ single-mode waveguide because of the surface damage resulting from PE.

The fabrication procedure of a $LiTaO_3$ QPM-SHG waveguide device is shown in Fig. 2. After depositing periodic Ta film stripes with a 3.5 μm period and a 2.0 μm stripe width on -c face of $LiTaO_3$, we put the sample for PE in pure benzoic acid melt at 220 °C for 40 min (Fig. 2(a)). After removing Ta stripes, a Ta-SiO_2 mask is deposited on the proton-exchanged surface to get a deep DI (Fig. 2(b)). The sample is heat-treated at 570 °C for 30 sec using a rapid thermal annealing(RTA) furnace (Fig. 2(c)). We use a rapid heat-up rate of 80 °C/sec. Both DI depth and width are equal to 1.8 μm as shown in Fig. 3. We form channel waveguides with a pattern width of 4 μm (Fig. 2(d)), perpendicular to the domain grating. PE is performed in pure benzoic acid melt at 220 °C for 40 min. After PE, a SiO_2 mask is deposited in the waveguide region to get a tight mode confinement[7] by suppressing the proton outdiffusion. PD with the SiO_2 mask is performed for 5 min in a furnace at 400 °C. After the PD is done, the exchange factor x of $Li_{(1-x)}H_xTaO_3$ in the whole region of our waveguide is estimated to be lower than the critical value[3] of 0.16. Below this critical value, the crystal phase is maintained in the single original α phase, and the crystal nonlinearity is completely restored[3].

The characteristics of our SHG device are measured by using a widely tunable Ti:Al_2O_3 laser as fundamental wave source. The measured results are shown in Fig. 4. The conversion efficiency is calculated by measuring the powers of the fundamental wave and the second-harmonic blue light through the waveguide end face. The SHG device with a length of 8 mm stably generates blue light of 1mW at 429 nm when the fundamental wave power is 10.3 mW. The conversion efficiency is almost 10 % and the normalized efficiency is 1500 %/Wcm^2. The dependence of SHG on the fundamental wave power is shown in Fig. 4(a). The second-harmonic wave power is proportional to the square of the fundamental wave power. The dependence of the fundamental and the second-harmonic wave power is shown in Fig. 4(b), which also demonstrates the maximum conversion of the fundamental

wave at 858.5 nm into the second-harmonic wave. The measured FWHM bandwidth is 0.17 nm that agrees reasonably with theoretical bandwidth of 0.12 nm.

In conclusion, we demonstrated that the SHG efficiency of $LiTaO_3$ waveguide is significantly enhanced by reducing the amount of PE in fabricating the SHG device. To reduce the amount of PE we used a Ta-SiO_2 mask in the heat-treatment for the domain grating and a SiO_2 mask in the proton diffusion process for the waveguide. In the fabricated device, the second-harmonic blue light of 1 mW at 429 nm was generated with the fundamental wave power of 10.3 mW. Its normalized efficiency is 1500 %/Wcm^2 which is the highest value for $LiTaO_3$ devices reported to date.

References

[1] K. Yamamoto, K. Mizuuchi, Y. Kitaoka, and M. Kato, Appl. Phys. Lett., vol. 62, pp. 2599-2601, 1993.

[2] T. Suhara and H. Nishihara, IEEE J. Quantum Electron., vol. 26, pp. 1265-1276, 1990.

[3] H. Å hlfeldt, J. Appl. Phys., vol. 76, pp. 3255-3260, 1994.

[4] S. Y. Yi and S. Y. Shin, Electron. Lett., vol. 31, pp. 1234-1235, 1995.

[5] K. Mizuuchi, K. Yamamoto, and H. Sato, J. Appl. Phys., vol. 75, pp. 1311-1318, 1994.

[6] Y. S. Son, H. J. Lee, and S. Y. Shin, IEEE Photon. Technol. Lett., vol. 2, pp. 184-186, 1990.

[7] S. S. Lee, M. C. Oh, Y. K. Jhee, and S. Y. Shin, IEEE J. Lightwave Technol., vol. 12, pp. 872-875, 1994.

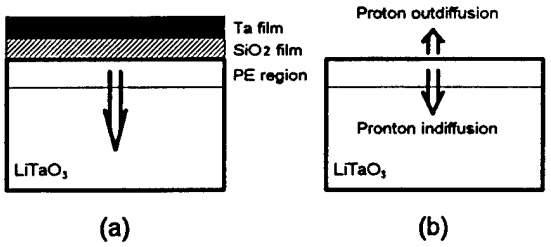


Fig. 1 Duffusion flux during the heat treatment (a) with the mask and (b) without the mask.

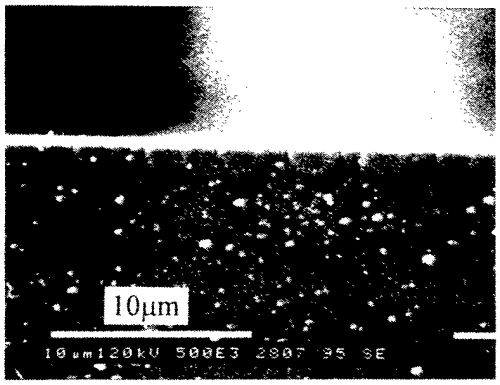


Fig. 3 Revealed domain-inversion structure. Both DI width and depth are 1.8μm.

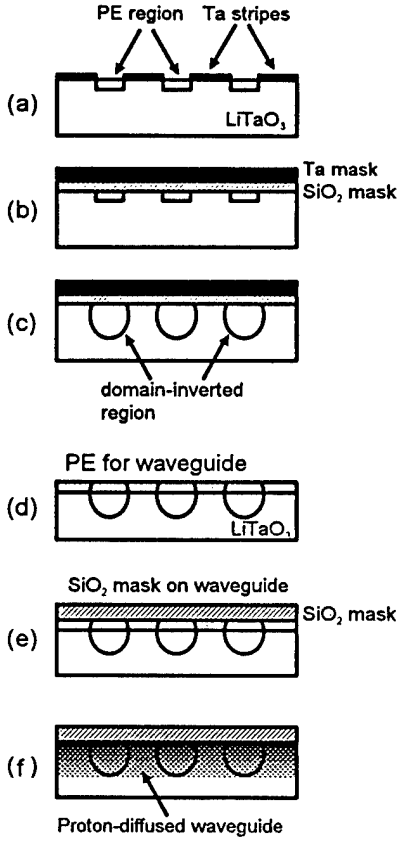


Fig. 2 Fabrication procedure of a QPM-SHG device: (a) selective PE for DI, (b) deposition of Ta-SiO_2 mask, (c) quick heat treatment with the Ta-SiO_2 mask, (d) PE for waveguide, (e) deposition of SiO_2 mask, and (f) proton diffusion with the SiO_2 mask.

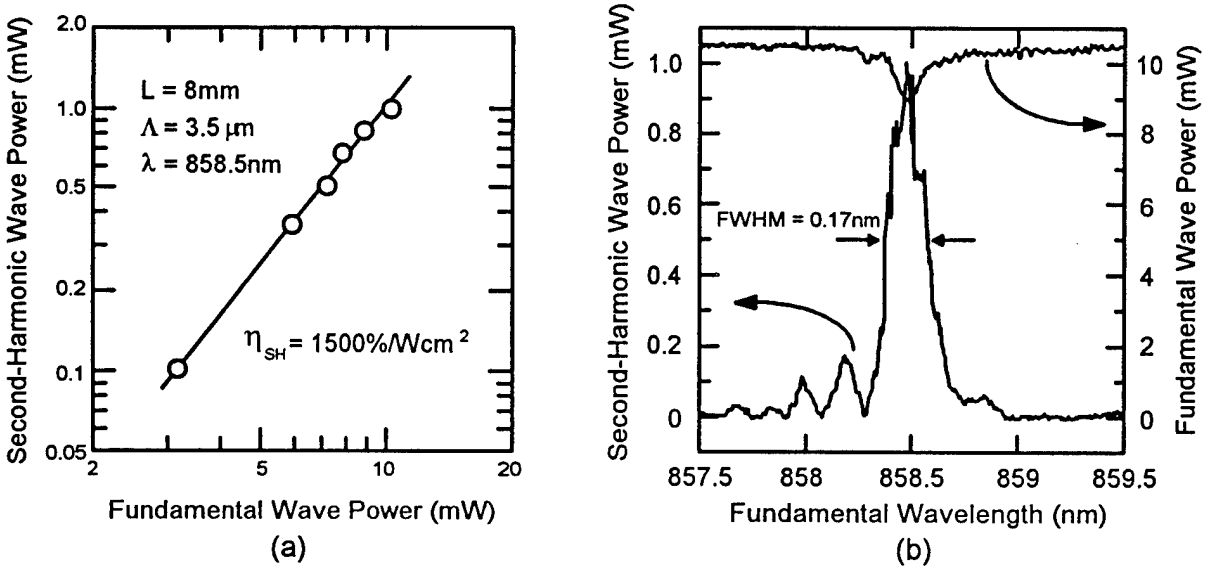


Fig. 4 Measured characteristics of SHG device (a) second-harmonic wave power against fundamental wave power and (b) second-harmonic wave power against fundamental wavelength.

Direct Observation of Buried Refractive-Index Profiles in Annealed Proton-Exchanged $LiTaO_3$ Waveguides

David B. Maring, Robert F. Tavlykaev, and Ramu V. Ramaswamy
Department of Electrical & Computer Engineering, University of Florida
135 Larsen Hall, Gainesville, FL 32611; Tel: (352) 392-9265, Fax: (352) 392-4963

Introduction

Recently, there has been an increasing interest in studying the properties of annealed proton-exchanged (APE) structures in $LiTaO_3$ due to its large electro-optical and nonlinear coefficients, as well as a higher optical damage threshold than that of $LiNbO_3$. Previous studies have indicated the anomalies of waveguides formed in $LiTaO_3$ [1-5], in particular, an increase of the extraordinary index increment upon annealing [1]. The feasibility of obtaining buried profiles in just a single-step diffusion has also been suggested [2,5], however, could not be verified due to the lack of data from direct measurements of refractive-index profiles. On the other hand, the presence of buried profiles would seriously undermine the adequacy of previous theoretical studies most of which relied on the inverse WKB procedure and monotonically decreasing depth profiles [2]. As for the ordinary index, very scarce information was available on its negative change on account of the absence of guided modes for this polarization and, as a consequence, inapplicability of conventional profile reconstruction methods. Overall, most of the previous studies have been based on indirect approaches, with associated, sometimes questionable, assumptions to deduce information of the actual index profile. Therefore, the importance of *direct optical characterization of index profiles* for developing and examining theoretical models is quintessential.

In this paper, we present the results of direct profile measurements of annealed proton-exchanged (APE) waveguides in X-cut $LiTaO_3$. A reflection technique was applied to directly profile waveguides with varying fabrication conditions for both extraordinary and ordinary polarizations. High spacial resolution was achieved by bevelling the substrate surface at a small angle. The existence of buried profiles and a dramatic increase of the extraordinary index upon short annealing have been directly proved, for the first time to the best of our knowledge. Also, we have obtained accurate scans of the ordinary profile showing a substantial negative change as well as expansion of the area delimited by the profile for increasing annealing time.

Fabrication and Profiling of Waveguides

A set of planar waveguides was fabricated by exchanging X-cut $LiTaO_3$ substrates in pyrophosphoric acid for 20 min at 260°C. Longer exchange times lead to cracks on the substrate surface caused by the difference in expansion along Z- and Y- axes and the associated in-plane stress component. The substrates were annealed at 300°C in air with annealing times varying from 0 (as-exchanged waveguides) to 60 min. A tantalum film was deposited on top of the substrate to serve as the reference for the air-substrate interface. Approximately half of the substrate surface was bevelled at an angle α of 2° to magnify the depth profiles by $1/\sin\alpha$ times (Fig.1). Finally, an AR coating (λ=0.633μm) was deposited on the back surface to minimize the interference between the backreflection from it and the light reflected by the bevelled surface.

The waveguide profiles were characterized, with a reflectivity technique [6], by scanning the focused beam of a He-Ne laser (Fig.1), polarized along the ordinary or extraordinary crystal axis, across the waveguide cross-section and measuring the variation of intensity of the reflected light due to a refractive index change. The variation ΔI of intensity I of reflected light is known to be related to the index profile as:

$$\frac{\Delta I}{I} = \frac{1}{4}\left(n_b - \frac{1}{n_b}\right)\frac{\Delta n}{n_b}$$

where Δn and n_b are the local increment and the bulk value of ordinary or extraordinary index, respectively.

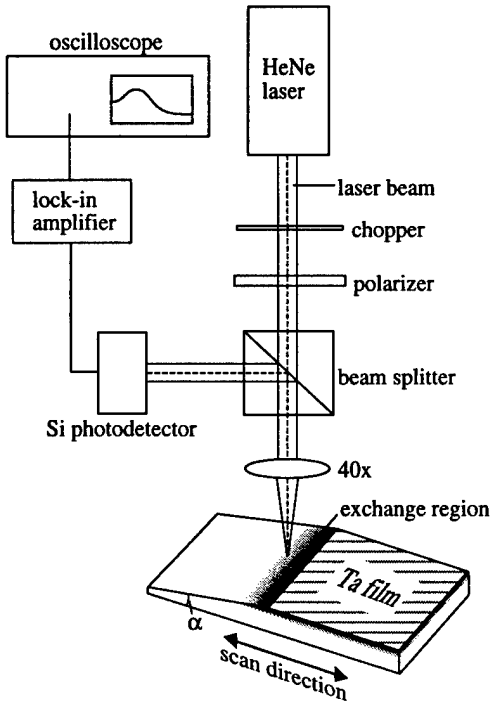


Fig. 1. Experimental setup for reflectivity measurements of index profiles.

The light incident on the sample was chopped and a lock-in amplifier was used at the photodetector output in order to improve SNR. Real-time index profiles were obtained by scanning the sample under the focused beam (in the depth direction) at a low frequency, feeding an oscilloscope with the output signal of the lock-in amplifier, and calibrating the absolute value of the index increment from the known bulk index of lithium tantalate. The position of the air-substrate interface was determined by monitoring a sharp peak in reflectivity when the beam moved onto the area covered by the Ta film.

Results and Discussion

Fig.2 shows the measured and a splined smooth fitted profile determined for the extraordinary polarization of incident light on a sample with annealing time t_a=15 min. It should be noted that the measured curve exhibited ripples whose origin still needs to be clarified. As seen, the magnitude of ripples is below ~ 15% of the maximum index increment. Taken alone, possible interference between the beam reflected from the bevelled (top) and bottom surfaces cannot explain this phenomenon, since practically no ripples were observed beyond the waveguide area. For presentation clarity, we fitted all the measured profiles (t_a=0 to 60 min), but that for the as-exchanged waveguide, with splined smooth curves which accentuate profile evolution upon annealing without adding substantial rounding errors as illustrated in Fig.3.

Fig.3 illustrates that index changes measured for as-exchanged waveguides were rather low and as a result, were significantly obscured by the aforementioned ripples preventing us from using any fit to the measured curve. The maximum index increment, however, dramatically increases upon short annealing, reaching ~0.02 for 30-min annealing time. The shape of the waveguide index also experiences rapid transformations revealing the presence of buried profiles for samples annealed for 7.5 and 15 min. This is the first, to the best of our knowledge, direct demonstration of the existence of buried APE profiles in $LiTaO_3$. The possibility of obtaining buried profiles in just a single-step diffusion due to a nonlinear dependence of the refractive index on proton concentration has been suggested in recent studies [2,5,7]. The current verification pinpoints the fact that a rigorous theoretical analysis of APE waveguides in $LiTaO_3$ is, to a large extent, hindered, if possible at all, until the phase diagram of this material is known. Some first results have indicated the nonlinearity of the refractive index versus proton concentration [7]. Yet, more accurate data is desired which we intend to obtain in the future by comparing optical profiles versus proton concentration distributions measured with an appropriate technique, such as SIMS.

Using the reflectivity technique, ordinary profiles were determined in the same straightforward manner with accuracy and resolution difficult to achieve if using conventional interferometric methods. Note again, curves fitted to the measured distributions with ripples are plotted in Figs.4 and 5. Summarized in Fig.5, the obtained results indicate that, as opposed to the extraordinary profiles, there no apparent buried profiles for this polarization. As expected, the measured index values are negative for ordinary polarization. By comparing Figs.3 and 5, it follows that for the same annealing time the index distributions for the two polarizations have an approximately identical width, however, the magnitude of the ordinary index decrease is substantially larger than the corresponding increase in the extraordinary increase for short annealing times. It is noted that the peak value of the negative ordinary change for the as-exchanged waveguides is comparable to those reported by Åhlfeldt et al [2,3].

We also performed preliminary measurements of temporal instabilities in APE profiles which had been reported to affect the waveguide properties in $LiTaO_3$. As an example, we observed a 15%-decrease of the extraordinary profile of a 15-min annealed sample over a 2-week period. Further investigation is in progress as well as the studies on the dispersion of the refractive index increment.

Conclusion

APE waveguides in X-cut $LiTaO_3$ were profiled by using reflectivity measurements. The existence of buried profiles was directly observed for the first time to the best of our knowledge, as well as the rapid evolution of the index profile during the annealing process. These facts substantiate the need for more adequate approaches than the routinely used WKB method, to analyze the profiles of APE waveguides in $LiTaO_3$, especially for short annealing times. New data on the ordinary index profiles and their modification upon annealing were also obtained. Experiments devised to obtain the dependence of the refractive index on proton concentration are currently in progress. The dispersion of the waveguide refractive-index increment needs to be determined over a spectral range up to 1.3 and 1.55 μm. At these wavelengths, the present technique can be applied for the characterization and design of single-mode channel waveguides where practically no other suitable approach is available.

References

1. T. Yuhara, K. Tada, and Y. Li, *J. Appl. Phys.*, **71**, p. 3966, 1992.
2. H. Åhlfeldt, J. Webjörn, F. Laurell, and G. Arvidsson, *J. Appl. Phys.*, **75**, p. 717, 1994.
3. H. Åhlfeldt, J. Webjörn, P. Thomas, and S. Teat, *J. Appl. Phys.*, **77**, p.4467, 1995.
4. P. J. Matthews and A. R. Mickelson, *J. Appl. Phys.*, **72**, p.2562, 1992.
5. G. M. Davis and N. A. Li, *J. Appl. Phys.*, **68**, p. 6513, 1990.
6. J. Steffen, A. Neyer, E. Voges, and N. Hecking, *Appl. Opt.*, **29**, p.4468, 1990.
7. K. Hadi et al, *Opt. Lett.*, **20**, p. 1698, 1995.

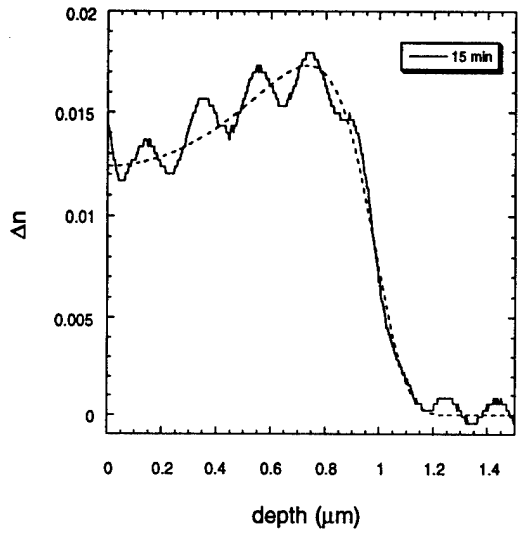


Fig. 2. Measured (solid) and fitted (dashed) extraordinary index profile for 15 minute annealing.

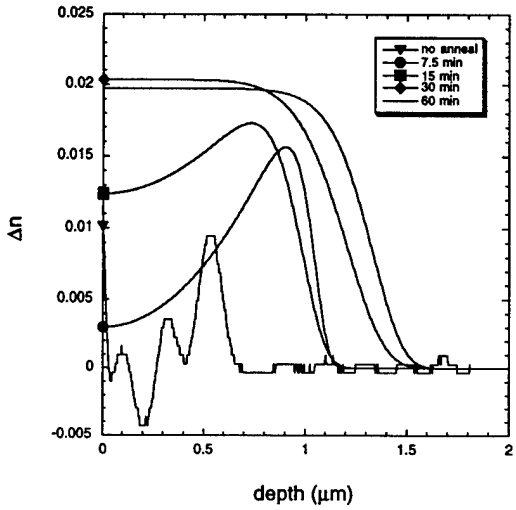


Fig. 3. Extraordinary index profiles for various annealing times.

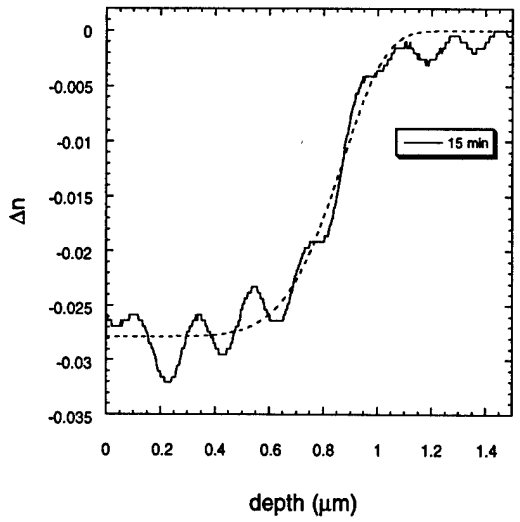


Fig. 4. Measured (solid) and fitted (dashed) ordinary index profile for 15 minute annealing.

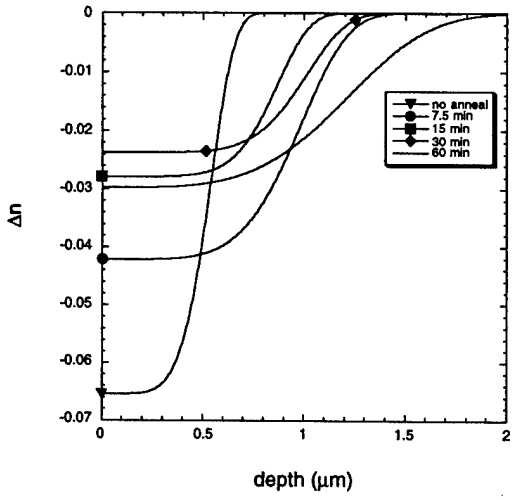


Fig. 5. Ordinary index profiles for various annealing times.

Measurement of Complex Coupling Coefficients of Directional Coupling by Thermo-Optic Modulation

H. Gnewuch
University of Cambridge, Institute of Biotechnology, Cambridge CB2 1QT, United Kingdom

J. E. Román, R. D. Harris, J. S. Wilkinson
University of Southampton, Optoelectronics Research Centre, Southampton SO17 1BJ, United Kingdom
Tel +44 1703 59 2792, Fax +44 1703 59 3149

R. Ulrich
Technische Universität Hamburg-Harburg, Optik und Meßtechnik, 21701 Hamburg, Germany
Tel +49 40 7718 3014, Fax +49 40 7718 2860

Introduction

Directional coupling between two parallel single-mode optical waveguides is the functional principle underlying numerous integrated optical devices, such as modulators [1], filters [2] and sensors [3, 4]. As the coupling efficiency depends critically on the synchronism of wave propagation and on the field overlap of the two guides, tight tolerances apply in waveguide fabrication, and a precise determination of the coupling parameters is essential.

Here we address the problem of measuring the coupling coefficient C which characterizes the coupling between the two guides which form a symmetric coupler. In a lossless coupler optical power is transferred completely back and forth between the guides, oscillating with a spatial periodicity $\Lambda = 2\pi/C$. When the guides are lossy, the oscillation is attenuated. Using an alternative description the oscillation and attenuation may be understood by as a "beating" phenomenon between the symmetric and antisymmetric 'supermode' ($m = 1, 2$) of the structure. These modes propagate independently of each other with complex propagation constants $\Gamma_m = \beta_m + j\alpha_m$. Their superposition varies according to the complex difference $C = \Gamma_2 - \Gamma_1 = \Delta\beta + j\Delta\alpha$, where $\Delta\beta = \beta_2 - \beta_1$ and $\Delta\alpha = \alpha_2 - \alpha_1$. This means a spatial periodicity $\Lambda = 2\pi/\Delta\beta$ and an attenuation of the beat amplitude proportional to $\exp(-\Delta\alpha z)$. In this paper we measure the difference C by scanning a small thermo-optic perturbation along the coupler and observing the induced periodic variation of the output power. In the earlier interpretation this C is the coupling constant between the two guides.

This thermo-optic method has recently been demonstrated for the measurement of the beat length Λ between two modes of orthogonal polarization [5]. It works equally well between the supermodes of a directional coupler, and its generalization to include the loss difference is straightforward. Compared to alternative techniques [6, 7, 8, 9] of measuring Λ, the thermo-optic method is advantageous because it does not require access to the evanescent field above the coupler. Therefore it permits application also to buried guides.

Theory

We consider the general case of a lossy symmetric directional coupler. It supports two guided waves ('supermodes') with complex propagation constants Γ_m, local amplitudes $A_m(z) = A_m(0)\exp(j\Gamma_m z)$, and vectorial field distributions $\mathbf{F}_m(x, y)$. In the absence of a perturbation they propagate independently along the coupler. Their total electrical field is the superposition $\mathbf{E}(x, y, z) = \sum_m A_m(0)\mathbf{F}_m(x, y)\exp(j\Gamma_m z)$. At a position z along the coupler the modal powers are $P_m(z) = |A_m(z)|^2 = |A_m(0)|^2 \exp(-2\alpha_m z)$, assuming that the $\mathbf{F}_m$ are normalized to $\int \mathbf{F}_m^* \mathbf{F}_n \, dx\, dy = \delta_{mn}$.

When a dielectric perturbation $\Delta\epsilon(x,y,z)$ is introduced by heating of a spot at $z = z_0$ on the coupler, the modal propagation constants Γ_m are modified by small amounts κ_{mm} and the supermodes become coupled by local coupling coefficients κ_{mn} which may be shown for $m,n = 1,2$ to be

$$\kappa_{mn}(z) = \frac{k_0^2}{2\beta_m} \int\int \mathbf{F}_m^*(x,y)\Delta\epsilon(x,y,z)\mathbf{F}_n(x,y)dxdy \tag{1}$$

with k_0 as the free space wavenumber. As a consequence the modal amplitudes are modified from their original values A_m to new values A_m^o in the region beyond z_0. These new amplitudes can be found by integrating the coupled mode equations

$$dA_m(z)/dz = j\sum \kappa_{mn}(z)\exp[j(\Gamma_m - \Gamma_n)z]\,A_n(z) \tag{2}$$

$$A_m^o(z_0^+) = A_m(z_0^+) + j\sum K_{mn}\,A_n(z_0) \tag{3}$$

$$\text{where} \quad K_{mn} = \int \kappa_{mn}(z - z_0)\,\exp[j(\Gamma_n - \Gamma_m)(z - z_o)]\,dz \tag{4}$$

The modified amplitudes propagate through the remaining distance $(L - z_0)$, and at the end of the guide, $z = L$, we have $A_m(L) = [A_m(0) + j\sum K_{mn}A_n(0)\exp[j(\Gamma_n - \Gamma_m)z_0]]$. The corresponding power $P_{m,L}^o$ in mode m is obtained as

$$P_{m,L}^o(z_0) = |A_m^o(L)|^2 = P_m(L) + 2\,K_{mn}\sqrt{P_m P_n}\,\exp(-\Delta\alpha\,z_0)\,\cos(\Delta\beta\,z_o + \phi_{mn}) \tag{5}$$

This equation shows the periodicity $\Delta\beta$ of the variation of the output power $P_m(L)$ when the position z_0 of the perturbation is scanned along the coupler. It also shows the attenuation with $\Delta\alpha$ of the oscillation amplitude. Therefore, a measurement of $P_{m,L}^o(z_0)$ yields the complex coupling coefficient C.

Experiments and Results

We start with the measurement of real coupling coefficients in nonabsorbing directional couplers. The symmetrical coupler supporting two modes comprised a single-ended input, the parallel coupling section, and a tapered section at the output, Fig. 1. The couplers were fabricated in soda-lime glass slides by thermal $K^+ - Na^+$–exchange. A thin black layer deposited on top of the waveguides was heated by local illumination inducing thermo-optic perturbation using thermo-optic and elasto-optic effects. In order to prevent absorption a transparent Teflon layer was deposited prior to the spin-coated absorbing film. Light from a 980 nm laser diode was coupled into a single mode fibre and directed onto the absorbing film, Fig. 1. The distance between fibre tip and the sample was $h \approx 20\,\mu m$, yielding a spot size of $\approx 9\mu m$ on the sample surface. The coupler modes were excited at 0.6328 μm via the input waveguide. At the output, light emerging from one branch of the coupler was TM-polarized and detected. By applying lock-in detection with a chopping frequency of $f_0 \approx 350\,Hz$ and having $\approx 8\,mW$ optical power at the fibre tip a relative modulation depth of $\approx 3 \cdot 10^{-4}$ was measured. For the measurement of the coupling coefficient the fibre was scanned along the waveguide and the lock-in reading was simultaneously monitored. Fig. 2 shows a typical measurement. With regard to Eq.(5), by fitting a sinusoid to the data, a relative error in the coupling coefficient below $\delta C/C = 1.6\,\%$ has been obtained. Finally, in Fig. 3 coupling coefficients corresponding to directional couplers with different edge-to-edge gap, d, in the original mask are shown. The plot shows to the first order an exponential dependence of the coupling coefficient on d, which is consistent with theory.

For the measurement of complex coupling coefficients of absorbing directional couplers we chose a compound structure comprising a dielectric waveguide in glass and a gold film covering the waveguide over a well defined length, Fig. 4. The dielectric waveguides were fabricated in Pyrex by thermal $K^+ - Na^+$–exchange. Subsequently, various goldfilms with varying thicknesses between $d = (20...50)$

nm were deposited and the coupler performance was measured dependent upon the superstrate index above the gold. Unlike the case of the directional coupler in glass we used the gold film itself as an inherent absorber. Again the absorber was illuminated using a laser diode, but now operating at 780 nm, via a single mode fibre whereby a thermo-optic perturbation was induced. The modes of the compound structure were excited at 0.6328 μm via the single mode input waveguide. At the output of the compound structure, the remaining fractions of the mode powers couple into the single mode of the output waveguide which is p-polarized and detected. In order to keep the perturbation region relatively small despite having a comparetively high thermal conductivity of gold we chose a modulation frequency of the perturbation source of $f_0 = 11$ kHz. For the measurement an index liquid was put onto the gold film. The fibre tip was then immersed into the index liquid and brought into close proximity to the gold film, $h \approx 50$ μm. The fibre was scanned along the whole length of the compound structure and the detected signal monitored simultaneously. For having $\approx$ 2 mW at the fibre tip a relative modulation depth of $\approx 1 \cdot 10^{-3}$ has been determined. Fig. 5 shows a modulation signal which is nearly point symmetric to the center of the coupling structure. By subtracting the modulation signals at points equally spaced to the center and subsequent normalization, an increase with increasing distance to the center is noticable which can be explained by the perturbation source becoming increasingly disaligned. Taking this into account, the mirror symmetry of the peaks is analogous to both cases of maximum modulation depth, [5], having either two modes excited and one mode at the output, or vice versa. Between the peaks coupling from the remaining less absorptive mode to the higher absorptive mode can not be seen at the output due to the excessive waveguide length for the higher absorptive mode. Note that part of the z-independent modulation signal between the peaks is therefore related to cross-coupling ! In Fig. 6 both the real and imaginary coupling coefficient can be determined. The real coupling coefficient has been determined with a relative error of 4 %.

Conclusions

In conclusion, we extended the theoretical description of the beatlength measurement technique based upon induced modal coupling to absorbing modes and applied the thermo-optical modulation technique to the measurement of the beatlength in nonabsorbing and absorbing directional couplers. The technique has been demonstrated for integrated optical directional couplers in glass and for a directional coupler comprising a dielectric waveguide in glass and a gold film covering the waveguide.

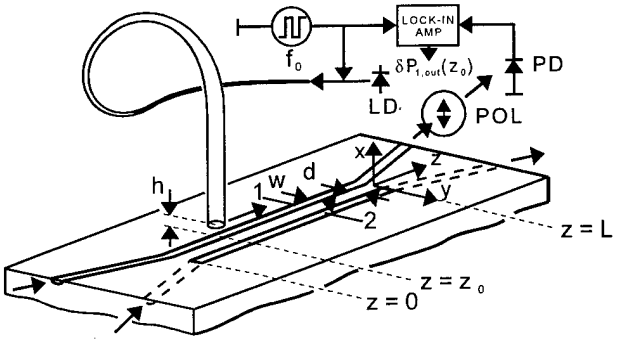


Fig. 1 : Experimental setup for the measurement of the coupling coefficient of directional couplers; waveguide width *w*, edge-to-edge waveguide gap *d*, distance between fibre tip and surface of sample *h*, laser diode LD, photodiode PD, linear polarisor POL.

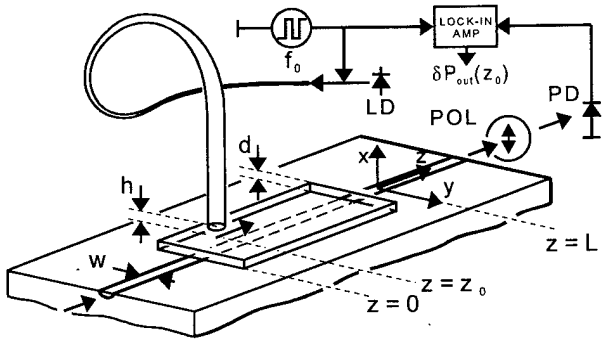


Fig. 4 : Experimental setup for the measurement of complex coupling coefficients of surface plasmon coupled dielectric waveguide modes; all abbreviations as in Fig. 1 but gold layer thickness *d*.

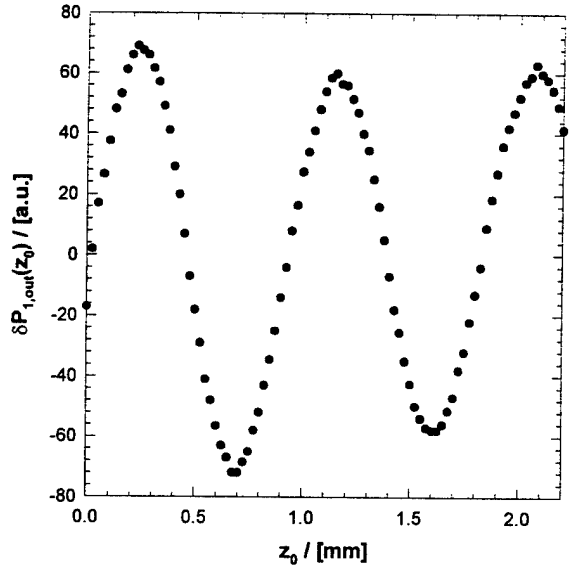


Fig. 2 : Measurement of the coupling coefficient for directional coupler with waveguide width w = (2.3 +/- 0.2)μm and gap d = (2.3 +/- 0.2)μm.

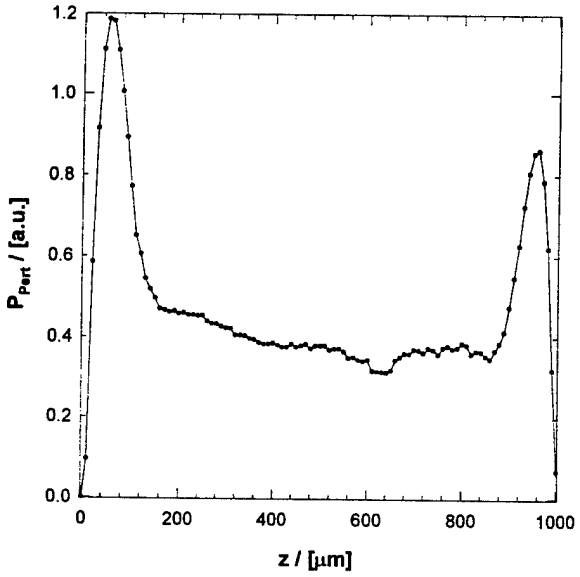


Fig. 5 : Modulation signal measured for waveguide covered by gold layer of thickness d = 33 nm; superstrate index n_0 = 1.390.

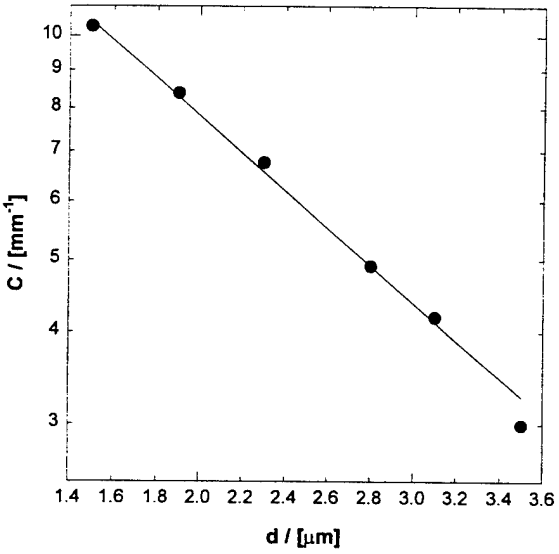


Fig. 3 : Log-linear plot of the coupling coefficient C versus waveguide gap d, waveguide width w = (2.3 +/- 0.2) μm.

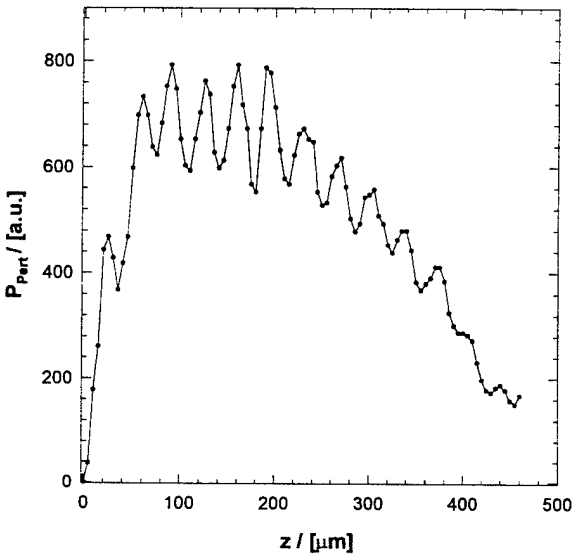


Fig. 6 : Modulation signal measured for waveguide covered by gold layer thickness d = 20 nm; superstrate index n_0 = 1.395.

References

[1] R. C. Alferness, Appl. Phys. Lett. **36**, 513 (1980).
[2] K. A. Winick, J. Lightwave Technol. **LT-9**, 1481 (1991).
[3] R. D. Harris, J. S. Wilkinson, Sensors & Actuators B **29**, 261 (1995).
[4] R. D. Harris et al, Proc. 7th Eur. Conf. on Int. Opt. (ECIO '95), 449 (1995).
[5] R. Stolte, R. Ulrich, Opt. Lett. **20**, 142 (1995).
[6] A. Miki, Y. Okamura, S. Yamamoto, J. Lightwave Technol. **LT-7**, 1912 (1989).
[7] K. Kishioka, G. L. Yip, Appl. Opt. **31**, 2807 (1992).
[8] A. G. Choo et al, Appl. Phys. Lett. **65**, 947 (1994).
[9] Y. Bourbin et al, J. Lightwave Technol. **LT-5**, 684 (1987).

Mechanisms of UV-induced refractive index changes in PECVD silica

M. V. Bazylenko, M. Gross and P.L. Chu
Electrical Engineering, University of New South Wales, Sydney, NSW, 2052, Australia.
(ph: Int-612-385-4027, fax: Int-612-385-5993)
D. Moss
Optical Fibre Technology Centre, University of Sydney, Sydney, NSW, 2006, Australia.
(ph: Int-612-335-0936, fax: Int-612-335-0910)

1. INTRODUCTION

Recently there has been considerable research into the process and applications of the UV induced refractive index change in germanosilicate glasses. Most of the Ge-doped planar structures reported to date have been formed by flame hydrolysis and require hydrogen loading for up to 2 weeks [1] to become reasonably photosensitive. An alternative deposition technique, which is able to produce photosensitive films without hydrogen loading, is Plasma Enhanced Chemical Vapour Deposition (PECVD). UV induced refractive index changes of up to +0.0035 [2] and in the range from -0.0036 to +0.0017 [3] have been reported for Ge-doped PECVD silica films without use of hydrogen loading.
In this paper we present more experimental data on Ge-doped PECVD silica with both positive and negative UV-induced refractive index changes and propose mechanisms which may account for each type of photosensitivity. The proposed mechanism for the negative change includes film relaxation due to UV-induced reduction of compressive stress. The positive change occurs in films which exhibit a significant degree of porosity and is attributed to UV-induced densification of the porous material.

2. EXPERIMENTAL

Ge-doped silica films were deposited on 50 mm diameter silicon substrates in a high plasma density hollow cathode reactor from mixtures of silane (SiH_4), germane (GeH_4) and oxygen. The dual opposing target hollow cathode reactor has been reported in detail elsewhere [4].
A series of deposition runs, with varying rf power densities, were carried out at a process pressure of 2 Pa and a GeH_4 flow rate of 6 sccm. The SiH_4 flow rate was fixed at 20 sccm with an SiH_4/O_2 ratio of 6:1. No electrode cooling was used in these experiments. In most of the deposition runs the film was deposited on one wafer clamped in the 'face down' position to the top electrode. In one run, however, two wafers were deposited simultaneously. The first wafer, labelled w1, was clamped to the top electrode in the normal manner, while the second wafer, w2, was placed on the bottom electrode, but supported slightly above it on three small ceramic spacers. The purpose of the spacers was to reduce the level of ion bombardment on w2 by reducing its voltage from the bias voltage of the electrode to a potential close to the floating potential of plasma glow. The reduction of ion bombardment was expected to result in porosity in the films, thus allowing us to investigate its effect on photosensitivity. We have previously found that the presence of w2 alters the deposition conditions of w1, so that the film properties of w1 (with and without w2) are different [3].
The film porosity was estimated by measuring its etching rate in standard 'P-solution'. The film stress was calculated from the substrate curvature, as measured by stylus profilometry.
The deposited films were UV exposed using a 193 nm excimer laser with a fluence of 10 kJ/cm^2. The refractive indices of the films were measured using the prism coupling technique at 633 nm wavelength with a measurement repeatability within ±0.00015.

3. RESULTS AND DISCUSSION

The change in refractive index after UV irradiation is shown in Fig. 1. Both increases and decreases in refractive index are observed, depending on the deposition conditions. All samples placed in direct contact with the electrode, and thus subjected to ion bombardment during deposition, exhibit a negative refractive index change. The negative refractive index change does not significantly depend on the power level for one wafer deposition. At the same time, the refractive index decrease for w1 (deposited simulateously with w2) is of the order of -0.006 which is about a three times larger change compared to the similar sample

deposited at the same power, but in the absence of the second wafer w2. Currently, we don't have any clear explanation for this effect, however, it may be looked at in terms of partial screening of the opposite electrode (and hence w1) by w2. This may lead to both an ion bombardment and temperature reduction on w1.

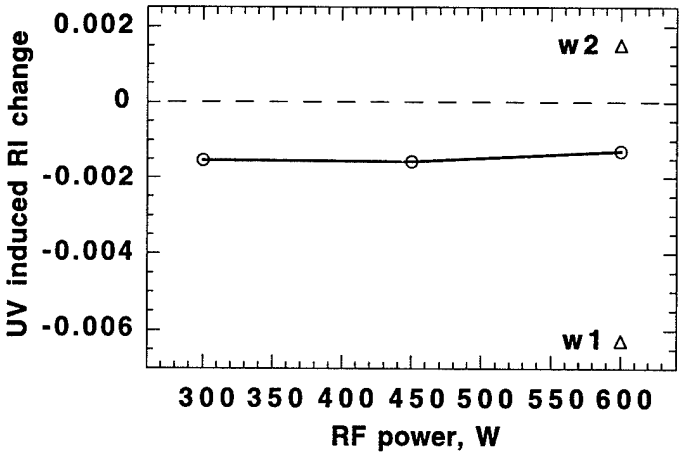
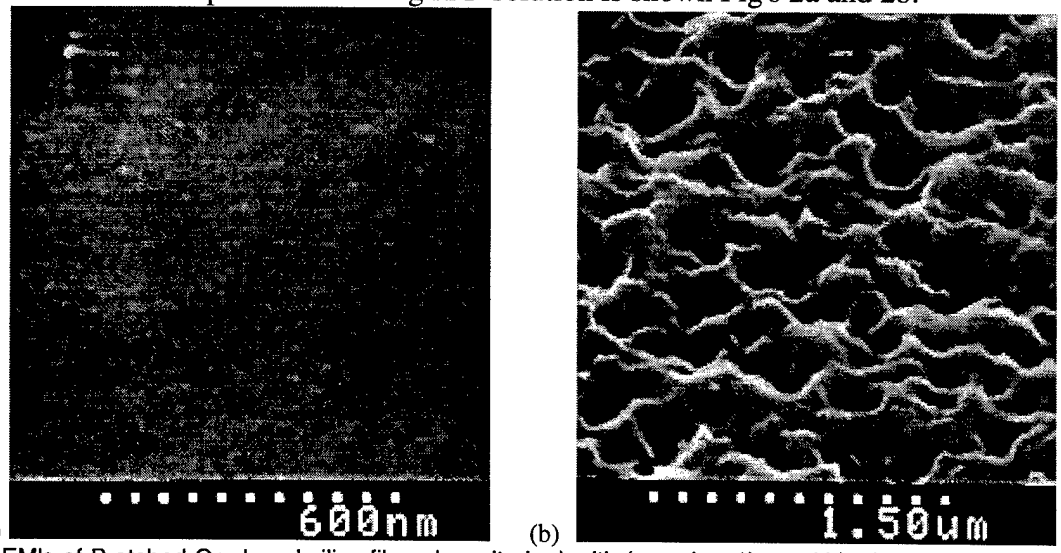


Fig. 1 UV induced index change of Ge-doped silica films deposited at various rf input powers.

At the same time, as can be seen in Fig. 1, sample w2, which was separated from the electrode during the deposition and thus received significantly decreased ion bombardment, exhibits a positive refractive index change after UV irradiation. By decreasing the level of ion bombardment it was intended to obtain a less dense (more porous) film compared to those normally obtained in the hollow cathode reactor. The results of P-etch rate measurements confirm that this indeed was achieved: the P-etch rates for samples w1 and w2 were 8 Å/s and 26 Å/s, respectively, which implies a less dense (porous) material in the latter case. The surface of the two samples after etching in P-solution is shown Fig's 2a and 2b.



(a) (b)

Fig. 2 SEM's of P-etched Ge-doped silica films deposited a) with (sample w1) , and b) without (sample w2) ion bombardment. The P-etch rates are 8 Å/s and 26 Å/s, respectively.

The rough appearance of the surface of sample w2 (deposited without ion bombardment) is consistent with the fact that its P-etch rate is on average 4 times higher than that of ion bombarded samples, and also implies a significant degree of porosity. It may be suggested, therefore, that positive refractive index changes after UV irradiation occur in porous PECVD material and can be attributed to film densification by UV light. A decrease in the film thickness of around 0.1µm (initial film thickness ≈ 3µm) has been measured for sample w2 after UV exposure, which seems to validate the material densification hypothesis.
From a practical point of view these results point to a limited usefulness for such 'positive'

photosensitive PECVD films, since the optical loss in such porous material is likely to be quite high. The high losses (>1dB/cm) previously reported for waveguides formed by direct UV writing in 'positive' photosensitive PECVD material [5] seem to support this conclusion. All deposited films were under compressive stress, which was observed to decrease after UV exposure. The film stress before and after UV exposure is shown in Fig 3. It is seen that the stress is reduced by around 100 to 120MPa for the ion bombarded samples and by about 50 MPa for the floating sample (w2).

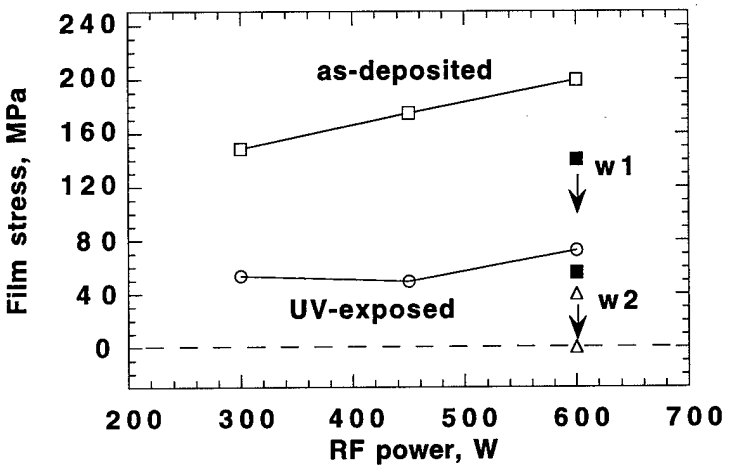


Fig. 3 Film stress before and after UV-exposure as a function of rf input power. Arrows point to UV exposed stress for w1 and w2.

Since UV exposure causes a stress reduction in the films (Fig. 3), it may be suggested that the observed negative refractive index change is related to a relaxation of stress-induced compression. The following simple calculation can prove the validity of this suggestion. The relation between the relative volume expansion and stress reduction for the plane stress case is given by [6]:

$$\Delta V/V = -2(1-2\nu)(\Delta P/E) \quad , \qquad (1)$$

where ΔP is the film stress reduction, E is Young's module and ν is Poisson's ratio. Taking E and ν values for thermal oxide (7×10^{10} Pa and 0.18, respectively) and an average value of the UV induced stress reduction of 100MPa (observed in the ion bombarded films in Fig. 4), we obtain a value of 0.18% volume expansion. We can now obtain the appropriate refractive index change by applying Clausius-Mosotti formalism, which relates the refractive index, n, to the molar volume of material. The appropriate expression is written as follows:

$$\frac{\varepsilon-1}{\varepsilon+2} = \frac{4\pi}{3}\frac{N}{V_m}\sum_{j=1}(f_j a_j), \qquad (2)$$

where $\varepsilon = n^2$ is the optical frequency dielectric constant, N is Avogadro's number, V_m is the molar volume, and the sum is taken over the bond polarizabilities a_j and f_j is the fraction of each bond type. Assuming the bond polarizabilities in the material remain unchanged during the UV exposure this expression gives a linear relationship between refractive index and molar volume. For a 0.18% volume expansion we thus obtain a refractive index change of -0.0026. This figure is in a reasonably good agreement with that observed for the single wafer deposition, ion bombarded samples. Thus we may attribute the observed negative refractive index change to the UV induced stress reduction in our films. The sample w1, which exhibits a 3 times larger UV induced index change (-0.006) while exhibiting the same degree of stress reduction (~100MPa), probably points to a concommitent decrease in the bond polarizabilities, which are assumed constant in the above calculation.

From a different point of view it is known that conventional PECVD silica has a refractive index which is typically higher than that of thermally grown silicon oxide. Film densification during the ion-assisted deposition process has been shown to account for the higher refractive index of PECVD silica [7]. After high temperature annealing however, the refractive index of PECVD silica decreases to that of thermal oxide, thus exhibiting a negative refractive index

change [7]. In order to investigate a possible relation between this intrinsic property of PECVD silica and the UV-induced refractive index decrease observed in this work, a partially UV-exposed sample was annealed at 600°C for 1 hour. The results are shown in Fig. 4.

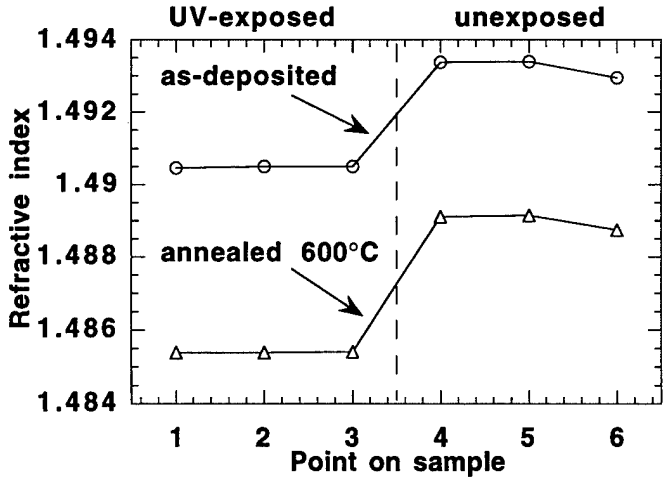


Fig. 4 Refractive index for as-deposited and 600°C annealed film in UV-exposed and unexposed areas .

It is seen that the refractive index decrease caused by the annealing does not effect the step in the refractive index induced by UV exposure. This suggests that different mechanisms are responsible for the refractive index decrease due to high-temperature annealing typical for PECVD silica (regardless of doping), and the UV-induced refractive index decrease obtained in this work for Ge-doped PECVD films.

5. CONCLUSIONS

Both positive and negative UV-induced refractive index changes have been demonstrated in Ge-doped silica films deposited using PECVD. The positive index change is observed in porous films and is attributed to film densification by UV light. Film stress reduction and the resulting volume expansion is shown to account for negative index changes. The negative UV-induced refractive index change mechanism is shown to be different from that suggested for typical PECVD silica following high temperature annealing.

Acknowledgements

The authors would like to thank J. Arkwright for helpful discussions. This work has been supported by the Australian Photonics Cooperative Research Centre (APCRC) of which the University of NSW and the Optical Fibre Technology Centre (OFTC) are members.

References

1. G. D. Maxwell and B. J. Ainslie: 'Demonstration of a directly written directional coupler using UV-induced photosensitivity in a planar silica waveguide'. Electron. Lett., 1995, **31**(2), pp. 95-96.
2. M. Svalgaard, C. V. Poulsen, A. Bjarklev and O. Poulsen: 'Direct UV writing of buried singlemode channel waveguides in Ge-doped silica films'. Electron. Lett., 1994, **30**(17), pp. 1401-1403.
3. M. V. Bazylenko, M. Gross, D. Moss and P.L. Chu 'Photosensitivity of Ge-doped silica films deposited in a PECVD hollow cathode reactor', Presented at the Photosensitivity and Quadratic Nonlinearity in Glass Waveguides Topical Meeting, Portland, USA, September 1995.
4. C.M. Horwitz, S. Boronkay, M. Gross and K.E. Davies: 'Hollow cathode etching and deposition', J. Vac. Sci. Technol, 1988, **A6**, pp. 1837-1844.
5. D. Moss et al 'All optically written planar germanosilicate waveguides gratings', Presented at the Photosensitivity and Quadratic Nonlinearity in Glass Waveguides Topical Meeting, Portland, USA, September 1995.
6. C. T. Wang, *Applied Elasticity*., McCraw-Hill, New York, 1953, p31.
7. M. V. Bazylenko, M. Gross, A. Simonian and P. L. Chu:'Pure silica and fluorine doped films deposited in a hollow cathode reactor for integrated optics application'. To be published in Journal of Vacuum Science and Technology.

Loss-reduction of deeply etched InP/InGaAsP waveguides by CBE-regrowth

C.G.M. Vreeburg[a], Y.S. Oei[a], T.L.M. Scholtes[c], J.W. Pedersen[d], H. Vonk[b], C.A. Verschuren[b], R.T.H. Rongen[b], M.R. Leys[b], J.H. Wolter[b]

[a,b]COBRA Interuniversity Research Institute
[a] Delft University of Technology, Department of Electrical Engineering
P.O. Box 5031, NL-2600GA Delft, The Netherlands
Phone: +31-15-2784950, Fax: +31-15-2784046

[b] Eindhoven University of Technology, Department of Physics
P.O. Box 513, NL-5600MB Eindhoven, The Netherlands

[c] Delft University of Technology, Department of Physics

[d] Royal PTT Nederland N.V., KPN Research
P.O. Box 421, NL-2260 AK Leidschendam, The Netherlands

Introduction

Low-loss waveguides are the basic components in photonic integrated circuits (PICs). A high degree of integration can only be obtained by the use of small components. In general the size of optical components can be reduced by increasing the optical contrast. The maximum contrast in a ridge waveguide structure can be achieved by etching through all the waveguiding layers. Recently, it has been shown [1] that, the size of MMI-couplers and bends can be significantly reduced by the application of this deep etch technology. In addition, device performance of deeply etched waveguides is insensitive to etch depth variations.

Waveguide losses in deeply reactive ion etched (RIE) waveguides have also been reported [2]. The wide and multimoded waveguides showed low loss, but the monomode waveguides (<1.6 μm) still have high losses. This is mainly caused by scattering at the sidewall roughness.

This effect of sidewall roughness can be reduced by regrowth of InP using chemical beam epitaxy (CBE) [3]. This work reports on a factor of two loss-reduction of deeply RIE-etched InP/InGaAsP(λ_{gap}=1.3 μm) waveguides by this approach.

Fabrication

On a SI-InP(100) substrate with 2° off-orientation non-intentionally doped layers consisting of a 1500 nm InP buffer layer, a 600 nm InGaAsP(λ_{gap}=1.3 μm) film layer and a 300 nm InP cladding layer have been grown by MOVPE. A 100 nm thick Si_3N_4 layer was deposited by plasma enhanced chemical vapour deposition and served as an etching mask for the waveguides. The pattern was defined in positive photoresist by contact illumination and transferred in the Si_3N_4 by using reactive ion etching with CHF_3.

After removal of the photoresist the waveguides were etched by reactive ion etching with an alternate etch/descum process [4] in a parallel-plate reactive ion etcher. First, InP was etched with CH_4:H_2 (7:35 sccm) at a power of 100 W and a reactor pressure of 50 mTorr for 150 s. The next step is removal of polymers on the wafer (descum) by an O_2 (100 sccm) plasma

for 18 s. Plasma power and reactor pressure were 70 W and 100 mTorr, respectively. In our system the etch rate of InP is about 35 nm/min. The two steps (etch and descum) were repeated upto the final etch depth of about 2 μm.

A SEM-micrograph of the waveguide ridge is shown in Fig. 1a. The Si_3N_4 mask is still visible, also the InGaAsP(1.3) film layer can be recognized in the sidewall. The waveguides are parallel to the [011]-direction. Striations (<20 nm) in the sidewall and the non-verticality can be observed from the picture.

CBE-regrowth

Before regrowth the residual polymers were removed by an O_2-plasma in a barrel stripper and two minutes etching in 5% phosphoric acid.

The sample with the RIE-etched waveguides were mounted on a molybdenum-block using indium solder alongside a quarter of a 2-inch InP(100) substrate as reference. Care was taken to mount the substrate containing the waveguides in such a way that the etched ridges are oriented radially on the holder. This ensures symmetrical growth on both sides of the waveguide [5]. After introduction into the CBE growth chamber the temperature was brought to 515 ^{o}C in approximately one hour under a (cracked) PH_3 flow of 12 sccm. The temperature was monitored by an optical pyrometer, focused on the InP reference piece. Growth was performed using a flow of 1.6 sccm trimethylindium and 6 sccm (cracked) PH_3. Under these conditions, the planar (100) growth rate of InP is 0.6 μm/hour.

In this particular growth experiment we made use of the fact that the growth rate of the {011} planes is extremely slow compared to the (100) plane. To prevent formation of (111)B facets we have chosen a relatively high V/III ratio as compared to our optimal planar growth conditions [6]. In order to achieve at least 50 nm sidewall thickness at the bottom of the waveguiding region it was estimated that a planar InP thickness of 0.7 μm was necessary. As can be seen in Fig. 1b-c true $(0\bar{1}1)$ and $(01\bar{1})$ facets have indeed been grown on the approximately 80° sloped RIE-etched sidewall.

Measurement results

The waveguide loss, before and after regrowth, has been measured with a Fabry-Perot resonance method at a wavelength of λ=1550 nm. Light of fixed polarization was end-fire coupled in the waveguides by an anti-reflection coated 40x microscope objective. Light emanating from the waveguides was imaged on a Ge-diode by a 40x microscope objective. The wavelength was tuned by heating the DFB-laser with a Peltier element. The reflection coefficients for different waveguide widths and polarization have been calculated.

On the wafer groups of waveguides with width varying for (1-5) μm in steps of 0.5 μm were present. Waveguide loss after RIE-etching as a function of the width and polarization, marked with TE_RIE and TM_RIE, are shown in Fig. 2. The results are the mean values of the seven best waveguides. Waveguides with a loss higher than 8 dB can not be measured accurately with our Fabry-Perot setup. The results of these measurements reproduced very well the earlier experiments (ECIO'95) [2]. Here the measurement results with a loss higher than about 5 dB were obtained from a cut back method.

Transmission losses versus waveguide width for smoothed waveguides are also depicted in Fig. 2 and marked by TE_RGR and TM_RGR for the two polarizations, respectively. Especially for the smaller waveguides (<2 μm) a significant loss reduction was obtained. The results are the mean value of the three best waveguides. It should be mentioned that after re-

growth significant spread in the loss results was found.

Discussion

The increased spreading in the loss results after regrowth is most probably caused by the varying degrees of roughness at the corners of (100) and the vertical planes. This roughness is most likely caused by the unevenness of the sidewalls after RIE-etching combined with impurity effects. The asymmetry which is clearly visible in Figs. 1c-d is typical for growth on off-oriented substrate containing (111)B steps [7]. Impurities together with sidewall imperfections are also responsible for the non-smooth surface between the waveguides. A more stringent cleaning process after the RIE is required.

Nevertheless, it has been demonstrated that, significant loss reduction of deeply etched InP/InGaAsP waveguides can be obtained by regrowth of InP using CBE. The loss reduction (for waveguide widths between 1 μm and 3 μm) is about a factor of 2, this reduction can be explained by a decrease in the index contrast at the rough interface. As described in [8] scattering loss scales up linearly with the squared indices difference ($\Delta n^2=n_1^2-n_2^2$) and the field intensity at the rough sidewall. By regrowth of about 150 nm InP Δn^2 is reduced by a factor of 7.3, but the field intensity is increased by a factor of 4 which results in an estimated loss reduction of about 1.8 which is in good agreement with the achieved results. Higher loss reduction can be obtained by matching the refractive indices of the filmlayer and the regrown layer.

References

1. L.H. Spiekman, Y.S. Oei, E.G. Metaal, F.H. Groen, I. Moerman and M.K. Smit, *"Extremely small multimode interference couplers and ultrashort bends on InP by deep etching"*, IEEE Photonics Techn. Lett., 6 (8), pp. 1008 (1994).
2. Y.S. Oei, L.H. Spiekman, F.H. Groen, I. Moerman, E.G. Metaal and J.W. Pedersen, *"Novel RIE-process for high quality InP-based waveguide structures"*, Proc. 7th Eur. Conf. on Int. OPt. (ECIO'95), pp. 205 (1995).
3. M. Gotoda, H. Sugimoto, S. Maruno, T. Isu, W.Susaki and M. Nunoshita, *"Fabrication of smooth facets of InP by selective sidewall epitaxy using CBE"*, Appl. Surf. Sci. (82/83) pp. 80 (1994).
4. Y.S. Oei, C. van Dam, L.H. Spiekman, B.H. Verbeek, F.H. Groen, E.G. Metaal and J.W. Pedersen, *"Improved RIE-technique for controled roughness and anistoropy in InP and related compounds"*, Proc. 18th State of the art program on compound semiconductors (SOTAPOCS XVIII), 134 (1993).
5. M. Gotoda, H. Sugimoto, S. Maruno, T. Isu, W. Susaki and M. Nunoshita, *"Symmetric InP mirror facets fabricated by chemical beam epitaxy on reactive ion etched sidewalls"*, J. Crystal Growth 150, pp. 399 (1995).
6. R.T.H. Rongen, M.R. Leys, P.J. Hall, C.M. van Es, H. Vonk and J.H. Wolter, *"Investigations on InP grown by chemical beam epitaxy"* , J. Electron. Mater., 24, pp. 1391 (1995)
7. H. Heinecke in Low dimensional structures prepared by epitaxial growth or regrowth on patterned sbustrates (eds. K. Eberl et al.), pp229-242, Kluwer Academic Publishers (1995).
8. H.G. Unger, Planar optical waveguides and fibres, Oxford, Clarendon Press (1977).

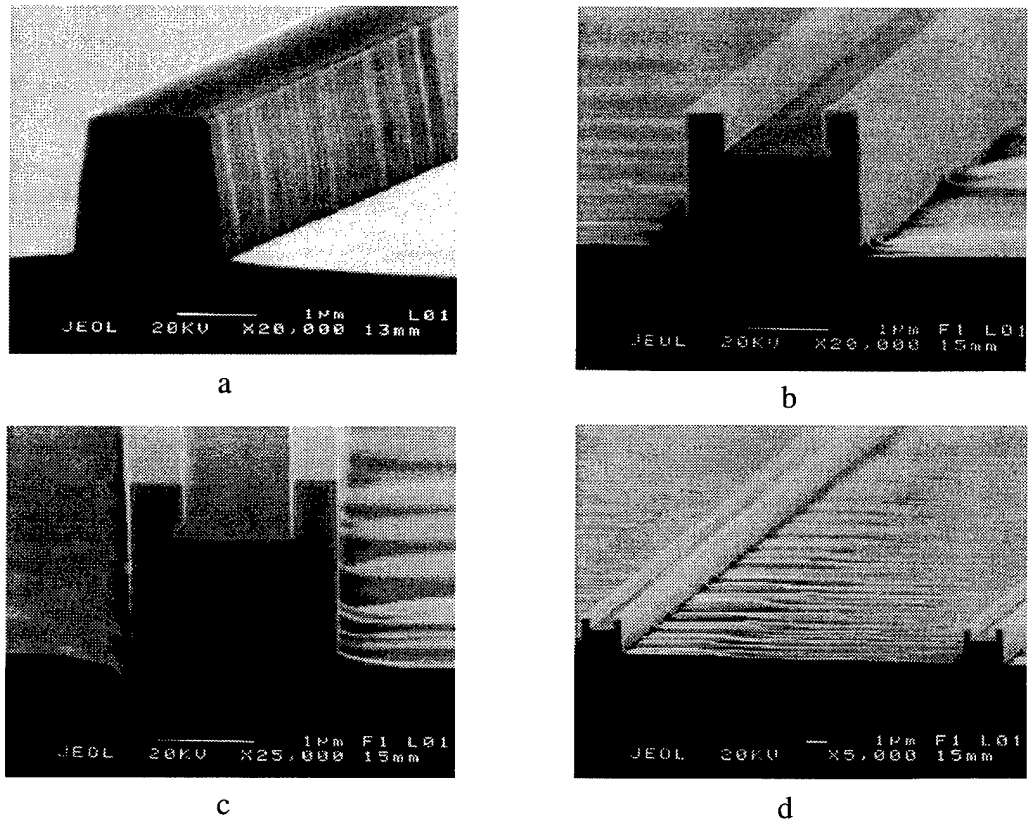


Fig. 1. SEM-micrographs of waveguides. a) Ridge waveguide after reactive ion etching. b) Ridge waveguide after regrowth with InP, the InGaAsP has been made visible with a stain etch. c) Front view of regrown waveguide. d) Surface morphology between two waveguides.

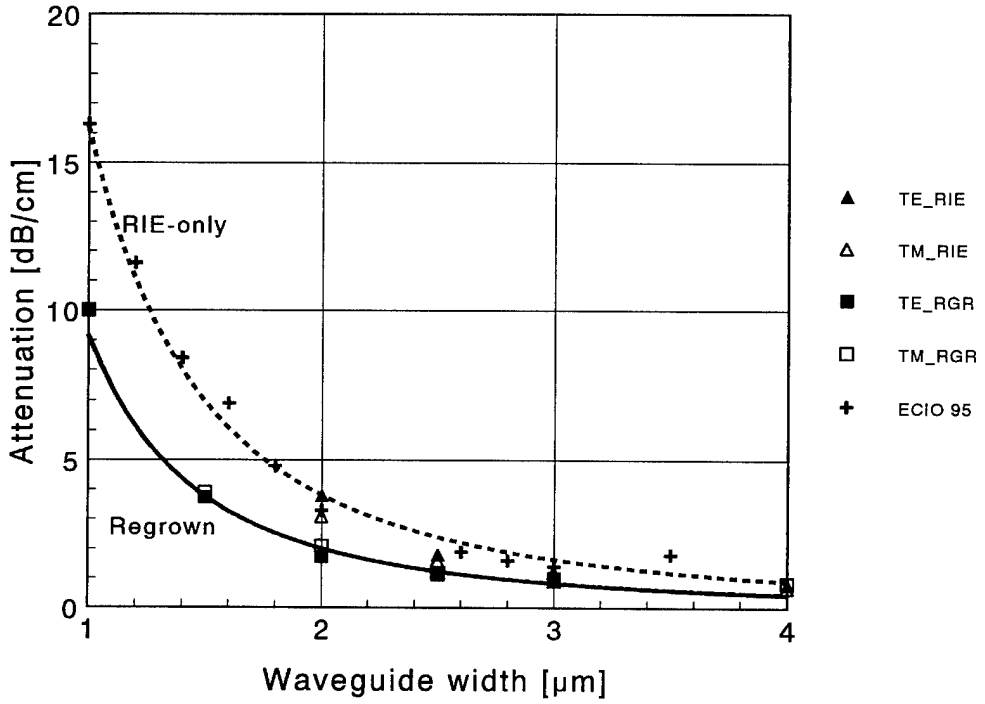


Fig. 2. Waveguide loss of RIE-waveguides (ECIO'95, TE_RIE, TM_RIE) and loss of regrown waveguides (TE_RGR and TM_RGR).

Wednesday, May 1, 1996

Polarization Selective Devices

IWC 10:30 am-12:00 m
Fairfax A

Ramu V. Ramaswamy, *Presider*
University of Florida

Poling-Induced Waveguide Polarizers in Electro-Optic Polymers

Min-Cheol Oh and Sang-Yung Shin
Dept. of Electrical Engineering, Korea Advanced Institute of Science and Technology, 373-1, Kusong-dong, Yusong-gu, Taejon, 305-701, Korea.
(Phone) +82-42-869-3420, (Fax) +82-42-869-3410

Wol-Yon Hwang and Jang-Joo Kim
Electronics and Telecommunications Research Institute, P.O.Box 8, Daedug Science Town, Taejon, 305-606, Korea.

Waveguide devices based on electro-optic (EO) polymers may play important roles in optical signal processing and optical communication. Because of their excellent velocity matching between microwave and optical signals, high speed modulators have been actively investigated [1], [2]. Recently, a polymeric wavelength-insensitive passive polarization converter was reported [3]. It demonstrated that the optic axis distribution in a poled polymer waveguide is controllable by specially designing the poling electrodes, and new types of polarization controlling devices may be designed based on this.

The electric field-assisted poling increases the refractive index of the EO polymer for the light polarized along the poling direction, while decreasing it for the light polarized perpendicular to the poling direction. Thus it may be utilized to fabricate channel waveguides that confine only one polarization component [4], [5]. On the other hand, the photobleached polymer waveguide supports both TE and TM modes [6]. In this work, we integrate poling induced waveguides in the middle of photobleached polymer waveguides and demonstrate polymeric waveguide polarizers. Although there are many kinds of integrated optic polarizers [7], polymeric waveguide polarizers have not been reported. The performance of the polarizer is usually evaluated by its excess loss and polarization filtering efficiency. To minimize the excess loss of polarizers, the poling-induced birefringence is controlled for matching the guided mode profiles between the photobleached waveguide and the poling-induced waveguide. The polarization filtering efficiency of the TE-pass polarizer is improved by using four electrodes instead of conventional coplanar electrodes.

Schematic diagrams of the two polarizers are shown in Fig. 1. The input and output sections consist of photobleached waveguides that support both TE and TM modes. Selective bleaching under UV light decreases the refractive index of the polymer and forms channel waveguides in the un-bleached area [9]. To fabricate a TM-pass polarizer, two vertically aligned electrodes may be used for poling the polymer. The poling induced birefringence produces a birefringent channel waveguide whose optic axis is aligned in the vertical direction. This vertically poled waveguide can confine only TM modes. Hence,

the TM mode passes the filtering section while the TE mode radiates. In a TE-pass polarizer four electrodes are used for the horizontal poling of polymer instead of conventional coplanar electrodes. The four electrodes make the electric fields to be aligned horizontally in the core layer of the waveguide and provide better uniformity of the poling-field directions than the coplanar electrodes [5]. After the electric-field assisted poling, a horizontally poled channel waveguide is formed. The refractive index of poled region is enhanced for TE modes and decreased for TM modes. Hence, the horizontally poled waveguide acts as a TE-pass polarizer.

The top views of both polarizers in Fig. 2 define the dimensions of waveguides. L_f is the length of the filtering section and W_s the strip width of the mask used for selective photobleaching. W_s affects the lateral mode profile of the bleached waveguide together with the bleaching time. W_e is the width of the poling electrodes in the TM-pass polarizer, and W_g the gap width between the poling electrodes in the TE-pass polarizer. They are important parameters that determine the resultant index profiles after poling.

For the low loss polarizers, the mode profiles of involved waveguides should be matched. The mode profile in vertical direction is determined by the refractive index of three layers forming planar waveguides. On the other hand, the lateral mode profiles are dependent on the device parameters and poling conditions. With parameters fixed by the dimensions of photomasks, it is necessary to find appropriate bleaching times and poling voltages to match the mode profiles between the different waveguides.

The two polarizers are fabricated on one substrate. The fabrication procedures are as follows. On a thermally oxidized Si wafer, bottom electrodes are constructed by vacuum evaporation of Ti-Au and by lift-off process. The EO polymer used in this work is the PMMA based copolymer with a stilbene derivative as a side chain (poly ((4 - dimethylamino - 4' - nitro - stilbene methylmethacrylate)$_x$ - co - (methylmethacrylate)$_{1-x}$); P2ANS) which is supplied by Hoechst-Celanese Co. For the lower cladding and core layers, P2ANS(x=0.35) and P2ANS(x=0.5) are spin-coated to be 3.5 μm and 4 μm thick, respectively. Then, the core layer is selectively photobleached under the UV light to form channel waveguides. For the upper cladding layer, a UV-curable epoxy, NOA61 (Norland Optical Adhesive 61) is spin-coated to be 2 μm thick, and cured by exposing under the UV light. After each spin-coating the polymer is baked sufficiently. The top electrodes are formed in the same way as the bottom electrodes. Over the top electrodes, the photoresist is spin-coated and baked completely. It serves as an electrical insulating layer to prevent the air-breakdown between adjacent top electrodes of the TE-pass polarizers during the poling. The device is poled on a hot-plate at 135 °C by applying poling voltages across the electrodes. Finally, the sample is cleaved for the light coupling.

To find the appropriate bleaching time and poling voltage for matched mode profiles, the guided mode profiles of the three waveguides were observed by a CCD-camera. Fig. 3 shows the lateral mode profile of each waveguide at the wavelength of 1.3 μm. A well confined single mode was obtained for the

bleached waveguide with W_s of 6 μm after bleaching 24 hours with the light intensity of 8 mW/cm^2. The vertically poled waveguide has W_e of 4 μm and the horizontally poled waveguide has W_g of 6 μm. They were poled at 400 V. It is shown that the three different waveguides have similar guided mode profiles. The measured spot sizes are 12.0 μm, 11.9 μm, and 12.4 μm for the vertically-poled, the horizontally-poled, and the photobleached waveguides, respectively. By integrating these waveguides, polarizers with low excess loss were fabricated.

To measure the polarization filtering efficiency, the polarization of the input light was set to have both TE and TM components. The light was butt coupled into the device. Then, the output light from the device was passed through a Glan-Thompson polarizer and detected by a photodiode. In front of the detector, an iris was used to block the radiated light out of channel waveguide. The power in each polarization component of the output light was measured by rotating the Glan-Thompson polarizer to the proper position. As a function of poling voltages, the polarization extinction ratio of each filter was measured and shown in Fig. 4. To measure the excess loss of the device, straight waveguides were also fabricated next to the polarizers by the photobleaching method. For the TM polarized input light, the throughputs of TM-pass polarizers and the bleached waveguides were measured. The excess loss was calculated by subtracting the throughput of the polarizer from that of the bleached waveguide. The excess loss of the TE-pass polarizer was also measured similarly. The measured excess losses are plotted in Fig. 4. The TM-pass polarizer with $W_e = 4$ μm, $W_s = 6$ μm, and $L_f = 1$ mm exhibited the best performance at the poling voltage of 400 V. The polarization extinction ratio was 20.7 dB and the excess loss was 0.2 dB. For the TE-pass polarizer with $W_g = 6$ μm, $W_s = 4$ μm, and $L_f = 3$ mm, the extinction ratio of 17.1 dB and the excess loss of 0.4 dB were obtained when it was poled by 300 V.

In conclusion, we successfully demonstrated TE-pass and TM-pass polymeric waveguide polarizers by integrating photobleached waveguides supporting both TE and TM modes and poling induced polymer waveguides that support either TE or TM modes. This work was partially supported by Korea Science and Engineering Foundation (KOSEF - OERC - 95K3 - 0809 - 01 - 01 - 1) and Korea Ministry of Information and Communications.

REFERENCES

[1] S. Ermer et al., *Organic Thin Films for Photonics Applications*, Oregon, USA, 1995, paper WA2-1.
[2] W. Wang et al., *IEEE Photon. Technol. Lett.*, Vol. 7, pp. 638-640, 1995.
[3] M. C. Oh, S. Y. Shin, W. Y. Hwang, and J. J. Kim, *Appl. Phys. Lett.*, Vol. 67, pp. 1821-1823, 1995.
[4] J. I. Thackara et al., *Appl. Phys. Lett.*, Vol. 52, pp. 1031-1033, 1988.
[5] M. C. Oh, S. S. Lee, and S. Y. Shin, *IEEE J. Quantum Electron.*, Vol. 31, pp. 1698-1704, 1995.
[6] M. B. J. Diemeer et al., *Electron. Lett.*, Vol. 26, pp. 379-380, 1990.
[7] P. G. Suchoski, T. K. Findakly, and F. J. Leonberger, *Optics Letters*, Vol. 13, pp. 172-174, 1988.

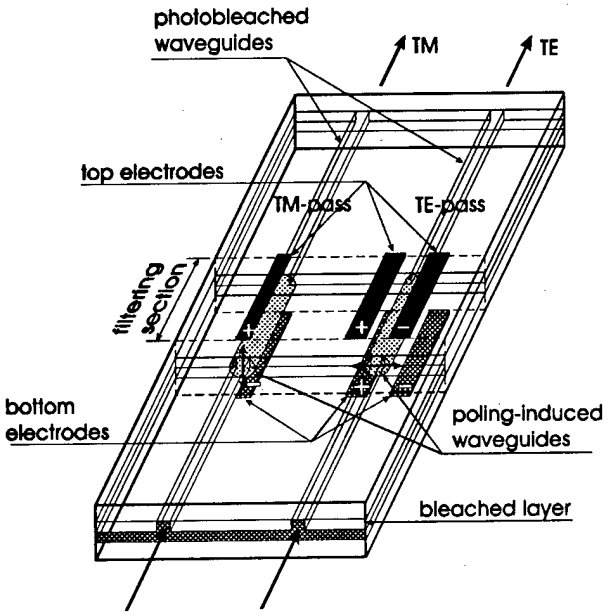


Fig. 1 Schematic diagram of the two types of polymeric waveguide polarizers.

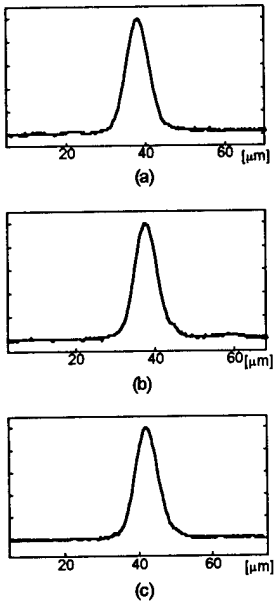


Fig. 3 Lateral mode profiles of various waveguides: (a) a vertically poled waveguide with W_e of 4 μm, (b) a horizontally poled waveguide with W_g of 6 μm, and (c) a photobleached waveguide with W_s of 6 μm.

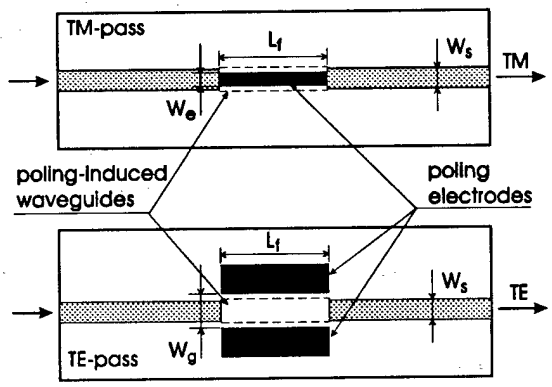


Fig. 2 Top views of the polarizers.

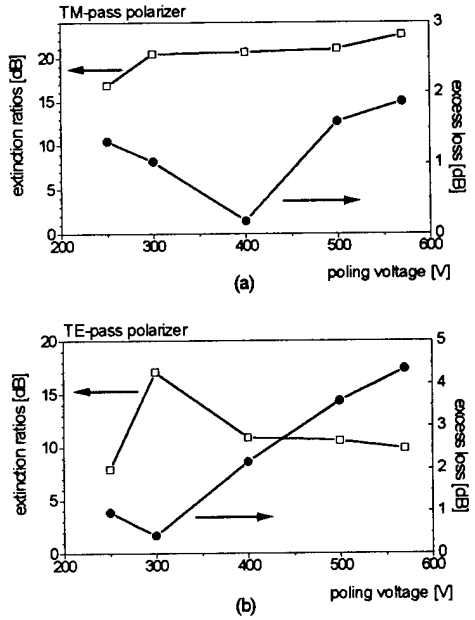


Fig. 4 Measured extinction ratios and excess losses: (a) TM-pass polarizer with W_e = 4 μm, W_s = 6 μm, and L_f = 1 mm, and (b) TE-pass polarizer with W_g = 6 μm, W_s = 4 μm, and L_f = 3 mm.

NEW METAL FREE POLARIZATION SPLITTER ON InGaAsP/InP

Jos J.G.M. van der Tol, Jørgen W. Pedersen, Ed G. Metaal, J. Jan-Willem van Gaalen
Royal PTT Nederland N.V., KPN Research, Leidschendam, The Netherlands,
tel +31 70 332 3642, fax +31 70 332 6477

Y. Siang Oei
Department of Electrical Engineering, Delft University of Technology, The Netherlands,
tel +31 15 2782438, fax +31 15 2784046

Fokke H. Groen
Department of Applied Physics, Delft University of Technology, The Netherlands,
tel +31 15 2784456, fax +31 15 2783251

I INTRODUCTION

Integrated optic polarization splitters are important components for many applications. An example is a coherent optical detection scheme, which uses the concept of polarization diversity. Various concepts for these splitters have been presented in the literature [1]-[10]. For a monolithic integration the polarization splitter must be realized in InGaAsP/InP, since only these semiconductors permit the realization of lasers, detectors, electronics and waveguide components in the 1.3 and 1.5 μm wavelength regions.

Polarization splitters can roughly be divided in two classes. One is based on the mode evolution (or mode sorting) effect [1]-[5]. Mode evolution components are capable of providing relaxed fabrication tolerances, good stability and operation over a broad wavelength range, but generally they are relatively long. The other class of devices is based on interference [6]-[10]. This leads to more stringent fabrication tolerances and to a limited operating wavelength region, but to shorter components. The birefringence needed to obtain different responses for the two polarizations in these splitters is usually created by depositing metal layers on top of the waveguides[8,10].

In this letter we present an interference polarization splitter based on InP. To facilitate integration it is desirable to limit the number of processing steps in the realization of this component. Therefore we developed a polarization splitter based on waveguide birefringence, which can be realized in one etching step and does not require metallization or other overlays.

II CONCEPT

The component utilizes the relatively large waveguide birefringence experienced by the first-order modes of the TE and TM-polarizations in a ridge-type waveguide made in a double heterostructure (DH). Fig. 1 shows the dispersion curves for the modes in such a waveguide.

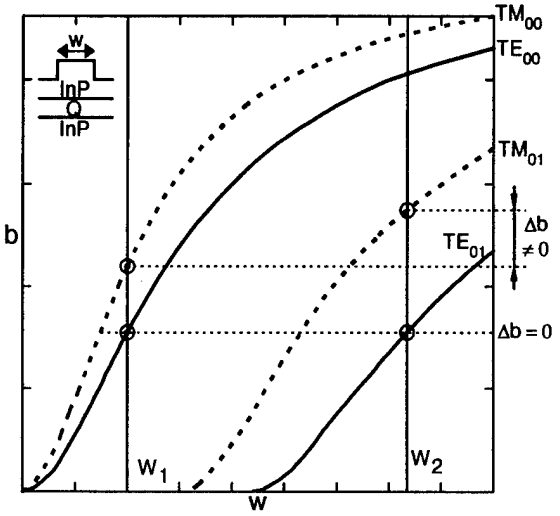


Figure 1: Dispersion curves for the two waveguides in the directional coupler polarization splitter. (Note that "b" is the normalized propagation constant, "W" the width of the ridge).

As indicated in this figure a bimodal and a monomodal waveguide are compared. The TE_{01}-mode in a bimodal waveguide of width W_2 has an identical propagation constant as the TE_{00}-mode of a monomodal waveguide of width W_1. If the two waveguides are used in a directional coupler (Fig. 2) the two modes will exchange energy. TE-polarized light injected in the narrow waveguide will couple completely to the first-order mode of the wide waveguide in a coupler having the right length L.

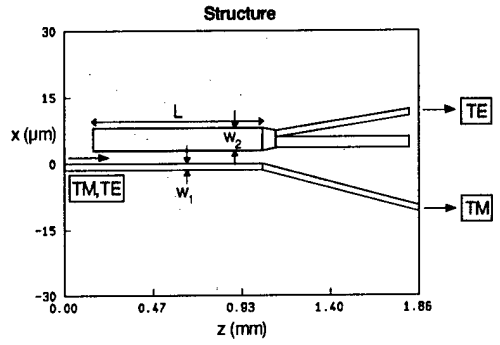


Figure 2: The directional coupler polarization splitter.

The TM_{01}-mode in the bimodal waveguide has a very different propagation constant from the TM_{00}-mode of the monomodal waveguide. Due to this phase mismatch light of this polarization is not transferred to the other waveguide in the directional coupler. In this way polarization splitting is obtained. An asymmetric Y-junction functioning as a mode converter can be used to couple the TE_{01}-mode of the bimodal waveguide to a monomodal output waveguide (Fig. 2).

III FABRICATION AND DESIGN

The device operates at a wavelength of 1.5 µm. The devices are fabricated in a DH InGaAsP/InP MOVPE layer structure. The InP-cover layer thickness is 500 nm and the Q-film layer thickness is 460 nm. The bandgap wavelength of the guiding layer is 1.3 µm.

A silicon nitride etch mask is defined using photolithography with contact UV exposure. All components are made on the same substrate in one etching step. The waveguide structures are realized with CH_4/H_2 reactive ion etching.

The design of the polarization splitter has been done with a film mode matching technique [11] for an etching depth of 325 µm. The width of the monomodal waveguide in the directional coupler is 1.5 µm, the bimodal waveguide is 5.0 µm wide. The gap between these two waveguides is 2 µm, leading to a predicted coupling length of 533 µm. In the actual mask design the length L of the coupler was varied to allow characterization of the coupling behavior. The bimodal waveguide is connected via a taper to the stem of the asymmetric Y-junction, which consists of two branches of 1.5 and 2.5 µm wide with a branching angle of 0.4 degree. To minimize coupling effects between the Y-junction and the outlet of the narrow waveguide in the directional coupler, this outlet makes an angle of 0.66 degree with the nearest branch of the Y-junction. The results of BPM-simulations on the splitter, reduced to two dimensions with the effective index method, are shown in Fig. 3. The simulated splitting ratio, defined in dB using the power ratio of the non-dominant (unwanted) and the dominant (wanted) exit port, is -20 dB for TE and -26 dB for TM-polarization. The BPM is also used to simulate the tolerance in etching depth of the device, which is the most critical fabrication parameter. It was found that for this design the splitting ratio is better than -10 dB for both polarizations over a range in etching depth of 25 nm.

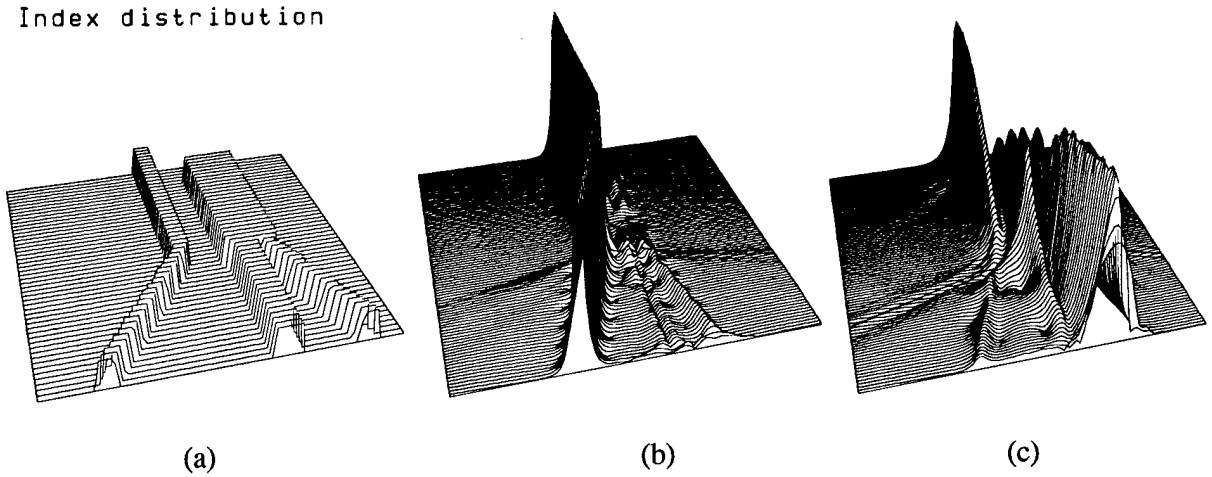


Figure 3: BPM-simulations of the component in figure 2.
(a): Effective index distribution, (b): propagation of a TM-polarized mode. (c): propagation of a TE-polarized mode.

IV RESULTS

The polarization splitters are characterized by transmission measurement using a FP-laser at a wavelength of 1.5 µm. In Fig. 4 the operation of the polarization splitters is demonstrated with photographs of the exit facet of the chip. It is seen that also the dummy channel of the asymmetric Y-junction captures some light, but this is never more than 20 percent of the total output power. The polarization splitters are characterized as a function of the length L of the coupling section (see Fig. 5). The fraction of the power from the straight through port ("TM"-port) is determined. This fraction shows an oscillating behavior with L for the TE-polarization, as is required in a directional coupler. The splitting ratio is -20 dB for the coupler with interaction length 400 µm, in agreement with BPM simulations. The coupling length is found from the oscillation to be 570 µm, which is comparable to the design value. The difference between the coupling length and the optimum interaction length indicates that some coupling is taking place in the taper and the Y-junction. For the TM-polarization, despite the phase mismatch between the guided modes, some undesirable coupling is found. This limited the best splitting ratio for the TM-polarization to -14 dB. It is presumably caused by spurious radiation modes, due to the roughness of the waveguides. Similar couplings between well-separated straight waveguides were observed for the TM-polarization on all chips realized with this etching depth. The splitter with the best performance for both polarizations simultaneously has an interaction length of 500 µm with splitting ratio of -10 dB for TE and -14 dB for TM. This is a sufficient performance for most applications, but reducing the influence of the radiation modes might improve the components strongly.

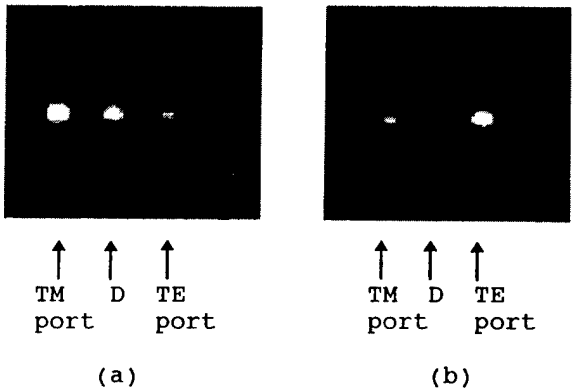


Figure 4: Output power distribution for the (a) TE- and (b) TM-polarization. "D" indicates the dummy exit via the wide branch of the Y-junction.

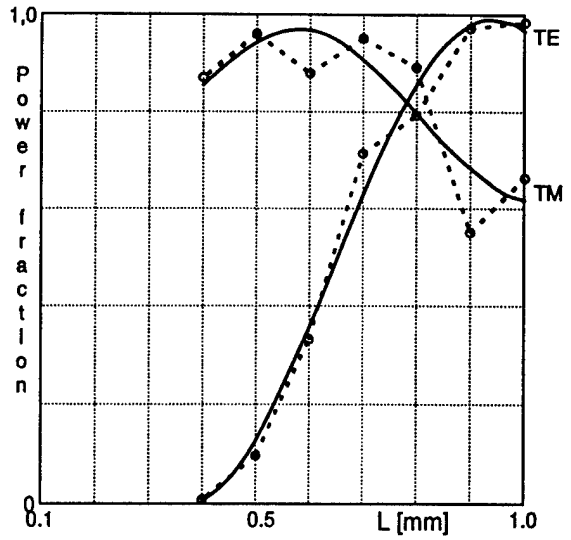


Figure 5: Experimental results. The fraction of the power emanating from the "TM"-port is shown as a function of the length of the directional coupling section, for both polarizations. The smooth curves indicate sine functions fitted to the data.

The excess loss of the splitters is measured by comparing the total throughput (but excluding the power from the dummy channel) with that of adjacent straight waveguides. This loss was found to be less than 1 dB for both the TM and the TE-polarization.

V CONCLUSIONS

A polarization splitter on InGaAsP/InP is presented which is based on a polarization selective directional coupler without the use of metal overlays. The length of the component is 1.5 mm, including an output section of 1 mm. This is the shortest polarization splitter without overlays reported to date.

If the polarization splitter is directly integrated with photo-detectors an output section is unnecessary, and a polarization splitter of sub-millimeter dimensions is obtained. The component does not require any extra processing beyond that necessary for waveguide fabrication. It is realized in a single etching step, which makes it attractive for integration. The realized components are characterized at 1.5 µm wavelength and show polarization splitting. Splitting ratio for the TE-polarization at the optimum interaction length are close to -20 dB, while fro the TM-polarization splitting ratios were limited to -14 dB due to spurious coupling effects. Excess losses are below 1 dB for both polarizations.

VI ACKNOWLEDGMENTS

The authors thank A.H.M. van der Hoff for his contribution in the design of the mask and in the characterization. M. Babeliowsky and P. Peters have reviewed the manuscript. Furthermore, the authors wish to thank G. Krijnen and H. Hoekstra of the University of Twente (The Netherlands) for the use of their BPM-program.

REFERENCES

[1] Y. Shani, C. H. Henry, R. C. Kistler, R. F. Kazarinov, and K. J. Orlowsky, "Integrated optic adiabatic polarization splitter on silicon," Appl. Phys. Lett., vol. 56, no. 2, pp. 120-121, 1990.

[2] N. Goto and G. L. Yip, "A TE-TM mode splitter in $LiNbO_3$ by proton exchange and Ti diffusion," J. Lightwave Technol., vol. 7, no. 10, pp. 1567-1574, 1989

[3] J.J.G.M. v.d. Tol and J.H.Laarhuis: "A polarization splitter on lithium niobate using titanium diffusion only," J. Lightwave Technol., vol. LT-9, no. 7, pp. 879-886, July 1991.

[4] M.B.J. Diemeer and J.J.G.M. van der Tol, "Integrated optical polarization splitter", US patent no. 5.056.883, Oct. 1991.

[5] J.J.G.M. van der Tol, J.W. Pedersen, E.G. Metaal, Y.S. Oei, H. van Brug and I. Moerman, "Mode evolution type polarization splitter on InGaAsP/InP", IEEE Photonic Technol. Letters, december 1993, Vol. 5, No. 12, pp. 1412-1414.

[6] D. Yap, L. M. Johnson, and G. W. Pratt, Jr., "Passive Ti:$LiNbO_3$ channel waveguide TE-TM mode splitter," Appl. Phys. Lett., vol. 44, no. 6, pp. 583-585, 1984.

[7] A.R. Vellekoop, and M.K. Smit, "A small-size polarization splitter based on a planar optical phased array," J. Lightwave Technol., vol. LT-8, no. 1, pp. 118-124, Jan. 1990.

[8] P. Albrecht, M. Hamacher, H. Heidrich, D. Hoffman, H.-P. Nolting, and C.M. Weinert, "TE/TM Mode Splitters on InGaAsP/InP," IEEE Phot. Technol. Lett., vol. 2, no. 2, pp. 114-115, Febr. 1990.

[9] J.W. Pedersen, J.J.G.M. van der Tol, E.G. Metaal, Y.S. Oei, F.H. Groen and I. Moerman, "Mode converting polarization splitter on InGaAsP/InP", paper We.C.2.2., ECOC'94.

[10] L. Soldano, A.H. de Vreede, M.K. Smit, B..H. Verbeek, E.G. Metaal and F.H. Groen, "Mach-Zehnder Interferometer Polarization Splitter in InGaAsP/InP", IEEE Photonic Technol. Letters, vol. 6, no. 3, march 1994, pp. 402-405.

[11] A.S. Sudbø, "Film mode matching: a versatile field calculation in dielectric waveguides", Pure and Applied Optics, vol. 2, 1993, pp. 211-233.

Integrated-Optics versus Micro-Optics - a Comparison

E.C.M. Pennings*, M.K. Smit#, A.A.M. Staring*, and G.-D. Khoe&

* *Philips Optoelectronics Centre, WY-61, Prof. Holstlaan 4, 5656 AA Eindhoven, The Netherlands*
Phone: +31-40-2743037 / Fax: +31-40-2743859 / E-mail: epenning@natlab.research.philips.com
Delft University of Technology, Fac. of Electr. Eng., Mekelweg 4, 2628 CD Delft, The Netherlands
Phone: +31-15-2782438 / Fax: +31-15-2784046 / E-mail: M.K.Smit@ET.TUDelft.NL
& *Technical University of Eindhoven, EH-12, PO Box 513, 5600 MB Eindhoven, The Netherlands*
Phone: +31-40-2473452 / Fax: +31-40-2455197 / E-mail: G.D.Khoe@ele.tue.nl

Introduction

It is the purpose of this paper to assess the relative merits and prospects of integrated-optic versus micro-optic devices for fiber-optic telecommunication systems. Firstly, this comparison is made from a market perspective. Then, the analogy between electronic and photonic integrated circuits is investigated. Finally, a specific comparison is made for wavelength demultiplexers for dense WDM applications. A comparison similar to this one but also including polarization-diversity hybrids can be found in Ref. 1.

In this paper, the following classification is used:

- *Fiber-based* devices, such as couplers, which are exclusively made from fiber.
- *Integrated-optic* devices, where light is guided in planar waveguides.
  - *Single-component* devices, such as lasers, laser amplifiers, and phase-modulators.
  - *Photonic integrated circuits*, where a number of optical devices are monolithically integrated.
- *Micro-optic* devices, which rely on diffractive or reflective bulk elements such as lenses or mirrors.
- *Modules*, which are assembled from any of the above elements.

The fiber-optic component market

Figure 1 shows the fiber-optic component market for 1992 and 1997 in the US. A direct comparison between integrated-optic and micro-optic techniques can only be made for passive components and Fig. 1 shows that the comparison therefore applies to the smaller part of the market (15%), since the larger part consists of active devices such as lasers and photodiodes. For passive components, the largest market segment is formed by couplers (11%) which are almost exclusively fiber-based. This shows that the market segments captured by integrated-optic and micro-optic products are both quite small (of the order of 1% - 2%). The micro-optic segment consists of products such as switches, isolators/circulators, attenuators, and filters. The integrated-optic segment mainly consists of $LiNbO_3$ switches and modulators. Another proven integrated-optic product (though active) is the DFB laser with integrated electro-absorption modulator.

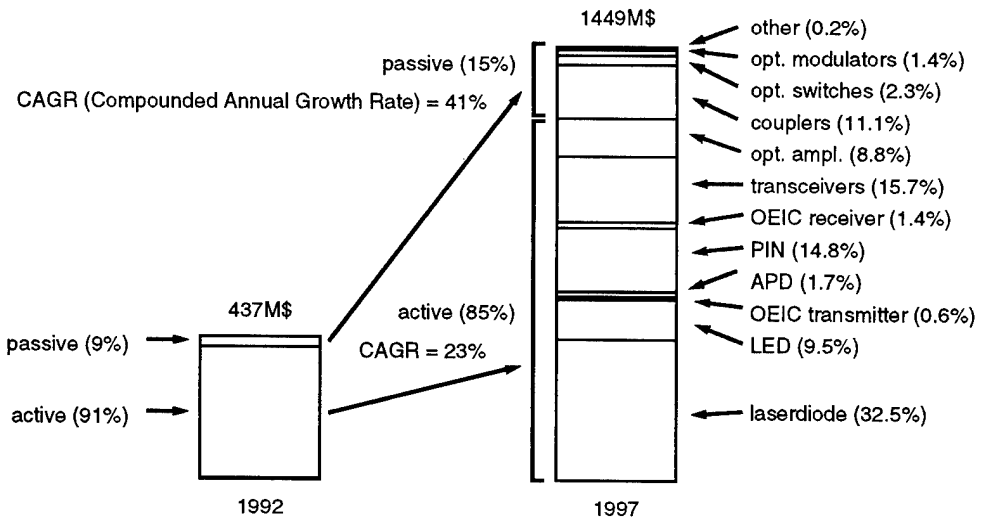


Figure 1: The 1997 US fiber-optic component market forecast (source: ElectroniCast'92).

The market analysis shows that the demand for components with a larger degree of optical functionality has been negligible so far. This is important because the competitive edge for PIC's is precisely in integrating complex optical functionality. This situation, however, is likely to change: the market is not only *growing* fast (more than 25% a year), but also *changing* due to the rapid commercialization of WDM systems. However, the first WDM transmission systems will merely require optical devices with a single functionality, so that the demand for complex optical functionality will only increase *later on*, i.e. when the wavelength domain is used to realize add-drop multiplexing and cross-connecting functions.

Technological considerations

It has been argued many times that the competitive edge of photonic IC's comes from increased scale of integration plus the corresponding cost reduction. This argument is in fact based on an implicit analogy between photonic and electronic IC's. This analogy, however, has to be treated with care. Firstly, the markets for photonic and electronic IC's are very different: as was argued in the previous section, the demand for complex optical functionality is still in its infancy. Secondly, there are several technical reasons why photonic and electronic IC's are quite different:

Packaging is much more difficult for photonic than for electronic IC's. Packaging related issues are the fiber-chip coupling problem which leads to the use of tapers and lenses, the influence of reflections and the accompanying use of isolators, and temperature sensitivity which can necessitate Peltier coolers and thermistors. It is important to notice that these packaging issues form, on one hand, the major *economic* incentive for integration, but that they, at the same time, form a *technical* obstacle against integration.

The scale of integration seen in electronic IC's is directly related to intrinsic on chip amplification and feedback which allow for accurate performance control and thus for the ability to cascade a large number of components. So far, optical feedback is not feasible in photonic IC's and integrated optical amplifiers are in their infancy. Even more important is that the characteristic size of the building blocks for photonic and electronic IC's differ by at least two to three orders of magnitude. Lastly, whereas electronic IC's contain many duplicates of a small set of building blocks, most photonic IC's integrate a number of very different elements. The accompanying problem of optimizing the performance of each individual sub-element complicates the design and leads to compromises in performance.

As a result, photonic IC's will follow their own rule of economy, different from electronic IC's, and will reach a more limited scale of integration. In order to reach that limit and speed up commercialization, additional effort will be required to reduce packaging costs, incorporate on-chip amplification, reduce component size, and to develop improved processes and fabrication-tolerant components.

Wavelength demultiplexers for dense WDM applications: a comparison

In this section, a specific comparison is made for a key component in OFDM networks, i.e. the wavelength demultiplexer for dense WDM applications. The development of these demultiplexers is shown in Fig. 2.

Fiber-based: The lack of fiber-based demultiplexers in Fig. 2 illustrates the unsuitability of fibers to demultiplex many closely spaced wavelengths *simultaneously*. Fibers are, on the other hand, very suitable to demultiplex two widely spaced wavelengths (i.e. duplexers), which are typically used for two-channel transmission systems (e.g. 1.31/1.55μm), or in EDFA's (0.98/1.55μm and 1.48/1.55μm). It is important to notice that duplexers form more than 90% of the demultiplexer market and are almost entirely fiber-based.

Modules: Fibers can, of course, be used in combination with *filters* to realize wavelength demultiplexers for dense WDM. These filters can be placed in series (cascaded) or in parallel by using a fiber splitter. Popular filters are the (fixed) interference filter[2] and the tunable (fiber) Fabry-Pérot filter.

Micro-optics: Fig. 2 shows that much of the work on micro-optical demultiplexers was already published in the early eighties[3-6] when MM fibers were used with wavelengths of λ=700-900nm. The subsequent reduction of interest was due to the shift of focus to coherent detection schemes. In the late eighties, when interest in WDM revived, work on micro-optical demultiplexers continued[7-11] and several earlier designs were commercialized. Micro-optical wavelength demultiplexers can be divided into the cascaded interference filter type and the grating-based type. Recently, the phased array design, which is typical for integrated optics, has also been realized in micro-optics[12].

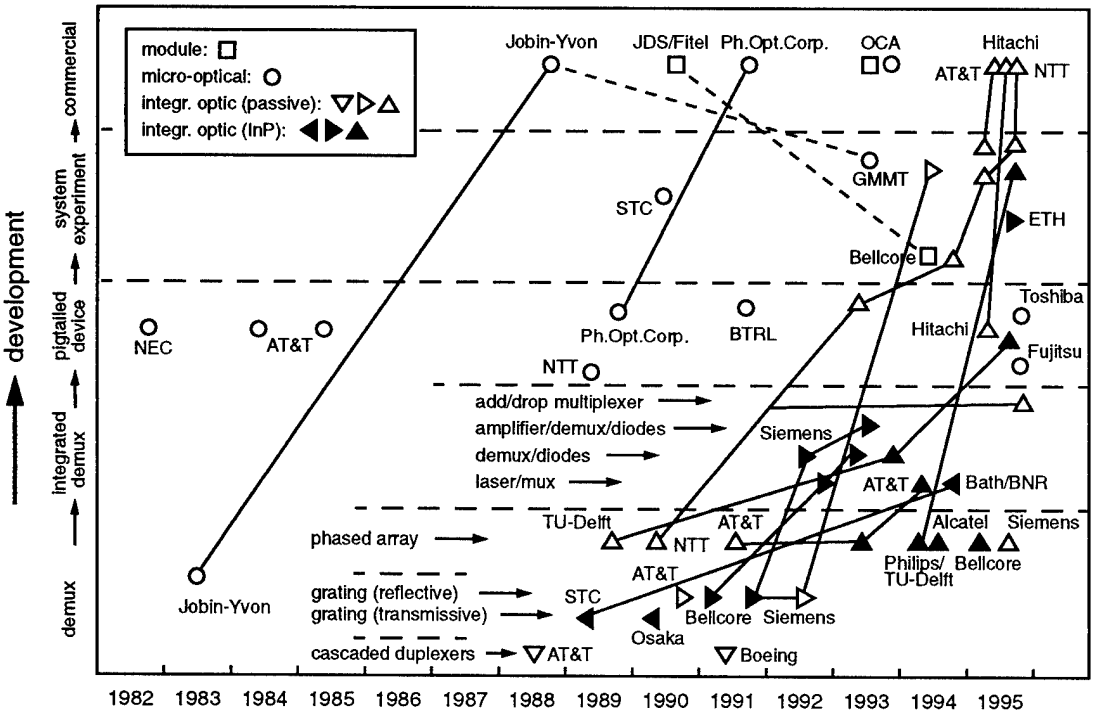


Figure 2. Overview of reported wavelength demultiplexers and their development in time.

Integrated optic: The first integrated optic demultiplexers appeared in the late eighties and relied on cascaded duplexers[13-14]. Soon afterward, planar versions of the micro-optic grating based demultiplexer were reported[15-20,21-22]. An alternative design is the phased array (PHASAR) or arrayed waveguide grating (AWG)[23-30]. This design has recently gained in importance due to superior performance and ease of processing. Fig. 2 shows how integrated-optic demultiplexers have subsequently been integrated into more complex PIC's (such as lasers[31-33], receivers[34-37,38], and an add/drop multiplexer[39]) and how they have been used in various system experiments[40,41-45]. It seems that this development is accelerating which is, for example, demonstrated by the rapid commercialization[46] of the Si-based demultiplexers.

Discussion and conclusion. The performance of a variety of commercial demultiplexers is compared in Table 1. The splitter plus filter configuration is rather popular due to its simplicity and tunability, but it poses an intrinsic splitter loss of 10·log(N) and may show unwanted back-reflections. *Fixed* demultiplexers will gain in importance, as soon as WDM channels have been *standardized*. For cascaded filters, the loss increases proportional to number of channels, which limits its suitability to 4-8 channels. Micro-optic demultiplexers offer proven reliability in addition to excellent performance in terms of number of

Table 1: Overview of performance of commercial wavelength demultiplexers.

Technique	Type	N	Δλ (nm)	Ins.Loss (dB)	Ret.Loss (dB)	X-talk (- dB)	Drift (nm/°C)	Pol.Dep. (dB)	Vendor
Module	Splitter + FFP-filter			<1.5-2.5	?	?	Act. tuning	<0.5	Micron Optics
				<4	>22-40	?	Act. tuning	?	Queensgate
	Cascaded filters			<1.5	>40-55	>15	0.004	?	OCA
Micro-Optic	Cascaded filter	4-8	1.6	<3-4	>40-55	>30	0.004	<0.1	OCA
	Grating	4-41	1-16	<3-5	?	>30-55	0.02-0.004	?	Jobin-Yvon
Integr.-Optic	PHASAR (passive)	8	?	<10	>25	>20	?	<1	Hitachi
		8	1.61	<10	>30	>20	0.01(tuning)	?	AT&T
		4-32	0.8-2	<6-7	>40	>20-22	Peltier/NTC	<0.3	NTT

channels, insertion loss, cross-talk, polarization-dependence and thermal stability[47]. Integrated optic demultiplexers, especially the phased array type, have seen an enormous development and the recently commercialized Si-based demultiplexers show a very competitive performance. The performance of these commercial versions can, however, not yet match that of micro-optic versions. This leads us to conclude that the real breakthrough for integrated optics has to be expected when both technology and market are ready for photonic IC's with increased functionality due to a larger scale of integration.

References

[1] E.C.M. Pennings *et al., Proc. MOC'95,* (Oct. 18-20, 1995, Hiroshima, Japan), paper J1.
[2] L. Eskildsen *et al., IEEE Photon. Technol. Lett.*, vol. 6, no. 11, pp. 1321-1323, 1994.
[3] M. Seki *et al., Electron. Lett.*, vol. 18, no. 6, pp. 257-258, 1982.
[4] J.P. Laude *et al., Proc. 9th ECOC '83,* (Oct. 23-26, 1983, Geneva, Switzerland), pp. 417-420.
[5] J. Hegarty *et al., Electron. Lett.*, vol. 20, no. 17, pp. 685-686, 1984.
[6] J. Lipson *et al., J. Lightw. Technol.*, vol. 3, no. 5, pp. 1159-1162, 1985.
[7] Y. Fujii *et al., Appl. Opt.*, vol. 28, no. 7, pp. 1305-1308, 1989.
[8] B. Moslehi *et al., Opt. Lett.*, vol. 14, no. 19, pp. 1088-1090, 1989.
[9] G.J. Cannell *et al., IEEE J. Sel. Areas. in Comm.*, vol. 8, no. 6, pp. 1141-1145, 1990.
[10] D.R. Wisely *et al., Electron. Lett.*, vol. 27, no. 6, pp. 520-521, 1991.
[11] K.J. Hood *et al., J. Lightw. Technol.*, vol. 11, no. 5/6, pp. 680-687, 1993.
[12] M. Shirasaki, *Proc. MOC'95,* (Oct. 18-20, 1995, Hiroshima, Japan), paper PD3.
[13] B.H. Verbeek *et al., J. Lightw. Technol.*, vol. 6, no. 6, pp. 1011-1015, 1988.
[14] J.P. Lin *et al., Opt. Lett.*, vol. 16, no. 7, pp. 473-475, 1991.
[15] M. Gibbon *et al., Electron. Lett.*, vol. 25, no. 21, pp. 1441-1442, 1989.
[16] S. Ura *et al., Appl. Opt.*, vol. 29, no. 9, pp. 1369-1373, 1990.
[17] C.H. Henry *et al., J. Lightw. Technol.*, vol. 8, no. 5, pp. 748-755, 1990.
[18] J.B.D. Soole *et al., Electron. Lett.*, vol. 27, no. 2, pp. 132-134, 1991.
[19] C. Cremer *et al., Appl. Phys. Lett.*, pp. 627-629, 1991
[20] P.C. Clemens *et al., IEEE Photon. Technol. Lett.*, vol. 4, no. 8, pp. 886-887, 1992.
[21] J.G. Bauer *et al., Proc. ECOC'94* (Sept. 25-29, 1994, Florence, Italy), pp.751-754.
[22] E. Gini *et al., Proc. ECOC'95,* (Sept. 17-21, 1995, Brussels, Belgium) pp. 207-210.
[23] A.R. Vellekoop *et al., Proc. ECOISA'89,* (Sept. 25-28, 1989, Amsterdam, The Netherlands), paper D3.
[24] H. Takahashi *et al., Electron. Lett.*, vol. 26, no. 2, pp. 87-88, 1990.
[25] C. Dragone, *IEEE Photon. Technol. Lett.*, vol. 3, no. 10, pp. 896-899, 1991.
[26] M. Zirngibl *et al., Electron. Lett.*, vol. 29, no. 2, pp. 201-202, 1993.
[27] B.H. Verbeek *et al., Proc. OFC'94,* (Febr. 20-25, 1994, San Jose, USA), post-deadline paper PDP13.
[28] H. Bissessur *et al., Electron. Lett.*, vol. 30, no. 4, pp. 336-337, 1994.
[29] M.R. Amersfoort *et al., Proc. IPR'95,* (Febr. 23-25, 1995, Dana Point, USA), post-deadline paper PD3.
[30] P.C. Clemens *et al., Proc. 7th ECIO'95,* (April 3-6, 1995, Delft, The Netherlands), pp. 505-508.
[31] J.B.D. Soole *et al., Electron. Lett.*, vol. 28, no. 19, pp. 1805-1807, 1992.
[32] M. Zirngibl *et al., Electron. Lett.*, vol. 30, no. 9, pp. 701-102, 1994.
[33] M. Asghari *et al., Electron. Lett.*, vol. 30, no. 20, pp. 1674-1675, 1994.
[34] C. Cremer *et al., IEEE Photon. Technol. Lett.*, vol. 4, no. 1, pp. 108-110, 1992.
[35] J.B.D. Soole *et al., Electron. Lett.*, vol. 29, no. 6, pp. 558-560, 1993.
[36] C. Cremer *et al., Proc. ECIO'93,* (April 18-22, 1993, Neuchâtel, Switzerland), p. 2-10.
[37] M.R. Amersfoort *et al., Proc. ECOC'93,* (Sept. 12-16, 1993, Montreux, Switzerland), post-deadline, pp. 49-52.
[38] C.A.M. Steenbergen *et al., Proc. ECOC'95,* (Sept. 17-21, 1995, Brussels, Belgium) pp. 211-214.
[39] K. Okamoto *et al., Proc. OFC'95,* (Febr. 26 - Mar. 3, 1995, San Diego, USA), paper PD10.
[40] Y. Tachikawa *et al., Electron. Lett.*, vol. 29, no. 24, pp. 2133-2134, 1993.
[41] S. Suzuki *et al., Electron. Lett.*, vol. 30, no. 13, pp. 1091-1092, 1994.
[42] O. Ishida *et al., Proc. OFC'95,* (Febr. 26 - Mar. 3, 1995, San Diego, USA), paper PD9.
[43] B.R. Hemenway *et al., Proc. OFC'95,* (Febr. 26 - Mar. 3, 1995, San Diego, USA), paper PD8.
[44] L.H. Spiekman *et al., Proc. ECOC'95,* (Sept. 17-21, 1995, Brussels, Belgium) pp. 1055-1058.
[45] K. Oda *et al., Proc. ECOC'95,* (Sept. 17-21, 1995, Brussels, Belgium) pp. 59-62
[46] H. Uetsuka *et al., Proc. OFC'95,* (Febr. 26 - Mar. 3, 1995, San Diego, USA), paper TuO7.
[47] M. Miyachi *et al., Proc. ECOC'95,* (Sept. 17-21, 1995, Brussels, Belgium) pp. 67-70.

High - Speed Polarization Scrambler with Adjustable Frequency Chirp

Fred Heismann and Robert W. Smith *

AT&T Bell Laboratories, 101 Crawfords Corner Road, Holmdel, NJ 07733-3030
** AT&T Bell Laboratories, 9999 Hamilton Blvd., Breinigsville, PA 18031-9359*

INTRODUCTION – High-speed polarization scramblers can substantially improve the performance of optically-amplified transoceanic lightwave systems by depolarizing the launched optical information signal, thus eliminating anisotropic gain saturation (polarization hole burning) in the erbium-doped fiber amplifiers [1]–[3]. Moreover, additional bit-synchronous phase modulation at the clock frequency of the optical information signal can further improve the performance of non-return-to-zero (NRZ) systems through a partial, nonlinear conversion of the phase modulation into amplitude modulation [4]–[5]. It is also well known that a conventional, single waveguide phase modulator on *z*-cut lithium niobate ($LiNbO_3$) generates a combination of polarization and phase modulation if the input light is linearly polarized at 45° [3], [6]. Applying a voltage, $V(t)$, to the drive electrode of this simple modulator induces different optical phase shifts for the TE- and TM-polarized modes via the r_{13} and r_{33} electro-optic coefficients, respectively. The induced phase shift for the TM-polarized mode, $\Phi_{TM}(t)$, is given by

$$\Phi_{TM}(t) = \Gamma \frac{r_{33}}{\lambda_0} V(t) \ , \qquad (1)$$

where Γ is a constant, λ_0 the optical wavelength in free space, and $r_{33} \approx 30.8 \times 10^{-12}$ m/V [3], [6]. Similarly, the induced phase shift for the TE-polarized mode, $\Phi_{TE}(t)$, is given by

$$\Phi_{TE}(t) = \Gamma \frac{r_{13}}{\lambda_0} V(t) \ , \qquad (2)$$

where $r_{13} \approx 8.6 \times 10^{-12}$ m/V. Note that the two phases are shifted in the same direction but at substantially different rates ($r_{33} \approx 3.6\, r_{13}$). This gives rise to a differential TE-TM phase retardation, $\Phi(t)$, with $\Phi(t) = \Phi_{TM}(t) - \Phi_{TE}(t) = (\Gamma/\lambda_0)(r_{33} - r_{13})\, V(t)$, and, in addition, to a common phase modulation, $\exp(j\Psi(t))$, with $\Psi(t) = (\Phi_{TM}(t) + \Phi_{TE}(t))/2 = (\Gamma/2\lambda_0)(r_{33} + r_{13})\, V(t)$, Hence, the relative amounts of phase and polarization modulation are determined by the ratio $(r_{33} + r_{13})/(r_{33} - r_{13})$ [3].

In this paper we report on the operation and performance of a novel high-speed polarization scrambler with independently adjustable phase and polarization modulation. In particular, this scrambler can produce chirp-free polarization modulation as well as pure phase modulation.

OPERATION – Fig. 1 shows two slightly different versions of this high-speed polarization scrambler / phase modulator. In both schemes, the adjustable phase / polarization modulation is generated by varying the optical phases of two orthogonally polarized modes independently of each other using two separate phase modulators. Both schemes are based on a Mach-Zehnder-type interferometer using a conventional Y-branch splitter in the input and a bulk-optic polarization splitter/combiner (PBS) in the output, which is connected to the two arms of the interferometer via polarization maintaining fibers (PMF). The Y-branch splitter and the two high-speed phase modulators are integrated on a *z*-cut $LiNbO_3$ substrate, using standard single-mode waveguides [7]. The modulator in Fig. 1 (b) comprises an additional 3-dB directional coupler on the $LiNbO_3$ substrate, located after the phase modulators.

In both cases, the input light to the $LiNbO_3$ modulator is TM-polarized and is equally divided between two parallel waveguide phase modulators which independently modulate the optical phases of the TM-polarized light in the two arms, $\Phi_1(t)$ and $\Phi_2(t)$, via the r_{33} electro-optic coefficient, similar to Eq. (1). In Fig. 1 (a), the two phase modulated waves are combined in orthogonal polarization states by converting one of the signals into TE-polarized light before it enters the PBS. The normalized amplitudes of the TE- and TM-polarized components after the PBS, A_{TM} and A_{TE}, are described by the Jones vector

$$\begin{bmatrix} A_{TM} \\ A_{TE} \end{bmatrix} = \frac{1}{\sqrt{2}} \begin{bmatrix} \exp(\Phi_1(t)) \\ \exp(\Phi_2(t)) \end{bmatrix} \ , \qquad (3)$$

where we have assumed identical optical path

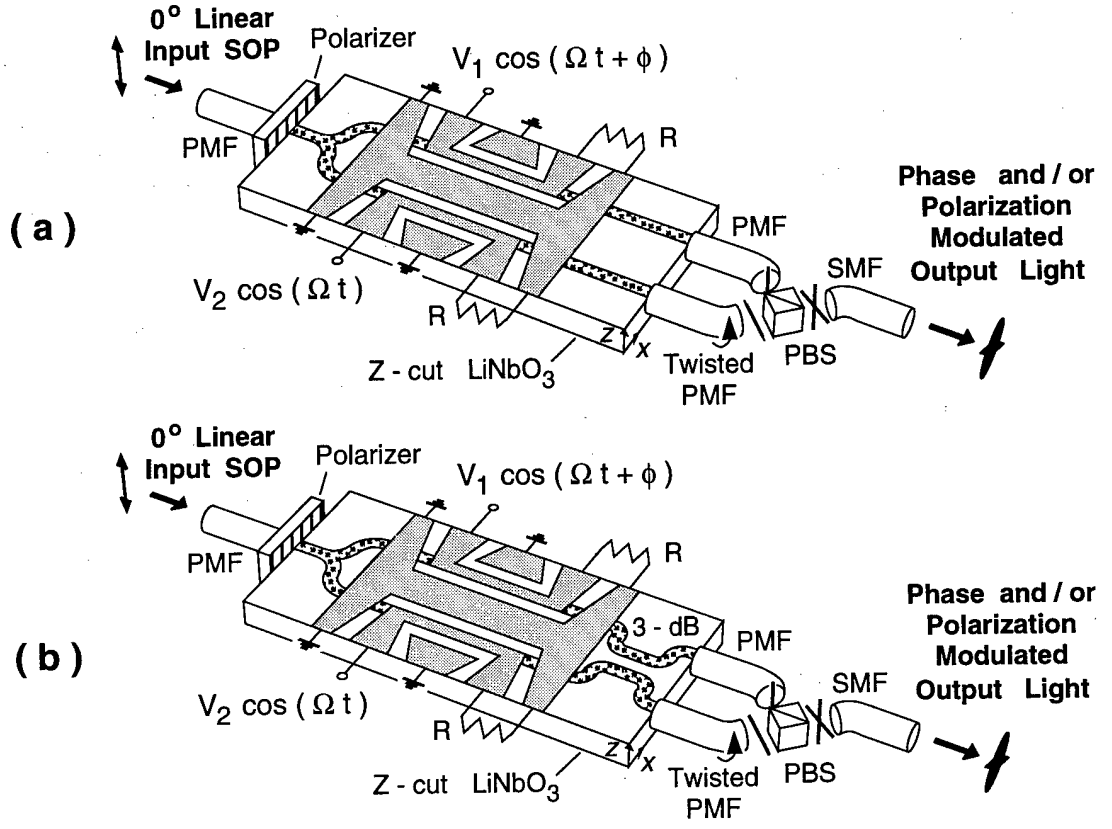


Fig. 1. *Schematic diagrams of two high-speed polarization scramblers with continuously adjustable phase modulation, implemented on z-cut lithium niobate ($LiNbO_3$) : (a), comprising two parallel phase modulators interconnected by an input Y-branch and an output polarization beam splitter (PBS); (b), based on an integrated-optic Mach-Zehnder interferometer followed by a PBS. In both cases, the TM-polarized light from the two output ports of the $LiNbO_3$ chip is combined in orthogonal polarization states using properly oriented polarization maintaining fiber (PMF).*

lengths in the two arms. The differential TE-TM phase retardation is then given by $\Phi(t)=\Phi_1(t)-\Phi_2(t)$ and the common phase shift by $\Psi(t)=(\Phi_1(t)+\Phi_2(t))/2$.

In the scheme of Fig. 1 (b), the two phase modulated signals are mixed in a 3-dB directional coupler before they are combined in orthogonal polarization states. The 3-dB coupler converts the differential phase retardation, $\Phi(t)$, into amplitude modulation while leaving the common phase modulation, $\Psi(t)$, essentially unchanged [8]. The output powers of the 3-dB splitter are proportional to $\cos^2(\Phi(t)/2+\pi/4)$ and $\sin^2(\Phi(t)/2+\pi/4)$. Thus, the amplitudes of the TE- and TM-polarized signals after PBS are then given by

$$\begin{bmatrix} A_{TM} \\ A_{TE} \end{bmatrix} = \begin{bmatrix} \cos(\Phi(t)/2+\pi/4) \\ \sin(\Phi(t)/2+\pi/4) \end{bmatrix} \times \times \exp\left[j(\Psi(t)-\pi/4) \right] . \quad (4)$$

The operation of this scrambler is therefore similar to that of a phase modulator followed by a variable polarization rotator.

In both schemes, the phase modulators are driven by sinusoidal voltages of the form $V_1 \cos(\Omega t+\phi)$ and $V_2 \cos(\Omega t)$ such that $\Phi_1(t)=\Delta\Phi_1 \cos(\Omega t+\phi)$ and $\Phi_2(t)=\Delta\Phi_2 \cos(\Omega t)$. From Eqs. (3) and (4) it is then easily seen that both scramblers are capable of generating any combination of differential phase retardation, $\Phi(t)$, and common phase modulation, $\Psi(t)$, simply by adjusting the relative drive phase, ϕ, and the

peak phase deviations, $\Delta\Phi_1$ and $\Delta\Phi_2$, generated by the two phase modulators via the drive voltage amplitudes V_1 and V_2. For example, if the two phase modulators are driven with equal voltage amplitudes, $V_1 = V_2$, such that $\Delta\Phi_1 = \Delta\Phi_2$, we obtain

$$\Phi(t) = -\Delta\Phi \sin(\Omega t + \phi/2)$$
$$\Psi(t) = \Delta\Psi \cos(\Omega t + \phi/2) \quad , \qquad (5)$$

with $\Delta\Phi = 2\Delta\Phi_1 \sin(\phi/2)$ and $\Delta\Psi = \Delta\Phi_1 \cos(\phi/2)$, such that $(\Delta\Phi/2)^2 + (\Delta\Psi)^2 = (\Delta\Phi_1)^2$. Note that Φ and Ψ are modulated in quadrature phase. The relative amounts of phase and polarization modulation are determined by the drive phase, ϕ: at $\phi = \pi$ we obtain chirp-free polarization modulation and at $\phi = 0$ pure phase modulation. Similarly, for fixed drive phase $\phi = \pi$ and variable peak phase deviations $\Delta\Phi_1$ and $\Delta\Phi_2$ we find

$$\Phi(t) = (\Delta\Phi_1 + \Delta\Phi_2) \cos(\Omega t + \pi)$$
$$\Psi(t) = \frac{\Delta\Phi_2 - \Delta\Phi_1}{2} \cos(\Omega t) \quad , \qquad (6)$$

where Φ and Ψ are modulated in phase (or anti-phase).

EXPERIMENTAL RESULTS - We have realized the scrambler shown in Fig. 1 (b) using a $LiNbO_3$ modulator with standard titanium-diffused waveguides. The two high-speed phase modulators employ identical, 2-cm-long traveling-wave electrodes. The $LiNbO_3$ modulator has a fiber-to-fiber insertion loss of 3.5 dB and a 3-dB modulation bandwidth of 14 GHz when operated as an intensity modulator. The overall fiber-to-fiber insertion loss of the entire scrambler is less than 5 dB (including fiber connectors). The optical powers in the two arms of the $LiNbO_3$ modulator and the two PMF connections to the PBS have to be well balanced in order to avoid undesired intensity modulation in the output light. Furthermore, the optical path lengths of the two interferometer arms need to be well matched to avoid polarization mode dispersion (PMD). The present device exhibits about 5 ps of PMD and 2 % residual intensity modulation. The coupling ratio in the 3-dB coupler of the MZI modulator, however, is less critical in this application.

Fig. 2 (a) displays the degree of polarization (DOP) in the output light of the scrambler, measured with a HP 8509B polarization analyzer, versus the drive phase ϕ and drive voltage amplitudes $V_1 = V_2$. The scrambler is operated here at a wavelength of 1558 nm and modulated at a frequency of 10 kHz. The first minimum in the DOP occurs at $V_1 = V_2 = 3.45$ V and $\phi = \pi$. At this operating point the scrambler generates chirp-free polarization modulation with $\Delta\Phi = 2.40$ rad and $\Delta\Psi = 0$ rad.

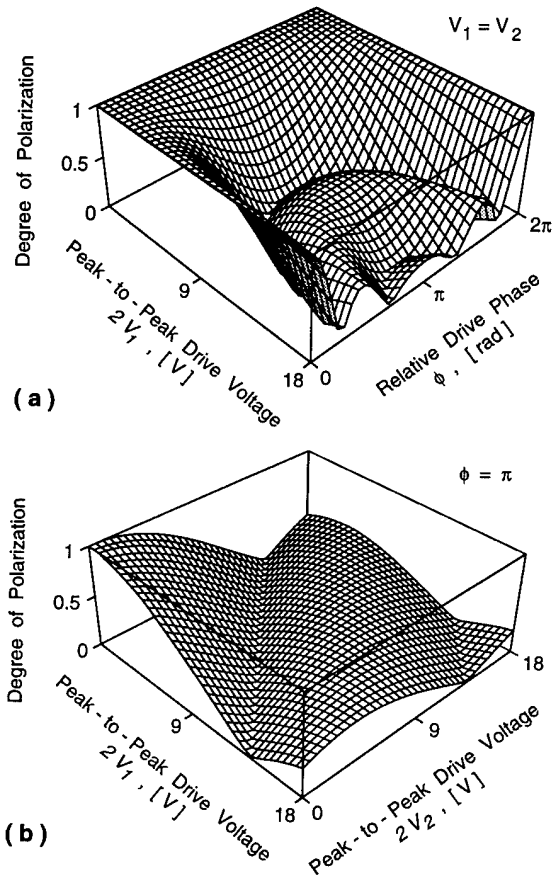


Fig. 2. *Degree of polarization in the output light versus drive voltage amplitudes and phases: (a), for $V_1 = V_2$; (b) for $\phi = \pi$. Modulation frequency is 10 kHz.*

At $V_1 = 3.45$ V and $\phi = 0$, the scrambler produces pure phase modulation with $\Delta\Psi = 1.20$ rad. At voltage amplitudes above 3.45 V, we always find at least two values of ϕ with minimum DOP and the depolarized output light is in general phase modulated. A second chirp-free DOP-minimum occurs at $V_1 = 7.9$ V and $\phi = \pi$, with $\Delta\Phi = 5.52$ rad. At the same voltage amplitude and $\phi = 0.90$, we find another

DOP minimum with large superimposed phase modulation, i.e., $\Delta\Psi = 2.48$ rad and $\Delta\Phi = 2.40$ rad.

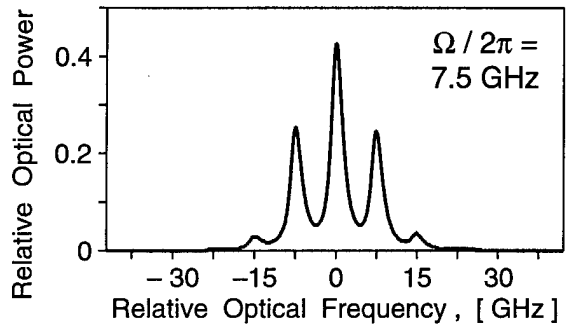


Fig. 3. *Optical output spectrum at the first DOP minimum with $V_1 = V_2$ and $\phi = \pi$. The scrambler is modulated at 7.5 GHz.*

Fig. 2 (b) shows the output DOP versus V_1 and V_2 for fixed drive phase $\phi = \pi$. For each voltage amplitude V_1 we find at least one value of V_2 with minimum DOP (and vice versa). Chirp-free polarization modulation, however, is only obtained for $V_1 = V_2$. Fig. 3 shows the optical output spectrum for chirp-free polarization modulation at the first DOP minimum with $\phi = \pi$. The scrambler is modulated here at a frequency of 7.5 GHz and with a total drive power of 560 mW. From Fig. 3 we deduce a peak phase deviation of 1.2 rad, indicating chirp-free polarization modulation with $\Delta\Phi \approx 2.4$ rad and $\Delta\Psi \approx 0$ rad. It should be noted that the sideband amplitudes in the output spectrum are independent of the drive phase ϕ. If ϕ is detuned from π, such that $\Delta\Phi < 2.4$ rad and $\Delta\Psi > 0$ rad, we obtain the same spectrum as in Fig. 3. This can be easily seen if we transform Eq. (4) into the components of linearly polarized light at +45° and −45°, which yields

$$\begin{bmatrix} A_{+45} \\ A_{-45} \end{bmatrix} = \frac{1}{\sqrt{2}} \begin{bmatrix} \exp\left(j\Delta\Phi_1 \cos\left(\Omega t + \phi\right)\right) \\ \exp\left(j\Delta\Phi_2 \cos\left(\Omega t\right)\right) \end{bmatrix}, \quad (7)$$

similar to Eq. (3). The power spectra of these two orthogonally polarized components are always identical and independent of ϕ. They are also insensitive to DC offsets in the drive voltages. The sideband amplitudes in both spectra, however, change with drive power in the same fashion as for pure phase modulation.

REFERENCES

[1] M. G. Taylor, "Observation of New Polarization Dependence Effects in Long Haul Optically Amplified Systems," *IEEE Photon. Technol. Lett.* **5**, p. 1244, 1993.

[2] M. G. Taylor and S. J. Penticost, "Improvement in Performance of Long Haul EDFA Link Using High Frequency Polarisation Modulation," *Electron. Lett.* **30**, p. 805, 1994.

[3] F. Heismann, D. A. Gray, B. H. Lee, "Electrooptic Polarization Scramblers For Optically-Amplified Long-Haul Transmission Systems," *IEEE Photon. Technol. Lett.* **6**, p. 1156, 1994.

[4] F. Heismann, "Polarization Scrambling and Multiplexing in Optically-Amplified Transoceanic Communication Systems," in *Tenth International Conference on Integrated Optics and Optical Fibre Communication*, Paper FD1, Vol. 4, Technical Digest (The Chinese University Press 1995), p. 92.

[5] N. S. Bergano, C. R. Davidson, and F. Heismann, "Bit-Synchronous Polarization and Phase Modulation Improves the Performance of Optical Amplifier Transmission Systems," to be published.

[6] M. M. Howerton and W. K. Burns, "Depolarized Source for High Power Remote Operation of an Integrated Optical Modulator," *IEEE Photon. Technol. Lett.* **6**, p. 115, 1994.

[7] S. K. Korotky, J. J. Veselka, C. T. Kemmerer, W. J. Minford, D. T. Moser, J. E. Watson, C. A. Mattoe, and P. L. Stoddard, "High-Speed, Low-Power Optical Modulator with Adjustable Chirp Parameter," in *Integrated Photonics Research*, Paper TuG 2, Vol. 8, 1991 Technical Digest Series (Optical Society of America 1991), p. 53.

[8] R. Calvani, R. Caponi, G. Marone, and P. Poggiolini, "High-Speed Polarization Modulation Through an Optical Guided-Wave Two-by-Two Switch," in *Coherent Lightwave Communications*, Vol. 1175, Proc. SPIE (The International Society for Optical Engineering 1989), p. 89.

Novel compact InP-based polarisation converters using ultra short bends

C. van Dam, L. H. Spiekman, F. P. G. M. van Ham, F. H. Groen*, J. J. G. M. van der Tol†, I. Moerman‡, W. W. Pascher§, M. Hamacher¶, H. Heidrich¶, C. M. Weinert¶, M. K. Smit

Delft University of Technology, Dept. of Electrical Engineering
P.O. Box 5031, NL-2600 GA Delft, The Netherlands
Phone: +31 - 15 - 2787089, Fax: +31 - 15 - 2784046
*Delft University of Technology, Department of Applied Physics
†PTT Research, Leidschendam.
‡Department for Information Technology, IMEC-University of Gent, Belgium
§FernUniversität, Department of Electrical Engineering, Hagen, Germany
¶Heinrich Herz Institut für Nachrichtentechnik Berlin GmbH, Germany

Introduction

Polarisation dependence is a main issue in optical communication systems. One way to make components polarisation independent is the use of a λ/2 plate inserted in the middle of a component, as has been demonstrated for phased-array demultiplexers [1]. This method can also be applied to InP-based demultiplexers and other components, but then the λ/2 plates must be replaced with integrated converters [2,3,4]. In this paper we present experimental results on novel compact InP-based polarisation converters with high conversion values, employing waveguide bends with very small bending radii. These converters are easy to fabricate (only one single etch step is required) and are thus well suited for integration with other devices.

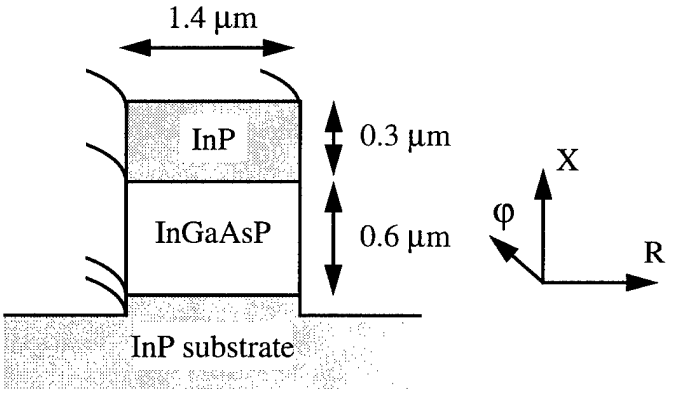


Figure 1. The deeply etched waveguide structure as used for the polarisation converter.

Design

Earlier experiments have shown that very small bending radii (down to 30 µm) can be applied with low insertion loss when using a deeply etched waveguide structure [5]. Such waveguide structure is shown in figure 1. Numerical analysis with a 2D vectorial method of lines mode solver reveals that in such waveguides the non-dominant transverse field component strongly increases if the bending radius is chosen sufficiently small, i.e. the polarisation plane is tilted if

the bending radius is reduced. In figure 2 the X- and R-components of the TE-polarised zero order mode are shown for a bending radius of 50 μm. Graphs of the TM-polarised zero order mode are almost identical. From the surface intensity plots of both components we can see that almost 40 % of the total field power is in the non-dominant X-component. This means that the state of polarisation is rotated by more than 35 degrees. By placing waveguide bends with opposite direction of curvature in series, the non-dominant field components will couple to the dominant field components of the other polarisation. The shape of the X- and R-components of both polarisations are almost identical, which results in low coupling losses of 0.2 dB in the case of a 50 μm bending radius.

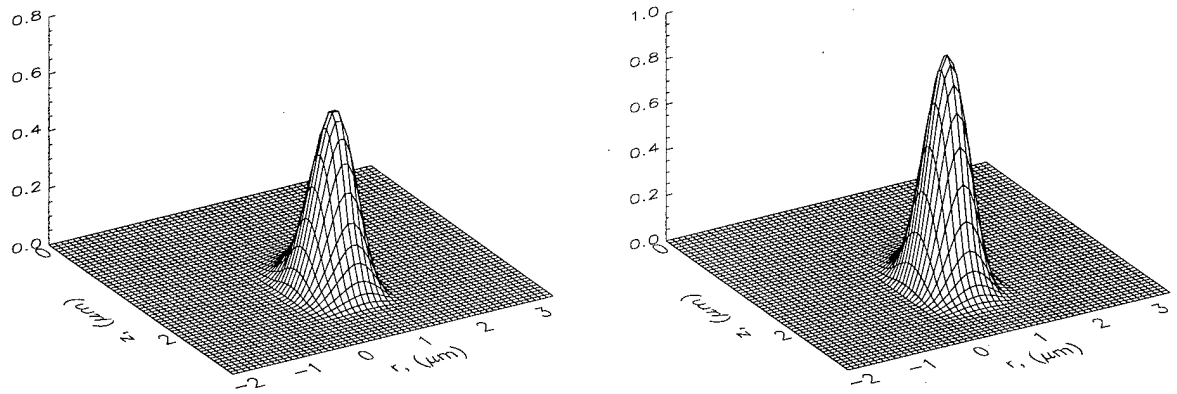


Figure 2. Surface intensity plots of the non-dominant X-component (left) and the dominant R-component (right) of the TE-polarised zero order mode in a waveguide bend with a 50 μm radius.

Maximum conversion will occur if the propagation length between two subsequent junctions is chosen equal to the beatlength of the TE and TM polarisation. This beatlength is defined as $L_\pi = \pi / (\beta_{TE} - \beta_{TM})$, in which β_{TE} and β_{TM} are the propagation constants of the TE and TM zero order mode, respectively. For measurement of the polarisation conversion we used the layout as shown in figure 3. Two U-bends are placed in series, connected to each other by 3.0 μm wide waveguides. The U-bends consist of four arc segments with a segment angle α. This angle is varied between 10 and 80 degrees, allowing for different beatlengths between two subsequent junctions. The in- and output waveguides of the U-bends are also 3.0 μm wide, because they are known to have low propagation losses [5]. The transition between these waveguides and the 1.4 μm wide bends was done using an adiabatic taper with a length of 50 μm. The total device size is 975 x 83 μm.

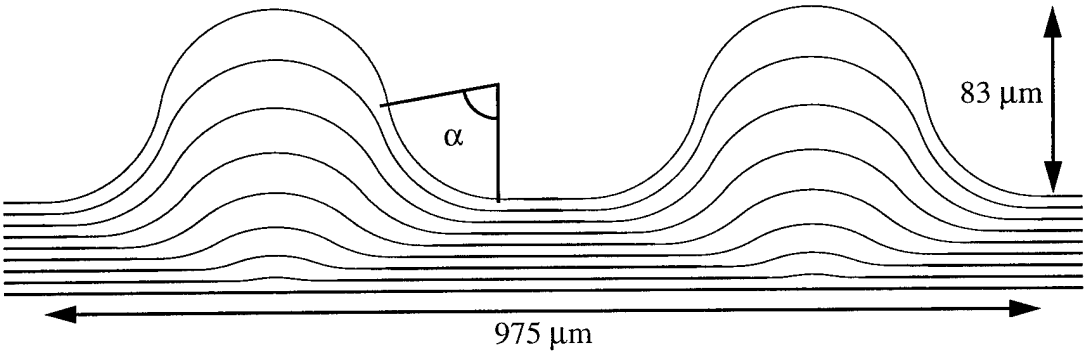


Figure 3. Schematic layout of the polarisation converter, in which the segment angle is depicted as α.

Fabrication

Waveguides have been fabricated in a MOCVD-grown InP/InGaAsP(λ_g = 1.3 μm)/InP ridge waveguide structure. A 100 nm thick PE-CVD deposited SiNx film was used as a masking layer, and waveguides were etched completely through the guiding layer into the substrate employing a CH_4/H_2 RIE etch/descum process to reduce the scattering losses [6]. Waveguide losses were measured 1.0 dB/cm and 2.2 dB/cm for widths of 3.0 μm and 1.4 μm respectively, both for TE and TM polarisation. The sidewall angle was measured to be 13 degrees off verticality.

Experimental results

The performance of the polarisation converters was measured using a Fabry-Perot laser operating at a wavelength of 1508 nm. TM polarised light was launched into the waveguide and at the output a polarisation filter was used for measuring the TE and TM response separately. In figure 4(a) the conversion values are shown versus the segment angle. The measurement results for the converters using a bending radius of 50 μm are of most interest. A high polarisation conversion of 85 % was measured at a segment angle of 70 degrees. Low conversion values (< 20 %) were measured for small bending radii (< 50 μm), and are not shown in the graph. Also a beat between TE and TM polarisation is clearly observed. The appropriate beatlengths are 120, 130, 140 and 300 μm, for bending radii of 50, 75, 100 and 150 μm, respectively, which deviate significantly from calculations (> 1 mm). This may be due to the non-vertical sidewalls which were not included in the modelling. Excess loss values, which are shown in figure 4(b), showed negligible dependence on the segment angle.

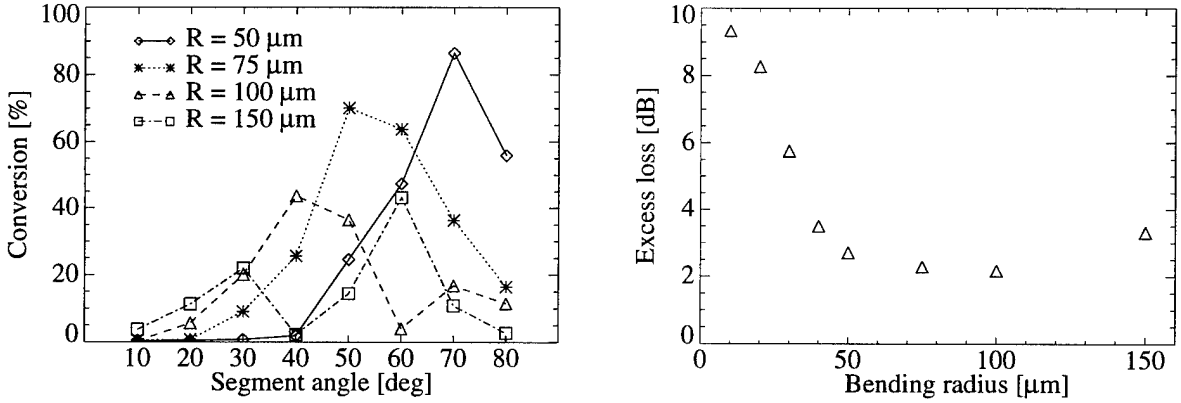


Figure 4. Measurement results of the first experiment polarisation converters: polarisation conversion (a), and excess loss (b).

For a second experiment another converter layout was used. In this case the converter consists of two S-bends, made of two arc segments, connected to each other with a 500 μm straight waveguide. Again the segment angle was varied in order to obtain different beatlengths between two subsequent junctions. Measurements of these converters are shown in figure 5. As can be seen in figure 5(a), a 45 % conversion was obtained at a bending radius of 70 μm. The corresponding excess loss value can be found in the graph of figure 5(b) and is only 0.4 dB. This is the lowest excess loss value for a polarisation converter reported so far. Also 45 % conversion is obtained with a 30 μm bending radius. The excess loss is then slightly higher: 0.6 dB.

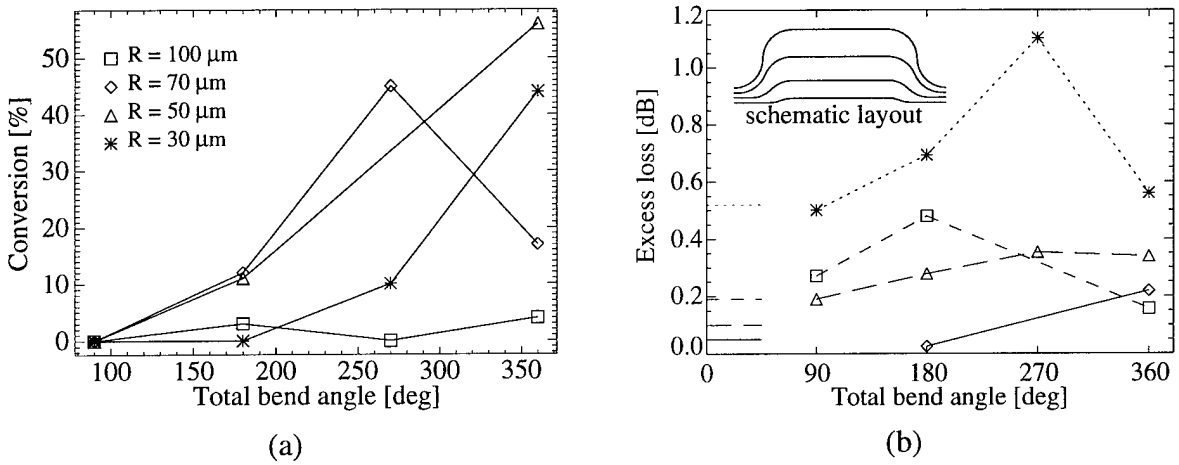


Figure 5. Measurement results of the second experiment polarisation converters: polarisation conversion (a), and excess loss (b).

Conclusion

A novel type of polarisation converter has been realised using deeply etched narrow InP/ InGaAsP ridge waveguide bends with small bending radius. It combines low loss (2.7 dB) with compact device size (975 x 83 μm) and high polarisation conversion (> 85 %). Also a 45 % converter was realised with extremely low excess loss (0.4 dB), and a device size of 760 x 86 μm. It is demonstrated that with deeply etched waveguide bends with small radii strong polarisation conversion can be obtained.

References

[1] H. Takahashi, Y. Hibino, and I. Nishi, "Polarization-insensitive arrayed-waveguide grating wavelength multiplexer on silicon", *Opt. Lett.*, vol. 17, pp. 499-501, April 1992.

[2] Y. Shani, R. Alferness, T. Koch, U. Koren, M. Oron, B. I. Miller, and M. G. Young, "Polarization rotation in asymmetric periodic loaded rib waveguides", *Appl. Phys. Lett.*, vol. 59, pp. 1278-1280, September 1991.

[3] H. Heidrich, P. Albrecht, M. Hamacher, H. P. Nolting, H. Schroeter-Janssen, and C. M. Weinert, "Passive mode converter with a periodically tilted InP/GaInAsP rib waveguide", *IEEE Phot. Tech. Lett.*, vol. 4, pp. 34-36, January 1992.

[4] J.J.G.M. van der Tol, J.W. Pedersen, E.G. Metaal, Y.S. Oei, F.H. Groen, and I. Moerman, "Efficient short passive polarization converter", Proc. 7th Eur. Conf. on Int. Opt. (ECIO'95), April 3-6, Delft, The Netherlands, pp. 319-322, 1995.

[5] L. H. Spiekman, Y. S. Oei, E. G. Metaal, F. H. Groen, P. Demeester, and M. K. Smit, "Ultrasmall waveguide bends: the corner mirrors of the future?", *IEE Proc. Optoelectron.*, vol. 142, pp. 61-65, February 1994.

[6] Y. S. Oei, C. van Dam, F. P. van Ham, L. H. Spiekman, B. H. Verbeek, F. H. Groen, E. G. Metaal and J. W. Pedersen, "Improved RIE technique for controlled roughness and anisotropy in InP-based devices", Procs. 18th State-of-the-art Program on Compound Semiconductors (SOTAPOCS XVIII), May 16-21, Honolulu, U.S.A., Volume 93-27, pp. 134-141, 1993.

Active Semiconductor Devices

IWD 10:30 am-12:00 m
Fairfax B

S. Chandrasekhar, *Presider*
Lucent Technologies-Bell Labs

A GAIN-CLAMPED, CROSSTALK FREE, VERTICAL CAVITY LASING SEMICONDUCTOR OPTICAL AMPLIFIER FOR WDM APPLICATIONS

J.D. Walker, F.G. Patterson, S.P. Dijaili and R. J. Deri
Lawrence Livermore National Laboratory, PO Box 808, Livermore, CA 94550
tel. (510) 422-3159, fax (510) 422-2783

INTRODUCTION:

In recent years, advancements in semiconductor optical amplifier (SOA) technology have solved many of the problems (e.g., polarization sensitivity[1] and low saturated output powers[2]) which have prevented their widespread deployment into optical networks. The most elusive and last remaining problem is the large crosstalk between channels in wavelength division multiplexing (WDM) and time division multiplexing (TDM) applications. The crosstalk arises from dynamic gain variations due to gain saturation. The most effective solution to these problems involves the use of a separate and simultaneous stimulated emission field in the SOA. Above threshold, the gain is clamped to the cavity losses and the effective carrier lifetime is significantly reduced due to stimulated emission. As a result, crosstalk, speed, and linearity of the SOA are significantly improved. Previous implementations of this gain-clamping approach to crosstalk reduction use a longitudinal lasing field[3-5] where a distributed Bragg reflector (DBR) or distributed feedback (DFB) laser structure is modified with lower reflectivities and then pumped above threshold. This approach, where laser light is collinear with the amplified signal, has a number of disadvantages. The creative challenge is to find a configuration where an "extra" lasing field can share the same gain medium and not hinder propagation of the signal beam through the device.

Our solution is to use an orthogonal lasing configuration as shown in Fig. 1(a). The orthogonal lasing field is provided by a vertical-cavity surface-emitting laser diode (VCSEL). A single-mode SOA ridge waveguide is formed in the upper VCSEL mirror. We will refer to this structure as a vertically lasing semiconductor optical amplifier (VLSOA). The advantages of a VLSOA over other gain clamped geometries are: 1) No separate spectral filtering of laser light along the fiber input or output is needed. 2) The full SOA gain spectrum is available for use since no wavelength dependent components are in the signal beam path (e.g., DBRs or dichroic coatings). 3) Since the internal power density is very large in a VCSEL, single mode rate equations show that the VLSOA is significantly faster than other gain clamped SOAs. Thus the VLSOA geometry can provide the highest channel speeds for WDM, TDM, and CATV/microwave applications. 4) Because the lasing field is orthogonal to the signal gain path, the device parameters for lasing (e.g. mirror reflectivities) can be independently tailored from SOA gain (e.g. length). As a result, the trade-off between high lasing field power (i.e. effective gain clamping) and gain along the ridge waveguide is eliminated.

The basic physics of the VLSOA device is now briefly discussed. As the device is electrically pumped, the gain of the amplifier increases until the VCSEL reaches lasing threshold. Above threshold, the gain is saturated or clamped to the passive losses (primarily mirror losses). Any further pumping of the medium results in the lasing power increasing. In the case of the VLSOA, there is good spatial overlap between the signal beam along the ridge waveguide and the lasing field in the vertical direction. The clamping of the gain to the passive losses via feedback (historically analogous to the electrical operational amplifier) by a lasing field implies that all the relevant parameters of a laser then apply such as speed of response, photon lifetime, etc. Since the VCSEL mirror reflectivities are relatively stable to variations in temperature, age, or drift in materials parameters, the SOA gain is also insensitive to these parameters. One benefit of gain clamping is that the WDM crosstalk is greatly reduced. The lasing field acts as a ballast and an input signal modulates the VCSEL power as opposed to a conventional SOA where an input signal modulates the gain. As the amplified signal output power is increased, the gain is clamped and linear until the laser power is exhausted. Hence, the effective SOA saturation output power equals

the lasing field power. Another benefit of the VLSOA is that the TDM gain recovery time is greatly reduced from ~1 ns to ~10 ps as result of stimulated emission from the lasing field. A third, but yet untested benefit, is the possibility of reducing the amplified spontaneous emission (ASE) noise in the ridge waveguide by microcavity noise reduction. Briefly, the ASE enhancement expected in the vertical direction [6] reduces the ASE for the horizontal direction. Stimulated emission is not affected and hence the SOA gain will not be reduced. It may be possible to exploit this effect to build low noise SOAs.

DEVICE FABRICATION:

An SEM photo of our first generation VLSOA is shown in Fig. 1(b). The device is essentially a tilted-facet ridge waveguide SOA, except that it uses a VCSEL epitaxial wafer in place of a conventional edge-emitting design. The ridge etched into the top Bragg reflector is used for electrical and optical confinement along the waveguide, and the tilted facets are used to suppress lasing along the amplifier direction. The VCSEL wafer is a molecular beam epitaxy (MBE) grown structure with GaAs/AlGaAs Bragg reflectors and a InGaAs multiple quantum well active region. The wafer used in these experiments produced room temperature CW output powers of 5 mW when processed into proton-implanted 30 μm square vertical cavity lasers [7]. Details of the VCSEL wafer design and epitaxial growth can be found in the literature [7]. Figure 1(b) is a view of the end facet of the VLSOA. The photo shows a 3 μm thick top Bragg reflector (20.5 Bragg pairs, 0.14 μm period), active region (white stripe) and 4.5 μm thick bottom Bragg reflector. The ridge is 9 μm wide, and was defined by etching about half way through the top Bragg reflector with a H_2SO_4:H_2O_2:H_2O based liquid etch. The top of the ridge is electrically contacted with e-beam and electroplated gold, and there is an insulating SiO_2 layer under the gold in the valley regions. The ridge stripes run at a seven degree angle to the (100) cleave planes to prevent longitudinal lasing.

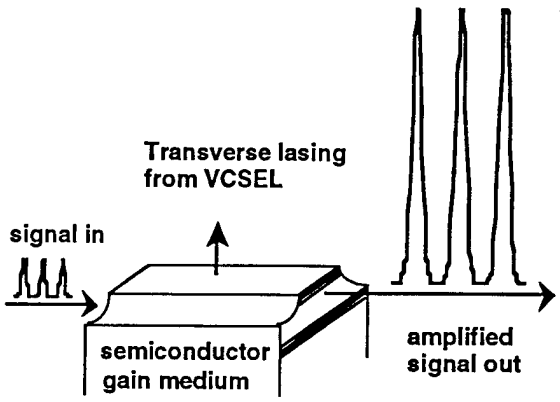


Fig. 1 (a) schematic of the VLSOA

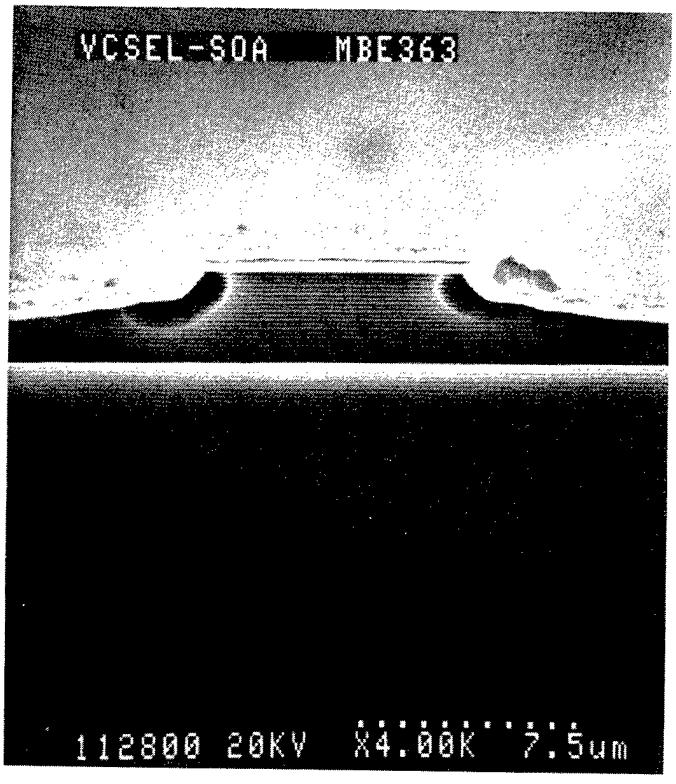


Fig. 1(b) SEM image of VLSOA cleaved facet.

EXPERIMENTAL RESULTS:

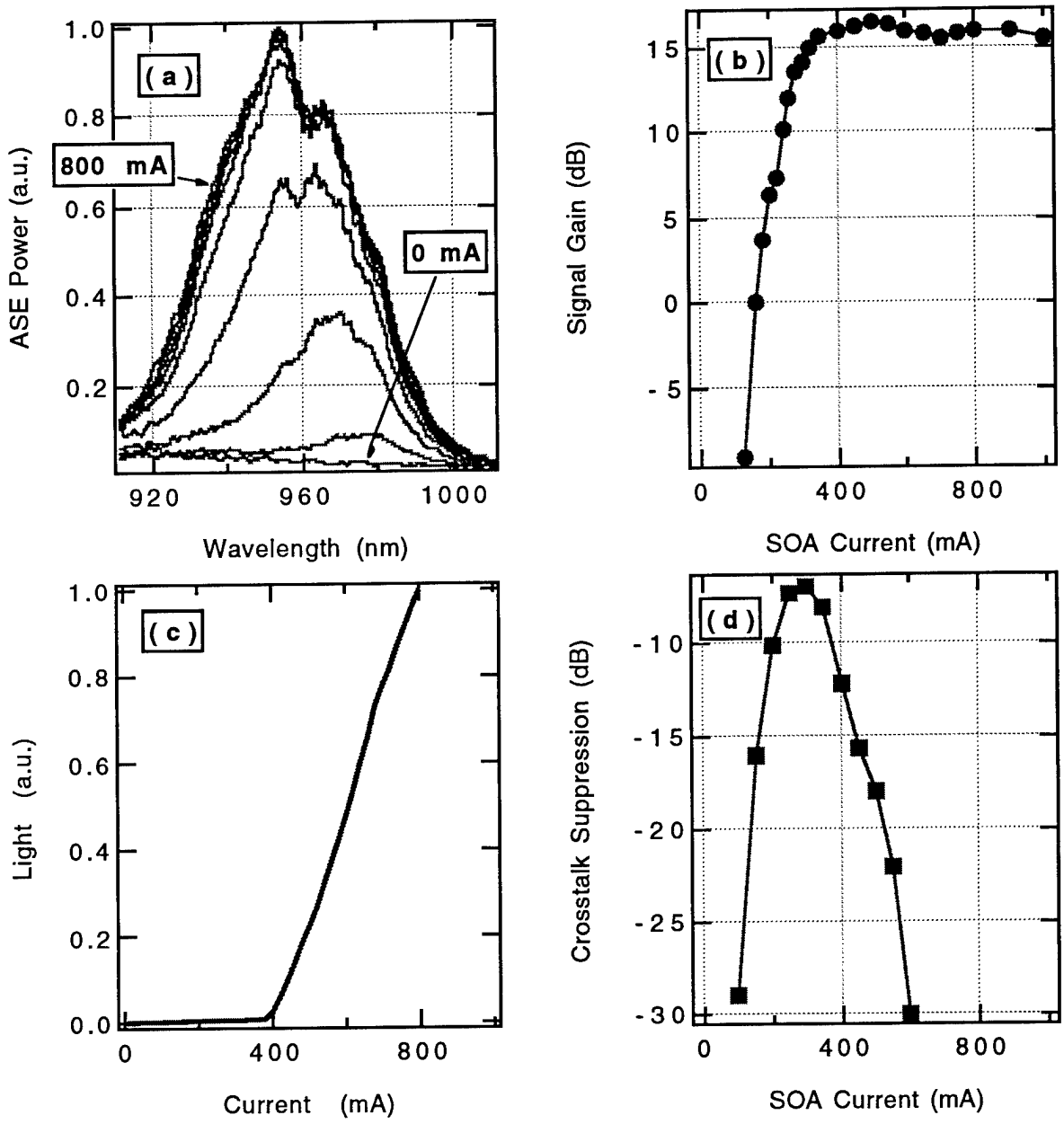


Fig. 2. (a) ASE spectra, I = 0 to 800 mA, 100 mA steps, res. bandwidth 0.1 nm; (b) VLSOA gain vs. bias current; (c) L-I curve for VCSEL lasing power; (d) VLSOA crosstalk signal vs. bias current

The VLSOAs were cleaved into individual die and mounted active-side up without solder onto a vacuum heat sink. In order to avoid adverse thermal effects, the bias current to the device is pulsed at a 0.2% duty cycle (1 μs, 2 kHz). (With properly soldered heat sinks CW operation is possible.) The pulsed L-I curve of the vertical-cavity laser is shown in Fig. 2(c). The VCSEL threshold current is observed to be 400 mA and thus the VLSOA is expected to be gain-clamped above this current level. The intensity in Fig. 2(c) is in arbitrary units because the devices are covered with gold on both sides and they have no output window to allow detection of the VCSEL light. To obtain the L-I curve, a hole was scratched through the gold on the substrate side of the device to allow some light to escape. The threshold current is higher than VCSEL devices in the literature for two reasons. First, our devices are ~100 times larger in area than the low threshold VCSELs in

the literature, and thus they are expected to have 100 times higher operating currents. Second, our devices have almost no lateral current confinement compared to other VCSEL structures in the literature. Our next generation VLSOA devices will incorporate improved current confinement and should operate CW at currents comparable to conventional ridge waveguide SOAs (<100 mA).

The ASE spectra, collected with a single-mode optical fiber from the VLSOA ridge waveguide, are shown as a function of bias current in Fig. 2(a). Nine bias current levels ranging from 0 to 800 mA in 100 mA steps are depicted. For a conventional SOA, the ASE power would continue to increase with bias current up to 800 mA; however, in these VLSOA devices the ASE power is clamped by the internal lasing field when the VCSEL reaches threshold at 400 mA. The second important result from Fig. 2(a) is that no detectable laser light is coupled into the single-mode optical fiber which defines the optical pathway for the amplified signal beam.

Figure 2(b) shows that as the VCSEL reaches threshold, the gain clamps at 16 dB. The gain in this first generation VLSOA is limited by a low and unoptimized mode confinement factor, poor lateral mode control, and low current confinement. These limitations can be overcome in future devices and 30 dB chip gains should be possible.

The crosstalk signal is measured by introducing a chopped (1μs, 1kHz) Ti:sapphire laser "pump" beam at 960 nm and a CW laser diode "probe" beam at 954 nm [8]. A Hewlett-Packard optical spectrum analyzer (OSA) is used to filter and detect only the 954 nm laser light. A lock-in amplifier is employed to sense the 1 kHz modulation of the pump beam induced onto the probe beam. The crosstalk signal is defined as the ratio of this 1 kHz AC component divided by the DC magnitude of the transmitted probe beam. The crosstalk signal is shown in Fig. 2(d) as a function of the bias current . A precipitous 25 dB drop in crosstalk is observed as the current is increased above the 400 mA VCSEL threshold current, consistent with the onset of gain clamping observed in Figs. 2(a,b,c). For a conventional SOA, the crosstalk signal would continue to increase with bias current up to 800 mA.

CONCLUSION:

We have proposed, fabricated and tested a vertically lasing semiconductor optical amplifier. The device exhibits a 16 dB clamped chip gain and 25 dB reduction in crosstalk relative to the maximum crosstalk which occurs just below the lasing threshold. Virtually no laser light is coupled into either the input or output optical fibers. Short wavelength VCSELs are commercially available and long wavelength VCSEL technology is progressing rapidly [9]. VCSEL epitaxial growth technology is compatible with strained multiple-quantum well material which can be made polarization insensitive [1]. We envision future crosstalk free VLSOAs with polarization insensitivity, low current consumption, high fiber-to-fiber gain, and availability at all major communications wavelengths.

This work was performed under the auspices of the U.S. Department of Energy by Lawrence Livermore National Laboratory under contract No. W-7405-Eng-48. The authors would like to acknowledge the efforts of Richard Combs, Holly Petersen, Bill Goward, and J.S. Smith.

REFERENCES:

[1] L. F. Tiemeijer et al., Appl. Phys. Lett. **62**, 826 (1994).
[2] T. Mamijoh et al., IEEE JQE **30**, 524 (1994).
[3] B. Bauer, F. Henry, and R. Shimpe, IEEE PTL **6**, 182 (1994).
[4] J. C. Simon et al., Electron. Lett. **30**, 49 (1994).
[5] L. F. Tiemeijer, et al., IEEE PTL **7**, 284 (1995).
[6] DeMartini et al., Phys. Rev. Lett. **60**, 1711 (1988).
[7] J. D. Walker, D. M. Kuchta, and J. S. Smith, Electron. Lett. **29**, 239 (1993).
[8] F.G. Patterson, S.P. Dijaili, and R.J. Deri, IPRC, Dana Point, CA, Feb. 1995, IFA3.
[9] D. I. Babic et al., IEEE PTL **7**, 1225 (1995).

Wavelength Accuracy and Output Power of Multiwavelength DFB Laser Arrays with Integrated Star Couplers and Optical Amplifiers

M. R.. Amersfoort, C. E. Zah, B. Pathak, F. Favire, P. S. D. Lin, A. Rajhel, N. C. Andreadakis
R. Bhat, C. Caneau, and M. A. Koza
Bellcore, NVC3Z391, 331 Newman Springs Rd., Red Bank, New Jersey 07701, USA,
Voice: +1-908-758-3468, Fax: +1-908-758-4372, E-mail: amers@nyquist.bellcore.com

Abstract

We report the static performance of multiwavelength DFB Laser Arrays with integrated star couplers and optical amplifiers. Wavelength deviations of ±0.2 nm or less from the eight-wavelength comb designated by ONTC have been achieved with high yield. High power into a single mode fiber of about −13 dBm and 0 dBm per wavelength has been measured without and with on-chip optical amplification, respectively.

I. INTRODUCTION

For WDM lightwave systems to be cost effective, it is important to reduce the per-wavelength component cost. One approach is to integrate devices with similar functionality to form arrays such as laser arrays [1], detector-preamplifier arrays, etc. For system applications, it is necessary to combine all the channels with different wavelengths into one single mode fiber at each transmitter site for signal transmission or distribution. One approach is to combine all the laser outputs with different wavelengths on the chip, and then couple the combined signal into one single mode fiber. Such a photonic integration reduces the packaging cost per wavelength since a single optical pigtailing including an optical isolator is shared by all the wavelengths [1]. As early as 1977, Y-branches were used to combine the light outputs from six 0.9 μm DFB lasers on a GaAs substrate [2]. More recently, star couplers were integrated with 21-wavelength DFB laser arrays [3] and 16-wavelength DBR laser arrays [4]. The star coupler is chosen for its compactness and wavelength insensitivity. To compensate for the inherent 1/N splitting loss, a semiconductor optical amplifier can be integrated on the same chip [3,4].

In the Optical Network Technology Consortium (ONTC) [6], we have improved the design and fabrication of multiwavelength laser arrays with integrated star couplers and optical amplifiers to meet the transmitter requirements of WDM network access modules. Here we report the static performance of our recent array chips, which is superior to that of first generation devices reported before [3].

II. ARRAY DESIGN AND FABRICATION

Fig. 1 shows the schematic top view of a 10-wavelength DFB laser array with an integrated star coupler and two optical amplifiers. The star coupler combines 20 DFB lasers on the left hand side. The waveguide structure employed is a 0.2 μm thick and 3 μm wide InGaAsP (1.25 μm bandgap wavelength) layer buried with regrown SI-InP [3, 7]. In order to compensate for the decreasing diffraction efficiency of the outer input waveguides, their apertures are increased from 3 μm for the center inputs to 7.5 μm for the outermost input, using 300 μm long tapers [7]. The minimum radius of curvature of the S-bends is 600 μm.

In the DFB laser region, the active layer consists of six strain-compensated quantum wells [8] grown on top of the above waveguide layer. At the transition from the active to the passive

waveguide region the light is evanescently coupled with a theoretically estimated loss of less than 0.5 dB. Gratings with 10 different pitches are patterned by e-beam direct writing. Although only eight wavelengths (1546-1560 nm in vacuum with 2 nm spacing) are needed for the ONTC optical network testbed, one extra grating is added on either side of the comb to increase the chance of covering the whole system wavelengths near room temperature. To improve the array yield, we have implemented two DFB lasers per wavelength. The laser with its wavelength closest to the designated system wavelength was selected to be wire bonded for final packaging.

Among the four output waveguides on the right hand side of Fig. 1, the two outer ones go through semiconductor optical amplifiers for on-chip amplification. To reduce the facet reflectivity a 60 μm long window region is incorporated at the output facet of each optical amplifier and the rear facet of each DFB laser. A single layer antireflection coating is applied to further reduce the facet reflectivity. The total chip size is only 4.3 mm x 1.4 mm.

III. STATIC PERFORMANCE

Among 20 DFB lasers within an array, the threshold current is measured to be around 25 mA at room temperature and its variation within an array is less than 10 % [7]. By operating one laser at 60 mA each time on the bench top, the power per laser coupled from a passive output waveguide into a single mode fiber is more than -13 dBm which is a significant improvement over the previous devices [3]. The high output power per wavelength is attributed to the high slope efficiency of the DFB lasers, low-loss integrated star coupler, and high-efficiency fiber coupling. The estimated loss breakdown is summarized in Table I.. Fig. 2. shows the optical spectrum of eight wavelengths from eight *selected* DFB lasers in an array under simultaneous operation in a fully packaged transmitter with a bias current of 60 mA per lasers [9]. The output power is about -13 ± 1.5 dBm and the wavelength deviations from the 2 nm wavelength comb are within ±0.2 nm for all eight wavelengths. Note that the power reading from the optical spectrum analyzer is about 2 dB lower that the reading from the power meter and the wavelength measured in air is about 0.7 nm shorter than in vacuum. The side mode suppression ratio is better than 35 dB for all eight wavelengths.

The output power can be further boosted by the on-chip semiconductor optical amplifier. Fig. 3. shows the light-current characteristics of DFB lasers with on-chip optical amplification for the shortest (solid line) and longest (dashed line) wavelengths as a function of the optical amplifier current. At a current bias of 200 mA, more than 10 mW facet power for a single laser has been obtained. The power coupled into a single mode fiber is about 0 dBm per wavelength if a single DFB-laser is operated at 60 mA. The net optical gain is estimated to be about 13 dB. To our knowledge, these power levels are the highest reported for integrated multiwavelength lasers [3, 4, 10]. The above results are measured under individual operation, one DFB laser at each time. It is important to note that the power per wavelength might be reduced when eight DFB lasers operate simultaneously because of the finite saturation output power of a semiconductor optical amplifier. The detailed study will be carried out in the future after the chip is packaged.

To find out the wavelength variation resulting from non-uniform material growth and device fabrication within a wafer, we have deliberately picked five integrated laser array chips from different parts of a wafer (1.7 cm x 1.8 cm). The absolute wavelength spread at 15 °C is about 1 nm for each channel and the channel spacing is 2 ± 0.04 nm. The current wavelength spread is small enough to obtain a good array yield for eight wavelengths. The minimized wavelength deviation from the designated ONTC wavelength comb shown in Fig. 4 is obtained by

adjusting the common heat sink temperature, and between two redundant lasers operating the one with its wavelength closer to the ONTC wavelength. Among five integrated laser array chips, the array yields for a wavelength tolerance of ±0.2 nm and ±0.1 nm are 80 % (4/5) and 40 %, (2/5) respectively. The high array yield is attributed to the two-to-one wavelength redundancy implemented on the chip [1] and the proximity effect i.e. good uniformity in both growth and fabrication within a small local area (0.95×0.37 mm^2) [1, 5].

IV. CONCLUSIONS

We have realized the second generation multiwavelength DFB laser arrays for the ONTC optical network testbed. High array yield has been demonstrated with 0.2 nm wavelength tolerance. With on-chip amplification, the integrated laser array output power can compete with the discrete DFB laser. The dynamical performance including crosstalk will be reported later.

ACKNOWLEDGMENT

We would like to acknowledge C. Dreze, D. Pollex and J. Stich of Bell-Northern Research Ltd., Canada, for transmitter packaging. We are also thankful to T. P. Lee, C. A. Brackett and P. Kaiser of Bellcore, and R. F. Leheny, B. Hui and A. Yang of ARPA for their encouragement and support of this work. This work was supported in part by ARPA contract # MDA972-92-H-0010.

REFERENCES

[1] For review, see: C. E. Zah *et al., J. of Optoelectronics - Devices and Technologies* **9**, pp. 153-166, 1994, and: C. E. Zah *et al., Int. J. of High Speed Electronics and Systems* **5** (1), pp. 91-109, 1994.

[2] K. Aiki *et al., IEEE, Journal of Quantum Electronics,* **QE-13**, pp. 220-223, 1977.

[3] C. E. Zah *et al., Electron. Lett.* **28**, pp. 824-826, 1992.

[4] M. G. Young *et al., IEEE, Photon. Technol.* Lett **5**, pp. 908-910, 1993.

[5] M. G. Young *et al., Electronics Letters* **31**, (20), pp. 1750-1752, 1995.

[6] C. A. Brackett *et al., J. of Lightwave Technol* **11**, pp. 736-753, 1993.

[7] C. E. Zah *et al., Proc. of IEEE LEOS Annual Meeting*, San Francisco, CA, October 30-November 2, pp. 239-240, 1995.

[8] A. Mircea *et al., Journal of Crystal Growth* **124**, pp. 737-740, 1992.

[9] C. Dreze *et al., Proc. of IEEE LEOS Annual Meeting*, PD1.5, San Francisco, CA, October 30-November 2, 1995

[10]M.C.Young *et al., Electron. Lett.* **31** (21), pp. 1835-1836, 1995

Table I. Power per wavelength and estimated loss breakdown

Laser power dBm	Waveguide loss dB	Transition loss dB	Bending loss dB	1/N loss dB	Excess loss dB	Net optical gain @ 200 mA dB	Fiber coupling loss dB	Power into a SM fiber dBm
7	-2	-0.5	-1	-13	-1	(+13)	-2.5	-13(0)

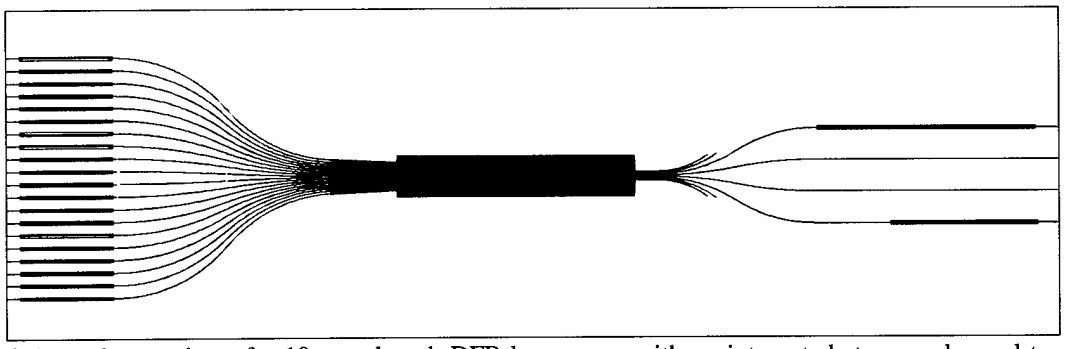


Fig. 1. Schematic top view of a 10-wavelength DFB laser array with an integrated star coupler and two optical amplifiers.

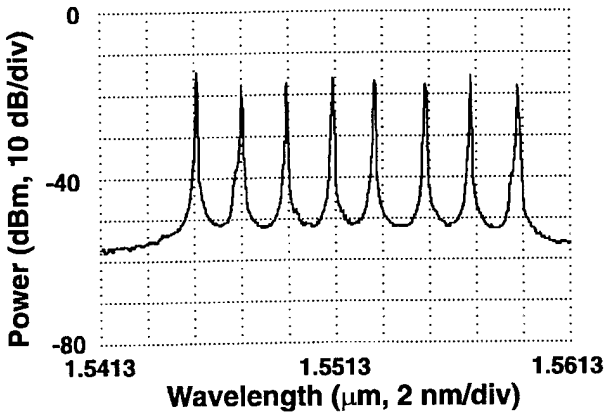


Fig. 2. Optical spectrum of eight wavelengths from eight selected DFB lasers in an array under simultaneous operation in a fully packaged transmitter with a bias current of 60 mA per laser.

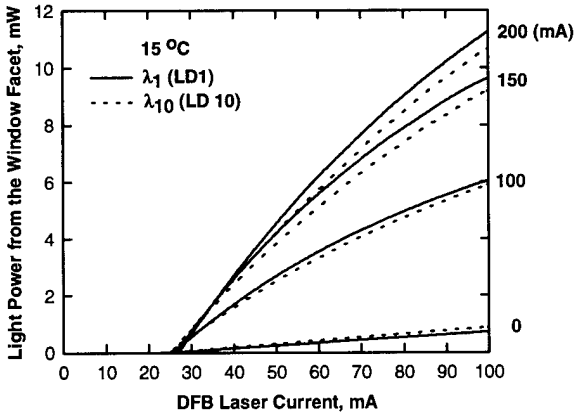


Fig. 3. LI-characteristics of DFB lasers with on-chip optical amplification for the shortest (solid line) and longest (dashed line) wavelengths as a function of optical amplifier bias current

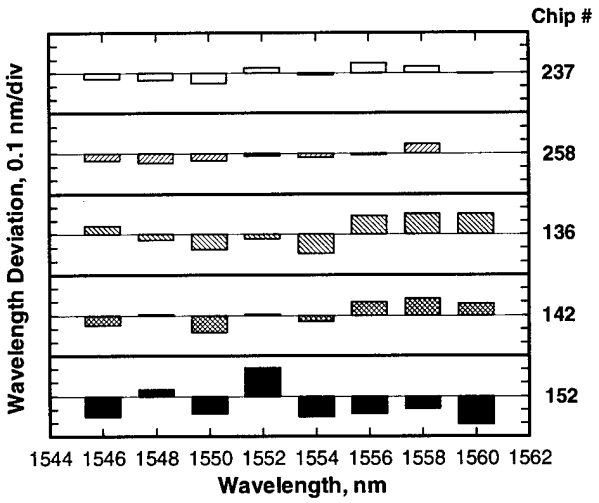


Fig. 4. Wavelength deviation of five randomly selected laser array chips from the designated ONTC wavelength comb, minimized by adjusting the common heat sink temperature and between two redundant lasers operating the one with its wavelength closer to the ONTC wavelength.

Flip-chip bonded 0.85-μm Vertical-cavity Surface-emitting Laser Array using an AlGaAs substrate

Yoshitaka Ohiso, Kouta Tateno, Yoshitaka Kohama, *Hideki Tsunetsugu, and Takashi Kurokawa

NTT Opto-electronics Laboratories
3-1 Morinosato-wakamiya, Atsugi,
Kanagawa 243-01, Japan.

*NTT Interdisciplinary Research Laboratories
9-11 Midori-Cho 3-Chome Musashino-Shi
Tokyo 180, Japan.

Telephone: +81-462-40-3282
Fax: : +81-462-40-3259
(e-mail ohiso@aecl.ntt.jp)

1. Introduction

Vertical-cavity surface emitting lasers (VCSELs) are promising for parallel optical interconnection and optical processing. 0.85-μm VCSELs offer some practical advantages over 0.98-μm ones [1-3] in that they can be used with standard optical fiber and more sensitive Si and GaAs-based receivers. However, it is generally difficult to fabricate 0.85-μm bottom-emitting VCSELs that have low parasitic capacitance and high thermal conductance by introducing flip-chip bonding. We previously reported 0.85-μm bottom-emitting VCSELs on an AlGaAs substrate [4-5]. However, their performance was not satisfactory and the utility of flip-chip bonding was not demonstrated.

In this paper, we report the high performance of a 0.85-μm bottom-emitting VCSEL array which is bonded on AlN sub-mount using flip-chip technique.

2. Experiment

The 0.85-μm VCSELs were grown on an $Al_{0.1}Ga_{0.9}As$ substrate (produced by Hitach Cable Co. Ltd.) by metal organic chemical vapor deposition (MOCVD). After Cl_2 gas etching in the MOCVD reactor, we grew a 100-nm-thick GaAs buffer layer, Si-doped distributed Bragg reflectors (DBRs), comprising 26.5 pairs of $Al_{0.15}Ga_{0.85}As$/AlAs, GaAs/$Al_{0.2}Ga_{0.8}As$, 6-multiple-quantum wells confined by spacer regions, a C-doped p-DBR comprising 29.5 pairs of $Al_{0.15}Ga_{0.85}As/Al_{0.5}Ga_{0.5}As$/AlAs, and a GaAs phase-matching layer. This structure is basically same as that previously reported [4-5] except the number of DBR. The individual 8 × 8 VCSEL elements were produced by reactive ion beam etching (RIBE) using Cl_2 gas and were buried with polymide. A Au mirror was deposited on phase-matching layer and the bottom side was coated with an antireflector.

was mounted in a face-down configuration on an AlN substrate with metallization tracks by using flip-chip bonding as shown in Fig. 1. The individual elements were 250 μm apart and the VCSEL array was 3 × 3 mm.

3. Results

The output power-current characteristics of 16-, 21-, and 26-μm diameter VCSELs under CW operation at 25°C was measured. The emission wavelength for all three VCSELs was the same: 855 nm at an injection current density of about 3 kA/cm^2. An external differential quantum efficiency η_d of 22% (previously reported: 2.6% [5]) was achieved due to the reduced bottom reflectivity. The threshold voltage was the same in all cases, 2.3 V, which is higher than the 2.1 V of VCSELs on a GaAs substrate [5]. The threshold voltage was higher because the number of p-DBR pairs was increased to obtain high reflectivity. The threshold current were 2.1, 2.4, and 4.35 mA and the differential resistance at the threshold were 173, 143 and 86 Ω for the 16-, 21- and 26-μm diameters respectively.

The offset-gain effect can be introduced to obtain higher output power. The maximum gain wavelength red-shifts with increasing carrier injection. Figure 2 shows the dependence of the threshold current and the maximum output power on the emission wavelength (measured @6 mA) for 16-μm diameter VCSELs at 25°C. In these devices, the PL emission peak from the quantum wells was 840 nm. The threshold current and maximum output power was optimal at around 863 nm, which coincides with a 23-nm offset-gain. The temperature increase of the active layer for a 3-kA/cm^2 injected current density was estimated to be 24°C, based on the emission wavelength under pulsed operation.

Figure 3 shows the output power and voltage against the injection current for VCSELs with an 863-nm emission wavelength. The maximum output power and power conversion efficiency were 4.2 mW and 11.7% at around 10 mA. The power conversion efficiency had little dependence on the diameters; the power conversion efficiency was 11.6 and 11.0% for the 21- and 26-μm diameter VCSELs, respectively. Reducing the resistance by implantation or oxidation techniques would further improve these values [6].

Figure 4 shows the temperature dependence of the light output-current characteristics of the 16-μm VCSELs. The maximum CW operating temperature was extended to 130°C due to the offset-gain of 23 nm. We were able to achieve a small variation in the threshold current of only 0.5 mA between 20 and 80°C. The VCSELs produced over 1 mW of output power up to 100°C, and the peak output power was reduced by only 50% as the operating temperature increased from 20 to 80°C. These characteristics are as good as those of 0.85-μm top-emitting VCSELs [7], and suggest that 0.85-μm bottom-emitting VCSELs on an AlGaAs substrate have great potential.

We also confirmed the advantage of flip-chip bonding in terms of thermal conductance. The average in the threshold current of the 16-μm diameter 8 × 8 VCSEL array elements was 1.6 mA with a variation less than ± 0.3 mA. For the VCSELs with an 855-nm emission wavelength, the threshold current was reduced from 2.2 to 1.6 mA after flip-chip bonding. This shows that it may be possible to reduce the thermal crosstalk between pixels caused by the facedown configuration. Moreover, with this flip-chip bonding technique, the parasitic capacitance of all VCSEL elements was lowered to less than 0.5 pF because metallization tracks are not directly applied to the VCSEL array. As a result, a 3-dB modulation bandwidth larger than 2.6 GHz across all array elements has been achieved for a bias current of just 4.2 mA.

4. Summary

We have demonstrated the high performance of 0.85-μm bottom emitting VCSELs on an AlGaAs substrate. The power conversion efficiency was 11.7% at 25°C and the maximum CW operating temperature was 130°C. We also demonstrated the utility of flip-chip bonding for reduced thermal conductance and improved high-speed modulation in the VCSEL array. These results strongly suggest that flip-chip bonded 0.85-μm VCSELs on an AlGaAs substrate can be promising as broadband and high-density optical light sources.

5. References

[1] K. L. Lear, K. D. Choquette, R. P. Schneider, S. P. Jr., Kilcoyne and K. M. Geib, *Electron. Lett.*, 1995, **31**, pp. 208-209

[2] E. Goobar, M. G. Peters, G. Fish and L. A. Coldren, *IEEE Photon. Technol. Lett.*, 1995, **7**, pp. 851-853

[3] G. Reiner, E. Zeeb, B. Moller, M. Ries and K. J. Ebeling, *IEEE Photon Technol. Lett.*, 1995, **7**, pp. 730-732

[4] Y. Kohama, Y. Ohiso, C. Amano and T. Kurokawa, Int. Symp. Compound Semicond., San Diego, 1994, pp. 559-562

[5] Y. Ohiso, Y. Kohama and T. Kurokawa, *Jpn. J. Appl. Phys.* 1995, **34** pp. 6073-6078

[6] R. A. Morgan, M. K. Hibbs-Brenner, R. A. Walterson, J. A. Lehman, T. M. Marta, S. Bounnak, E. L. Kalweit, T. Akinwande, and J. C. Nohava, *Electron. Lett.*, 1995, **31** pp. 462-464

[7] J. M. Catchmark, R. A. Morgan, M. T. Asom, G. D. Guth, M. W. Foucht, T. Mullally, and D. N. Christidoulides, *Electron. Lett.*, 1994, **25**, pp. 2136-2137

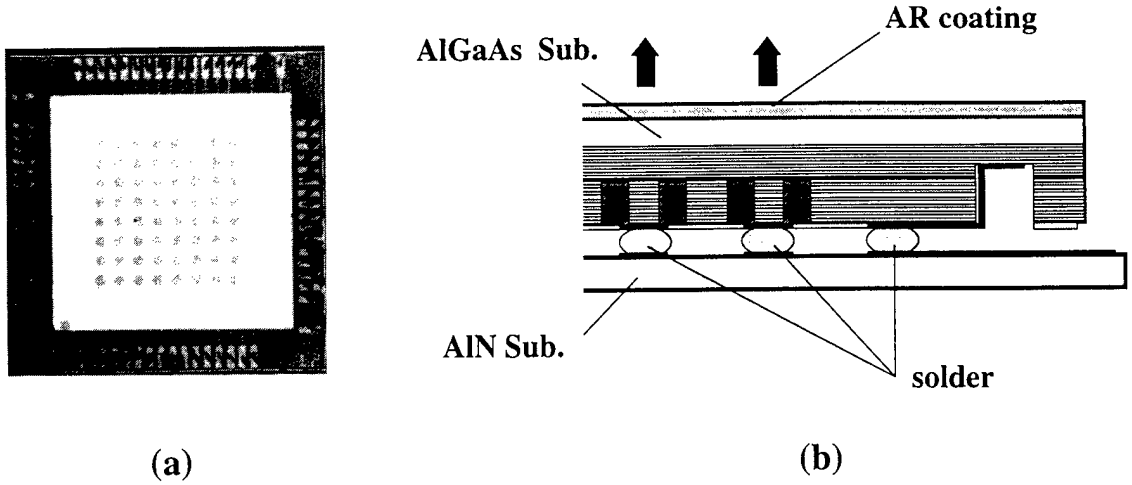


Fig. 1. (a) Photograph (b) Schematic of flip-chip fabrication of 0.85-μm bottom-emitting VCSELs on an AlGaAs substrate.

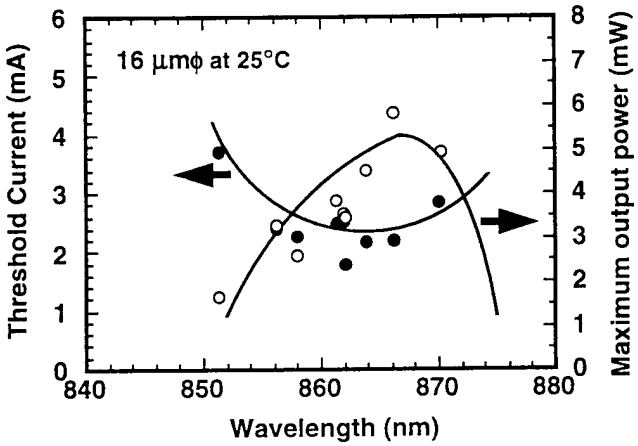


Fig. 2. Dependence of threshold current and maximum output power on the emission wavelength (25 °C) .

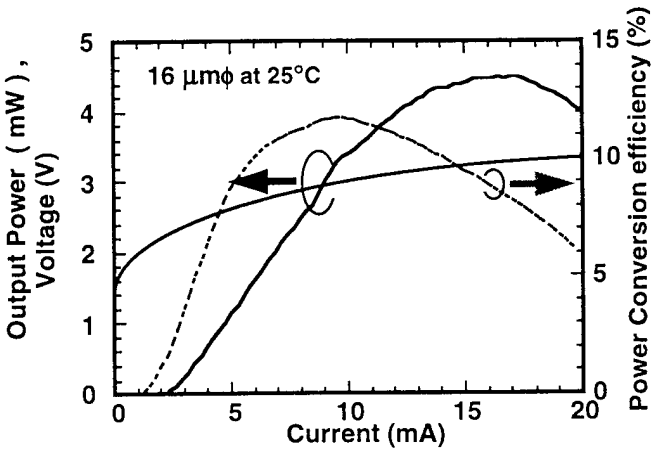


Fig. 3. Light output power, voltage and power conversion efficiency against current characteristics for16-μm diameter VCSELs .

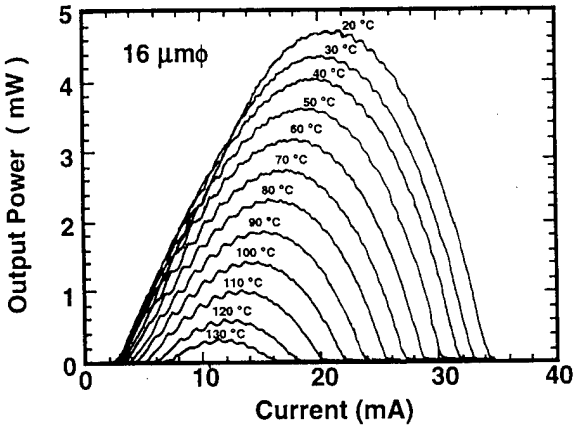


Fig. 4. Temperature dependence of the light output-current curve for 16-μm VCSELs. The maximum CW operating temperature was 130 °C.

Integrable Polarization Insensitive InGaAsP/InP Mach-Zehnder Switch

T. Uitterdijk[a], H. van Brug[a], F. H. Groen[a], H. J. Frankena[a]
C. G. M. Vreeburg[b], J.J.G.M. van der Tol[c]

[a] Delft University of Technology, Department of Applied Physics
P.O. Box 5046, NL-2600 GA Delft, The Netherlands
Fax: +31 152788105, Phone: +31 152781444
E-mail: uitterd@optica.tn.tudelft.nl

[b] Delft University of Technology, Department of Elecrical Engineering
P.O. Box 5031, NL-2600 GA Delft, The Netherlands
Fax: +31 152784046, Phone: +31 152784950

[c] Royal PTT Nederland, KPN Research
P.O. Box 421, NL-2260 AK Leidschendam, The Netherlands
Fax: +31 703326477, Phone: +31 7033225732

I. INTRODUCTION

The availability of suitable electro optical switches is one of the main conditions for the implementation of optical networks based on III-V semiconductor material. Especially for telecommunication applications, switches are indispensable components in, for example, cross-connects, add-drop nodes, transceivers and wavelength routers. The benefit of using an InGaAsP film layer, instead of an MQW film layer, is the lower absorption loss and the possibility to integrate active and passive structures in a single epitaxial step. The advantage of a Mach-Zehnder switch is that it changes the refractive index by reverse biasing a diode instead of injecting a current like in certain Digital Operating Switches (DOS)[1,2]. Reverse biasing enables higher switching frequencies and leads to lower heat dissipation. Because the present fibre network does not maintain the state of polarization, independency of polarization is one of the main properties of a switch. A possible disadvantage of a single 2×2 Mach-Zehnder switch is that a polarization independent crosstalk lower than -20 dB is hard to realize. On the contrary the crosstalk can easily be enhanced by a factor of two using dilated schemes[3,4].

II. DESIGN

The design of the switch consists of two Multi Mode Interference couplers (MMI's) as 3-dB splitting and combining elements and 2 mm long intervening waveguides, on which Ti/Pt/Au-contacts are deposited, as phase shifting sections (Fig. 1). Etch depth, doping profiles and dimensions of the switch are depicted in Fig. 2. The width of the in- and output waveguides are chosen to be 3 μm to ensure low waveguide losses and the width of the phase shifting sections are 4 μm to enable alignment of 2 μm wide contacts on top of them. To

avoid high losses for TM polarized light due to the contacts in these active regions, the InP top layer is chosen as thick as 1000 nm. A 300 nm thick intrinsic InP layer is included to avoid high losses due to absorption in the p-doped top layer. Phase modulation is achieved by changing the effective refractive index by applying a reverse bias voltage between the two top contacts or between one top contact and the substrate. To ensure electrical isolation between the two top contacts, 1 μm wide gaps are etched into the waveguide adjacent to the contacts (Fig. 2). The switch is produced in an InP/InP/InGaAsP(λ_{gap}=1.3 μm)/InP p-i-n-n layer stack and is oriented in the [0-11] direction. The film layer is n-doped to enhance the polarization independent carrier induced effects instead of the polarization dependent electric field induced Pockels effect[5].

Fig. 3 shows the theoretical switching curve of a single Mach-Zehnder switch in case only linear electro-optic effects are considered. The tolerance in the switching voltage for a crosstalk value of -30 dB is less than 5% which means that polarization independent switching is only possible if the electro-optic coefficients for TE- and TM polarization also differ less than 5%. At the moment this seems rather difficult and therefore we propose dilated schemes in case crosstalk values below -20dB are needed.

III. FABRICATION

The layer stack is grown by low pressure metal organic vapor phase epitaxy at 625°C on a 2" n^+-type (100) InP wafer. Zn is used as p-doping for the InP top layer and the InGaAsP contact layer.

The first production step is selective removal of the p^+ InGaAsP contact layer, exept in the active regions, by wet chemical etching. This reduces the loss of the passive waveguides. A 120 nm thick SiO_2 layer is deposited using plasma enhanced chemical vapour deposition. Next the waveguide pattern is defined in positive photoresist and transferred into the SiO_2 layer by reactive ion etching (RIE) using CHF_3. After removal of the photoresist, the waveguides are etched using an alternating CH_4/H_2-etching and O_2-descumming RIE-process. Dry etching of p-n junctions in an H_2-surrounding causes passivation of acceptors which results in high leakage currents[6]. The acceptors are reactivated during the annealing of the contacts. On top of the etched waveguides the Ti/Pt/Au-contacts are deposited by lift-off using image reversal photo resist. Finally, the active regions are passivated with cured polyimide.

IV. MEASUREMENT RESULTS

Fig. 4 shows typical switching curves for TE and TM polarization at a wavelength of 1540 nm. The crosstalk values for the cross and the bar state are respectively -14 dB and -17 dB for TE and -14 dB and -12 dB for TM. At 6.2V reverse bias the switch acts polarization independent with a crosstalk of -12 dB. Without applying a reverse bias voltage the switches are in the cross state. Light is coupled in- and out of the waveguides by (50×) microscope objectives. The switching characteristics are measured with an automated setup which varies

the reverse bias voltage via probe needles on a contact pad and records the transmission of one of the two outputs selected by a slit diafragm in front of the detector. Using the substrate as back contact, grounding the second top contact has no influence on the switching curves which proves that the gaps in the waveguides provide sufficient electrical isolation.

Loss values are obtained using the Fabry-Perot resonance technique. Waveguide losses for TE- and TM-polarization are 1 dB/cm and 2 dB/cm, respectively. This is an increase of less than 0.5 dB/cm with respect to an undoped film layer. Excess losses of the switches, determined from transmission measurements with respect to a straight waveguide, are typically 3 dB for TE- and 5 dB for TM-polarization.

V. CONCLUSIONS

We have developed a polarization insensitive InGaAsP/InP Mach-Zehnder switch in a layer stack similar to layer stacks used for the production of phased arrays[7] and polarization splitters[8] which eases the integration of these components. N-doping of the film layer increases the polarization independent carrier induced effects and hardly (< 0.5 dB/cm) increases the waveguide losses. Because of the small tolerance (<5%) in the switching voltage it is hard to realize a single polarization independent Mach-Zehnder switch with a crosstalk better than -20 dB. At the price of increased size the crosstalk can however easily be improved by a factor of two using a dilated scheme.

REFERENCES

[1] W. H. Nelson, A. N. M. Masum Choudhury e.a., "Wavelength- And Polarization-Independent Large Angle InP/InGaAsP Digital Optical Switches with Extinction Ratios Exceeding 20dB," IEEE Phot. Techn. Lett., vol. 6, no. 11, p. 1332-4, 1994.

[2] T. Kirihara e.a., "Lossless and Low-Crosstalk Characteristics in an InP-Based 4x4 Optical Switch with Integrated Single-Stage Optcal Amplifiers," IEEE Phot. Techn. Lett., vol. 6, no. 2, pp. 218-221, 1994.

[3] H. S. Hinton, *An Introduction to Photonic Switching Fabrics,* Plenum, New York, '93.

[4] G. H. Song, M. Goodman, "Asymmetrically-Dilated Cross-Connect Switches for Low-Crosstalk WDM Optical Networks," Proc. LEOS '95, San Francisco,vol. 1, p. 212-213.

[5] J. F. Vinchant e.a., "InP/GaInAsP Guided-Wave Phase Modulators Based on Carrier-Induced Effects: Theory and Experiment," J. Lightwave Techn., vol. 10, no. 1, 1992.

[6] T. H. Hayes e.a., "Passivation of Acceptors in InP Resulting from CH_4/H_2 Reactive Etching," Appl. Phys. Lett., vol. 55, no. 1, 1989.

[7] M. R. Amersfoort e.a., "Small-size low-loss 4-channel phased-array wavelength division (de)multiplexer on InP," *Proc. 6th ECIO,* April 18-22, 1993.

[8] L. B. Soldano e.a., "Mach-Zehnder Interferometer Polarization Splitter in InGaAsP/InP," IEEE Photon. Techn. Lett., vol. 6, no. 3, 1994.

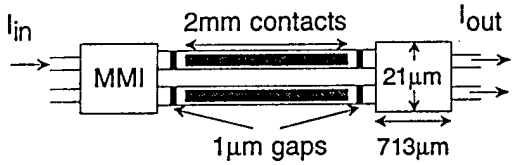


Fig. 1: Layout of the electro-optical Mach-Zehnder switch.

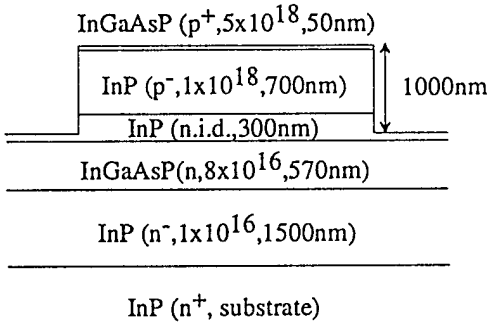


Fig. 2: Cross-section of the layer stack showing materials, dimensions and doping concentrations.

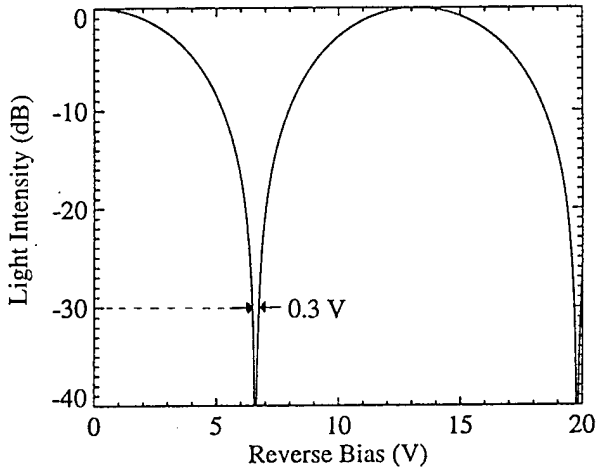


Fig. 3: Theoretical switching curve, assuming only lineair e.o. effects, showing a switching voltage tolerance of 5% at a crosstalk value of -30dB.

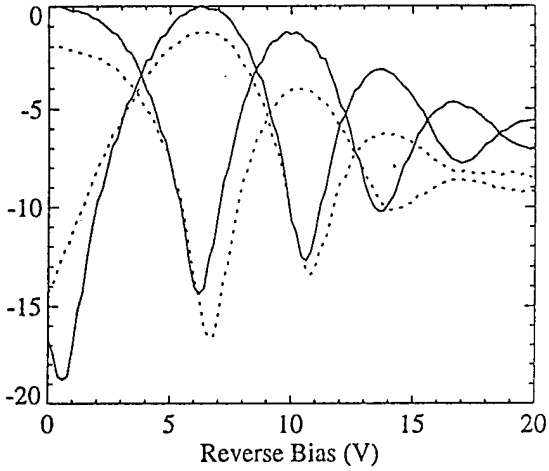


Fig. 4: Switching curves of the bar- and cross output ports at a wavelength of 1540nm for TE- (solid) and TM-polarization (dotted).

Terahertz Tunable Polarization-Switching VCSELs

S.Y. Chou, M.Y. Liu, R.C. Shi, L. Zhuang, S. J. Schablitsky
Nanostructure Lab, Department of Electrical Engineering
University of Minnesota, Minneapolis, MN 55455
Tel: (612) 625-1316, Fax: (612) 625-4583

Generation of ultra-high frequency laser pulses has enormous impact to many areas in science and engineering. Two common approaches are gain switching and mode-locking. The frequency in former is intrinsically limited by the carrier relaxation frequency which is typically about 100 GHz [1]. The frequency in latter is primarily determined by the laser cavity length, and currently is 350 GHz in mode-locked edge emitting lasers [2] and 6 GHz for polarization switching vertical cavity surface-emitting laser (VCSEL) where the cavity length is limited by the thickness of a quarter wave plate [3]. In this paper, we propose polarization-switching VCSELs that can have a tunable oscillation frequency as high as several terahertz. The substantial increase in frequency comes from using a new quarterwave plate made of an amorphous-silicon subwavelength transmission grating that is only one-third of the wavelength thick. The frequency tuning is provided by fabricating the waveplate and a mirror monolithically on a movable microcantilever.

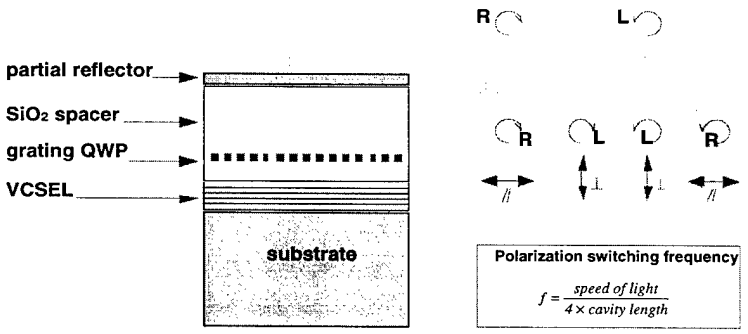


Figure 1. Schematic of an ultra-high frequency polarization switching VCSEL using a subwavelength-grating quarter-wave plate.

As depicted in Fig 1, a polarization-switching VCSEL has an external cavity consisting of a conventional VCSEL, a partial reflector (PR), and a quarter-wave plate (QWP) between the VCSEL and the PR. The VCSEL can lase in two orthogonal modes that are linearly polarized in the two <011> crystal directions of the semiconductors. The axis of the quarter-wave plate is placed 45 degrees from the <011> crystal direction. A linear polarized laser beam first comes out the VCSEL and passes through the QWP becoming circularly polarized (say, right-hand circularly polarized, RHCP). Then a part of the RHCP light is reflected back by the PR becoming left-hand circularly polarized (LHCP) and traveling back to the VCSEL. The reflected LHCP light becomes, after passing through the QWP, linearly polarized in the direction orthogonal to the polarization of the initial beam coming out of the VCSEL. When the orthogonal polarized wave is injected into the VCSEL cavity, it will force the laser to switch into the new polarization direction. As the process continues, the polarization of the laser and the output of the external cavity oscillate between the two orthogonal directions. The period of the oscillations is equal to two round-trip time of the external cavity.

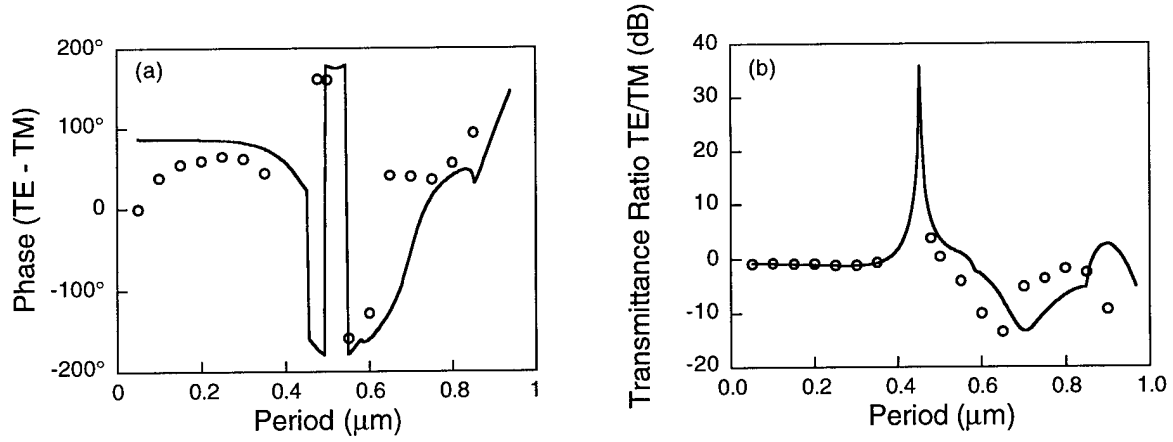


Figure 2. (a) The phase retardation between TE and TM waves (zeroth order). The dots are the measured and the lines are the simulation. (b) Transmission ratio of TM and TE waves (zeroth order). The dots are the measured and the lines are the simulation.

To increase the oscillation frequency, the cavity length must be reduced. This is achieved by using a new QWP made of amorphous Si subwavelength gratings. The dielectric constant of the

gratings in the direction parallel to the grating fingers is significantly larger than that normal to the grating fingers. This leads to a colossal birefringence that is over two orders of magnitude higher than that in a typical natural birefringence crystal, therefore a quarter wave plate of over two orders of magnitude thinner. Fig. 2 shows transmissions and phase difference for TE (the polarization parallel to the grating finger) and TM waves in a set of amorphous Si subwavelength gratings of 240 nm thick, specially designed for 850 nm VCSELs. As the grating period is less than that 0.4 μm, the gratings become good quarterwave plates. In case of a typical natural birefringence crystal, a zero order quarterwave shift would require a thickness of about 0.2 mm.

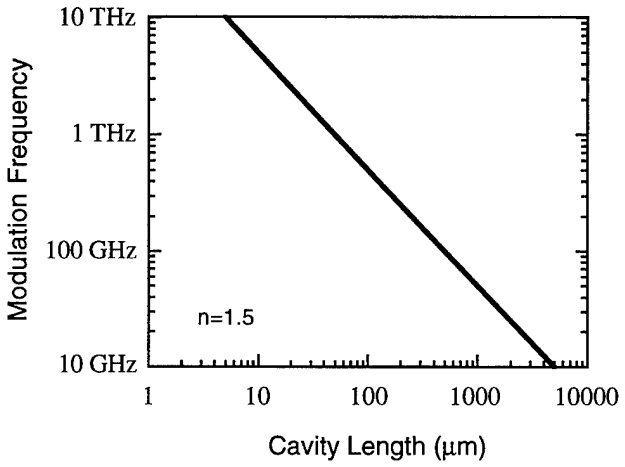


Figure 3. Oscillation frequency of a polarization-switched VCSEL vs. the total cavity length.

The maximum modulation frequency can be estimated from the minimum external cavity length (Fig. 3). Using the subwavelength QWPs, the total cavity length can be reduced to 5 μm, and for a refraction index of 1.5, this leads to a the modulation frequency of 10 THz. Another frequency limiting factors such as laser gain spectral width and photon lifetime, which seem not to pose serious problems until the frequency over 10 THz, will be discussed. The waveplate and a mirror will be fabricated monolithically on a movable microcantilever to tune the cavity length and therefore the modulation frequency.

References:

[1] K. Y. Lau, " Gain switching of semiconductor injection lasers," Appl. Phys. Lett. vol. 52, pp. 257-259. 1988.

[2] Y. K. Chen, M. C. Wu, T. Tanbun-Ek, R. A. Logan, and M. A. Chin, "Subpicosecond monolithic colliding pulse mode-locked multiple quantum well laser," Appl. Phys. Lett. vol. 58, pp. 1253-1255, 1991.

[3] S. Jiang, Z. Pan, M. Dagenais, R. A. Morgan, and K. Kojima, "High-frequency polarization self-modulation in vertical-cavity surface-emitting lasers," Appl. Phys. Lett. vol. 63, pp. 3545-3547, 1993.

Cryogenic Vertical-Cavity Laser for Low Power Free-Space Optical Interconnects.

Y. A. Akulova, B. J. Thibeault, J. C. Ko, E. Goobar, and L. A. Coldren

Electrical and Computer Engineering Dept.
University of California at Santa Barbara
Santa Barbara, CA 93106
Tel: (805) 893-8465
Fax: (805) 893-4500
E-mail: 6500yul@ucsbuxa.ucsb.edu

Optical interconnections in combination with low-temperature system operation provide an opportunity for enhanced performance of advanced high-speed, high-density electronic computing, imaging, and communication systems [1]. Furthermore, optical interconnects provide low thermal loading on the cryostat. Vertical-Cavity Lasers (VCLs) represent a promising approach for low temperature optical interconnect applications, because of their potential for low cost manufacture in arrays, their desirable optical properties, and superior performance achievable at cryogenic temperatures [2, 3]. The potential of VCLs in cryogenic high-speed optical links has been demonstrated [3, 4], but the required drive powers at low optical output power (0.1-0.2 mW) have still been higher than desired.

In this paper we report a VCL that has been designed for low power (P_{out} = 0.1-0.2 mW) optical interconnect applications at 77 K. The low power design also enables the device to operate over the entire range from 77 to 300 K, an important characteristic for many applications. Thus, the design is superior to previously published results.

The VCLs are bottom-emission index-guided lasers that incorporate a dielectric aperture for current constriction (Fig.1). The MBE grown structure consists of a 22.5-period n-doped $Al_{0.9}Ga_{0.1}As$/GaAs quarter-wave DBR, a 2λ-cavity formed by a 5/4λ n-GaAs intracavity contact layer and an $Al_{0.2}Ga_{0.8}As$-GaAs-$In_{0.2}Ga_{0.8}As$ separate confinement active region, p-doped intracavity contact, and a 28-period undoped $Al_{0.9}Ga_{0.1}As$/GaAs quarter-wave DBR. The n-type contact layer is incorporated into the structure for the future realization of double intracavity contact scheme and is not used in the present work. The p-doped contact includes a λ/4 $Al_{0.98}Ga_{0.02}As$/AlAs current constriction layer and a 3/4λ GaAs intracavity contact layer. The processing includes self-aligned double-mesa etching [5] and lateral oxidation step to form the current constriction aperture[6].

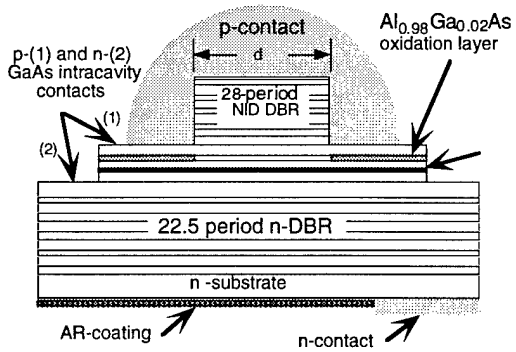


Fig.1. Schematic cross-section of the bottom-emission VCL with oxide-defined current constriction aperture.

Figure 2 shows the light and voltage versus current characteristics for a 6 μm diameter VCL at several temperatures. The threshold of 130 μA (J_{th} = 460 A/cm^2) is achieved at the design temperature (77 K), but the device still operates CW up to 300 K with a threshold below 1 mA. At room temperature the wavelength of the resonant cavity mode is 45 nm shorter than the wavelength of the maximum gain corresponding to the transition between the first electron and heavy hole subbands of the QW at low pumping levels. When the pumping level is increased the gain spectrum widens and the shoulder corresponding to the transition between the second subbands of

the QW appears on the short wavelength wing of the spectra. The alignment of the cavity mode with this second maximum provides enough gain for the low temperature optimized VCL to operate at 300 K. Threshold current as a function of temperature for various device diameters is shown in Fig.3. The lowest thresholds are observed at 77 K in agreement with the design. The lowest threshold current density (265 A/cm^2) is measured for a 12 μm diameter device.

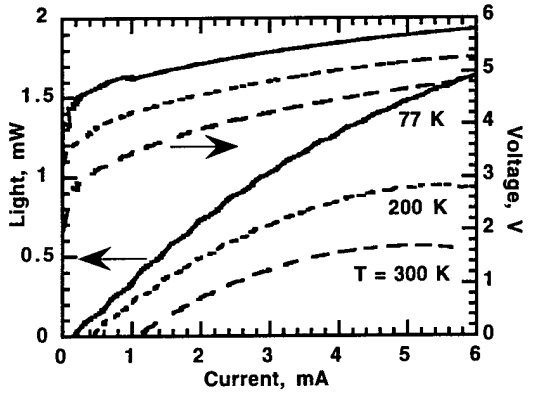


Fig.2. The L-I and I-V characteristics of a 6-μm diameter VCL at different temperatures.

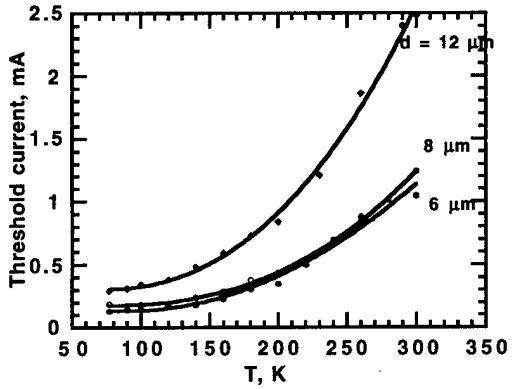


Fig.3. Threshold current as a function of tempe-ratureture. The diameters of the devices are shown.

Single-mode operation of VCLs is necessary for free-space optical interconnect applications. However, dielectric-apertured VCLs tend to be multimode even for relatively small (3-4 μm) device diameters [7]. Thus, we made use of the natural mode-selective loss that occurs in the etched-pillar structures by only oxidizing to the edge of the pillar. This results in a slight increase in the threshold current, but it provides single-mode operation for all bias levels in a 6-μm diameter VCL. Spectral characteristics of a 6-μm diameter VCL measured for the different bias levels up to 38 times I_{th} at 77 K are shown in Fig.4. In fact, with this design 6-μm diameter devices operate single-mode over the entire temperature range (77-300 K) and for all measured bias levels.

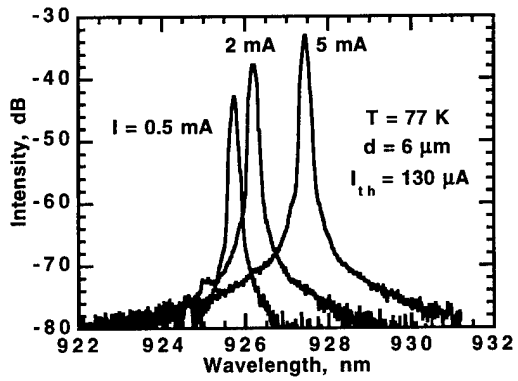


Fig.4. Spectra of a 6-μm diameter VCL at 77 K.

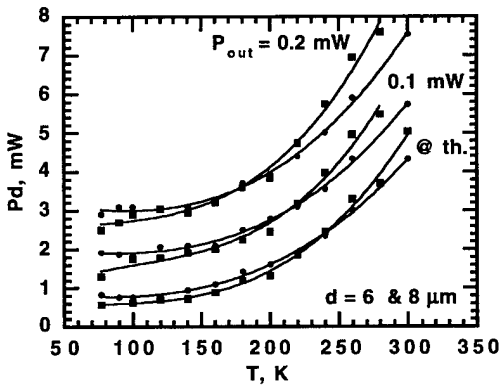


Fig.5. Dissipated power as a function of measured temperature for several output power levels for 6 (squares) and 8 (dots) μm diameter VCLs

The VCL design (single QW active and 22.5 periods of output coupler) was optimized for an output optical power level of 0.1-0.2 mW. Fig.5 shows the power dissipation as a function of temperature at these power levels for 6- and 8- μm diameter VCLs. At the optimum temperature (77 K), the power dissipation for the single-mode 6 μm diameter device is 0.6 mW at threshold, 1.4 mW for P_{out} = 0.1 mW, and 2.6 mW for P_{out} = 0.2 mW. The low power dissipation at 77 K is achieved due to the reduction of threshold current. However, it could be further improved by

adjusting the composition and doping profiles of the p-type contact and utilization of a double intracavity contact scheme to lower the operation voltage.

In summary, we have designed and fabricated dielectrically apertured VCLs optimized for operation at cryogenic temperatures. 6-μm diameter VCLs with relatively low threshold currents ~130 μA, 1.5 mW of single-mode output power, and total power dissipation of 1.4 mW for optical output of 0.1 mW at 77 K are demonstrated. Operation up to 300 K with submilliamp thresholds is also demonstrated in the same devices. By using smaller oxide aperture diameters further reduction in threshold currents can be achieved at the expense of poorer side-mode suppression.

The authors would like to acknowledge the support of SBRC/Hughes via the UC-MICRO program.

[1] L.A.Hornak, S. K. Tewksbury, J. C. Barr, W. D. Cox et al., *Proc. SPIE* **2400**, 224 (1995).

[2] E. Goobar, M. Peters, G. Fish, and L. A.Coldren, *IEEE Photon. Technol. Lett.* **7**, 851 (1995).

[3] Bo Lu, Wen-Lin Luo, C. Hains, J. Cheng, R.P. Schneider, R.P Choquette, K. L. Lear, S. P. Kilcoyne, and J. C. Zolper, *IEEE Photon. Technol. Lett.* **7**, 447 (1995).

[4] E. Goobar, M. Peters, D. Cohen, G. Fish, and L. A.Coldren, *CLEO'95*, paper CTuB7, Baltimore, MD, May 1995.

[5] B. J. Thibeault, J. W. Scott, M. G. Peters, F. H. Peters, D.B. Young, and L.A. Coldern, *Electron. Lett.* **29**, 2197 (1993).

[6] B. J. Thibeault, E. R. Hegblom, P. D. Floyd, Y. Akulova, and L. A. Coldren, *LEOS'95* post deadline paper 2.1, San Francisco, CA (1995).

[7] D. L. Huffaker, D. G. Deppe, and K.Kumar, *Appl. Phys. Lett.* **65**, 97 (1994).

Wednesday, May 1, 1996

Diffractive and Reflective Elements

IWE 2:00 pm-3:00 pm
Fairfax A

Leon McCaughan, *Presider*
University of Wisconsin–Madison

High Efficiency Focusing Waveguide Grating Coupler with Parallelogramic Groove Profiles

Tingdi Liao, Stephen Sheard and Ming Li
Department of Engineering Science, University of Oxford
Parks Road, Oxford, OX1 3PJ, UK
Telephone : +44 1865 273094; Fax : +44 1865 273905.

Jianguo Zhu and Philip Prewett
Central Microstructure Facility, Rutherford Appleton Laboratory
Chilton, Didcot, Oxon, OX11 0QX, UK
Telephone : +44 1235 821900; Fax : +44 1235 44570.

INTRODUCTION

Focusing waveguide grating couplers (FWGCs) play important roles in many integrated–optic devices, such as the integrated–optic disk pickup device[1]. Such a FWGC can be evaluated in terms of : (i) coupling efficiency as a grating coupler and (ii) focusing performance as a focusing lens. Fabrication of diffraction–limited focusing waveguide grating couplers by electron–beam lithography has been previously reported by other researchers[2]. However, high focusing performance as well as high coupling efficiency is of great importance for obtaining high signal–to–noise ratio in a practical device. The coupling efficiency theoretically obtained so far is around 60% when using a buffer layer reflector[1]. The other possible method to achieve higher efficiency is to utilize a multi–layered high–reflectivity dielectric stack[3], providing a radiation directionality of greater than 95%. In this paper, a high efficiency focusing waveguide grating coupler using a new waveguide grating structure is proposed, designed and fabricated by direct–write electron beam lithography.

DESIGN

Principles We are concerned with a focusing waveguide grating coupler. It is well known that locally any grating coupler can be treated as a plane, uniform grating coupler that can be fully described by the grating pitch and groove direction. Based on this consideration, a focusing waveguide grating coupler can be treated as one which consists of several uniform sub–gratings each of which corresponds to a given pitch $\Lambda \equiv \Lambda(y,z)$. Thus the perturbation method developed for a uniform grating coupler can be used to deal with each sub–grating that forms one part of a chirped and curved grating coupler.

A new structure for the grating coupler with parallelogramic groove profiles[4,5] is shown in Fig.1. The parallelogramic shape is etched into both layers simultaneously. Such a waveguide grating system can be treated as a five–layered waveguide structure. However, based on the gen-

eralised volume–average method by W. Streifer et al[6], a double–layered grating coupler with index and depth (n_g, g_1), and (n_{ad}, g_2) for each layer, can be reduced to a single–layered waveguide grating coupler with an equivalent index value. Based on the above, computer simulations shows that the proposed structure has two main advantages : (1) both large radiation decay factors and high directionality are achievable; (2) a wide range of radiation decay factors is conveniently available by varying the thickness of the additional grating layer.

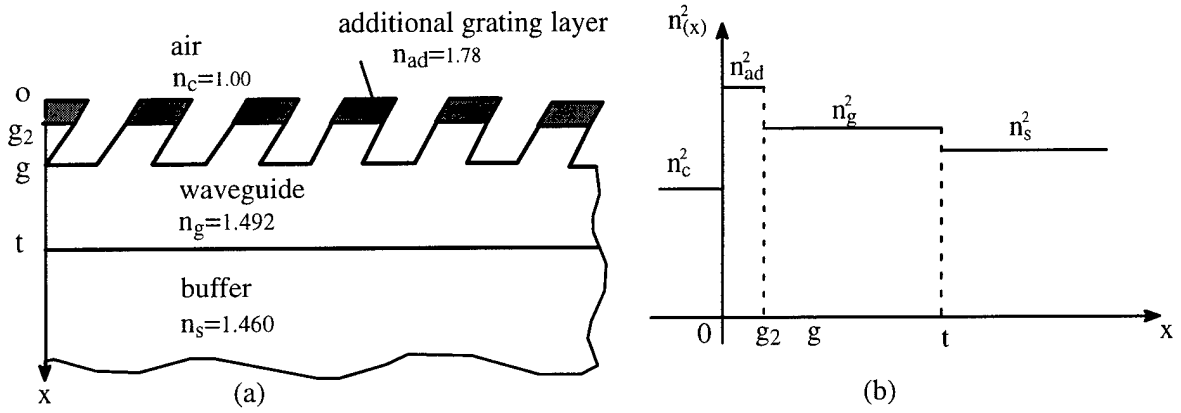


Fig. 1: Proposed structure for a focusing grating coupler with parallelogramic profiles (a) and its squared refractive index (b). The grating is etched into both additional layer and guiding layer.

FWGC parameters : Laser–to–grating waveguide distance r = 10.50mm. FWGC working distance WD = 2.00mm, FWGC aperture L = 1.00mm, focal length f = 1.56mm. Central output angle θ_o=15°. Laser wavelength λ=1. 30μm.

Waveguide parameters : The grating design is based on silica waveguide technology developed under the "SOPHI" project funded by the EPSRC and Department of Trade and Industry, UK. The buffer layer is SiO_2 with n_b = 1.460, t_b = 10.0μm, and the guiding layer is arseno–silicate glass (ASG) with n_g = 1.492, t=2.0μm. The effective index of guided mode (TE_0) N_{eff} = 1. 474; the grating pitch Λ = 1.289 ~ 0.877μm; the grating total thickness g = 0.40μm, the blaze angle θ_B = 45°; the SiN layer has a thickness of g_2 = 0.17μm. The theoretical directionality η^c obtained here is 95. 1%, while the coupling efficiency, η, is 90. 7%, about 30% higher than that obtained previously[1].

FABRICATION

To achieve high coupling efficiency, a large radiation decay factor is desired. In our device a high index SiN thin film (n_{ad}=1. 78, g_2=0. 17μm) is sputter–deposited on top of the waveguide structure. E–beam direct writing was used to pattern the focusing grating. The e–beam resist (950PMMA CS) was spin–coated on top of the waveguide sample at 6000rpm for 40 seconds, forming a thickness of 0. 30μm. After soft baking at 170°C in an oven for 60 minutes, the sample was directly transferred to an evaporator. A thin Al layer (about 7nm) is evaporated on top of the PMMA in order to avoid charging problems during e–beam writing on the waveguide structure. Before conventional development, the thin Al layer is removed in photoresist developer

(MF319). An e–beam energy of 20KeV, a beam current of 2.0nA and a dose of 300μC/cm^2 was used to expose the pattern. To achieve high addressing accuracy and reduce pattern distortion, the grating pattern was written with stitched field of 0.4mm×0.4mm having a grid size of 12.5nm. Fig.2 shows an SEM picture of the resist profiles for fabrication of the focusing grating coupler.

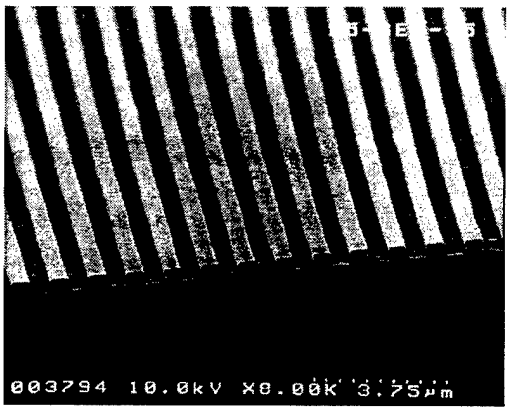


Fig. 2: SEM picture of resist profiles of a focusing grating coupler

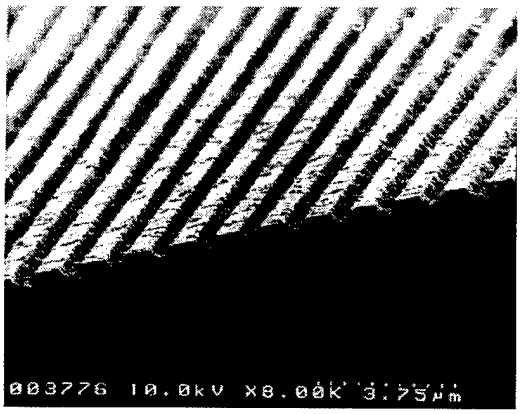


Fig. 3: SEM picture of cross section of fabricated focusing grating coupler in SiN/ASG layer.

To fabricate a grating with parallelogramic groove profiles, a metal grating is required as a mask layer for transferring the grating pattern onto the waveguide structure during etching. The metal grating is prepared using the lift–off process. An oxygen plasma descum was carried out to remove traces of organic residue in the exposed resist pattern. This ensures good adhesion of the metal grating lines to the substrate and guarantees that the lift–off process is successful. After lift–off, a metal mask is formed only over the exposed grating regions. Therefore, a metal mask with an open grating window (1mm×1mm) needs to be defined by conventional photolithography and lift–off in order to define the FWGC aperture. Finally, the metal grating pattern is transferred onto waveguide structure by an oblique reactive ion etching process[7,8]. In our device, the grating is fabricated on both SiN layer and ASG guiding layer. The following processes were employed : a CF_4 plasma was used to etch the SiN and then a CF_3H plasma was used to etch the ASG. Fig.3 shows an SEM picture of the cross section of the fabricated device.

RESULTS

The focused spot is magnified by a microscope objective (20×) and detected by an IR CCD camera. The CCD image and the intensity profiles of the focused spot are illustrated in Fig.4 and Fig.5, from which the spot size (FWHM) is determined to be 9.52μm.

To measure the radiation directionality of the fabricated device, a focusing waveguide grating coupler with complementary blaze angle was prepared as above. This complementary FWGC should be exact the same as the original FWGC device except for the blaze angle, which is given by 180–θ_B. Based on theoretical calculations, the directionality can be determined by

$$\eta^c = \frac{P_{c1}}{P_{c1} + \varkappa P_{c2}} \times 100 \qquad (1)$$

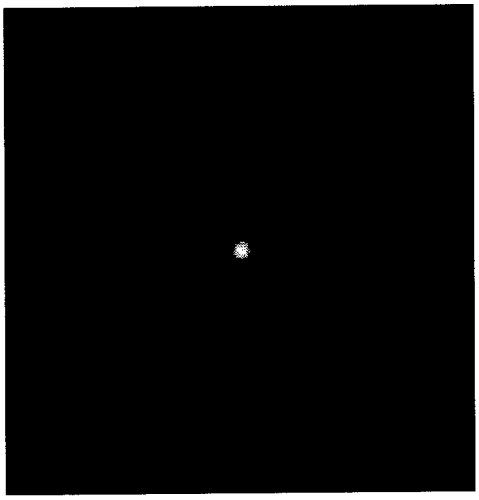


Fig. 4: The CCD image of focused spots produced by the fabricated focusing grating coupler.

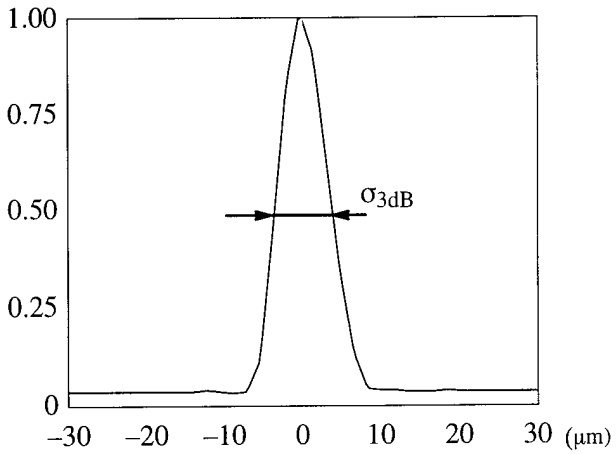


Fig. 5: Normalized intensity profile of focusing spot produced by the fabricated focusing waveguide grating coupler. The focused spot size (FWHM) is determined to be 9.52μm.

where P_{c1} and P_{c2} are the radiation powers into cladding measured from the FWGC and the complementary FWGC, respectively. The parameter $\varkappa$ is a theoretically determined coefficient that depends on the waveguide structure and the experimental setup. In our device $\varkappa \approx 0.5$, and the absolute error in determining the directionality is expected to be within 2% for the blaze angle ranging from 25° to 55°. By this method, the directionality of the fabricated devices is measured to be 91.2 %. In addition, a uniform grating coupler with pitch of 1. 0μm was fabricated together with the FWGC and the complementary FWGC. From the intensity profiles of the radiation beam, the radiation decay factor of the uniform grating coupler is estimated to be 28.3cm^{-1}. Therefore the coupling efficiency of the FWGC is estimated to be 85.6%.

CONCLUSIONS

Focusing waveguide grating couplers using parallelogramic groove profiles have been successfully fabricated by electron beam lithography. A directionality of greater than 90% was obtained and coupling efficiency of 85.6% determined. Although the focused spot size (FWHM) obtained was around 10μm due to fabrication and alignment errors, it has been demonstrated that high coupling efficiency can be achieved with the proposed FWGC structure.

REFERENCES

1.S Ura, T Suhara, and H Nishihara et al, J of Lightwave Techno., vol.LT–4, 913–917, 1986.
2.F Sogawa, Y Hori, and M Kato, Appl. Opt., vol. 29, 5103–5105, 1990.
3.R L Roncone, Lifeng Li, and K A Bates et al, Appl. Opt. , vol. 32, 4522–4528, 1993.
4.M Matsumoto, IEEE J QE–28, 2016–2023, 1992.
5.M Li and S J Sheard, Opt. Commun., vol. 109, 239–245, 1994.
6.W Streifer, R D Burnham and D R Scifres, IEEE J QE–12,494–499, 1976.
7.M Li, J C H Lin, M J Cherrill, and S J Sheard, Electron. Lett., vol.30, 2126–2128, 1995.
8.G D Boyd, L A Coldren, and F G Storz, Appl. Phys. Lett.,vol. 36, 583–585, 1980.

Gratings with parallelogramic-shape grooves for unidirectional coupling in large guidance waveguides

V.A.Sychugov, A.V.Tishchenko
General Physics Institute of Russian Academy of Sciences, Vavilov Street 38,
117942 Moscow, Russia. Phone:+7 095 1328113; Fax: +7 095 1350270
O.Parriaux
Formerly CSEM, Switzerland

Introduction

Waveguide coupling gratings are bound to be widely used in future integrated-optic devices and microsystems. However, the problem of grating coupling efficiency has not received a convincing and practicable solution so far. The main reason is that light radiation into a medium with lower refractive index n_c (air, for instance) is always accompanied by light radiation into the medium with larger refractive index n_s (substrate). The relative intensity of the radiation into the substrate is n_s/n_c or more. It is known that only coupling at an angle larger than critical provides high excitation efficiency; but this solution is difficult to implement in practice. Therefore the problem of unidirectional coupling, which has been constantly addressed during the last 20 years, remains very actual. Recently, a new and promising solution to this problem was proposed by M. Matsumoto [1] and by M. Li and S.Y. Sheard [2]. They consider light propagation in a waveguide having a grating with a parallelogram groove shape and obtain a definite "blazing effect", i.e. unidirectional light outcoupling from a waveguide.

An experiment [3] confirmed the theoretical results of [2]. The cited papers deal only with TE polarized light and the considered waveguide structures have small guidance. Grating coupling to/from weak guidance waveguides is however of little practical interest since the inherently small grating radiation coefficient imposes very long gratings for a significant power ratio to be coupled in/out. We are presenting here new results, which also consider TM polarization, on large guidance waveguides which are, and will be, the most often used structures in practical applications such as displacement encoders and biological sensors for non-labelled species [4]. In such large guidance structures, the blazing effect of parallelogramic-shape grooves can not be achieved with grooves defined within the waveguide film since the grooves are necessarily very shallow (a few nanometers as in biochemical sensors [4]). It is therefore necessary to consider a 4-layer structure where the parallelograms are defined in a low-index film deposited on the waveguide film as illustrated in Fig. 1. This work is part of a collaborative effort on grating coupling within BRITE project FOA.

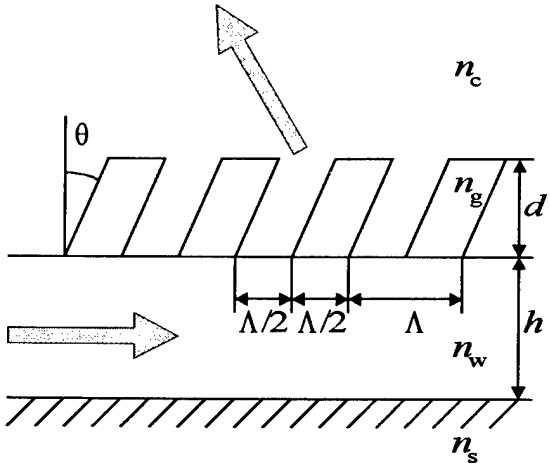


Figure 1. Parallelogramic grating loaded slab waveguide

Theoretical treatment and calculation results

For computer analysis of periodical waveguide structures, we use the R-T matrix method [5]. In this method, the grating region is represented in the form of an stack of thin layers. We calculate the diffraction R-T matrix for each thin layer grating using a Rayleigh-Fourier technique [6]. We then combine all R-T matrices in order to get the diffraction R-T matrix of the whole grating. This method is valid for deep gratings with arbitrary groove shapes.
We first analyze the waveguide structure described in [2]. The comparison of our results with those of [2] confirms the good agreement between the two methods. The TM mode analysis reveals a very similar blazing effect. A maximum radiation coefficient contrast is obtained for a blazing angle of 30^0 for near to normal radiation.

We consider next the case of a high guidance structure. The refractive index of the single mode waveguide is n_f = 2.1, substrate (silica) refractive index is n_s = 1.457. The grating is formed in the same material as the substrate n_g = 1.457, the waveguide is covered with water, n_c = 1.33. The incidence of light is from the substrate at the angle $\theta = -10^0$. This structure is typical for an evanescent wave biosensor. We first calculated the angular dependence of the radiation coefficient for two different groove depths for both TE and TM modes, again with incidence from the substrate. These are presented in Fig. 2.

We can see that the blazing effect also exists in the case of high waveguide refractive index difference. Fig. 3a shows the calculated radiation loss coefficient of the TE mode versus groove depth in the condition of maximum coupling into the substrate and cover.

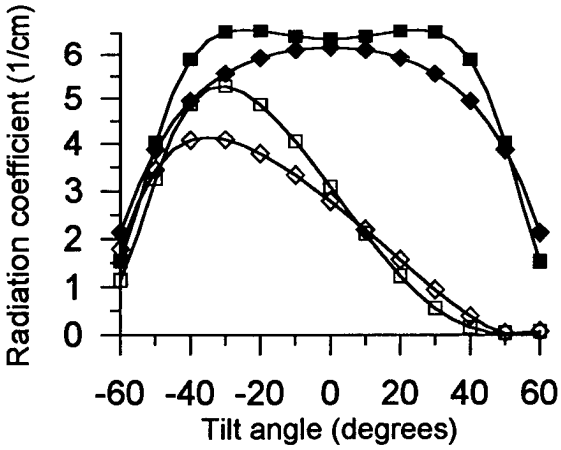


Figure 2a. Total radiation coefficient (plein) and its part due to the radiation into the substrate (void); TE mode;
◆ - d = 0.15 μm, ■- d = 0.25 μm.

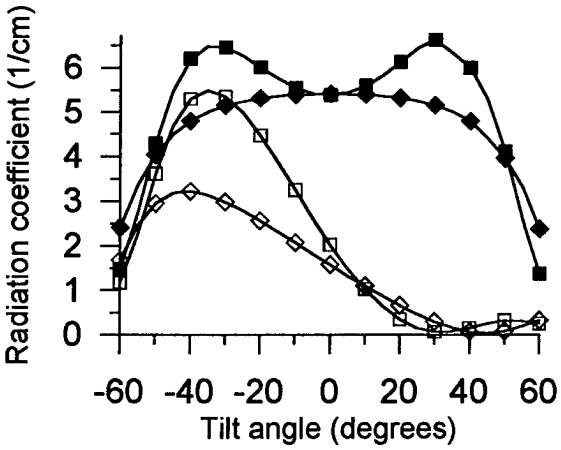


Figure 2b. Total radiation coefficient (plein) and its part due to the radiation into the substrate (void); TM mode;
◆ - d = 0.15 μm, ■- d = 0.25 μm.

In contrast with the case of [2], the radiation loss coefficient in the present large guidance structure exhibits a saturation effects which starts at d = 0.2 μm in our structure. The reason for this is clear if we realize that the mode field in the considered structure decreases sharply in the grating region. Unidirectionality can be appreciated by defining the ratio ν of the radiation coefficient into the cover α_c at the optimum blazing angle, relative to the total radiation loss coefficient α. ν = 1 corresponds to complete single-sided radiation into the

cover. Fig. 3b represents ν versus the grating depth. As expected, ν does saturates but, in the case of TE mode radiation in the cover, ν does not reach 1. The condition of fully single-sided radiation is very little dependent on d as from d = 0.15 μm.

We can conclude that parallelogramic grating in and out coupling to/from large guidance waveguide is very tolerant on the grating depth in the saturation region, and essentially depends on the groove angle.

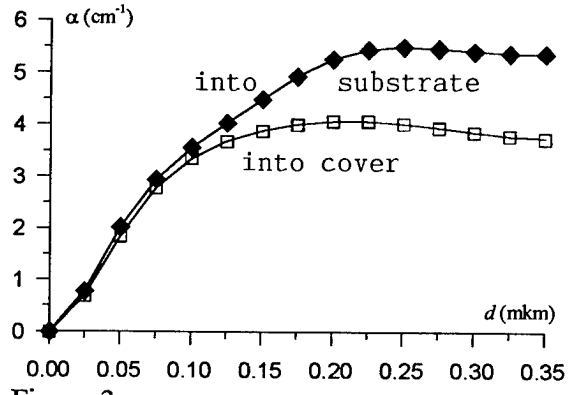


Figure 3a

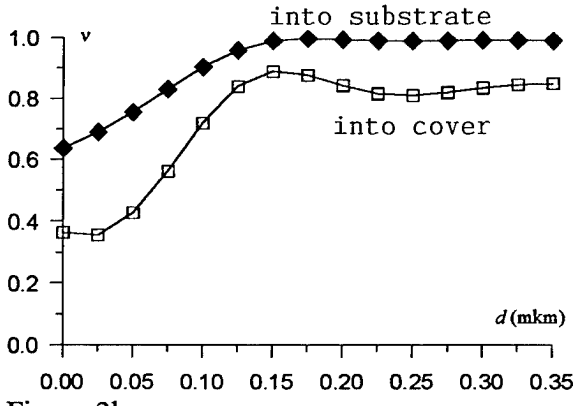


Figure 3b

Earlier in [7], a detailed study of a corrugated waveguide mode excitation by a normally incident light beam was made assuming that the grating has a symmetric groove profile. This excitation configuration is of obvious practical interest but its solution must take in account second order intraguide resonance between the two contrapropagating excited waveguide modes.

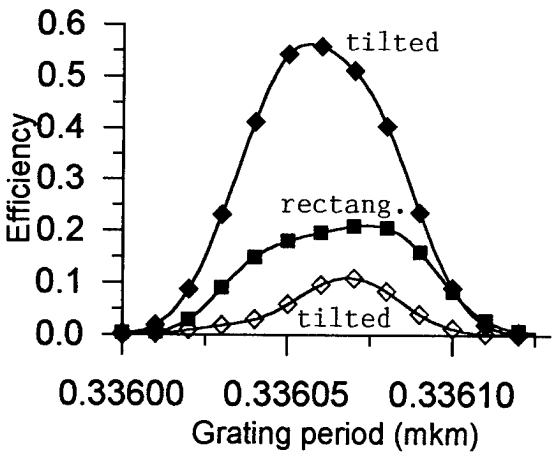


Figure 4. Excitation efficiency of the TE waveguide mode under normal incidence from the substrate for a groove tilt of 50^0 and for symmetrical rectangular grooves.

In the case of parallelogramic grooves, the symmetry is broken and the problem becomes more complicated. The reason is that, in case of parallelogramic grooves, radiation loss coefficients and intraguide resonance coefficients depend on mode propagation direction. Fig. 4 shows the excitation efficiencies of two contradirected waveguide modes versus grating period at fixed tilt angle of the grooves. The grating length L is equal to the exciting beam diameter $2w_0$ = 2.4 mm. It is clear that one can still find the grating period at which Gaussian excitation efficiency in the preferred direction is maximum. The difference between excitation in the two directions is due to the same blazing effect of the grating and thus depends on the tilt angle. As a qualitative conclusion about normal incidence coupling by means of a parallelogramic grating, it can be said that the unidirectional feature is still present but it is only slightly degraded by the existence of second order intra-guide coupling. Therefore no particular care must be taken to avoid a normal incidence condition.

The choice of the tilt angle for the blazing effect is thus very important in the design of a waveguide coupling device. We have just revealed that the angle is actually the only parameter that determines the coupler operation in the case of large guidance structures. The authors of [2] propose to use K. Chang and T. Tamir approach [8] for the determination of the groove angle. According to this approach, in a waveguide structure where a grating is considered as a layer with an average refractive index, the blazing condition is realized when a diffracted waveguide mode is reflected at the Bragg condition. The authors of [2] report that this relation is correct for a structure of low guidance. In our large guidance case, their formula does not give a very accurate estimate. However, we have shown that the proposed relation can be used as an initial guess for the tilt angle.

Conclusion

In conclusion, we have completed the analysis of unidirectional coupling in low index waveguide by means of parallelogramic grating in showing that a significant blazing effect is obtainable for the TM polarization also. The same unidirectionality feature is shown to be obtainable in the more practical case of large guidance waveguides by means of a loaded parallelogramic grating. In large guidance structures, the condition for high efficiency unidirectional coupling is shown to be largely independent of the grating groove depth. This renders the parallelogram groove solution especially interesting practically. Second-order intra-guide resonance in the case of normal incidence is shown to slightly deteriorate the unidirectionality.

Experimental results on large guidance waveguide for biosensors will be reported at the conference.

Acknowledgement

This work was performed within the BRITE programme, project number BE-5720, "High-efficiency wavefront shaping Flat Optical Antennae".

References

1. M.Matsumoto, "Analysis of the Blazing Effect in Second-Order Gratings". IEEE J. of Quant Electronics. 28, 2016-2023 (1992).
2. M. Li, S.Y. Sheard, "Waveguide couplers using parallelogramic-shaped blazed gratings". Opt.Commun., 109, 239-245 (1994).
3. M. Li, S.Y. Sheard, "Demonstration of Blazing Effect Using Grating Couplers with Parallelogramic Tooth Profiles". Proceedings 7 th European Conference on Integrated Optics, April 3-6, 1995, Post-deadline Papers, Thp.1, p.33-36.
4. C. Fattinger, C. Mangold, M.T. Gale, H. Shutz, "Bidiffractive optical coupler: universal transduser for optical interface analytics", Opt. Eng., 34, 2744-2753 (1995).
5. S.T. Peng, T. Tamir, and H.L. Bertoni, "Theory of periodic dielectric waveguides", IEEE Trans. Microwave Theory Tech., MTT-23, 123-133 (1975).
6. I.A. Avrutskii, V.A. Sychugov, A.V. Tishchenko, "The study of excitation, radiation and reflection processes in corrugated waveguides", Proc. IOFAN, 34, 3-98, Moscow, Nauka, 1991.
7. O. Parriaux, V.A. Sychugov, A.V. Tishchenko, "Excitation of a ridge waveguide by a normally incident light beam", Quantum Electronics 25, no. 6, 582-586 (1995).
8. K.C. Chang, T. Tamir, "Simplified approach to surface-wave scattering by blazed dielectric gratings", Appl. Optics, 19, no. 2, 282 (1980).

Periodically-segmented tapered waveguide for mode-size transformation and fundamental mode excitation

M. H. Chou, M. A. Arbore and M. M. Fejer

E. L. Ginzton Laboratory, Stanford University, Stanford, CA 94305
Tel: (415) 723-9100, Fax: (415) 723-2666

Transformation of modal properties through axial tapering of the structure of a dielectric waveguide is useful in several contexts. Mode size transformation with a tapered waveguide allows independent optimization of the mode size in different portions of a waveguide to simultaneously achieve effective input and output coupling and for efficient performance of active or electrooptic devices. An adiabatic taper from a single to a multimode waveguide also allows robust coupling into the fundamental mode of a multimode waveguide, important in certain types of nonlinear waveguide devices, such as difference frequency generators, that involve interactions between modes at widely disparate wavelengths. Periodically-segmented waveguides (PSWs), investigated both theoretically[1,2,3] and experimentally[4,5] in the literature, allow independent control over vertical and lateral confinement, and thus can be used to tailor the size and shape of waveguide modes. In this paper we report tapers in annealed-proton-exchanged (APE) waveguides in $LiNbO_3$ through the use of segmented waveguides with axially varying duty cycle.

PSWs consist of segments that repeat with a period Λ, each segment consisting of a region of length l indiffused with a dopant to produce an index change Δn, separated by undoped regions. Both theoretical[2] and experimental[4] investigations in the literature show that an average index model, where the behavior of the PSW is approximated by an equivalent waveguide in which the effective refractive index step is taken to be

$$\Delta n_{eff} = \Gamma \Delta n \ , \qquad (1)$$

where the duty cycle $\Gamma = l/\Lambda$, accurately predicts the modal properties of the waveguide. Nir *et al.* showed that under appropriate fabrication conditions the propagation losses are not significantly increased over a similarly confining uniform waveguide.[5] With independently controllable optical confinement in both width (with physical width and segmentation duty cycle) and depth (with segmentation duty cycle), the segmented waveguide with axially varying duty cycle is a practical method to make tapered waveguides, as shown in Fig. (1). Another major advantage of PSWs for tapers is that they can be integrated with essentially any existing integrated-optic device without requiring additional lithography or diffusion steps.

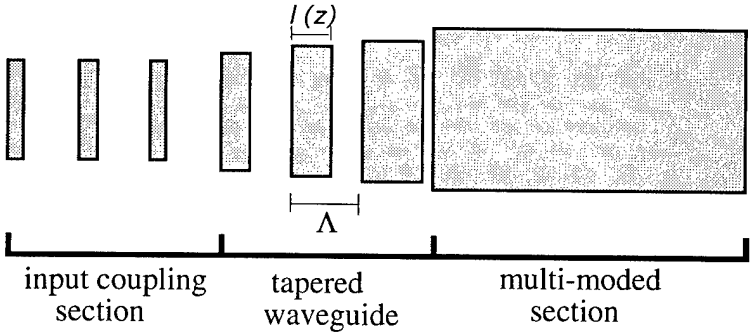


Fig. 1. Tapered waveguide using a segmented structure. Both the input coupling section and the taper are made from periodically segmented waveguides. Duty cycle and waveguide width can be modulated simultaneously to optimize the device.

We verified the reported mode and loss properties of PSWs in APE $LiNbO_3$ at a 1.3 μm wavelength. The results for samples with a proton exchange depth of 0.4 μm, a waveguide width of 5 μm, a 12 hour anneal at 333°C, and various duty cycles and segmentation periods are shown in Figs. 2. Figure 2a shows the measured 1/*e* mode full-width vs. duty cycle for three different segmentation periods. The lines on the graph, calculated based on the average index model of Eq. (1) with transverse refractive index distributions calculated from the fabrication conditions according to the model obtained by Bortz,[6,7] show good agreement with the experimental data. Figure 2b shows the losses *vs.* duty cycle, measured with the Fabry-Perot technique.[8] The results show that the waveguide properties do not depend significantly on the segmentation period, and, for duty cycles sufficiently large that the effective waveguide is not close to cutoff, the loss does not increase significantly above that of a uniform waveguide.

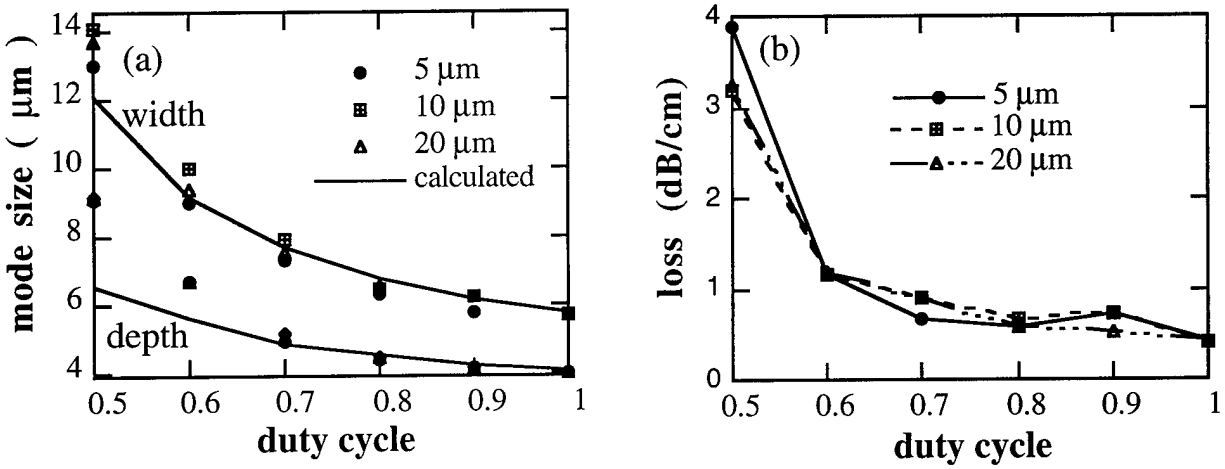
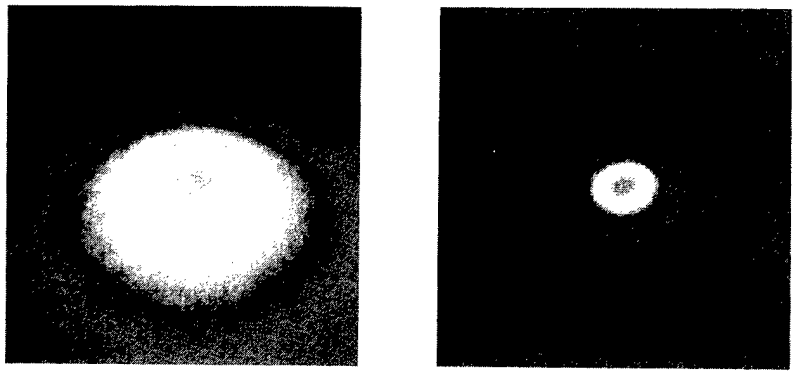


Fig. 2. (a) measured 1/e full-width power mode size vs. duty cycle (b) measured loss vs. duty cycle for three segmentation periods (5 μm, 10 μm, and 20 μm).

We chose as a demonstration a taper that allows robust coupling of pump radiation (780 nm) into the fundamental mode of a highly-multimode waveguide, designed for near-degenerate difference frequency mixing at 1.56 μm. For the main waveguide, we used the APE-LiNbO3 waveguide model of Ref. 7 to choose a proton-exchange depth and width of 0.5 μm and 5.5 μm, respectively, and annealing time of 9 hours at 333°C, giving a nominally 13 moded waveguide for the pump. The full device consists of a 1.5 mm long single mode input coupling waveguide with a period 10 μm and a duty cycle 0.2, followed by a taper region in which the duty cycle was gradually increased from 0.2 to 1, with a linear taper function $\Gamma(z) = 0.2 + 0.8\ (z/L)$ or a concave taper function $\Gamma(z) = 0.2 + 0.8\ (z/L)^3$ (where z is the distance along the taper and L is taper length), followed by the uniform multimode waveguide. The width was constant throughout the device. Samples fabricated according to these designs were tested at 780 nm for spatial mode profiles, taper losses, mode conversion efficiency (defined as the ratio of the power output in the fundamental mode to the total output power) and, dependence of output mode on input coupling conditions. The measured spatial profiles, with 1/*e* intensity dimensions of the fundamental mode 6.0 x 4.4 μm in the input coupling sections and 2.0 μm x 1.3 μm in the multi-mode sections (with a 2.5 mm long concave taper), are shown in figure 3.

To measure the excess loss for the fundamental mode in the taper, we fabricated 11 mm long straight segmented waveguides with and without back-to-back tapers. Both of these waveguides are single-mode at their input and output ends, and so could be tested by the Fabry-Perot method.[8] The total propagation loss of the straight segmented guide was 1.1 dB (1.0

dB/cm). The total loss for the segmented waveguide with two 1 mm long concave tapers was 2.3 dB. Subtracting the losses of the straight sections (assumed the same as in the waveguide without tapers) leaves excess loss of 0.6 dB for each of the 1 mm concave tapers. Similarly, we obtained excess losses 1.5 dB for 1mm long linaer tapers and 0.4 dB for 2.5 mm long concave tapers.



(a) (b)

Fig. 3. Measured mode spatial profiles at wavelength 780nm (a) in the input coupling section (b) in the multi-moded section.(with a 2.5 mm long cancave taper). Image fields are 11.7 μm x 11.7 μm.

We used modal interference to measure the mode conversion efficiency. When more than one mode is excited in the waveguide, the output intensity distribution is determined by the coherent sum of the modal fields present at the output of the waveguide. This coherent summation of fields (rather than intensities) means that a small power fraction in a higher order mode causes a large change in the output intensity distribution. To quantify the fraction of the power in the fundamental mode, we observed the output intensity distribution while tuning the wavelength of the 780 nm diode laser used to excite the waveguide. Wavelength dependence of the output intensity distribution results from the difference in propagation constants of the fundamental and higher order modes, which then add in or out of phase with each other as the wavelength is varied. Assuming (as predicted by simulations) that the second higher order width mode (i.e. the first even

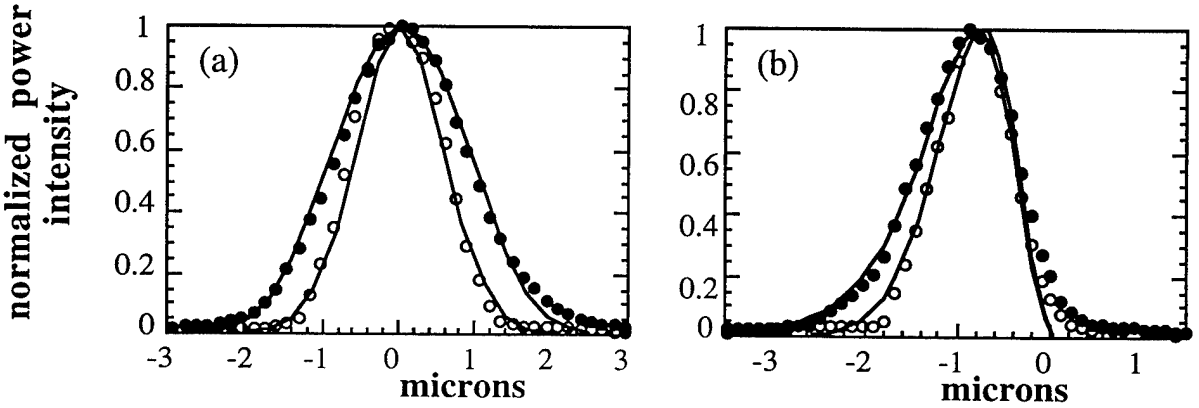


Fig. 4. Output intensity profiles resulting from modal interference for two different wavelengths. Circles are measured results; solid lines are curve fits for 0 and π relative phases between the fundamental and first allowed high order transverse modes (a) in the width direction. (b) in the depth direction.

higher order width mode) and the first higher order depth mode dominate the undesired modal excitation, the observed output intensities can be fit with respect to the ratio of fundamental mode to higher order mode power. Figure 4 shows the measured intensity profiles of maximum and minimum widths for a 1 mm concave taper. The solid lines are fits for 0 and π relative phases of the fundamental and higher order mode, corresponding to mode conversion efficiencies of 97% in width and 98% in depth, resulting in 95% overall.

We tested the sensitivity of the output intensity distribution to the input coupling conditions to illustrate that the filtering action of the input coupling region prevents launching of undesired modes. Figure 5 shows measured output intensity distributions observed with different input coupling conditions for a waveguide without any taper and one with a 1 mm long concave taper. The waveguides were moved laterally (shown) and vertically about 1.7 μm. It can be seen that the output mode mixture for the waveguide with no taper is highly sensitive to input coupling conditions, while the mode mixture for the waveguide with the coupling taper is essentially independent of coupling conditions.

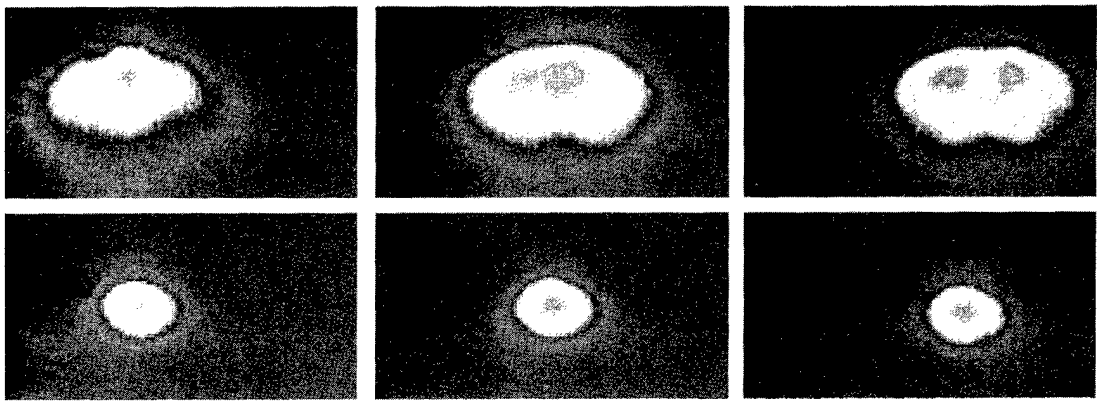


Fig. 5. Measured output intensity profiles for different input coupling conditions for launching the light into a waveguide (a) straight multimode waveguide (b) multimode waveguide with imput through single mode section and cancave taper. In this example, waveguides are moved in the width direction about 1.7 microns relative to the incident beam to change coupling conditions.

In summary, we have observed that the effective index of PSWs can be accurately modeled by spatially averaging the increased index of the proton exchange and the waveguide propagation losses will not be increased significantly by using PSWs. We have used a segmented structure to fabricate tapered annealed proton exchanged channel waveguides in $LiNbO_3$. Spot size transformations of 3:1 have been obtained, with excess losses 0.4 dB. Robust, efficient coupling to the fundamental mode of a multimode waveguide was demonstrated. The mode size transformation can also be used to simplify free-space coupling or fiber pig-tailing by loosening alignment tolerances.

REFERENCES:

1. Z. Weissman and A. Hardy, Electron. Lett. **28**, 1514 (1992).
2. Z. Weissman and A. Hardy, J. Lightwave Technol. **11**, 1831 (1993).
3. L. Li and J. J. Burke, Opt. Lett, 17,1195 (1992).
4. K. Thyagarajan, C. W. Chein, R. V. Ramaswany, H. S. Kim, and H. C. Cheng, Opt. Lett. **19**, 880 (1994).
5. D. Nir, S. Ruschin, A. Hardy and D. Brooks, Elec. Lett., **31**, 186 (1995).
6. M. L. Bortz, M. M. Fejer, Opt. Lett. **16**, 1844, (1991).
7. M. L. Bortz, L. A. Eyres, M. M. Fejer, Appl. Phys. Lett, **62**, 2012 (1993).
8. R. Regener and W. Sohler, Appl. Phys. **B, 36**, 143 (1985).

Low-loss GaAs/AlGaAs waveguide corners for compact optical delay lines.

J.M. Heaton, M.M. Bourke, S.B. Jones, K.P. Hilton, and D.R. Wight.
Defence Research Agency, St Andrew's Road, Malvern, Worcestershire, WR143PS U.K.
Tel. : +44 1684 895585 Fax. : +44 1684 896150 E-mail : jmheaton@taz.dra.hmg.gb

To make compact delay lines it is essential to have low-loss single-mode straight guides, and compatible low-loss, small radius corners (or mirrors). Straight guide losses of a few tenths of a dB per centimetre have been achieved in III-V semiconductor waveguides, but these are not usually compatible with small radius corners [1,2]. Alternatively, very low excess corner losses have been achieved with a bend radius as small as 30 μm using deep-etched guides, but the corresponding straight guide losses were very high [3]. In this paper we use deep-etched, vertical-walled GaAs/AlGaAs waveguides (λ = 1.064 μm). We compare sets of straight guides and corners for two wafer designs: 1) a smaller-guide wafer, with a 2.6 μm single-mode width; and 2) a larger-guide wafer, with a 4.2 μm single-mode width. We also compare measured losses of different waveguide corner designs, and demonstrate the advantages of using corners with an optimised near-hyperbolic shape, designed to minimise straight to curved guide mode mismatch. We show, for example, results for an optimised 90° corner, which has an excess loss of 0.5 dB for an equivalent radius of 100 μm.

The epitaxial layers (on a GaAs substrate) for the two types of guide were as follows:

Layer	**Smaller-guide**			**Larger-guide**		
Upper cladding	30%	AlGaAs	1.1 μm	20%	AlGaAs	1.2 μm
Waveguide core		GaAs	1.6 μm	5%	AlGaAs	2.5 μm
Lower cladding 1	20%	AlGaAs	0.3 μm	15%	AlGaAs	0.3 μm
Spacer layer		GaAs	0.5 μm	5%	AlGaAs	0.5 μm
Lower cladding 2	4%	AlGaAs	2.0 μm	6.5%	AlGaAs	2.8 μm

Both guides were etched to about 0.1 μm into the spacer layer. All modes except the fundamental leaked strongly into the high index GaAs substrate. This was because the second cladding layer index was lower than the effective index of the fundamental mode but higher than those of all other modes. Waveguides were made with these two wafer designs using conventional photolithography and reactive ion etching to give smooth, vertical sidewalls. Sets of 36 straight guides of different widths from 1.0 μm to 8.0 μm in steps of 0.2 μm were made and tested. The optical loss was measured using the Fabry-Perot method [2,5] for guide lengths of 0.5 cm, 1.0 cm and 2.95 cm, and the measured loss was found to be independent of length for single-mode guides. Note, however, that the Fabry-Perot method is not very reliable for multimode guides and will in general overestimate the guide loss. The number of modes supported by each guide at each length was determined by viewing the output surface of the guide using a 0.95 NA lens and an infra-red camera (to form a high resolution microscope) and looking at the way that the camera image changed as the input spot was moved. Figure 1 shows the measured results for four sets of guides all of length 2.95 cm. The guide loss, and the points at which the different higher order modes appeared were in

good agreement with theoretical predictions using the leaky-mode Spectral Index method [4]. There is a cut-off guide width for each lateral mode, determined by the index step between the core and the second cladding layer. The minimum single-mode larger-guide loss occurred for guide widths around 4.0 μm, and was 0.8 dB/cm (0.6 dB/cm for some multi-mode guides). We believe that most of this loss was due to side wall effects, but the theory predicts a loss due to leakage into the substrate of 0.3 dB/cm which may also account for some of the loss. The minimum single-mode smaller-guide loss occurred for guide widths around 2.6 μm, and was 1.5 dB/cm (0.9 dB/cm for some multi-mode guides).

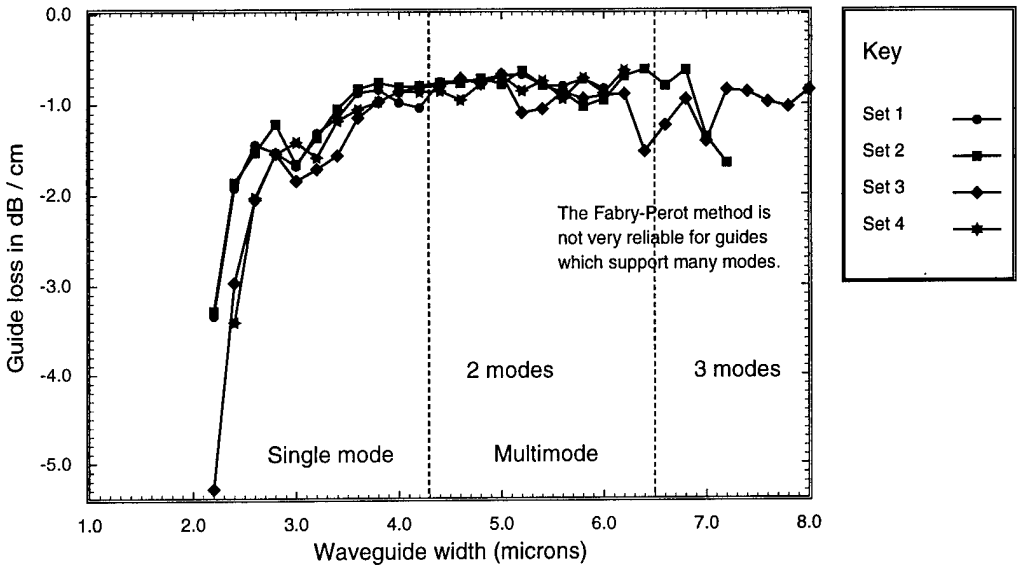


Figure 1. *Straight guide losses and mode cut-off points for larger-guide wafer. The four different sets correspond to measurements made on different parts of the wafer.*

The corners were designed to change the guide direction by 90°, and we measured the excess loss due to each corner type for five different input/output guide widths (2.0, 2.5, 3.0, 4.0 and 5.0 μm), and for both wafer designs. The corner types tested were: 1) conventional curves; 2) conventional curves with an offset to reduce straight/curved transition losses [3,6]; 3) whispering gallery corners [2] with offsets; 4) three types of near-hyperbolic curves [7] designed to minimise straight /curved transition losses; 5) two sizes of 45° plane mirrors [2]; and 6) a focusing mirror. These corners types were designed and made for four different effective radii (100, 200, 500 and 1000 μm), i.e. each corner type had the same input/output guide positions as a conventional curve with the corresponding radius. The loss of each corner type was measured using the Fabry-Perot method, to determine the overall loss of a fixed length of straight guide and four 90° corners. We assumed that the Fabry-Perot method was reliable for measuring these losses if the input/output guides were single-moded. The near-hyperbolic corners (Figure 2) were designed using a simple theoretical method in which the curve was considered to be made from short sections of straight guide joined together with small, abrupt angle changes at each join. The behaviour of the light in the curve was analysed in terms of straight guide modes, and each angle change was assumed to change the set of complex mode amplitudes. To simplify the calculations the straight guide mode fields were approximated by sine functions with propagation constants determined analytically using Pythagoras' theorem. In a more accurate method the mode fields and propagation constants

(including loss) could be determined using the leaky-mode Spectral Index method, for example. The number of modes was limited to 20, because the higher modes, although very lossy, could be very significant in the short straight sections. The curve was described as a set of subsections joined together in series. Each subsection was defined by two line lengths (L_1 and L_2), and a half-angle α, as shown in Figure 2.

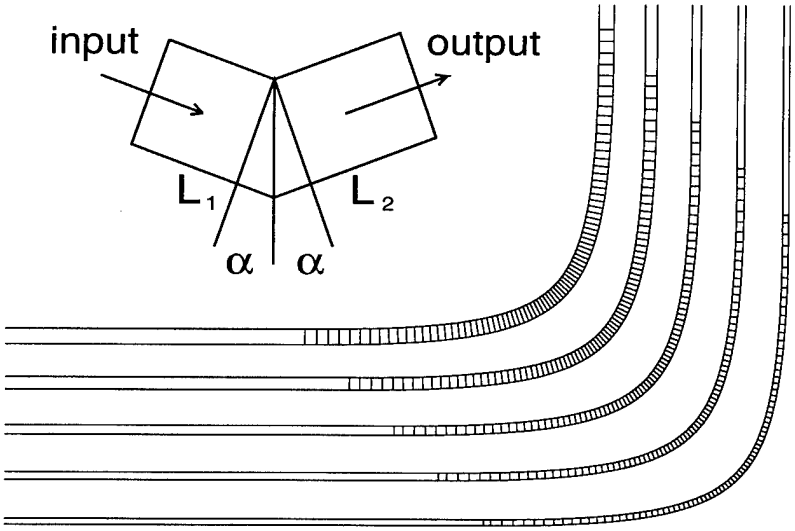


Figure 2. *Near-hyperbolic curves for five guide widths (100 μm equivalent radius). The inset shows a subsection (with an exaggerated bend angle) used for designing these corners.*

The straight line widths were all assumed to be the same as those of the input and output guides. The propagation of light through each subsection was represented by a complex matrix M_{ij} which mapped the input set of complex mode amplitudes A_j on to the output set of complex mode amplitudes A_i. The matrix elements were determined by mode overlap calculations applied across the intersection boundary between the two lengths of straight guide. By multiplying the individual matrices together, a matrix which described the whole corner could be determined. The eigenvectors of this matrix correspond to sets of straight guide mode amplitudes, which when multiplied by the relevant mode fields and summed over the number of modes, give a set of 'corner modes' which correspond to input fields which emerge from the corner unchanged. To design the near-hyperbolic corners which were tested, we described the corner as a simple analytic function and varied the shape until the fundamental corner mode was as close to the fundamental straight guide mode as possible.

Corner losses measured for the larger-guides were found to be quite high, typically around 1.5 dB/90° for a 1000 μm radius, 2.5 dB/90° for a 200 μm radius, and 5 dB/90° for a 100 μm radius. However, much lower corner losses were achieved for the smaller-guides. Figure 3 shows a summary of the minimum losses from measurements taken on a number of sets of 100 μm effective radius corners (and mirrors). Results for the larger radius curves will be presented at the conference. These results show (for each corner type and guide width) the total Fabry-Perot measured loss determined for four 90° corners and a length of straight guide. The total path length of each test guide depended on the curve type but was approximately 1.14 cm. For comparison, the loss of a 1.0 cm straight guide is also included in Figure 3. The results show trends which can also be seen on the results for other radius corners and for

the larger-guide wafer. The near-hyperbolic corners were generally found to give the lowest loss, especially for smaller radius corners. The minimum excess losses for 100 μm, 200 μm, and 500 μm radius near-hyperbolic corners (3.0 μm wide) were 0.5 dB, 0.3 dB, and 0.2 dB respectively. The plane mirror losses were typically around 1.5 dB/mirror for the smaller-guides, but were unmeasurable for the larger-guides suggesting that the wall verticality was more significant for larger-guides. In general the offset curves gave similar losses to the conventional curves for all corner radii and wafer designs measured, and for larger radius corners these losses were very similar to the corresponding near-hyperbolic corner losses.

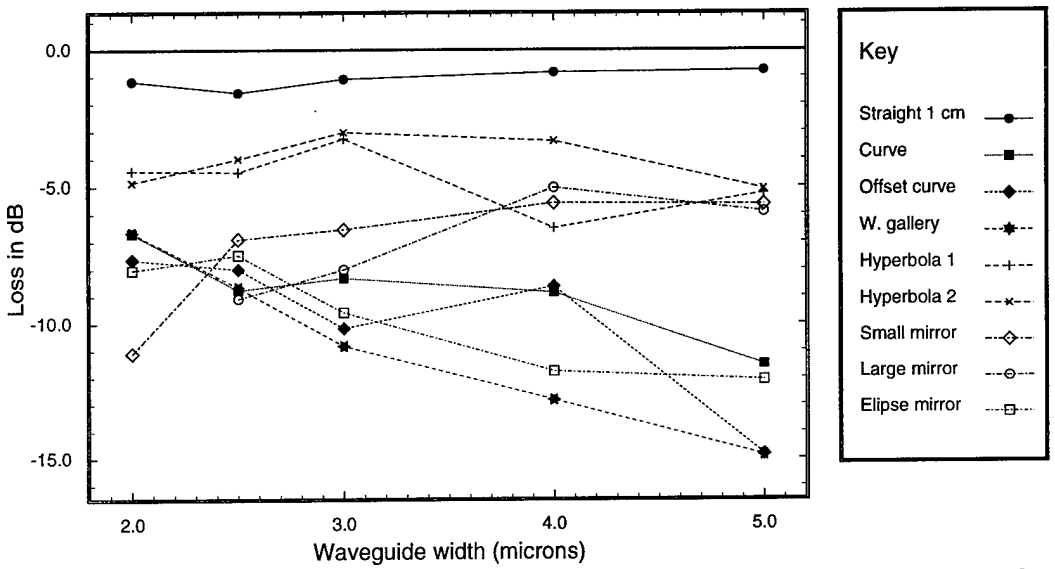


Figure 3. *Corner losses for eight corner types (in five widths) on the smaller-guide wafer. The total losses for four 90° corners and ~1.14 cm of straight guide are plotted, as well as the loss of 1.0 cm of the corresponding straight waveguide for comparison.*

In conclusion we have made loss measurements on a wide range of deep-etched straight guides and corners. We have demonstrated 0.5 dB/90° for a 100 μm radius near-hyperbolic corner, which is compatible with a 1.5 dB/cm single-mode straight guide.

References:

[1] R.J. Deri, A. Shahar, E. Colas, R.N. Thurston, W.J. Tomlinson, A. Yi-Yan, and M. Seto, 'Single-mode semiconductor optical waveguides with large dimensions suitable for compact bend applications,' Appl. Phys. Lett. 57, 2396-2398, 1990.

[2] R.J. Deri, and E. Kapon, 'Low-loss III-V semiconductor optical waveguides,' IEEE J. Quantum Elect. 27, 626-640, 1991.

[3] L.H. Spiekman, Y.S. Oei, E.G. Metaal, F.H. Groen, I. Moerman and M.K. Smit, 'Extremely small multimode interference couplers and ultrashort bends on InP by deep etching,' IEEE Photonics Tech. Lett. 6, 1008-1010, 1994.

[4] G.M. Berry, S.V. Burke, J.M. Heaton, and D.R. Wight, 'Analysis of multilayer semiconductor rib waveguides with high refractive index substrates,' Electronics Lett. 29 1941-1942, 1993.

[5] R.G. Walker, 'Simple and accurate loss measurement technique for semiconductor optical waveguides,' Electron. Lett. 21 581-583, 1985; erratum: ibid., 21 714, 1985.

[6] E.C.M. Pennings, 'Bends in optical ridge waveguides, modelling and applications,' PhD Thesis, Delft University of Technology, Delft, the Netherlands, ISBN 90-9003413-7 1990.

[7] E.A.J. Marcatili, 'Dielectric tapers with curved axes and no loss,' IEEE J. Quantum Elect. 21 307-314, 1985.

Wednesday, May 1, 1996

Advanced Laser Structures

IWF 1:45 pm-3:00 pm
Fairfax B

Uziel Koren, *Presider*
AT&T Bell Laboratories

Impact of current blocking structure on the coupling characteristics in 1.3-μm spot-size converted laser diodes

Y. Suzaki, O. Mitomi, Y. Tohmori, H. Okamoto, Y. Kondo,
Y. Sakai, M. Okamoto and Y. Kadota
NTT Opto-electronics Laboratories
3-1, Morinosato-Wakamiya, Atsugi-shi, Kanagawa, 243-01, Japan

Introduction

Recently, laser diodes used in optical network systems must have not only a large alignment tolerance to optical fiber and waveguides to reduce module alignment cost, but also a low threshold current and high temperature operation. The spot-size converted laser diodes (SSC-LDs) are attractive for their large tolerance and low-loss coupling without lenses [1]-[11], and we have demonstrated SSC-LDs with butt-joint -selective (BJ-selective) growth. This structure is very advantageous because it enable us to optimize both laser and SSC regions independently [5-6].

In this paper, we clarify that the buried heterostructure (BH) has a strong influence on the performance of FFPs and on the coupling characteristics. We obtain a low-loss coupling by considering the design of the pn-BH to avoid the influence of the n-doped current blocking layer whose refractive index is much different from the p-doped cladding layer. We fabricated SSC-LDs whose SSC region was easily formed by BJ-selective growth. With the proposed design, a low-loss coupling of less than 2 dB with a low threshold current of less than 6 mA is demonstrated.

Analysis of pn-BH structure dependence

A waveguide in the SSC region is buried in the pn-BH together with the active layer. Previously, the position of the n-doped current blocking layer in the pn-BH has been designed only for laser performance, not coupling characteristics.

Figure 1 shows the proposed concept for designing the pn-BH for both laser and coupling performance. To reduce leakage current, the n-doped current blocking layer should be located near the active layer. Furthermore, the doping concentration of this layer should be high enough to block leakage current, as shown in Fig. 1 (a).

On the other hand, the refractive index of n-doped InP is much lower than that of p-doped InP in the pn-BH due to the effect of dopants. Therefore, the position of the n-doped current blocking layer is very important in avoiding the influence of refractive index difference as shown in Fig. 1 (b).

Figure 2 (a) shows the calculated coupling loss to an optical fiber (spot size = 4 μm), when the height of the n-doped blocking layer is varied. We assume that the thickness T and width W of the core are 0.1 and 1.5 μm, respectively. This calculation doesn't include the radiation loss which increases as the height difference decreases [12]. The position of the n-doped current blocking layer has a strong influence on the FFPs and the coupling loss. In conventional pn-

BH design, when the height difference between the center of the active layer and the upper surface of the n-doped current blocking layer is small that corresponds to Fig. 1 (a), the coupling loss is ~ 1.8 dB. As the height difference is increased, which corresponds to Fig. 1 (b), the coupling loss can be reduced to 1.3 dB. Furthermore, the coupling loss can be drastically improved by reducing the doping concentration of the n-doped current blocking layer.

Figure 2 (b) also shows the coupling loss, when the n-doped current blocking layer is moved parallel to the surface and the height difference is set to 0.4 μm. We can obtain a low-loss coupling at the distance of 0.1 μm, which is narrow enough to prevent leakage current through the side of the active layer.

Fabrication of SSC-LDs

The structure of the proposed LD is shown in Fig. 3. This is grown in five steps of MOVPE. An active layer consisting of a GaInAsP (λ_{LD} = 1.3 μm) MQW layer and GaInAsP (λ_g = 1.1 μm) SCH layers is grown. Using a SiN_X mask, the active layer on the SSC region is removed by wet etching, and tapered GaInAsP (λ_g = 1.1 μm) SSC layer is formed by BJ-selective growth. Then a thin InP cladding layer is grown and a mesa stripe is fabricated by CH_4 dry etching. After the mesa stripe is buried in the pn-BH, an over-cladding layer is formed as final growth step. Finally, electrodes are formed at both sides of the laser. A highly reflective film (95 % reflectivity) is coated on the rear facet. The length of both the active and the SSC region is 300 μm. The core thickness and width at the output facet are 0.1 and 1.5 μm, respectively. We have fabricated tapered SSC layer by BJ-selective growth because the thickness at the border between the laser and the SSC region and the thickness of the SSC region at the output facet can be flexibly adjusted. Furthermore, we can obtain nearly exponentially tapered shape as designed for low-loss coupling [12]. SEM view of the SSC region at the output facet is shown in Fig. 4.

Characteristics

The dependence of the height difference for measured coupling losses is shown in Fig. 5. We obtained a low-loss coupling below 2 dB at the height difference of 0.4 μm that corresponds to Fig. 1 (b). The coupling loss tends to be reduced as the height difference is increased. In Fig. 5, the distribution of the coupling losses is considered to be caused by the effects with the difference of the doping concentration of the n-doped current blocking layer and the difference of the core size at the output facet.

Figure 6 shows the performance of the SSC-LDs with the height difference of 0.4 μm. At the room temperature, a very low threshold current of less than 6 mA has been achieved with reducing coupling loss to less than 2 dB .

Conclusion

The influence of the n-doped current blocking layer in the pn-BH is described. We clarified that the position and doping concentration of the n-doped current blocking layer in the SSC region is very important in obtaining a low-loss coupling, and that a coupling loss of less than 2

dB is attainable by designing the position. Accordingly, we built SSC-LDs using BJ-selective growth that have a low-loss coupling of less than 2 dB with a low threshold current of less than 6 mA.

References

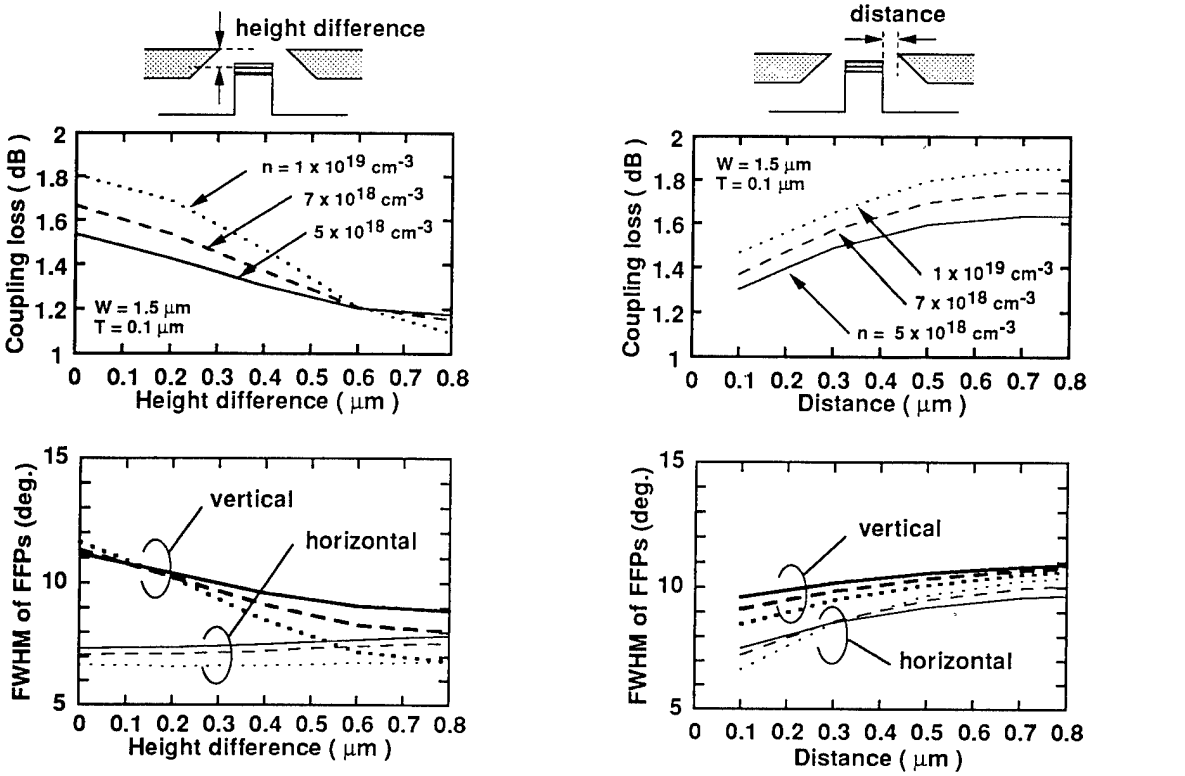
[1] T. L. Koch et al., IEEE Photonics Technol. Lett, 2, pp. 88-90., 1990
[2] K. Kasaya et al., Electron. Lett., 29, pp. 2067-2068, 1993
[3] I. F. Lealman et al., Electron. Lett., 30, pp. 857-859, 1994
[4] P. Doussiere et al., Appl. Phys. Lett., 64, pp. 539-541, 1994
[5] Y. Tohmori et al., Electron. Lett., 31, pp. 1069-1070, 1995
[6] Y. Tohmori et al., Electron. Lett., 31, pp. 1838-1840, 1995
[7] H. Kobayashi et al., IEEE Photonics Technol. Lett., 6, pp. 1080-1081, 1994
[8] A. Kasukawa et al., Electron. Lett., 31, pp. 559-560, 1995
[9] A. Takemoto et al., IOOC '95, PD 1-4, Hong Kong
[10] I. Moerman et al., ECOC'94, Th.C.2.4, Firenze, Italy
[11] H. J. Brückner et al., Electron. Lett., 30, pp. 1290-1291, 1994
[12] O. Mitomi et al., IEEE J. Quantum Electron., QE-30, pp. 1787-1793, 1994



(a) design for laser performance

(b) design for FFPs performance

Fig. 1 Design concept for a low-loss coupling



(a) dependence of the height difference between a core and an n-doped current blocking layer

(b) dependence of the distance between a core and an n-doped current blocking layer

Fig. 2 Influence of an n-doped current blocking layer

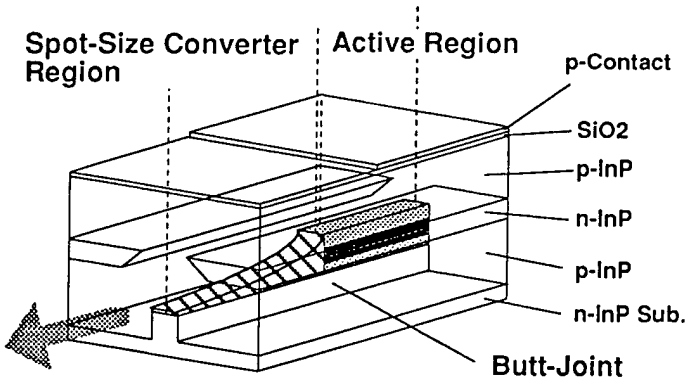


Fig. 3 Structure of SSC-LDs

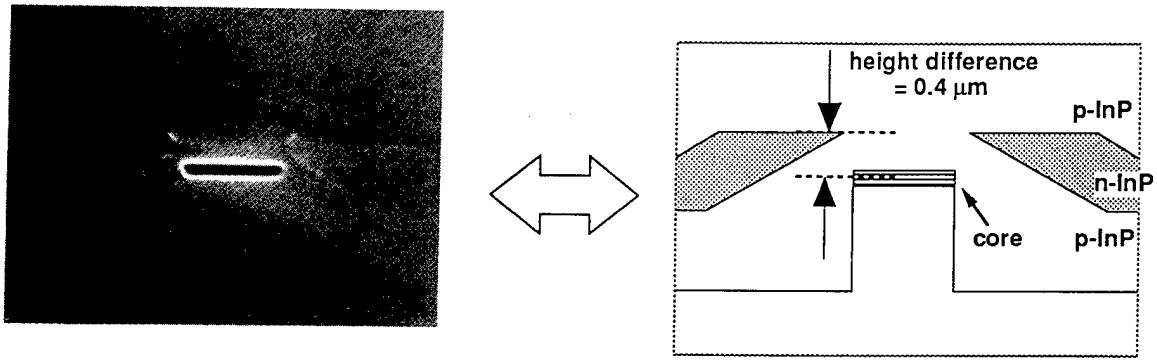


Fig. 4 Structure of SSC region at an output facet

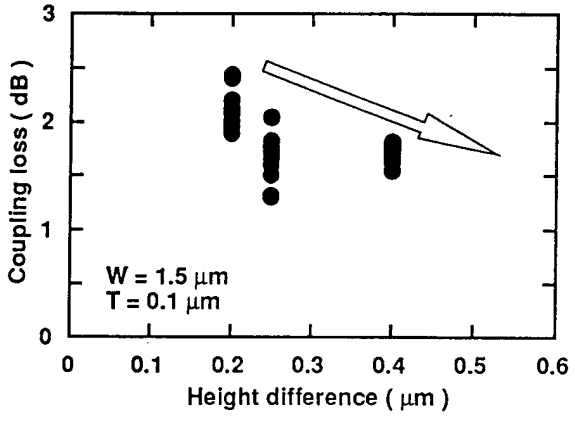


Fig. 5 Measured coupling loss to a fiber

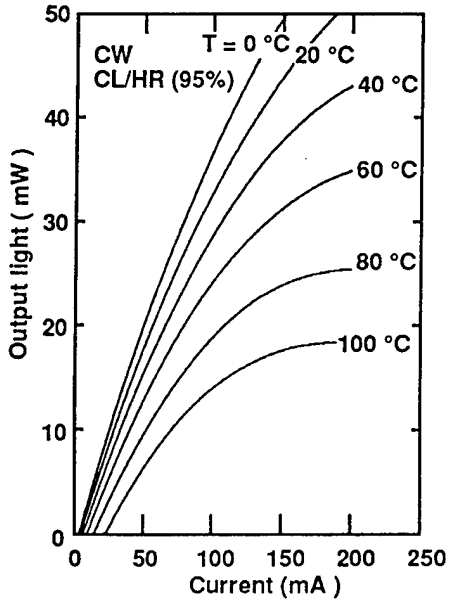


Fig. 6 Temperature dependence of L-I curve

Large diameter semiconductor ring lasers in tensile strained InP/InGaAsP material

Thomas F.Krauss, Hanson Pottinger, A. Catrina Bryce, John H.Marsh and Richard M. De La Rue

Optoelectronics Research Group, Department of Electronics and Electrical Engineering
Glasgow University, Glasgow, G12 8LT, Scotland, U.K.
Tel: +44 141 330 5220 Fax: +44 141 330 6002

Chris C. Button and John S. Roberts

Department of Electronics and Electrical Engineering,
Sheffield University, Sheffield, S1 3JD, U.K.

Introduction

Semiconductor lasers with ring cavities are attractive as possible sources for future fibre-to-the-home systems that require affordable components. Ring resonator lasers can readily be integrated and do not require gratings or facets for feedback. They can be operated cw [1] in a single transverse and longitudinal mode [2] without the need for accurate gratings or overgrowth and hence offer themselves strongly for low-cost mass-production.
Due to the bidirectional light circulation and the inherent symmetry, these devices are particularly suited for colliding pulse mode-locked (CPM) operation. The repetition rate is a function of the cavity length which can be accurately determined by lithography alone, unlike in cleaved Fabry-Peror lasers. This feature is an important requirement for applications in communication systems where devices operating at well-defined pulse repetition rates are required. It is with this mode-locking application in mind that we designed the 3mm long cavity, aiming for repetion rates in the 20-40GHz regime. Comparable devices in the GaAs/AlGaAs material system have already produced evidence for mode-locking at 28GHz [3].

The majority of ring lasers reported so far have been fabricated in the GaAs/AlGaAs material system [2, 4, 5]. Although many aspects of ring lasers have already been studied at 0.85μm wavelength, it is important to demonstrate low threshold operation in the more relevant communications wavelength regime around 1.55 μm, where, to our knowlege, only a few results have been published [6, 7].

Material

The material was designed with two strained quantum wells (L_z=120Å) embedded in a GRINSCH-structure (Fig.1a). The Indium content of the two InGaAs wells was 32%, resulting in 1.5% tensile strain, a design which has previously resulted in very low threshold current laser operation [8]. We chose to introduce tensile instead of compressive strain, because the thicker quantum wells (>100Å instead of ≈25Å in the compressive case) allow a greater degree of control during growth.

The epitaxial growth was performed in an MR Semiconductors MR350 horizontal low pressure MOVPE reactor, at a reactor pressure of 150 Torr and a growth temperature of 650°C. The reagents used were 100% phosphine, 100% arsine, trimethylgallium and trimethylindium entrained in a palladium-diffused hydrogen carrier gas flowing at 18 slm. The output of the TMIn source was monitored by an Epison ultrasonic cell, and controlled via a feedback system to maintain a stable output from the bubbler. The n-dopant source was disilane, 10ppm in helium, and the p-dopant was zinc from a 5000 ppm dimethylzinc-in-hydrogen gas source. The step-graded GaInAsP cladding regions were achieved by maintaining a constant flow of the P and the In precursors to the reactor, and switching

between pre-calibrated As and Ga sources to minimise gas flow disruptions. Growth rates for the GaInAsP material ranged from 1.5-1.8μm/hr. An undoped spacer layer was introduced into the upper InP cladding layer to allow for the inevitable diffusion of the p-dopant during the final stages of growth.

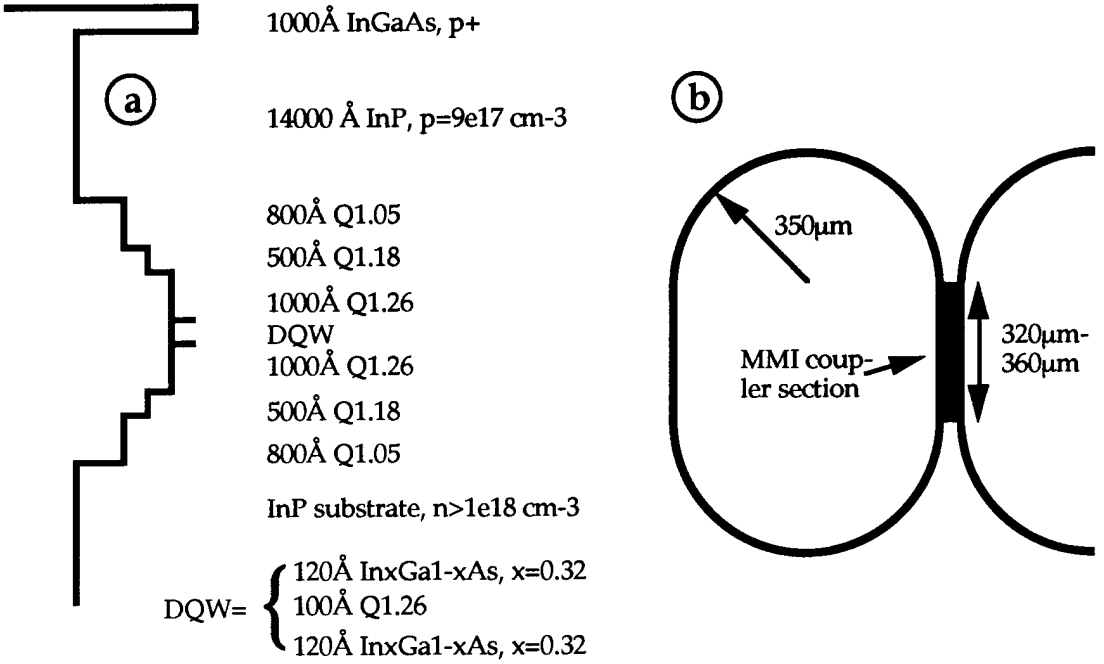


Figure 1. *a) Material structure, the approximate refractive index being indicated on the horizontal and the layer thickness on the vertical axis. b) Sketch of the device layout. The cavity, coupler and two output branches are pumped and the output branches are angled at 4 ° to normal to minimise backreflections; the output facets are, however, not anti-reflection (AR) coated.*

50μm wide broad area lasers were fabricated for material assessment (Fig.2). The extrapolated threshold current density of 193 A/cm² for infinite cavity length devices represents state-of-the-art performance for double quantum well (DQW) long wavelength material. For comparison, Thijs et al. [8] achieved 92 A/cm² using a single quantum well, Yokouchi [9] and Yamamoto [10] achieved slightly over 100 A/cm² per well for DQW material.

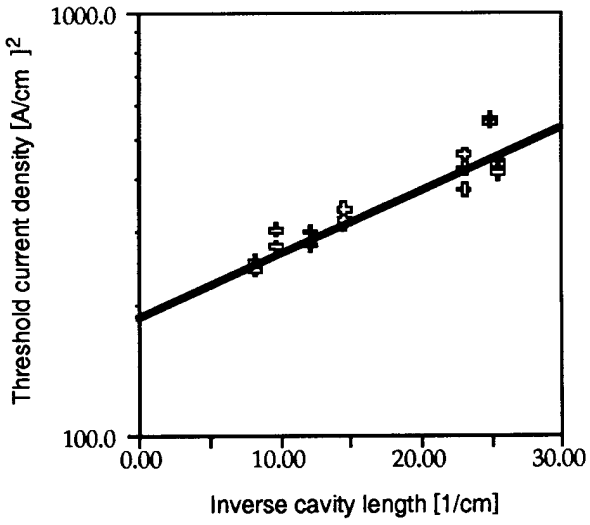


Figure 2 *Threshold current density vs. inverse cavity length for the material MR 396 used in our experiments. The threshold for infinite cavity length is at 193 A/cm².*

Devices

Devices were fabricated using our self-aligned process described previously [5]. Lasers were designed as racetracks with 3 μm wide strip-loaded waveguide ridges and 350μm radius in the curved parts, using multi-mode interference (MMI) sections for output coupling. The length of the MMI section for a 3dB coupler according to [11] is

$$L_{MMI} = \frac{1}{2}\frac{4nw^2}{\lambda} \qquad (1)$$

Assuming a width w of 9.2 μm, a wavelength λ of 1.55 μm and an effective index n of 3.28, L_{MMI} = 360μm. Previous investigations [12] have shown that the optimum MMI coupler length, if the MMI section is part of an active ring laser cavity, is 5-10% shorter than the length suggested by (1). We found this result confirmed (Fig.3), and obtained the best results with devices with an MMI coupler length of 320 μm or 340 μm, i.e. 90% and 95%, respectively, of the length suggested by (1).

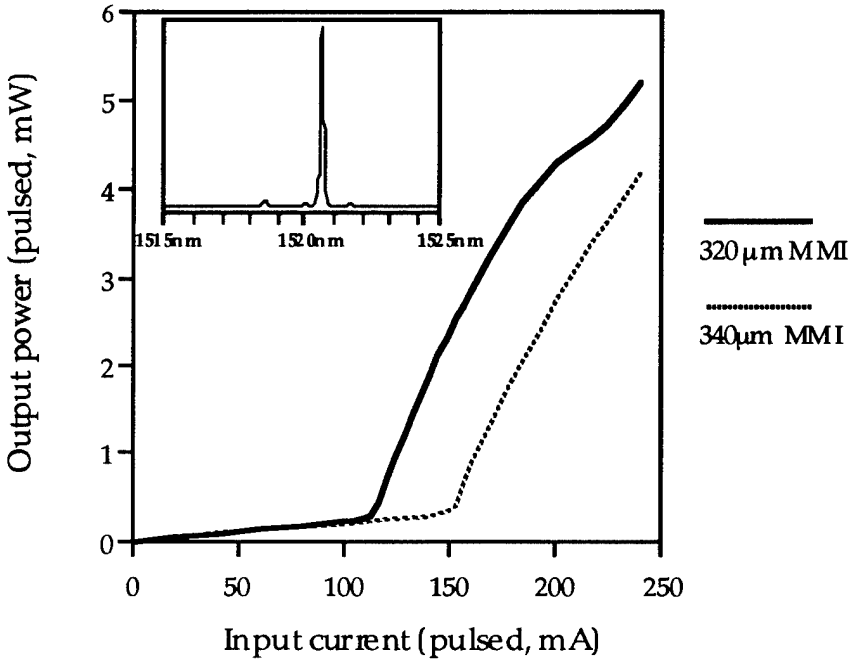


Figure 3. L-I curve and spectrum of ring lasers with MMI sections of different length. The lowest threshold was 110 mA for a device with a 320 μm long MMI section, whereas the device with the 340 μm long MMI section operated single mode between threshold and 240mA. The spectrum was taken for the 340 μm device at 220 mA. The efficiency (sum of both laser outputs) was between 8 % and 10 % for different devices.

The lowest threshold of 110 mA is very encouraging and comparable to the results obtained with similar devices in the GaAs/AlGaAs material system [5]. In comparison to other published results achieved with InP/InGaAsP material [6, 7], where thresholds between 150mA - 200mA were obtained, this result is a considerable advance, which is mainly due to the superior characteristics of our tensile strained DQW material. Unlike our GaAs/AlGaAs lasers, we were not able to operate these devices cw, because of the low T_0 (i.e. poor performance at elevated temperatures), which is typical of lasers in the InP/InGaAsP material system. It is well known [13] that although it improves the threshold current and high speed operation characteristics, the incorporation of strain does not significantly increase the T_0 of a laser device, hence proper heatsinking arrangements are required.

Further improvements in device operation are expected from the introduction of better electron confinement, e.g. through proton implant isolation, passive cavity extension

through a suitable quantum well intermixing process [14] and the addition of saturable absorbers into the cavity for mode-locked operation.

Acknowledgements

This work was in part supported in part by the Engineering and Physical Sciences Research Council (EPSRC), (Grant Number GR/H/82471) and by the MOD (UK) through DRA. TFK acknowledges support through an EPSRC personal fellowship.

References

1. Krauss, T. and Laybourn, P.J.R."Cw operation of semiconductor ring lasers", El.Lett., 1990, 26, pp.2095-2097.
2. Hohimer, J.P., Craft, D.C., Hadley, G.R., Vawter, G.A. and Warren, M.E., "Single-frequency continuous-wave operation of ring resonator diode lasers", Appl.Phys.Lett., 1991, 59, pp.3360-3362.
3. Krauss, T. F., Martins-Filho, J. F., Ironside, C.N., Laybourn, P.J.R. and De La Rue, R. M., "Mode-locking in semiconductor ring lasers with two saturable absorbers", Proceedings of the European Conference on Integrated Optics, (ECIO), Delft, The Netherlands, April 1995, pp.55-58.
4. Krames, M.R., Minervi, A.D. and Holonyak, Jr., N., "Deep-oxide curved resonator for low-threshold AlGaAs-GaAs quantum well heterostructure ring lasers", Appl.Phys.Lett., 1995, 67, pp.73-75.
5. Krauss, T.F., De La Rue, R.M., Laybourn, P.J.R., Vögele, B. and Stanley, C.R., "Efficient semiconductor ring lasers made by a simple self-aligned fabrication process", IEEE Journal on Selected Topics in Quantum Electronics, 1995, 1, pp757-761.
6. van Roijen, R., Pennings, E.C.M., van Stralen, M.J.N., van der Heijden, J.M.M., van Dongen, T. and Verbeek, B.H., "Compact InP-based ring lasers employing multi-mode interference couplers and combiners", Appl.Phys.Lett., 1994, 64, pp.1753-1755.
7. Hansen, P.B., Raybon, G., Chien, M.-D., Koren, U., Miller, B.I., Young, M.G., Verdiell, J.-M. and Burrus, C.A., "A 1.54μm monolithic semiconductor ring laser: cw and mode-locked operation", IEEE Phot.Tech.Lett., 1992, 4, pp. 411-413, 1992.
8. Thijs, P.J.A., Binsma, J.J.M., Tiemeijer, L.F. and T.van Dongen, "Submilliamp threshold current (0.62mA at 0° C) and high output power (220mW) 1.5μm tensile strained InGaAs single quantum well lasers", Electron. Lett., 1992, 28, pp.829-830.
9. Yokouchi, N., Yamanaka, N., Iwai, N. and Kasukawa, A., "$Ga_xIn_{1-x}As_yP_{1-y}$ - InP tensile-strained quantum wells for 1.3-μm low threshold lasers", Phot.Technol. Lett., 1995, 7, pp.842-844.
10. Yamamoto, T., Nobuhura, H., Tanaka, K., Inoue, T., Fuji, T., Wakao, K., "Well width dependence of threshold current density in tensile strained InGaAs/InGaAsP quantum-well lasers", Japn. Journ. of Appl.Phys., 1994, 33, pp.6199-6200.
11. Ulrich, R. and Ankele, G., "Self-imaging in homogenous planar optical waveguides", Appl.Phys.Lett., 1975, 27, pp.337-339.
12. Krauss, T., De La Rue, R.M. and Laybourn, P.J.R., "Impact of the output coupler configuration on the operation of semiconductor ring lasers", Journal of Lightwave Technology, 1995, 13, pp.1500-1507.
13. O'Reilly, E.P. and Adams, A.R., "Band-structure engineering in strained semiconductor-lasers", Journ. of Quant. Electron., 1994, 30, pp.366-379.
14. McLean, C., McKee, A., Lullo, G., Bryce, A.C., De La Rue, R.M. and Marsh, J.H., "Quantum-well intermixing with high spatial selectivity using a pulsed-laser technique", Electron. Lett, 1995, 31, pp.1285-1286.

Output Characteristics Of High Power GaAs/GaAlAs Double Heterostructure Rib-Waveguide Bow-tie Lasers

I.Middlemast

School of Electronic and Electrical Engineering

University of Bath

Bath - BA2 7AY, England , U.K.

phone: (44)(1225) 826826 x5070 ; fax: (44)(1225) 826305 ;

J. Sarma

School of Electronic and Electrical Engineering

University of Bath

Bath - BA2 7AY, England , U.K.

phone: (44)(1225) 826863 ; fax: (44)(1225) 826305 ;

P.S.Spencer

School of Electronic Engineering and Computer Systems

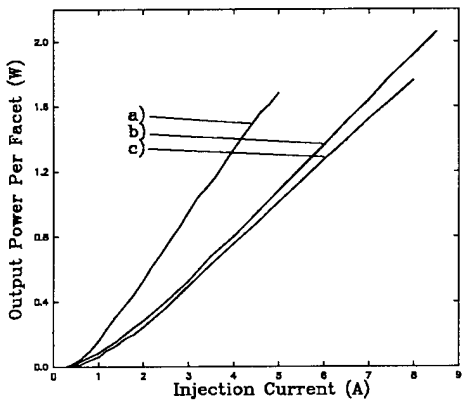
University of Wales

Dean St., Bangor, Gwynedd - LL57 1UT, Wales , U.K.

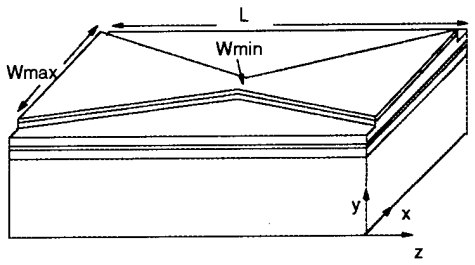
phone: (44)(1248) 351151 x2738

1) Introduction

In the quest for high power semiconductor laser diodes much of the latest research has been devoted to tapered structures, e.g. tapered amplifiers, [1], integrated laser/amplifiers, [2], and tapered lasers, [3]. Tapered amplifiers have the disadvantage that they must either be used with external signal injection or be integrated with a DFB laser. Tapered lasers have problems associated with catastrophic optical damage, (COD), at the facet with the narrow stripe contact. This problem has been alleviated to some extent by A-R coating the facet at the broad end of the stripe contact, however this adds to the complexity and cost of the lasers. Recently double tapered or Bow-tie lasers have been used to produce high power Q-switched pulses, [4]. Typical dimensions of these Bow-tie lasers were 300μ long with a 5μ narrow section tapering to 30μ at the output facets. Subsequently double tapered (Bow-tie) lasers 2mm long, 5μ wide in the middle, and flaring to 175μ at each facet have been fabricated. These devices are cabable of producing 2W quasi-CW output power per facet and up to 4W per facet at a low duty cycle. The advantage of using double tapered lasers over the single tapered laser is that the narrow region is located either at or towards the centre of the structure so that each facet has a wide output area. Preliminary results from a computer model which is currently under development, shows good agreement with the experimental near and far-field intensity distributions emanating from the Bow-tie lasers, at currents just above threshold.



Fig(2) Light/current characteristics of 3 Bow-tie lasers each having L=2mm, Wmin=5μ and tapering out to Wmax= a) 150μ, b) 175μ and c) 200μ.



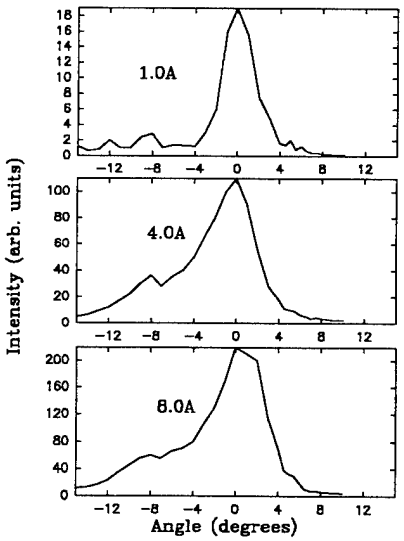
Fig(1) Schematic diagram of a Bow-tie Laser.

2) Experimental Work

The Bow-tie lasers were fabricated in the School of Electronic and Electrical Engineering, University of Bath, from DQW AlGaAs material obtained from the EPSRC III-V facility at Sheffield University. Rib-waveguides were ion beam etched to provide weak index guiding and reduce current spreading so that the narrowest section of the guide supports only one lateral mode, fig(1). Deflectors were included to stop unwanted stray light coupling into the taper and preserve the purity of the fundamental mode, [3]. The light/current characteristics of 3 devices, each 2mm long, but with different taper angles are shown in fig(2). The devices were driven with 1μs pulses with a 5:1 duty cycle at room temperature. The maximum quasi-cw output power achieved was 2.1W per facet at an injection current of 8A with a slope efficiency of 0.3W/A per facet, from device b), fig(2). Most of the Bow-tie lasers that were tested had output powers exceeding 1.5W/facet. The narrowest taper angle bow-tie laser that was measured proved to have the highest slope efficiency,

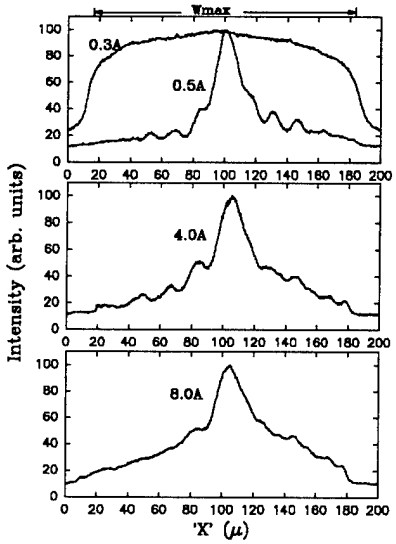
0.4W/A getting progressively worse as the taper angle increased. The light/current characteristics of the bow-tie lasers were also measured under low duty cycle conditions, 1000:1, with 500ns pulse widths. Under these conditions it was possible to obtain 4W per facet at 7A with a slope efficiency of 0.6W/A from a Bow-tie laser which was, 2mm long, 5μ at the centre, and tapering linearly to 150μ. The threshold current of this laser was 400mA.

The near-field intensity profiles of the bow-tie lasers, were measured using a vidicon camera. The devices were pulsed at a low duty cycle, 1000:1, and neutral density filters used to reduce the output power. Some typical near-field intensity profiles are shown as a function of current in fig(3). A dramatic narrowing of the near-field distribution occurs as the injection current is increased from 0.3A, below threshold, where spontaneous emission dominates, to 0.5A, above threshold, into the stimulated emission regime.



Fig(4) Far-field intensity profiles of Bow-tie laser (b) shown as a function of injection current.

In addition to the central lobe, it is noticeable that there are a number of subsidiary peaks, which correspond to power transferred from the fundamental lateral waveguide mode into higher order modes, as the optical field travels along the length of the taper. As the current is increased the central lobe broadens and the fraction of power outside of the central lobe increases. This is thought to be a consequence of spectral hole burning altering the carrier distribution, and hence the refractive index profile, thus causing more power to be transferred to the higher order lateral modes.



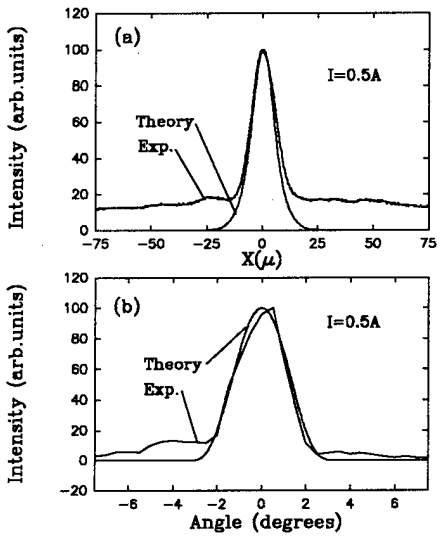
Fig(3) Near field intensity profiles of Bow-tie laser (b) shown as a function of injection Current.

The far-field intensity profiles of the Bow-tie lasers, fig(4), were measured by accurately placing the lasers at the centre of a rotating base and using a small area detector, 1mm in diameter, at a distance of 200mm. At 1A the full width half maximum (FWHM) of the far-field distribution is approximately 3.5°. As the current is increased the far-field becomes lop-sided and broadens to give a FWHM of 6°. The lop-sided shape of the far-field distribution is likely to be caused by asymmetries introduced into the bow-tie laser during

fabrication. The broadening of the far-field provides further evidence that more power is being transferred to the higher order modes as the current is increased.

3) Theoretical Model

A theoretical model of tapered devices has been developed to obtain a better understanding of how a bow-tie laser works and hence to improve on it's design. The intensity distribution within the device is of particular interest as this determines the saturation characteristics and also the COD limit for the near-field intensity distribution at the output facet. Of course, the near-field intensity distribution coupled with the phase also defines the far-field intensity distribution. Consequently a modal analysis, similar to that of Bendelli et al, [5], was chosen to model the tapered devices. In this method the taper is discretised along the length of the device, into slab waveguides of piece-wise constant width, and the step transition method applied at each of the discretising interfaces. This technique has been verified by comparing the near-field intensity distributions from the model with experimental measurements made on passive tapered rib-waveguides, [6]. To extend the analysis to a tapered or Bow-tie laser, the time independent diffusion equation is solved, to obtain the carrier profile, in each longitudinal section. Note that, unlike the 'Bendelli model', [5], the refractive index dependence on the carrier profile is explicitly included. The distribution of the carriers and the optical field are not independent of each other and in this analysis they have been solved in a self-consistent manner by using a piece-wise constant inversion population method. Within each longitudinal section, the carrier profile, and hence the gain/absorption, has been assumed to be z independent, so that each lateral mode will grow or decay exponentially. The lateral modes which make up the total optical field are allowed to propagate forwards and backwards along the tapered structure until the boundary conditions at the facets are satisfied to within a specified accuracy. Spontaneous emission is assumed to be negligible in the present analysis.



Fig(5) Comparison of theoretical and experimental a) near-field and b) far-field intensity profiles of Bow-tie laser (a).

Calculations corresponding to the Bow-tie lasers described in section (2) have been carried out. It can be seen from fig(5) that the experimental near-field and far-field intensity distributions, can be simulated quite accurately with the model. at currents just above threshold.

4) Summary

In conclusion we have demonstrated that the Bow-tie laser can provide high output powers, 2W quasi-cw. The far-field profile is stable at and above 1.0A with half power points of 3° rising to 6.5° at 8A. A theoretical model of the tapered laser has been developed which describes the near and far-field intensity

profiles accurately at currents just above the lasing threshold. Bow-tie lasers are expected to provide a low cost, high power, alternative to the MOPA and single tapered lasers.

References

1) 1) E. Kintzer, J. Walpole, S. Chinn, C. Wang and L. Missagia, 'High-power strained-layer amplifiers and lasers with tapered gain regions.' IEEE Photonics Technol. Lett., v.5, n.6, p.605, 1993.

2) D. Mehuys, L. Goldberg and D. Welch, '5.25W cw near-diffraction-limited tapered-stripe optical amplifier.'IEEE Photonics Technol. Lett., v.5, n.10, p.1179, 1993.

3) S. O'Brien, D. F. Welch, R. A. Parke, D. Mehuys, K. Dzurko, R. J. Lang, R. Waarts and D. Scifres, 'Operating characteristics of a high-power monolihically integrated flared amplifier master oscillator power amplifier.' IEEE J. of Quant. Electon., v.29, n.6, p.2052, 1993.

4) K.A.Williams, J.Sarma, I.H.White, R.V.Penty, I.Middlemast, T.Ryan, F.R.Laughton and J.S Roberts, 'Q-switched Bow-tie Lasers for High-energy Picosecond Pulse Generation', Electron. Letts., v.30, n.4, p.320, 1994.

5) Bendelli, K.Komori and A.Shigehisa, 'Gain saturation and propagation characteristics of index-guided tapered-waveguide travelling-wave semiconductor laser amplifiers (TTW-SLA's)', IEEE J. of Quant. Electron., v.28, pp.447-457, 1992.

6) I.Middlemast, J.Sarma, P.S.Spencer and K.A.Shore, 'Characterisation of tapered D-H semiconductor rib-waveguides at optical wavelengths', submitted to IEEE J. of Lightwave Technology.

A SIMPLE, BUT ACCURATE EXPRESSION FOR THE STATIC AND DYNAMIC CHIRP IN DFB LASERS

Geert Morthier, Piet Verhoeve, Roel Baets
Department of Information Technology, University of Gent - IMEC
Sint-Pietersnieuwstraat 41, B-9000 Gent, Belgium
Tel. +32 9 264 33 44 , Fax. +32 9 264 35 93

1. Introduction

High bitrate long distance optical communication systems operating at 1.55μm require a DFB laser source with low chirp. A considerable amount of research has therefore been dedicated to the study of special laser structures with low chirp. In the theoretical analysis, it is generally believed that a low chirp can only be achieved with structures with a small effective linewidth enhancement factor α_{eff} and hence several structures with small α_{eff} and assumed low chirp have been reported [1-3].

Below we will show that only the chirp caused by gain suppression can be related somehow to the value of α_{eff}. The intrinsic chirp, caused by the time-dependence of the optical power and dominating at high bit rates, is proportional with the linewidth enhancement factor α of the active layer material. We also give an analytical expression for the chirp caused by spatial hole burning, a contribution that can be dominating at low power levels. This expression also shows how this spatial hole burning contribution depends on a structural parameter on one hand and on parameters such as threshold gain, linewidth enhancement factor, carrier lifetime and differential gain on the other hand. Our derivation of the analytical formula for the chirp is based on a similar approach as the one used to arrive at the α_{eff}-based linewidth formula [4].

2. Theory

We derive the variation of the pulsation $\Delta\omega$ from the dynamic coupled wave equations:

$$\begin{aligned} &\frac{\partial R^+}{\partial z} + \frac{1}{v_g}\frac{\partial R^+}{\partial t} + j\Delta\beta\ R^+ = \kappa R^- \\ &-\frac{\partial R^-}{\partial z} + \frac{1}{v_g}\frac{\partial R^-}{\partial t} + j\Delta\beta\ R^- = -\kappa^*\ R^+ \end{aligned} \qquad (1)$$

and expand the field amplitudes and the complex Bragg deviation as:

$$\begin{aligned} R^{\pm}(z,t) &= R_0^{\pm}(z) + \delta R^{\pm}(z,t) \\ \Delta\beta(z,t) &= \Delta\beta_0(z) + \delta(\Delta\beta)\ (z,t) \end{aligned} \qquad (2)$$

From a first order approximation of the coupled wave equations one can derive the following equation [5]:

$$\int_0^L \delta(\Delta\beta)\, R_0^+ R_0^- \, dz = \frac{j}{2v_g} \frac{\partial}{\partial t} \left(\int_0^L (R_0^+ \delta R^- + R_0^- \delta R^+) \, dz \right) \tag{3}$$

We normalise the fields such that the photon density $S(z) = |R^+|^2 + |R^-|^2$. We also assume that the modulation does not change the field profiles, i.e. that:

$$\delta S(z) = S_0(z)\, f(t) \;,\; \delta R^- = R_0^- \frac{f(t)}{2} \text{ and } \delta R^+ = R_0^+ \frac{f(t)}{2} \tag{4}$$

with f a real, z-independent function of time. In equation (3), we expand $\delta(\Delta\beta)$ as follows:

$$\delta(\Delta\beta) = \frac{\Delta\omega}{v_g} + j \frac{1+j\alpha}{2} \Gamma \frac{\partial g}{\partial N} \delta N(z) - \frac{j}{2} \Gamma g_{th} \xi \, \delta S(z) \tag{5}$$

with α the linewidth enhancement factor, $\partial g/\partial N$ the differential gain of the active layer and ξ the gain suppression coefficient. The variation of the local carrier density follows from a linearisation of the longitudinal carrier density equation and is [5]:

$$\begin{aligned} \delta N &= \int_0^t \left[\frac{\delta J}{qd} - G(N_{av})\, S_{av} f - \frac{G(N_{av})\, f\, (S_0(z) - S_{av})}{1 + G'\tau_d\, S_{av}} \right] \exp\left[- \frac{(t-t')}{\tau_d} (1 + G'\tau_d S_{av}) \right] dt' \\ &= A(t) - B(t)\, (S_0(z) - S_{av}) \end{aligned} \tag{6}$$

with $G' = \Gamma v_g \partial g/\partial N$, τ_d the differential carrier lifetime and N_{av}, resp. S_{av} the axial average of $S_0(z)$ and $N_0(z)$. Substitution of (4)-(6) in (3) and elimination of A gives the following expression for $\Delta\omega(t)$:

$$\begin{aligned} \Delta\omega(t) \;=\; & \frac{\alpha}{2} \frac{d\ln P(t)}{dt} + \frac{\xi G_{th} S_{av}}{2} (\alpha\chi' - \chi'') \frac{\delta P(t)}{P_0} \\ & - \frac{G' G_{th}\, S_{av} (1+\alpha^2)}{2\,(1 + G'\tau_d\, S_{av})} \chi'' \int_0^t \left(\frac{\delta P(t')}{P_0} \right) \exp\left[- \frac{(t-t')}{\tau_d} (1 + G'\tau_d\, S_{av}) \right] dt' \end{aligned} \tag{7}$$

with P the output power and:

$$\chi = \chi' + j\chi'' \;=\; \frac{\int_0^L \left(\frac{S_0(z)}{S_{av}} \right) R_0^+ R_0^- \, dz}{\int_0^L R_0^+ R_0^- \, dz} \tag{8}$$

The first term in this expression is the dynamic chirp, the second term the chirp caused by gain suppression and the third term the chirp caused by spatial hole burning. This equation implies that for the calculation of the dynamic chirp not the effective α-parameter, but the material α-factor must be used.

3. The low-frequency chirp: discussion and numerical results

At low frequencies, expression (7) reduces to:

$$\Delta\omega = \frac{\xi G_{th} S_{av}}{2}(\alpha\chi' - \chi'')\frac{\delta P(t)}{P_0} - \frac{G' G_{th} S_{av}(1+\alpha^2)\tau_d}{2(1+G'\tau_d S_{av})^2}\chi''\frac{\delta P(t)}{P_0} \qquad (9)$$

χ depends only the specific DFB laser structure (i.e. on coupling coefficients and facet reflectivities). It is purely real for lasers emitting at the Bragg wavelength. Real and imaginary part of χ are displayed as a function of the κL-product in Fig. 1-3 for AR-coated lasers, $\lambda/4$-shifted AR-coated lasers and for a laser with cleaved facets. It can be noticed that χ' exceeds χ'' by a factor of at least 20 in all cases.

The contribution from gain suppression is proportional with $\alpha\chi'-\chi'' \approx \alpha\chi'$ and with the threshold gain. This contribution is dominant at high bias powers. Since χ' and the ratio of S_{av} to bias output power increase with κL while the threshold gain decreases with κL, an optimum κL-value with minimum chirp caused by gain suppression will exist. The optimum value depends on the internal loss however. The contribution from spatial hole burning is proportional with χ'', but also increases with the square of α, with threshold gain, carrier lifetime and differential gain. For constant optical modulation depth $m = \delta P/P_0$, the chirp first increases with bias power, then reaches a maximum $G_{th}(1+\alpha^2)\chi''m/2$ at $S_{av}=1/(G'\tau_d)$ and then decreases as $1/S_{av}$.

The accuracy of the formula (9) for $\xi=0$ has been investigated more in detail for an AR-coated DFB-laser with κL=2. To this end, the results obtained with (9) have been compared with results obtained with a more rigourous numerical model [6]. The chirp as a function of bias output power for m=0.35 obtained with the analytical and the numerical model is shown in Fig. 4. As can be seen, a good agreement is obtained.

4. Conclusion

We have presented an accurate analytical formula for the chirp in laser diodes. The fomula includes gain suppression, spatial hole burning and dynamic effects. It shows that the chirp caused by spatial hole burning is proportional with α^2 and that the dynamic chirp is proportional with α and not with α_{eff}.

Acknowledgement

This work was supported partly by the European ACTS project AC065 (BLISS).

References:
[1] K. Kudo, J. I. Shim, K. Komori, S. Arai, IEEE Phot. Techn. Lett., Vol. 6, pp. 531-534, 1992.
[2] A. J. Lowery, El. Lett., Vol. 28, pp. 2295-2297, 1992.
[3] M. Blez, D. Mathoorasing, C. Kazmierski, M. Quillec, M. Gilleron, J. Landreau, H. Nakajima, IEEE Journ. Quant. El., Vol. 29, pp. 1676-1681, 1993.
[4] M.-C. Amann, El. Lett., Vol. 26, pp. 569-571, 1990.
[5] G. Morthier, P. Verhoeve, R. Baets, to be published.
[6] P. Vankwikelberge, G. Morthier, R. Baets, IEEE Journ. Quant. El., Vol. 26, pp. 1728-1741, 1990.

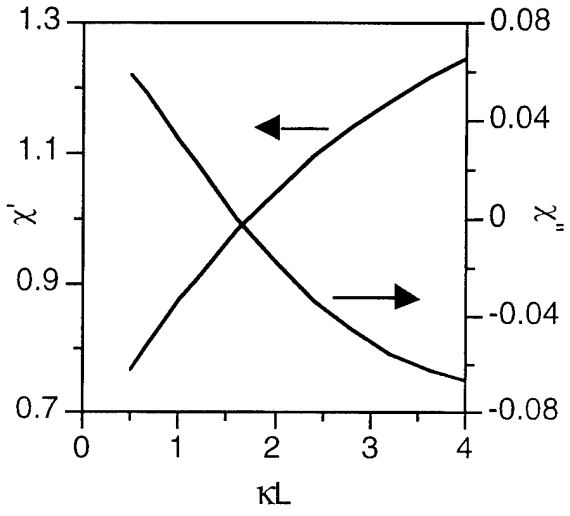


Fig.1: χ for an AR-coated laser (mode with $\lambda > \lambda_B$)

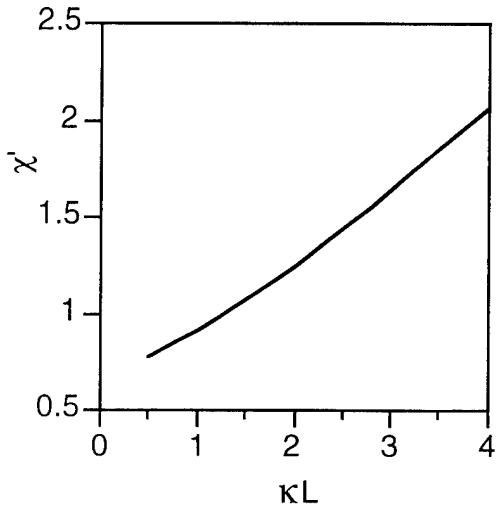


Fig. 2: χ for an AR-coated, $\lambda/4$-shifted laser ($\chi'' = 0$)

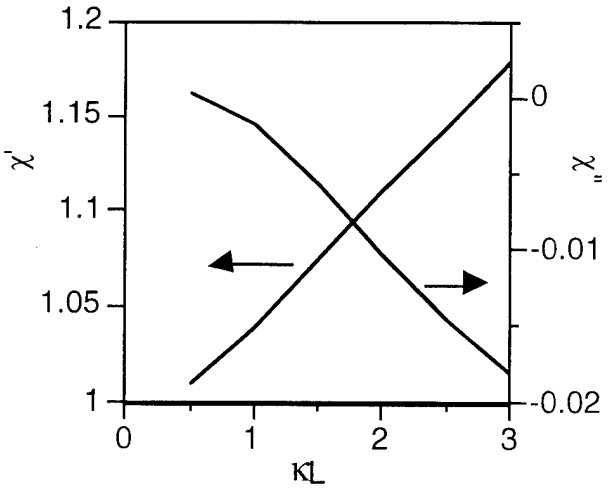


Fig.3: χ for a cleaved laser

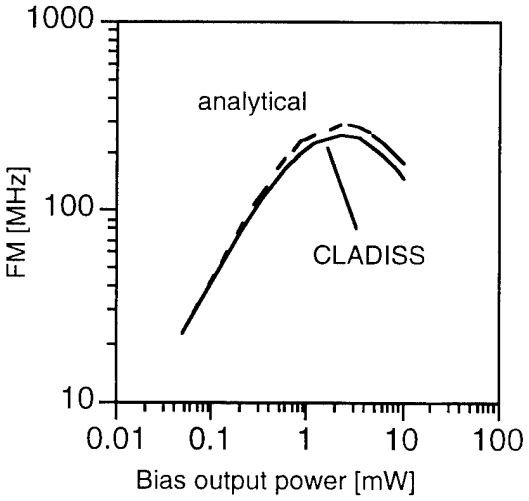


Fig. 4: FM calculated using (9) and using CLADISS

The Microstrip Laser

D. A. Tauber [1], M. Horita [2], A. L. Holmes, Jr.[1], B. I. Miller [3], and J. E. Bowers [1]

[1] Department of Electrical and Computer Engineering
University of California, Santa Barbara, CA 93106
Phone: (805) 893-4883 FAX: (805) 893-3262

[2] KDD R&D Laboratories, Opto-electronics Group
2-1-15 Ohara, Kamifukuoka-shi, Saitama 356, Japan
Phone: 81-492-78-7832

[3] AT&T Bell Laboratories
Holmdel, NJ 07733

Introduction

Semiconductor lasers that operate at high power and high frequency are important components for optical communication networks and systems. High power operation requires efficient heat removal from the active region of the device and high frequency operation requires careful consideration of electrode structure to minimize the deleterious effects of electrical parasitics and poor microwave signal propagation [1-3]. Efficient heat removal has often been achieved by mounting the laser ridge side down onto a diamond heat sink. The highest frequency lasers have utilized a coplanar waveguide electrode geometry with thick metallization to minimize the electrical problems [3]. The microstrip laser, a schematic of which is shown in Figure 1, is inherently an excellent thermal and microwave structure because of the thick gold layer beneath the lower cladding. The schematic drawing is for a polyimide ridge waveguide laser. The improved thermal properties result from the high thermal conductivity of the gold layer which acts as a heat spreader. The improved microwave properties result from the high electrical conductivity of the gold layer, which minimizes slow wave effects and microwave signal attenuation at high frequency [1-2].

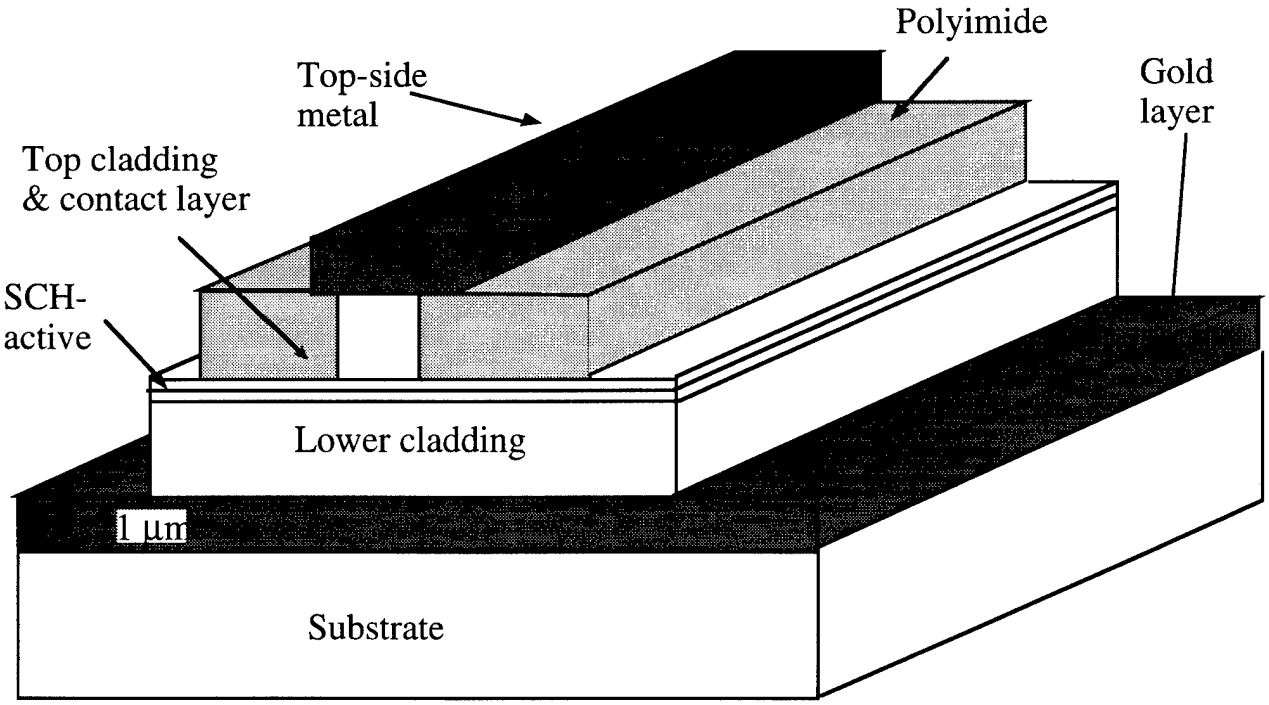


Figure 1. Schematic of a polyimide ridge waveguide microstrip laser.

Fabrication Process

The vertical structure of the microstrip laser cannot be made by standard growth and fabrication procedures, since it is not possible to grow metal on a semiconductor and then grow crystalline semiconductor on top of the metal. Instead a gold-to-gold fusion process is used. For the results presented here, a standard laser structure consisting of 6 strained InGaAsP quantum wells is grown in a metal organic chemical vapor deposition (MOCVD) reactor. The unpatterned wafer is then metallized with a Chrome (Cr)/Platinum (Pt)/ Gold (Au) metallization. Simultaneously we metallize an unpatterned semi-insulating (SI) InP substrate with the same metallization. Approximately 5000 angstroms (Å) of gold are put down on each wafer. Special attention is paid to wafer cleanliness and surface preparation both before and after the metal is evaporated. Following this step, the wafers are placed in intimate contact with each other, the contact being made between the gold faces. The wafers are then subject to high pressure in a special fixture at a temperature of 300 °C for 4 hours. The gold layers are fused together into a single layer during this process. The original substrate upon which the epitaxial structure was grown is removed in a hydrochloric acid solution which stops on an InGaAs stop etch layer. The epitaxial layers (which now are upside down relative to the original growth) are then processed into a ridge waveguide structure. A step is required in which a broad mesa under the ridge is formed by etching through the active region and the lower cladding to the fused gold layer, since the fused

gold is one of the contacts and must be accessible by probes. A scanning electron microscope (SEM) cross section of a finished device is shown in Figure 2 below.

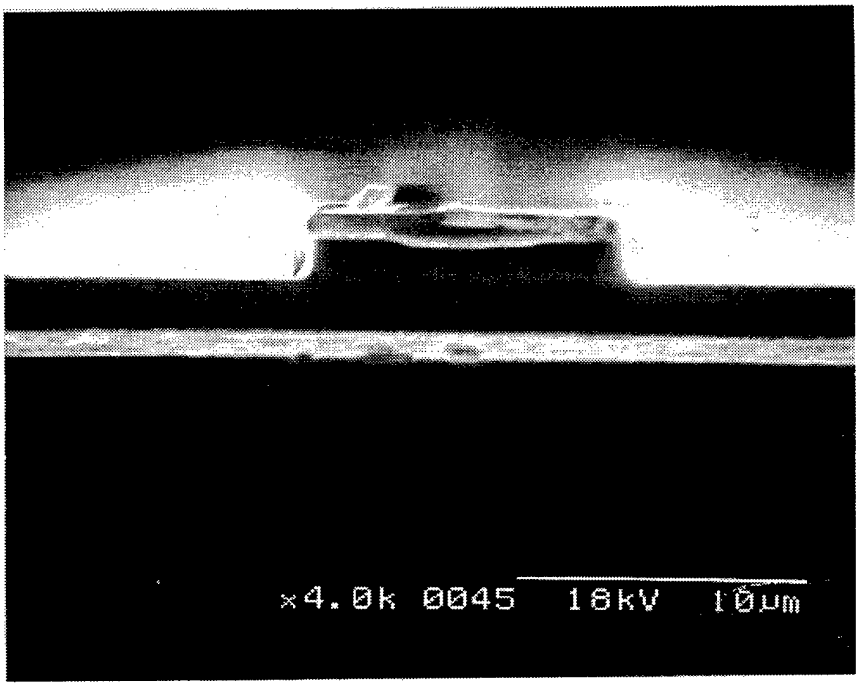


Figure 2. SEM cross section of a 10 µm ridge waveguide microstrip laser.

Results

Ridge waveguide devices with 10 µm wide ridges were fabricated from material with a p-doped, 6 quantum well active region. These devices were probed directly on the ridge and did not include any dielectric (such as polyimide) planarization around the ridges. In addition to fabricating 10 µm ridge microstrip lasers, 10 µm conventional ridge lasers were made from the same original wafer. The conventional ridge laser is a device which was processed directly from the grown wafer: there is no gold fused layer nor substrate removal and the epitaxial layers sit on the orignal substrate on which the layers were grown. Since the material used to fabricate these devices was grown p-side up, the microstrip lasers had n-ridges and the standard lasers had p-ridges. Additionally, standard broad area lasers with 50 µm ridges were also fabricated to test the material quality and as a means of comparison for the 10 µm ridges. Threshold current densities versus device length are shown in Figure 3 for all structures. The threshold current behavior of the microstrip laser is not degraded relative to the broad area structure or the standard 10 µm ridge device. Variations in the threshold current density from sample to sample may be related to surface nonuniformity of the original wafer.

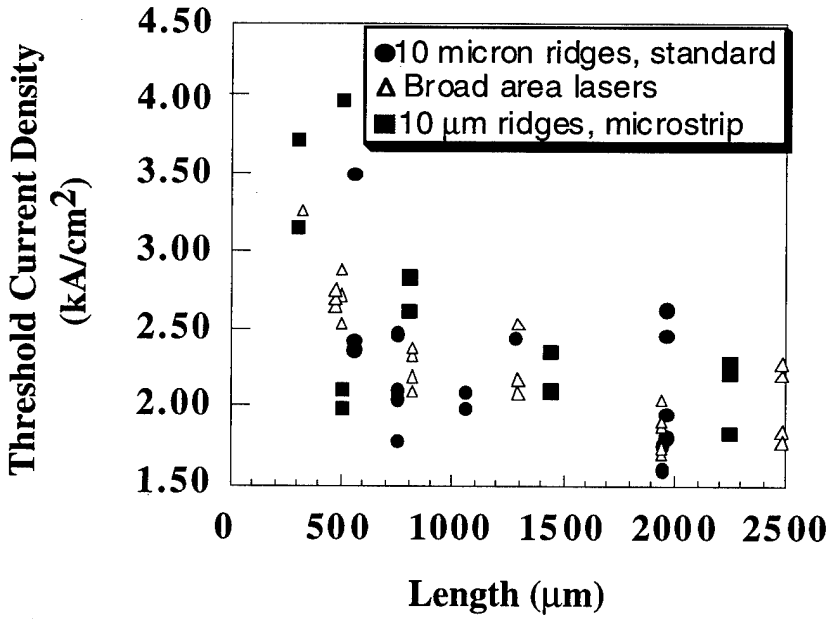


Figure 3. Threshold current densities vs. device length for 10 micron ridge waveguide microstrip lasers, 10 micron ridge waveguide conventional lasers, and broad area lasers.

In addition to the 10 micron ridge structures, narrow polyimide ridge waveguide microstrip devices, such as shown in the schematic Figure 1 were also fabricated. These structures demonstrated extremely high current continuous wave (cw) operation even when mounted ridge side up. A 5 μm wide, 620 μm long device operated cw at currents above 400 mA. The threshold currents in these devices were high however, and thus did not exhibit the expected higher power operation that one might otherwise see at such high current levels. As Figure 3 shows, good threshold operation is possible in these devices and we expect that the capability to run the devices at very high current levels will result in very high power operation.

The microwave propagation characteristics on the polyimide ridge structures were also measured. Previous measurements on conventional ridge waveguide lasers [1] reported microwave attenuation along the laser ridge on the order of 500-600 dB/cm at a freqency of 40 GHz. This high frequency attenuation is problematic for large bandwidth performance. Similar measurements on the microstrip structure show an attenuation between 150 and 300 dB/cm at 40 GHz depending on the bias current. This level of attenuation reduces the bandwidth problem caused by microwave attenuation and should permit higher bandwidth operation than is possible in a standard structure.

References

1. D. Tauber et al., Appl. Phys. Lett. **64**, 325 (1994).
2. B. Wu et al., Appl. Phys. Lett. **67**, 467 (1995).
3. J. D. Ralston et al., IEEE Photon. Technol. Lett. **6**, 1076 (1994).

Wednesday, May 1, 1996

Integrated Optics and Micromachining

IWG 3:30 pm-5:15 pm
Fairfax A

Robert J. Deri, *Presider*
Lawrence Livermore National Laboratory

Integrated-Optical Nanomechanical Systems

W. Lukosz
Optics Laboratory, Swiss Federal Institute of Technology, CH-8093 Zürich, Switzerland
phone: ++41-1-633 28 10 fax: ++41-1-633 11 12

Introduction

The functioning of all active integrated-optical (IO) systems, such as modulators, switches, and wavelength-tunable filters, is based on changes ΔN of the effective refractive indices N of the guided modes. The required ΔN-changes are normally induced either electro-optically (with ns-response times) or thermo-optically (with ms-response times).

We describe IO nanomechanical systems where the ΔN-changes are induced by the IO nanomechanical effect (with µs-response times). No electro-optic materials are required; no use is made of thermo- or elasto-optic effects. The systems comprise waveguides on oxidized silicon (Si/SiO_2) or glass substrates and "effective-refractive-index-shifting elements E" micromachined from Si/SiO_2 in the form of bridges or cantilevers, respectively, spanned or projecting over a waveguide. The ΔN-changes are induced by (elastic) nanometer-deflections of the element E under external forces. Potential applications are: active IO systems, electrically actuated by electrostatic forces, and all-optical acoustical sensors.

IO nanomechanical effect

The evanescent tail of a guided mode penetrates through the air gap of width $d < \lambda$ into the effective-refractive-index-shifting element E (see Fig. 1). This interaction causes the effective refractive index N of the guided mode to depend on d. Element E is a nonabsorptive dielectric material, such as SiO_2 or glass, with refractive index $n < N$. Consequently, the guided modes are not attenuated by absorption or radiation into element E. For suitably designed waveguides and small median air-gap widths d_0, width variations $\Delta d(t)$ of the order of nanometers induce effective-refractive-index changes $\Delta N(t) = (\partial N/\partial d)_{d=d_0} \cdot \Delta d(t)$ required for IO device operation [1,2]. The sensitivities $(\partial N/\partial d)$ versus d_0 were calculated for planar and rib waveguides. A wavelength-scaling law holds: the required gap-width changes Δd scale with λ if the thickness and width of the waveguide are also scaled proportional to λ.

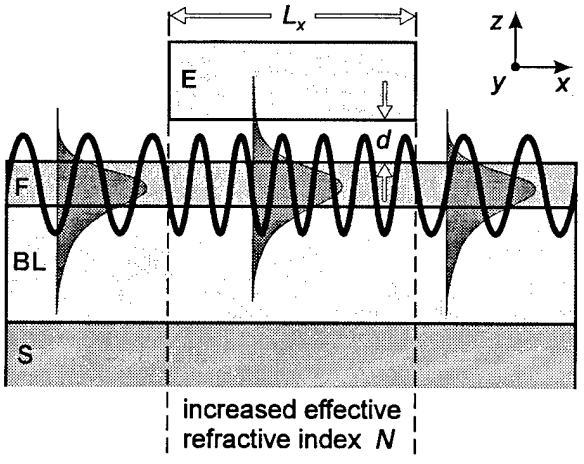


Fig. 1. Schematic cross-sectional view of effective-refractive-index-shifting element E and waveguide F.

C, air gap; d, air-gap width; L_x, interaction length; BL, SiO_2 buffer layer; S, substrate (Si).
The evanescent field of the guided mode interacts with the dielectric element E.

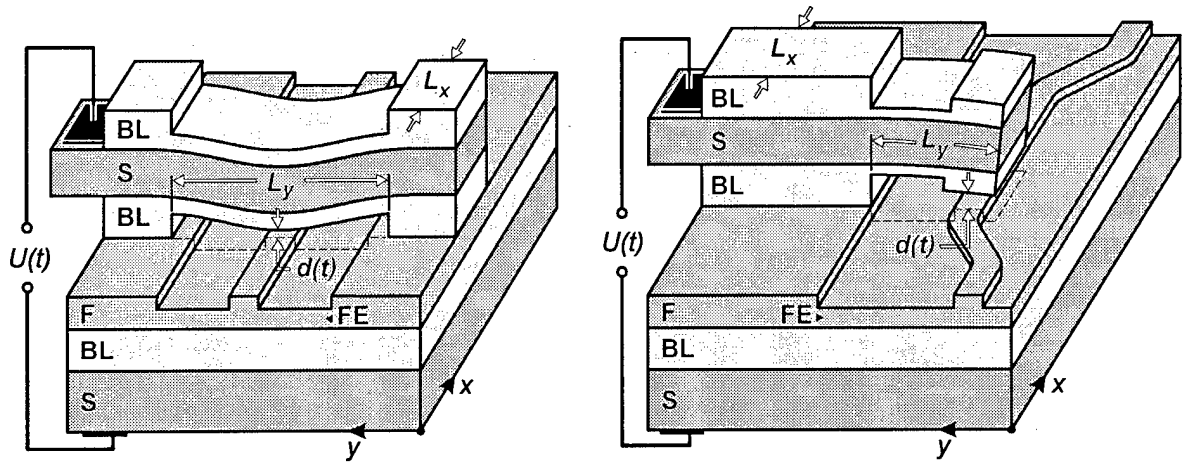


Fig. 2. Electrically actuated effective-refractive-index-shifting elements E in the form of (left) a bridge spanned over or (right) a cantilever projecting over a rib waveguide. $U(t)$, time-dependent voltage; $d(t)$, air-gap width; S, substrate (Si); BL, SiO_2 layer; F, waveguiding film (e.g., Si_3N_4); FE, etched film areas.

Examples of nanomechanical systems

Phase modulators

A guided mode propagating in a planar or rib waveguide under the effective-refractive-index-shifting element E experiences a phase shift of $\Delta\Phi(t) = 2\pi(L_x/\lambda)\Delta N(t)$.

Interferometric intensity modulators/switches

An effective-refractive-index-shifting element E is provided in one leg of a Mach-Zehnder interferometer; the phase modulation $\Delta\Phi(t)$ is transformed into an intensity modulation. In a Mach-Zehnder interferometer with two output ports, a phase shift of $\Delta\Phi = \pi$ switches the system from the cross to the bar state. In a polarimetric interferometer two guided modes of orthogonal polarization propagate simultaneously in a waveguide under element E; the difference $\Delta\tilde{\Phi}(t)$ of their phase shifts is transformed into an intensity modulation.

Wavelength-tunable Bragg reflector

An element E is positioned over a waveguide section with a surface relief grating acting as a Bragg reflector. The centre wavelength λ_m of the Bragg-reflected band is shifted by $\Delta\lambda_m$, where $\Delta\lambda_m/\lambda_m = \Delta N/N$.

These and other examples are explained in more detail in Refs. [1-4].

The temporal response of the IO nanomechanical systems is determined by the (micro- or nano-) mechanics and dynamics of the element E. From elasticity theory, the elastic deflections of bridges, cantilevers, and membranes under external forces or pressures are calculated, and thus their compliances and eigenfrequencies. The response time is given by the reciprocal of the lowest eigenfrequency.

Electrically actuated nanomechanical systems

Electrically actuated nanomechanical systems with cantilevers or bridges as effective-refractive-index-shifting elements E are schematically shown in Fig. 2. An electric voltage $U(t) = U_0 + \Delta U(t)$ is applied between the two plates of the capacitor. The resulting attractive

force is proportional to $[U(t)]^2 \approx U_0^2 + 2U_0\Delta U(t)$. With the d.c. voltage U_0 the median gap width d_0, and, thus, the system's sensitivity is adjusted; the a.c. voltage produces the gap-width variations $\Delta d(t)$ and the effective-refractive-index changes $\Delta N(t)$. We demonstrated intensity modulation with a polarimetric interferometer [5-7] and with a Mach-Zehnder interferometer [8], also wavelength-tunable Bragg-reflectors [9] and Fabry-Perot's [6].

IO microphone

With an effective-refractive-index-shifting element E in form of a thin membrane a polarimetric (or Mach-Zehnder) interferometer becomes an IO microphone. We demonstrated the functioning of such a microphone with an a-few-mm^2-large membrane etched in silica [10]. The compliance of the membrane has to be high and the compressibility of the air cushion in the gap and damping by viscous air flow have to be taken into account.

Conclusions and outlook

IO nanomechanical systems were fabricated with waveguides on oxidized silicon and by micromachining of the effective-refractive-index-shifting elements E in form of cantilevers, bridges, or membranes. Bulk micromachining was employed; the two chips with the waveguides and the element E, respectively, were bonded. Surface micromachining may be preferable.

All-optical IO microphones which directly transform sound-pressure variations into light-intensity modulation are feasible.

Electrically actuated nanomechanical systems have attractive features as follows: low switching energies, low operating voltages, and μs-response times. Their integration with IC's on the same silicon chip should be possible.

References

[1] W. Lukosz, "Integrated Optical Chemical Sensors and New Nanomechano-Integrated Optical Devices as Modulators, Switches, and Microphones; Integrated Optical (Bio-)Chemical Sensors," Micro System Technologies '90, Ed.: H. Reichl, Springer Berlin, 1990, pp. 725-732.

[2] W. Lukosz, "Integrated Optical Nanomechanical Devices as Modulators, Switches, and Tunable Frequency Filters, and as Acoustical Sensors," Proc. SPIE Vol. 1793 (1992), 214-234 [OE/Fibers '92, Boston].

[3] US patent 5.091.983.

[4] P. Pliska and W. Lukosz, "Electrostatically Actuated Integrated Optical Nanomechanical Devices, Proc. SPIE Vol. 1793 (1992), 259-272 [OE/Fibers '92, Boston].

[5] P. Pliska and W. Lukosz, "Electrically Actuated Nanomechanical Integrated Optical Switches," Photonics in Switching, Technical Digest (Opt. Soc. Am., Washington, D.C., 1993), pp. 164-167.

[6] P. Pliska, R. Dangel, and W. Lukosz, "Electro-Nanomechanically Actuated Integrated-Optical Modulators, Switches, and Deflectors and Tunable Fabry-Perot Interferometers," Proc. Europ. Conf. on Integrated Optics (ECIO '93), Neuchâtel, April 1993; paper 14-30.

[7] R. Dangel and W. Lukosz, "SiO_2-TiO_2 Rib-Waveguides for Electrostatically Actuated IO Nanomechanical Devices," Proc. ECIO '95, Delft, April 1995, p. 371-374.

[8] R. Dangel and W. Lukosz, "Electro-nanomechanically actuated IO Mach-Zehnder interferometer," Integrated Photonics Research, Boston April 29-May 3, 1996 (submitted).

[9] W. Gabathuler and W. Lukosz, "Electro-Nanomechanically Tunable IO Bragg Reflectors," Proc. ECIO '93, Neuchâtel, April 1993; paper 4-18.

[10] P. Pliska and W. Lukosz, "Integrated-Optical Acoustical Sensors," Sensors and Actuators A, 41-42, 93-97 (1994).

Actuated micromachined microreflector with two degrees of freedom for integrated optical systems

Michael J. Daneman, Norman C. Tien, Olav Solgaard, Kam Y. Lau, Richard S. Muller

University of California at Berkeley
211-70 Cory Hall, #1772
Berkeley, CA 94720-1772
Phone: (510) 642-1023
Fax: (510) 642-6330

Introduction

The growing optical communications and measurement market requires low-cost, high-performance optoelectronic modules such as laser-to-fiber couplers, tunable lasers, scanners, interferometers, etc. Unlike integrated electronic circuits, integrated optical systems require precise alignment of components. A misalignment of less than 1 μm can dramatically decrease system performance. While silicon-optical-bench (SOB) technology provides for hybrid integration of semiconductor lasers, lenses, and optical fibers on a silicon chip, it is typically limited to ±1 μm alignment tolerances (without external adjustment). Another limitation is the lack of on-chip actuated optical components (such as mirrors, gratings, lenses, etc.) As a result, SOB technology applications have been limited to simple systems with no more than three or four components. To overcome these limitations a micromachined free-space optical platform has been proposed [1, 2]. By combining micromachined movable optical components with lasers, lenses, and fibers on a silicon substrate, we can produce complex self-aligning optical systems on a chip. In order to function in a self-contained optical module, the micromachined components must have sufficient precision and, where required, must have on-chip actuation. In this paper, we present an actuated micromachined microreflector with two degrees of freedom and on-chip resonant electrostatically driven impact actuations.

Design

The actuated microreflector (Figure 1) was designed for laser-to-fiber coupling and external-cavity-laser applications. It consists of a polysilicon mirror plate hinged to a support beam. Each of these is, in turn, hinged to a vibromotor-actuated slider. Microhinge technology [3] allows the joints to rotate out of the plane of the substrate to achieve large aspect ratios. Common-mode actuation of the sliders results in translational motion, while differential slider motion produces out-of-plane mirror rotation. These motions permit the microreflector to position an optical beam in two dimensions.

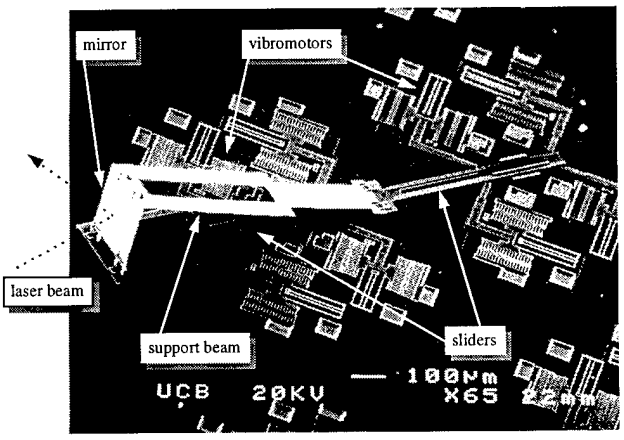


Figure 1. Scanning electron micrograph of a released and assembled actuated microreflector.

Each of the two sliders is actuated with an integrated microvibromotor. The vibromotor consists of four electrostatic-comb resonators with attached impact arms driving a slider through oblique impact. To balance the forces, two opposing impacters are used for each direction of travel. The comb structures are driven at their resonance frequency (roughly 8.2 kHz) thereby achieving an amplification of the electrostatic force by the resonator quality factor (typically 30 to 100 in air [4,5]). Since energy is transferred to the slider only during impact (typically lasting only a few microseconds), the impacters can deliver short-duration forces that are large enough to overcome static friction in the sliders and hinges. Slider velocity can be controlled by driving the comb drives with gated bursts of the resonant waveform.

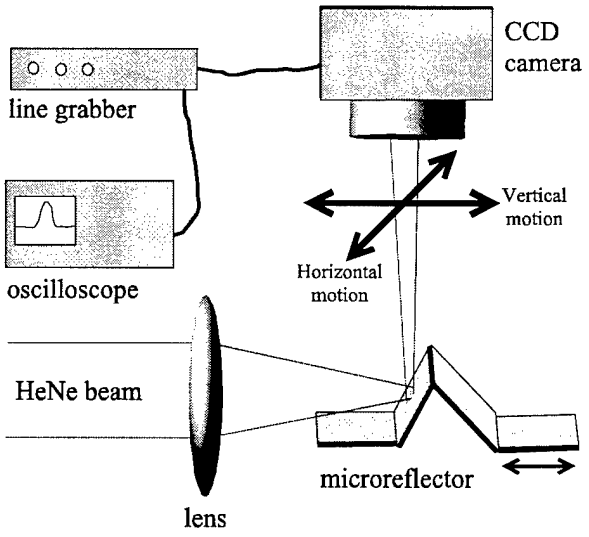


Figure 2. Experimental setup for actuated microreflector scanning precision measurements.

Fabrication

The actuated microreflector was fabricated on a silicon substrate using silicon-surface micromachining technology. The fabrication process is described in detail in [1,6]. A special pre-release etch in 5:1 HF followed by a vigorous rinse is used to eliminate stringers. Finally, the structure is released for 10 minutes in concentrated HF and dried using a critical-point CO_2 drier [7] to avoid sticktion.

Characterization

Characterization of the vibromotor alone has been described in a previous publication and has shown the slider motion to have a step resolution of less than 0.3 μm [8]. In this paper,

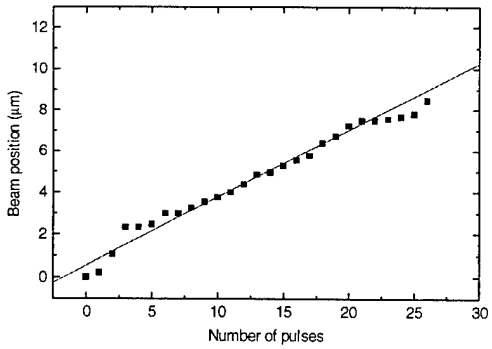


Figure 3. Vertical beam position 200 μm from the micromirror. These data show a 0.6 μm standard deviation from an ideal response. Standard deviations upto 0.81 μm were measured.

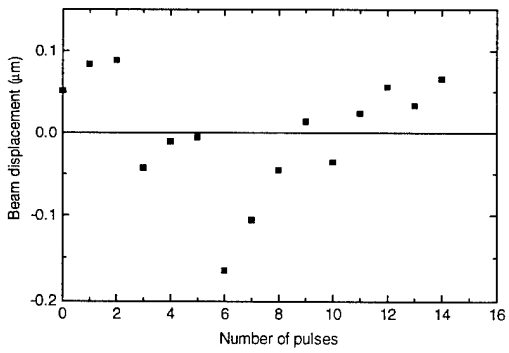


Figure 4. Horizontal beam deviation 200 μm from the micromirror during a vertical scan. A standard deviation of 0.05 μm and a maximum deviation of 0.16 μm was measured.

vibromotor performance in an integrated microreflector system is characterized. The precision of the actuated microreflector is measured using the experimental setup shown in Figure 2. A HeNe laser is reflected from the micromirror surface onto a CCD camera. As the rear slider is actuated, the beam position along each of the two axes is measured on the CCD and extrapolated to a location 200 μm in front of the mirror (where a fiber would typically be positioned for a laser-to-fiber coupling application). The micromirror is able to position the beam with a standard deviation of 0.81 μm and a maximum deviation of 1.5 μm (Figure 3) in the vertical dimention. This deviation is due primarily to the wobble in the slider structure. The horizontal beam deviation is 0.05 μm (Figure 4) and is comparable to the 0.07 μm deviation measured in externally actuated structures. This precision is sufficient for laser to single-mode fiber coupling applications where, due to lens magnification, the beam only needs to be within 1-2 μm for high coupling. However, for external cavity laser applications a higher precision is necessary. Since in earlier experiments a microreflector with no on-chip actuators and an alternate hub design has shown a vertical precision of 0.17 μm [6], a redesign of the actuated slider should greatly improve its precision.

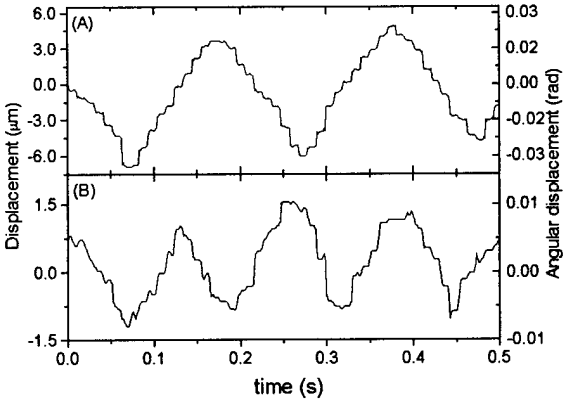


Figure 5. Beam scanning with the actuated micro-reflector. In (a) a 40 V dc offset was used, resulting in 0.7-1.1 μm step size on the plane 200 μm from the micromirror, while in (b) a 38 V dc offset produces 0.3-0.6 μm steps.

To demonstrate the use of the actuated micromirror in scanning and beam-positioning applications, a reflected HeNe beam was imaged on a position-sensitive detector while the angular position of the mirror was swept in real time. The vibromotor was driven with bursts of four 20 V (p-p) resonant (8.2 kHz) square-wave cycles spaced 10 ms apart in series with a 40 or 38 V dc offset. The resulting output (Figure 5) clearly shows the stepwise nature of the mirror motion. The average speed of the sweep can be changed by varying the spacing of the bursts. Figures 5a and 5b also demonstrate that the size of the step itself depends on the applied voltage and can be controlled. With an average angular step size of 5 mrad, the microreflector has a maximum estimated scan rate of 10.2 rad/s or a beam speed of 2 mm/s on a plane 200 μm in front of the reflector.

Conclusion

In conclusion, we have fabricated and characterized an on-chip actuated micromachined microreflector for use in integrated optical systems on a silicon chip. The microreflector has two degrees-of-freedom and is able to position an optical beam in two dimensions. It is designed for use in self-contained laser-to-fiber coupling modules, integrated external-cavity devices, as well as other silicon-optical-bench applications requiring precise optical alignment. The reflector is capable of positioning an optical beam a fiber with a resolution of 0.81 μm, and a significantly higher precision is expected in future designs. We have also demonstrated repeatable beam scanning, with the scanning speed and step size determined by the applied electrical signal. The

actuated microreflector and devices like it mark an important step towards making useful and cost-effective miniaturized integrated optical system.

1. O. Solgaard, M. Daneman, N.C. Tien, A. Friedberger, R.S. Muller, K.Y. Lau, "Optoelectronic packaging using silicon surface-micromachined alignment mirrors," IEEE Photonics Technology Letters, vol. 7, no. 1, 1995, pp. 41-43.
2. L.Y. Lin, S.S. Lee, K.S.J. Pister, M.C. Wu, "Micro-machined three-dimentional micro-optics for free-space optical systems," IEEE Photonics Technology Letters, vol. 6, no. 12, 1994, pp. 1445-1447.
3. K.S.J. Pister, M.W. Judy, S.R. Burgett, R.S. Fearing, "Microfabricated hinges," Sensors and Acutators (A), vol. 33, no. 3, 1992, pp. 249-256.
4. W.C. Tang T.-C. H. Nguyen, M.W. Judy, R.T. Howe, "Electrostatic-comb drive of lateral polysilicon resonators, " Sensors and Actuators, vol. A21-23, 1990, pp. 328-331.
5. Y.H. Cho, A.P. Pisano, R.T. Howe, "Viscous Damping Model for Laterally Oscillating Microstructures," Journal of Microelectromechanical Systems, vol. 3, no. 2, 1994, pp.81-87.
6. M.J. Daneman, O. Solgaard, N.C. Tien, K.Y. Lau, R.S. Muller, "Integrated Laser-to-Fiber Coupling Module Using a Micromachined Alignment Mirror," Photonics Technology Letters, March, 1996.
7. G.T. Mulhern, D.S. Soane, R.T. Howe, "Supercritical Carbon Dioxide Drying of Microstructures," 7th International Conference on Solid State Sensors and Actuators, 1993, pp. 296-299.
8. M.J. Daneman, N.C. Tien, O. Solgaard, A.P. Pisano, K.Y. Lau, R.S. Muller, "Linear Microvibromotor for Positioning of Optical Elements," Microelectromechanics Strucutres Conference, Amsterdam, The Netherlands, January 1995, pp. 55-60.

Design and Fabrication of High-Performance Silicon Micromachined Resonant Microscanners for Optical Scanning Applications

Meng-Hsiung Kiang, Olav Solgaard, Richard S. Muller and Kam Y. Lau
Department of Electrical Engineering and Computer Sciences
University of California at Berkeley
Berkeley, CA 94720
Tel: (510) 643-5849, Fax: (510) 642-2739

Introduction

Resonant and galvanometric optical scanners have long been used for various scientific and industrial applications. The typical attributes of these scanners are fast scan speeds, large scan angles, and low mass. In this paper, we present the design and fabrication of a silicon-surface-micromachined resonant microscanner that has a large scan angle, a fast scan rate, extremely small mass, and a low operating power. The integration of the scanner optics and the driving motor(s) and potentially the electronics is carried out as part of the fabrication process, which avoids major technical challenges such as the assembly of mirrors and motors in the bulk optical scanner system. The compact microscanner also makes packaging a much easier task. With the scanner module integrated on a silicon chip, the microscanner can be packaged in a vacuum which alleviates the adverse effects from the environment. Vacuum packaging is, however, very difficult and costly to do in a bulk-scanner system. We will discussed single-mirror scanners that are capable of high-speed scanning with a large scan angle. These single-mirror scanners can be combined to form more complicated microscanners like the system shown in Fig. 1, which is an SEM micrograph of one of the microscanner systems that we have fabricated. The two-mirror, two-axis raster scanner finds a wide range of applications in areas such as communications, medicine, and entertainment, among others.

Silicon-surface-micromachining technology has been used to fabricate micro-optical devices such as movable-micromirrors for building optical components and communication subsystems [1-5]. Motorized micromirrors with actuators integrated on the same chip (such as those in [1, 2]) are of particular interest because they make possible truly miniaturized systems. Several authors have proposed different microscanner schemes [6, 7] to be used for optical scanning. For practical optical-scanner systems, however, the smallest optical aperture (such as that of the mirror in our case) has to be large enough to insure sufficient image resolution. In order to create high-aspect-ratio optical surfaces with dimensions in the hundreds of μms while taking advantage of the planar integrated-circuit processing technology, polysilicon microhinges [8] are incorporated in our microscanner structure. The microhinges allow the micromirrors to be lifted out of the plane of the substrate after processing is completed.

Scanner Fabrication

Three layers of structural polysilicon (each 2 μm thick) are used to build the resonant scanner. Oxide is used as the sacrificial material separating the different polysilicon layers. The silicon substrate is first passivated by thermal silicon dioxide and nitride. Then on top of a 0.5-μm-thick film of phosphorous-doped polysilicon ground plane for the electrostatic comb motor, a layer of sacrificial oxide is deposited. Indentations are made on the oxide surface to create dimples in the subsequent polysilicon layer. The dimples reduce the surface-contact area and, therefore,

the "stiction" between the two surfaces. The first structural polysilicon layer is then deposited and patterned to form the electrostatic comb drive, the back support, the slider and the bottom plate of the hinge structures. The pins in the hinges and the guide for the slider are defined in the second polysilicon layer. Lastly, the third structural polysilicon layer is used to form the mirror and the staples of the pins to finish the hinge structures. Through-holes are etched in the larger polysilicon areas in the last processing step to reduce the final wet-etching time in concentrated HF used to "free" the mechanical parts. Once the sacrificial oxide is removed, the released polysilicon structures are free to be moved and assembled.

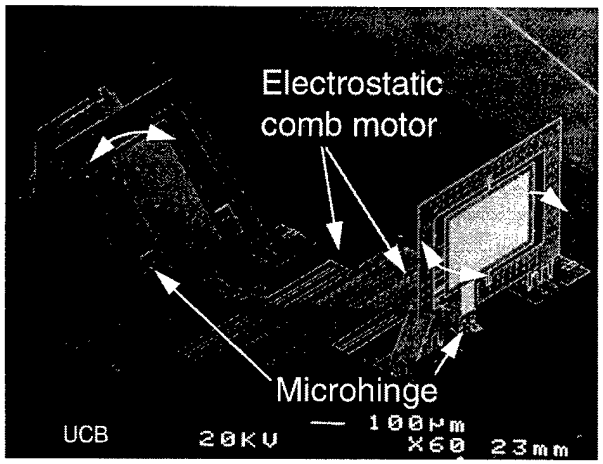


Fig. 1 SEM photograph of a two-mirror, two-axis microscanner. An electrostatic-comb motor is attached to the bottom of each of the two scanning micromirrors. The size of both of the micromirrors is 300 by 500 μm.

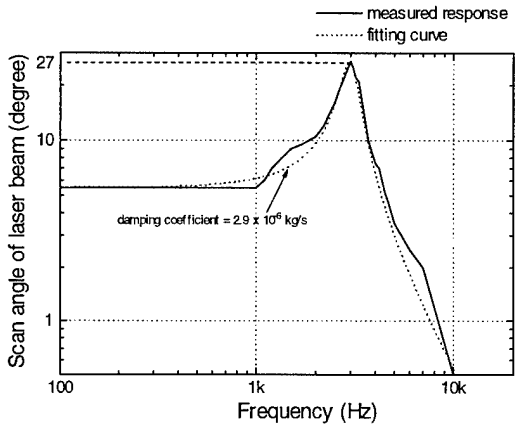


Fig. 2 The frequency response of the resonant microscanner. A 9-V ac voltage on top of a 30-V dc voltage is applied to the driving motor. The dotted trace is the theoretical curve modeling the scanner as a linear forced-oscillation system.

Characterization

To characterize the performance of our resonant microscanner systems, an one-mirror microscanner, similar to the one shown in the left of Fig. 1, is used in the experiments described in the following paragraphs. The micromirror in the scanner measures 200 by 250 μm, and the shafts around which the mirror pivots are 160 μm below the top of the mirror. The maximum excursion of the bottom of the mirror is limited to below 20 μm each side (swings two sides when the scanner is driven on resonance) from its rest position in our initial design. At 150 μm away from the rotation axis of the mirror, a 20 μm displacement results in a 7.6° rotation of the mirror. In other words, the upper-limit of the scan angle of this resonant scanner is 15° (30° optical) if the motor is driven by a sufficiently large voltage. This scan angle compares favorably with typical performance characteristics obtained in bulk resonant scanners available at present [9].

The frequency response and the maximum scan range of the resonant microscanner are measured by bouncing the light beam of a He-Ne laser off the scanning micromirror and observe the scan-line imaged on a screen that has the angular vernier marks on it. In addition to a 30-V dc supply, an sinusoidal voltage (9 V in amplitude) with varying frequencies is applied to the electrostatic comb motor. The force exerted by the electrostatic comb on the scanning mirror can be written as

$$F = \tfrac{1}{2} C \bullet V^2 = \tfrac{1}{2} C \bullet (V_{dc} + V_{ac} \cos \omega t)^2$$

$$= \tfrac{1}{2} C \bullet (V_{dc}^2 + 2\, V_{dc}\, V_{ac} \cos \omega t + V_{ac}^2 \cos^2 \omega t)$$
$$= \tfrac{1}{2} C \bullet (V_{dc}^2 + \tfrac{1}{2}\, V_{ac}^2 + 2\, V_{dc}\, V_{ac} \cos \omega t + \tfrac{1}{2}\, V_{ac}^2 \cos 2\omega t) \quad (1)$$

where C is the capacitance of the electrostatic comb drive and V is the applied voltage amplitude. V_{dc} and V_{ac} stands for the dc and ac voltage amplitude, respectively, and ω is the angular frequency of the ac input. The measured large-signal frequency response of the resonant microscanner system is plotted in Fig. 2. The microscanner resonates at 3 kHz with a system Q-factor calculated to be 2.8. The dotted curve is the theoretical model of a forced-damped-oscillation with a damping force proportional to the linear velocity of the moving parts in the mechanical system. The optical scan angle shown in this plot has a peak value of 27°. The 28° maximum-scan-angle of this microscanner, limited by the geometry of the structure in this particular design, is obtained when the ac voltage input amplitude is increased to 9.5 V. The hump around 1.5 kHz in the measured curve is due to the second harmonic (the last term in equation (1)) of the ac voltage.

One important issue for optical scanners is the scan-line repeatability between scans. To characterize it, the resonant microscanner is put in an optical interferometric setup similar to the one depicted in Fig. 5 of [1]. The cleaved facet of the optical fiber forms a Fabry-Perot interferometer with the tip of the scanning micromirror (Fig. 3a) that can measure the mirror displacement with a resolution of 10 nm. The detected interference pattern with a 1.5 kHz ac voltage applied to the motor is shown in Fig. 3b. The scan repeatability is determined by comparing the turning points of the periodic interference pattern, at which points the mirror changes its scan direction and therefore are the end points of the scan lines. For our present microscanner system, the deviation for the ends of the scan lines is typically measured to be less than 1/4 of an optical cycle, or 0.16 μm for a 1.3 μm laser source in the interferometer. This small inaccuracy is caused by the sloppiness in the hinges that we have used in our current scanner structures and can be further improved by employing different types of mirror hinges such as torsion bars.

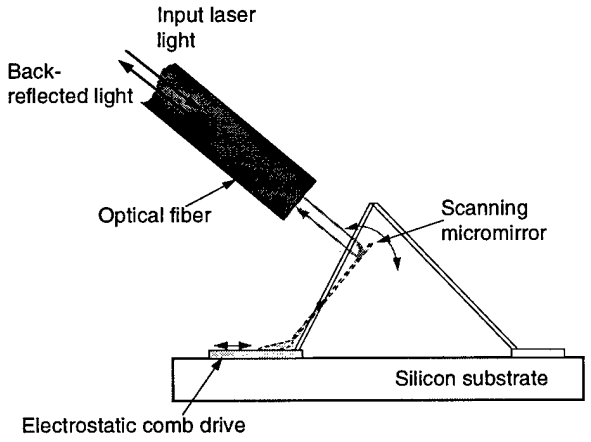


Fig. 3a Schematic drawing of the Fabry-Perot interferometer formed between the fiber front facet and the top of the scanning micromirror.

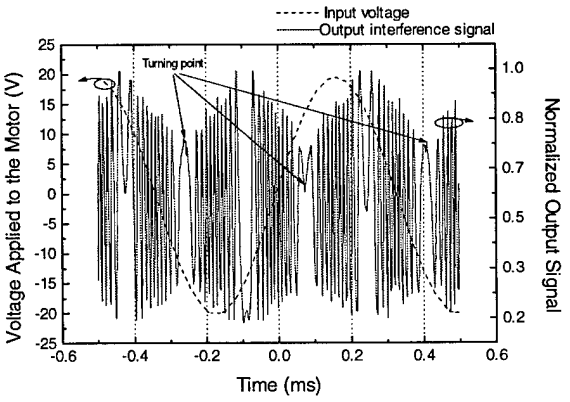


Fig. 3b Detected interference signal from the setup shown in Fig. 3a. The microscanner is driven on resonance at 3 kHz with a 20-V ac voltage.

Application

One application of resonant scanners are as barcode readers which are widely used for automatic object-identification in many industries. We have demonstrated barcode scanning using our

resonant microscanner with the experimental setup as depicted in Fig. 4 [10]. The universal product code (UPC) barcode from the package of a commercial product is used in the experiment, and Fig. 5 shows the recorded signal that corresponds to the center portion of the barcode as indicated by the arrow. This result is obtained by driving the scanning micromirror off resonance (at ~ 2 kHz) with a sinusoidal voltage of 20 V in amplitude (i.e. the mirror is scanning at an angle of ~ 4.5°). The linear scan-range can be increased to cover the entire barcode with sufficient resolution for code recognition when the driving voltage amplitude to the microscanner is increased or the frequency of the ac voltage is set on resonance.

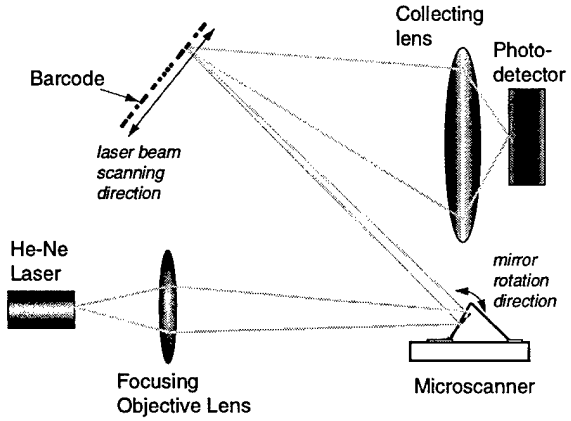


Fig. 4 Experimental setup for barcode scanning using the resonant microscanner.

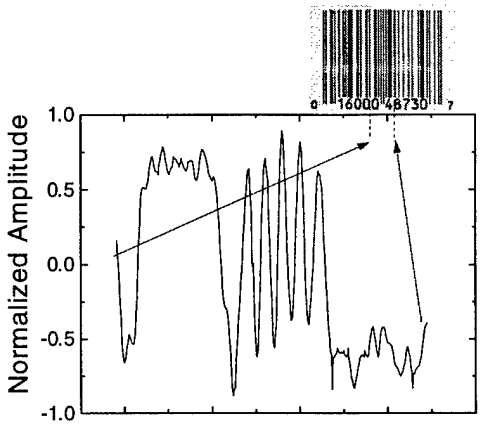


Fig. 5 The detected signal corresponding to the center portion of the barcode (as indicated by the arrows).

Conclusion

To summarize, we have designed and fabricated resonant optical microscanners using silicon-surface-micromachining technology. Constructed with an electrostatic comb motor to drive a 200 by 250 μm micromirror, the microscanner has a maximum scan angle of 28° (optical) and a resonant frequency of 3 kHz. The microscanner has been demonstrated to be a viable building block as the scanning component in a barcode reader. The small size, light weight, low operating power, and potentially low cost make it attractive for numerous applications of optical scanning systems.

References

[1] M.-H. Kiang, O. Solgaard, R. S. Muller, and K. Y. Lau, *IEEE Photon. Technol. Lett.,* Vol. 8, no. 1, 1996 (in press).

[2] M.-H. Kiang, O. Solgaard, M. Daneman, N. C. Tien, R. S. Muller, and K. Y. Lau, in *Conference on Lasers and Electro-Optics,* 1995 Technical Digest Series, Vol. 15, pp. 248-249, Baltimore, MD, May 1995.

[3] M. Daneman, O. Solgaard, N. C. Tien, R. S. Muller, and K. Y. Lau, in *Conference on Lasers and Electro-Optics,* 1995 Technical Digest Series, Vol. 15, pp. 249-250, Baltimore, MD, May 1995.

[4] O. Solgaard, M. Daneman, N. C. Tien, A. Friedberger, R. S. Muller, and K. Y. Lau, *IEEE Photon. Technol. Lett.*, Vol. 7, no. 1, pp. 41-43, 1995.

[5] Y. Lin, S. S. Lee, K. S. Pister, and M. C. Wu, *IEEE Photon. Technol. Lett.*, Vol. 6, no. 12, pp. 1445-1447, 1994.

[6] K. Deng, H. Miyajima, V. R. Dhuler, M. Mehregany, S. W. Smith, F. L. Merat. and S. Furukawa, in *Tech. Dig., Solid-State Sensor & Actuator Workshop*, Hilton Head, SC, June 1994, pp. 234-238.

[7] A. Yasseen, S. W. Smith, M. Mehregany, and F. L. Merat, in *Proceed. IEEE Micro Electro Mechanical Systems*, pp. 175-180, Amsterdam, the Netherlands, Jan. 1995.

[8] K. S. J. Pister, M. W. Judy, S. R. Burgett, and R. S. Fearing, *Sensors and Actuators (A),* Vol. 33, no. 3, pp. 249-256, 1992.

[9] J. I. Montagu, in *Optical Scanning,* chap. 10, edited by G. F. Marshall, Marcel Dekker, Inc., New York, NY, 1991.

[10] M.-H. Kiang, O. Solgaard, R. S. Muller, and K. Y. Lau, in *Proceed. IEEE Micro Electro Mechanical Systems,* San Diego, CA, Feb. 1996.

Photonic integrated circuits for optical displacement sensing

Hans P. Zappe and Daniel Hofstetter

Paul Scherrer Institute
Badenerstrasse 569
8048 Zurich
Switzerland
Phone +41 1 492 6350
Fax +41 1 491 0007
email zappe@psi.ch

ABSTRACT

We discuss a III-V-based monolithically integrated measurement microsystem for optical displacement sensing. The sensor, consisting of a Michelson interferometer with an integrated DBR laser and waveguide photodetector, has been fabricated on a single GaAs substrate. Alignment requirements are reduced to that of a lens for beam collimation; displacement measurements with sub-100 nm resolution have been performed. The same technology may also be employed for integrated optical refractometric chemical sensors.

INTRODUCTION

Photonic integrated circuits (PICs), well developed for telecommunications applications [1], show considerable promise for use in sensors and metrology. The ability to integrate most or all optical functions on a single semiconductor chip will yield small, robust and highly functional optical sensor microsystems. The small size and reduced need for complex optical alignment suggests that such integrated optical chips may be used as components in micro-optical systems, as part of a more complex MEMS device or in environments where the use of a bulk optical approach is precluded. As a demonstration of the potential utility and attractiveness of such a monolithic system, we discuss here the use of III-V devices and integration technology for the fabrication of a monolithic optical displacement sensor circuit.

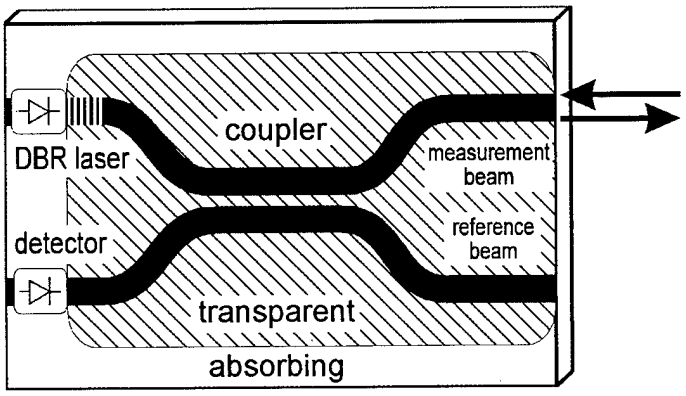


Figure 1 - Schematic view of a Michelson interferometer used for displacement measurement. The measurement beam is reflected from an external object and returns to the interferometer chip.

This physical displacement measurement chip was configured as a Michelson interferometer and included a monolithically integrated DBR laser, waveguide coupler and waveguide photodetector as shown schematically in Figure 1. While requiring only the alignment of an external GRIN lens for beam collimation, the chip was used for displacement measurements with sub-100 nm resolution at a measurement distance of up to 0.45 m [2].

TECHNOLOGY AND COMPONENT CHARACTERISTICS

The integration of the waveguides, lasers and photodetectors for the Michelson interferometer was accomplished by the use of a single heterostructure layer design. On a GaAs substrate, a 1.1 μm thick n-type $Al_{0.8}Ga_{0.2}As$ lower cladding, 165 nm thick $Al_{0.3}Ga_{0.7}As$ core region with a single, 7 nm wide quantum well, and a 0.8 μm thick p-type $Al_{0.8}Ga_{0.2}As$ upper cladding were grown by MOVPE; the structure was capped by a 100 nm thick highly-doped p^+ GaAs layer. Most process details have appeared elsewhere [3]; we discuss here a few relevant points.

An optical integrated circuit requires that, at the operating wavelength, the waveguide regions be transparent whereas the laser pumped region and detector should be absorbing; this is shown schematically by the hatched and clear regions, respectively, of Figure 1. A controlled change in the shape of the quantum well allows tuning of the emission or absorption wavelength; this was accomplished through vacancy-enhanced disordering (VED), a process which uses two different surface dielectrics (SiO_2 and SrF_2) during a high temperature anneal step. During VED, the absorption edge of the waveguide regions could be selectively blue-shifted by up to 68 nm while shifting the photodetector and pumped regions of the DBR laser less than 10 nm. For the Michelson interferometer chip, a smaller wavelength shift was used; measurements showed that laser performance was not notably degraded by this short high-temperature anneal step [4].

The DBR laser was designed for simple fabrication, without epitaxial re-growth. A 3rd order, holographically-defined grating with a period of 385 nm was positioned in a dry-etched recess in which most, but not all, of the upper cladding was removed. The depth of this recess, and the depth of the dry-etched grating, allow accurate determination of the grating coupling coefficient, κ; κL ~ 4 for the L = 200 μm long grating. This value is high enough for good laser performance but low enough to allow sufficient light to enter the interferometer. The grating was used as a reflector on the interferometer-side of the laser; the opposite mirror was formed by a cleaved facet (see Figure 3).

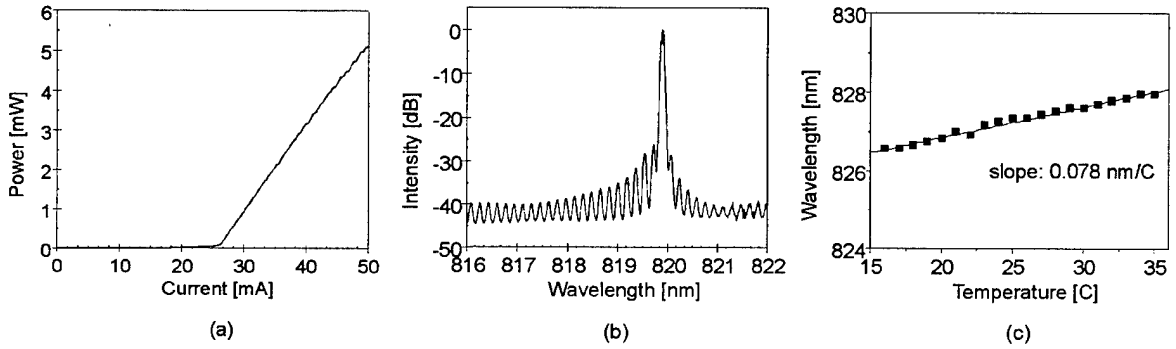


Figure 2 - Output characteristics of the DBR laser used to drive the interferometer circuits: (a) output power from the cleaved facet; (b) optical spectrum; (c) temperature wavelength tuning.

In Figure 2a, the PI characteristic of a discrete DBR laser shows a threshold current of 26 mA, implying $J_{th} = 1.3$ kA/cm^2; total internal quantum efficiency is $\eta = 26\%$. Maximum optical output power exceeded 5 mW. Emission wavelength was nominally 820 nm at room temperature, as seen in the spectrum of Figure 2b. The wavelength could be temperature tuned ($\Delta T = 20°$) over 600 GHz without mode-hops as seen in Figure 2c, as measured on a different sample; temperature sensitivity of J_{th} is given by $T_0 = 101$ K. The monomode behavior of the

laser is evident from the spectrum; side mode suppression ratio is greater than 27 dB. Self-heterodyne measurements showed an optical linewidth value of 500 kHz, giving a coherence length of 600 m.

The 500 μm long waveguide detectors remained absorbing after the VED step. Typical responsivity values were 0.6 A/W at 820 nm, implying a quantum efficiency of 91%. Measured dark currents were 500 pA for 3×500 μm^2 area. The detectors were optically isolated from the DBR laser by an etched isolation trench and electrically isolated by patterned H^+ implantation.

INTEGRATED DISPLACEMENT SENSOR

As shown in the photograph of Figure 3, the monolithically integrated displacement measurement chip includes the DBR laser, waveguide interferometer and photodetector on a single piece of GaAs, thus requiring no physical alignment of these components. The interferometers are less than 300 μm wide and total chip length is 2 mm.

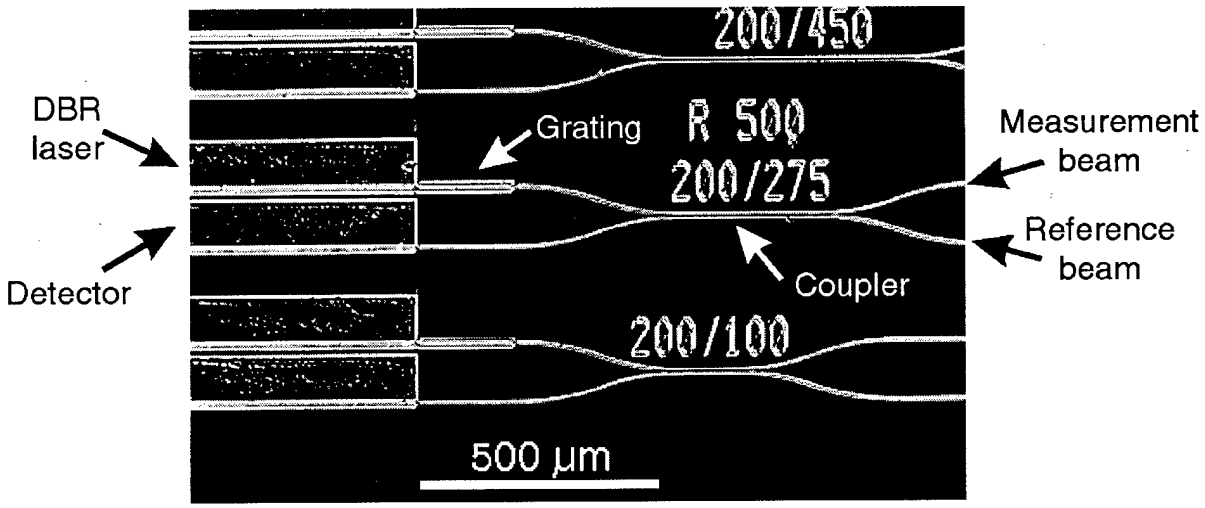


Figure 3 - Photograph of the Michelson interferometer chip used for displacement measurements. Cleaved facets form the left and right edges of the chip.

A GRIN lens, with pitch 0.23, was used for collimation of the measurement beam leaving the interferometer; this alignment was the only physical adjustment of the microsystem necessary. A semi-transparent mirror was used as a test measurement object; a CCD camera behind the mirror was used to adjust the system into autocollimation. The detector output current, giving the interference signal, for a measurement distance of 3 cm, is shown in Figure 4. Mirror displacement was limited to 20 μm by the piezo actuators, but we see that 49 interference fringes are traversed for this displacement. Based on this output signal, which corresponds to an object displacement of about 400 nm per fringe, sub-100 nm system resolution is easily achieved. Higher resolution values may be reached with additional optical signal processing and improved system contrast. Maximum measurement distance was about 45 cm, the contrast of the signal decreasing for longer distances.

The interference characteristic shows a considerable offset current, due to optical coupling directly from the laser into the detector despite the etched optical isolation; this crosstalk may be reduced by inclusion of optically non-transparent layers on the trench sidewalls. The limitation of measurement distance (45 cm) is due to the increased linewidth of the emitted measurement beam: a linewidth of 300 MHz was measured for optical signal emitted from the

interferometer. A linewidth in this range implies a coherence length of 1 m, and is likely due to interface reflections and feedback into the DBR laser. Improved facet coatings and process optimization should diminish this effect.

Future designs will incorporate a phase-shifted second reference beam, induced by an integrated waveguide phase modulator, for measurement of two signals in phase quadrature and thus determination of displacement *direction*. In addition, the use of a vertically emitting, focusing grating coupler [5] would remove the necessity for the alignment step still required, namely that of the GRIN lens.

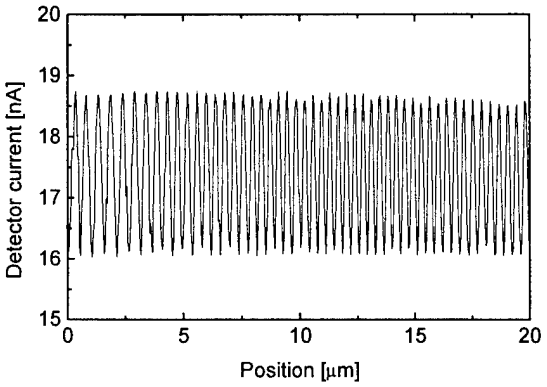


Figure 4 - Measured interferogram for an external object at a distance of 3 cm displaced by 20 μm. 49 interference fringes are seen.

The fabrication and device technology developed for this monolithic displacement sensor has also been demonstrated to be suitable for other types of optical sensing platforms, particularly for chemical analysis. Using a Mach-Zehnder interferometer configuration, for example, changes in the refractive index of an external medium, such as a chemical or biological solution, can be measured. Since the same process technology for the optoelectronic components as described above is used for this type of chemical sensor, arrays of highly functional optical sensors based on GaAs may be fabricated.

APPLICATIONS AND CONCLUSIONS

We have discussed the design and performance of a monolithically integrated optical sensor microsystem based on III-V technology. Accurate displacement measurement using a sensor PIC such as that described may be relevant as a monitor of the position or movement of micromachined actuators, diaphragms or microbeams or as part of a micro-metrology system. The small physical size of the optical chip and its reduced optical assembly requirements suggest that uses in microsystems where space is at a premium, or robustness essential, may be attractive. The monolithically integrated approach implies that robust and sensitive physical and chemical measurement microsystems may be fabricated in a single chip, with the attendant opportunity of directly integrating multi-sensor arrays.

1 Koch, T.L. and Koren, U., "Semiconductor photonic integrated circuits", *IEEE Journal of Quantum Electronics*, **27**(3), 1991, p. 641

2 Hofstetter, D., Zappe, H.P. and Dändliker, R. "A monolithically integrated optical displacement sensor in GaAs/AlGaAs", *Electronics Letters*, **31**, 27 November 1995

3 Zappe, H.P., Arnot, H.E.G., and Kunz, R.E., "Technology for III-V-based integrated optical sensors", *Sensors and Materials*, **6**, 1994, p. 261

4 Hofstetter, D., Zappe, H.P., Epler, J.E. and Riel, P., "Multiple-wavelength Fabry-Perot lasers fabricated by vacancy-enhanced quantum well disordering", *Applied Physics Letters*, **67**, 1995, p. 1978

5 Suhara, T., Taniguchi, T., Uemakai, M., Nishihara, H., Hirata, T. and Suehiro, M., "Monolithic integrated-optic position/displacement sensor using waveguide gratings and QW-DFB laser", *IEEE Photonics Technology Letters*, **7**, 1995, p. 1195

Widely Tunable Micromachined Optical Filters

*M.S. Wu, E.C. Vail, C.J. Chang-Hasnain**
E.L. Ginzton Laboratory, Stanford University, 94305
*presently at Cory Hall, University of California at Berkeley, 94720

Abstract: We demonstrate a surface-normal GaAs Fabry-Perot filter with 70 nm continuous tuning range requiring 5V tuning voltage. Micromechanical tuning is achieved by electrostatically deflecting the top mirror of the resonator which is freely suspended as a cantilever.

Introduction

Wavelength division multiplexing (WDM) has shown great promise for increasing both the transmission bandwidth and the routing capability of optical communication systems [1]. However, although many proposals for WDM systems exist, implementation of practical systems has been limited by currently available device technology [2,3].

In this talk, we discuss a widely tunable micro-mechanical surface-normal transmission filter. The filter is part of a family of surface normal devices including tunable detectors [4], LED's [5], and lasers [6] which use micromechanical motion for tuning. The advantage of using micromechanical tuning is that wide *continuous* tuning can be achieved ($\Delta\lambda/\lambda >> 1\%$). Indeed, micromechanical filters have achieved record tuning of 70 nm. In addition, because the devices are voltage tuned, tuning power is negligible. Further, the surface-normal geometry offers the advantages of circular modes, compatibility with multi-mode fiber, 2-D arrays, and polarization insensitivity. Finally, the device fabrication process is simple and high yield, requiring only two non-critical lithography steps. We feel that these merits combine to make these filters ideal cost-effective components for practical implementation of WDM systems.

Device Operation

Figure 1 shows a schematic of the tunable filter. A resonant cavity fabry-perot (FP) cavity is formed between two distributed bragg reflector (DBR) mirrors which are doped to form a p-n junction. The upper DBR mirror is freely suspended 1.2 μm above the substrate by a cantilever structure. The lower DBR mirror is fixed in the substrate. As a tuning voltage is applied to reverse bias the junction between the cantilever and the substrate, electrostatic attraction causes deflection of the cantilever towards the substrate. As the cantilever is deflected toward the substrate, the FP cavity length decreases thereby tuning the resonant wavelength of the cavity. Deflection of only 0.33 μm causes the FP resonant wavelength to tune from 970 nm to 900 nm. Since the top mirror is moved over only 30% of the gap size, no sticking or hysteresis is observed.

The upper DBR mirror is undercut and suspended by using a selective isotropic dry etch [8] to remove a 1.2 μm sacrificial layer between the upper and lower DBR mirrors. The use of a dry etching allows the formation of high aspect ratio features by avoiding surface tension, which causes structures to collapse during wet etching. Cantilevers with lengths of 25, 50, 75, 100 μm; widths of 2, 4, 6 μm, and filter (end-circle) diameters of 10, 15, 20 μm were formed. The entire structure is grown using MBE, ensuring single crystalline material with excellent mechanical properties.

Device Performance

The devices were tested using a Ti-sapphire tunable laser with the light coupled into and out of the device using microscope objectives. The Ti-sapphire power was monitored, while the transmitted light was recorded. Figures 2 and 3 show the tuning of 2 μm wide, 100 μm long cantilever devices with 20 μm end-circles when a reverse biased voltage is applied to the p-n junction. In Figure 2, a constant tuning voltage is applied to the device and the transmittance of the filter is measured as the wavelength

of the incident light is scanned. In Figure 3, the incident light is held at a fixed wavelength while the tuning voltage is scanned. The FP resonance can be tuned over 70 nm with a control voltage ranging up to 4.9 V. The corresponding static control current is limited to 50 pA; thus the DC power dissipation of our filter is only 250 pW. The filter extinction ratio is 19 dB and the insertion loss is 5.5 dB, of which, we estimate that 1.5 dB is due to reflection for the substrate/air interface and 1.7 dB is due to absorption in the heavily doped substrate. The high insertion loss for wavelengths less than 910 nm is due to substrate absorption. The remaining excess loss is likely due to either scattering loss or reflectivity mismatch of the resonator mirrors. These loss mechanisms may be reduced in future designs.

The tuning speed of the filter is limited by the mechanical response of the cantilever which is a damped mechanical oscillator. The modulation response in air is illustrated in Figure 4 for 6 μm wide cantilevers of varying lengths with 10 μm end-circles. The resonance frequency dictates both the modulation bandwidth and the step-response switching speed. A resonance of 1.1 MHz was measured for 1 25 μm cantilever. Because this structure is so underdamped, the step response demonstrates significant ringing. For a critically damped system, however, the rise time can be as fast as 0.3 times the resonance period. Increasing the ambient pressure or increasing the air drag of the structure to approach critical damping would yield a switching time of 300 ns. The cantilever tuning speed may be further increased by making the lever stiffer to increase the resonant frequency and correspondingly increase the damping.

Both the mechanical resonance frequency of the device and tuning voltage decrease with increasing cantilever length. Hence, there is a trade-off between high tuning speed and low tuning voltage. For example, a resonance of 1.16 MHz was measured for a 25 μm long, 6 μm wide cantilever, but this device required 54 V to tune the first 10 nm. In contrast, the 100 μm long 2 μm wide cantilever required only 4.3 V to tune over 70 nm and 1.7 V to the first 10 nm, but had a resonance frequency of 76 kHz. However, the longer cantilever also had greater damping and no ringing was observed in the step response. A 4 μs switching speed was measured for 10 nm of tuning.

Conclusions

Micromechanical tunable devices are promising components for practical implementation of WDM networks. They can be made as wavelength tunable filters, detectors, or sources and possess record continuous wavelength tunability, low tuning voltages and powers, good spectral characteristics and low insertion loss. They exhibit good tuning speeds and easy fiber coupling and are polarization insensitive, easy to fabricate and naturally formed as 2-D arrays.

References

[1] C.A. Brackett, "Dense Wavelength Division Multiplexing Networks: Principles and Applications," *IEEE J. Select. Areas Commun.*, vol. 8, no. 6, p. 948-64, 1990.

[2] L.L Buhl et al, "Grating Assisted Vertical Coupler/Filter for Extended Tuning Range," *Electron Lett.*, vol. 29, no. 1 p. 81-2, 1993.

[3] K.W. Goosen et al, "Silicon modulator based on mechanically-active anti-reflection layer for fiber-in -the loop applications," *Optical Fiber Conference* 1994, San Jose, paper PD-10.

[4] M.S. Wu et al, "Widely and Continuously Tunable Micromachined Resonant Cavity Detector with Wavelength Tracking", *Photon. Technol. Lett.*, vol. 8, no. 1, p. 98-100, 1996.

[5] M.C. Larson et al, "Broadly-tunable resonant cavity light-emitting diode," *Conference on Lasers and Electro-Optics*, 1995, Baltimore, paper CPD17.

[6] E.C. Vail et al, "Tunable Micromachined Vertical Cavity Surface Emitting Lasers," *Quantum Electronics and Laser Science Conference* 1995, Baltimore, paper QPD12.

[7] S. Saliman et al, "Selective dry etching of GaAs over AlGaAs in SF_6 / $SiCl_4$ mixtures," *J. Vac. Sci. Technol. B*, vol. 6, no. 6, p. 1641-4, 1988.

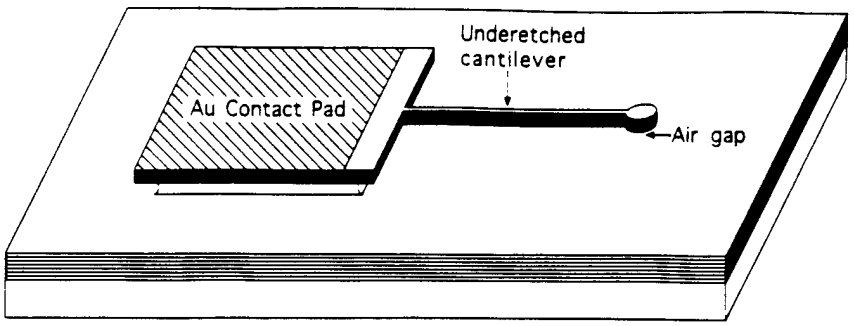


Fig. 1 Device schematic.showing under etched cantilever supported at contact pad and tunable air gap.

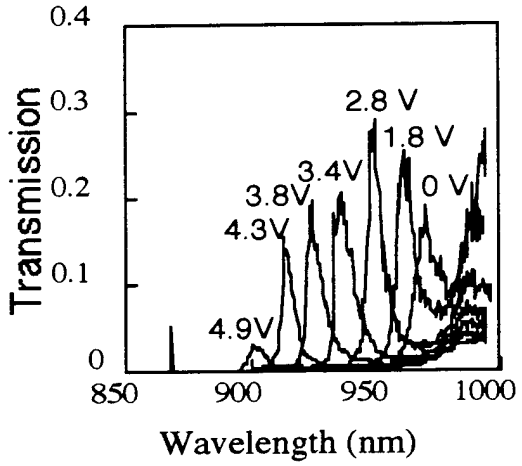


Fig. 2 Filter transmission spectra for fixed applied tuning voltages.

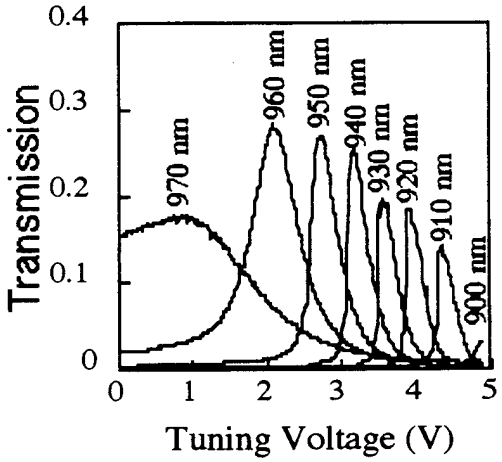


Fig. 3 Filter transmission vs. tuning voltage for fixed wavelength of incident light.

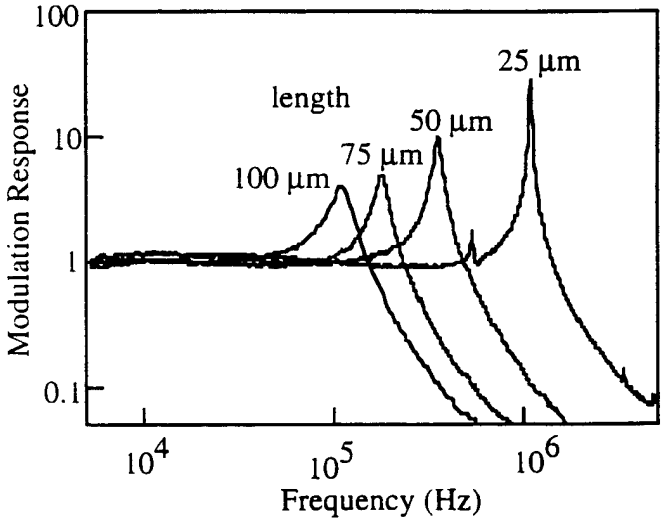


Fig. 4 Filter small signal modulation response for various length cantilevers.

Wednesday, May 1, 1996

Symposium on Parallel Optical Interconnects and Avian Technologies

IWH 3:30 pm-5:00 pm
Fairfax B

Mark Lowry, *Presider*
Lawrence Livermore National Laboratory

POLO - Gigabyte/s parallel optical links for multimedia, computer cluster and switching systems

Kenneth H. Hahn, Kirk S. Giboney, Robert E. Wilson, Joseph Straznicky, Tuochuan Huang, Michael R. Tan, Joseph Straznicky, David W. Dolfi
Hewlett-Packard Laboratories
3500 Deer Creek Rd., Palo Alto, CA 94303

The POLO (Parallel Optical Link Organization) is a collaborative development consortium of Hewlett-Packard, AMP, Du Pont, SDL, and the University of Southern California. The goal of the POLO program is to develop low cost, high performance parallel optical links for applications in central office switching environments, clustered computing, and multimedia. Previous reports have described preliminary results and the general design of the POLO interconnect module [1]. In this paper, we discuss the performance results of the 1st generation POLO module (POLO-1) and progress in the design and assembly of the 2nd generation optimized module.

The components of the POLO module include VCSELs (vertical-cavity surface emitting lasers) [2], Polyguide™ polymer optical waveguides [3], PIN detector arrays, silicon bipolar transceiver ICs, and high-speed ceramic packages. Polyguide waveguides with 45° out-of-plane mirrors are packaged with MT-style ferrules to couple the transmitter and receiver arrays with the ribbon fiber connector. The POLO module accommodates 10-bit wide transmission and 10-bit wide receiver paths, allowing bidirectional transmission of 9 data + 1 clock or 10 data channels. Each channel operates at 622 Mb/s, although the performance will be increased to 1 Gb/s per channel in future designs. An application platform to test the POLO module in a system environment is provided by the development of an interface chip set for workstation interconnections at USC. Figure 1 shows the POLO-1 module mounted on an evaluation board. In order to test the waveguide-ribbon fiber interface, the POLO-1 module features an optical connector which does not incorporate the full push/pull latched design.

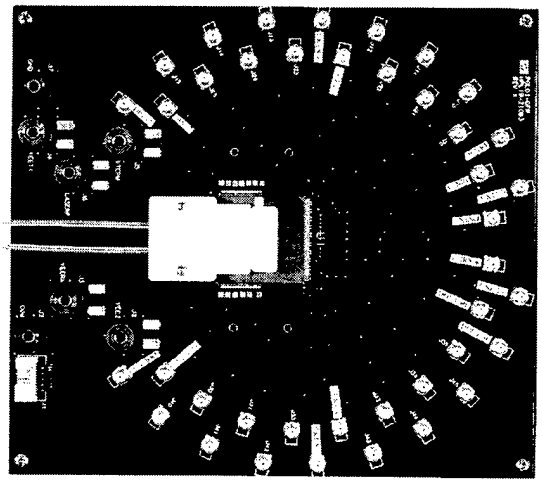


Figure 1. POLO-1 module on evaluation board

The modules are typically tested in "loopback" mode, where the transmitter and receiver of one module are connected together by a single ribbon fiber. To test BER with worst-case crosstalk conditions, all 10 Tx and Rx channels of one module are operated at the same time. A multiple channel data generator is used to modulate all channels with independent PRBS streams.

Figure 2 shows the eye patterns of all 10 channels in simultaneous operation at 622 Mb/s at the output of the receiver. The BER for each channel was $< 10^{-11}$, and an extended measurement of one channel resulted in BER $< 10^{-14}$ with 400 m of low-skew ribbon fiber [4]. While some pattern dependent jitter is observed, the eyes are clearly open at 622 Mb/s. The rise and fall times are < 500 ps, and channel-to-channel skew (excluding ribbon fiber skew) is < 100 ps. The phase margin for BER $< 10^{-9}$ is typically > 1 ns.

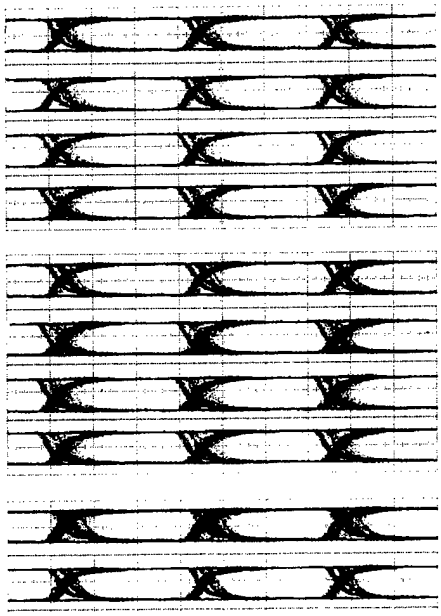


Figure 2. Output eye patterns of POLO-1 module at 622 Mb/s per channel.

Similar results have been obtained with the latched version of the POLO-1 module, which incorporates a clock channel. A 622 MHz clock signal synchronizes the 9 output data channels to eliminate any accumulated skew at the receiver output.

The second generation of POLO module (POLO-2) will incorporate several key modifications. POLO-2 will accommodate both 980 nm bottom emitting and 850 nm top emitting VCSELs. At 850 nm, monolithic arrays of VCSELs will be used, with GaAs MSM or Si PIN detectors in the receiver. The ceramic package footprint will be reduced from 4 x 4 cm to less than 2.5 x 2.5 cm to allow a fully assembled module width of ~ 1". Finally, the speed of the module will be increased to accommodate a data rate greater than 622 Mb/s.

POLO-2 will also feature push-pull ribbon fiber connectors from AMP. This connector is based on the precision molded MT array ferrule housed inside a push-pull SC style housing. The housing of the module will provide a mechanism for optically coupling the push-pull

connector with the Polyguide waveguide circuit. Figure 3 shows the design of the assembled POLO-2 module.



Figure 3. POLO-2 module design

In conclusion, we have demonstrated operation of the 10-channel POLO-1 module at 622 Mb/s per channel with up to 400 m of ribbon fiber. The development and test of the POLO-1 module has been successfully completed, and the design and assembly of the optmized POLO-2 module is underway.

The support of ARPA under the guidance of Anis Husain is gratefully acknowledged.

References

[1] K. H. Hahn. "POLO - Parallel Optical Links for Gigabyte Data Communications," *1995 Proceedings, , 45th Electronics Components and Technology Conference*, pp. 368-375, IEEE, New York, 1995.

[2] M.R. Tan, K.H. Hahn, Y.M. Houng, and S.Y. Wang, "SELs for short distance optical links using multimode fibers," *Conference on Lasers and Electro-Optics 1995*, pp. 54-55, Optical Society of America, Washington D.C., 1995.

[3] B.L. Booth, J.E. Marchegiano, C.T. Chang, R.J. Furmanak, and D.M. Graham, "Polymer waveguides for optical interconnect applications," *Conference on Optical Fiber Communications 1994*, p. 74, Optical Society of America, Washington D.C., 1994.

[4] S. Siala, A.P. Kanjamala, R.N. Nottenburg, and A.F.J. Levi, "Low skew multimode ribbon fibres for parallel optical communications," *Electronics Lett.*, vol. 30, pp. 1784-1786, October 1994.

An easily-assembled optical device for coupling single-mode planar waveguides to a fiber array

M. Takaya, M. Kihara, and S. Nagasawa

NTT Access Network Systems Laboratories
Tokai, Ibaraki, 319-11, Japan
(TEL : +81-29-287-7272, FAX : +81-29-287-7860,
E-mail : takaya@nttlsl.iecl.ntt.jp)

Optical interconnection is a key technology for computer optical data links.[1][2] It is important to connect optical fibers to such devices as planar waveguides, LD arrays, and PD arrays. The connection must be high in density, easy to assemble, and low in cost. As regards connecting single-mode planar waveguides to a multifiber array, we have already proposed a basic passively aligned coupling method using two guide-pins.[3] However, there are some aspects of device fabrication which need to be improved. In this paper we propose a novel easily fabricated optical device for coupling single-mode planar waveguides to a multifiber array. This device uses fully passive alignment, which makes the assembly process easier, and also contributes to cost effectiveness.

Figure 1 shows the structure of the proposed coupling device. This device consists of two MT-type plastic connector plugs for multifiber array joints and a waveguide chip with plug components which are compatible with the MT-type plug. The MT-type plug is assembled by inserting a multifiber array into an MT-type plastic ferrule, which is fabricated by a transfer molding method, and fixing them together with adhesive.[4]

The waveguide chip with MT-compatible plug components is fabricated as follows. Many waveguide chips are fabricated in a silicon wafer using flame hydrolysis deposition (FHD) and reactive ion etching (RIE).[5] Two V-grooves for alignment are formed on each chip of the wafer. Here, the V-grooves are fabricated at a predetermined position in relation to the waveguide core. The wafer is cut with a dicing saw to form individual chips with V-grooves. In addition, MT-compatible plug components are fabricated with two V-grooves and guide-holes with predetermined relative positions. These components can be made by the transfer molding method. Two pins for alignment are

placed in the V-grooves in the chip. One MT-compatible plug is passively aligned on each end portion of the chip, based on the positions of the pins and two V-grooves in the plug. Adhesive is used to fix the components to the chip. This fabrication without active core alignment allows the coupling device to be both easily assembled and mass produced.

The above design has been applied to fabricate 1×8 star couplers for silica-based waveguides with a core size of 8×8 μm. A photograph of the device is shown in Figure 2. The waveguide chip and MT-type plugs are aligned with two guide-pins and then held with two clamp springs. Index-matching material is used between the chip and plug endfaces. This coupling structure enables waveguides and fibers to be directly connected and disconnected. Figure 3 (a) shows the endface of a waveguide chip with an MT-compatible plug component and also that of an MT plug. The origin for the endface geometry is defined as the midpoint on a straight line between the centers of two guide-holes. The designed core centers are arranged along the line at intervals of 250 μm. The relative positions between the cores and the guide-holes in the chips are determined on the basis of the pins for alignment and the V-grooves. The core centers of the chip and the MT plug are aligned using two guide-pins. Connection losses occur when the core positions in a fabricated chip and MT plug deviate from their designed positions. We measured the core position deviation in the fabricated 1×8 chip and MT plugs, and calculated the connection losses. Moreover, we measured the actual connection losses. Figure 3 (b) shows the relation between the estimated and measured losses. All the results were in good agreement. This reveals that the connection loss between a chip and an MT plug is mainly due to the positional deviation of the cores.

Figure 4 shows the insertion loss of the fabricated 1×8 coupler device, which includes two connection losses at a wavelength of 1.3 μm. The average insertion loss is 10.66 dB. The average excess loss is 0.81dB and this is mainly due to connection losses. We also measured the return loss, which was greater than 40 dB. We carried out a reconnection test (100 times) and a heat cycle test in the -25℃ to 70℃ temperature range. The loss change in the reconnection test was less than 0.2 dB. The loss change from the value at 20℃ was less than 0.3 dB in the heat cycle test.

In conclusion, we have developed a simple and compact device for coupling single-mode planar waveguides to a multifiber array using passive alignment. The fabricated 1×8 coupling device exhibits a low insertion loss of 10.7 dB. This device will be effective for use in the construction of optical communication networks.

References

[1] K.P.Jackson, E.B.Flint, M.F.Cina, D.Racey, Y.Kwark, J.M.Trewhella, T.Caulfield, P.Buchmann, Ch.Harder, and P.Vettiger, J. Lightwave Technol., vol. 12, No. 7, 1994.

[2] C.A. Armiento, A.J. Negri, M.J. Tabasky, R.A. Boudreau, M.A.Rothman, T.W. Fitzgerald, and P.O.Haugsjaa, IEEE Trans. Hybrids Manuf. Technol., vol. CHMT-15, No.6, pp.1072-1080, 1992.

[3] M. Kihara, S. Nagasawa, and T. Tanifuji, in conference on Optical Fiber Communication, 1995 Technical Digest, paper WS4, 1995.

[4] T. Satake, S.Nagasawa, N. Kashima, and F. Ashiya, J. Lightwave Technol., vol. LT-3, No. 6, 1985.

[5] M.Kawachi, Optical and Quantum Electronics, 22, pp391-416, 1990.

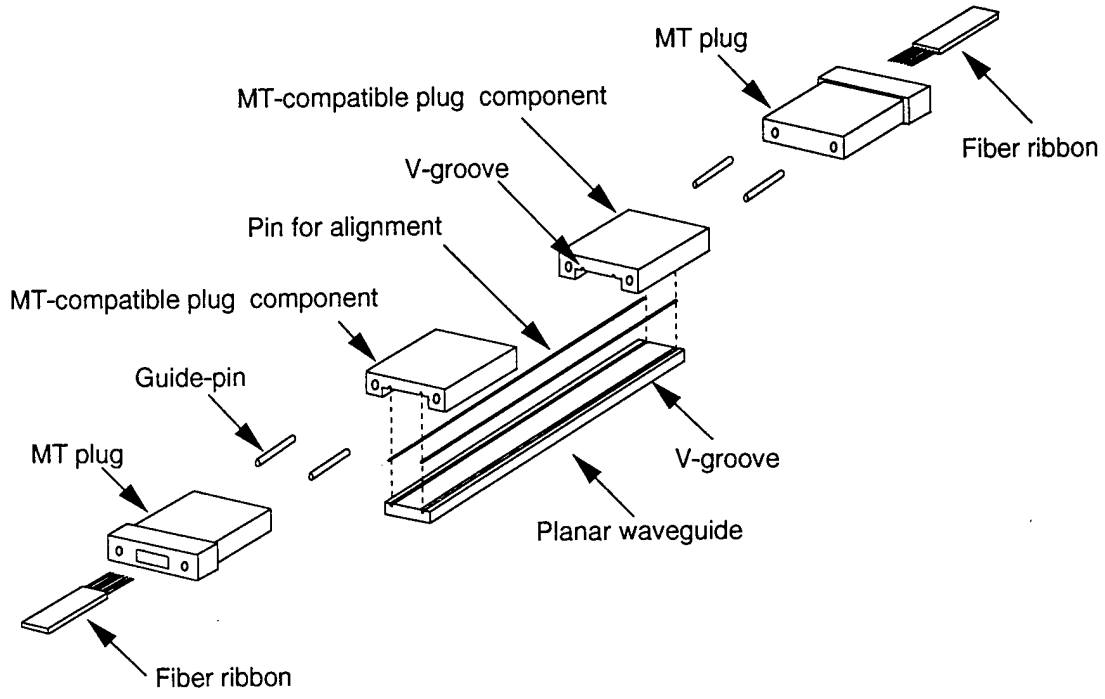


Figure 1 Structure of single-mode planar waveguide to multifiber array coupling device.

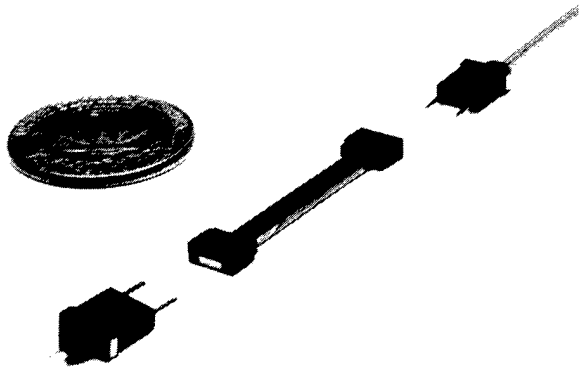


Figure 2 Single-mode planar waveguide to multifiber array coupling device.

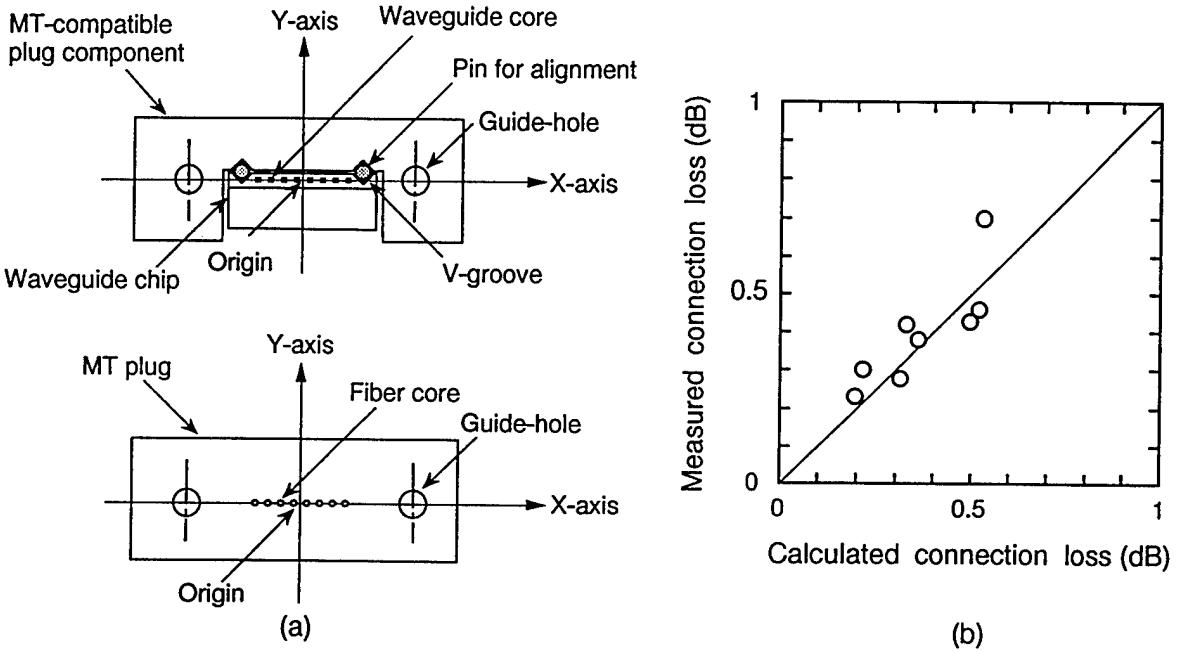


Figure 3 (a) Endface of a waveguide chip with an MT-compatible plug component and endface of an MT plug. (b) Relation between estimated losses caused by relative position deviation and measured losses.

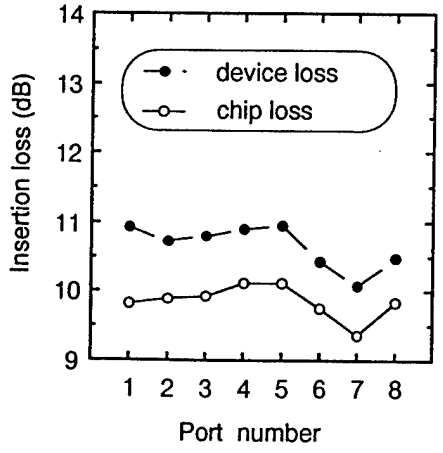


Figure 4 Insertion loss of a 1 ×8 coupling device assembled with passively aligned components.

Passive Alignment Technique for All-Silicon Integrated Optics

R. MOOSBURGER, B. SCHÜPPERT, U. FISCHER AND K. PETERMANN

Technische Universität Berlin, Institut für Hochfrequenztechnik,
Einsteinufer 25, 10587 Berlin, Germany

Tel.: +49 30 314 22934, Fax: +49 30 314 24626

Introduction

A useful technique for the coupling of single-mode fibres and integrated optical devices is crucial for cost-effective packaging. This is especially a critical issue for multiport devices [1].
In the case of integrated optical devices IN or ON silicon it seems straight-forward to etch V-grooves for the fibre alignment into the same substrate as the waveguides. However, until now, no promising technique has been found for preparing the end-faces of the integrated waveguides at the extremity of the etched V-grooves. For this reason we have chosen a flip-chip approach so that the end-faces can be prepared by polishing or cleaving. Since we use silicon for the IO-chip as well as for the micro-optical bench, no instabilities due to differences in the coefficients of thermal expansion are to be expected. Furthermore, a "smart" chip-bench attachment becomes possible.

Micro-Optical Bench

The flip-chip mounting of III/V- compound optical circuits on a V-grooved silicon motherboard has already been demonstrated to be feasible for integrated-optic applications [2][3]. The overall usage of silicon in our work allows an advantageous design regarding cost, manufacturability and stability. Figure 1 shows the realized arrangement. It is designed for the passive coupling between an SOI (silicon-on-insulator) integrated optical chip and standard single-mode fibers. The self-aligned mounting of the chip is achieved by a rib-groove combination as shown in Fig. 2 in more detail. Note that the rib is the exact negative of the groove so that the flip-chip is put on precisely defined planes rather than on sensitive edges, which would be the case when using rectangular alignment ribs. These structures as well as the V-grooves for the fibre alignment are fabricated by wet chemically etching with KOH. In principle, this orientation-dependent etch process allows a precision in the sub-μm range. However, if the structures are not well aligned to the crystal axis greater deviations occur resulting in wider fibre alignment grooves and narrower chip alignment ribs. Since both structures are composed of the same crystal planes, the undercutting is the same for the V-grooves and for the ribs. Provided that the gap shown in Figure 2 is wide

enough the effects of the undercutting are balanced since the fibres and the flip-chip experience the same vertical offset. The precise crystal orientation may be taken into account by means of a separate etching process [4]. Our samples have been fabricated by a wafer-mask alignment using the wafer-flat as a reference only.

Integrated-Optical Testchip

To investigate the coupling of fibres to waveguides, a testchip has been fabricated that contains a number of straight rib waveguides. The substrate material used here was silicon-on-insulator (BE-SOI) with a thickness of the silicon top layer of 4 μm. The rib dimensions (2μm high, 3 μm wide) were chosen to assure single-mode operation [5][6]. We found that the end-faces of the integrated waveguides can be well prepared by simple cleaving. For this purpose marks at the brim of the wafer are made by either etching or sawing (20-100 μm deep). Then the wafer can be separated by slightly bending it around a pointed needle (see Figure 3). This is an attractive alternative to the very time consuming polishing of each substrate edge.

Simultaneous definition of alignment grooves and waveguides

The alignment grooves and the waveguides on the testchip have to be etched in separate steps since these structures differ in depth and profile. However, the limited positioning accuracy of the second masking step would cause a lateral offset of the waveguides relative to the alignment structures. To solve this problem we developed a process that allows the simultaneous definition of both structures that can nevertheless be etched separately.

For this process a thin layer of SiO_2/Si_3N_4 (35nm/150nm) is deposited on the SOI-wafer by chemical vapour deposition. The waveguides and the alignment grooves are then defined photolithographically and windows in the SiO_2/Si_3N_4-layer are opened by reactive-ion etching (RIE). By thermal oxidation, a covering of certain areas with resist and etching of the thermal SiO_2 in buffered HF, one is able to temporarily reclose some of the mask-windows without affecting the Si_3N_4-mask.

Measuring the misalignment

The misalignment can be determined by comparing the optical insertion loss of the self-aligned pigtailed device with the optimal-aligned fibre-chip coupling. Excess loss due to misalignment of 1.5 dB was measured which implies a positioning accuracy of better than 2 μm.

Currently we are processing an optimised design using SOI-wafers with a thickness of the silicon top layer of 11 μm. The cross-section of the rib waveguides then becomes compatible with the standard fibre permitting very low coupling losses and somewhat less stringent alignment tolerances (e.g. the excess loss caused by a 2 μm offset would be reduced to 0.9 dB). Additionally a thicker top layer is advantageous for the bench-chip align structure so that we expect an improved positioning accuracy.

Summary

We have proposed and experimentally demonstrated a technique for self-aligned pig-tailing of all-silicon based integrated optical devices. Close attention was paid to the manufacturability of the devices with standard semiconductor technologies. The achieved positioning accuracy is about 2 μm. Self-alignment and coupling efficiency is expected to be improved by tuning the design parameters and using SOI-material with greater thickness of the silicon top layer.

Acknowledgements

The authors thank M. Gruse and B. Malik for their assistance with sample preparation. We also kindly acknowledge the fruitful discussions with B. Müller (Institut für Mikroelektronik, TU-Berlin).

References

[1] E.J. Murphy, T.C. Rice, „Self-Alignment Technique for Fiber Attachment to Guided Wave Devices", IEEE Journal of Quantum Electronics, Vol. QE-22, No. 6 (1986), pp. 928-932

[2] G. Grand, C. Artigue, „Hybridisation of Optoelectronic Components on Silicon Substrate", ECOC'94, pp 193-200

[3] W. Hunziker et al., „Self-Aligned Optical Flip-Chip OEIC Packaging Technologies", ECOC'93, WeP7.1, Montreux

[4] A. Steckenborn, et al., „High Precision Wafer Orientation for Micromachining", Micro Systems Technologies 1991, Berlin, Germany

[5] R. A. Soref, J. Schmidtchen, K. Petermann, „Large Single-Mode Rib Waveguides in GeSi-Si and Si-on-SiO_2", IEEE Journal of Quantum Electronics, Vol. 27 No. 8 (1991), pp. 1971-1974

[6] T. Zinke, U. Fischer, B. Schüppert, A. Splett und K. Petermann, „Comparison of optical waveguide losses in silicon-on-insulator", Electronics Letters, Vol. 29, Nr. 23, (1993), pp. 2031-2033

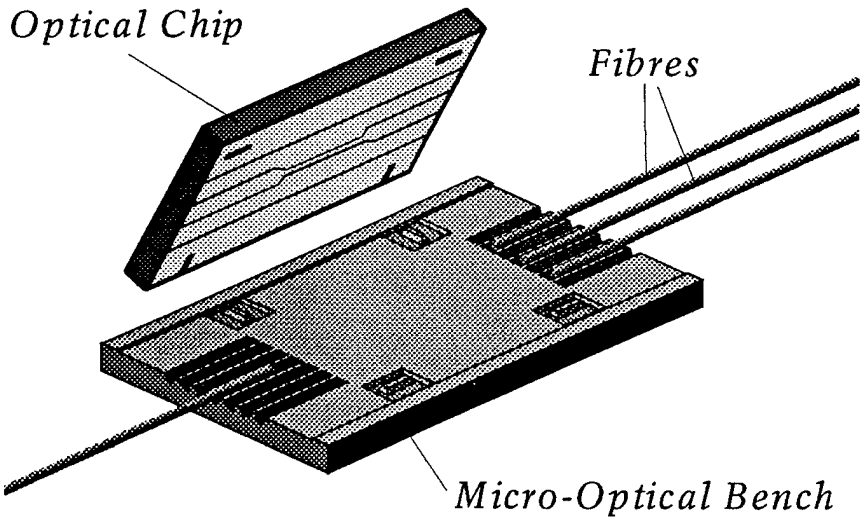


Fig. 1: Micro-Optical Bench

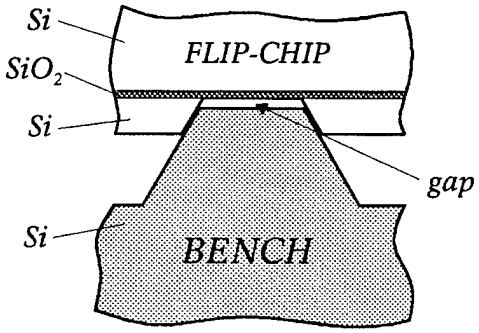


Fig. 2: Chip-Bench Alignment Element

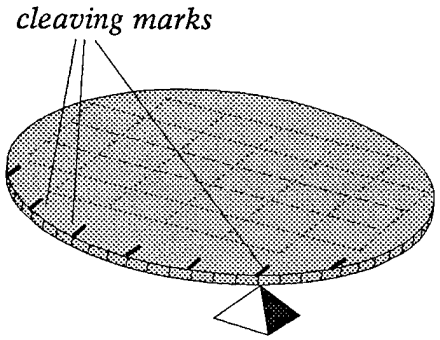


Fig. 3: Cleaving

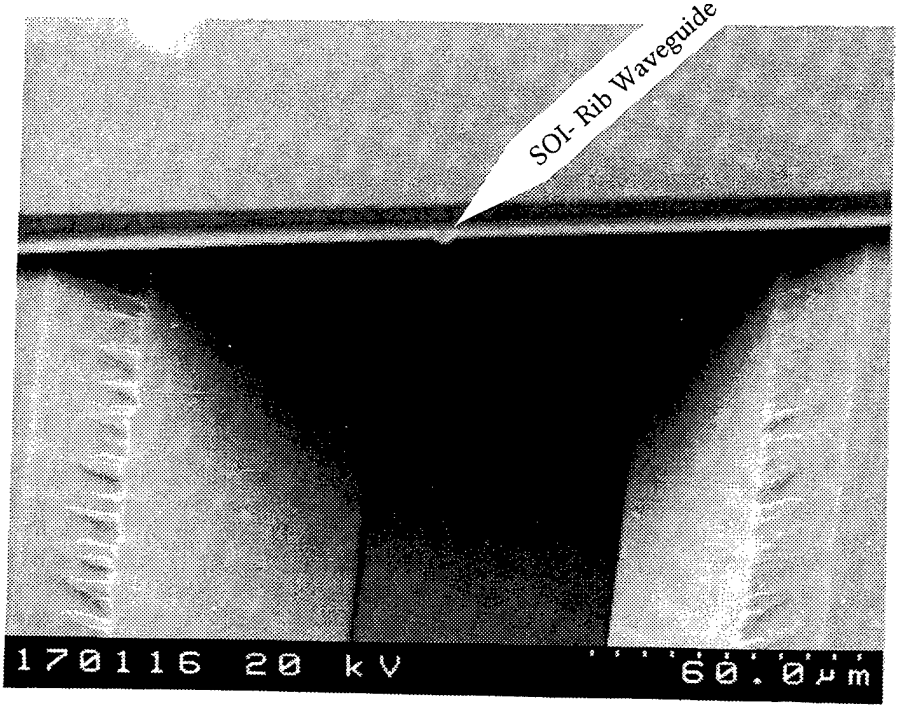


Fig. 4: V-groove and flip-chip

Passively Aligned PIN Photodetector Array's on Silicon Waferboard Platforms

A. J. Negri, J. F. Mehr, G. A. Duchene, M. J. Tabasky, C.A. Armiento and P. O. Haugsjaa
GTE Laboratories, 40 Sylvan Road, Waltham, MA 02254

D. Yap, H. P. Hsu, W. W. Ng, D. M. Bohmeyer, and H. W. Yen,
Hughes Research Laboratories,

Hybrid integration utilizing silicon waferboard as a platform for mounting discrete and array components, is an attractive alternative to using conventional sub-mounted devices when building low-cost, high-performance, multichannel optical transmitter and receiver modules. Silicon substrates are extremely versatile as a platform material for the following reasons: 1) both multimode and single mode fiber can be mounted into v-grooves etched into the silicon surface; 2) alignment fiducials formed on the silicon surface, provide a registration feature for optoelectronic devices such as emitters and detectors; 3) signal traces can be defined using conventional photo-lithography techniques on a common silicon substrate; one that carries the components as well as the optical fibers; and 4), heat can be efficiently transported away from the active devices mounted on the silicon surface through the silicon platform.

The silicon waferboards were designed to hold a commercially available 4 or 8 fiber, fiber ribbon and included an etched well that, when used with a silicon cap, provided a strain relief for holding the jacketed portion of the fiber ribbon. Alignment fiducials formed on the silicon surface for butting the precision-cleaved PIN arrays against, permitted passive detector alignment, to fibers previously embedded into v-grooves etched into the silicon surface. The PIN arrays were back-illuminated with light reflecting off turning mirrors formed at the etched end surface of each v-groove.

Images of infrared light patterns observed, as reflecting off the turning mirrors during waferboard characterization, and light patterns exiting the top surface of each photodetector, were documented and analyzed for presence of any light-scattering defects. Optical power insertion loss measurements at the turning mirrors, and the analysis of the infrared light patterns, provided information relating to the origins of the insertion loss. Optical losses were found to depend on mirror surface quality, optical fiber placement including epoxy effects, and fiber end face quality. In addition, from these measurements we are able to differentiate between mirror quality, fiber placement, and mechanical alignment effects on PIN array

performance. These characterization techniques provided insight into the dynamics of passive fiber alignment to PIN arrays using fiber ribbon and silicon waferboard.

Silicon waferboard optical insertion loss measurements including infrared light patterns and responsivity data will be presented.

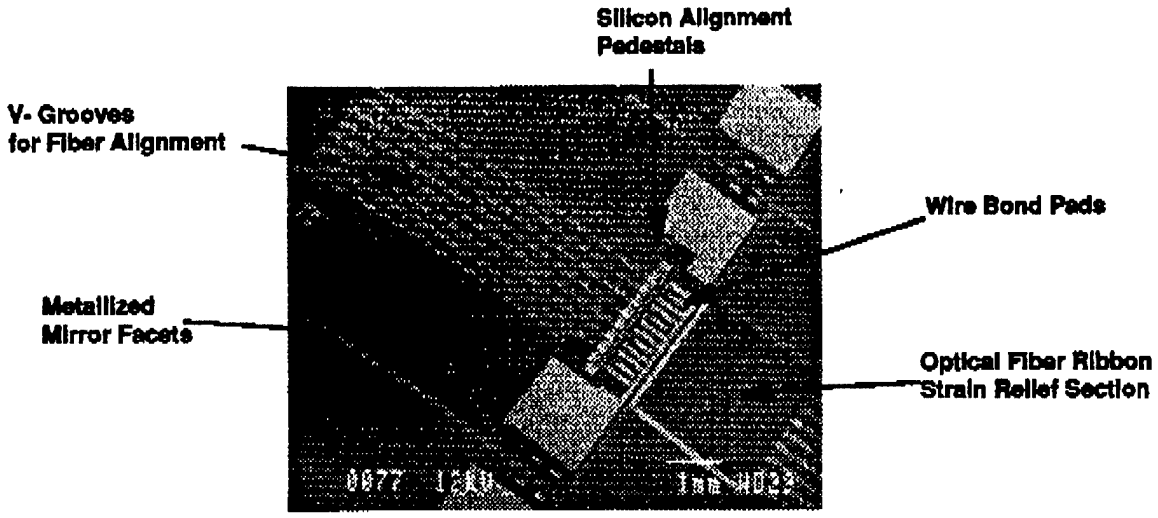


Fig1: Top view of receiver silicon waferboard

Thursday, May 2, 1996

Optical System Modeling

IThA 8:00 am-10:15 am
Fairfax A

Alan E. Willner, *Presider*
University of Southern California

MODELING THE PERFORMANCE OF WDM LIGHTWAVE SYSTEMS

Fabrizio Forghieri

AT&T Research
Crawford Hill Laboratory
Holmdel, NJ 07733-0400
phone: (908) 888–7286
fax: (908) 888-7190
e-mail: biccio@big.att.com

The introduction of Erbium-doped fiber amplifiers (EDFAs) has revolutionized the field of lightwave systems. EDFAs are capable of compensating fiber loss over an optical bandwidth of tens of nanometers. Several optical channels can be amplified simultaneously without appreciable crosstalk due to the EDFA's slow gain dynamics. The use of EDFAs in place of opto-electronic regenerators allows to design *transparent*, high-capacity, wavelength-division-multiplexed (WDM) systems over thousand of kilometers, as shown by laboratory experiments and field trials.

The performance of lightwave systems using EDFAs is determined by the optical signal-to-noise ratio (SNR) at the receiver. The SNR can be increased by either spacing the EDFAs closer or by increasing their output power. Reducing the amplifier spacing is an expensive solution and spacings below 30 km are not helpful. Increasing the EDFAs output power, a more viable solution from a cost point of view, raises the issue of fiber nonlinearities. High powers, multiple channels and long unregenerated distances conspire together to enhance the deleterious effects of fiber nonlinearities. Nonlinearity-induced power loss, pulse-shape distorsion and crosstalk can severely limit the performance of lightwave systems. In the system design, a compromise must be reached between the opposite requirements placed on launched power by SNR and fiber nonlinearities. It is therefore essential to develop models to gain a good understanding of fiber nonlinearities and their impact on lightwave systems. A deeper understanding can also help to devise techniques to suppress or at least to mitigate the performance degradation introduced by fiber nonlinearities.

The nonlinearities in silica fibers can be classified into two categories: stimulated scattering (Raman and Brillouin), and effects arising from the nonlinear index of refraction. Stimulated scattering is manifested as intensity dependent gain or loss, while the nonlinear index gives rise to intensity dependent phase [1].

In stimulated Brillouin scattering (SBS), power transferred to the backward direction, due to amplification of spontaneous scattering, depletes the forward traveling signal [2]. SBS does not couple channels in a WDM system. Its threshold is about 10 mW for intensity-modulated

transform limited data, and can be easily increased by frequency-dithering the laser. Stimulated Raman scattering (SRS), is a similar, but much weaker effect [2]. The main differences are that SRS can occur in either the forward or backward direction, and the gain bandwidth for SRS is on the order of 100 nm. Thus SRS can couple WDM channels and give rise to crosstalk. The nonlinear index of refraction of silica fiber gives rise to three effects: self phase modulation (SPM), where fluctuations in the signal power induce phase modulation and lead to broadening of the signal spectrum; cross phase modulation (CPM), in which intensity fluctuations of other channels modulate the phase of the signal; four photon mixing (FPM), where the beating between two channels at their difference frequency modulates the signal phase at that frequency, generating new tones as sidebands [3].

The dominant nonlinear effect in high-speed WDM systems is FWM, since the low fiber chromatic dispersion and the high launched power per channel required by high-bit-rate operation enhance the efficiency of generation of FWM waves. Unequal channel spacing reduces interference from FWM and permits an increase of the launched power by 7 dB, making possible WDM upgrade of lightwave systems with embedded dispersion-shifted fiber [4]. The generation of FWM waves itself can be suppressed by using fiber with a magnitude of the chromatic dispersion of 2 ps/nm/km or above [5]. In this case, depending on the actual values of dispersion, system length and per-channel bit rate, dispersion compensation may be necessary. Dispersion-managed systems, in which fibers with opposite signs of dispersion are alternated to ensure low cumulated dispersion, have been demonstrated with per-channel bit rates up to 20 Gb/s [5]. High-speed WDM upgrade of conventional fiber requires dispersion compensation at each amplified segment to avoid excessive dispersion accumulation. In systems with conventional fiber and dispersion-compensating fiber, FWM is completely suppressed by the large dispersion, but the interaction between the large local dispersion and SPM in both fibers might lead to performance degradations, particularly at bit-rates of 20 Gb/s or above. A good dispersion-compensating fiber for high-speed WDM systems should have low nonlinearity [6] and negative dispersion slope [7].

The performance of high-speed WDM systems is determined by the interplay of several factors, such as power, dispersion map, fiber nonlinearities, channel frequency allocation, and amplifier spacing. The combined optimization of all these parameters to achieve high performance at reasonable cost is a challenging task. In the absence of an analytical solution of the overall problem, good insight has been gained by studying the different nonlinear effects separately. Ideally, though, one would like to have a "black box", say a powerful computer, able to simulate a real experiment including all possible effects, from transmitter to receiver through fiber and EDFAs. If the black box was fast enough, one could imagine using it to optimize all the systems parameters by repeated simulations (Monte Carlo), without ever resorting to expensive test beds, or at least building one only for the optimized system.

For single-channel systems, computer simulations using the split-step Fourier method, or beam-propagation method (BPM), [3] to solve the nonlinear Schrödinger equation that expresses the electric field propagation in the fiber have come close to this goal. In single-channel systems, indeed, neglecting SBS, the only effect left is SPM, and the interaction between SPM and chromatic dispersion can be very effectively studied using the BPM. A rough idea of the system performance can be gained by looking at the *eye opening*, defined as the separation between the minimum "one" level and the maximum "zero" level at the best sampling time divided by twice the average power. The intersymbol interference (ISI) introduced by the interplay of SPM and dispersion, or even by optical or electrical filters, does not extend beyond the neighbouring bits. Therefore a short pseudo-random bit sequence (PRBS) of 2^7 bits is sufficient to capture all possible cases of interference. Furthermore, the worst-case eye opening is very likely to happen, hence the worst-case eye closure gives a good measure of the power penalty at the receiver. Computer simulations can also be used to evaluate bit-error rate (BER) or, equivalently, Q [8], by computing mean and standard deviation of both the "one" and the "zero" level distribution and assuming that they can be approximated by a Gaussian. With large ISI, the Gaussian approximation is not valid. In this case it is necessary to compute the BER individually for each of the possible cases of interference. Q can then be computed finding the BER for each pattern and weighting it by its occurrence likelihood [9].

Computer simulation studies, even for single-channel systems, are less useful when the impairment is generated by the tail of an unknown distribution or by some rare event. For example it is very hard to study the interaction between polarization-mode dispersion (PMD) and SPM, because it is necessary to run a very large number of simulations with different (independent) choices of the fiber polarization properties. Also degradations due to low frequency components have been observed in many experiments when using a long PRBS. Simulating these effects (and their interaction with nonlinearities) would require the use of unpractically large Fourier transforms.

In WDM systems the interplay between fiber nonlinearities and dispersion becomes much more complicated, and a quick look at the eye diagrams of the channels can be very misleading. The result of computer simulations in WDM systems depends on the initial relative optical phases of the channels, the bit patterns used and their relative time delay. Finding the worst case may be difficult, because of the large dimension of the variables space. In addition, although it may be possible to carefully select the input signals to make sure to hit the worst case, knowledge of the worst-case eye opening is useless when its occurrence probability is very low. Predicting system performance based on the power penalty relative to a very unlikely worst case would lead to a large overestimation of the degradation. Applying the method in [9] to WDM systems may also be difficult, since typically each rail, even in the absence of noise, has a continuous probability distribution, generally unknown a priori and often not Gaussian, rather then a simple four-level, discrete distribution, as seen for single-channel ISI.

For WDM systems, computer simulations are still very useful to determine the pulse shape evolution and the interplay between chromatic dispersion and self- and cross-phase modulation, but analytical modeling is necessary to correctly include the effects of random relative optical phases, modulation statistics and amplifier noise. A careful combination of computer simulations and analytical modeling is required to evaluate BER in WDM systems. Feedback from experimental measurements on a testbed is essential for WDM systems to test the validity of the modeling assumption. This three-fold interaction between simulation, modeling and experiments makes optimization of WDM systems a difficult and lengthy process, and there is room for additional modeling tools to be developed for this purpose.

Several examples will be given of how computer simulations for WDM systems can be misleading. "Tricks" and countermeasures to avoid these problems will be described. Accurate modeling techniques will be reviewed for FWM [10] and SRS crosstalk [11]. It will be shown how the insight gained with accurate modeling has helped to design a method to suppress SRS crosstalk [12]. Finally, as an example of using modeling for WDM system optimization, a heuristic approach to the granularity issue will be described; two systems with same total capacity and fiber length but different number of channels will be compared from a transmission penalty point of view.

References

[1] A. R. Chraplyvy, "Limitations on lightwave communications imposed by optical-fiber nonlinearities," *J. Lightwave Technol.*, vol. 8, pp. 1548–1557, Oct. 1990.

[2] R. G. Smith, "Optical power handling capacity of low loss optical fibers as determined by stimulated Raman and Brillouin scattering," *Appl. Opt.*, vol. 11, pp. 2489–2494, Nov. 1972.

[3] G. P. Agrawal, *Nonlinear fiber optics.* Academic Press, 1989.

[4] F. Forghieri, R. W. Tkach, and A. R. Chraplyvy, "WDM systems with unequally spaced channels," *J. Lightwave Technol.*, vol. 13, no. 5, pp. 889–897, May 1995.

[5] R. W. Tkach, A. R. Chraplyvy, F. Forghieri, A. H. Gnauck, and R. M. Derosier, "Four-photon mixing and high-speed WDM systems," *J. Lightwave Technol.*, vol. 13, no. 5, pp. 841–849, May 1995.

[6] F. Forghieri, R. W. Tkach, A. R. Chraplyvy, and A. M. Vengsarkar, "Dispersion compensating fiber: is there merit in the figure of merit?," in *Proc. OFC '96, San Jose, Ca.*, paper ThM5, pp. 255–257, Feb. 1996.

[7] R. W. Tkach, R. M. Derosier, F. Forghieri, A. H. Gnauck, A. M. Vengsarkar, D. W. Peckham, J. L. Zyskind, J. W. Sulhoff, and A. R. Chraplyvy, "Transmission of eight 20-Gb/s channels over 232 km of conventional single-mode fiber," *IEEE Photon. Technol. Lett.* vol. 7, no. 11, pp. 1369–1371, Nov. 1995.

[8] N. S. Bergano, F. W. Kerfoot, and C. R. Davidson, "Margin measurements in optical amplifier systems," *IEEE Photon. Technol. Lett.*, vol. 5, pp. 304–306, Mar. 1993.

[9] C. J. Anderson and J. A. Lyle, "Technique for evaluating system performance using Q in numerical simulations exhibiting intersymbol interference," *Electron. Lett.*, vol. 30, pp. 71–72, Jan. 1994.

[10] F. Forghieri, R. W. Tkach, and A. R. Chraplyvy, "Statistics of four-wave mixing crosstalk," *Proc. NLGW '95, Dana Point, Ca.*, paper NSaD1, pp. 256–258, Feb. 1995.

[11] F. Forghieri, R. W. Tkach, and A. R. Chraplyvy, "Effect of modulation statistics on Raman crosstalk in WDM systems," *IEEE Photon. Technol. Lett.*, vol. 7, pp. 101–103, Jan. 1995.

[12] F. Forghieri, R. W. Tkach, and A. R. Chraplyvy, "Suppression of Raman crosstalk in WDM systems," in *Proc. OAA '95, Davos, Switzerland*, paper SaB3, pp.212–215, June 1995.

Feasibility of 40 Gbit/s Single-Channel Transmission over Embedded Standard Fiber

Dirk Breuer and Klaus Petermann

Technische Universität Berlin, Institut für Hochfrequenztechnik
Einsteinufer 25, 10587 Berlin, Germany
Phone: 0049-30-314-22437 Fax: 0049-30-314-24626

Introduction

The system performance of future high-speed TDM-systems beyond 10 Gbit/s is severely degraded by the large chromatic dispersion when transmitted over the already installed standard single-mode fiber (SMF) network at 1.55 μm. An unchirped 40 Gbit/s conventional NRZ-modulated signal will suffer a 1 dB dispersion penalty after about 4 km. To cope with this stringent limitation the most attractive schemes are Dispersion-Compensating Fibers (DCFs) and Optical-Phase Conjugation (OPC), which both have already shown their potential in various experiments [1-6]. In particular a 10 Gbit/s transmission over 2245 km standard fiber with the use of DCFs was reported [1]. It is the goal of the present work to conclude on the suitability of both concepts for future high speed systems operating at 40 Gbit/s over the embedded standard-fiber.

Model

The pulse propagation in the nonlinear dispersive fiber is solved by the split-step Fourier method. At the transmitter a chirp-free modulated Mach-Zehnder modulator is driven by a $2^7 - 1$ PRBS-NRZ bit-pattern. The modulator bandwidth is chosen to be equal to the bit rate. The dispersion D, the effective cross section area A_{eff} and the fiber attenuation α of the transmission fiber and the DCF are assumed as shown in figure 1a. For both fibers a nonlinear refractive index of $n_2 = 2.6{\cdot}10^{-20}\mathrm{m}^2/\mathrm{W}$ and a dispersion slope $\mathrm{d}D/\mathrm{d}\lambda$ of 0.08 ps/(km nm^2) was chosen. Fig. 1a shows the principle setup for the DCF-based pre- and postcompensating systems. Assuming a single ideal Optical-Phase Conjugator at the system midpoint fig. 1b depicts the setup for the OPC-based system. At the receiver the signal is optically filtered, detected and then electrically filtered. The optical filter bandwidth is set to 160 GHz and the electrical filter bandwidth is chosen to be 65 % of the bit rate.

Optical-Phase Conjugation

For an OPC-based system fig. 2 shows the power penalty as a function of the average fiber-input power for a 1000 km standard fiber transmission at 40 Gbit/s assuming an amplifier spacing Δ_{oa} of 25 km and 50 km. It turns out that in the nonlinear power regime ($\geq$ 4.5 dBm) the power penalty increases significantly due to the non-ideal power symmetry within the transmission line with respect to the OPC. From the linear point of view at lower fiber input powers the system performance is

mainly limited by the accumulated amplifier noise. At higher input powers the length is limited by the non-perfect power symmetry. At 50 km amplifier spacing the penalty is about 1.1 dB at a fiber-input power of 0 dBm. Due to increasing power symmetry at 25 km amplifier spacing the penalty is then reduced to about 0.8 dB. These considerations show the feasibility of 1000 km OPC-based 40 Gbit/s systems over standard single-mode fibers.

Dispersion-Compensating Fiber

Dispersion-Compensating Fiber schemes work perfect as long as the system is opearted within the linear regime. With increasing optical power, as required for very high speed systems, it turns out [7] that the DCFs must be placed at distances comparable to the linear dispersion length ($\approx$ 4 km at 40 Gbit/s over standard single-mode fiber), which is unrealistic, in order to get a virtually dispersion-free system. If the Dispersion-Compensating Fibers are placed at the optical amplifiers, the spacing should at least exceed 20 km for practical systems. For 40 Gbit/s such DCF-based systems are then feasible *only* if the system is operated within the linear regime, as expressed by a maximum allowable nonlinear phase shift ϕ_{nl}

$$\phi_{nl} = \phi_{nl,SMF} + \phi_{nl,DCF} \overset{!}{<} 0.4 \tag{1}$$

over the whole fiber span. Only if eq.(1) is satisfied the exact position of the DCF-segments is of minor importance.

In fig. 3 the achievable standard-fiber length L_{SMF}, yielding a power penalty of 1 dB is plotted as a function of the average fiber-input power for different amplifier spacings and thus DCF-spacings [9]. Assuming a noiseless transmission it is shown in fig. 3 that the analytical solution according to (1) yields a good estimate for the maximum power level. For a 400 km standard-fiber transmission at 100 km amplifier spacing an upper power level of about -2 dBm is allowable. However, as depicted in fig. 3 taking the ASE-noise into account the system performance is severely degraded. At an amplifier spacing of 20 km and 60 km the achievable standard-fiber length is limited to 340 km and 240 km at an average fiber-input power of about -5 dBm and -3 dBm, respectively.

Conclusion

The performance of future high-speed single-channel optical communication systems operating at 40 Gbit/s over the embedded standard fiber was analyzed by numerical simulations. Two different transmission schemes Optical-Phase Conjugation and Dispersion Compensating Fibers were compared. In the DCF scheme it has been shown that the system must be operated in the linear regime of the transmission fiber, if the spacing of consecutive Dispersion-Compensating Fibers exceeds 20 km. A maximum achievable transmission distance of about 240 km at 60 km amplifier spacing is feasible within this scheme. In contrast, however, in a system equipped with a single midpoint Optical-Phase Conjugator a transmission of 40 Gbit/s over 1000 km at an amplifier spacing of about 50 km is feasible.

The polarization-mode dispersion (PMD), however, yields another limitation for the r.m.s. PMD for a 40 Gbit/s transmission. It should not exceed 2 ps [10], corresponding to a required PMD-coefficient of $< 0.13\text{ps}/\sqrt{\text{km}}$ and $< 0.06\text{ps}/\sqrt{\text{km}}$ for a 240 km and 1000 km transmission, respectively.

References

[1] K. Kikuchi, S. Sasaki, and K. Sekine, "10 Gbit/s Dispersion Compensated Transmission over 2245-km conventional (non-dispersion shifted) fibers in a re-circulating loop", in *Technical Digest, Conference on Optical Fiber Commununication*, 1995, number FB5, pp. 306–307.

[2] A.D. Ellis and D.M. Spirit, "Unrepeatered transmission over 80 km standard fibre at 40 Gbit/s", *Electronics Letters*, vol. 30, pp. 72–74, 1994.

[3] A.D. Ellis, M.C. Tatham, D.A.O. Davies, D. Nesset, D.G. Moodie, and G. Sherlock, "40 Gbit/s transmission over 202 km of standard fibre using midspan spectral inversion", *Electronics Letters*, vol. 31, pp. 299–301, 1995.

[4] A.H. Gnauck, R.M. Jopson, and R.M. Derosier, "10-Gb/s 360-km Transmission Over Dispersive Fiber Using Midsystem Spectral Inversion", *Photonics Technology Letters*, vol. 5, pp. 663–666, 1993.

[5] S. Watanabe, T. Naito, and T. Chikama, "Compensation of chromatic dispersion in a single-mode fibre by optical phase conjugation", *Photonics Technology Letters*, vol. 5, pp. 92–95, 1993.

[6] W. Pieper, C. Kurtzke, R. Schnabel, D. Breuer, R. Ludwig, H.G. Weber, and K. Petermann, "Nonlinearity-insensitive standard-fibre transmission based on optical-phase conjugation in a semiconductor-laser amplifier", *Electronics Letters*, vol. 30, pp. 724–726, 1994.

[7] D. Breuer, C. Kurtzke, and K. Petermann, "Optimum dispersion management for nonlinear optical single-channel systems", in *Technical Digest, Conference on Optical Fiber Commununication*, 1995, number WQ6, pp. 196–197.

[8] M. Onishi, C. Fukuda, Y. Koyano, M. Shigematsu, and H. Kanamori, "Dispersion Compensating Fiber with a Figure of Merit of 273 ps/nm/dB and its Compact Packaging", in *Fifth Optoelectronics Conference (OEC'94), Technical Digest*, 1994, number 14B1-3, pp. 126–127.

[9] D. Breuer, and K. Petermann, "Design Guidelines for 40 Gbit/s TDM-Systems over Embedded Standard Fibre", *submitted to Electronics Letters.*

[10] B. Clesca, J.-P. Thiery, L. Pierre, V. Harvard, and F. Bruyere, "Impact of polarisation mode dispersion on 10 Gbit/s terrestrial systems over non-dispersion-shifted fibre", in *Prodeedings, European Conference on Optical Communication*, 1995, number We.B.1.6, pp. 581–584.

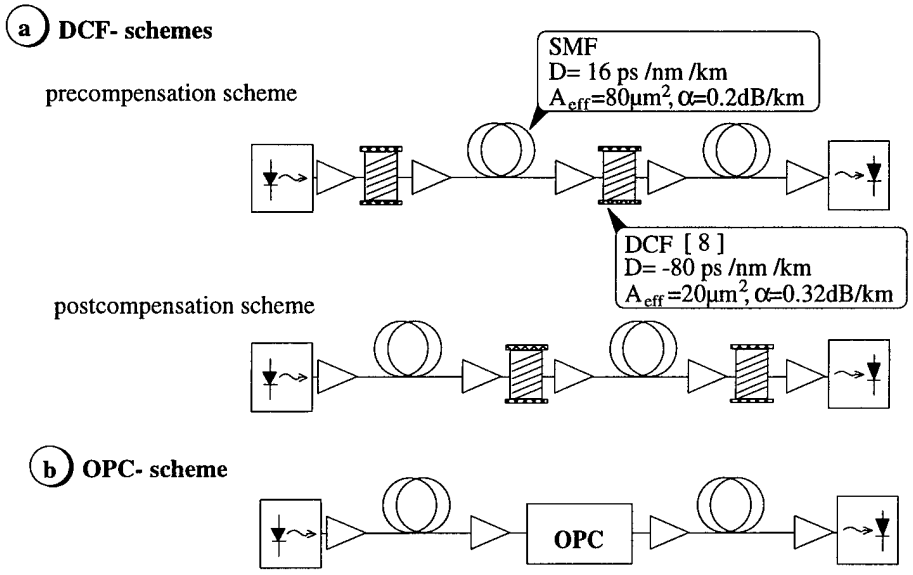


Fig. 1: Principle setup for **a)** a system based on Dispersion-Compensating Fibers (DCF) and **b)** a system based on Optical-Phase Conjugation (OPC)

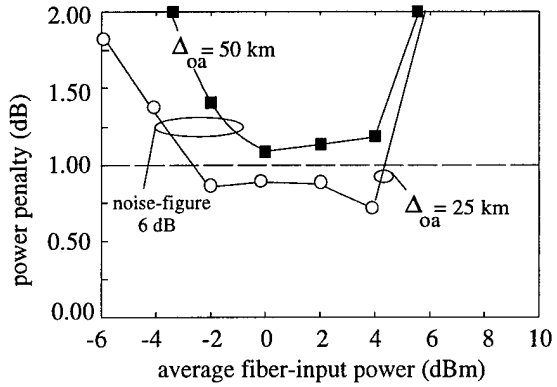


Fig. 2: Power penalty as a function of fiber-input power in a 1000 km OPC-based system operating at 40 Gbit/s for different amplifier spacings

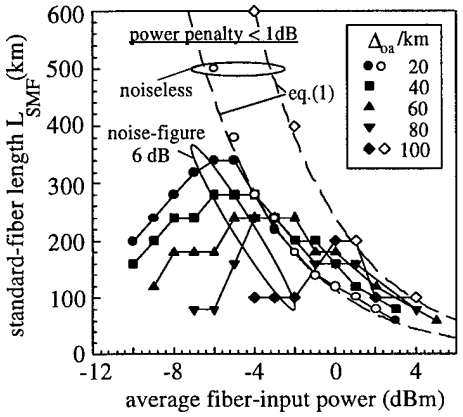


Fig. 3: Achievable standard-fiber length as a function of average fiber-input power for 1 dB power penalty and different amplifier spacings.

Novel tapped delay line transmitter pulse shaping for reducing dispersion penalty of a 10 Gbit/s transmission system

Y. R. Zhou and L. R. Watkins
School of Electronic Engineering & Computer Systems, University of Wales-Bangor,
Dean Street, Bangor, Gwynedd, LL57 1UT, United Kingdom
Tel: +44.1248.382719, Fax: +44.1248.361429

1. Introduction

Most of the installed fibre systems are based on standard single mode fibres operating at the low loss window around 1.55 μm. Such optical fibre system with zero dispersion at 1.3 μm suffers from severe limitation due to chromatic dispersion, for example, the limited transmission distance of a 10 Gbit/s fibre system is about 65 km [1]. Much effort has been given to overcome the dispersion limitation, thus upgrading the existing fibre system and increasing the repeaterless transmission distance. Techniques using dispersion compensating fibres and mid-system spectral inversion have been shown to extend the dispersion limited transmission distance greatly [2, 3]. A duobinary signalling scheme has also been investigated [4, 5], which increases the transmission distance of a 10 Gbit/s system to beyond 100 km by reducing the signal bandwidth. In comparison dispersion compensation in the electrical part of the optical link is expected to provide relatively simple and more flexible ways to tackle the chromatic dispersion [6].

In this paper, we propose a new technique, which uses a tapped delay line transfer function to shape the drive signal of the external modulation at the transmitter. From computer simulation, it is found that this modulation scheme with an appropriate chirp can extend the dispersion limited distance to 170 km for a 10 Gbit/s system.

2. Modeling

The system configuration is as follows: a transmitter is an externally modulated laser source, its output signal at 10 Gbit/s is propagated along a standard single mode fibre with attenuation of 0.2 dB/km at 1.55 μm, the fibre chromatic dispersion is 17 ps/km/nm, the Kerr coefficient is $2.42 \times 10^{-20}\mathrm{m}^2/\mathrm{W}$ and mode area 50 $\mu\mathrm{m}^2$, the launch power of the transmitted signal is 10 mW to avoid the effect of nonlinearity, such as Stimulated Brillouin Scattering (SBS), at the receiver end the signal is detected by a pre-amplified PIN receiver. Signal propagation in single mode fibre is governed by the nonlinear Schrödinger equation and the distorted signal after transmission is obtained by numerically solving this equation. To estimate system performance the modified Chernoff bound (MCB) is used to calculate the bit error rate, which is a tight upper bound on bit error rate [7].

A block diagram of the transmitter is shown in Fig.1, which consists of a laser diode and a Mach-Zehnder (M-Z) modulator. A model of the M-Z modulator with adjustable chirp is given in [8], where two branches of the modulator are drived by signals of same waveform but opposite sign. The chirp parameter is defined as

$$\alpha = \frac{V_1 + V_2}{V_1 - V_2} \tag{1}$$

where V_1, V_2 are respectively the peak-to-peak amplitude of the drive signals and their sign depends on the relative polarity. Hence, the modulator chirp can be adjusted by changing the relative peak-to-peak driving voltages and their polarities. In this work, the

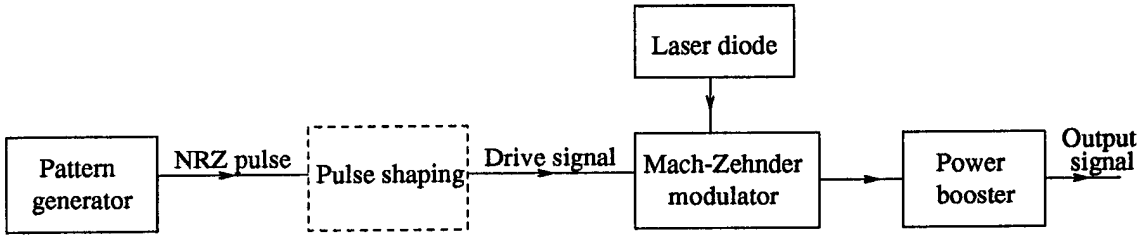


Fig.1 block diagram of the transmitter

drive signal is generated by a pulse shaping circuit with a non-return-to zero (NRZ) input signal from a pseudo random signal generator. The pulse shaping circuit is a tapped delay line in cascade with a low pass filter, which can be a Butterworth filter or just the equivalent low pass feature of the driving signal route. The transfer function of the tapped delay line is given by:

$$Tr(s) = \sum_{k=-L}^{L} c_k \exp\{-sk(\frac{T}{N})\} \tag{2}$$

where T is bit period, T/N is the tap spacing and s the transform variable. The number of taps is $(2L+1)$ and c_k are the tap weights. The tap weights c_k, where $k \neq 0$, are less than one with c_0 normalized to one. A tapped delay line with positive values of tap weights can modify the amplitude and broaden the pulse according to the data pattern, here a tapped delay line of 3 taps and tap spacing of the bit period is used. Fig.2 illustrates the output signal of a transmitter with the pulse shaping. Compared with the NRZ pulse sequence, it is seen that different shapes of output waveform are obtained by varying the tap weights. In addition, such pulse shaping also introduces more intersymbol interference (ISI).

3. Results

We present here results to demonstrate the effect of the pulse shaping at transmitter for compensating chromatic dispersion. In our calculation, the sampling time is set to that at which an isolated '1' reaches its maximum value after receiver electrical filtering and system performance is measured by the receiver sensitivity, which is the received signal power needed to maintain a bit error rate of 10^{-9}.

Fig.3 shows that the receiver sensitivity varies with transmission distance for the system with pulse shaped signal, the results for NRZ signal are also plotted for comparison. We see that the back to back receiver sensitivity of the pulse shaped signal is about 2.0 dB lower than that of NRZ signal. For zero chirp modulation, the pulse shaped signal reaches 1 dB penalty just after 100 km transmission. With negative chirp -1.0, it is seen that the dispersion penalty goes to negative value first and is 1 dB at about 170 km. Whereas for the NRZ signal, 1 dB power penalty is incurred before 100 km, after that the penalty increases rapidly. With negative chirp its performance only improves slightly. Therefore, we see that combining the pulse shaping of the drive signals and chirping of the Mach-Zehnder modulator, the system dispersion penalty is greatly reduced.

In Fig.4, we compare the system performance with pulse shaping for tap weights c_{-1}, c_1 of (0.25,0.25), but varying the chirp parameters. Relative to the receiver sensitivity curve at zero chirp, it is seen that a positive chirp parameter increases the power penalty, in contrast, negative chirp parameter improves system performance. For chirp parameter

-0.5, the 1 dB dispersion penalty occurs at around 150 km, with chirp parameter -1.0 and -1.5 a similar trend is shown in the receiver sensitivity curves, but a greater improvement in dispersion penalty is obtained, leading to an increased tansmission distance of over 170 km for 1 dB dispersion penalty.

Fig.5 shows the influence of different tap weights on the system performance achieved. Comparing the back-to-back case, larger value of tap weights results in lower receiver sensitivity due to larger amount of ISI induced. Note it is not necessary for the tap weights c_{-1}, c_1 to be equal. It is seen that with tap weights (0.15,0.15) there is a relatively larger dispersion penalty compared with the other cases. For larger tap weights (0.35,0.35) and (0.4,0.4) the system reaches 1 dB dispersion penalty after 170 km, but gives lower receiver sensitivity. Pulse shaping with tap weights (0.25,0.25) is a good choice with both low dispersion penalty and higher receiver sensitivity.

4. Summary

We have introduced a new technique using pulse shaping in an externally modulated transmitter as a means of compensating the chromatic dispersion in a 10 Gbit/s transmission system with conventional single mode fibre. The tapped delay line pulse shaping circuit with positive tap weights modifies the amplitude and width of the transmitter output. It has been shown that this pulse shaping of the drive signals in combination with the negative chirp parameter of a M-Z modulator is effective in reducing the dispersion penalty so that the dispersion limit can be extended to 170 km. Appropriate values of tap weights can offer both low dispersion penalty and higher receiver sensitivity. Further more, the pulse shaping is relatively easy to implement with a microwave circuit since only positive tap weights are required.

References

[1] A. F. Elrefaie, R. E. Wagner, D. A. Atlas, and D. G. Daut. Chromatic dispersion limitations in coherent lightwave transmission systems. *J. Lightwave Technology*, **vol.6**(5):pp. 704 – 709, 1988.

[2] B. L. Patel, E. M. Kimber, N. E. Jolley, and A. Hadjifotiou. Repeaterless transmission at 10 Gb/s over 215 km of dispersion shifted fibre, and 180 km of standard fibre. *Proc. OFC '93*, **San Jose, USA**:PD6, 1993.

[3] A. H. Gnauck, R. M. Jopson, and R. M. Derosier. 10-Gb/s 360-km transmission over dispersive fiber using midsystem spectral inversion. *IEEE Photonics Technology Letters*, **vol.5**(5):pp. 663 – 666, 1993.

[4] X. Gu, S. J. Pycock, D. M. Spirit, A. D. Ellis, and C. J. Anderson. 10 Gbit/s, 138 km uncompensated duobinary transmission over installed standard fibre. *Electronics Letters*, **vol.30**(23):pp. 1953 – 1954, 1994.

[5] G. May, A. Solheim, and J. Conradi. Extended 10 Gb/s fiber transmission distance at 1538 nm using a duobinary receiver. *IEEE Photonics Technology Letters*, **vol.6**(5):pp. 648 –650, 1994.

[6] M. Schiess. Extension of dispersion limit by pulse shaping and profiting of fibre nonlinearities. *Digest ECOC'94*, **Firenze, Italy**:pp. 423 – 426, September 1994.

[7] J. J. O'Reilly and J. R. F. Da Rocha. Improved error probability evaluation methods for direct detection optical communication systems. *IEEE Trans. Inform. Theory*, **IT-33**(6):pp.839–848, 1987.

[8] A. H. Gnauck and S. K. Korotky et. al. Dispersion penalty reduction using an optical modulation with adjustable chirp. *IEEE Photonics Technology Letters*, **vol.3**(10):pp. 916 – 918, 1991.

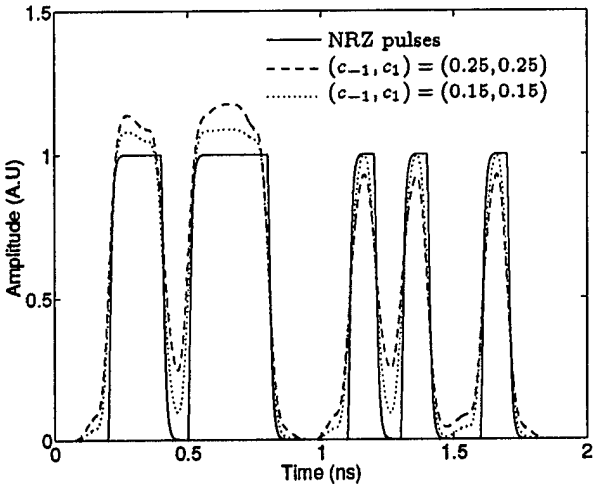


Fig.2 tranmitter output waveforms with and without pulse shaping

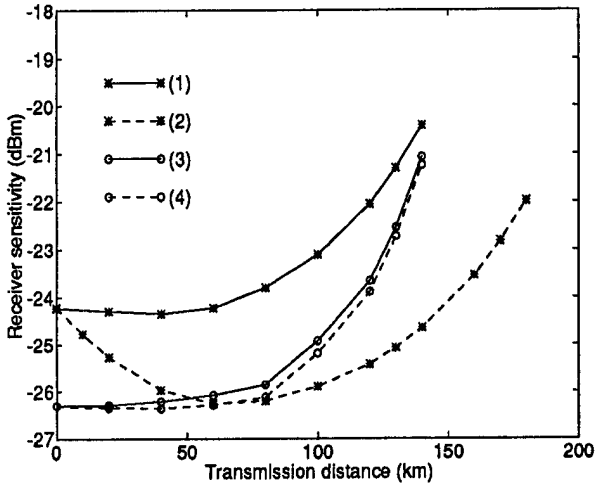


Fig.3 receiver sensitivity vs. transmission distance (1) zero chirp, $(c_{-1}, c_1) = (0.25, 0.25)$
(2) chirp −1.0, $(c_{-1}, c_1) = (0.25, 0.25)$
(3) zero chirp and NRZ pulse
(4) chirp −1.0 and NRZ pulse

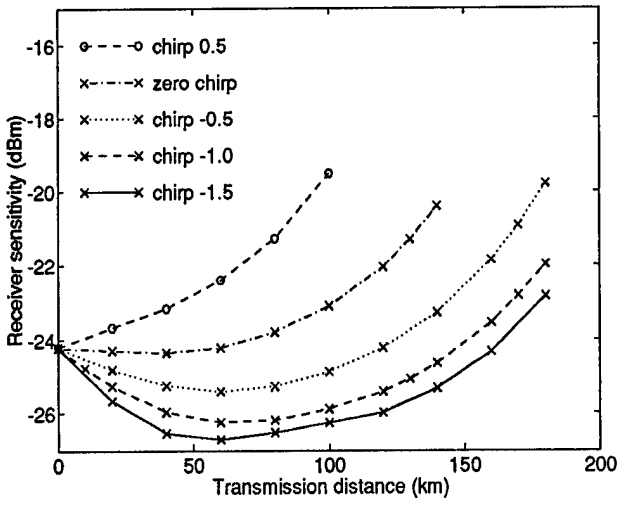


Fig.4 receiver sensitivity vs. transmission distance for $(c_{-1}, c_1) = (0.25, 0.25)$ and various chirp parameters

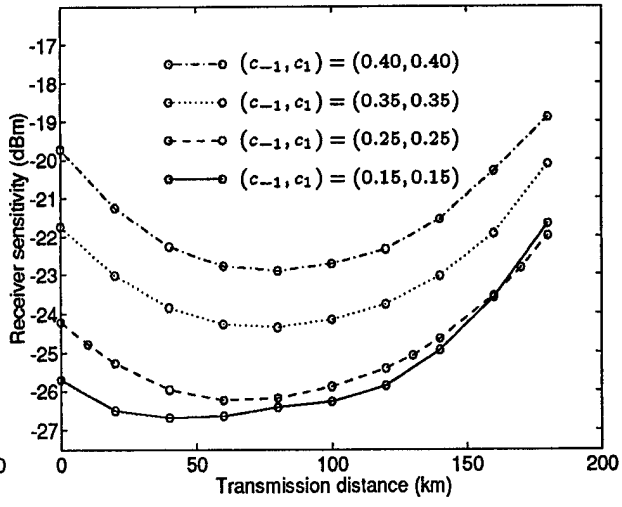


Fig.5 receiver sensitivity vs. transmission distance for chirp −1.0 and various extents of pulse shaping

An Optical Correlation Receiver Employing Phase Modulated Optical Orthogonal Codes

Gordon R. Strachan, Member, IEEE (strachan@waterloo.hp.com)
S. K. Chaudhuri, Senior Member, IEEE (sujeet@maxwell.uwaterloo.ca)
Department of Electrical and Computer Engineering
University of Waterloo
Waterloo, Ontaria
N2L - 3G1
Email: strachan@waterloo.hp.com
Email: sujeet@maxwell.uwaterloo.ca

1. Introduction

A traditional optical to electrical receiver consists of a simple PIN diode followed by a number of electrical signal processing elements which are required to detect and decode the incoming optical signal. The speed of the data on the optical fiber is limited by the bandwidth of these electrical signal processing devices which is typically only a small fraction of the available bandwidth on the optical fiber. With the recent advent of practical optical amplifiers it is now feasible to implement a number of the important receiver functions in the optical domain prior to detection by the PIN diode with out a loss in receiver sensitivity. By implementing these functions optically we can simplify the electrical section of the receiver and thus increase its bandwidth and yield significant gains in the transmission rate.

In this work we present a novel line coding scheme that can be used to realize all optical clock recovery in the receiver and completely remove the need for a phase lock loop (PLL). In addition, the receiver employs a bank of optical correlators which allows multiple data bits to be transmitted per symbol period.

2. The Receiver Design

The primary signal processing element employed in this work is the coherent tapped delay line filter. The filter consists of series of coupled optical waveguides of varying lenghts. The different lengths impose a different propagation delay on the signal in each arm and hence cause them to recombine out of phase at the output of the filter. By controlling the amount of signal coupled into each arm, and the relative delay between the arms, a wide variety of transfer functions can be realized. With the addition of electro-optic phase modulators, one can control the propogation delay to a fraction of a wavelength. This precise phase control allows one to realize practical coherent optical filtering[1-3]. In this work, we employ coherent optical tapped delay line filters to realize a line coding scheme employing both amplitude and phase coding.

Figure 1. shows the implementation details of the transmitter and receiver pair. The transmitter consists of a pulsed laser and a series of optical delay lines. The laser generates one pulse per symbol interval which is split and subjected to different delays in the delay arms. The output of the transmitter will be a series of pulses whose positions correspond to an optical orthogonal code (OOC)[4, 5]. In addition, each branch in the delay arm contains a phase modulator which is used to give each pulse a fixed phase shift. The data is transmitted as a train of pulses with a unique set of phase shifts imposed upon them. There is only a finite number of distinct symbols that can be sent which is determined by the size of the correlation bank in the receiver. Mathematically the output of the transmitter when it is transmitting symbol I is given as:

$$p_I(t) = \sum_{i=1}^{W} \sin(\omega_c - d_i T) + \phi_i^I) rect\left(\frac{t - d_i T}{T}\right) \quad (1)$$

where ω_c is the optical frequency, W is the number of delay arms, d_i is the pulse delay and ϕ_i^I its the phase shift.

The receiver is constructed from N + 1 optical correlators as is shown in figure 1. The delays introduced in each correlator correspond to the inverses of the delays in the transmitter. Since the pulse position correspond to an optical orthogonal code the output of each correlator will be a single pulse centered at the middle of the symbol interval. However, because the transmitted pulses are phase coded, the output will be the *vector* sum of the pulses. The $(N+1)^{th}$ filter performs an incoherent summation on the delay arm outputs and so it will be insensitive to the phase coding and will always generate the same output irrespective of the symbol transmitted. This will form the recovered clock. All that is required to complete the clock recovery circuit is a PIN diode and a threshold detector. The bandwidth of the circuit will be limited by the response time of the PIN diode only and not the bandwidth of an electrical PLL.

In each of the other N correlators, phase delays are introduced to cancel the phase shifts introduced in the transmitter. This is equivalent to match filtering. At the sample instant, which is determined using the recovered clock, the output of the Jth filter when the Ith symbol is transmitted is given by:

$$i_{IJ} = \left[\sum_{i=1}^{W} \sin(\phi_i^I - \phi_i^J)\right]^2 + \left[\sum_{i=1}^{W} \cos(\phi_i^I - \phi_i^J)\right]^2 \quad (2)$$

The phase shifts used are then selected such that i_{IJ} is minimized for all $I \neq J$, and

maximized for $I = J$. A Simulated Annealing algorithm was employed to solve for the optimal phase shifts[6].

3. Results

The line coding scheme parameters which are of interest are: code efficiency (bits sent/OOC chip length) and receiver sensitivity. The two parameters are interrelated through the maximum cross-correlation achievable for a given symbol set size (N). Figure 2 shows the achieved optimal cross-correlation values and figure 3 shows the sensitivity as a function of N. For the presented results it is shown that our scheme can be upto twice as efficient as other self clocked receiver designs such as Manchester Coding[7, 8]. Finally, extensive error analysis has been performed which show the proposed line coding method to be relatively immune to random phase errors.

4. Conclusions

We have proposed and studied a novel line coding scheme which can be used to implement an all clock recovery circuit. The bandwidth of the receiver is limited only by the response time of the PIN diode and no other electrical signal processing device. This scheme has been shown to more efficient than other self clocked receiver schemes while only slightly less sensitive.

5. References

1. M. E. Marhic and Y. L. Chang, Pulse Coding and Coherent Decoding in Fibre-Optic Ladder Networks, *Electronics Letters* **25**(22) pp. 1535-1536 (26 October 1989).
2. D. E. N. Davis and G. W. James, Fibre-Optic Tapped Delay Line Filter Employing Coherent Optical Processing, *Electronics Letters* **20**(2) pp. 95-97 (January 19, 1984).

3. Kaname Jinguji and Masao Kawachi, Synthesis of Coherent Two-Port Lattice-Form Optical Delay-Line Circuit, *Journal of Lightwave Technology* **13**(1) pp. 73-82 (January 1995).
4. Fan R. K. Chung, Jawad A. Salehi, and Victor K. Wei, Optical Orthogonal Codes: Design, Analysis, and Applications, *IEEE Transactions on Information Theory* **35**(3) pp. 595-604 (May 1989).
5. Jawad A. Salehi, Code Division Multiple-Access Techniques in Optical Fiber Networks - Part I: Fundamental Principles, *IEEE Transactions on Communications* **37**(8) pp. 824-833 (August 1989).
6. Lester Ingber, Simulated annealling: Practice versus Theory, *Mathl. Comput. Modelling* **18**(11) pp. 29-58 (1993).
7. Tran Van Muoi, Receiver Design for Digital Fiber Optic Transmission Systems Using Manchester (Biphase) Coding, *IEEE Transactions on Communications* **COM-31**(5) pp. 608-619 (May 1983).
8. Noriaki Yoshikai, Shigendo Nishi, and Jun-ichi Yamada, Line Code and Terminal Configuration for Very Large-Capacity Optical Transmission System, *IEEE Journal on Selected Areas in Communications* **SAC-4**(9)(Dec. 1986).

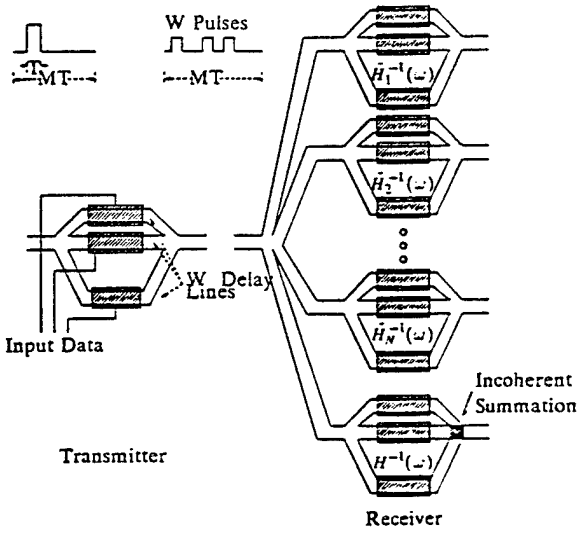


Figure 1a: The Correlation Transmitter-Receiver Pair

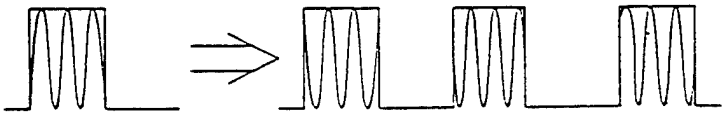


Figure 1b: The Resultant Output of the Transmitter

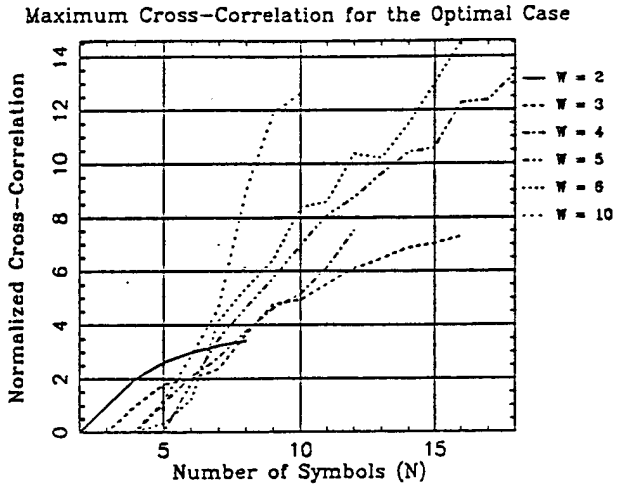


Figure 2: Optimal Maximum Cross-Correlation for Different Signal Set Sizes

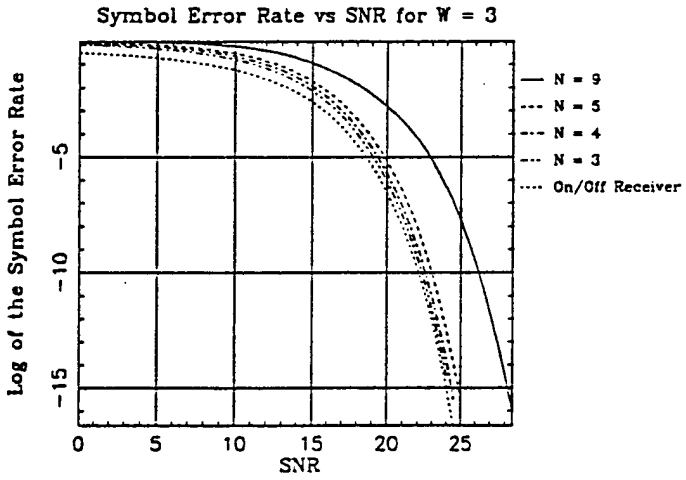


Figure 3: Receiver Sensivity for a Normalized Decision Threshold of ¼

Multiple Length Scales and Averaging in Modelling of Long-Distance Optical Fiber Transmission

C. R. Menyuk
Department of Computer Science and Electrical Engineering
University of Maryland Baltimore County
Baltimore, MD 21228-5398
tel. no. (410)-455-3501

When scientists model long-distance optical fiber communication systems, we must deal with a wide range of length scales extending from 1.5 μm, which is the wavelength of the transmitted light signal, to 27 Mm, which the length of the FLAG cable network. In between, there are a host of other length scales whose values depend on the fiber parameters. These include the pulse scale lengths which are in the range of 0.3–30 cm, the polarization beat length which is 3–30 m, and the fiber polarization orientation correlation length which is on the order of 10–100 m. The attenuation scale length is 20–30 km, and the scale lengths for polarization mode dispersion and chromatic dispersion can be as small as 100 km and can be almost arbitrarily large. These scale lengths depends on both the fiber parameters and the data rate. Nonlinear scale lengths are typically on the order of 1000 km. The gap of 13 orders of magnitude between the shortest and the longest scale lengths seems like a serious challenge, and it would in fact be an insuperable challenge if we really attempted to solve Maxwell's equations on a scale length of micrometers to determine the behavior over the many thousands of kilometers that exist in real systems. While there have been some attempts to directly solve Maxwell's equations in optical fibers over short lengths and in special parameter regimes,[1] my own view is that it does not make much sense to apply this sort of brute force approach to optical fiber transmission. Instead, we should take advantage of the very powerful mathematical averaging techniques that exist to, in effect, leap over the shortest length scales and focus on the length scales of interest. These techniques have a long and distinguished history that dates back to the 19th century,[2] and the well-known slowly varying envelope approximation that is used in optics can be viewed as an application of these techniques.

In this talk, I will present applications of this approach. I will first focus on the derivation of the nonlinear Schrödinger equation which takes advantage of the wide disparity between the wavelength and the fiber radius on one hand and the pulse lengths on

the other hand. I will also describe the derivation of the averaged nonlinear Schrödinger equation which takes into account the disparity between the attenuation length and the length scale on which the dispersion varies on one hand and the dispersive and nonlinear lengths scales on the other hand. Finally, I will discuss the coupled nonlinear Schrödinger equation which appears when polarization effects are important and recent work by my own research group in which we use the large disparity between the beat length and fiber decorrelation length on one hand and the nonlinear and dispersive length scales on the other hand to obtain the Manakov-PMD equation.

If polarization effects can be ignored, then many of the length scales that I mentioned in the first paragraph can be ignored, and Hasegawa and Tappert[3] showed heuristically as far back as 1973 that single-mode optical fibers can be described by the equation

$$i\frac{\partial\psi}{\partial z} + \frac{i}{2}k''\frac{\partial^2\psi}{\partial t^2} + \gamma|\psi|^2 = -i\alpha\psi, \tag{1}$$

where ψ is the complex wave envelope, normalized so that $|\psi|^2$ is the pulse power, z is distance along the fiber, t is time, k'' is the dispersion coefficient, γ is the nonlinear coefficient, and α is the attentuation/gain coefficient. Several averages occur in the derivation of Eq. (1) from Maxwell's equation, and the best discussion of this issue in my opinion has been given by Kodama.[4] One averages over the transverse profile to reduce the problem from three spatial dimensions to one, and one averages over the temporal oscillations to obtain the evolution equation for the complex envelope. Equation (1) is the lowest order equation in an expansion in which the small parameters are a/L and λ/L, where a and λ are the fiber radius and the light's wavelength, while L is the length scale over which ψ changes. Carrying out the expansion to higher order, one obtains corrections terms that play a role in certain parameter regimes — notably terms that contribute to higher-order dispersion and the Raman effect.

It is possible to go farther. Noting that k'' and α vary on a scale of 10 to 20 km, while the nonlinear and average dispersive scale lengths are 100 – 1000 km, one can average once again to obtain[5]

$$i\frac{\partial\psi}{\partial z} + \frac{i}{2}\bar{k}''\frac{\partial^2\psi}{\partial t^2} + \gamma|\psi|^2 = 0, \tag{2}$$

where $\bar{\alpha} = 0$ and the overbars indicate averages. Equation (2) is just the nonlinear Schrödinger equation. I note that this approach was used at a very early stage by Wai, et al.[6] to show that when $\bar{k}'' = 0$, the effect of k''' is visible even if k'' is locally large. I also note that Bronski and Kutz[7] have recently used this approach to elucidate the evolution of NRZ pulses in the presence of dispersion maps.

When polarization effects cannot be ignored, Menyuk[8] showed in 1987 that pulse evolution is described by the coupled nonlinear Schrödinger equation, which may be written after normalization as

$$i\frac{\partial \mathbf{U}}{\partial z} + i\alpha\mathbf{U} + \beta\begin{pmatrix}\cos\theta & \sin\theta \\ \sin\theta & -\cos\theta\end{pmatrix}\mathbf{U} + i\beta'\begin{pmatrix}\cos\theta & \sin\theta \\ \sin\theta & -\cos\theta\end{pmatrix}\frac{\partial \mathbf{U}}{\partial t}$$
$$-\frac{1}{2}k''\frac{\partial^2 \mathbf{U}}{\partial t^2} + \frac{\omega_0}{c}n_2\begin{pmatrix}|u_1|^2u_1 + \frac{2}{3}|u_2|^2u_1 + \frac{1}{3}u_2^2u_1^* \\ \frac{2}{3}|u_1|^2u_2 + |u_2|^2u_2 + \frac{1}{3}u_1^2u_2^*\end{pmatrix} = 0. \tag{3}$$

In communication fibers, the length scale on which θ varies is 10–100 m which is far shorter than the dispersive and nonlinear length scales. It was shown by members of my research group and others in 1991[9] that Eq. (3) reduces to the Manakov equation when averaged over the Poincaré sphere, but a careful justification of this averaging was lacking and the nature of the higher-order corrections was unclear. We have recently resolved this problem completely. Our approach is based on the observation that while a single frequency, continuous wave at low intensity undergoes a rapid and random evolution on the Poincaré sphere, the trajectories on the Poincaré sphere of different frequencies in the bandwidth of a typical communication signal differ only slightly, and, likewise, the difference due to nonlinearities is small. By mathematically "freezing out" the rapid motion of the continuous wave on the Poincaré sphere, we can examine the gradually developing deviations at different frequencies and due to nonlinearity. In detail, we begin by solving the equation

$$i\frac{\partial \mathbf{U}_0}{\partial z} + i\alpha\mathbf{U}_0 + \beta\begin{pmatrix}\cos\theta & \sin\theta \\ \sin\theta & -\cos\theta\end{pmatrix}\mathbf{U}_0 = 0 \tag{4}$$

for a single continuous wave at the central frequency of the optical signal whose complex amplitude is labeled $\mathbf{U}_0$. In principle, we need to solve Eq. (4) on the short length scale,

but that is strictly necessary only when we wish to benchmark our results against Eq. (3) for a given realization. Otherwise, we obtain equations with known statistical properties that allow us to obviate the short step altogether. In any case, Eq. (4) is a simple, second order ordinary differential equation that can be rapidly solved. Solving Eq. (3) yields the evolution in the form $\mathbf{U}_0(z) = \mathsf{T}\mathbf{U}_0(0)$. Defining now $\mathbf{V}(z,t) = \mathsf{T}^{-1}\mathbf{U}(z,t)$, we find that the equation that describes the evolution of $\mathbf{V}$ may be written

$$i\frac{\partial \mathbf{V}}{\partial z} - \frac{1}{2}k''\frac{\partial^2 \mathbf{V}}{\partial t^2} + \frac{8}{9}\frac{\omega_0}{c}n_2\left(|v_1|^2 + |v_2|^2\right)\mathbf{V} + i\bar{\beta}'\mathsf{A}\frac{\partial \mathbf{V}}{\partial t} + \mathbf{N}(\mathbf{V}) = 0. \tag{5}$$

where A is a matrix with known statistical properties, and $\mathbf{N}(\mathbf{V})$ is a vector whose properties are also known. In contrast to the other transformations that I have discussed, this one is *exact*! The fourth term on the right corresponds to the usual linear polarization mode dispersion (PMD) and the fifth term includes effects due to incomplete mixing on the Poincaré sphere that we refer to as nonlinear PMD. We have already carried out careful numerical studies of this equation.

This work was supported by ARPA through AFOSR, DOE, and NSF.

REFERENCES

1. R. M. Rose, P. M. Goorjian, and A. Taflove, Opt. Lett. **18**, 491 (1993).
2. H. Poincaré, *Les méthodes nouvelles de la mécanique céleste. Tome II* (Gauthiers-Villars, Paris, 1893).
3. A. Hasegawa and F. D. Tappert, Appl. Phys. Lett. **23**, 142 (1973).
4. Y. Kodama, J. Stat. Phys. **39**, 597 (1985).
5. A. Hasegawa and Y. Kodama, Opt. Lett. **15**,1443 (1990); L. F. Mollenauer, S. G. Evangelides, and H. A. Haus, J. Lightwave Technol. **9**, 194 (1991).
6. P. K. A. Wai, C. R. Menyuk, H. H. Chen, and Y. C. Lee, IEEE J. Quantum Electron. **QE-24**, 373 (1988).
7. J. C. Bronski and J. N. Kutz, Opt. Lett. (submitted for publication).
8. C. R. Menyuk, IEEE J. Quantum Electron. **QE-23**, 174–176 (1987).
9. P. K. A. Wai and C. R. Menyuk, J. Lightwave Technol. **14**, 148 (1996).

Dynamics of Stimulated Brillouin Scattering and Its Effects on Fibre Supported Millimeter-Wave Communication Systems

S. L. Zhang and J. J. O'Reilly
Department of Electronic and Electrical Engineering
University College London
Torrington Place, London WC1E 7JE, U.K.
Tel: 0171 419 3974
Fax: 0171 388 9325
E-mail: szhang@eleceng.ucl.ac.uk

1. Introduction

Fibre supported millimeter-wave communication (FSMWC) is attracting considerable attention in the literature[1,2,3]. The generation of millimeter-wave in such communication systems is based on the mixing of two optical carriers on a PIN photodiode. The frequency difference of the two optical carriers should be the required millimeter-wave frequency. The two optical carriers can be produced by using two lasers or by using only one laser and a Mach-Zehnder (MZ) modulator which is modulated by a sinusoidal wave at half of the required millimeter-wave frequency[4,5]. Since the fibre length for FSMWC systems can be several tens of kilometers and the powers of the optical carriers can approach tens of milliwatts, stimulated Brillouin scattering (SBS) may have great effects on system performance[6,7,8]. Numerical results have been published in [9] based on steady-state analysis (SSA), however, for systems operating at a low bit rate such as 2Mbit/s, the total signal bits travelling inside the whole length of the optical fibre may not be large enough to validate SSA. For such a case the study of the dynamics of SBS[10] can provide more information about the potential effects of SBS on the system performance. In this paper we have analyzed the effects of SBS on FSMWC system by studying the dynamics of SBS. Results are shown for SBS power distribution and received signal eye opening. For comparison results from SSA are also shown. The analysis of the dynamics of SBS not only provides the time-averaged values but also approximated probability density functions of the SBS wave and the received signal therefore should provide more useful insight for system designers to understand and to deal with the SBS effects on FSWMC systems.

2. System Configuration of FSMWC Systems

A block diagram for FSMWC system is shown in Fig.1. A dual frequency optical source generates two optical carriers, which can be produced by two lasers, or by a semiconductor laser and a MZ modulator, or by any other ways. One of the two optical carriers is modulated by the 'data' signal at the modulator. After the modulation a directional coupler is used to combine the two optical carriers, which are then transmitted through the optical fibre to a photodiode. The desired millimeter wave signal is generated at the output of the photodiode as a result of the beating of the two optical carriers on it. The millimeter wave signal is then filtered , amplified and sent to an antenna. If the power of the optical carriers are high enough, significant SBS wave will be produced by the two optical carriers in the optical fibre because of fibre nonlinearity and subsequently system performance will be degraded.

3. Mathematical Model for the Dynamics of SBS

For FSMWC systems, the frequency separation of the two optical carriers is equal to or greater than 30GHz, with the 60GHz band currently of especial interest[11]. This frequency separation is much greater than the SBS shift frequency of about 11GHz in an optical fibre, therefore the SBS produced by the two optical carriers can be considered separately. The differential equations for the slowly varying amplitudes

of the electrical waves of the optical carrier $E_c(z,t)$ and SBS $E_{sbs}(z,t)$ and the density perturbation $A(z,t)$ are as follows[10]:

$$\left[\frac{\partial}{\partial z}+\frac{1}{\nu_g}\cdot\frac{\partial}{\partial t}\right]E_c(z,t) = \frac{i}{4}\cdot\frac{\omega_c^2}{k_c\cdot c_0^2}\cdot\frac{\partial\epsilon_r}{\partial\rho}\cdot E_{sbs}(z,t)\cdot A(z,t)-\alpha\cdot E_c(z,t) \quad (1)$$

$$\left[\frac{\partial}{\partial z}-\frac{1}{\nu_g}\cdot\frac{\partial}{\partial t}\right]E_{sbs}(z,t) = -\frac{i}{4}\cdot\frac{\omega_{sbs}^2}{k_{sbs}\cdot c_0^2}\cdot\frac{\partial\epsilon_r}{\partial\rho}\cdot E_c(z,t)\cdot A^*(z,t)+\alpha\cdot E_{sbs}(z,t) \quad (2)$$

$$\left[\frac{\partial}{\partial t}+\Gamma_B\right]A(z,t) = \frac{i}{4}\cdot\frac{k_a}{\nu_a}\cdot\rho_0\cdot\epsilon_0\cdot\frac{\partial\epsilon_r}{\partial\rho}\cdot E_c(z,t)\cdot E_{sbs}^*(z,t) \quad (3)$$

where ρ_0 is the material density, ρ is the relative material density, ϵ_0 is the free-space dielectric permittivity, ϵ_r is the relative dielectric permittivity, Γ_B^{-1} is the characteristic photon damping time, ν_a is the acoustic wave velocity, k_{sbs} and k_c are the wave numbers for the SBS and the optical carrier, ω_{sbs} and ω_c are the angular frequencies of the SBS and the optical carrier, c_0 is the light velocity in the vacuum, ν_g is the group velocity of light inside the fibre, α is the fibre loss. The above differential equations can be normalized by assuming that approximately $\omega_c=\omega_{sbs}=\omega$ and $k_c=k_{sbs}=k$ and using the following definitions:

$$E_{cn}(z,t) \triangleq -i\cdot r_1\cdot E_c(z,t) \quad (4)$$

$$E_{sbsn}(z,t) \triangleq -i\cdot r_2\cdot E_{sbs}(z,t) \quad (5)$$

$$A_n(z,t) \triangleq -i\cdot r_a\cdot A(z,t) \quad (6)$$

$$\zeta \triangleq \frac{z}{L} \quad (7)$$

$$\tau \triangleq \frac{t}{(L/\nu_g)} \quad (8)$$

$$\delta \triangleq \frac{\Gamma_B\cdot L}{\nu_g} \quad (9)$$

where $r_1=r_2=|E_c(z=0,t=0)|^{-1}$ and $r_a=\frac{\omega^2\cdot L}{4\cdot k\cdot c_0^2}\cdot\frac{\partial\epsilon_r}{\partial\rho}$. The normalized differential equations are as follows:

$$\left[\frac{\partial}{\partial\tau}+\frac{\partial}{\partial\zeta}\right]E_cn(\zeta,\tau) = -E_{sbsn}(\zeta,\tau)\cdot A_n(\zeta,\tau)-\alpha_n\cdot E_cn(\zeta,\tau) \quad (10)$$

$$\left[\frac{\partial}{\partial\tau}-\frac{\partial}{\partial\zeta}\right]E_{sbsn}(\zeta,\tau) = E_{cn}(\zeta,\tau)\cdot A_n^*(\zeta,\tau)-\alpha_n\cdot E_{sbsn}(\zeta,\tau) \quad (11)$$

$$\left[\frac{\partial}{\partial\tau}+\delta\right]A_n(\zeta,\tau) = \gamma\cdot E_{cn}(\zeta,\tau)\cdot E_{sbsn}^*(\zeta,\tau) \quad (12)$$

where α_n is the fibre loss after the normalization and

$$\gamma=\rho_0\cdot\epsilon_0\cdot\left(\frac{\partial\epsilon_r}{\partial\rho}\right)^2\cdot\frac{\omega^2}{16\cdot k\cdot c_0^2}\cdot\frac{L^2\cdot k_a}{\nu_g\cdot\nu_a}\cdot|E_c(z=0,t=0)|^2 \quad (13)$$

The above three normalized differential equations can be solved numerically with appropriate boundary and initial conditions.

4. Results and Discussion

This section shows some calculated results. The optical carriers are assumed to have very narrow linewidth before modulation and the powers of the optical carriers are 4mW. Amplitude modulation of a hurdred percent is assumed on one of the optical carriers. Signal bit rate is assumed to be 2Mbit/s, fibre length is assumed 20km. Other parameters used are listed in Table 1. Fibre dispersion effects can be neglected for such a low bit rate. The SBS power variation with time and signal patterns is shown in Fig.2. The three curves correspond to random bit sequency starting from different initial states. We see that the SBS power changes significantly with time and transmitted signal bit patten. Fig.3 shows the calculated probability density function (pdf) of SBS power which is plotted by the solid line, the best fit curve by 20

order polynormal which is plotted by dashed and dotted line and an approximation of it using function $a_1x^2 \cdot e^{-b_1x}$ which is plotted by dotted line. Also shown are the average SBS power calculated using the pdf which is marked by 'a' and the average and worst case SBS powers by SSA which is marked by 'b' and 'c' respectively. The pdf provides much more information for calculating the bit error rate then the average or worst case values by SSA. Comparing the three marked values we see that the worst case value by SSA is too pessimistic and can be several times larger than the average value calculated from the pdf and the average power by SSA is optimistic, which is caused by the nonlinear increase of SBS power near and above the SBS threshold. Also worth noticing is that the pdf of the SBS power can be approximated quite well by function $a_1x^2 \cdot e^{-b_1x}$.

Fig.4 shows the normalized received signal eye diagram. We see that SBS causes quite great eye closure, however, it is also quite obvious that the received signal has a higher chance taking a value near the top of the eye. To illustrate this more clearly, the pdf for the normalized eye opening for receiving bit '1's at the middle of the bit duration is calculated and shown in Fig.5 together with the results from SSA. The same marks as in Fig.3 are used, however, the approximation of the pdf for this figure is done by a mirrored and shifted curve of function $a_2x^2 \cdot e^{-b_2x}$. we see that the worst case value by SSA is still too pessimistic and the average power by SSA a bit optimistic for the same reason given above. The pdf can still be approximated quite well by a mirrored and shifted curve of function $a_2x^2 \cdot e^{-b_2x}$.

5. Summary

The dynamics of SBS and its effects on the eye opening of FSMWC systems has been studied and compared with the results by SSA. Much more information can be provided by the study of the dynamics of SBS than by SSA as pdfs of both SBS power and received signal can be calculated approximately for the former analysis. Comparing the average value calculated from the pdf and the average and worst case SBS powers by SSA we see that the worst case power by SSA overestimates the effect very much while the average power by SSA underestimates it. Therefore the analysis of the dynamics of SBS is much better for estimating the effects of SBS on FSMWC systems, especially for low bit rate and short length systems.

References

1. J. J. O'Reilly and P. M. Lane, "Remote delivery of video services using mm-wave and optics", *J. Lightwave Technol.*, vol. 12, no. 2, pp. 369-375, February, 1994

2. D. Wake, I. C. Smith, N. G. Walker, I. D. Henning, and R. D. Carver, "Video transmission over a 40GHz radio-fibre link", *Electron. Lett.*, vol. 28, no. 21, pp. 2024-2025, October, 1992

3. J. J. O'Reilly, P. M. Lane, M. H. Capstick, H. M. Salgado, R. Heidemann, R. Hofstetter, and H. Schmuck, "RACE R2005: Microwave optical duplex attenna link", *IEE Proc., Pt. J*, vol. 140, no. 6, pp. 385-391, December, 1993

4. J. J. O'Reilly, P. M. Lane, R. Heidemann, and R. Hofstetter, "Optical generation of very narrow linewidth millimeter wave signals', *Electron. Lett.*, vol. 28, no. 25, pp. 2309-2311, December, 1992

5. J. J. O'Reilly and P. M. Lane, "Optical fibre supported cable television with a mm-wave drop", *IEE Colloquium on Optical Fibre Systems for Cable Television*, pp. 3/1-3/4, 12 October, 1993

6. Y. Aoki, K. Tajima, and I. Mito, "Input power limits of single-mode optical fibers due to stimulated Brillouin scattering in optical communication systems", *J. Lightwave Technol.*, vol. 6, no. 5, pp. 710-719, May, 1988

7. E. Lichtman, R. G. Waarts, and A. A. Friesem, "Stimulated Brillouin scattering excited by a modulated pump wave in single-mode fibers", *J. Lightwave Technol.*, vol. 7, no. 1, pp. 171-174, January, 1989

8. R. G. Waart, A. A. Friesem, E. Lichtman, H. H. Yaffe, and R. -P. Braun, "Nonlinear effects in coherent multichannel transmission through optical fibers", *Proc. of the IEEE*, vol. 78, no. 8, pp. 1344-1368, August, 1990

9. S. L. Zhang and J. J. O'Reilly, "Modelling of stimulated Brillouin scattering effects on optical fiber supported millimeter-wave system", *IEEE 1995 Global Telecommunications Conference*, pp. 1982-1986, 13-17 November, 1995

10. A. Hook and A. Bolle, "Transient dynamics of stimulated Brillouin scattering in optical communication systems", *J. Lightwave Technol.*, vol. 10, no. 4, pp. 493-502, April, 1992

11. M. Chelouche and A. Plottner, "RACE 2067: Mobile broadband system (MBS): Trends and impact on 60GHz band MMIC development", *IEE Electronics and Communication Engineering Journal*, vol.5, no.3, pp. 187-197, June, 1993

Fibre core diameter = 8.0μm
Fibre loss = 0.2dB/km
Fibre intrinsic SBS gain constant = 5×10^{-8}km/W
Fibre dispersion parameter $\beta_1 = 0$
Fibre dispersion parameter $\beta_2 = 2.17 \times 10^{-23}$s·s/km
Fibre dispersion parameter $\beta_3 = 0$
Frequency band of millimeter wave = 60GHz
SBS gain spectrum bandwidth = 20MHz
SBS frequency shift = 11GHz

Table 1. Parameters used in the Illustrative Calculations

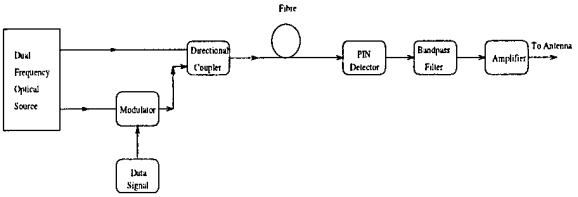


Fig.1 Block Diagram of Fibre Supported Millimeter-Wave Communication Systems

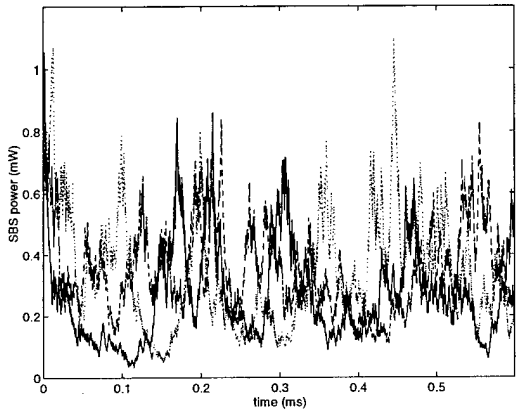


Fig.2 Variation of SBS Power with Time and Signal Pattern

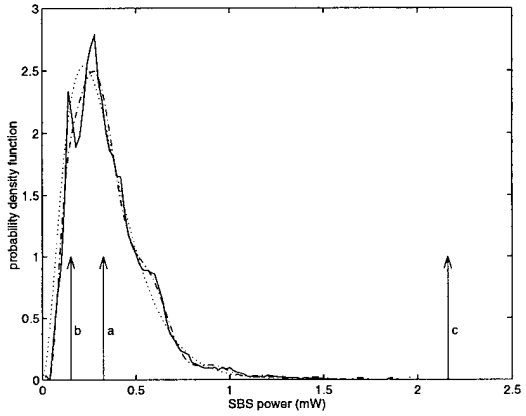


Fig.3 Probability Density Function of SBS Power and Results from Steady State Analysis

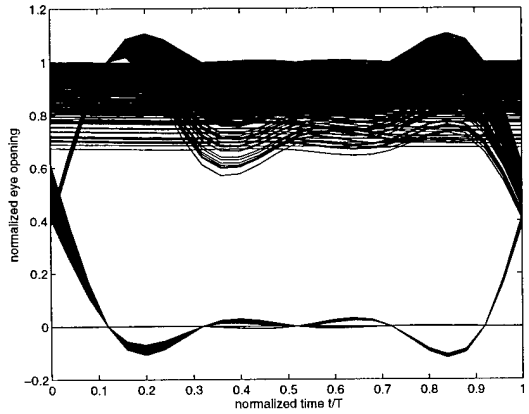


Fig.4 Effect of SBS on the Normalized Received Signal Eye Diagram

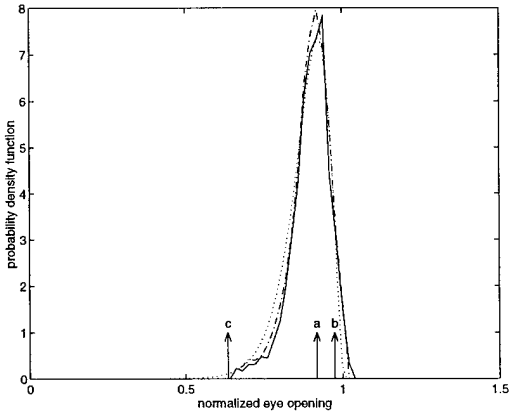


Fig.5 Probability Density Function for Normalized Eye Opening for Receiving Bit '1's at the Middle of Bit Duration

Dispersion and Self-Phase Modulation Compensation Based on a Negative Nonlinearity

C. Paré, A. Villeneuve, P.-A. Bélanger, N. Bélanger

Centre d'Optique, Photonique et Laser, Département de Physique, Université Laval, Québec, PQ, Canada G1K 7P4; Tel.: (418) 656-3752; FAX: (418) 656-2623; e-mail: cpare@phy.ulaval.ca

and

N.J. Doran

Photonics Research Group, Department of Electronic Engineering and Applied Physics, Aston University, Birmingham, B4 7ET, United Kingdom.

Dispersion compensation is of crucial importance in optical fiber communication systems. Various approaches have been suggested to combat the dispersive broadening of optical pulses and then increase data transmission rates. A well-known procedure consists in launching the signal at the output of a first fiber segment (characterized by its dispersion parameter β_{21}) in a second section presenting a dispersion parameter of opposite sign. As long as the condition $\beta_{22}L_2 = -\beta_{21}L_1$ ($L_{1,2}$ being the medium lengths) is satisfied, pulse restoration at the output of the second segment is ensured. This approah, however, is valid only in the linear regime. Spectral broadening caused by nonlinear self-phase modulation distorts the pulse and the above technique is unable to compensate for this.

Some time ago [1,2], it was suggested that the -then new- technique of phase conjugation might represent an interesting solution to this problem. Phase conjugation of the signal at the end of a first fiber section would induce a spectral inversion which implies that a subsequent propagation in an *identical* fiber section would reshape the pulse in its initial form. The recent experimental confirmation of the validity of this proposition[3-5] has renewed the interest for phase conjugation and has simultaneously motivated the search of alternate compensation schemes. In this report, we describe a new procedure for achieving the same goal. Basically, we extend the technique of alternate dispersions described above to the nonlinear regime by suggesting the use of a second dispersive medium with a *negative* nonlinear refractive index parameter n_2 (optical fibers are characterized by a positive n_2). As a possible candidate, let us mention AlGaAs which can present a strong negative nonlinearity, as well as a high dispersion parameter[6].

Through numerical simulations of nonlinear pulse propagation based on the Nonlinear Schrödinger Equation (plus higher-order terms), we demonstrate how the impact of dispersion and nonlinear Kerr effect (responsible for self-phase modulation), accumulated over tens of kilometers of propagation in a fiber could, in principle, be cancelled out following a short additional propagation of the signal in such a material. This is illustrated, for example, in Figs 1 and 2 in the context of ultra-long distance communications. Figure 1 first displays the signal degradation along a communication line consisting of a periodic sequence of fiber segments (medium 1) of length $L_1 = 20$ km spaced by *linear* ($n_{22} = 0$) waveguides (medium 2) of length L_2 only compensating for the dispersion. The condition $\beta_{22}L_2 = -\beta_{21}L_1$ is assumed satisfied with $L_2 << L_1$ by using, for example, a chirped grating as a dispersion compensator. An amplifier serves to reestablish the input energy before re-launching the signal in each fiber segment. The parameters are: $\alpha_1 = 0.2$ dB/km, $L_1 = 20$ km, $\beta_{21} = -1$

ps^2/km, T_0= 15 ps (implying a dispersion length L_{D_1} equal to 225 km), P_0= 0.28 mW. One can observe the gradual deformation of each pulse, due to the uncompensated spectral broadening in the fiber segments. This culminates in a strong interaction between the two pulses. In contrast, Fig. 2 demonstrates that the signal can be preserved if the ideal conditions (described by simple analytical expressions) of the proposed technique are fulfilled. Here the waveguide is assumed to have a negative nonlinearity (n_{22}= -2.0 x 10^{-13} cm^2/W [6] and the ratio of effective areas is fixed at A_{eff_2} / A_{eff_1} =0.1) and this ensures that the alterations to the pulse spectrum in each fiber segment do not accumulate (as is the case in Fig.1) but are instead cancelled out before passing through the next fiber segment.

We will discuss of the viability of this method when the ideal conditions are not satisfied. It will be shown that the compensating system can be simplified and still perform very well. The influence of two-photon absorption and higher-order dispersion will be evaluated and a comparison with soliton-based communication systems will also be presented. The possibility of experimental demonstration of this approach will be addressed.

[1] A. Yariv, D. Fekete, and D.M. Pepper, *Opt. Lett.* **4**, 42 (1979).

[2] R.A. Fisher, B.R. Suydam, and D. Yevick, *Opt. Lett.* **8**, 611 (1983).

[3] S. Watanabe, T. Naito, and T. Chikama, *IEEE Photonics Technol. Lett.* **5**, 92 (1993).

[4] S. Watanabe, T. Chikama, G. Ishikawa, T. Terahara, and H. Kuwahara, *IEEE Photonics Technol. Lett.* **5**, 1241 (1993).

[5] M.C. Tatham, G. Sherlock, and L.D. Westbrook, *Electron. Lett.* **29**, 1851 (1993).

[6] P. Dumais, A. Villeneuve and J.S. Aitchison, (to be published in *Optics Letters*); M.J. Lagasse, K.K. Anderson, C.A. Wang, H.A. Haus and J.G. Fujimoto, *Appl. Phys. Lett.* **56**, 417 (1990).

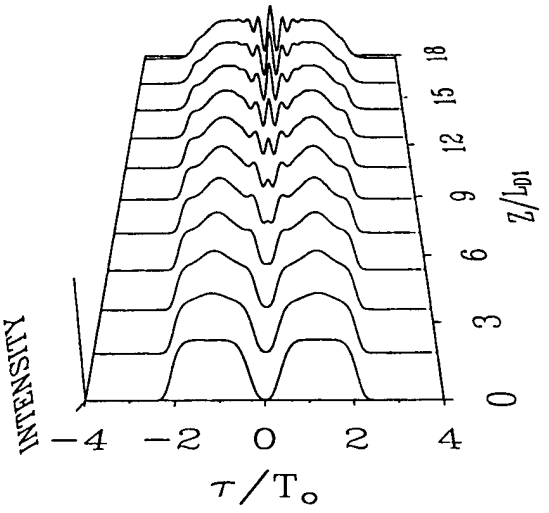


Figure 1. Signal degradation when only the dispersion is compensated for.

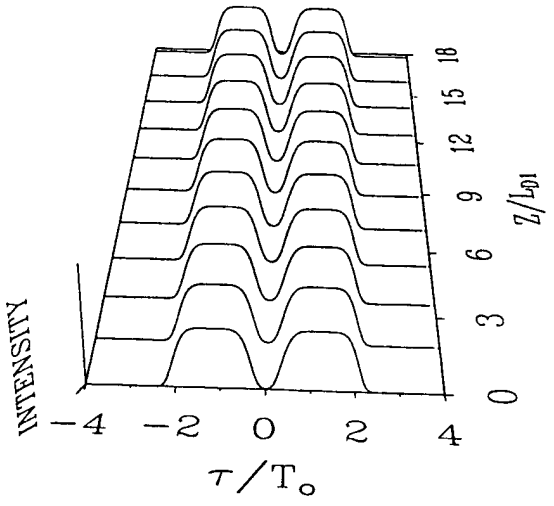


Figure 2. Signal preservation with the proposed compensation scheme.

Thursday, May 2, 1996

Symposium on Hybrid Packaging of III-V Components to Single-Mode Fibers

IThB 8:30 am-10:00 am
Fairfax B

Joseph Shmulovich, *Presider*
AT&T Bell Laboratories

HYBRID INTEGRATION USING SILICA-ON-SILICON OPTICAL MOTHERBOARDS

Carole Jones, Ken Cooper, Maurice Nield, Robert Waller, Jim Rush, John Collins, Phil Fiddyment and Ian Lealman

BT Laboratories, Martlesham Heath, Ipswich, Suffolk, IP5 7RE, UK.
Telephone: +44 1473 642020, Fax: +44 1473 646885.

INTRODUCTION

Silicon micromachining can be used to fabricate motherboards onto which optical, optoelectronic and electronic components can be aligned using low-cost passive alignment techniques. Further functionality can be added by incorporating planar silica waveguides, which route the optical signal within the motherboard and may also perform optical processing functions. This paper begins by describing some motherboard elements developed at BT Laboratories, then discusses examples of two modules which have been fabricated, combining several of these elements to form optical sub-systems.

MOTHERBOARD ELEMENTS

A series of "building blocks" for hybrid integration has been developed at BT Laboratories. A generic processing route has been devised, which enables these elements to be fabricated on a single motherboard substrate, with many processing steps being common to several building blocks. Thus, virtually any combination of hybrid components can be selected to produce the desired module.

V-grooves for fibre attachment are produced by anisotropic etching, with sub-micron control over dimensional and positional accuracy. Since the fibres are held in place using adhesive, a slot is also etched perpendicular to the V-grooves, to allow the glue to flow freely underneath the fibres. The sloping end-face of the V-grooves can be removed by placing a shallow diamond saw-cut across the end of the V-grooves, allowing the fibres to be brought close to other devices on the motherboard.

Passive alignment of laser chips has been achieved with sub-micron precision, giving coupling efficiencies of up to 27% to silica waveguides and in excess of 50% to singlemode fibres. The alignment technique relies on precision cleaving of the laser chip and butting its edges against silica stops on the silicon motherboard, so that the laser active region is accurately aligned to other features or components on the motherboard. Once the laser chip has been aligned against the stops, a known thickness of solder beneath the laser chip is reflowed, which holds the laser in place and forms one electrical contact to the laser. A short wire-bond connecting the laser to an adjacent bond pad forms the other electrical contact.

Precision cleaved laser chips are fabricated by defining channels in the quaternary layer of the laser, which are then etched to form U-shaped grooves. These grooves act as scribe lanes, and their top corners locate the edge of the chip very accurately with respect to the laser active region. The silica stops on the motherboard, which are between 8 and 15 μm thick, are deposited by PECVD and patterned using a combination of reactive ion and wet etching.

Planar silica waveguides based on arseno-silicate glass (ASG) have been used as an optical routing medium within the motherboard, and can also perform optical processing functions such as routing, switching and multiplexing. Although ASG has a relatively high optical loss at around 0.4 dB/cm, its high δn means that the excess loss at waveguide bends is very low, even for very small bend radii. This enables very dense and intricate optical interconnect patterns to be defined in the waveguides.

Micromachined mirrors are formed from metallised V-groove facets and may be used to deflect the light emerging from a waveguide into a substrate entry photodetector. Photodetectors with active diameters of 55 and 90 μm have been used, and are passively aligned using a series of visual alignment markers on the motherboard surface. Because of the large alignment tolerance for these large area photodetectors, this alignment technique yields coupling efficiencies of 40-50%, which are as high as those achieved using active alignment.

Electrical interconnects can be formed from thick aluminium layers deposited onto the motherboard and patterned into the correct geometries to give matched impedance transmission lines, enabling high frequency operation. Vias etched in a silica dielectric layer and coated with a layer of Ti/Pt/Au are used to provide contact to the electrical interconnect layer. Components can be bonded to these metal pads using either solder or silver-loaded epoxy. In order to achieve accurate vertical alignment of lasers, a precise solder thickness is required. The bond pads to which lasers are soldered therefore include a 10 μm wide constriction, so that surface tension prevents the flow of solder from the region directly beneath the laser chip.

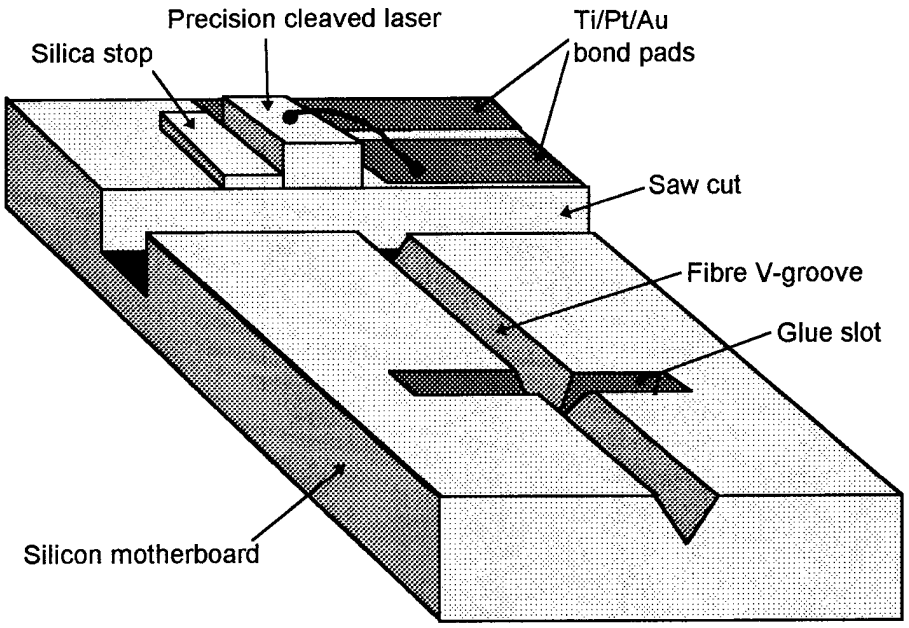


Figure 1 - Silicon laser optical bench

EXAMPLE MODULES

1. Silicon Laser Optical Bench

The silicon laser optical bench combines fibre V-grooves and passive alignment of a 1.55 μm laser. In order to give a high coupling efficiency, a large spot laser was used, which incorporates a tapered region to expand the laser mode to match that of the fibre [1]. The hybrid system is shown schematically in Figure 1.

Coupling efficiencies in excess of 50% have been reproducibly achieved [2]. This compares with values of around 62% for fibres actively aligned to similar lasers, indicating the accuracy of the passive alignment mechanism. The thermal properties of the lasers on the silicon bench compare favourably with test devices bonded on diamond headers, as the poorer thermal conductivity of silicon compared to diamond is compensated for by the large footprint of the motherboard. Back-to-back bit error rate measurements indicate that the device is capable of modulation at rates in excess of 600 Mbit/s.

2. High Speed Silicon Motherboard Transceiver

A hybrid optical transceiver [3] has been developed under the "SOPHI" project funded by the UK Department of Trade and Industry, and is shown schematically in Figure 2. The transmitter uses a 1.3 μm laser, passively aligned to a silica waveguide. A back facet monitoring photodiode monitors the laser output. The transmitted signal is routed via a planar silica directional coupler to the edge of the motherboard, where the waveguide is interfaced to a single mode fibre. The received 1.55 μm signal enters the motherboard via the same fibre and the directional coupler routes this signal to a photodetector, which is interfaced to the waveguide using a micromachined mirror. The photodetector is connected to a hybrid integrated amplifier chip through a short length of bond-wire. Aluminium coplanar waveguide electrodes are used to carry the receiver output to the edge of the motherboard and to bring the laser drive signal from an external driver to the integrated laser chip.

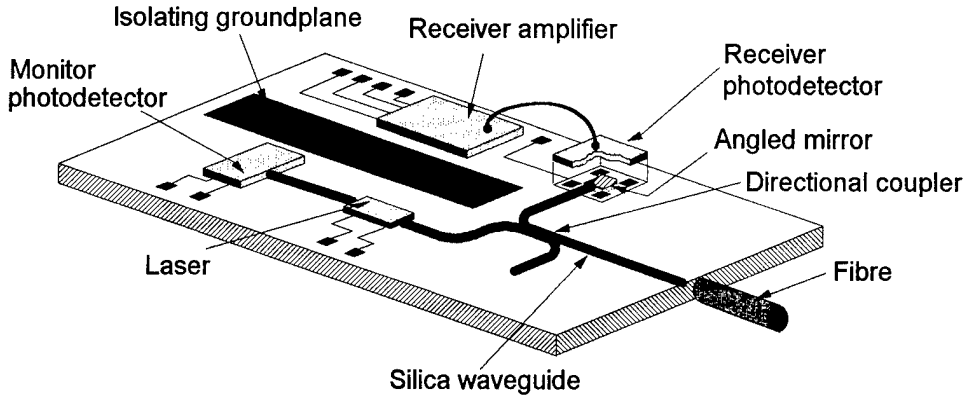


Figure 2 - Silicon motherboard transceiver

Modulation experiments have shown that both the transmitter and receiver operate at frequencies of 2.4 Gbit/s, with bit error rates below 10^{-9}.

CONCLUSIONS

A generic processing route has been devised, which enables any combination of hybrid building blocks to be fabricated on a motherboard substrate. Two example modules have been described: an optical bench for high efficiency passive laser to fibre coupling and a high speed transceiver.

REFERENCES

[1] I. F. Lealman, L. J. Rivers, M. J. Harlow and S. D. Perrin, "InGaAsP/InP tapered active layer multiquantum well laser with 1.8 dB coupling loss to cleaved singlemode fibre", Electronics Letters, **30** (20) 1685 (1994).

[2] J. V. Collins, I. F. Lealman, P. J. Fiddyment, C. A. Jones, R. G. Waller, L. J. Rivers, K. Cooper, S. D. Perrin, M. W. Nield and M. J. Harlow, "Passive alignment of a tapered laser with more than 50% coupling efficiency", Electronics Letters, **31** (9) 730 (1995).

[3] C. A. Jones, K. Cooper, M. W. Nield, J. D. Rush, A. R. Thurlow, R. G. Waller, P. J. Ayliffe and P. M. Harrison, "A 2.4 Gbit/s transceiver using silica waveguides on a silicon optical motherboard", Electronics Letters, in the press.

Silica based optical waveguide devices, with novel fiber guide structure for alignment-free fiber coupling

N.Kitamura , S.Mizuta, T.Shimoda and M.Kitamura
Opto-Electronics Research Laboratories , NEC Corporation
4-1-1 , Miyazaki , Miyamae-ku , Kawasaki City ,
Kanagawa 216 , Japan +81-44-856-8087
S.Nakamura
2nd Transmission Division Transmission Operations Unit , NEC Corporation
1753 , Shimonumabe , Nakahara-ku , Kawasaki City ,
Kanagawa 211 , Japan +81-44-435-5664

1. Introduction

Devices with silica based optical waveguides are attracting much attention for various optical communication systems, such as optical subscriber systems, optical interconnects and so on [1-3] . Among them, silica waveguide devices with V-groove fiber guide, giving rise to cost reduction in module assembly, are particularly attractive for optical subscriber systems. However, conventional V-groove design requires precise mask alignment along specific crystal orientation, which may deteriorate total throughput of devices. In this paper, the authors demonstrate silica based optical waveguide devices, with novel fiber guide design. Average coupling loss, as low as 0.36dB, with single mode fiber, has been achieved from 80 individual devices.

2. Silica waveguides with novel Si fiber guides

a) Concept of novel Si fiber guides

For easy coupling between single mode optical fibers(SMFs) and optical waveguides, fiber guides, employing Si V-groove structure, are effective. Optical waveguide devices on Si, with such fiber guide structure have been demonstrated [4] . However, in conventional V-groove structure, very precise mask alignment along specific Si crystal orientation is required. Even subtle misalignment of etching mask, relative to crystal orientation, may cause displacement of optical axis between SMF and optical waveguide, resulting in increasing optical coupling loss(Fig.1a).

To overcome this problem, we propose novel fiber guide with multiple Si mesas (Fig.1b). In our novel structure, the tolerance of etching mask alignment can be much enhanced. The corner of each Si mesa can support SMF in accordance with waveguide optical axis, even if the etching mask is not completely parallel to crystal orientation. Fig.2 shows the SEM photograph of novel fiber guides with multiple Si mesas.

b) Silica waveguide formed by APCVD

To obtain well defined fiber guides, it is preferred that etching masks for the fiber guide are directly formed on Si substrate. Since under clad silica layer needs to be thicker than 10 μ m, etching masks need to be patterned on Si, before silica glass layers are deposited. However, conventional methods of waveguides layer deposition, such as FHD, require high temperature(about 1300℃) treatment [5] , and may deteriorate etching mask quality, resulting in fiber guides deformation.

For well defined fiber guides on Si, we have employed atmosphere pressure

chemical vapor deposition(APCVD). Tetraethoxysilane(TEOS) was employed as precursor. Thick(about 30 μ m) silica glass layers have been deposited at as low temperature as 450℃. Clad layer and core layer consist of Germanium and Phosphorus doped silica glass(GPSG). The difference of refractive index between core layer and clad layer can be controlled by controlling tetramethoxygermanium(TMG) flow rate. For fundamental characterization of optical waveguides, we have fabricated straight optical waveguide structure with fiber guide structure. The core layer is 6 μ m thick and 6 μ m wide. The thickness of under and upper clad layers are 15 μ m and 10 μ m, respectively. The relative refractive index difference was 0.35%. As low as 0.05dB/cm optical propagation loss was obtained at the wavelength of 1.3 μ m.

Process flow, forming waveguide with fiber guide, is shown in Fig.3 . The thickness of the under clad layer need to be controlled precisely, since vertical position of waveguide relative to optical fiber, is determined by this thickness. The APCVD method enables to control the film thickness distribution below 5% on 4 inches diameter Si substrate. After the core layer is deposited, photoresist mask is patterned for waveguide at the position corresponding to the fiber guide. The core layer is etched by reactive ion etching (RIE). After upper clad layer is deposited, the silica layers on the part of fiber guide is removed. Finally using this exposed mask, fiber guide is formed by anisotropic chemical etching.

c) Coupling characteristics with SMF

We have measured straight waveguide devices with fiber guides fabricated by above process, utilizing alignment-free coupling. Fig.4 shows measured insertion loss values as a function of mask pattern width for fiber guide. Single mode fiber was used at input port, and multi mode fiber was used at output port. Insertion losses are measured at 1.3 μ m. The insertion loss includes straight waveguide loss, coupling loss caused by spot size diameter mismatch between waveguide and optical fiber, and excess loss caused by displacement. The waveguide loss and coupling loss are estimated as about 0.05dB and 0.15dB respectively. Therefore excess loss by displacement is deduced as about 0.1dB in case of 126.5 μ m wide pattern. Using optimum mask width, we have fabricated optical waveguide devices. Fig.5 shows the histogram of coupling losses measured for 80 devices. The average coupling loss as low as 0.36dB was obtained.

3. Transmitter/receiver optical module

Using above result, we have fabricated a hybrid integrated bi-directional transmitter／receiver optical module shown in Fig.6 The module consists of LD,PD and optical fiber, which are connected to the waveguide. The waveguide contains Y branch and directional coupler for 1.3 μ m /1.55 μ mWDM. LD and waveguide are connected through short length single mode fiber with hemispherical lens facet. The short length fiber and other fibers are connected to the waveguide using fiber guide fabricated on the Si substrate. Ordinary 1.3 μ m InGaAsP BH-LD and InGaAs PIN-PD were employed. Output optical power from module of more than +0dBm, and conversion efficiency of PD of about 0.25A/W were obtained.

4.Conclusion

The authors have developed silica based optical waveguide devices with novel fiber guide structure fabricated on Si substrate. Optical waveguide are formed by

APCVD method at low temperature. As a result, very low (~0.1dB) excess coupling loss by displacement, between fiber and waveguide, was obtained. Further, using this technique, transmitter/receiver optical modules have been demonstrated.

References:
[1] R.Adar, et al., J. Lightwave Tech., vol.10, pp.46-50, 1992.
[2] M.Okuno, et al., J. Lightwave Tech., vol.12, pp.1597-1606, 1994.
[3] K.P.Jackson, et al., J. Lightwave Tech.,vol.12, pp.1185-1191,1994.
[4] Y.Omori, et al., 6th international workshop on optical access networks, S3.5, 1994.
[5] M.Kawachi, Optical and Quantum Electronics, vol.22, pp.391-416,1990.

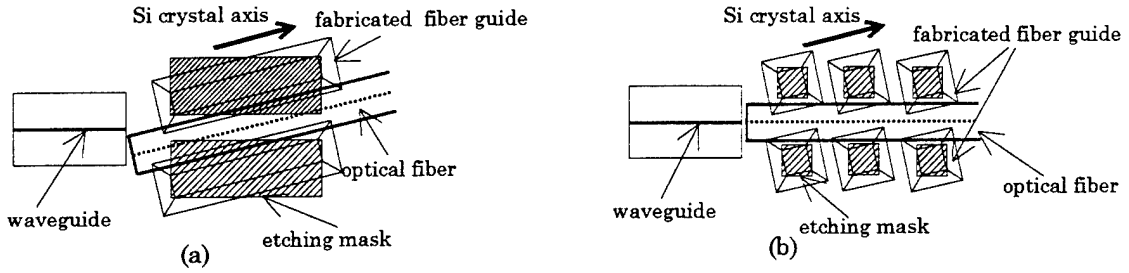


Fig.1 Schematic diagram showing coupling using fiber guide
(a) conventional (b) novel fiber guide

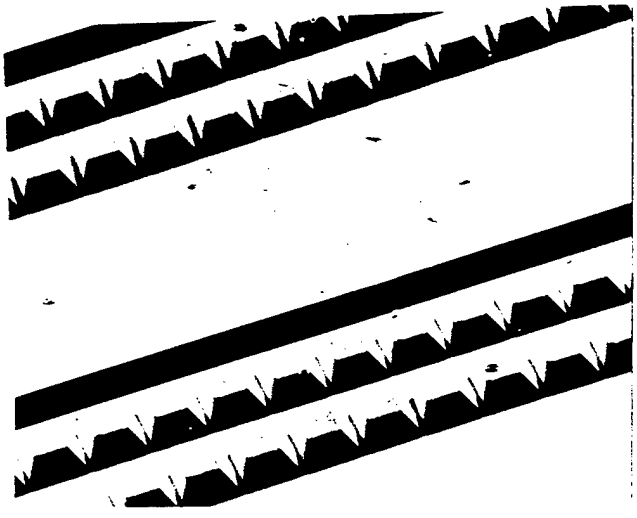


Fig.2 SEM photograph of fiber guide with Si multiple mesas

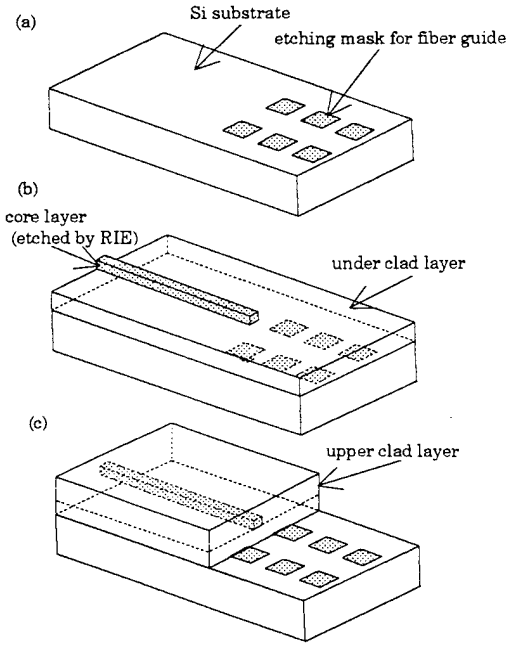


Fig.3 Schematic diagram of process flow

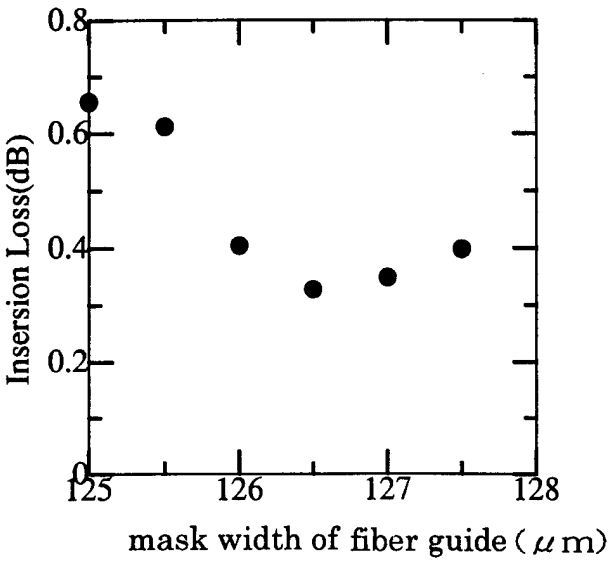


Fig.4 Insertion loss vs. mask width of fiber guide

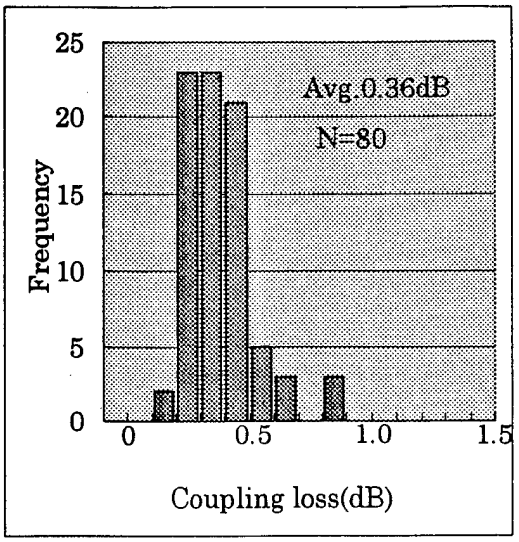


Fig.5 Histogram of couplihg losses

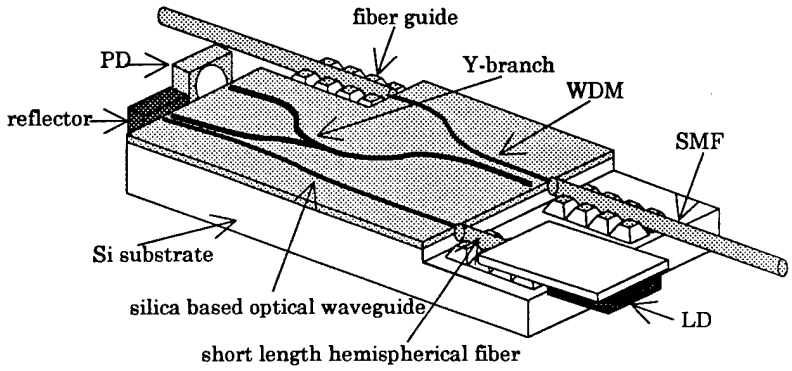


Fig.6 Schematic diagram showing transmitter/ receiver optical module with fiber guide

An Integrated Opto-Electronic Transceiver Module

R.E. Scotti, P.J. Anthony, and J.V. Gates
Lucent Technologies Bell Labs Innovations
600 Mountain Ave. , Murray Hill, NJ 07974 US.
Telephone: 908 582 5675, Fax: 908 582 2024

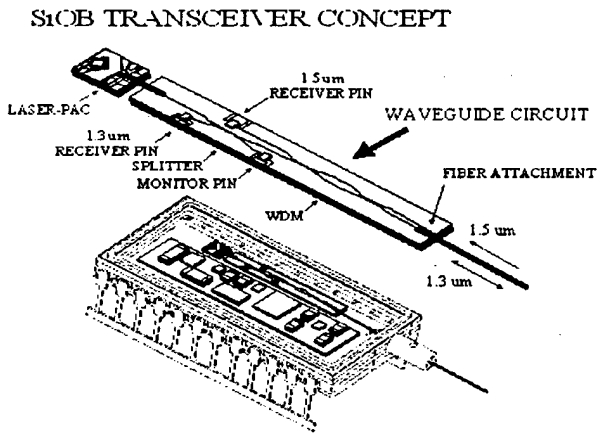
J.Goodwin, D. Siebert
Allied Signal R&T, Government Electronics Systems
Route 48, Teterboro, NJ 07608
Telephone: 201 393 2350, Fax: 201 393 8644

MOTIVATION

The current fiber optic component market has reached a level of maturity in that fiber optics has spread quickly and easily into long haul communication applications and cable TV trunks. The next phase of their deployment could be in connecting the last mile between the outside plant locations and the subscriber. This will require either a significant justification for increased subscriber fees or a large reduction in the cost of these items. The market for fiber optic gyros is in a similar position. Fiber optic gyros present improved performance and increased reliability over existing mechanical gyros, but at an increase in cost. If the cost of the components for both of these applications could be reduced, vast new markets could be available to them. A team, consisting of Lucent Technologies, Bell Labs Innovations (formely the equipment business of AT&T), Allied Signal Aerospace (ASA), and the Advanced Research Projects Agency (ARPA), brought together by the Technology Reinvestment Project (TRP) [1] process aims to bring about this cost reduction through the development of an Integrated Electro-Optic Module (IOEM). In October 1995, Fibersense Technology joined the consortium and is adding their expertise to the venture.

TRANSCEIVER

The prototype opto-electronic module, schematically depicted in Fig. 1, contains a compact optical subassembly (OSA) and either a hybrid electronic circuit or an ASIC circuit organized on a multi-chip module (MCM). The design implements, in a single 24 pin dip package, an encapsulated diode laser source subassembly, a waveguide splitter with two PIN photodiodes mounted on top for a receiver and for a laser monitor, and an external fiber attachment, along with the laser driver electronics, with a feedback stabilization circuit, the receiver pre-amp and post amp, an A-to-D converter and the required voltage regulator circuits. The electrical specification, design and production of the prototype components was provided by Allied Signal. The proposed application for this design is a to replace what is currently an assemblage of



individually packaged components for a reduced cost fiber optic gyro. The current state of the art has separate packages for the source, the receiver, the bi-directional splitter and the electronics. Each optical package contains a fiber pigtail and assembly requires individual fiber attachment to the devices and splicing of the fibers to interconnect devices. The IOEM module eliminates much of the time and cost associated with these processes.

Fig. 1 Silicon Optical Bench Transceiver

SILICON OPTICAL BENCH

The design of the optical subassembly utilizes Lucent Technologies existing Silicon Optical Bench Technology [2]. This technology utilizes 5" silicon wafer processing to implement passive wave guide designs and Si micro-machining for packaging to achieve low cost, high yield component integration. The passive waveguide technology allows for high density distribution of optical signals and functional device integration. The baseline transceiver uses a single fiber bi-directional approach. The main kernel of the design centers around a passive waveguide chip which forms an integrated tap. The waveguide chip (see Fig. 2) contains photolithographically defined waveguides, turning mirrors with metalization for high coupling efficiency (> 75%), metal bonding pads , deposited solders, and solder dams. The waveguides are formed in glass layers grown and deposited on the Si surface through CVD techniques. Standard photolithography is used to define the waveguide position, structure and function. The functions the waveguides perform for this device are simply to split the source light between the monitor photodiode and the fiber output and split off half of the incoming signal to the receiver photodiode. Two ends of the waveguides terminate at fiber attach points and the other two ends terminate at turning mirror structures etched into the glass surface. The PIN photodiodes are soldered over the turning mirrors utilizing a self-centering technique that is made possible by the mask defined metalization and solder. The detectors are tack bonded in position and are aligned during a solder reflow step. Wire bonds are used to make the electrical connections to the P-contact.

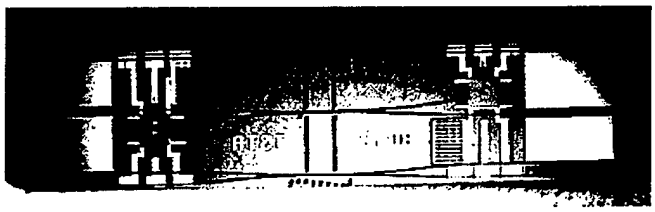


Fig 2. Integrated Tap Waveguide Chip

SiOB piece parts are also used to fabricate the Laser OSA. This component contains metal bonding pads for laser, fiber alignment, thermistor attachment, and electrical routing, deposited solder and solder dams, and heater strips for implementing the solder fiber attachment. The light is coupled from the laser into the fiber using a highly efficient (> 50%) and highly reproducible chemically etched lens at the fiber tip. This source component also forms the kernel of the LASERPAC component (ref. 1) The source is encapsulated with a Si machined lid which protects both the laser and the fiber attachment. This source pill can then be safely handled for polishing and subsequent attachment to the waveguide integrated tap component.

ELECTRICAL

The design includes the light source drive, receiver and source monitor detector signal amplification and filtering, and receiver detector analog-to-digitial (A/D) conversion functions. The circuit design is based on already established fiber optic gyroscope electronics, but will be applicable to a multitude of continuous wave sensor applications. The key element is the selectively coated ceramic metal substrate material. The metal core can be selected to provide the optimum combination of strength, thermal conductivity, and cost. The thin film multichip module allows for high density interconnects. The process is based on photo-definable polyimide dielectric layers. Two forms of the design exist. One is the hybrid layout shown in Fig. 3, with 14 integrated circuits and numerous resistors and capacitors. The other consists of an ASIC design, which integrates all of the above functions onto a single integrated circuit.

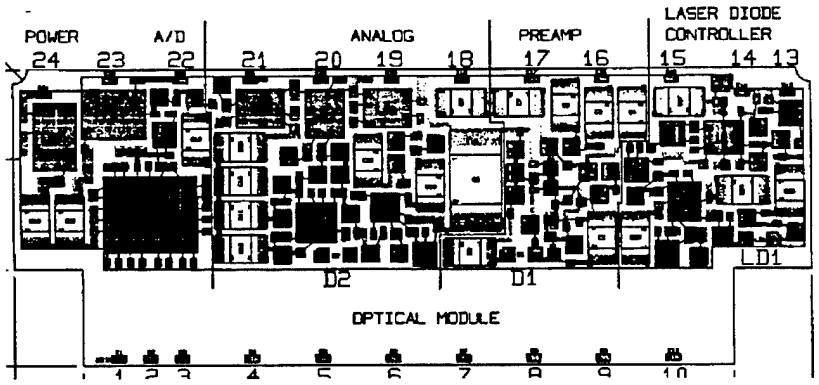


Fig 3. Electrical Hybrid MCM

PERFORMANCE

A completely functional transceiver device has been fabricated utilizing the components described in this talk. The device performance results are listed in the tables below. The transmitter characteristics showed stable optical power output to over 1 mW, and the receiver operated with a responsivity of .38 A/W with a gain of 200,000 in its operating frequency range of up to 1 MHz.

OSA Characteristics:

Optical Power	Current	Monitor	Receiver
1 mW	50 mA	0.32 A/W	0.38 A/W

Transmitter Characteristics:

Optical Power (μW)	Rsat (V)	LD Power (V)	LD Current (mA)	Temperature (Deg C)
100	1.6	3.59	21	22
200	3	3.57	24	22

Receiver Characteristics:

Input Signal (P-P)	Freg. (kHz)	Dmon (P-P)	LP 1 (P-P)	Rise Time (nsec)
125 nW	200	5 mV	1.1 V	500

CONCLUSIONS

A hybrid integrated bi-directional single mode electro-optic transceiver has been fabricated utilizing processes that are consistent with potentially low cost manufacturability for large volume applications. Work continues on implementing the passive attachment of fibers and the integration of passive alignment of beam expanded lasers to the waveguides.

REFERENCES

[1] Technology Reinvestment Project (TRP), Technology Development Agreement between The Integrated Opto-electronic Module Consortium (IOEMC) and The Advanced Research Project Agency Agreement No. MDA972-94-3-0017

[2] C.H. Henry, G.E. Blonder and R. F. Kazarinov, " Glass Waveguide on Silicon for Hybrid Optical Packaging", J. Lightwave Technol., vol. 7, No. 10, October 1989

[3] J.V. Gates, G. Henein, J. Shmulovich, D.J. Muehlner, W.M. MacDonald and R. E. Scotti, "Uncooled laser packaging based on Silicon Optical Bench Technology", SPIE Proc., Vol. 2610, October, 1995

Estimation of waveguide loss of 1.3μm narrow beam lasers fabricated by selective MOCVD

A. Kasukawa, N. Yamanaka and N. Iwai

Yokohama R&D Laboratories, The Furukawa Electric Co., Ltd.

2-4-3, Okano, Nishi-ku, Yokohama 220, Japan

Phone: +81-45-311-1219 Fax: +81-45-322-6961

Laser diodes with a narrow and circular output beam are of great importance because they enable us to get high coupling into single mode fiber with a large alignment tolerance. LDs with mode-field-converter (MFC-LD) to increase the optical spot size are intensively investigated [1]-[4]. Monolithically integrated either vertically or laterally tapered waveguide is usually used for MFC. A simple fabrication of integrated vertically tapered waveguide has been reported utilizing selective area epitaxy of QW structure onto the dielectric patterned substrate [3].

In this paper, we report the estimation of waveguide loss of MFC region and excellent lasing characteristics of 1.3μm MFC-LDs.

The MFC LD, fabricated by use of MOCVD selective area epitaxy, is schematically shown in Fig.1. It consists of gain and MFC regions. Strained-layer five quantum wells (SL-MQW) structure with GRIN-SCH is grown on the patterned substrate with dielectric film. The thickness of the MFC region is about one third that of the gain region. A high resolution scanning electron microscope (HR-SEM) measurement reveals that the thickness distribution of the tapered waveguide along the cavity decreases exponentially.

Figure 2 shows the threshold current density (J_{th}) versus the length of MFC region (L_{wg}) as a parameter of L_{act}. The J_{th} increases with L_{act} for all cases. Assuming the logarithmic gain of the quantum wells, J_{th} is given as follows:

$$J_{th}=N_w J_0 \exp\left\{\frac{\alpha_i+(L_{wg}/L_{ac})\alpha_{wg}+(1/2L_{ac})\ln(1/C^2R_1R_2)}{\Gamma G_0}\right\} \quad (1)$$

Here, N_w is the number of wells, J_0 is the transparent current density per well, G_0 is the gain coefficient, α_i and α_{wg} are the internal loss of the gain and MFC regions, respectively. R_1 and R_2 are the facet reflectivity of the front and rear facets, respectively. Γ is the optical confinement factor of the gain region. C is the coupling coefficient of the electric field between the gain and MFC regions. We assumed C as to be unity since thickness and composition at the jointed section connected smoothly in this manner. From eq. (1), J_{th} increases with L_{wg} and shows small dependence for the longer L_{ac}. If the α_{wg} is a constant value, logarithm of J_{th} ($\ln(J_{th})$) increases linearly in respect to L_{wg}.

However, it is experimentally shown that $\ln(J_{th})$ has a different slope for all L_{ac} at around L_{wg}=100μm. This means that the waveguide loss is not a constant value. If we assume the loss as a function of the distance from the end of the gain region, z as $\alpha_{wg}(z)=\alpha_{wg}(0)\exp(-hz)+\alpha_{wgc}$, we can explain the experimental results. Here, $\alpha_{wg}(0)$, h and α_{wgc} are the constant values. α_{wgc} is assumed to be $10cm^{-1}$, which is a loss value of the GaInAsP layer with a bandgap wavelength of 1.2μm, PL peak wavelength of the MFC region, for the 1.31μm lasing wavelength. If we assume the loss of the MFC region as in Fig.3, calculated threshold current density agrees well with the experimental data as shown in Fig.4. The assumed loss curve coincides with the thickness measurement along the cavity by HR-SEM.

Figure 5 shows the temperature dependence of CW L/I characteristics for a cleave/HR device with L_{act}=700μm and L_{wg}=100μm. The maximum output power over 50mW was achieved from the MFC facet at 25°C. The inset shows the far-field-pattern (FFP) parallel and perpendicular to the junction plane at an output power of 20mW. The full widths at half maximum of FFPs parallel and perpendicular to the junction plane are 11° and 11°, respectively. The maximum operating temperature was as high as 120°C. The characteristic temperature T_0 of 58K is measured in the temperature range of 20-85°C.

In conclusion, waveguide loss of narrow beam lasers using selective MOCVD is experimentally verified for the first time. A low threshold current of 12mA and high output power over 50mW are obtained in a 1.3μm MFC-LD with a narrow beam angle of 11°x11°.

References

[1] T.L. Koch et al., *IEEE Photon. Technol. Lett.*, **2**, pp.88-90, 1990.

[2] I.F. Lealman et al., *Electron. Lett.*, **30**, pp.857-859, 1994.

[3] H. Kobayashi et al., *IEEE Photon. Technol. Lett.*, **6**, pp.1080-1081, 1994.

[4] Y. Tohmori et al., *Electron. Lett.*, Vol. 31, pp.1069-1070, 1995.

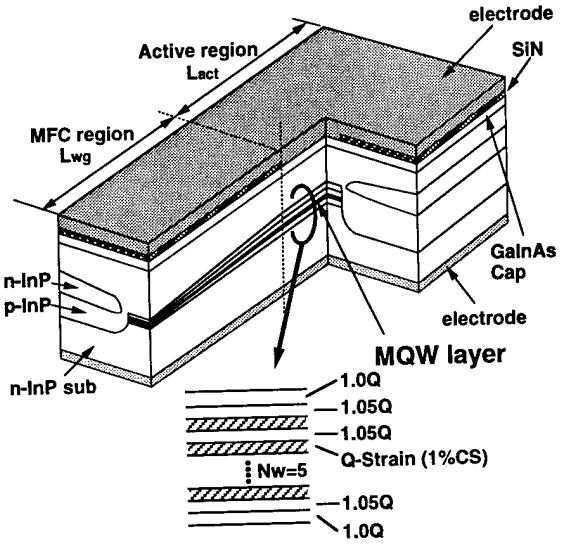


Fig.1 Schematic diagram of a 1.3μm MFC-LD fabricated using selective area growth of MOCVD.

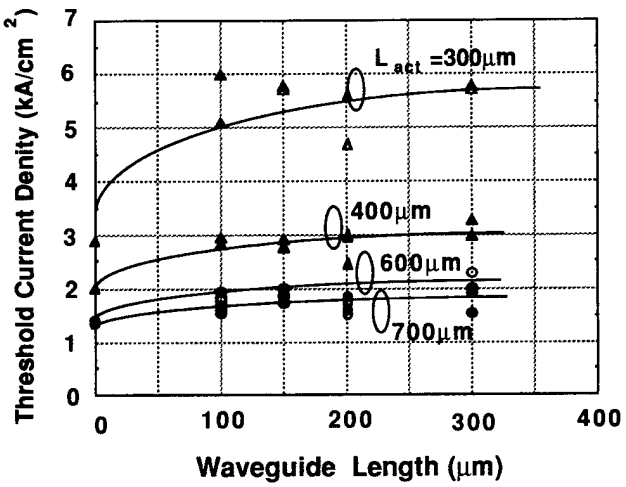


Fig.2 Threshold current density versus L_{wg} as a parameter of L_{act}.

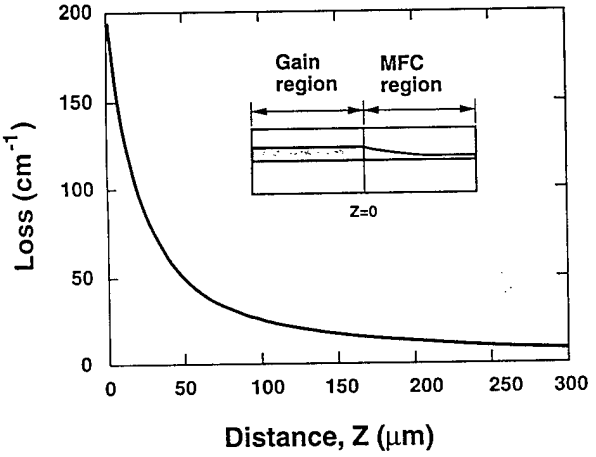


Fig.3 Estimated loss curve of the MFC region. The loss curve is similar to the thickness distribution in the MFC region, measured by HR-SEM measurement.

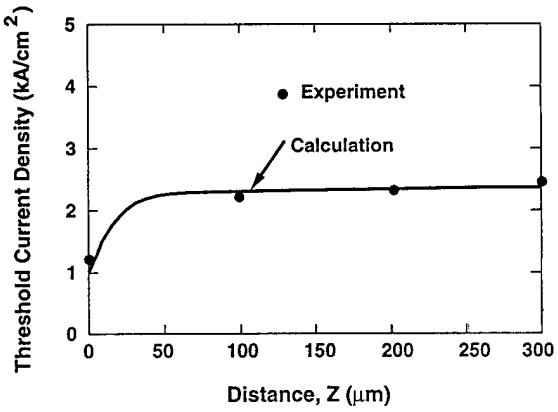


Fig.4 Calculated threshold current density versus waveguide length for a L_{act}=500μm device. Experimantal data are also shown.

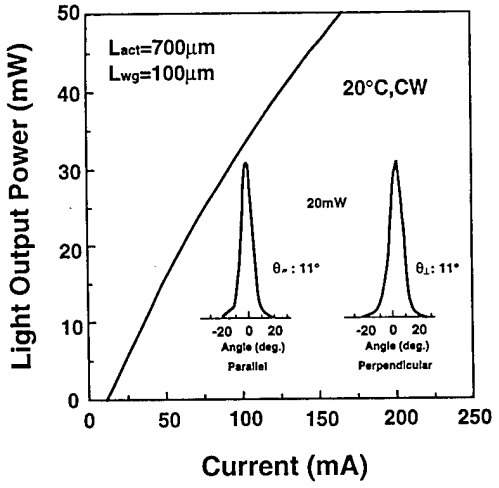


Fig.5 Light output versus injection characteristics of a 800μm-long MFC-LD with HR coating on rear facet. The threshold current is 12mA. Inset shows the FFP pararell and perpendicular to the junction plane. The FWHMs of FFP are 11° (parallel) and 11° (perpendicular), respectively.

Low-loss and low-cost fiber coupling of 980 nm laser diodes

J-M Verdiell, M. Ziari, and D.F. Welch
SDL, 80 Rose Orchard Way, San Jose, CA 95134

Low loss coupling and passive alignment of lasers to single mode fibers are key technologies for opto-electronic packaging. Single-mode fiber coupling of semiconductor lasers usually results in a significant insertion loss of several dB. This excess loss stems from the undesirable waveguide properties of laser diodes. A new design for 980 nm laser featuring low divergence (15°) and low ellipticity (1.5) is presented and shown to result in less than 1 dB coupling loss into a cleaved fiber. The active alignment cost of the single-mode fiber to the laser laser has a important impact on the the cost of photonic packages. We also report on a low-cost packaging technique based on passive alignment of a laser array to a Silica-on-Silicon waveguide array, with 36% coupling efficiency.

Conventional semiconductor lasers support a highly divergent and elliptical mode with a small spot size that does not match the mode size of single mode fibers. The high beam divergence of semiconductor lasers in the vertical direction exceeds the acceptance angle (numerical aperture) of key optical elements such as single mode fibers and many lenses. This large numerical aperture in the perpendicular plane also causes large aberrations in spherical lenses such as ball lenses or lensed fibers with spherical tips and results in large phase front distortion and additional coupling losses. Finally, the beam asymmetry of the laser beam, typically 3:1, seriously degrades the coupling efficiency into single mode optical fibers with symmetric modes. The small waist size also translates into very tight alignment tolerances. Low loss fiber coupling requires lasers with more symmetric circular beams and low vertical divergence angles.

The main challenge of the design large spot size lasers with a circular output beam is to reduce the divergence in the vertical direction. In our structure, the low divergence was achieved solely by waveguide engineering. Mode shaping was obtained by introducing extra layers of low index materials in the structure around the waveguide core, as shown in Fig. 1. As a result, the effective index of the mode is reduced and the mode penetrates further into the cladding (Fig. 1).

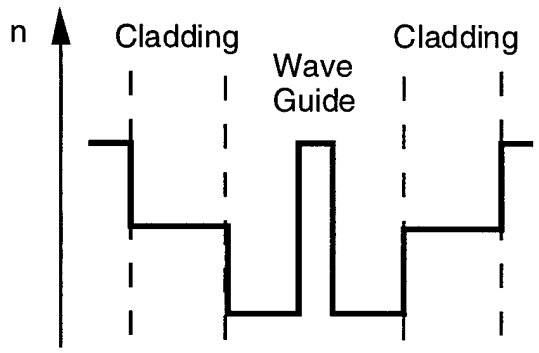


Fig 1) Waveguide structure of a narraow divergence 980 nm laser.

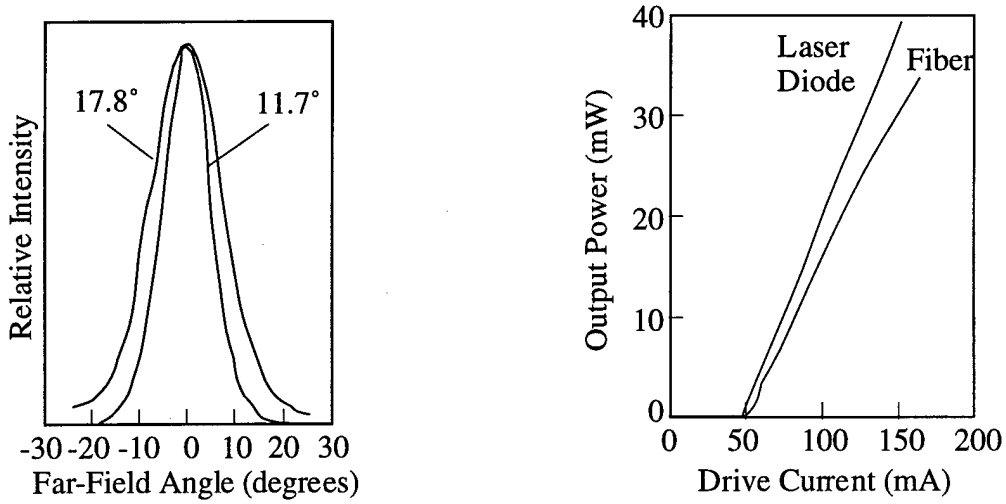


Figure 2a) Measured mode profile of the low-divergence laser. The FWHM divergence angles parallel and perpendicular to the junction are mentioned on the left and right side respectively.2b) Light-current curve demonstrating 80% coupling efficiency between the low divergence laser diode and cleaved PF-1 fiber.

Lasers incorporating this waveguide design were fabricated in GaAs/AlGaAs/InGaAs by MOCVD. The laser characteristics are shown in figures 2. The measured far-field divergence at FWHM is 9×15.2°, with an aspect ratio of only 1.5 .

Figure 2b) also shows the fiber coupling results. The laser was directly butt-coupled to a cleaved single mode fiber (PF-1). A coupling efficiency of 80% or –0.98 dB was measured. This is very close to the estimated theoretical maximum coupling efficiency of -0.68 dB (using overlap integration of Gaussian beam shapes and zero spacing) for this arrangement. One important aspect that has a major impact on the manufacturing cost and performance of a fiber-coupled package is the alignment tolerance. We tested the alignment sensitivity and measured the coupling loss as function of the vertical offset of the single mode fiber from its optimum position. The measured tolerance at ± 1 dB range was 2.4 μm and a ± 3 dB range of 4.45 μm, starting from an absolute minimum coupling of -1 dB.

Another important research direction in photonics packaging is to reduce the cost and time of alignment between the laser and the single mode waveguide or fiber. We report an efficient coupling method from a laser array mounted on a Silica-on-Silicon using an entirely passive alignment method. The passive alignment principle relies on a Silica-on-Silicon platform where etched alignment ridges and optical waveguides match similar grooves etched on the laser diode array. The Silica-on-Silicon chip had three set of features: an array of 4 straight waveguides (500 μm pitch), an array of contact pads to provide bonding area and individual p-down contacting of each element of the array, and alignment ridges on which the matching grooves on the laser were aligned during the passive alignment. The alignment features on the Silicon platform were realized in the same glass

material as the waveguides. All features (waveguide and alignment) were fabricated in the same lithography step and etch, guaranteeing perfect alignment of the rails with respect to the waveguides. In this experiment, the waveguides were not strictly single mode in the lateral direction, but they were single mode in the transverse direction, which is the most difficult to align. An array of four 980 nm laser diode was processed with an additional groove etched on the p-side to match the alignment rails of the carrier chip. Thin solder was patterned on the Silicon carrier over the contact pad with characteristics similar to the solder used for bonding of high-power lasers. The solder was then molten and the laser was lowered onto the Silicon platform and pushed until it clicked into the alignment rails. The mounted array is shown in Fig. 3.

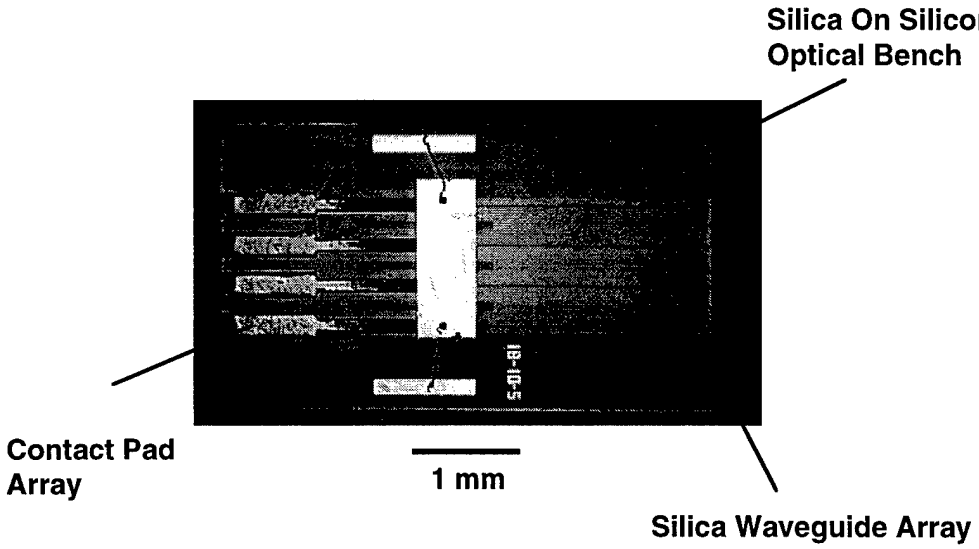


Fig. 3: Mounted array on a Silica on Silicon package.

Three of the 4 lasers were successfully coupled to the waveguides. Excess solder in front of the fourth laser at the edge prevented the light to couple in the last waveguide. The power measured out of the first glass waveguide is compared to the power of an uncoupled laser diode in Fig. 3. A coupling efficiency of about 36% is inferred from these curves. CW measurements revealed that as much as 30 mW were coupled into the waveguide. This indicates good thermal quality of the p-down bonding. Unfortunately, other waveguides were broken in the middle of the chip which prevented the light to reach the ouput and be measured. Scattered light seen by a CCD camera looking from the top of the package indicates that the light was efficiently coupled in waveguide the portion before the break.

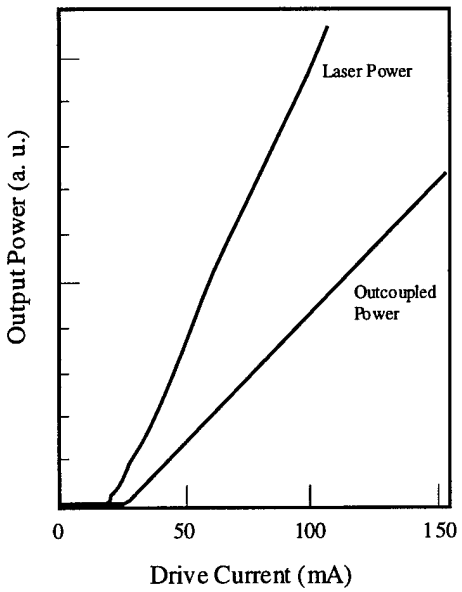


Fig. 4: Light output from one waveguide compared to a diode L-I before coupling suggests 30 % coupling efficiency.

In conclusion, we report on two important packaging techniques:

- a low divergence circularized laser design with a 1 dB coupling loss to a cleaved fiber.

- a passive alignment technique that allows p-down mounting of an array of laser diodes to a Silica-on-Silicon photonic integrated circuit.

These low-loss and low-cost packaging methods are believed to become more and more important for future commercial development of optoelectronics.

References

1 B. Acklin et. al, IEEE Photon. Technol. Lett. **7,** 406-408 (1995).

2 W. Hunziker et. al, IEEE Photon. Technol. Lett. **7,** 1324-1326 (1995).

3 A. P. McDonna and B. M. Macdonald, in *Optical components technologies for FTTH applications*, Las Vegas, NV, 1995.

Switches and Modulators

IThC 10:30 am-11:45 am
Fairfax A

Catherine H. Bulmer, *Presider*
U.S. Naval Research Laboratory

Reflective Linearized Modulator

G.E. Betts, F.J. O'Donnell, K.G. Ray
Lincoln Laboratory, Massachusetts Institute of Technology
Lexington, MA 02173-9108
(617) 981-4429 FAX (617) 981-5793

D. K. Lewis, D. E. Bossi, K. Kissa, and G. W. Drake
Uniphase Telecommunication Products (UTP)
1289 Blue Hills Ave., Bloomfield, CT 06002
(203) 769-3058 FAX (203) 769-3007

Linearized modulators are desirable for improving the dynamic range of fiber optic links used in analog applications such as cable TV transmission, distributed antenna networks for cellular telephone systems, phased-array antenna control, and other antenna remoting applications. We report here a very simple and practical modulator that is useful in many of these applications.

A variety of linearized modulator designs that reduce both second- and third-order distortion have been proposed, and some demonstrated, over the last several years. These generally have proven so difficult to build and/or control that they have not been used much in practical systems. Also, these broadband linearized designs all involve some penalty in modulator response compared to standard designs such as the Mach-Zehnder interferometric modulator. Many of the analog applications mentioned above require only a sub-octave bandwidth, so second-order distortion signals fall out of the system's frequency range and can be ignored. Modulators designed to reduce only third-order distortion, such as the devices reported here, are much simpler than broadband linearized modulators and can be made with no penalty in response.

The connection of two standard Mach-Zehnder interferometers (MZ) in series [1], as shown in Fig. 1, efficiently reduces third-order distortion. The two bias points ϕ_1 and ϕ_2 and the voltage splitting ratio r can be adjusted so the third derivative of the electrical-to-optical transfer function is zero, which reduces the third-order distortion (it does not eliminate it because some still comes from fifth-degree and higher terms). This modulator is a simplification of the broadband linearized series interferometer [2], in which the extinction of one MZ must be reduced to achieve simultaneous second-order linearization. There are a variety of choices for r, ϕ_1 and ϕ_2 that give linearization. The second modulator must be driven in phase with the first, though. If we require r=1 and $\phi_1=\phi_2$, the modulator is symmetric. With these additional constraints, there is a unique solution, $\phi_1=\phi_2=104.5°$. In this case, the series MZ can be cut in half and a mirror placed in the middle. Input light travels through the modulator, is reflected, and travels through the modulator again, giving the desired series effect. The fundamental drawback to this simple lumped-element design is that the second modulator is no longer driven in phase with the first. The light is delayed by the transit time to the mirror and back. This limits the frequency at which the linearization works; we will discuss this further below. The big advantage to using the mirror is that the modulator is now as simple as a standard MZ modulator:

it has one electrical input, one bias point to control, and the third-order distortion has a single minimum in the $0°<\phi_1<180°$ range so it is easy to find.

We fabricated the double-Y devices (the type shown in Fig. 2) on $LiNbO_3$ using Ti-indiffused waveguides. The fiber-to-fiber loss of the modulator was ≈7.0 dB. We tested the devices in an analog link by using an optical circulator to separate the input and output light, as shown in Fig. 2 (the circulator added 2.6 dB optical loss). In a two-tone intermodulation test, the third-order intermodulation signal falls as the fifth degree of the input power, as expected for a linearized modulator. The dynamic range was 85.5 dB for a 1 MHz noise bandwidth; for modulation depths where the fifth-degree slope holds, the bandwidth-normalized dynamic range was 134 dB-$Hz^{4/5}$. At 405 mW optical input power (1321 nm Nd:YLF laser), a link noise figure (no amplifiers!) of 6 dB was achieved at 150 MHz with a resonant impedance-matching circuit connected to the 36-mm-long modulator electrodes [3]. This very low noise figure is due to a combination of the high optical power, the lack of a response penalty for linearization, and the very low V_π of 470 mV with the resonant circuit (V_π at dc, without the matching circuit, was 1.4V). At the 1 MHz noise bandwidth, a bias error of ±2° reduced the dynamic range by about 5 dB, eliminating only half of the 11 dB dynamic range advantage this device has over a standard MZ. We normally control the bias point to within ±0.5°, so the bias control tolerance required is easily achieved.

The experimental devices were designed for applications below 500 MHz, and had very long electrodes and long distances to the mirror which limited their dynamic range improvement to low frequencies because of the phase error mentioned above. The devices with 36 mm electrode length (33 mm electrode-center-to-mirror distance) had their dynamic range degraded by 3 dB at 300 MHz, and devices with 18 mm electrode length (24 mm electrode-center-to-mirror distance) had their dynamic range degraded by 3 dB at 500 MHz. This roughly agreed with our theoretical calculations. With shorter electrodes and shorter electrode-to-mirror distances, lumped-element mirrored devices on $LiNbO_3$ should be able to linearize at frequencies up to 2 GHz. If the devices were built using semiconductor integrated optics, where much shorter devices can be made, the useful frequency range could be extended to several GHz.

The device shown in Fig. 2, which used a Y-branch to split the light at both ends of the interferometer, is inflexible in two ways: it requires a circulator, and it allows only one choice of bias point. The circulator is expensive and has a small leakage of light from port 1 to port 3. The light leakage provides a second path to the detector from the laser, and the interference between this and the main path produces a small amount of intensity noise at very low frequencies (a typical number is -70 dB/Hz at 100 Hz). The 104.5° bias point results in 14% dc optical transmission; this is actually too high when one is trying to get optimum performance by biasing for a very low transmission [4]. To address these concerns, we developed the half-coupler device shown in Fig. 3. (Simply replacing both Y branches with couplers does not give the required flexibility: linearized light will still come back only on the input fiber unless both outputs at the mirror end are reflected back, which requires a separate phase adjustment and makes the device complicated.)

The half-coupler device allows linearized light to be returned on a fiber separate from that of the input light, so no circulator is required. The electrical-to-optical transfer function is adjustable by adjusting the values of the coupling angles Θ_1 and Θ_2. (The coupling angle Θ is the product of the coupling coefficient and the length; the optical crossover fraction is $\sin^2\Theta$.)

Θ_2 here refers to the total value due to transmission through the half-coupler to the mirror and then back through it again. If Θ_1=22.5° and Θ_2=45°, the transfer function is exactly like that of the double-Y device, with a linearizing bias point of 104.5° phase difference between the interferometer arms. We built devices with Θ_1=26.5° and Θ_2=37.5°, where the linearizing bias point was 98.3° and the dc optical transmission was 7.5%, which gave better performance in our analog links. There is a linearizing bias point for a wide range of combinations of Θ_1 and Θ_2, although the link performance is poor for some choices. Although this device is complicated to analyze and design, it operates much like the double Y: a single bias adjustment is all that is required, and there is a single linearizing bias point in the $0°<\phi<180°$ range.

The half-coupler modulators were fabricated on $LiNbO_3$ with annealed proton exchange waveguides. The half-coupler itself was fabricated by first making a normal coupler with coupling angle Θ_2, then cutting it exactly in half and putting a mirror on it. If done exactly right, the mirrored half-coupler still has a coupling angle Θ_2. We found that a length tolerance of ±30μm was required to achieve the ±5° tolerance we required on Θ_2. The mirrors were fabricated by metallizing a fiber coupling block (a polished 1-mm cube of $LiNbO_3$) with gold and attaching it to the end of the modulator. These devices also had detectors bonded to the top surfaces of their input and output waveguides to tap off a small amount of power to sense the modulator bias point. The initial devices had electrode lengths of 18 and 36 mm, and the total fiber-to-fiber loss of the first devices was 5.3 to 6.3 dB.

The half-coupler modulators were tested in analog links with performance results similar to those reported above for the double-Y devices. We used optical power as high as 320 mW, and achieved two-tone, third-order intermodulation free dynamic ranges of up to 85 dB. These devices showed an unusual optical damage effect that we did not see with the other reflective linearized designs. When powered with a single-frequency or nearly single frequency laser, the transfer function shape changed over time with powers as low as 80 mW input. There was always a linearizing point, but when this type of drift occurred, the bias had to be controlled with an active feedback loop to keep the third harmonic minimized. This damage did not occur when a multimode laser was used, even at much higher power. Our conjecture at this point is that a photorefractive grating is being created when a single frequency laser is used, and that the grating cannot form efficiently when too many laser frequencies are present. This device design is more sensitive than the double-Y design to a small additional reflectivity within the waveguides.

REFERENCES

[1] G.E. Betts, "A linearized modulator for sub-octave-bandpass optical analog links," *IEEE Trans. Microwave Theory Tech.*, vol. 42, pp. 2642-2649, 1994.

[2] H. Skeie and R. V. Johnson, "Linearization of electro-optic modulators by a cascade coupling of phase modulating electrodes," *Proc. SPIE*, vol. 1583, pp. 153-164, 1991.

[3] G. E. Betts and F. J. O'Donnell, "Improvements in passive, low-noise-figure optical links," presented at Photonics Systems for Antenna Applications V, 18-20 January 1995.

[4] M. L. Farwell, W. S. C. Chang, and D. R. Huber, "Increased linear dynamic range by low biasing the Mach-Zehnder modulator," *IEEE Photon. Tech. Lett.*, vol. 5, pp. 779-782, 1993.

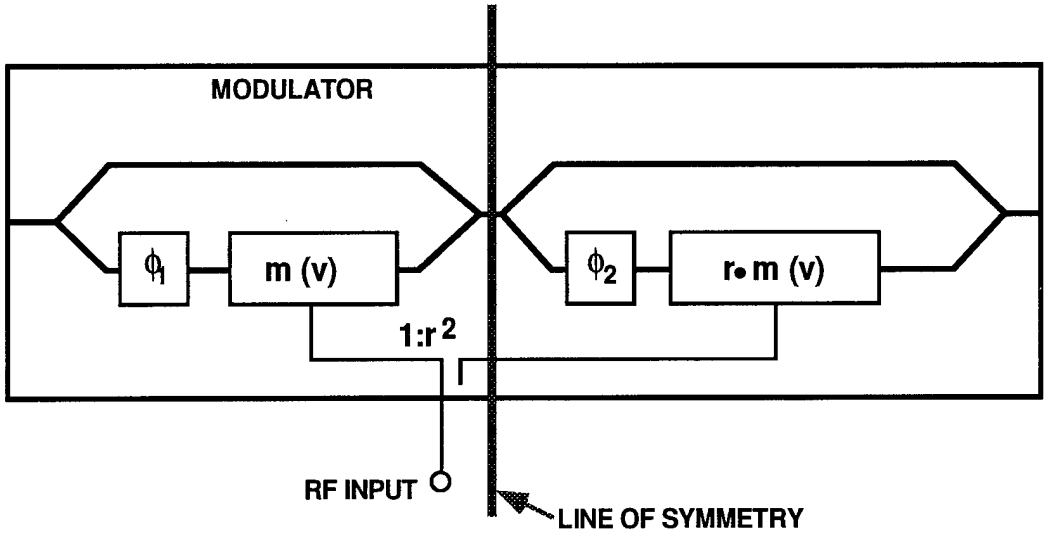


Fig. 1 The series linearized modulator is symmetric about the center if the bias points $\phi 1$ and $\phi 2$ are equal and the voltage ratio r=1.

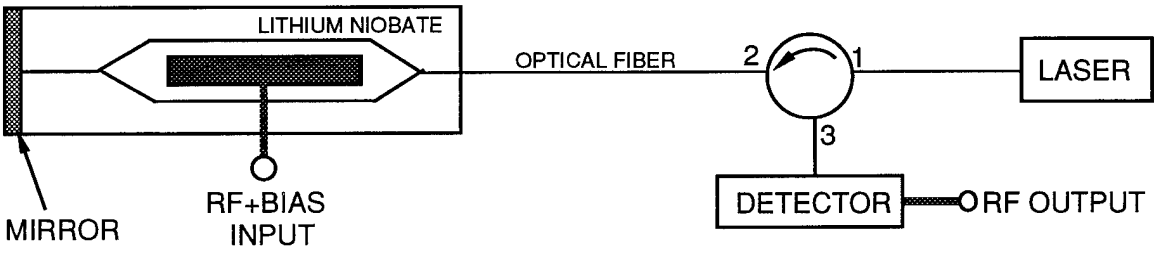


Fig. 2 Initial reflective linearized modulator design requiring optical circulator.

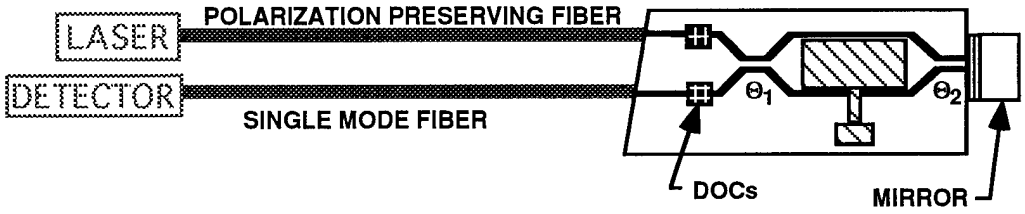


Fig. 3 The half-coupler modulator. DOC refers to detector-on-chip.

Space Switching and Wavelength Routing with Polymer Components

Marc Donckers

Akzo Nobel Photonics
PO Box 9300, 6800 SB Arnhem, The Netherlands

Introduction

After a decade of research, polymer-based components such as passive couplers and splitters and also optical fiber have matured and are now commercially available. Recently, space switches were added to this list after Akzo Nobel's introduction of their Solid State Optical Switches. These single-mode switches combine wavelength- and polarization-independent switching characteristics with a switching time of 1 ms [1,2]. The need for switching in the optical domain is increasing rapidly with the growing importance of protection switching and dynamic reconfiguration of fiber-optic networks. To further utilize network capacity, the use of multiple wavelengths (WDM) is expanding [3,4]. The first polymer-based wavelength multiplexers have been demonstrated by NTT as well as Akzo Nobel [5,6]. Below, recent developments in polymeric space switches and wavelength multiplexers are reviewed. First, the breakthroughs in polymer properties that enabled the development of the aforementioned components are summarized.

State of the art polymers for integrated optics

A polymer system with low light loss is a prerequisite for the fabrication of practical integrated-optic components. Channel waveguides with a loss of 0.1 dB/cm at 1.31 μm have been reported by Imamura et al. [7]. At 1.55 μm, the loss of those polymers was estimated to be above 0.4 dB/cm or more. More recently, Akzo Nobel has developed a polymer system with a loss of 0.15 dB/cm or less (as measured in a thin film) in both the 1.31-μm and the 1.55-μm window [8]. The refractive index of these materials can be tuned between 1.48 and 1.54, allowing for the fabrication of channel waveguides with a mode that is nearly perfectly matched to that of a single mode fiber. In addition, these polymers are chemically stable and can be used at temperatures well above 100 °C.
One method for device fabrication is based on spincoating a cladding/core/cladding structure on a Si or other substrate. Channel waveguide can be defined in the polymeric multilayer by photobleaching of chromophores contained in the core layer or by reactive-ion etching [9]. Alternatively, waveguide grooves can be made in a polymeric substrate by means of injection molding, embossing, or reactive-ion etching. These grooves are subsequently filled with a second (reactive) polymer [10].

Space switches

For their operation, most polymer-based space switches rely on the thermo-optic effect, which is particularly large for polymers ($dn/dT \sim 10^{-4}$). Two fundamentally different

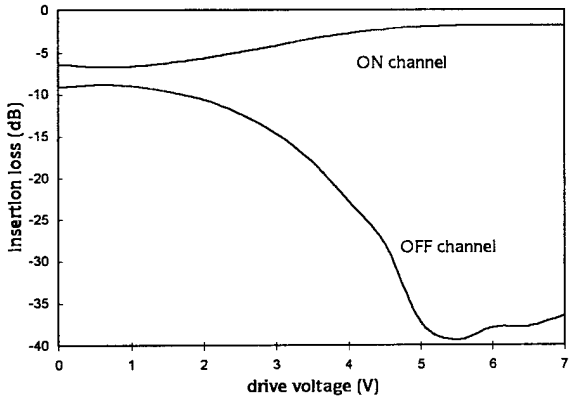


Figure 1:
Switching chracteristic of 1x2 Solid State Optical Switch at 1.55 μm

categories can be discerned: interferometric switches and digital switches. Interferometric switches are based on thermo-optic phase modulation in a directional coupler, a concept which has been explored by Imamura et al. at NTT [11] and Keil et al. at the Heinrich Hertz Institute [12]. These switches are compact and the power consumption is low, but the performance is susceptible to changes in environment, drive signal, and polarization and wavelength of the light. As a consequence, active bias control is needed to warrant stable operation and simultaneous use at 13.1 μm and 1.55 μm is not possible. In addition, the extinction ratio is typically limited to about 20 dB.

In digital switches, thermo-optic control of the mode evolution in an adiabatic Y-branch is used [1]. Selective heating of one of the arms of the Y-branch results in a local decrease of the refractive index such that the propagating light is switched to the other arm. This concept was first pioneered by Akzo Nobel and PTT Telecom of the Netherlands, and more recently the Technical University Berlin also reported results on digital switches. The first commercial 1x2, 1x4, 1x8, and 2x2 digital switches became available in 1995 [2]. These switches exhibit a quasi digital switching characteristic (figure 1) that is essentially the same in the 1.31-μm and the 1.55-μm communication window. The extinction ratio is better than 30 dB and the ON-state insertion loss is polarization independent, ranging from < 2 dB for the 1x2 switch to < 5 dB for the 1x8 switch.

Wavelength multiplexers

The first phased array wavelength multiplexer in polymer was demonstrated in 1994 by Imamura et al. of NTT [5]. This component was intended for operation at 1.31 μm. More recently, Akzo Nobel realized a 8x8 phased array wavelength multiplexer for operation in the EDFA window around 1.55 μm [6]. The transmission characteristics of this prototype are shown in figure 2. The channel spacing is 3.2 nm, as designed. The crosstalk between the channels is better than -20 dB. Due to birefringence in the polymer films that were used for this first prototype, the transmission characteristics exhibit some polarization dependence, which is responsible for the asymmetry in the transmission peaks.

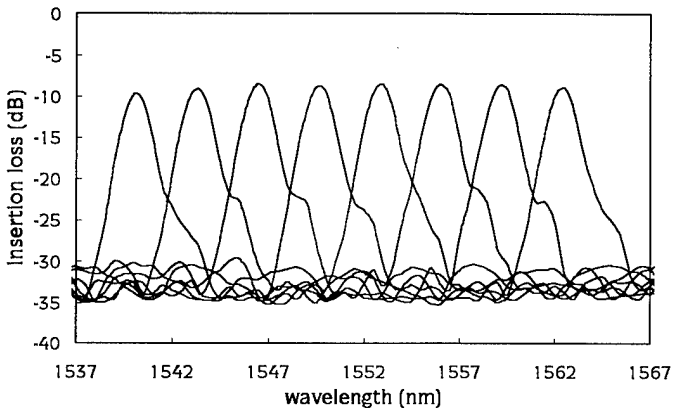


Figure 2: Transmission characteristic of 8x8 polymer-based phased-array wavelength multiplexer.

Conclusion

Competitive polymer-based Solid State Optical Switches are available and wavelength multiplexers are under development. The demand for these components is rapidly growing with the increasing importance of protection switching and dynamic network reconfiguration and with the advent of WDM systems. The versatile processing technology of polymer components allows for flexible scaling and integration of the switching and multiplexing functionality. Polymer-based switches and wavelength multiplexers can therefore be tailored for deployment in optical cross connect systems and wavelength add-drop multiplexers.

References

1) H.M.M. Klein Koerkamp, M.C.J.M. Donckers, B.H.M. Hams, W.H.G. Horsthuis, H. Lausen, T. Klein, and L. Bersiner, *Integrated Photonics Research*, San Francisco 1994, Technical Digest Series Volume 3, p. 274
2) W.H.G. Horsthuis, B. Hendriksen, M.B.J. Diemeer, M.C.J.M. Donckers, T.H. Hoekstra, H.M.M. Klein Koerkamp, G.F. Lipscomb, J. Thackara, T. Ticknor, and R. Lytel, European Conference on Optical Communication, Brussels 1995
3) Scott Kingsley, *Business Communications Review*, June 1994, p.61
4) Charles A. Brackett and Matthew S. Goodman, *Exchange*, February 1994, p. 14
5) Y. Hida, Y. Inoue, and S. Imamura, *Electron. Lett.* 30 (1994) p. 959
6) Paper submitted for pressentation at *Integrated Photonics Research 1996*
7) S. Imamura, R. Yoshimura, and T. Izawa, *Electron. Lett.* 27 (1991) p. 1342
8) M.B.J. Diemeer, T. Boonstra, M.C.J.M. Donckers, A.M. van Haperen, B.H.M. Hams, T.H. Hoekstra, J.W. Hofstraat, J.C. Lamers, W.Y. Mertens, R. Ramsamoedj, M. van Rheede, F.M.M. Suijten, U.E. Wiersum, R.H. Woudenberg, B. Hendriksen, W.H.G. Horsthuis, and H. M.M. Klein Koerkamp, *Proceedings SPIE*, San Diego, USA, 1995
9) M.B.J. Diemeer, F.M.M. Suijten, E.S. Trommel, A. McDonach, J.M. Copeland, L.W. Jenneskens, and W.H.G. Horsthuis, *Electron. Lett.* 26 (1990) p. 379
10) A. Neyer, *Integrated Photonics Research*, San Francisco 1994, Technical Digest Series Volume 3, p. 268
11) Y. Hida, H. Onose, and S. Imamura, *IEEE Phot. Technol. Lett.* 5 (1993) p.782
12) N. Keil, H.H. Yao, C. Zawadzki, and B. Strebel, *Electron. Lett.* 30 (1994) p. 639

Low crosstalk polymer waveguide optical switch and switching matrix

N. Keil, H. H. Yao, C. Zawadzki

Heinrich-Hertz-Institut für Nachrichtentechnik Berlin GmbH
Department Material Technology
Einsteinufer 37, D-10587 Berlin, Germany
Tel.: 00 49 30 31002 590; Fax: 00 49 30 31002 213
e-mail: keil@hhi.de; yao@hhi.de; zawadzki@hhi.de

Introduction:

Polymer waveguide thermo-optic (TO) space switching elements show great promise for practical integrated photonic applications [1 - 4]. These devices are expected to be employed in future optical telecommunication systems as routing elements in optical cross-connects. One of the challenges of the optical waveguide space switches is to reduce the crosstalk which is vital to all-optical communication networks. All-optical communication networks have not been implemented in the real world because of the lack of a compact, low cost switching matrix with low crosstalk and insertion loss. For system applications, the crosstalk of a switching matrix should be < -30 dB, leading to the requirement for a single switching element to exhibit values < -40 dB. Up to now, such a switch can be only realized by fiber mechanical devices which, however, are bulky and not suitable for large switching matrices used in telecommunications. The switching matrix suitable for communications may be realized by integrated photonic technologies. The first polymer based (4x4)-switching matrix which integrated eight (2x2)-directional coupler switches and operated at λ = 1.55 µm was reported in 1995 [3]. Due to the asymmetrical heating electrode configuration employed, crosstalk in the unbiased 'cross' state turned out to be limited to typically -25 dB, leading to a minimum crosstalk value of only -21.5 dB in the (4x4)-matrix. Low crosstalk in conjunction with low switching power operated at λ = 1.3 µm was obtained by NTT using a Mach-Zehnder interferometer (MZI) switch in 1993 [1]. However, in comparison with a directional coupler type switch the total length of a MZI is about three times as large which renders this type of switch less suitable for the implementation of larger switching matrices.

Here we demonstrate for the first time a polymer TO (2x2)-directional coupler switch exhibiting an extremely low polarization independent crosstalk value of < -40 dB by using a novel electrode configuration to combine the symmetrical and the asymmetrical version of a coupler switch into one switch. The measured crosstalk values are -42 dB at 'cross' state and -45 dB at 'bar' state. The required switching power amounts to only 3 mW and 20 mW respectively. A rearrangeable nonblocking (4x4)-switching matrix incorperating eight of these new switches has also been fabricated. The whole switching matrix exhibits a crosstalk of <-30 dB for all switching states. To the best of our knowledge these data represent the best crosstalk performance hitherto reported for polymer based switching devices.

Design consideration:

It is well known that optical directional couplers are characterized by (1) the interaction length, L, (2) the coupling coefficient, κ, or the corresponding conversion length $L_C = \pi/2\kappa$ which gives the minimum length required to obtain complete crossover, and (3) the propagation constant mismatch between waveguides WG1 and WG2, $\Delta\beta = \beta_1 - \beta_2$. For an asymmetrical coupler switch to obtain the perfect 'cross' state the exact odd-integer values of L/L_C must be ensured during device fabrication. There is no means of electrical adjustment to compensate for fabrication errors. The conventional TO coupler switch reported in [3] exhibited an unsatisfactory crosstalk value at the unbiased 'cross' state due to fabrication tolerances. On other hand, a symmetrical type coupler switch can reach the perfect 'cross' and 'bar' states by changing β_1 and β_2 simultaneously to keep $\Delta\beta = 0$ and to change the ratio L/L_C from an odd-integer ('cross' state) to an even-integer ('bar' state), or reverse. For inducing this change in L_C, the symmetrical coupler switch needs high switching power. In order to obtain a switch with low crosstalk values at both the 'cross' and the 'bar' state and with low switching power, we have designed a coupler switch operating as a symmetrical version coupler ($\Delta\beta = 0$) at low bias to turn the coupler to the perfect 'cross' state and then as an asymmetrical version coupler ($\Delta\beta \neq 0$) to reach the 'bar' state at a low switching power level. For this purpose, the coupler has been designed with an interaction length L slightly longer than the corresponding conversion length L_C to assure that only a small increment in L_C can drive the switch into its perfect 'cross' state. A metal TO electrode has been employed with features two parallel branches on top of the two waveguides WG1 and WG2, interconnected at the common earth E. The electrode is shifted by a small distance Δ (~ 0.5 µm) to the left with respect to the waveguides. The switching power can be applied to branch E1 or branch E2. Fig. 1 shows the schematic layout and the cross-section AA' of the coupler switch.

Due to the high thermal conductivity of the metal electrode the temperature of the right branch E2 will be raised even if only the left branch E1 is heated. Combined with the small shift Δ, the propagation constants β_1 and β_2 of the two waveguides will be

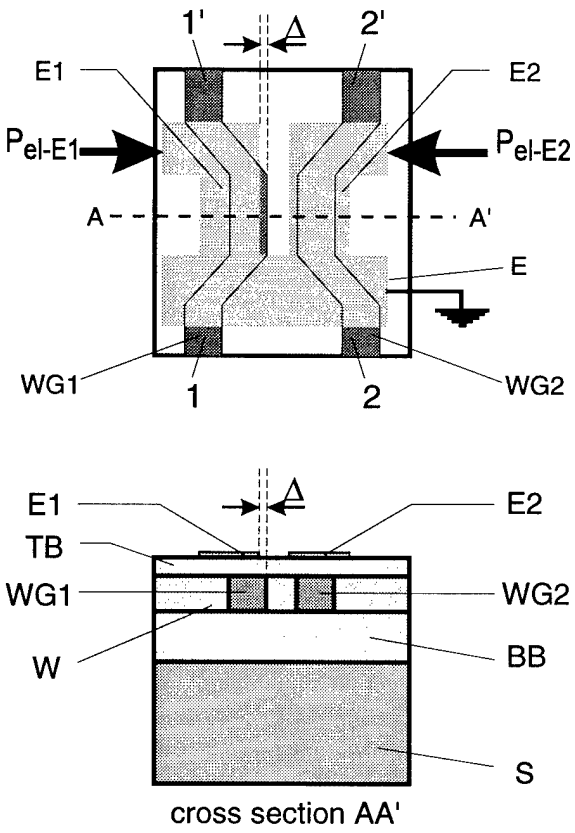


Fig. 1: Schematic layout and cross section AA' of a polymer waveguide TO switch with a noval electrode configuration.

changed almost synchroneously to keep $\Delta\beta \cong 0$ when the applied heating power is at a very low power level. The change of the propagation constants leads to a change in the conversion length L_C. Because the interaction length of the switch is very near the conversion length, only a slightly change ΔL_C suffices to drive the switch into the perfect 'cross' state. By increasing the heating power the temperature difference between the two branches E1 and E2 will be dominant leading to $\Delta\beta \neq 0$. The switch behaves asymmetrically to reach the 'bar' state. Therefore, it can be expected that this switch can reach the 'cross' and the 'bar' states even if only the left branch E1 is fed with the heating current whereas the branch E2 is kept electrically open.

Experimental results:

The switches were fabricated using a standard fabrication process as described previously [4]. The multi-layer structure is shown in Fig. 1. The polymer TO switch consists of a substrate (S), a bottom buffer layer (BB), a waveguide layer (W), a top buffer layer (TB) and the TO electrode branches (E1 and E2). In order to characterize the switch, light from a 1.55 µm laser diode was coupled into port 1, and the optical output power at port 1' (through port) and 2' (coupled port) was measured at TE and TM polarization, showing < ±0.5 dB polarization dependence. Therefore only the measurement results for the TM polarization are presented.

Fig. 2 shows the measured results when only the branch E1 is heated. The device is switched into perfect 'cross' state first, reaching an extinction ratio of -42 dB at 3 mW. If the accuracy of the heating power is kept within ±0.4 mW (±13%) around the working point, a crosstalk value of < -30 dB can be guaranteed. By increasing the power the device is switched into its 'bar' state with an extinction ratio of -45 dB at 19.7 mW. Here to guarantee a crosstalk of < -30 dB, the accuracy of the heating power has to be adjusted within ±1 mW (±5%) relative to the working point. This result confirms that the switch combines the advantage of a symmetrical switch to achieve low crosstalk in the 'cross' state and the advantage of an asymmetrical switch to reach the 'bar' state with low switching power.

A fibre-to-fibre insertion loss of 6 dB of which some 4 dB is estimated to be due to fiber-chip coupling was measured at λ = 1.55 µm on a 20 mm long chip. The waveguide loss at λ = 1.55 µm was determined to be 0.85 dB/cm. The length of the switch is only 7 mm, and the response time of the device is less than 1 ms.

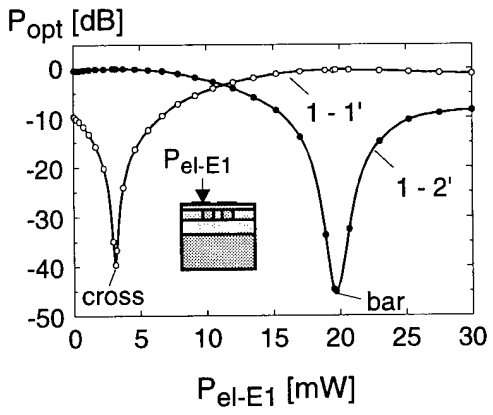


Fig. 2: Measured transfer characteristics; heating power applied to left branch E1.

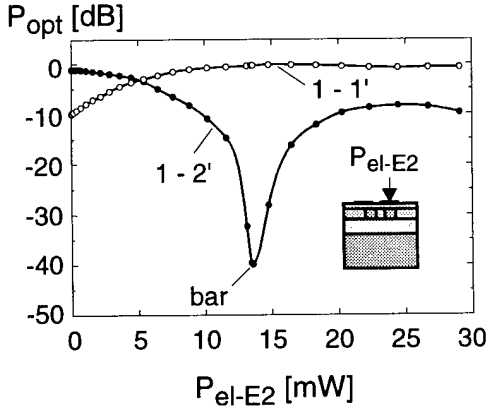


Fig. 3: Measured transfer characteristics; heating power applied to right branch E2.

Fig. 2 shows that the initial crosstalk value of the coupler switch is only -10 dB. We have found that, in order to achieve low crosstalk values at both the 'cross' and the 'bar' state, the maximum deviation ΔL of the coupler interaction length from the conversion length L_C may be as high as 25% of L_C. Therefore, this new type of switch shows high fabrication tolerance in the manufacturing process. If the right branch E2 is powered, the switch behaves asymmetrically even at a very low power level and cannot reach the 'cross' state, as is confirmed by the measurement results shown in Fig. 3.

Due to the excellent device performance, compactness and high fabrication tolerance, this (2x2)-switching element is considered to be a highly suitable building block for constructing larger polymer based switching matrices. A rearrangeable nonblocking (4x4)-switching matrix consisting of eight of the new (2x2)-switches described above has been fabricated and tested. The preliminary results show that the new matrix exhibits a crosstalk of < -30 dB for all switching states which is about 10 dB lower than with the previous matrix incorporating conventional switches [3]. The performance of the switch and switching matrix can be further improved through the optimization of the switch structure, such as the shift Δ, the electrode and waveguide dimensions.

Conclusion:

We have demonstrated a novel type of polymer waveguide integrated photonic (2x2)-switch which exhibits extremely low polarization independent crosstalk (< -40 dB) in conjunction with low electric power consumption at λ = 1.55 µm. A (4x4)-rearrangeable nonblocking switching matrix which consists of eight of these switches has been demonstrated to show very low crosstalk levels (< -30 dB) as well.

References:

[1] HIDA, Y., ONOSE, H., and IMAMURA, S.: 'Polymer waveguide thermooptic switch with low electric power consumption at 1.3 µm', IEEE Photonic Technol. Lett., Vol. 5, pp. 782-784, 1993.

[2] HORSTHUIS, W., HENDRIKSEN, B., DIEMEER, M., DONCKERS, M., HOEKSTRA, T., KOERKEMP, M. K., LIPSCOMB, F., THACKARA, J., TICKNOR, T., LYTEL, R.: 'Packaged polymeric 1x8 digital optical switches', ECOC'95, Postdeadline Papers, pp. 1059-1062, 1995.

[3] KEIL, N., YAO, H. H., ZAWADZKI, C., STREBEL, B., G. UNTERBÖRSCH: 'Polarization insensitive rearrangeable nonblocking (4x4)-switching module at λ = 1.55 µm realized by low-cost polymer waveguide technology', OFC'95, Postdeadline Papers, PD-17, 1995.

[4] KEIL, N., YAO, H. H., ZAWADZKI, C., STREBEL, B.: 'Rearrangeable nonblocking polymer waveguide (4x4)-switching matrix and its applications to future OFDM systems', EFOC&N'95, Proc. Vol. 2, pp. 240-243, 1995.

Crosstalk Reduced Digital Optical Switch with Single Electrode Designed for InP

H. - P. Nolting, M. Gravert, Heinrich-Hertz Institut für Nachrichtentechnik Berlin GmbH
Einsteinufer 37, 10587 Berlin, Germany, ++ (4930) 31002 427
M. Bachmann, M. Renaud, Alcatel Alsthom Recherche, Route de Nozay, 91460 Marcoussis, France

Abstract

Coherent crosstalk of optical space switch matrices is a key problem of optical transparent networks. A new crosstalk compensating technique based on the integration of a *single* electrode mode converter as correcting device into a 1x2 or 2x2 digital optical switch (DOS) is proposed and theoretically investigated. Introduction of the mode converter stage enhances a -20 dB crosstalk DOS device to -40 dB with only a small increase of the device length. The new scheme with one common electrode for DOS and converter simplifies a recently published architecture needing 4 additional electrodes and a special control algorithm. A realistic design of a -40 dB crosstalk DOS based on InP is presented.

Introduction

The all-optical multiwavelength network is a prime candidate for future "information highways". Space switch matrices are key components in an optical cross-connect. For the construction of larger networks[1], switching nodes have to be cascaded. Thus coherent crosstalk[2,3] of the individual switching component is a problem, where signals from sources of nominally the same wavelength can interfere coherently if their frequency separation is within the receiver bandwidth. As has been pointed out recently, one main disadvantage of electro-optical switches is the high crosstalk or low contrast of the output ports in the order of about -20 dB[4]. To realize a higher crosstalk suppression, cascading[5] of identical switches is an often used solution with the disadvantage of increasing the device length. Recently, we have proposed the CRDOS (Crosstalk Reduced DOS) in which the crosstalk is compensated with an integrated *general mode converter*. This architecture is able to compensate all kinds of crosstalk sources including fabrication tolerances with the additional use of 4 different control voltages or currents for tuning. Here we propose and theoretically investigate an architecture, which uses one single electrode for crosstalk reduction. Control signals on the convertor electrode and the DOS switching electrode are correlated such that only one control signal has to be applied from the outside world. This opens the way to use the CRDOS as building block in larger switching matrices.

Mode matching in DOS for crosstalk compensation

optical 1x2 DOS matrices (see Fig. 1), but the basic ideas can easily be applied to a 2x2 DOS. Following the argumentation given in [4], we know that the (conventional) DOS uses the adiabatic coupling behavior of a mode travelling along an asymmetric Y-junction[6] consisting of two different waveguides. Here we use a *symmetrical Y-branch* waveguide structure in the passive state. Switching is performed by introducing an asymmetry using an electro-optical refractive index change Δn_{EO} in one of the output waveguides of the Y-branch. Input (see Fig. 1: section A to B) and output waveguides (H to J) are identical monomode waveguides. The splitting region of the Y-branch (B to D) supports the fundamental and the second order mode of a local directional coupler causing two mode interference (TMI). Here we introduce the *one electrode mode matching device* for crosstalk suppression (D to F). Following [4] we can look at the Y-branch (F to H) as an adiabatic mode converter ("Y-branch mode converter") from quasi isolated waveguide modes outside the device at the output port to the fundamental and second order mode at the TMI input port (F) with complex amplitudes E_1 and E_2, respectively. We represent the normalized field amplitudes by their absolute value $|E_i|$ and their phase difference φ. If the switch is activated, one of the two electrodes introduces a refractive index change in the underlying waveguide, leading to an asymmetric Y-branch. A wrong linear combination of both

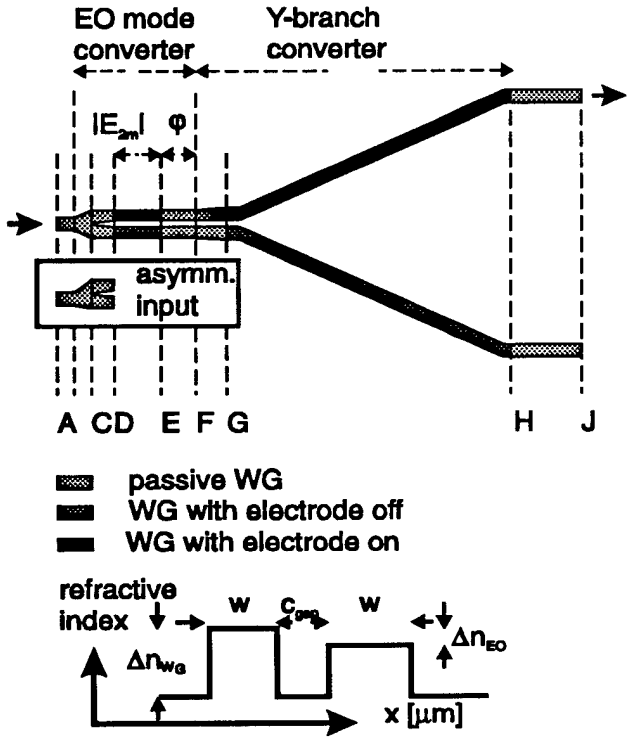


Fig. 1 : Device architecture of crosstalk reduced Y-DOS

modes E_1 and E_2 at the interface F leads to crosstalk. The correct values can be determined by calculating the Y-branch in the backward direction with starting values of unity and zero, respectively, and resulting in amplitude E_{2m} and phase difference φ_μ at the interface F of Fig. 1. This can be done by eigenmode expansion methods or by beam propagation methods and using overlap calculation of both eigenmodes. Thus we have to generate the same amplitude E_{2m} and the negative phase difference $-\varphi_\mu$ at the interface E by introducing the one electrode mode matching device (D to E) between input waveguide and interface F.

Limiting interface

In fact we cascade two devices. A balance between the both is good strategy, because we are interested to design a large window in terms of fabrication tolerances, switching voltage or current and wavelength independence. The DOS itself has a digital response. The window width is, however, limited by the cosine characteristic of the mode converter. This leads to the condition, that $|E_{2m}|^2$ (power of the second mode) has to be in the order of 10^{-2} (or -20 dB) for getting a crosstalk below -40 dB. Each abrupt waveguide change caused by waveguide disturbances due to electrodes, refractive index changes, bends and fabrication errors is the source of mode conversion. The abrupt change of the refractive index by electro-optical effects can severely limit the crosstalk of the DOS and is therefore called limiting interface. To give a realistic example we use the design parameters of an actual working DOS[7] with $\Delta n_{WG} = 0.011$ and $\Delta n_{EO} = -0.003$ (for definition of the parameters see insert Fig. 1). The separation of the Y-branch at the output is 12 µm, to reduce the inter waveguide crosstalk to -50 dB. A lateral waveguide geometry of two waveguides of the width w = 2.5 µm separated by the gap g = 1 µm limits the crosstalk due to the abrupt interface to $|E_{2m}|^2$ = -8.7 dB. This has to be improved. A reduction to -20 dB is possible by tapering the width of the waveguides to 1.5 µm and a linear increase of the refractive index change from zero to Δn_{EO} over a length of 200 µm as schematically shown in Fig.1, F to G. A few examples of Y-branches are shown in Table 1 together with the results of a Beam Propagation Method (BPM) and a Bidirectional Eigenmode Propagation (BEP) calculation. Note that the BEP calculation represents the mode conversion due to the interface only, whereas the BPM calculation includes the Y-branch with an opening angle of 0.35 degrees.

w	g	Δn_{WG}	Δn_{EO}	BEP	BPM	
2.5	1.	0.011	0.003	-8.7 dB	-9.2 dB	strong guiding
1.5	1.	0.011	0.003	-14.3 dB	-18.9 dB	weak guiding
1.5	1.	0.011	0.003	----------	-20.9 dB	electrode taper

Table 1: Examples of Y-branches and their crosstalk

The actual device with the results shown in Fig. 2 and 3 has the following lengths in µm: converter electrode DE = 22, phase section EF = 31 and electrode taper FG = 325, resulting in an overall length of ≈1600 µm. This device may be further improved by shaping the Y-branch. Here we will demonstrate the combination of DOS and converter. We know that $|E_{2m}|^2 < 10^{-2}$ and determine the matching linear combination as described above. We further assume that the amplitudes $|E_{2m}|$ are identical for both switching states, which can be implemented by properly watching the symmetry of the Y-branch.

Compensation of 2. mode with passive and electro-optic techniques

We can easily generate a second mode of the required amplitude $|E_{2m}|$ by connecting the input waveguide and the TMI section with an asymmetrical taper as shown in the insert of Fig. 1. The amplitude $|E_{2m}|$ increases with increasing shift of input waveguide relative to TMI waveguide and can theoretically be determined together with the phase difference. We determine the length L of the TMI section (D to F) such as to match the phase using the well known phase constants. This looks like a pure passive compensation technique, but by arguments of symmetry, to compensate the crosstalk for switching the other electrode, we would have to shift the asymmetrical taper to the other side. A pure passive compensation is therefore not possible. Two architectures using active compensation are discussed below.

The desired second mode can be generated by activating an additional electrode on one of both waveguides of the TMI section (D to E) and match the phase by the proper choice of the length L_φ (E to F) between converter and DOS electrode. Converter electrodes and DOS electrodes are synchronously switched. The generated amplitude of the second mode $|E_{2m}|$ and the phase φ are a function of electrode length and refractive index change Δn_{EO}. We discuss two configurations.

a) $\Delta n_{DOS} \neq \Delta n_{Conv}$

We can work with different currents or voltages for DOS and converter, but with a fixed relation between them (e. g. voltage divider). In this case we choose the length of the electrode to half of the beatlength Λ which leads to a phase shift of π. The needed Δn_{Conv} for operation can be determined by eigenmode expansion technique

(see Appendix). For the case of an abrupt DOS electrode as the limiting interface, Δn_{Conv} is always lower than the used Δn_{DOS}.

b) $\Delta n_{DOS} = \Delta n_{Conv}$

We can use identical refractive index changes for DOS and converter electrodes. In this case we control the converter efficiency ($|E_{2m}|$) by the length of the electrode L. The electrode consists of two interfaces. The maximum amplitude generation of the second mode in this case is 2 times that of a singular interface (see Appendix), which should be enough to compensate all mismatch of the DOS, if the interface is the limiting factor.

Window of performance

We have investigated the fabrication tolerances in the following way. The rib height and the layer thicknesses determine the effective refractive index Δn_{WG} of the waveguides. Any change influences the phase balance of these devices. Therefore we have investigated the crosstalk as a function of variation of the waveguide parameter Δn_{WG} and have determined the window with crosstalk values better than -40 dB (see Fig. 2). We find that the same Δn_{EO} for the converter and the DOS electrode gives the best results. In addition, the width of this window is a measure for the TE / TM mode behaviour. For the actually used waveguides, the polarisation dependence of the effective index is 0.002. Further we have investigated the switching characteristic, shown in Fig.3, where we compare the conventional and the crosstalk reduced DOS. To remain within the -40 dB window of crosstalk performance the voltage or current has to be controlled in the order of ±5%. The wavelength variation has been demonstrated to be a flat response over the width of the EDFA window with a 3 dB penalty by using BPM calculations for the general mode convertor [4]. This broadband behavior is achieved, because the number of periods is only one. The introduction of the mode converter into the DOS requires an additional length of 400 µm only (Fig. 1).

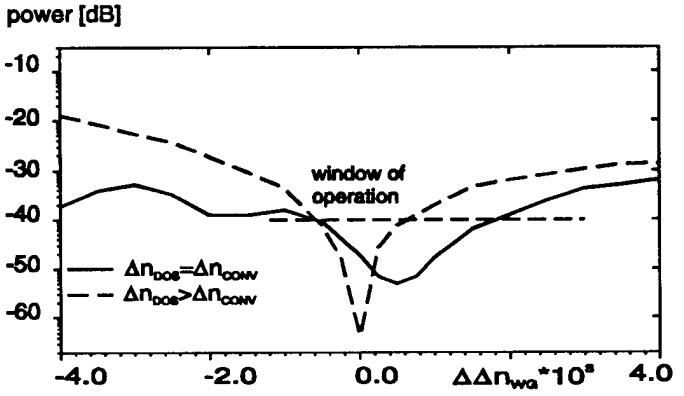


Fig. 2 Crosstalk behaviour of two architectures as a function of the variation of the refractive index difference of the waveguide: $\Delta n_{WG}=11*10^{-3}$

Conclusion

The principle developed earlier to compensate the crosstalk of a X-DOS has been successfully used for a Y-DOS. We have introduced a one electrode architecture for simpler operation than the 4 voltage general solution. The combination of a DOS with a mode converter has the advantage that it acts as a cascadation of two different devices, both with a switching effect in the order of 10^{-2} or -20 dB leading to about -40 dB. The length of the mode converter is rather short, in the order of one beatlength. The more stringent fabrication tolerances as compared to the 4 electrode solution are justified by the simplification to the one electrode control. The proposed DOS is a promising switching element to build larger switching matrices.

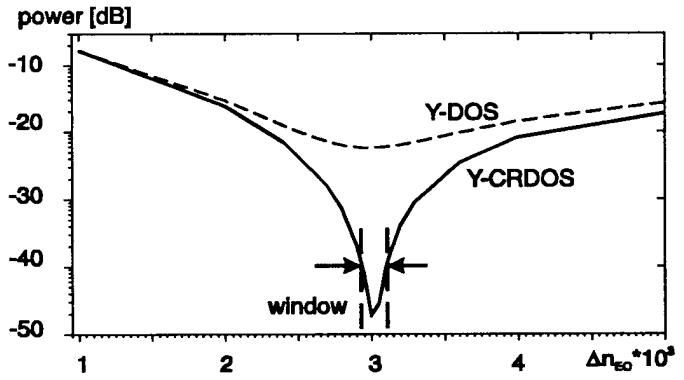


Fig. 3 : Switching characteristic of Y-DOS and Y-CRDOS

Appendix

The influence of an electrode with the switching efficiency Δn_{EO}, the length L and the phase mismatch δ can be calculated following [8]. The overlap integrals a_{ik} of the two eigenmodes between the unperturbed and the switched waveguide and the transfermatrix of the switched waveguide are given by ($^{l}X_i(x)$ are the field distibutions of the eigenmode i in section l):

$$ {}^{l+1,l}\overline{\overline{O}} = \begin{pmatrix} a_{11} & a_{12} \\ a_{21} & a_{22} \end{pmatrix} \quad {}^{l,l-1}\overline{\overline{O}} = \begin{pmatrix} a_{11} & a_{21} \\ a_{12} & a_{22} \end{pmatrix} \quad {}^{l}\overline{\overline{T}} = \begin{pmatrix} e^{+j\delta \cdot L} & 0 \\ 0 & e^{-j\delta \cdot L} \end{pmatrix} \qquad (1) $$

with $ {}^{l+1,l}a_{ik} = \int {}^{l+1}X(x) \cdot {}^{l}X(x)dx $ and $ \int {}^{l}X(x) \cdot {}^{l}X(x)dx = \delta_{ik} $

The matrix describing the electrode than is the product of the three matrices, resulting in equation 2 for the amplitude E_{2m} of the second mode:

$$ {}^{sys}\overline{\overline{M}} = {}^{l+1,l}\overline{\overline{O}} \cdot {}^{l}\overline{\overline{T}} \cdot {}^{l,l-1}\overline{\overline{O}} \qquad E_{2m} = {}^{sys}M_{12} \approx 2 \cdot a_{12} \cdot \sin(\delta \cdot L) \qquad (2) $$

Literature

1 M. J. O' Mahoney, "The Potential of Multi-Wavelength Transmission", Proceedings Vol 2, 20th European Conference on Optical Communication, ECOC 94, Sept. 25-29. 1994, Firenze,Italy, pp 907-913

2 A. Ehrhardt, M. Eiselt, G. Großkopf, L. Küller, R. Ludwig, W. Pieper, R. Schnabel, H. G. Weber, "Semiconductor Laser Amplifier as Optical Switching Gate", IEEE J. of Lightwave Techn. Vol. 11, No. 8, (1993), p.1287-1295

3 D. J. Blumenthal, L. Thylen, "Coherent Crosstalk Induced BER Floors in NxN Space Photonic Switches", IEEE/LEOS Summer Topical Meeting on Optical Networks and their Enabling Technologies, July 11-13, 1994, Lake Tahoe, NV, Postdeadline Paper

4 H.-P. Nolting, M. Grawert, „Architecture of Crosstalk Reduced Digital optical 2x2 Switches (CRDOS)", IEEE J. of Photonic Technologies Letters, Nov 1995

5 M. Kondo, N. Takado, K. Komatsu, Y. Ohta, Proc. 5th Intern. Conf. on Integrated Optics and Optical Fibre Communic. IOOC, 11th European Conf. on Optical Communic.(ECOC) 1985, Venice (Italy), Techn. Dig. I, pp. 361-364

6 W. Burns, A. F. Milton, "An Analytic Solution for Mode Coupling in Optical Waveguide Branches", IEEE J. Quantum Electronics, Vol. QE 16, No. 4, (1980), p 446-454.

7 M. Renaud, J. F. Vinchant, A. Goutelle, B. Martin, G. Ripoche, M. Bachmann, P. Pagnod, F. Gaborit "Compact Digital Optical Switches for Low Insertion Loss Large Switch Arrays on InP", ECOC 95, 17-21-Sept. 1995, Brussels, Mo.L.3.1., Vol 1, pp.99-102

8 H.-P. Nolting, M. Grawert, "A Comparison between Different Methods to Calculate Grating Assisted Asymmetrical Couplers", Linear and Nonlinear Integrated Optics, 11-13 April 1994 Lindau 94, Germany, Proceedings Europto Series Vol 2212, p 328-336

Thursday, May 2, 1996

Semiconductor Components for Fiber in the Loop

IThD 10:30 am-12:00 m
Fairfax B

Jun Yu, *Presider*
Bell-Northern Research, Ltd., Canada

Optical Hybrid Integration Technology using a PLC Platform and Spot-Size Converted Devices

Yasufumi Yamada
NTT Opto-electronics Laboratories

162, Tokai, Ibaraki-ken, 319-11, Japan
Tel:+81-29-287-7688; Fax:+81-29-287-7877
e-mail: yyamada@nttiba.ntt.jp

I. Introduction

Cost reduction is a major concern in optical modules for Fiber-To-The-Home (FTTH) applications. Optical hybrid integration, where laser diodes (LDs) and/or photo-diodes (PDs) are flip-chip bonded onto a waveguide substrate, is considered as a promising way to achieve this. A V-grooved silicon has been used as a hybrid integration platform on which to assemble an LD or a PD, and a fiber[1][2]. However, there seem to be two major problems with this technology. First, the conventional silicon platform is not equipped with a waveguide, and seems to be of use only in a limited application field. Second, the coupling loss for the conventional LD to the fiber is as high as 10 dB because of its small spot-size. To achieve a low-cost optical module both the platform and the semiconductor device should be improved. This paper reviews recent progress in optical hybrid integration technology toward inexpensive optical modules.

II. PLC platform

A silica-waveguide on a silicon substrate is the most promising candidate as a hybrid integration platform[3]-[7]. This is because the silica waveguide offers a highly functional planar lightwave circuit (PLC) such as NxM splitters or WDM/FDM filters. However, the conventional SiO_2/Si substrate is not suitable for hybrid integration because a thick cladding layer formed on the substrate prevents the silicon from being used as a platform.

To overcome this difficulty, we have developed a PLC platform with a silica-on-terraced- silicon (STS) structure as shown in Fig.1[8][9]. The silica-waveguide is formed on the ground plane of the silicon substrate to form various types of PLCs such as a Y-branch and a WDM circuit. The silicon terrace functions both as an alignment plane and a heat-sink for a semiconductor optical device. Therefore, a highly functional optical module can be formed simply by the flip-chip bonding of LDs or PDs.

III. Spot-size converted semiconductor devices

To reduce the coupling loss between an LD and a waveguide (or a fiber), the spot-sizes of the LD and the waveguide should be adjusted. A spot-size converted LD (SSLD) in which the spot size of an output light is converted to match an optical fiber is attractive because it offers the advantages of low-coupling loss as well as relaxed alignment tolerance. Several types of SSLD which reduce the fiber-to-LD coupling loss to less than 3 dB have been reported[11]-[14].

The SSLD has recently been successfully applied in a hybrid integration experiment. BT laboratories succeeded in the passive alignment of the SSLD and cleaved fiber using the V-grooved silicon platform[15]. The LD was a 1.55 μ m spot-size converted MQW BH laser which facilitates a tapered MQW active layer and an underlying passive guide. The coupling loss was estimated to be about 3 dB. NTT has performed the hybrid integration of the SSLD onto the PLC platform[16] (Fig. 1). The SSLD has a tapered passive waveguide region which is butt-jointed to the active layer[14] (Fig. 2). The output power from the fiber connected to the PLC platform was 6 mW at 50 mA with an SSLD-waveguide coupling loss of 3.2 dB.

Concerning PDs, a planar PD has been commonly used. In the hybrid integration experiment, the planar PD is coupled with an optical waveguide (or fiber) through an additional optical element such as a small mirror[4][6][7]. To simplify the device assembly, however, a PD should be integrated onto the platform in the same way as the LD integration. A side-illuminated waveguide PD (WGPD) is one solution to this problem[16][17]. NTT has developed a 1.3 μ m WGPD in which the optical field distribution was enlarged by facilitating a doped intermediate-band gap layer between a core layer and a cladding layer[18]. The WGPD had a high responsivity of 0.95 A/W at a wavelength of 1.31 μ m. The coupling loss between the WGPD and dispersion shift fiber was 0.44 dB with a 1-dB tolerance of ± 17 μ m in the horizontal and ± 2 μ m in the vertical.

IV. Application to optical module for FTTH

By combining the spot-size converted devices and the PLC platform, we have fabricated a WDM transceiver module consisting of a PLC with a 1.3/1.55-μ m WDM and a Y-branch for 1.3-μ m light, and a 1.3-μ m SSLD and a 1.3-μ m WGPD integrated on the silicon terrace as shown in Fig. 3 [19][20]. It should be noted that the number of the module components was reduced to only five including the fiber pigtails, and that the LD and PD assembly was simplified by adopting passive alignment procedure.

V. Conclusion

Recent progress in hybrid integration technology using a PLC platform and spot-size converted devices was reported. Since this technology enables us to fabricate an optical module with the simplest structure, it should be able to provide a low-cost optical module for FTTH.

References

[1] C. A. Arminento et al, Electron. Lett., vol.27, pp. 1109-1111, 1991.
[2] K. Kurata et al., Proc. 45th ECTC, Las Vegas, 1995, pp. 759-765.
[3] Y. Yamada et al., Opt. Eng., vol. 28, pp. 1281-1287, 1989.
[4] C. H. Henry et al, J. Lightwave Technol., vol. 7, pp. 1530-1539, 1989.
[5] C. A. Jones et al., Electron. Lett., vol. 30, pp. 215-216, 1994.
[6] C. G. Grookes et al., Electron. Lett., vol. 30, pp. 1002-1003, 1994.
[7] K. P. Jackson et al., Proc. 42nd ECTC, San Diego, CA, 1992, pp. 93-97.
[8] Y. Yamada et al., Electron. Lett., vol. 29, pp. 444-445, 1993.
[9] S. Mino et al., Electron. Lett., vol. 30, pp. 1888-1889, 1995.
[10] T. L. Kock et al, IEEE Photon. Technol. Lett., vol. 2, pp. 88-90, 1990.

[11] K. Kasaya et al, Electron. Lett., vol. 29, pp. 2067-2068, 1993.
[12] I. F. Lealman et al. Electron. Lett, vol. 30, pp. 857-859, 1994.
[13] Y. Tohmori et al., Electron. Lett., vol .31, pp. 1069-1070, 1995.
[14] J. V. Collins et al, Electron. Lett., vol. 31, pp. 730-731, 1995.
[15] T. Hashimoto et al, Tech. Digest 5th Microoptics Conf., 1995, Hiroshima, pp. 66-69.
[16] M. Yamada et al., Electron. Lett., vol. 23, pp. 1056-1057, 1987.
[17] K. Kato et al., IEEE Photon. Technol. Lett., vol. 6, pp. 719-721, 1994.
[18] A. Akatsu et al., Proc. ECOC '95, 1995, Mo.B.4.4.
[19] Y. Yamada et al., Proc. OFC '95, 1995, San Diego, PD2.
[20] Y. Yamada et al., Electron. Lett., vol. 31, pp. 1366-1367, 1995.

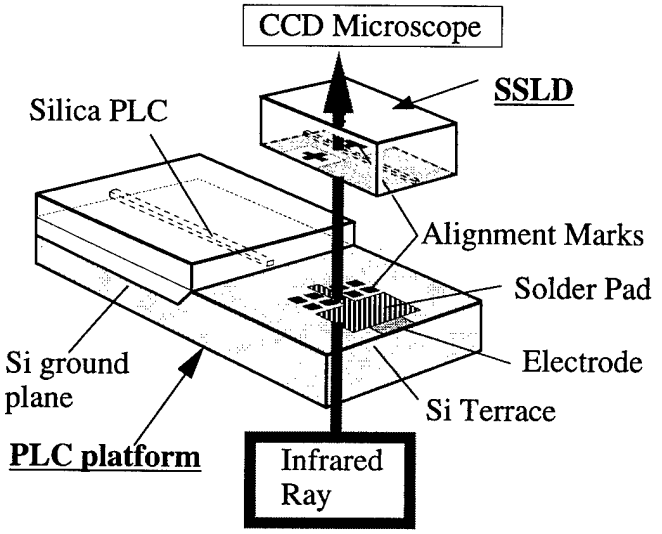


Fig. 1. Passive alignment procedure of SSLD onto PLC platform

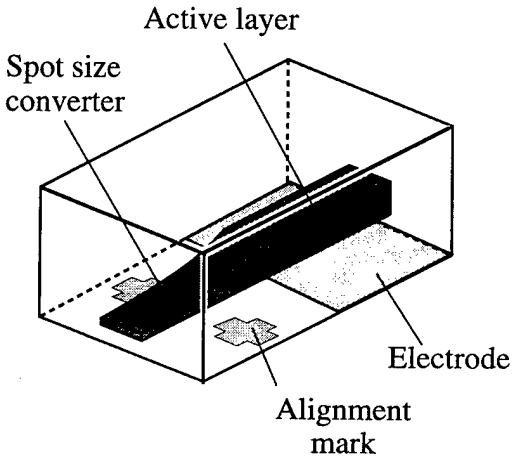


Fig. 2. Schematic structure of SSLD

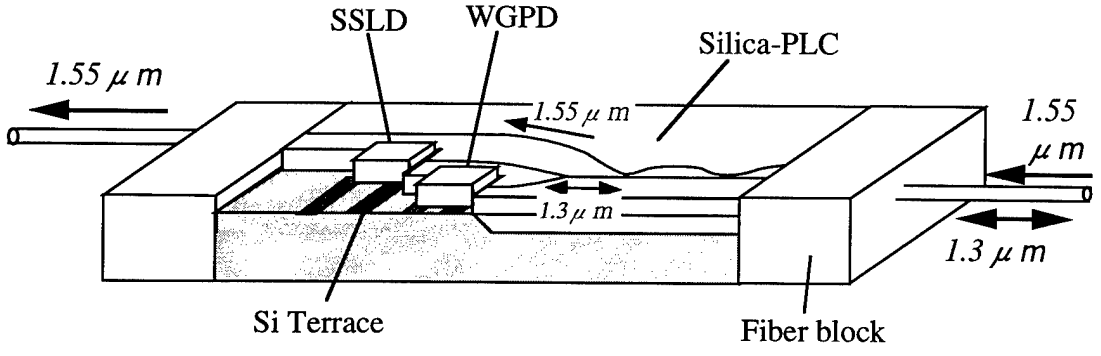


Fig. 3. WDM transceiver module using a PLC platform and spot-size converted devices

A Polarization Insensitive Semiconductor Optical Amplifier with Integrated Electroabsorption Modulators

U.Koren, B.I. Miller, M.G. Young, M. Chien, G. Raybon, T. Brenner, R. Ben-Michael, K. Dreyer, R.J. Capik, AT&T Bell Laboratories, Holmdel, N.J. 07733

As optical access to the loop becomes more advanced, using emerging fiber to the loop (FTTL) architectures, and with the possible use of wavelength division multiplexing (WDM) to enhance transmission capacity and networking flexibility, it is important to consider new components that may be useful as building blocks for the upcoming local access networks. Obviously, for FTTL applications, low cost is an important prerequisite for components that are not widely shared. This may require uncooled operation, ease of packaging, and perhaps integration of opto-electronic devices. One of the new FTTL-WDM architectures that was recently demonstrated is RITE-Net [1,2], which is based on a WDM signals from a central office sent downstream to a remote node, and then to the local optical network unit (ONU). The carrier wavelength is modulated at the ONU using an on site optical modulator and returned upstream to the central office. One parameter that effects the performance is the insertion loss of the modulator. To improve the power budget of the system, it might be useful to employ a component that has integrated modulators and a semiconductor optical amplifier (SOA) resulting in a modest fiber to fiber gain rather than a large insertion loss. The proposed component can also enable WDM networks where frequency conversion and/or signal equalization over a large dynamic input range is required. It may be useful to integrate two modulators, so that one can be used for data encoding and the other for power level equalization.

In the present work we demonstrate a polarization insensitive integrated device composed of an SOA with two electroabsorption modulators at the input and output ports. The geometry is similar to a recent design proposed by Souli et al [3,4], where one modulator was used for very high speed pulse generation, and the other for data encoding. However, the above mentioned design is not suitable for most other applications as it has a large insertion loss (-9dB) and is not polarization insensitive [4]. In the present device we have used integrated passive waveguide beam expanders [5,6] to reduce coupling loss to lensed fibers and increase the tolerance to coupling misalignment. As a result, fiber to fiber insertion gain as high as 9 dB has been obtained. Polarization independence is obtained by using bulk quaternary modulators [6] and a polarization insensitive strained multiple quantum well (MQW) amplifier [7]. A schematic description of the present device is shown in Fig. 1. The optical amplifier section is 600 μm long, composed of 4 compressively strained InGaAsP QW's and 4 tensile strained InGaAsP QW's with strain compensating

InGaAsP barriers operating with peak photoluminescence at 1.55 μm wavelength [7]. The input and output electroabsorption modulators employ a separately grown 2000Å thick bulk InGaAsP layer with peak photoluminescence at 1.44μm wavelength. Each of the two modulator sections is 150 μm long. These bulk modulators can have excellent polarization insensitivity, as recently shown by several groups [6,8]. The length of the integrated passive beam expanders is 250 μm on each side. The total length of the device is 1400 μm. The device was made with four MOCVD epitaxial growth steps using process technology similar to that previously described for electroabsorption modulated lasers (EML's) [9] and for beam expanded lasers [5].

Fig. 2. shows the response of the output modulator as a function of reverse bias voltage, for different polarizations and input wavelengths. The amplifier current is held at 120 mA and the input fiber power level is kept at -9.2 dBm. A maximum fiber to fiber gain of 9.0 dB was obtained at 150 mA amplifier current. The observed polarization dependence of the combined amplifier-modulators configuration was less than 1 dB, and extinction ratios over 15 dB were obtained over a spectral range larger than 35 nm. The power budget of the device can be determined by sequential measurements of photocurrent using the modulators and amplifier as photodetectors. The internal propagation losses of the modulators are 2 dB per modulator and the fiber coupling losses are 2 dB per facet, indicating 17 dB maximum chip gain for the amplifier. This result is in accordance with the previously measured gain for MQW polarization insensitive SOA's [7]. The amplified spontaneous emission (ASE) fiber coupled power level is -8.5 dBm at zero modulator bias. This low ASE level is partially due to the filtering effect of the integrated modulator which effectively cuts off spontaneous emission below 1.5 μm wavelength. The ASE ripple for both polarizations is lower than 2 dB.

The small signal frequency response of the output modulator is shown in Fig. 3 for several biasd voltages. The 3-dB modulation bandwidth is 5.5 GHz, and is limited by the parasitic capacitance of the contact pads. The tolerances for fiber coupling misalignments in the vertical, lateral and z directions, using standard AT&T etched lensed fibers are shown in Fig. 4. The full width 1-dB excess loss ranges are 1.8 μm , 2.2μm and 15 μm respectively. These relaxed tolerances, together with the very low 2 dB measured coupling loss per facet, demonstrate the advantage of using the passive waveguide beam expanders in these devices. The wide spectral response of the device indicates that operation over a wide temperature range is possible [6]. These relaxed tolerances may result in simplified packaging schemes and reduced costs for packaged devices.

In conclusion, we demonstrate a polarization independent semiconductor optical amplifier integrated with two electroabsorption modulators, with moderate - 9dB fiber to fiber optical gain. Such devices may be useful for low cost FTTL and WDM systems.

REFERENCES

1. N.J. Frigoet al. OFC -94 paper PD-8 post deadline proc. page 434 , (1994).
2. N.J. Frigo et al Photonic Tech. Lett. 6, 1365, (1994).
3. N. Souli et al. Electronics Lett. 30, 1706, (1994)
4. N. Souli et al. OFC 95, conf. procc. p 39, paper TUl4, (1995).
5. R. Ben-Michael et al, Photonic Tech Lett. 16. 1412, (1994).
6. U. Koren et al.Electronics Lett. 30, 1852, (1994).
7. M.A. Newkirk et al. Photonic Tech Lett. 4, 406, (1993).
8. K. Yamada et al. OFC-95 paper TuF4 pp24-25, (1995).
9. K.C. Reichmann, et al. Photonic Tech. Lett. September (1993).

FIGURE CAPTIONS

1. Schematic description of the device.
2. Response of the electroabsorption modulator for different polarizations and input wavelengths.
3. Small signal frequency response of the output modulator.
4. Misalignment tolerances for coupling into a lensed fiber.

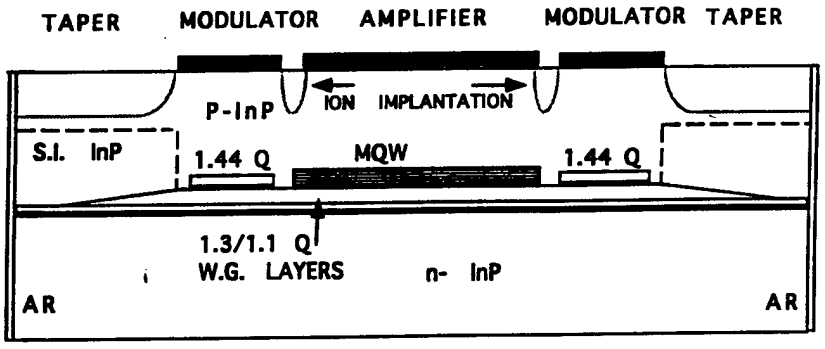


Fig. 1.

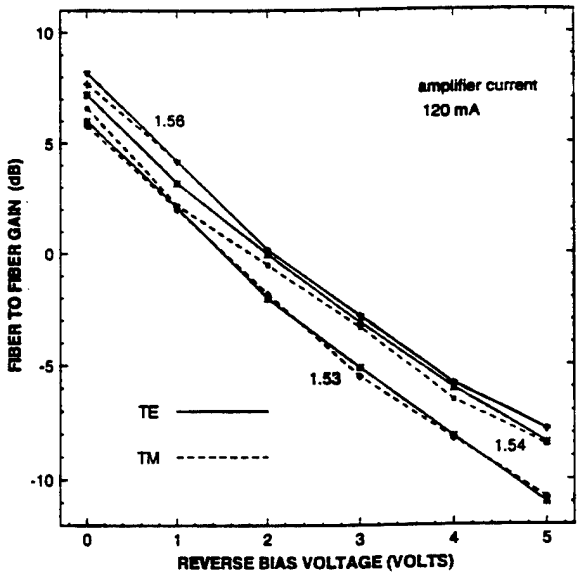


Fig.2.

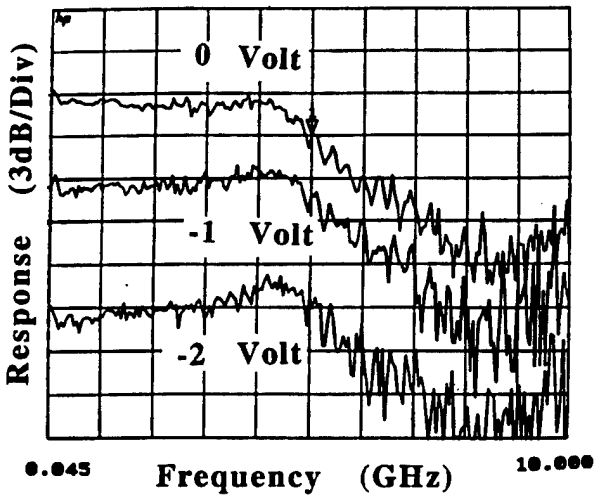
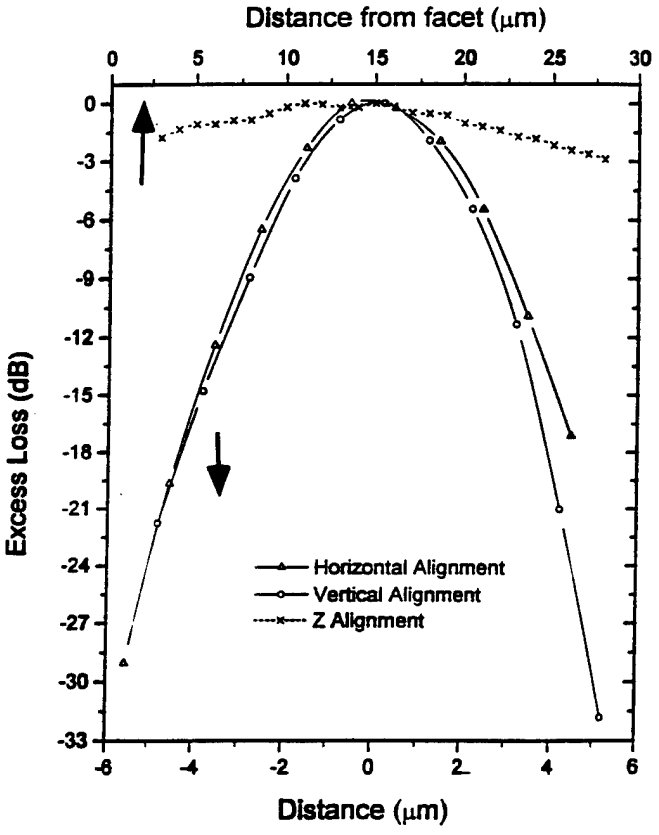


Fig. 3.

Fig. 4.



Large-Spot Laser Diodes with Stable Carrier Frequency by an External Fiber Grating

R. Zengerle, H. Burkhard, R. Ries, B. Hübner*, Ch. Gréus, E. Kuphal

Deutsche Telekom AG, Technologiezentrum,
Am Kavalleriesand 3, 64295 Darmstadt, Germany,
Phone: +49 6151 838380 Fax: +49 6151 834988

*Technische Physik, Universität Würzburg,
Am Hubland, 97074 Würzburg, Germany

1 Introduction:

Low-cost, wavelength stabilized laser modules are an important prerequisite for large-scale applications of passive optical transmission systems in the access network. One way to achieve this is to use a laser diode coupled to a lensed fiber incorporating a UV written grating [1]. Here, the wavelength stability is mainly determined by the low temperature dependence of fiber Bragg gratings. In order to reduce costs further, low-loss chip fibre coupling with large alignment tolerances is required. Spot-size transformation by a separate intermediate waveguide chip using tapers has been shown [2] to be a convenient way for the necessary spot-size adaption. However to reduce the problem of all alignment tolerances significantly, monolithic integration of the spot-size adaption on a semiconductor chip itself has been demonstrated using a vertical [3] or lateral [4] taper. Replacing the upper passive waveguide by an active one leads to a Fabry-Pérot laser with integrated spot-size transformation [5]. The integration of a DBR laser with a bulk active region using a simple taper structure was also published [6]. We recently reported on the successful integration of a DFB laser and a spot-size transformer, combining the good lasing characteristics and low loss chip fiber coupling [7]. Here we present a modification of this design, using a fiber grating as external wavelength reference, suitable for operation at bitrates of at least 2.5 Gbit/s.

Device structure:

The complete fiber grating laser with integrated spot-size adaption is shown in Fig. 1 and is based on our layout for a large spot GaInAsP/InP DFB laser, however, without the phase-shifted grating. The semiconductor structure consists of two parts, the amplification section and the double waveguide spot-size transformer. The amplification section is a constricted mesa multiple quantum well (MQW) type with 8 quantum wells. To simplify the processing sequence, the laser waveguide is also used as the tapered upper waveguide of the spot-size transformer. A mushroom fabrication technique [8] is used for the lateral definition of the laser waveguide.

The overall (not jet optimized) chip length was around 900 µm (240 µm for the amplification section, 560 µm for the linear taper section, followed by the fiber matched output waveguide). As wavelength reference a cleaved commercially

available grating (length: 2 mm) in a standard single-mode fiber with a peak reflectivity of about 45 % (bandwidth 0.5 nm, FWHM) was directly butt-coupled. Instead of a glue, we used refractive index liquid between chip and fiber, matching the fiber refractive index. On the fiber side of the chip an AR coating was sputtered with a residual reflectivity of about 1 % between the chip and matching liquid, whereas the other end of the chip was left as cleaved.

Experimental results:

Threshold currents down to 40 mA (at 25° C) were achieved for the fiber-grating semiconductor lasers. In the output power/current (P-I) characteristics at the end of the single-mode fiber no kinks were observed in the measured range of the driving current (up to I_p = 90 mA, Fig. 2). The present differential quantum efficiency of the grating stabilized laser is 4.4% in our setup. This value includes the loss of the optical isolator and the fiber connectors. Using an appropriate high reflection coating at the rear facet of the laser diode will reduce the optical power loss and thus increase the efficiency.
Only one strong emission line at the wavelength of 1534 nm was measured in the CW emission spectrum with a side-mode suppression ratio (SMSR) of more than 45 dB (Fig. 3). The measured modulation transfer function (Fig. 4) indicates a modulation bandwidth of more than 3.5 GHz (-3 dB value, measured at a driving current of 70 mA).

The large output spot size together with its smaller (unguided) angular divergence leads to drastically increased alignment tolerances for several important device parameters. Stable operation with a sidemode suppression still exceeding 30 dB was maintained for a lateral displacement in a total range of 9 µm horizontally and 8 µm vertically with the grating in a standard single-mode fibre. For larger fiber displacements the stabilization effect of the grating is reduced and the laser diode eventually starts lasing at its gain maximum, which is near 1525 nm. The tolerance values for a 1 dB decay in the output power are +/- 2.1 µm horizontally and +/- 1.7 µm vertically, thus beeing only slightly smaller than in the case of coupling between two standard single mode fibers.
In comparison to the lensed fiber design with a relatively small depth of focus, longitudinal alignment requirements are also significantly reduced. In the range between 5 µm and 25 µm (for the facet to fiber distance) the maximum reduction of the output power was less than 1 dB.
The laser has been operated with 1 mW of output power at temperatures up to 45°C without significant reduction in its spectral purity.

Conclusions:

The emission characteristics of a semiconductor laser chip with monolithically integrated laterally tapered spot-size transformer on InGaAsP/InP and external wavelength stabilization by a fiber grating were demonstrated. Despite the relatively simple design good high speed modulation performance exceeding 3.5 GHz were demonstrated and therefore confirm the attractivity of this setup for low-cost laser

components in optical transmission systems, especially in the access network. Even this simple design can be used for systems with bitrates of up to 2.5 Gbit/s.
Stable operation was demonstrated for lateral fiber alignment tolerances even in the 2 µm range. Thus our concept is well suited for low-cost silicon motherboard or polymer packaging techniques.

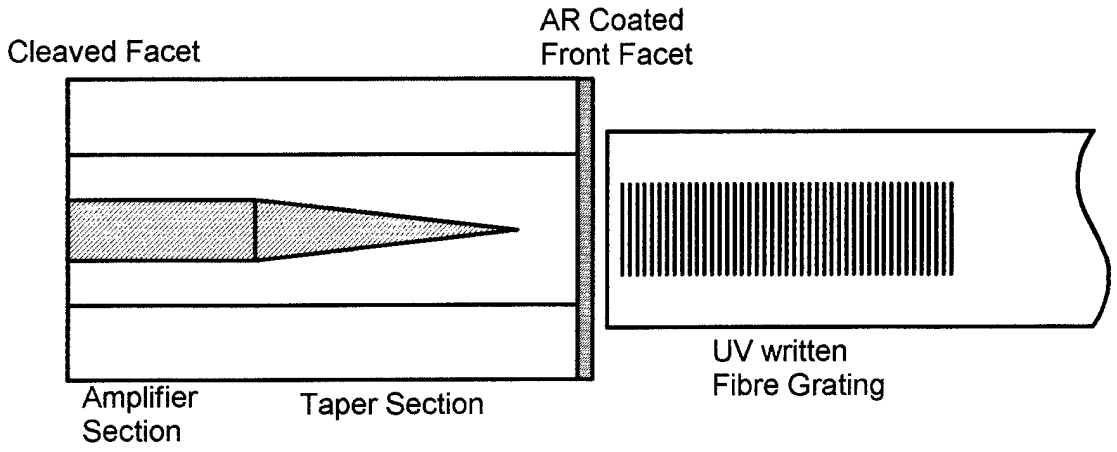


Fig. 1: Schematic diagram of the laser with monolithically integrated spot-size transformer and external fiber grating.

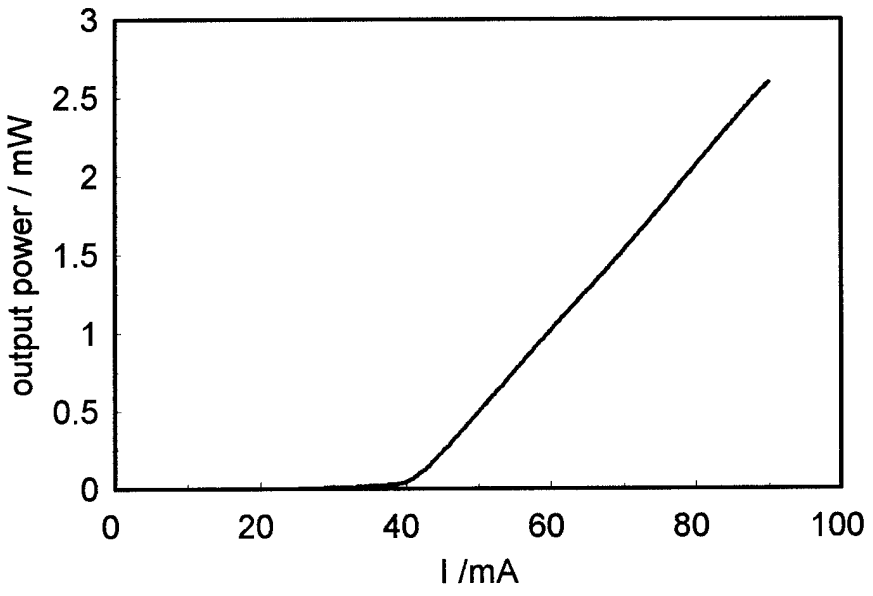


Fig. 2: P-I characteristics for the complete fiber grating laser at the end of the fiber, containing the Bragg grating.

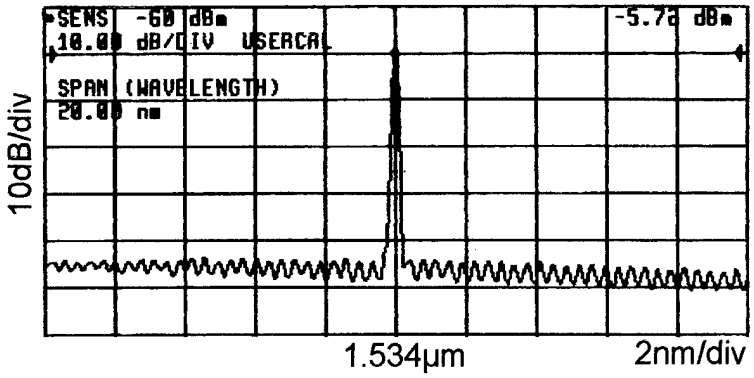


Fig. 3: Laser spectrum for I_p =70 mA at the output of a standard single-mode fiber.

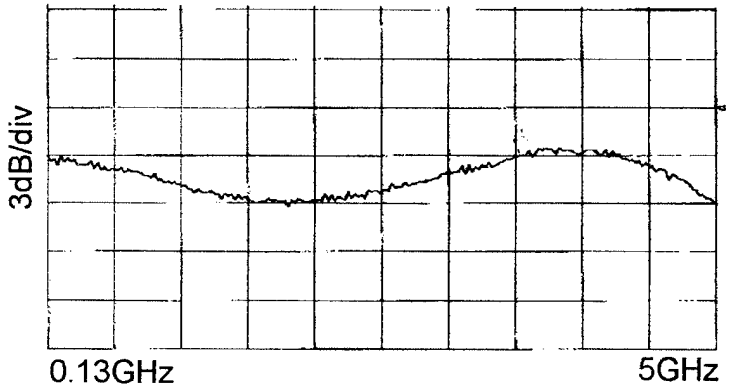


Fig. 4: Modulation transfer function of the fiber grating laser (I_p =70 mA).

References:

1 R.J. Campbell, G. Sherlock, D.L. Williams, R. Payne, R. Wyatt, M. Robertson, J.R. Armitage; Proc. ECOC'95, Bruxelles, pp. 545-548

2 Y. Shani, C. H. Henry, R.C. Kistler, K.J. Orlowsky, D.A. Ackerman; Appl. Phys. Lett., 1989, 55, (23), pp.2389-2391

3 T.L Koch, U. Koren, G. Eisenstein, M.G., Young, M. Oron, C.R. Giles, B. I Miller; IEEE Photonics Technol. Lett., 1990, 2, (2), pp. 88-90

4 R. Zengerle, H.J. Brückner, E. Kuphal, O. Leminger; Proc. ECOC'93, Montreux, 2, pp. 249-252.

5 I.F. Lealman, L.J. Rivers, M.J. Harlow, S.D. Perrin, M.J. Robertson; Electron. Lett. 1994, 30, (11), pp. 857-859

6 K. Kasaya, Y. Kondo, M. Okamoto, O. Mitomi, M. Naganuma; Electron. Lett., 1993, 29, (23), pp. 2067-2068

7 R. Zengerle, B. Hübner, C. Gréus, H. Burkhard, H. Janning, E. Kuphal; Electron. Lett. 1995, 31, (14), pp. 1142-1143

8 H. Burkhard, E. Kuphal, H.W Dinges; Electron. Lett., 1986, 22, (15), pp. 802-803

Re-Engineering the Receiver: Creating a Low Cost Fiber-in-the-Loop Component

S.Chandrasekhar and Leda M. Lunardi*
Bell Labs, Lucent Technologies
* AT&T Research
Crawford Hill Laboratory, Holmdel, NJ 07733

The last several years has seen increased research and development in bringing the enormous information bandwidth to homes through the medium of the glass fiber and using optical communication techniques. World-wide research on semiconductor devices for fiber-to-the-home (FTTH) and fiber-in-the-loop (FITL) applications has concentrated on realizing components for this large market which have special attributes as compared to other application areas. The devices need to be low cost, highly reliable, in large volume, and have good performance. Cost of manufacturing a semiconductor device is related to the complexity of fabrication, the number of epitaxial growths needed and to the overall yield of the process technology. Packaging also adds to cost, particularly when there are optical interfaces. In an effort to drive down costs, one must not sacrifice performance. Several research laboratories around the world are actively investigating these issues for different semiconductor photonic and electronic devices that are envisioned to form the backbone of FTTH systems. In this talk, we shall examine the photoreceiver in particular, consisting of a photodetector followed by a preamplifier, and consider issues related to its role in FTTH/FITL systems.

There are essentially four types of photodetectors that could be of particular use in optical communication systems. These are the p-i-n, the M-S-M, the APD, and the phototransistor. Among these, the M-S-M photodetector, though a very simple device, has not been used in any communication system, though it has found use in optical back planes of computers. The device has several non-linear characteristics that make it unsuitable for FTTH applications. The phototransistor has potential in this area, but is a more complicated device, and certainly needs more fabrication steps than a simple p-i-n. However, its strength lies in the fact that it can be monolithically integrated with preamplifier electronics using the same epitaxial material. Both high speed and high performance has been demonstrated. Nevertheless, it must be borne in mind that the phototransistor needs to be physically a small device relative to a p-i-n, and therefore could make coupling of light into it a little more harder than a p-i-n. Fabricating an integral lens on the back of the wafer to ease the coupling of light from the fiber into the phototransistor is a distinct possibility, as is being done in the case of some p-i-n photodetectors. The avalanche photodiode (APD) improves system performance by atleast 8-10 dB and is an attractive candidate for systems that require that additional margin. However, it is a more subtle device, and proper performance can only be achieved with careful device fabrication, epitaxy, and device design. Moreover, it also requires higher operating voltages, which may not be an issue for certain types of superlattice APDs. Nevertheless, an APD is probably the most costly photodetector in the market today, and

it would not be used in most FTTH systems except where the additional performance overrides the cost issues. Also, it would also not be possible to re-engineer the device to meet the low-cost, high volume, large yield targets of FITL.

That leaves the simple p-i-n photodiode as the most viable and cost-effective photodetector for most applications. Both planar- and mesa-type p-i-ns are available and been used in real systems with excellent performance. Intergral lenses have eased optical coupling from a fiber and reduced packaging costs. Development of solder bumps on the surface have enabled flip-chip bonding the p-i-n directly to preamplifier electronics. Waveguide p-i-n photodiodes have now been engineered for use with guided-wave platforms such that the optical coupling from the waveguide into the p-i-n is optimized without complicating the alignment procedures. Since most FTTH/FITL systems today are not very high speed, the requirements on the photodetector are very relaxing and therefore helps in achieving a high-yield-low-cost target.

As the knowledge-base on FTTH systems increases, there are newer architectures that are being constantly proposed. Some of these architectures are based on wavelength division multiplexed (WDM) systems. A very important component in these approaches is a multichannel receiver array, which can simultaneously detect optical signals originating from different sources. The only cost effective solution to realizing such a component is the monolithic integration of the array of photodetectors with an array of preamplifier electronics. Several groups world-wide have demonstrated such photoreceivers with excellent performance and reasonable yield. The primary issue in such implementation is the electrical crosstalk arising between channels due to shared power supplies and close-proximity of the signal paths. Proper engineering of the chip and the chip carrier should minimize the problem and make monolithic array photoreceivers a viable solution for ceratin WDM systems in FTTH/FITL architectures. Another component which could have some practical use is a multiwavelength demultiplexed receiver, capable of spectrally resolving each of the multiple wavelengths received on a single fiber and detecting the optical signals. Such a monolithic demultiplexed receiver would minimize the number of optical interfaces and therefore the cost of the complete subsystem. Research groups around the world are working on such photoreceivers and the performance has been steadily improving. There is nevertheless much engineering to be done for such a component to become viable in a real system.

In summary, although the photoreceiver is a relatively simple component in any optical communication system, there are several issues to be considered when such a component is be used in a FTTH/FITL system. We have highlighted key device and technology issues that influence the cost, yield and performance of a variety of photodetectors. Merits of monolithic integration of the photodetector with preamplifier electronics have been enumerated, particularly for applications in multichannel architectures. Re-engineering the photoreceiver appears to be the path towards realizing cost-effective solution for applications in the expanding field of delivering broadband services to the home on a fiber.

Abe, Makoto — ITuD5
Ackerman, D. A. — ITuA1
Adams, A. R. — ITuA2
Adams, D. M. — ITuG1
Adesida, I. — IMC4
Agboatwalla, A. M. — IME1
Agrawal, N. — ITuG3
Ahlers, E. — ITuE5
Ahn, Doyeol — ITuA4, ITuA5
Akulova, Y. A. — IWD6
Alles, M. — ITuG5
Alt, Kevin — ITuB2
Amano, C. — ITuA6
Amersfoort, M. R. — IMC4, IWD2
Anada, T. — IMF4, ITuD3
Andreadakis, N. C. — IMC4, IWD2
Anthony, P. J. — IThB3
Aoki, Masahiro — IMH18
Aoki, Shin'ichi — IWA5
Arbore, M. A. — IWE3
Aren-Fischer, R. — ITuD3
Armendariz, M. — ITuG6
Armiento, C. A. — IWH4
Aronson, Lewis B. — ITuH
Arrand, H. — ITuD3
Artigue, Claude — ITuD1

Bachmann, M. — IThC4
Baets, Roel — IMH14, ITuE4, IWA4, IWF5
Balle, S. — IMH15
Balsamo, S. — IMD3
Bao, Z. — IME1
Baraff, G. A. — ITuA1
Baran, J. E. — IME1
Barla, A. — IWA2
Bazylenko, M. V. — IWB5
Belanger, N. — IThA7
Belanger, P.-A. — IThA7
Ben-Michael, R. — IThD2
Benson, T. M. — IMF4, ITuD3
Berger, M. G. — ITuD3
Betts, G. E. — IThC1
Bhat, R. — IMC4, IWD2
Binsma, J. J. M. — IMC6, IMG3
Blixt, P. — IMD3
Blok, Hans — IMB4
Bohmeyer, D. M. — IWH4
Bossert, David — IMH19
Bossi, D. E. — IThC1
Bourke, M. M. — IWE4
Bowers, J. E. — IMD3, IWF6
Bozeat, R. J. — ITuD3
Braasch, Th. — ITuG5
Bradshaw, Scott — ITuG1, ITuG4
Brenner, T. — IThD2
Breuer, Dirk — IThA2
Brook, J. — IMC5
Brorson, Stuart D. — IMG4
Bryce, A. Catrina — IMH22
Bulmer, Catherine H. — IThC
Burkhard, H. — IThD3
Button, Chris C. — IWF2
Buus, J. — IWA4

Calciu, S. — IMH23
Caneau, C. — IMC4, IWD2
Capik, R. J. — IME5, IThD2
Cappuzzo, M. A. — ITuF2
Chakravarthy, R. S. — IME1
Chan, P. W. L. — ITuD2
Chandrasekhar, S. — IWD, IThD4
Chang-Hasnain, C. J. — IWG5
Chaudhuri, Sujeet K. — IMD2, IThA4
Chen, J. C. — IWA1
Chen, Ray T. — ITuD4
Chien, M. — IME5, IThD2
Choquette, K. D. — ITuE6
Chou, M. H. — IWE3
Chou, S. Y. — IWD5
Chu, P. L. — IWB5
Clapp, T. — IMC5
Clements, S. J. — IMC5
Cocorullo, G. — ITuB3
Coldren, L. A. — IWD6
Coleman, James J. — ITuA
Collins, John — IThB1
Cooper, Ken — IThB1
Cox, III, Charles — IMH18
Croston, Ian R. — ITuF
Ctyroky, Jiri — IMD5

Daneman, Michael J. — IWG2
Dangel, R. — IMH9
Daub, K. — IMG6
Day, S. — IMC5
De Bernardi, C. — IWA2
de Hoop, Maarten V. — IMB4
de Jong, J. F. — ITuH3
De La Rue, Richard M. — IWF3
De Micheli, M. P. — IMH4
Della Corte, F. G. — ITuB3
Dellunde, J. — IMD4, ITuE2, ITuE3
Demeulenaere, Bart — ITuE4
Deri, Robert J. — IWD1, IWG
Dhoedt, Bart — ITuE4
Diemeer, M. B. J. — IMC2
Dijaili, S. P. — IWD1
Doerr, C. R. — IMG1, IMG2
Dolfi, David W. — IWH1
Donckers, Marc — IThC2
Donnelly, Joseph P. — ITuE
Doran, N. J. — IThA7
Drake, G. W. — IThC1
Dreyer, K. — IME5, IThD2
Dubinovsky, Michael — ITuD4
Duchene, G. A. — IWH4
Dutting, K. — IMG6

Ehrke, H. J. — ITuG3
Eng, T. T. H. — ITuD2
Ershov, Oleg — ITuD4
Ersoni, M. — IMH8
Esquivias-Moscardo, Ignacio — ITuA3

Favire, F. — IWD2
Fedorov, V. A. — IMH4
Fejer, M. M. — IWE3
Fiddyment, Phil — IThB1
Fischer, Russell J. — IME6
Fischer, U. — IWH3
Fontaine, Marie — IMH12
Forghieri, Fabrizio — IThA1
Fraile-Pelaez, Francisco Javie — ITuA3
Franke, D. — ITuG3
Frankena, H. J. — IWD4
Fuchs, B. A. — ITuG6
Funke, Stefan — ITuG2
Furst, W. — ITuG3

Gates, J. V. — ITuF2, ITuH3, IThB3
Giboney, Kirk S. — IWH1
Giuliano, C. — IMD3
Gnazzo, A. — IWA2
Gnewuch, H. — IWB4
Goeman, Stefan — ITuE4
Gomez-Alcala, Rafael — ITuA3
Goobar, E. — IWD6
Goodwin, J. — IThB3
Gopinath, Anand — IMB2, IMD1, IMF
Grattan, K. T. V. — IMH17
Gravert, M. — IThC4
Grawert, M. — IMD5
Greus, Ch. — IThD3
Griffel, G. — IMH13
Groen, Fokke H. — IMH1, IWC2, IWC5, IWD4
Gross, M. — IWB5

Hadley, G. Ronald — IMH6, ITuE6
Haes, J. — IMH14, IWA4
Hafich, M. — ITuG6
Hahn, Kenneth H. — IWH1
Hall, Dennis G. — ITuB5
Hamacher, M. — IWC5
Harris, R. D. — IWB4
Hattori, Kuninori — ITuD5
Haugsjaa, Paul O. — ITuF1, IWH4
Haus, H. A. — IWA1
Heaton, J. M. — IWE4
Heidrich, H. — IWC5
Heismann, Fred — IWB, IWC4
Helfert, S. F. — ITuE5
Helkey, Roger — IMH18
Helmy, A. Saher — IMH21
Henein, G. E. — ITuH3
Henry, Charles H. — IME6
Hietala, V. M. — ITuG6
Hilton, K. P. — IWE4

Himeno, Akira — ITuD5
Ho, J. Y. L. — ITuD2
Ho, Kwang C. — IMH13
Hoekstra, T. H. — IMC2
Hofstetter, Daniel — IWG4
Holmes, Jr., A. L. — IWF6
Horita, M. — IWF6
Houghton, D. C. — ITuB1
Housel, M. — ITuG6
Hsu, H. P. — IWH4
Huang, Chi-hung — IWB1
Huang, F. Y. — ITuB2
Huang, Tuochuan — IWH1
Huang, Wei-Ping — IMB5, IMB6
Huang, W. P. — IMH11
Hubner, B. — IThD3
Hwang, Wol-Yon — IWC1
Hybertsen, M. S. — ITuA1

Idler, W. — IMG6
Ilic, Igor — IMF5
Imam, N. — IME1
Inoue, Yasuyuki — IMC1
Iwai, N. — IThB4

Jackel, J. L. — IME, IME1
Jager, D. — ITuG5
Jahn, E. — ITuG3
Jalali, Bahram — ITuB4, ITuD
Jansen, E. J. — IMC6, IMG3
Jessop, P. E. — IMH8
Jin, Yong-Sung — IWB2
Joannopoulos, J. D. — IWA1

Jones, Carole — IThB1
Jones, G. — ITuA2
Jones S. B. — IWE4
Jones, Wynn — IMH22
Jopson, R. M. — IME5
Joyner, C. H. — IMG1, IMG2

Kadota, Y. — IME3, IWF1
Kallman, J. — IME1
Kan, S. C. — ITuD2
Kane, C. F. — ITuF2
Kapon, Eli — ITuC1, ITuE1
Kasukawa, A. — IThB4
Kazarinov, R. F. — ITuA1
Keil, N. — IThC3
Kendall, P. C. — IMF4
Kerns, John A. — ITuF3
Khoe, G. D. — IWC3
Kiang, Meng-Hsiung — IWG3
Kihara, M. — IWH2
Kim, H. B. — ITuG1
Kim, Jang-Joo — IWC1
Kim, Sangin — IMB2
Kissa, K. — IThC1
Kitagawa, Takeshi — ITuD5
Kitamura, M. — IThB2
Kitamura, N. — IThB2
Klem, J. F. — IMH6
Klenk, M. — IMG6
Ko, J. C. — IWD6
Koch, T. L. — IMA1
Kohama, Yoshitaka — IWD3
Kohnke, Glenn E. — IME6
Kondo, Y. — IME3, IWF1
Koren, U. — IME5, IWF, IThD2
Korkishko, Yu. N. — IMH4
Koza, M. A. — IMC4, IWD2
Krauss, Thomas F. — IWF3
Krueger, M. — ITuD3
Kuphal, E. — IThD3
Kurokawa, Takashi — ITuA6, IWD3

Lach, E. — IMG6
Larson, Donald R. — IMH20
Laskowski, Edward J. — IME6
Lau, Kam Y. — IWG2, IWG3
Laube, G. — IMG6
Lealman, Ian — IThB1
Lear, K. L. — ITuE6
LeBlanc, H. P. — IMC4
Lewis, D. K. — IThC1
Leys, M. R. — IWB6
Li, Feiming — ITuD4
Li, Hua — IMH19
Li, Ming — IWE1
Liao, Tingdi — IWE1
Liem, I. H. M. — ITuD2
Lin, P. S. D. — IWD2
Lin, Y. S. — IMH23
Liu, Karen — IMG4
Liu, M. Y. — IWD5
Logan, R. A. — ITuA1
Loktev, S. M. — IMH2
Loni, A. — ITuD3
Lowry, Mark — IWH
Lui, Wayne W. — IMB5, IMB6
Lukosz, W. — IMH9, IWG1
Lunardi, Leda — IThD4
Lundqvist, Lennart — ITuG2
Lusse, P. — IMF2, ITuC5
Luth, H. — ITuD3
Lyndin, N. M. — IMH2

Madsen, Christi K. — IMH5
Maring, David B. — IWB3
Marsh, John H. — IMH21, IMH22, IWF3
Martin-Regalado, J. — IMH15
McCaughan, Leon — IWB1, IWE
McIlvaney, Karen — IMH22
McKee, Andrew — IMH22
Mehr, J. F. — IWH4
Menyuk, Curtis — IThA, IThA5
Metaal, Ed. G. — IWC2
Middlemast, I. — IWF4
Miller, B. I. — IME5, IWF6, IThD2
Mitomi, O. — IWF1
Mizuta, S. — IThB2
Moerman, I. — IMH1, IWC5
Monneret, S. — ITuC3
Montrosset, I. — IMD3
Moore, R. S. — ITuG1
Moosburger, R. — IWH3
Morley, J. — IMC5
Morthier, Geert — IWF5
Morton, P. A. — ITuA1
Moss, D. — IWB5
Moule, D. — IMC5
Muller, Richard S. — IWG2, IWG3
Mulligan, L. J. — ITuH3
Munder, H. G. — ITuD3

Naddeo, C. — IMD3
Nagasawa, S. — IWH2
Nakamura, S. — IThB2
Nakano, Hisamatsu — IMF3, IMH16, IWA5
Nakazawa, T. — IME2
Negri, A. J. — IWH4
Ng, W. W. — IWH4
Nield, Maurice — IThB1
Nishio, Koji — IMH16
Noad, J. P. — IMH8
Nolting, H. P. — IMD5, IThC4

O'Donnell, F. J. — IThC1
O'Reilly, Eoin P. — ITuA2, ITuC
O'Reilly, J. J. — IThA6
Obarski, Gregory E. — IMH20
Oberg, Olof — IME4
Oei, Y. S. — IWB6, IWC2
Oh, Min-Cheol — IWC1
Ohiso, Yoshitaka — ITuA6, IWD3
Ohmori, Yasuji — ITuD5
Ojha, S. — IMC5
Okamoto, H. — IWF1
Okamoto, M. — IWF1
Onischenko, A. — ITuC2
Ooi, B. S. — IMH21
Osgood, Jr., Richard M. — IMF5

Pabla, A. S. — IMH7
Pare, C. — IThA7
Parker, David G. — ITuH1
Parriaux, O. M. — IWE2
Pascher, W. W. — IWC5
Pathak, B. — IWD2
Patil, A. A. — IME1
Patterson, F. G. — IWD1
Pedersen, Jorgen W. — IWB6, IWC2
Pennings, E. C. M. — IWC3
Perrone, G. — IMD3

Petermann, Klaus — IWH3, IThA2
Phelan, Robert J. — IMH20
Pieper, W. — ITuG3

Pier, Harald — ITuE1
Piscani, Emil C. — IMH3
Pocha, Michael D. — ITuF3
Pottinger, Hanson — IWF3
Pregla, R. — ITuE5
Presby, H. M. — IMG1, ITuH3
Prewett, Philip — IWE1
Puetz, N. — ITuG1

Rahman, B. M. A. — IMH17
Rajhel, A. — IMC4, IWD2
Rajkomar, P. — ITuH4
Ramaswamy, Ramu V. — IWB3, IWC
Rashid, H. — IME1
Ray, K. G. — IThC1
Raybon, G. — IME5, IThD2
Renaud, M. — IThC4
Rendina, I. — ITuB3
Ries, R. — IThD3
Rigneault, H. — ITuC3
Rivera, Michael — IMB3
Robert, S. — ITuC3
Roberts, Charles W. — IMH3
Roberts, John S. — IWF2
Rogers, C. — IMC5
Rolland, Claude — ITuG1, ITuG4
Roman, J. E. — IWB4
Rongen, R. T. H. — IWB6
Roussell, Harold — IMH18
Rubino, A. — ITuB3
Rush, Jim — IThB1
Ryan, John P. — IMA2

Sahlen, Olof G. — ITuG2
Sakai, Y. — IWF1
Sale, T. E. — ITuA6
san Miguel, M. — IMH15
Sancho, J. M. — ITuE2
Sano, Hirohisa — IMH18
Sarlet, G. — IMH14
Sarma, J. — ITuC2, IWF4
Sartori, F. — IMD3
Scarmozzino, Robert — IMF5
Schablitsky, S. J. — IWD5
Schilling, M. — IMG6
Schobel, J. — ITuC5
Scholtes, T. L. M. — IWB6
Schuppert, B. — IWH3
Schwander, T. — ITuC5
Scotti, R. E. — IThB3
Seino, M. — IME2
Seki, Shunji — IMB
Sekiguchi, Minoru — IMF3
Sewell, P. — IMF4
Shain, Sang-Yung — IWC1
Shams-Zadeh-Amiri, Ali M. — IMH11
Sheard, Stephen — IWE1
Shepherd, F. R. — ITuG1
Shetengel, G. E. — ITuA1
Shi, R. C. — IWD5
Shibayama, Jun — IMF3
Shimoda, T. — IThB2
Shin, Sang-Yung — IWB2, IWC1
Shirasaki, M. — IMC3
Shmulovich, Joseph — ITuF2, IThB
Shore, K. A. — IMD4, ITuE2, ITuE3, IWA
Siebert, D. — IThB3
Silver, M. — ITuA2
Sin, S. Y. S. — ITuD2
Sink, R. K. — IMD3
Smit, M. K. — IMC2, IMC6, IMG3, IMH1, IWC3, IWC5
Smith, D. A. — IME1
Smith, R. E. — IMH6
Smith, Robert W. — IWC4
Smith, S. W. — IME1
Snipes, B. — IMH6
Solgaard, Olav — IWG2, IWG3
Somani, Azmina — ITuG4
Son, Yung-Sung — IWB2
Soole, J. B. D. — IMC4, IMG
Soref, Richard A. — ITuB
Spencer, P. S. — IWF4
Spiekman, L. H. — IMC2, IMG3, IWC5
Stagg, J. P. — IMC5
Staring, A. A. M. — IMC6, IMG3, IWC3
Stoltz, Bjorn — IME4
Strachan, Gordon R. — IThA4
Strand, Oliver T. — ITuF3, ITuH2
Strasser, Thomas A. — IME6
Straznicky, Joseph — IWH1
Stuart, Howard R. — ITuB5
Stulz, L. W. — IMG1
Sullivan, C. T. — IMH6, ITuG6
Suzaki, Y. — IWF1
Sychugov, V. A. — IMH2, IWE2
Szalkowski, J. M. — ITuF2
Sztefka, G. — IMD5

Tabasky, M. J. — IWH4
Takaya, M. — IWH2
Tamir, T. — IMH13
Tan, Michael R. — IWH1
Tanbun-Ek, T. — ITuA1
Taniguchi, S. — IME2
Tanobe, H. — IME3
Tateno, Kouta — IWD3
Tauber, D. A. — IWF6
Tavlykaev, Robert F. — IWB3
Terzini, E. — ITuB3
Thibeault, B. J. — IWD6
Thijs, P. J. A. — IMG3
Tien, Norman C. — IWG2
Tishchenko, A. V. — IWE2
Togher, P. — ITuA2
Tohmori, Y. — IWF1
Tong, F. — IMB1
Tony, Essam S. — IMD2
Torrent, M. C. — ITuE2
Trinh, P. D. — ITuB4
Tsai, C. S. — IMH23
Tsunetsugu, Hideki — IWD3
Turovets, S. I. — IMD4
Tzolov, Velko P. — IMH12

Uitterdijk, T. — IWD4
Ulrich, R. — IWB4
Unger, H. -G. — IMF2
Usievich, B. A. — IMH2

Vail, E. C. — IWG5
Valle, A. — ITuE3
van Brug, H. — IWD4
van Dam, C. — IMC6, IMH1, IWC5
van der Tol, Jos J. G. M. — IMH1, IWC2. IWC5, IWD4
van Dongen, T. — IMC6, IMG3
van Gaalen, J. Jan-Willem — IWC2
van Ham, F. P. G. M. — IMH1, IWC5
van Stralen, Mattheus J. N. — IMB4
van Tartwijk, G. H. M. — IMH15
Vassallo, Charles — IMF1
Vawter, G. A. — IMH6, ITuG6
Verbeek, B. H. — IMC6, IMG3
Verdiell, J. M. — IThB5
Verhoeve, Piet — IWF5
Verschuren, C. A. — IWB6
Villeneuve, A. — IThA7
Villenueve, P. R. — IWA1
Vonk, H. — IWB6
Vreeburg, C. G. M. — IWB6, IWD4

Wakita, Koichi — ITuC4
Walker, J. D. — IWD1
Waller, Robert — IThB1
Wang, K. L. — ITuB2
Wang, W. -K. — IMB1
Watkins, L. R. — IThA3
Weber, H. G. — ITuG3
Weber, Jean-Pierre — IME4
Weidman, David L. — IMC
Weinert, C. M. — IWA3, IWC5
Welch, D. F. — IThB5
Weller-Brophy, Laura — IMA2
Wendt, J. R. — IMH6, ITuG6
West, Lawrence C. — IMH3
White, Alice E. — IME6
Wiesenfeld, Jay M. — IMG5
Wight, D. R. — IWE4
Wilkinson, J. S. — IWB4
Willner, Alan E. — IThA
Wilson, Robert E. — IWH1
Wolter, J. H. — IWB6
Wong, G. K. L. — ITuD2
Wongcharoen, T. — IMH17
Wu, M. S. — IWG5
Wu, X. — IMH8
Wunstel, K. — IMG6

Xu, C. L. — IMB5

Yamada, Yasufumi — IThD1
Yamanaka, N. — IThB4
Yamanaka, Takayuki — ITuC4
Yamauchi, Junji — IMF3, IMH16, IWA5
Yang, Wei — IMD1
Yao, H. H. — IThC3
Yap, D. — IWH4
Yasaka, H. — IME3
Yegnanarayanan, S. — ITuB4
Yen, H. W. — IWH4
Yevick, David O. — IMA, ITuG4
Yi, Sang-Yun — IWB2
Yokoyama, Kiyoyuki — IMB5, IMB6, ITuC4
Yoshikuni, Y. — IME3
Young, M. G. — IME5, IThD2
Youtsey, C. — IMC4
Yu, Jun — ITuG1, ITuG4, IThD
Yue, Chaoyu — IMG4

Zah, C. E. — IWD2
Zappe, Hans P. — IWG4
Zavada, J. M. — IMD
Zawadzki, C. — IThC3
Zengerle, R. — IThD3
Zhang, S. L. — IThA6
Zhao, Jian H. — IMH5
Zhou, Y. R. — IThA3
Zhu, Jianguo — IWE1
Zhuang, L. — IWD5
Zhuber-Okrog, Kuno — IMH10
Ziari, M. — IThB5
Zirngibl, M. — IMG1, IMG2
Zucker, Jane E. — ITuG

INTEGRATED PHOTONICS RESEARCH
TECHNICAL PROGRAM COMMITTEE

David Yevick, *Queen's University at Kingston, Canada, General Chair*
Robert J. Deri, *Lawrence Livermore National Laboratories, Program Chair*
Anand Gopinath, *University of Minnesota, Program Chair*
Laura Weller-Brophy, *3M Telecom Systems Division, Technical Applications Representative*

SUBCOMMITTEE I: ACTIVE SEMICONDUCTOR DEVICES

Jane Zucker, *AT&T Bell Laboratories, Chair*
Dan Botez, *University of Wisconsin*
S. Chandrasekhar, *Lucent Technology*
Greg Magel, *Texas Instruments*
Monique Renaud, *Alcatel Alstrom, France*
Claude Rolland, *Bell Northern Research, Canada*
Hirohisa Sano, *Hitachi, Japan*
Joseph Shmulovich, *AT&T Bell Laboratories*
Meint Smit, *Delft University of Technology, The Netherlands*
Mike Wale, *GEC-Marconi, UK*
Chung-En Zah, *Bellcore*

SUBCOMMITTEE II: DIELECTRIC WAVEGUIDES AND WAVEGUIDE DEVICES

Fred Heismann, *AT&T Bell Laboratories, Chair*
Catherine H. Bulmer, *Naval Research Laboratory*
Dennis Hall, *University of Rochester*
Winfried H.G. Horsthuis, *Akzo Research Laboratories, The Netherlands*
Janet Lehr Jackel, *Bellcore*
Bahram Jalali, *University of California, Los Angeles*
Yuan P. Li, *AT&T Bell Laboratories*
Leon McCaughan, *University of Wisconsin–Madison*
Patrick Mottier, *LETI, France*
Yasuji Ohmori, *NTT Opto-Electronics Laboratories, Japan*
Ramu V. Ramaswamy, *University of Florida*
Wolfgang Sohler, *University of Paderborn, Germany*
Julian B. Soole, *Bellcore*
Richard Soref, *USAF Rome Laboratory*
David L. Weidman, *Corning, Inc.*
Laura Weller-Brophy, *3M Corporate Research Laboratories*

SUBCOMMITTEE III: MODELING, NUMERICAL, SIMULATION AND THEORY

Shunji Seki, *NTT Opto-Electronics Laboratories, Japan, Chair*
Sujeet K. Chaudhuri, *University of Waterloo, Canada*
James J. Coleman, *University of Illinois*
Joseph Donnely, *Lincoln Laboratory*
Aly F. Elrefaie, *Bellcore*
Michaeil D. Feit, *Lawrence Livermore National Laboratory*
G. Ronald Hadley, *Sandia National Laboratory*
Jonathan A. Nagel, *AT&T Bell Laboratories*
Yoshiaki Nakano, *University of Tokyo, Japan*
John J. O'Reilly, *University College of London*
Eoin O'Reilly, *University of Surrey*
Klauss Petermann, *Technical University of Berlin, Germany*
K. Alan Shore, *University of Wales, Bangor, UK*
Bjarne Tromborg, *Telecommunication Research Laboratory, Denmark*
Carl M. Weinert, *Heinrich Hertz Institute, Germany*
Alan E. Willner, *University of Southern California*
John Zavada, *U.S. Army Research Office*

SUBCOMMITTEE IV: IMPLEMENTATION OF PHOTONIC COMPONENT TECHNOLOGY: MANUFACTURING, PACKAGING, AND SUBSYSTEM PROTOTYPING

Mark Lowry, *Lawrence Livermore National Laboratories, Chair*
Robert Ade, *United Technologies Photonics*
Philip J. Anthony, *AT&T Bell Laboratories*
Lewis B. Aronson, *Hewlett Packard*
Richard Becker, *Integrated Optics Circuit Consultants*
Ghazi Chaoui, *AT&T Bell Laboratories*
Ian Croston, *Integrated Optical Components, UK*
Paul Haugsjaa, *GTE Laboratories*
Anis Husain, *Advanced Research Projects Agency*
W. J. Tomlinson, *Bellcore*
Marc Verdiell, *Spectra-Diode Laboratories*

IPR ADVISORY COMMITTEE

Steven Korotky, *AT&T Bell Laboratories, Chair*
Stephen R. Forrest, *Princeton University*
Curtis Menyuk, *University of Maryland*
David A. Smith, *Case Western Reserve University*
David Yevick, *Queen's University at Kingston, Canada*
Meint Smit, *Technical University of Delft, The Netherlands*